Published in Journals: Climate, Drones, Forests, Land, Remote Sensing and ISPRS International Journal of Geo-Information

Topic Reprint

Advances in Multi-Scale Geographic Environmental Monitoring

Theory, Methodology and Applications, Volume II

Edited by
Jingzhe Wang, Yangyi Wu, Yinghui Zhang, Ivan Lizaga and Zipeng Zhang

mdpi.com/topics

MDPI

Advances in Multi-Scale Geographic Environmental Monitoring: Theory, Methodology and Applications—Volume II

Advances in Multi-Scale Geographic Environmental Monitoring: Theory, Methodology and Applications—Volume II

Topic Editors

Jingzhe Wang
Yangyi Wu
Yinghui Zhang
Ivan Lizaga
Zipeng Zhang

MDPI

Basel • Beijing • Wuhan • Barcelona • Belgrade • Novi Sad • Cluj • Manchester

Topic Editors

Jingzhe Wang
School of Artificial Intelligence
Shenzhen Polytechnic University
Shenzhen
China

Yangyi Wu
School of Urban Design
Wuhan University
Wuhan
China

Yinghui Zhang
MNR Key Laboratory for Geo-Environmental Monitoring of Great Bay Area
Shenzhen University
Shenzhen
China

Ivan Lizaga
Environmental Hydrology and Interactions with Climate and Human Activities
Instituto Pirenaico de Ecología (IPE-CSIC), Spanish National Research Council
Zaragoza
Spain

Zipeng Zhang
College of Geography and Remote Sensing Sciences
Xinjiang University
Urumqi
China

Editorial Office
MDPI AG
Grosspeteranlage 5
4052 Basel, Switzerland

This is a reprint of the Topic, published open access by the journals *Climate* (ISSN 2225-1154), *Drones* (ISSN 2504-446X), *Forests* (ISSN 1999-4907), *Land* (ISSN 2073-445X), *Remote Sensing* (ISSN 2072-4292) and *ISPRS International Journal of Geo-Information* (ISSN 2220-9964), freely accessible at: https://www.mdpi.com/topics/O6HOQ639Y3.

For citation purposes, cite each article independently as indicated on the article page online and as indicated below:

Lastname, A.A.; Lastname, B.B. Article Title. *Journal Name* **Year**, *Volume Number*, Page Range.

Volume II
ISBN 978-3-7258-4711-2 (Hbk)
ISBN 978-3-7258-4712-9 (PDF)
https://doi.org/10.3390/books978-3-7258-4712-9

Set
ISBN 978-3-7258-4707-5 (Hbk)
ISBN 978-3-7258-4708-2 (PDF)

© 2025 by the authors. Articles in this book are Open Access and distributed under the Creative Commons Attribution (CC BY) license. The book as a whole is distributed by MDPI under the terms and conditions of the Creative Commons Attribution-NonCommercial-NoDerivs (CC BY-NC-ND) license (https://creativecommons.org/licenses/by-nc-nd/4.0/).

Contents

About the Editors . . . . . **ix**

Preface . . . . . **xi**

Suyan Yi, Hongwei Wang, Ling Xie, Can Wang and Xin Huang
Spatio-Temporal Dynamics and Drivers of Ecosystem Service Bundles in the Altay Region: Implications for Sustainable Land Management
Reprinted from: *Land* **2024**, *13*, 805, https://doi.org/10.3390/land13060805 . . . . . **1**

Xingmeng Ma, Xin Su, Yanlong Guo and Linfu Zhang
Research on Rural Environments' Effects on Well-Being:The Huizhou Area in China
Reprinted from: *ISPRS Int. J. Geo-Inf.* **2024**, *13*, 189, https://doi.org/10.3390/ijgi13060189 . . . . **17**

Jie Chen, Yankun Wang, Jingzhe Wang, Yinghui Zhang, Yue Xu, Ou Yang, et al.
The Performance of Landsat-8 and Landsat-9 Data for Water Body Extraction Based on Various Water Indices: A Comparative Analysis
Reprinted from: *Remote Sens.* **2024**, *16*, 1984, https://doi.org/10.3390/rs16111984 . . . . . **38**

Yue Zhao, Yuning Feng, Mingyi Du and Klaus Fraedrich
Annual and Seasonal Dynamics of CO_2 Emissions in Major Cities of China (2019–2022)
Reprinted from: *ISPRS Int. J. Geo-Inf.* **2024**, *13*, 181, https://doi.org/10.3390/ijgi13060181 . . . . **65**

Tingting Xia, Xuan Xue, Haowei Wang, Zhen Zhu, Zhi Li and Yang Wang
Mechanism of Vegetation Greenness Change and Its Correlation with Terrestrial Water Storage in the Tarim River Basin
Reprinted from: *Land* **2024**, *13*, 712, https://doi.org/10.3390/land13050712 . . . . . **78**

Guanting Lyu, Xiaoyi Wang, Xieqin Huang, Jinfeng Xu, Siyu Li, Guishan Cui and Huabing Huang
Toward a More Robust Estimation of Forest Biomass Carbon Stock and Carbon Sink in Mountainous Region: A Case Study in Tibet, China
Reprinted from: *Remote Sens.* **2024**, *16*, 1481, https://doi.org/10.3390/rs16091481 . . . . . **99**

Peng Chen, Hongzhong Pan, Yaohui Xu, Wenxiang He and Huaming Yao
Spatial-Temporal Evolution Characteristics and Driving Force Analysis of NDVI in Hubei Province, China, from 2000 to 2022
Reprinted from: *Forests* **2024**, *15*, 719, https://doi.org/10.3390/f15040719 . . . . . **115**

Maoling Ayitikan, Xia Li, Yusufu Musha, Qing He, Shuting Li, Yuting Zhong and Kai Cheng
Characteristics of Foehn Wind in Urumqi, China, and Their Relationship with EI Niño and Extreme Heat Events in the Last 15 Years
Reprinted from: *Climate* **2024**, *12*, 56, https://doi.org/10.3390/cli12040056 . . . . . **138**

Enyan Zhu, Dan Fang, Lisu Chen, Youyou Qu and Tao Liu
The Impact of Urbanization on Spatial–Temporal Variationin Vegetation Phenology: A Case Study of the Yangtze River Delta, China
Reprinted from: *Remote Sens.* **2024**, *16*, 914, https://doi.org/10.3390/rs16050914 . . . . . **153**

Ting Zhang, Jiaquan Wang, Qiming Ma and Liping Fu
Improving the Detection Effect of Long-Baseline Lightning Location Networks Using PCA and Waveform Cross-Correlation Methods
Reprinted from: *Remote Sens.* **2024**, *16*, 885, https://doi.org/10.3390/rs16050885 . . . . . **171**

Yizhuo Liu, Tinggang Zhou and Wenping Yu
Analysis of Changes in Ecological Environment Quality and Influencing Factors in Chongqing Based on a Remote-Sensing Ecological Index Mode
Reprinted from: *Land* **2024**, *13*, 227, https://doi.org/10.3390/land13020227 . . . . . **190**

Huifang Chen, Jingwei Wu and Chi Xu
Monitoring Soil Salinity Classes through Remote Sensing-Based Ensemble Learning Concept: Considering Scale Effects
Reprinted from: *Remote Sens.* **2024**, *16*, 642, https://doi.org/10.3390/rs16040642 . . . . . **207**

Yin Du, Zhiqing Xie, Lingling Zhang, Ning Wang, Min Wang and Jingwen Hu
Machine-Learning-Assisted Characterization of Regional Heat Islands with a Spatial Extent Larger than the Urban Size
Reprinted from: *Remote Sens.* **2024**, *16*, 599, https://doi.org/10.3390/rs16030599 . . . . . **223**

Zhichao Zhang, Yang Wang, Haisheng Tang and Zhen Zhu
Analysis and Prediction of Spatial and Temporal Evolution of Ecosystem Service Value on the Northern Slopes of the Kunlun Mountains Based on Land Use
Reprinted from: *Land* **2023**, *12*, 2123, https://doi.org/10.3390/land12122123 . . . . . **243**

Jin Zhu, Yao Gong, Changchang Liu, Jinglong Du, Ci Song, Jie Chen and Tao Pei
Assessing the Effects of Subjective and Objective Measures on Housing Prices with Street View Imagery: A Case Study of Suzhou
Reprinted from: *Land* **2023**, *12*, 2095, https://doi.org/10.3390/land12122095 . . . . . **264**

Taotao Zhang and Xiaoyi Wang
Dynamics of Spring Snow Cover Variability over Northeast China
Reprinted from: *Remote Sens.* **2023**, *15*, 5330, https://doi.org/10.3390/rs15225330 . . . . . **289**

Lei Peng, Yanbo Wan, Haobo Shi, Abudureyimu Anwaier and Qingdong Shi
Influence of Climate, Topography, and Hydrology on Vegetation Distribution Patterns—Oasis in the Taklamakan Desert Hinterland
Reprinted from: *Remote Sens.* **2023**, *15*, 5299, https://doi.org/10.3390/rs15225299 . . . . . **305**

Ziqiang Bu, Jingying Fu, Dong Jiang and Gang Lin
Production–Living–Ecological Spatial Function Identification and Pattern Analysis Based on Multi-Source Geographic Data and Machine Learning
Reprinted from: *Land* **2023**, *12*, 2029, https://doi.org/10.3390/land12112029 . . . . . **324**

Degefie Tibebe, Mekonnen Adnew Degefu, Woldeamlak Bewket, Ermias Teferi, Greg O'Donnell and Claire Walsh
Homogenous Climatic Regions for Targeting Green Water Management Technologies in the Abbay Basin, Ethiopia
Reprinted from: *Climate* **2023**, *11*, 212, https://doi.org/10.3390/cli11100212 . . . . . **341**

Yongjuan Guan, Jinling Quan, Ting Ma, Shisong Cao, Chengdong Xu and Jiali Guo
Identifying Major Diurnal Patterns and Drivers of Surface Urban Heat Island Intensities across Local Climate Zones
Reprinted from: *Remote Sens.* **2023**, *15*, 5061, https://doi.org/10.3390/rs15205061 . . . . . **355**

Emmanuel Chinkaka, Julie Michelle Klinger, Kyle Frankel Davis and Federica Bianco
Unexpected Expansion of Rare-Earth Element Mining Activities in the Myanmar–China Border Region
Reprinted from: *Remote Sens.* **2023**, *15*, 4597, https://doi.org/10.3390/rs15184597 . . . . . **377**

Bin Liu, Xiaomei Yang, Zhihua Wang, Yaxin Ding, Junyao Zhang and Dan Meng
A Comparison of Six Forest Mapping Products in Southeast Asia, Aided by Field Validation Data
Reprinted from: *Remote Sens.* **2023**, *15*, 4584, https://doi.org/10.3390/rs15184584 . . . . . **400**

Edvinas Tiškus, Martynas Bučas, Diana Vaičiūtė, Jonas Gintauskas and Irma Babrauskienė
An Evaluation of Sun-Glint Correction Methods for UAV-Derived Secchi Depth Estimations in Inland Water Bodies
Reprinted from: *Drones* **2023**, *7*, 546, https://doi.org/10.3390/drones7090546 . . . . . **426**

About the Editors

Jingzhe Wang

Jingzhe Wang is currently a lecturer at the School of Artificial Intelligence, Shenzhen Polytechnic University, Shenzhen, China. He received a B.Sc. degree from Anqing Normal University, Anqing, China, in 2014 and a Ph.D. degree from Xinjiang University, Urumqi, China, in 2019. His research interests focus on Earth observation and remote sensing, spectral modeling, the quantitative estimation of soil properties, digital soil mapping, GIS, spatial analysis, and environmental sustainability.

Yangyi Wu

Yangyi Wu is currently an Associate Researcher (Assistant Professor) at the School of Urban Design, Wuhan University, Wuhan, Hubei, China. He received a B.E. degree from Wuhan University, Wuhan, China, in 2013; an M.S. degree from the University of Texas at Dallas, Dallas, U.S.A.; and a Ph.D. degree from the University of Utah, Salt Lake City, U.S.A. His research interests are concentrated on analyzing uneven urban development in the United States and China, relying on advanced spatial analysis and statistics.

Yinghui Zhang

Yinghui Zhang is currently an Assistant Professor at the School of Architecture and Urban Planning, Shenzhen University, Shenzhen, China. He received his B.S. degree from the Shandong Agricultural University, Taian, China, in 2014, and M.S. and Ph.D. degrees from the Institute of Geographic Sciences and Natural Resources Research, CAS, China, in 2017 and 2021, respectively. His research focuses on surface monitoring at fine spatiotemporal resolutions, including the measurement of vegetation parameters, urban environments, etc.

Ivan Lizaga

Ivan Lizaga is a permanent researcher at the Pyrenean Institute of Ecology (IPE-CSIC) in Spain. His work focuses on understanding human-induced land and soil degradation, with particular attention to the interaction between geomorphological processes and environmental risks such as landslides and flash floods. His research adopts a comparative approach, examining catchments around the world, with a special focus on contrasts between European and sub-Saharan African basins—particularly in the Great Lakes region—to explore how natural systems and human populations respond to environmental stressors. Ivan's scientific contributions advance knowledge on soil erosion and fine sediment transport, two major challenges in sustainable agriculture and ecosystem resilience. His areas of expertise include soil science, geomorphology, sediment fingerprinting, remote sensing, land degradation assessment, and water and risk management. Through interdisciplinary projects and international collaboration, his work supports the development of science-based strategies to address climate change's impact on vulnerable landscapes.

Zipeng Zhang

Zhang Zipeng is currently an Associate Professor at the College of Geography and Remote Sensing Sciences, Xinjiang University. He received his B.S. degree from Suzhou University of Science and Technology in 2017, and earned his Ph.D. degree (through a combined master's and Ph.D. program) from Xinjiang University in 2022. His research focuses on analyzing the responses of soil organic carbon to climate change and human activities using advanced spatial analysis and statistical methods.

Preface

Geographic environments are essential for a stable Earth system, usually characterized by complex interactions among biophysical processes, ecological patterns, and human activities. However, the Anthropocene has presented a series of challenges to the geographic environment, particularly due to intensified urbanization pressures, underscoring the critical importance of effectively monitoring the interactions of environmental elements across multiple spatial and temporal scales.

Recent advancements in Earth observation technologies, sophisticated sensor networks, and the rapidly evolving field of geospatial data science have enabled researchers to observe environmental changes at unprecedented spatial and temporal resolutions. To stay at the forefront of research, this reprint compiles forty-four innovative studies, addressing a wide range of critical topics in geographical environment monitoring, including land-use change, ecosystem services, vegetation dynamics, water resource management, atmospheric processes, and the significant impacts of human activities on environmental systems. The investigations presented here span diverse geographic contexts—from densely populated urban centers and vital agricultural zones to sensitive border regions, desert–oasis ecosystems, and the environmentally significant Qinghai–Tibet Plateau. The methodologies illustrate the integration of multi-source data—including satellite imagery, UAV observations, ground-based sensors, and social media—alongside sophisticated analytical methods such as machine learning, spatial modeling, and innovative scale transformation techniques.

Rather than assembling isolated studies, this reprint offers a cohesive, forward-looking narrative on the methodological, technological, and conceptual progression of multiscale environmental monitoring. It further underscores the importance of scalable, integrative solutions for sustainable development and effective environmental governance by intentionally bridging disciplines, including remote sensing, ecology, urban studies, and data science.

Building upon these studies, we sincerely hope that this reprint will serve as a valuable reference for researchers, planners, and policymakers. We firmly believe that deepening our collective understanding of multiscale environmental monitoring is essential for fostering interdisciplinary collaboration and achieving integrated environmental governance. This reprint was jointly supported by the National Natural Science Foundation of China (42401065 and 42201347), Guangdong Basic and Applied Basic Research Foundation (2023A1515011273), the Specific Innovation Program of the Department of Education of Guangdong Province (2023KTSCX315), and the Shenzhen Polytechnic University Research Fund (6025310064K).

Jingzhe Wang, Yangyi Wu, Yinghui Zhang, Ivan Lizaga, and Zipeng Zhang
Topic Editors

land

MDPI

Article

Spatio-Temporal Dynamics and Drivers of Ecosystem Service Bundles in the Altay Region: Implications for Sustainable Land Management

Suyan Yi [1,2], Hongwei Wang [1,2,*], Ling Xie [3], Can Wang [1,2] and Xin Huang [1,2]

[1] School of Geography and Remote Sensing Sciences, Xinjiang University, Urumqi 830017, China; yisuyan@stu.xju.edu.cn (S.Y.); wangcan_geo@stu.xju.edu.cn (C.W.); huangxin@stu.xju.edu.cn (X.H.)
[2] Xinjiang Key Laboratory of Oasis Ecology, Xinjiang University, Urumqi 830017, China
[3] College of Environment and Resources, Guangxi Normal University, Guilin 541004, China; xl_geo@mailbox.gxnu.edu.cn
* Correspondence: wanghw_777@xju.edu.cn

Abstract: Understanding the dynamics of ecosystem services (ESs) in arid landscapes and socio-ecological systems is crucial for sustainable development and human well-being. This study uses the Invest model to quantify the spatio-temporal changes in four key ecosystems services in Altay from 1990 to 2020: water yield (water yield), carbon stock (carbon stock), soil retention (soil retention), and habitat quality (habitat quality). The trade-offs/synergies between different ESs were investigated via Spearman's correlation analysis. Ecosystem service bundles (ESBs) were mapped using self-organizing mapping (SOM), and the key drivers of ES relationships and the spatio-temporal dynamics of ESBs were revealed through redundancy analysis. The results showed that water yield increased by 33.7% and soil retention increased by 1.2%, while carbon stock and habitat quality decreased by 3.5% and 1.24%, respectively. The spatial distribution pattern had a clear zonal pattern, with the northern mountainous areas higher than the southern desert areas. The six pairs of ESs, in general, showed mainly low trade-off and high synergistic relationships, with trade-offs between water yield and carbon stock, soil retention and habitat quality, and a decreasing trend of trade-offs over time. Four types of ESBs were distinguished, and the compositional differences and spatial distribution within each ESB were determined by interactions between ESs and landscape types. There are complex non-linear relationships between the drivers and the four ESBs in different years. Before 2010, ecological factors were the key drivers influencing the spatio-temporal changes in ESBs, whereas social and environmental factors combined to drive changes in ESB allocations after 2010. Additionally, this study found that the implementation of conservation measures, such as reforestation and sustainable land management practices, positively influenced the provision of ecosystem services in the Altay region. These findings underscore the importance of integrating conservation efforts into land use planning and decision-making processes to ensure the sustainable delivery of ecosystem services in arid landscapes.

Keywords: ecosystem services; ecosystem services bundles; trade-offs; anthropogenic activities; spatial dynamics; Altay region

1. Introduction

As global ecological and environmental issues become more prominent and sustainable development becomes more widely accepted, ecosystem services (ESs), as a theoretical and practical framework to solve human–land issues, play a vital role in advancing the agenda of social and environmental justice and achieving the sustainable development of socio-ecological systems [1–3]. ESs refer to various products and services that humans derive directly or indirectly from ecosystems, including provisioning, regulating, supporting, and cultural services [4]. The variety of ES types, the spatial heterogeneity of ES, and

human activities may generate complex interactions among ESs, which include trade-offs, synergies, and bundles [5]. In this context, exploring trade-offs/synergies in ecosystem services on the basis of long-term time series can help to prioritize conservation and restoration actions in areas where multiple services are under threat [6]. Remote sensing (RS) and geographic information system (GIS) technologies are becoming increasingly important in this field, not only to make up for the shortcomings of traditional monitoring data [7], but also to effectively track spatial and temporal trends in ecosystem services [8–10].

Ecosystem service bundles (ESBs), defined as spatially and temporally recurring collections of ESs [11], are an effective means of identifying patterns of multi-service aggregation in ecosystems [12,13]. ESBs are often quantified using cluster analysis [14,15], which captures the relationship of specific ESs to human-dominated land use and associated ESs [16]. In general, trade-offs and synergies between ESs are usually reflected in differences in the spatial distribution of ESBs and the intrinsic component of ESs. However, the direction and strength of these dyadic and synergistic ES relationships may be spatially heterogeneous and dependent on regional backgrounds [13]. ESBs provide a perspective for characterizing the complex interactions of multiple ESs and can be used to divide regions with homogeneous ES types and magnitudes. They also provide a solid foundation for effective spatial planning and decision-making to promote sustainable development and conservation efforts. Nonetheless, their composition, spatial distribution, and temporal dynamics are influenced by various drivers [17,18]. It has been reported that climate, vegetation, and human activities are important drivers of ESBs [19–21]. However, existing studies concentrated on regression analysis and scenario modeling to investigate the drivers of ESs, with some limitations. In regression analysis, the focus is often on linear relationships [22], yet this approach heavily is influenced by subjective human assumption [23]. Although interactions between drivers and spatial variations in driver effects have been considered in some studies [21], there is still a need to delve deeper into the spatio-temporal variability of ES clustering and its driving mechanisms. Understanding the driving mechanisms behind ESBs can provide valuable insights for enhancing ecosystem resilience and adapting to changing environmental conditions. Therefore, there is a critical need to refine our understanding of ESBs and the complex interactions of ESs within ecosystems.

The Altay region is a relatively abundant water area and a mountain grassland ecological function area in Xinjiang, which is composed of mountain–oasis–desert ecosystems by topography and climate. However, this region faces ecological challenges stemming from long-term mineral resource exploitation, grassland overgrazing, and oasis agriculture practices, compounded by anthropogenic and natural factors like climate change. These issues have resulted in the fragmentation of habitats and the degradation of forests, posing a threat to the sustainable social and economic development of the region [24]. Considering the rich ecological and functional complexity of this region, which is subjected to various external pressures, it is essential to conduct an in-depth investigation into the spatial and temporal evolution of ecosystem services in Altay, and the underlying driving forces, in order to discern the interconnections between diverse ecosystem services and the resulting socio-ecological impacts. This approach can facilitate a comprehensive understanding of the vulnerability of the regional ecosystems and their restoration potential, thereby providing a scientific foundation for the development of effective conservation and management measures.

2. Materials and Methods

2.1. Study Area

Altay region is situated in the northernmost part of the Xinjiang Uygur Autonomous Region, China. Its geographic coordinates are 85°31′–91°04′ E and 45°00′–49°10′ N (Figure 1). The Altay region has a natural geographic barrier in the north and an open terrain in the west, forming three major first-class geomorphological units: mountains, plains, and deserts. The mountain ranges vary in height from west to east, and the hilly plains gradually increase in elevation from east to west, presenting a more pronounced

stepped topography. Three main types of land use can be identified: forests, grasslands, and bare areas. To the south are vast deserts, while the northern mountains are rich in water resources and mixed tree–grass areas [24]. This region has a typical temperate continental climate, with average annual precipitation of 139.3–268.4 mm and average annual temperatures of 0.7–4.9 °C. Considerable inter-annual variability exists in runoff. In terms of spatial distribution, there are more water resources in the west and north than in the east and south [25]. The region has several nature reserves with many rare and endangered plants and animals, including the Castor fiber birulai, which is found only in the Ulungu River basin in northern Xinjiang, China [26]. The Altay Region consists of seven county-level administrative units. In 2020, the total population of the region was 668,600 people, and the gross domestic product (GDP) reached CNY 33.632 billion. The expansion of human activities, such as tourism development and agricultural production, has resulted in the degradation of biological habitats to some extent.

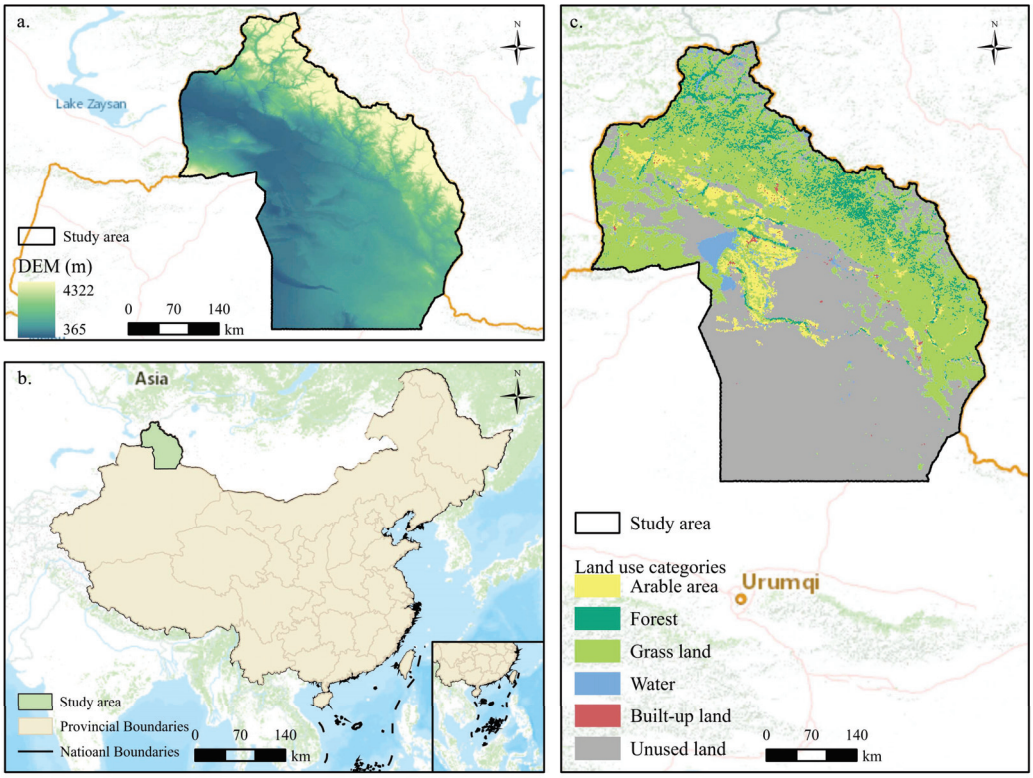

Figure 1. Location of the Altay region in China. (**a**) Elevation distribution; (**b**) map inspection number GS (2019) 1822; (**c**) land-use categories of Altay in 2020.

2.2. Data Sources

In this study, ESs and socio-ecological drivers were quantified using multi-source data on land use/land cover, climate, vegetation, and socio-economics from 1990 to 2020 (Table 1). The land use/land cover data represent 25 thematic categories. All the raster data with different spatial resolutions in Table 1 were resampled to have a standard spatial resolution of 1 km × 1 km for quantifying ESs and the spatio-temporal socio-ecological drivers.

Table 1. Data sources for this study.

Data Type	Application	Data Format	Data Source/Processing	Spatial-Resolution
Land use/land cover	water yield, carbon stock, soil retention, habitat quality, social–ecological drivers	Raster	Resource and Environment Science and Data Center (http://www.resdc.cn (accessed on 3 June 2024))	30 m
Precipitation	water yield, social–ecological drivers	Raster	National Earth System Science Data Center, National Science & Technology Infrastructure of China (http://www.geodata.cn (accessed on 3 June 2024))	1 km
Temperature	social–ecological drivers	Raster	National Earth System Science Data Center, National Science & Technology Infrastructure of China (http://www.geodata.cn (accessed on 3 June 2024))	1 km
Evapotranspiration	water yield, social–ecological drivers	Raster	National Earth System Science Data Center, National Science & Technology Infrastructure of China (http://www.geodata.cn (accessed on 3 June 2024))	1 km
Root depth, soil texture, and organic carbon content	water yield	Raster	China soil map based harmonized world soil database (HWSD) (v1.1)	30 arc-second
Carbon density	carbon stock	Spreadsheet	A dataset of carbon density in Chinese terrestrial ecosystems (2010s) (http://www.doi.org/10.11922/sciencedb.603 (accessed on 3 June 2024))	/
Digital elevation model (DEM)	soil retention, social–ecological drivers	Raster	Resource and Environment Science and Data Center (http://www.resdc.cn/ (accessed on 3 June 2024))	90 m
Normalized difference vegetation index (NDVI)	social–ecological drivers	Raster	Resource and Environment Science and Data Center (http://www.resdc.cn/ (accessed on 3 June 2024))	1 km
Gross domestic product (GDP)	social–ecological drivers	Raster	Resource and Environment Science and Data Center (http://www.resdc.cn/ (accessed on 3 June 2024))	1 km
Population density	social–ecological drivers	Raster	Resource and Environment Science and Data Center (http://www.resdc.cn/ (accessed on 3 June 2024))	1 km

2.3. ES Quantification

In this study, four ES categories of the region were finalized based on the variability of geomorphology, climate, vegetation, water system, and intensity of anthropogenic disturbances, i.e., water yield, soil retention, carbon Stock, and habitat quality (Table 2). With the help of the InVEST software (3.7.0), the ESs in 1990, 2000, 2010, and 2020 were quantified, and the spatial distribution pattern of ES, interaction characteristics, and major ecological threats were then analyzed.

Table 2. Overview of ecosystem services.

Ecosystem Service	Description
Water yield	The yield of annual water
Habitat quality	The ability of ecosystems to provide conditions suitable for the persistence of individuals and populations.
Carbon storage	The amount of carbon stored by terrestrial ecosystems
Soil retention	Sediment delivery ratio

2.3.1. Water Yield (WY)

Using the water balance method, the annual water production of the Altay region was estimated based on the "water harvesting" module of the InVEST model, and the water conservation capacity of the Altay region considering the streamflow, soil permeability, and other factors (Equations (1)–(2)) [27]:

$$WY = \min(1, 249/Velocity) \times \min(1, 0.3TI) \times \min(1, K_{sat}/300) \times Y_x \quad (1)$$

$$Y_X = (1 - AET_X/P_X) \quad (2)$$

where WY is water yield (mm), Velocity represents flowing rate, TI is topography index, Ksat is saturated hydraulic conductivity of soil (mm/d), Yx denotes annual water yield (mm), AETx is average annual actual evapotranspiration of grid cell x (mm), and Px indicates average annual precipitation of grid cell x (mm).

2.3.2. Soil Retention (SR)

In the current work, the soil conservation module of the InVEST model was employed to calculate the average annual soil loss and soil conservation for each land-class grid using geomorphic, climatic, vegetative, and management capacity data, primarily based on the Universal Soil Loss Equation (USLE) (Equation (3)) [28]:

$$SR = R \times K \times LS \times C \times P \quad (3)$$

where SR is the soil erosion volume; R is the rainfall erosive force; K is the soil erodibility factor; LS is the sloping length factor; C is the vegetation cover factor and management factor; and P is the soil and water conservation measures factor.

2.3.3. Carbon Stock

Carbon sequestration model in InVEST was adopted for assessment. This model was constructed based on the main principle of accumulation of carbon densities, including surface carbon density, soil carbon density, subsurface carbon density, and dead carbon density.

2.3.4. Habitat Quality

The habitat quality module of the InVEST model was used to assess habitat quality in the Altay region. This model links habitat distance and threat sources to compute habitat quality (Equation (4)) [29]:

$$Q_j = H_j\left(1 - \frac{D_j^2}{D_j^2 + k^2}\right) \quad (4)$$

where Qj is the habitat quality of land use type j; Hj is the habitat suitability of land use type j; Dj represents the level of stress to which land use type j is subjected; and k is the half-saturation constant.

2.4. Quantification of Relationships between ESs

The interactions among the four ESs are subject to uncertainty and thus require a dynamic understanding of their relationships. Spearman correlation analysis was employed to assess the correlations between the four ESs [14,18]. The "Corrplot" package in R software (4.3.3) was used to calculate the Spearman correlation coefficient.

2.5. Identification of ESBs

To facilitate comparison between different years, ESs were normalized from 0 to 1 (low to high); a total of 4898 ecological grid units of 5 km × 5 km each were partitioned within the study area by using the grid method. We conducted self-organizing mapping analysis using the "kohonen" package from software R (4.3.3).

2.6. Identification and Analysis of Socio-Ecological Drivers of ESBs

Potential socio-ecological drivers affecting ESB formation were categorized into three groups, i.e., landscape configuration, natural ecology, and human activity indicator. To reduce the redundancies among the indicators and to identify the main drivers, SPSS (26.0 software) was used to diagnose multiple covariances, eliminating indicators that had a VIF of >10 [30], leaving twelve possible social–ecological drivers for further analysis (Table 3).

Table 3. Social–ecological drivers.

Category	Indicator	Abbreviation
Biophysical indicators	Topographic position index	TPI
	Normalized difference vegetation index	NDVI
	Drought index	K
	Temperature	TEM
Anthropogenic indicators	Land-use development intensity	LDI
	Population density	POP
	Gross domestic product	GDP
	Human activity intensity	HAI
Landscape configuration	Aggregation index	AI
	Contagion index	CONTAG
	Patch density	PD
	Number of patches	NP

To facilitate comparisons between years, potential drivers were standardized [14,31] and then used to perform redundancy analyses (RDAs) to select different combinations of key social-ecological drivers that significantly affect ESs in different ESB types. For each ESB, socio-environmental drivers were identified and tested for significance (999 permutations). The results were used to check the statistical significance of these factors. In addition, hierarchical partitioning analyses were conducted to obtain independent explanations for each socio-ecological driver of multiple ESs in each ESB.

3. Results

3.1. Spatial–Temporal Variations in ESs

In this study, four ES categories (including water yield, soil retention, carbon stock, and habitat quality) were quantitatively analyzed. The results showed that the spatio-temporal patterns of ESs were heterogeneous. Over the past 30 years, water yield and soil retention in the Altay region showed an inverted U-shaped trend (Figure 2a,b). From 1990 to 2000, there was a significant increase in both soil retention and water yield values. Water yield increased by 29.27% and soil retention by 32.44%. However, from 2010 to 2020, the soil retention value showed a decreasing trend, decreasing by 2.27%, while the water yield value decreased by 29.12%. Compared to 1990, the total soil retention and water yield in the region increased by 33.7% and 1.2%, respectively, in 2020. Changes in carbon stock and habitat quality showed consistency across years (Figure 2c,d). The peak year was 1990, showing the lowest value by 2020. Carbon stock and habitat quality showed similar rates of decline, with decreases of 3.5% and 1.24%.

According to the spatial distribution map, water yield and soil retention show similarities, with high values in the north hilly regions and northwestern mountainous regions, while low value regions are clustered in the plains and desert of the south and center (Figure 2a,b). It was evident that the water yield amount in the northwestern region was significantly more increased in 2010 than in the other years (Figure 2a). The overall distribution pattern of carbon stock in Altay showed a gradual decline from north to south (Figure 2c). Areas with high carbon stock values are distributed in the northeast, with water systems in the west belonging to the mountainous forested areas with high vegetation cover and a more complete landscape. The main distribution area of desert is located in the south, which is also the distribution area with low carbon stock and habitat quality

values. In contrast, the central region exhibits more apparent fluctuations in carbon stock and habitat quality.

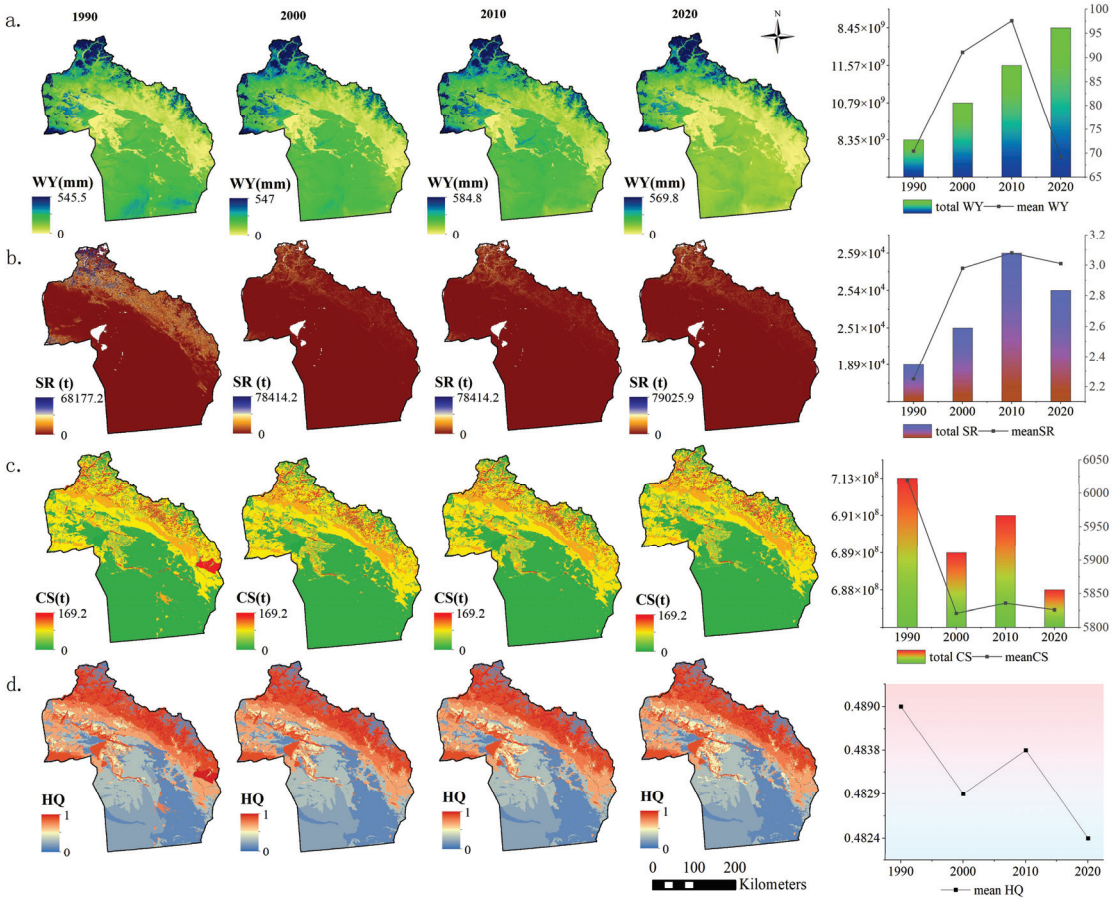

Figure 2. Spatial–temporal patterns and variability in ecosystem services. (**a**) WY: water yield; (**b**) SR: soil retention; (**c**) CS: carbon stock; (**d**) HQ: habitat quality.

3.2. Trade-Offs and Synergies between ES Pairs

By quantifying the correlations between the five categories of ESs in different historical periods, we found statistically significant ($p < 0.001$) correlations between six ES pairs (Figure 3). Carbon stock, habitat quality, and soil retention all exhibited synergies with each other, while water yield showed a trade-off with these three ES categories, with the highest trade-offs between water yield and carbon stock, and the lowest between water yield and soil retention. During 1990–2020, the trade-offs between water yield and carbon stock, habitat quality, and soil retention weakened. Notably, the highly significant negative correlation between water yield and carbon stock shifted to a highly significant positive correlation. The synergy between soil retention, carbon stock, and habitat quality has shown a stable trend. Overall, the relationship between these four ESs in the Altay region is characterized by low trade-offs and high synergies. There is a clear conflict between water yield on one side and carbon stock, soil retention, and habitat quality on the other side, leading to a gradual weakening of the trade-offs over time.

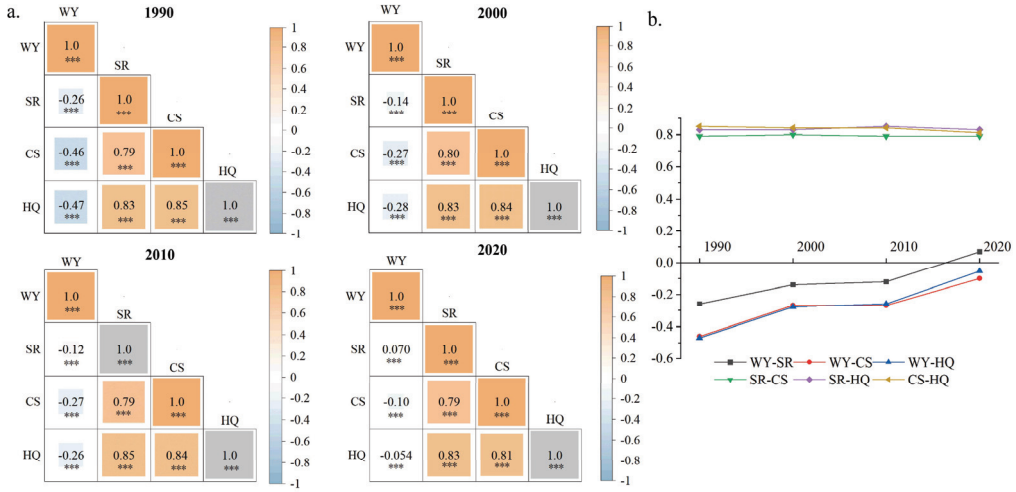

Figure 3. (**a**) Trade-offs and synergies amongthe relationships of ecosystem services in the Altay region from 1900 to 2020; (**b**) Correlation changes in 1990 to 2020. *** $p < 0.001$.

3.3. Spatial–Temporal Distributions of ESB

The self-organizing mapping identified four ESB bundles at the grid scale, and the trajectory change in ESBs from 1990 to 2020 was further explored based on the classification result (Figure 4a). According to the ESB composition (Figure 4b), bundle 1 includes three types of ESs, including soil retention, carbon stock, and habitat quality; this bundle demonstrated the spatial synergy of high soil retention, carbon stock, and habitat quality. The distribution of bundle 1 was mainly concentrated in the gentle mountainous regions and low hills. Bundle 2 is widely distributed in the south-central region and displayed a distinct vertical pattern. It was characterized by a sizable supply of water yield and habitat quality, with carbon stock being less prominent. Bundle 3 has a more limited function type, consisting only of soil retention and water yield, with soil retention's proportion being much higher than that of water yield. This bundle has the smallest area and highly concentrated spatial distribution. Bundle 4 was primarily spread across the mountainous regions with high elevation in the northwest and has the most balanced distribution of proportions of each type of ES, demonstrating its ability to provide an integrated ES advantage. The spatial variation in the four ESBs is mainly concentrated in the gently sloping mountain and oasis regions.

Figure 5 reflects the shift in area of different ESBs at the grid scale and the proportion of landscape types from 1990 to 2020. Over the past 30 years, the change in the area covered by Bundle 1 has exhibited a consistent pattern with the change in the area of forests within its corresponding landscape type. Bundle 2 exhibits the highest proportion of unused land in the regional landscape type, which is primarily composed of bare rock and sandy soil. The Gobi encompasses a considerable area of undeveloped wasteland, resulting in a lower proportion of soil retention in this bundle. The landscape composition of bundle 3 is dominated by river, which accounts for more than 50% of the area. Bundle 4 exhibits the greatest proportion of forested grassland in comparison with the other three ESB landscape types, displaying an upward and subsequent downward trend in the change in its area.

From 1990 to 2000, the land use type of the region where bundle 1 is located exhibited a higher proportion of forests and grasslands. Concurrently, the area occupied by bundle 1 decreased by 11.6% due to an increase in the proportion of unused land. In contrast, the area of bundle 4 exhibited an increasing trend, accompanied by an increase in the proportion of forests in the landscape type and a concomitant decrease in the proportion of unused land. The reduction in bundle 1 was accompanied by an increase in the areas of bundle 2 and bundle 4 (Figure 5e). The area covered by bundle 1 showed an increasing trend from 2010 to 2020, which was reflected in a decrease in the share of cropland and an increase in the share of forests in its land use type. The area covered by bundle 4 was

the highest in 2010, with an area share of 9.7%. This was mainly due to an increase in the proportion of grassland, a continuous decrease in the proportion of unused land, and an increase in vegetation cover. The proportion of area covered by bundle 2 was 51.1% in 2020, with the proportion of arable land showing an increasing trend and the proportion of unused land showing a decreasing trend.

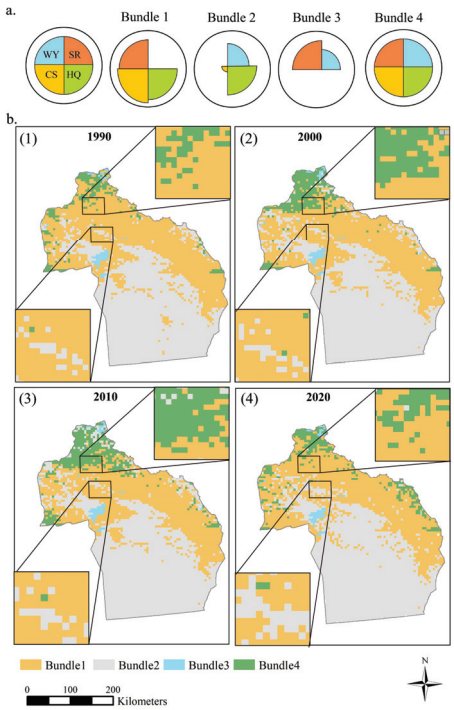

Figure 4. (**a**) Composition and relative magnitude of ESs in ES bundles at the grid scale; (**b**) the area of inter-conversion among different ES bundles in 1990–2020 at the grid scale.

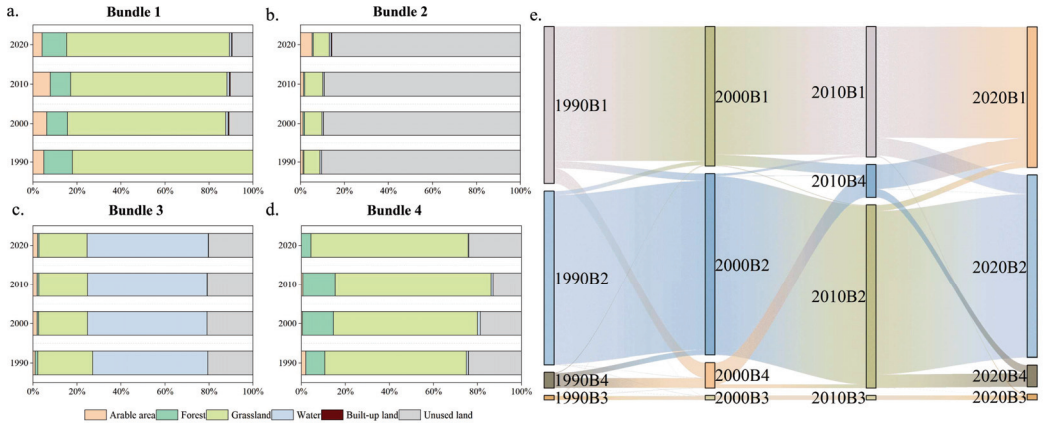

Figure 5. (**a**–**d**) Spatial–temporal patterns of ES bundles at the grid scale; (**e**) land-use structures of the landscapes with different bundles of ecosystem services in 1990–2020.

3.4. Drivers of the Spatio-Temporal Heterogeneity of ESBs

The proportion of socio-ecological factor composition was found to significantly affect the distribution of ESBs (p-value < 0.05). Moreover, the explanatory power of different socio-ecological drivers in ESBs similarly varied (Figure 6). This suggests that the same drivers may show consistent effects on some ESs across the four ESBs over time, or they may have opposite effects on the same function across ESBs. The RDA demonstrated inter-annual fluctuations in the explanatory potential of the 12 socio-ecological factors for different ESBs and the four types of ES. The initial two principal components (RDA1

and RDA2) accounted for a substantial proportion of the data variability observed in the distinct ESBs (Figure 7).

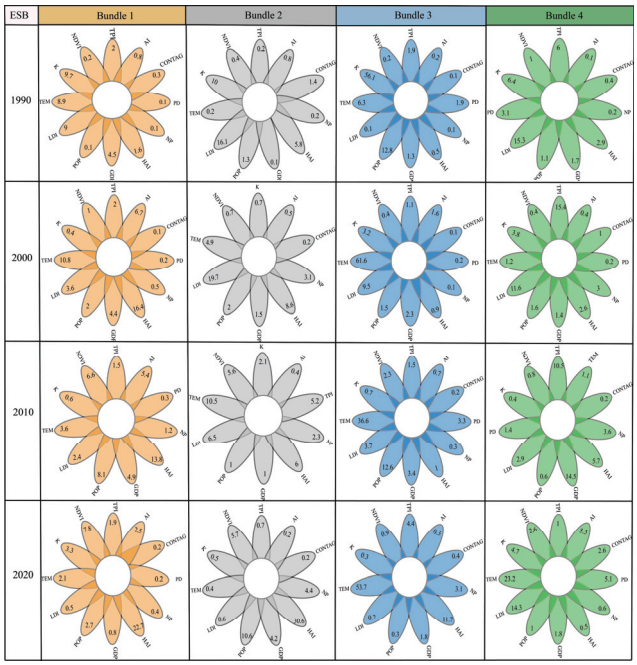

Figure 6. The explanatory ability of socio-ecological drivers for ESBs in Altay (1990–2020).

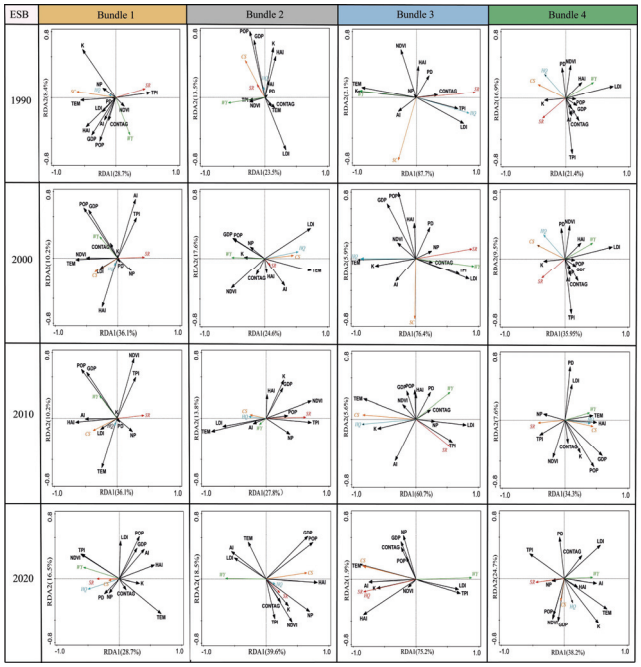

Figure 7. Impact of socio-ecological drivers on ESBs in Altay (1990–2020).

During 1990–2000, the main drivers affecting the changes in bundle 1 and bundle 3 were K and TEM, respectively. The contribution of K demonstrated an upward trajectory, while the explanatory potential of NP and PD was less than 2%. The spatio-temporal drivers of bundle 2 were mainly K and LDI. In this case, the influence of K exhibited a decreasing trend, while the influence of LDI gradually increased. The key drivers affecting changes in bundle 4 were TPI and LDI, with the influence of TPI increasing significantly and a contribution rate of 15.4% in 2000. From 2010 to 2020, the main drivers affecting

bundle 1 were HAI and NDVI. The effect of these drivers gradually increased. For bundle 2, in addition to LDI, the HAI driver has become one of the key drivers. For bundle 3, the social driver POP became a key driver in 2010, along with the impact of the ecological driver. However, the social driver of this cluster changed from population density to HAI in 2020. For bundle 4, the social driver was replaced by GDP from the previous LDI, and the impact of the social driver exceeded the impact of the ecological driver, contributing 23.2% in 2020.

The positive and negative effects of different driving factors on the improvement in ESs in different ESBs fluctuate or have phased effects, eventually leading to the spatio-temporal differentiation of ESBs. For some ESBs, the driving factors will change over time, and even the driving mechanism of the same factor will evolve. This shows that the driving factors have different nonlinear effects on ESs in different years.

For ESs comprising internal ESBs (Figure 7), K and TEM are the primary negative drivers influencing the quantity of water yield, namely the greater water yield in low-temperature, low-dryness regions. NDVI was positively correlated with water yield, carbon stock, and habitat quality, suggesting that the greater the vegetation cover in the region, the higher the corresponding ES function. In 2010 and 2020, the status of LDI reversed from a positive indicator to a key negative indicator, with the exception of TEM, in regulating soil retention. On the other hand, TPI emerged as the primary positive indicator influencing soil retention, showing a negative impact on water yield, carbon stock, and habitat quality. The contribution of HAI to each ES is uncertain. In 2010, POP became the main determinant of the number of water yield reverse drivers, while GDP was positively correlated with water yield and habitat quality in 2020.

In summary, the driving factors of bundles 1, 2, and 4 have shifted from being primarily ecological factors to being jointly driven by social and ecological factors. On the contrary, the driving factors of bundle 3 remain relatively stable. Among the ecological factors, K, TEM, NDVI, and TPI are the main driving factors of ESBs and ESs. In contrast, the social factors of LDI, HAI, GDP, and POP have more significant driving effects.

4. Discussion

4.1. Spatio-Temporal Changes in ESs and Interaction Characteristics

The water yield, soil retention, carbon stock, and habitat quality exhibit distinct spatial heterogeneity characteristics due to the geographical differentiation of the natural environment. This has led to the development of a unique arid "mountain–oasis–desert" system in the Altay region [24]. The northeastern mountainous areas are characterized by high ES values and high forest coverage rates. Despite strong rainfall erosion, lower evapotranspiration contributes to soil conservation, resulting in higher water yield and soil retention values [31]. In addition, high soil retention areas were significant in the northern region and closely associated with areas of steep slope, suggesting a correlation between soil retention and topography. Conversely, land degradation affected the southern region, resulting in low vegetation cover, mainly unused land, leading to high ecological degradation and low carbon stock and habitat quality values. Changes in land cover types significantly affected the capacity of carbon stock services in different areas. Where forests and grasslands are found in the north and south of carbon stock, there is more variety in the value distribution than elsewhere. This study also reveals that ES variations are primarily concentrated within high-value ES zones, followed by central oasis areas. This phenomenon suggests a heightened sensitivity towards disturbances within these locations due to the impact of significant human activity, as previously indicated [32]. The traditional seasonal grazing practices of Altay herders, particularly during the spring and summer months, have led to significant damage to the high-elevation grasslands and alpine meadows [33]. And the expansion of agricultural land, urbanization, livestock grazing, and other factors has resulted in a reduction in carbon stock, water yield, and habitat quality, ultimately leading to a decline in ESs [34].

This study also reveals the interactive relationships between ESs in the Altay region from 1990 to 2020. There is a trade-off between water yield and soil retention, carbon stock, and habitat quality, which is mainly influenced by precipitation and land cover [35]. Changes in climate and land use conversion impact regional vegetation coverage, leading to significant splash erosion and scouring from excessive precipitation that can result in a decrease in soil retention [36]. Meanwhile, population growth and economic demands have led to an increase in the intensity of human activities, the destruction of vegetation growth conditions, and increased soil erosion, while retention has gradually declined. Studies in arid inland river basins have reported similar findings [37]. Soil erosion is also a major problem faced by the ecology of the region today [38–40]. It is noteworthy that the high trade-off relationship between the two types gradually converged to a low synergistic relationship between 1990 and 2020, suggesting some potential for ecological optimization in the region. Jia et al. showed that constructing ecological restoration projects, such as the Grain for Green Project in China, has the potential to alleviate the trade-off between water yield and soil retention [41]. Additionally, the initiation of these projects in 2000 coincided with the observed trend of changes in the relationship strength of trade-offs between ESs in the study region [42]. The synergistic relationships in the Altay region are reflected in the relationships between soil retention, carbon stock, and habitat quality. The synergistic relationship between carbon stock and soil retention in the Altay region is due to the increase in vegetation cover, which enhances carbon stock and reduces rainfall-induced soil erosion, thus enhancing soil retention [43]. Soil retention maintains a stable level of species diversity and improves the development of habitat quality [44].

4.2. ESBs and Dynamic Drivers in Land Management

This study found significant variations in the types and proportions of ESs provided by different ESBs. Furthermore, ESBs exhibited multi-dimensional and multi-temporal correlations [45]. The dynamic changes observed can reflect the potential causes of ES changes and the speed of change. Identifying the social drivers of ESBs is favorable for formulating spatial management and planning strategies that promote the multifunctionality of the research area and enable the sustainable development of the region [46,47].

It was shown that water yield exhibited a trade-off relationship with soil retention, carbon stock, and habitat quality, in accordance with the internal ES composition of bundle 1. K and TEM exhibited a more pronounced driving effect on bundle 1. The warming and drying climate conditions led to a decline in ESs, and drought exacerbated the risk of desertification, posing a greater threat to the ecological security of oasis regions [25]. Since 2010, NDVI has become the main positive driving factor for bundle 1; ecological protection projects (e.g., the "Grain for Green" project) have expanded the area covered by vegetation and vegetation restoration enhances the synergistic benefits between carbon stock and water yield in the arid northern region [48], enhancing the ESs of the region and facilitating the transition from bundle 1 to bundle 4. According to ESB classification, bundle 1 is spanning the mountain oasis ecological zone and river buffer zone. Under the impact of climate change and water resource inequality, the ecological functions of the region are severely limited. The rapid expansion of urban construction areas due to intensified human activities has significantly altered the spatial pattern of ESBs in the region. For bundle 1, future management should prioritize soil conservation, restrict grazing activities [49], and make efforts to restore vegetation in areas of severe land fragmentation. Furthermore, it may also be beneficial to consider expanding the Altay Nature Reserve to limit human activities and increase the stability of vegetation in order to mitigate the impact of climate change [50].

The internal composition of bundle 2 includes water yield, habitat quality, and carbon stock, whose distribution area is subject to a combination of environmental constraints and anthropogenic interventions. LDIs and HAIs are key socioeconomic factors influencing the spatial differentiation of bundle 2, highlighting the significant impact of complex human activities on ecological disturbance [51]. The expansion of the build-up area has caused

a reduction in carbon stock, leading to a decrease in regulatory services [52]. Meanwhile, the increase in surface hardening has contributed to an upward trend in water yield [53]. This suggests that the advancement of regional economic development has contributed to the implementation of ecological conservation policies, thereby facilitating ecosystem restoration and reconstruction. The land-use structure should be adjusted based on ecological suitability and environmental carrying capacity in order to alleviate the ecological stress caused by construction expansion.

As a crucial source of water supply, bundle 3 is primarily driven by K and TEM. Despite increased rainfall amounts across much of the Altay region experiencing arid climates with evaporative rates often surpassing actual rainfall totals, drought-induced water scarcity hampers vegetation growth, while adverse ecological impacts due to climate warming are emerging [54]. As the distribution of ESBa is concentrated in riverine landscapes comprising watersheds and other land use types, the limited interception of runoff facilitates water storage due to low-to-moderate grass cover. Management objectives should adhere to the principle of ecological prioritization, focusing on water retention and storage.

Bundle 4 is predominantly distributed in high-altitude mountainous areas, which serve as primary sources of ecosystem services, with the high-altitude northern glaciers providing abundant water and thermal resources [33]. TPI exerts a positive driving force in the formation of bundle 4, topographically redistributes water and thermal conditions, influences soil properties, and leads to interannual variations in soil retention, thus playing a crucial role in the spatio-temporal patterns of bundle 4. Bundle 4 is also in an area with excellent natural conditions, where human interventions have led to changes in land cover, consisting mainly of forests and grasslands. In 2000, China began to implement the "Grain for Green" project, and the supply and regulation services in the Altay region were improved [17]. Future management objectives should take into account the establishment of an ecological red line, the active protection of the pristine ecological environment, and the restriction of the artificial and unreasonable expansion of the northwestern mountainous areas. These actions are necessary to promote environmental protection and sustainable development. Additionally, in order to safeguard or enhance the carbon sequestration surplus in densely vegetated areas, it may be beneficial to consider utilizing carbon trading platforms and fiscal transfer payments as a means of providing or enhancing ecological compensation for establishing ecological redlines [55,56].

5. Conclusions

In the current study, we analyzed the spatio-temporal variation driving factors of the ES relationships and ESBs in the Altay region from 1990 to 2020 and provided related ecological management suggestions for each ESB.

This research can be concluded as follows: (1) During 1990–2020, there was a consistent pattern in the intensity and trend of changes in water yield and soil retention. Soil erosion has been shown to be one of the most important environmental challenges in the region. The spatial disparities in the four categories of ecosystem services are associated with regional variations in natural geographical environments. (2) The trade-off intensity between water yield and the three other types of ESs is gradually decreasing, indicating a positive trend towards improved ecological quality in the Altay region. (3). The clustering results led to the categorization of the Altay region into four distinct types of ESBs. The internal compositional differences and spatial distribution of ESBs are assigned by the interaction relationships between ESs and landscape types. (4) There is a complex non-linear dynamic in the relationship of the different drivers to the four types of ESBs over different years. Natural conditions and climatic factors emerge as the key ecological elements influencing the spatio-temporal variations in ESBs. In contrast, societal factors (e.g., land expansion for construction and human activity intensity) drive the changes in ecosystem service functionality. Overall, by identifying the specific areas and times where certain ESs are most critical or vulnerable, decision-makers can better allocate resources

and prioritize conservation efforts. This targeted approach could lead to more effective land-use planning, sustainable resource management, and enhanced ecosystem resilience in the face of environmental challenges.

Author Contributions: Conceptualization, S.Y.; data curation, S.Y. and L.X.; formal analysis, S.Y. and H.W.; investigation, X.H.; methodology, S.Y.; resources, S.Y. and H.W.; software (ArcGIS 10.8), S.Y. and L.X.; validation, C.W. and H.W.; visualization, X.H. and H.W.; writing—original draft, S.Y. and L.X.; writing—review and editing, H.W. and S.Y. All authors have read and agreed to the published version of the manuscript.

Funding: This research was supported by the Ministry of Science and Technology of the People's Republic of China under the Third Xinjiang Scientific Expedition Program (No. 2021xjkk0902).

Data Availability Statement: The data presented in this study are available on request from the corresponding author. The data are designed to be used in other ongoing research and should be protected before official publication.

Acknowledgments: Thanks to all the reviewers and editors.

Conflicts of Interest: The authors declare no conflicts of interest.

References

1. Costanza, R. Valuing natural capital and ecosystem services toward the goals of efficiency, fairness, and sustainability. *Ecosyst. Serv.* **2020**, *43*, 101096. [CrossRef]
2. Torralba, M.; Fagerholm, N.; Hartel, T.; Moreno, G.; Plieninger, T. A social-ecological analysis of ecosystem services supply and trade-offs in European wood-pastures. *Sci. Adv.* **2018**, *4*, 2176. [CrossRef]
3. Loos, J.; Benra, F.; Berbes-Blazquez, M.; Bremer, L.L.; Chan, K.M.A.; Egoh, B.; Felipe-Lucia, M.; Geneletti, D.; Keeler, B.; Locatelli, B.; et al. An environmental justice perspective on ecosystem services. *Ambio* **2023**, *52*, 477–488. [CrossRef] [PubMed]
4. Jaligot, J.B.M. Assessing spatial temporal patterns of ecosystem services in Switzerland. *Landsc. Ecol.* **2019**, *34*, 1379–1394. [CrossRef]
5. Raudsepp-Hearne, C.; Peterson, G.D. Scale and ecosystem services: How do observation, management, and analysis shift with scale—Lessons from Québec. *Ecol. Soc.* **2016**, *21*, 316. [CrossRef]
6. Ji, Y.; Xie, M.; Liu, Y.; Zhu, R.; Tang, Z.; Hu, R. How Do Ecological Restoration Projects Affect Trade-Offs and Synergies between Ecosystem Services? *Land* **2024**, *13*, 384. [CrossRef]
7. Nemec, K.T.; Raudsepp-Hearne, C. The use of geographic information systems to map and assess ecosystem services. *Biodivers. Conserv.* **2013**, *22*, 1–15. [CrossRef]
8. Zaehringer, J.G.; Schwilch, G.; Andriamihaja, O.R.; Ramamonjisoa, B.; Messerli, P. Remote sensing combined with social-ecological data: The importance of diverse land uses for ecosystem service provision in north-eastern Madagascar. *Ecosyst. Serv.* **2017**, *25*, 140–152. [CrossRef]
9. Cao, W.; Wu, D.; Huang, L.; Liu, L. Spatial and temporal variations and significance identification of ecosystem services in the Sanjiangyuan National Park, China. *Sci. Rep.* **2020**, *10*, 6151. [CrossRef] [PubMed]
10. Balkanlou, K.R.; Müller, B.; Cord, A.F.; Panahi, F.; Malekian, A.; Jafari, M.; Egli, L. Spatiotemporal dynamics of ecosystem services provision in a degraded ecosystem: A systematic assessment in the Lake Urmia basin, Iran. *Sci. Total Environ.* **2020**, *716*, 137100. [CrossRef]
11. Raudsepp-Hearne, C.; Peterson, G.D.; Bennett, E.M. Ecosystem service bundles for analyzing tradeoffs in diverse landscapes. *Proc. Natl. Acad. Sci. USA* **2010**, *107*, 5242–5247. [CrossRef]
12. Mo, W.; Zhao, Y.; Yang, N.; Xu, Z. Ecological function zoning based on ecosystem service bundles and trade-offs: A study of Dongjiang Lake Basin, China. *Environ. Sci. Pollut. Res. Int.* **2023**, *30*, 40388–40404. [CrossRef]
13. Cortinovis, C.; Geneletti, D.; Hedlund, K. Synthesizing multiple ecosystem service assessments for urban planning: A review of approaches, and recommendations. *Landsc. Urban Plan.* **2021**, *213*, 104129. [CrossRef]
14. Dou, H.; Li, X.; Li, S.; Dang, D.; Li, X.; Lyu, X.; Li, M.; Liu, S. Mapping ecosystem services bundles for analyzing spatial trade-offs in inner Mongolia, China. *J. Clean. Prod.* **2019**, *256*, 120444. [CrossRef]
15. Zhou, S.; Li, W.; Lu, Z.; Cheng, R. An ecosystem-based analysis of urban sustainability by integrating ecosystem service bundles and socio-economic-environmental conditions in China. *Ecol. Indic.* **2020**, *117*, 106691. [CrossRef]
16. Zhao, M.; Peng, J.; Liu, Y.; Li, T.; Wang, Y. Mapping Watershed-Level Ecosystem Service Bundles in the Pearl River Delta, China. *Ecol. Econ.* **2018**, *152*, 106–117. [CrossRef]
17. Li, T.; Lü, Y.; Fu, B.; Hu, W.; Comber, A.J. Bundling ecosystem services for detecting their interactions driven by large-scale vegetation restoration: Enhanced services while depressed synergies. *Ecol. Indic.* **2019**, *99*, 332–342. [CrossRef]
18. Xu, J.; Wang, S.; Xiao, Y.; Xie, G.; Lei, G. Mapping the spatiotemporal heterogeneity of ecosystem service relationships and bundles in Ningxia, China. *J. Clean. Prod.* **2021**, *294*, 126216. [CrossRef]

19. Zhang, T.; Zhang, S.; Cao, Q.; Wang, H.; Li, Y. The spatiotemporal dynamics of ecosystem services bundles and the social-economic-ecological drivers in the Yellow River Delta region. *Ecol. Indic.* **2022**, *135*, 108573. [CrossRef]
20. Hamann, M.; Biggs, R.; Reyers, B. Mapping social-ecological systems: Identifying 'green-loop' and 'red-loop' dynamics based on characteristic bundles of ecosystem service use. *Glob. Environ. Chang.* **2015**, *34*, 218–226. [CrossRef]
21. Dong, W.; Wu, X.; Zhang, J.; Zhang, Y.; Dang, H.; Lü, Y.; Wang, C.; Guo, J. Spatiotemporal heterogeneity and driving factors of ecosystem service relationships and bundles in a typical agropastoral ecotone. *Ecol. Indic.* **2023**, *156*, 111074. [CrossRef]
22. Liu, Q.; Qiao, J.; Li, M.; Huang, M. Spatiotemporal heterogeneity of ecosystem service interactions and their drivers at different spatial scales in the Yellow River Basin. *Sci. Total Environ.* **2024**, *908*, 168486. [CrossRef]
23. Zheng, H.; Li, Y.; Robinson, B.E.; Liu, G.; Ma, D.; Wang, F.; Lu, F.; Ouyang, Z.; Daily, G.C. Using ecosystem service trade-offs to inform water conservation policies and management practices. *Front. Ecol. Environ.* **2016**, *14*, 527–532. [CrossRef]
24. Hanchu, L.; Jie, F.; Baoyin, L.; Li, W.; Qin, Q. Practical Exploration of Ecological Restoration and Management of the Mountains-Rivers-Forests-Farmlands-Lakes-Grasslands System in the Irtysh River Basin in Altay, Xinjiang. *J. Resour. Ecol.* **2021**, *12*, 766–776. [CrossRef]
25. Fu, Q.; Li, B.; Hou, Y.; Bi, X.; Zhang, X. Effects of land use and climate change on ecosystem services in Central Asia's arid regions: A case study in Altay Prefecture, China. *Sci. Total Environ.* **2017**, *607–608*, 633–646. [CrossRef]
26. Chu, H.; Jiang, Z. Distribution and conservation of the Sino-Mongolian beaver *Castor fiber birulai* in China. *Oryx* **2009**, *43*, 197–202. [CrossRef]
27. Zhou, W.; Liu, G.; Pan, J.; Feng, X. Distribution of available soil water capacity in China. *J. Geogr. Sci.* **2005**, *15*, 3–12.
28. Williams, J.R. The Erosion-Productivity Impact Calculator (EPIC) Model: A Case History. *Philos. Trans. R. Soc. B Biol. Sci.* **1990**, *329*, 421–428.
29. Chen, Y.; Qiao, F.; Jiang, L. Effects of Land Use Pattern Change on Regional Scale Habitat Quality Based on InVEST Model—A Case Study in Beijing. *Acta Sci. Nat. Univ. Pekin.* **2016**, *3*, 553–562.
30. Williams, S.; Maree, N.; Taylor, P.J.; Belmain, S.R.; Keith, M.; Swanepoel, L.H. Predation by small mammalian carnivores in rural agro-ecosystems: An undervalued ecosystem service? *Ecosyst. Serv.* **2018**, *30*, 362–371. [CrossRef]
31. Shen, J.; Li, S.; Liang, Z.; Liu, L.; Wu, S. Exploring the heterogeneity and nonlinearity of trade-offs and synergies among ecosystem services bundles in the Beijing-Tianjin-Hebei urban agglomeration. *Ecosyst. Serv.* **2020**, *43*, 101103. [CrossRef]
32. Ren, Q.; Liu, D.; Liu, Y.; Liu, Y. Spatio-temporal dynamics and socio-ecological determinants of ecosystem service interplays in Shandong Province's coastal region (2000–2020): Implications for environmental protection and sustainable ecosystem management. *Environ. Res.* **2024**, *243*, 117824. [CrossRef]
33. Fu, Q.; Li, B.; Yang, L.; Wu, Z.; Zhang, X. Ecosystem Services Evaluation and Its Spatial Characteristics in Central Asia's Arid Regions: A Case Study in Altay Prefecture, China. *Sustainability* **2015**, *7*, 8335–8353. [CrossRef]
34. Polasky, S.; Nelson, E.; Pennington, D.; Johnson, K.A. The Impact of Land-Use Change on Ecosystem Services, Biodiversity and Returns to Landowners: A Case Study in the State of Minnesota. *Environ. Resour. Econ.* **2011**, *48*, 219–242. [CrossRef]
35. Deng, Z.; Cao, J. Incorporating ecosystem services into functional zoning and adaptive management of natural protected areas as case study of the Shennongjia region in China. *Sci. Rep.* **2023**, *13*, 18870. [CrossRef]
36. Wang, C.; Su, K.; Jiang, X.; You, Y.; Zhou, X.; Yu, Z.; Chen, Z.; Liao, Z.; Zhang, Y.; Wang, L. Increase in precipitation and fractional vegetation cover promote synergy of ecosystem services in China's arid regions—Northern sand-stabilization belt. *Front. Ecol. Evol.* **2023**, *14*, 3389.
37. Pan, J.; Li, Z. Analysis on trade-offs and synergies of ecosystem services in arid inland river basin. *Trans. Chin. Soc. Agric. Eng.* **2017**, *17*, 280–289.
38. Hao, R.; Yu, D.; Wu, J. Relationship between paired ecosystem services in the grassland and agro-pastoral transitional zone of China using the constraint line method. *Agric. Ecosyst. Environ.* **2017**, *240*, 171–181. [CrossRef]
39. Deng, X.; Li, Z.; Gibson, J. A review on trade-off analysis of ecosystem services for sustainable land-use management. *J. Geogr. Sci.* **2016**, *26*, 953–968. [CrossRef]
40. Zhang, X.S. Ecological restoration and sustainable agricultural paradigm of mountain-oasis-ecotone-desert system in the North of the Tianshan Mountains. *Acta Bot. Sin.* **2001**, *43*, 1294–1299.
41. Jia, X.; Fu, B.; Feng, X.; Hou, G.; Liu, Y.; Wang, X. The tradeoff and synergy between ecosystem services in the Grain-for-Green areas in Northern Shaanxi, China. *Ecol. Indic.* **2014**, *43*, 103–113. [CrossRef]
42. Wen, X.; Wang, J.; Han, X.; Ma, L. Where Are the Trade-Offs in Multiple Ecosystem Services in the Process of Ecological Restoration? A Case Study on the Vegetation Restoration Area in the Loess Plateau, Northern Shaanxi. *Land* **2024**, *13*, 70. [CrossRef]
43. Lu, Y.; Xu, X.; Zhao, J.; Han, F. Spatiotemporal Evolution of Mountainous Ecosystem Services in an Arid Region and Its Influencing Factors: A Case Study of the Tianshan Mountains in Xinjiang. *Land* **2022**, *11*, 2164. [CrossRef]
44. Yan, K.; Wang, W.; Li, Y.; Wang, X.; Jin, J.; Jiang, J.; Yang, H.; Wang, L. Identifying priority conservation areas based on ecosystem services change driven by Natural Forest Protection Project in Qinghai province, China. *J. Clean. Prod.* **2022**, *15*, 132453. [CrossRef]
45. Xia, H.; Yuan, S.; Prishchepov, A.V. Spatial-temporal heterogeneity of ecosystem service interactions and their social-ecological drivers: Implications for spatial planning and management. *Resour. Conserv. Recycl.* **2023**, *189*, 106767. [CrossRef]
46. Yang, Y.; Zheng, H.; Kong, L.; Huang, B.; Xu, W.; Ouyang, Z. Mapping ecosystem services bundles to detect high- and low-value ecosystem services areas for land use management. *J. Clean. Prod.* **2019**, *225*, 11–17. [CrossRef]

47. Chen, T.; Feng, Z.; Zhao, H.; Wu, K. Identification of ecosystem service bundles and driving factors in Beijing and its surrounding areas. *Sci. Total Environ.* **2020**, *711*, 134687. [CrossRef]
48. Li, T.; Ren, Y.; Ai, Z.; Qiao, Z.; Ren, Y.; Ma, L.; Yang, Y. Revealing the Spatial Interactions and Driving Factors of Ecosystem Services: Enlightenments under Vegetation Restoration. *Land* **2024**, *13*, 511. [CrossRef]
49. Luo, K.; Wang, H.; Yan, X.; Yi, S.; Wang, C.; Lei, C. Integrating CVOR and circuit theory models to construct and reconstruct ecological networks: A case study from the Tacheng-Emin Basin, China. *Ecol. Indic.* **2024**, *165*, 112170. [CrossRef]
50. Zhang, B.; Zhang, Y.; Wang, Z.; Ding, M.; Liu, L.; Li, L.; Li, S.; Liu, Q.; Paudel, B.; Zhang, H. Factors Driving Changes in Vegetation in Mt. Qomolangma (Everest): Implications for the Management of Protected Areas. *Remote Sens.* **2021**, *13*, 4725. [CrossRef]
51. Wei, H.; Xu, Z.; Liu, H.; Ren, J.; Fan, W.; Lu, N.; Dong, X. Evaluation on dynamic change and interrelations of ecosystem services in a typical mountain-oasis-desert region. *Ecol. Indic.* **2018**, *93*, 917–929. [CrossRef]
52. Sun, Q.; Qi, W.; Yu, X. Impacts of land use change on ecosystem services in the intensive agricultural area of North China based on Multi-scenario analysis. *Alex. Eng. J.* **2021**, *60*, 1703–1716. [CrossRef]
53. Li, H.; Calder, C.A.; Cressie, N. Beyond Moran's I: Testing for Spatial Dependence Based on the Spatial Autoregressive Model. *Geogr. Anal.* **2010**, *39*, 357–375. [CrossRef]
54. Piao, S.; Nan, H.; Huntingford, C.; Ciais, P.; Friedlingstein, P.; Sitch, S.; Peng, S.; Ahlstr, M.A.; Canadell, J.G.; Cong, N. Evidence for a weakening relationship between interannual temperature variability and northern vegetation activity. *Nat. Commun.* **2014**, *5*, 5018. [CrossRef]
55. Yang, B.; Wong, C.P.; Bo, J.; Hughes, A.C.; Min, W.; Qing, W. Developing China's Ecological Redline Policy using ecosystem services assessments for land use planning. *Nat. Commun.* **2018**, *9*, 3034.
56. Schirpke, U.; Wang, G.; Padoa-Schioppa, E. Editorial: Mountain landscapes: Protected areas, ecosystem services, and future challenges. *Ecosyst. Serv.* **2021**, *49*, 101302. [CrossRef]

Disclaimer/Publisher's Note: The statements, opinions and data contained in all publications are solely those of the individual author(s) and contributor(s) and not of MDPI and/or the editor(s). MDPI and/or the editor(s) disclaim responsibility for any injury to people or property resulting from any ideas, methods, instructions or products referred to in the content.

International Journal of
Geo-Information

MDPI

Article

Research on Rural Environments' Effects on Well-Being: The Huizhou Area in China

Xingmeng Ma [1], Xin Su [2,*], Yanlong Guo [1] and Linfu Zhang [3]

[1] Social Innovation Design Research Center, Anhui University, Hefei 203106, China; 20106@ahu.edu.cn (Y.G.)
[2] Community Development Research Center, Anhui University, Hefei 203106, China
[3] Faculty of Arts and Social Sciences, Lancaster University, Lancaster LA1 4YW 122, UK
* Correspondence: suxin@ahu.edu.cn

Abstract: The Huizhou region is an important area of traditional Chinese culture, and currently, the state of the village's surroundings in this area is still not perfect. In this study, seven districts (counties) in the Huizhou region were selected for research. The Rural Habitat Environment (RHES) Indicator Program is based on the concept of Socio-Economic-Natural Complex Ecosystems (SENCE) and constructs 18 metrics in three dimensions. Trends and influencing factors were analyzed using entropy weight TOPSIS and a Grey Relational Analysis (GRA) for the years 2013–2022, and spatial and temporal evolution was measured using Geographic Information Systems (GISs). The findings show that the composite index for the Huizhou region grew from 2013 (0.3197) to 2022 (0.6806). Second, the Tunxi District belongs to the high index–high economy category. The Shexian, Xiuning, and Qimen counties belong to the high index–low economy category. Huizhou District and Huangshan District belong to the low index–high economy category. Yixian County belongs to the low index–low economy category. Third, all districts (counties) show an upward trend, and Huangshan District has the best RHES condition. Shexian County ranks relatively low in the comprehensive index.

Keywords: Huizhou area; RHES; GIS; composite ecosystem; well-being effects

1. Introduction

The RHES is a general term for the natural, economic, social, and cultural environments related to human residential life within a rural space [1]. In practice, it refers to the organic combination of the material and non-material needs of farmers in their productive lives [2,3]. Good working conditions are the material foundation. The term livable represents living conditions. Harmony is a spiritual concept. The interaction of these three factors is externalized, representing the "beauty" of the countryside (Figure 1). The concept of "harmony and beauty" incorporates the traditional Chinese culture of "harmony" and reminds people that beauty is not only about appearance.

Environmental livability refers to living conditions, focusing on infrastructure and public services. An area with environmental livability is a settlement with a good spatial environment and a humanistic and social environment with modern living conditions [4]. From the perspective of production relations, rural construction is carried out for farmers to meet their expectations and requirements for rural living conditions and a good living environment [5]. "Livable" means farmers can live a modern life where they are residing and realize sustainable ecological livability [6].

Good working conditions depend on industrial and economic development. Areas that are suitable for entrepreneurship and employment [7] can create more local and nearby employment opportunities for farmers. Providing a material foundation for farmers to lead a modern life is a good way to liberate and develop rural productivity and realize farmers' prosperity. From the perspective of productivity development, without supporting materials, rural construction can only be carried out at a low level.

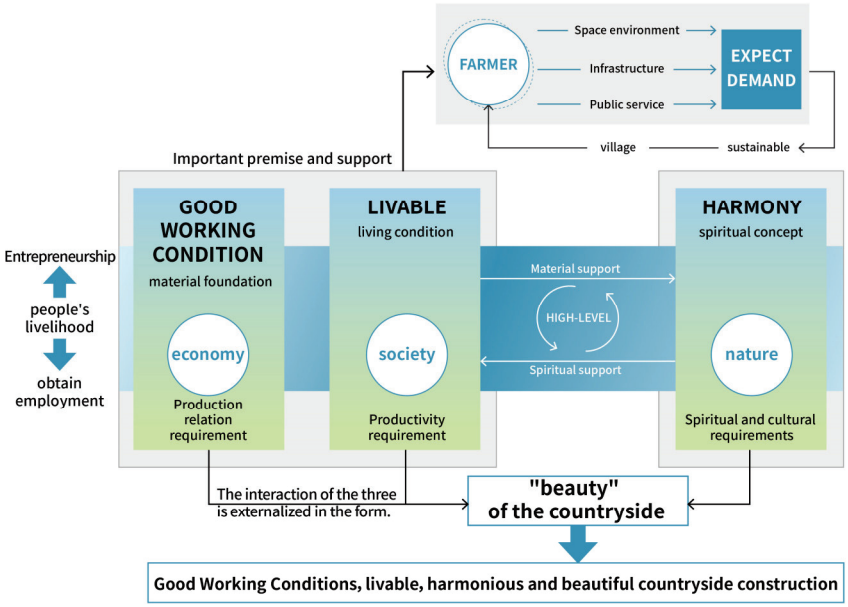

Figure 1. Logical relationship between "livable, workable and beautiful countryside".

Life and beauty are spiritual concepts that highlight the intrinsic attributes of spiritual civilization. This means having a stable and harmonious social environment. "Beauty" is the external appearance of material civilization. From the perspective of spiritual culture, the idea of beauty provides a conceptual guarantee and a spiritual kernel for rural construction [8]. It is an important concept in traditional Chinese culture, emphasizing the harmonious relationship between people, nature, and society.

2. Synthesis of Research

Well-being is understood as welfare, advantage, and benefits [9]. Well-being continues to represent the degree to which conditions are maintained and improved in all areas. The level of well-being of people depends on their living conditions and the degree of economy. A high level of well-being is measured using the Human Settlement Environment (HSE) index [10,11]. National development for the promotion of people's well-being enhances residents' senses of acquisition, happiness, and security.

To promote people's well-being, the state has taken the growth of people's demand for a better life as its core objective [12]. Research has shown that China's studies on the effects of health, safety, and environmental well-being have mainly focused on more developed urban areas. However, the unbalanced and insufficient development of urban and rural areas is a major challenge in Chinese society. Rural areas have long been a weak link in national development [13]. Farmers face low income levels, low labor productivity, a lack of public service facilities, and backward environmental governance in contrast to the prosperity of cities [14]. In view of this, the well-being of rural residents in China needs to be assessed and studied in depth.

The geographic work conducted by geographers on the concept of well-being is valued from the perspectives of psychology and welfare economics. Simandan presents a perspective on geography in personal and social change, emphasizing the role of the unexpected and surprising in shaping personal well-being and social change [15]. Furthermore, Smith and Reid explore the role of presence in the construction of well-being and how it relates to geographies of health and well-being [16]. By integrating these critical geographic perspectives, this study extends the understanding of the differences in well-being between rural and urban residents, emphasizing the importance of space and place in shaping lived experiences and perceived well-being. These geographic perspectives provide frameworks to reassess and reinterpret data while offering new directions for future research to explore how spatiality affects human well-being.

The HSE in Huizhou has the advantages of having natural beauty, a pleasant climate, a rich culture, and a quiet atmosphere. On the one hand, it provides a livable environment for rural residents and attracts many tourists to explore and experience the area. On the other hand, it benefits the well-being of residents while promoting local economic prosperity and social progress. Although the Huizhou region possesses several advantages, there is also a series of unfavorable conditions in terms of the HSE. The Huizhou region is in the mountainous area, and the terrain is mostly hilly and mountainous, which affects residents' traveling abilities and the transportation of materials. The regionalization of rural areas in Huizhou varies greatly, resulting in a mismatch between the HSE and infrastructure development [17]. An excessive influx of tourists and residents may affect the original ecological environment and cultural heritage [18].

RHSE includes a variety of elements associated with an individual's residential environment. They are commonly categorized into the following four types: The first type is rural buildings and infrastructure [19]. This factor mainly includes buildings, commercial facilities, roads, bridges, water, electricity, and gas infrastructure. The planning, design and construction of these facilities should consider the needs, safety, and sustainability of residents. The second type is rural housing [20]. The RHES involves different types of housing styles, such as bungalows, village-style buildings, and buildings. This includes the layouts, sizes, and functions of the houses as well as the planning and design of residential areas. The third type is community facilities [21]. The RHES also includes community facilities, such as education, healthcare, transportation, and elderly care. The existence and quality of these facilities are essential to provide convenience, promote social interaction, and enhance quality of life. The fourth type is the rural natural environment and green spaces. The HSE should be harmonized with the natural environment [22]. The presence of green spaces and natural landscapes helps to improve air quality, regulate climate, provide recreational space, and promote ecological balance.

The current academic research on the RHES from a GIS perspective focuses on the definition, meaning, and dynamic evolution levels. First, the RHES can be defined as a livable countryside that people living in the city would envy. A livable countryside makes industries more prosperous. A harmonious countryside makes farmers' homes happier. The RHES is a modern living condition that can satisfy farmers' material consumption needs and spiritual life pursuits. Industry, talent, culture, ecology, and the organization of the overall coordinated development of the countryside are factors involved in achieving a livable countryside [23]. Second, the important value of the RHES, from the perspective of Chinese-style modernization, constitutes the inherent requirements and prerequisites for the construction of a strong agricultural country and has both far-reaching historical and practical significance. Third, there has been dynamic evolution in the process of building a livable, workable, and beautiful countryside [24]. Since the 1990s, with the introduction of new technologies such as computers and GISs, quantitative research methods have become mainstream in the field of RHES research.

The RHES is a complicated dynamic megasystem [25], and establishing livable and beautiful villages is the main aim of the RHES. With the continuous upgrading of the urban and rural economy comes economic pressure. The main directions of comfort and coordination are used to carry out comprehensive evaluations and research on the HSE. They lay the foundation for development to narrow the urban–rural gap and provide data support for green growth in the countryside. Although there are some disadvantages in the Huizhou area, these problems are not insurmountable. Scholars often measure the level of RHES development by constructing an indicator system for a comprehensive evaluation [26]. This study explores the quality of the RHES in Huizhou and investigates its spatial and spatio-temporal patterns of distribution based on existing research results with the help of entropy weight TOPSIS and GRA. It promotes Huizhou to build a development pattern involving harmony and symbiosis among human beings and nature, which, in turn, promotes the sustainable development of the RHES in China.

3. Material and Methodology

3.1. Research Scope

The Huizhou region is a region in the Anhui province of China. The Huizhou region carries rich Huizhou culture, and its political and economic influences have covered a wide area in various historical periods. According to the approval of the State Council in November 1987, the Huizhou Prefecture was reorganized into the prefecture-level city of Huangshan. Jixi County was assigned to the Xuancheng region, and Shitai County was assigned to the Chizhou region. In July 1988, the prefecture-level city of Huangshan was formally established. It includes Huangshan District, Tunxi District, Yixian County, Shexian County, Huizhou District, Qimen County, and Xiuning County (Figure 2).

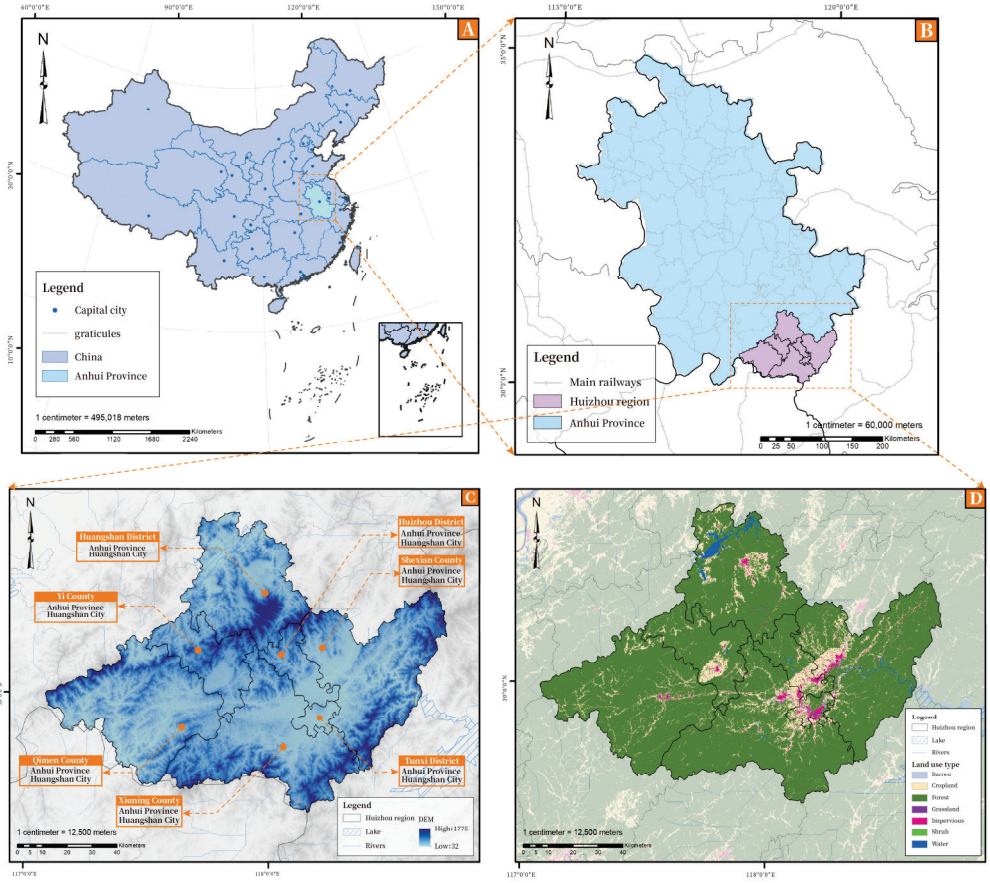

Figure 2. Regional location of Huizhou.

The HSE in the Huizhou region has numerous advantages that attract residents and tourists to live and visit the region. First of all, the Huizhou region is in a mountainous area with rich natural resources and magnificent natural scenery. Clear lakes, ancient villages, and green mountains constitute the unique natural ecological environment of the Huizhou region. It brings a fresh and pleasant living atmosphere to residents. Secondly, the Huizhou area is one of the more well-preserved ancient village settlements in China with many ancient villages of unique style. The most famous of them are Hongcun, Xidi, Qimen, and so on. Thirdly, Huizhou has a long history and unique Huizhou culture. Preserving many Huizhou-style buildings from the Ming and Qing dynasties, it has become a favorite tourist destination for domestic and foreign tourists.

This shows that the Huizhou area is rich and diverse in ancient villages, traditional handicrafts, and historical and cultural relics. Residents live in a cultural atmosphere and feel the unique historical heritage and cultural essence. The HSE is an important source of happiness and security for residents. Compared with the city, the living environment in

the Huizhou area is more peaceful and quieter, and the pace of life is relatively slow. Thus, residents enjoy a peaceful life and have a higher quality of life.

3.2. Research Process

In this study, a comprehensive RHES indicator system was constructed using the SENCE conceptual framework. GRA and entropy weight TOPSIS were selected to measure the level of RHES growth in Huizhou. The process of the study (Figure 3) is described below.

First, the composite ecosystem–SENCE conceptual framework is used. The first task involved in scientifically measuring the level of livable and beautiful countryside construction in the Huizhou region is choosing appropriate measurement indicators. A complete, scientific, and objective evaluation index system is constructed. Second, the collection and compilation of data are carried out. A total of 18 indicators in 7 regions (counties) include three major types of data: social, economic, and environmental. Social and economic data were obtained from the Statistical Yearbook (2013–2022) for each district (county). The data on the environment are from the China Environmental Statistics Yearbook (2013–2022). Third, entropy weight TOPSIS is used to compare the effect gaps between different regions and time through a comprehensive evaluation of the RHES. Composite scores are derived for each subsystem to analyze the variance demonstrated at the substrate layer. Diagnosis of the effectors is carried out using GRA to derive the major factors of influence. The purpose is to obtain information on the rational exploitation and use of rural Huizhou.

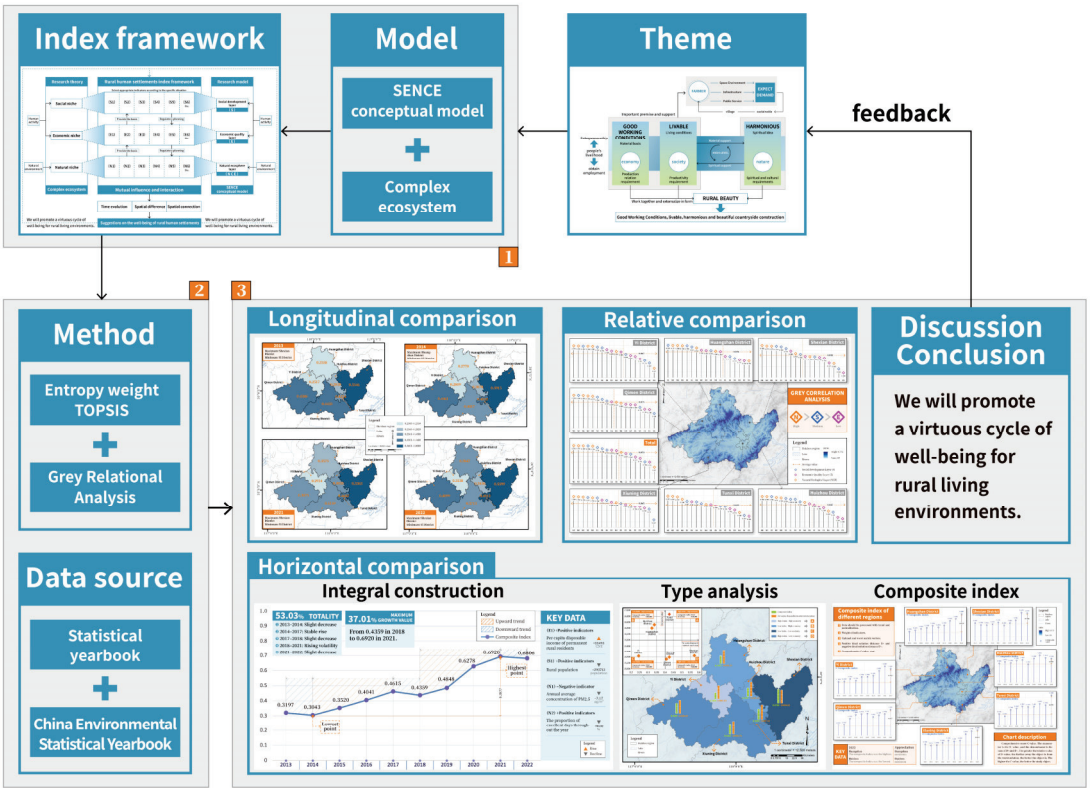

Figure 3. Processes of research on RHES well-being effects in Huizhou region.

3.3. Indicator Construction

A composite ecosystem will use the HSE to refer to human behavior as the subjective consciousness, the natural environment as the auxiliary conditions, and economic and social needs as the multi-level needs of society, the economy, and nature. It will combine the single economic, social, and ecological fields into a composite ecosystem with vitality [27]. Its core concept is to integrate the internal relationships of the three subsystems. The coupling of high-quality coordinated and interoperable development is emphasized to achieve the sustainability of the composite relationship [28]. The SENCE framework of

perception is a unifying body of society, economy, and nature and is known as SENCE—Complex Ecosystems [29]. The SENCE conceptual framework was combined with the concept of a composite ecosystem (Figure 4). The three subsystems were divided according to the principles of targeting, relevance, systematicity, and operability.

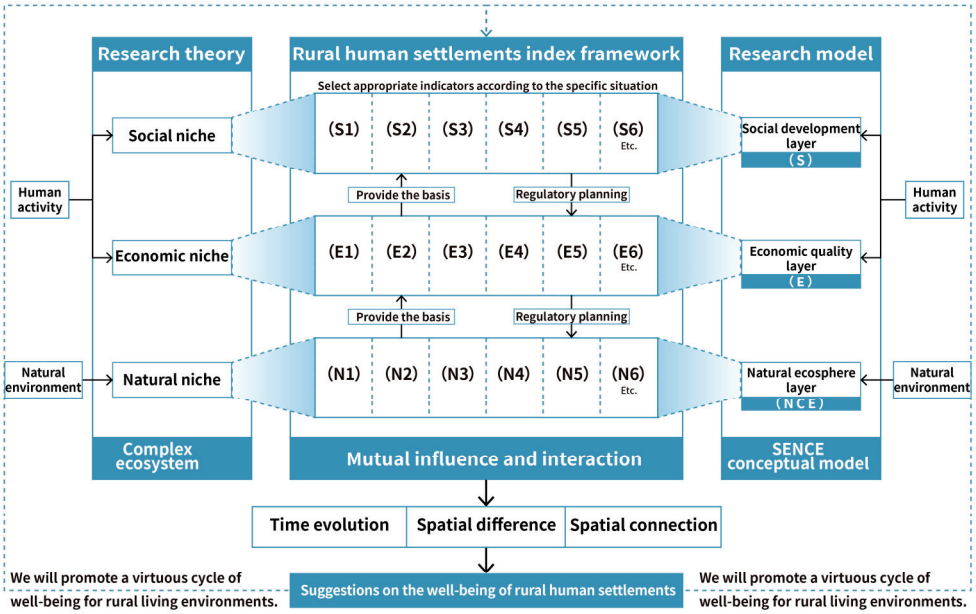

Figure 4. Complex ecosystem–SENCE conceptual framework.

Studies have shown that the SENCE conceptual framework has the advantages of completeness, systematicity, and operability. Firstly, the SENCE conceptual framework embraces key elements such as economy, community, natural resources, and setting. It can accurately represent the connection between ecology and other elements [30]. It provides a scientific theoretical basis for the study of RHES well-being in Huizhou. Second, the environment, agriculture, and ecology domains are integrated into the SENCE framework. This offers a fundamental framework for the establishment of a rational RHES indicator system. Finally, its assessment logic is simpler to understand and use, bringing convenience to researchers. Thus, this research adopts the SENCE conceptual framework as the study model and the composite ecosystem as the study concept. This study constructs a framework of indicators for evaluating the well-being effects of livability and beauty RHES in Huizhou.

The objective layer is the general objective of the indicator framework for the well-being of the RHES in the Emblem area (M). The guideline layer (subsystem) is a subdivision and normalization of the indicator framework's level of ambition. The indicator elements are organized into three groups, namely social development (S), economic quality (E), and natural ecology (NCE). The indicator level is the concretization of the guideline level and extends the indicators on that basis. Through generalization and screening, the guideline layer is expanded to S1–S6, E1–E6, and N1–N6, totaling 18 secondary assessment indicators (Table 1). The detailed implications of the structure of the guidelines and indicators tier are set out below.

First, the social development layer (S) responds to the social component of the evaluation index framework, that is, the relationships and community systems that result from human contact, including social connections, cultural identity, public administration, and economic growth. A geographical environment with a common cultural background and social relationship network formed to meet the needs of people's daily activities, such as residence, consumption, and leisure. The evaluation indicators selected correspond to the number of people in the countryside (S1), the number of village practitioners (S2),

village-run health centers (S3), the per capita housing floor area of rural residents (S4), rural electricity (S5), and the number of automobiles per 100 rural households (S6).

Next, the economic quality layer (E) corresponds to the economy sub-system in the evaluation indicator system, that is, all kinds of production and business activities on which human beings rely for survival and development. The level of economic output is the functioning force behind the establishment of the RHES, which is representative of the economic level and living and production conditions in the countryside. The evaluation indicators selected are the per capita income of permanent residents in villages (E1), the per capita consumption expenditure of rural permanent residents (E2), expenditure on rural minimum subsistence allowance (E3), rural employment subsidies (E4), village conservation and building tax (E5), and elements of the gross value of agricultural output (E6).

Third, the natural ecological layer (NCE) responds to the natural sub-systems in the assessment index system. It is the natural substrate for the development of the RHES in Huizhou, which is a geographical place that provides the required ecological products and services for the rural residents of Huizhou. It mainly includes the local climate, topography, water, land, pollution level, and so on. The evaluation indicators selected are the annual average intensity of PM2.5 (N1), the proportion of good and excellent weather in a year (N2), green coverage area (N3), annual precipitation (N4), the annual average temperature (N5), and forest cover (N6). The selected evaluation indicators may express the developing condition of Huizhou's natural environment and promote Huizhou to build a development pattern of harmonious coexistence between human and nature.

Table 1. Framework of RHES well-being indicators for Huizhou region.

Objective Level	Criterion Level	Indicator Layer (Attributes)	Unit	References	Weights
M: Well-being of RHES in Huizhou	Social development layer (S)	S1: Number of people in countryside (+)	Population	Pan, Y. et al. (2023) [31]	2.321
		S2: Number of village practitioners (+)	Population		3.435
		S3: Village-run health centers (+)	Individual		11.302
		S4: Per capita housing floor area of rural residents (+)	Square meters		4.821
		S5: Rural electricity (+)	Million watt-hours		10.938
		S6: Number of automobiles per 100 rural households (+)	Vehicle		7.276
	Economic quality layer (E)	E1: Per capita income of permanent residents in villages (+)	Yuan	Zhao, H., et al. (2021) [32]	3.534
		E2: Per capita consumption expenditure of rural permanent residents (+)	Yuan		6.015
		E3: Expenditure on rural minimum subsistence allowance (+)	Million yuan		5.126
		E4: Rural employment subsidies (+)	Million yuan		3.302
		E5: Village conservation and building tax (+)	Million yuan		4.245
		E6: Elements of gross value of agricultural output (+)	Million yuan		8.694
	Natural ecological layer (NCE)	N1: Annual average intensity of PM2.5 (−)	$\mu g/m^3$	Zhang, Y. et al. (2024) [33]	9.269
		N2: Proportion of good and excellent weather in a year (+)	%		3.406
		N3: Green coverage area (+)	Hectare		4.443
		N4: Annual precipitation (+)	Millimeter		3.986
		N5: Annual average temperature (+)	Celsius		5.484
		N6: Forest cover (+)	%		2.404

("+" represents positive indicators and "−" represents negative indicators).

3.4. Data Sources

The data on the objective status of the HSE in Huizhou are mainly derived from sources such as the Huangshan City Statistical Yearbook (2012–2022), the China County Statistical Yearbook (2000–2022), and the CECN statistical database (Table 2). Considering the feasibility of data acquisition and the focus of this study, the 10-year period of 2013–2022 is taken as the evaluation period. To address the issue of missing data, Stata MP software is used to estimate missing values. This method uses the available data to infer the most likely values for missing entries, ensuring that the overall trend and distribution of the data set is maintained.

Table 2. RHES data sources and descriptions for the Huizhou region.

Name of Data	Year	Description of Data	Source of Data
China's Digital Elevation Model (DEM)	2023	Digital elevation model with 250 m spatial resolution	30 m yearly data set on land coverage
Land Use Structure	2022	30 m yearly data set on land coverage	30 m yearly data set on land coverage
Administrative Division Data	2023	Used to extract study area boundaries	http://www.geodata.cn/ (accessed on 20 April 2024)
Objective Status Statistics	2013–2022	Contains population, land, economic, and other statistics	Huangshan Statistical Yearbook, China County Statistical Yearbook, etc.

4. Evaluation Methodology

4.1. Entropy Weight TOPSIS

The entropy weight TOPSIS evaluation model can objectively and comprehensively evaluate the degree of strengths and weaknesses of multiple objects in the same field. By exploring the principle of the superiority and inferiority solution distance method [34], the degree of superiority and inferiority of the HSE status of Huizhou is defined as the comprehensive evaluation value of the objective status. The assessment process includes two steps: indicator assignment and comprehensive evaluation. In particular, the entropy weight approach is utilized to identify the weights of the basic internal indicators, and the TOPSIS approach is utilized to synthesize the evaluation of the research object [35]. The specific steps are outlined below.

If there are y items to be assessed and x indicators, then we can form the statistics indicator data matrix $M = \left(N_{ij}\right)_{y \times xo}$. M_{ij} values are normalized using the following equation:

$$M_{ij} = \frac{N_{ij} - \min\left(N_{1j}, N_{2j}, \ldots, N_{xi}\right)}{\max\left(N_{1j}, N_{2j}, \ldots, N_{xi}\right) - \min\left(N_{1j}, N_{2j}, \ldots, N_{xj}\right)} \tag{1}$$

The value of M_{ij} when the index is an inverse indicator is as follows:

$$M_{ij} = \frac{\max\left(N_{1j}, N_{2j}, \ldots, N_{xi}\right) - N_{ij}}{\max\left(N_{1j}, N_{2j}, \ldots, N_{xi}\right) - \min\left(N_{1j}, N_{2j}, \ldots, N_{xj}\right)} \tag{2}$$

The normalized data matrix is used to determine the entropy weight of each indicator and is calculated as follows:

$$M_j = -\frac{1}{\ln x} \sum_{i=1}^{x} Z_{ij} \ln Z_{ij} \tag{3}$$

The normalized matrix formula, $M = \left(N_{ij}\right)_{m \times n}$, can be used to obtain Formula (4) as follows:

$$Q = \left(q_{ij}\right)_{m \times n} \tag{4}$$

where $q_{ij} = N_{ij} W_j$.

The composite score for each indicator is obtained by the formula. The formula for the optimal solution is as follows:

$$C^{+} = \left\{c_{i1}^{+}, c_{i2}^{+}, \ldots, c_{in}^{+}\right\} \tag{5}$$

The worst solution formula is as follows:

$$C^{-} = \left\{c_{i1}^{-}, c_{i2}^{-}, \ldots, c_{in}^{-}\right\} \tag{6}$$

The Euclidean distances between each assessment subject and the positive and negative ideal solutions are calculated, and the composite scores are obtained as follows.

The formula for the distance to the optimal solution is

$$D^{+} = \sqrt{\sum_{j=1}^{n} \left(q_{ij} - c_{ij}^{+}\right)^{2}} \tag{7}$$

The distance from the worst solution is given by the following equation:

$$D^{-} = \sqrt{\sum_{j=1}^{n} \left(q_{ij} - c_{ij}^{-}\right)^{2}} \tag{8}$$

The relative proximity of each measurement scheme to the ideal scheme is calculated, and the combined score formula is as follows:

$$F_i = \frac{D_i^{-}}{\mathrm{D}_i^{+} + \mathrm{D}_i^{-}} \tag{9}$$

When $F_i = 1$, this represents the highest evaluation level; when $F_i = 0$, this represents the lowest evaluation level. On the contrary, this also means the RHSE system construction indicators in Huizhou are closer to the optimal solution.

Combining the characteristics of the entropy weight method and the TOPSIS method to supplement each other's deficiencies and applying them to the construction of a RHES construction assessment system in Huizhou has many advantages. First of all, the entropy weight method is chosen to assign weights to the dimensions to avoid the problem of subjective weighting bias caused by the insufficient understanding of different experts about the environmental governance and the actual development of the region, as well as the problem of insufficient research by HSE scholars on the weights of the evaluation indexes across the urban and rural areas that are unique to Huizhou and the problem of not being able to determine fair weights. Secondly, the choice of using the TOPSIS method was decided based on the reality of rapid and uneven development in Huizhou. Since Huizhou is not only limited to the rural environment and natural geography, its unique cross-rural and urban geographical characteristics make its evaluation objects involve multiple HSE types, and its environmental characteristics are diverse and complex.

At the same time, to analyze the temporal and spatial evolution of the HSE construction in Huizhou, it is necessary to carry out a comprehensive and multi-level study in different regions and years, and entropy weight TOPSIS is chosen based on such a realistic background, considering the complexity of the temporal and spatial changes in the sample data.

4.2. GRA

The gray system theory holds that, in the process of people's cognition of objective things, people cannot fully grasp all information. Rather, they can only grasp part of the known information, and at the same time, they will also encounter some unknown information or uncertainty factors. Therefore, the gray system theory emphasizes the need to consider these unknown or uncertain factors when dealing with and analyzing problems [36] to understand and recognize these problem more objectively and accurately. Among them, an unknown system is known as a gray system. To explore and measure this unknown gray system, a GRA analysis is used to quantitatively describe and compare its development and change dynamics [37].

First, the maximum value $\underset{i}{max}$ and the minimum value $\underset{i}{min}$ of the Huizhou indicator are found. The maximum value $\underset{i}{max}$ and minimum value $\underset{i}{min}$ for all participating indicators in Huizhou are found. The GRA value is obtained for the indicator.

$$S_{ij}^{+} = \frac{\underset{i}{min}\underset{j}{min}\left|c_{ij}^{+} - q_{ij}\right| + \delta \underset{i}{max}\underset{j}{max}\left|c_{ij}^{+} - q_{ij}\right|}{\left|c_{ij}^{+} - q_{ij}\right| + \delta \underset{i}{max}\underset{j}{max}\left|c_{ij}^{+} - q_{ij}\right|} \tag{10}$$

where $\delta = 0.5$ and S_{ij}^{+} is the GRA value of region i with a positive ideal solution indicator about the j participating indicator.

$$S_{ij}^{-} = \frac{\underset{i}{min}\underset{j}{min}\left|c_{ij}^{-} - q_{ij}\right| + \delta \underset{i}{max}\underset{j}{max}\left|c_{ij}^{-} - q_{ij}\right|}{\left|c_{ij}^{-} - q_{ij}\right| + \delta \underset{i}{max}\underset{j}{max}\left|c_{ij}^{-} - q_{ij}\right|} \tag{11}$$

where S_{ij}^{-} is the GRA value of region i with a negative value of the desired resolution index relative to the j participation index.

$$S_{i}^{+} = \frac{1}{n}\sum_{j=1}^{n} S_{ij}^{+} \tag{12}$$

where S_{i}^{+} is the GRA value of the sample with the positive ideal solution.

$$S_{i}^{-} = \frac{1}{n}\sum_{j=1}^{n} S_{ij}^{-} \tag{13}$$

where S_{i}^{-} is the GRA value of the sample with the negative ideal solution.

The research group tries to quantify the relationship between indicators and evaluation targets by using a GRA in the gray system theory. The association between the profiles is the comparative strength of the RHES indicator for the Huizhou region as influenced by the indicators it evaluates. This comprehensive research method can effectively avoid the subjectivity of questionnaire measurement and has good application prospects.

4.3. GIS

A GIS is a technology that can manage, analyze, and present geographic data to help researchers better understand the spatial distribution, characteristics, and changes in the RHES by combining geographic data with attribute data. By using a GIS to explore the RHES in Huizhou, the RHES is studied and analyzed in depth from a geospatial perspective. A more comprehensive understanding of the link between the RHES and geospatial characteristics from holistic and spatialized research perspectives is needed to offer scientific support and references to policy makers and planners.

Researchers use GISs to organize, process, and analyze spatial data collected through a variety of field and remote methods. The data come from a variety of sources, such as satellite remote sensing, mapping data, and social surveys. Through GIS technology, the collected spatial data are analyzed. Visualizing the status of the RHES in Huizhou can help researchers better understand geospatial characteristics and differences. By utilizing the spatial analysis function of a GIS, different spatial data layers can be superimposed to discover the correlation and influence between different geographic elements. For example, the per capita disposable income and RHES quality are overlaid and analyzed to understand the relationship between them.

By collecting, organizing, processing, and analyzing spatial data and using the GIS methodology, the research team has gained a comprehensive understanding of the current

situation and problems of the rural housing system in Huizhou from a geospatial perspective. This approach provides a scientific basis for the government and relevant departments to improve and develop the rural housing system in Huizhou. A GIS is utilized to support evidence-based decision making and provide management references for urban and rural planning, community building, and ecological protection. By integrating and analyzing different spatial data sets, the main strengths and challenges of Huizhou's regional ecological system are clarified, contributing to the sustainable development of the area and the improvement of residents' quality of life.

5. Results

5.1. Horizontal Comparison between Different Regions

In this section, the research team will delve into the performance of different regions in terms of their overall level of construction and how they compare with each other. Horizontal comparison is an important means of understanding the development status of various regions. It not only reveals the construction achievements of individual regions, but also provides the research team with a perspective to assess and analyze the differences in the development of various regions. Through such comparisons, the research team was able to identify the strengths and weaknesses of each region in the development process, thus providing a basis for the formulation of targeted policies and measures.

5.1.1. The Overall Level of Construction in the Huizhou Area

Over the ten-year period from 2013 to 2022, the RHES in the Emblem area shows a significant growth trend. Specifically, this composite index gradually increased from 0.3197 in 2013 to 0.6806 in 2022 (Figure 5). This reflects the continuous improvement of the region in terms of rural habitat.

Overall, the status of the RHES in Huizhou has experienced a fluctuating upward trend and a slight decline in some periods. The trend of change can be subdivided into five main stages, each reflecting different development characteristics and challenges. In the next section, the research team will analyze these stages in detail, explore the influencing factors behind them, and assess how the corresponding policies and measures have contributed to the improvement of the RHES in Huizhou.

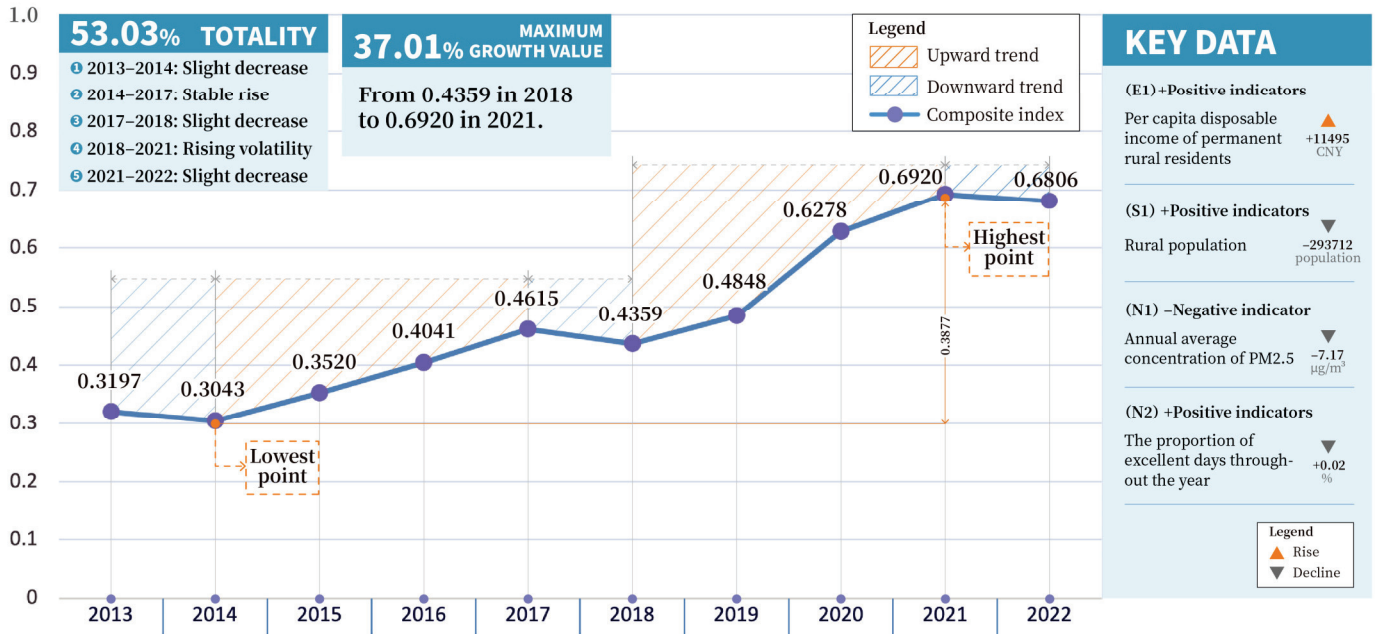

Figure 5. A composite index for the Huizhou region from 2013 to 2022.

In 2013 and 2014, the Huizhou region experienced a slight decline in the Rural Habitat Environment Composite Index (RHES). This downward trend can be attributed to the relatively poor rural environmental infrastructure in the region. The challenge facing Huizhou region is determining how to improve the rural living environment while maintaining the traditional characteristics and features of the countryside. In order to meet this challenge, the local government and community workers have begun to work closely together, relying on the active participation of local residents, to jointly explore a model of good rural construction that is suitable for the Huizhou region.

From 2014 to 2017, the RHES in the Emblem region experienced a steady upward trend. During this period, the composite index increased, but the growth was relatively small. The growth in this phase reflects the effectiveness of the Huizhou region's decision to incorporate the construction of a better countryside into key livelihood projects. The construction of a better countryside in the Huizhou region is also reflected in efforts to build harmonious urban–rural relations. Regional policy makers realized that there should be a complementarity and free flow of resources between urban and rural areas rather than simply transforming the countryside according to the urban model. Guided by this philosophy, Huizhou respects the respective functional positions of urban and rural areas and is committed to realizing the complementarity and overall coordination of urban and rural development.

In 2017 and 2018, the RHES in the Huizhou region experienced a small decline. During this phase, despite the decline in the composite index, this phenomenon also prompted the regions to start paying more attention to the protection and development of the rural environment. Realizing the importance of the rural environment, the Huizhou region began to take measures aimed at restoring and upgrading the quality of the rural habitat. This shift marks a new direction in regional policy and practice, one that places greater emphasis on sustainability and ecological balance.

From 2018 to 2021, the Rural Habitat Environment Composite Index (RHES) of the Huizhou region experienced a fluctuating upward phase. During this period, the Huizhou region placed agriculture and rural development at the forefront of policy planning and firmly implemented a new development concept centered on innovation, coordination, greenness, openness, and sharing. In order to enhance the overall development level of the countryside, the Huizhou region has made reference to the standards of the advanced regions in the Yangtze River Delta and has begun to explore the construction of an advanced demonstration area for rural revitalization.

In 2021 and 2022, there was a small decline in the RHES in Huizhou. This downward trend suggests the complexity of the rural spatial composition, including the mutual integration and harmonization of rural production space, living space, and ecological space [38,39]. At this stage, the Huizhou region faces the challenge of how to balance these three spatial types. To meet this challenge, the Huizhou region insists on the synchronized development of production, living, and ecology. Specifically, the Huizhou region has implemented a series of major ecological and environmental protection projects, taking the construction of a model area for ecological protection and compensation from Xin'anjiang River to Qiandao Lake as an opportunity. Through a variety of efforts, the Huizhou region continues to explore the development path of rural transformation and open up new ways to achieve rural economic development.

5.1.2. Typological Analysis of Different Regions

RHES conservation and socio-economic development are interlinked. The implementation of the RHES requires a large amount of financial investment, including infrastructure construction, environmental management, and agricultural development. The limited financial resources of villages are often unable to fulfill the requirements of comprehensive development, and this shortage of funds has become a major challenge. However, economic development should not be sacrificed for the RHES, and the construction of harmonious villages is more economically sustainable. The research team combined the economic levels

of each area in Huizhou region and divided the zones into different latitudes. Including four kinds, high index–high economy, high index–low economy, low index–high economy, and low index–low economy. These divisions are based on the composite index and rural disposable income per capita. The delineation criteria are that a composite index greater than or equal to 0.4 is considered high ecological security, and a rural per capita disposable income GDP greater than or equal to 16,000 is considered a high economic level. Accordingly, the seven districts (counties) of the Huizhou region are distributed on the map (Figure 6).

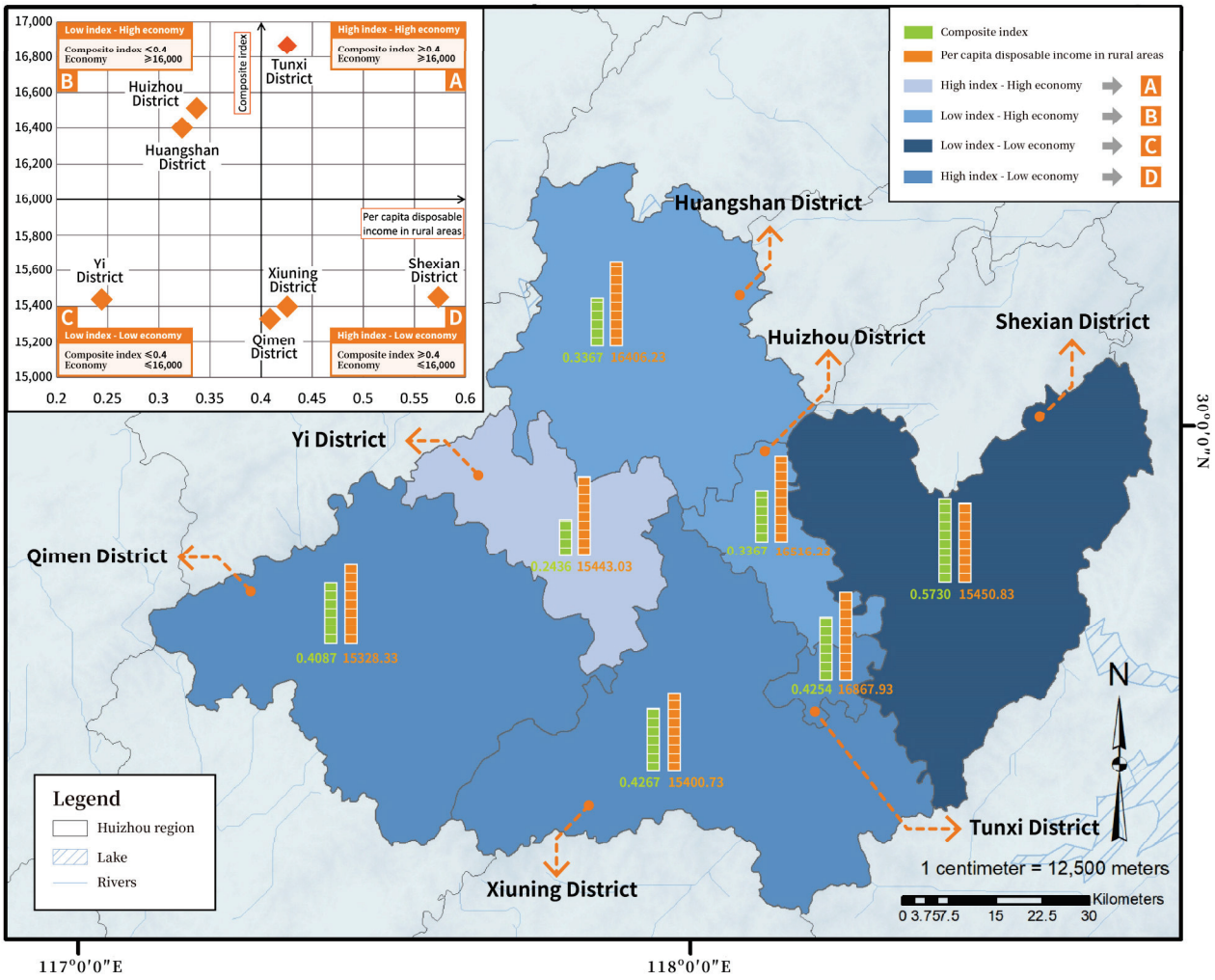

Figure 6. Composite index for Huizhou region from 2013 to 2022.

According to the official website of the Huizhou region, the expert group derived the per capita disposable income of villagers in the Huizhou region (county) in the 2013–2022 period. The per capita disposable income of village inhabitants can be organized in the following order: Tunxi District (16,867.93), Huangshan District (16,406.23), Huizhou District (16,516.23), Shexian County (15,450.83), Xiuning County (15,400.73), Yixian County (15,443.03), and Qimen County (15,328.33). The results show that the Tunxi District belongs to the high index–high economy category. The Shexian, Xiuning, and Qimen counties belong to the high index–low economy category. Huizhou District and Huangshan District belong to the low index–high economy category. Yixian County belongs to the low index–low economy category.

5.1.3. Composite Index for Different Regions

For a more detailed description of the RHES, the composite index of each district in Huizhou was calculated from 2013 to 2022 (Figure 7). Each area (county) showed an increasing trend, and the best RHES conditions were found in Huangshan District based on the following order: Huangshan District (0.2395–0.6809), Huizhou District (0.4205–0.5238), Tunxi District (0.2436–0.1943), Yixian County (0.3039–0.6351), Shexian County (0.4003–0.6189), Qimen County (0.2473–0.5950), and Xiuning County (0.3481–0.6643). An analysis of the comparative vicinity and rank of Huizhou's regions based on the 2013–2022 period is shown below.

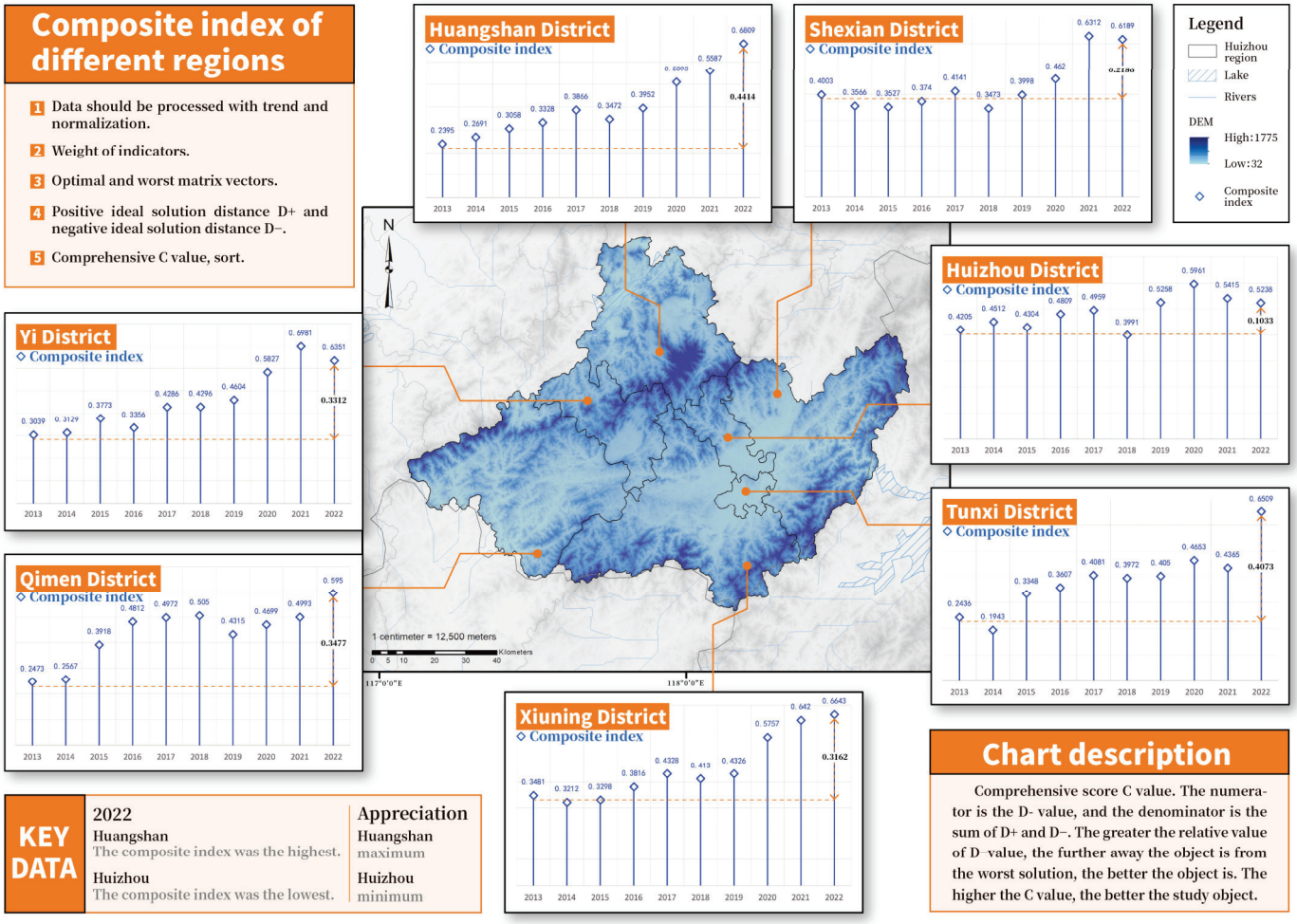

Figure 7. Composite index for different regions.

First, the Huangshan District has the largest ten-year increase, with a difference of 0.4414. Moreover, the composite index for 2022 (0.6809) is the highest among all regions. In 1990, the region's Huangshan Scenic Area was included in the World Heritage List. It is accelerating the promotion of world-class leisure and vacation destinations in Huangshan District and vigorously developing rural tourism. Meanwhile, Huangshan Maofeng and Taiping Houkui are known worldwide as Chinese tea varieties. The Huangshan District supports family farms and farmers' cooperatives and accelerates the cultivation of rural specialty industries. Data from 2023 show that four villages in Huangshan District are on the list of Harmonious Countryside Boutique Demonstration Village Construction. They are the Tangjiazhuang Village in the Jiao Village Township, the Monkey Pit Village in the Xinming Township, the Shanqiao Village in the Tangkou Township, and the Ferry Village in the Longmen Township. Taking Xinming Township in Huangshan District as

an example, the Xinming Village has clean and tidy village roads and increasingly perfect supporting facilities.

Second, the province with the greatest number of provinces sorted in the first place is Huizhou District. Huizhou District ranks first with overall indexes of 0.4205, 0.4512, 0.4304, 0.5258, and 0.5961 in 2013, 2014, 2015, 2019, and 2020, respectively. The main reason for this may be that Huizhou District has a forest coverage rate of 76.24%, and the Fengle River of the Xin'an River runs through the north and south, which gives it a good natural environment advantage. At the same time, Huizhou District has refined its construction, and now there are seven fine demonstration villages of the Hemei Countryside. Among them, there are three at the provincial level and four at the municipal level. However, since 2021, the RHES index of the Huizhou District has shown a decreasing trend. There are more than 300 ancient Huizhou-style buildings preserved in Huizhou District. Huizhou-style dwellings have the problems of summer heat and winter cold, especially the dilemma of high humidity, which aggravates the ecological pressure in Huizhou District. This suggests that developing an effective compensation mechanism for the residential environment in Huizhou District appears to be very necessary.

Third, Tunxi District and Shexian County rank relatively low on the composite index. The composite index of these two districts has been low in the time dimension. Although Tunxi District is not as rich and colorful as Huangshan District in terms of scenic spots, the local area possesses a profound history and culture. A total of 197 items of intangible cultural heritage exists in the district, covering a wide range of fields. Among them, the Cheng Da Bit bead algorithm has been awarded the list of Intangible Cultural Heritage of Humanity by UNESCO. Tunxi District should be evaluated based on local characteristics and regional features and adhere to cultural resources as a carrier, strengthening the integrated development of farming, culture, and transportation and cultivating new brands with influence. Second, the governance system in rural areas of Shexian is relatively weak, bringing obstacles. It is necessary to improve the basic supporting facilities and upgrade the levels of education, medicine, pension, culture, sports, and other public services.

5.2. Longitudinal Comparison between Years

By combining the data, the comprehensive score index of the Huizhou region was calculated for 2013, 2014, 2021, and 2022 (Figure 8). Using the ArcGIS software, the RHES index was divided into five levels. The overall state of the Huizhou region has been improved smoothly. Most of the districts (counties) have been improved, and the Huangshan District has the best status. As before, Huangshan District shows an upward trend, improving from 0.2558 to 0.3847. The rural conditions of the Qimen and Huining counties in 2022 have declined since 2013. Rural areas face problems of low quality and insufficient resources. The remaining five districts (counties) gradually improved. Therefore, the Qimen and Xiuning counties should strengthen their rural resource management, improve their levels of rural operation, and effectively supplement ecological resources.

First, Yixian County's per capita disposable income (E1) rankings for rural residents are of the "low index–low economy" double-low type. On the economic front, the rising prices of agricultural fertilizers and seeds have increased the cost of agricultural production and dampened farmers' incentive to grow food. In the social aspect, most of the young people in the countryside go out to work, and the labor force at home for farming is weak. Expanding production and quality improvement are difficult to realize. In terms of natural ecology, the strong development of the lodging industry and the dilution of the concept of environmental protection by most operators of ecological protection have brought potential damage to the ecological environment of the villages.

Secondly, regarding the rankings of the disposable income per capita of rural residents (E1), Qimen County ranked back but belongs to the "high index–low economic" type according to their agricultural resource advantages and development status. The development of the green food industry is an essential way to transform the mode of agricultural growth and promote the county's farmers to achieve sustained and rapid

income growth. In summary, from 2013 to 2022, Huizhou's regional economic integration increased significantly, but there remain variations among the regions (counties).

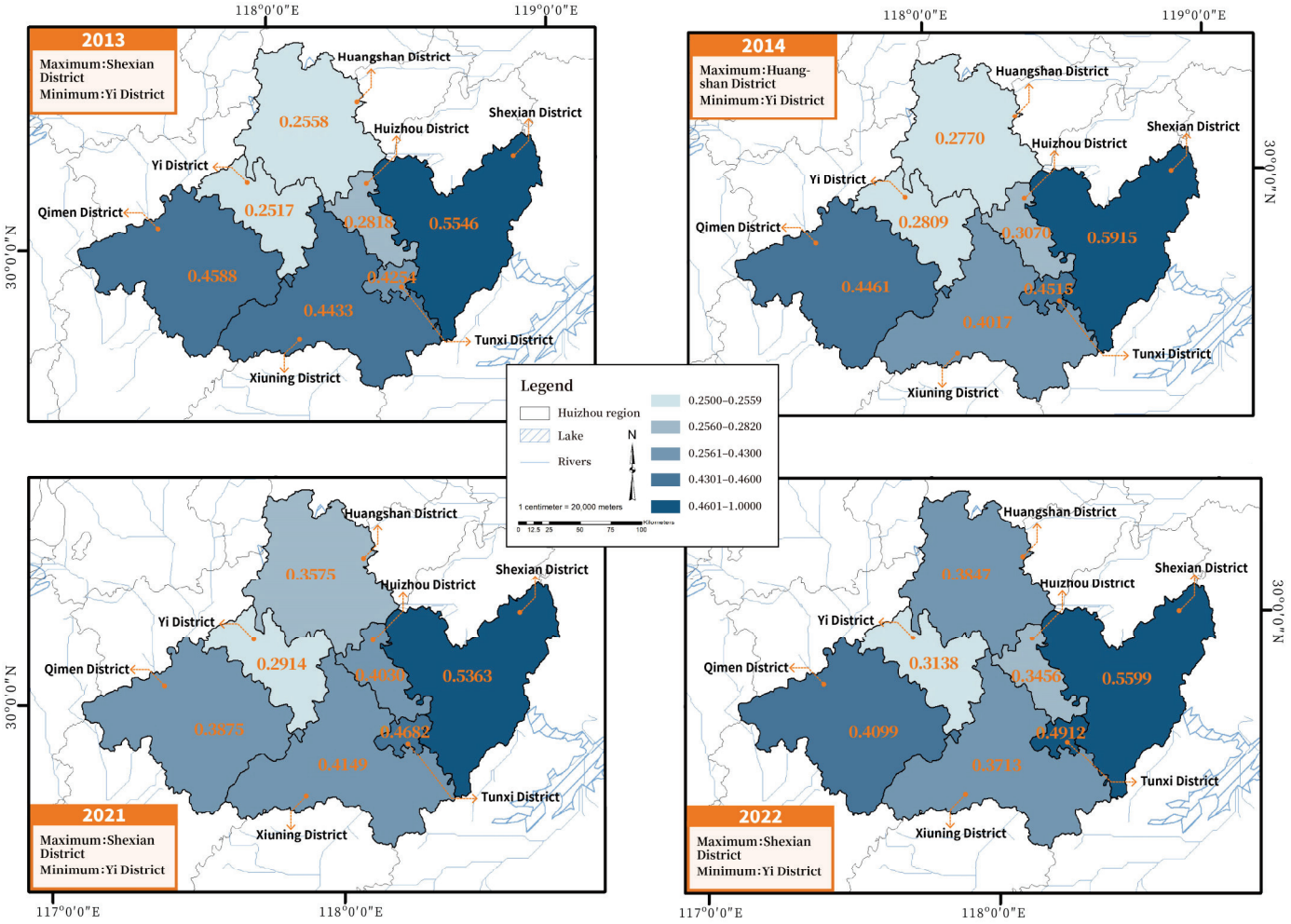

Figure 8. Spatial distribution of RHES in Huizhou in 2013–2022 period.

5.3. Comparison of Different Indicators Relative to Each Other

GRA is founded on the geometrical similarity between the evaluating units and the orthogonal and antithetical "ideal solutions". The research team utilized GRA to rank the three criteria layers and 18 indicator correlations of the RHES in Huizhou. This helped them determine the extent of impact of each index on the study population (Figure 9).

According to the summary table for the Huizhou region, the factors with higher-than-average values on the regional RHES were mainly the natural ecosystem (NCE) and the social development system (S). The top five rankings of the degree of effect are, in descending order, N6 (0.993), N3 (0.991), N2 (0.989), S2 (0.988), and N5 (0.984). Among them, four indicators are out of the natural ecosystem. Realizing the abundance of rural industries and improving the rural ecological environment are the key ways to enhance the Huizhou region.

In recent years, the villages in the Huizhou region have seized the opportunity to tap their own characteristic elements and strengthen creative planning. At the same time, they continued to enrich the product industry and innovate the product system, and they have transformed the beautiful scenery into a beautiful economy. Located in the south of China's Anhui Province, the Huizhou region is an area full of historical flavor and natural beauty. It not only has deep cultural heritage, but also many natural landscapes that attract tourists. Huangshan Mountain, one of the ten most famous mountains in

China, is famous for its stunning scenery. It is both majestic and magnificent, as well as delicate and soft. Hongcun, known as "the countryside in Chinese paintings", is famous for its unique Huizhou architecture and beautiful natural scenery. Hongcun, known as the countryside in Chinese painting, is famous for its unique Huizhou architecture and beautiful natural scenery.

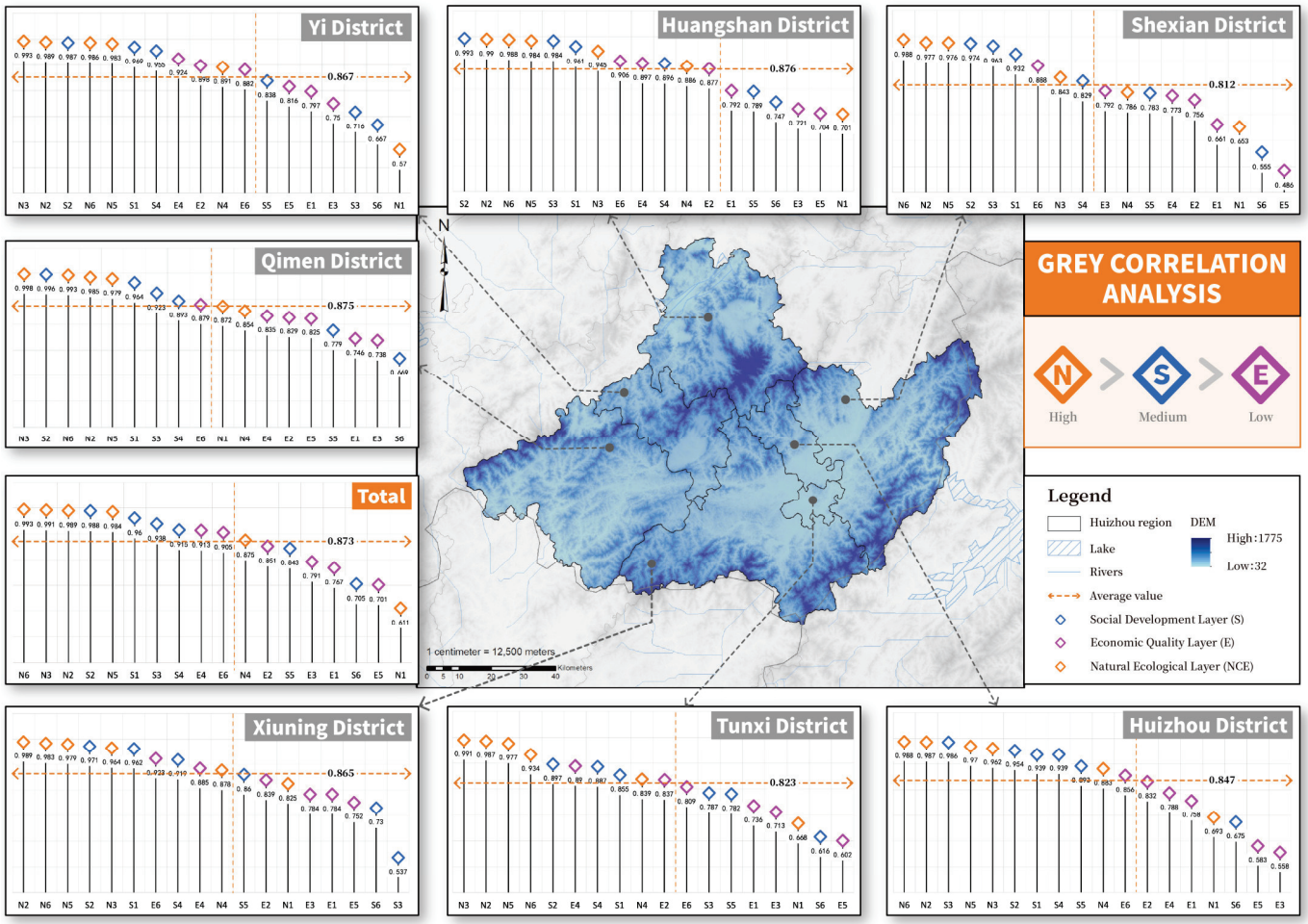

Figure 9. Ranking of evaluation indicators based on level of impact.

6. Discussion

In the assessment of the carrying level, the RHES status of the Huizhou region shows a slight downward trend after a fluctuating increase. Overall, the RHES development level from 2013 to 2022 can be specifically categorized into five stages: small decline stage (2013 to 2014), stable rise stage (2014 to 2017), small decline stage (2017 to 2018), fluctuating rise stage (2018 to 2021), and small decline stage (2021 to 2022). At the local level, the seven districts (counties) are categorized into four types based on the composite index and rural disposable income per capita. Tunxi District belongs to the high index–high economy category. The Shexian, Xiuning, and Qimen counties belong to the high index–low economy category. Huizhou District and Huangshan District belong to the low index–high economy category. Yixian County belongs to the low index–low economy category.

Through an in-depth analysis of the composite indices of different regions, this study found that the RHES of all districts (counties) showed an upward trend, with Huangshan District's performance being particularly outstanding. This achievement is attributed to the fact that Huangshan District has taken the creation of the National Rural Revitalization Demonstration County as an opportunity to strengthen systematic planning. Analyzed from a time-series perspective, the overall RHES status of the Huizhou region shows a

steady upward trend. Although most of the districts (counties) have made progress, Tunxi District and Shexian County are still deficient in the RHES. This study not only emphasizes the excellent practice of Huangshan District in China's rural construction, but also points out the deficiencies in infrastructure in other districts (counties), thus providing specific policy recommendations for rural revitalization in Huizhou. These findings fit with the national rural revitalization strategy and provide lessons to be learned for other regions.

Among the effector associations, the natural ecosystem (NCE) was the most dominant effector in Huizhou. N6 (0.993), N3 (0.991), and N2 (0.989) played strong roles in influencing the RHES in Huizhou. Similar studies have found that natural factors influence changes in the countryside [40]. In addition, according to the degree of impact of the evaluation indicators in Figure 9, the average value of each research object in the Huizhou region is above 0.8. Overall, this study reveals that the enhancement of the RHES in the Huizhou region requires more than surface-level improvements and should delve deeper into the level of cultural and historical heritage preservation. This study emphasizes the importance of whole-village preservation and the development of traditional villages, which not only echoes China's national policy on cultural heritage preservation but also provides a viable model for other regions with similar historical backgrounds.

7. Conclusions

The RHES is an integral part of the urban–rural composite HES system and a synthesis of human–land relations in the countryside. This refers to the function of maintaining the integral blend of physical and non-physical structures required for the activities of village dwellers. Based on the composite ecosystem–SENCE conceptual framework, the research team explored the degree of relevance of the indicators through a comprehensive assessment of the Huizhou region for the period of 2012–2021. The complexity and uncertainty of the RHES system were considered to make the assessment results more science-based and rational. Taking seven districts (counties) in Huizhou region as the research objects, entropy weight TOPSIS was applied and combined with GRA to judge the key effect factors. The results can offer a decision-making basis for the stable use and science-based administration of rural renewable energy systems and to promote the stable development of rural integration.

(1) Harmonious villages are villages with "livable" environments and basically modern living conditions. At present, the rural society in Huizhou is in a period of profound change and adjustment. The level of basic living facilities and public services in rural areas has been continuously upgraded. Rural roads and logistics and other infrastructure are complete. The level of public services, for example, education, health care, and pensions, is close to that of the cities. Some rural areas have experienced some decline. The trend of population aging is obvious, and the hollowing out phenomenon also exists, to a certain extent, in the countryside. Considering the development patterns of different types of villages, the focus is on upgrading the shortcomings of inadequate infrastructure and public services in accordance with local conditions.

(2) Harmonious villages are villages in which development is "workable". We innovated the operation system for utilizing the resources of traditional villages and are actively exploring the operation mechanism of "one platform management, multiple main body operation" for building, sharing, and enrichment. Xidi and Hongcun adopted a differentiated development strategy relying on the richness of ancient residential resources and preserving the work of the villages. The village's layout allows for a variety of experiential, interactive activities that can benefit the tourism industry, and sightseeing is free of charge. For example, the Huimo Ink Production Experience Center was built and put into operation. It attracts more than 30,000 researchers every year. It actively mobilizes rural agricultural workers to seek employment and entrepreneurship in their hometowns, attracting nearly 100 people to return to their hometowns to engage in catering, tourism, construction, and other service industries.

(3) Harmonious villages are villages that live "harmoniously" and have a stable and harmonious social environment. Villages integrate production, living, and ecological functions and have distinctive village styles. They need to be developed based on the regional characteristics of the countryside and be integrated with the natural ecology. They must also adhere to the strictest ecological protection system with the goal of improving the ecological security pattern; consider industrial development, population layout, public services, land use, and ecological protection in an integrated manner; plan the spatial distribution and building of agricultural production and living facilities in a scientific and rational manner; preserve outstanding traditional vernacular culture; and promote the integration and development of traditional vernacular culture with modern civilization.

This study provides an in-depth assessment of the RHES in Huizhou by analyzing the HSE index. However, well-being is a multidimensional concept, and its comprehensive assessment needs to consider a wider range of factors. Although this study involves the natural ecosystem subsystem (NCE), it still has shortcomings. Future work will explore the effects of biodiversity and cultural identity on the well-being of residents and determine how rural residential environments can be enhanced through the protection and enhancement of native ecosystems. These factors will be incorporated into rural development strategies as recommended by the United Nations Convention on Biological Diversity (CBD).

Author Contributions: Conceptualization, Yanlong Guo and Xingmeng Ma; methodology, Xin Su and Linfu Zhang; software, Xingmeng Ma; validation, Xingmeng Ma and Yanlong Guo; formal analysis, Yanlong Guo; investigation, Xin Su and Yanlong Guo; resources, Yanlong Guo; data curation, Linfu Zhang; writing—original draft preparation, Yanlong Guo and Xingmeng Ma; writing—review, Yanlong Guo; editing, Linfu Zhang; visualization, Xingmeng Ma; supervision, Yanlong Guo; project administration, Yanlong Guo. All authors have read and agreed to the published version of the manuscript.

Funding: This study obtained the research topic of Anhui Province's social science innovation and development from the study titled "Study on the Driving factors of living and Working Conditions in Huizhou Area and the American Countryside" (2023CX137) and the study by the Huizhou Ancient Village Digital Protection and Inheritance of Creativity, Anhui Province Key Laboratory, titled "Huizhou Ancient Village Digital creative Product Design under the Background of Cultural and Tourism Integration" (PA2023GDSK0118). This study was also supported by the Anhui Provincial Research Planning Project titled "Research on Living Conservation Mode of Huizhou Cultural and Ecological Protection Area" (2022AH050038).

Data Availability Statement: The experimental data used to support the findings of this study are included in the article.

Conflicts of Interest: The authors declare no conflicts of interest.

References

1. Wang, Y.; Zhu, Y. Exploring the Effects of Rural Human Settlement on Rural Development: Evidence from Xianju County in Zhejiang Province, China. *Environ. Dev.* **2023**, *16*, 100845. [CrossRef]
2. Zhang, T.; He, D.; Kuang, T.; Chen, K. Effect of Rural Human Settlement Environment around Nature Reserves on Farmers' Well-Being: A Field Survey Based on 1002 Farmer Households around Six Nature Reserves in China. *Int. J. Environ. Res. Public Health* **2022**, *19*, 6447. [CrossRef]
3. Dou, H.; Ma, L.; Li, H.; Bo, J.; Fang, F. Impact Evaluation and Driving Type Identification of Human Factors on Rural Human Settlement Environment: Taking Gansu Province, China as an Example. *Open Geosci.* **2020**, *12*, 1324–1337. [CrossRef]
4. Sanchez, T.W.; Ye, X. The Implications of Human Mobility and Accessibility for Transportation and Livable Cities. *Urban Sci.* **2023**, *7*, 107. [CrossRef]
5. Zhang, H.; Cong, R.; Luan, S. Utilization Quality Evaluation and Barrier Factor Diagnosis of Rural Residential Areas in Agricultural Regions of the Northeast Plain: A Case Study of Wangkui County, Heilongjiang Province, China. *Land* **2023**, *12*, 870. [CrossRef]
6. Yan, Z.; Peng, L.; Wu, X. Evaluation System for Agricultural and Rural Modernization in China. *Agriculture* **2023**, *13*, 1930. [CrossRef]

7. Santilli, S.; Valbusa, I.; Rinaldi, B.; Ginevra, M.C. Life Satisfaction, Courage, and Career Adaptability in a Group of Italian Workers. *Soc. Sci.* **2024**, *13*, 106. [CrossRef]
8. Yao, Q.; An, N.; Gu, G.; Yang, E.; Yang, H.; Li, C.; Yan, K. Research Progress on Features and Characteristics of Rural Settlements: Literature Distribution, Key Issues, and Development Trends. *Buildings* **2023**, *13*, 2457. [CrossRef]
9. Hidalgo-Fuentes, S.; Martínez-Álvarez, I.; Sospedra-Baeza, M.J.; Martí-Vilar, M.; Merino-Soto, C.; Toledano-Toledano, F. Emotional Intelligence and Perceived Social Support: Its Relationship with Subjective Well-Being. *Healthcare* **2024**, *12*, 634. [CrossRef]
10. Han, Y.; Huang, J. Evolution of Social Welfare in Rural China: A Developmental Approach. *Int. Soc. Work* **2019**, *62*, 390–404. [CrossRef]
11. Jiang, S.; Ma, H.; Yang, L.; Luo, S. The Influence of Perceived Physical and Aesthetic Quality of Rural Settlements on Tourists' Preferences—A Case Study of Zhaoxing Dong Village. *Land* **2023**, *12*, 1542. [CrossRef]
12. Beltramo, R.; Peira, G.; Pasino, G.; Bonadonna, A. Quality of Life in Rural Areas: A Set of Indicators for Improving Wellbeing. *Sustainability* **2024**, *16*, 1804. [CrossRef]
13. Zhou, F.; Guo, X.; Liu, C.; Ma, Q.; Guo, S. Analysis on the Influencing Factors of Rural Infrastructure in China. *Agriculture* **2023**, *13*, 986. [CrossRef]
14. Shi, B.; Liu, H.; Huang, L.; Zhang, Y.; Xiang, Z. Increasing Vulnerability of Village Heritage: Evidence from 123 Villages in Aba Prefecture, Sichuan, China. *Land* **2023**, *12*, 2048. [CrossRef]
15. Simandan, D. Being Surprised and Surprising Ourselves: A Geography of Personal and Social Change: A Geography of Personal and Social Change. *Prog. Hum. Geogr.* **2020**, *44*, 99–118. [CrossRef] [PubMed]
16. Smith, T.S.J.; Reid, L. Which 'Being' in Wellbeing? Ontology, Wellness and the Geographies of Happiness. *Prog. Hum. Geogr.* **2018**, *42*, 807–829. [CrossRef]
17. Welch-White, V.; Langan, R. Co-Ops Advocate for Rural Infrastructure: At Capitol Hearing, Co-Op Leaders Address Critical Need for Modern Infrastructure. *N. Y. For. Own.* **2017**, *55*, 12–17.
18. Wang, Y.; Zhao, Z.; Xu, M.; Tan, Z.; Han, J.; Zhang, L.; Chen, S. Agriculture–Tourism Integration's Impact on Agricultural Green Productivity in China. *Agriculture* **2023**, *13*, 1941. [CrossRef]
19. Bigiotti, S.; Costantino, C.; Marucci, A. Agritourism Facilities in the Era of the Green Economy: A Combined Energy Audit and Life Cycle Assessment Approach for the Sustainable Regeneration of Rural Structures. *Energies* **2024**, *17*, 1101. [CrossRef]
20. Yang, Y.; Wang, K.; Zhou, D.; Wang, Y.; Zhang, Q.; Xu, D. Improvement of Human Comfort in Rural Cave Dwellings via Sunrooms in Cold Regions of China. *Buildings* **2024**, *14*, 734. [CrossRef]
21. Meng, J.; Yang, L.; Lei, H. Promoting Elderly Care Sustainability by Smart Village Facilities Integration—Construction of a Public Service Field with Introduction of Fall Posture Monitoring. *Buildings* **2023**, *13*, 2144. [CrossRef]
22. Kuczman, G.; Bechera, D.; Rózová, Z.; Tóth, A. Roadside Vegetation Functions, Woody Plant Values, and Ecosystem Services in Rural Streetscapes: A Qualitative Study on Rural Settlements in Western Slovakia. *Land* **2024**, *13*, 272. [CrossRef]
23. Zuo, Y.; Yang, C.; Xin, G.; Wu, Y.; Chen, R. Driving Mechanism of Comprehensive Land Consolidation on Urban–Rural Development Elements Integration. *Land* **2023**, *12*, 2037. [CrossRef]
24. Dai, X.; Zhang, J.; Sun, X.; Li, J.; Liu, B. Differentiation Governance of Rural Human Settlement Environments in China: Knowledge Mapping and Visualization. *Int. J. Environ. Res. Public Health* **2023**, *20*, 4209. [CrossRef] [PubMed]
25. Hu, Q.; Wang, C. Quality Evaluation and Division of Regional Types of Rural Human Settlements in China. *Habitat Int.* **2020**, *105*, 102278. [CrossRef]
26. Tong, S.; Zhu, Y.; Li, Z. Correlation Study between Rural Human Settlement Health Factors: A Case Study of Xiangxi, China. *Comput. Intell. Neurosci.* **2022**, *2022*, 2484850. [CrossRef] [PubMed]
27. Bian, D.; Yang, X.; Wu, F.; Babuna, P.; Luo, Y.; Wang, B.; Chen, Y. A Three-Stage Hybrid Model Investigating Regional Evaluation, Pattern Analysis and Obstruction Factor Analysis for Water Resource Spatial Equilibrium in China. *J. Clean. Prod.* **2022**, *331*, 129940. [CrossRef]
28. Zhu, S.; Feng, H.; Shao, Q. Evaluating Urban Flood Resilience within the Social-Economic-Natural Complex Ecosystem: A Case Study of Cities in the Yangtze River Delta. *Land* **2023**, *12*, 1200. [CrossRef]
29. Tai, X.; Xiao, W.; Tang, Y. A Quantitative Assessment of Vulnerability Using Social-Economic-Natural Compound Ecosystem Framework in Coal Mining Cities. *J. Clean. Prod.* **2020**, *258*, 120969. [CrossRef]
30. Jin, C.; Guan, Q.; Gong, L.; Zhou, Y.; Ji, Z. Evaluation of Regional Water Environmental Carrying Capacity and Diagnosis of Obstacle Factors Based on UMT Model. *Water* **2022**, *14*, 2621. [CrossRef]
31. Pan, Y.; An, Z.; Wang, J.; Weng, G. Dynamic Evolution Characteristics and Drivers of Tourism-Related Ecological Security in the Beijing–Tianjin–Hebei Region. *Systems* **2023**, *11*, 533. [CrossRef]
32. Zhao, H.; Li, J. Energy Efficiency Evaluation and Optimization of Industrial Park Customers Based on PSR Model and Improved Grey-TOPSIS Method. *IEEE Access* **2021**, *9*, 76423–76432. [CrossRef]
33. Zhang, Y.; Zhang, J.; Li, Y.; Liang, S.; Chen, W.; Dai, Y. Revealing the Spatial-Temporal Evolution and Obstacles of Ecological Security in the Xiamen-Zhangzhou-Quanzhou Region, China. *Land* **2024**, *13*, 339. [CrossRef]
34. Wei, H.; Gao, Y.; Han, Q.; Li, L.; Dong, X.; Liu, M.; Meng, Q. Quality Evaluation and Obstacle Identification of Human Settlements in the Qinghai–Tibet Plateau Based on Multi-Source Data. *Land* **2022**, *11*, 1479. [CrossRef]
35. Lin, S.; Hou, L. SDGs-Oriented Evaluation of the Sustainability of Rural Human Settlement Environment in Zhejiang, China. *Heliyon* **2023**, *9*, e13492. [CrossRef] [PubMed]

36. Rehman, A.U.; AlFaify, A.Y. Evaluating Industry 4.0 Manufacturing Configurations: An Entropy-Based Grey Relational Analysis Approach. *Processes* **2023**, *11*, 3151. [CrossRef]
37. Chen, Z.; Zhang, C.; Raza, S.T. Evaluation of Forest Ecological Security and Its Influencing Factors in Multi-Climatic Zones: A Case Study of Yunnan Province. *Appl. Sci.* **2023**, *13*, 12345. [CrossRef]
38. Bi, G.; Yang, Q. Spatial Reconstruction of Rural Settlements Based on Multidimensional Suitability: A Case Study of Pingba Village, China. *Land* **2022**, *11*, 1299. [CrossRef]
39. Zhang, Z.; Fang, B.; Li, X.; Wang, Y. Evaluation of Human Settlement Environment and Identification of Development Barriers Based on the Ecological Niche Theory: A Case Study of Northern Shaanxi, China. *Int. J. Environ. Res. Public Health* **2023**, *20*, 1772. [CrossRef]
40. Yu, L.; Xie, D.; Xu, X. Environmental Suitability Evaluation for Human Settlements of Rural Residential Areas in Hengshui, Hebei Province. *Land* **2022**, *11*, 2112. [CrossRef]

Disclaimer/Publisher's Note: The statements, opinions and data contained in all publications are solely those of the individual author(s) and contributor(s) and not of MDPI and/or the editor(s). MDPI and/or the editor(s) disclaim responsibility for any injury to people or property resulting from any ideas, methods, instructions or products referred to in the content.

remote sensing

MDPI

Article

The Performance of Landsat-8 and Landsat-9 Data for Water Body Extraction Based on Various Water Indices: A Comparative Analysis

Jie Chen [1,†], Yankun Wang [2,†], Jingzhe Wang [1,3,*], Yinghui Zhang [4], Yue Xu [5], Ou Yang [1,3], Rui Zhang [6], Jing Wang [7], Zhensheng Wang [8], Feidong Lu [9] and Zhongwen Hu [4]

1 Institute of Applied Artificial Intelligence of the Guangdong-Hong Kong-Macao Greater Bay Area, Shenzhen Polytechnic University, Shenzhen 518055, China; 2022220206@jou.edu.cn (J.C.); yangou@szpu.edu.cn (O.Y.)
2 Internet of Things Research Institute, Shenzhen Polytechnic University, Shenzhen 518055, China; wyk20210152@szpu.edu.cn
3 School of Artificial Intelligence, Shenzhen Polytechnic University, Shenzhen 518055, China
4 MNR Key Laboratory for Geo-Environmental Monitoring of Great Bay Area & Guangdong Key Laboratory of Urban Informatics & Guangdong-Hong Kong-Macau Joint Laboratory for Smart Cities & Shenzhen Key Laboratory of Spatial Smart Sensing and Services, Shenzhen University, Shenzhen 518060, China; zyhui@szu.edu.cn (Y.Z.); zwhoo@szu.edu.cn (Z.H.)
5 College of Urban and Environmental Sciences, Central China Normal University, Wuhan 430079, China; xuyue2022010474@mails.ccnu.edu.cn
6 School of Marine Technology and Geomatics, Jiangsu Ocean University, Lianyungang 222005, China; rzhang@jou.edu.cn
7 Vanke School of Public Health, Tsinghua University, Beijing 100091, China; jingjing0330@mail.tsinghua.edu.cn
8 Department of Strategic and Advanced Interdisciplinary Research, Peng Cheng Laboratory, Shenzhen 518000, China; wangzhsh@pcl.ac.cn
9 Tongji Architectural Design (Group) Co., Ltd., Shanghai 200092, China; feidonglu@tongji.edu.cn
* Correspondence: jzwang@szpu.edu.cn
† These authors contributed equally to this work.

Abstract: The rapid and accurate extraction of water information from satellite imagery has been a crucial topic in remote sensing applications and has important value in water resources management, water environment monitoring, and disaster emergency management. Although the OLI-2 sensor onboard Landsat-9 is similar to the well-known OLI onboard Landsat-8, there were significant differences in the average absolute percentage change in the bands for water detection. Additionally, the performance of Landsat-9 in water body extraction is yet to be fully understood. Therefore, it is crucial to conduct comparative studies to evaluate the water extraction performance of Landsat-9 with Landsat-8. In this study, we analyze the performance of simultaneous Landsat-8 and Landsat-9 data for water body extraction based on eight common water indices (Normalized Difference Water Index (NDWI) and Modified Normalized Difference Water Index (MNDWI), Augmented Normalized Difference Water Index (ANDWI), Water Index 2015 (WI_{2015}), tasseled cap wetness index (TCW), Automated Water Extraction Index for scenes with shadows ($AWEI_{sh}$) and without shadows ($AWEI_{nsh}$) and Multi-Band Water Index (MBWI)) to extract water bodies in seven study sites worldwide. The Otsu algorithm is utilized to automatically determine the optimal segmentation threshold for water body extraction. The results showed that (1) Landsat-9 satellite data can be used for water body extraction effectively, with results consistent with those from Landsat-8. The eight selected water indices in this study are applicable to both Landsat-8 and Landsat-9 satellites. (2) The NDWI index shows a larger variability in accuracy compared to other indices when used on Landsat-8 and Landsat-9 imagery. Therefore, additional caution should be exercised when using the NDWI for water body analysis with both Landsat-8 and Landsat-9 satellites simultaneously. (3) For Landsat-8 and Landsat-9 imagery, ratio-based water indices tend to have more omission errors, while difference-based indices are more prone to commission errors. Overall, ratio-based indices exhibit greater variability in overall accuracy, whereas difference-based indices demonstrate lower sensitivity to variations in the study area, showing smaller overall accuracy fluctuations and higher robustness. This study can provide necessary references for the selection of water indices based on the newest

Landsat-9 data. The results are crucial for guiding the combined use of Landsat-8 and Landsat-9 for global surface water mapping and understanding its long-term changes.

Keywords: water extraction; water index; Landsat-8 OLI; Landsat-9 OLI-2; remote sensing; comparative analysis

1. Introduction

Surface water, a vital component of Earth's environmental system, plays a significant role in supporting human productivity and providing immense environmental and ecological benefits [1,2]. However, the rapid and substantial fluctuations in these water bodies, driven by climatic change and human activities, have led to a series of detrimental water-related phenomena, including water scarcity, flooding, and pollution [3–7]. The importance of accurately identifying the dynamic changes in water bodies is undisputed. Correspondingly, it has emerged as an enduring research hotspot over recent decades [8,9]. This research theme not only aids in understanding and predicting the impacts of water body changes on the environment and society but also provides a framework for more effective management and protection of our water resources [10,11]. Therefore, it is of great significance to continue delving into this topic to better understand and manage global water resources.

Remote sensing technology offers a powerful tool for the large-scale, long-term monitoring of water bodies [1,12]. Its advantages include rapid, wide-area, and periodic imaging capabilities, which are invaluable for tracking dynamic changes in water bodies over time [13]. Several multispectral satellites have been extensively used for water body extraction. These include the Landsat series, MODIS, Sentinel-2, and Chinese Gaofen series [1,14–17]. These satellites provide rich spectral information, broad swath coverage, and short revisit periods, making them ideal for mapping large-scale surface water. Among these, the Landsat series satellites, launched by the United States for civilian land resource monitoring, has played a pivotal role in water body remote sensing research [18]. Their extensive temporal coverage, dating back to 1972 with the launch of Landsat-1 (also known as ERTS-1), have provided invaluable data for studying long-term changes in water bodies [19,20]. The latest addition to this series, Landsat-9, was launched in September 2021 as the successor to Landsat-8. The Operational Land Imager-2 (OLI-2) onboard Landsat-9 is largely identical to the Landsat-8 onboard OLI, offering calibrated imagery covering the solar-reflected wavelengths [21,22]. However, the performance of Landsat-9 in water body extraction is yet to be fully understood. Therefore, it is crucial to conduct comparative studies to evaluate the water extraction performance of Landsat-9 with its predecessor.

There exists a broad spectrum of methodologies designed for water body extraction based on medium-resolution optical satellite imagery [23,24]. These include pixel-level classification methods such as single-band thresholding segmentation, multi-band spectral relationship analysis, water index methods, and supervised classification methods (including popular machine learning and deep learning techniques) [10,25]. Object-level classification methods, such as object-based image analysis, are also employed [26]. Among these, the water index method stands out due to its simplicity and ease of use, making it a popular choice for large-scale or long-term water body extraction [27]. The water index method is grounded in the analysis of spectral characteristics of water bodies. It involves the selection of spectral bands closely associated with water body identification [28,29]. Through simple mathematical operations and the application of appropriate thresholds, this method facilitates the extraction of water body information. This approach leverages the unique spectral signatures of water bodies to distinguish them from other features in a landscape, providing a straightforward and effective means of water body extraction [30]. A variety of prominent water indices have been developed, including Normalized Difference Water Index (NDWI) [31], Modification of Normalized Difference Water Index

(MNDWI) [32], Automated Water Extraction Index (AWEI) [28], Multi-Band Water Index (MBWI) [33], Water Index 2015 (WI_{2015}) [34], Augmented Normalized Difference Water Index (ANDWI) [35] and Tasseled Cap Transformation (TCT) [36]. Existed publications have demonstrated their exceptional performance in water body extraction [1,5,16,37,38]. At present, whether at regional, national, or global scales, water body identification and mapping are inseparable from remote sensing water index methods. However, these indices were developed based on various existing remote sensing data, such as Landsat MSS, TM, ETM+, and OLI and other multi-spectral remotely sensed imagery. Therefore, it is crucial to analyze their applicability to new sensors, i.e., the OLI-2 sensor onboard Landsat-9.

The launch of the Landsat-9 satellite marks the start of a new era for the Landsat series. Compared to the Operational Land Imager (OLI) on Landsat-8, the OLI-2 on Landsat-9, while similar in terms of band configuration to its predecessor, has seen improvements in spectral response characterization and radiometric resolution [21,22]. Since the launch of Landsat-9, there have been some cross-comparisons of data from Landsat-8 and Landsat-9. Xu et al. [39] found that the surface reflectance data from Landsat-8 and Landsat-9 are almost consistent. However, there were significant differences in the average absolute percentage change in the bands for water detection [40,41]. It remains uncertain whether this deviation will be amplified in the calculation of water indices. This underscores the need for further research to fully understand the implications of these differences for water body extraction using Landsat-9 data. Consequently, it is urgent to conduct a systematic analysis of the performance of water body extraction based on Landsat-9 satellite imagery and a global comparison with the currently most widely used satellite in the Landsat series, i.e., Landsat-8. Our research aims to evaluate the differences between Landsat-9 and its predecessors, particularly in terms of water body extraction. This is crucial for assessing whether Landsat-9 can succeed Landsat-8 in continuing Earth observations, sensing global water resource dynamics, and supporting the achievement of sustainable development goals (SDGs).

Specifically, this study aims to compare the performance of multiple water indices for water extraction based on Landsat-8 and Landsat-9 datasets. Based on almost simultaneous Landsat-8 and Landsat-9 data, we employed eight common water indices to extract water bodies in seven study sites worldwide and further analyzed the application of water indices based on Landsat-9. This study aims to answer the following questions: (1) Are water indices applicable to Landsat-8 also applicable to Landsat-9? (2) Are there any differences in water extraction performance between Landsat-9 and Landsat-8? (3) Are Landsat-9 better in water extraction compared to Landsat-8? These results can guide our exploration of the capabilities and potential of the new Landsat-9 satellite in the field of remote sensing for water body extraction.

2. Study Areas and Data Source

2.1. Study Area

To ensure a rigorous and representative comparative analysis, the variations in remote sensing image acquisition times, elevation, climate, terrain, vegetation cover types, and geological features were carefully considered. A total of seven test sites (Mille Lacs Lake, Lake Nipissing, the Tongling section of the Yangtze River, Lianhuan Lake, Sai Lake, Liangzi Lake, and Lake Wivenhoe) were selected (Figure 1). Various sites can enhance the diversity of the water body dataset and enable a robust validation of water index applications across varying geographical contexts.

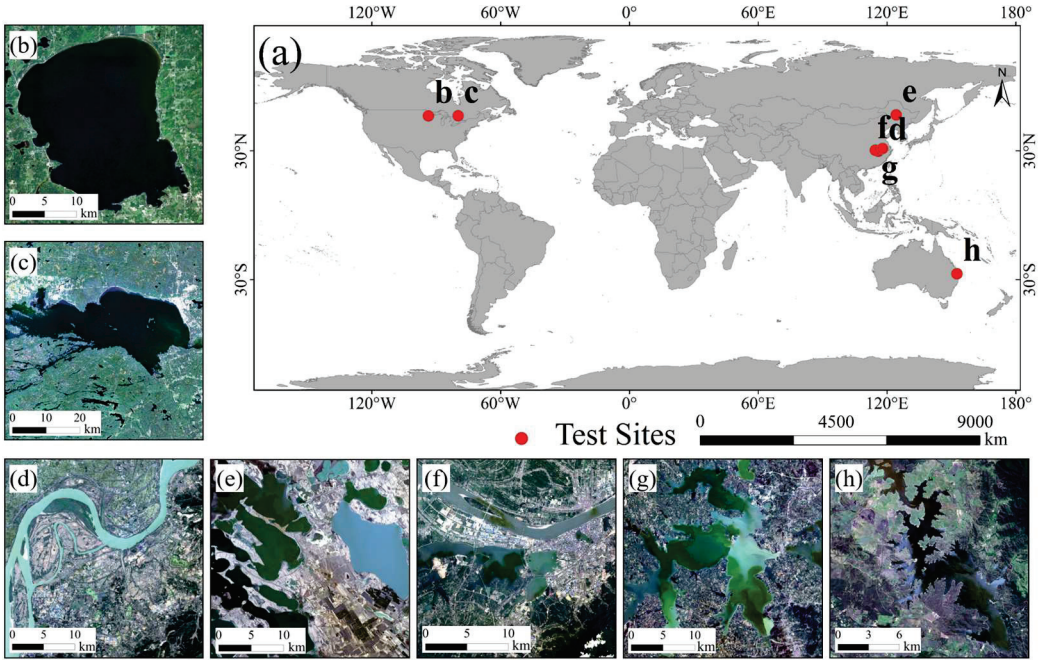

Figure 1. Overview of all selected test sites. (**a**) Locations of the seven test sites, (**b**) Mille Lacs Lake, (**c**) Lake Nipissing region, (**d**) Tongling section of Yangtze River, (**e**) Lianhuan Lake, (**f**) Sai Lake, (**g**) Liangzi Lake, and (**h**) Lake Wivenhoe. All satellite maps are produced via Landsat-9 data (standard true color composite).

Geographically, the selected areas span Asia, North America, and Oceania. Morphologically, the aquatic landscapes at these sites comprise a mixture of small ponds encircled by larger lakes, rivers of linear or irregular shapes, human-made reservoirs, and water channels in coastal zones. For the climatic features, these sites extend from coastal to inland settings, each characterized by unique climatic conditions, as detailed in Table 1.

Table 1. Description of the seven test sites in this study.

No.	Names	Country	Climate	Water Type	Major Background Noise
1	Mille Lacs Lake	The United States of America	Temperate continental climate	Lake	Vegetation
2	Lake Nipissing	Canada	Temperate continental climate	Lake	Vegetation and Artificial building
3	Tongling section of Yangtze River	China	Temperate monsoon climate	River	Paddy field and Mountain shadow Wetland
4	Lianhuan Lake	China	Temperate monsoon climate	Lake cluster	Wetland
5	Sai Lake	China	Temperate monsoon climate	River and Lake	Artificial building
6	Liangzi Lake	China	Temperate monsoon climate	Lake	Artificial building
7	Lake Wivenhoe	Australia	Subtropical monsoon and humid climate	Artificial reservoir	Mountain shadow and Artificial building

2.2. Remote Sensing Data

In this study, data were utilized from both Landsat-8 OLI and Landsat-9 OLI-2 satellites. To minimize inter-dataset discrepancies and ensure accuracy in the extraction of

aquatic information, it is crucial to acquire remote sensing images from both sensors, captured over the same area one day apart. Although Landsat-9 and Landsat-8 have an 8d temporal misalignment, making exact date-over-date comparisons infeasible, images from adjacent paths overlap within approximately 24 h. This overlap allows for the acquisition of nearly concurrent images. Accordingly, a total of fourteen sets of images from both Landsat-9 and Landsat-8, captured over the same scene and within a 24 h interval, were collected (Table 2).

Table 2. Summary of the employed Landsat-8 OLI and Landsat-9 OLI-2 imagery and corresponding reference data in this study.

No.	Test Site	Path/Row	Acquisition Date	Data Source
1	Mille Lacs Lake	028/028	2022/08/31	Landsat-8 Collection 2 Level-2
		027/028	2022/09/01	Landsat-9 Collection 2 Level-2
2	Lake Nipissing	019/028	2023/09/04	Landsat-8 Collection 2 Level-2
		018 /028	2023/09/05	Landsat-9 Collection 2 Level-2
3	Tongling section of Yangtze River	120/039	2022/11/08	Landsat-8 Collection 2 Level-2
		121/038	2022/11/07	Landsat-9 Collection 2 Level-2
4	Lianhuan Lake	120/027	2022/11/08	Landsat-8 Collection 2 Level-2
		119/028	2022/11/09	Landsat-9 Collection 2 Level-2
5	Sai Lake	122/039	2022/08/18	Landsat-8 Collection 2 Level-2
		121/040	2022/08/19	Landsat-9 Collection 2 Level-2
6	Liangzi Lake	123/039	2022/05/05	Landsat-8 Collection 2 Level-2
		122/039	2022/05/06	Landsat-9 Collection 2 Level-2
7	Lake Wivenhoe	089/079	2022/10/29	Landsat-8 Collection 2 Level-2
		090/079	2022/10/28	Landsat-9 Collection 2 Level-2

All data were collected from the Google Earth Engine (GEE) platform (https://developers.google.cn/earth-engine (accessed on 12 May 2024)). The remote sensing image data primarily consisted of Tier 1 Level 2 Science Products (L2SP), which have undergone rigorous geometric correction based on ground control points, radiometric and atmospheric corrections, and solar zenith angle adjustments. These products feature a spatial resolution of 30 m. They can provide surface reflectance data that are ready for subsequent processing. More details of the employed data can be found at https://developers.google.cn/earth-engine/datasets/catalog/landsat (accessed on 12 May 2024). To further enhance image quality, the study employed image selection criteria on the GEE platform, prioritizing images with less than 20% cloud cover for subsequent analysis. After careful investigations, all the acquisition dates of employed satellite imagery were sunny clear-sky days, with no obvious precipitation in the previous and subsequent days. It is noted that the selection of imagery is a trade-off between the overlapping acquisition date and imagery quality.

3. Methodology

3.1. Water Index

In this study, various water indices were employed to enhance water body information for subsequent water extraction. To evaluate the applicability of these indices, the study categorized various water indices and selected representative ones to assess extraction accuracy and analyze the mechanisms influencing their performance. The effective extraction of water body information was facilitated by binarizing the index images via the appropriate threshold. This study incorporated eight water indices, including the commonly utilized Normalized Difference Water Index (NDWI) and Modified Normalized Difference Water Index (MNDWI), Augmented Normalized Difference Water Index (ANDWI), Water Index 2015 (WI_{2015}), tasseled cap wetness index (TCW), automated water extraction index for scenes with shadows ($AWEI_{sh}$) and without shadows ($AWEI_{nsh}$), and Multi-Band Water

Index (MBWI). The aim was to explore the differences in effectiveness and practicality of extracting surface water body information using Landsat-8 and Landsat-9 imagery. Detailed methodologies for calculating each water index, along with their respective sensor bases, are presented in Table 3.

Table 3. Basic information of the employed water indices in this study.

Type	Water Index	Equation	Sensor	Reference
Ratio-based	NDWI	$(\text{Green} - \text{NIR})/(\text{Green} + \text{NIR})$	MSS	[31]
	MNDWI	$(\text{Green} - \text{SWIR1})/(\text{Green} + \text{SWIR1})$	TM	[32]
	ANDWI	$(\text{Blue} + \text{Green} + \text{Red} - \text{NIR} - \text{SWIR1} - \text{SWIR2})/(\text{Blue} + \text{Green} + \text{Red} + \text{NIR} + \text{SWIR1} + \text{SWIR2})$	ETM+/OLI	[35]
Difference-based	WI_{2015}	$1.7204 + 171 \times \text{Green} + 3 \times \text{Red} - 70 \times \text{NIR} - 45 \times \text{SWIR1} - 71 \times \text{SWIR2}$	TM/ETM+/OLI	[34]
	TCW	$0.1446 \times \text{Blue} + 0.1761 \times \text{Green} + 0.3322 \times \text{Red} + 0.3396 \times \text{NIR} - 0.6210 \times \text{SWIR1} - 0.4186 \times \text{SWIR2} - 3.3828$	TM/ETM+	[36]
	$AWEI_{sh}$	$\text{Blue} + 2.5 \times \text{Green} - 1.5 \times (\text{NIR} + \text{SWIR1}) - 0.25 \times \text{SWIR2}$	TM	[28]
	$AWEI_{nsh}$	$4 \times (\text{Green} - \text{SWIR1}) - (0.25 \times \text{NIR} + 2.75 \times \text{SWIR2})$	TM	[28]
	MBWI	$(2 \times \text{Green}) - \text{Red} - \text{NIR} - \text{SWIR1} - \text{SWIR2}$	OLI	[33]

Note: Blue, Green, Red, NIR, SWIR1, and SWIR2 represent the surface reflectance of blue band, green band, red band, near-infrared band, and shortwave infrared band-1 and -2 in Landsat-8 and Landsat-9 imagery, respectively. MSS, TM, ETM+, and OLI represent the Landsat Multispectral Scanner, Thematic Mapper, Enhanced Thematic Mapper Plus, and Operational Land Imager (OLI) data, respectively.

3.2. Threshold Determination

The water body index can effectively enhance the class separability between water and non-water classes. On this basis, selecting an appropriate threshold to achieve the best possible separation effects is also the key to water mapping [13]. Consequently, a series of multi-modal density slicing methods were developed, such as Otsu, K-Means, Inter-modes, Maximum Entropy, Median, Concavity, Percentile, Inter-means, and Iterative Self-organizing Data Analysis (ISODATA) [42,43]. Among them, the Otsu algorithm is a typical adaptive thresholding technique for image segmentation, commonly used to convert grayscale images into binary images [44]. The fundamental advantage of the Otsu method lies in its ability to automatically select a threshold that divides the image into foreground and background, minimizing within-class variance and maximizing between-class variance.

The Otsu method is good at determining the best threshold automatically in a straightforward and effective way, which is particularly valuable in images with varying lighting conditions or contrast levels [45]. Compared to traditional methods that require manual threshold setting, the Otsu method significantly reduces subjectivity and the complexity of experimental operations [13]. In other words, this specific method is featured with satisfactory slicing effect and high efficiency. Although other advanced methods are also employed for threshold determination in water mapping, the Otsu method allows for keeping accuracy without sacrificing efficiency [12,46].

The application of Otsu's method is suitable for the binarization of remote sensing water indices under bimodal distribution conditions [47]. Remote sensing images typically contain complex geographical and environmental information, with clear distinctions in gray levels between water and non-water regions in water index images [13]. The Otsu method effectively isolates water regions from these complex datasets by automatically identifying the optimal threshold based on the image's statistical characteristics [25,48]. This capability is crucial for enhancing the accuracy and efficiency of water body extraction, especially in large-scale or automated water monitoring projects, thereby significantly improving processing speed and the reliability of results.

3.3. Accuracy Assessment

To comprehensively evaluate the classification accuracy of water indices, this study utilizes four key metrics: Overall Accuracy (OA), User Accuracy (UA), Producer Accuracy (PA), and the Kappa coefficient [49]. In addition, the Matthew Correlation coefficient (MCC) is also used for evaluating the extraction performance, which is particularly suited for unbalanced binary distributions [50]. MCC values range between -1 and 1, where a value of 1 represents a perfect classifier, whereas a value of 0 describes a classifier making random guesses [51]. These parameters are employed to analyze interpretative discrepancies across different test sites and to identify the spatial distribution of error-prone pixels.

In this study, validation data for the water and non-water samples were obtained through the visual interpretation of employed Landsat-8 and Landsat-9 imagery. For samples that are challenging to distinguish on 30 m Landsat imagery, we utilize high-resolution Google Earth and Chinese MapWorld imagery (<1 m) from similar time periods to assist in their identification. The satellite imagery utilized in this study was acquired during periods of sunny, clear skies, with no significant precipitation or flooding events. Moreover, the water extents in the seven test sites exhibited relative stability, showing minimum pixel changes over a short temporal span of 1 d, even in transitional areas. This consistency underscores the reliability of the data for accurate analysis and interpretation.

Additionally, these data were also used for extracting "pure" pixel samples from the same locations in both Landsat-8 and Landsat-9 imagery to provide a reference for the spectral differences between the two sets of images. Commonly, the ground area corresponding to a "pure" pixel contains only a single object (land cover type), and then the recorded information by this pixel (30×30 m corresponding to the pixel size of a 30 m-Landsat image) is the spectral characteristic of the pure object [33,52]. In this study, these points were randomly generated from the map and then manually confirmed to ensure the stable distribution of land cover types, including shadows, water, vegetation, and soil. The corresponding spectral features were used for analyzing the differences between both satellite images.

4. Results

4.1. Effects of Different Water Indices

To enhance the comparative analysis of the extraction performance of various water indices utilizing Landsat-9 OLI-2 data, this study systematically selected eight water indices. The effects of these indices were evaluated through a multi-dimensional framework, examining image discrepancies, correlations, and difference metrics.

4.1.1. Comparison of Different Water Indices in Landsat-9

Focusing on the Tongling section of the Yangtze River region, a total of eight water maps were generated (Figure 2). The visual analysis of the results from these water indices reveals that each index effectively enhances the contrast between aquatic and non-aquatic areas, clearly delineating the distribution of water bodies within the watershed.

The ratio-based indices NDWI, ANDWI, and MNDWI, as depicted in Figure 2b–d, exhibit significant and uniform distinctions between land and water areas, with NDWI showing the greatest difference (-0.827–0.983), resulting in a range of 1.810. In contrast, ANDWI shows a somewhat narrower range (ranging from -0.890 to 0.857), a difference of 1.747. The corresponding difference-based indices retain a considerable amount of surface detail, which is characteristic of these indices. Due to the inherent nature of difference-based indices, we did not conduct a comparative analysis of the highest and lowest values here. However, visually, the difference-based indices slightly lag behind the ratio-based indices, as they do not as effectively suppress information related to water fields. Overall, all eight water body indices we employed were capable of supporting subsequent analyses for water body extraction.

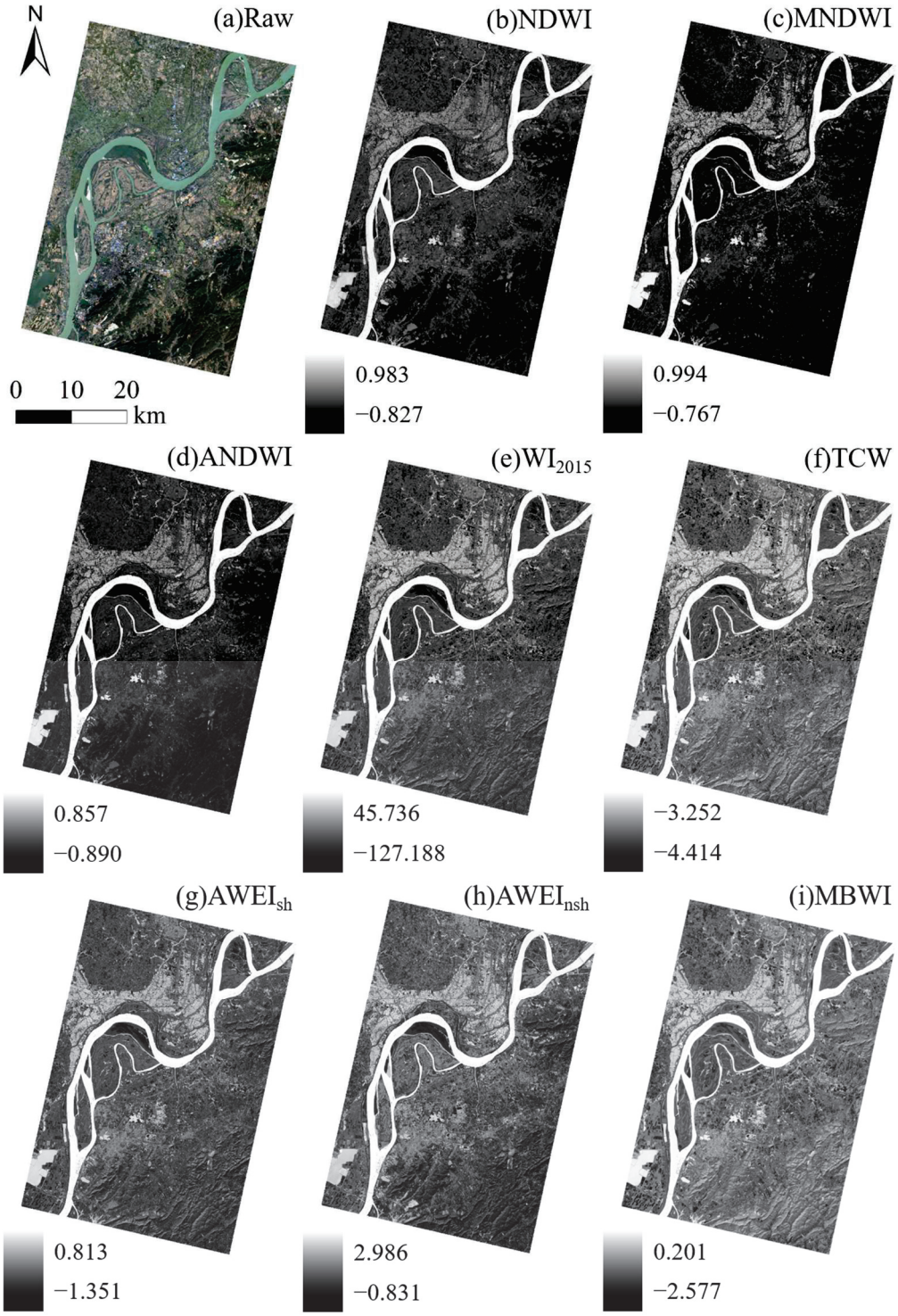

Figure 2. Satellite map (standard true color composite) and various water indices map based on Landsat-9 in Tongling section of Yangtze River region.

4.1.2. Differences of Seven Water Indices in Landsat-8 and Landsat-9

To better evaluate the differences between the water indices derived from Landsat-8 and Landsat-9 data, we examined the differences of index images (Landsat-8 scene minus Landsat-9 scene) from both satellites, focusing on the Lake Wivenhoe as illustrated in Figure 3. The differences are calculated by subtracting the index values derived from Landsat-8 data from those obtained using Landsat-9 data. In the water areas, differences are predominantly positive, indicating that the water indices calculated from Landsat-8

generally yield higher values than those from Landsat-9. For the terrestrial areas, the ratio-based indices (Figure 3a–c) tend to approach zero, indicating the minimal discrepancies between both datasets.

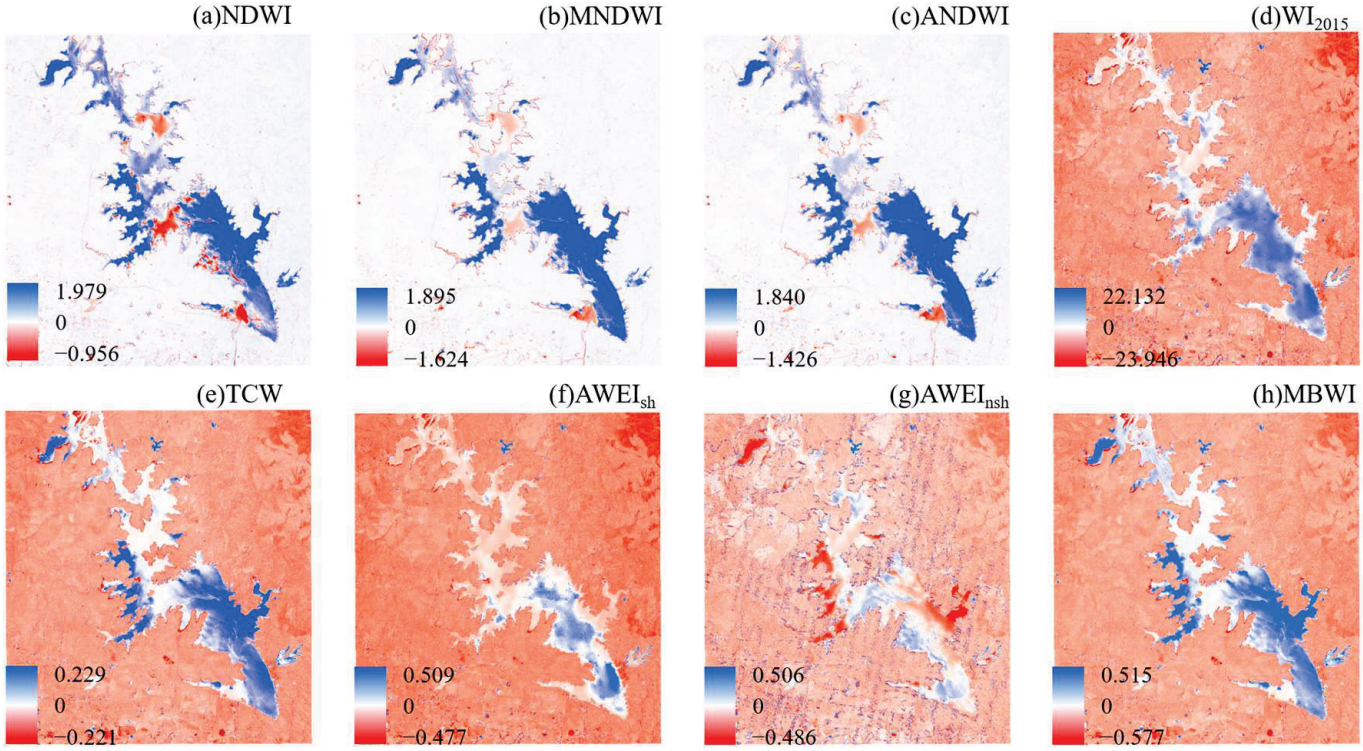

Figure 3. Differences of water indices maps between Landsat-8 and Landsat-9 data in Lake Wivenhoe region.

In the non-water areas, difference-based indices typically exhibit negative values, indicating that water indices calculated from Landsat-8 are generally lower than those derived from Landsat-9. As shown in Figure 3c, the difference in values between the two imagery indices of $AWEI_{sh}$ is smaller compared to other indices. In Figure 3, it is obvious that most water regions appear lighter or near white, reflecting minimal disparities. The difference plot for $AWEI_{sh}$ shows a maximum value of 0.509 and a minimum value of −0.477, with a total range of 0.986. Similar trends of small disparities in $AWEI_{sh}$ index values are observed in other study areas, as detailed in Figures S1–S5.

However, the test site of Mille Lacs Lake (Figure 4) displays opposite characteristics to Lake Wivenhoe, with water indices predominantly showing negative differences. In non-water areas, the ratio-based water indices in both test sites tend to approach zero, while the difference-based indices display positive values, indicating that the majority of water index values calculated from Landsat-8 are greater than those from Landsat-9. More difference maps are shown in Figures S1–S5. These above results indicate that the performance of various water indices varies with geographical regions; however, there remains a strong consistency between Landsat-8 and Landsat-9 data across these areas.

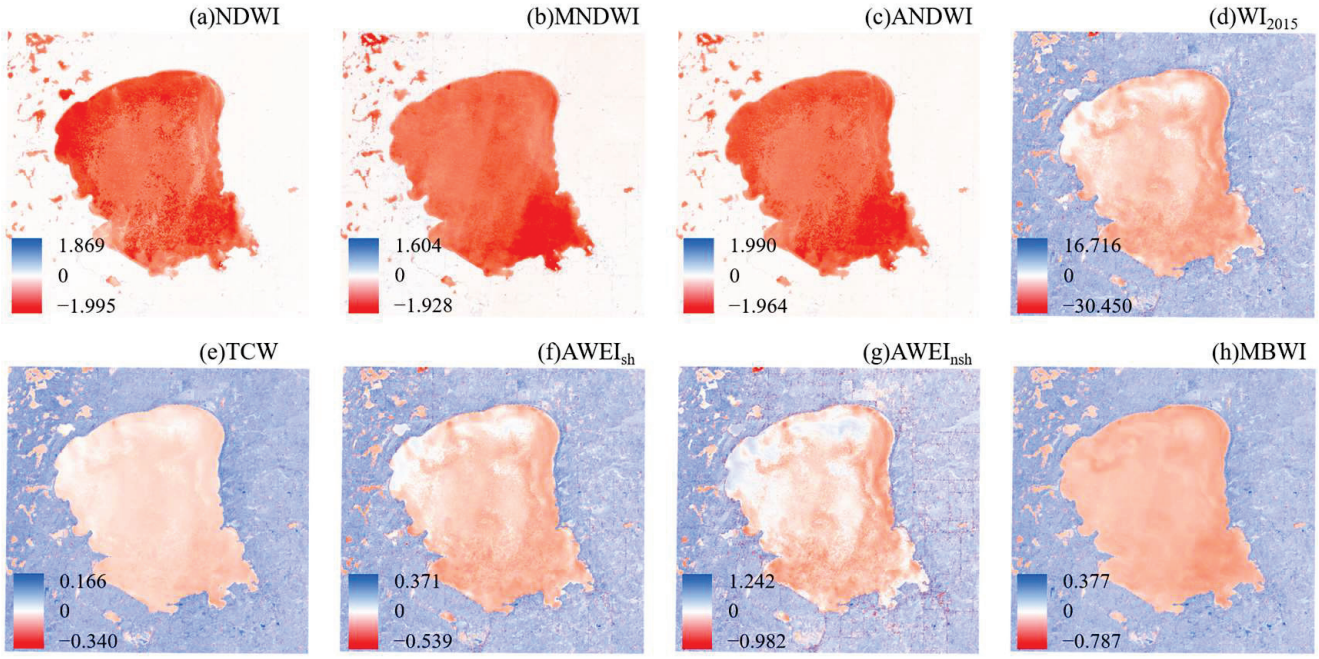

Figure 4. Differences of water index maps between Landsat-8 and Landsat-9 data in Mille Lacs Lake region.

4.1.3. Correlation among Various Water Indices

Based on the GEE platform, a total of 3000 data points were randomly selected for extracting the water index values in each pair of Landsat-8 and Landsat-9 imagery. Subsequently, a correlation analysis was conducted on the water indices calculated from two scenes within the Lake Wivenhoe area (Figure 5). Overall, both sets of data demonstrate high correlations across all eight indices, with R^2 values exceeding 0.990 for each. Notably, the highest correlations were observed in MBWI, TCW, and WI_{2015}, all reaching an R^2 of 0.998, while the lowest was in NDWI (R^2 = 0.990). The graphical representation shows that the 3000 data points for all water body indices are predominantly positioned at the extremes of the fitted line. However, the distribution of ratio-based indices, especially NDWI, is more pronounced, with data points distinctly clustered at the extremes (Figure 5a). In contrast, TCW points are more densely concentrated at one end, associated with non-water body points. The R^2 values for MNDWI, NDWI, ANDWI, and $AWEI_{nsh}$ are 0.995, 0.990, 0.991, and 0.994, respectively, indicating a slightly lower correlation compared to other indices. The additional correlation results are shown in Figures S6–S11.

4.2. Separation of the Water Index

To assess the impact of spectral band differences on water extraction, the separability of water index values was analyzed within the Lake Wivenhoe region (Figure 6). The relationships between the indices and the corresponding spectral bands were also analyzed. Generally, there is consistency in the separability of water indices derived from both Landsat-8 and Landsat-9 data, with indices such as NDWI demonstrating identical reflectance distributions in the Green and NIR bands across both satellite images. However, indices like $AWEI_{nsh}$, $AWEI_{sh}$, and WI2015 show no distinct separation gaps, leading to significant uncertainty in their segmentation thresholds. Conversely, indices such as NDWI, MNDWI, MBWI, and ANDWI display clear gaps near zero, facilitating their direct application for water body segmentation across the entire study area based on established thresholds. As illustrated in Figure 6, the division of water bodies using NDWI and MNDWI is predominantly determined by the greater reflectance values in the Green band compared to the NIR and SWIR1 bands. In the other test sites, the separations of the water index are similar (Figures S12–S17).

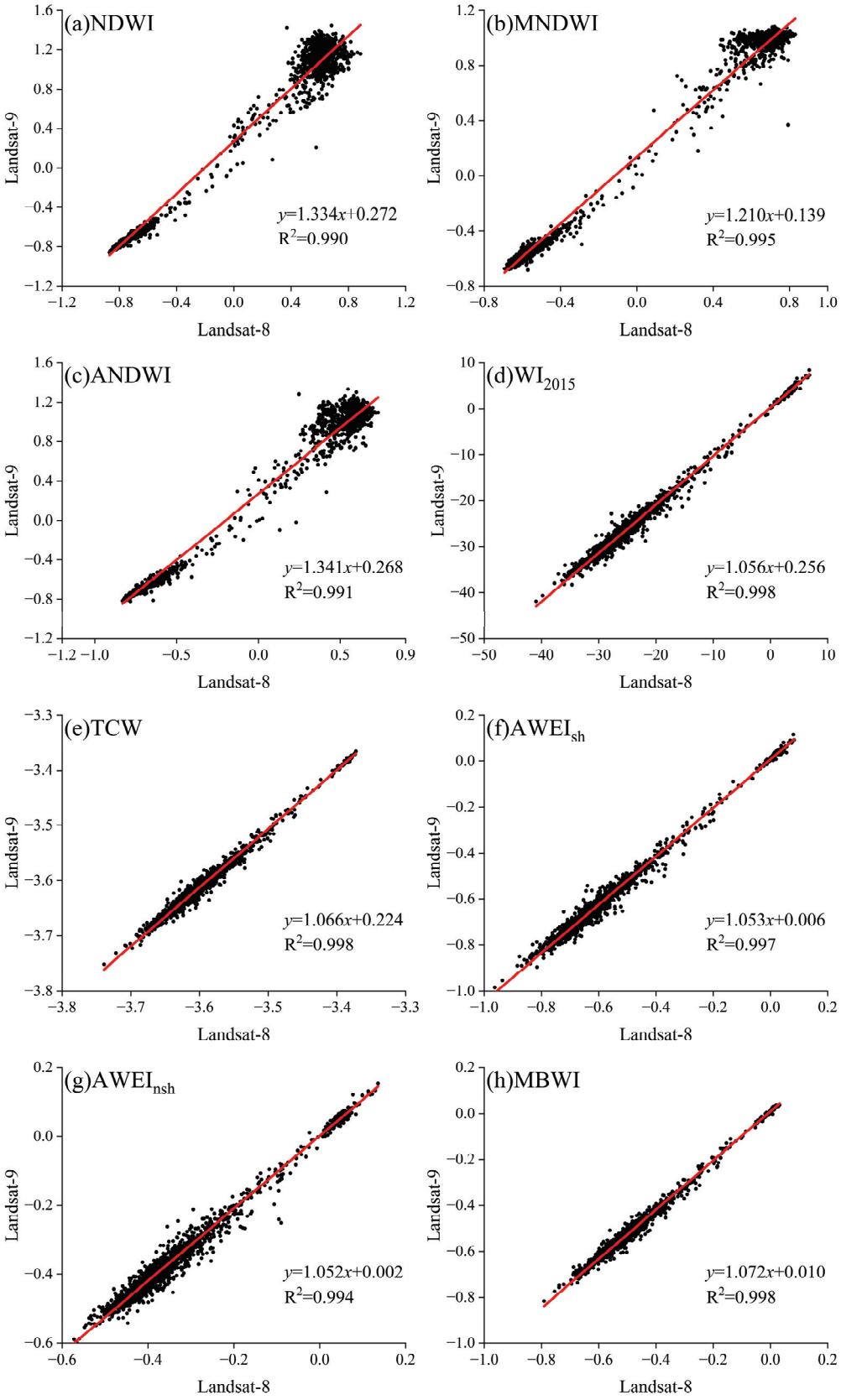

Figure 5. Correlation analysis of water indices in the Lake Wivenhoe region based on Landsat-8 and Landsat-9 imagery (Note: red line denotes the fitted line).

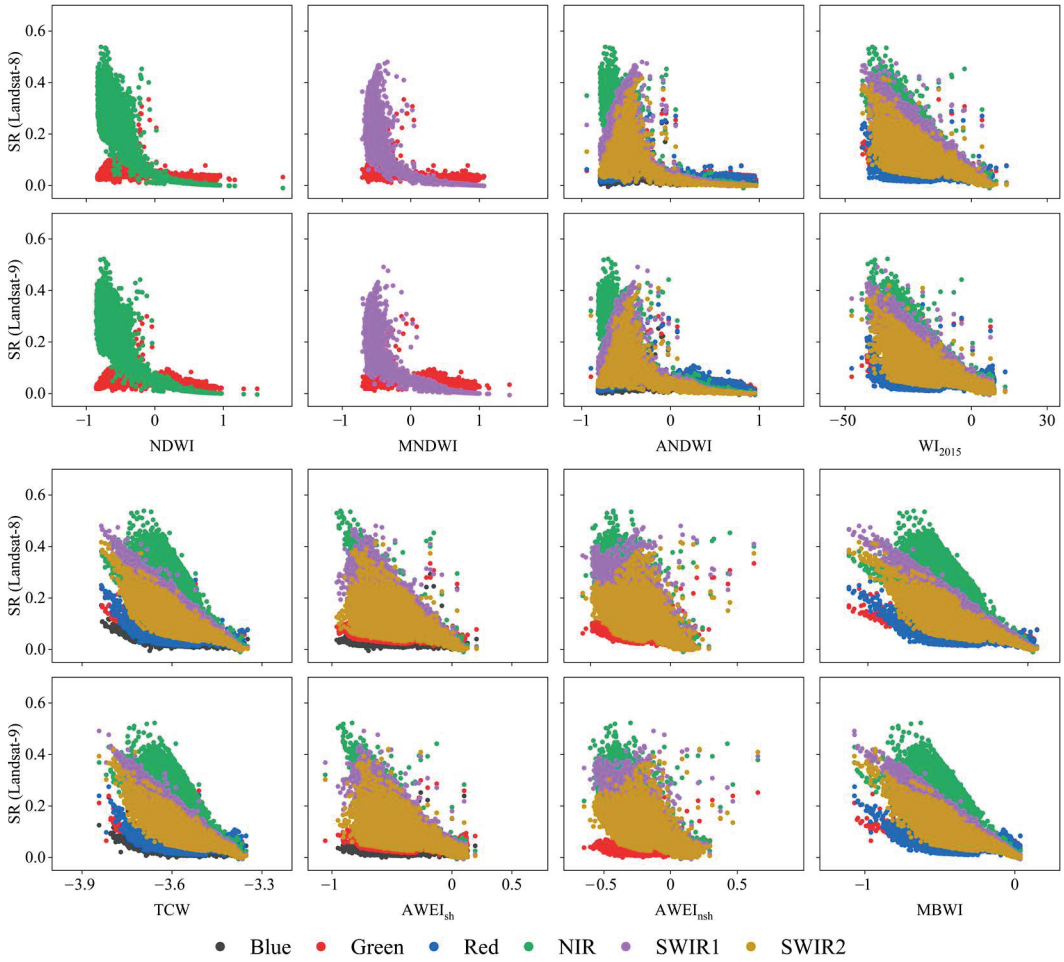

Figure 6. Comparison of the separability of different water indices based on Landsat-8 and Landsat-9 imagery in Lake Wivenhoe.

For the threshold, histograms were generated using Lake Wivenhoe as a case study (Figure 7). Eight different water indices were utilized, all designed to suppress the differences in surface reflectance between water and non-water bodies, resulting in more concentrated pixel values ranging from −1 to 1 for indices like NDWI. These indices amplify the distinction between water and non-water areas. Typically, the histogram of a water index image displays two peaks, with the right peak representing water areas, as seen in the WI_{2015} index image, and the left peak representing non-water areas.

As shown in Figure 7, it is evident that although some water peaks are quite low due to the small proportion of water in the study area, both Landsat-8 and Landsat-9 exhibit similar morphologies, with most images showing a bimodal distribution. This characteristic makes it straightforward to distinctly differentiate between the index values of water and non-water bodies. The ratio-based indices, such as NDWI, MNDWI, and ANDWI, feature a large separation between the two peaks, where water (right peak) and non-water (left peak) are far apart and do not overlap. This clear separation facilitates the setting of thresholds for water body segmentation. Conversely, the difference-based indices like $AWEI_{nsh}$ and MBWI (Figure 7g,h) show a shorter distance between peaks, resulting in minimal separation.

In this specific test site, the thresholds for ratio-based water indices differ significantly between Landsat-8 and Landsat-9 imagery (Figure 7a–c). For example, the Otsu threshold for the NDWI index is 0.005 on Landsat-8 images and −0.095 on Landsat-9 images, a difference of 0.100. In contrast, the thresholds for difference-based indices show smaller

discrepancies; the MBWI index has an Otsu threshold of −0.285 on Landsat-8 images and −0.275 on Landsat-9 images, with a minimal difference of 0.010.

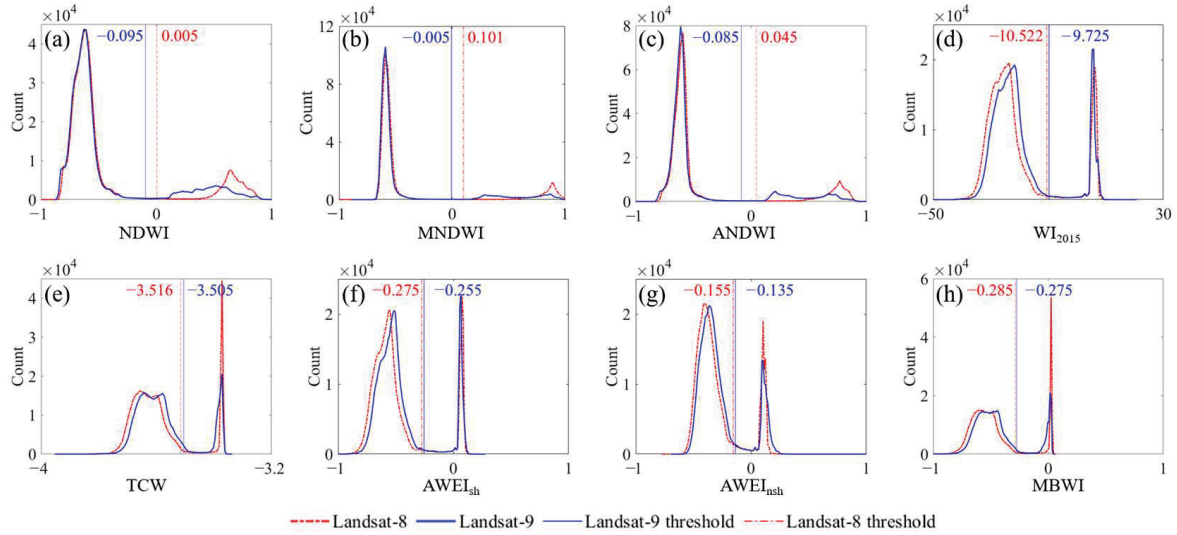

Figure 7. Comparison of the applicability of different water body index thresholds based on Landsat-8 and Landsat-9 imagery in Lake Wivenhoe. (**a**) NDWI, (**b**) MNDWI, (**c**) ANDWI, (**d**) WI_{2015}, (**e**) TCW, (**f**) $AWEI_{sh}$, (**g**) $AWEI_{nsh}$, and (**h**) MBWI.

Overall, the histograms of the index images from Landsat-8 and Landsat-9 are consistent (Figure 7 and Figures S18–S23). The ratio-based indices, being greater than 0, demonstrate a distinct difference in the crest of the water peak between the two satellite images; hence, the threshold for ratio-based indices exhibits more variability between Landsat-8 and Landsat-9 imagery.

4.3. Comparison of Water Body Extraction

To evaluate the extraction performance of different water indices, three test sites featuring complex water body boundaries, large watersheds, and rivers of varying morphologies were selected. Overall, the eight water indices successfully captured the distribution of water bodies within each test site.

An analysis of the Lake Wivenhoe region using Landsat-9 imagery serves as a case study. Figure 8 illustrates that the primary areas of omission occur with the ratio-based indices NDWI, MNDWI, and ANDWI (Figure 8a–c), which tend to miss finer water bodies. In contrast, $AWEI_{nsh}$ (Figure 8g) demonstrates the least amount of omission in capturing fine water bodies. The main misclassifications in the difference-based indices $AWEI_{nsh}$, MBWI, and TCW are related to mountain shadows and buildings. $AWEI_{nsh}$ (Figure 8g) shows the highest misidentification of building shadows as water bodies, whereas WI_{2015} (Figure 8d) is less prone to this error. TCW (Figure 8e) tends to misclassify mountain shadows the most, whereas WI_{2015} (Figure 8d) effectively minimizes such errors.

The Mille Lacs Lake area shares similarities with the Lake Wivenhoe region in its inclusion of omissions in fine stream areas. In terms of ratio-based indices, NDWI, MNDWI, and ANDWI lack precision in identifying the boundaries of water bodies, resulting in more frequent omissions at the edges of smaller water areas (Figure 9a–c).

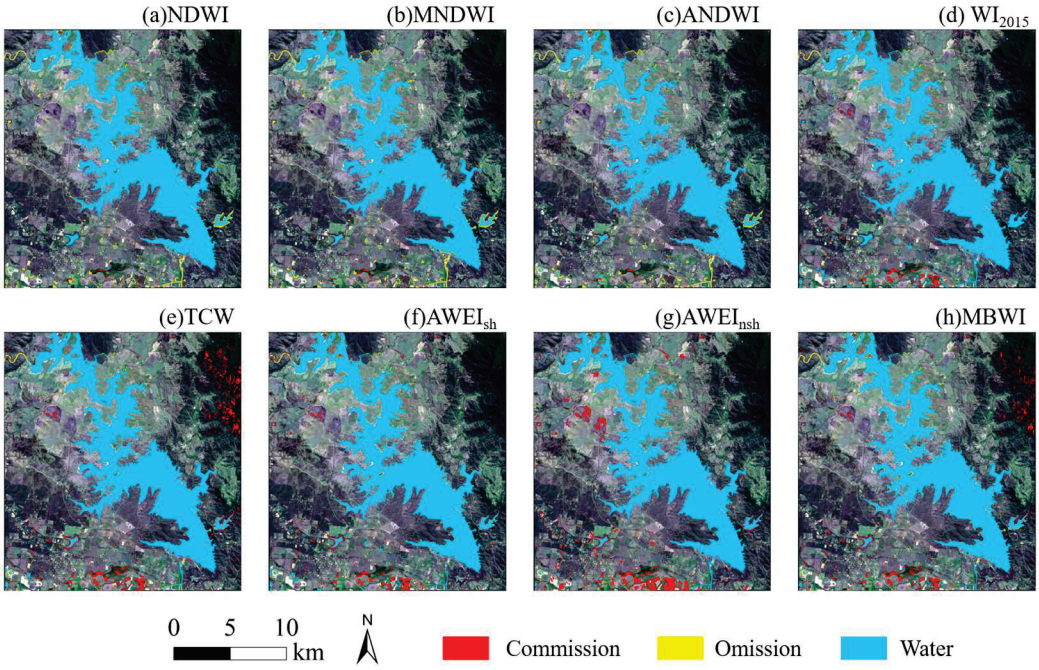

Figure 8. Spatial differences in water index extraction capacity in the Lake Wivenhoe region based on Landsat-9 imagery.

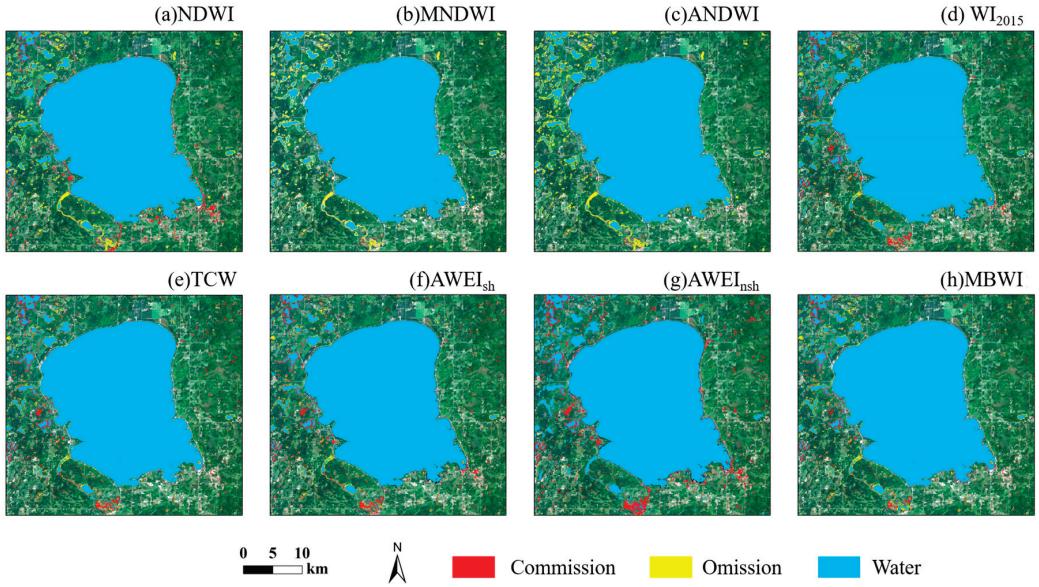

Figure 9. Spatial differences in water index extraction capacity in the Mille Lacs Lake region based on Landsat-9 imagery.

In the Tongling section of the Yangtze River region, disturbances from paddy fields and mountain shadows are prevalent, leading to high rates of misclassification across all eight water indices (Figure 10). TCW and MBWI (Figure 10e,h) show less effectiveness in suppressing mountain shadows and building shadows, often misidentifying these features as bodies of water. WI_{2015}, $AWEI_{sh}$, and $AWEI_{nsh}$ exhibit fewer errors with mountain shadows but tend to misclassify building shadows as water more frequently. In the other test sites, similar results were also observed (Figures S24−S27).

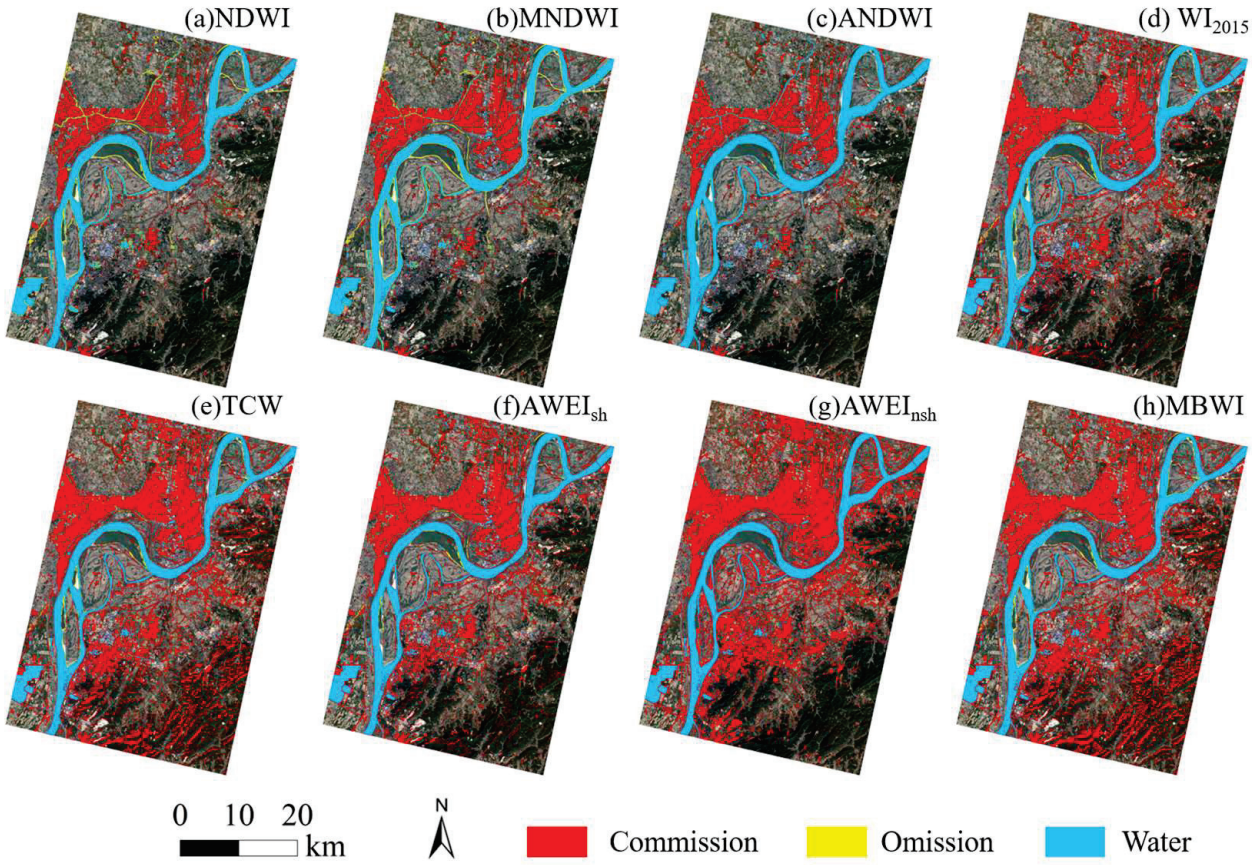

Figure 10. Spatial differences in water index extraction capacity in the Tongling section of the Yangtze River region based on Landsat-9 imagery.

To compare the accuracy of different water indices using Landsat-8 and Landsat-9 imagery, an analysis was performed focusing on the extraction accuracies and Kappa and MCC statistics for each index. The results, summarized in Table 4, demonstrate the consistency of extraction accuracies between Landsat-8 and Landsat-9, with the largest discrepancy observed in the PA of the NDWI index within Lake Nipissing, showing a difference of −0.279. In contrast, the smallest gaps (close to 0) in PA were detected in the Mille Lacs Lake (MBWI), Lake Wivenhoe (TCW and MBWI), Liangzi Lake (TCW), Sai Lake (AWEIsh), and Lianhuan Lake (TCW and $AWEI_{sh}$). Among all MCC results, the largest difference was observed in the NDWI of Mille Lacs Lake (−0.101); however, the smallest difference (close to 0) is the MBWI of Mille Lacs Lake, the $AWEI_{sh}$ of Lake Nipissing and WI_{2015} of the Tongling section of the Yangtze River, indicating the perfect classifiers for water detection.

Among the indices, the NDWI index exhibited the greatest variability in accuracy differences, with several test sites showing a precision difference greater than 0.15 (in absolute value) between Landsat-8 and Landsat-9 data. For instance, the Kappa difference in the Mille Lacs Lake region reached −0.170, and the UA difference in Lake Nipissing was 0.156. The PA difference in Lianhuan Lake reached 0.151, and in Nipissing reached −0.279. The largest MCC difference of the NDWI reaches −0.101, and the smallest difference (−0.018) was observed in the Tongling section of the Yangtze River. The accuracy differences for all other indices across Landsat-8 and Landsat-9 data were below 0.1 (in absolute value), suggesting more attention should be given to the use of the NDWI index when applying Landsat-8 and Landsat-9 imagery concurrently.

Table 4. Accuracy metrics of water mapping based on the Landsat-8 OLI and Landsat-9 OLI-2 data. (Note: red font represents the negative value).

Site		Landsat-9								Landsat-8 Minus Landsat-9							
		NDWI	MNDWI	ANDWI	WI_{2015}	TCW	$AWEI_{sh}$	$AWEI_{nsh}$	MBWI	NDWI	MNDWI	ANDWI	WI_{2015}	TCW	$AWEI_{sh}$	$AWEI_{nsh}$	MBWI
Mille Lacs Lake	Kappa	0.574	0.364	0.437	0.822	0.843	0.820	0.780	0.838	−0.170	0.055	−0.089	0.015	−0.006	0.001	0.011	0.000
	OA	0.825	0.660	0.718	0.937	0.944	0.937	0.924	0.942	−0.132	0.048	−0.073	0.005	−0.002	0.000	0.005	0.000
	PA	0.834	0.561	0.645	0.980	0.986	0.986	0.986	0.980	−0.226	0.074	−0.108	0.003	−0.003	−0.003	0.011	0.000
	UA	0.925	0.976	0.970	0.939	0.942	0.933	0.918	0.945	0.048	−0.012	0.011	0.003	0.000	0.003	−0.002	0.000
	MCC	0.583	0.454	0.505	0.826	0.847	0.826	0.790	0.840	−0.101	0.034	−0.060	0.014	−0.007	−0.000	0.017	0.000
Lake Nipissing	Kappa	0.362	0.344	0.310	0.580	0.581	0.561	0.519	0.581	−0.129	0.071	0.041	−0.011	−0.020	0.000	−0.016	−0.016
	OA	0.675	0.658	0.639	0.791	0.791	0.782	0.763	0.791	−0.078	0.039	0.024	−0.006	−0.010	0.000	−0.007	−0.008
	PA	0.545	0.381	0.334	0.793	0.789	0.797	0.820	0.782	**−0.279**	0.069	0.066	−0.007	−0.024	−0.004	0.019	−0.006
	UA	0.784	0.957	0.981	0.813	0.816	0.797	0.758	0.820	0.156	0.011	−0.045	−0.004	−0.001	0.003	−0.017	−0.008
	MCC	0.382	0.439	0.421	0.581	0.581	0.561	0.521	0.582	−0.040	0.060	0.015	−0.011	−0.019	0.000	−0.013	−0.016
Tongling section of Yangtze River	Kappa	0.731	0.701	0.706	0.674	0.618	0.667	0.607	0.609	−0.030	−0.007	−0.023	0.002	−0.020	−0.014	−0.038	−0.014
	OA	0.867	0.851	0.854	0.836	0.806	0.832	0.801	0.801	−0.014	−0.003	−0.011	0.001	−0.010	−0.007	−0.019	−0.007
	PA	0.804	0.827	0.814	0.918	0.954	0.922	0.914	0.960	−0.070	−0.006	−0.031	−0.009	−0.015	−0.011	0.008	−0.019
	UA	0.903	0.852	0.867	0.775	0.723	0.768	0.731	0.715	0.038	−0.001	0.004	0.006	−0.006	−0.005	−0.026	−0.001
	MCC	0.735	0.701	0.707	0.685	0.647	0.679	0.624	0.642	−0.018	−0.006	−0.021	−0.000	−0.022	−0.015	−0.030	−0.019
Lianhuan Lake	Kappa	0.823	0.835	0.838	0.832	0.757	0.844	0.844	0.772	0.061	0.003	0.011	0.018	0.015	0.014	0.003	0.017
	OA	0.912	0.918	0.919	0.916	0.878	0.922	0.922	0.886	0.030	0.001	0.006	0.009	0.008	0.007	0.001	0.008
	PA	0.834	0.863	0.857	0.968	0.974	0.971	0.968	0.974	0.151	0.009	0.023	0.003	0.000	0.000	0.009	0.003
	UA	0.986	0.967	0.977	0.876	0.817	0.883	0.885	0.827	−0.080	−0.006	−0.012	0.012	0.010	0.012	−0.003	0.011
	MCC	0.833	0.840	0.844	0.837	0.771	0.848	0.847	0.784	0.055	0.002	0.009	0.016	0.013	0.013	0.004	0.016
Sai Lake	Kappa	0.668	0.681	0.674	0.715	0.726	0.670	0.580	0.735	−0.016	0.020	0.022	−0.012	−0.018	0.006	0.012	−0.034
	OA	0.831	0.838	0.834	0.859	0.864	0.838	0.797	0.868	−0.007	0.010	0.012	−0.006	−0.008	0.002	0.005	−0.016
	PA	0.743	0.744	0.736	0.844	0.841	0.848	0.872	0.834	0.004	0.020	0.030	−0.009	0.007	0.000	−0.008	0.004
	UA	0.951	0.963	0.965	0.903	0.914	0.865	0.793	0.927	−0.020	−0.001	−0.009	−0.004	−0.020	0.004	0.011	−0.032
	MCC	0.689	0.704	0.699	0.717	0.729	0.671	0.584	0.740	−0.020	0.016	0.015	−0.012	−0.019	0.005	0.010	−0.037
Liangzi Lake	Kappa	0.863	0.885	0.888	0.782	0.732	0.770	0.736	0.767	0.025	−0.041	−0.029	−0.019	0.022	−0.010	0.032	−0.013
	OA	0.933	0.943	0.945	0.890	0.864	0.884	0.866	0.882	0.012	−0.020	−0.015	−0.010	0.011	−0.005	0.017	−0.007
	PA	0.874	0.936	0.914	0.988	0.986	0.986	0.988	0.984	0.046	0.017	0.026	−0.009	0.000	−0.007	−0.017	−0.002
	UA	0.972	0.936	0.959	0.806	0.771	0.798	0.772	0.797	−0.018	−0.055	−0.053	−0.009	0.015	−0.003	0.033	−0.009
	MCC	0.866	0.885	0.889	0.798	0.755	0.787	0.759	0.784	0.022	−0.038	−0.029	−0.019	0.018	−0.011	0.022	−0.012
Lake Wivenhoe	Kappa	0.808	0.798	0.795	0.857	0.860	0.836	0.802	0.866	−0.043	−0.056	−0.053	−0.003	−0.006	−0.002	−0.026	−0.012
	OA	0.909	0.905	0.904	0.930	0.932	0.920	0.902	0.935	−0.019	−0.025	−0.024	−0.001	−0.003	−0.002	−0.013	−0.006
	PA	0.793	0.718	0.775	0.929	0.929	0.929	0.954	0.921	−0.050	−0.061	−0.057	−0.004	0.000	0.007	−0.015	0.000
	UA	0.987	0.99	0.991	0.906	0.909	0.884	0.834	0.921	0.003	−0.001	−0.001	0.000	−0.006	−0.008	−0.015	−0.013
	MCC	0.821	0.813	0.810	0.857	0.860	0.837	0.808	0.866	−0.036	−0.047	−0.044	−0.003	−0.006	−0.002	−0.027	−0.012

The analysis shows that within the same test site, the PA for ratio-based indices was lower than that for difference-based indices. For example, in the Sai Lake region on Landsat-9 imagery, the PA for the three ratio-based indices (NDWI, MNDWI, and ANDWI) were 0.743, 0.744, and 0.736, respectively, while the PA for the other difference-based indices were all above 0.800. Similar patterns were observed in other sites on both datasets, where the PA for ratio-based indices was consistently lower than that for difference-based indices, and omissions were more frequent in ratio-based indices. In general, the results of OA and MCC are similar and complemental.

Furthermore, the UA for ratio-based indices was higher than that for difference-based indices within the test sites. For instance, in the Liangzi Lake region on Landsat-9 imagery, the UA for the three ratio-based indices (NDWI, MNDWI, and ANDWI) were 0.972, 0.936, and 0.959, respectively, whereas the UA for the other difference-based indices were all below 0.900. Accuracy results on both datasets in other sites showed the same trend (Table 4), where the UA for ratio-based indices was greater than the PA for difference-based indices, and the difference-based indices had a higher rate of misclassification compared to ratio-based indices.

5. Discussion

5.1. Performance and Effectiveness of Various Water Indices

The computation of remote sensing indices for water body detection is straightforward, eliminating the need for intricate training processes. This simplicity facilitates the rapid extraction of water body information over large areas, making it an essential technique for global and regional assessments of water distribution and area estimation. Despite a trend towards more complex water body indices, existing studies suggest that more elaborate indices do not always outperform their simpler counterparts [27]. In our research, we utilized eight different water indices for water extraction.

NDWI effectively minimizes the influence of non-aquatic elements like vegetation and soil, proving particularly effective for large lakes and reservoirs. However, it still includes substantial interference when applied to urban water bodies [29]. MNDWI, building upon the NDWI approach, uses the Landsat TM short-wave infrared band (TM5) instead of the near-infrared band (TM4). This modification enhances the index's ability to reduce the impacts of soil and buildings, thereby improving the removal of shadows from urban structures [32]. AWEI, including its variants $AWEI_{nsh}$ and $AWEI_{sh}$, is formulated based on TM image data. AWEI aims to maximally separate aquatic from non-aquatic pixels through band subtraction and the application of varying coefficients. Validation has shown that AWEI achieves higher accuracy in water extraction than MNDWI [28]. Building on WI_{2006}, the WI_{2015} introduces a new extraction algorithm based on linear discriminant analysis (LDA), employing the LDA classification (LDAC) to determine optimal coefficients for segregating training area classes, thereby enhancing classification precision [35]. The MBWI mitigates the effects of mountain shadows and dark building pixels while also lessening seasonal variations caused by changes in solar conditions [33]. The TCT, an empirical orthogonal transformation introduced by Kauth et al. [53] during studies on crop growth stages, effectively extracts water information through its wetness component (i.e., TCW), as utilized in our research.

Figure 11 displays the precision statistics across eight water indices at various test sites. Under differing surface water environmental conditions, the OA fluctuations of the NDWI, MNDWI, and ANDWI indices are notably larger compared to the other indices, highlighting the superior robustness of $AWEI_{nsh}$, $AWEI_{sh}$, WI_{2015}, TCW, and MBWI in water body extraction, which can be mutually confirmed with MCC results. Generally, the results of OA and MCC are similar. Analyzing PA results, the ratio-based indices (NDWI, MNDWI, and ANDWI) exhibit greater variability and generally lower mean values compared to the difference-based indices, resulting in a higher incidence of omission errors, as depicted in Figures 8–10. Conversely, UA analysis shows that ratio-based indices have higher mean

values, indicating fewer commission errors, while difference-based indices exhibit lower mean values and, thus, more commission errors.

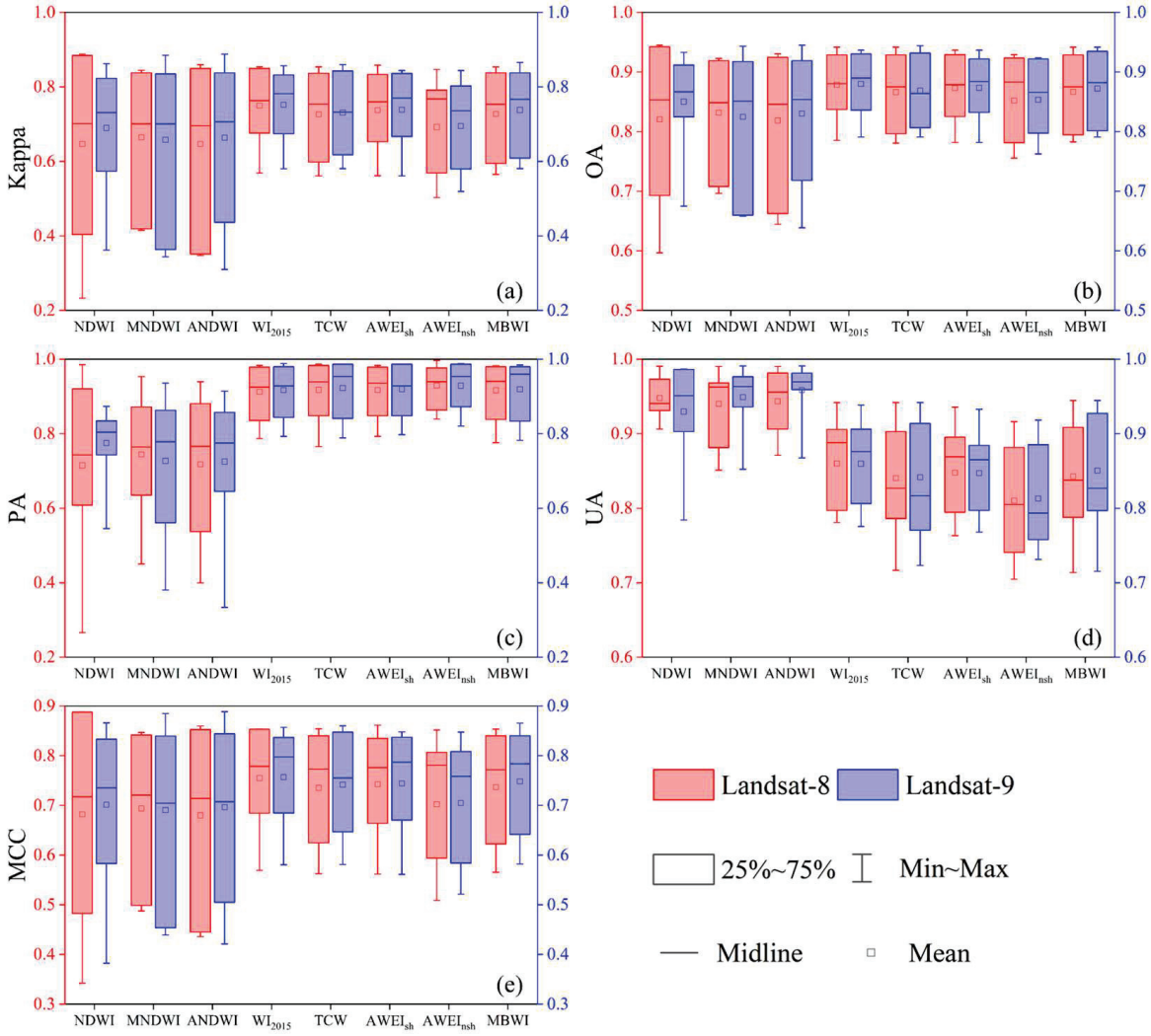

Figure 11. Statistical results of statistical parameters across eight water indices. (**a**) Kappa, (**b**) OA, (**c**) PA, (**d**) UA, and (**e**) MCC.

As shown in Figures 11 and 12 across various study areas, the NDWI index performs less effectively in water body extraction compared to $AWEI_{sh}$. $AWEIs_h$ demonstrates superior capability in identifying small water bodies within images, outperforming NDWI, which tends to misclassify water body edges as non-water, leading to increased omission errors and impacting overall accuracy. According to our findings, the water extraction accuracy based on Landsat-8 and Landsat-9 imagery is consistent. The related results suggest that the subtle differences between the two sensors do not lead to significant variations in accuracy. Consequently, we can confidently utilize data from both sensors in tandem for water body mapping across various temporal and spatial scales.

Through systematic analysis and comparison of various water body indices applied to Landsat-8 and Landsat-9 imagery, the results demonstrated the distinct advantages and limitations inherent to both ratio-based and difference-based indices. Our results confirm that ratio-based indices like NDWI, MNDWI, and ANDWI exhibit significant variability in accuracy, especially in complex urban and boundary water body scenarios. They offer stable performance across diverse environments and satellites due to their ability to mitigate the effects of clouds and shadows without the need for coefficients. On the other hand, difference-based indices such as $AWEI_{sh}$, WI_{2015}, TCW, and MBWI, despite

their empirical coefficients and potential for variability, have shown higher robustness in extracting water bodies, particularly in challenging conditions where the precision and minimization of omission and commission errors are critical.

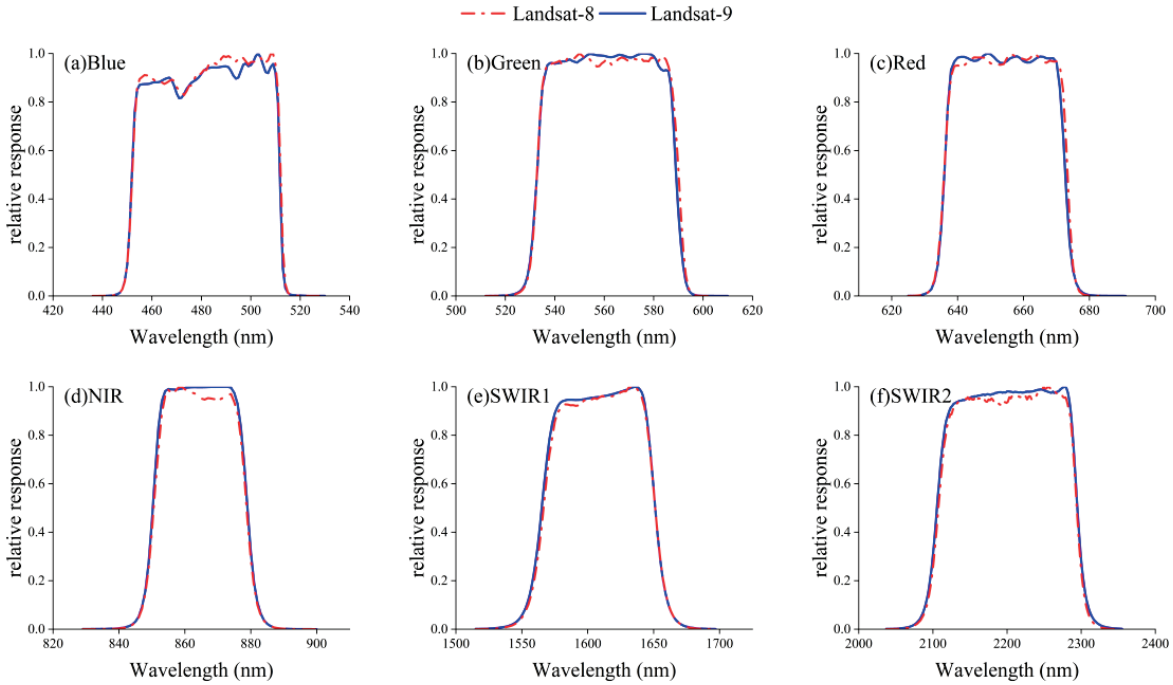

Figure 12. Comparison of spectral response curves between Landsat-8 OLI and Landsat-9 OLI-2. Spectral response functions obtained from https://landsat.gsfc.nasa.gov/satellites/landsat-8/spacecraft-instruments/ (last accessed on 12 May 2024) and https://landsat.gsfc.nasa.gov/satellites/landsat-9/landsat-9-instruments (last accessed on 12 May 2024), respectively.

5.2. Spectral Response and Reflectance of Landsat-8 and Landsat-9 Data

Landsat-9 is the latest addition to the Landsat satellite series, continuing the mission of Earth observation established by its predecessors. Moreover, one of its significant roles is to work in tandem with Landsat-8 to halve the Earth observation cycle from 16 d to 8 d [21,39]. This necessitates a high degree of consistency in the imagery data between Landsat-9 and Landsat-8 to ensure the results from both are strictly comparable [54]. The primary distinctions between them stem from differences in spectral reflectance attributed to their spectral response functions [21].

Regarding the remote sensors, there are some disparities in the spectral band ranges of the Landsat-8 OLI and Landsat-9 OLI-2 (Table 5). For instance, the bands used to calculate NDWI, the Green and NIR bands, have wavelengths of 525–600 nm and 845–885 nm for Landsat 8 OLI, compared to 533–590 nm and 851–879 nm for Landsat 9 OLI-2, respectively. Additionally, there are differences in reflectance in the SWIR bands. This is because they share similar spectral response functions with some differences (Figure 12). The spectral response peaks for SWIR2, SWIR1, NIR, Green, and Red bands on Landsat-9 OLI-2 are higher than those on Landsat-8 OLI, suggesting that OLI-2 is more sensitive to these wavelengths.

Another critical metric for assessing the performance of remote sensing instruments is the signal-to-noise ratio (SNR) [54]. Under typical radiation conditions, the SNR of data transmitted by OLI-2 on Landsat-9 is improved by 25%, offering higher radiometric precision in observing the Earth's surface. Landsat-9's OLI-2 downlink transmits all 14-bit data produced by the spacecraft's electronic equipment to Earth, providing images with greater bit depth and redundancy [41,55].

Table 5. The basic specifications for the spectral characteristics and spatial resolution of OLI and OLI-2 sensors.

Band	Acronym	Spatial Resolution	Landsat-8 OLI		Landsat-9 OLI2	
			Spectral Range	Band Center	Spectral Range	Band Center
Coastal aerosol	B1	30 m	433–453	443	435–451	443
Blue (B)	B2	30 m	450–515	483	452–512	482
Green (G)	B3	30 m	525–600	561	533–590	562
Red (R)	B4	30 m	630–680	655	636–673	655
Near-infrared (NIR)	B5	30 m	845–885	865	851–879	866
Shortwave infrared 1 (SWIR1)	B6	30 m	1560–1660	1610	1566–1651	1610
Shortwave infrared 2 (SWIR2)	B7	30 m	2100–2300	2200	2107–2294	2201
Panchromatic	B8	15 m	500–680	591	503–676	590
Cirrus	B9	30 m	1360–1390	1373	1363–1384	1374

Reflectance serves as the data foundation for distinguishing different land cover types. The varying chemical compositions, physical structures, and surface states influence the capacities for reflecting, absorbing, and transmitting electromagnetic waves. In this study, we selected "pure" pixel samples from the same locations in both Landsat-8 and Landsat-9 imagery to provide a reference for the spectral differences between the two sets of images. These "pure" pixels with a size of 30 × 30 m were obtained from seven test sites covered by Landsat-8 and Landsat-9 imagery. Figure 13 displayed the typical "pure" pixels in the Landsat scene. They encompass all the challenging factors of identifying surface water: mountain shadows, urban areas (buildings), vegetation, and bare soil.

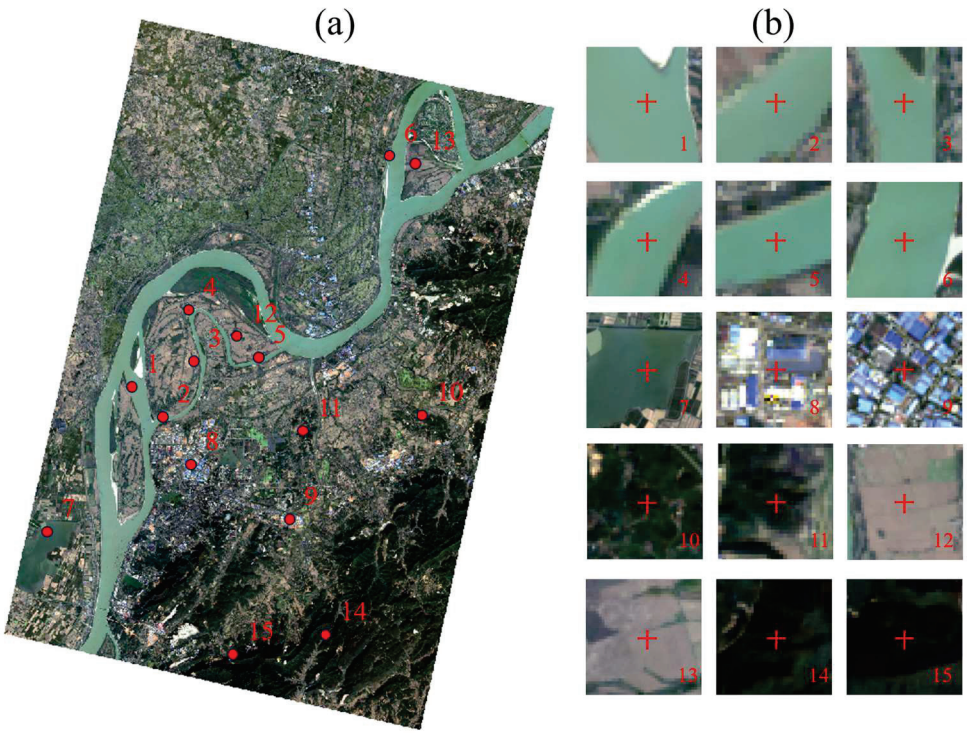

Figure 13. Spatial distribution of "pure" pixels in Landsat scene (standard true color composite) in Tongling section of Yangtze River. The number in (**a**) is the image id, and the number in (**b**) is the scene that corresponds to each image, where id (1–7) represent water, id (8–9) represent building, id (10–11) represent vegetation, id (12–13) represent bare soil, and id (14–15) represent mountain shadows.

Utilizing remote sensing imagery, high-resolution Google Earth images, and the Chinese MapWorld database, a total of 1768 pure pixel samples were selected. Regardless of the land cover type, certain discrepancies exist in the reflectance of pure land cover pixels across the six spectral bands between Landsat-8 and Landsat-9 data (Figure 14). Notably, the reflectance of the NIR band exhibits a significant difference between Landsat-8 OLI and Landsat-9 OLI-2, impacting the construction of various water indices. Except for the MNDWI index, which does not utilize the NIR band, all others in this study incorporated this specific band in their formulation. The comparative analysis revealed a smaller discrepancy in water body extraction accuracy between Landsat-8 and Landsat-9 for the MNDWI index compared to others, likely due to the exclusion of the NIR band.

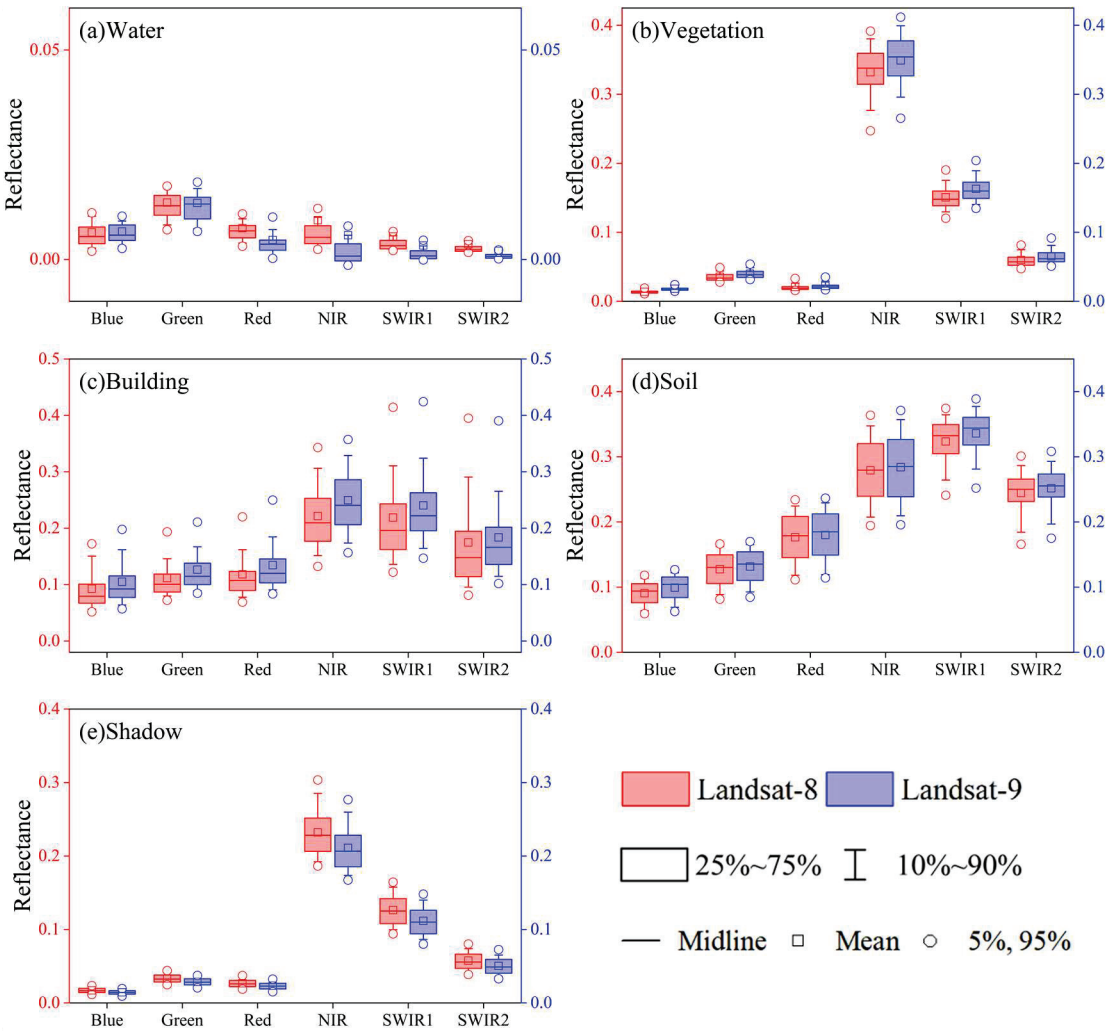

Figure 14. Surface reflectance of various land cover pixels in Landsat-8 and Landsat-9 imagery.

5.3. Uncertainty and Perspective

Some existed studies analyzed the differences between Landsat-8 and Landsat-9 satellite data, and the results suggest that Landsat 9 closely resembles Landsat 8 in various aspects and has similar reflected wavelengths and find suitability for both satellite datasets for water detection [21,56]. The significant differences in the average absolute percentage change in the bands may affect the water detections. However, whether the deviation in the calculation of water indices affects the mapping performances is still unclear. Therefore, we conducted a comparative analysis of the performance in water body extraction between Landsat-8 and Landsat-9 satellite data in this study. Our research, leveraging eight distinct water indices, aimed to extract water bodies at seven sites globally from Landsat-8 and

Landsat-9. That is the main academic contribution and novelty of this study. The findings indicate a good consistency between the Landsat-9 and Landsat-8 satellites, with the former demonstrating superior performance.

The selection of image data is pivotal to ensuring the accuracy of cross-comparisons, necessitating the use of synchronized image pairs. The most reliable data are the cross under-fly data provided by the United States Geological Survey (USGS), where Landsat 9 and Landsat 8 pass overhead almost simultaneously, with temporal discrepancies as minimal as a few seconds and no more than three minutes and nearly identical solar azimuth and elevation angles [55]. This minimizes the potential discrepancies arising from atmospheric and illumination conditions. The results in [39,54] have leveraged these data to analyze the differences between the two sensors, illustrating this approach.

It is crucial to note, however, that the Landsat-8 and Landsat-9 data used in this study were still separated by 1d. Water bodies can undergo changes within a single day, particularly in arid regions [13], which may influence the outcomes of this study. Moreover, the selection of water bodies was somewhat limited, primarily due to the multiple considerations of acquisition date (minimum temporal gap), image quality (cloud cover), geographical distribution, and water body coverage in our selection of remote sensing imagery. For the accuracy assessment, this study mainly relied on visual interpretation results of employed Landsat-8 and Landsat-9 imagery. The high-resolution Google Earth imagery and Chinese MapWorld database were also utilized to distinguish between water and non-water classes, especially for indistinguishable pixels on 30 m Landsat scenes. However, these datasets might have been compiled and integrated from remote sensing images acquired over adjacent periods (within several weeks before or after the primary acquisition dates). Although the temporal differences between the Landsat and high-resolution reference datasets may introduce potential uncertainties, in this study, the imagery was captured over the same scene and within a 24 h interval, minimizing any impact on the final results. In future studies, we aim to increase the number of reference data by incorporating additional field sites to reduce uncertainty and enable more robust comparisons.

In this study, we utilized level 2 science products (L2SP) available on the Google Earth Engine (GEE) platform, employing the atmospheric correction algorithm from the Land Surface Reflectance Code (LaSRC) algorithm (Version 3.5.5) [57]. Although Landsat-8 and Landsat-9 are sibling satellites, certain improvements or modifications to the OLI-2 sensor on Landsat-9 compared to the OLI sensor could account for some of the observed discrepancies in water body extraction results caused by identical surface reflectance computations. In addition, the different performance of various indices between Landsat-8 and Landsat-9 data can be attributed to variability of reflectance spectra caused by concentrations of phytoplankton and sediments, depth, and/or substratum type [58]. For example, Lianhuan Lake is a typical shallow water area (average depth < 0.5 m), and regional aquatic plants are flourishing. Liangzi Lake is characterized by dense phytoplankton. These facts might result in possible spectral variations (as well as water index values) affecting the water mapping accuracy.

Threshold segmentation is a commonly employed method for water body extraction, yet the setting of the threshold significantly influences the separation outcome [8]. An excessively high threshold may lead to omission errors, particularly for smaller water bodies, while a low threshold can introduce considerable noise [46]. The subjectivity inherent in manually setting thresholds is undeniable. Beyond logical operations, water index thresholds predominantly utilize empirical (global) thresholds and bisection (local adaptive) thresholds, with the key to threshold applicability lying in its ability to differentiate the subtle distinctions between mixed water and non-water pixels [59]. In fact, the optimal threshold is only available in ideal conditions since it is dependent not only on the sensor but also on the scene. To mitigate the subjectivity of empirical thresholds, this study employed the Otsu method for determining the segmentation threshold. Algorithms like the Otsu method and histogram bimodality are standard for threshold segmentation but are not without limitations, especially in complex environments. Li et al. [56] explored

the usability of Landsat-9 images in the relationship between the extraction accuracy and the algorithm; the results indicated that the fixed threshold may cause the significantly distorted overall accuracy of water mapping. Studies have shown that the Otsu method's optimal threshold for the NDWI index is 0.18 [59], significantly lower than the actual optimal value (0.38) obtained by the minimum thresholding method. Further research demonstrated that the accuracy gap between the Otsu threshold and manually determined optimal thresholds could reach up to 9–200% [60,61], suggesting the Otsu threshold may not be suitable for all case areas or for indices with unimodal distributions. In addition, this specific method is sensitive to the proportion of water vs. non-water pixels. In this study, we found that the impact of the polygon size on Otsu threshold and subsequently on water extraction accuracy is limited. This can be attributed to the distinctive class separability between water and non-water classes. Nevertheless, it is noted that the performance of Otsu method for threshold segmentation in this study is satisfactory. In addition, though not implemented in our current study, we intend to do so in the future so the modified Otsu method can identify the robust threshold of various water indices and believe we can further reduce the uncertainty and improve the accuracy of the water mapping.

The pivotal role of the Landsat series in water body remote sensing research is undeniable. With the confirmation that the Landsat-9 satellite can accurately map surface water, the future holds promise for achieving high-spatiotemporal resolution Earth observations at more detailed temporal intervals [21]. By integrating emerging technologies such as deep learning, we can precisely depict land cover changes and their impacts on surface water resources, crafting comprehensive solutions for assessing progress towards SDG-6 indicators.

6. Conclusions

The Landsat program has functioned much like a relay runner, launching a series of satellites that have conducted Earth observations for over 50 years. This enduring initiative has continually passed the baton from one satellite to the next, ensuring a consistent and valuable flow of data to monitor and study our planet's environment and changes. In this study, we analyze the performance of almost simultaneous Landsat-8 and Landsat-9 data for water body extraction based on eight common water indices (NDWI, MNDWI, ANDWI, WI_{2015}, TCW, $AWEI_{sh}$, $AWEI_{nsh}$, and MBWI) to extract water bodies in seven study sites worldwide. The Otsu algorithm is utilized to automatically determine the optimal segmentation threshold for water body extraction. From the perspective of the extraction performance of each index, we investigated the effect of both satellite data. The results showed the following:

(1) Landsat-9 satellite data can be used for water body extraction effectively, with results consistent with those from Landsat-8. The selected eight water indices in this study are applicable on both Landsat-8 and Landsat-9 satellites.
(2) The NDWI index shows a larger variability in accuracy compared to other indices when used on Landsat-8 and Landsat-9 imagery. Therefore, additional caution should be exercised when using the NDWI for water body analysis with both Landsat-8 and Landsat-9 satellites simultaneously.
(3) For Landsat-8 and Landsat-9 imagery, ratio-based water indices tend to have more omission errors, while difference-based indices are more prone to commission errors. All water indices can enhance water information and suppress background noise. Among them, TCW and MBWI show less effective suppression of mountain shadows, while $AWEI_{nsh}$ performs well in extracting fine rivers but poorly in suppressing building information, leading to more misclassification. Overall, ratio-based indices exhibit greater variability in overall accuracy, whereas difference-based indices demonstrate lower sensitivity to variations in the study area, showing smaller overall accuracy fluctuations and higher robustness.

Last but not least, the combined use of Landsat-8 and Landsat-9 is promising, particularly for water extraction. However, different water index methods exhibit unique

characteristics under various environmental conditions, and the most suitable method should be selected based on specific circumstances.

Supplementary Materials: The following supporting information can be downloaded at: https://www.mdpi.com/article/10.3390/rs16111984/s1, Figure S1: Differences of water indices maps between Landsat-8 and Landsat-9 data in Lake Nipissing region; Figure S2: Differences of water indices maps between Landsat-8 and Landsat-9 data in Tongling section of Yangtze River region; Figure S3: Differences of water indices maps between Landsat-8 and Landsat-9 data in Lianhuan Lake region; Figure S4: Differences of water indices maps between Landsat-8 and Landsat-9 data in Sai Lake region; Figure S5: Differences of water indices maps between Landsat-8 and Landsat-9 data in Liangzi Lake region; Figure S6: Correlation analysis of water indices in the Mille Lacs Lake region based on Landsat-8 and Landsat-9 imagery; Figure S7: Correlation analysis of water indices in the Lake Nipissing region based on Landsat-8 and Landsat-9 imagery; Figure S8: Correlation analysis of water indices in the Tongling section of Yangtze River region based on Landsat-8 and Landsat-9 imagery; Figure S9: Correlation analysis of water indices in the Lianhuan Lake region based on Landsat-8 and Landsat-9 imagery (Note: red line denotes the fitted line); Figure S10: Correlation analysis of water indices in the Sai Lake region based on Landsat-8 and Landsat-9 imagery; Figure S11: Correlation analysis of water indices in the Liangzi Lake region based on Landsat-8 and Landsat-9 imagery); Figure S12: Comparison of separability of different water indices based on Landsat-8 and Landsat-9 imagery in Mille Lacs Lake region; Figure S13: Comparison of separability of different water indices based on Landsat-8 and Landsat-9 imagery in Lake Nipissing region; Figure S14: Comparison of separability of different water indices based on Landsat-8 and Landsat-9 imagery in Tongling section of Yangtze River region; Figure S15: Comparison of separability of different water indices based on Landsat-8 and Landsat-9 imagery in Lianhuan Lake region; Figure S16: Comparison of separability of different water indices based on Landsat-8 and Landsat-9 imagery in Sai Lake region; Figure S17: Comparison of separability of different water indices based on Landsat-8 and Landsat-9 imagery in Liangzi Lake region; Figure S18: Comparison of the applicability of different water body index thresholds based on Landsat-8 and Landsat-9 imagery in Mille Lacs Lake region; Figure S19: Comparison of the applicability of different water body index thresholds based on Landsat-8 and Landsat-9 imagery in Lake Nipissing region; Figure S20: Comparison of the applicability of different water body index thresholds based on Landsat-8 and Landsat-9 imagery in Tongling section of Yangtze River region; Figure S21: Comparison of the applicability of different water body index thresholds based on Landsat-8 and Landsat-9 imagery in Lianhuan Lake region; Figure S22: Comparison of the applicability of different water body index thresholds based on Landsat-8 and Landsat-9 imagery in Sai Lake region; Figure S23: Comparison of the applicability of different water body index thresholds based on Landsat-8 and Landsat-9 imagery in Liangzi Lake region; Figure S24: Spatial differences in water index extraction capacity in the Lake Nipissing region based on Landsat-9 imagery; Figure S25: Spatial differences in water index extraction capacity in the Lianhuan Lake region based on Landsat-9 imagery; Figure S26: Spatial differences in water index extraction capacity in the Sai Lake region based on Landsat-9 imagery; Figure S27. Spatial differences in water index extraction capacity in the Liangzi Lake region based on Landsat-9 imagery.

Author Contributions: Conceptualization, J.C., J.W. (Jingzhe Wang) and Y.W.; methodology, J.C., J.W. (Jingzhe Wang), Y.X., Y.Z., O.Y., R.Z. and Z.H.; software, J.C., Y.X., Y.Z. and Z.W.; validation, J.W. (Jing Wang), Y.W. and Z.W.; formal analysis, J.C., Y.W., J.W. (Jingzhe Wang), Y.X., Y.Z., O.Y. and R.Z.; investigation, J.C. and J.W. (Jing Wang); resources, J.W. (Jingzhe Wang) and Z.H.; data curation, J.C., Y.X. and F.L.; writing—original draft preparation, J.C., J.W. (Jingzhe Wang) and Y.Z.; writing—review and editing, J.W. (Jingzhe Wang), Y.Z., O.Y., R.Z. and Z.H.; visualization, J.C., Y.X., J.W. (Jing Wang) and F.L.; supervision, J.W. (Jingzhe Wang), Y.W. and Z.H.; project administration, J.W. (Jingzhe Wang) and Y.W.; funding acquisition, J.W. (Jingzhe Wang) and Y.Z. All authors have read and agreed to the published version of the manuscript.

Funding: This research was supported by the Guangdong Basic and Applied Basic Research Foundation (2023A1515011273 and 2021A1515110910), Basic Research Program of Shenzhen (20220811173316001), Specific Innovation Program of the Department of Education of Guangdong Province (2023KTSCX315), Guangdong Key Scientific Research Platform and Projects for the Higher-educational Institution (2022ZDZX4101), Shenzhen Polytechnic Research Fund (6023310031K and 6023271008K), and Open Research Fund Program of MNR Key Laboratory for Geo-Environmental

Monitoring of Great Bay Area (GEMLab-2023014). The funders had no role in study design, data collection and analysis, decision to publish, or preparation of the manuscript.

Data Availability Statement: Data will be made available upon request.

Acknowledgments: We appreciate the valuable comments offered by the anonymous reviewers and editors for the improvement of this manuscript. In addition, the authors would like to thank the USGS Landsat program for providing Landsat-8 and Landsat-9 satellite data.

Conflicts of Interest: The authors declare no conflicts of interest.

References

1. Pekel, J.-F.; Cottam, A.; Gorelick, N.; Belward, A.S. High-resolution mapping of global surface water and its long-term changes. *Nature* **2016**, *540*, 418–422. [CrossRef] [PubMed]
2. Huang, C.; Chen, Y.; Zhang, S.; Wu, J. Detecting, Extracting, and Monitoring Surface Water From Space Using Optical Sensors: A Review. *Rev. Geophys.* **2018**, *56*, 333–360. [CrossRef]
3. Jordan, Y.C.; Ghulam, A.; Hartling, S. Traits of surface water pollution under climate and land use changes: A remote sensing and hydrological modeling approach. *Earth-Sci. Rev.* **2014**, *128*, 181–195. [CrossRef]
4. Chang, N.-B.; Imen, S.; Vannah, B. Remote Sensing for Monitoring Surface Water Quality Status and Ecosystem State in Relation to the Nutrient Cycle: A 40-Year Perspective. *Crit. Rev. Environ. Sci. Technol.* **2015**, *45*, 101–166. [CrossRef]
5. Sogno, P.; Klein, I.; Kuenzer, C. Remote Sensing of Surface Water Dynamics in the Context of Global Change—A Review. *Remote Sens.* **2022**, *14*, 2475. [CrossRef]
6. Tran, T.N.D.; Do, S.K.; Nguyen, B.Q.; Tran, V.N.; Grodzka-Łukaszewska, M.; Sinicyn, G.; Lakshmi, V. Investigating the Future Flood and Drought Shifts in the Transboundary Srepok River Basin Using CMIP6 Projections. *IEEE J. Sel. Top. Appl. Earth Obs. Remote Sens.* **2024**, *17*, 7516–7529. [CrossRef]
7. Ge, X.; Ding, J.; Amantai, N.; Xiong, J.; Wang, J. Responses of vegetation cover to hydro-climatic variations in Bosten Lake Watershed, NW China. *Front. Plant Sci.* **2024**, *15*, 1323445. [CrossRef] [PubMed]
8. Yang, X.; Qin, Q.; Yésou, H.; Ledauphin, T.; Koehl, M.; Grussenmeyer, P.; Zhu, Z. Monthly estimation of the surface water extent in France at a 10-m resolution using Sentinel-2 data. *Remote Sens. Environ.* **2020**, *244*, 111803. [CrossRef]
9. Pickens, A.H.; Hansen, M.C.; Hancher, M.; Stehman, S.V.; Tyukavina, A.; Potapov, P.; Marroquin, B.; Sherani, Z. Mapping and sampling to characterize global inland water dynamics from 1999 to 2018 with full Landsat time-series. *Remote Sens. Environ.* **2020**, *243*, 111792. [CrossRef]
10. Luo, X.; Tong, X.; Hu, Z. An applicable and automatic method for earth surface water mapping based on multispectral images. *Int. J. Appl. Earth Obs. Geoinf.* **2021**, *103*, 102472. [CrossRef]
11. Palmer, S.C.; Kutser, T.; Hunter, P.D. Remote sensing of inland waters: Challenges, progress and future directions. *Remote Sens. Environ.* **2015**, *157*, 1–8. [CrossRef]
12. Yang, X.; Chen, L. Evaluation of automated urban surface water extraction from Sentinel-2A imagery using different water indices. *J. Appl. Remote Sens.* **2017**, *11*, 026016. [CrossRef]
13. Wang, J.; Ding, J.; Li, G.; Liang, J.; Yu, D.; Aishan, T.; Zhang, F.; Yang, J.; Abulimiti, A.; Liu, J. Dynamic detection of water surface area of Ebinur Lake using multi-source satellite data (Landsat and Sentinel-1A) and its responses to changing environment. *CATENA* **2019**, *177*, 189–201. [CrossRef]
14. Yang, X.; Zhao, S.; Qin, X.; Zhao, N.; Liang, L. Mapping of Urban Surface Water Bodies from Sentinel-2 MSI Imagery at 10 m Resolution via NDWI-Based Image Sharpening. *Remote Sens.* **2017**, *9*, 596. [CrossRef]
15. Duan, Y.; Zhang, W.; Huang, P.; He, G.; Guo, H. A New Lightweight Convolutional Neural Network for Multi-Scale Land Surface Water Extraction from GaoFen-1D Satellite Images. *Remote Sens.* **2021**, *13*, 4576. [CrossRef]
16. Petrakis, R.E.; Soulard, C.E.; Waller, E.K.; Walker, J.J. Analysis of Surface Water Trends for the Conterminous United States Using MODIS Satellite Data, 2003–2019. *Water Resour. Res.* **2022**, *58*, e2021WR031399. [CrossRef]
17. Li, L.; Skidmore, A.; Vrieling, A.; Wang, T. A new dense 18-year time series of surface water fraction estimates from MODIS for the Mediterranean region. *Hydrol. Earth Syst. Sci.* **2019**, *23*, 3037–3056. [CrossRef]
18. Ogilvie, A.; Belaud, G.; Massuel, S.; Mulligan, M.; Le Goulven, P.; Calvez, R. Surface water monitoring in small water bodies: Potential and limits of multi-sensor Landsat time series. *Hydrol. Earth Syst. Sci.* **2018**, *22*, 4349–4380. [CrossRef]
19. Alsdorf, D.E.; Rodríguez, E.; Lettenmaier, D.P. Measuring surface water from space. *Rev. Geophys.* **2007**, *45*, RG2002. [CrossRef]
20. Hemati, M.; Hasanlou, M.; Mahdianpari, M.; Mohammadimanesh, F. A Systematic Review of Landsat Data for Change Detection Applications: 50 Years of Monitoring the Earth. *Remote Sens.* **2021**, *13*, 2869. [CrossRef]
21. Masek, J.G.; Wulder, M.A.; Markham, B.; McCorkel, J.; Crawford, C.J.; Storey, J.; Jenstrom, D.T. Landsat 9: Empowering open science and applications through continuity. *Remote Sens. Environ.* **2020**, *248*, 111968. [CrossRef]
22. Showstack, R. Landsat 9 Satellite Continues Half-Century of Earth Observations: Eyes in the sky serve as a valuable tool for stewardship. *BioScience* **2022**, *72*, 226–232. [CrossRef]
23. Chen, J.; Chen, S.; Fu, R.; Li, D.; Jiang, H.; Wang, C.; Peng, Y.; Jia, K.; Hicks, B.J. Remote Sensing Big Data for Water Environment Monitoring: Current Status, Challenges, and Future Prospects. *Earth's Future* **2022**, *10*, e2021EF002289. [CrossRef]

24. Bijeesh, T.V.; Narasimhamurthy, K.N. Surface water detection and delineation using remote sensing images: A review of methods and algorithms. *Sustain. Water Resour. Manag.* **2020**, *6*, 68. [CrossRef]
25. Liu, S.; Wu, Y.; Zhang, G.; Lin, N.; Liu, Z. Comparing Water Indices for Landsat Data for Automated Surface Water Body Extraction under Complex Ground Background: A Case Study in Jilin Province. *Remote Sens.* **2023**, *15*, 1678. [CrossRef]
26. Kaplan, G.; Avdan, U. Object-based water body extraction model using Sentinel-2 satellite imagery. *Eur. J. Remote Sens.* **2017**, *50*, 137–143. [CrossRef]
27. Zhou, Y.; Dong, J.; Xiao, X.; Xiao, T.; Yang, Z.; Zhao, G.; Zou, Z.; Qin, Y. Open surface water mapping algorithms: A comparison of water-related spectral indices and sensors. *Water* **2017**, *9*, 256. [CrossRef]
28. Feyisa, G.L.; Meilby, H.; Fensholt, R.; Proud, S.R. Automated Water Extraction Index: A new technique for surface water mapping using Landsat imagery. *Remote Sens. Environ.* **2014**, *140*, 23–35. [CrossRef]
29. Zhang, F.; Tiyip, T.; Kung, H.-t.; Johnson, V.C.; Wang, J.; Nurmemet, I. Improved water extraction using Landsat TM/ETM+ images in Ebinur Lake, Xinjiang, China. *Remote Sens. Appl. Soc. Environ.* **2016**, *4*, 109–118. [CrossRef]
30. Ma, S.; Zhou, Y.; Gowda, P.H.; Dong, J.; Zhang, G.; Kakani, V.G.; Wagle, P.; Chen, L.; Flynn, K.C.; Jiang, W. Application of the water-related spectral reflectance indices: A review. *Ecol. Indic.* **2019**, *98*, 68–79. [CrossRef]
31. McFeeters, S.K. The use of the Normalized Difference Water Index (NDWI) in the delineation of open water features. *Int. J. Remote Sens.* **1996**, *17*, 1425–1432. [CrossRef]
32. Xu, H. Modification of normalised difference water index (NDWI) to enhance open water features in remotely sensed imagery. *Int. J. Remote Sens.* **2006**, *27*, 3025–3033. [CrossRef]
33. Wang, X.; Xie, S.; Zhang, X.; Chen, C.; Guo, H.; Du, J.; Duan, Z. A robust Multi-Band Water Index (MBWI) for automated extraction of surface water from Landsat 8 OLI imagery. *Int. J. Appl. Earth Obs. Geoinf.* **2018**, *68*, 73–91. [CrossRef]
34. Fisher, A.; Flood, N.; Danaher, T. Comparing Landsat water index methods for automated water classification in eastern Australia. *Remote Sens. Environ.* **2016**, *175*, 167–182. [CrossRef]
35. Rad, A.M.; Kreitler, J.; Sadegh, M. Augmented Normalized Difference Water Index for improved surface water monitoring. *Environ. Model. Softw.* **2021**, *140*, 105030. [CrossRef]
36. Baig, M.H.A.; Zhang, L.; Shuai, T.; Tong, Q. Derivation of a tasselled cap transformation based on Landsat 8 at-satellite reflectance. *Remote Sens. Lett.* **2014**, *5*, 423–431. [CrossRef]
37. Du, Z.; Li, W.; Zhou, D.; Tian, L.; Ling, F.; Wang, H.; Gui, Y.; Sun, B. Analysis of Landsat-8 OLI imagery for land surface water mapping. *Remote Sens. Lett.* **2014**, *5*, 672–681. [CrossRef]
38. Liu, Z.; Yao, Z.; Wang, R. Assessing methods of identifying open water bodies using Landsat 8 OLI imagery. *Environ. Earth Sci.* **2016**, *75*, 873. [CrossRef]
39. Xu, H.; Ren, M.; Lin, M. Cross-comparison of Landsat-8 and Landsat-9 data: A three-level approach based on underfly images. *GIScience Remote Sens.* **2024**, *61*, 2318071. [CrossRef]
40. Markham, B.; Jenstrom, D.; Masek, J.; Dabney, P.; Pedelty, J.; Barsi, J.; Montanaro, M. *Landsat 9: Status and Plans*; SPIE: Bellingham, WA, USA, 2016; Volume 9972. [CrossRef]
41. Niroumand-Jadidi, M.; Bovolo, F.; Bresciani, M.; Gege, P.; Giardino, C. Water Quality Retrieval from Landsat-9 (OLI-2) Imagery and Comparison to Sentinel-2. *Remote Sens.* **2022**, *14*, 4596. [CrossRef]
42. Albertini, C.; Gioia, A.; Iacobellis, V.; Manfreda, S. Detection of surface water and floods with multispectral satellites. *Remote Sens.* **2022**, *14*, 6005. [CrossRef]
43. Zhao, B.; Wu, J.; Han, X.; Tian, F.; Liu, M.; Chen, M.; Lin, J. An improved surface water extraction method by integrating multi-type priori information from remote sensing. *Int. J. Appl. Earth Obs. Geoinf.* **2023**, *124*, 103529.
44. Ostu, N. A threshold selection method from gray-level histograms. *IEEE Trans. Syst. Man Cybern.* **1979**, *9*, 62–69.
45. Rosser, J.F.; Leibovici, D.G.; Jackson, M.J. Rapid flood inundation mapping using social media, remote sensing and topographic data. *Nat. Hazards* **2017**, *87*, 103–120. [CrossRef]
46. Yang, X.; Chen, Y.; Wang, J. Combined use of Sentinel-2 and Landsat 8 to monitor water surface area dynamics using Google Earth Engine. *Remote Sens. Lett.* **2020**, *11*, 687–696. [CrossRef]
47. Günen, M.A.; Atasever, U.H. Remote sensing and monitoring of water resources: A comparative study of different indices and thresholding methods. *Sci. Total Environ.* **2024**, *926*, 172117. [CrossRef] [PubMed]
48. Pan, F.; Xi, X.; Wang, C. A Comparative Study of Water Indices and Image Classification Algorithms for Mapping Inland Surface Water Bodies Using Landsat Imagery. *Remote Sens.* **2020**, *12*, 1611. [CrossRef]
49. Haas, E.M.; Bartholomé, E.; Lambin, E.F.; Vanacker, V. Remotely sensed surface water extent as an indicator of short-term changes in ecohydrological processes in sub-Saharan Western Africa. *Remote Sens. Environ.* **2011**, *115*, 3436–3445. [CrossRef]
50. Matthews, B.W. Comparison of the predicted and observed secondary structure of T4 phage lysozyme. *Biochim. Et Biophys. Acta (BBA)-Protein Struct.* **1975**, *405*, 442–451. [CrossRef]
51. Prakash, N.; Manconi, A.; Loew, S. Mapping Landslides on EO Data: Performance of Deep Learning Models vs. Traditional Machine Learning Models. *Remote Sens.* **2020**, *12*, 346. [CrossRef]
52. Chen, F.; Chen, X.; Van de Voorde, T.; Roberts, D.; Jiang, H.; Xu, W. Open water detection in urban environments using high spatial resolution remote sensing imagery. *Remote Sens. Environ.* **2020**, *242*, 111706. [CrossRef]
53. Kauth, R.J.; Thomas, G. *The Tasselled Cap—A Graphic Description of the Spectral-Temporal Development of Agricultural Crops as Seen by Landsat*; Purdue University: West Lafayette, IN, USA, 1976; p. 159.

54. Xu, H.; Ren, M.; Yang, L. Evaluating the consistency of surface brightness, greenness, and wetness observations between Landsat-8 OLI and Landsat-9 OLI2 through underfly images. *Int. J. Appl. Earth Obs. Geoinf.* **2023**, *124*, 103546. [CrossRef]
55. Gross, G.; Helder, D.; Begeman, C.; Leigh, L.; Kaewmanee, M.; Shah, R. Initial Cross-Calibration of Landsat 8 and Landsat 9 Using the Simultaneous Underfly Event. *Remote Sens.* **2022**, *14*, 2418. [CrossRef]
56. Li, X.; Zhang, D.; Jiang, C.; Zhao, Y.; Li, H.; Lu, D.; Qin, K.; Chen, D.; Liu, Y.; Sun, Y. Comparison of lake area extraction algorithms in Qinghai Tibet plateau leveraging google earth engine and landsat-9 data. *Remote Sens.* **2022**, *14*, 4612. [CrossRef]
57. Vermote, E.; Justice, C.; Claverie, M.; Franch, B. Preliminary analysis of the performance of the Landsat 8/OLI land surface reflectance product. *Remote Sens. Environ.* **2016**, *185*, 46–56. [CrossRef] [PubMed]
58. Wang, J.; Shi, T.; Yu, D.; Teng, D.; Ge, X.; Zhang, Z.; Yang, X.; Wang, H.; Wu, G. Ensemble machine-learning-based framework for estimating total nitrogen concentration in water using drone-borne hyperspectral imagery of emergent plants: A case study in an arid oasis, NW China. *Environ. Pollut.* **2020**, *266*, 115412. [CrossRef] [PubMed]
59. Sekertekin, A. A Survey on Global Thresholding Methods for Mapping Open Water Body Using Sentinel-2 Satellite Imagery and Normalized Difference Water Index. *Arch. Comput. Methods Eng.* **2021**, *28*, 1335–1347. [CrossRef]
60. Mukherjee, A.; Kumar, A.A.; Ramachandran, P. Development of new index-based methodology for extraction of built-up area from landsat7 imagery: Comparison of performance with svm, ann, and existing indices. *IEEE Trans. Geosci. Remote Sens.* **2020**, *59*, 1592–1603. [CrossRef]
61. Li, C.; Shao, Z.; Zhang, L.; Huang, X.; Zhang, M. A comparative analysis of index-based methods for impervious surface mapping using multiseasonal Sentinel-2 satellite data. *IEEE J. Sel. Top. Appl. Earth Obs. Remote Sens.* **2021**, *14*, 3682–3694. [CrossRef]

Disclaimer/Publisher's Note: The statements, opinions and data contained in all publications are solely those of the individual author(s) and contributor(s) and not of MDPI and/or the editor(s). MDPI and/or the editor(s) disclaim responsibility for any injury to people or property resulting from any ideas, methods, instructions or products referred to in the content.

International Journal of
Geo-Information

MDPI

Article

Annual and Seasonal Dynamics of CO_2 Emissions in Major Cities of China (2019–2022)

Yue Zhao [1], Yuning Feng [1,*], Mingyi Du [1] and Klaus Fraedrich [2]

[1] School of Geomatics and Urban Spatial Information, Beijing University of Civil Engineering and Architecture, Beijing 100044, China; 2108160222002@stu.bucea.edu.cn (Y.Z.); dumingyi@bucea.edu.cn (M.D.)
[2] Max Planck Institute for Meteorology, 20146 Hamburg, Germany; klaus.fraedrich@mpimet.mpg.de
* Correspondence: fengyuning@bucea.edu.cn; Tel.: +86-152-0125-5273

Abstract: To control the growth of CO_2 emissions and achieve the goal of carbon peaking, this study carried out a detailed spatio-temporal analysis of carbon emissions in major cities of China on a city-wide and seasonal scale, used carbon emissions as an indicator to explore the impact of COVID-19 on human activities, and thereby studied the urban resilience of different cities. Our research re-vealed that (i) the seasonal patterns of CO2 emissions in major cities of China could be divided into four types: Long High, Summer High, Winter High, and Fluctuations, which was highly related to the power and industrial sectors. (ii) The annual trends, which were strongly affected by the pan-demic, could be divided into four types: Little Impact, First Impact, Second Impact, and Both Impact. (iii) The recovery speed of CO2 emissions reflected urban resilience. Cities with higher levels of de-velopment had a stronger resistance to the pandemic, but a slower recovery speed. Studying the changes in CO2 emissions and their causes can help to make timely policy adjustments during the economic recovery period after the end of the pandemic, provide more references to urban resilience construction, and provide experience for future responses to large-scale emergencies.

Keywords: CO_2 emissions; time series decomposition; annual dynamics; seasonal dynamics; urban resilience; social emergencies (COVID-19)

1. Introduction

Global warming is broadly agreed to be mainly caused by human activity, and is currently an important issue facing sustainable human development [1]. Evidence shows that the heat-trapping gases released by burning fossil fuels, referred to as greenhouse gases, are responsible for causing global warming [2], which is related to multiple sectors such as power, industry, transportation, and residential consumption [3]. Thus, greenhouse gas emissions (GHG), such as carbon dioxide (CO_2), are critical for understanding and addressing the climate crisis [4]. In this context, many countries have set clear targets to reduce their CO_2 emissions in order to face the challenges of climate change. China promises to peak carbon by 2030 and achieve carbon neutrality by 2060 [5]. Correspondingly, despite facing many difficulties, China is taking a series of measures to achieve this goal, making a positive contribution to promoting global governance in response to climate change. These measures include developing and widely promoting low-carbon technologies; developing a new energy industry to promote energy transformation; and implementing comprehensive low-carbon policies and laws [6–8]. So far, CO_2 emissions per unit of energy consumption, energy consumption per unit of gross domestic product (GDP), and CO_2 emissions per unit of GDP all present downward trends in China, but China is yet to reach its peak in CO_2 emissions per capita, which is the key factor of CO_2 emission measurements [9]. Therefore, accurately characterizing the dynamics of CO_2 emissions (before the carbon peak is attained as a turning point) is critical for China to formulate and implement corresponding policies in order to fulfill its commitment of reducing CO_2 emissions.

At present, China's total CO_2 emissions rank first in the world, but their growth rate is constantly decreasing and has been effectively controlled. In addition, China's CO_2 emissions are unevenly distributed in space, with significant differences among different sectors [10]. According to studies in recent years, there was an initial dip in CO_2 emissions due to the COVID-19 pandemic, followed by varying degrees of rebounds [11]. Studying the dynamics of CO_2 emissions can observe the impact of the COVID-19 pandemic on human socio-economic activities and reveal patterns of urban resilience occurring during the pandemic period (2019–2022). Urban resilience is the capacity of a city to rebound from major and minor disasters [12], which shows whether a city can cope with risks or events and is an important goal in SDG 11 (making cities and human settlements inclusive, safe, resilient, and sustainable). According to the recovery of CO_2 emissions, we can adjust the relevant policies in the post-pandemic period in a timely manner and study the laws of urban resilience through the recovery rate of CO_2 emissions. This can also provide experience for dealing with disturbances in the future and improve the adaptability of cities to risks [13].

As the world's current major economic power and emitter of CO_2, there are abundant CO_2 emissions studies focusing on China [14]. However, due to the lack of high-spatiotemporal-accuracy CO_2 emission data, studies of CO_2 dynamics are mostly analyzed on an annual basis [15], lacking a high temporal accuracy. Moreover, most studies choose the whole country or certain provinces as their research object, but less focus on the urban scale [16], which lacks fine-scale conclusions for the guidance of emission reduction. Furthermore, the contribution of each CO_2 emission sector is worth considering, but the specific classification of various CO_2 emission sources is needed now [17]. According to relevant research, the influencing factors of CO_2 emissions are mainly divided into three categories: technology, scale, and structure, which are also the main ideas involved in implementing CO_2 reduction policies [18–20]. In recent years, some studies have noticed the impact of seasonal changes on carbon emissions [21], which provides new possible methods for emission reduction, but there is a lack of more extensive and detailed research. The development of CO_2 emission datasets brings new possibilities for finer-scale studies. Fine temporal–spatial CO_2 emission management becomes the inevitable trend, keeping the goals of carbon peak and carbon neutrality. More precision in terms of the accuracy of timing allows us to grasp the dynamic changes occurring due to the impact of major social events on human activities in a more timely and accurate manner. The precise spatial scale allows us to focus on typical research areas. In addition, detailed sources of CO_2 emissions make it easier for us to study the causes of CO_2 emission changes.

In order to summarize the patterns of CO_2 emission changes occurring during the pandemic period and provide new ideas for the implementation of future emission reduction policies, this study separated the seasonal and annual trends of CO_2 emissions by time series decomposition. Taking COVID-19 from 2019 to 2022 as an example, we analyzed the relationship between the impact of major social events and changes in CO_2 emissions, as well as the relationship between seasons and CO_2 emissions during this period, which is lacking in previous relevant studies. This study fills the gap in related research by conducting more refined studies (urban and monthly scales), comparing and analyzing CO_2 emissions from different sectors and cities, and studying the seasonal trends of CO_2 emissions. In addition, we studied the recovery rates of CO_2 emissions in different cities after COVID-19 (2019.1–2022.12) and analyzed their patterns.

2. Data and Methods

This study contains three major steps (Figure 1): (1) Data collection and the preprocession of CO_2 emissions and relevant variables. (2) Time series decomposition of CO_2 emission trends into annual and seasonal patterns, and then an analysis of both patterns by types and causes. (3) Evaluation of urban resilience during the COVID-19 pandemic based on the annual patterns of CO_2 emissions. The following sub-sections detail the data and main methods.

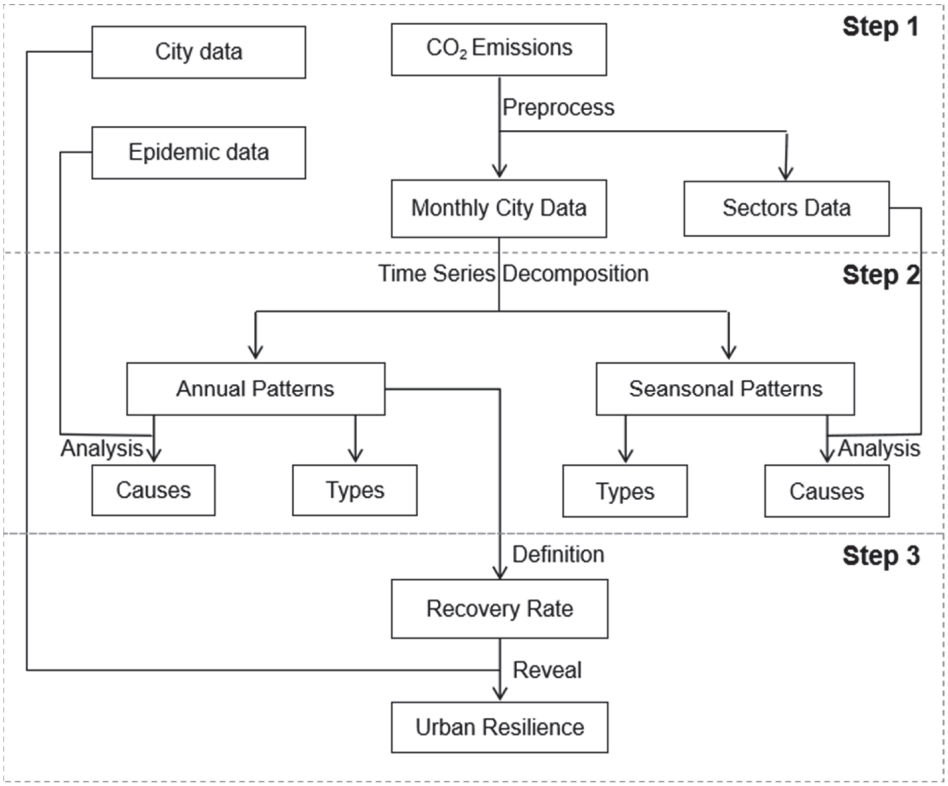

Figure 1. The process in this study.

2.1. Raw Data Collection and Pre-Procession

Thirty-one major cities in China with intensive human activities were selected as the research areas to be analyzed, which have high carbon footprints and become the main locations for controlling CO_2 emissions. The research period lasted from January 2019 to December 2022, which includes the period from the outbreak to the end of the pandemic.

The raw data for this article came from Global gRidded dAily CO_2 Emissions Dataset (GRACED) [22–25], which provides near-real-time global gridded daily CO_2 emissions data from fossil fuel and cement production with a global spatial resolution of 0.1° by 0.1° and a temporal resolution of 1 day, and the measure in kilograms of CO_2 per hour (kgC/h). The data satisfy the demand for high-quality, high-precision, and near-real-time data on CO_2 emissions to support global emissions monitoring across various spatial scales.

We calculated the monthly CO_2 emission data for provincial capital cities in China. For each city, we obtained the total CO_2 emission data, as well as specific CO_2 emission data for each of the four sectors: Power, Industry, Residential, and Ground Transportation. GRACED also provided CO_2 emission data from three sectors: International Aviation, International Shipping, and Domestic Aviation, which were not studied in detail in this work, due to their small contributions and their very low or even zero CO_2 emissions. A data summary is provided in Table 1 to provide readers with a general understanding of the data.

Table 1. Summary of total CO_2 emissions data for the studied cities (unit: kgC/h).

Year	2019	2020	2021	2022
Max	13,005,368	12,957,019	13,696,092	12,686,413
Min	71,630	73,133	77,953	71,983
Mean	2,255,063	2,333,183	2,470,084	2,413,396
STDEV	2,297,401	2,331,765	2,438,838	2,279,562

Other relevant data, such as population and gross domestic product (GDP). etc., were obtained from the China Statistical Yearbook to serve as a reference for exploring the causes of CO_2 emission changes in the subsequent experiments [26].

2.2. Time Series Decomposition of CO_2 Emissions Trend

A time series Y_t with seasonal factors can be decomposed into the following three components: (1) a trend component (T_t) representing long-term changes; (2) a seasonal component (S_t) which reveals periodic changes over time; and (3) an error component (E_t) as a mutation caused by errors [27]. Thus, Y_t can be decomposed by an additive model.

$$Y_t = T_t + S_t + E_t \quad (1)$$

This seasonal trend decomposition based on LOESS (STL) is a time series data analysis method, which makes the curve smoother and employs locally weighted regression models to decompose a time series into trend, seasonal, and remaining contributions. STL consists of an inner and an outer loop; the inner loop calculates the trend and seasonal components and the outer loop provides the robustness weights for the next inner loop. The process of STL is shown in Figure 2.

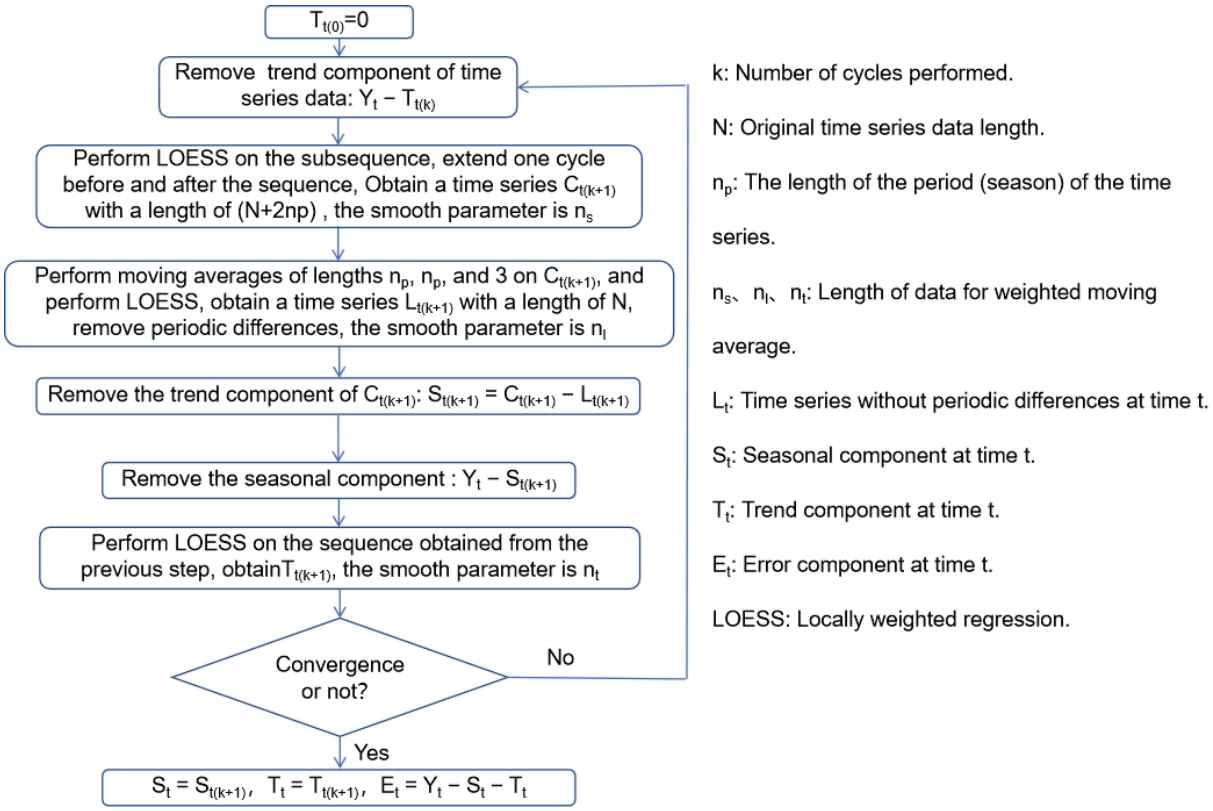

Figure 2. The process of STL.

STL is a simple and easy-to-use method for obtaining robust trend and seasonal components, and has a better applicability for complex long-term time series. The advantages of STL is that it can identify seasonal components changing over time, it is responsive to nonlinear trends, and it is robust in the presence of outliers [28]. The STL procedure was developed and implemented in the R software (version 4.2.1), and decomposed the CO_2 emissions into seasonal and annual patterns. Further, we analyzed the types and causes of the seasonal and annual patterns from the perspectives of CO_2 emission sectors and urban development, respectively.

2.3. Evaluation of Urban Resilience

A city is a huge artificial ecosystem in the sense that we can deal with the city problem as an ecological entity. We found that when cities were facing the impact of the pandemic, their human activity levels reflected in CO_2 emissions exhibited different fluctuations, which were related to their different levels of development. In this study, we used the per capita GDP of 2019 to represent the development levels of different cities during normal periods. Some cities, which revealed strong resistance to external influences and quickly recovered after being affected, we identified as urban resilient. Due to the fact that CO_2 emissions levels can reflect the strength of human activity levels, the recovery rate of CO_2 emissions can reflect the recovery rate of human activity levels, thereby reflecting the resistance of different cities (Equation (2)). Note that, in order to quantitatively compare cities with different levels of CO_2 emissions, their variations in CO_2 emission levels were measured by the ratio of the increase in CO_2 emissions to the initial value per time interval of the recovery period,

$$\mathrm{V} = \frac{\frac{\Delta E}{E_0}}{T_{end} - T_{star}} \tag{2}$$

with the recovery rate of CO_2 emissions V, the total increase in CO_2 emissions during the recovery period is represented by ΔE. E_0 is the initial value of CO_2 emissions (the average CO_2 emissions in the first half of 2019, which represents the normal CO_2 emissions without experiencing the pandemic); T_{star} denotes the time when CO_2 emissions begin to show a long-term upward trend; and T_{end} defines the time when CO_2 emissions do not show an upward trend or the monthly increase is very small. Furthermore, we used per capita GDP as an indicator to represent the development level of the city to investigate the relationship between the development level of the city and its own recovery rate, and then reveal the patterns of urban resilience.

3. Results

We decomposed the CO_2 emission variation patterns into seasonal and annual variations by STL, and then classified and summarized the results. In Section 3.1, we discuss the seasonal patterns of total CO_2 emissions and further investigate the seasonal patterns of the four specific CO_2 emission sectors, power, industry, residential, and others. As the power and industry sectors were the main sources of CO_2 emissions, we focused on their discussion. In Section 3.2, we analyze the annual patterns of total CO_2 emissions divided into four types. Then, we choose a city as an example for more detailed analysis. In Section 3.3, we calculate the recovery rate of the city and plot it.

3.1. Seasonal Patterns of CO_2 Emissions

The seasonal patterns of the total CO_2 emissions in major cities in China can be generally classified into the following four categories in Figure 3. The number on the vertical axes in Figure 3 represents the proportion of seasonal components of CO_2 emissions relative to the initial value. The distribution of these patterns is shown in Figure 4. More detailed data can be found in Table 2. Power and Industry, respectively, represent the proportion of CO_2 emissions from the power sector and industry sector in the total CO_2 emissions. Type represents the classification of the seasonal components of CO_2 emissions in cities. No data represents missing relevant raw data.

Long-term High: CO_2 emissions have a low peak around February and a high to medium level during other time periods, such as Shanghai.

Summer High: CO_2 emissions have a high peak during summer and a low level during other time periods, such as Beijing.

Winter High: CO_2 emissions have a high peak during winter and a low level during other time periods, such as Guangzhou.

Fluctuations: CO_2 emissions fluctuate frequently throughout the year, such as Hohhot.

Considering the sectors of CO_2 emissions, we found that CO_2 emissions from the same sector in different cities had similar patterns. The power sector peaked in summer, in winter, or both, and often fluctuated in the other months. For the industry sector, all cities' CO_2 emissions revealed a low peak around February, and most of them stayed at a high level in the other months. Note that all cities' CO_2 emissions from the residential sector showed the same pattern: peaking around January and remaining at low levels at all other times. Due to the significant impact of the pandemic on CO_2 emissions from the transportation sector, the data could not be decomposed into a trend component and seasonal component. But we can find patterns by observing the original data in Figure 5: during the pandemic, there were two time periods (January to October 2021 and March to December 2022) during which CO_2 emissions were at very low levels, while CO_2 emissions fluctuated greatly at other times. The other sectors were not studied in detail, due to their small contributions and the very low or even zero CO_2 emissions.

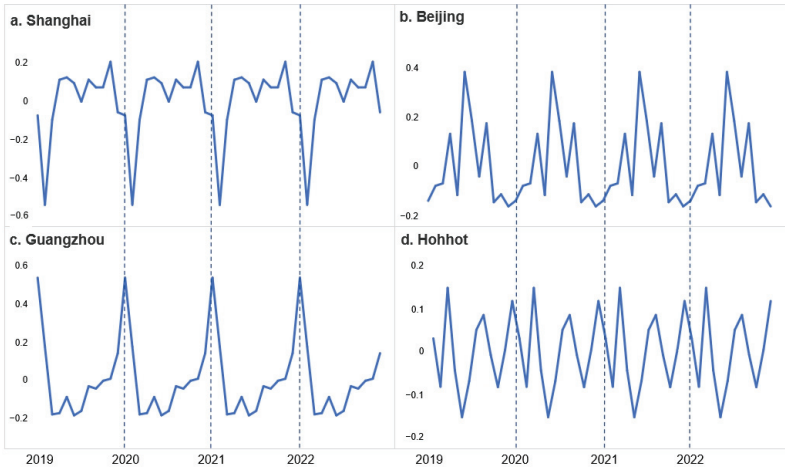

Figure 3. Seasonal patterns of CO_2 emissions in cities: (**a**) Shanghai, (**b**) Beijing, (**c**) Guangzhou, and (**d**) Hohhot.

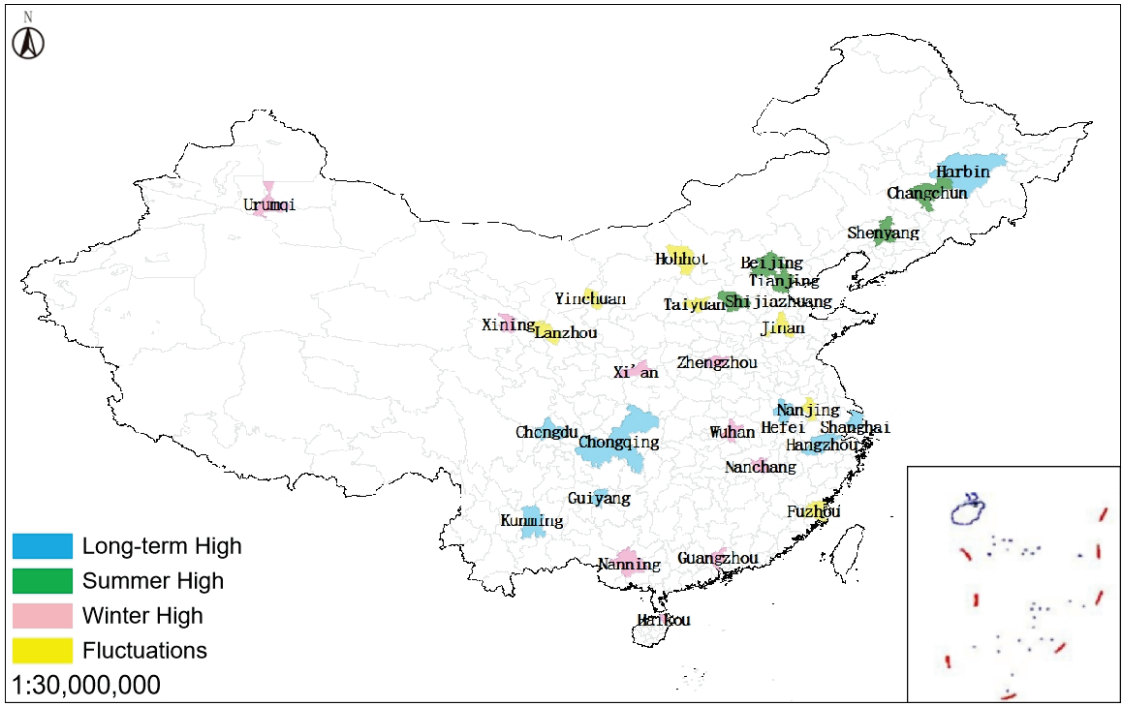

Figure 4. Major cities analyzed in this study and their seasonal patterns.

Table 2. The composition and seasonal classification of CO_2 emissions in cities.

City	Power/%	Industry/%	Type
Chengdu	11.04	69.58	Long-term High
Guiyang	39.74	36.79	
Hangzhou	11.05	65.63	
Hefei	36.07	48.58	
Kunming	18.86	57.83	
Shanghai	8.36	83.53	
Chongqing	37.02	41.87	
Nanjing	31.32	56.47	
Harbin	-	-	
Beijing	17.98	60.2	Summer High
Shenyang	26.4	57.03	
Changchun	69.38	14.65	
Tianjing	55.11	24.19	
Shijiazhuang	63.91	25.33	
Guangzhou	40.58	34.15	Winter High
Haikou	72.29	13.53	
Nanchang	58.97	26.73	
Nanning	30.34	53.59	
Urumqi	40.97	38.19	
Wuhan	27.15	62.87	
Xi'an	41.99	31.99	
Zhengzhou	58.28	28.99	
Xining	-	-	
Lhasa	10.31	28.96	
Changsha	28.83	45.89	
Taiyuan	67.06	22.25	Fluctuations
Hohhot	79.97	11.11	
Lanzhou	59.74	24.84	
Jinan	63.59	23.46	
Yinchuan	86.51	7.74	
Fuzhou	58.23	28.04	
Mean	43.14	38.76	
Max	86.51	83.52	
Min	8.36	7.74	
SD	22.40	19.52	

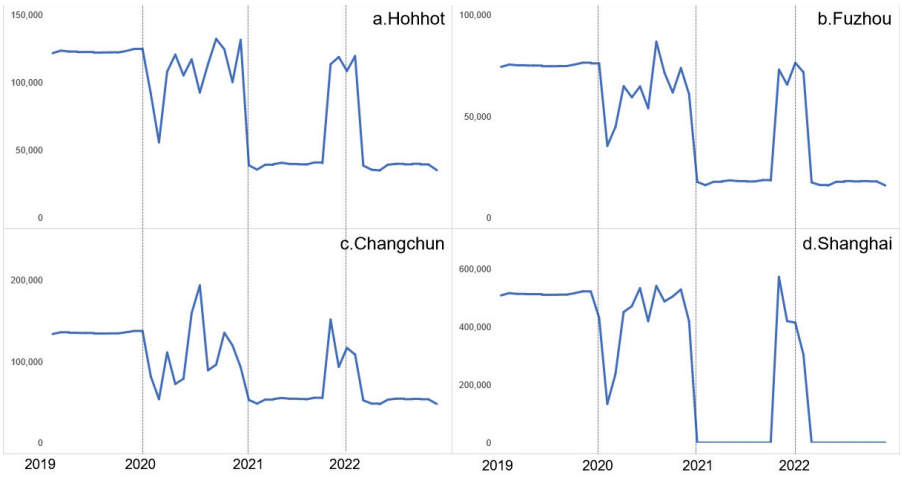

Figure 5. Line charts of CO_2 emissions in the transportation sector of (**a**) Hohhot, (**b**) Fuzou, (**c**) Changcun, and (**d**) Shanghai.

3.2. Annual Patterns of CO_2 Emissions

In our study, city CO_2 emissions showed an upward trend most of the time. However, almost all cities fluctuated during specific time periods, which coincided highly with the outbreaks of the pandemic. Based on these specific fluctuations, we divided the annual patterns of total CO_2 emissions into the following four types in Figure 6. First and Second represent the time of the first and second outbreaks of the pandemic.

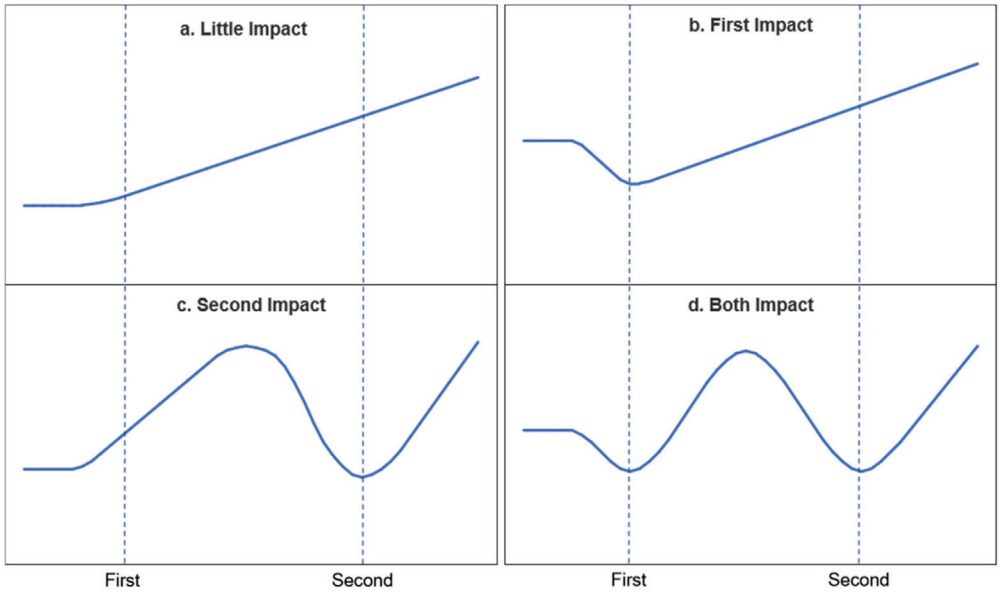

Figure 6. Conceptual charts of the four trend patterns of CO_2 emissions: (**a**) Little Impact, (**b**) First Impact, (**c**) Second Impact, and (**d**) Both Impacts.

Little Impact: CO_2 emissions showed a stable upward trend or little change, such as in Hohhot.

First Impact: CO_2 emissions showed a low peak in early 2020, followed by a slow upward trend, such as in Fuzhou.

Second Impact: CO_2 emissions showed a low peak at the end of 2021, such as in Beijing.

Both Impacts: CO_2 emissions showed low peaks in early 2020 and at the end of 2021, such as in Changchun.

For each type, we selected a typical city to display the STL results (Figure 7). The number on the vertical axes in Figure 7 represents the proportion of seasonal components of CO_2 emissions relative to the initial value. To more specifically describe the relationship between the impact of the pandemic and the changes in CO_2 emissions, we selected Changchun as an example. During the period from January 2020 to April 2020, Changchun City had a cumulative increase of 49 new infected individuals, which led to the implementation of strict control measures and a reduction in human activities, so, accordingly, CO_2 emissions decreased during this period. For a long time afterwards, there were no new infections and CO_2 emissions increased during this period. At the beginning of 2022, there was a large number of new infections, while CO_2 emissions decreased again at the same time. Due to China's implementation of the policy of liberalization at the end of the pandemic, this subsequent part was not within the scope of this study. It can be seen that the CO_2 emissions of Changchun significantly decreased during the two time periods of sudden increases in the number of infected individuals, since the levels of human activities were significantly affected by the pandemic at those times. Almost all cities showed a similar pattern: when the impact of the pandemic was severe or aggravated, CO_2 emissions decreased, and vice versa, when the impact was mild, CO_2 emissions rose.

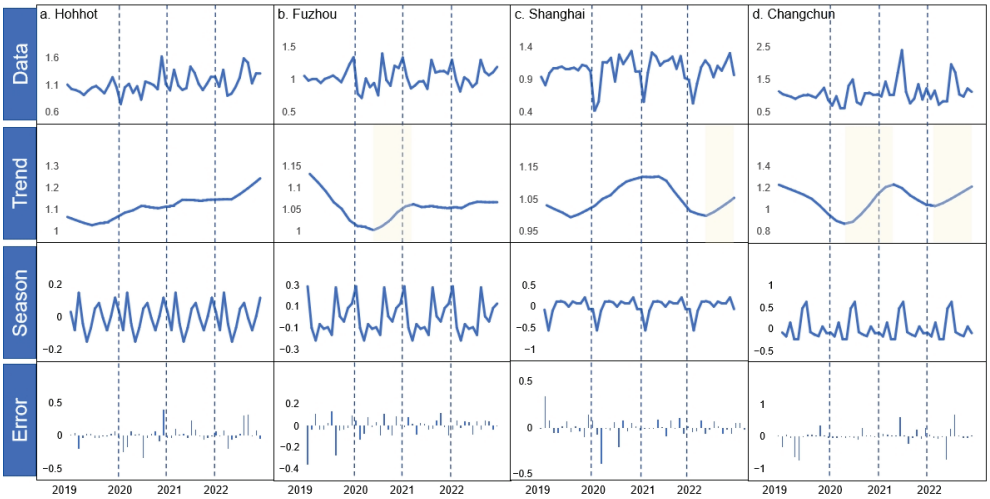

Figure 7. Seasonal trend decomposition result of total CO_2 emissions in (**a**) Hohhot, (**b**) Fuzhou, (**c**) Shanghai, and (**d**) Changchun. (The shaded areas represent that the city was in a period of recovery.)

3.3. Urban Resilience

We calculated the rates of increase in CO_2 emissions in cities and indicated which post-pandemic recovery rate they belonged to; the results are presented in Table 3. The Recovery Speed I and Recovery Speed II represent the recovery speeds of CO_2 emissions in cities after experiencing the impact of the first and the second outbreak of the pandemic. Recovery Value I and Recovery Value II represent the proportion of CO_2 emissions increasing relative to the initial value after experiencing the impacts of the first and second pandemic outbreaks. No data means that the city did not experience a decrease in CO_2 emissions due to the pandemic during this period, or it did not recover until the end of the research period. Then, we plot the calculation results in Figure 8. Blue means the recovery rate after the first outbreak of the pandemic, while red means the second.

Table 3. The recovery rate of CO_2 emissions in cities and other data.

City	Per Capita GDP /$\times 10^4$ Yuan	Recovery Speed I	Recovery Speed II	Recovery Value I	Recovery Value II
Fuzhou	13.53	0.54%	-	9.62%	-
Hefei	12.12	1.17%	-	7.5%	-
Jinan	12.31	1.66%	-	18.6%	-
Lhasa	8.68	1.15%	-	−0.72%	-
Nanchang	10.48	1.00%	-	−1.78%	-
Nanning	5.82	1.21%	-	18.76%	-
Tianjing	11.37	1.07%	-	14.39%	-
Urumqi	9.08	2.02%	-	1.57%	-
Wuhan	13.53	0.98%	-	15.24%	-
Xi'an	8.37	0.75%	-	3.52%	-
Xining	6.26	1.89%	-	−0.65%	-
Changsha	13.07	0.47%	-	8.27%	-
Nanjing	17.45	-	1.43%	-	6.25%
Shanghai	17.54	-	0.78%	-	3.72%
Beijing	18.75	-	1.71%	-	14.49%
Shijiazhuang	5.78	-	1.22%	-	12.5%
Taiyuan	9.56	-	1.37%	-	9.79%
Shenyang	7.97	2.31%	0.85%	13.71%	5.37%
Changchun	7.83	2.54%	1.70%	3.39%	1.75%
Harbin	5.07	1.69%	1.36%	5.01%	14.43%
Zhengzhou	10.01	1.66%	1.09%	10.93%	9.19%
Kunming	8.51	0.98%	0.51%	7.57%	6.12%
Guangzhou	15.04	1.10%	0.89%	−1.68%	1.19%
Hangzhou	14.99	0.51%	0.47%	1.27%	−2.06%
Chengdu	9.46	0.62%	0.48%	8.08%	8.45%
Hohhot	8.98	-	-	-	-
Guiyang	7.79	-	-	-	-
Haikou	7.1	-	-	-	-
Lanzhou	7.38	-	-	-	-
Yinchuan	7.88	-	-	-	-
Chongqing	8.75	-	-	-	-

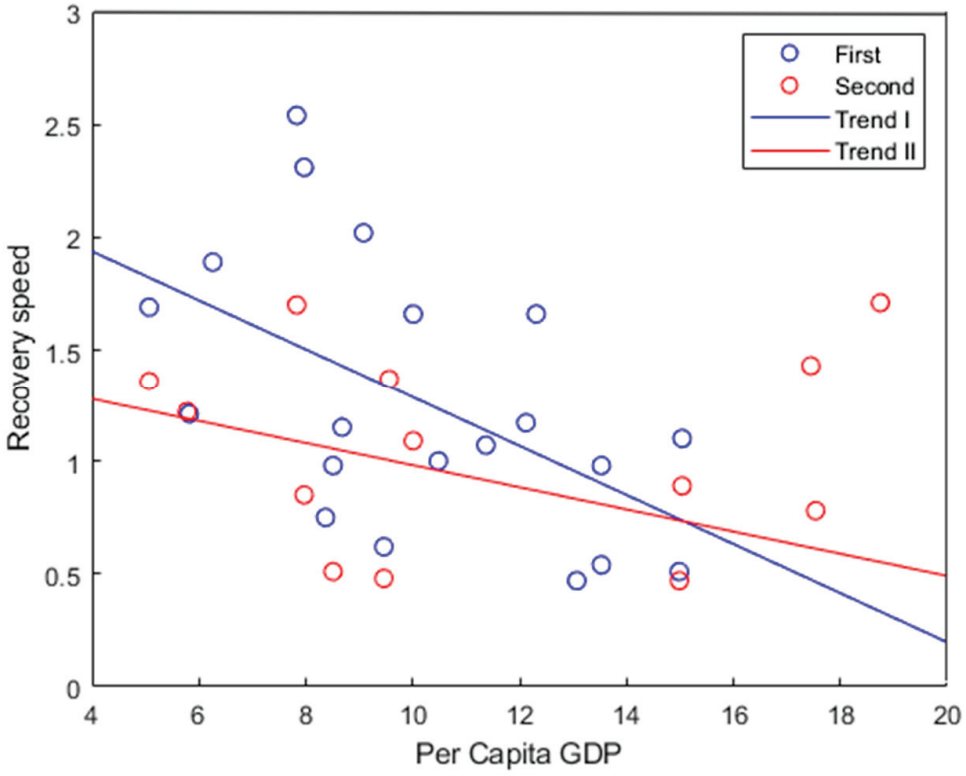

Figure 8. Scatter plot of urban per capita GDP and recovery rate of CO_2 emissions.

4. Discussion

4.1. Seasonal Patterns and the Causes

The data sources used in this study, which provide the CO_2 emissions, include many sources (such as industrial electricity and building electricity). For the power sector, about half of the cities saw seasonal fluctuations in CO_2 emissions, while the others peaked only during summer or winter. In most cities, the CO_2 emissions from the industry sector were at high levels throughout the year, but lower peaks were experienced during the Spring Festival (traditional Chinese festival during which many companies, factories, enterprises, and schools give employees and students a long holiday). However, different from the industry sector, due to the impact of the pandemic, most people choose to celebrate the Spring Festival at home, resulting in an increase in CO_2 emissions from the residential sector during this period. As for CO_2 emissions from the transportation sector, due to the uncertainty of people's travel willingness during the pandemic and other possible factors, various transportation modes, such as express delivery, saw fluctuation. When implementing travel restriction policies, it will drop to a very low or even close to zero level.

For all cities in this study, the CO_2 emissions of the power and industrial sectors accounted for at least 75% of the total CO_2 emissions; that is, these two sectors are the main contributors to changes in the total CO_2 emissions. In general, cities with the industry sector as their main source of CO_2 emissions reveal more obvious seasonal patterns of CO_2 emissions, while cities with the power sector dominating as the main source of CO_2 emissions are more prone to fluctuations in their seasonal CO_2 emission patterns. In addition, we also found that most cities with similar seasonal patterns in their CO_2 emissions are geographically clustered (see Figure 3). As for the residential and transportation sectors, both have undergone significant changes at certain times, but CO_2 emissions from the industrial and electricity sectors have not shown significant fluctuations during these times. This indicates that emissions reduction in the power and industrial sectors is important for achieving carbon peaking, while low-carbon transportation and residential energy saving cannot make sufficient contributions to this. Although seasonal components account for a relatively small proportion of CO_2 emissions, they are more prone to significant changes

in the short-term time scale. Therefore, in order to observe the changes in CO_2 emissions more accurately, it is necessary to remove seasonal effects. This way, we can grasp the rising and falling trends of CO_2 emissions in a timely and accurate way, which is conducive to a fast-responding policy to achieve carbon peaking.

4.2. Resilience of Annual Patterns in CO_2 Emissions

The impact of the pandemic on cities varied in degree and duration, and thus on human activities, which could be reflected through the changes in the CO_2 emission trends. At the same time, different cities had varying levels of resistance and resilience to the impact of the pandemic. We compared the changes in the number of infected individuals and the annual patterns in CO_2 emissions during the pandemic period, and obtained the relationship between the two:

(i) When the impact of the pandemic did not exceed the city's resistance to the pandemic, CO_2 emissions showed an upward trend associated with the normal development of the economy and the acceleration of various production activities.

(ii) When the impact of the pandemic exceeded the city's resistance, CO_2 emissions rapidly decreased in the short-term time scale and then rose after the impact ended.

During the pandemic, the period when urban CO_2 emissions suddenly decreased is similar to the period when the number of infected people in the city suddenly increased significantly (which also indicates that the impact of the pandemic is increasing). This result indicates that it is feasible to measure the impact of large-scale emergencies on cities through real-time observations of changes in CO_2 emissions. When a city is affected by large-scale emergencies, we can react in a timely manner and respond accordingly. It can be seen that cities with a higher per capita GDP have a lower recovery rate. In fact, a higher level of development means that the internal structure of the city is more complex, which means that a small amount of impact can not only lead to the paralysis of the urban system, but also to a more difficult recovery after destruction.

In this sense, urban resilience means "resistance", "quick transformation", and "rapid recovery". But from the results, most cities have been more or less affected by the pandemic, indicating that the current construction of urban resilience is insufficient. Therefore, the construction of urban resilience is important and should consider different levels of urban development. The improvement in urban resilience can reduce the impact of large-scale emergencies such as COVID-19, and accelerate the recovery rate of cities after the city is affected. In addition, our study found that the CO_2 emission levels of most cities after the recovery period had exceeded the initial levels, with some even approaching a 20% increase. For cities affected by two outbreaks, we found that the recovery rate of CO_2 emissions had an unreasonably high value after the first impact ended. In addition, comparing the two trend lines in Figure 8, we found that the recovery rate of CO_2 emissions after the first impact of the pandemic was faster than the second. This means that the rising rate of CO_2 emissions during the period was not under control, which may be due to the lack of experience in responding to the pandemic. This also indicates that there are still many risks that need to be carefully addressed during the urban recovery period. Achieving a fast recovery speed of cities after disasters is important, but ensuring that recovery is not too excessive is also highly important. How to achieve these goals is what we need to focus on in the future.

5. Conclusions

The impact of the pandemic on human activities is analyzed accurately and in more detail, thereby studying the urban resilience of different cities. This included the seasonal and annual patterns of CO_2 emissions by STL, and urban resilience by calculating and comparing the recovery rates of CO_2 emissions in different cities.

Seasonal trends can be classified into four types, mainly generated by the power and industrial sectors, which are also the focus of emission reduction. The seasonal portion of CO_2 emissions generally does not exceed 15% overall, but can change significantly in the

short term, which means that we must consider it when observing the short-term trend of CO_2 emissions. When facing large-scale emergencies such as the pandemic, we need to consider the seasonal trends of human activities when evaluating the short-term impacts of the event. In addition, due to the significant differences in seasonal patterns between different seasons, implementing emission reduction policies tailored to the seasons can achieve better results. Due to the fact that cities with the same seasonal pattern are not geographically dispersed, it is feasible to implement this differentiated policy nationwide. However, this study still has the following limitations: (1) It is difficult to explain seasonal trends related to the power sector due to the lack of more detailed classifications from the raw data. (2) There is no analysis of urban resistance to compare with urban resilience (existing research indicates an inverse relationship between the two). (3) Due to the significant impact of the pandemic on the transportation sector, time series decomposition cannot be performed.

The annual trend can also be classified into four types, which are related to the impact of the pandemic. During the pandemic, CO_2 emissions in many cities rose or recovered with normal economic development, and rapidly decreased if severely affected by the pandemic. Many cities are experiencing economic development or recovery, but uncontrolled CO_2 emissions are detrimental to achieving the goal of carbon peaking. In our study, most cities had already exceeded their initial CO_2 emission levels after rebounding. Especially after the end of the first pandemic outbreak, the rebound rate in some cities showed abnormally high values, and their CO_2 emissions eventually exceeded the initial value. When facing large-scale emergencies, apart from the degree of impact, we also need to consider factors such as urban development, economy, and population, etc., which can reflect the strength of the city's resistance to such events and play an important role in the achievement of SDG 11. During the recovery period after the impact of the event, we also need to achieve economic recovery while preventing excessive rebounds in CO_2 emissions. Especially in recent years, when SDG11 and the carbon peak target date are approaching, it is crucial to control the growth rate of CO_2 emissions and even achieve a reduction. In future research, we can construct an urban resilience evaluation system based on CO_2 emissions to achieve the goals of urban health assessment, sustainable development, and carbon peaking.

Author Contributions: Conceptualization, Yue Zhao; Software, Yue Zhao; Validation, Klaus Fraedrich; Investigation, Yue Zhao; Data curation, Yue Zhao; Writing-original draft, Yue Zhao; Writing-review & editing, Yuning Feng and Klaus Fraedrich; Supervision, Yuning Feng and Mingyi Du; Project administration, Mingyi Du. All authors have read and agreed to the published version of the manuscript.

Funding: This research was funded by: National Natural Science Foundation of China: 41930650; Youth Research and Innovation Project—Young teachers research ability enhancement program: X23002.

Data Availability Statement: Raw data were generated at https://carbonmonitor-graced.com/ (accessed on 19 March 2024). Derived data supporting the findings of this study are available from the corresponding author Y.F. on request.

Conflicts of Interest: All authors have no conflicts of interest. On behalf of all authors, the corresponding author states that there is no conflict of interest.

References

1. Matthews, H.; Gillett, N.; Stott, P.; Zickfeld, K. The proportionality of global warming to cumulative carbon emissions. *Nature* **2009**, *459*, 829–832. [CrossRef] [PubMed]
2. Luo, L. The Warming Trend Influenced by Human Activities. *China Meteorological News*, 11 November 2021; p. H3. (In Chinese) [CrossRef]
3. Liu, Z.; Guan, D.B.; Wei, W. Accounting of China's carbon dioxide emissions data. *Sci. China Earth Sci.* **2018**, *48*, 878–887. (In Chinese) [CrossRef]
4. Xin, Y.; Xu, Y. IPCC: Controlling Global Warming Is Crucial in the Coming Years. *China Science Daily*, 4 April 2022; p. H1. (In Chinese) [CrossRef]
5. Yu, B.Y.; Zhao, G.P.; An, R.Y.; Chen, J.M.; Tan, J.X.; Li, X.Y. Research on China's Carbon Emission Path under the Carbon Neutrality Goal. *J. Beijing Inst. Technol. (Soc. Sci. Ed.)* **2021**, *23*, 17–24. (In Chinese) [CrossRef]

6. Zhang, W. China Makes Positive Contributions to Promoting Global Governance in Response to Climate Change. *Legal Daily*, 3 November 2023; p. H6. Available online: http://www.legaldaily.com.cn/government/content/2023-11/03/content_8922843.html(accessed on 28 May 2024). (In Chinese)
7. Sun, Q.S. The current situation and specific strategies of China's low-carbon economic development. *Financ. Theory Teach.* **2023**, *6*, 76–81. (In Chinese) [CrossRef]
8. Kartal, M.T.; Erdogan, S.; Alola, A.A.; Pata, U.K. Impact of renewable energy investments in curbing sectoral CO_2 emissions: Evidence from China by nonlinear quantile approaches. *Environ. Sci. Pollut. Res.* **2023**, *30*, 11267–112685. [CrossRef] [PubMed]
9. Guan, J.W.; Zhou, Q.; Mao, B.H. International Comparison and Experience Reference of Carbon Emission Control. *J. Transp. Syst. Eng. Inf. Technol.* **2022**, *22*, 281–290. (In Chinese) [CrossRef]
10. Wang, J.; Feng, L.; Palmer, P.I.; Liu, Y.; Fang, S.X.; Bösch, H.; O'Dell, C.W.; Tang, X.P.; Yang, D.X.; Liu, L.X.; et al. Large Chinese land carbon sink estimated from atmospheric carbon dioxide data. *Nature* **2020**, *586*, 720–723. [CrossRef] [PubMed]
11. UNEP. *Emissions Gap Report 2021: The Heat Is On—A World of Climate*; U. N. Environ. Programme UNEP DTU Partnership: Nairobi, Kenya, 2021.
12. Campanella, T.J. Urban resilience and the recovery of New Orleans. *J. Am. Plan. Assoc.* **2006**, *72*, 141–146. [CrossRef]
13. Qu, S.; Chen, W.M.; Liu, L.J.; Hu, Y.C.; She, Y.L.; Di, B.Y.; Zhou, Q. Research on carbon emission trends and emission reduction strategies in the post epidemic reconstruction stage. *Environ. Manag. Coll. China* **2021**, *13*, 8–18. (In Chinese) [CrossRef]
14. Li, Z.X.; Zhang, J.W. Visual analysis of hot research topics on economic development and carbon emissions. *Coop. Econ. Technol.* **2023**, *12*, 12–15. (In Chinese) [CrossRef]
15. Yang, H.X.; Yang, G. Research on the spatiotemporal evolution and influencing factors of provincial-level carbon emissions in China based on modernization. *Adv. Clim. Chang. Res.* **2023**, *19*, 457–471. (In Chinese)
16. Huang, H.; Zhou, J. Study on the Spatial and Temporal Differentiation Pattern of Carbon Emission and Carbon Compensation in China's Provincial Areas. *Sustainability* **2022**, *14*, 7627. [CrossRef]
17. Liu, Y.S.; Yang, M.; Cheng, F.Y.; Tian, J.Z.; Du, Z.Q.; Song, P.B. Analysis of regional differences and decomposition of carbon emissions in China based on generalized divisia index method. *Energy* **2022**, *256*, 124666. [CrossRef]
18. Guan, W.; Wang, Y.; Xu, S.T. Research on the Network Structure and Influencing Factors of Industrial Carbon Emissions in China. *Resour. Ind.* **2023**, *25*, 40–49. (In Chinese) [CrossRef]
19. Wang, B.; Wang, L.M.; Xiang, N.; Qu, Q.S.; Xiong, C.R. Analysis of the driving factors of carbon emissions and counter measures for carbon emission reduction in Hebei province. *J. Resour. Ecol.* **2022**, *13*, 220–230. [CrossRef]
20. Peng, X.; Tao, X.M.; Zhang, H.; Chen, J.D.; Feng, K.S. CO_2 emissions from the electricity sector during China's economic transition: From the production to the consumption perspective. *Sustain. Prod. Consum.* **2021**, *28*, 1010–1020. [CrossRef]
21. Ouyang, D.; Cui, J. A Study on the Spatiotemporal Dynamics of Air Pollutants in Harbin City under the Carbon Neutrality Strategy: Based on the Holt Winters Time Series Model. *Environ. Prot. Sci.* **2023**, *49*, 112–119. (In Chinese) [CrossRef]
22. Global gRidded dAily CO2 Emission Dataset. Available online: https://carbonmonitor-graced.com/ (accessed on 13 March 2023).
23. Dou, X.Y.; Wang, Y.L.; Ciais, P.; Chevallier, F.; Davis, J.S.; Crippa, M.; Janssens-Maenhout, G.; Guizzardi, D.; Solazzo, E.; Yan, F.F.; et al. Near-real-time global gridded daily CO_2 emissions. *Innovation* **2022**, *3*, 100182. [CrossRef] [PubMed]
24. Liu, Z.; Ciais, P.; Deng, Z.; Lei, R.X.; Davis, S.J.; Feng, S.; Zheng, B.; Cui, D.; Dou, X.Y.; Zhu, B.Q.; et al. Near-real-time monitoring of global CO_2 emissions reveals the effects of the COVID-19 pandemic. *Nat. Commun.* **2020**, *11*, 5172. [CrossRef]
25. Liu, Z.; Ciais, P.; Deng, Z.; Davis, S.J.; Zheng, B.; Wang, Y.L.; Cui, D.; Zhu, B.Q.; Dou, X.Y.; Ke, P.Y.; et al. Carbon Monitor, a near-real-time daily dataset of global CO_2 emission from fossil fuel and cement production. *Sci. Data* **2020**, *7*, 392. [CrossRef]
26. National Bureau of Statistics of China. Available online: http://www.stats.gov.cn/sj/ndsj/ (accessed on 13 March 2023).
27. Kirchgässner, G.; Wolters, J.; Hassler, U. *Introduction to Modern Time Series Analysis*; Springer: Berlin/Heidelberg, Germany, 2008.
28. Cristina, S.; Cordeiro, C.; Lavender, S.; Costa Goela, P.; Icely, J.; Newton, A. MERIS Phytoplankton Time Series Products from the SW Iberian Peninsula (Sagres) Using Seasonal-Trend Decomposition Based on Loess. *Remote Sens.* **2016**, *8*, 449. [CrossRef]

Disclaimer/Publisher's Note: The statements, opinions and data contained in all publications are solely those of the individual author(s) and contributor(s) and not of MDPI and/or the editor(s). MDPI and/or the editor(s) disclaim responsibility for any injury to people or property resulting from any ideas, methods, instructions or products referred to in the content.

land

MDPI

Article

Mechanism of Vegetation Greenness Change and Its Correlation with Terrestrial Water Storage in the Tarim River Basin

Tingting Xia [1], Xuan Xue [2], Haowei Wang [2], Zhen Zhu [1], Zhi Li [3] and Yang Wang [1,*]

[1] College of Grassland Science, Xinjiang Agricultural University, Urumqi 830052, China; 320220036@xjau.edu.cn (T.X.); 320222416@xjau.edu.cn (Z.Z.)
[2] College of Resources and Environment, Xinjiang Agricultural University, Urumqi 830052, China; 320223630@xjau.edu.cn (X.X.); 320223653@xjau.edu.cn (H.W.)
[3] State Key Laboratory of Desert and Oasis Ecology, Xinjiang Institute of Ecology and Geography, CAS, Urumqi 830011, China; liz@ms.xjb.ac.cn
* Correspondence: wangyang@xjau.edu.cn; Tel.: +86-13999252425425

Abstract: The response of dryland vegetation to climate change is particularly sensitive in the context of global climate change. This paper analyzes the characteristics of spatial and temporal dynamics of vegetation cover in the Tarim River Basin, China, and its driving factors in order to investigate the response of vegetation growth to water storage changes in the basin. The Enhanced Vegetation Index (EVI), the GRACE gravity satellite, and meteorological data from 2002 to 2022 are used to decipher the characteristics of the response of water storage changes to vegetation changes, which is of great significance to the realization of regional ecological development and sustainable development. The results of the study show the following: (1) The vegetation in the Tarim River Basin has an overall increasing trend, which is mainly distributed in the Aksu Basin and the Weigangkuche River Basin and is spatially distributed in the form of a ring. (2) Vegetation distribution greatly improved during the 20-year study period, dominated by high-cover vegetation, with a change rate of 200.36%. Additionally, vegetation changes are centered on the watersheds and expand to the surrounding area, with a clear increase in vegetation in the Kumukuri Basin. Areas with a vegetation Hurst index of <0.5 account for 63.27% of the study area, and the areas with a continuous decrease were mainly located in the outer contour area of the Tarim River and Kumu Kuri Basins. (3) There are obvious spatial differences in the correlation between EVI and temperature and precipitation elements. The proportion of areas with positive correlation with temperature within the study area is 64.67%. EVI tends to be consistent with the direction of migration of the center of gravity of the population and GDP, and the areas with positive correlation between vegetation and terrestrial water reserves are mainly distributed in the northern slopes of the Kunlun Mountains, with an area proportion of about 50.513%. The Kumukuli Basin also shows significantly positive correlation.

Keywords: EVI; terrestrial water storage; climate change; human activities; Tarim River Basin

1. Introduction

Vegetation is an important component of terrestrial ecosystems as well as a key hub linking soil, atmosphere, and water, especially in arid and semi-arid zones. Vegetation also plays a key role in wind and sand stabilization, soil and water conservation, and ecological stability maintenance [1], which is of great significance to the sustainable development of regional socioeconomics and ecology [2,3]. The Enhanced Vegetation Index (EVI) is an optimized vegetation measure that improves vegetation monitoring by decoupling the background signal of the vegetation canopy and reducing the atmospheric effect [4]. This index has been widely used in recent years in the monitoring of vegetation growth and cover changes. Compared with the Normalized Difference Vegetation Index (NDVI), the EVI is better able to weaken the influence of aerosol and sub-surface bedding to a certain extent, distinguish sparse vegetation, and reflect the growth change of luxuriant vegetation.

As well, the EVI can improve the sensitivity of vegetation in high biotic areas and reduce the influence of soil background and atmosphere. Given its higher sensitivity and superiority in monitoring vegetation change, the EVI is currently being broadly applied in the study of grassland degradation and in the quantitative analysis of grassland resources [4–6].

Scholars in China and elsewhere have recently carried out extensive research on EVI data, including spatial changes in vegetation [7,8] and trends in vegetation evolution [9] as well as the driving factors behind these changes [10]. Depending on the topic, the research scale of these studies was global [11], area-limited [12,13], regional [9,14], or watershed-related [15,16]. Vegetation growth under the influence of climate change is often affected by multiple factors, with the main ones being water and heat conditions. Some studies have shown that when temperature increases at low latitudes, vegetation growth is inhibited, whereas when temperature increases at high latitudes, vegetation growth is promoted [17]. Furthermore, the feedback of vegetation to the combined effects of temperature and precipitation is more obvious than the effects of either temperature or precipitation alone.

Human activities are also a major factor affecting vegetation growth. Their intensification leads to changes in the structure and function of regional land use, thus affecting the environment for vegetation growth [18–20]. Under the driving force of climate and human activities, the response of vegetation changes to the two drivers demonstrates stark regional differences [21,22]. At present, most studies investigate the comprehensive influencing factors of the vegetation index [23] or conduct linear correlation analyses of the influencing factors [24,25]. Only a few studies have focused on the spatial expression of the influencing factors of the vegetation index, especially in arid areas with complex topography and geomorphology. In such areas, spatial expression is particularly important.

The Tarim River Basin (TRB) is the core area of the "Silk Road Economic Belt" in northwest China. The basin is located in the interior of the Central Asian continent and has a unique geomorphological pattern of "mountain–oasis–desert", with vegetation changes that are highly sensitive to climate change. Due to the region's ecological sensitivity, the present study has chosen the TRB as its target area, exploring the spatial and temporal evolution of vegetation changes over the past 20 years based on multi-source remote sensing data for temperature, precipitation, and terrestrial water storage. The study analyzes the response characteristics of vegetation EVI to climatic factors by using correlation analysis and significance testing. Additionally, we use the Hurst index to estimate the future evolution trend of vegetation indices and to gauge the sustainability of vegetation change in the context of climate change, with a view to providing theoretical references for ecological environment changes and sustainable development.

2. Materials and Methods

2.1. Overview of the Study Area

The Tarim River Basin is located in the southern part of Xinjiang (73°10′–94°05′ E, 34°55′–43°08′ N), in the hinterland of the Asia-Europe continent (Figure 1). Renowned as China's largest inland river basin and as the central hub of the Silk Road Economic Belt initiative, the TRB has extremely complex geomorphological patterns, with mountains, plains, and deserts forming a typical mountain–oasis–desert system. The basin is bordered by the Tianshan Mountains to the north, the Kunlun Mountains to the south, and the Pamir Plateau to the west. It covers an area of about 102×10^4 square kilometers and accounts for approximately 61.82% of the total area of Xinjiang.

The high mountains bordering the TRB on three sides are interspersed with sub-basins, making the terrain generally higher in the south and west and lower in the north and east. Despite its relatively abundant natural resources, the basin has an extremely fragile ecological environment, with a climate that is classified as continental arid due to scarce precipitation and strong evaporation. There is a significant difference between daytime and nighttime temperatures in the study region, but the number of daily sunshine hours is

high, making the area rich in light and heat resources. The average annual temperature in the TRB is 10.6 °C, and the average annual precipitation is about 89.1 mm.

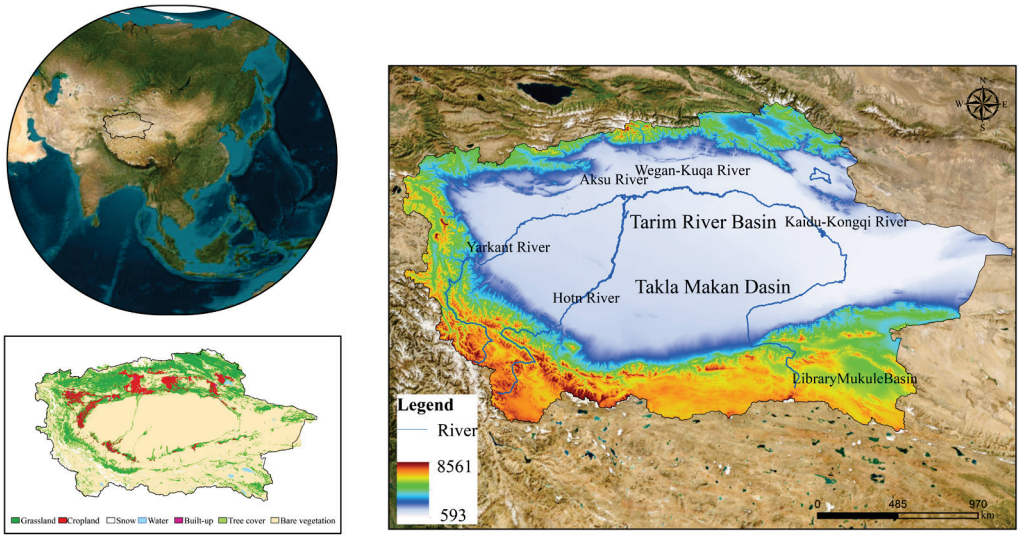

Figure 1. Overview map of the study area (note: review drawing No. GS (2020) 4619).

2.2. Data Sources

The land-use data for this study were adopted from the land-use dataset of the Sentinel-2 Land Cover Explorer introduced by Esri, with a data accuracy of 10 m. The data classifications include watershed, woodland, grassland, flooded vegetation, crops, shrubs, built-up area, bare ground, glaciers, and permanent snow and ice. The EVI data were obtained from NASA EOS/MODIS MOD13A1 (http://ladsweb.modaps.eosdis.nasa.gov/, accessed on 15 January 2024), with a spatial resolution of 1 km and a time span of 2002–2022. Temperature and precipitation data were obtained from the high-precision meteorological indicator raster data released by the National Tibetan Plateau Science Data Center, with a spatial resolution of 1 km. Terrestrial water storage data were obtained from GRACE RL06 data released by NASA based on the seasons of CSR, GFZ, and JPL, with a spatial resolution of 0.25° and a time span of 2002–2022. To maintain the integrity of spatial accuracy within the datasets and accommodate the scope of the study area, the data were processed utilizing cropping and resampling tools. This processing resulted in a consistent format of raster files, each precision-aligned to a 0.25° × 0.25° grid (Figure 2).

2.3. Research Methods and Modeling

2.3.1. Enhanced Vegetation Index

EVI is an optimized vegetation index with increased sensitivity to areas of high biomass and improved vegetation monitoring capabilities through decoupling of the vegetation canopy background signal and reduction of atmospheric effects. In this study, the EVI values of healthy vegetation varied between 0.2 and 0.8, as expressed in the following formula:

$$\mathrm{EVI} = 2.5 \times ((\mathrm{NIR} - \mathrm{Red})/(\mathrm{NIR} + 6\mathrm{R} - 7.5\mathrm{Blue} + 1)) \quad (1)$$

2.3.2. Sen+ Mann-Kendall Trend Analysis

The Theil-Sen Median method is also known as the Sen slope estimation. Trend analysis is a method of predicting the trend of a variable over time by performing a linear regression analysis on it. The formula for slope can be written as

$$\beta = \mathrm{Median}\left(\frac{x_j - \mathrm{x}_i}{j - i}\right), \forall\, j > i \quad (2)$$

where β represents the slope of the meta-regression equation, x_i, x_j denotes the length of the time series of this dataset. When $\beta > 0$, the data analyzed for the respective image show an increasing trend; when $\beta = 0$, the data are essentially unchanged; and when $\beta < 0$, the data show a decreasing trend.

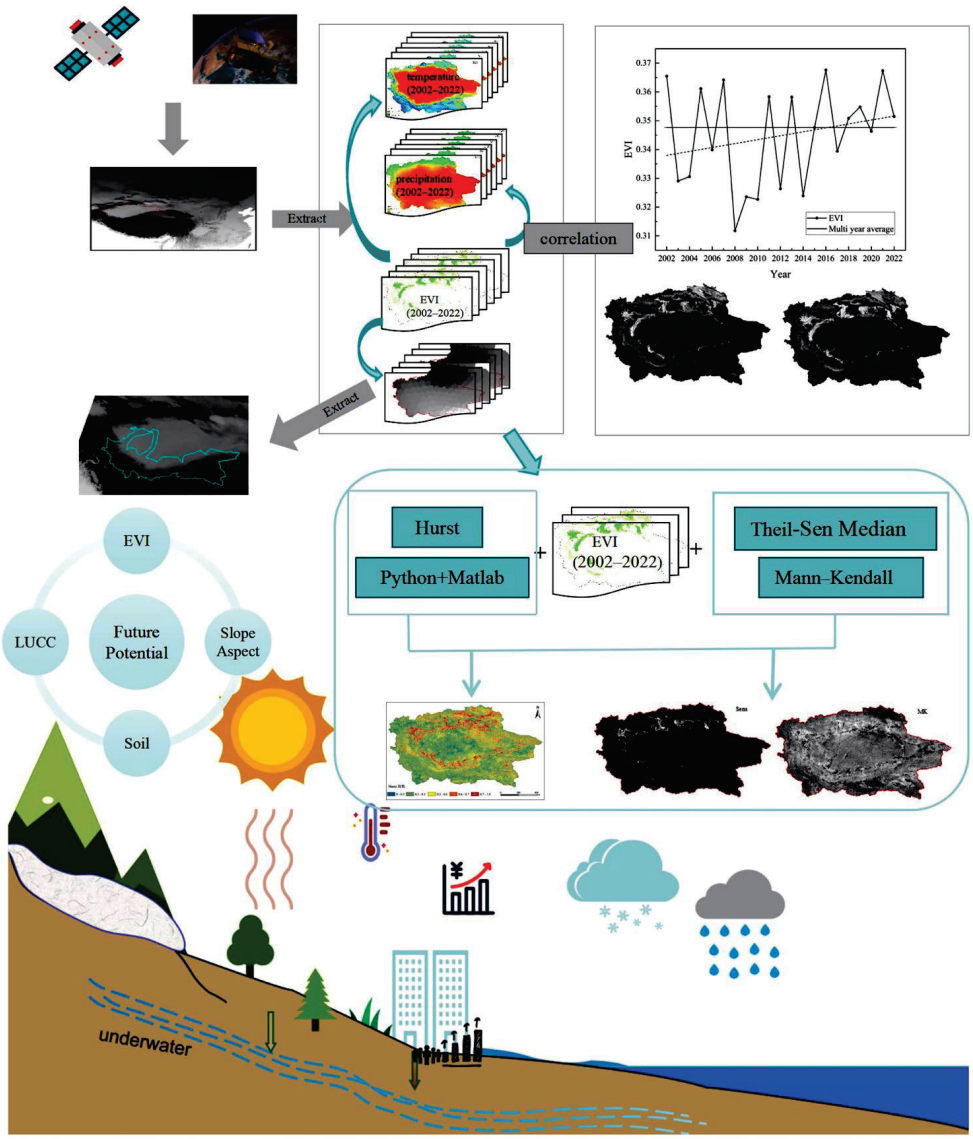

Figure 2. Flow chart of data processing.

2.3.3. Mann–Kendall Significance Test

The M-K trend test is a non-parametric test proposed by Mann [26] to test for the presence of a trend in a dataset. It can detect monotonic trends in datasets, including linear and nonlinear trends, and does not require assumptions about the data distribution. The M-K test is widely used in research on trend testing for climate and hydrology [27–30].

The present paper analyzes the inter-annual trend of vegetation indices using the M-K trend test based on Python language. The principle of calculation is as follows: Assuming that the statistic S constructed by the M-K test is denoted when trend detection is performed on a dataset with time series X_1,X_2,. . .,X_n,

$$s = \sum_{i=1}^{n-1} \sum_{j=i+1}^{n} sign(x_i - x_j) \quad (3)$$

Sign( ) for

$$sign = \begin{Bmatrix} 1,\ if\ x_i - x_j > 0 \\ 0,\ if\ x_i - x_j = 0 \\ -1,\ if\ x_i - x_j < 0 \end{Bmatrix} \tag{4}$$

where n denotes the length of the time series of this dataset, x_i is the observed value of the data at time i, and x_j is the observed value of the data at time j.

When the distribution of S is approximately normal, the mean and variance are expressed as

$$E(S) = 0 \tag{5}$$

$$\mathrm{Var}(S) = \frac{n(n-1)(2n-5)}{18} = \sigma^2 \tag{6}$$

where σ is the standard deviation.

The statistic Z of a normalized data set can be expressed as follows:

$$Z = \begin{Bmatrix} \frac{S-1}{\sigma},\ for\ S > 0 \\ 0\quad ,\ for\ S = 0 \\ \frac{S=1}{\sigma},\ for\ S < 0 \end{Bmatrix} \tag{7}$$

Also, the p-value of the statistic S can be calculated using the normal cumulative distribution function:

$$P = 2[1 - \varnothing(|Z|)] \tag{8}$$

where $\varnothing(|Z|)$ denotes the cumulative distribution function of a standard normal variable. When the data significance level is $p \leq 0.05$, the change in trend of the group in this time series is significant.

2.3.4. Correlation Analysis and Significance Test

The Pearson's correlation coefficient is a statistical measure of the strength and direction of the linear relationship between two continuous variables. It takes values between -1 and 1 and can indicate whether the relationship between two variables is negative, uncorrelated, or positive. The Pearson's formula is written as

$$r_{xy} = 1 - \frac{\sum_{i=1}^{N}(x_i - \overline{x})(y_i - \overline{y})}{\sqrt{\sum_{i=1}^{N}(x_i - \overline{x})^2 (y_i - \overline{y})^2}} \tag{9}$$

where r_{xy} is the correlation coefficient between the variables x and y; x_{ij}, y_{ij} are the variable values in year i and month j; and $\overline{x}$ and $\overline{y}$ are the mean values of the variables at each time scale, respectively.

2.3.5. Hurst Index

The Hurst index (H) is an effective method for quantitatively describing the self-similarity and long-range dependence of a time series [31,32], i.e., the extent to which past information affects the future; it can be used to determine future trends in the data.

$$\overline{EVI}_{(T)} = \frac{1}{T}\sum_{\mathrm{t}=1}^{T} EVI_{(\mathrm{T})} \quad T = 1,\ 2,\ \cdots,\ n \tag{10}$$

$$X_{(\mathrm{t},T)} = \sum_{\mathrm{t}=1}^{t}\left(EVI_{(\mathrm{T})} - \overline{EVI}_{(\mathrm{T})}\right) \quad 1 \leq \mathrm{t} \leq T \tag{11}$$

$$R_{(T)} = \max X_{(t,T)} - \min X_{(t,T)} \quad T = 1,\ 2,\ \cdots,\ n \tag{12}$$

$$S_{(T)} = \left[\frac{1}{T}\sum_{\mathrm{t}=1}^{T}\left(EVI_{(\mathrm{t})} - EVI_{(\mathrm{T})}\right)^2\right]^{\frac{1}{2}} \quad T = 1,\ 2,\ \cdots,\ n \tag{13}$$

$$\frac{R_{(T)}}{S_{(T)}} \alpha\ T^H \tag{14}$$

H takes values from 0 to 1. When $H = 0.5$, the time series are random sequences that are independent of each other with finite variance; when $0.5 < H < 1$, the time series changes are persistent, and future changes will be consistent with past trends; when $0 < H < 0.5$, the time series is anti-persistent, i.e., past changes are unsustainable.

2.3.6. Gaussian Filter Smoothing

The smoothing algorithm of Gaussian filtering can effectively reduce the error generated by GRACE in the observation process. Applied to the spherical harmonic function, it can also reduce the interference generated by other geophysical signals. Selecting the appropriate smoothing radius of Gaussian filtering can reduce the error and noise pollution at the same time, without losing the effective information on the change of water storage or the more effective inversion of spatial and temporal changes of terrestrial water storage. The expanded expression for the spherical harmonic coefficient is

$$N(\theta,\lambda) = \alpha\sum_{l=0}^{\infty}\sum_{m=0}^{l}\overline{P}_{lm}(\cos\theta)(C_{lm}\cos(m\lambda) + S_{lm}\sin(m\lambda)) \tag{15}$$

where $N(\theta, \lambda)$ represents the shape of the geoid, θ denotes the geocentric residual latitude, λ is the longitude, α indicates the mean radius of the Earth, C_{lm} and S_{lm} denote the fully specified spherical harmonic coefficients, l and m are the order and magnitude of the spherical harmonic coefficients, respectively, and $lm(\cos\theta)$ is the normalized summed Legendre function.

The change in the geoid is expressed as $\Delta N(\theta, \lambda)$, which can be expanded into a change in the spherical harmonic coefficient, as follows:

$$\Delta N(\theta,\lambda) = \alpha\sum_{l=0}^{\infty}\sum_{m=0}^{l}\overline{P}_{lm}(\cos\theta)(\Delta C_{lm}\cos(m\lambda) + \Delta S_{lm}\sin(m\lambda)) \tag{16}$$

Based on the above equation, we can see that the change in the gravity field is due to the redistribution of the mass of the Earth system. This change can be expressed by the following equation:

$$\begin{Bmatrix}\Delta\overline{C}_{lm}\\ \Delta\overline{S}_{lm}\end{Bmatrix} = \frac{3}{4\pi\alpha\rho_{\alpha ve}(2l+1)}\int \Delta\rho(r,\theta,\lambda)\overline{P}_{lm}(\cos)\left[\frac{r}{\alpha}\right]\begin{Bmatrix}\cos(m\lambda)\\ \sin(m\lambda)\end{Bmatrix}\sin\theta d\theta d\lambda dr \tag{17}$$

where $\rho\alpha ve$ denotes the average density of the Earth, and $\Delta\rho(r, \theta, \lambda)$ represents the change in the bulk density of matter.

The Earth's mass change can be obtained from the gravity level. By calculating the change in mass, it can be directly converted to a change in equivalent water height:

$$TWS(\theta,\varphi) = \frac{2\alpha\rho_{\alpha ve}\pi}{3\rho_{water}}\sum_{l=0}^{N}\sum_{m=0}^{l}\frac{2l+1}{1+kl}WlP_{lm}\cos\theta[\Delta C_{lm}\cos(m\varphi) + \Delta S_{lm}\sin(m\varphi)] \tag{18}$$

3. Results

3.1. Characteristics of Vegetation Dynamics and Their Influencing Factors

3.1.1. Spatial Distribution of EVI

From 2002 to 2022, the vegetation cover of the TRB displayed spatial distribution characteristics of "high in the surrounding area, low in the middle, high in the northwest, and low in the southeast". The spatial difference of the vegetation cover in the basin is significant because the cover was constrained by numerous driving factors, among which climate and human activities predominated. As shown in the spatial distribution of vegetation in 2022 (Figure 3), the medium and high vegetation cover in the basin region

is distributed in the mountainous areas in the north and the plains in the center, while the low vegetation cover is mainly distributed at the edge of the mountainous areas and in the transition zones of the desert oases. The overall percentage of the area covered by each vegetation cover type is in the order of low vegetation cover > medium vegetation cover > high vegetation cover.

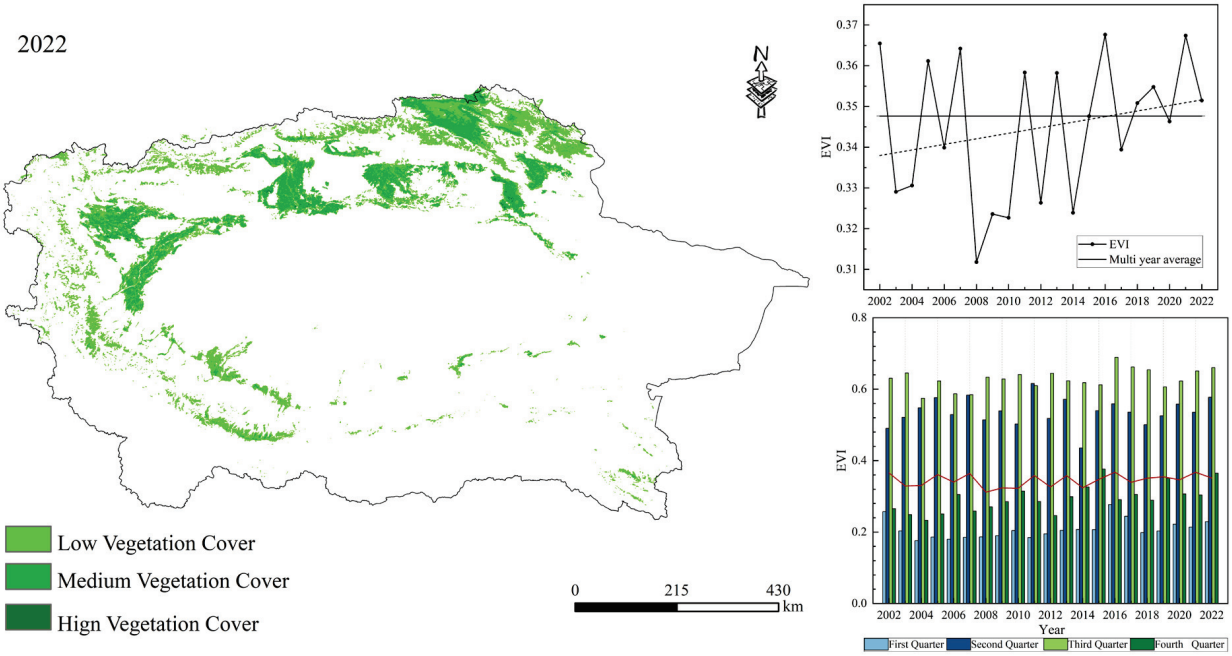

Figure 3. Spatial distribution of vegetation in the TRB.

According to the changes in vegetation cover area in the TRB during the study period (Table 1), the vegetation index fluctuates and increases mainly in the low and medium vegetation cover, but the high vegetation cover shows a slight decreasing trend. Furthermore, the rate of change of the medium vegetation cover is 86.937%, and the increase in area (25,437 km^2) only occurs from 2017 to 2022, on the heels of a slight decreasing trend. The low and medium vegetation cover showed a decreasing trend in 2002–2007, with decreasing areas of 9394 km^2 and 139 km^2 and change rates of 11.067% and 32.028%, respectively. The high vegetation cover had a higher change rate, but the overall fluctuation was not large.

Table 1. Area change of vegetation index in the TRB.

	2002–2007		2007–2012		2012–2017		2017–2022		2002–2022	
	Magnitude of Change	Rate of Change	Magnitude of Change	Rate of Change	Magnitude of Change	Rate of Change	Magnitude of Change	Rate of Change	Magnitude of Change	Rate of Change
low vegetation cover	−9394	−11.067%	13,203	17.490%	5639	6.358%	−5280	−5.597%	4168	4.910%
medium vegetation cover	4115	14.064%	15,249	45.691%	6967	14.329%	−894	−1.608%	25,437	86.937%
high vegetation cover	−139	−32.028%	582	197.289%	45	5.131%	−527	−57.158%	−39	−8.986%

The period of greatest change was 2007–2012, during which the low, medium, and high vegetation cover all showed an increasing trend. For the high vegetation cover, the rate of change was as high as 197.289%. For the medium and low vegetation cover, the change rate was smaller, but the amount of change was larger (13,203 km^2 and 15,249 km^2, respectively). For the period 2012–2017, the area of increase of medium vegetation cover was 6967 km^2, which is an increase of 14.328% over 2012. For the period 2017–2022, the area

of increase of vegetation cover mainly decreased. The reduction was especially obvious in the high vegetation cover, with a rate of change as high as 57.58%, while the area of medium and low vegetation cover decreased only slightly, showing reductions of 5280 km^2 and 894 km^2 and rates of change of 5.597% and 1.608%, respectively.

Figure 3 presents interannual trends for the TRB based on the vegetation index dataset. As can be seen in the figure, the overall variation range of the vegetation index is between 0.311 and 0.368. The multi-year average value of vegetation cover in the TRB from 2002 to 2022 is 0.346, with the smallest value (0.346) occurring in 2008. The average value of the vegetation cover reached its maximum value (0.368) in 2016. Moreover, the fluctuating and decreasing growth of EVI in the watershed during the study period, with an annual growth rate of 0.013/10a, indicates a slightly degrading trend of vegetation growth. The mean value of the vegetation index fluctuated from 2002 to 2015, except for the years 2002, 2005, 2007, and 2011, when the mean FVC values were at or above the multi-year mean line; the mean EVI values for the remaining years were below the multi-year mean line. After 2018, the vegetation cover showed an increasing trend compared with the previous 11 years. In general, the data indicate that the vegetation activity in the TRB over the past two decades has developed in the direction of enhancement, with ample room for improvement.

3.1.2. Characterization of the Spatial and Temporal Evolution of EVI

This study investigated the natural vegetation changes in the Tarim River Basin by comparing and analyzing the characteristics of natural vegetation EVI from 2002 to 2022. The spatial distribution of natural vegetation EVI in the study area is characterized as being "high in the surrounding area, low in the middle, high in the northwest, and low in the southeast". The spatial distribution characteristics of natural vegetation EVI are divided into the following five classes: $0 < EVI \leq 0.1$, $0 < EVI \leq 0.2$, $0.2 < EVI \leq 0.4$, $0.4 < EVI \leq 0.6$, $0.6 < EVI \leq 0.8$, and $0.8 < EVI \leq 1$.

Natural vegetation is mainly concentrated in the northern edge of the TRB, including in the Yarkant River Basin (Figure 4a–e). Because desert comprises the central part of the study region and is the main geomorphological type, vegetation is relatively scarce. However, the vegetation in the middle and high value zones of the Tarim's mainstream and tributaries have luxuriant growth. Moreover, there is a marked change in the growth status of the natural vegetation after 2012, showing a significant increase. The transformation type is mainly from low value zones to middle and high value zones, and the transformation area is concentrated around the Tarim's mainstream.

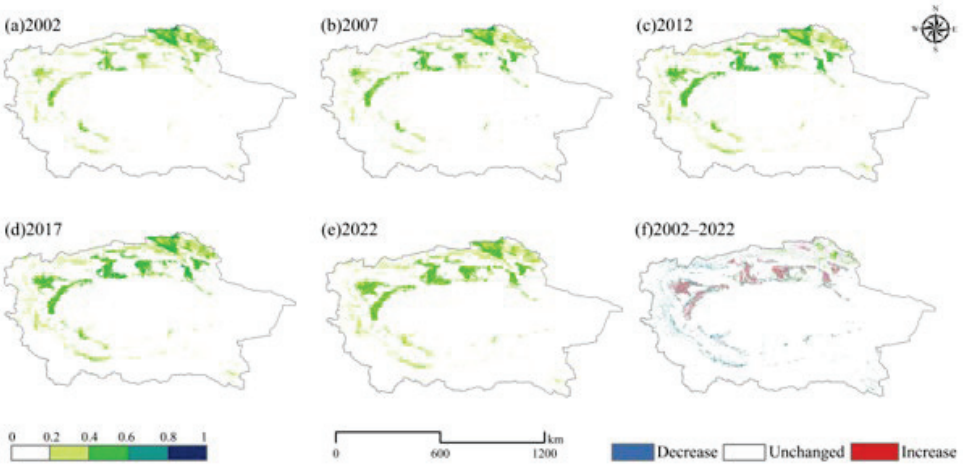

Figure 4. Characteristics of spatial and temporal evolution of vegetation in the TRB. ((**a**–**e**) show the characteristics of the spatial distribution for each five-year period, and figure (**f**) shows the characteristics of the changes in the period 2002–2022).

Figure 4f illustrates that the growth area of natural vegetation is significantly higher than the decrease area, and that the overall natural vegetation growth condition is improving, indicating that the status quo of ecological environment degradation has been alleviated. As shown, the 0 < EVI $\leq$ 0.2 area is the most widely distributed level of natural vegetation in the study region. It displays a fluctuating decreasing trend (i.e., initial decrease followed by an increase). The decreasing area of 2.13 $\times$ 10^4 km is mainly transformed to a high value area, at a rate of change of 1.79% (Table 2). The 0.2 < EVI $\leq$ 0.4 area also has a wide distribution of vegetation, with EVI > 0.2 indicating healthy natural vegetation. It also shows a fluctuating growth trend. The total area in 2022 of this part of the study region was 8.91$\times$$10^4$ km, and the rate of change was 4.91%.

Table 2. Changes in the area of different classes of vegetation index in the vegetated TRB from 2002 to 2022 (km^2).

$\times$**10^4 km^2**	**2002**	**2007**	**2012**	**2017**	**2022**	**Change%**	**Magnitude of Change**
0–0.2	118.87	119.67	116.41	115.53	116.74	−1.79	−2.13
0.2–0.4	8.49	7.55	8.87	9.43	8.91	4.91	0.42
0.4–0.6	2.76	3.21	4.42	5.01	4.92	78.19	2.16
0.6–0.8	0.19	0.15	0.53	0.64	0.58	200.36	0.39
0.8–1	0.012	0.005	0.0045	0.0037	0.0017	−85.59	−0.018

The 0.4 < EVI $\leq$ 0.6 area is mainly distributed in the upper reaches of the Kaidu River, the lower reaches of the Weigan River, Bosten Lake, and the lower reaches of the Aksu River. This vast stretch of the TRB showed a clustered vegetation distribution that increased significantly, with a change rate of 78.19% during the 20-year study period. The largest increase in area (5.01 $\times$ 10^4 km) occurred in 2017, with a rate of increase of 0.108 $\times$ 10^4 km/a. Most significantly, the 0.6 < EVI $\leq$ 0.8 area has the highest rate of change during the study period (200.36%). However, the overall distribution within this zone is relatively small and sporadically distributed in the upper reaches of the Kaidu River, the lower reaches of the Peacock River, the lower reaches of the Aksu River, and the upper reaches of the Yarkant River. Still, the area of this region increased markedly, indicating that the vegetation is shifting to a high vegetative covering. Finally, the 0.8 < EVI $\leq$ 1 area is sporadically distributed only in the northern edge of the TRB, with the area showing a slightly decreasing trend.

3.1.3. EVI Trends and Shift Analyses

From 2002 to 2022, there were frequent transformations and significant differences in the characteristics of the natural vegetation classes across the study region (Figure 5). The total transfer area (80,414 km^2) was dominated by transformations between classes b, c, and d. Specifically, classes a and b were dominated by transfers out, classes b, c, and d were dominated by transfers in, class e did not have significant changes during the study period, and transformations occurred only between classes d and e.

Class a is the most widely distributed area in the TRB. It is also the location with the most transferred area, mainly converting to classes b (28,507 km^2) and c (8320 km^2). These sections of the study region are dominated by very sparse vegetation, and the distribution of the current status of land use is mostly underutilized land, with a transfer rate of 48.15%. It is worth noting that the transferred area of class a in 2022 is much lower than that in 2002. This change of situation also indicates improvements in the growing conditions of some natural vegetation in the study region.

Class b is mostly in the intertwined desert-oasis zone. The vegetation growth conditions in this type of area are generally poor, but due to the influence of irrigation and the abandonment of farmland to grass in some areas, the natural vegetation in these locations shows a growing trend. Class b is the second largest class in terms of area transferred during the study period, with a total area of 31,554 km^2. The shifts from class b mainly

occurred to classes a (9104 km^2) and c (21,136 km^2), at a conversion rate of 39.24%. Class b is primarily distributed in the Kaidu River Basin and the west, with sporadic distribution in the southeast, mainly in the upper reaches of the Kaidu, Aksu, and Yarkand rivers and the lower reaches of the Hotan River. The basin, at its center, shows diffuse growth in all directions, which also partially increases the Kumukuli Basin of the East Kunlun River.

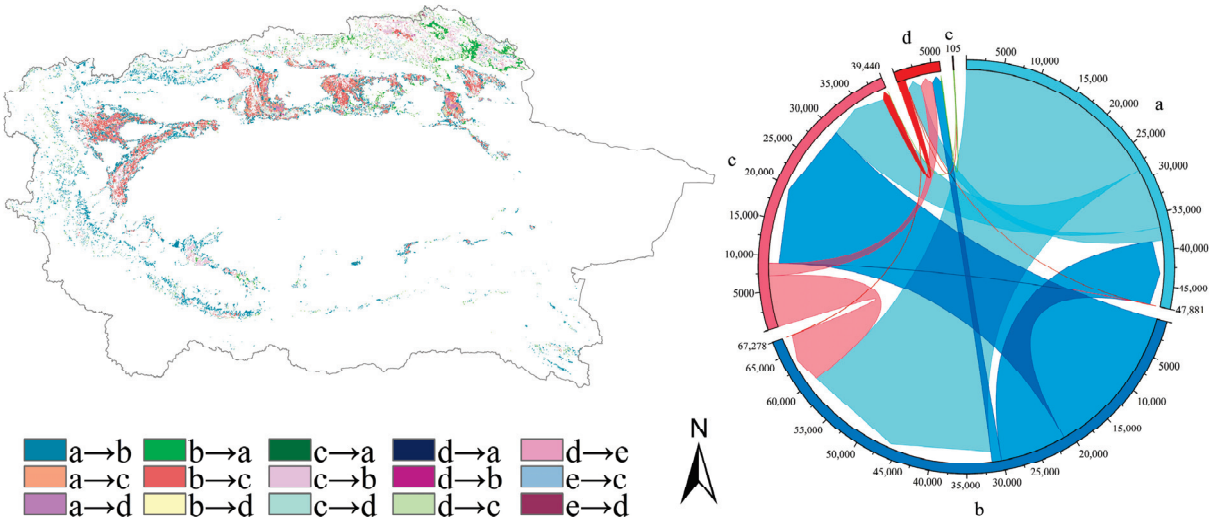

Figure 5. Spatial distribution of vegetation conversion in the TRB. (**a**) 0 < EVI < 0.2; (**b**) 0.2 ≤ EVI < 0.4; (**c**) 0.4 ≤ EVI < 0.6; (**d**) 0.6 ≤ EVI < 0.8; (**e**) 0.8 ≤ EVI < 0.1.

Class c refers to locations with medium vegetation cover. In these places, vegetation growth is relatively stable and mostly transforms with class b, but the transformed area is much smaller than class b. Spatial distribution of class c along the middle reaches of the Yulongkash River and the upper reaches of the Yarkant River is sporadic, while in the upper reaches of the Kaidu River, class c sections are increasing.

Class d denotes a high-coverage area, with less area converted in the study region. In class d locations, the natural vegetation grows luxuriantly and is generally unaffected by climatic conditions. Its diversion is mainly to the medium-coverage area, at a diversion rate of 1.39%. The class e transfer-out area accounts for a relatively small percentage (0.13%) of the study region. It has sporadic distribution along the northern edge of the TRB.

Grade a denotes sections with very low vegetation cover. It is mainly located in the central portion of the study area and the Gobi desert and is characterized by scant precipitation. Grade a locations are affected by multiple factors, such as human activities and desertification, and show a decreasing trend in vegetation cover, with the area transferred out exceeding the area transferred in. Increases in grade a area mainly occur at the southern edge of the TRB and at the upper reaches of the Kaidu River.

Somewhat anomalous to the general trend of vegetation coverage in the TRB is the northern edge of the study region, which has rich vegetation. Thanks to good thermal and hydrological conditions, vegetation growth in this location is abundant, and transformations between vegetation classes are plentiful, trending to an overall favorable development.

In order to deeply understand the spatial trend of natural vegetation across all locations in the study region, the image-by-image trend of the vegetation index in the TRB was calculated using the Sen trend and combined with the M-K test to obtain a trend map of EVI. The spatial variation of vegetation EVI is shown in Figure 6. From the spatial trend, it can be seen that the improved area exceeds that of the degraded area, and that the improved area accounts for 84.13% of the TRB. Of this total, 45.70% exhibits a significant or highly significant increase, while 38.43% shows either an insignificant or a non-significant increase. Furthermore, the proportion of stable and unchanged area is 7.23%, the proportion of non-significantly decreasing area is 7.32%, and the proportion of significantly decreasing

and very significantly decreasing area is 1.71%. Overall, the trend is one of increase in improved area across the entire basin.

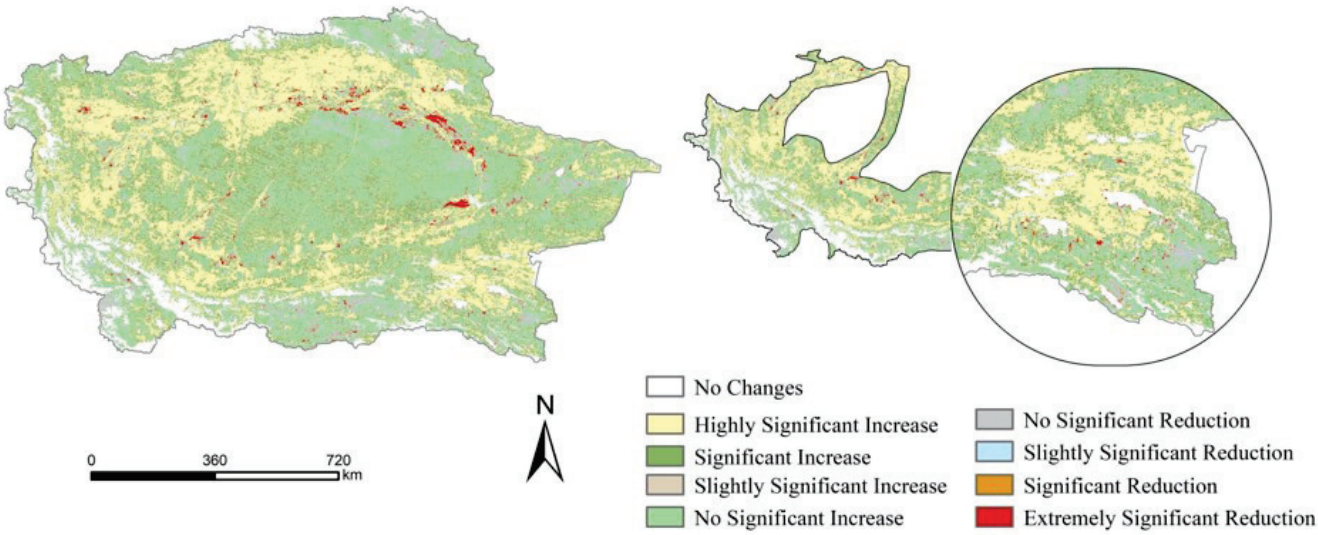

Figure 6. Trends in vegetation change in the TRB and the northern slopes of the Kunlun Mountains.

Significantly and very significantly reduced area was mainly concentrated in the lower Tarim River, with sporadic distribution near the Yarkant River. Non-significantly reduced area was distributed throughout the TRB but was mainly located at its southern edge as well as along the lower reaches of the Tarim River and in the Weigangkuche River Basin. The area of very significant increase involved spreading distribution that was centered on the various sub-basins of the TRB, with less distribution in the outer contour area and the hinterland of the Taklamakan Desert and a wider distribution area in the Kumkuli Basin. Locations showing significant increase were adjacent to those showing very significant increase, with the area of expansion more evenly distributed and less distributed around the outer contour. Locations exhibiting non-significant increase were distributed throughout the study region.

In analyzing vegetation change trends for the northern slope of the Kunlun Mountains and the Kumukuli Basin, it can be seen that they are mainly on the rise. Specifically, the trends manifest as highly significant and significant increases in degradation that are sporadically distributed throughout the Kumukuli Basin.

3.2. Analysis of Vegetation Cover Drivers and Characterization of Future Changes in the TRB

3.2.1. Impact of Climate Change on EVI

Temperature is one of the main factors affecting the spatial distribution of terrestrial water storage. The correlation coefficients between EVI and temperature over the past 20 years were calculated based on the image metric scale, using year as the time unit. Significance tests were then performed to derive the spatial distribution of the correlation between EVI and air temperature in the TRB (Figure 7a). The results show that the response of EVI to temperature varies spatially and is correlated with temperature, with positive and negative correlations co-existing. Under controlled precipitation conditions, the correlation coefficients between EVI and air temperature ranged from −0.849 to 0.899, with an average correlation coefficient of 0.080. The locations where EVI was positively correlated with air temperature accounted for 64.67% of the total area of the TRB and were widely distributed throughout the region.

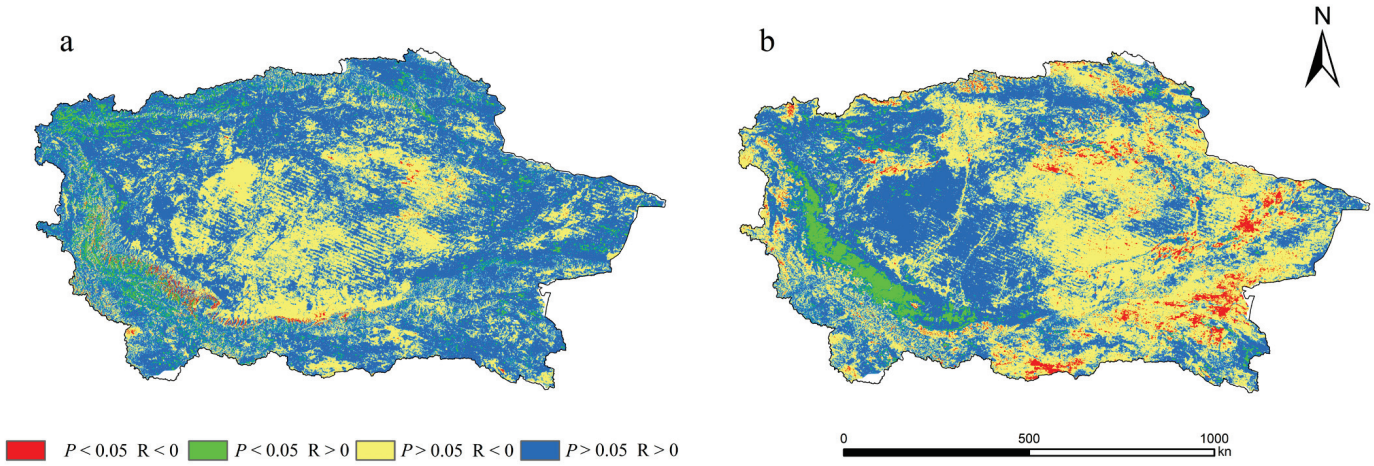

Figure 7. Spatial distribution of correlation coefficients between vegetation, air temperature, and precipitation in the TRB: (**a**) temperature–vegetation phase coefficient; (**b**) precipitation–vegetation phase coefficient.

For the significance test, the apportioned area where the relevant distribution was significant comprised 4.97% of the study region. The significant positive correlation was mainly distributed in the Yarkant River Basin, where the significant positive correlation accounted for 6.54% of the positive correlation distribution area ($p < 0.05$) or 4.23% of the total area. Persistent extremely calorimetric conditions inhibited the expansion of vegetation cover and also indicated that heat is the main limiting factor for the growth of sparse vegetation. The location exhibiting negative correlation of air temperature accounted for 35.33% of the total area of the region. In addition, the natural vegetation in the hinterland of the Taklamakan Desert mainly showed a non-significant negative correlation with air temperature in the significance test. The distribution of locations with significant negative correlation was even less, accounting for only 2.11% of negatively correlated area ($p < 0.05$). With the rise in air temperature, there was an increase in potential evaporation, placing the growth and expansion of the sparse vegetation under duress.

Unlike temperature, precipitation had a significant influence on spatial differences in the positive and negative correlation distribution of the EVI response. These differences were also very geographically diverse (Figure 7b). The correlation coefficients between EVI and precipitation ranged from −0.869 to 0.893 under controlled temperature conditions. Locations with positive correlations between EVI and precipitation accounted for 48.50% of the total area of the study region and were mainly situated in the western part of the TRB, with sporadic distribution in the Bayinguoleng Mongol Autonomous Prefecture. Locations with negative correlations between EVI and precipitation accounted for 51.50% of the total area and were primarily situated in the eastern portion of the study region, indicating that the vegetation growth in this location is more affected by climate change and less by precipitation.

Under the significance test, the significant portions accounted for a relatively small amount (7.34%) of the total area, with significant positive correlations and significant negative correlations showing obvious spatial distribution. The significant positive correlations were mainly distributed in the Kumukuli Basin in a strip-like pattern and accounted for 4.02% ($p < 0.05$). This percentage indicates that the southwest portion of the study region has restricted vegetation growth due to the decrease in precipitation, whereas greater amounts of precipitation would promote increases in sparse vegetation. The significant negative correlation (3.32%) ($p < 0.05$) may be due to the increase in surface evaporation caused by increases in temperature and the high consumption of water, both of which the precipitation amounts were insufficient to offset.

3.2.2. Impact of Human Activities on EVI

Based on the standard deviation ellipse center of gravity formula, we calculated the coordinates of the center of gravity of the vegetation index, population, and GDP of the TRB for 2002, 2007, 2012, 2017, and 2022, identifying both the location of the center of gravity and the direction of the transfer. The results are shown in Figure 8. Figure 8a depicts the migratory trend of the change of the center of gravity of the EVI, revealing that the whole of the EVI during the study period migrated from the northeast to the northwest. Further, we found that the center of gravity change ranges from 79.117° E–80.292° E to 39.053° N–39.562° N and that the center of gravity migration distance is 209.245 km. The migration trend occurs roughly over two phases: the first phase is 2002–2012, where the overall migration is to the southeast and the migration distance is shorter; the second phase is 2012–2022, with the majority of the migration occurring from east to west at a migration distance of 131.887 km. With the passage of time, the vegetation changes in the western part of the study region improved more than those in the eastern part.

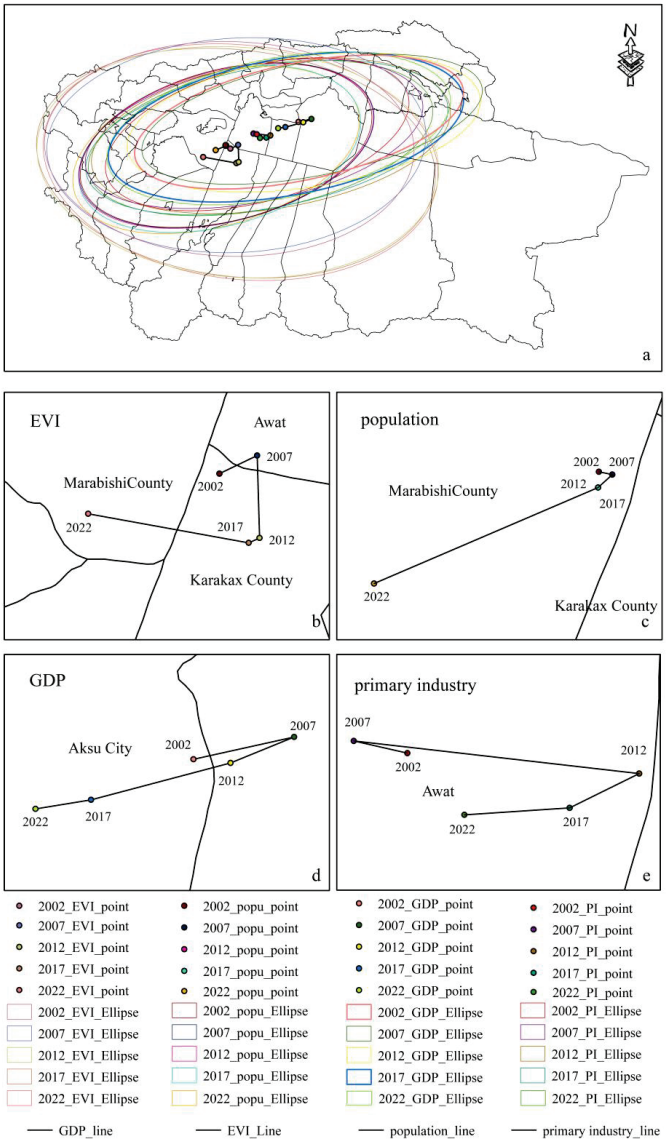

Figure 8. EVI, population, and GDP center of gravity migration trajectory in the TRB. ((**a**): Multifactor center of gravity migration trajectories in the TRB, (**b**): EVI center of gravity migration trajectory, (**c**): population center of gravity migration trajectory, (**d**): GDP center of gravity migration trajectory, (**e**): primary industry center of gravity migration trajectory).

More specifically, the center of gravity shifted from Moyu to Bachu County, passing through Awati County along the way, thus spanning three prefectures. The rotation angle of the standard deviation ellipse showed irregular changes from 2002 to 2022, with the rotation angle ranging from 79.057° to 85.258°. The smallest and largest rotation angles occurred in 2007 and 2017, respectively, and the direction of the rotation angle shifted in the opposite direction of the center of gravity migration trend. This shift suggests that the EVI is changing in the spatial and horizontal directions, indicating that the trend is enhanced in horizontal spatial directionality.

The trend of population center of gravity change is relatively uniform, mainly showing northeast to southwest migration. The center of gravity mainly occurs within Bachu County and ranges from 79.509° E–79.807° E to 39.305° N–39.5484° N, for a total migration distance of 41.117 km. The degree of offset in the direction of longitude is greater than that in latitude, indicating that the center of gravity of the study region population is more imbalanced in the former than in the latter. The rotation angle of the standard deviation ellipse shows regular changes, with the rotation angle gradually shifting from east to west. The migration of the center of gravity of GDP exhibits the characteristic of migrating from the southwest to the northeast, mainly towards Aksu (Figure 8d). In the direction of longitude, GDP migrates westward by 1.019°, while in the direction of latitude, it migrates southward by 0.411°.

The GDP migration trajectory changes twice during the study period, showing an overall migratory trajectory toward cities with high economic development. The majority of the economic development is primarily centered around Korla and Aksu, with a migration distance of 170.068 km and a migration rate of 8.5 km/a. The rotation angle of the GDP standard deviation ellipse exhibits regular changes throughout the study period, with the rotation angle ranging from 82.443° to 85.863°. The minimum and maximum rotation angles occur in 2002 and 2012, respectively. The year 2012 is the turning point for the standard deviation ellipse change.

The above results indicate that the EVI of the TRB is consistent with the migration direction of population and GDP. As the population increases and the economy grows at a rapid pace, the corresponding human-generated activities increase the demand for land, and the area of arable land increases, which in turn affects changes in vegetation structure. Furthermore, the migration of the center of gravity of the population is inseparable from the living environment and the economic development of the region, as the increase in population boosts the demand for arable land and various resources. Population rises also lead to changes in the local economic structure and the rapid development of urbanization, since the increase in the number of people in a region is also one of the reasons for the rapid development of the region's economy. On the other hand, the migration of population and economic centers of gravity will change land use, which will have an impact on vegetation type, growth, and expansion.

3.2.3. Future Trends in Vegetation Cover Change in the TRB

The Hurst index can predict future development trends for certain time or spatio-temporal sequences. In this paper, the RS algorithm was used to calculate the Hurst index EVI for the TRB from 2002 to 2022 and to generate a spatial distribution map. Figure 9 visualizes whether the changes in the EVI for each vegetation type are persistent over the years. A Hurst index result greater than 0.5 indicates a positive continuation of future EVI change conditions, while a result less than 0.5 indicates reverse persistence. In terms of the proportion of spatial image elements of the Hurst index, 63.27% of the study region had results less than 0.5, and 36.73% had results greater than 0.5. These findings indicate that most of the locations of future vegetation changes showed reverse persistence. In other words, the future change trends for the EVI across the entire TRB were opposite to the trends that occurred over the past two decades, suggesting that improved area would be greater than degraded area.

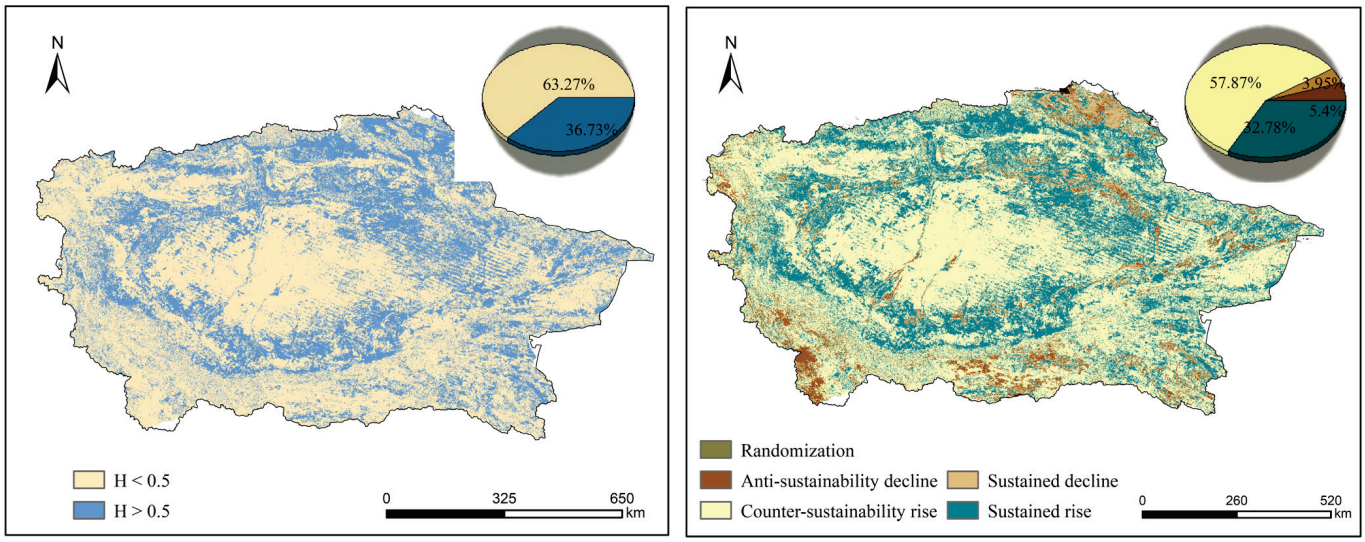

Figure 9. Hurst index for vegetation in the TRB.

In order to further study the future change trends for vegetation in the study region, the calculated Hurst index results were spatially superimposed on the Sen trend results to obtain the future trend map of the EVI (Figure 10). The outcomes were divided into five main categories: random change, inverse sustained decline, sustained decline, inverse sustained rise, and sustained rise. Among these, the anti-continuous decline was mainly distributed in the area north of the Tarim River mainstream and in the high mountainous area of the Yarkant River Basin, with sporadic distribution at the edge of the TRB accounting for a smaller proportion of 5.4%. Continuous decline was mostly distributed in the area north of the Tarim River mainstream, with a small amount distributed in Mongolia's Bayin'guolengmeng Autonomous Prefecture, accounting for a proportion of 3.95%. The anti-continuous rise accounts for the largest proportion of the basin as a whole (57.87%) and is mainly concentrated in the hinterland of the Taklamakan Desert, the Yarkant River Basin, and the Bayin'guolengmeng Autonomous Prefecture. The persistent uplift portion is situated throughout the TRB, particularly around the Weigang Kucha River, forming a ring-like distribution in the center. This persistent uplift is second only to the persistent uplift in the future trend.

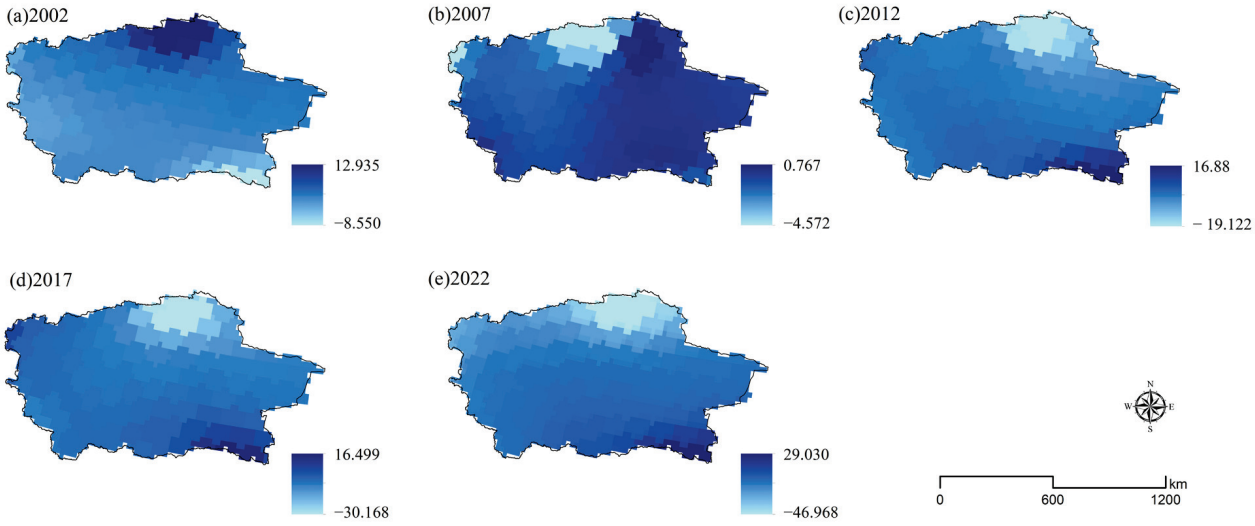

Figure 10. Spatial distribution of terrestrial water storage on the northern slopes of the Kunlun Mountains in 2002–2022.

3.3. Relationships between Water Storage Changes and Vegetation in the TRB

3.3.1. Characterization of Spatial and Temporal Variations in Terrestrial Water Storage

The CSR and MANCON gravity field data were used to analyze the spatial distribution characteristics of the terrestrial water storage data in the TRB from 2002 to 2022 and to explore the spatial distribution of the regional water storage data and the process of change (Figure 10). The results highlight obvious differences in the spatial distribution of land water reserves on the northern slopes of the Kunlun Mountains, giving an overall deficit rate between −2.99 and 1.88 mm/a. Moreover, the surplus and deficit status of land water reserves in 2002 showed obvious distribution patterns. The surplus was mainly distributed in the northern portion of the Tarim River mainstream, while the deficit primarily appeared in the south. However, both of these land water reserves were evenly distributed in area, with 47.93% apportioned to the north and 52.07% to the south.

In 2007, the surplus and deficit of terrestrial water reserves were mainly distributed in the west and east of the study region, with some surplus in the southwest and a deficit in the Kumukuli Basin. At that time, the surplus status of terrestrial water reserves was increased from the original 47.93% to 55.73%. After 2007, a slight decreasing trend emerged, but the surplus status then showed an increasing trend until 2022, with the surplus rising from 0.77 to 29.03. For locations that were in the deficit status, there is an increase in the degree of deficit. The distribution of water reserves after 2007 gradually results in a stable state, with the surplus status mostly distributed in Bayin'guoleng Autonomous Prefecture. The southeast is the primary distribution area, where the northern slope of the Kunlun Mountains and the water reserves in the Kumukuli Basin all exhibit surpluses.

According to the line graph depicting water storage changes (Figure 11), terrestrial water storage shows a fluctuating upward trend from 2002 to 2022 at a range of −60.565~307.208 mm. Storage changes significantly after 2015, with the maximum value appearing in the summer of 2019. From the second half of 2019 to 2022, the overall water reserves show a surplus state, and the increasing trend is more obvious after 2011; the increasing trend tends to stabilize in 2020–2022. The overall change in land water reserves in the Kumkuli Basin is thus dominated by growth, with more years in surplus than in deficit. Under the influence of global changes, the Kumkuli Basin experienced a significant increase in the number and area of lakes during the study period due to a rise in temperature, accelerated glacier melting, and increased precipitation. All of these changes resulted in the recharging of terrestrial water reserves and a marked uptick in the change trend.

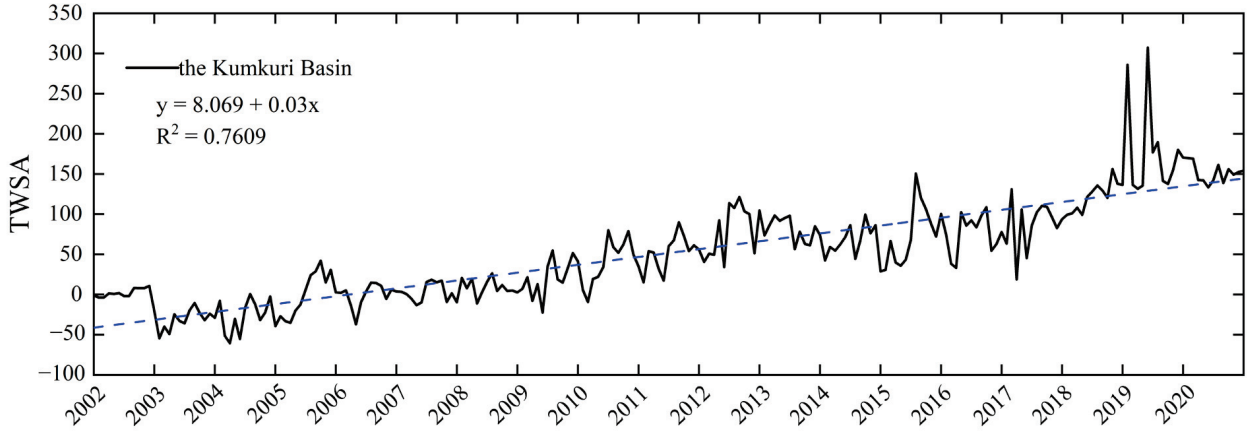

Figure 11. Change map of terrestrial water storage in the Kumkuri Basin.

3.3.2. Response of Water Storage Changes to EVI

Hydrothermal conditions are important resources for the growth of vegetation, as changes in water resources also controls growth. The study analyzed the correlation and significance test between terrestrial water reserves and the EVI. However, because the

spatial resolution of the terrestrial water reserves data is 0.25°, the correlation analysis was carried out after re-sampling the EVI data in order to ensure data accuracy.

Overall, the TWSA change process is not unlike the EVI change process, in that the change trends are similar and the interannual change characteristics are more consistent. As can be seen from Figure 12, the response of the TWSA to the EVI shows obvious spatial differences, with correlation coefficients ranging from −0.606 to 0.535. The locations with positive correlations between TWSA and EVI accounted for 50.513% of the total area and were mainly distributed in the southern and southwestern parts of the study region. The locations with negative correlations accounted for 49.487% of the total area.

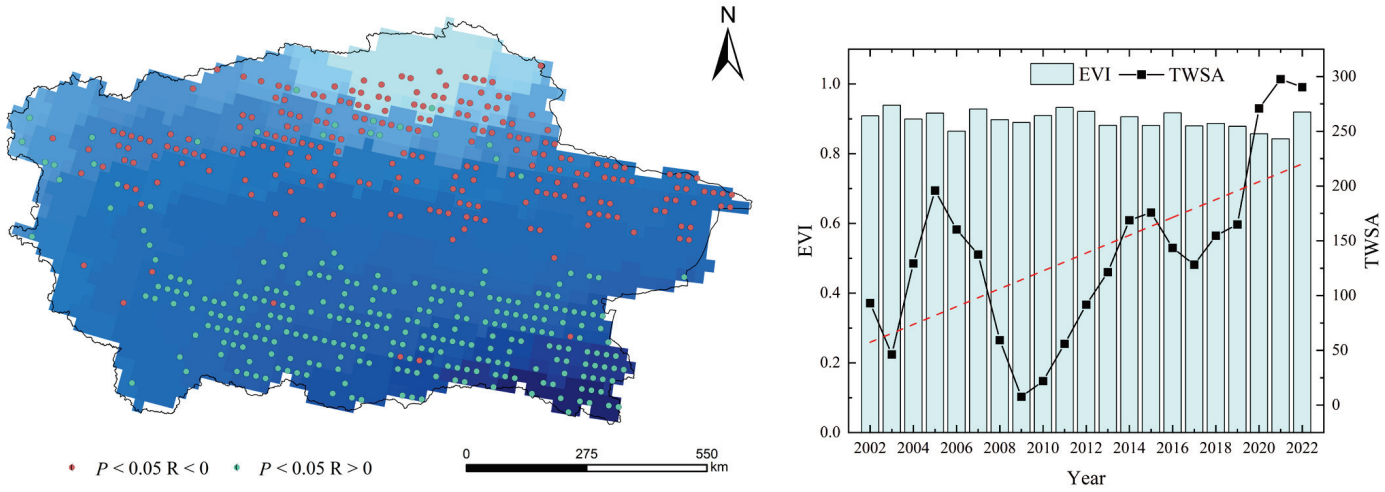

Figure 12. Spatial distribution of correlation coefficients between vegetation and terrestrial water storage in the TRB.

The correlation coefficients were also tested for significance. We found that 30.57% of the correlation coefficients of the TWSA passed the test at the level of $p < 0.05$. Significantly the positive correlation area was mainly located in the southern part of the study region, namely in the Kriya and Hotan river basins as well as in the Kumkuri Basin, which suggests that the favorable conditions for water storage in these areas can promote vegetation growth. The TWSA is critical to the growth of vegetation in this location because of its complex topographic features, sparse rainfall, and dependence on groundwater and soil moisture.

Meanwhile, additional test results indicate that, in the context of global climate change, temperatures are beginning to rise. At the same time, soil moisture and groundwater will increase as the southern part of the TRB continues a melting trend of seasonal permafrost. The area of significant negative correlation is mainly concentrated in the northern portion of the study region, in the transition zone of desert oases and plains. The rapid urbanization process in the northern part of the TRB along with the strong disturbances caused by human activities have led to various degrees of shrinkage of the groundwater resources in the region. The result has been a decline in groundwater levels, the reclamation of arable land, and the increase in land use for construction purposes. Agriculture and construction consume a large amount of water resources, which is one of the reasons for the significant negative correlation between the TWSA and the EVI in this part of the study region.

4. Discussion

To analyze the spatial distribution characteristics of the vegetation index in the Tarim River Basin, the response of vegetation to climate and terrestrial water storage is further explored by integrating climatic factors, changes in terrestrial water storage, and human activities. The results of trend analysis and the significance test of the EVI showed an overall upward trend of gradual "greening". Vegetation in the Kumukuli Basin increased significantly, which was basically consistent with Zhang Qifei's [33] results. Furthermore,

the vegetation in the watershed exhibited a spatial distribution characterized by "low in the middle and high in the surroundings". There were some differences in the vegetation growth area and pattern in each location across the TRB, and the transformation of the vegetation index varied for each class. Overall, the complexity and diversity of vegetation and climate types in the study region led to differences in the numerical and spatial distributions of the effects of temperature and precipitation on the EVI of the vegetation.

With the frequent transformation between land-use types in the TRB [34], the intensity of water resources development increased, resulting in uneven distribution of water resources and problems such as water poverty in some parts of the region [35,36]. There was a significant increase in terrestrial water reserves in the Kumukuli Basin, but a significant decrease in the Weigangkuche River Basin. Considering the special geographic location and geomorphological topography of the study area, the accelerated urbanization in the northern part of the basin led to water scarcity as well as an imbalance in water use between the inhabitants and the ecology [37]. The implementation of projects such as the ecological water conveyance in the lower Tarim River has generally improved the vegetation cover and compensated for the adverse impacts of urban sprawl. The changes in terrestrial water storage have accordingly shifted from deficit to surplus.

Climate change and human activities are the main factors affecting changes in vegetation cover. The TRB has been vigorously promoting the construction of ecological civilization in recent years. The Tarim River Basin Comprehensive Management Plan prevents the expansion of desertification by rationally allocating water resources and guaranteeing water supply to vegetation in the lower reaches of the river; it also constructs ecological water transfer projects in the basin to improve the natural environment and gradually restore natural vegetation. Relevant studies show that cultivated land, grassland, and forest land in the lower reaches of the Tarim River all show an increasing trend after ecological water transfer, and unutilized land shows a decreasing trend. Meanwhile, the value of ecosystem services in the study area showed an increasing trend [38]. Due to the improved vegetation growth conditions after the water transfer, the area of woodland and grassland has increased significantly, with a 33.3% increase in the area of vegetation compared to the area before the water transfer [39].

Human activities will, to a certain extent, reduce the degree of vegetation response to climate change, but it has also been shown that among the main factors that affect vegetation, climate change is the main driver [40]. Warmer temperatures and increased precipitation generally positively contribute to vegetation. However, discussing the interrelationships between vegetation and climate change only considering a time series does not reflect their spatial differences well enough to directly express their relevance. Soil type and topography dominate the spatial distribution of vegetation cover in the study area, but soils and topography are more stable on their own and have a weaker influence on vegetation change. Therefore, this study relied on the correlation analysis model and significance test to explore the correlations between vegetation, climate, and terrestrial water storage. The results of the study have a certain degree of reliability.

Precipitation and temperature conditions are the most critical factors influencing the vegetation growth process. The study region is located in the inner part of the Asian-European continent, which has a temperate, arid continental climate and major spatial differences in temperature, precipitation, and vegetation cover. The increased temperature in the hinterland of the TRB shows notable inhibition of vegetation, while the oases and desert–oasis transition zones are gradually turning into better ecological environments with increased precipitation. In the Kunlun Mountains portion of the study region, precipitation is mainly in the form of snowfall, and its special geographical location and altitude are more conducive to the development of glaciers. With global climate change, temperatures are on the rise, and precipitation is increasing in winter and summer, causing water vapor to fall to the Kunlun Mountains in the form of solid precipitation. This, along with glacial meltwater, is the main reason for the increase in the amount of terrestrial water storage in the Kunlun Mountains and for the increase in vegetation cover in the Kumkuli Basin.

Our study employed the enhanced vegetation index, which can effectively reduce the interference of dryness in the accuracy of data. The EVI was then combined with terrestrial water storage to analyze the influencing factors, aiming to make up for the results of earlier studies conducted only from the aspects of climate or topography. In addition to this novel approach, the study limited the factor selection to climate, economy, population, and terrestrial water reserves only in order to explore the influence of nature on the EVI. Nonetheless, studies exploring the driving mechanisms, such as land-use change, topography, slope, slope orientation, etc., are still lacking in the literature, and a more comprehensive investigation of the driving mechanisms of the EVI in the TRB could be helpful in the future.

5. Conclusions

(1) The spatial distribution of the EVI of vegetation in the Tarim River Basin from 2002 to 2022 was characterized as "high all around, low in the center, high in the northwest, and low in the southeast". There were frequent transformations between classes of the vegetation index and significant vegetation growth over the 20-year study period. Among these conversions, the area of highest change rate was $0.6 < \text{EVI} \leq 0.8$, at a rate of change of 200.36%. Additionally, vegetation in the TRB increased more than it decreased, and the locations boasting improved vegetation accounted for 84.13% of the total area. The places showing highly significant increases and significant increases accounted for 45.70% of the study region, so the overall ecological environment improved. Vegetation in the Kumukuli Basin also showed an increasing trend. For future vegetation changes, the area of degradation is slightly larger than the area of improvement, the overall trend is toward degradation, and the proportion of anti-sustained upward movement area is 57.87%.

(2) Temperature and precipitation were demonstrated to be the most critical factors affecting the vegetation growth process. The areas with positive correlations between vegetation EVI and temperature accounted for 64.67% of the study region, with 6.54% showing significant positive correlations. The locations exhibiting positive correlations between precipitation and vegetation accounted for 7.3% of the total area, which is a relatively small percentage, and vegetation showed a lower sensitivity to precipitation compared to temperature. The EVI remained consistent with the direction of population and GDP migration, and the impact of human activities on the EVI was mainly generated through the increase in the area of cultivated land.

(3) The spatial distribution of terrestrial water storage in the basin was geographically significant during the study period. The spatial changes showed a gradual shift from deficit to surplus from the northeast to the southwest, with an overall fluctuating upward trend. Changes in terrestrial water storage in the Kumkuli Basin were most obvious after 2011 and resulted in a 0.993 mm/month change rate. Terrestrial water storage changes had only indirect effects on vegetation, with a positive correlation of 50.513% for the total area. The locations exhibiting significant positive correlations were mainly distributed along the northern slopes of the Kunlun Mountains, and the Kumukuli Basin gave the highest performance.

Author Contributions: Y.W. and Z.L. conceived the study design; T.X. implemented the field research and collected and analyzed the field data; X.X., H.W. and Z.Z. applied mathematics or other forms of technology to analyze or research data; T.X. wrote the paper. All authors have read and agreed to the published version of the manuscript.

Funding: This research was support by the Third Xinjiang Scientific Expedition Program, grant number 2021xjkk010202.

Data Availability Statement: The data presented in this study are available on request from the corresponding author due to privacy restrictions.

Conflicts of Interest: The authors declare no conflicts of interest.

References

1. Shi, S.H.; Wang, X.L.; Hu, Z.R.; Zhao, X.; Zhang, S.R.; Hou, M.; Zhang, N. Geographic detector-based quantitative assessment enhances attribution analysis of climate and topography factors to vegetation variation for spatial heterogeneity and coupling. *Glob. Ecol. Conserv.* **2023**, *42*, e02398. [CrossRef]
2. Zhang, H.; Yu, J.D.; Jiang, T.L.; Yu, S.C.; Zhou, C.L.; Li, F.Q.; Chen, X.T. Natural Vegetation Area Design in an Arid Region Based on Water Resource Carrying Capacity-Taking Minqin County as an Example. *Water* **2023**, *15*, 3238. [CrossRef]
3. Sur, K.; Chauhan, P. Dynamic trend of land degradation/restoration along Indira Gandhi Canal command area in Jaisalmer District, Rajasthan, India: A case study. *Environ. Earth Sci.* **2019**, *78*, 472. [CrossRef]
4. Zhang, G.L.; Biradar, M.C.; Xiao, X.M.; Dong, J.W.; Zhou, Y.T.; Qin, Y.W.; Zhang, Y.; Liu, F.; Ding, M.J.; Thomas, R.J.; et al. Exacerbated grassland degradation and desertification in Central Asia during 2000-2014. *Ecol. Appl. A Publ. Ecol. Soc. Am.* **2018**, *28*, 442–456. [CrossRef] [PubMed]
5. Zhang, Q.; Wang, G.; Yuan, R.Y.; Singh, V.P.; Wu, W.H.; Wang, D.Z. Dynamic responses of ecological vulnerability to land cover shifts over the Yellow river Basin, China. *Ecol. Indic.* **2022**, *144*, 109554. [CrossRef]
6. Zhang, D.; Geng, X.L.; Chen, W.X.; Fang, L.; Yao, R.; Wang, X.R.; Zhou, X. Inconsistency of Global Vegetation Dynamics Driven by Climate Change: Evidences from Spatial Regression. *Remote Sens.* **2021**, *13*, 3442. [CrossRef]
7. Sun, X.; Li, G.Y.; Wu, Q.Q.; Li, D.Q.; Lu, D.S. Examining the Effects of Soil and Water Conservation Measures on Patterns and Magnitudes of Vegetation Cover Change in a Subtropical Region Using Time Series Landsat Imagery. *Remote Sens.* **2024**, *16*, 714. [CrossRef]
8. Xiao, X.; Guan, Q.Y.; Zhang, Z.P.; Liu, H.Q.; Du, Q.Q.; Yuan, T.W. Investigating the underlying drivers of vegetation dynamics in cold-arid mountainous. *Catena* **2024**, *237*, 7107831. [CrossRef]
9. He, B.; Wu, X.; Liu, K.; Yao, Y.Z.; Chen, W.J.; Zhao, W. Trends in Forest Greening and Its Spatial Correlation with Bioclimatic and Environmental Factors in the Greater Mekong Subregion from 2001 to 2020. *Remote Sens.* **2022**, *14*, 59825982. [CrossRef]
10. Gu, Z.V.; Zhang, Z.; Yang, J.H.; Wang, L.L. Quantifying the Influences of Driving Factors on Vegetation EVI Changes Using Structural Equation Model: A Case Study in Anhui Province, China. *Remote Sens.* **2022**, *14*, 42034203. [CrossRef]
11. Li, C.H.; Song, Y.F.; Qin, T.L.; Yan, D.H.; Zhang, X.; Zhu, L.; Dorjsuren, B.; Khalid, H. Spatiotemporal Variations of Global Terrestrial Typical Vegetation EVI and Their Responses to Climate Change from 2000 to 2021. *Remote Sens.* **2023**, *15*, 4245. [CrossRef]
12. Zhang, T.; Zhou, J.Z.; Yu, P.; Li, J.Z.; Kang, Y.F.; Zhang, B. Response of ecosystem gross primary productivity to drought in northern China based on multi-source remote sensing data. *J. Hydrol.* **2023**, *616*, 128808. [CrossRef]
13. Fan, X.Y.; Zhu, D.P.; Sun, X.F.; Wang, J.B.; Wang, M.; Wang, S.Q.; Watson, A.E. Impacts of Extreme Temperature and Precipitation on Crops during the Growing Season in South Asia. *Remote Sens.* **2022**, *14*, 6093. [CrossRef]
14. Amantai, N.; Meng, Y.; Wang, J.; Ge, X.Y.; Tang, Z.Y. Climate overtakes vegetation greening in regulating spatiotemporal patterns of soil moisture in arid Central Asia in recent 35 years. *GIScience Remote Sens.* **2024**, *61*, 2286744. [CrossRef]
15. Qin, J.S.; Ma, M.L.; Shi, J.B.; Ma, S.R.; Wu, B.G.; Su, X.H. The Time-Lag Effect of Climate Factors on the Forest Enhanced Vegetation Index for Subtropical Humid Areas in China. *Int. J. Environ. Res. Public Health* **2023**, *20*, 799. [CrossRef]
16. Ge, X.Y.; Ding, J.L.; Amantai, N.; Xiong, J.; Wang, J.Z. Responses of vegetation cover to hydro-climatic variations in Bosten Lake Watershed, NW China. *Front. Plant Sci.* **2024**, *15*, 1323445. [CrossRef] [PubMed]
17. Yuan, H.; Wu, C.; Gu, C.; Wang, X.Y. Evidence for satellite observed changes in the relative influence of climate indicators on autumn phenology over the Northern Hemisphere. *Glob. Planet. Chang.* **2020**, *187*, 103131. [CrossRef]
18. Sun, R.; Chen, S.H.; Su, H.B. Trend Analysis and Driving Factors of Vegetation Dynamics in Northern China from 1982 to 2015. *Remote Sens.* **2022**, *14*, 6163. [CrossRef]
19. Mei, L.; Tong, S.Q.; Yin, S.; Bao, Y.H.; Huang, X.J.; Tuya, A. Variation Characteristics of Ecosystem Water Use Efficiency and Its Response to Human Activity and Climate Change in Inner Mongolia. *Remote Sens.* **2022**, *14*, 54225422. [CrossRef]
20. Yu, M.Z.; Song, S.; He, G.Z.; Shi, Y.J. Vegetation Landscape Changes and Driving Factors of Typical Karst Region in the Anthropocene. *Remote Sens.* **2022**, *14*, 5391. [CrossRef]
21. Matta, E.; Bresciani, M.; Tellina, G.; Schenk, K.; Bauer, P.; Von, T.F.; Ruther, N.; Bartosova, A. Data Integration for Investigating Drivers of Water Quality Variability in the Banja Reservoir Watershed. *Water* **2023**, *15*, 607. [CrossRef]
22. Yang, X.Y.; Yang, Q.K.; Yang, M.M. Spatio-Temporal Patterns and Driving Factors of Vegetation Change in the Pan-Third Pole Region. *Remote Sens.* **2022**, *14*, 4402. [CrossRef]
23. Chen, L.F.; Michishita, R.; Xu, B. Abrupt spatiotemporal land and water changes and their potential drivers in Poyang Lake, 2000–2012. *ISPRS J. Photogramm. Remote Sens.* **2014**, *98*, 9885–9893. [CrossRef]
24. Liu, H.; Yu, Y.; Xia, D.S.; Ma, X.; Dong, L. Analysis of the relationship between dust aerosol and precipitation in spring over East Asia using EOF and SVD methods. *Sci. Total Environ.* **2023**, *908*, 168437. [CrossRef] [PubMed]
25. Sur, K.; Dave, R.; Chauhan, P. Spatio—Temporal changes in NDVI and rainfall over Western Rajasthan and Gujarat region of India. *J. Agrometeorol.* **2018**, *20*, 189–195.
26. Mann, H.B. Nonparametric tests against trend. *Econom. J. Econom. Soc.* **1945**, *13*, 245–259. [CrossRef]
27. Jumai, M.; Kasimu, A.; Liang, H.; Tang, L.N.; Aizizi, Y.; Zhang, X.L. A Study on the Spatial and Temporal Variation of Summer Surface Temperature in the Bosten Lake Basin and Its Influencing Factors. *Land* **2023**, *12*, 1185. [CrossRef]

28. Fang, L.J.; Gao, R.Z.; Wang, X.X.; Zhang, X.; Wang, Y.L.; Liu, T.X. Effects of coal mining and climate-environment factors on the evolution of a typical Eurasian grassland. *Environ. Res.* **2024**, *2024*, 244117957. [CrossRef]
29. Yang, Y.; Tang, S.N.; Yu, L.L.; Chen, F.; Ding, Y.Y.; Zhang, P.Z. Trend analysis on temperature and precipitation over North China Plain for past five decades. *IOP Conf. Ser. Earth Environ. Sci.* **2021**, *675*, 012014. [CrossRef]
30. Li, J.; Peng, X.; Tang, R.; Tang, R.; Geng, J.; Zhang, J.P.; Xu, D.; Bai, T. Spatial and Temporal Variation Characteristics of Ecological Environment Quality in China from 2002 to 2019 and Influencing Factors. *Land* **2024**, *13*, 0110. [CrossRef]
31. Zhang, X.C.; Chen, L.X.; Zhou, C. Deformation Monitoring and Trend Analysis of Reservoir Bank Landslides by Combining Time-Series InSAR and Hurst Index. *Remote Sens.* **2023**, *15*, 619. [CrossRef]
32. Hu, J.Y.; Chritakos, G.; Wu, J.P.; Li, M.; Leng, J.X. Spatiotemporal BME characterization and mapping of sea surface chlorophyll in Chesapeake Bay (USA) using auxiliary sea surface temperature data. *Sci. Total Environ.* **2021**, *794*, 148670.
33. Zhang, Q.F.; Chen, Y.N.; Sun, C.J.; Xiang, Y.Y.; Hao, H.C. Changes in terrestrial water storage and evaluation of oasis ecological security in the Tarim River Basin. *Arid Land Geogr.* **2024**, *47*, 1–14.
34. Wang, S.; Zuo, Q.; Zhou, K.; Wang, J.L.; Wang, E. Predictions of Land Use/Land Cover Change and Landscape Pattern Analysis in the Lower Reaches of the Tarim River, China. *Land* **2023**, *12*, 1093. [CrossRef]
35. Lu, Q.; Liu, F.J.; Li, Y.J.; Wang, D.Z. Study on the Relationship between Water Resources Utilization and Economic Growth in Tarim River basin from the Perspective of Water Footprint. *Water* **2022**, *14*, 16551655. [CrossRef]
36. Wang, J.; Din, J.; Li, G.; Liang, J.; Yu, D.L.; Aishan, T.J.; Zhang, F.; Yang, J.M.; Abulimiti, A.; Liu, J.; et al. Dynamic detection of water surface area of Ebinur Lake using multi-source satellite data (Landsat and Sentinel-1A) and its responses to changing environment. *Catena* **2019**, *177*, 189–201. [CrossRef]
37. Lu, S.B.; Shang, Y.Z.; Li, W. Assessment of the Tarim River basin water resources sustainable utilization based on entropy weight set pair theory. *Water Supply* **2019**, *19*, 908–917. [CrossRef]
38. Zhang, S.; Wang, Y.; Wang, Y.; Li, Z.; Hou, Y.F. Spatiotemporal Evolution and Influencing Mechanisms of Ecosystem Service Value in the Tarim River Basin, Northwest China. *Remote Sens.* **2023**, *15*, 591. [CrossRef]
39. Sun, Q.; Tasipurat, T.; Zhang, F. Dynamics of land use/cover changes in the Weigan and Kuqa rivers delta oasis based on Remote Sensing. *Acta Ecol. Sin.* **2012**, *32*, 3252–3265.
40. Yue, S.J.; Huang, J.C.; Zhang, Y.L.; Chen, W.Q.; Guo, Y.L.; Cheng, M.Y.; Ji, G.X. Quantitative Evaluation of the Impact of Vegetation Restoration and Climate Variation on Runoff Attenuation in the Luan River Basin Based on the Extended Budyko Model. *Land* **2023**, *12*, 1626. [CrossRef]

Disclaimer/Publisher's Note: The statements, opinions and data contained in all publications are solely those of the individual author(s) and contributor(s) and not of MDPI and/or the editor(s). MDPI and/or the editor(s) disclaim responsibility for any injury to people or property resulting from any ideas, methods, instructions or products referred to in the content.

remote sensing

MDPI

Article

Toward a More Robust Estimation of Forest Biomass Carbon Stock and Carbon Sink in Mountainous Region: A Case Study in Tibet, China

Guanting Lyu [1,2], Xiaoyi Wang [1,*], Xieqin Huang [3], Jinfeng Xu [1,4], Siyu Li [5], Guishan Cui [5] and Huabing Huang [6]

[1] State Key Laboratory of Tibetan Plateau Earth System, Resources and Environment (TPESRE), Institute of Tibetan Plateau Research, Chinese Academy of Sciences, Beijing 100101, China; guantinglv@itpcas.ac.cn (G.L.); jinfengxu@itpcas.ac.cn (J.X.)
[2] University of Chinese Academy of Sciences, Beijing 100101, China
[3] Department of Computer Science and Technology, Tsinghua University, Beijing 100084, China; hxq23@mails.tsinghua.edu.cn
[4] College of Ecology, Lanzhou University, Lanzhou 730000, China
[5] College of Geography and Ocean Sciences, Yanbian University, Yanji 133002, China; honertjecodin@gmail.com (S.L.); cuiguishan@ybu.edu.cn (G.C.)
[6] School of Geospatial Engineering and Science, Sun Yat-sen University, Zhuhai 519082, China; huanghb55@mail.sysu.edu.cn
* Correspondence: xiaoyiwang@itpcas.ac.cn; Tel.: +86-010-8409-7037

Abstract: Mountainous forests are pivotal in the global carbon cycle, serving as substantial reservoirs and sinks of carbon. However, generating a reliable estimate remains a considerable challenge, primarily due to the lack of representative in situ measurements and proper methods capable of addressing their complex spatial variation. Here, we proposed a deep learning-based method that combines Residual convolutional neural networks (*ResNet*) with in situ measurements, microwave (Sentinel-1 and VOD), and optical data (Sentinel-2 and Landsat) to estimate forest biomass and track its change over the mountainous regions. Our approach, integrating in situ measurements across representative elevations with multi-source remote sensing images, significantly improves the accuracy of biomass estimation in Tibet's complex mountainous forests (R^2 = 0.80, root mean squared error = 15.8 MgC ha^{-1}). Moreover, *ResNet*, which addresses the vanishing gradient problem in deep neural networks by introducing skip connections, enables the extraction of complex spatial patterns from limited datasets, outperforming traditional optical-based or pixel-based methods. The mean value of forest biomass was estimated as 162.8 $\pm$ 21.3 MgC ha^{-1}, notably higher than that of forests at comparable latitudes or flat regions in China. Additionally, our findings revealed a substantial forest biomass carbon sink of 3.35 TgC year^{-1} during 2015–2020, which is largely underestimated by previous estimates, mainly due to the underestimation of mountainous carbon stock. The significant carbon density, combined with the underestimated carbon sink in mountainous regions, emphasizes the urgent need to reassess mountain forests to better approximate the global carbon budget.

Keywords: mountain forest; Sentinel-1; VOD; landsat; forest biomass; carbon sink; deep learning

1. Introduction

Mountainous forests, spanning extensive territories, are pivotal in the sequestration of atmospheric carbon [1]. Refining our estimates of carbon reservoirs within these biomes is crucial for climate change mitigation strategies and to inform sustainable forestry [2–5]. Nonetheless, the diverse forest types, challenging topography, and heterogeneous climate of mountain regions impose significant difficulties in calculating forest biomass and carbon sequestration rates [6,7]. Across the elevational gradient, forest types transition from broadleaf to mixed, and then to coniferous forests and eventually an alpine tree line, which

occurred over short horizontal spans, and paralleled by varied biomass. Marked biomass differences also persist between sunlit and shaded slopes in mountain regions. Traditional assessment methods could not capture the intricate spatiotemporal dynamics of mountain forests, hindered by limited in situ measurements and methods suitable for their complex spatial variations [8]. Consequently, accurate biomass and carbon sequestration estimates for mountainous terrain remained challenging [9].

First, in situ measurements in mountainous areas were limited, as monitoring sites often were unevenly distributed and too few to accurately reflect the complex spatial variations, especially across large elevational gradients. Such insufficiency compromised the accuracy of forest carbon stock assessments and their variation within these complex landscapes. For example, a widely used forest biomass inventory dataset for Eurasia [10] included only 30.6% of measurements from mountain regions as defined by the Global Mountain Biodiversity Assessment (GMBA) datasets [11], and included only 19.9% of measurements which were located in rugged regions with slopes greater than 10°. This deficiency was more pronounced across China, where only 6.45% of measurements were located in mountain regions with an elevation higher than 1000 m. Therefore, there was an emergent need to conduct widespread measurements over mountain regions [12,13]. However, the remoteness and access difficulties in mountainous regions made extensive field surveys challenging, often precluding the collection of widespread observational data [14,15]. Thus, determining whether representative sampling along elevational gradients could enable efficient monitoring and enhance forest biomass estimations emerged as a primary issue to address.

Second, forest biomass carbon stock and sink estimations had increasingly relied on remote sensing data, ranging from optical images (e.g., Landsat, Sentinel-2, IKONOS, QuickBird) to SAR (e.g., Sentinel-1, SSDD, ALOS-2) and VOD (e.g., L-VOD, X-VOD, P-VOD) datasets, each offering unique insights into vegetation structure [16–18]. However, how to effectively combine multi-source remote sensing data remained to be solved. Specifically, optical remote sensing imagery provided spectral reflectance of the forest canopy, enabling the acquisition of features related to the forest's top canopy, notably leaves [19,20]. However, it fell short in detecting the structural components of trunks and branches, resulting in potential bias in forest carbon estimations [21]. Advanced remote sensing techniques such as LiDAR [22,23] and microwave remote sensing [24,25] could effectively penetrate the forest canopy, provide forest structure for biomass analysis, and were less susceptible to weather conditions [26]. For example, C-band SAR data provided by Sentinel-1A/B satellites aboard the ESA (European Space Agency) had been consistently providing valuable data on forest vertical structure through multiple polarization modes since 2014 [27,28]. There have been studies showing the proficiency of SAR data in regional biomass studies [29,30], yet the penetration power of SAR has limitations in dense or high-biomass forests where it might underestimate biomass [31]. The L-band vegetation optical depth (L-VOD), which correlates with aboveground biomass carbon and water content within vegetation, had been extensively utilized as a proxy for vegetation biomass to monitor changes in carbon stocks [32,33]. VOD data, notably sensitive to woody biomass and non-saturating at high levels due to low-frequency microwaves [34], offered an effective biomass proxy. For instance, Fan et al. [35] detected changes in terrestrial tropical carbon stocks using L-VOD and found that the tropics were roughly carbon neutral during 2010–2017. Wigneron et al. [36] further showed that tropical forest biomass was a carbon source during the strong 2015–2016 El Niño event and did not recover to the pre-event level. While methods utilizing L-VOD were constrained by the assumption that the plant water-holding capacity remained constant. This assumption could potentially be challenged by climate variations and the physiological responses of vegetation [37–39]. Therefore, how to effectively combine the multi-source remote sensing data that reflect the multi-dimensional forest structure and attributes to accurately quantify forest biomass remained an unresolved issue.

Third, traditional methods that upscaled in situ measurements to regional wall-to-wall maps failed to capture the detailed spatial variations present in mountainous terrain. Such methods often employed pixel-based modeling, which neglected neighboring pixel information, including textural patterns crucial for depicting spatial variation [40,41]. However, with advancements in deep learning, particularly Convolutional Neural Networks (CNNs), these methods showed promise in overcoming various geospatial challenges, as evidenced by numerous researchers [42–44]. Unlike traditional pixel-based approaches that formed predictions from isolated pixels, CNNs leveraged the spatial context by considering information from neighboring pixels, thus offering a more complex representation of forest biomass distribution [45]. Integrating CNNs with multi-source remote sensing data, which provided insights into different forest components such as leaves, branches, and trunks, held the potential to significantly improve the mapping of regional biomass and carbon sinks.

Forests in Tibet, characterized by intact and natural state [45–47], potentially hold considerable carbon stock and serve as substantial carbon sinks. The elevation of forest over Tibet ranges from 8 to 4900 m. The rugged and complex terrain poses challenges for traditional methods of estimating biomass in mountainous forests, making it an ideal case study for our research. Hence, our objective is to devise a robust methodology for estimating forest biomass and biomass carbon sink, with a particular focus on mountainous forests, exemplified by those in the mountain regions of Tibet. Our research aimed to answer the following key questions: (1) whether representative in situ measurements along elevation could improve mountain forest biomass. (2) Do multi-source remote sensing data outperform single source results? (3) Whether the patch-based deep learning method outperforms the traditional pixel-based method in mountain forest biomass and carbon sink estimation. (4) The size of forest biomass carbon stock and carbon sequestration rate over Tibet.

2. Data Collection

2.1. Study Area

The Tibet Autonomous, situated in southwestern China, boasts a significant altitude range. This considerable variation in altitude harbors diverse climate types across Tibet [48], facilitating the growth of plants ranging from subtropical to boreal species. Consequently, Tibet harbors a forest ecosystem of exceptional biodiversity, earning recognition as one of China's three major forested regions [46]. Forest distribution in Tibet is predominantly concentrated in the mountains and valleys of the Himalayas and the Hengduan Mountains in the southeast. Noteworthy is the Nyingchi Prefecture, home to China's largest primeval forest area and revered as one of the most representative regions for global biodiversity.

2.2. Forest Inventory Data

We conducted in situ measurements (N = 67, red dots in Figure 1) during 2019 and 2023 with a special focus on the elevational gradient. Here, we set the elevation intervals as 100 m, ensuring that at least one sample was collected every 100 m from 33 m (a.s.l.) to 4500 m (a.s.l.). Each plot was set as a square of 10 $\times$ 10 m. We then measured the diameter at breast height (DBH), and height of each tree (DBH > 5 cm) and also recorded tree types. The forest aboveground biomass was obtained using the allometric model of each tree type. The average biomass of these sample points is 135.4 MgC ha^{-1}, with an average elevation of 4673.4 m. In addition, we compiled data documented in the literature (N = 98, blue dots in Figure 1). Data should be measured near or after the year 2015, and satisfy the following two criteria (1) the inventory should be conducted at the plot scale rather than at the individual tree level [49]; (2) data should be collected from stable sites with no recent fires or human disturbances, verified through high-resolution imagery on Google Earth (interpreted manually from Google Earth high-resolution images). Data recorded only forest aboveground biomass was transformed into biomass by the shoot-to-root ratio of 0.35, following Liu et al. [8]. The distribution of inventory data which met

those criteria is shown in Figure 1. However, the observation data were obtained between 2015 and 2023, while our analysis focused on the period from 2015 to 2020. This temporal mismatch could potentially introduce uncertainties in our estimation.

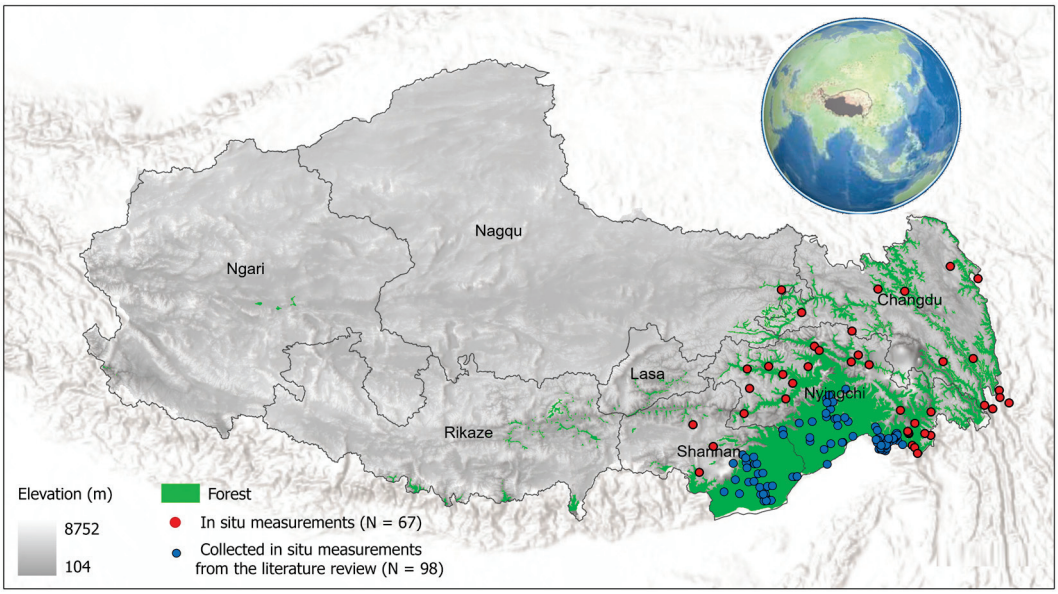

Figure 1. Distribution of forests and in situ measurements over Tibet.

2.3. Microwave Remote Sensing Images

The Sentinel-1 data offer backscatter information in the Interferometric Wide Swath (IW) mode, capturing both VV (Vertical transmit–Vertical receive) and VH (Vertical transmit–Horizontal receive) polarizations at a spatial resolution of 10 m. We acquired median value data spanning the growing seasons (May to September) in 2015 and 2020 using the Google Earth Engine (GEE) platform [50] (https://earthengine.google.org/, accessed on 10 January 2024). These datasets underwent meticulous pre-processing, including noise elimination, terrain correction, and radiometric calibration, to ensure accuracy and reliability.

The vegetation optical depth (VOD) data were from the SMOS-ICV2-RE06 L-VOD product (L-VOD), which provides monthly VOD data at different microwave band frequencies since 2010. The VOD measured at microwave frequencies is related to the vegetation water content. And the vegetation water content can be related to the biomass and to its moisture status, which can be parameterized by the gravimetric moisture content Mg (%). The VOD data we utilized also originate from both the 2015 and 2020 periods, and we downscaled L-VOD data to 10 m resolution by linear spatial interpolation.

2.4. Optical Remote Sensing Image

We also obtained top-of-atmosphere reflectance data from Sentinel-2 level 2A and Landsat 8 images during the growing seasons (June to September) of 2015 and 2020 via the GEE platform. We selected five bands, including green, red, near-infrared, and two shortwave infrared bands (Table 1). To ensure compatibility with the Sentinel-1 data, we applied the nearest-neighbor resampling method to adjust the Landsat data to a 10-m resolution, thereby minimizing uncertainties due to disparities of spatial scale between the two datasets.

Table 1. Details of the multi-source remote sensing imagery used in this study.

Multi-Source Remote Sensing Dataset	Band	Description	Spatial Resolution
Sentinel 1	VV VH	Vertical transmit–Vertical receive Vertical transmit–Horizontal receive	10 m
VOD SMOS-ICV2-RE06	L-VOD	VOD	0.25°
Sentinel-2A	Band 3 Band 4 Band 8 Band 11 Band 12	Green Red Near-infrared Shortwave infrared Shortwave infrared	10 m
Landsat 8 OLI	Band 3 Band 4 Band 5 Band 6 Band 7	Green Red Near-infrared Shortwave infrared Shortwave infrared	30 m

3. Method

To provide a benchmark of mountainous forest biomass and estimated changes in biomass, that is the biomass carbon sink, we proposed a deep learning method that integrated a Residual Convolutional Neural Networks based model, *ResNet*, with a relatively large number of in situ measurement data, microwave remote sensing (Sentinel-1 and VOD), and optical imagery (Sentinel-2A and Landsat 8). Initially, we compiled multi-source remote sensing data covering the years 2015 to 2020. We then aligned in situ measurements with the remote sensing data to ensure spatial consistency, incorporating neighboring information as additional input for *ResNet* regression (Step 1 in Figure 2). Subsequently, we trained and optimized the *ResNet* model to minimize the loss value (Step 2 in Figure 2). The well-optimized *ResNet* model was then deployed to predict regional forest biomass at the pixel level. Changes in forest biomass were subsequently translated into forest biomass carbon sink (Steps 3 and 4 in Figure 2).

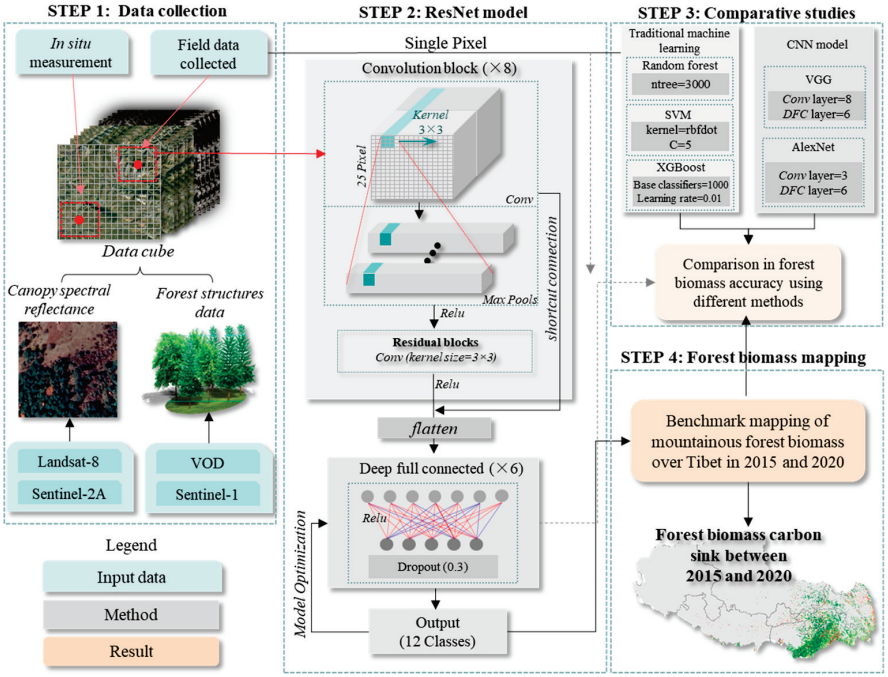

Figure 2. Schematic flow of the mountain forest biomass and biomass carbon sink mapping proposed in this study.

3.1. ResNet CNN Model

The principle of Convolutional Neural Networks (CNN) was that the convolutional structure was added to the traditional Deep Neural Network (DNN) model. The *ResNet* model introduced a novel architectural innovation known as residual learning to the traditional CNN model, primarily through the use of residual blocks [51]. Each block contained a shortcut connection that bypassed one or more layers with an identity mapping. This approach allowed the model to learn the additive residuals of the underlying mapping, rather than the entire mapping at once, which avoided the vanishing gradients and the degradation problem, and enabled much deeper networks to be trained effectively. Furthermore, the core of the algorithm are convolutional layers, which apply convolution operations to the input images using learnable filters. These filters act as feature detectors, capturing patterns and spatial relationships within the images. Following convolution, pooling layers are employed to down-sample the feature maps, reducing computational complexity and preventing overfitting by retaining only the most relevant information. The extracted features are then passed through fully connected layers, where they are transformed and aggregated to produce the final regression output. Each layer is activated using rectified linear unit (ReLU) activation functions, facilitating non-linear transformations and enhancing model expressiveness. In our case, we constructed *ResNet* model under the Google TensorFlow framework [52]. Our *ResNet* architecture comprises a series of convolution layers, repeated four times in this instance, followed by a pooling layer and six fully connected layers. The parameters employed in this architecture include Convolution layers: these utilize a kernel size of 3×3, a stride size of 1×1, and a filter size initially set to 64, with an increment by a factor of 2 as the model depth increases. The filter size regulates the number of features extracted by convolution. Pooling layers: utilizing max pooling, these layers extract the maximum value of each feature with a stride size of 1×1. Residual blocks: these blocks consist of multiple convolutional layers followed by identity shortcut connections, which skip one or more layers. Fully connected layers: the architecture includes six fully connected layers. These parameters are carefully chosen to optimize feature extraction and model performance across varying depths. To optimize the algorithm's performance, we employed techniques such as grid search to fine-tune hyperparameters, weight regularization (L2 regularization) to prevent overfitting, and dropout layers to randomly deactivate neurons during training, thereby promoting model generalization.

3.2. Other Machine Learning

To demonstrate the proficiency of the *ResNet* model in estimating forest biomass carbon, we conducted a comparative analysis with traditional machine learning approaches, including Random Forest (RF), Support Vector Machine (SVM), eXtreme Gradient Boost (XGBoost) and a Deep Neural Network (DNN) that had no convolutional layers to extract neighboring information, and two advanced deep learning methods, AlexNet and VGG. We optimized and fine-tuned all the models to ensure that the superior performance of *ResNet* was not solely due to model tuning. The RF model consisting of 3000 decision trees (ntree = 3000), an SVM model with a "*rbfdot*" kernel and a penalty coefficient of $C = 5$ and a XGBoost with 1000 base-classifiers and 0.01 learning rate was ultimately selected (Figure 2). Furthermore, to determine whether the convolutional structure was the main reason the *ResNet* model effectively captured forest biomass in mountainous areas, we also established a DNN model without a convolutional structure. Parameters were set to be consistent with the fully connected structure in a CNN. AlexNet and VGG share the same convolutional layer parameters (3×3 kernel size; 64 filter size) and fully connected structure (6 layers with L2 regularization and Dropout) with *ResNet*. However, they lack residual modules, and AlexNet has shallower convolutional layers (3 layers) compared to VGG and *ResNet* (8 layers).

3.3. Validation and Accuracy Assessment

We employed a 10-fold cross-validation method to randomly reserve 20% of the training data as independent validation data to assess the uncertainty of biomass mapping at field measurement scales. Specifically, the cross-validation process was repeated 10 times, with each validation dataset being non-repeated to reduce the particularity of validation results. In addition, we extracted biomass values corresponding to the training sample locations from the forest biomass dataset used for comparison, and evaluated the dataset accuracy by contrasting their differences with the true values at sample points. We also randomly selected 80% of the training samples for model training, with the remaining 20% used for model validation. For accuracy quantification, we utilized the coefficient of determination (R^2) and root mean square error (*RMSE*) (Equations (1) and (2)).

$$R^2 = 1 - \frac{\sum_i (\hat{y}_i - y_i)^2}{\sum_i (\overline{y_i} - y_i)^2} \tag{1}$$

$$RMSE = \sqrt{\frac{1}{m}\sum_{i=1}^{m} (\hat{y}_i - y_i)^2} \tag{2}$$

where m is the number of observations, y_i and $\hat{y}_i$ is the ith observed dependent variable value and the predicted y value for the ith observation from the regression model, respectively; and $\overline{y_i}$ is the mean of all y values.

4. Result and Discussion

4.1. Validation of Mountain Forest Biomass Mapping

To validate the robustness of our proposed deep learning-based algorithm, we randomly reserved 20% of in situ measurements as independent validation samples. Figure 3 illustrates the scatter plot presenting this comparison. Each point on the plot represented a measured biomass value along with the corresponding prediction generated by our *ResNet* model. The validation showed that the proposed model could capture well the variation in mountain forest biomass at the plot scale, revealing a high coefficient of determination (R^2) of 0.80. Furthermore, the root mean square error (*RMSE*) was found to be 15.8 MgC ha^{-1}, indicating a low level of discrepancy between the measured and predicted forest biomass values. Notably, the *RMSE* constituted only 10.1% of the average forest biomass estimated by the *ResNet* model, highlighting the model's robust performance in accurately estimating forest biomass in mountainous regions.

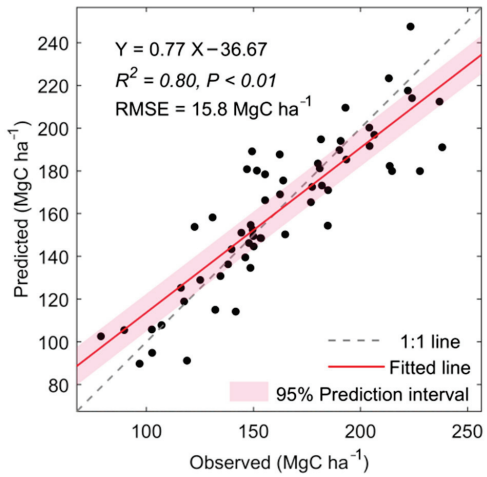

Figure 3. Relationship between the independent in situ measurement and the predicted forest biomass. The solid blue line and the dashed black line represent the regression line and 1:1 line, respectively. Here, independent samples (N = 62) were only used for verification. R^2 represents the coefficient of determination, and RMSE is the root mean squared error.

4.2. Comparative Studies

4.2.1. Comparison in Different Field Sampling Strategies

To reveal the importance of in situ observations across elevational gradients in estimating mountainous forest biomass, we compared results using elevation gradient sampling (N = 67), and with traditional random sampling from the literature review (N = 98). The comparison revealed that elevational gradient sampling strategy, though small in numbers (67 vs. 98), surpassed traditional random sampling strategy in R^2 by 15.1% (Table 2) in terms of estimating mountain forest biomass. We further assessed the impact of elevational interval settings of in situ measurements on the results, considering intervals of 100 m (N = 67), 200 m (N = 32), 300 m (N = 19), and 500 m (N = 12). Here, one measurement was randomly selected at each interval, and the Monte Carlo method [53] was used to augment the sample size, ensuring a consistent sample size after sampling. The results showed that as the elevational interval increased, the accuracy of the results decreased rapidly, with R^2 dropping from 0.63 to 0.51 and *RMSE* increasing from 22.4 to 24.8 MgC ha^{-1}. These results highlighted the crucial role of field observation data spanning different elevational gradients, and emphasizes the need for comprehensive sampling strategies that capture the variability in forest characteristics along elevation gradients to improve the accuracy of biomass estimates in complex mountain ecosystems.

Table 2. Estimations using different field sampling strategies.

	R^2	*RMSE* (MgC ha^{-1})
Elevation gradient sampling (Total, N = 67)	0.63	22.4
Traditional random sampling (N = 98)	0.53	24.6
Elevation gradient sampling (interval = 200 m, N = 32)	0.59	23.9
Elevation gradient sampling (interval = 300 m, N = 19)	0.56	24.7
Elevation gradient sampling (interval = 500 m, N = 12)	0.51	24.8

4.2.2. Comparison of Different Sources of Remote Sensing Data

Multi-source remote sensing data offer a comprehensive view of vegetation structure, with Sentinel-2 and Landsat providing information on leaf characteristics; Sentinel-1 C band backscatter reflecting trunk and branch features, and L-VOD indicating vegetation water content. We first revealed a relationship between each remote sensing data and forest biomass at the field measurement scale. Scatter plots (Figure 4) indicated that the Sentinel-1 VV and VH bands (Figure 4a,b) outperform L-VOD (Figure 4c) and optical data from Sentinel-2 (Figure 4d–g) and Landsat (Figure 4h,i) in predicting field-measured forest biomass. However, Sentinel-1 data still saturated at high forest biomass above 150 MgC ha^{-1}, potentially underestimating high-biomass forests. Here, it should be emphasized that the weaker performance of L-VOD for biomass may be due to the loss of information and blurring caused by its lower resolution data. Furthermore, we conducted a comparative analysis using different sources of remote sensing data. Our analysis revealed that relying solely on single-source remote sensing data yielded limited accuracy in estimating forest biomass (Table 3). For instance, using Sentinel-2 and Landsat data alone to capture leaf characteristics resulted in an incomplete representation of forest structure and subsequently led to suboptimal biomass estimates (R^2 = 0.65, *RMSE* = 23.3 MgC ha^{-1}). It was noted that using optical data alone could significantly bias mountain forest biomass, as the underestimation could reach ~50% when compared with multi-source data results (107.0 ± 11.0 MgC ha^{-1} vs. 162.8 ± 21.9 MgC ha^{-1}). Similarly, employing Sentinel-1 data, which primarily reflects trunk and branch characteristics, provided only a partial

insight into forest biomass dynamics (R^2 = 0.57, *RMSE* = 28.7 MgC ha^{-1}). In contrast, when integrating multi-source remote sensing data, including Sentinel-2, Landsat, Sentinel-1, and L-VOD, our model achieved significantly improved performance in estimating forest biomass (R^2 = 0.80, *RMSE* = 15.8 MgC ha^{-1}). By leveraging the complementary information from each data source, our model was able to capture a more comprehensive range of vegetation structure features, leading to enhanced accuracy in biomass estimation.

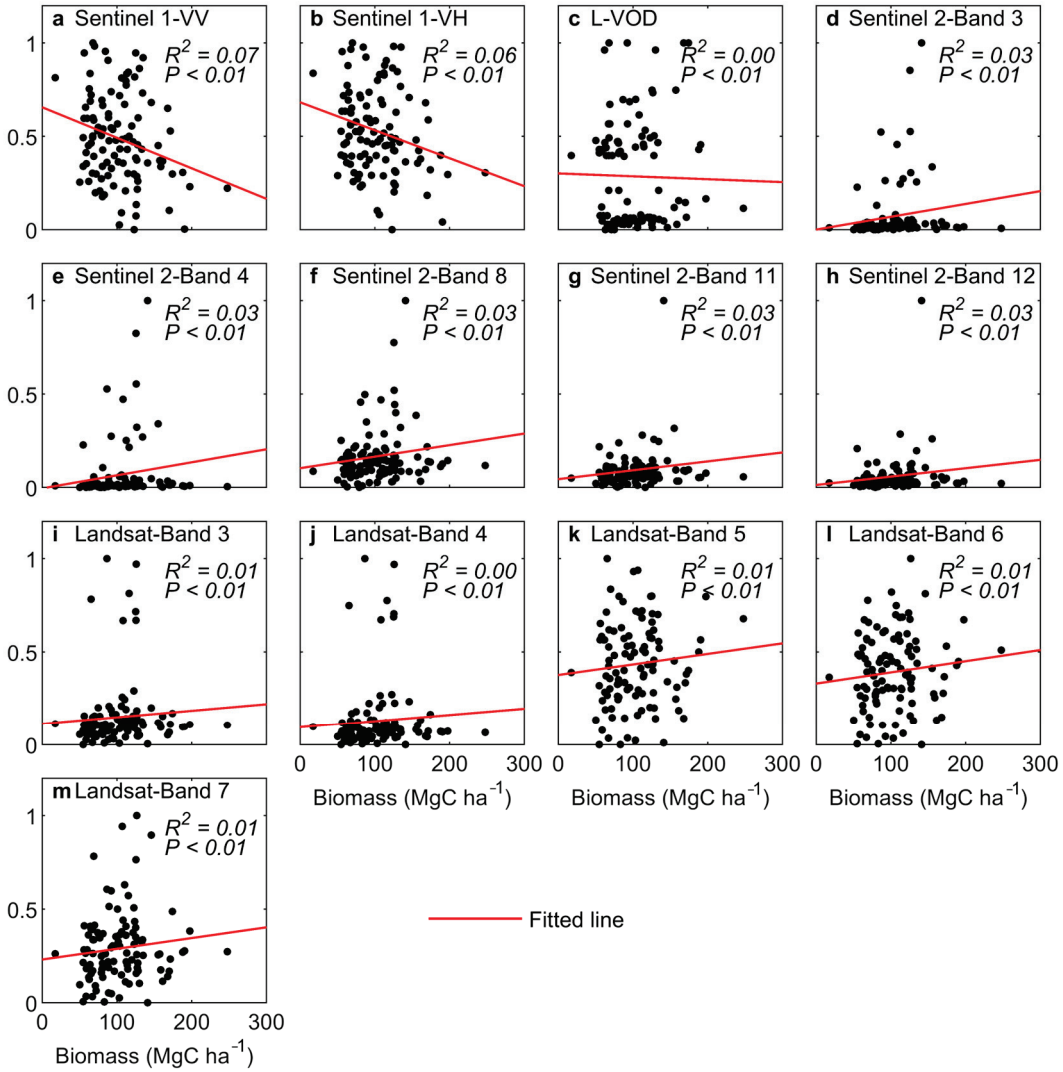

Figure 4. Relationship between the forest biomass and the multi-source remote sensing data at field measurement scale. The subplots reveal data using multi-source remote sensing data, including (**a**) VV, (**b**) VH bands from Sentinel-1, (**c**) Vegetation Optical Depth (VOD), (**d**–**g**) reflectance data from Sentinel-2, and (**h**–**l**) Landsat 8. All remote sensing-based data have been normalized.

Table 3. Comparison in forest biomass accuracy using different sources of remote sensing data.

Features	R^2	*RMSE* (MgC ha^{-1})
Sentinel-2A + Landsat OLI	0.65	23.3
Sentinel-1	0.57	28.7
Sentinel-2A + Landsat OLI + Sentinel-1	0.78	18.1
Sentinel-2A + Landsat OLI + Sentinel-1 + VOD	**0.80**	**15.8**

4.2.3. Comparison with Pixel-Based Method

To reveal the effectiveness of incorporating spatial context into the *ResNet* model for enhancing forest biomass estimation, we conducted a comparative analysis with traditional pixel-based machine learning methods. Here, training and validation samples were kept the same. The *ResNet* model, equipped with convolutional layers capable of capturing spatial features within the forest canopy, outperformed traditional pixel-based methods such as RF (R^2 = 0.59, *RMSE* = 29.3 MgC ha^{-1}) and SVM (R^2 = 0.56, *RMSE* = 30.4 MgC ha^{-1}). This superiority was evident in the evaluation results presented in Table 4, where *ResNet* exhibited higher accuracy levels, particularly during validation at the plot scale. Additionally, XGBoost outperformed other machine learning methods with an R^2 value of approximately 0.66. However, its performance remains weaker than that of the *ResNet* model. This is primarily because XGBoost, despite algorithmic improvements [21,54], operates on individual pixels and lacks a convolutional structure, which prevents it from fully exploring spatial distributions like *ResNet* does. To ascertain the impact of the convolutional structure, that could consider the spatial context in *ResNet*, we constructed a pixel-based DNN model devoid of convolutional layers. This model relied solely on single-pixel information for forest biomass estimation and has other structures same to *ResNet*. Our analysis revealed a marked discrepancy in performance, with the DNN model trailing behind CNN notably (R^2 = 0.68 vs. 0.81, *RMSE* = 24.1 vs. 15.6 MgC ha^{-1}). This disparity highlighted the critical role played by the convolutional structure. Incorporating spatial context allowed a model like *ResNet* to "understand" and process such multi-dimensional data, enabling it to recognize and analyze complex patterns and relationships within the data that are essential for accurate forest biomass estimation, especially in challenging and varied landscapes like mountainous regions.

Table 4. Comparison with the pixel-based method for forest biomass estimation.

Algorithm	R^2	*RMSE* (MgC ha^{-1})
ResNet	**0.80**	**15.8**
DNN	0.68	24.1
XGBoost	0.66	23.3
RF	0.59	29.3
SVM	0.56	30.4

4.2.4. Comparison with Other Advanced Deep Learning Methods

To reveal the effectiveness of including residual learning and deep neural network structures in the *ResNet* model for enhancing forest biomass estimation, we compared results with two other advanced convolution-based deep learning methods: AlexNet and VGG. AlexNet, with its simple three-layered architecture, offered a baseline with shallow depth, while VGG presented a more intricate setup with eight layers, yet without the residual learning integral to *ResNet*. Our comparative analysis indicated that the shallow depth model AlexNet performed poorly, achieving a model accuracy of only 87.5% (Table 5). Although increasing the depth of the model appeared to improve the performance of VGG, it still did not match that of *ResNet*. VGG's accuracy lagged by 7.5%, potentially owing to the absence of residual connections, which are vital for the efficient training of deep networks. Residual connections streamline in *ResNet* introduced "shortcuts" that skip layers, simplifying gradient backpropagation and preventing diminishing gradients. This approach speeded up training while maintaining data integrity, enabling deeper network structures without added complexity. In this way, *ResNet* could reach high accuracy with complex deep networks in forest biomass mapping.

Table 5. Comparison in forest biomass accuracy using different CNN models.

Algorithm	R^2	*RMSE* (MgC ha^{-1})
ResNet	**0.80**	**15.8**
VGG	0.74	18.2
AlexNet	0.70	21.1

4.3. Benchmark Mapping of Mountainous Forest Biomass over Tibet

After obtaining satisfactory validation results at the plot scale, we proceeded to generate a comprehensive wall-to-wall forest biomass map for the year 2020 (Figure 5). Our analysis revealed that regional forest biomass ranges from 95.2 to 275.3 MgC ha^{-1}, with an average of 162.8 ± 21.3 MgC ha^{-1}. This equals a total carbon storage of approximately 2.05 PgC, constituting 40.2% of the entire forest carbon storage 5.10 PgC on the Tibetan Plateau [55]. Notably, the mountainous forests harbor high carbon density, with nearly 90% of the forest biomass exceeding 135 MgC ha^{-1}. This is significantly higher than forests in eastern regions at similar latitudes in China (86.0 ± 10.6 MgC ha^{-1}) [56], as well as flat regions (slopes lower than 10 degrees) in China (61.3 ± 22.4 MgC ha^{-1}). Forest biomass reveals large spatial variation, regions with higher forest biomass are predominantly concentrated in Shannan City, situated in the southeastern part of Tibet, where the average biomass is approximately 1.24 times higher than that of the entire Tibetan region (202.4 ± 24.3 MgC ha^{-1}). Conversely, regions such as Nagqu and Chamdo in northeastern Tibet exhibit relatively lower forest biomass, attributed to the constraints of low temperature and limited water availability. Furthermore, forest biomass exhibits significant variation with the elevation. With increasing elevation, the forest biomass accumulation began to be inhibited.

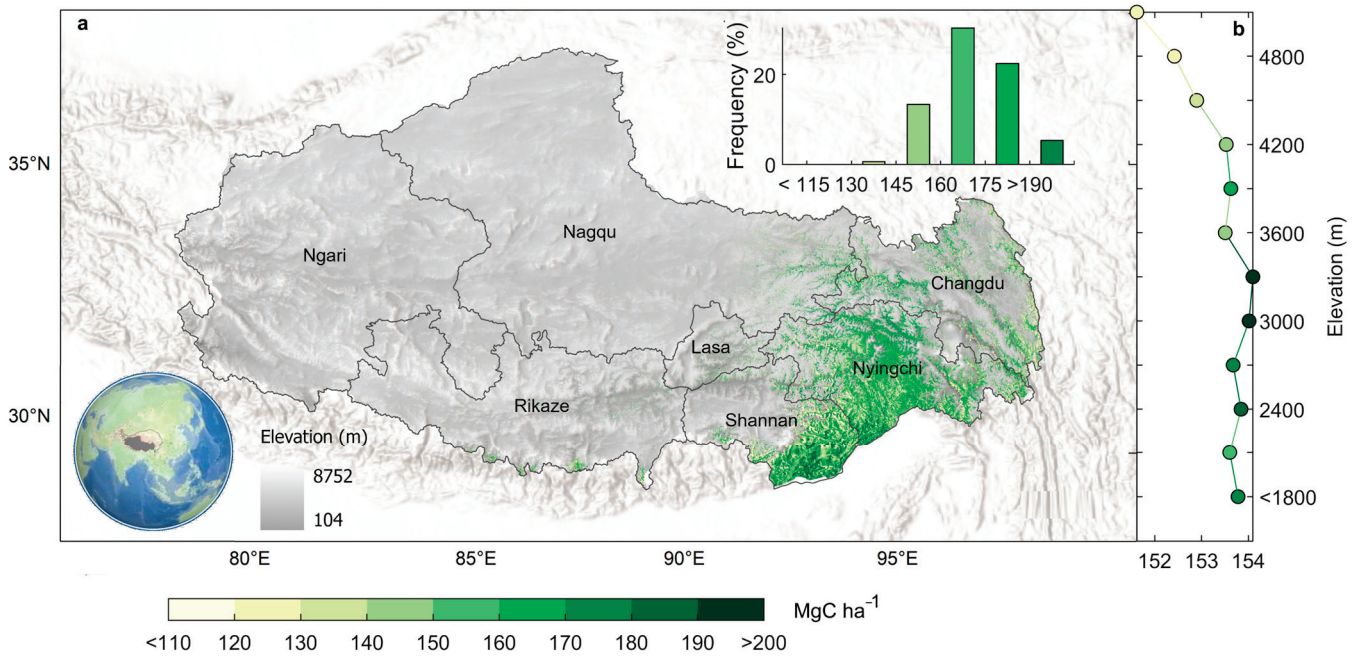

Figure 5. Spatial pattern of mountain forest biomass over Tibet in 2020. (**a**) Distribution of forest biomass estimated by the newly proposed deep learning method, that integrates CNN with Sentinel-1 and Landsat data. The inset displays the frequency of forest biomass. (**b**) Mean elevational value of forest biomass over Tibet.

4.4. Forest Biomass Carbon Sink over Tibet

We then estimate changes in forest biomass during 2015–2020 (Figure 6). The mean forest biomass increased from 162.3 to 168.2 MgC ha^{-1}, resulting in regional carbon storage increasing from 0.85 to 1.07 PgC. This indicates an annual forest biomass carbon sink of

3.35 ± 0.08 TgC year^{-1}. Warming and wetting climate, along with CO_2 fertilization contributed to the forest biomass carbon sink [57,58]. The size of the carbon sink varied significantly across the elevation, with lower elevation forests (below 2500 m) generally experiencing a larger carbon sink. Local forest afforestation and natural forest protection projects likely contributed to this observed increase in carbon sink size [59]. High-elevation forests (above 4000 m) constitute only 32.9% of the total forest area in Tibet, yet their carbon sink capacity accounts for 41.8% (1.40 TgC year^{-1}) of the total carbon sink. Notably, forests near the treeline (elevation > 4500 m) also make a substantial contribution to carbon sequestration, with an annual carbon sink of 0.97 ± 0.03 TgC year^{-1}. The warming climate would facilitate trees upslope expansion [60], which also contributes to the regional carbon sink.

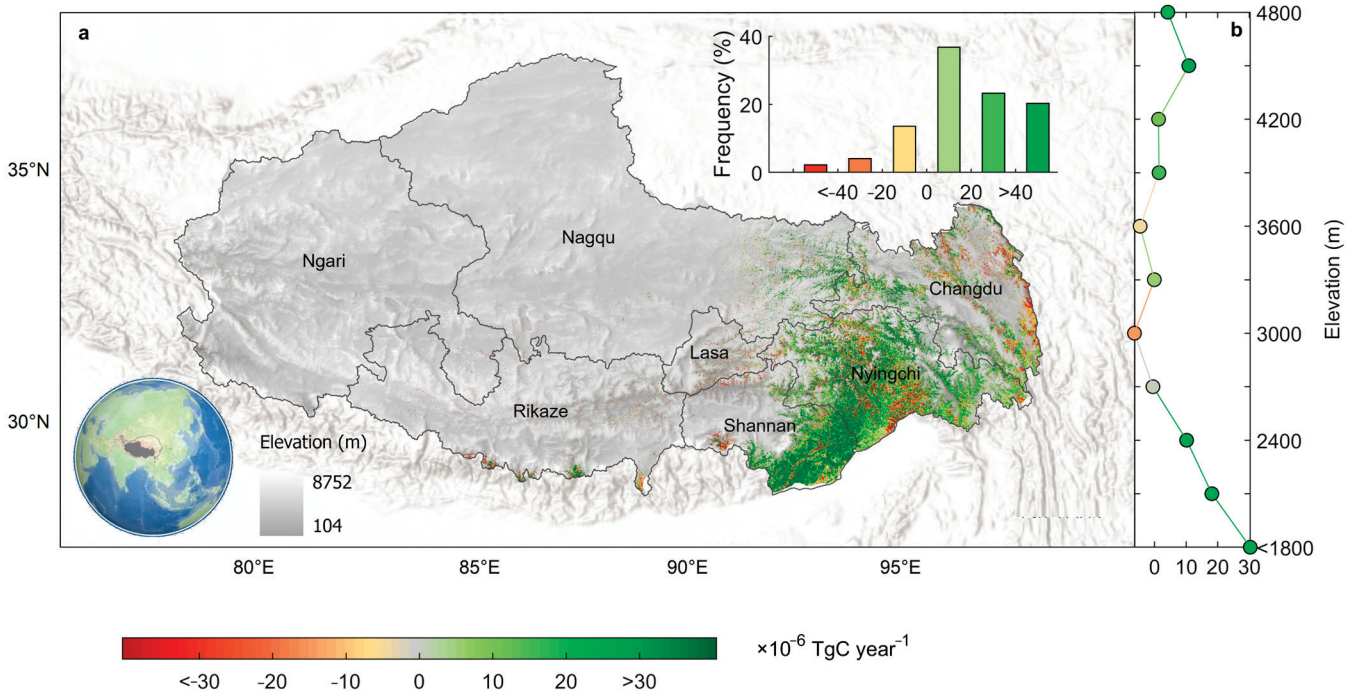

Figure 6. Spatial pattern of the forest biomass carbon sink between 2015 and 2020. (**a**) Distribution of forest biomass carbon sink. The inset displays the frequency of forest biomass carbon sink. (**b**) Mean elevational value of forest biomass carbon sink over Tibet. The red region indicates a decrease in biomass and the green region is an increase.

We further compared our results with existing forest biomass carbon sink estimation (Table 6). Xu et al. [24] estimated global forest aboveground biomass and biomass carbon sink using a random forest method combined with ICESat/GLAS lidar data, MODIS, SRTM digital elevation model, and climate variables. We transformed aboveground biomass into total biomass, considering the root-to-shoot ratio. Liu et al. [8] provide changes in forest biomass based on VOD datasets. However, compared to our results, the previous estimation of mountainous forest biomass carbon sink (0.0068–1.19 TgC year^{-1}) [8,24] is less than half of our results. The underestimation of forest biomass carbon sink is primarily attributed to the underestimation of mountain forest carbon stocks (0.01–0.7 PgC) in Tibet due to the lack of forest structure information and valid in situ measurement data. Specifically, the mean forest biomass over mountainous Tibet reaches only 40.0 and 102.9 MgC ha^{-1}, which is 4 times less than our estimation. The validation results using our independent samples (N = 62) indicate that neither of these datasets effectively estimates the biomass of forests in the Tibetan region (Figure 7). This comparison shows models lacking representative field observation and spatial context can notably undervalue the biomass of mountain forests.

Table 6. Comparison in existing mountain forest biomass carbon sink estimation in Tibet.

	Biomass (MgC ha^{-1})	Carbon Stocks (PgC)	Carbon Sink (TgC year^{-1})	Method	Data
This study	**162.6**	**5.10**	**3.35**	***ResNet***	**Sentinel-2A Landsat OLI Sentinel-1 VOD**
Liu et al. [8]	40.0	0.01	0.0068	The empirical relationship of convert VOD to aboveground biomass carbon	VOD
Xu et al. [24]	102.9	0.7	1.19	Random forest	GLAS MODIS QuikSCAT WorldClim SRTM

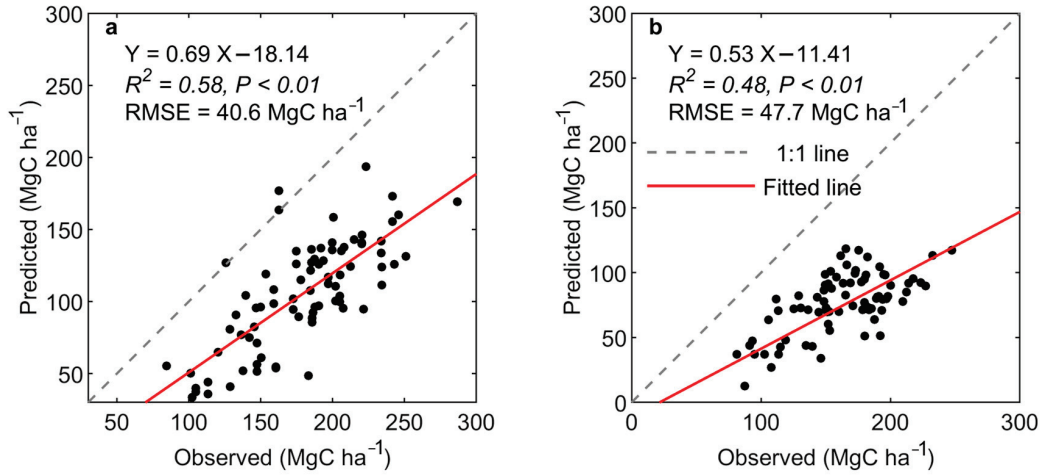

Figure 7. Validation of existing forest biomass maps in mountainous areas of Tibet based on measured samples. (**a**,**b**) are the estimated results of Liu et al. [8] and Xu et al. [24], respectively.

4.5. Limitation and Perspective

Here, we revealed significant elevational distribution of mountain forest biomass carbon stock and sink. However, the temporal mismatch between observation data (2015–2023) and our analysis period (2015–2020) could introduce uncertainties. Field observations were scarce at high elevations, especially near the treeline, and we lack repeated sampling to quantify biomass changes at the field scale. Future studies should include repeated sampling, particularly at high elevations. Furthermore, forest biomass varied greatly across sunny and shaded slopes, but we lack detailed comparative data on terrain aspect-related differences along the elevation gradient. Finer sampling could refine our understanding of microtopography's impact on forest biomass and the carbon cycle in mountainous regions. Regarding remote sensing, we utilized optical, SAR, and VOD data for mapping forest biomass but omitted satellite LiDAR data from sources like ICESat/GLAS, ICESat-2 and GEDI. Integrating canopy height and direct vertical structure data from these sources might enhance our biomass estimates and provide better insights into the carbon cycle of mountain forests.

5. Conclusions

In summary, our study advances the benchmark mapping of forest biomass and biomass carbon sinks in mountainous regions. We introduce a deep learning-based method

that integrates microwave remote sensing (C band data from Sentinel-1, and L-VOD data) with optical images (Sentinel-2A and Landsat 8). The *Resnet* model used in our study could automatically learn information from complex spatial features and distribution characteristics unique to mountainous forests, evidenced by comparison with the pixel-based method, advanced deep learning methods, and single-source remote sensing data. Our research also presents high-resolution (10 m) mapping of biomass and biomass carbon sink dynamics across mountainous forests during 2015–2020, thereby aiding in our understanding of how forests respond to climate change, especially in rugged mountainous regions. The magnitude of the forest carbon sink across high elevations of mountains can serve as a basis for formulating regional strategies to enhance carbon sequestration in response to climate change. However, it should be noted that our estimation still lacks observation data near the upper range limit of trees, especially near the treeline position due to the difficulty of access. The use of UAV-based or satellite-based LiDAR may be promising in those high-elevational forest carbon accounting.

Author Contributions: Conceptualization, X.W.; methodology, X.W. and G.L.; writing—original draft preparation, G.L., X.W. and J.X.; writing—review and editing, X.W., X.H., S.L., G.C. and H.H.; funding acquisition, X.W. and H.H. All authors have read and agreed to the published version of the manuscript.

Funding: This work was supported by the Second Tibetan Plateau Scientific Expedition and Research Program (2019QZKK0606), the National Natural Science Foundation of China (42371118, 41977401), and the Science and Technology Plan Project of Tibet Autonomous Region (XZ202201ZD0005G01).

Data Availability Statement: All computer codes used in this study can be provided by the corresponding author upon reasonable request.

Acknowledgments: We thank the reviewers for their valuable comments and suggestions, and gratefully acknowledge the INRAE BORDEAUX remote sensing products for providing the SMOS-ICV2-RE06 L-VOD product (L-VOD) data.

Conflicts of Interest: The authors declare no conflicts of interest.

References

1. Price, M.F.; Gratzer, G.; Duguma, L.A.; Kohler, T.; Maselli, D.; Romeo, R. *Mountain Forests in a Changing World: Realizing Values, Adressing Challenges*; FAO/SDC: Rome, Italy, 2011; pp. 1–86.
2. Yang, Y.; Shi, Y.; Sun, W.; Chang, J.; Zhu, J.; Chen, L.; Wang, X.; Guo, Y.; Zhang, H.; Fang, J.; et al. Terrestrial carbon sinks in China and around the world and their contribution to carbon neutrality. *Sci. China Life Sci.* **2022**, *65*, 861–895. [CrossRef] [PubMed]
3. Piao, S.; Yue, C.; Ding, J.; Guo, Z. Perspectives on the role of terrestrial ecosystems in the 'carbon neutrality'strategy. *Sci. China Earth Sci.* **2022**, *65*, 1178–1186. [CrossRef]
4. Pan, Y.; Birdsey, R.A.; Fang, J.; Houghton, R.; Kauppi, P.E.; Kurz, W.A.; Phillips, O.L.; Shvidenko, A.; Lewis, S.L.; Canadell, J.G.; et al. A Large and Persistent Carbon Sink in the World's Forests. *Science* **2011**, *333*, 988–993. [CrossRef] [PubMed]
5. Bonan, G.B. Forests and climate change: Forcings, feedbacks, and the climate benefits of forests. *Science* **2008**, *320*, 1444–1449. [CrossRef] [PubMed]
6. Diogo, I.J.S.; dos Santos, K.; da Costa, I.R.; dos Santos, F.A.M. Effects of topography and climate on Neotropical mountain forests structure in the semiarid region. *Appl. Veg. Sci.* **2021**, *24*, e12527. [CrossRef]
7. Greenwood, S.; Chen, J.C.; Chen, C.T.; Jump, A.S. Strong topographic sheltering effects lead to spatially complex treeline advance and increased forest density in a subtropical mountain region. *Glob. Chang. Biol.* **2014**, *20*, 3756–3766. [CrossRef] [PubMed]
8. Liu, Y.Y.; Van Dijk, A.I.J.M.; De Jeu, R.A.M.; Canadell, J.G.; Mccabe, M.F.; Evans, J.P.; Wang, G. Recent reversal in loss of global terrestrial biomass. *Nat. Clim. Chang.* **2015**, *5*, 470–474. [CrossRef]
9. Cutler, M.; Boyd, D.S.; Foody, G.M.; Vetrivel, A. Estimating tropical forest biomass with a combination of SAR image texture and Landsat TM data: An assessment of predictions between regions. *ISPRS J. Photogramm. Remote Sens.* **2012**, *70*, 66–77. [CrossRef]
10. Schepaschenko, D.; Shvidenko, A.; Usoltsev, V.; Lakyda, P.; Luo, Y.; Vasylyshyn, R.; Lakyda, I.; Myklush, Y.; See, L.; McCallum, I.; et al. A dataset of forest biomass structure for Eurasia. *Sci. Data* **2017**, *4*, 170070. [CrossRef]
11. Körner, C.; Donoghue, M.; Fabbro, T.; Häuse, C.; Nogués-Bravo, D.; Arroyo, M.T.K.; Soberon, J.; Speers, L.; Spehn, E.M.; Sun, H.; et al. Creative use of mountain biodiversity databases: The Kazbegi research agenda of GMBA-DIVERSITAS. *Mt. Res. Dev.* **2007**, *27*, 276–281. [CrossRef]
12. Li, A.; Wang, A.; Liang, S.; Zhou, W. Eco-environmental vulnerability evaluation in mountainous region using remote sensing and GIS—A case study in the upper reaches of Minjiang River, China. *Ecol. Model.* **2006**, *192*, 175–187. [CrossRef]

13. Xie, X.; Li, A. An adjusted two-leaf light use efficiency model for improving GPP simulations over mountainous areas. *J. Geophys. Res. Atmos.* **2020**, *125*, e2019JD031702. [CrossRef]
14. Bian, J.; Li, A.; Lei, G.; Zhang, Z.; Nan, X. Global high-resolution mountain green cover index mapping based on Landsat images and Google Earth Engine. *ISPRS J. Photogramm. Remote Sens.* **2020**, *162*, 63–76. [CrossRef]
15. Xie, X.; Li, A. Development of a topographic-corrected temperature and greenness model (TG) for improving GPP estimation over mountainous areas. *Agric. For. Meteorol.* **2020**, *295*, 108193. [CrossRef]
16. Forkuor, G.; Zoungrana, J.B.B.; Dimobe, K.; Ouattara, B.; Vadrevu, K.P.; Tondoh, J.E. Above-ground biomass mapping in West African dryland forest using Sentinel-1 and 2 datasets-A case study. *Remote Sens. Environ.* **2020**, *236*, 111496. [CrossRef]
17. Nandy, S.; Srinet, R.; Padalia, H. Mapping forest height and aboveground biomass by integrating ICESat-2, Sentinel-1 and Sentinel-2 data using Random Forest algorithm in northwest Himalayan foothills of India. *Geophys. Res. Lett.* **2021**, *48*, e2021GL093799. [CrossRef]
18. Reiche, J.; Mullissa, A.; Slagter, B.; Gou, Y.; Tsendbazar, N.-E.; Odongo-Braun, C.; Vollrath, A.; Weisse, M.J.; Stolle, F.; Pickens, A.; et al. Forest disturbance alerts for the Congo Basin using Sentinel-1. *Environ. Res. Lett.* **2021**, *16*, 024005. [CrossRef]
19. Zhao, P.; Lu, D.; Wang, G.; Wu, C.; Huang, Y.; Yu, S. Examining Spectral Reflectance Saturation in Landsat Imagery and Corresponding Solutions to Improve Forest Aboveground Biomass Estimation. *Remote Sens.* **2016**, *8*, 469. [CrossRef]
20. López-Serrano, P.M.; Cárdenas Domínguez, J.L.; Corral-Rivas, J.J.; Jiménez, E.; López-Sánchez, C.A.; Vega-Nieva, D.J. Modeling of aboveground biomass with Landsat 8 OLI and machine learning in temperate forests. *Forests* **2019**, *11*, 11. [CrossRef]
21. Li, Y.; Li, M.; Li, C.; Liu, Z. Forest aboveground biomass estimation using Landsat 8 and Sentinel-1A data with machine learning algorithms. *Sci. Rep.* **2020**, *10*, 9952. [CrossRef]
22. Sinha, S.; Jeganathan, C.; Sharma, L.K.; Nathawat, M.S. A review of radar remote sensing for biomass estimation. *Int. J. Environ. Sci. Technol.* **2015**, *12*, 1779–1792. [CrossRef]
23. Braun, A.; Wagner, J.; Hochschild, V. Above-ground biomass estimates based on active and passive microwave sensor imagery in low-biomass savanna ecosystems. *J. Appl. Remote Sens.* **2018**, *12*, 046027. [CrossRef]
24. Xu, L.; Saatchi, S.S.; Yang, Y.; Yu, Y.; Pongratz, J.; Bloom, A.A.; Bowman, K.; Worden, J.; Liu, J.; Yin, Y.; et al. Changes in global terrestrial live biomass over the 21st century. *Sci. Adv.* **2021**, *7*, eabe9829. [CrossRef] [PubMed]
25. Gleason, C.J.; Im, J. Forest biomass estimation from airborne LiDAR data using machine learning approaches. *Remote Sens. Environ.* **2012**, *125*, 80–91. [CrossRef]
26. Mitchard, E.T.A.; Saatchi, S.S.; Woodhouse, I.H.; Nangendo, G.; Ribeiro, N.S.; Williams, M.; Ryan, C.M.; Lewis, S.L.; Feldpausch, T.R.; Meir, P. Using satellite radar backscatter to predict above-ground woody biomass: A consistent relationship across four different African landscapes. *Geophys. Res. Lett.* **2009**, *36*. [CrossRef]
27. Rostan, F.; Riegger, S.; Pitz, W.; Torre, A.; Torres, R. The C-SAR instrument for the GMES sentinel-1 mission. In Proceedings of the 2007 IEEE International Geoscience and Remote Sensing Symposium, Barcelona, Spain, 23–28 July 2007; pp. 215–218.
28. Sonobe, R. Combining ASNARO-2 XSAR HH and Sentinel-1 C-SAR VH/VV polarization data for improved crop mapping. *Remote Sens.* **2019**, *11*, 1920. [CrossRef]
29. Ghosh, S.M.; Behera, M.D. Aboveground biomass estimation using multi-sensor data synergy and machine learning algorithms in a dense tropical forest. *Appl. Geogr.* **2018**, *96*, 29–40. [CrossRef]
30. Santi, E.; Paloscia, S.; Pettinato, S.; Fontanelli, G.; Mura, M.; Zolli, C.; Maselli, F.; Chiesi, M.; Bottai, L.; Chirici, G. The potential of multifrequency SAR images for estimating forest biomass in Mediterranean areas. *Remote Sens. Environ.* **2017**, *200*, 63–73. [CrossRef]
31. Berninger, A.; Lohberger, S.; Staengel, M.; Siegert, F. SAR-Based Estimation of Above-Ground Biomass and Its Changes in Tropical Forests of Kalimantan Using L- and C-Band. *Remote Sens.* **2018**, *10*, 831. [CrossRef]
32. Tian, F.; Brandt, M.; Liu, Y.Y.; Verger, A.; Tagesson, T.; Diouf, A.A.; Rasmussen, K.; Mbow, C.; Wang, Y.; Fensholt, R. Remote sensing of vegetation dynamics in drylands: Evaluating vegetation optical depth (VOD) using AVHRR NDVI and in-situ green biomass data over West African Sahel. *Remote Sens. Environ.* **2016**, *177*, 265–276. [CrossRef]
33. Wang, M.; Fan, L.; Frappart, F.; Ciais, P.; Sun, R.; Liu, Y.; Li, X.; Liu, X.; Moisy, C.; Wigneron, J.-P. An alternative AMSR2 vegetation optical depth for monitoring vegetation at large scales. *Remote Sens. Environ.* **2021**, *263*, 112556. [CrossRef]
34. Rodríguez-Fernández, N.J.; Mialon, A.; Mermoz, S.; Bouvet, A.; Richaume, P.; Al Bitar, A.; Al-Yaari, A.; Brandt, M.; Kaminski, T.; Le Toan, T.; et al. An evaluation of SMOS L-band vegetation optical depth (L-VOD) data sets: High sensitivity of L-VOD to above-ground biomass in Africa. *Biogeosciences* **2018**, *15*, 4627–4645. [CrossRef]
35. Fan, L.; Wigneron, J.-P.; Ciais, P.; Chave, J.; Brandt, M.; Fensholt, R.; Saatchi, S.S.; Bastos, A.; Al-Yaari, A.; Hufkens, K.; et al. Satellite-observed pantropical carbon dynamics. *Nat. Plants* **2019**, *5*, 944–951. [CrossRef] [PubMed]
36. Wigneron, J.P.; Fan, L.; Ciais, P.; Bastos, A.; Brandt, M.; Chave, J.; Saatchi, S.; Baccini, A.; Fensholt, R. Tropical forests did not recover from the strong 2015–2016 El Niño event. *Sci. Adv.* **2020**, *6*, eaay4603. [CrossRef] [PubMed]
37. Dou, Y.; Tian, F.; Wigneron, J.-P.; Tagesson, T.; Du, J.; Brandt, M.; Liu, Y.; Zou, L.; Kimball, J.S.; Fensholt, R. Reliability of using vegetation optical depth for estimating decadal and interannual carbon dynamics. *Remote Sens. Environ.* **2023**, *285*, 113390. [CrossRef]
38. Konings, A.G.; Saatchi, S.S.; Frankenberg, C.; Keller, M.; Leshyk, V.; Anderegg, W.R.L.; Humphrey, V.; Matheny, A.M.; Trugman, A.; Sack, L.; et al. Detecting forest response to droughts with global observations of vegetation water content. *Glob. Chang. Biol.* **2021**, *27*, 6005–6024. [CrossRef] [PubMed]

39. Holtzman, N.M.; Anderegg, L.D.L.; Kraatz, S.; Mavrovic, A.; Sonnentag, O.; Pappas, C.; Cosh, M.H.; Langlois, A.; Lakhankar, T.; Tesser, D.; et al. L-band vegetation optical depth as an indicator of plant water potential in a temperate deciduous forest stand. *Biogeosciences* **2021**, *18*, 739–753. [CrossRef]
40. Luo, K.; Wei, Y.; Du, J.; Liu, L.; Luo, X.; Shi, Y.; Pei, X.; Lei, N.; Song, C.; Li, J.; et al. Machine learning-based estimates of aboveground biomass of subalpine forests using Landsat 8 OLI and Sentinel-2B images in the Jiuzhaigou National Nature Reserve, Eastern Tibet Plateau. *J. For. Res.* **2022**, *33*, 1329–1340. [CrossRef]
41. Li, T.; Zou, Y.; Liu, Y.; Luo, P.; Xiong, Q.; Lu, H.; Lai, C.; Axmacher, J.C. Mountain forest biomass dynamics and its drivers in southwestern China between 1979 and 2017. *Ecol. Indic.* **2022**, *142*, 109289. [CrossRef]
42. Huang, J.; Wang, X.; Zhao, Y.; Xin, C.; Xiang, H. Large Earthquake Magnitude Prediction In Taiwan Based On Deep Learning Neural Network. *Neural Netw. World* **2018**, *28*, 149–160. [CrossRef]
43. Liang, P.; Wang, X.; Sun, H.; Fan, Y.; Wu, Y.; Lin, X.; Chang, J. Forest type and height are important in shaping the altitudinal change of radial growth response to climate change. *Sci. Rep.* **2019**, *9*, 1336. [CrossRef] [PubMed]
44. Zhong, L.; Hu, L.; Zhou, H. Deep learning based multi-temporal crop classification. *Remote Sens. Environ.* **2019**, *221*, 430–443. [CrossRef]
45. Kattenborn, T.; Leitloff, J.; Schiefer, F.; Hinz, S. Review on Convolutional Neural Networks (CNN) in vegetation remote sensing. *ISPRS J. Photogramm. Remote Sens.* **2021**, *173*, 24–49. [CrossRef]
46. Wang, G.; Ran, F.; Chang, R.; Yang, Y.; Luo, J.; Fan, J. Variations in the live biomass and carbon pools of Abies georgei along an elevation gradient on the Tibetan Plateau, China. *For. Ecol. Manag.* **2014**, *329*, 255–263. [CrossRef]
47. Sun, X.; Wang, G.; Huang, M.; Chang, R.; Ran, F. Forest biomass carbon stocks and variation in Tibet's carbon-dense forests from 2001 to 2050. *Sci. Rep.* **2016**, *6*, 34687. [CrossRef]
48. Zhu, H. The Tropical Forests of Southern China and Conservation of Biodiversity. *Bot. Rev.* **2017**, *83*, 87–105. [CrossRef]
49. Li, W.; Ciais, P.; Guenet, B.; Peng, S.; Chang, J.; Chaplot, V.; Khudyaev, S.; Peregon, A.; Piao, S.; Wang, Y.; et al. Temporal response of soil organic carbon after grassland-related land-use change. *Glob. Chang. Biol.* **2018**, *24*, 4731–4746. [CrossRef]
50. Gorelick, N.; Hancher, M.; Dixon, M.; Ilyushchenko, S.; Thau, D.; Moore, R. Google Earth Engine: Planetary-scale geospatial analysis for everyone. *Remote Sens. Environ.* **2017**, *202*, 18–27. [CrossRef]
51. Simonyan, K.; Zisserman, A. Very deep convolutional networks for large-scale image recognition. *arXiv* **2014**, arXiv:1409.1556.
52. Abadi, M.; Barham, P.; Chen, J.; Chen, Z.; Davis, A.; Dean, J.; Devin, M.; Ghemawat, S.; Irving, G.; Isard, M.; et al. TensorFlow: A system for large-scale machine learning. In Proceedings of the 12th USENIX Symposium on Operating Systems Design and Implementation (OSDI 16), Savannah, GA, USA, 2–4 November 2016; Volume 16, pp. 265–283.
53. Del Moral, P.; Doucet, A.; Jasra, A. On adaptive resampling strategies for sequential Monte Carlo methods. *Bernoulli* **2012**, *18*, 252–278. [CrossRef]
54. Bartold, M.; Kluczek, M. A Machine Learning Approach for Mapping Chlorophyll Fluorescence at Inland Wetlands. *Remote Sens.* **2023**, *15*, 2392. [CrossRef]
55. Wang, T.; Wang, X.; Liu, D.; Lv, G.; Ren, S.; Ding, J.; Chen, B.; Qu, J.; Wang, Y.; Piao, S. The current and future of terrestrial carbon balance over the Tibetan Plateau. *Sci. China Earth Sci.* **2023**, *66*, 1493–1503. [CrossRef]
56. Spawn, S.A.; Sullivan, C.C.; Lark, T.J.; Gibbs, H.K. Harmonized global maps of above and belowground biomass carbon density in the year 2010. *Sci. Data* **2020**, *7*, 112. [CrossRef] [PubMed]
57. Ruehr, S.; Keenan, T.F.; Williams, C.; Zhou, Y.; Lu, X.; Bastos, A.; Canadell, J.G.; Prentice, I.C.; Sitch, S.; Terrer, C. Evidence and attribution of the enhanced land carbon sink. *Nat. Rev. Earth Environ.* **2023**, *4*, 518–534. [CrossRef]
58. Piao, S.; Zhang, Y.; Zhu, Z.; Lian, X.; Huang, K.; He, M.; Zhao, C.; Liu, D. Socioeconomic and Environmental Changes in Global Drylands. In *Dryland Social-Ecological Systems in Changing Environments*; Springer: Singapore, 2014; pp. 161–201.
59. Wang, W.; Feng, C.; Liu, F.; Li, J. Biodiversity conservation in China: A review of recent studies and practices. *Environ. Sci. Ecotechnol.* **2020**, *2*, 100025. [CrossRef]
60. Wang, X.; Wang, T.; Xu, J.; Shen, Z.; Yang, Y.; Chen, A.; Wang, S.; Liang, E.; Piao, S. Enhanced habitat loss of the Himalayan endemic flora driven by warming-forced upslope tree expansion. *Nat. Ecol. Evol.* **2022**, *6*, 890–899. [CrossRef]

Disclaimer/Publisher's Note: The statements, opinions and data contained in all publications are solely those of the individual author(s) and contributor(s) and not of MDPI and/or the editor(s). MDPI and/or the editor(s) disclaim responsibility for any injury to people or property resulting from any ideas, methods, instructions or products referred to in the content.

forests

MDPI

Article

Spatial-Temporal Evolution Characteristics and Driving Force Analysis of NDVI in Hubei Province, China, from 2000 to 2022

Peng Chen [1], Hongzhong Pan [1], Yaohui Xu [1], Wenxiang He [1,*] and Huaming Yao [1,2,3]

[1] College of Resources and Environment, Yangtze University, Wuhan 430100, China; cp.stu@yangtzeu.edu.cn (P.C.); 500440@yangtzeu.edu.cn (H.P.); xuyaohui@yangtzeu.edu.cn (Y.X.); huaming.yao@ce.gatech.edu (H.Y.)
[2] China Yangtze River Power Co., Ltd., Yichang 443000, China
[3] Hubei Key Laboratory of Intelligent Yangtze River and Hydropower Science, Yichang 443000, China
* Correspondence: hwx@yangtzeu.edu.cn; Tel.: +86-071-6806-0524

Abstract: Exploring the characteristics of vegetation dynamics and quantitatively analyzing the potential drivers and the strength of their interactions are of great significance to regional ecological environmental protection and sustainable development. Therefore, based on the 2000–2022 MODIS NDVI dataset, supplemented by climatic, topographic, surface cover, and anthropogenic data for the same period, the Sen+Mann–Kendall trend analysis, coefficient of variation, and Hurst exponent were employed to examine the spatial and temporal characteristics and trends of NDVI in Hubei Province, and a partial correlation analysis and geographical detector were used to explore the strength of the influence of driving factors on the spatial differentiation of NDVI in vegetation and the underlying mechanisms of interaction. The results showed that (1) the mean NDVI value of vegetation in Hubei Province was 0.762 over 23 years, with an overall increasing trend and fluctuating upward at a rate of 0.01/10a ($p < 0.005$); geospatially, there is a pattern of "low east and high west"; the spatial change in NDVI shows a trend of "large-scale improvement in the surrounding hills and mountains and small-scale degradation in the middle plains"; it also presents the spatial fluctuation characteristics of "uniform distribution in general, an obvious difference between urban and rural areas, and a high fluctuation of rivers and reservoirs", (2) the future trend of NDVI in 70.76% of the region in Hubei Province is likely to maintain the same trend as that of the 2000–2022 period, with 70.78% of the future development being benign and dominated by sustained improvement, and (3) a combination of partial correlation analysis and geographical detector analysis of the drivers of vegetation NDVI change shows that land cover type and soil type are the main drivers; the interactions affecting the distribution and change characteristics of NDVI vegetation all showed two-factor enhancement or nonlinear enhancement relationships. This study contributes to a better understanding of the change mechanisms in vegetation NDVI in Hubei Province, providing support for differentiated ecological protection and project implementation.

Keywords: NDVI; land cover type; trend analysis; geographical detector; partial correlation analysis

1. Introduction

Vegetation, as an important indicator of the ecological sustainability of a biosphere, plays an important role in the material cycle, energy flow, and information transfer in terrestrial ecosystems [1]. Changes in vegetation cover reflect not only changes in the ecosystem itself but also the impact of natural factors and human activities on the ecological environment [2,3]. Therefore, monitoring vegetation dynamics has also become one of the topical issues of continuing interest in regional change research. Normalized Difference Vegetation Index (NDVI) has the advantages of clear physical meaning, elimination of radiometric errors, and strong responsiveness to vegetation. It has been widely used as an indicator to characterize the vegetation cover of the ground surface in the fields of

vegetation pattern change, vegetation productivity estimation, and ecological effectiveness assessment [4,5].

A large number of scholars have conducted numerous studies on the spatial and temporal changes in vegetation and their drivers in different study areas using different scales of NDVI. The characterization of spatial and temporal changes in vegetation uses a one-way linear regression analysis [6], Sen+Mann–Kendall trend analysis [7], coefficient of variation [8], and Hurst exponent [9]. Based on datasets, such as climate, topography, and human activities, partial correlation analysis [10], principal component regression [11], geographical detector [12], multiple regression residual analysis [13], and redundancy analysis variance decomposition [14] were used, exploring the driving mechanisms of vegetation change. NDVI is affected by human activities, and the urban heat island (UHI) is strongly negatively correlated with NDVI and strongly positively correlated with NDBI [15]. NDVI is utilized to study the response of vegetation and plants to environmental changes, and vegetation is affected by both natural factors and human activities, where the natural factors of climate and topography are closely related to the growth and distribution of vegetation [16]. In recent decades, the magnitude of NDVI changes in China has been decreasing from high to low latitudes [17], and temperature, precipitation, and solar radiation are the main climatic factors affecting NDVI changes [18].

Hubei Province is situated in the transitional zone from the second to the third topographical tier in China and is located in the middle reaches of the Yangtze River, which includes diverse vegetation types, such as forests, grasslands, and wetlands. The implementation of ecological projects, such as returning farmland to forests and soil and water conservation in Hubei Province, has effectively improved the ecological condition of the land, making Hubei Province a provincial area with significant vegetation recovery. At present, the research on the vegetation of Hubei Province has made some progress. Based on the analysis of summer MODIS vegetation NDVI trends in Hubei Province from 2005 to 2015, it was found that human socio-economic activities were important driving factors influencing the landscape pattern and vegetation changes in the study area, and the urbanization expansion in the study area was the main reason for the vegetation changes in Hubei Province [19]. In terms of natural influences, the correlation between the NDVI of the vegetation in Hubei Province and precipitation, elevation, and land-use type was more significant, and there was a hysteresis in the response of the vegetation growth to the precipitation [20].

Previous studies have considered elements such as climatic factors (precipitation [21] and temperature [22]) and elevation [23], or climatic factors and nighttime lighting [24], ignoring the systematic effects of soil type [25], land cover type [26,27], slope [28], aspect [29], and population density [30] on vegetation growth. It also focuses on qualitative discussions and fails to quantitatively separate the impacts of climate change, topographic conditions, land cover, and human activities on vegetation change; there have not been enough studies conducted on the sustainability and future trend of vegetation development in Hubei Province.

In view of this, this paper is based on annual maximized MODIS NDVI data for the years 2000–2022, combined with natural and anthropogenic factor datasets. Sen+Mann–Kendall trend analysis, coefficient of variation, and Hurst exponent analysis were used to investigate the spatial and temporal characteristics and trends of vegetation NDVI, and partial correlation analysis and geographical detector were used to quantitatively analyze the effects of natural and anthropogenic factors on the spatial variation in vegetation NDVI and quantitatively assess the relative roles of climate change and human activities in vegetation improvement and degradation under different scenarios in order to provide a scientific basis for the dynamic monitoring, management, and protection of vegetation in Hubei Province, which has an important application value for the development of reasonable ecological protection programs.

2. Materials and Methods

2.1. Study Area

Hubei Province (29°05′–30°20′ N, 108°30′–116°20′ E, Figure 1) is located in the center of China and the core of the Yangtze River Economic Belt. The region is vast, with a land area of 185,000 km^2, with mountains, hills and plains, and lakes accounting for 56%, 24%, and 20% of the total area, respectively [31]. The topography of Hubei Province varies greatly in height, with the terrain showing an incomplete basin area that is elevated on three sides, flat in the center, open to the south, and with a gap in the north [32]. Located in the north–south climate transition zone and belonging to the subtropical monsoon humid climate, there is rain and heat at the same time, it is cold in the winter and hot in the summer, and precipitation is mainly concentrated from June to July, with the average annual precipitation of 800 to 1600 mm and the average annual temperature of 15 to 22 °C [33]. The vertical distribution of natural vegetation is distinctive, rich in biological resources, characterized by the transition between the north and the south, with broad-leaved forests as the main type of vegetation, and at the same time, includes diversified vegetation types, such as coniferous forests, mixed forests, wetland forests, etc. It is in the transition zone between the east and the west of China's flora and is one of the provinces in China that are richer in botanical resources. It has 32 national-level ecological civilization demonstration zones in China, four forest ecological stations, one bamboo forest ecological station and one wetland ecological station [34].

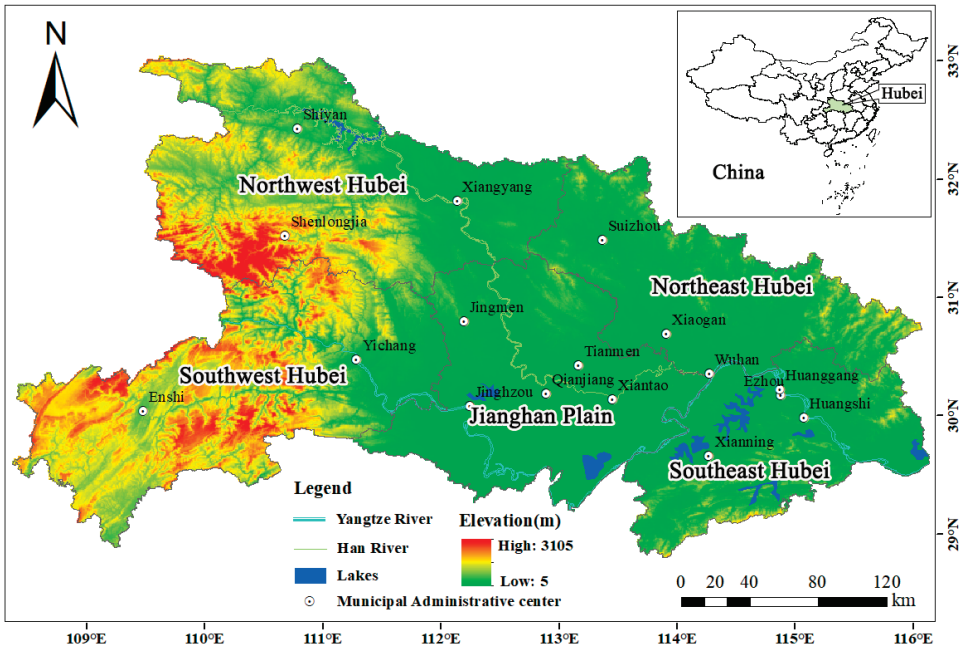

Figure 1. Overview of the study area.

2.2. Data Sources

The data used in this study mainly include remote sensing data, climatic data, topographic data, surface cover data, and anthropogenic data (Table 1). The spatial rasterization of the data for each year was achieved using ArcGIS 10.8.2, with a resolution of 1 km after projection transformation, study area boundary masking, and resampling, and the projected coordinate system was the UTM projection. In modeling the geographical detector, NDVI was used as the Y variable and the 10 factors data as the X variable for detection. The NDVIs in this paper, unless otherwise noted, are annual NDVIs synthesized using the maximum value composites (MVCs) method.

Table 1. Data source and data preprocessing.

Data Type	Code	Data Content	Year	Resolution	Data Source	Product
Remote sensing data	Y	MODIS NDVI	2000–2022	1 km	NASA website (https://ladsweb.modaps.eosdis.nasa.gov/search/ accessed on 25 February 2024)	MOD13Q
Climate data	X_1	Total annual precipitation	2000–2022	1 km	National Tibetan Plateau Science Data Center (https://data.tpdc.ac.cn accessed on 25 February 2024)	Peng, S. [35]
	X_2	Annual mean temperature	2000–2022	1 km	National Tibetan Plateau Science Data Center (https://data.tpdc.ac.cn accessed on 25 February 2024)	Peng, S. [36]
	X_3	Solar radiation	2000–2022	1 km	National Tibetan Plateau Science Data Center (https://data.tpdc.ac.cn accessed on 25 February 2024)	Wang, K. [37]
Topographic data	X_4	elevation	2022	1 km	NASA website (https://ladsweb.modaps.eosdis.nasa.gov/search/ accessed on 25 February 2024)	SRTM 30 m DEM
	X_5	Slope	2022	1 km	Derived from elevation data	/
	X_6	Aspect	2022	1 km	Derived from elevation data	/
Land cover data	X_7	Soil type	2022	1 km	Usda website (https://www.usda.gov/ accessed on 25 February 2024)	OpenLandMap
	X_8	Land cover type	2000–2022	1 km	Zenodo (https://www.zenodo.org/ accessed on 25 February 2024)	Jie Yang, & Xin Huang [38]
Anthropogenic data	X_9	Population density	2000–2020	1 km	The Word Pop (https://hub.worldpop.org/ accessed on 25 February 2024)	WorldPop Global Project Population Data
			2021–2022	1 km	Hubei statistical yearbook (https://tjj.hubei.gov.cn/tjsj/ accessed on 25 February 2024)	Provincial statistical yearbook
	X_{10}	nighttime light	2000–2022	1 km	National Earth System Science Data Center (http://www.geodata.cn/ accessed on 25 February 2024)	Chen Zuoqi et al. [39]

2.3. Research Methods

2.3.1. Sen+Mann–Kendall Significance Tests

The Theil–Sen Median method, also known as the Sen slope estimation, is a nonparametric statistical method for trend calculation, which has become an important method for judging the characteristics of changes in long time series of vegetation, hydrology, climate, etc. data, because of its high computational efficiency and insensitivity to outliers, which is more robust than Slope analysis [40]. The formula is as follows:

$$\beta = \text{Median}\left[\frac{x_j - x_i}{j - i}\right] \quad \forall\, j > i \tag{1}$$

where x_i and x_j are the data for the year i or j in the NDVI time series; median indicates the median value. β is the median value of the slopes of all pairs of data, and when $\beta > 0$, it reflects an increasing trend of NDVI in this time series; on the contrary, it is a decreasing trend. The significance of the trend was tested by the Mann–Kendall method. The formula is

$$Z = \begin{cases} \frac{S-1}{\sqrt{\text{VAR}(S)}} & S > 0 \\ 0 & S = 0 \\ \frac{S-1}{\sqrt{\text{VAR}(S)}} & S < 0 \end{cases} \tag{2}$$

with:

$$S = \sum_{i=1}^{n-1} \sum_{j=i+1}^{n} sgn(x_j - x_i) \tag{3}$$

$$\mathrm{VAR}(S) = \frac{n(n-1)(2n+5)}{18} \tag{4}$$

$$sgn(x_i - x_j) = \begin{cases} +1 & x_j - x_i > 0 \\ 0 & x_j - x_i > 0 \\ -1 & x_j - x_i > 0 \end{cases} \tag{5}$$

where Z is the standardized test statistic; S is the test statistic; VAR(S) is the variance; sgn is the sign function; x_j and x_i are the sample time series data; and n is the number of data in the time series. The hypothesis is tested using a bilateral trend test, where the original hypothesis is rejected and the trend is considered significant when $|Z| > Z_{1-\alpha/2}$ at a given significance level α. $Z_{1-\alpha/2}$ is the value corresponding to the distribution table of the standard normal distribution function at the confidence level α. At $|Z| \geq 2.58$, $|Z| \geq 1.96$ indicates that the trend passes the significance test with 99% and 95% confidence levels, which are highly significant and significant, respectively, and $|Z| < 1.96$ indicates that the trend is not significant.

Combining the β and $|Z|$, the trend of change was categorized into six classes [41], including extremely significant degradation/improvement, significant degradation/improvement, and non-significant degradation/improvement (Table 2).

Table 2. Grading of Change Trends.

β	$\|Z\|$	NDVI Trend Characteristics
$\beta > 0$	2.58≤	Extremely significant improvement
	1.96≤	Significant improvement
	<1.96	non-significant improvement
$0 < \beta$	<1.96	non-significant degradation
	1.96≤	Significant degradation
	2.58≤	Extremely significant degradation

2.3.2. Stability Analysis

The coefficient of variation, also known as the standard deviation rate or unit risk, is used to reflect the degree of dispersion of the data and can be calculated as the relative degree of fluctuation in the spatial and temporal distributions of geographic elements. The larger the value obtained from the calculation indicates that the data series are more dispersed. Refer to reference [42] for the specific calculation method. Combined with the results of previous research [43], the coefficient of variation was categorized into five classes from low to high: low volatility change ($Cv \leq 0.05$), relatively low volatility change ($0.05 < Cv \leq 0.10$), medium volatility change ($0.10 < Cv \leq 0.15$), relatively high volatility change ($0.15 < Cv \leq 0.20$), and high volatility change ($Cv > 0.20$).

2.3.3. Future Variation Trend

The Hurst exponent is a research method based on the calculation of R/S re-scaled extreme variance analysis, proposed by the British scholar Hurst [44], which can effectively and quantitatively describe the sustainability of the time series and forecast its future evolution trend. The process of its calculation methodology is as follows.

For the time series $NDVI_t$, $t = 1, 2, 3 \ldots n$, defines its mean series:

$$\overline{NDVI_\tau} = \frac{1}{\tau} \sum_{t=1}^{\tau} NDVI_\tau,\ \tau = 1,\ 2,\ 3 \ldots n \tag{6}$$

Cumulative deviation calculation:

$$X_{(t,\,\tau)} = \sum_{t=1}^{\tau} \left(NDVI_\tau - \overline{NDVI_\tau}\right),\ 1 \le t \le \tau \tag{7}$$

Polar deviation calculation:

$$R_\tau = \max_{1 \le t \le \tau}(t,\ \tau) - \min_{1 \le t \le \tau}(t,\ \tau),\ \tau = 1,\ 2,\ 3 \ldots n \tag{8}$$

Standard deviation calculation:

$$S_\tau = \left\{ \frac{1}{\tau} \sum_{t=1}^{\tau} (NDVI_t - NDVI_\tau)^2 \right\}^{1/2},\ \tau = 1,\ 2,\ 3 \ldots n \tag{9}$$

Hurst exponent calculation:

$$\frac{R_\tau}{S_\tau} = c\tau^H \tag{10}$$

A straight line was fitted to obtain the Hurst exponent:

$$\ln\left(R/S\right)_n = a + H \ln n \tag{11}$$

where c is the relationship constant, H is the Hurst exponent, and a is the intercept. The Hurst exponent ranges from 0 to 1. When $0 \le H < 0.4$, it indicates that the future has strong inverse sustainability with the past. The closer H is to 0, the stronger the inverse is; when $0.4 \le H < 0.5$, it indicates that the future has weak inverse sustainability with the past; when $H = 0.5$, it indicates that the time series change is random; when $0.5 < H \le 0.6$, it indicates that the future change trend is the same as the past, weak forward sustainability; and when $0.6 < H \le 1$, it indicates that the future trend of change is the same as the past, with strong forward sustainability, and the closer the value of H is to 1, the stronger the sustainability is [45]. Coupling and superimposing the NDVI trend results with the Hurst exponent results can be used to analyze the future trend of vegetation.

2.3.4. Partial Correlation Analysis

There are many factors influencing vegetation cover, and changes in any one of these influences may affect changes in another [5,46]. With the help of first and second-order partial correlation analyses, the correlation between a single variable and vegetation NDVI was characterized by controlling for the effects of other variables. Its second-order partial correlation analytical expression is (first-order identically):

$$R_{xy \cdot z\lambda} = \frac{r_{xy \cdot z} - r_{x\lambda,\,z} \times r_{y\lambda \cdot z}}{\sqrt{\left(1 - r_{x\lambda \cdot z}^2\right)\left(1 - r_{y\lambda \cdot z}^2\right)}} \tag{12}$$

where $R_{xy \cdot z}$ is the second-order partial correlation coefficient of x and y after the control variables z and λ; $R_{xy \cdot z\lambda} > 0$ is positively correlated; and $R_{xy \cdot z\lambda} < 0$ is negatively correlated. Second-order partial correlation analysis was used to study the degree of partial correlation of NDVI and mean annual temperature, total annual precipitation, and solar radiation, and first-order partial correlation analysis was used to study the NDVI and population density in this study. The second-order partial correlation analysis was used to study the degree of partial correlation between NDVI and population density, nighttime lighting. In addition, a t-test was used to test the significance of the partial correlation coefficients.

2.3.5. Geographical Detector Model

The geographical detector is an open-source statistical model for spatial data analysis (http://www.geodetector.cn/ accessed on 25 February 2024) that determines the similarity

of spatial distributions of two variables through the lens of spatial hierarchical heterogeneity [47]. In this study, we selected the driving factors in Table 1 and analyzed the potential drivers of vegetation cover changes in Hubei Province using two modules of the geographical detector (factor detector and interaction detector). In addition, the continuous variables in the independent variables were discretized, and the continuous data were reclassified using the natural breakpoint method, which classified the land cover types into 9 categories, the soil types into 6 categories, and the rest of the continuous variables into 9 categories uniformly.

Factor Detector

The factor detector was used to test the extent to which each influencing factor explained the spatial heterogeneity of NDVI. A q-value metric was used. The calculation formula is as follows:

$$q = 1 - \frac{SSW}{SST} \tag{13}$$

$$SSW = \sum_{h=1}^{L} N_h \rho_h^2 \tag{14}$$

$$SST = N\rho^2 \tag{15}$$

where q is the explanatory power of the metric factor on NDVI, with a value range of [0, 1], and larger values indicate stronger explanatory power of the factors and stronger influence on the spatial distribution of vegetation NDVI. The symbol h = 1, 2,... L is the classification or zoning of the dependent or independent variable, N_h and N are the number of cells in stratum h and the whole region, respectively; ρ_h^2 and ρ^2 are the variance of NDVI in stratum h and the whole region, respectively; SSW and SST are the sum of the variance within the stratum and the total variance of the region, respectively [48].

Interaction Detector

This detector is used to identify the interaction between different factors, whether the drivers x_1 and x_2, acting together, increase or decrease the explanatory power of vegetation NDVI or whether these drivers are independent of each other in their explanatory power of vegetation NDVI. The specific determination method is shown in Table 3.

Table 3. Type of independent variable interaction.

Interaction Types	Interaction Criteria
Bivariate-enhancement	$q(x_1 \cap x_2) > \text{Max}\,[\,q(x_1)\,,\,q(x_2)]$
Nonlinear-enhancement	$q(x_1 \cap x_2) > q(x_1) + q(x_2)$
Univariate-weakening	$\text{Min}\,[\,q(x_1)\,,\,q(x_2)] < q(x_1 \cap x_2) < \text{Max}\,[\,q(x_1)\,,\,q(x_2)]$
Nonlinear-weakening	$q(x_1 \cap x_2) < \text{Min}\,[\,q(x_1)\,,\,q(x_2)]$
Independent	$q(x_1 \cap x_2) = q(x_1) + q(x_2)$

3. Results

3.1. Spatiotemporal Variation Characteristics of the NDVI

3.1.1. Interannual Variation Characteristics of the NDVI

The annual NDVI (MVC) and NDVI (average) were calculated separately from 2000 to 2022 to characterize the vegetation changes in Hubei Province in the last 23 years. As can be seen in Figure 2, the annual NDVI (MVC) is 0.74 to 0.79, the annual NDVI (average) is 0.48 to 0.57, and the minimum and maximum values of the annual NDVI (MVC) and NDVI (average) occur in 2001 and 2021. The overall change in NDVI showed a fluctuating upward trend, and the annual NDVI (MVC) growth rate was 0.01/10a ($p < 0.005$), which was lower than the annual NDVI (average) growth rate of 0.28/10a ($p < 0.001$). In terms of inter-annual trends, the trends of annual NDVI (MVC) and annual NDVI (average) converge roughly.

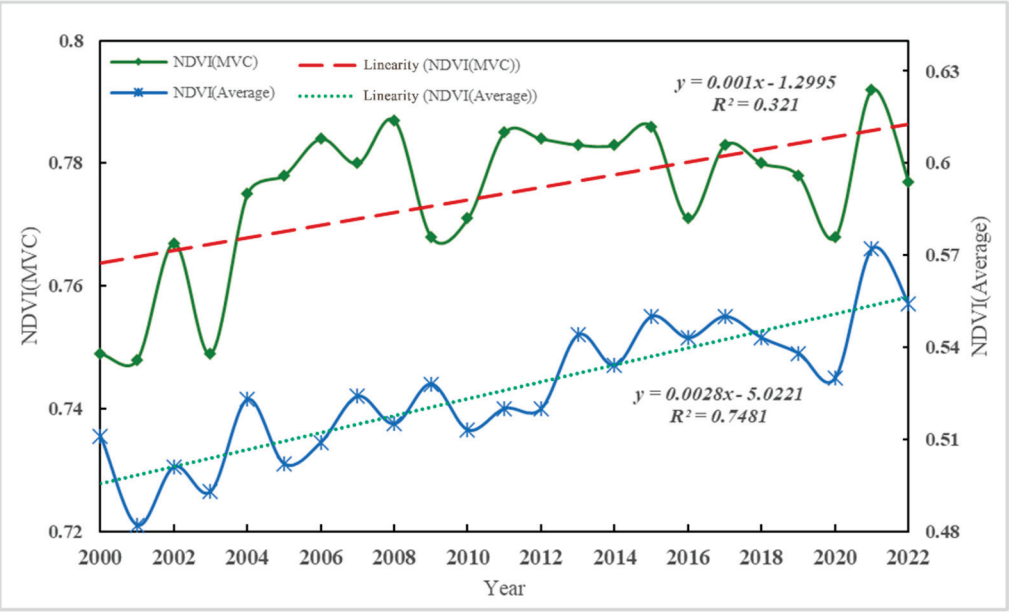

Figure 2. Interannual changes of NDVI in Hubei Province from 2000 to 2022.

3.1.2. Spatial Variation Characteristics of the NDVI

The multi-year mean NDVI values in Hubei Province from 2000 to 2022 ranged from 0.025 to 0.898, with a mean value of 0.762. Combined with the actual situation in Hubei Province, this study used the equal-interval method to classify the spatial distribution of NDVI into five types: low vegetation cover ($0 < NDVI \leq 0.2$), medium-low vegetation cover ($0.2 < NDVI \leq 0.4$), medium vegetation cover ($0.4 < NDVI \leq 0.6$), medium-high vegetation cover ($0.6 < NDVI \leq 0.8$), high vegetation cover ($0.8 < NDVI \leq 1.0$). The spatial distribution of NDVI in Hubei Province shows a pattern of "low in the east and high in the west" (Figure 3). Among them, the proportion of medium-high and high vegetation-covered areas reached 94.4%, indicating that the overall vegetation-cover condition in Hubei Province is at a high level. The proportion of areas with less than medium vegetation cover is only 5.6 percent, concentrated in and around cities with a high level of urbanization and development, and consisting mainly of various types of urban built-up areas, reservoirs, lakes, and rivers.

Combined with the Sen+Mann–Kendall trend analysis to obtain the spatial distribution of vegetation NDVI trends and the percentage of area occupied by trend classes (Figure 4), it is found that in the past 23 years, the NDVI of the vegetation in Hubei Province has shown a trend of continuous improvement, in general, and the NDVI of the vegetation in Hubei Province has shown a trend of continuous improvement in the past 23 years. Vegetation NDVI showed an improving trend in 85.91% of the total area of Hubei, and the significant improvement trend ($p < 0.05$) accounted for 63.89% of the study area, which was mainly concentrated in northwestern Hubei, southwestern Hubei, and part of northeastern Hubei and southeastern Hubei. Vegetation NDVI showed a decreasing trend that was mainly distributed in the more densely populated Jianghan Plain area, with a significant degradation trend of 4.71% of the area ($p < 0.05$). Generally speaking, the proportion of areas with improving vegetation cover in Hubei Province is much higher than that of degrading trend, and the state of vegetation cover is improving, which is characterized by the spatial change in "large improvement in the surrounding hills and mountains, and small degradation in the middle plains".

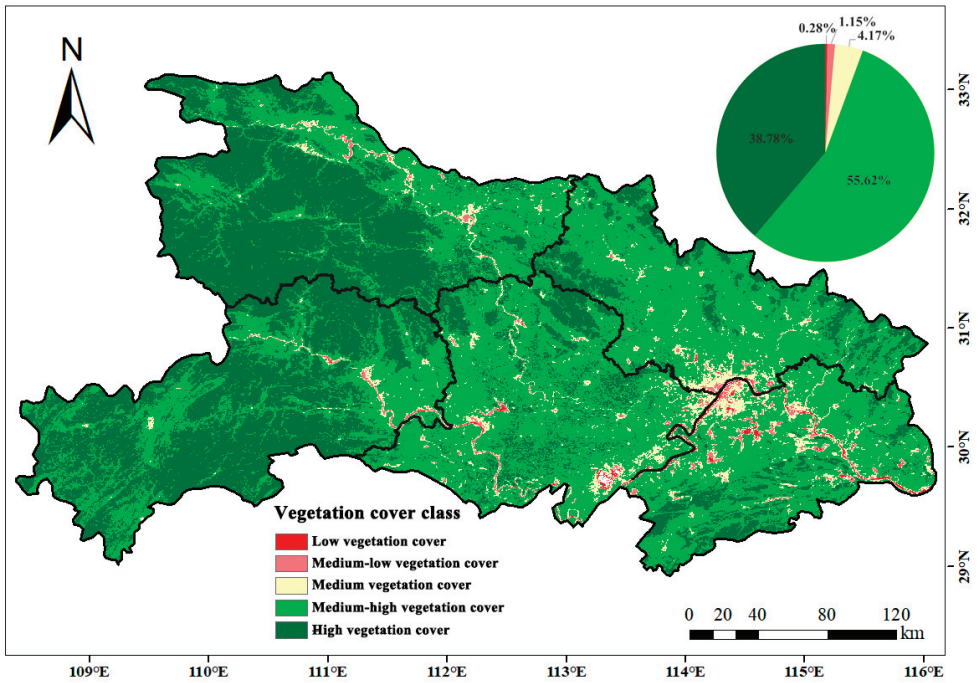

Figure 3. Spatial distribution of NDVI in Hubei Province from 2000 to 2022.

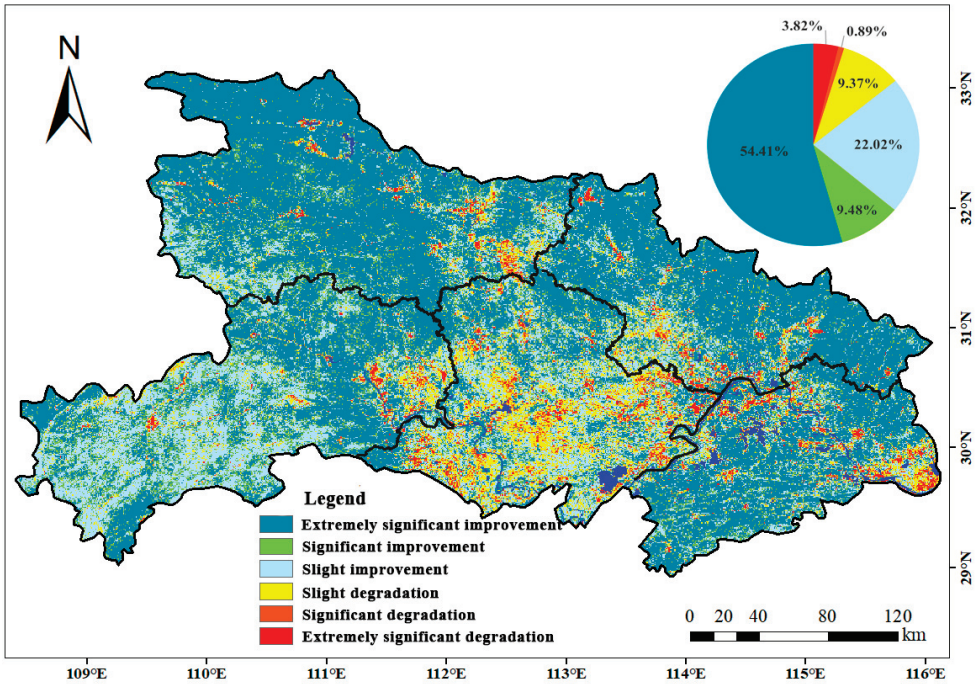

Figure 4. The spatiotemporal variation trend in NDVI in Hubei Province from 2000 to 2022.

3.1.3. Stability Analysis of the NDVI

The coefficient of variation (*Cv*) can be used to characterize the degree of dispersion and volatility of NDVI within a time series, and it was calculated that the *Cv* in Hubei Province ranged from 0 to 1.39 from 2000 to 2022. During the study period, the stability of spatial changes in NDVI in the study area (Figure 5) was characterized by "uniform distribution, in general, obvious differences between urban and rural areas, and fluctuations in river and reservoir heights". Among them, the areas with low and lower fluctuation changes are 17.26% and 69.70%, respectively, the area with medium fluctuation changes

is 8.58%, and the area with high and higher fluctuation changes is only 4.46%, which is consistent with the range of the area covered by less than medium vegetation.

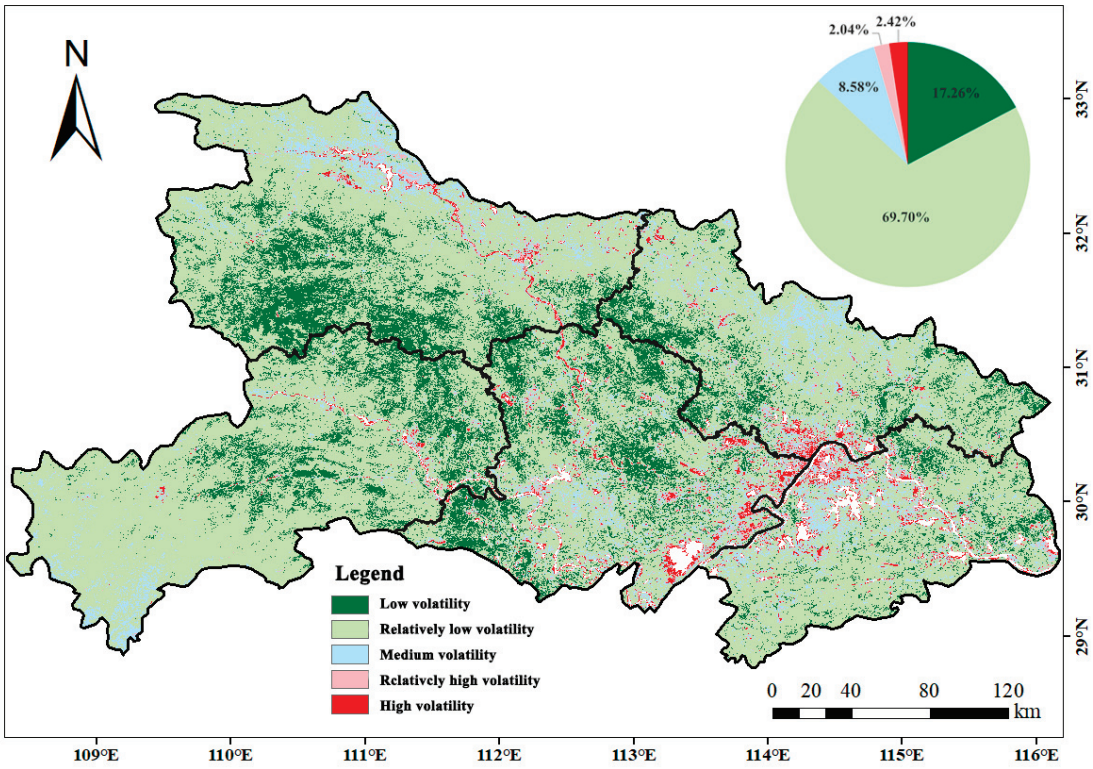

Figure 5. Spatial fluctuation characteristics of NDVI in Hubei Province from 2000 to 2022.

3.1.4. Stability Analysis of the NDVI

Spatial characterization of vegetation changes in Hubei Province over the past 23 years has been carried out, but its future development trend is unclear. Combined with the Hurst exponent to predict the future trend of NDVI change in Hubei Province, as shown in Figure 6, the overall tendency of vegetation changes towards sustainability accounted for 70.76%, indicating that the trend of NDVI change in most of the regions in the future is likely to be maintained in line with the trend of change in the period from 2000 to 2022. Among them, the strong forward sustainability trend accounted for 33.83%, which was mainly distributed to the west of Hubei. On the contrary, the overall tendency of vegetation changes to anti-sustainability accounted for 29.24%.

In order to further explore the characteristics of the future vegetation development trend of NDVI in Hubei Province, the spatial distribution of the Hurst exponent and the trend of NDVI were superimposed and analyzed to obtain the future trend of NDVI (Figure 7). Among them, the proportion of areas with sustainability improvement amounted to 64.05%, the proportion of areas with anti-sustainability degradation from degradation to improvement accounted for 6.73%, and the proportion of benign development in the future totaled 70.78%, indicating that the future trend of NDVI change in Hubei Province will be dominated by improvement. Sustained degradation areas account for 5.82%, anti-sustained improvement areas from improvement to degradation accounted for 21.91%, and future malignant development accounted for a total of 27.73%, which were mainly distributed in the Jianghan Plain, Wuhan Urban Agglomeration, Xiangyang-Shiyan-Suizhou Urban Agglomerations, etc. For potentially degraded areas, it is necessary to strengthen ecological environmental protection and management according to the local conditions in order to minimize the risk of vegetation degradation in the future.

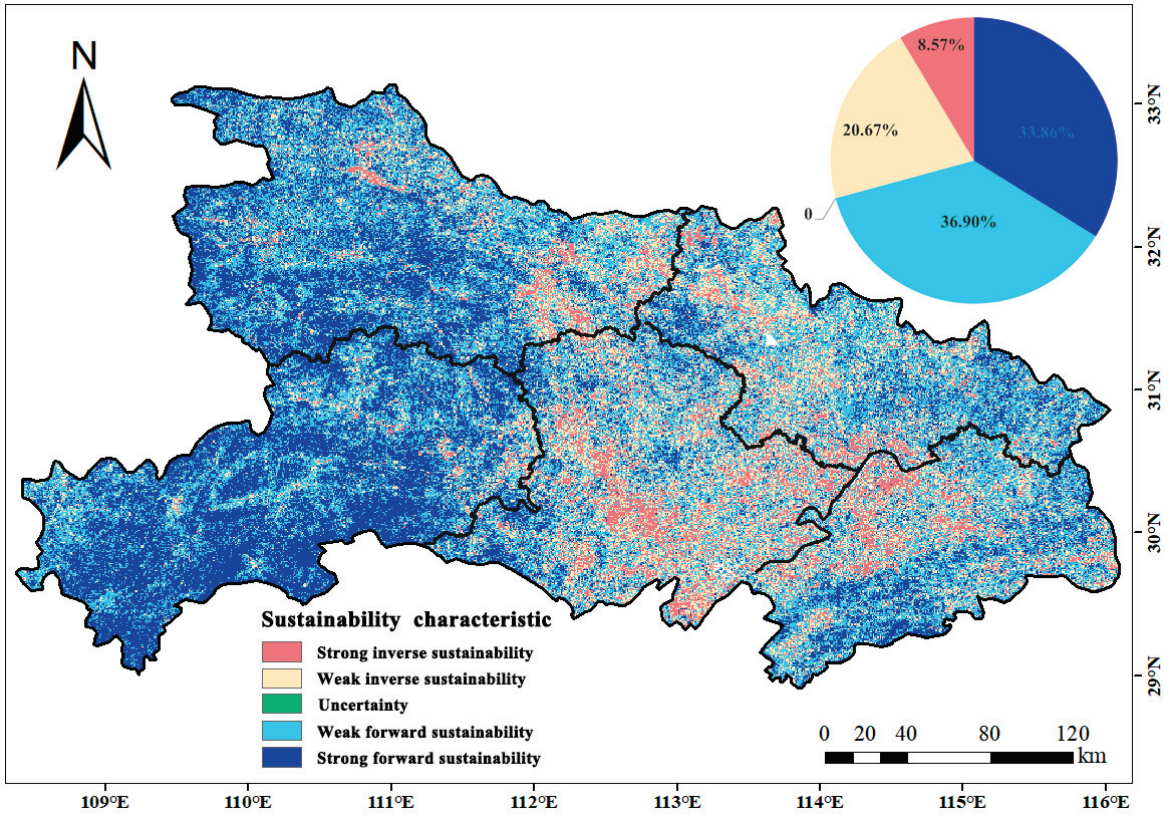

Figure 6. Persistence characteristics of NDVI in Hubei Province from 2000 to 2022.

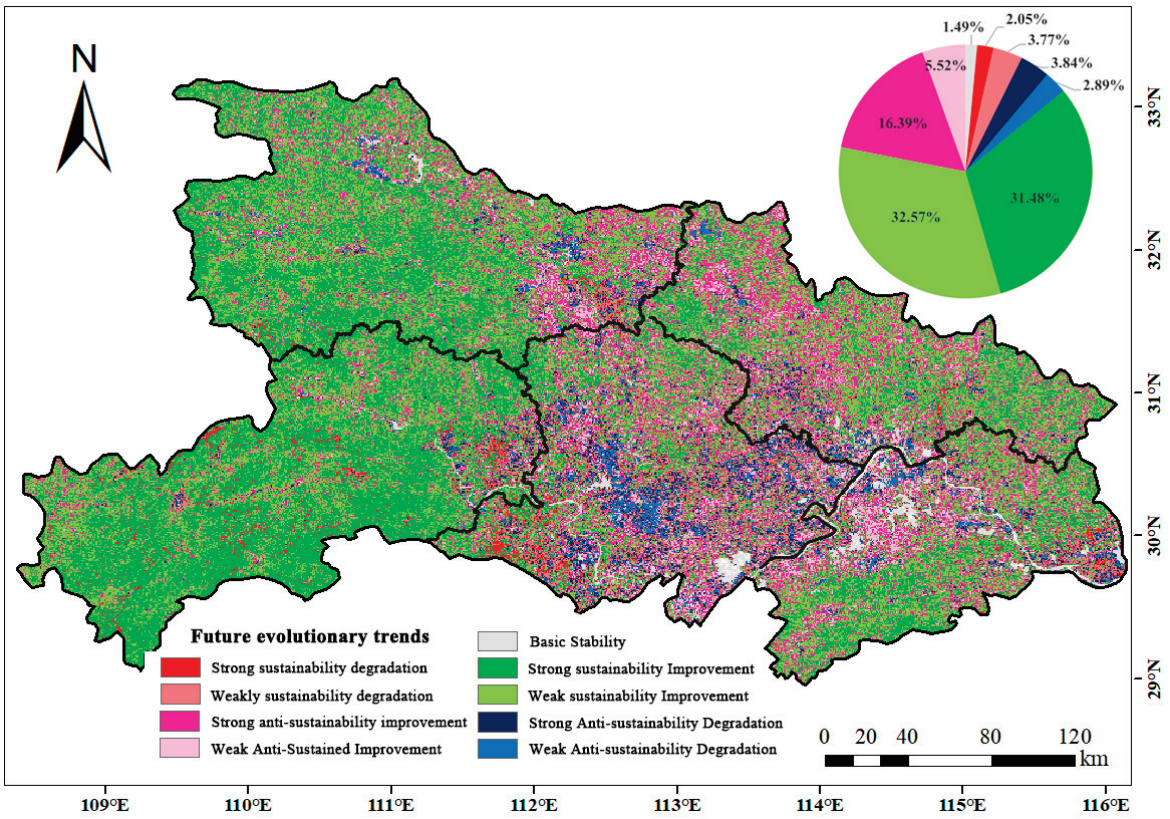

Figure 7. Future evolutionary trends of NDVI in Hubei Province.

3.2. NDVI Driver Analysis

3.2.1. Influence of Climatic Factors on Vegetation NDVI

Changes in temperature and precipitation affect the ecological adaptation of vegetation and climatic phenomena, while solar radiation directly affects plant photosynthesis. From the partial correlation coefficients between climate factors and vegetation, it can be seen (Figure 8) that the mean values of the partial correlation coefficients of vegetation NDVI with precipitation, temperature, and solar radiation are 0.04, 0.14, and −0.05. The partial correlation coefficients between vegetation NDVI and precipitation ranged from −0.87 to 0.85, in which the coefficients greater than 0 indicate that precipitation had a facilitating effect on the growth of vegetation, which accounted for about 54.57% of the area of the study area and was mainly distributed in the southwest of Hubei. On the contrary, the coefficients less than zero indicated that precipitation had an inhibitory effect on the growth of vegetation, and it was mainly distributed in the Jianghan Plain, southeast Hubei, and northwest Hubei. The significance test of the partial correlation coefficient shows that 3.64% of the area passes the significance test of $p < 0.05$, with sporadic distribution in West Hubei and other places. The areas with a positive and negative correlation between NDVI and air temperature in the study area account for 74.2% and 25.8% of the total study area, of which the proportion of the area passing the $p < 0.05$ significance test was 4.59%, which was mainly distributed in northwestern and southeastern Hubei, and there were sporadic distributions in other areas.

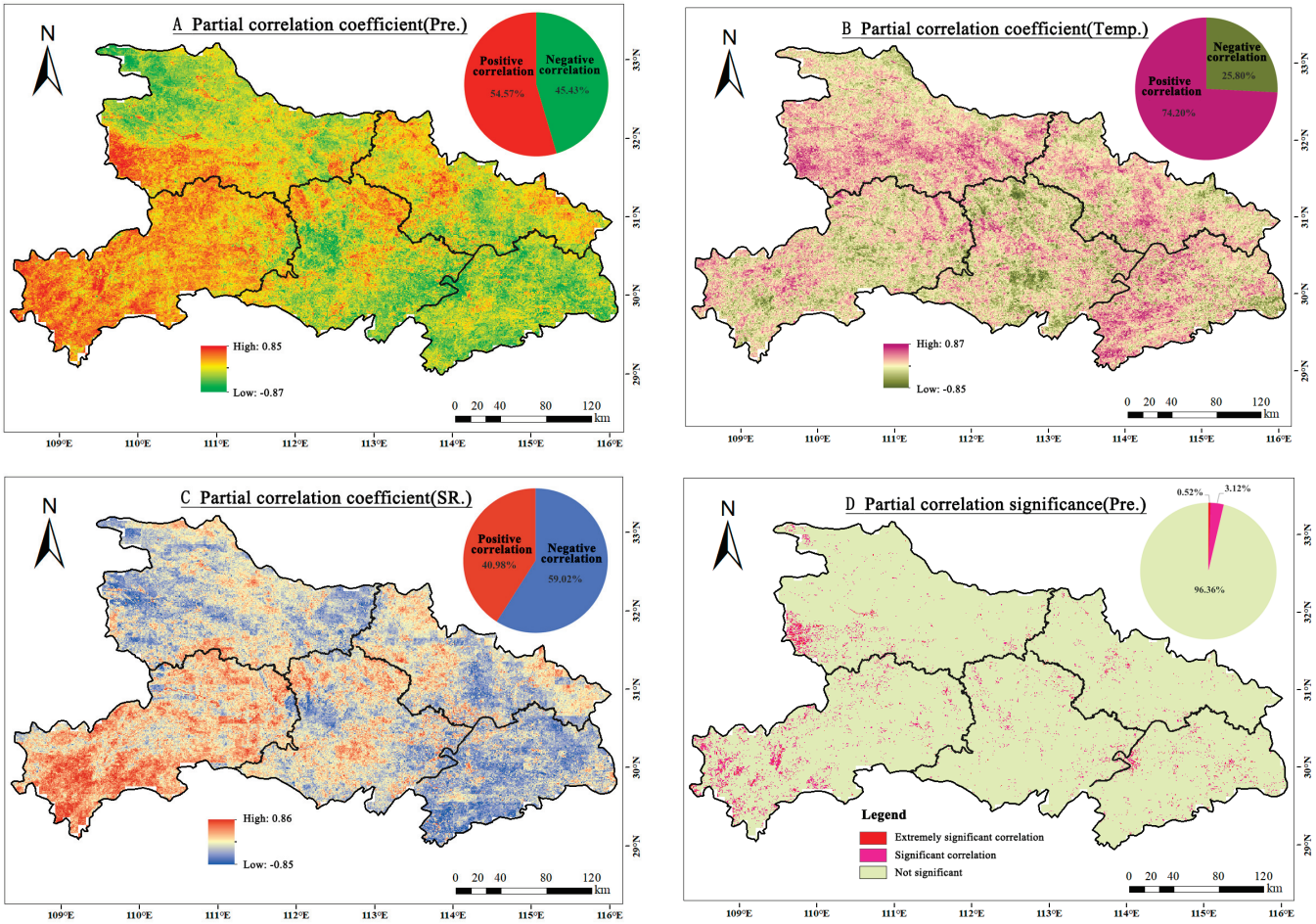

Figure 8. *Cont.*

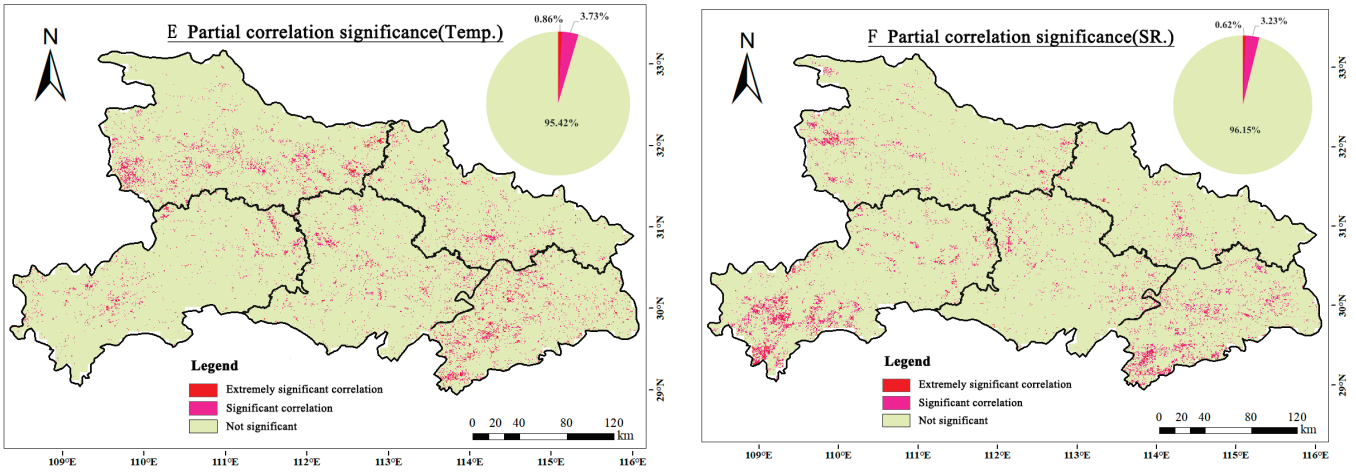

Figure 8. Spatial distribution of partial correlation coefficient (**A**–**C**) and partial correlation significance (**D**–**F**) between NDVI and climate factors in Hubei Province from 2000 to 2022.

In the study area, NDVI was positively and negatively correlated with solar radiation, accounting for 40.98% and 59.02% of the total area, of which the proportion of the area that passed the significance test of $p < 0.05$ was 3.85%, which was mainly distributed in the south and southeast of Hubei and sporadically distributed in other areas. At the same time, the partial correlation coefficients of the climate factors were absolute-valued, and the factor with the largest absolute value within the raster image was taken as the dominant climate-driving factor affecting the regional vegetation NDVI (Figure 9), and the results showed that the proportion of the area driven by precipitation, air temperature, and solar radiation factors ranged between 32.40%, 33.60%, and 34.01%, respectively, and was evenly distributed within the study area, indicating that the contributions of the three climatic factors to drive the vegetation NDVI change were relatively even, and there was no obvious dominant factor.

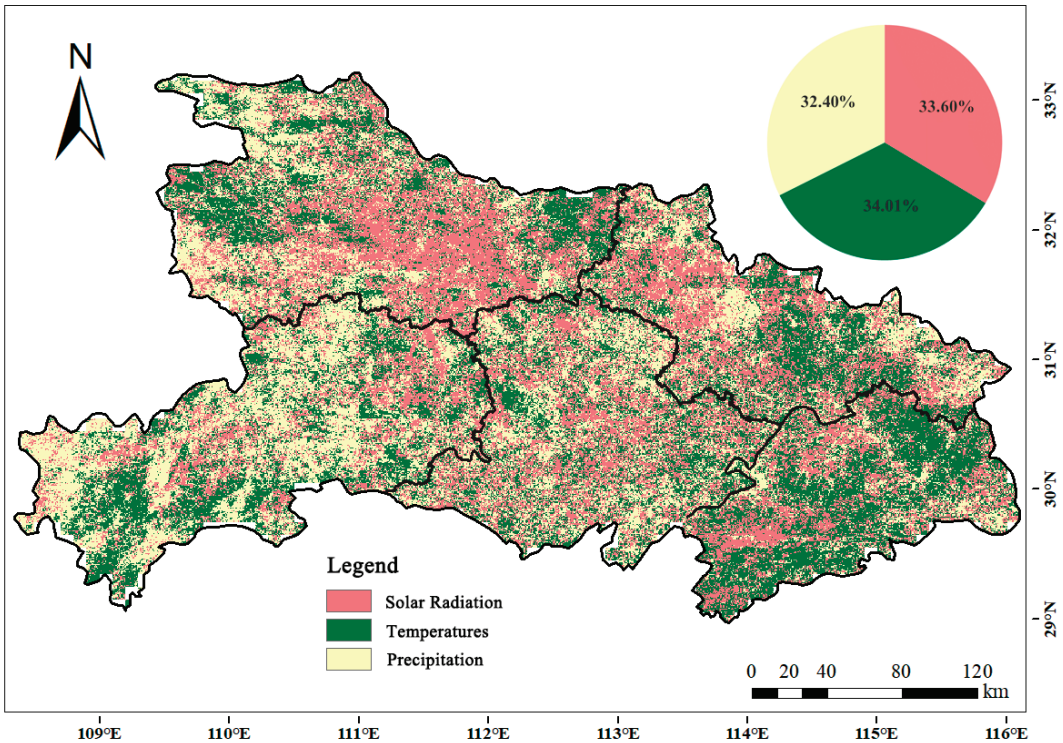

Figure 9. Spatial distribution of dominant climate factors of NDVI change in Hubei Province from 2000 to 2022.

3.2.2. Anthropogenic Effects on Vegetation NDVI

As can be seen from Figure 10, the population of Hubei Province is mainly distributed in East Hubei and the Jianghan Plain, and the areas with higher population density are mainly distributed in Wuhan City and its surroundings. The distribution of nighttime lights in Hubei Province has a high degree of overlap with the distribution of population density, which indicates that there are frequent human-related activities in the overlapping areas. NDVI was negatively correlated with population density in 73.08% of the study area, of which 23.98% were significantly negatively correlated ($p < 0.05$), mainly in northwest Hubei, northeast Hubei, southwest Hubei, etc. NDVI was negatively correlated with nighttime light in 56.67% of the study area, mainly in West Hubei, and the region with a significant negative correlation ($p < 0.05$) accounted for 2.55%. The area where NDVI is negatively correlated with both population density and nighttime lighting suggests that human activities in the region inhibit vegetation NDVI, especially population density.

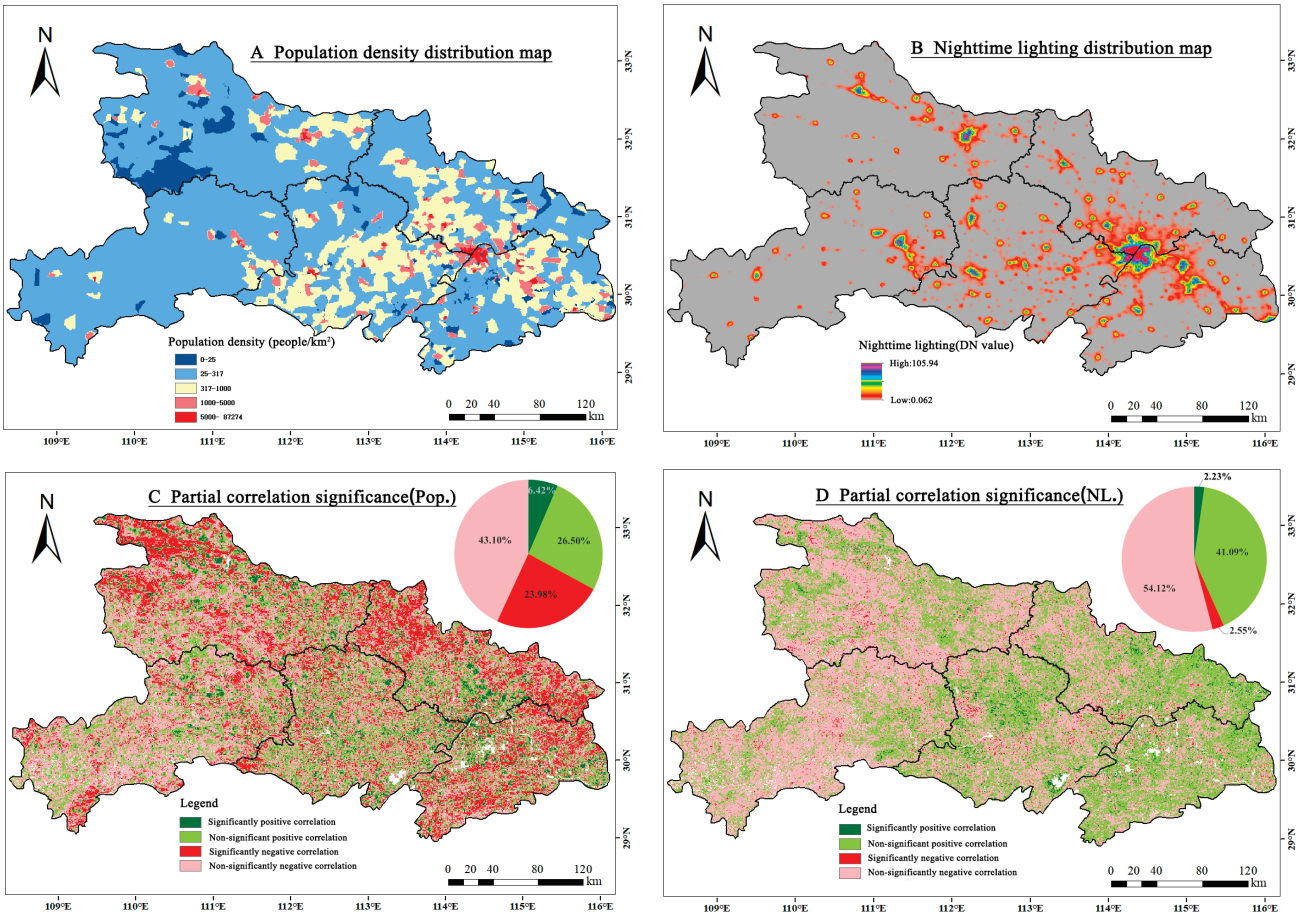

Figure 10. Population Density and night Light Index Distribution and partial correlation between NDVI and them in Hubei Province from 2000 to 2022.

Combined with the inter-annual changes of NDVI in Hubei Province (Figure 2) and the spatial distribution of its trend (Figure 4), it is concluded that the changes in NDVI in the cities within the built-up area show a gradual improvement, whereas for the urban-rural combined belt around the built-up area, the natural vegetation is degraded, indicating that the urbanization process has contributed to the decline of vegetation cover at the periphery of built-up urban areas.

3.2.3. Impact of Land Cover on Vegetation NDVI

As can be seen from Figure 11, land cover in Hubei Province from 2000 to 2022 is mainly Woody Savannas, Croplands, Savannas, Cropland/Natural Vegetation Mosaics, Mixed

Forests, and Deciduous Broadleaf Forests (Figure 11), accounting for 93.81% of the study area. Among them, Woody Savannas, Mixed Forests, and Deciduous Broadleaf Forests are mainly distributed in northwest and southwest Hubei, as well as some mountainous areas of Dabie and Mufu Mountains, accounting for about 48.96% of the study area; Croplands and Cropland/Natural Vegetation Mosaics are mainly distributed in the Jianghan Plain, Nanxiang Basin and some low hillock areas, such as Huanggang City, accounting for about 29.10% of the study area; In addition, Savannas are mainly found in the woodland-cropland interface area, which accounts for about 15.75% of the study area.

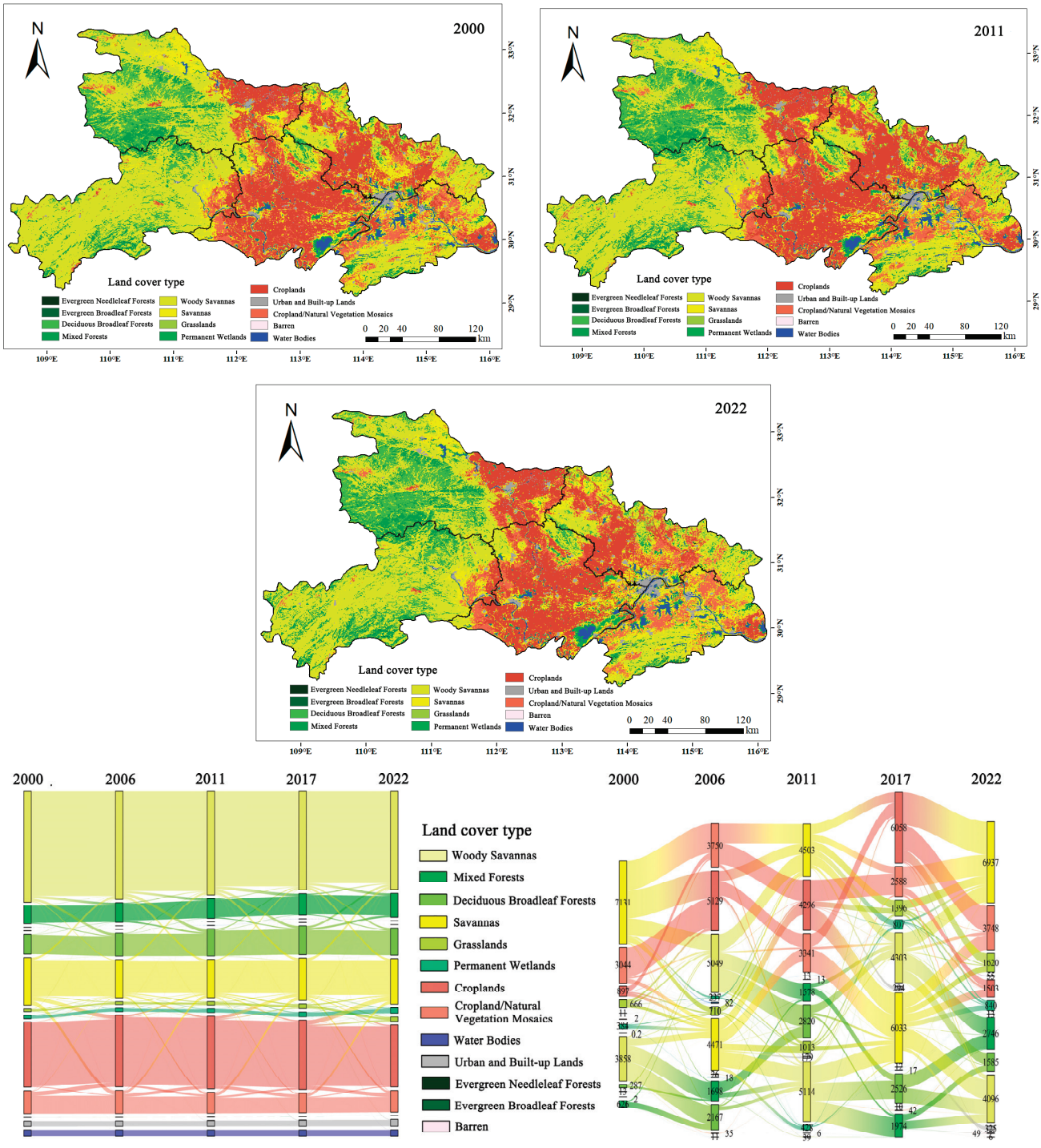

Figure 11. The spationtemporal variation in NDVI in different land cover from 2000 to 2022.

The analysis of land cover transfer shows that in the past 23 years, the transfer between land cover types in the four time periods in Hubei Province is generally characterized by changes in the range of changes from small to large and in the form of simple to diversified changes (Figure 11). From 2000 to 2006, Hubei Province saw the most significant increase in Croplands, with 2534 km^2 and 2371 km^2 transferred from Cropland/Natural Vegetation Mosaics and Savannas, respectively, and the greatest loss of Savanna, with a decrease of 7131 km^2. The overall change in land cover from 2006 to 2011 was relatively smooth, with a more pronounced shift away from Woody Savannas and mainly towards Deciduous Broadleaf Forests. From 2011 to 2017, Woody Savannas in Hubei Province shrank significantly, decreasing by about 2945 km^2, and the Savannas increased by 1730 km^2. Land cover changed dramatically in 2017–2022, with a decrease of 4555 km^2 of Croplands, mainly draining to the Savannahs and an additional area of 325 km^2 of Urban and Built-up Lands.

In addition, over the past 23 years, 907 km^2 of cultivated land and Woody Savannas in Hubei Province have been converted to forested land, which is mainly due to the implementation of the Returning Cultivated Land to Forestry Project in Hubei Province, which began in 2000, resulting in an increase in the area of vegetation. The addition of 880 km^2 to the Urban and Built-up Lands indicates that Hubei Province has experienced rapid urbanization during the study period, but the urbanization process also constrains the vegetation NDVI, resulting in a reduction in vegetation cover.

3.2.4. Geographical Detection of Factors Influencing the NDVI

(1) Factor detection

The factor detector results (q-value) revealed the magnitude of the explanatory power of each factor on the spatial differentiation of vegetation NDVI in Hubei Province. As can be seen from Figure 12, the ranking of factors influencing the distribution and change in vegetation cover in Hubei Province are as follows: land cover factor > anthropogenic factor > topographic factor > climatic factor. The explanatory power of the two driving factors, land cover type (X_8) and soil type (X_7), on the spatial distribution of vegetation cover, was over 60%, and the explanatory power of the land cover type (X_8) factor was over 70%. Different land cover types can significantly affect the effectiveness of soil moisture, and the soil is the growth substrate for plants, which has a significant impact on the growth of vegetation and the efficiency of rainwater reuse. The average annual temperature (X_1) and population density (X_9) are secondary driving factors, with an explanatory power of more than 50%, and the temperature has an impact on the dissolution of nutrients in the soil and the uptake of the plant root system, and the fluctuating increase in the explanatory power of the average annual temperature from 2000 to 2022, with the explanatory power of the average annual temperature increasing to 70.7% in 2022, which indicates that the NDVI of the vegetation in Hubei Province by the temperature. The influence of temperature on the NDVI of vegetation in Hubei Province gradually increased, and land use changes caused by human activities, such as urban expansion, agricultural expansion, and deforestation, negatively affected the distribution of vegetation. Those with 30% to 50% explanatory power include elevation (X_4), nighttime light (X_{10}), and a total of five factors, slope (X_5), slope direction (X_6), solar radiation (X_3), and precipitation (X_2), have the least explanatory power for vegetation cover characterized by NDVI among the 10 drivers.

(2) Interaction detection

The interaction detection mainly assesses the influence of the interaction of different driving factors on the spatial distribution pattern of vegetation NDVI in Hubei Province.

Figure 13 shows that there are only two types of interactions between the factors: bivariate enhancement and nonlinear enhancement. Most of the factor interactions showed bivariate enhancement effects, of which the nonlinear enhancements were temperature ∩ solar radiation, precipitation ∩ solar radiation, slope direction ∩ solar radiation, and precipitation ∩ slope, all of which were climatic and topographic factor interactions, suggesting a synergistic enhancement effect of the natural factors on the vegetation NDVI.

In addition, the interaction between land cover type and other factors was the most significant, with the largest q of 0.95 for the interaction with elevation, which further indicated that land cover type was the main factor influencing vegetation NDVI, and the q of 0.91 and 0.92 for the interactions of population density and nighttime lighting associated with human activities, which indicated that human activities had an important influence in interpreting the NDVI; a smaller interaction was that of solar radiation and slope.

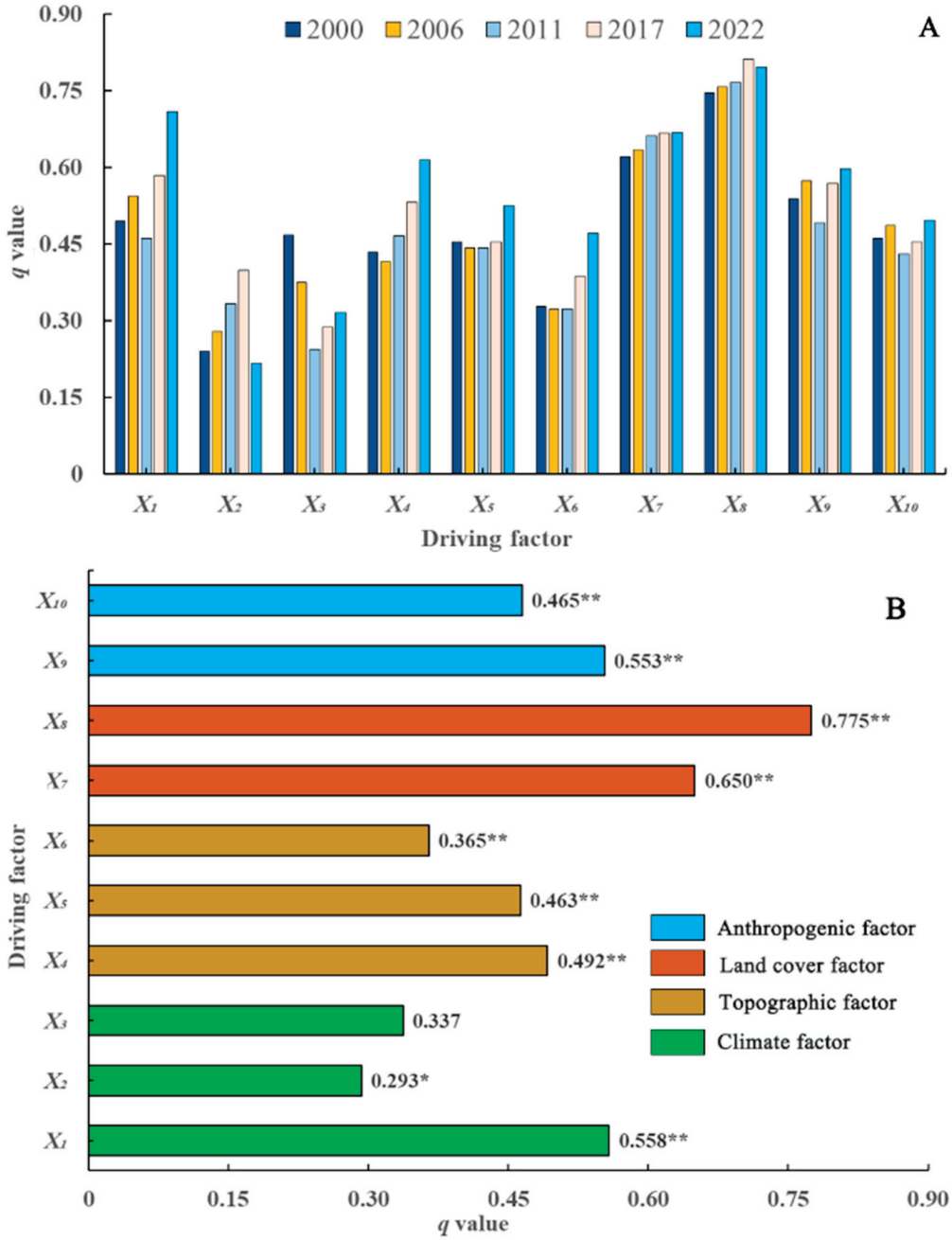

Figure 12. Influence of driving factors (q value) for Normalized Difference Vegetation Index (NDVI) in Hubei Province. ((**A**) q value in 2000, 2006, 2011, 2017and 2022. (**B**) Mean value of q during 2000–2022. X1–X10, driving factors name, see Table 3. * $p < 0.05$; ** $p < 0.01$).

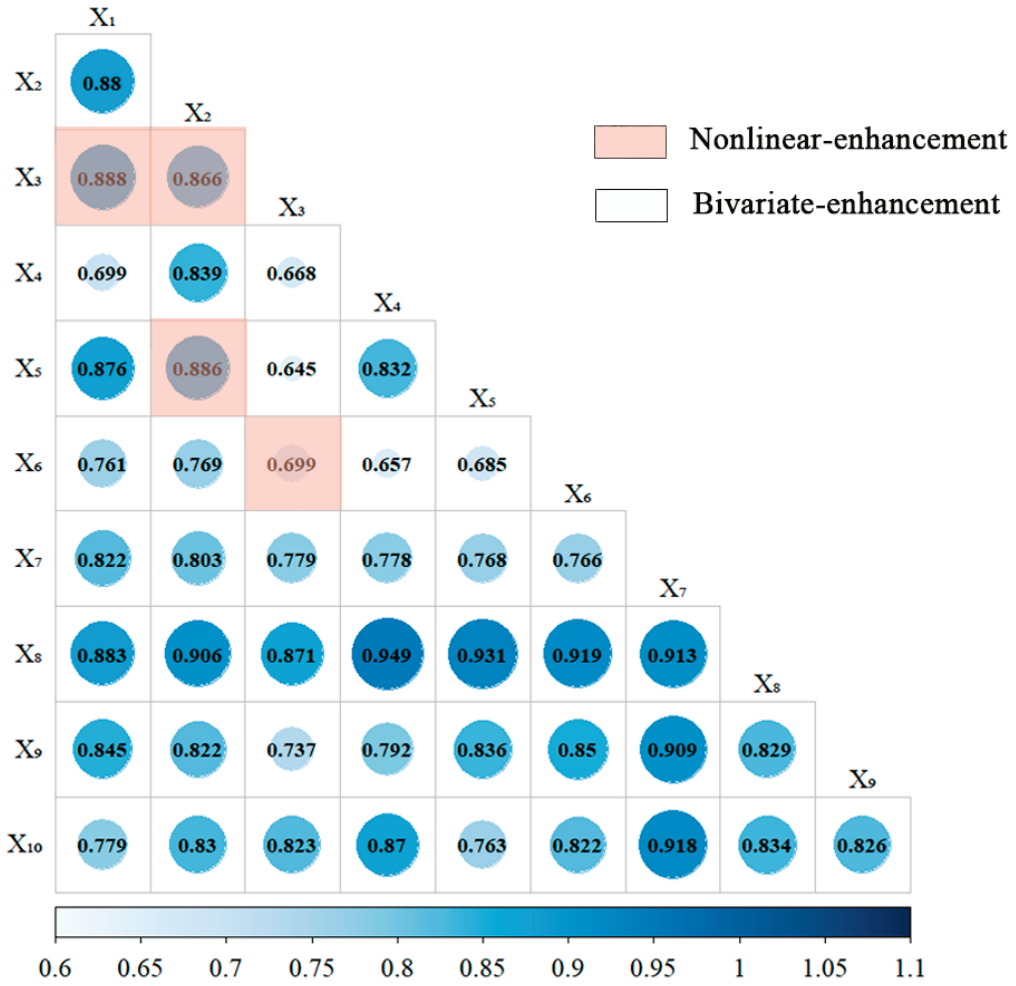

Figure 13. Interaction of driving factors in Hubei Province. (X_1–X_{10}, driving factors' name, see Table 3. Circle size denotes the magnitude of the interaction, numbers in circle indicates *q* value of driving factors interaction).

4. Discussion

4.1. Spatiotemporal Variation Characteristics in the NDVI in Hubei Province

Hubei Province is situated in the transitional zone from the second to the third topographical tier in China, characterized by significant elevation differences. The variation in vegetation cover within the study area is influenced by a combination of natural and human factors. Temporally, the mean value of vegetation NDVI was 0.762 from 2000 to 2022 and fluctuated upward at a rate of 0.01/10a, and the vegetation NDVI showed an increasing trend, which was consistent with the results of [19,20]. In 2003, 2009, 2016, 2020, and 2022, there was a significant decline in vegetation cover. This is due to extreme droughts in 2003 and 2016, rain, snow, and ice storms in 2008, the worst flooding since 1998 in 2020, and the recovery of the New Crown epidemic in 2022 with the orderly movement of people and an increase in human activities leading to a decline in vegetation cover. Vegetation cover recovery is most significant in 2021, which is largely due to a dramatic reduction in anthropogenic as a result of closure measures during the early stages of the COVID-19 pandemic. From a spatial perspective, the state of vegetation cover in Hubei Province is mainly improving and the future evolution trend is mainly continuous improvement, which indicates that the vegetation cover in Hubei Province has not been significantly degraded during the past rapid economic development, which may be related to the climatic conditions of the middle and lower reaches of the Yangtze River in which Hubei Province is situated, and the future evolution trend is mainly continuous improvement, which indicates that Hubei Province has a certain degree of continuity in the protection

of the natural environment. This may be related to the climatic conditions of the middle and lower reaches of the Yangtze River in Hubei Province. In addition, in the hilly and mountainous areas of Hubei Province, the improvement in vegetation cover is relatively large and forest degradation is low. On the contrary, small-scale degradation occurs in the plains in the middle of the area. This is closely related to the topography of the study area, where the vegetation cover of the Jianghan Plain shows a degradation trend due to the high population density and the increasing number of man-made buildings, which further suggests that high human activities can cause low NDVI and vegetation degradation.

During the period 2000–2022, the higher and more volatile areas of NDVI in Hubei Province are mainly distributed along rivers and reservoirs, in cities, and in built-up areas, which are mainly affected by human activities; the low and relatively low volatile areas are mainly distributed in higher elevation hills and mountains, which are less disturbed by human beings, with suitable water and heat conditions, and with vegetation types dominated by forested land, which have a strong resistance to soil and water runoff. The region is less disturbed by human beings and has suitable water and heat conditions [49].

At present, the percentage of areas with significant degradation trends in Hubei Province is 4.71%, but according to the results of the analysis of future development trends, there are still 27.73% of the areas with vegetation that may have the potential risk of deterioration of sustained degradation or change from improvement to degradation in the future. The region is mainly located in the Jianghan Plain, the Wuhan urban agglomeration, Xiangyang-Shiyan-Suizhou Urban Agglomerations, etc. For the potentially deteriorating areas, ecological environmental protection and management need to be strengthened in accordance with the local conditions in order to reduce the risk of vegetation degradation in the future. This is crucial to the sustainable and green development of Hubei Province.

4.2. Drivers of Spatial Variability in Vegetation NDVI

In this study, we analyzed the relationship between vegetation NDVI and climate, topography, surface, and anthropogenic factors in Hubei Province, and the results showed that surface factors were the main drivers of the spatial differentiation of vegetation cover in Hubei Province, for which the explanatory power of the land cover type and the soil type on the spatial distribution of the cover of the vegetation was 76% and 65%, respectively, which was in line with the results of the studies by [50,51]. In the last 23 years, 907 km^2 of cultivated land and Woody Savannas in Hubei Province have been converted to forested land, which is mainly due to the implementation of the Returning Cultivated Land to Forestry Project in Hubei Province, which started in 2000, resulting in an increase in the area of vegetation. At the same time, rapid urbanization during the study period resulted in a significant reduction in vegetation cover in the urban and peripheral areas of the study area, with an additional area of 880 km^2 in the Urban and Built-up Lands.

The influence of temperature on vegetation NDVI in Hubei Province, among the climate factors, fluctuated and increased, and the explanatory power of annual mean temperature increased to 70.7% in 2022, while the explanatory power of precipitation was the smallest, and at the level of inter-annual variability, the annual mean temperature had a closer relationship with the NDVI in Hubei Province, which was in line with the findings of [52], who concluded that the influence of temperature was greater than the effect of precipitation on vegetation in the Yangtze River Basin. Among the human-related activities, the explanatory power of population density and nighttime light index was 55% and 47%, and they were mainly negatively correlated with NDVI, with 23.98% of the regional NDVI significantly negatively correlated with population density ($p < 0.05$), indicating that vegetation cover tended to decrease in regions with higher population density, which was in line with the conclusion of the study conducted by [53]. In addition, the interaction of each factor showed enhanced explanatory power without any weakening or independent phenomenon [54], and the bivariate-enhancement effect accounted for 80% of the total, of which the nonlinear enhancement was all due to the interaction of climatic

and topographic factors, which indicated that there was a synergistic enhancement effect of the natural factors on the NDVI of the vegetation.

In addition, the use of fairly standardized pixel-by-pixel statistics and *p*-value-based hypotheses in the spatial analyses in this paper has some limitations and needs to be combined with other analyses to reach final conclusions, such as the use of geostatistical methods to investigate forest ecosystems.

5. Conclusions

(1) During the period over 23 years, the average value of NDVI of vegetation in Hubei Province was 0.762. The overall change in NDVI showed a fluctuating upward trend, and the growth rate was 0.01/10a ($p < 0.005$); the spatial distribution of NDVI showed a pattern of "low in the east and high in the west", and the vegetation cover condition of Hubei Province was at a relatively high level, in general. The spatial change in NDVI is characterized by "large improvement in the surrounding hills and mountains and small degradation in the middle plains"; the stability of the spatial change in NDVI is characterized by "uniform distribution in general, with obvious differences between urban and rural areas and fluctuation of the river reservoirs and reservoir heights".

(2) In terms of trend prediction, 70.76% of the regions in Hubei Province are likely to maintain the same NDVI trend as that of the 2000–2022 period in the future, and the future evolution of NDVI tends to be mostly benign, accounting for 70.78% of the total; however, 27.73% of the regions may still have the potential deterioration of sustained degradation or change from improvement to degradation of vegetation cover in the future.

(3) The results of partial correlation analysis showed that at the level of interannual variation, NDVI was positively correlated with precipitation and air temperature and negatively correlated with solar radiation, population density, and nighttime lighting in most of the study areas in Hubei Province, for which 23.98% of the areas had a significant negative correlation between NDVI and population density ($p < 0.05$) and, furthermore, among the climatic factors.

(4) The results of the factor detector showed that the influencing factors of vegetation distribution and change in Hubei Province were ranked as follows: land cover factor > human activities > topographic factor > climatic factor, and land cover type and soil type were the main drivers; mean annual air temperature and population density were the secondary drivers, and the influence of air temperature on the NDVI of the vegetation in Hubei Province increased gradually, and the precipitation had the smallest explanatory power of the NDVI characterization of the vegetation cover.

(5) The results of interaction detection showed that, at full scale, the interactions affecting the distribution and change characteristics of NDVI vegetation all showed two-factor enhancement or nonlinear enhancement relationships, which were significantly enhanced compared with the single-factor effects, and most of the factor interactions showed two-factor enhancement effects, and the nonlinear enhancements were all climate and topographic factor interactions. The strongest interaction explanatory power was between land cover type and elevation.

Author Contributions: Conceptualization, P.C. and H.P.; methodology, P.C.; software, P.C.; data curation, Y.X. and W.H.; writing—original draft preparation, P.C.; writing—review and editing, H.P. and W.H.; visualization, P.C. and H.Y.; supervision, H.Y.; project administration, H.Y. All authors have read and agreed to the published version of the manuscript.

Funding: This work was funded by the Youth Fund of the National Natural Science Foundation of China (No. 41902257) and the Smart Yangtze River and Hydropower Science Key Laboratory of Hubei Province Open Research Fund project (ZH2002000113).

Data Availability Statement: All data, models, or code generated or used during the study are available from the author by request (cp.stu@yangtzeu.edu.cn).

Acknowledgments: The authors would like to thank the data support provided by various data source websites in the article. I would like to thank Huaming Yao and Hongzhong Pan for their guidance on the paper, and support of these projects for the paper.

Conflicts of Interest: Author Huaming Yao was employed by the company China Yangtze River Power Co., Ltd. The remaining authors declare that the research was conducted in the absence of any commercial or financial relationships that could be construed as a potential conflict of interest.

References

1. Li, X.; Xin, Z.; Yang, J.; Liu, J. The spatiotemporal changes and influencing factors of vegetation NDVI in the Hehuang Valley of Qinghai Province from 2000 to 2020. *J. Soil Water Conserv.* **2023**, *13*, 79–90.
2. Lai, J.-L.; Qi, S.; Cui, R.-R.; Liao, R.-E.; Tang, Y.; Li, P. Analysis of Vegetation Change and Influencing Factors in Southwest Alpine Canyon Area. *Huan Jing Ke Xue = Huanjing Kexue* **2023**, *44*, 6833–6846. [PubMed]
3. Zhu, L.; Sun, S.; Li, Y.; Liu, X.; Hu, K. Effects of Climate Change and Anthropogenic Activity on the Vegetation Greening in the Liaohe River Basin of Northeastern China. *Ecol. Indic.* **2023**, *148*, 110105. [CrossRef]
4. Yang, J.; Wan, Z.; Borjigin, S.; Zhang, D.; Yan, Y.; Chen, Y.; Gu, R.; Gao, Q. Changing Trends of NDVI and Their Responses to Climatic Variation in Different Types of Grassland in Inner Mongolia from 1982 to 2011. *Sustainability* **2019**, *11*, 3256. [CrossRef]
5. Liu, D.; Pan, P.; Fu, J.; OUYANG, X. Spatiotemporal variation and driving factor of vegetation coverage in southern Jiangxi Province, China from 2000 to 2020. *Chin. J. Appl. Ecol.* **2023**, *34*, 2919–2928.
6. Wang, J.; Wang, K.; Zhang, M.; Zhang, C. Impacts of Climate Change and Human Activities on Vegetation Cover in Hilly Southern China. *Ecol. Eng.* **2015**, *81*, 451–461. [CrossRef]
7. Liu, S.; Li, W.; Qiao, W.; Wang, Q.; Hu, Y.; Wang, Z. Effect of Natural Conditions and Mining Activities on Vegetation Variations in Arid and Semiarid Mining Regions. *Ecol. Indic.* **2019**, *103*, 331–345. [CrossRef]
8. Gao, S.; Dong, G.; Jiang, X.; Nie, T.; Guo, X. Analysis of Factors Influencing Spatiotemporal Differentiation of the NDVI in the Upper and Middle Reaches of the Yellow River from 2000 to 2020. *Front. Environ. Sci.* **2023**, *10*, 1072430. [CrossRef]
9. Shi, S.; Li, W.; Lin, X.; Zhai, Y.; Ding, Y. Spatiotemporal Variations of Vegetation NDVl and Influencing Factors in Heilonjiang Province. *Res. Soil Water Conserv.* **2023**, *30*, 294–305.
10. Zhang, L.; Cong, Z.; Zhang, D.; Li, Q. Response of Vegetation Dynamics to Climatic Variables across a Precipitation Gradient in the Northeast China Transect. *Hydrol. Sci. J.* **2017**, *62*, 1517–1531. [CrossRef]
11. Jia, X.; You, G.; McKenzie, S.; Zou, C.; Gao, J.; Wang, A. Inter-Annual Variations of Vegetation Dynamics to Climate Change in Ordos, Inner Mongolia, China. *PLoS ONE* **2022**, *17*, e0264263. [CrossRef]
12. Zhang, Y.; Zhang, L.; Wang, J.; Dong, G.; Wei, Y. Quantitative Analysis of NDVI Driving Factors Based on the Geographical Detector Model in the Chengdu-Chongqing Region, China. *Ecol. Indic.* **2023**, *155*, 110978. [CrossRef]
13. Liang, Z.; Sun, R.; Duan, Q. Spatiotemporal variation of NDVI in the Yellow River water conservation zone and its driving factors. *Prog. Geogr.* **2023**, *42*, 1717–1732. [CrossRef]
14. Pan, J.; Ren, Z.; Xu, S.; Li, P.; Zhang, X.; Xu, Y.; Ren, Z. Variation Characteristics of NDVl of Different Vegetation Types in Ningxia, China and Their Responses to Climate. *J. Earth Sci. Environ.* **2023**, *45*, 819–832.
15. Cetin, M.; Ozenen Kavlak, M.; Senyel Kurkcuoglu, M.A.; Bilge Ozturk, G.; Cabuk, S.N.; Cabuk, A. Determination of land surface temperature and urban heat island effects with remote sensing capabilities: The case of Kayseri, Türkiye. *Nat. Hazards* **2024**, *120*, 5509–5536. [CrossRef]
16. Pettorelli, N.; Vik, J.O.; Mysterud, A.; Gaillard, J.-M.; Tucker, C.; Stenseth, N.C. Using the Satellite-Derived Normalized Difference Vegetation Index (NDVI) to Assess Ecological Responses to Environmental Change. *Trends Ecol. Evol.* **2005**, *20*, 503–510. [CrossRef]
17. Sun, H.; Wang, C.; Niu, Z. Analysis of the Vegetation Cover Change and the Relationship between NDVI and Environmental Factors by Using NOAA Time Series Data. *J. Remote Sens. Beijing* **1998**, *2*, 210–216.
18. Ma, M.; Wang, J.; Wang, X. Advance in the Inter-Annual Variability of Vegetation and Its Relation to Climate Based on Remote Sensing. *J. Remote Sens. Beijing* **2006**, *10*, 421.
19. Yuan, M.; Zhou, L.; Lin, A.; Zhu, H. Analyzing dynamic vegetation change and response to climatic factors in Hubei Province, China. *Acta Ecol. Sin.* **2016**, *36*, 5315–5323.
20. Zhao, W.; Li, J.; Chu, L.; Wang, T.; Li, Z.; Cai, C. Analysis of spatial and temporal variations in vegetation index and its driving force in Hubei Province in the last 10 years. *Acta Ecol. Sin.* **2019**, *39*, 7722–7736.
21. Dastigerdi, M.; Nadi, M.; Sarjaz, M.R.; Kiapasha, K. Trend analysis of MODIS NDVI time series and its relationship to temperature and precipitation in Northeastern of Iran. *Env. Monit Assess* **2024**, *196*, 346. [CrossRef]
22. Degerli, B.; Çetin, M. Evaluation from rural to urban scale for the effect of NDVI-NDBI indices on land surface temperature, in Samsun, Türkiye. *Turk. J. Agric. Food Sci. Technol.* **2022**, *10*, 2446–2452. [CrossRef]

23. Chen, T.; Xia, J.; Zou, L.; Hong, S. Quantifying the Influences of Natural Factors and Human Activities on NDVI Changes in the Hanjiang River Basin, China. *Remote Sens.* **2020**, *12*, 3780. [CrossRef]
24. Zhong, H.; Wang, H. Temporal and spatial variation of normalized vegetation index in Hubei Province from 2007 to 2016. *J. Cent. China Norm. Univ. (Nat. Sci.)* **2018**, *52*, 582–588.
25. Whetton, R.; Zhao, Y.; Shaddad, S.; Mouazen, A.M. Nonlinear parametric modelling to study how soil properties affect crop yields and NDVI. *Comput. Electron. Agric.* **2017**, *138*, 127–136. [CrossRef]
26. Cetin, M. The effect of urban planning on urban formations determining bioclimatic comfort area's effect using satellitia imagines on air quality: A case study of Bursa city. *Air Qual. Atmos. Health* **2019**, *12*, 1237–1249. [CrossRef]
27. Degerli, B.; Çetin, M. Using the remote sensing method to simulate the land change in the year 2030. *Turk. J. Agric. Food Sci. Technol.* **2022**, *10*, 2453–2466. [CrossRef]
28. Guerrero FJ, D.T.; Hinojosa-Corona, A.; Kretzschmar, T.G. A comparative study of NDVI values between north-and south-facing slopes in a semiarid mountainous region. *IEEE J. Sel. Top. Appl. Earth Obs. Remote Sens.* **2016**, *9*, 5350–5356. [CrossRef]
29. Fan, J.; Fan, Y.; Cheng, J.; Wu, H.; Yan, Y.; Zheng, K.; Shi, M.; Yang, Q. The Spatio-Temporal Evolution Characteristics of the Vegetation NDVI in the Northern Slope of the Tianshan Mountains at Different Spatial Scales. *Sustainability* **2023**, *15*, 6642. [CrossRef]
30. Chen, S.; Zhu, Z.; Liu, X.; Yang, L. Variation in Vegetation and Its Driving Force in the Pearl River Delta Region of China. *Int. J. Environ. Res. Public Health* **2022**, *19*, 10343. [CrossRef]
31. Li, Q.; Zhou, Y.; Wang, L.; Zuo, Q.; Yi, S.; Liu, J.; Su, X.; Xu, T.; Jiang, Y. The Link between Landscape Characteristics and Soil Losses Rates over a Range of Spatiotemporal Scales: Hubei Province, China. *Int. J. Environ. Res. Public Health* **2021**, *18*, 11044. [CrossRef] [PubMed]
32. Chen, J.; Song, X.; Zang, L.; Mao, F.; Yin, J.; Zhang, Y. Spatio-temporal association mining of intercity PM2. 5 pollution: Hubei Province in China as an example. *Environ. Sci. Pollut. Res.* **2023**, *30*, 7256–7269. [CrossRef] [PubMed]
33. Zhang, Y.; Guo, L.; Chen, Y.; Shi, T.; Luo, M.; Ju, Q.; Zhang, H.; Wang, S. Prediction of Soil Organic Carbon Based on Landsat 8 Monthly NDVI Data for the Jianghan Plain in Hubei Province, China. *Remote Sens.* **2019**, *11*, 1683. [CrossRef]
34. Guo, H.; Wang, B.; Niu, X. A Plan for a Forest Ecosystem Observation Research Network, Based on GIS. *Hubei Prov. Acta Ecol. Sin. China* **2015**, *35*, 6829–6837.
35. Peng, S. *1-Km Monthly Precipitation Dataset for China (1901–2022)*; National Tibetan Plateau Data Center: Beijing, China, 2020.
36. Peng, S. *1-Km Monthly Mean Temperature Dataset for China (1901–2022)*; National Tibetan Plateau Data Center: Beijing, China, 2019.
37. Wang, K. *Homogeneous Grid Dataset of Chinaese Land Surface Observation (Surface Solar Radiation, Surface Wind Speed, Relative Humidity and Land Surface Evapotranspiration)*; National Tibetan Plateau Data Center: Beijing, China, 2022.
38. Yang, J.; Huang, X. The 30 m Annual Land Cover Datasets and Its Dynamics in China from 1985 to 2022. 2023. Available online: https://zenodo.org/records/8176941 (accessed on 25 February 2024).
39. Chen, Z.; Yu, B.; Yang, C.; Zhou, Y.; Yao, S.; Qian, X.; Wang, C.; Wu, B.; Wu, J. An Extended Time Series (2000–2018) of Global NPP-VIIRS-like Nighttime Light Data from a Cross-Sensor Calibration. *Earth Syst. Sci. Data* **2021**, *13*, 889–906. [CrossRef]
40. Sen, P.K. Estimates of the Regression Coefficient Based on Kendall's Tau. *J. Am. Stat. Assoc.* **1968**, *63*, 1379–1389. [CrossRef]
41. Lie, Q.; Hu, Z.; Wang, J.; Zhang, Y.; Wu, G. Spatiotemporal Dynamics of NDVI in China from 1985 to 2015: Ecosystem Variation, Regional Differences, and Response to Climatic Factors. *Acta Ecol. Sin.* **2023**, *43*, 6378–6391.
42. Alavi, N.; King, D. Evaluating the Relationships of Inter-Annual Farmland Vegetation Dynamics with Biodiversity Using Multi-Spatial and Multi-Temporal Remote Sensing Data. *Remote Sens.* **2020**, *12*, 1479. [CrossRef]
43. Jiang, W.; Yuan, L.; Wang, W.; Cao, R.; Zhang, Y.; Shen, W. Spatio-Temporal Analysis of Vegetation Variation in the Yellow River Basin. *Ecol. Indic.* **2015**, *51*, 117–126. [CrossRef]
44. Rivas-Tabares, D.A.; Saa-Requejo, A.; Martín-Sotoca, J.J.; Tarquis, A.M. Multiscaling NDVI Series Analysis of Rainfed Cereal in Central Spain. *Remote Sens.* **2021**, *13*, 568. [CrossRef]
45. Duo, A.; Zhao, W.; Gong, Z.; Zhang, M.; Fan, Y. Temporal analysis of climate change and its relationship with vegetation cover on the north China plain from 1981 to 2013. *Acta Ecol. Sin.* **2016**, *37*, 576–592.
46. Wang, F.; Ma, Y.; Darvishzadeh, R.; Han, C. Annual and Seasonal Trends of Vegetation Responses and Feedback to Temperature on the Tibetan Plateau since the 1980s. *Remote Sens.* **2023**, *15*, 2475. [CrossRef]
47. Jinfeng, W.; Chengdong, X. Geodetector: Principle and Prospective. *Acta Geogr. Sin.* **2017**, *72*, 116–134.
48. Wang, J.-F.; Zhang, T.-L.; Fu, B.-J. A Measure of Spatial Stratified Heterogeneity. *Ecol. Indic.* **2016**, *67*, 250–256. [CrossRef]
49. Fan, J.; Xu, Y.; Ge, H.; Yang, W. Vegetation Growth Variation in Relation to Topography in Horqin Sandy Land. *Ecol. Indic.* **2020**, *113*, 106215. [CrossRef]
50. Feng, X.; Zeng, Z.; Jing, M.; Gao, K.; Xiao, Y. Influence of driving factors under different vegetation indices of NDVI and EVI in Guangdong-Hong Kong-Macao Greater Bay Area. *J. Huazhong Agric. Univ.* **2023**, *42*, 116–124.
51. Chen, X.; Zhao, X.; Zhang, J.; Wang, R.; Lu, J. Variation of NDVI spatio-temporal characteristics and its driving factors based on geodetector model in Horqin Sandy Land, China. *Chin. J. Plant Ecol.* **2023**, *47*, 1082–1093. [CrossRef]
52. Qu, S.; Wang, L.; Lin, A.; Yu, D.; Yuan, M.; Li, C. Distinguishing the Impacts of Climate Change and Anthropogenic Factors on Vegetation Dynamics in the Yangtze River Basin, China. *Ecol. Indic.* **2020**, *108*, 105724. [CrossRef]

53. Seto, K.C.; Fragkias, M. Quantifying Spatiotemporal Patterns of Urban Land-Use Change in Four Cities of China with Time Series Landscape Metrics. *Landsc. Ecol.* **2005**, *20*, 871–888. [CrossRef]
54. Tang, J.; Xu, M.; Mo, Y.; Wu, W.; Zhang, J.; Li, Z.; Bao, Y. Spatial and temporal variation in normal difference vegetation index of vegetation in Liaoning Province from the perspective of ecogeographic zoning. *Chin. J. Appl. Ecol.* **2023**, *34*, 3271–3278.

Disclaimer/Publisher's Note: The statements, opinions and data contained in all publications are solely those of the individual author(s) and contributor(s) and not of MDPI and/or the editor(s). MDPI and/or the editor(s) disclaim responsibility for any injury to people or property resulting from any ideas, methods, instructions or products referred to in the content.

climate

MDPI

Article

Characteristics of Foehn Wind in Urumqi, China, and Their Relationship with EI Niño and Extreme Heat Events in the Last 15 Years

Maoling Ayitikan [1,2,3,4], Xia Li [2,3,*], Yusufu Musha [2,3], Qing He [1,5,*], Shuting Li [2,3], Yuting Zhong [2,3] and Kai Cheng [2,3]

1 School of Geography and Remote Sensing Science, Xinjiang University, Urumqi 830002, China; maoling@stu.xju.edu.cn or maoln@idm.cn
2 Institute of Desert Meteorology, China Meteorological Administration, Urumqi 830002, China; ysfbs5@aliyun.com (Y.M.); lishuting@idm.cn (S.L.); zhongyuting@idm.cn (Y.Z.); chengkai@idm.cn (K.C.)
3 Field Scientific Experiment Base of Akdala Atmospheric Background, China Meteorological Administration, Urumqi 830002, China
4 Dabancheng Special Test Field Base of National Integrated Meteorological Observation, Urumqi 830002, China
5 Xinjiang Meteorological Observatory, Urumqi 830002, China
* Correspondence: lixia@idm.cn (X.L.); qinghe@idm.cn (Q.H.)

Abstract: Dry and hot Foehn wind weather often occurs in Urumqi, China, due to its canyon terrain. This directly impacts the lives and health of local people. Using surface meteorological variables (including the hourly wind, temperature, humidity, and pressure) measured in situ at the Urumqi Meteorological Station and ERA5 reanalysis from the European Centre for Medium-Range Weather Forecasts in the past 15 years (2008–2022), the characteristics of Foehn wind and their relationship with EI Niño and extreme high-temperature events in Urumqi are analyzed. The results show that the annual distributions of Foehn wind present a fluctuating pattern, and the highest frequency occurred in 2015. Compared to the summer (July) and winter (February) seasons, Foehn wind occurs most frequently in spring (March, April, May) and autumn (September, October, and November). Daily variations in Foehn wind occur most frequently from 9:00 a.m. to 14:00 p.m. In particular, high levels are found at 10:00 a.m. and 11:00 a.m. in April and May. In 2011, 2012, and 2014, the average wind speed of FW exceeded 6 m/s, and the lowest average wind speed was 3.8 m/s in 2021. The temperature and relative humidity changes (ΔT and ΔRH) caused by Foehn wind are the most significant in winter and when Foehn wind begins to occur. The high-temperature hours related to Foehn wind weather in Urumqi represented 25% of the total in the past 15 years. During the EI Niño period, the amount of Foehn wind in Urumqi significantly increased; The correlation coefficient beteewn slide anomaly of Foehn days and the Oceanic Niño Index is as high as 0.71. Specifically, Foehn wind activity aggravates extreme high-temperature events. This study provides indications for Foehn wind weather forecasting in Urumqi.

Keywords: Foehn wind; wind speed; temperature; relative humidity; EI Niño; extreme heat; Urumqi; China

1. Introduction

1.1. Foehn Wind (FW)

Foehn wind (FW) is a type of dry and hot wind formed by an increase in temperature and a decrease in humidity due to the adiabatic motion of sinking air. FW usually occurs on the lee slope of mountain ranges, which experiences a localized form of air movement caused by a mountainous region [1]. FW occurs in many mountainous areas around the world, such as the Alps in Europe, the Rockies in America, and the Taihang Mountains

in China [2–14]. It often poses a threat to local people's safety, the infrastructure, transportation, agricultural production, etc. In winter, FW is the one of the main factors that contribute to heavy urban pollution [15–17].

Urumqi is located on the northern slope of the Central Tianshan Mountains and is the capital of Xinjiang province in China. It is the political, economic, cultural, and transportation center of Xinjiang and has significant regional influence. Urumqi is in a canyon area, surrounded by mountains on three sides, with large differences in terrain. When Urumqi is located at the bottom of a high-pressure system, southeast winds blow, and the airflow is forced by the terrain to sink rapidly after crossing the mountains, causing adiabatic heating of the air and a decrease in humidity. This is the unique FW weather in the Urumqi region [13,14,18–20]. FW in Urumqi has had a significant impact on local socio-economic development, and thus a thorough investigation and exploration of the activity patterns of FW is urgent.

There has been extensive research on the weather and climate characteristics of FW both domestically and internationally, and the results vary in different regions. Research on the northern slope of the Central Tianshan Mountains shows that the frequency of FW in the urban area of Urumqi is the highest in spring and the lowest in winter. The northern suburb of Urumqi Airport is prone to frequent and high-speed FWs during the morning to noon period, but they occur less frequently with relatively low wind speeds from the afternoon to night, lasting less than 5 h [19–21]. Scholars have found that European fine-grid numerical forecasting products can improve the spatiotemporal resolution and forecasting performance in predicting FW in Urumqi [13,21]. In addition, some scholars have pointed out that winter FW in Urumqi has a significant impact on the formation and enhancement of boundary layer inversion and plays an important role in the initiation of heavily polluted weather [15–17]. However, the above-mentioned studies mostly used short-term data, and the understanding of the spatiotemporal distribution and variation characteristics of the temperature and humidity of Urumqi FW is not detailed or in-depth enough.

1.2. EI Niño

EI Niño Southern Oscillation (ENSO) events refer to the periodic weather phenomena caused by the interaction between the tropical sea surface temperature (SST) and atmospheric circulation in the Pacific region, which have a wide influence on the global climate system. The ENSO event consists of two main stages: EI Niño and La Niña [22,23]. El Niño events are closely related to global cooling and warming, as well as droughts and floods, and therefore are of great concern. In recent years, the National Oceanic and Atmospheric Administration (NOAA) of the United States and the National Climate Center of the China Meteorological Administration have used the Oceanic Niño Index (ONI) to define the intensity of El Niño events: $0 \leq \text{ONI} \leq 0.5$ (normal), $0.6 \leq \text{ONI} \leq 0.9$ (weak), $1 \leq \text{ONI} \leq 1.4$ (moderate), $1.5 \leq \text{ONI} \leq 1.9$ (strong), and $\text{ONI} \geq 2$ (very strong) [24].

El Niño indirectly affects the weather and climate of Xinjiang. Previous researchers found that the impact of El Niño events on weather and climate is almost global. This impact is significant in Northern Xinjiang and insignificant in Southern Xinjiang. Warm winters and dry springs often occur during El Niño, and precipitation increases as the phenomenon moves away [25–28]. However, previous research has mainly focused on the impact of El Niño events on temperature and precipitation in Xinjiang, but there have been few related studies on the impact of El Niño events on FW in the northern slope of the Central Tianshan Mountains.

1.3. Extreme High Temperatures

In Chinese meteorology, a daily maximum temperature reaching or exceeding 35 °C is generally referred to as a high temperature. In 2015, the average temperature in Urumqi was higher than usual. In July, historically rare large-scale, long-term, and high-intensity high-temperature weather swept through the Urumqi region, generating widespread attention [29,30]. Some meteorologists have pointed out that an extreme heat event is

mainly caused by the strong intensity and eastward position of Iranian subtropical high pressure [30,31]. However, no previous research has identified whether southeast winds cause the Foehn wind effect due to the influence of terrain, which also intensifies this high-temperature weather. The understanding of the extreme heat caused by the Urumqi FW is still relatively weak.

Based on observation data from the Urumqi Meteorological Station, this paper analyzes in detail the characteristics of the occurrence frequency, intensity, and temperature and humidity changes during FW weather in Urumqi. In addition, combined with the Oceanic Niño Index and the ERA5 global reanalysis data from the ECMWF, the impact of the El Niño event on FW weather and the effect of FWs on extreme heat weather in Urumqi are analyzed.

2. Study Region, Data, and Methods

2.1. Study Region

The Tianshan Mountains are in the central part of Xinjiang, China, with an average elevation of above 4000 m and stretching for ~2000 km from east to west. Xinjiang is divided into two different climatic zones: Northern Xinjiang and Southern Xinjiang. The Middle Tianshan Valley from Dabancheng to Urumqi runs through the Tianshan Mountains in the southeast–northwest direction. The narrowest part of the Valley has a width of ~15 km, and both ends are very prone to mountain pass winds or downhill storms. Urumqi is located at the opening of the northern end of the Middle Tianshan Valley. The urban area is surrounded by mountains with a height of 1300~5000 m on three sides, and the northern opening faces the Junggar Basin, with a "bell mouth" shape (see Figure 1). The terrain of the urban area slopes from southeast to northwest, with an average elevation of 800 m and a drop of 300–400 m. When the cold air mass around the Mongolian high-pressure system flows back to the southern slope of the Tianshan Mountains, a pressure gradient across the Tianshan Mountains is easily formed at both ends of the Middle Tianshan Valley, which in turn leads to airflow passing through the Middle Tianshan Valley, invading Urumqi and its downstream areas and easily generating FWs (see Figure 2).

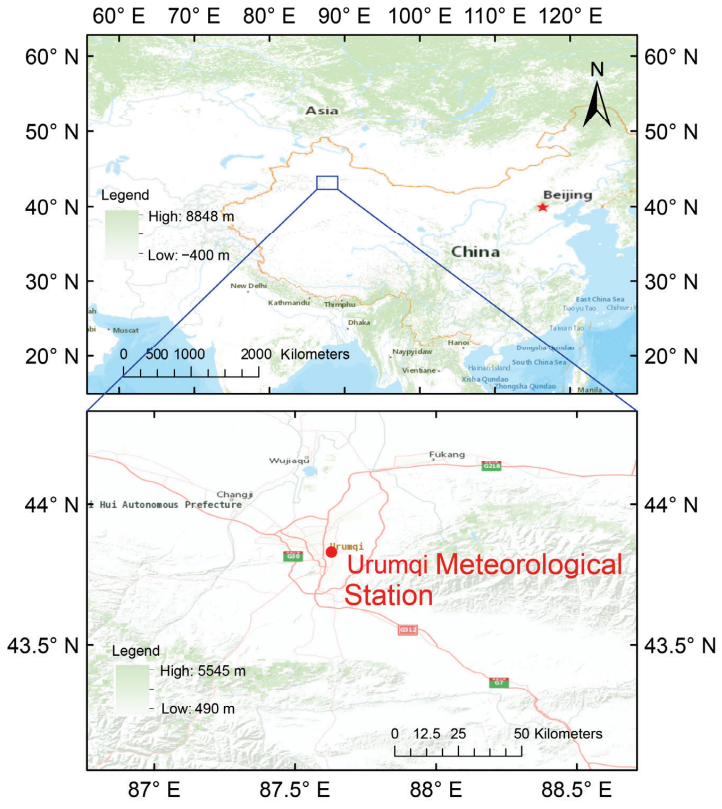

Figure 1. A sketch of the topography of Urumqi.

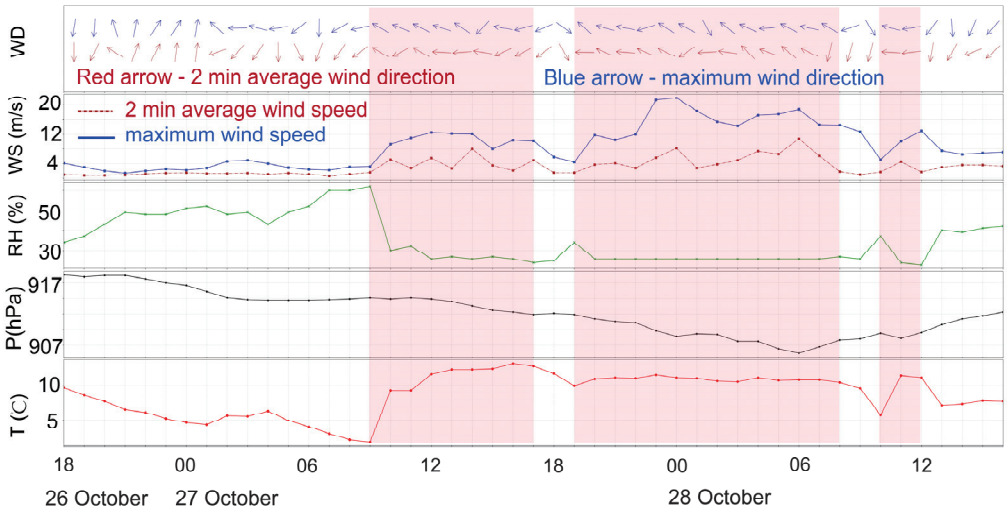

Figure 2. Typical Foehn Wind events in Urumqi. Changes in surface meteorological elements in Urumqi from 27 to 28 October 2020. The pink shaded area represents the Foehn wind period.Green line represents relative humidity; black line is pressure; red line is temperature.

2.2. Data and Methods

(1) Meteorological station observation data. This study selected meteorological variables such as hourly 2 min average, 10 min average, instantaneous, and maximum wind speeds and directions; atmospheric and sea level pressure; temperature; and relative humidity from Urumqi Station from 2008 to 2022.The beginning and end periods of Foehn wind, the duration of FW weather, and the distribution of various meteorological elements over time in Urumqi over the past 15 years were analyzed based on the southeast winds in Urumqi, the conditions in the upper level during the Foehn period, the surface pressure situation of "high in the south and low in the north", and the sudden rise/drop in temperature/humidity [14]. The selection criteria for strong FW are as follows: an instantaneous wind speed $\geq$ 17 m/s or a 2 min average wind speed $\geq$ 10.8 m/s. The selection criterion for a Foehn day is as follows: a day with one hour of FW from 20:00 of the current day to 20:00 of the following day. When analyzing the temperature and humidity changes during FW, the hourly temperature/relative humidity change ($\Delta T/\Delta RH$) is calculated as the difference between the temperature/relative humidity at the previous and present moment. Using the statistical method, the characteristics of FW in Urumqi were analyzed.

(2) The Oceanic EI Niño Index (ONI). The ONI was obtained from the USA National Center for Environmental Prediction (https://origin.cpc.ncep.noaa.gov/products/analysis_monitoring/ensostuff/ONI_v5.php, accessed on 6 December 2023) and the literature [24]. There have been three El Niño events in the past 15 years (Table 1): from June 2009 to April 2010, from October 2014 to April 2016, and from September 2018 to June 2019. The period of October 2014 to April 2016 was regarded as a very strong El Niño event. To match the ONI, a three-month sliding anomaly (DJF, JFM, FMA, MAM, AMJ, MJJ, JJA, JAS, ASO, SON, OND, and NDJ) was calculated for the past 15 years of Urumqi FW days. The relationship between the two parameters was analyzed through the regression analysis and correlation analysis methods.

Table 1. Three EI Niño events in the past 15 years.

Time	Intensity
June 2009–April 2010	moderate
October 2014–April 2016	very strong
September 2018–June 2019	weak

(3) ERA5 reanalysis data. This paper uses ECMWF ERA5 hourly reanalysis meteorological variables with a spatial resolution of 0.25° × 0.25° (including temperature, pressure, and wind speed) to analyze the regional geopotential height field and anomaly field during the extreme heat weather induced by FW. The climate average field refers to the 30-year average from 1991 to 2020.

3. Results

3.1. The Characteristic of FW in Urumqi

3.1.1. The Time Distribution of FW

Annual Distribution Characteristic

In the past 15 years, Urumqi has experienced a total of 3110 h of FW. The annual average duration is 207.3 h; of this, the duration was higher than the average in 5 years, and lower than the average in the remaining 10 years. In 2015, the peak duration of FW reached 346 h, and the lowest was 125 h in 2012 (not shown in tables and figures). Figure 3 presents the statistics of the number of days of FW in Urumqi from 2008 to 2022; the total number of FW days in the past 15 years is 526, with an annual average of 35.1 days. The maximum and minimum number of FW days is 49 in 2010 and 2015 and 23 in 2021, respectively. In particular, there was strong FW in Urumqi for total of 149 h and 53 days over the past 15 years, and the annual average was 9.9 h and 3.5 days. It is noted that the number of hours (162 h) and days (23 d) of FW in 2012 was lower than for other years, but the duration of strong FW was the highest in nearly 15 years, reaching 24 h. Consequently, the time distribution of FW in Urumqi over the past 15 years has shown a fluctuating pattern. In 2015 (top occurrence frequency of FW in the past 15 years), we have preliminarily found better consistency between the anomaly of diurnal FW days and the variation in the ONI, which was mainly associated with atmospheric circulation anomalies caused by super strong El Niño events. The detailed analysis can be found in Section 4.

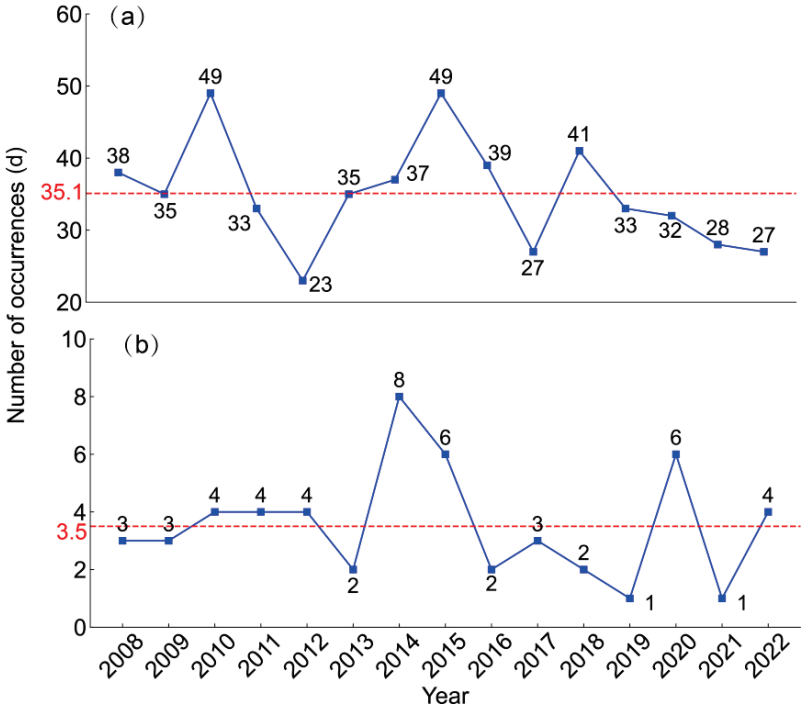

Figure 3. Annual distribution of Foehn wind (FW) in Urumqi in the past 15 years: (**a**) FW, (**b**) strong FW. The red dashed line represents the mean value.

Monthly and Daily Distribution Characteristics

Figure 4 shows the monthly distribution of FW (days and hours) in Urumqi in the past 15 years. In general, the occurrence of FW peaks in spring (March, April, and May) and autumn (September, October, and November), and there are 715 h and 65 days of FW in April (more than other months). FW occurs infrequently, and for about 70 h (30 days) and 73 h (25 days) in summer and winter, especially in February and July, respectively. The duration (hours) of FW in winter is lower than in other seasons, but there is an insignificant difference in the number of days between seasons. It can be inferred that the duration of FW is generally shorter in winter. For example, the duration of FW is 82 h (43 days), indicating that the duration of FW is relatively short in January.

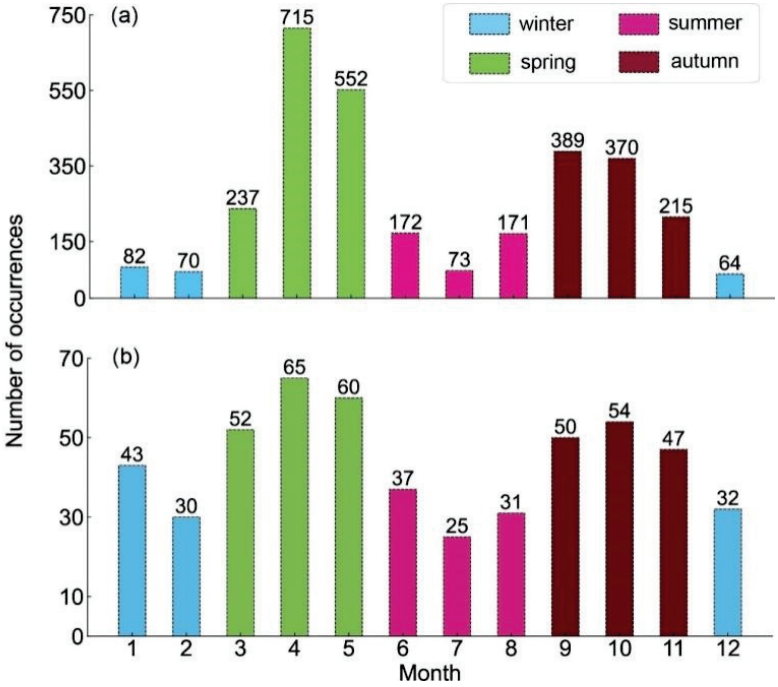

Figure 4. Seasonal variation in Foehn wind (FW) in Urumqi in the past 15 years: (**a**) hourly FW per month and (**b**) daily FW per month.

FW dominates in spring and autumn, which is mainly due to the frequent activity of cold air, the high background temperature, and the pressure difference between the south (high) and the north (low) causing the temperature to alternate easily between cold and warm. Therefore, the favorable thermal conditions and special terrain contribute to the high occurrence of FW. In winter, the frequency of FW is relatively low, which is likely due to the existence of a deep inversion layer in the Urumqi area. Meanwhile, FW is blocked by the inversion layer and cannot enter the urban area, and instead blows through the low-altitude area in Urumqi. As a result, FW rarely touches the ground in winter.

In addition, we calculated the daily variation in FW for each month in the past 15 years (Figure 5). Overall, FW has the highest frequency from 9:00 to 14:00 and the lowest from 21:00 to 02:00 every day, and mainly dominates at 10:00 and 11:00 in April and May (and does not dominate at night in July). At night, there is often a mixed airflow of mountain wind and FW, and distinguishing between the dominant effect of FW and mountain wind is worthy of further discussion.

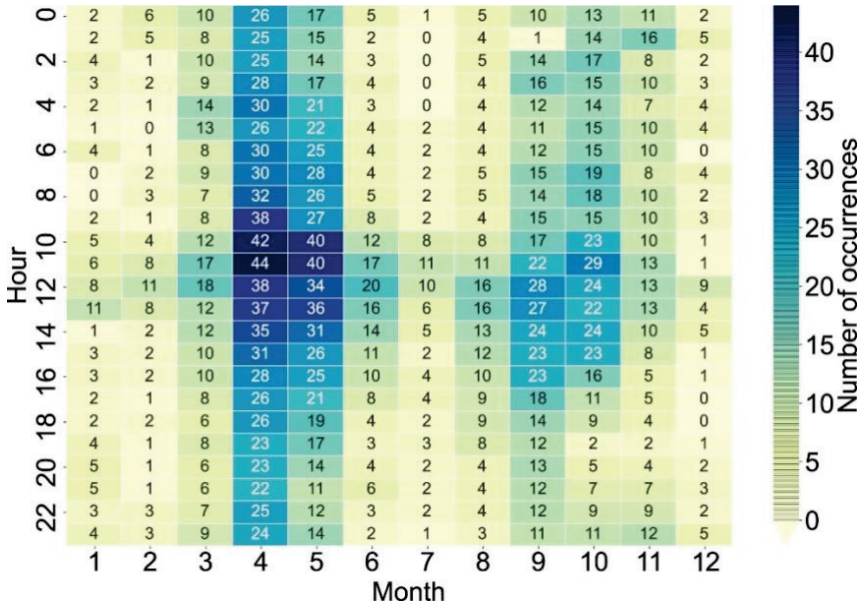

Figure 5. Daily variation in Foehn wind (FW) per month in Urumqi in the past 15 years.

3.1.2. The Characteristics of FW Speed in Urumqi

FWs in Urumqi are often very strong, causing many disasters. The maximum average 2 min wind speed was 18 m/s at 13:00 on 30 March 2012. Figure 6 shows the distribution of the annual average FW speed (yellow color) and the annual average wind speed (green color) in Urumqi from 2008 to 2022. Generally, the annual average FW speed (5 m/s) is more than twice the annual average wind speed (2 m/s) in Urumqi. In 2011, 2012, and 2014, the annual average FW speed exceeded 6 m/s, and the lowest wind speed was 3.8 m/s in 2021.

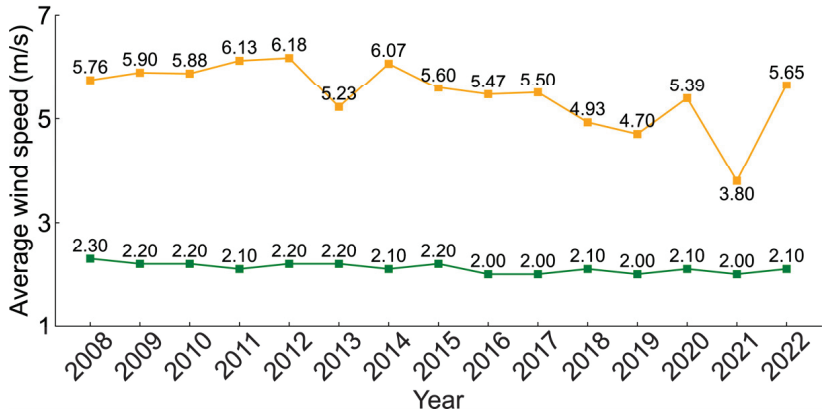

Figure 6. Annual distribution of average wind speed in Urumqi from 2008 to 2022. Yellow refers to the average wind speed of Foehn wind (FW); green is the average wind speed.

Figure 7 shows the monthly distribution of average wind speed in Urumqi from 2008 to 2022. The maximum monthly average wind speed in Urumqi (green) reached 2.60 m/s, 2.60 m/s, and 2.40 m/s in March, April, and May, and the minimum reached less than 2 m/s in December, January, and February, respectively. Conversely, the yellow line fluctuates more than the green line, which is related to the high frequency of FW in Urumqi. The average wind speeds caused by FW are relatively high in March, April, May, and June (5.92 m/s, 5.95 m/s, 6.05 m/s, and 5.80 m/s), and relatively low in December, January, and July (3.61 m/s, 3.95 m/s, and 4.18 m/s, respectively). The wind speed is often low in winter, and the unique canyon terrain in Urumqi is not conducive to the diffusion of pollutants, which contributes to the severe air pollution in the region.

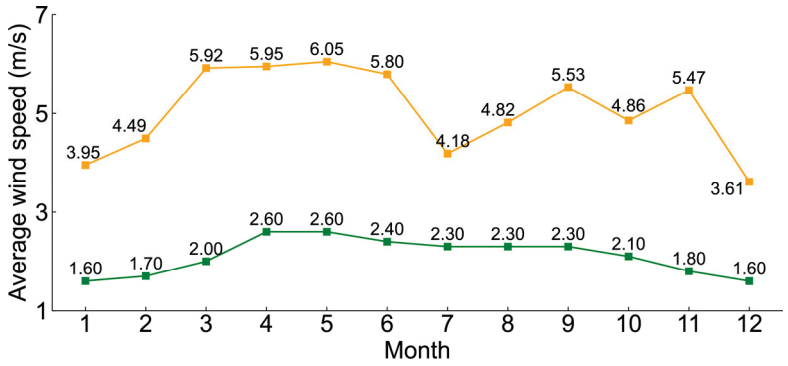

Figure 7. Monthly distribution of average wind speed in Urumqi from 2008 to 2022. Yellow refers to the average wind speed of Foehn wind (FW); green is the average wind speed.

3.1.3. The Characteristics of Temperature and Relative Humidity of FW in Urumqi

Monthly Distribution of Average Temperature

During the FW period, the temperature significantly increases due to adiabatic heating during the movement of air downhill on the leeward slope. Figure 8 shows that the monthly average temperature over 15 years in Urumqi is generally lower than the temperature of the FW. The average temperature is around 25 °C in the summer in Urumqi, which is lower than the average temperatures of FW of 32.3 °C and 30.9 °C in July and August, respectively. That indicates that FW weather can easily cause high temperatures in Urumqi. Table 2 also presents the difference in average temperature. The average temperature is −9.2 °C in February, and the average temperature induced by FW reaches 1.4 °C. The most significant average temperature differences, in descending order, are 11.5 °C, 10.6 °C, and 9.5 °C in March, February, and January, and the most insignificant are around 5 °C in April, May, and June, respectively. In addition, there is a relatively large temperature difference of above 8 °C in October and November.

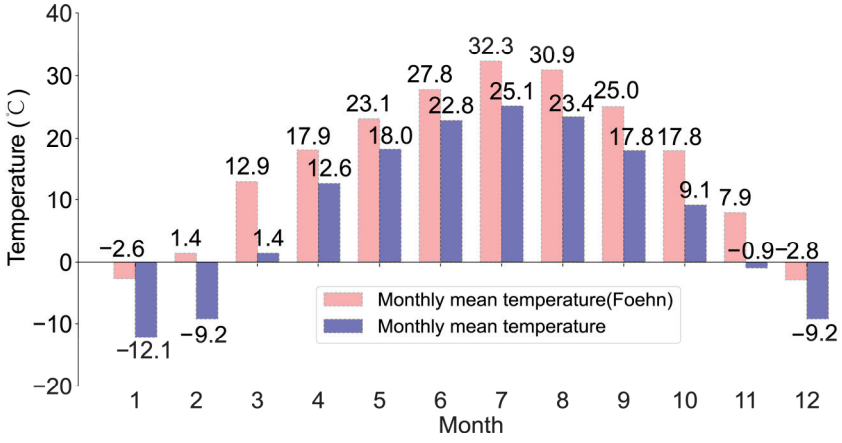

Figure 8. Monthly distribution of average temperature in Urumqi in the past 15 years. Purple represents the monthly average temperature; pink is the average temperature of Foehn wind (FW).

Table 2. The difference in average temperature between full months and Foehn wind (FW) periods in Urumqi in the past 15 years.

T (°C)	January	February	March	April	May	June	July	August	September	October	November	December
FW	−2.6	1.4	12.9	17.9	23.1	27.8	32.3	30.9	25.0	17.8	7.9	−2.8
Full month	−12.1	−9.2	1.4	12.6	18.0	22.8	25.1	23.4	17.8	9.1	−0.9	−9.2
Difference	9.5	10.6	11.5	5.3	5.1	5.0	7.2	7.5	7.2	8.7	8.8	6.4

Urumqi has experienced a total of 289 h of high temperature (temperature $\geq$ 35 °C) in the past 15 years, and 25.3% (73 h) of these are affected by FW weather. Table 3 summarizes the hours of high temperature during the FW period. The peak is 32 h in 2015, followed by 14 h and 8 h in 2008 and 2022, respectively. The highest temperature of 40.5 °C in Urumqi in the past 15 years occurred at 17:00 on 21 July 2015 (more than 35°C from July 21 to 23). The high-temperature weather corresponded to an FW period, which also intensifies extreme heat. Therefore, the duration of extreme heat exceeded historical extremes in the summer of 2015 in Xinjiang; this also represented one of the top ten weather and climate events in China in 2015. A detailed analysis of the causality of the heat waves in Urumqi on 21 July 2015 is presented in Section 5.

Table 3. The hours of high temperature during the FW period.

Year	2008	2009	2010	2011–2013	2014	2015	2016	2017	2018–2020	2021	2022
Hour	14	0	7	0	2	32	2	3	0	5	8

In summary, the effect of FW on temperature changes is significant in Urumqi and has been shown to cause significant warming and high-temperature weather. Active efforts should be made to prevent the impact of abrupt temperature increases caused by FW.

The Distribution of Temperature and Relative Humidity Changes in FW

Figure 9 shows the variations in the hourly temperature and relative humidity of FW during different seasons in Urumqi in the past 15 years. Overall, the temperature variation presents a positive phase during the FW period, while humidity presents a negative phase. A maximum hourly temperature variation of 15.5 °C occurred in winter on 19 February 2021, when the FW had a southeast direction and a wind speed of 5 m/s at 04:00 a.m., and was interrupted by a northwest wind at 05:00 a.m. The hourly temperature change was very sharp during this process (temperature increased from −7.1 °C at 03:00 a.m. to 8.4 °C at 04:00 a.m., and then dropped to −10.2 °C at 05:00 a.m.). In Urumqi, 15 h of hourly temperatures reaching $\geq$10 °C total and 177 h of hourly temperatures reaching $\geq$5 °C were related to FW in the past 15 years. The greatest variation in humidity was a decrease of 63% in spring on March 3, 2013; the relative humidity dropped from 89% at 21:00 p.m. to 26% at 22:00 p.m. The changes in the temperature and relative humidity of FW during the winter period are more significant than in other seasons. The variation in hourly temperature ranged from 0.9 °C to 5.9 °C, and that of relative humidity ranged from −1% to −19%. The variations in hourly temperature and humidity in the other three seasons were similar, with a higher positive temperature change of 13.1 °C in spring and autumn.

In addition, Figure 10 presents the changes in hourly temperature and humidity of FW at the beginning, duration, and end periods in Urumqi in the past 15 years. At the beginning of FW, the changes in temperature and humidity are relatively severe, with the temperature increasing by 0.4 °C to 6.9 °C and the relative humidity decreasing by −2% to −32%. At the end of FW, the temperature decreases significantly from 5.4 °C to −0.7 °C, and the relative humidity increases from −1% to 23%. The duration of FW shows insignificant changes in temperature and relative humidity, with a slight increase in temperature and a slight decrease in relative humidity.

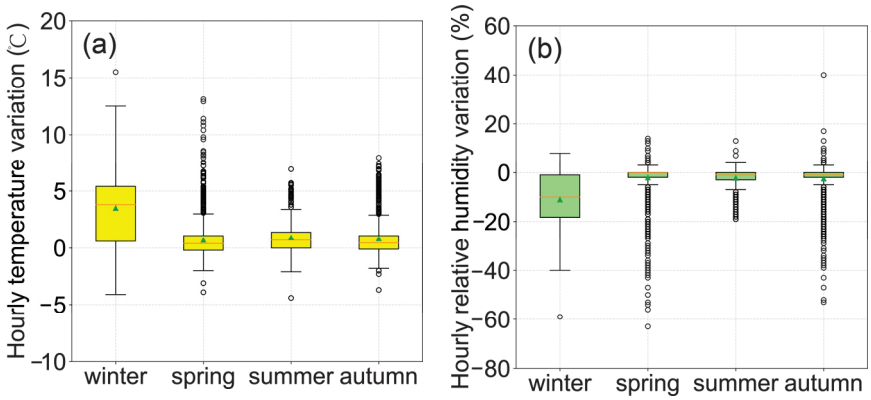

Figure 9. Variations in the hourly temperature (**a**) and relative humidity (**b**) of Foehn wind (FW) during the different seasons in Urumqi in the past 15 years.

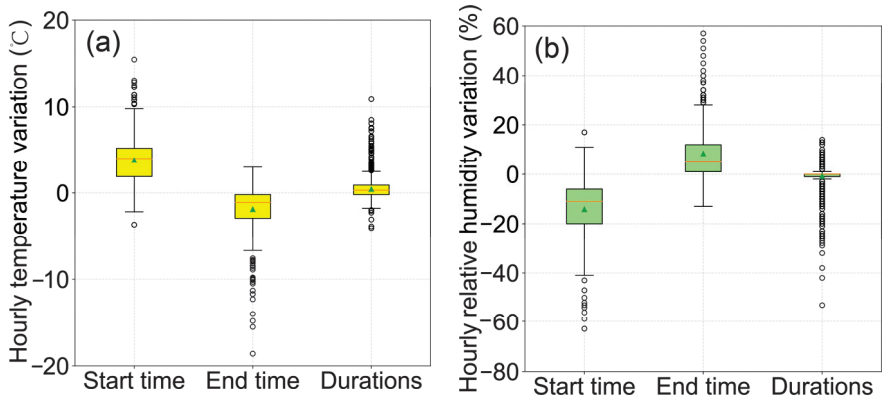

Figure 10. Variations in hourly temperature (**a**) and relative humidity (**b**) in the three periods (start, end, and during) of Foehn wind (FW).

3.2. The Effect of EI Niño Events on FW in Urumqi

Figure 11 shows the distribution of the ONI and the sliding anomaly of FW days in Urumqi over the past 15 years. Overall, the ONI (black solid line) is consistent with the sliding anomaly trend line (blue solid line) and with the corresponding peak and valley value. The days of FW significantly increased during the three El Niño events from June 2009 to April 2010, October 2014 to April 2016, and September 2018 to June 2019 (Table 1). In particular, the highest frequency of FW occurred in Urumqi during the super strong El Niño event from October 2014 to April 2016. The above analysis in Section 3 also found that FW occurred for 346 h and 49 days in 2015, which was more frequent than other years. The periods of moderate El Niño events from June 2009 to April 2010 also present a high frequency of FW, at 230 h and 49 days. The correlation coefficient between the ONI and the anomaly of FW days is 0.71 (at a significance level of 95%; $\alpha = 0.05$) in Urumqi. This indicates a good correlation between the abnormal occurrence of FW in Urumqi and the corresponding El Niño events.

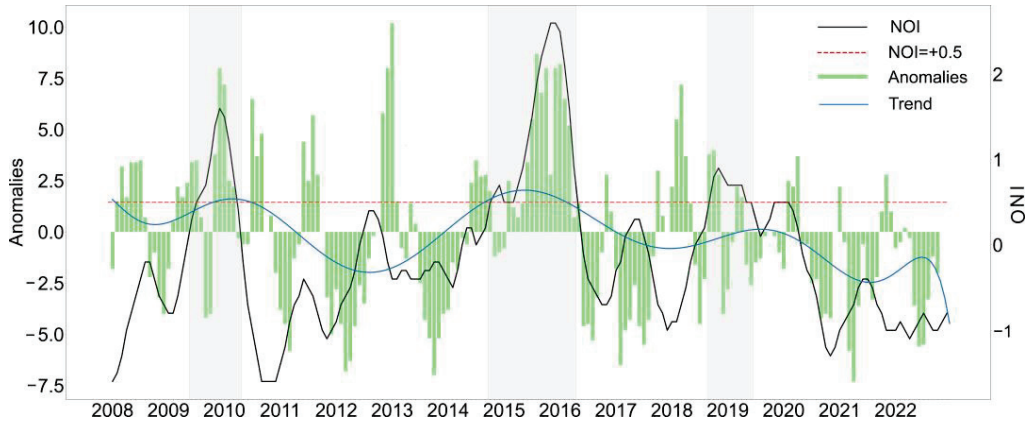

Figure 11. Distribution of the ONI and sliding anomaly of FW days in Urumqi in the past 15 years (the black solid line represents the ONI, and the red dashed line represents ONI = +0.5; the green histogram represents the sliding anomaly of FW days for three months; and the blue solid line represents the trend of the anomaly).

3.3. Effect of FW Intensifies Heat Waves

A rare heat wave occurred in Urumqi from 21 to 23 July 2015. In Figure 12, the 500 hPa circulation pattern and anomaly illustrate that an unusually strong Iranian subtropical high pressure is the main factor that caused the rare sustained high temperatures. The high-pressure center and the ridge line on the north side of the high-pressure system are both located over the Xinjiang region, with a strong central intensity. The anomaly center is in the northern region of the high-pressure system, and the variation magnitude exceeds 10 hPa in Northern Xinjiang. Both Northern Xinjiang and the Tianshan Mountains are influenced by the positive anomaly center. Figure 13 demonstrates the surface circulation pattern. It shows that the low-pressure system in the north and the strong Mongolian high-pressure system in the south of Urumqi form a "high in the south and low in the north" pressure field pattern. Urumqi is located in the southwest of the Mongolian high-pressure system, and FW occurred in the valley area.

Figure 14 shows the changes in surface meteorological elements in Urumqi from 21 to 23 July 2015. On 21 July 2015, FW began to occur in Urumqi at 10:00 a.m. and ended at 6:00 p.m. At 07:00 a.m. on the 22nd, FW began again and ended at 01:00 a.m. on the 23rd. The temperature reached 40.5 °C on 21 July at 17:00, and the temperature was relatively high from 21 to 23 July. Thus, the high-temperature weather occurred during the period of FW. Generally, the temperature in Urumqi suddenly rises once a FW occurs. Except for the first few hours of the FW, the temperature was usually $\geq$35 °C (even on the night of the 22nd). The temperature gradually dropped when the FW ended. In addition, the relative humidity was very low (below 20%), and the sky was clear or slightly cloudy, resulting in strong solar radiation during the FW period. Based on this, it can be concluded that the characteristics of a rise in temperature and a decrease in humidity during the FW period aggravate the intensity of heat waves.

Through the analysis of changes in ground meteorological elements and circulation patterns, it has been found that the eastward movement of high pressure in Xinjiang is the direct cause of this high temperature process, which is consistent with previous research [29–31]. In addition, Urumqi is located in the southwestern part of the Mongolian high-pressure system. When FW blows along the ground, the airflow is forced to sink rapidly by the terrain after crossing the mountain, causing adiabatic warming of the air. During FW periods, the relative humidity decreases, the air becomes dry, and the weather is clear, which are all conducive to local radiation warming. Therefore, the high-temperature weather process is also significantly affected by the FW effect. In summary, three factors contribute to these heat waves: an abnormally strong Iranian subtropical high pressure, the FW effect, and radiation heating.

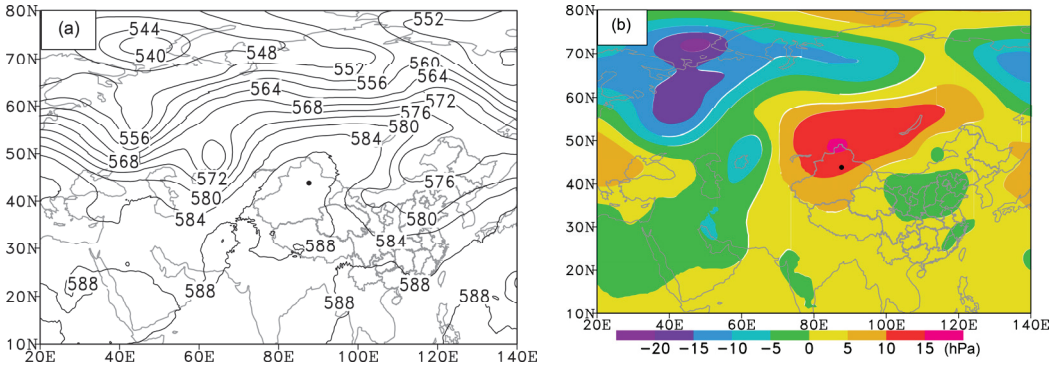

Figure 12. (**a**) The 500 hPa circulation pattern on 21 July 2015, and (**b**) an anomaly. Black dot represents Urmqi Meteorological stations.

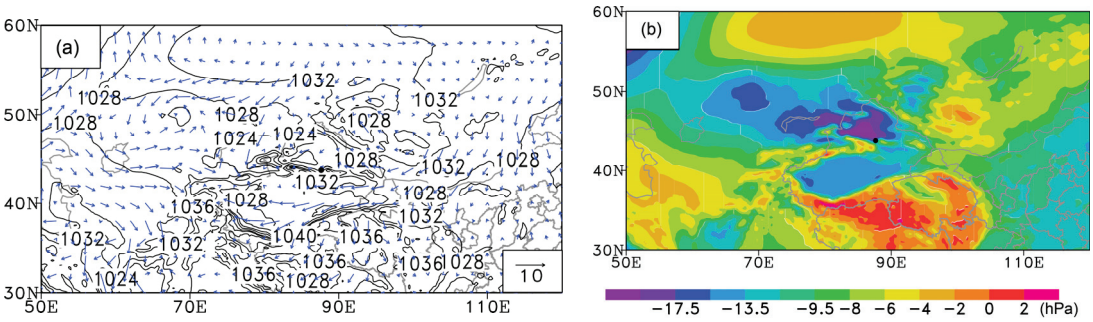

Figure 13. (**a**) Surface circulation pattern on 21 July 2015, and (**b**) an anomaly. Black dot represents Urmqi Meteorological stations.

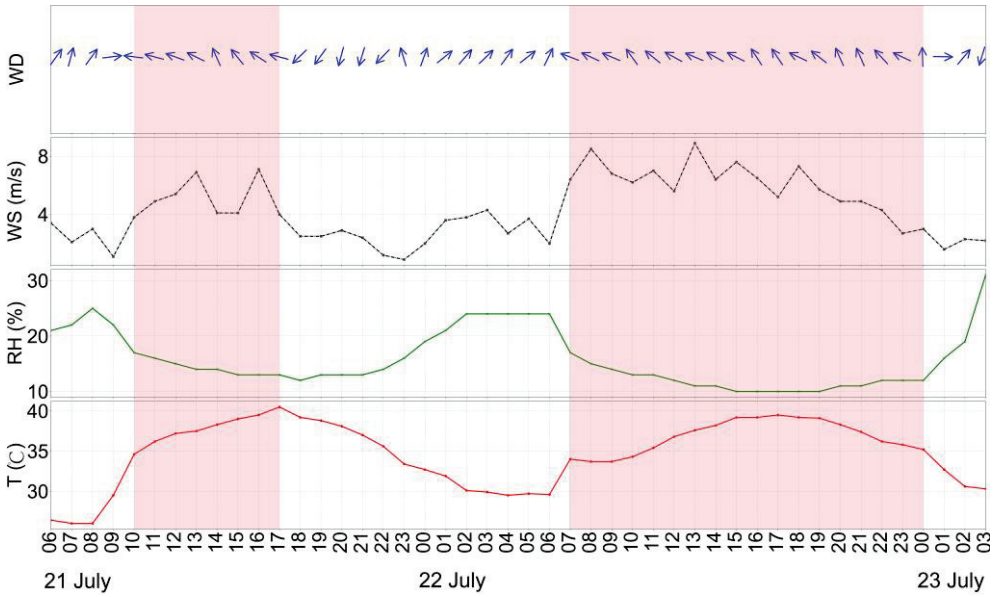

Figure 14. Changes in surface meteorological elements in Urumqi from 21 to 23 July 2015. The pink shaded area represents the Foehn wind (FW) period. Blue arrow represents 2 min average wind direction; black line is 2 min average wind speed; green line is relative humidity; red line is temperature.

4. Discussion

FW has brought many disasters to the local area in Urumqi due to its high wind speed and dry and hot characteristics. In the spring and autumn seasons, FW occurs frequently

and with high wind speeds, which often cause strong wind disasters in the area. The low FW speeds and high emissions of pollutants from winter heating are meteorological conditions that are not conducive to the diffusion of local pollutants in winter. Therefore, severe pollution easily occurs during winter FW periods. In summer, the airflow loses moisture on the windward slope and becomes dry. After crossing the mountain, airflow is forced to sink rapidly due to the terrain, causing adiabatic warming of the air. In the meantime, the weather is generally fair or slightly cloudy, which is favorable to local radiation warming during the FW period. Therefore, Urumqi is prone to high-temperature weather, which is related to the FW in summer. It has been noted that FW has different impacts on the local area in different seasons, so it is necessary to comprehensively monitor and forecast FWs.

Previous studies have shown that Xinjiang mostly experienced warm winters and dry springs during the El Niño period. This study found that the frequency of FW in Urumqi was relatively high during the El Niño period. The highest number of FW days and the highest temperatures in the past 15 years occurred during the strong El Niño event in 2015. During an El Niño period, the air–sea interaction causes abnormal atmospheric circulation, resulting in frequent and strong FW in Urumqi. In summer, FW also further intensifies high-temperature weather. Therefore, it is necessary to pay more attention to FW weather and prevent the occurrence of strong winds and extreme high temperatures in Urumqi during the El Niño period.

FW processes differ in different regions of the northern slopes of the Middle TianShan Mountains. In this paper, we used the data from Urumqi meteorological stations to determine the characteristics of FW speed, temperature, and humidity changes during FW in the last 15 years. Currently, more than 60 ground-based automatic meteorological stations have been deployed in and around Urumqi, providing valuable basic data for monitoring and early warning of FW in complex terrain. Our next step will be to classify the intensity of the FW process based on these 60 stations' long-term data to carry out a more detailed statistical analysis of FW at different stations by year, season and month, so as to more comprehensively reveal the distribution characteristics and change rules of different-intensity FWs on the north slope of the Middle Tianshan Mountains in China.

5. Conclusions

This article uses hourly ground meteorological data to analyze the annual, monthly, and daily variations in FW in Urumqi over the past 15 years, as well as the annual and monthly variations in the speed of FWs. A comparative analysis is also conducted on the difference between the monthly average temperature and the monthly average temperature during FW periods in Urumqi. In addition, the characteristics of changes in hourly temperature and relative humidity are investigated during the FW period. Using reanalysis data and the Oceanic Niño Index, the impact of the El Niño event on FW and the heat waves caused by the FW process is primarily discussed and verified. The specific conclusions are as follows:

(1) The annual distribution of FW days in Urumqi in the past 15 years presents a fluctuating pattern. The highest numbers of FW days occurred in 2010 and 2015, and the lowest number occurred in 2012; this year also had the most hours of strong FWs. The monthly distribution of FW dominates in spring (March, April, and May) and autumn (September, October, and November), with the lowest occurrence in February and July. The daily distribution of FW shows the highest frequency from 09:00 a.m. to 14:00 p.m.; in particular, the highest occurrence was at 10:00 a.m. and 11:00 a.m. in April and May.

(2) The annual average wind speed of ~2 m/s in Urumqi is much lower than the values of ~5 m/s during the FW period. In 2011, 2012, and 2014, the average FW speed exceeded 6 m/s, and the wind speed was the lowest at 3.8 m/s in 2021. The monthly average FW speed is higher in March, April, May, and June, while it is lower in December, January, and July.

(3) A significant impact of FW on temperature changes in Urumqi is found. The monthly average temperature is lower than that during the FW period, and the most significant temperature differences are 11.5 °C, 10.6 °C, and 9.5 °C in March, February, and January, respectively. This indicates that FW can easily cause high-temperature weather in summer. There was a total of 289 h of high temperature in Urumqi in the past 15 years, and 25.3% (73 h) were affected by FW weather. The highest number of hours of high temperature of 32 occurred in 2015.

(4) Through observational analysis, we confirmed that FW causes significant warming and reductions in humidity. The most significant temperature and relative humidity changes related to FW occurred in winter compared to other seasons. At the beginning of FWs, the changes in temperature and humidity are relatively severe, with the temperature increasing by 0.4 °C to 6.9 °C, and the relative humidity decreasing by −2% to −32%. At the end of FWs, the temperature decreases significantly from 5.4 °C to −0.7 °C, and the relative humidity increases significantly from −1% to 23%. During FW, there are insignificant changes in temperature and relative humidity, with a slight increase in temperature and a slight decrease in relative humidity.

(5) The abnormal occurrence of FW in Urumqi is consistent with EI Niño periods, with a correlation coefficient of 0.71.

(6) Urumqi experienced a heat wave from 21 to 23 July 2015, and the highest temperature reached 40.5 °C. Three factors contribute to the extreme high-temperature weather: the abnormally strong subtropical high pressure in Iran, the FW effect, and radiation heating. The effect of FW on intensifying extreme high temperatures cannot be ignored.

Author Contributions: Conceptualization, M.A., Q.H. and X.L.; data curation, M.A., Y.M. and S.L.; formal analysis, M.A., X.L. and Q.H.; funding acquisition, S.L. and Y.Z.; investigation, M.A., K.C., S.L. and Y.Z.; methodology, M.A. and X.L.; project administration, M.A.; resources, M.A., X.L. and K.C.; software, M.A. and Y.M.; supervision, X.L. and Q.H.; validation, M.A. and X.L.; visualization, M.A., X.L., Q.H. and Y.M.; writing—original draft, M.A. and X.L.; writing—review and editing, M.A. and X.L. All authors have read and agreed to the published version of the manuscript.

Funding: This research was funded by the National Natural Science Foundation of China (Grant No. 42205010) and the Xinjiang Meteorological Bureau Science and Technology Innovation Development Fund Project (MS202303).

Institutional Review Board Statement: Not applicable.

Informed Consent Statement: Not applicable.

Data Availability Statement: The data used in this paper can be provided by M.A. (maoln@idm.cn) upon request.

Conflicts of Interest: The authors declare no conflicts of interest.

References

1. Brinkmann, W. What is a foehn? *Weather* **1971**, *26*, 230–239. [CrossRef]
2. Seibert, R. South foehn studies since the ALPEX experiment. *Meteorol. Atmos. Phys.* **1990**, *43*, 91–103. [CrossRef]
3. Lentink, H.S. Extreme foehn in Switzerland: A Climatology and the Relation to Large Scale Flow. Master's Thesis, University Utrecht, Utrecht, Switzerland, 2012; pp. 1–65. Available online: https://studenttheses.uu.nl/handle/20.500.12932/15889 (accessed on 20 December 2023).
4. Richner, H.; Gutermann, T. Statistical analysis of foehn in Altdorf, Switzerland. In Proceedings of the International Conference on Alpine Meteorology, Chamb'ery, France, 1 January 2007; pp. 457–460.
5. Richner, H.; Hächler, P. Understanding and Forecasting Alpine Foehn. In *Mountain Weather Research and Forecasting*; Springer Atmospheric Sciences: Berlin/Heidelberg, Germany, 2013; pp. 219–260.
6. Vergeiner, J. South Foehn Studies and a New Foehn Classification Scheme in the Wipp and Inn Valley. Ph.D. Thesis, University of Innsbruck, Innsbruck, Austria, 2004; pp. 1–111.
7. Mayr, G.J.; Armi, L.; Arnold, S.; Banta, R.M.; Darby, L.S.; Durran, D.D.; Flamant, C.; Gaberšek, S.; Gohm, A.; Mayr, R.; et al. Gap flow measurements during the Mesoscale Alpine Programme. *Meteorol. Atmos. Phys.* **2004**, *86*, 99–119. [CrossRef]

8. Nishi, A.; Kusaka, H. Future changes of the extreme high-temperature events influenced by foehn winds in Niigata, Japan. *Atmos. Sci. Lett.* **2023**, *24*, e1137. [CrossRef]
9. Zhao, S.L.; Wang, R.K.; Guo, Y.B.; Tan, J.L.; Shi, Z.Z. The Foehn in the Middle Rang of Taihang Mountain. *Meteor Mon.* **1993**, *19*, 3–6.
10. Wang, Z.; Ding, Y.; Zhang, Y.; Fan, J.; Zhang, S.; Tian, L. Statistical Characteristics and Mechanism Analysis of Foehn Weather in the Eastern Foothills of Taihang Mountain II: Case analysis of the influence of leeward wave on the generation and propagation of Foehn wind. *Plateau Meteorol.* **2012**, *31*, 555–561.
11. Li, D.; Zhang, Q.; He, K.; Sun, J.; Zhao, Z. Analysis of Temporal and Spatial Characteristics of Foehn in Xingtai City. *J. Agric. Catastrophol.* **2022**, *12*, 122–124. [CrossRef]
12. Zhao, Z.; Ma, H.; Ding, Z.; Xu, Y. The Influence of the Foehn Wind on the Temperature of Baoding Area. *Shanxi Sci. Technol.* **2016**, *31*, 88–91. [CrossRef]
13. Maulen, A.; Li, X.; Wang, S.; Mu, S.; Li, S.; Zhong, Y. Temporal and Spatial Characteristics of Foehn on the North Slope of the Tianshan Mountains of China and Prediction Ability of European Fine Grid Numerical Products. *Mt. Res.* **2022**, *40*, 823–834. [CrossRef]
14. Ayitikan, M.; Li, X.; He, Q.; Musha, Y.; Tang, H.; Li, S.; Zhong, Y.; Ren, G. Characteristics and Establishment of Objective Identifification Criteria and Predictors for Foehn Winds in Urumqi, China. *Atmosphere* **2023**, *14*, 1206. [CrossRef]
15. Li, X.; Zhao, K.; Zhong, S.; Yu, X.; Feng, Z.; Zhong, Y.; Maulen, A.; Li, S. Evolution of Meteorological Conditions during a Heavy Air Pollution Event under the Influence of Shallow Foehn in Urumqi, China. *Adv. Atmos. Sci.* **2023**, *40*, 29–43. [CrossRef]
16. Li, X.; Xia, X.; Zhong, S.; Luo, L.; Yu, X.; Jia, J.; Zhao, K.; Li, N.; Liu, Y.; Ren, Q. Shallow foehn on the northern leeside of Tianshan Mountains and its influence on atmospheric boundary layer over Urumqi, China—A climatological study. *Atmos. Res.* **2020**, *240*, 104940. [CrossRef]
17. Li, X.; Xia, X.A.; Wang, L.; Cai, R.; Zhao, L.; Feng, Z.; Ren, Q.; Zhao, K. The role of foehn in the formation of heavy air pollution events in Urumqi, China. *J. Geophys. Res. Atmos.* **2015**, *120*, 5371–5384. [CrossRef]
18. Zhang, J.; Su, Q.; Sun, S. *Xinjiang Short-Term Weather Forecast Guidebook*; Urumqi, Xinjiang People's Publishing House: Urumqi, China, 1986; pp. 341–347.
19. Diao, P. The statistical characteristics and forecast of southeast gale in Urumqi in spring. *Xinjiang Meteorol.* **1991**, *14*, 16–18.
20. Meng, Q.; Lyu, B.; Diao, P. Research on the Distribution Law of Southeast Gale in Urumqi Area. *Xinjiang Meteorol.* **1995**, *18*, 6–10.
21. Wan, Y.; Cao, X.; Dou, X.; Lu, H. The Application of ECMWF Refined Net Numerical Forecast Data in the Southeast Gale in Urumqi. *Desert Oasis Meteorol.* **2014**, *8*, 32–38. [CrossRef]
22. Berknes, J. Atmospheric teleconnections from the equatorial Pacific. *Mon. Weather Rev.* **1969**, *97*, 163–172. [CrossRef]
23. Cane, M.A.; Zebiak, S.E. A theory for El Niño and the Southern Oscillation. *Science* **1985**, *228*, 1085–1087. [CrossRef]
24. Zhao, Z.C.; Luo, Y.; Huang, B. Global warming and El Niño events. *Clim. Chang. Res.* **2023**, *19*, 663–666. [CrossRef]
25. Lian, T.; Chen, D.; Tang, Y.; Wu, Q. Effects of westerly wind bursts on El Niño: A new perspective. *Geophys. Res. Lett.* **2014**, *41*, 3522–3527. [CrossRef]
26. Lian, T.; Wang, J.; Chen, D.; Liu, T.; Wang, D. A strong 2023/24 El Niño is staged by tropical Pacific Ocean heat content buildup. *Ocean-Land-Atmos. Res.* **2023**, *2*, 0011. [CrossRef]
27. Huang, B.; Thorne, P.W.; Banzon, V.F.; Boyer, T.; Chepurin, G.; Lawrimore, J.H.; Menne, M.J.; Smith, T.M.; Vose, R.S.; Zhang, H.M. Extended Reconstructed Sea Surface Temperature version 5 (ERSSTv5), upgrades, validations, and intercomparisons. *J. Clim.* **2017**, *30*, 8179–8205. [CrossRef]
28. Ren, H.-L.; Lu, B.; Wan, J.; Tian, B.; Zhang, P. Identification standard for ENSO events and its application to monitoring and prediction in China. *China J. Meteorol. Res.* **2018**, *32*, 923–937. [CrossRef]
29. Lei, Y.-N.; Gong, D.-Y.; Zhang, Z.-Y.; Guo, D.; He, X.-Z. Spatial-temporal characteristics of high-temperature events in summer in eastern China and the associated atmospheric circulation. *Geogr. Res.* **2009**, *28*, 653–662. [CrossRef]
30. Mao, W.; Chen, P.; Shen, Y. Characteristics and effects of the extreme maximum air temperature in the summer of 2015 in Xinjiang under global warming. *J. Glaciol. Geocryol.* **2016**, *38*, 291–304. [CrossRef]
31. Zhang, L.; Zhang, T.; Mao, W.; Si, J.; Zhang, T.; Wang, S. Analysis of the upper-air temperature change in Xinjiang region. *Arid Zone Res.* **2021**, *38*, 133–143.

Disclaimer/Publisher's Note: The statements, opinions and data contained in all publications are solely those of the individual author(s) and contributor(s) and not of MDPI and/or the editor(s). MDPI and/or the editor(s) disclaim responsibility for any injury to people or property resulting from any ideas, methods, instructions or products referred to in the content.

remote sensing

MDPI

Article

The Impact of Urbanization on Spatial–Temporal Variation in Vegetation Phenology: A Case Study of the Yangtze River Delta, China

Enyan Zhu [1], Dan Fang [2], Lisu Chen [2,3,*], Youyou Qu [1] and Tao Liu [1]

[1] College of Transport and Communications, Shanghai Maritime University, Shanghai 201306, China; eyzhu@shmtu.edu.cn (E.Z.); 202010612028@stu.shmtu.edu.cn (Y.Q.); liutao2@shmtu.edu.cn (T.L.)
[2] College of Ocean Science and Engineering, Shanghai Maritime University, Shanghai 201306, China; 202030410142@stu.shmtu.edu.cn
[3] State Key Laboratory of Marine Environmental Science, Xiamen University, Xiamen 361005, China
* Correspondence: lschen@shmtu.edu.cn; Tel.: +86-0213-8282-362

Abstract: The response of vegetation phenology to urbanization has become a growing concern. As impervious surfaces change as urbanization advances, the variation in vegetation phenology at the dynamic urbanization level was analyzed to significantly quantify the impact of urbanization processes on vegetation phenology. Based on the MOD13Q1 vegetation index product from 2001 to 2020, vegetation phenology parameters, including the start of the growing season (SOS), the end of the growing season (EOS), and the length of the growing season (GSL), were extracted, and the spatial–temporal variation in vegetation phenology, as well as its response to urbanization, was comprehensively analyzed. The results reveal that (1) from 2001 to 2020, the average rates of change for the SOS, EOS, and GSL were 0.41, 0.16, and 0.57 days, respectively. (2) The vegetation phenology changes showed significant spatial–temporal differences at the urbanization level. With each 10% increase in the urbanization level, the SOS and EOS were advanced and delayed by 0.38 and 0.34 days, respectively. (3) The urban thermal environment was a major factor in the impact of urbanization on the SOS and EOS. Overall, this study elucidated the dynamic reflection of urbanization in phenology and revealed the complex effects of urbanization on vegetation phenology, thus helping policymakers to develop effective strategies to improve urban ecological management.

Keywords: vegetation phenology; urbanization; spatial–temporal analysis; urbanization level; urban temperature; remote sensing

1. Introduction

Vegetation phenology refers to the sprouting, leaf expansion, flowering, fruiting, and defoliation of vegetation responding to external factors (temperature, precipitation, etc.) during the growth [1] period and is the most flexible biological indicator of seasonal environmental changes [2]. Research has shown that the phenology of vegetation changes over time. For example, the EOS, SOS, and GSL in the temperate regions of China tended to be delayed, advanced, and extended, respectively [3]. From 2001 to 2016, the trend in the SOS in freshwater swamps in northeastern China was for it to occur earlier, and the SOS in the Greater Khingan Mountains was earlier than that in the Songnen Plain [4]. With the development of society, human activities such as population growth, land use changes, and extensive resource exploitation have led to a range of environmental changes [5]. For instance, an increase in the impermeable surface area impacts the process of energy exchange between the atmosphere and the surface, which, in turn, changes the environment for vegetation growth [6]. Overall, with the development of climate warming and urbanization, the influence of urbanization on vegetation phenology has attracted growing attention and become a new urgent issue in phenology research.

Previous studies have found that with the advancement of urbanization, phenology will also change [7,8]. A study of 32 cities in China presented an EOS that was 5.4 days earlier while the SOS was 11.9 days later in rural areas compared to urban areas [9]. Using the percentage of the impervious layer to express the urbanization level, another research work found that an increase in the impervious layer will lead to an advanced SOS and a delayed EOS [10]. A tenfold increase in urban size may lead to a 1.3-day advance in the SOS and a 2.4-day delay in the EOS [11]. Previous studies have differed in their approach to dividing the urbanization level. However, most of them have only considered urban impacts on vegetation phenology under a fixed urbanization level, ignoring the process of urban expansion [12,13]. The percentage of impervious surfaces has also changed during the urbanization process, resulting in the urbanization level changing from year to year [14]. Thus, this study used a dynamic level that can be quantified using remote sensing technology, taking into account the process of urban sprawl. The impervious surface was used instead of the traditional method of establishing an urban–rural differential between rural and urban areas, which allows for a more significant quantification of the urbanization process affecting vegetation phenology.

In contrast to traditional ground-based methods, remote sensing images are not restricted by time or space. They not only facilitate the acquisition of long time series of vegetation phenology information but also compensate for the limited-scale coverage of field observation sites, which greatly promotes the development of vegetation phenology research [15]. MODIS remote sensing monitoring data have a suitable spatial resolution and a stable vegetation index, which is extensively used in vegetation phenology research. Thompson et al., used MODIS NDVI data to extract phenology information in the Alps and found that the higher the elevation, the shorter the GSL [16]. Sarvia et al., used MOD13Q1 data and found that different vegetation types have different responses to climate change [17]. Vegetation phenology parameters were extracted using MOD13Q1-NDVI data with spatial and temporal resolutions of 250 m and 16 days, respectively, for a total of 460 periods (https://search.earthdata.nasa.gov/, accessed on 1 February 2022). MOD11A2 surface temperature data with spatial and temporal resolutions of 1000 m and 8 days, respectively, were used (https://search.earthdata.nasa.gov/, accessed on 20 March 2022). MODIS product data have the advantages of good time continuity and a high spatial resolution [18–20] and are widely used in vegetation growth monitoring [21], soil moisture monitoring [22], and research on vegetation phenology changes [23,24]. The impervious surface data constitute global high-resolution impervious-surface-mapping products released by Prof. Peng Gong et al. for the period of 2001 to 2018 with a spatial resolution of 30 m [25] (https://data-starcloud.pcl.ac.cn/zh, accessed on 18 June 2022). The impervious surface data for 2019 and 2020 were supplemented using land use data sourced from 30 consecutive years of land use in China from 1990 to 2021 (China Land Cover Dataset, CLCD) [26], and the accuracy rate reaches 80%.

The maximum-slope-of-change method, the dynamic threshold method, and the sliding average method are commonly used to extract vegetation phenology parameters from remote sensing data [27,28]. Human factors such as the setting of the threshold and the window size in the dynamic threshold method and the sliding average method can produce errors in the results, while the maximum-slope-of-change method can avoid such errors. So, in this paper, the maximum-slope-of-change method was utilized to extract the vegetation phenology parameters, as it utilizes the slope of a fitted linear function to reflect the vegetation phenology trend more objectively and accurately, thus effectively avoiding the interference of human subjective factors with the vegetation phenology inversion.

This paper hypothesized a relationship between the ISP, LST, and vegetation phenology parameters. We defined phenological changes due to an increase in the impervious surface (ISP) as the effect of urbanization on phenology and phenological changes due to land surface temperature (LST) as the effect of the thermal environment on phenology as caused by urbanization. The processing flow of this study was as follows. Firstly, MODIS NDVI data from 2001 to 2020 were utilized to extract the vegetation phenology parame-

ters for the Yangtze River Delta region, including the EOS, SOS, and GSL. Secondly, the spatial–temporal features of vegetation phenology were analyzed. Thirdly, the vegetation phenology variation, along with the dynamic urbanization level, was analyzed to significantly quantify the impact of the urbanization process on vegetation phenology. Finally, the contribution of the urban thermal environment to the physical climate was explored.

2. Data and Methods

2.1. Study Area

The Yangtze River Delta region (29°12′ to 35°20′N and 114°54′ to 121°28′E) is located in eastern China, downstream of the Yangtze River, covering a total area of approximately 359,000 square kilometers. The region is dominated by a subtropical monsoon and temperate monsoon climate, and it is warm and humid year-round. Plains, hills, and mountains are the main terrain types, and the three main vegetation types are mixed evergreen deciduous broad-leaf forest, green broad-leaved forest, and temperate deciduous broad-leaved forest (Figure 1). As a region with strong economic power and rapidly developing urbanization levels in China, its total GDP reached CNY 24.5 trillion, and its total population reached 235 million people in 2020, which profoundly changed the urban ecological environment [29] (Table 1). In addition, the urbanization level was complete in the selected study area, making it an excellent natural experimental area for exploring the effects of urbanization on vegetation phenology. In addition, compared to existing research focusing on the area within the city and its surrounding limited areas, our selected study area covers areas with different urbanization levels, including rural areas and urban areas with various development levels, making the study area a natural experimental area for exploring the effects of urbanization on plant phenology.

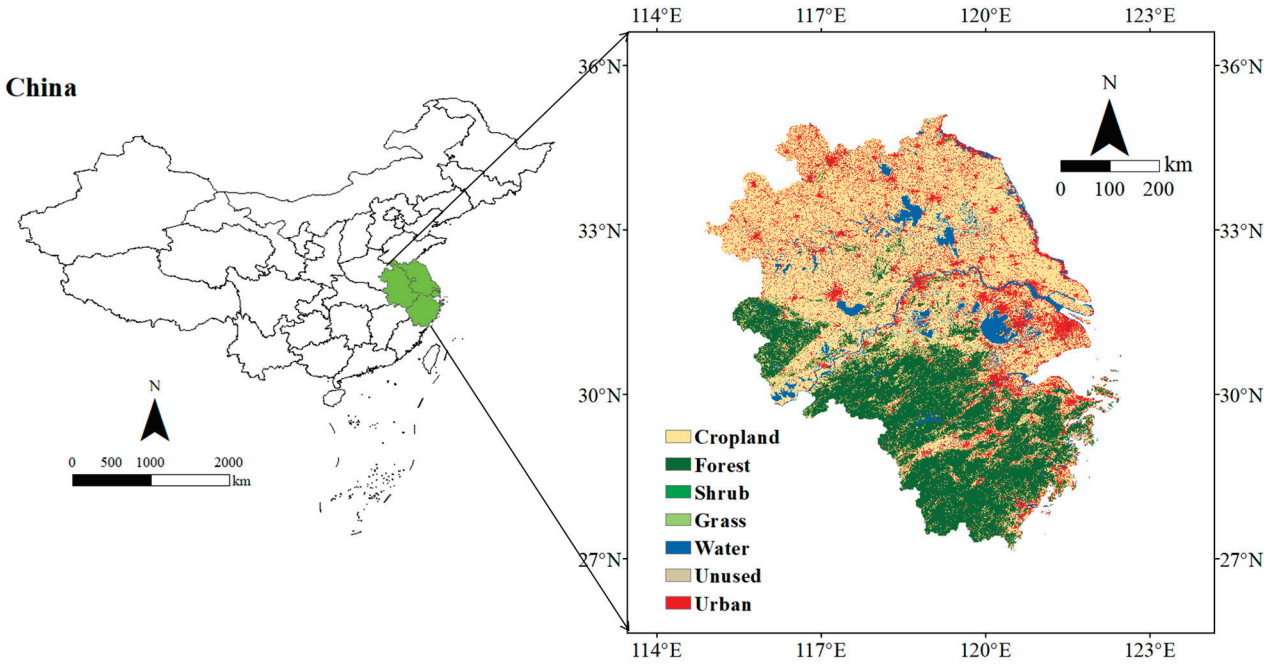

Figure 1. Land cover map of the study area in 2020.

Table 1. Population and GDP of provinces in the Yangtze River Delta region in 2020.

	Province	Population	GDP (Billion CNY)
1	Shanghai	24,870,895	38,700.58
2	Jiangsu	84,748,016	102,719
3	Zhejiang	64,567,588	64,613
4	Anhui	61,027,171	38,680.6

2.2. Data Source

The data used in this study include the MOD13Q1-NDVI dataset, the MOD11A2-surface temperature dataset, a land use dataset, and urban boundary data, as detailed in Table 2.

Table 2. Data sources and uses.

	Data	Year	Source	Uses
1	MOD13Q1-NDVI	2001–2020	https://search.earthdata.nasa.gov/, accessed on 1 February 2022	Extraction of vegetation phenological parameters
2	Impervious surface data	2001–2020	https://data-starcloud.pcl.ac.cn/zh, accessed on 18 June 2022	Definition of urbanization level
3	MOD11A2-Surface temperature data	2001–2020	https://search.earthdata.nasa.gov/, accessed on 1 February 2022	Extraction of surface temperature
4	Land use data	2001–2020	https://zenodo.org/record/5816591#.ZEOxa3ZBzIV, accessed on 11 August 2022	Selection of different types phenological changes in vegetation

2.3. Methods

2.3.1. Time-Series Reconstruction

MODIS is an important sensor onboard the Terra and Aqua satellites, generating the land vegetation data product MOD13Q1 with a spatial resolution of 250 m and a temporal resolution of 16 days, of which the normalized difference vegetation index (NDVI) layer is extensively used in large-scale vegetation phenology research [30]. However, cloud and snow cover, haze effects, and the performance of the sensor itself can have an impact on the radiant energy output from the sensor, resulting in valleys and peaks in the synthesized NDVI curves. These anomalies cause the accuracy of the parameter inversion results to decrease and deviate from the real vegetation activity on the surface. Therefore, reconstructing and smoothing the time series of NDVI data are necessary to improve the accuracy and effectiveness of the data. In this paper, the Savitzky–Golay (S-G) filtering method was chosen to fit the raw NDVI time-series data [31]. The S-G filtering method is a sliding window weighting algorithm proposed by Savitzky and Golay in 1960, where the weighting coefficients are obtained by the least-squares fitting of a given high-order polynomial within a sliding window [32]. The new curve obtained by the S–G filtering method can retain complete detailed information in the process of filtering out the noise interference and can describe the changes in long time-series data in more detail [33].

The Savitzky–Golay filtering (S–G) filtering method is as follows:

$$Y_j^* = \sum_{i=-m}^{m} \frac{C_j Y_{j+1}}{2m+1} \quad (1)$$

where Y represents the initial NDVI value, Y_j^* is the smoothed NDVI data, C_j is the filter coefficient for the least-squares fit, j is the initial coordinate of the sliding window, Y_{j+1} is the jth initial value in the sliding window, and $2m+1$ is the sliding window size.

2.3.2. Vegetation Phenology Parameter Extraction

Three phenological parameters, namely, SOS, GSL, and EOS, were selected to investigate the response of vegetation phenology to urbanization. In this study, the maximum-slope-of-change method was used to retrieve vegetation phenology parameters, which can effectively avoid the interference of human subjective factors and reflect vegetation phenology trends more objectively and accurately. The maximum-slope-of-change method is used to identify the date when the fitted curve first reaches the maximum rate of change, which is the vegetation phenology start time; similarly, the end time of vegetation phenology is the date when the curve reaches the maximum rate of decline in change. The length of the season is the length of time between the start time and the end time of the vegetation

phenology period. To eliminate the uncertainty caused by errors, the ranges of the SOS and EOS were restricted to a certain interval. The SOS and EOS were limited to Days 50–180 and Days 240–330 of the year, respectively [34,35]. Additionally, to minimize errors, we used only areas where there was no change in the land cover type (Figure 2).

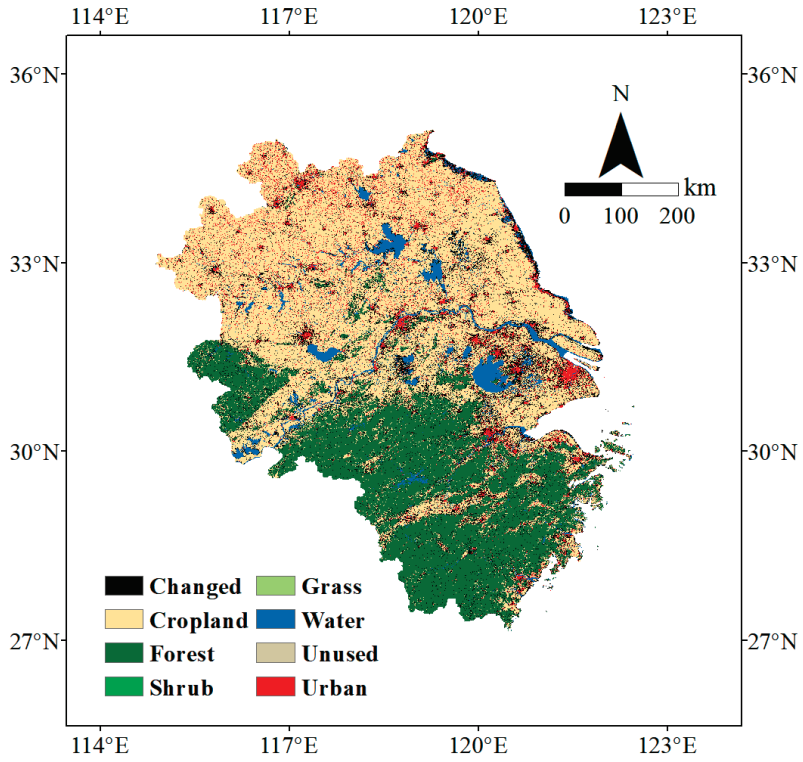

Figure 2. Changed and unchanged areas.

2.3.3. Dynamic Urbanization Level Setting

In this paper, we use the percentage of impervious surfaces to indicate different urbanization levels within the region. We first used remote sensing data to calculate the percentage of impervious surfaces (P_{ISP}) in every 1 km × 1 km grid and then used the P_{ISP} to classify the urbanization level. The following equation was used to calculate the P_{ISP}:

$$P_{ISP} = \frac{S_{ISP}}{S_{1km^2}} \times 100\% \quad (2)$$

where P_{ISP} is the percentage of impervious surfaces, and S_{ISP} is the area of impervious surfaces.

The P_{ISP} values are listed in descending order, from 100% to 0%, of the percentage value. Then, we divided the P_{ISP} into 100 equal-scale intervals (0–1%, 1–2%, . . ., 99–100%) as the urbanization levels. The urbanization level is the first level when the P_{ISP} is between 0% and 1%, the second level when it is between 1% and 2%, and so on. Areas with a proportion greater than 80% were defined as urban cores, areas with a proportion less than 20% were defined as rural areas, and areas with a proportion between 20% and 80% were defined as suburban areas. As the urban landscape changes, the percentage of impervious surfaces in the city also changes from year to year. The endpoints of the level change depending on the urbanization level in different locations, creating a dynamic urbanization level that allows for a better exploration of how the urban environment affects vegetation phenology. The dynamic effects of urbanization on vegetation phenology were expressed by phenological parameters at each level to determine the spatial–temporal variability in phenology at the urbanization level. The grid at 0% impervious surface was used as the initial base, and all initial grid values were averaged. The process of determining the level is shown in Figure 3. Figure 4 shows the urbanization levels in 2001 and 2020.

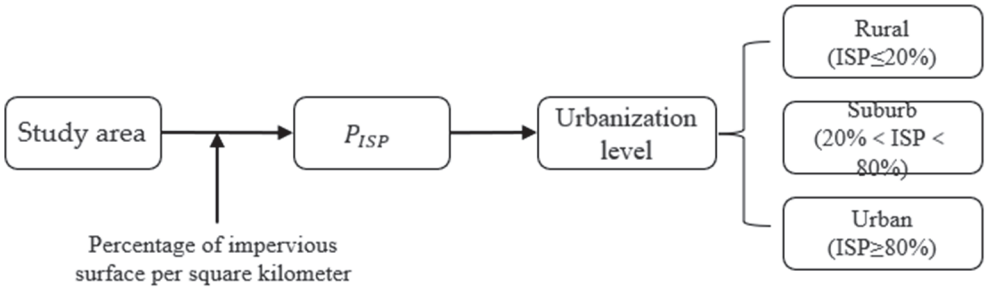

Figure 3. Process for determining the urbanization level.

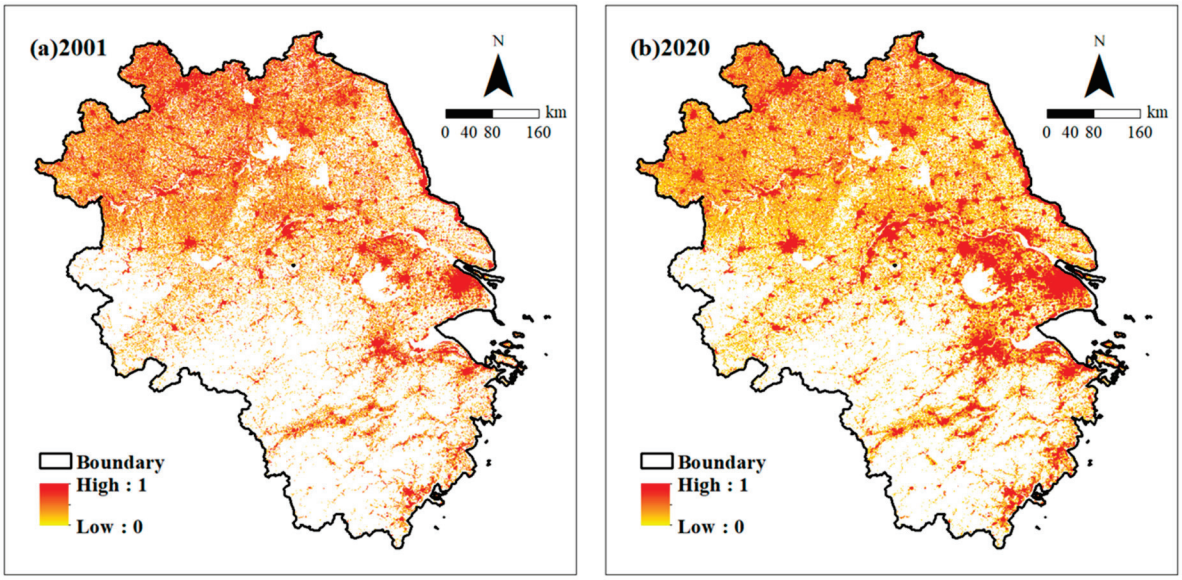

Figure 4. Maps of the urbanization levels in the study area in 2001 and 2020.

2.3.4. Trend Analysis of Vegetation Phenology

We used linear regression to explore variations in phenology indicators during 2001–2020, which was calculated as follows:

$$S = \frac{n\sum_{t=1}^{n} t \times P_t - \sum_{t=1}^{n} t \sum_{t=1}^{n} P_t}{n \times \sum_{t=1}^{n} t^2 - \left(\sum_{t=1}^{n} t\right)^2} \quad (3)$$

where t is the year, P_t is the SOS, EOS, or GSL in year t, S is the trend in the SOS, EOS, or GSL over time in days/year, and n is equal to 20. A slope greater than 0 indicates a trend in which the SOS or EOS is delayed or a trend in which the GSL is extended. A slope smaller than 0 indicates that the GSL tends to shorten, while the SOS and EOS tend to advance. The magnitude of the slope indicates the speed at which the SOS and EOS are delayed or advanced or the GSL is extended or shortened.

2.3.5. The Impact of Urbanization on Vegetation Phenology

We quantified the differences between different levels and nonurbanized areas (ISP = 0) as ΔSOS, ΔEOS, and ΔGSL. To explore the effect of urbanization over the course of a year, we calculated trends in phenology using the following equations:

$$\Delta SOS_{ti} = a_1 \Delta ISP_{ti} + c \quad (4)$$

$$\Delta SOS_{ti} = b_1 \Delta LST_{ti} + c_1 \quad (5)$$

$$\Delta EOS_{ti} = a_2 \Delta ISP_{ti} + d \quad (6)$$

$$\Delta EOS_{ti} = b_2 \Delta LST_{ti} + d_1 \quad (7)$$

$$\Delta GSL_{ti} = a_3 \Delta ISP_{ti} + e \quad (8)$$

$$\Delta GSL_{ti} = b_3 \Delta LST_{ti} + e_1 \quad (9)$$

where ΔSOS_{ti}, ΔEOS_{ti}, and ΔGSL_{ti} are the ΔSOS, ΔEOS, and ΔGSL, respectively, of the i-th urbanization level in year t; ΔISP_{ti} is the difference between the nonurbanized area (ISP = 0) and the urbanization level in year t; and the value range of i is 1–100.ΔLST_{ti} represents the temperature difference between the i-th level in year t and nonurban areas (ISP = 0) in year t. When exploring the relationships between the SOS, EOS, and GSL and temperature, spring and fall temperatures and average annual temperatures were used. The parameter *a* indicates the effects of urbanization on phenology, and the parameter b indicates the effects of temperature changes on phenology.

2.3.6. Distinguishing the Influences of Urban Thermal Environments on Changes in Vegetation Phenology

Thermal and nonthermal environmental factors are the two main categories of factors of urbanization that affect vegetation phenology. In this paper, we previously hypothesized a relationship between ISP, LST, and vegetation phenology parameters, which we quantified using linear regression with a known fixed-intercept model [36]. First, all the data were normalized, and then the phenological changes caused by the increase in impervious surfaces were defined as the influence of urbanization on phenology. Second, the change in phenology owing to surface temperature was defined as the effect of the urban thermal environment on phenology. The following equations were used to calculate the contribution rates of the LST and ISP:

$$\Delta LST_{ti} = \beta \Delta ISP_{ti} + c \quad (10)$$

$$CR = \frac{\beta * b_i}{a_i} \times 100\% \quad (11)$$

where CR indicates the contribution rate of the urban thermal environment to the effect of urbanization on vegetation phenology. A CR > 100% indicates that the thermal environment is the only factor affecting vegetation phenology caused by urbanization.

3. Results and Discussion

3.1. Average Rate of Changes in Vegetation Phenology

The variation in vegetation phenology is shown in Figure 5, with a clear trend in vegetation phenology over time. The variation in the SOS was more erratic, with an average advance of 0.41 days/year. The amplitude of change from 2006 to 2009 was relatively uniform (Figure 5a). The variation in the EOS showed a trend of being delayed, but the delay trend was less variable than that in the SOS. The average delay was 0.16 days per year, and all SOSs fell between Days 286 and 291 (Figure 5b). The duration between the SOS and EOS was defined as the length of the growing season of the vegetation. The SOS showed an advancing trend, while the EOS showed a trend of being delayed, leading to a trend of the GSL being extended. The findings indicated that the GSL was extended by 0.57 days per year on average, with a relatively stable change from Days 208 to 210 from 2015 to 2020 (Figure 5c).

To explore the variations in vegetation phenology among urban, rural, and suburban areas, this study extracted the average values of phenology in urban, rural, and suburban areas and fitted them with a linear regression equation. The results are shown in Figure 6. From 2001 to 2020, the average SOSs were on Days 86, 82, and 77 in rural, suburban, and urban areas, respectively, all showing early trends. Rural areas advanced by an average of 0.46 days per year, and suburban areas showed the greatest change, advancing by an average of 0.52 days per year. The trend in urban areas was not obvious, with an increase of 0.16 days per year (Figure 6a). Figure 6b shows the interannual variation in the average EOSs, all of which exhibit a trend of being delayed. The average EOSs for urban, rural, and

suburban areas were on Days 293, 278, and 285, respectively. The largest variation was in rural areas, with an average delay of 0.58 days per year, and the smallest variation was in urban areas, with a delay of 0.14 days per year. The change in suburban areas was between those in rural and urban areas, with a delay of 0.4 days/year. The GSLs in rural, suburban, and urban areas all tended to extend due to the advance in the SOS and the delay in the EOS (Figure 6c). The greatest variation in the GSL was observed in suburban areas, with a lengthening of 1.05 days per year and a mean GSL of 203 days. The average GSL in rural areas was 192 days, with a mean delay of 1.02 days per year. The lowest amplitude of GSL was found in urban areas, where the average prolongation was 0.32 days per year, with a mean GSL of 216 days.

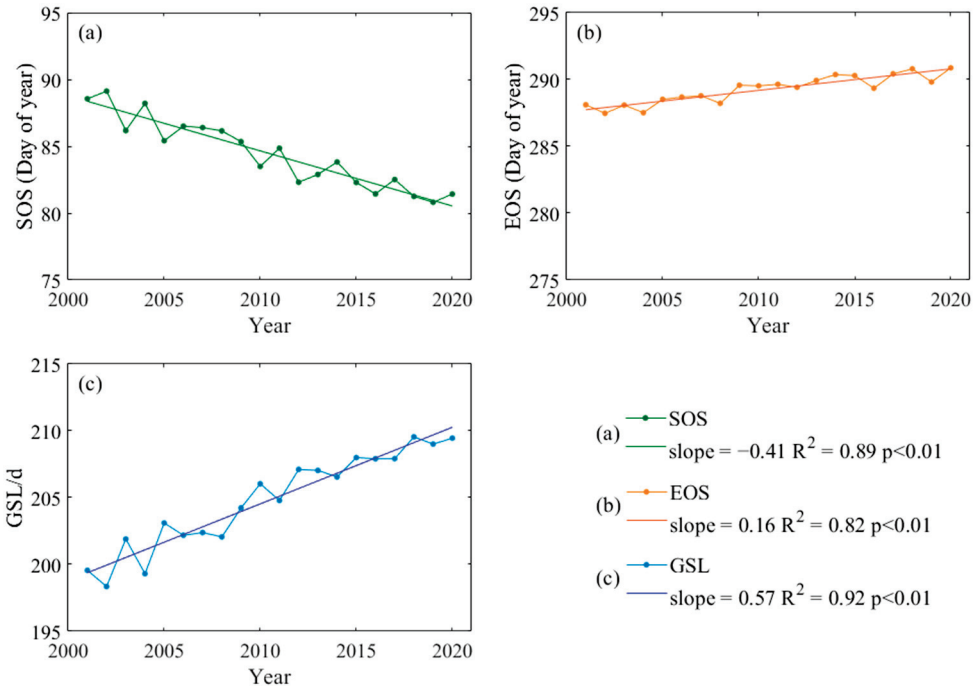

Figure 5. Variation in vegetation phenology.

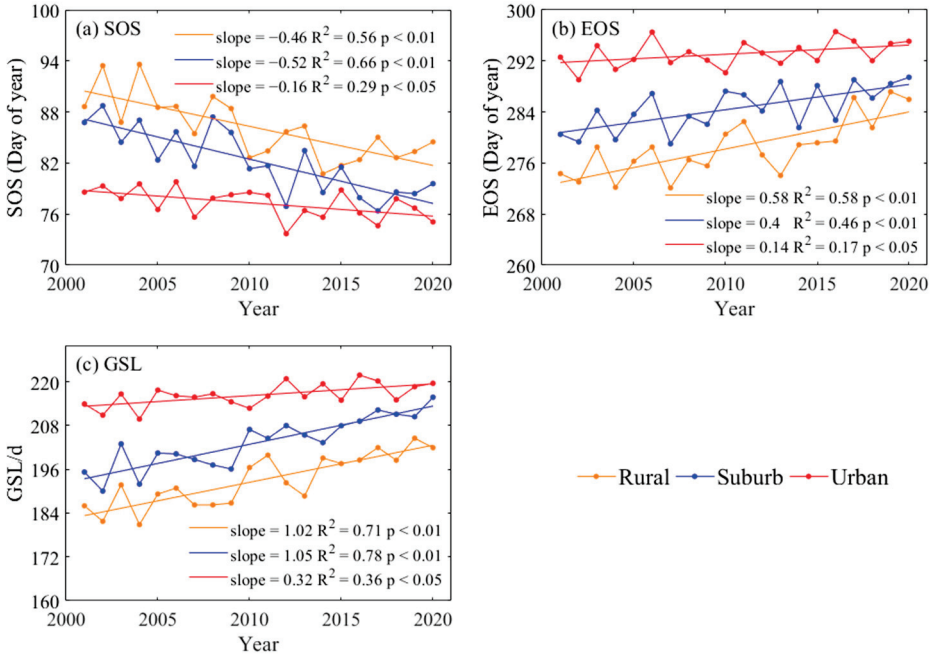

Figure 6. Variation in vegetation phenology in urban, suburban, and rural areas.

We also analyzed the variability in phenology for different land cover types, and the results are shown in Figure 7. The built-up area contains green vegetation such as green belts, so phenological parameters can also be extracted. The trends in the SOS and EOS were the same for all five types, with the SOS showing a trend of advancing and the EOS showing a trend of being delayed. The SOS advanced by 0.29 days/year (grassland), 0.13 days/year (shrub), 0.13 days/year (crop), 0.08 days/year (built-up area), and 0.06 days/year (forest). The EOS was delayed by 0.39 days/year (grassland), 0.31 days/year (forest), 0.14 days/year (crop), 0.14 days/year (built-up area), and 0.1 days/year (shrub).

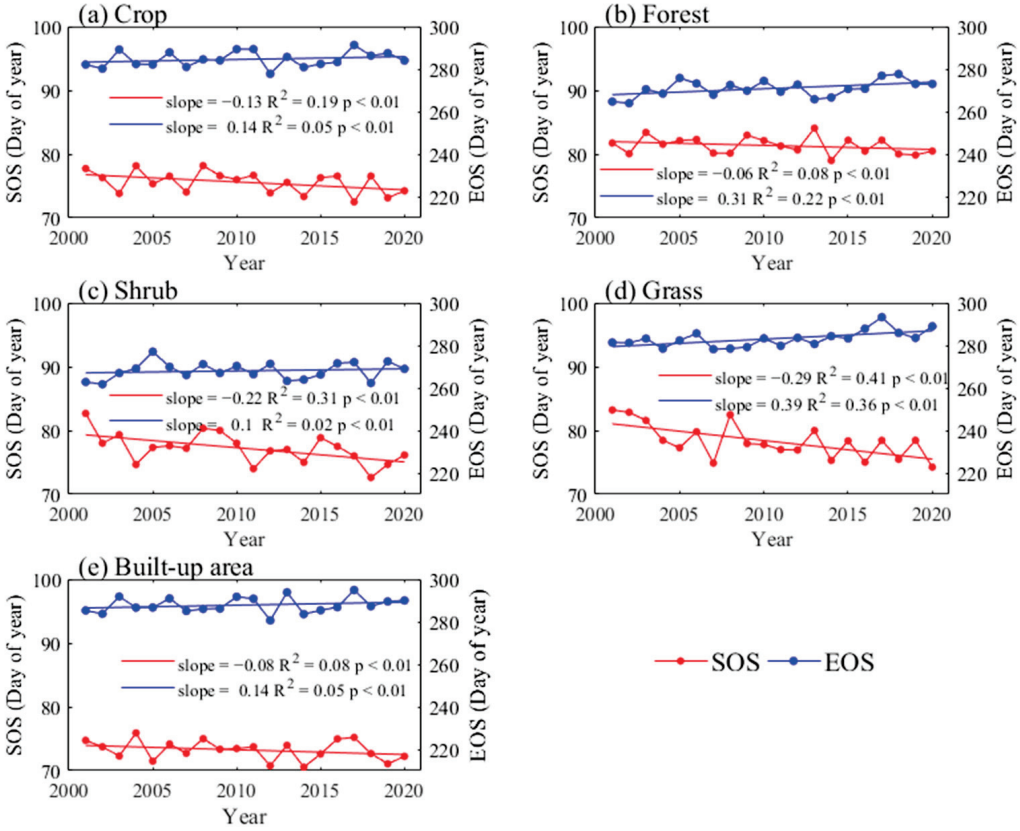

Figure 7. Variability in the phenology of five different land types.

The results of the SOS, EOS, and GSL of the five land cover types (farmland, shrub, grassland, forest, and built-up area) are displayed in Figure 8. The SOS on the five land cover types began in March, with an average distribution between Day 73 and Day 82. The built-up area had the earliest onset time, with the average on Day 74. Excluding built-up areas, the earliest average start time among the four vegetation types was for agricultural land, occurring on around Day 75, followed by shrubs and grasslands, occurring on Days 77 and 78, respectively. The EOS of forests was evenly distributed on Day 81, with the latest SOS (Figure 8a). The EOS started in September, with an average distribution between Days 268 and 287. The built-up areas had the latest EOS, with the average being on Day 287. The EOS occurred later in agricultural and grassland areas on Day 284 and Day 283, respectively. The EOS of forests was evenly distributed on Day 271, and shrubs had the latest EOS, distributed on Day 268 (Figure 8b). The GSL was distributed between 190 and 215 days, with the longest time GSL occurring in built-up areas at 215 days and the shortest time GSL occurring in forested areas at 190 days (Figure 8c).

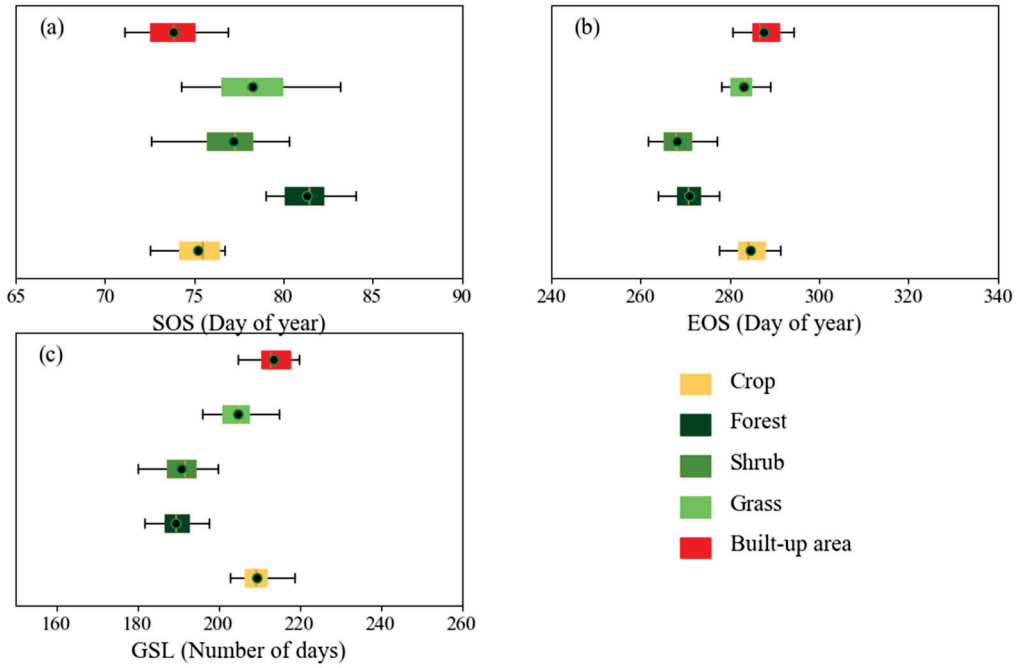

Figure 8. Box plots of the different land cover types. (**a**) shows the distribution of SOS per year for the five land types. (**b**) shows the distribution of EOS per year for the five land types. (**c**) shows the distribution of GSL per year for the five land types.

The vegetation phenology changed over time, with the SOS, EOS, and GSL showing trends of being advanced, delayed, and extended, respectively, which is similar to the findings of previous related studies. For example, Wang et al. studied the spring vegetation phenology in 292 cities in China and found that 78.3% of the cities showed an early trend in spring vegetation phenology [37]. Jiao et al., used integrated empirical mode decomposition (EEMD) to explore the changes in regional phenology in China and reported that the national average SOS advanced by 0.01 days/year and that the average delay in the EOS was 0.20 days/year [38]. This phenomenon can be attributed to several factors, such as global warming and precipitation. Research suggests that adequate precipitation may advance the SOS on the Tibetan Plateau, while the advancement of the SOS in meadow areas may be associated with increased temperature [39]. The EOS and GSL were obviously positively correlated with temperature in arid Central Asia, while the SOS was obviously negatively correlated with temperature [40]. The discrepancies in the variation in phenology between urban, rural, and suburban areas indicate that different levels of urbanization lead to different trends in phenology. The changes were more dramatic in suburban areas than in urban areas, which may be because the urban environment has stabilized, while the suburbs are in a rapid stage of urbanization.

3.2. Spatial Distribution Characteristics of Vegetation Phenology

The results of the spatial distribution of vegetation phenology are shown in Figure 9. Figure 9a shows the average SOS, with an early trend from northwest to southeast. The SOS in northern Anhui (including Fuyang, Bozhou, Huabei, Suizhou, and northern Liuan) and Xuzhou and Jiangsu were significantly later than those in other regions, with the SOS concentrated on Days 93 to 107. Compared with those in other regions, the SOSs in Anqing and southern Liuan in Anhui and the remaining part of Jiangsu were earlier than in other regions, with the SOS concentrated on Days 72 to 79. Figure 9b shows the average EOS distribution, with time gradually advancing from north to south. The EOSs in northern Anhui, Jiangsu, and Shanghai were significantly later, mostly concentrated between Days 285 and 300. In the southern region, the EOS was significantly earlier due to the higher altitude, and it was mostly concentrated between Days 270 and 280. Figure 9c shows

the average GSL distribution, which was mostly concentrated between 180 and 200 days. The early SOS and late EOS resulted in a significantly longer GSL in Jiangsu than in the other regions. Since the EOS was significantly later than in other regions, the GSL was longer in northern Anhui.

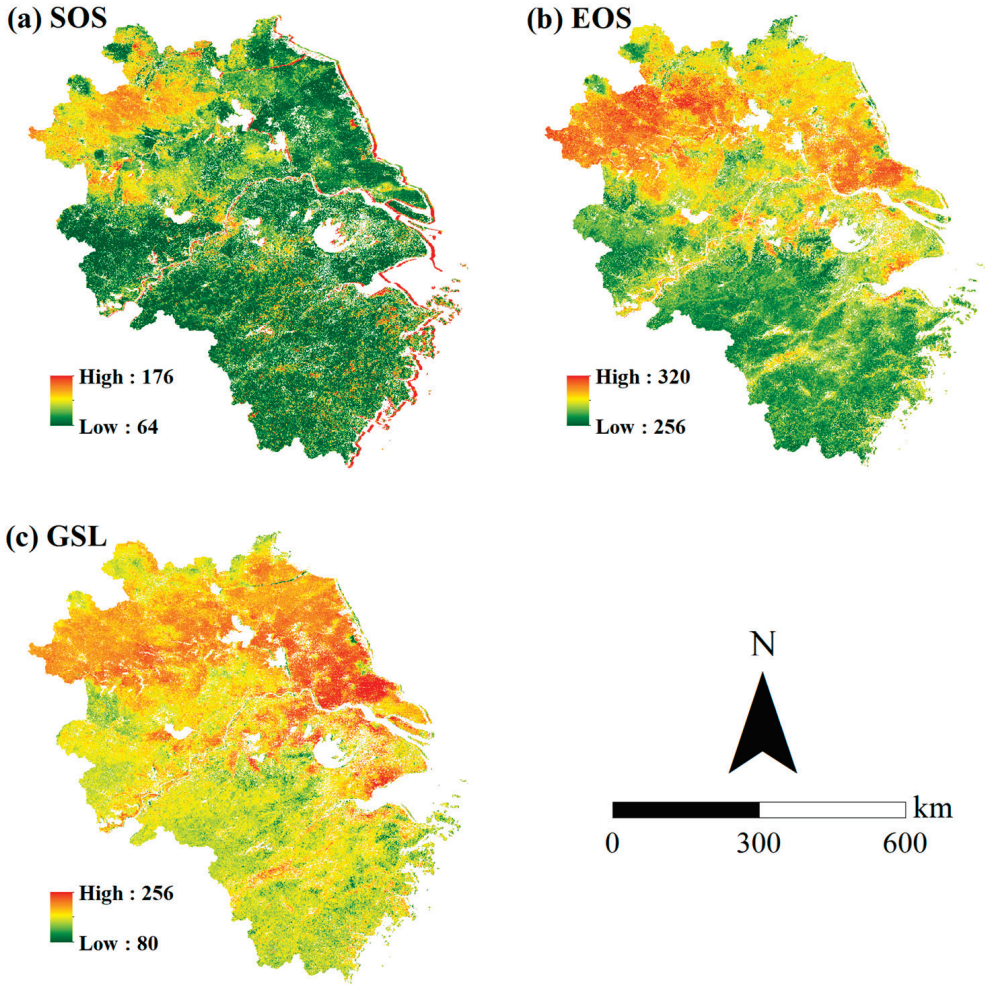

Figure 9. The average vegetation phenology from 2001 to 2020.

The results showing the trends in vegetation phenology changes are shown in Figure 10. Figure 10a shows the distribution of SOS variation, where the proportion of areas with an early SOS (slope < 0) was 40.33%, and the proportion of areas with a delayed SOS (slope > 0) was 59.67%. The SOS in Fuyang, Bozhou, Huabei, Suizhou, and northern Bengbu in Anhui showed obvious trends of being delayed, with delays of 1.75, 3.18, 2.86, 2.80, and 2.2 days, respectively. Figure 10b shows the distribution of EOS changes, and most of them showed trends of being delayed. Delayed areas accounted for 95.27%, and advanced areas accounted for only 4.73%. The junction of Anqing, Chizhou, Tongling, and Wuhu in Anhui Province and the southern part of Yancheng in Jiangsu Province showed early trends, with variations ranging from 1 to 3 days. The phenology in other regions showed a trend of being delayed, with variations ranging from 1 to 2 days. Figure 10c shows the distribution of GSL changes, and the percentages of regions with longer and shorter GSLs were 61% and 39%, respectively.

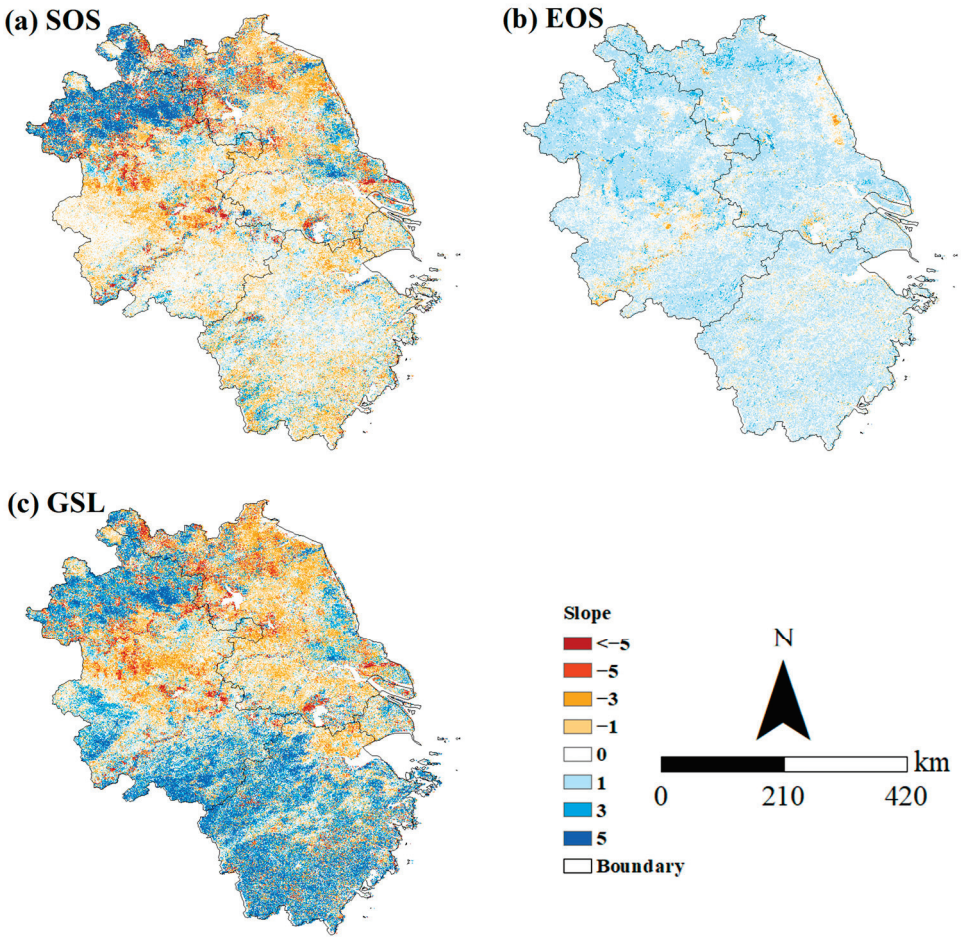

Figure 10. Spatial–temporal variation in phenology from 2001 to 2020.

The vegetation phenology showed significant spatial differences, with the EOS being earlier in the south than in the north and the GSL being shorter than in the north. The possible reason for this phenomenon is the altitude factor. Studies have shown that the higher the altitude, the later the SOS and the earlier the EOS, resulting in a shorter GSL [41,42]. The southern part of the research area is at a higher elevation than the northern part and, therefore, has a shorter growing season length. In contrast to the distribution of EOS changes, the distributions of SOS and GSL changes were not uniform, and the rates of change varied greatly. There were some areas where the level of SOS delay was greater, such as northern Anhui. The EOS variation was equally distributed and less variable than the SOS variation, ranging between 1 and 2 days. This suggests that the SOS is more sensitive to surrounding environmental factors than is the EOS, and similar conclusions have been reached in prior studies. Lukasová et al., studied the influence of altitude on the phenology of beech and reported that spring phenology was closely related to altitude, while fall phenology was not closely related to altitude [43]. Hou et al. reported that the daytime temperature was the main element that promoted the SOS in the northeast region, while the effect on the EOS was not significant [44].

3.3. Trends in Vegetation Phenology at the Urbanization Level

Figure 11a shows that the SOS advanced with changing rural–urban levels, with the average SOS in rural areas (Day 86.75, ISP $\leq$ 20%) occurring 3.09 days later than the average SOS in urban areas (Day 83.66, ISP $\geq$ 80%). When the urbanization level was below 60%, the SOS advanced significantly as the urbanization level increased; when the urbanization process exceeded 60%, the SOS gradually stabilized and did not become significantly earlier. Figure 11b shows that the EOS showed a trend of being delayed at the rural–urban level,

with the average EOS in rural areas (Day 280.34, ISP $\leq$ 20%) delayed by 81 days compared with the average EOS in urban areas (Day 283.15, ISP $\geq$ 80%). When the urbanization level was less than 50%, the EOS showed a trend of being delayed with increasing urbanization levels; when the urbanization level was more than 50%, the EOS tended to stabilize and did not change significantly. Figure 11c shows that the GSL exhibited an increasing trend at the rural–urban level, with an average GSL of 193.60 days in rural areas, which was 6.1 days shorter than the average GSL in urban areas (199.70 days). The GSL gradually stabilized when urbanization exceeded 60%.

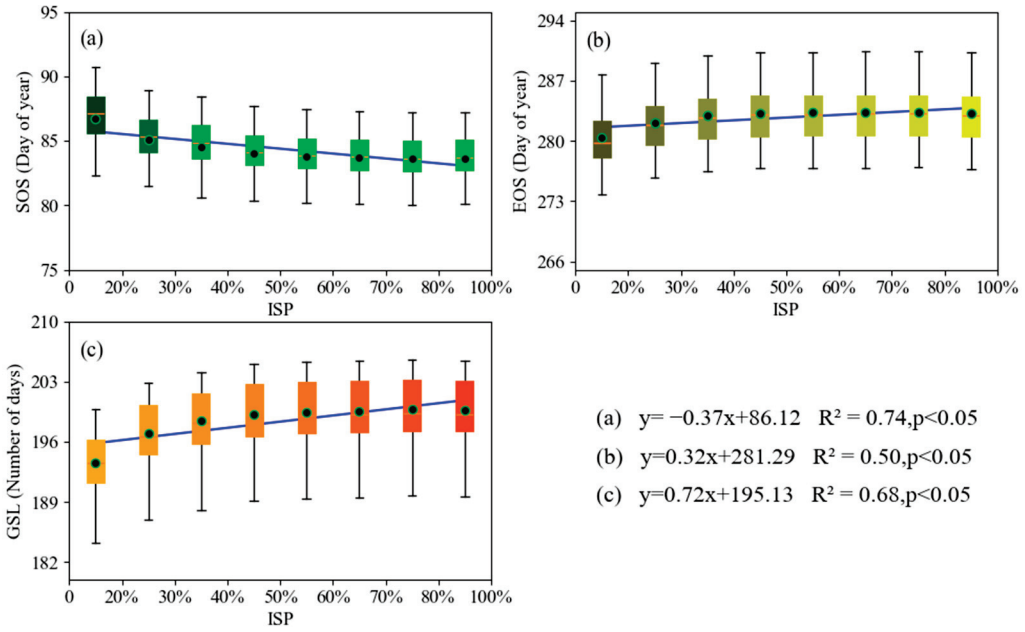

Figure 11. Vegetation phenology changes with increasing urbanization levels. (**a**) shows the changes in the SOS with the changes in the urbanization level. (**b**) shows the changes in the EOS with the changes in the urbanization level. (**c**) shows the changes in the GSL with the changes in urbanization level.

With accelerated urbanization, the urban environment has undergone significant changes, with profound effects on vegetation phenology. Studies have shown that urbanization changes the land cover type and has an impact on the surrounding environment, thus profoundly altering the vegetation phenology in the region. As the level of urbanization increases, the SOS, EOS, and GSL appear to be advanced, delayed, and prolonged, respectively, which is similar to the findings of prior studies. Li et al., reported a later SOS and earlier EOS in rural areas than in urban areas [10]. Ren et al., explored the relationship between urbanization and vegetation phenology and reported that the vegetation SOS occurred approximately 2.4 days earlier, the EOS occurred approximately 0.7 days later, and the GSL was 3.1 days longer in urban areas than in rural areas [45].

3.4. The Impact of Urbanization on Urbanization-Level Phenology

To quantify the effect of urbanization on vegetation phenology, a linear regression of the difference in vegetation phenology and the difference in urbanization level was performed. The results of the study are presented in Figure 12. The evolution of the ΔSOS showed a clear trend toward advancement at the urbanization level. With each 10% increase in the percentage of impervious surfaces, the ΔSOS decreased by 0.38 days, indicating a general trend of SOS advancement with increasing levels of urbanization. The average ΔSOS in rural and urban areas was 0.57 days and 3.72 days, respectively (Figure 12a). Figure 12b shows that the change in ΔEOS exhibited a trend of being delayed at the urbanization level. When the urbanization level increased by 10%, the ΔEOS was delayed by 0.34 days. The average ΔEOS was 1.14 and 3.97 days for rural and urban areas, respectively. The ΔGSL showed a positive trend at the urbanization level, with the ΔGSL

increasing by 0.57 days for each 10% increase in impervious surfaces. The average ΔGSLs for the rural and urban areas were 0.23 and 4.58 days, respectively (Figure 12c). Overall, from 2001 to 2020, there was a tendency for the SOS to be advanced with changing rural-to-urban levels and for the EOS and GSL to be delayed with changing rural-to-urban levels.

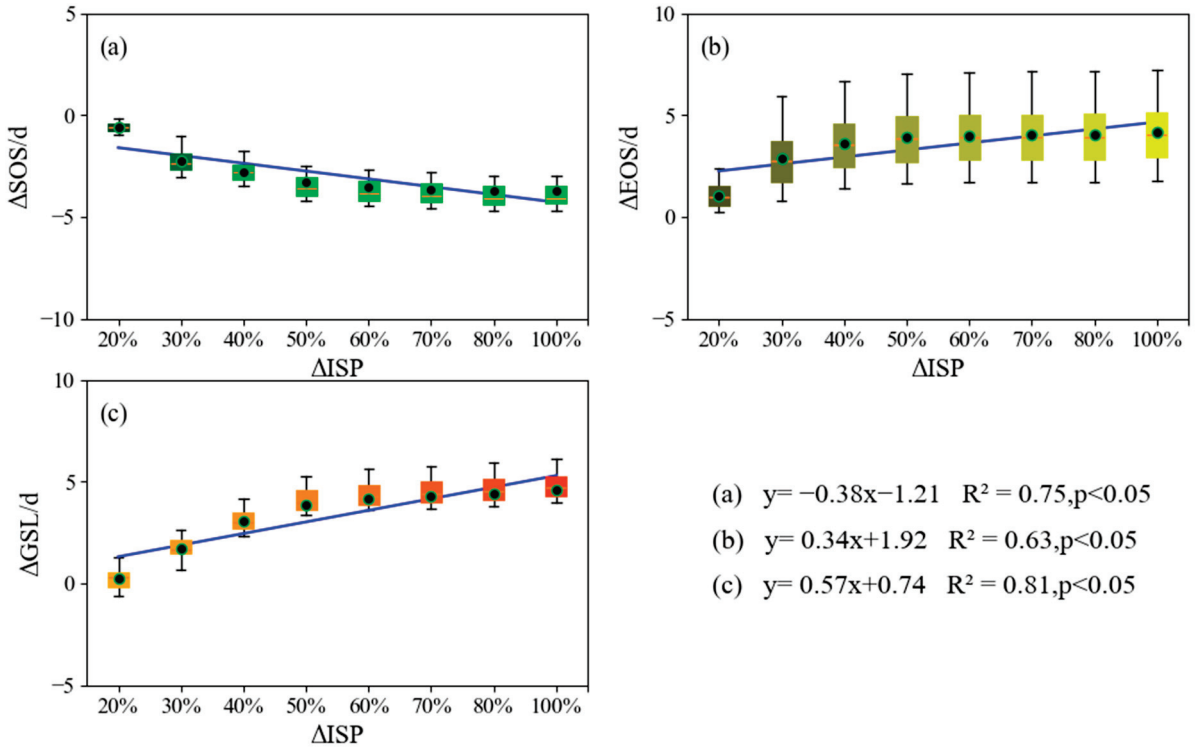

Figure 12. Effect of changing P_{ISP} on urbanization-level phenology. (**a**) shows the variation in ΔSOS with urbanization level differences. (**b**) shows the variation in ΔEOS with urbanization-level differences. (**c**) shows the variation in ΔGSL with urbanization-level differences.

The results showed that the discrepancy in vegetation phenology among urban areas and rural areas increased with increasing urbanization levels. When the urbanization level reaches a certain height, the differences between the two areas gradually tend to level off. The differences in vegetation phenology under different levels of urbanization are likely related to several factors [15]. First, areas with low urbanization levels (e.g., less than 20% impervious surfaces) are dominated by nonurban factors, and their phenology is mainly attributed to natural vegetation (e.g., forests, farmland, etc.). Areas with high levels of urbanization (e.g., >80% impervious surfaces) are subject to phenological changes due to the effects of urbanization (e.g., the urban thermal environment). This finding is congruent with existing findings. Ruan et al. investigated the relationship between phenology and the urban–rural distance in 32 major cities in the Northern Hemisphere and found that 22 cities experienced earlier SOSs and 19 cities experienced delayed EOSs as the distance increased, leading to greater differences in phenology between rural and urban areas [46].

3.5. Impacts of Rising Temperatures on Phenology across Urbanization Levels

To explore the relationships between temperature and phenology at the rural–urban level, this paper analyzed the relationships between spring temperature differences and the ΔSOS, between fall temperature differences and the ΔEOS, and between annual mean temperature differences and the ΔGSL using linear regression. Figure 13a shows that the ΔSOS was negatively correlated with the difference in spring surface temperature, and the ΔSOS of vegetation phenology increased with increasing spring temperatures. The results suggest that increased spring temperatures can advance the SOS. For each 1 °C increase in spring surface temperature, the ΔSOS was advanced by 0.47 days. The advancement of the

SOS was more obvious when the temperature was increased by 2–10 °C. Figure 13b shows a positive correlation between the ΔEOS and the difference in surface temperature in autumn. As the autumn temperature increased, the ΔEOS increased, indicating that the autumn surface temperature promoted a delay in the EOS. The effect of the fall surface temperature on the EOS was not strong, with the ΔEOS delayed by 0.13 for each 1 °C increase in the fall surface temperature. Figure 13c shows that the ΔGSL was positively correlated with the difference in the mean annual temperature. As the mean annual temperature increased, the GSL increased. The GSL increased by 0.6 days for each 1 °C increase in the annual mean temperature.

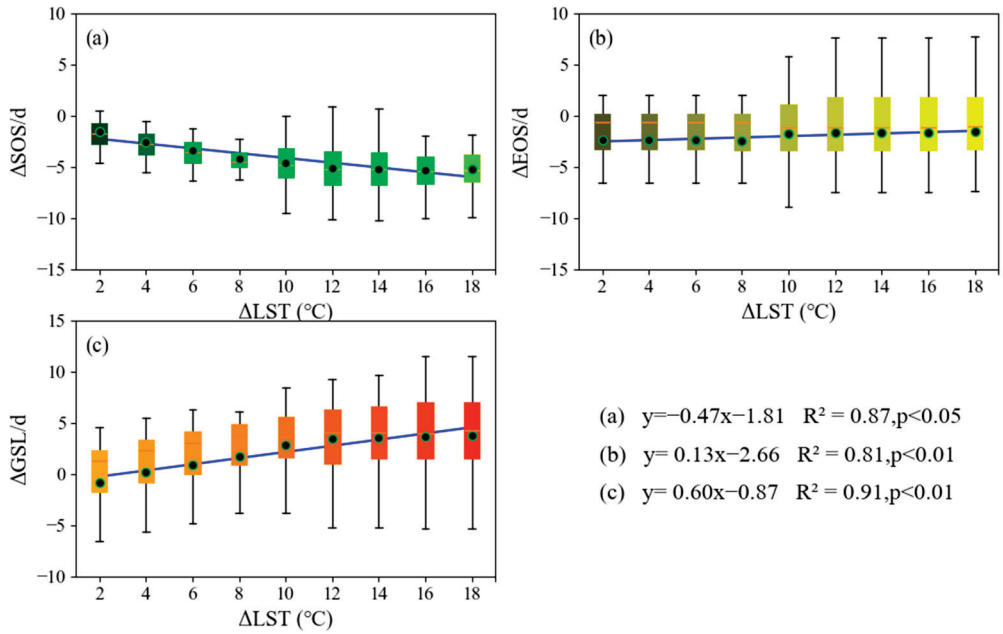

Figure 13. The effect of surface temperature on urbanization-level phenology. (**a**) shows the variation in ΔSOS with temperature differences. (**b**) shows the variation in ΔEOS with temperature differences. (**c**) shows the variation in ΔGSL with temperature differences.

We calculated the contribution rate of temperature changes to vegetation phenology to distinguish the warming effect from the environmental effect of urbanization. For the relationships between ΔISP, ΔLST, and ΔSOS, the slopes of the ΔISP − ΔSOS normalization ranged from −0.75 to −0.95 when anchored to a given level. For ΔISP − ΔLST − ΔSOS, the slope ranged from −0.76 to −0.90 days per year. In terms of the relationships between ΔISP, ΔLST, and ΔEOS, the slopes of the ΔISP − ΔEOS normalized curves ranged from 0.80 to 0.96, and the slopes of the ΔISP − ΔLST − ΔEOS curves ranged from 0.75 to 0.95. Overall, the contribution of the LST in spring and fall ranged from 87 to 99%, indicating that urban warming was a major factor in the impact of urbanization on the SOS and EOS (Figure 14).

A combination of factors due to urbanization affected vegetation phenology. Studies have shown that there is a warming trend in temperature with increasing urbanization [47]. Warming can contribute to an earlier SOS and a delayed EOS. The urban thermal environment caused by rising temperatures was a major factor in the difference between urban and rural levels, which is identical to the results of existing studies [48].

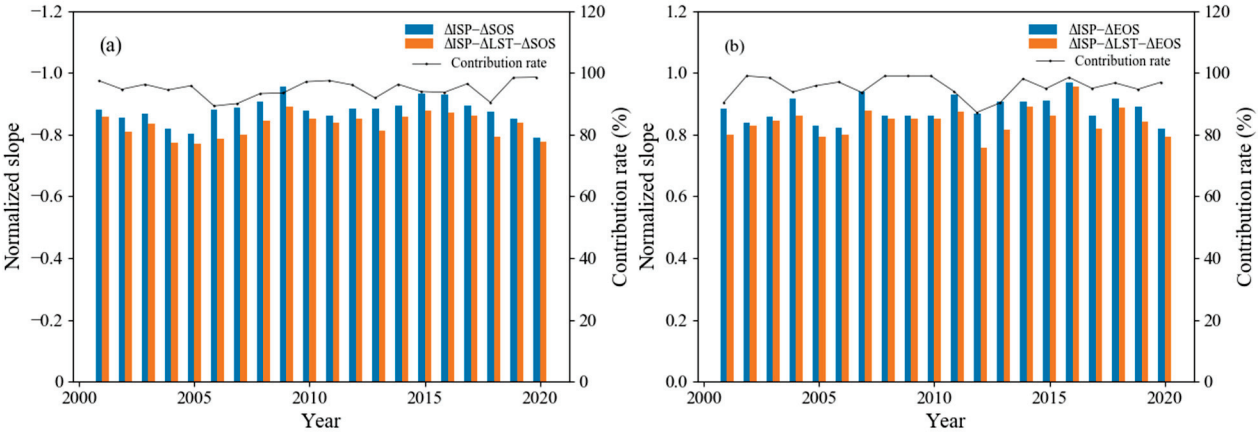

Figure 14. The contribution of the surface temperature increase to phenological changes. (**a**) shows the contribution of surface temperature to the impact of urbanization on the SOS. (**b**) shows the contribution of surface temperature to the impact of urbanization on the EOS.

4. Conclusions

This study extracted vegetation phenology based on MOD13Q1 vegetation index products from 2001 to 2020 and explored its spatial–temporal variation in the Yangtze River Delta. Furthermore, using impervious surface data and land cover data, the impact of urbanization on vegetation phenology was explored through a dynamic-level approach. The results showed that the SOS, EOS, and GSL were advanced by 0.41 days, delayed by 0.16 days, and extended by 0.57 days per year, respectively. Spatially, there were differences in the variability in phenology among rural, suburban, and urban areas, where suburban areas had the strongest variation in phenology, mainly because suburban areas are still experiencing the most dramatic stage of urban expansion and environmental changes. Additionally, due to the higher altitude of the southern region, the GSL in the southern region was shorter than that in the northern region. The correlation between vegetation phenology and the urbanization process is obvious. With each 10% increase in the urbanization level, the SOS, EOS, and GSL were advanced by 0.38 days, delayed by 0.34 days, and extended by 0.57 days per year, respectively, which was attributed to the temperature discrepancy in the city. The SOS was advanced by 0.47 days for every 1 °C increase in surface temperature, and the EOS was delayed by 0.13 days for every 1 °C increase in surface temperature. Overall, this study provides information on the dynamic response of vegetation phenology to urbanization and can aid in understanding the complex effects of urbanization on vegetation phenology, which is crucial for ecological planning in the process of urbanization.

Author Contributions: Conceptualization, E.Z. and L.C.; methodology, D.F.; software, D.F.; validation, E.Z.; formal analysis, Y.Q.; writing—original draft preparation, E.Z.; writing—review and editing, L.C. and T.L.; visualization, D.F.; funding acquisition, E.Z. All authors have read and agreed to the published version of the manuscript.

Funding: This research was funded by the National Natural Science Foundation of China, grant number 72104139; the Shanghai "Innovation Action Plan" Soft Science Project, grant number 23692120200; the MEL Visiting Fellowship, grant number MELRS2333; and the Science and Technology Commission of Shanghai Municipality (STCSM) Capacity Building Project of Local Universities, grant number 23010502200.

Data Availability Statement: The data that support the findings of this study are available by request to the corresponding author. The data are not publicly available due to data confidentiality.

Acknowledgments: The authors would like to acknowledge the editor and anonymous reviewers for improving the paper's quality.

Conflicts of Interest: The authors declare no conflicts of interest.

References

1. Zeng, L.; Wardlow, B.D.; Xiang, D.; Hu, S.; Li, D. A review of vegetation phenological metrics extraction using time-series, multispectral satellite data. *Remote Sens. Environ.* **2020**, *237*, 111511. [CrossRef]
2. Shen, X.; Liu, B.; Henderson, M.; Wang, L.; Wu, Z.; Wu, H.; Jiang, M.; Lu, X. Asymmetric effects of daytime and nighttime warming on spring phenology in the temperate grasslands of China. *Agric. For. Meteorol.* **2018**, *259*, 240–249. [CrossRef]
3. Wang, Y.Y.; Yuan, J.G.; Zhang, Y.; Wu, C.Y. Temporal and spatial variation of vegetation phenology in temperate China and its impact on gross primary productivity. *Remote Sens. Technol. Appl.* **2019**, *34*, 377–388.
4. Shen, X.; Liu, B.; Xue, Z.; Jiang, M.; Lu, X.; Zhang, Q. Spatiotemporal variation in vegetation spring phenology and its response to climate change in freshwater marshes of Northeast China. *Sci. Total Environ.* **2019**, *666*, 1169–1177. [CrossRef] [PubMed]
5. Singh, N.; Singh, S.; Mall, R. Urban ecology and human health: Implications of urban heat island, air pollution and climate change nexus. In *Urban Ecology*; Elsevier: Amsterdam, The Netherlands, 2020; pp. 317–334. [CrossRef]
6. Yan, S.J.; Wang, H.; Jiao, K.W. Spatiotemporal Dynamics of NDVI in the Beijing-Tianjin-Hebei Region based on MODIS Data and Quantitative Attribution. *J. Geo-Inf. Sci.* **2019**, *21*, 767–780. [CrossRef]
7. Du, H.; Wang, M.; Liu, Y.; Guo, M.; Peng, C.; Li, P. Responses of autumn vegetation phenology to climate change and urbanization at northern middle and high latitudes. *Int. J. Appl. Earth Obs. Geoinf.* **2022**, *115*, 103086. [CrossRef]
8. Li, X.; Zhou, Y.; Asrar, G.R.; Meng, L. Characterizing spatiotemporal dynamics in phenology of urban ecosystems based on Landsat data. *Sci. Total Environ.* **2017**, *605*, 721–734. [CrossRef]
9. Zhou, D.; Zhao, S.; Zhang, L.; Liu, S. Remotely sensed assessment of urbanization effects on vegetation phenology in China's 32 major cities. *Remote Sens. Environ.* **2016**, *176*, 272–281. [CrossRef]
10. Qiu, T.; Song, C.; Zhang, Y.; Liu, H.; Vose, J.M. Urbanization and climate change jointly shift land surface phenology in the northern mid-latitude large cities. *Remote Sens. Environ.* **2020**, *236*, 111477. [CrossRef]
11. Li, X.; Zhou, Y.; Asrar, G.R.; Mao, J.; Li, X.; Li, W. Response of vegetation phenology to urbanization in the conterminous United States. *Glob. Chang. Biol.* **2017**, *23*, 2818–2830. [CrossRef]
12. Zhao, C.; Weng, Q.; Wang, Y.; Hu, Z.; Wu, C. Use of local climate zones to assess the spatiotemporal variations of urban vegetation phenology in Austin, Texas, USA. *GISci. Remote Sens.* **2022**, *59*, 393–409. [CrossRef]
13. Zhang, W.; Randall, M.; Jensen, M.B.; Brandt, M.; Wang, Q.; Fensholt, R. Socio-economic and climatic changes lead to contrasting global urban vegetation trends. *Glob. Environ. Chang.* **2021**, *71*, 102385. [CrossRef]
14. Jia, W.; Zhao, S.; Zhang, X.; Liu, S.; Henebry, G.M.; Liu, L. Urbanization imprint on land surface phenology: The urban–rural gradient analysis for Chinese cities. *Glob. Chang. Biol.* **2021**, *27*, 2895–2904. [CrossRef]
15. Zhang, Y.; Yin, P.; Li, X.; Niu, Q.; Wang, Y.; Cao, W.; Huang, J.; Chen, H.; Yao, X.; Yu, L. The divergent response of vegetation phenology to urbanization: A case study of Beijing city, China. *Sci. Total Environ.* **2022**, *803*, 150079. [CrossRef]
16. Thompson, J.A.; Paull, D.J. Assessing spatial and temporal patterns in land surface phenology for the Australian Alps (2000–2014). *Remote Sens. Environ.* **2017**, *199*, 1–13. [CrossRef]
17. Sarvia, F.; De Petris, S.; Borgogno-Mondino, E. Exploring climate change effects on vegetation phenology by MOD13Q1 data: The piemonte region case study in the period 2001–2019. *Agronomy* **2021**, *11*, 555. [CrossRef]
18. Zhang, R.; Zhou, Y.; Hu, T.; Sun, W.; Zhang, S.; Wu, J.; Wang, H. Detecting the Spatiotemporal Variation of Vegetation Phenology in Northeastern China Based on MODIS NDVI and Solar-Induced Chlorophyll Fluorescence Dataset. *Sustainability* **2023**, *15*, 6012. [CrossRef]
19. Zhou, Y.K.; Liu, J.W. Spatio-temporal analysis of vegetation phenology with multiple methods over the Tibetan Plateau based on modis NDVI data. *Remote Sens. Technol. Appl.* **2018**, *33*, 486–498. [CrossRef]
20. Wu, Y.; Tang, G.; Gu, H.; Liu, Y.; Yang, M.; Sun, L. The variation of vegetation greenness and underlying mechanisms in Guangdong province of China during 2001–2013 based on MODIS data. *Sci. Total Environ.* **2019**, *653*, 536–546. [CrossRef]
21. Ahmed, T.; Singh, D. Probability density functions based classification of MODIS NDVI time series data and monitoring of vegetation growth cycle. *Adv. Space Res.* **2020**, *66*, 873–886. [CrossRef]
22. Tao, L.; Ryu, D.; Western, A.; Boyd, D. A new drought index for soil moisture monitoring based on MPDI-NDVI trapezoid space using MODIS data. *Remote Sens.* **2020**, *13*, 122. [CrossRef]
23. Hu, P.; Sharifi, A.; Tahir, M.N.; Tariq, A.; Zhang, L.; Mumtaz, F.; Shah, S.H.I.A. Evaluation of vegetation indices and phenological metrics using time-series modis data for monitoring vegetation change in Punjab, Pakistan. *Water* **2021**, *13*, 2550. [CrossRef]
24. Xin, Q.; Li, J.; Li, Z.; Li, Y.; Zhou, X. Evaluations and comparisons of rule-based and machine-learning-based methods to retrieve satellite-based vegetation phenology using MODIS and USA National Phenology Network data. *Int. J. Appl. Earth Obs. Geoinf.* **2020**, *93*, 102189. [CrossRef]
25. Gong, P.; Li, X.; Wang, J.; Bai, Y.; Chen, B.; Hu, T.; Liu, X.; Xu, B.; Yang, J.; Zhang, W. Annual maps of global artificial impervious area (GAIA) between 1985 and 2018. *Remote Sens. Environ.* **2020**, *236*, 111510. [CrossRef]
26. Yang, J.; Huang, X. The 30 m annual land cover dataset and its dynamics in China from 1990 to 2019. *Earth Syst. Sci. Data* **2021**, *13*, 3907–3925. [CrossRef]
27. Li, N.; Zhan, P.; Pan, Y.; Zhu, X.; Li, M.; Zhang, D. Comparison of remote sensing time-series smoothing methods for grassland spring phenology extraction on the Qinghai–Tibetan Plateau. *Remote Sens.* **2020**, *12*, 3383. [CrossRef]
28. Bornez, K.; Descals, A.; Verger, A.; Peñuelas, J. Land surface phenology from VEGETATION and PROBA-V data. Assessment over deciduous forests. *Int. J. Appl. Earth Obs. Geoinf.* **2020**, *84*, 101974. [CrossRef]

29. Yu, Z.; Yao, Y.; Yang, G.; Wang, X.; Vejre, H. Spatiotemporal patterns and characteristics of remotely sensed region heat islands during the rapid urbanization (1995–2015) of Southern China. *Sci. Total Environ.* **2019**, *674*, 242–254. [CrossRef] [PubMed]
30. Cai, Z.; Jönsson, P.; Jin, H.; Eklundh, L. Performance of smoothing methods for reconstructing NDVI time-series and estimating vegetation phenology from MODIS data. *Remote Sens.* **2017**, *9*, 1271. [CrossRef]
31. Li, S.; Xu, L.; Jing, Y.; Yin, H.; Li, X.; Guan, X. High-quality vegetation index product generation: A review of NDVI time series reconstruction techniques. *Int. J. Appl. Earth Obs. Geoinf.* **2021**, *105*, 102640. [CrossRef]
32. Liu, X.; Ji, L.; Zhang, C.; Liu, Y. A method for reconstructing NDVI time-series based on envelope detection and the Savitzky-Golay filter. *Int. J. Digit. Earth* **2022**, *15*, 553–584. [CrossRef]
33. Tang, L.; Zhao, Z.; Tang, P.; Yang, H. SURE-based optimum-length SG filter to reconstruct NDVI time series iteratively with outliers removal. *Int. J. Wavelets Multiresolut. Inf. Process.* **2020**, *18*, 2050001. [CrossRef]
34. Cong, N.; Piao, S.; Chen, A.; Wang, X.; Lin, X.; Chen, S.; Han, S.; Zhou, G.; Zhang, X. Spring vegetation green-up date in China inferred from SPOT NDVI data: A multiple model analysis. *Agric. For. Meteorol.* **2012**, *165*, 104–113. [CrossRef]
35. White, M.; de Beurs, K.; Didan, K.; Inouye, D.; Richardson, A.; Jensen, O.; O'Keefe, J.; Zhang, G.; Nemani, R.; Van Leeuwen, W.; et al. Intercomparison, interpretation, and assessment of spring phenology in North America estimated from remote sensing for 1982–2006. *Glob. Chang. Biol.* **2009**, *15*, 2335–2359. [CrossRef]
36. Liu, Z.; Zhou, Y.; Feng, Z. Response of vegetation phenology to urbanization in urban agglomeration areas: A dynamic urban–rural gradient perspective. *Sci. Total Environ.* **2023**, *864*, 161109. [CrossRef] [PubMed]
37. Wang, L.; De Boeck, H.J.; Chen, L.; Song, C.; Chen, Z.; McNulty, S.; Zhang, Z. Urban warming increases the temperature sensitivity of spring vegetation phenology at 292 cities across China. *Sci. Total Environ.* **2022**, *834*, 155154. [CrossRef] [PubMed]
38. Jiao, F.; Liu, H.; Xu, X.; Gong, H.; Lin, Z. Trend evolution of vegetation phenology in China during the period of 1981–2016. *Remote Sens.* **2020**, *12*, 572. [CrossRef]
39. Cheng, M.; Jin, J.; Zhang, J.; Jiang, H.; Wang, R. Effect of climate change on vegetation phenology of different land-cover types on the Tibetan Plateau. *Int. J. Remote Sens.* **2018**, *39*, 470–487. [CrossRef]
40. Wu, L.; Ma, X.; Dou, X.; Zhu, J.; Zhao, C. Impacts of climate change on vegetation phenology and net primary productivity in arid Central Asia. *Sci. Total Environ.* **2021**, *796*, 149055. [CrossRef] [PubMed]
41. Deng, C.; Ma, X.; Xie, M.; Bai, H. Effect of altitude and topography on vegetation phenological changes in the Niubeiliang nature reserve of Qinling Mountains, China. *Forests* **2022**, *13*, 1229. [CrossRef]
42. Shen, X.; Jiang, M.; Lu, X. Diverse impacts of day and night temperature on spring phenology in freshwater marshes of the Tibetan Plateau. *Limnol. Oceanogr. Lett.* **2023**, *8*, 323–329. [CrossRef]
43. Lukasová, V.; Bucha, T.; Škvareninová, J.; Škvarenina, J. Validation and application of European beech phenological metrics derived from MODIS data along an altitudinal gradient. *Forests* **2019**, *10*, 60. [CrossRef]
44. Hou, X.; Gao, S.; Sui, X.; Liang, S.; Wang, M. Changes in day and night temperatures and their asymmetric effects on vegetation phenology for the period of 2001–2016 in northeast China. *Can. J. Remote Sens.* **2018**, *44*, 629–642. [CrossRef]
45. Ren, Q.; He, C.; Huang, Q.; Zhou, Y. Urbanization impacts on vegetation phenology in China. *Remote Sens.* **2018**, *10*, 1905. [CrossRef]
46. Ruan, Y.; Zhang, X.; Xin, Q.; Ao, Z.; Sun, Y. Enhanced vegetation growth in the urban environment across 32 cities in the Northern Hemisphere. *J. Geophys. Res. Biogeosci.* **2019**, *124*, 3831–3846. [CrossRef]
47. Kabano, P.; Lindley, S.; Harris, A. Evidence of urban heat island impacts on the vegetation growing season length in a tropical city. *Landsc. Urban Plan.* **2021**, *206*, 103989. [CrossRef]
48. Meng, L.; Mao, J.; Zhou, Y.; Richardson, A.D.; Lee, X.; Thornton, P.E.; Ricciuto, D.M.; Li, X.; Dai, Y.; Shi, X. Urban warming advances spring phenology but reduces the response of phenology to temperature in the conterminous United States. *Proc. Natl. Acad. Sci. USA* **2020**, *117*, 4228–4233. [CrossRef]

Disclaimer/Publisher's Note: The statements, opinions and data contained in all publications are solely those of the individual author(s) and contributor(s) and not of MDPI and/or the editor(s). MDPI and/or the editor(s) disclaim responsibility for any injury to people or property resulting from any ideas, methods, instructions or products referred to in the content.

remote sensing

MDPI

Article

Improving the Detection Effect of Long-Baseline Lightning Location Networks Using PCA and Waveform Cross-Correlation Methods

Ting Zhang [1,2,3,4], Jiaquan Wang [5], Qiming Ma [5] and Liping Fu [1,3,4,*]

[1] National Space Science Center, Chinese Academy of Sciences, Beijing 100190, China; zhangting221@mails.ucas.ac.cn
[2] University of Chinese Academy of Sciences, Beijing 100049, China
[3] Beijing Key Laboratory of Space Environment Exploration, Beijing 100190, China
[4] Key Laboratory of Science and Technology on Environmental Space Situation Awareness, CAS, Beijing 100190, China
[5] Institute of Electrical Engineering, Chinese Academy of Sciences, Beijing 100190, China; wangjiaquan@mail.iee.ac.cn (J.W.); maqiming@mail.iee.ac.cn (Q.M.)
* Correspondence: fuliping@nssc.ac.cn

Abstract: Ultra-long-distance and high-precision lightning location technology is an important means to realize low-cost and wide-area lightning detection. This paper carried out research on the high-precision location technology of very-low-frequency (VLF) lightning electromagnetic pulse based on the Asia-Pacific Lightning Location Network (APLLN) deployed in 2018. Two key technologies are proposed in this paper: one is the calculation method of signal arrival time using very-low-frequency lightning electromagnetic pulse waveform, and the other is the compression transmission technology of lightning electromagnetic pulse waveform based on a signal principal component analysis. The results of a comparison and evaluation of the improved APLLN with the ADTD system show that the APLLN has a relative location efficiency of 69.1% and an average location error within the network of 4.5 km.

Keywords: APLLN; VLF lightning location; waveform cross-correlation; PCA; data compression

1. Introduction

Thunderstorms or lightning are common severe convective weather phenomena in nature, with an average of tens to hundreds of lightning flashes per second worldwide, including cloud and cloud-to-ground flashes. Accurate and efficient detection of lightning event information can help people to obtain information about thunderstorms, avoid lightning accidents, and reduce economic losses.

Lightning emits a significant number of electromagnetic pulse signals. The signals cover a wide frequency range, from a few hertz (long continuing currents) to 10^{20} Hz (hard X-rays) [1]. Measuring electromagnetic pulses is the fastest and most effective way to detect lightning events. Considering the propagation attenuation of electromagnetic signals in the Earth–ionosphere waveguide, ground-based lightning location systems generally operate in the extremely-low- to very-high-frequency band. A ground-based lightning location network usually consists of at least four electromagnetic pulse detection sites, a data processing center, and a network transmission link. The distance between the two stations is called the baseline. Baseline sizes typically range from tens to thousands of kilometers depending on the detection range. The lightning location network uses the time difference and direction parameters of the signal to locate each event.

Very-high-frequency lightning electromagnetic pulse signals carry richer information, and the steep peaks of electromagnetic pulses are easily detected by sensors, thus achieving precise lightning imaging [2–6]. However, the propagation distance of high-frequency

LEMP signals is short, and the amplitude rapidly decreases after a long distance. The effective detection range of lightning electromagnetic pulse sensors working in high-frequency bands is usually within several dozen kilometers.

At present, the regional commercial lightning location systems are working in the VLF and LF bands, such as the U.S. National Lightning Detection Network (NLDN), European Cooperation for Lightning Detection (EUCLID), and China Advanced Direction-time Lightning Detection (ADTD). These systems are usually composed of hundreds of lightning detection sites; the baseline of the sites is generally about 100 km, which can be better compatible with the detection efficiency of cloud-to-ground (CG) lightning and intracloud (IC) lightning, and the location accuracy is better than 500 m. The signals in the VLF band could propagate long distances in the Earth–ionosphere waveguide, and long-range lightning detection can be realized by using VLF signals. Considering the long-distance propagation of VLF signals in Earth–ionosphere waveguides [7–11], more and more studies have begun to focus on using VLF lightning electromagnetic pulse signals to achieve low-cost, large-area, and high-precision lightning detection.

The World Wide Lightning Location Network (WWLLN) [12–14] currently operates more than 70 detection sites in the frequency band of 3 kHz to 30 kHz. WWLLN uses lightning electromagnetic pulse signals detected by at least five sites for localization calculation. The lightning strokes could be located by calculating the time difference between the signals arriving at each site based on the time of the group arrival method. Recent research indicates that the detection efficiency of WWLLN for strokes with about 30 kA is approximately 30% globally.

The Institute of Electrical Engineering of the Chinese Academy of Sciences has deployed the Asia-Pacific Lightning Location Network (APLLN), which operates in the VLF band. The average distance between the detection sites is about 1000 km. Wang et al. [15] proposed a calculation method of signal arrival time based on envelope peak, and the location accuracy in the network is around 10 km.

Wang et al. [16] adopted the time-difference location method to realize lightning location. The network boasts a baseline distance of approximately 2000 km and operates in the VLF band. The Gauss–Newton iteration method was utilized to find the optimal fitting point of the arrival time difference, thereby enhancing both the efficiency and accuracy of the location algorithm. Comparisons with lightning location results in the Jiangsu area of the China Power Grid demonstrate a detection accuracy that can reach 12 km.

Overall, the baseline of the VLF lightning location systems is about 1000 km, and the location accuracy is about 10 km. Compared with VLF/LF lightning location system whose location accuracy is better than 500 m, the location accuracy of 10 km is not ideal. To enhance the detection performance of the long-baseline lightning location system, this paper presents an improved localization method based on the lightning electromagnetic pulse waveform.

The rest of this article is arranged as follows: Section 2 provides a brief overview of the APLLN and its components. Section 3 introduces the data processing and localization methods used in the study. Section 4 describes the location results. Section 5 compares and evaluates the results of the new method. Finally, Section 6 summarizes the article.

2. Network and Data

Since 2018, the APLLN [15] has established 16 long-baseline LEMP detection sites in China and neighboring countries, which have been in stable operation for five years. The detection sites are distributed between 75 and 134°E and 7 and 53°N, with a baseline range of 800~1500 km. The deployment of the APLLN detection site and the appearance of the electromagnetic pulse detection equipment are shown in Figure 1. In the case of at least four sites detecting signals simultaneously, the real-time two-dimensional location of lightning activity in China and the Asia–Pacific region can be realized based on the time difference of arrival (TDOA).

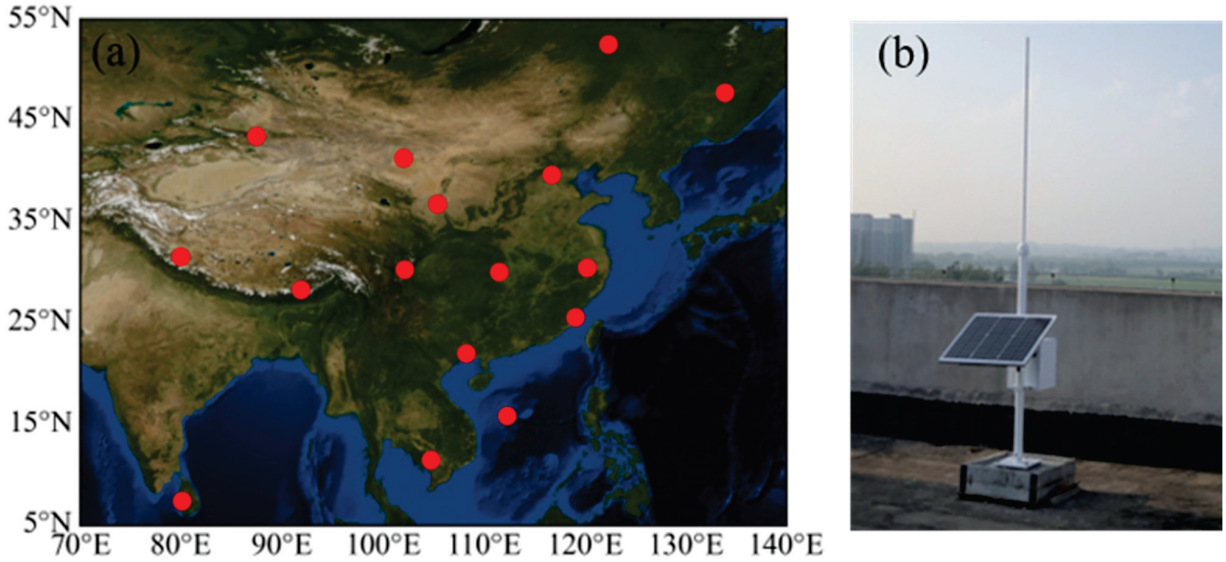

Figure 1. (**a**) The deployment of the APLLN detection site; the red dots indicate the locations of the sites. (**b**) The appearance of the electromagnetic pulse detection equipment.

Each detection site of the APLLN is mainly composed of a whiplash electric field antenna, signal amplifier, filter, analog and digital conversion circuit, signal processor, and high-precision GPS/Beidou timing module. The detection equipment adopts the trigger sampling method to record the LEMP signal with a duration of 2 ms. The sampling rate of the device is 500KSPS, which fully meets the sampling requirements of signals in the 3–30 kHz frequency band according to the Nyquist sampling theorem. Figure 2 shows the LEMP waveform data recorded by a device. One single records 1000 sampling points, and each sampling point is stored with 4-byte floating-point data, so the memory needs at least 4K bytes of storage space to record a single sample of data.

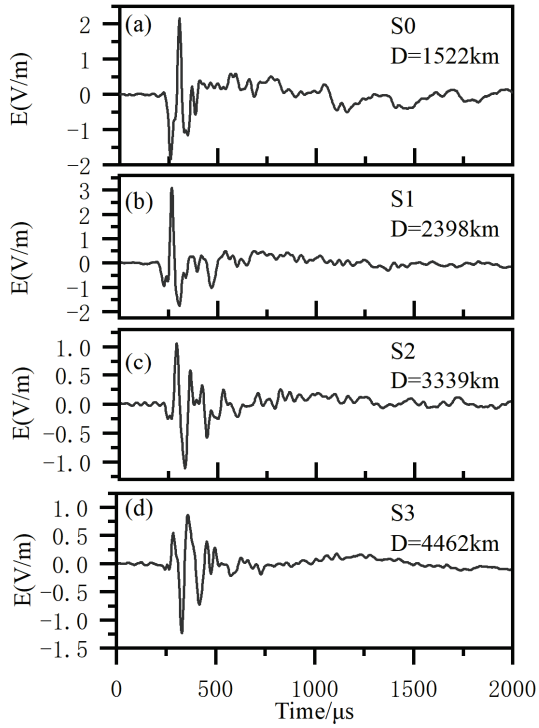

Figure 2. (**a–d**) The LEMP waveform data from different distance.

3. Method

3.1. Real-Time Data Compression

Before describing the lightning location method, it is necessary to introduce the compression technology of LEMP waveform data. In recent years, the research team has upgraded the data processing system of APLLN. The detection system can work at a lower trigger threshold. A lower trigger threshold would result in the detection system capturing weaker LEMP signals, thus improving the lightning detection efficiency. However, this also brings new challenges, as data transmission requires larger bandwidth resources.

When processing large amounts of LEMP waveform data, data compression is an effective way to save transmission bandwidth and improve transmission efficiency [17]. The conventional lossless compression method has the disadvantages of slow computation speeds and low compression rates, which cannot meet the real-time LEMP data processing. This paper presents a method of real-time lossy compression of LEMP waveform data based on principal component analysis (PCA) [18,19] and transmits the compressed LEMP waveform data back to the data processing center in real-time. As far as we know, this is the first time that PCA method has been applied in the field of LEMP waveform compression transmission. The data processing center decompresses the data and performs subsequent data processing and location calculation. The process diagram of data compression and decompression using the PCA method is shown in Figure 3.

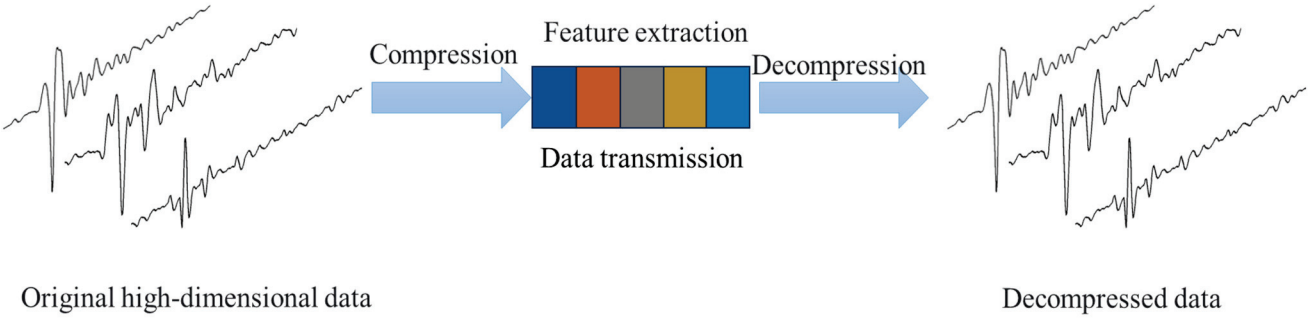

Figure 3. Data compression transmission flow diagram.

The main idea of the PCA method is to find the most significant components in the data and replace the original data with the most significant components to achieve the purpose of data dimensionality reduction [19]. To minimize the loss of data information, we removed the correlation of the data and preprocessed the data in a lower-dimensional space in the case of high-dimensional space.

For an LEMP waveform data set x of length n, the mean value of x is:

$$\overline{x} = \frac{1}{n}\sum_{i=1}^{n} x_i \tag{1}$$

Decentralization of LEMP waveform data:

$$d_i = x_i - \overline{x} \tag{2}$$

The covariance matrix of the LEMP waveform data sample is:

$$C_{n*n} = \frac{1}{n-1}\sum_{i=1}^{n} d_i {d_i}^T \tag{3}$$

Using the covariance matrix of the LEMP waveform data, we obtained the eigenvalues and eigenvectors. Then, we sorted the eigenvalues of the LEMP waveform data samples from large to small and selected the top K values [20]. Then, the corresponding K eigen-

vectors are formed into the eigenvector matrix P_K in the form of row vectors. With the eigenvector set to P_K, LEMP waveform data x can be projected into the eigenspace y_K:

$$y_K = {P_K}^T(x - \overline{x}) \tag{4}$$

The LEMP waveform data x are compressed, transmitted back, and finally decompressed. The decompressed LEMP waveform data can be expressed as:

$$x = \overline{x} + \sum_{K=1}^{n} y_K P_K \tag{5}$$

Taking an example of the LEMP waveform data recorded by the APLLN detector as a reference, the blue line in Figure 4a represents the waveform of the original data, and the red line represents the waveform data obtained after PCA compression and decompression. The dimension of the LEMP waveform data is 1000. Through experiments, it was found that when the dimensionality of the data was reduced to 90, i.e., compressed from the original 1000 sampling points to 90 feature points, the correlation between the transformed data and the original data was 98.87%. If only 90 feature points need to be transmitted through the network instead of all 1000 sampling points, it can fully meet the real-time transmission and processing of LEMP data. Figure 4b shows the results of compressing the original data using the PCA method. It can be seen from Figure 4 that the original data and the extracted data are generally consistent in the time domain.

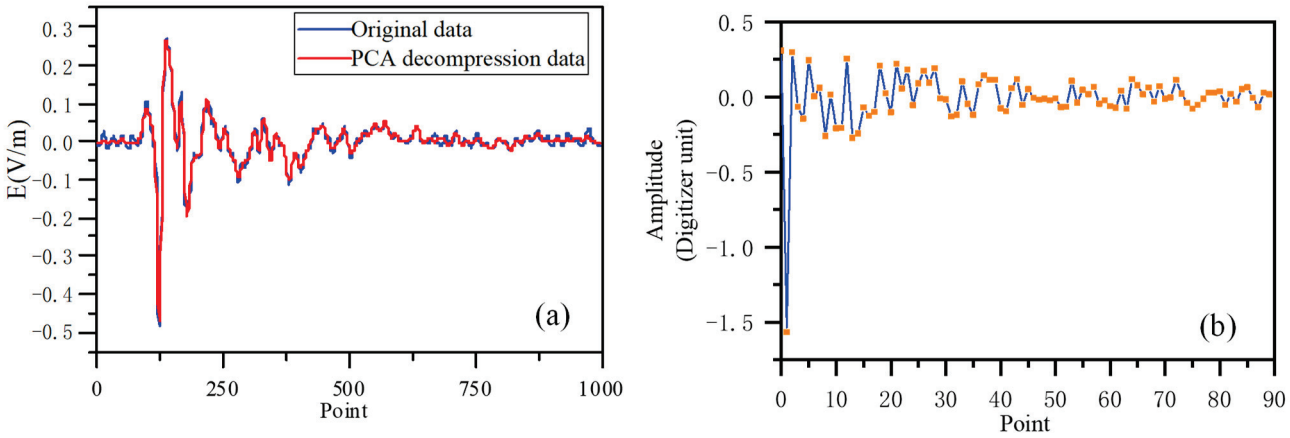

Figure 4. (**a**) The blue line represents the waveform of the original data, and the red line represents the waveform data obtained after PCA compression and decompression. (**b**) The feature data compressed using PCA method, and each colored point represents a feature.

In practical applications, P_K and $\overline{x}$ are fitted from a large amount of historical data and stored in the memory of detection devices and data processing centers, respectively, for the compression and decompression of LEMP waveform data. Considering the presence of a large amount of electromagnetic noise during the propagation process, as well as factors such as propagation distance and terrain that can affect the waveform, we analyzed the LEMP data received from multiple detection sites. All LEMP signals were generated by the same lightning event. Figure 5 below shows a set of homologous LEMP signals collected from four different sites, with propagation distances ranging from 720 km to 3062 km. It can be seen that the PCA conversion results can effectively restore the original LEMP data. Using the method of signal cross-correlation to calculate the similarity of signals, the average similarity is 98.46%. This indicates that the PCA method can effectively restore the principal components of the original LEMP data without causing significant information loss due to electromagnetic noise.

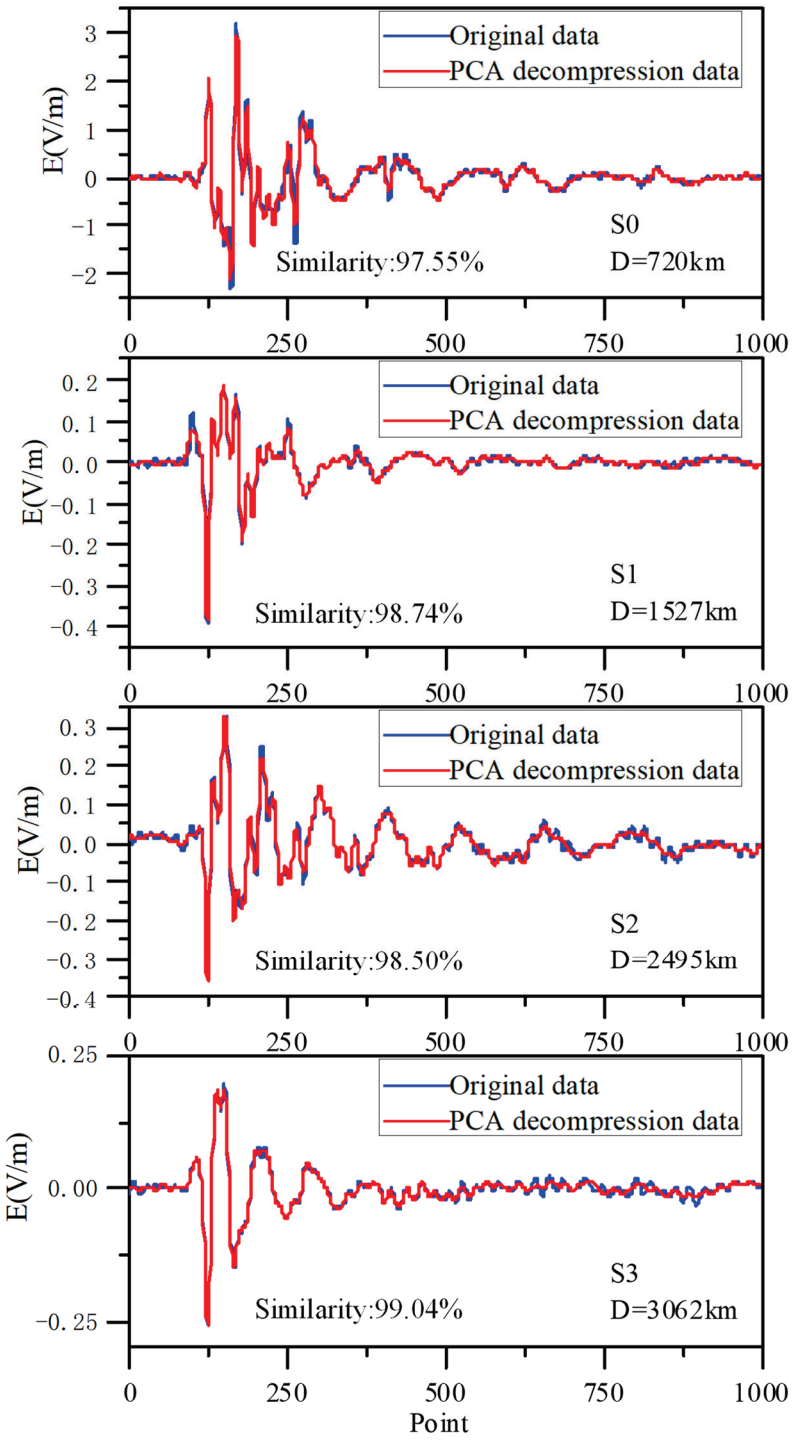

Figure 5. Original data of LEMP waveform with different propagation distance and PCA conversion data. The data are all from the same lightning event and were recorded by different detection stations. Each subplot is labeled with the propagation distance of the LEMP signal.

This paper compares the time consumption and compression ratio of bzip2 [21,22] lossless compression and PCA lossy compression for different amounts of data. It can be seen from Table 1 that the compression rate of PCA lossy compression is much higher than that of bzip2 lossless compression, which greatly reduces the bandwidth occupation of the channel during data transmission. The time consumed by PCA lossy compression is also much less than that consumed by bzip2 lossy compression, and using PCA lossy compression can improve the efficiency of data transmission.

Table 1. Comparison of bzip2 lossless compression and PCA lossy compression.

Data Number	bzip2 Lossless Compression		PCA Lossy Compression	
	Consumption of Time (s)	Compressibility (%)	Consumption of Time (s)	Compressibility (%)
100	0.84	0.63	0.0882	0.09
200	1.83	0.63	0.1764	0.09
300	2.75	0.66	0.2646	0.09
400	3.76	0.63	0.3528	0.09
500	4.48	0.60	0.441	0.09
600	5.57	0.63	0.5292	0.09
700	6.49	0.64	0.6174	0.09
800	8.55	0.72	0.7056	0.09

3.2. Location Algorithm

Based on the efficient transmission method of LEMP data explained in Section 3.1, this section mainly discusses the second key issue of VLF lightning detection: how to improve the location accuracy of VLF lightning detection? In general, the mainstream lightning location systems use the TDOA method for location [23–25]. The TDOA method locates the radiation source according to the time difference between the LEMP signals arriving at each detection site. The number of sites ranges from four to more, typically. The long-baseline lightning location system has a large baseline over 1000 km, which is different from the short- and medium-baseline location system with the baseline between 30 and 150 km. The LEMP signals received by the long-baseline lightning location system have a large attenuation of ground wave propagation due to the long distance between the signal source and the detection site. Then, the signal received by the detection site could not calculate the arrival time of the ground wave accurately, which leads to the poor location accuracy of the long-baseline lightning detection system.

In the past few years, APLLN has used a localization method that calculates the envelope of LEMP using the Hilbert transform and then calculates the arrival time of the signal based on the peaks of the envelope [15]. At the same time, the location result of lightning was calculated by the TDOA method, and an improved Levenberg–Marquardt nonlinear least squares iterative algorithm was used to optimize the lightning location results. This location algorithm is collectively referred to as the envelope peak method in the following content.

However, the arrival time of the LEMP calculated by the envelope peak method is biased with respect to the true value. As shown in Figure 6, the first pulse peak S_2 of the gray waveform can be regarded as the arrival time of the LEMP signal. The envelope peak S_3 of the red waveform is the signal arrival time determined by the envelope peak method. S_1 is the theoretical arrival time of the LEMP signal, which is the actual time it takes for the signal to travel from lightning to the detection station. From Figure 6, it can be seen that the arrival time of the real signal is earlier than the time of the envelope peak. When the distance between the detection site and the lightning is nearer, such as less than 100 km, S_1 is approximately S_2. As the signal propagation distance increases, S_2 gradually lags behind S_1.

Moreover, the anti-noise ability of the envelope peak method is weak. Figure 7 lists several typical electromagnetic pulse signals that may affect the accuracy of VLF lightning location. The duration of an LEMP signal ranges from tens of microseconds to hundreds of microseconds. Therefore, we generally assumed that there is only one LEMP signal within a sampling window. As shown in Figure 2, the collected signals only have one LEMP signal, which is the case handled by most calculation processes. However, in practical applications, signals such as those in Figure 7a,b may also be encountered, where Figure 7a is a dense lightning electromagnetic pulse signal emitted by cloud flash radiation. Figure 7b shows the presence of multiple LEMP signals within a sampling window. Although both cases collect LEMP signals, the use of signal's envelope or peak methods cannot accurately determine lightning homology, resulting in incorrect location results. Figure 7c,d show two

common electromagnetic pulse interference signals, which are usually similar to LEMP and cannot be accurately removed. At the same time, due to the large amount of interference signals generated in a short period of time, it seriously affects the location calculation. When using signal's envelope or peak methods, it can also produce incorrect location results.

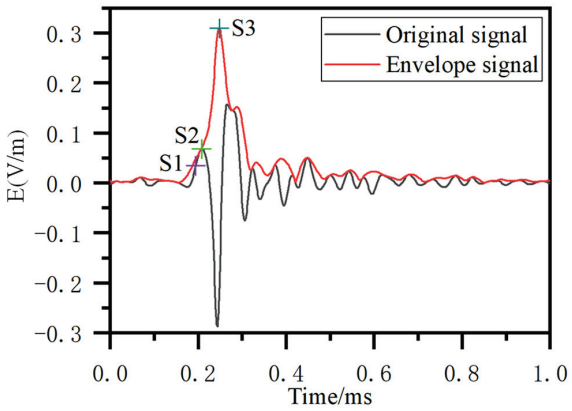

Figure 6. Gray line represents the original signal waveform, and red line represents the envelope waveform after the Hilbert transformation.

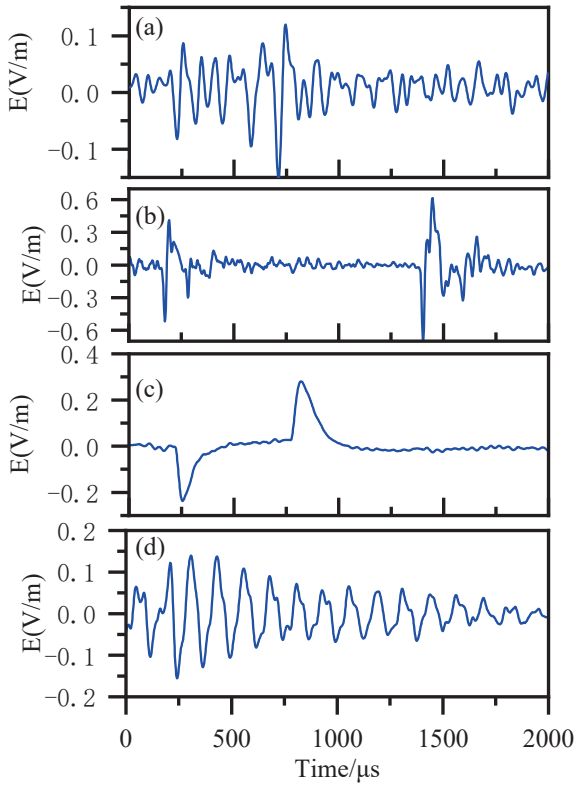

Figure 7. Typical waveform of LEMP and interference signals. (**a**) Electromagnetic pulse signals from cloud flash. (**b**) Two LEMPs within the same sampling window. (**c**) Pulse interference signal from switching power supply. (**d**) Radio interference signal.

In order to improve the location capability of the APLLN, the arrival time of LEMP was calculated using the cross-correlation method [26–29] of waveforms in this paper. The waveform is used to find homologous events, remove noise interference, and reduce the influence of noise signals on location. Previously, very-low-frequency lightning positioning systems were limited by data transmission rates and typically calculated the arrival time at

the detection equipment end. Due to the arrival time ambiguity caused by the long-distance propagation of signals in the Earth–ionosphere waveguide, this method cannot accurately calculate the arrival time of signals. Therefore, after using the PCA method to solve the real-time compression and transmission of signals, the signal cross-correlation method was applied in the field of very-low-frequency lightning detection. This location algorithm is collectively referred to as the cross-correlation method in the following content.

The APLLN obtains the real-time high-precision time through the GPS/Beidou satellite timing system and marks the trigger time of the original waveform data. The detected data less than the set threshold are defined as homologous data. The detailed steps of the improved signal arrival time algorithm are as follows:

For a set of homologous data sequences $\{x_1, x_2, x_3, \ldots x_n\}$, the earliest time LEMP waveform data x_1 were selected as the reference data. The time t_{x1} of the pulse peak of LEMP waveform data x_1 was taken as the reference time.

The dimension of the LEMP waveform data is 1000, which is expressed as l. We extended the dimension of x_1 according to Formula (6).

$$x_1' = \{m, x_1, m\} \tag{6}$$

The dimension of m is 500, and the values are zeros. We calculated the value of the correlation between $x_1'[a : l + a]$ and x_2. Then, we obtained the correlation coefficient sequence $C = \{C_1, C_2, C_3 \ldots . C_a\}$, where a is the first point of the data x_1', $a \in [1, 2l]$.

The index value corresponding to C_{max} with the largest correlation coefficient can be used to calculate the arrival time t_{x2} of the electromagnetic pulse waveform data x_2. By traversing the homologous data sequence $\{x_1, x_2, x_3, \ldots x_n\}$, the time of each waveform arriving at the detection site can be found.

Figure 8a shows the electromagnetic pulse waveform data received by the detection sites S1 and S2. According to the above method, the LEMP waveform data received by the detection sites S1 and S2 were cross-correlated, and the results were obtained as shown in Figure 8b. It can be seen from Figure 8b that at time 0, the maximum correlation coefficient is obtained when the two waveforms are not translated [28].

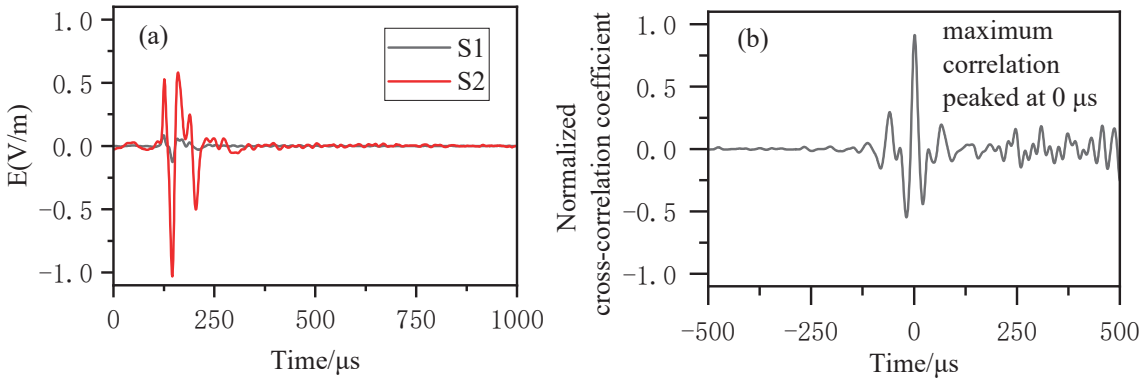

Figure 8. (**a**) The LEMP signals from different detection sites. (**b**) Cross-correlation results between the LEMP signals from two different detection sites.

3.3. Simulated Analysis

The simulation analysis is mainly used to evaluate the performance of the location algorithm and lightning location network. This paper used Monte Carlo simulation method [30–32]. The geographical range of the simulation is 10°S~70°S, 40°E~165°E. The simulation area was divided into grids with the size of 0.1° × 0.1°. We supposed there are 1000 lightning events in each grid. We calculated the arrival time t_{si} of the electromagnetic pulse signal radiated by the lightning source to each detection site. For the

convenience of calculation, we calculated the arrival time of the ground wave signal as t_{si}, which is

$$t_{si} = t_0 + \frac{1}{c} D_{si} \tag{7}$$

t_0 is the assumed time of lightning occurrence; D_{si} is the great circle distance from the lightning to the ith detection site, and c is the speed of light. Considering the calculation error caused by signal propagation factor in real environment, random error was added to the arrival time t_{si} in the simulation process, which was defined as $\Delta\varepsilon_{si}$ in this paper. For 1000 simulation calculations within each grid, we set the mean of the random error to 0 and the variance to 1. Regarding the range of error $\Delta\varepsilon_{si}$, ref. [33] used a smaller error range of -0.4~0.4 μs.

Due to the fact that the TDOA calculation method ultimately assumes signal propagation along the Earth, when using envelope peak or signal peak methods to calculate signal arrival time, the position represented by the peak is generally sky waves rather than ground waves. Therefore, there is an error in the calculation of the signal arrival time. If the signal propagation distance is over a thousand kilometers, $\Delta\varepsilon_{si}$ can reach several tens of microseconds. On the other hand, the propagation of very-low-frequency LEMP signals in the Earth–ionosphere waveguide is affected by the height changes in the D region of the ionosphere, and the arrival time of sky waves will also have varying degrees of lag or lead, which mainly affects the propagation of signals at longer distances. Based on these factors, the time error introduced by APLLN is larger, and simulation requires a larger error range, which is completely different from lightning location systems with a baseline of around 100 km. Similar to [34], this article set the simulation error range to $[-5, 5]$ μs, making the simulation results closer to the real situation.

The distance between each location result and the simulated lightning location was calculated, and the location error of lightning in each grid was obtained. Figure 9 shows the results of location error using the Monte Carlo simulation method. The results show that the location error is less than 5 km for lightning events in APLLN network by using the location method proposed in this paper. With the increase in the signal propagation distance, the location error would be larger, and the location error is about 5 thousandths of R, where R is the average distance from the lightning source to the detection site. At the same time, it can also be seen that due to the uneven deployment of detection sites, large location errors may occur in the Indian Ocean, the Pacific Ocean, and other regions.

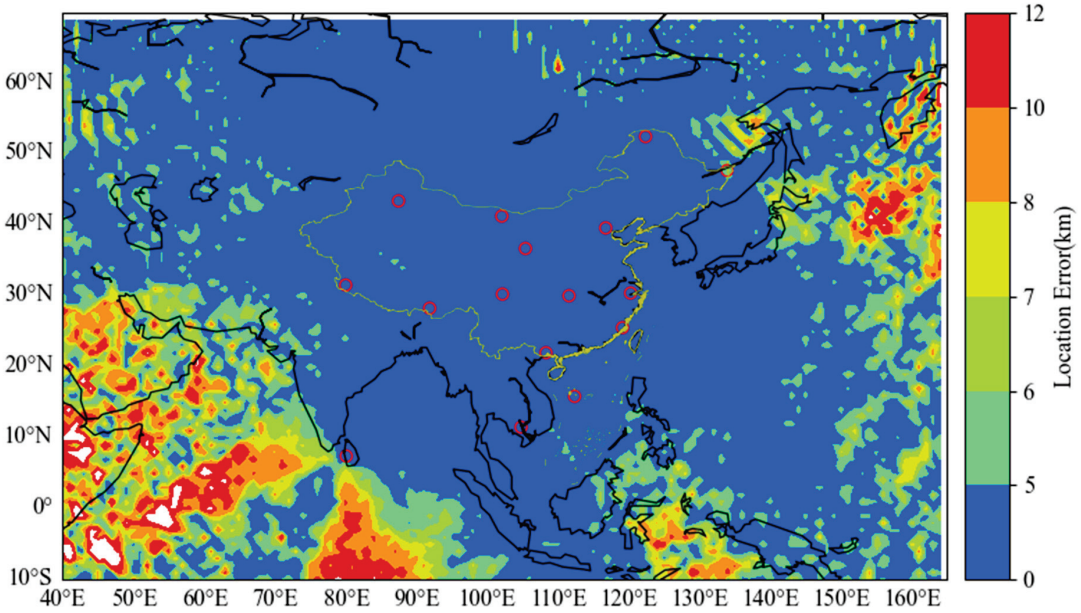

Figure 9. Simulation results of lightning location error. The red circles represent the geolocation of the detection sites.

4. Results

4.1. The Location Result of Cross-Correlation Method

This article selected a thunderstorm process in southern China for data comparison and analysis. The thunderstorm process lasted for 9 h. The thunderstorm took place from 19:00 on 22 March 2023 to 4:00 on 23 March 2023, Beijing time. By analyzing the data detected by APLLN, we could visually observe the development process of thunderstorms. The process of this thunderstorm was analyzed in the range of 113.5~117.3°E and 26.4~28.3°N. The location results of the APLLN (cross-correlation method) showed that a total of 10,604 lightning strokes were detected.

As can be seen from Figure 10, the thunderstorm began at 19:00 on 22 March 2023. In the next several hours, the range of thunderstorms gradually expanded and the intensity gradually increased. The pattern displayed a westward trend, reaching its strongest within 23:00–24:00 (00:00) on 22 March 2023. Then, the thunderstorm began to weaken. The weather radar reflectivity is superimposed in Figure 10. It can be seen that the lightning location results are strongly consistent with the areas with high radar reflectivity, which verifies the accuracy of the detection results. Figure 11 shows the number of lightning events detected by the APLLN (cross-correlation method) over different periods. As can be seen from Figure 11, the maximum number of lightning strokes was 2565 at around 23:00–24:00 on 22 March 2023. The whole thunderstorm process developed rapidly and lasted a long time.

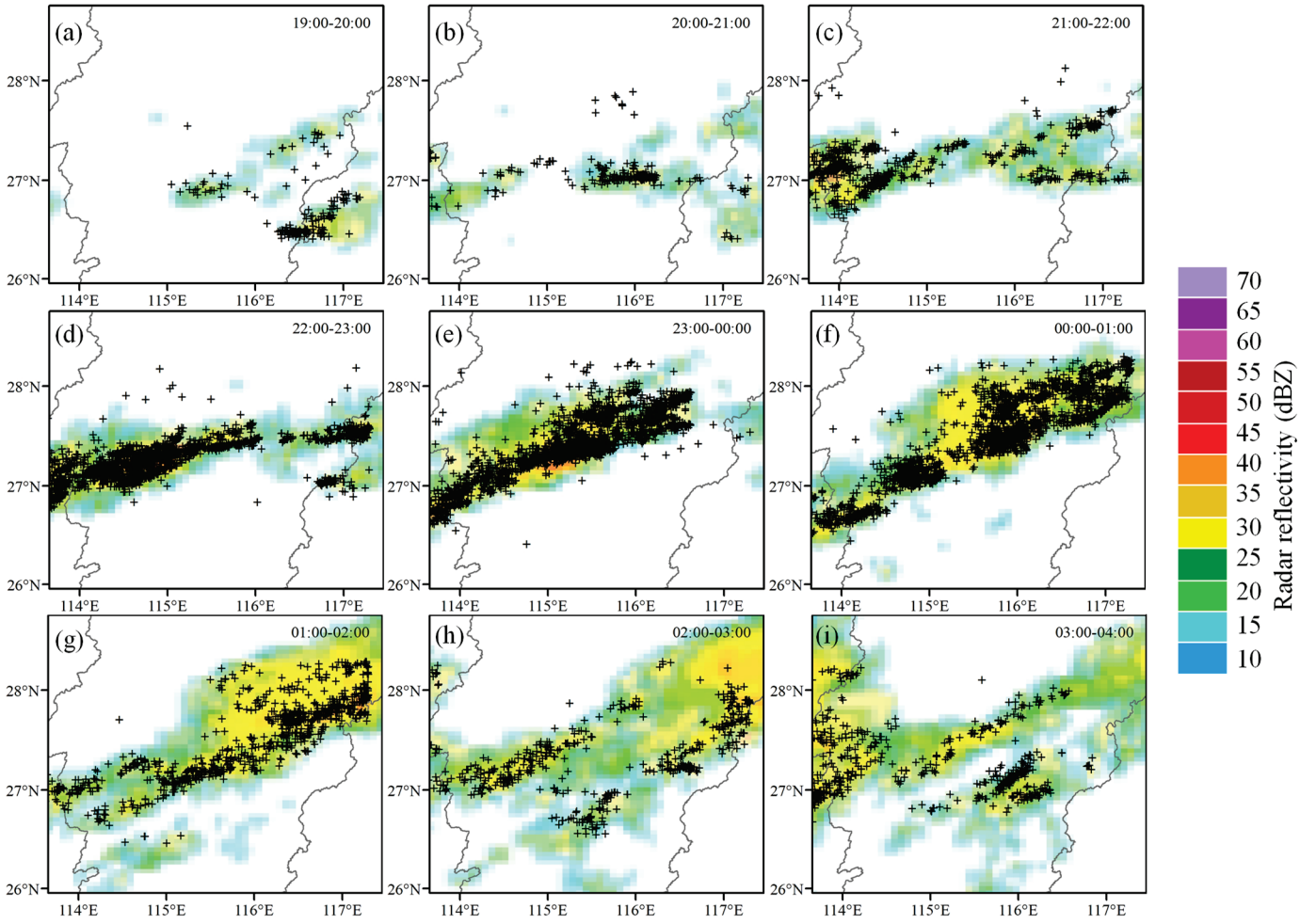

Figure 10. The location result of the APLLN by using the method proposed in this paper. Subplots (**a**–**i**) show the lightning location results for each hour, respectively. The symbol '+' indicates the location of each lightning event.

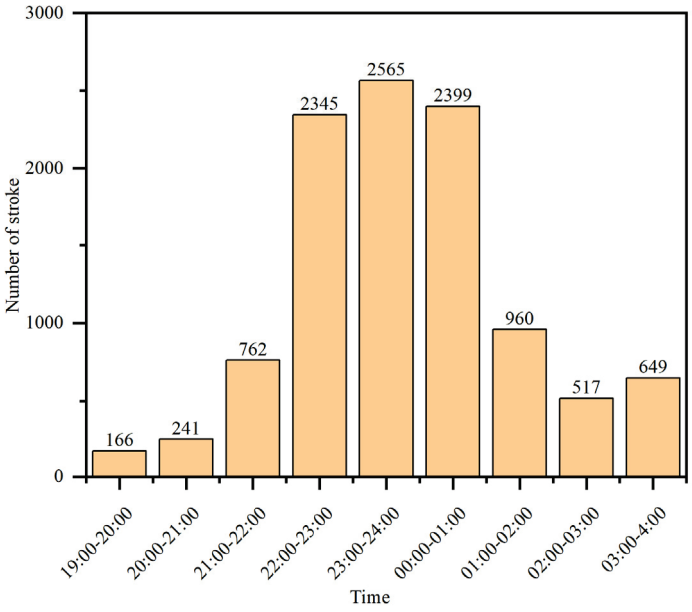

Figure 11. The number of lightning events detected by APLLN at different times using PCA and cross-correlation methods.

4.2. The Location Result of Envelope Peak Method

Within the same time, latitude, and longitude as described in Section 4.1 above, the location results of the APLLN (envelope peak) showed that a total of 9470 lightning strokes were detected. Figure 12 shows the lightning scatter distribution by hour. It can be seen that the development trend of thunderstorm activity monitored by the above cross-correlation method is consistent. However, from 00:00 to 01:00, it can be seen that the anti-noise ability of the envelope peak method is poor, and the monitored data are doped with a lot of noise signals.

Figure 13 shows the number of lightning events detected by the APLLN (envelope peak method) over different periods. As can be seen from Figure 13, the maximum number of lightning strokes was 3286 from 00:00 to 01:00 on 23 March 2023. The whole thunderstorm process developed rapidly and lasted a long time. Comparing Figure 10 to Figure 13, it can be observed that using the envelope peak localization method resulted in a large amount of discrete data. Among them, the most obvious period is from 00:00 to 1:00, with scattered data covering almost all the analysis areas. These scattered points did not coincide with the radar echo reflection area, which fully indicates that this is an incorrect lightning location result. In order to analyze the reasons for the incorrect results, we analyzed the incorrect lightning location data and the original LEMP data. Figure 14 shows a set of raw LEMP data participating in localization calculations. Figure 14a shows typical types of LEMP data. During thunderstorms, two or even more LEMP data points may appear within a sampling time window. If the envelope method is used for calculation, the detection site will only select the signal with the strongest amplitude for calculation. This method cannot guarantee that the data involved in localization are homologous. An incorrect location result arises when there is at least one non-homologous LEMP data point present. When using the signal cross-correlation method for localization calculation, the algorithm first selects homologous LEMP signals from the received LEMP data. Taking Figure 14 as an example, conducting a cross-correlation analysis between Figure 14a–d can exclude Figure 14a from the candidate queue. Several other typical electromagnetic interference signals are also listed in Figure 7. It should be emphasized that Figure 7c,d, which are electromagnetic interference signals, usually generate continuously. If cross-correlation calculations are not performed, the phenomenon shown in Figure 12f is inevitable.

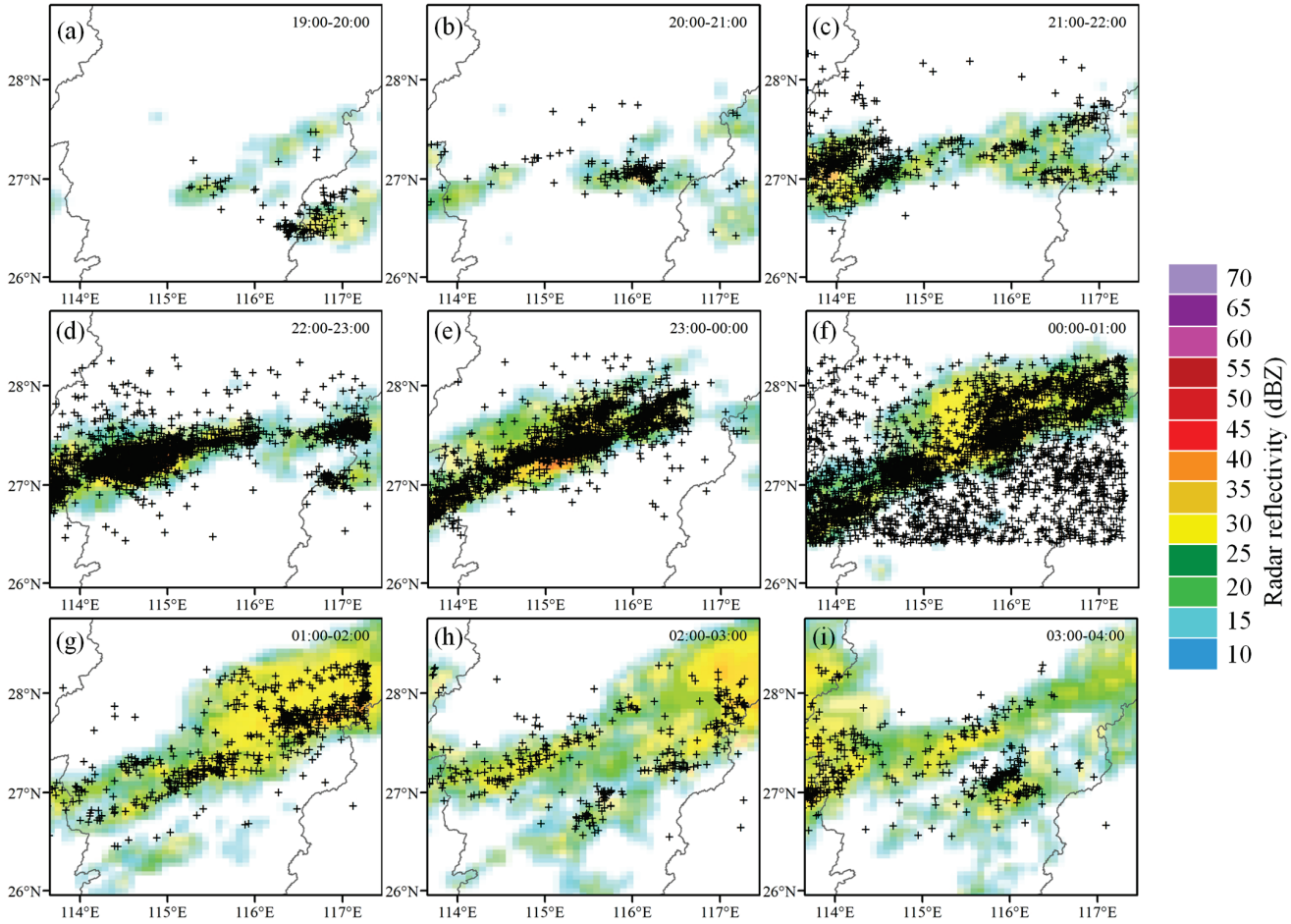

Figure 12. The location result of the APLLN by using envelope peak method. Subplots (**a**–**i**) show the lightning location results for each hour, respectively. The symbol '+' indicates the location of each lightning event.

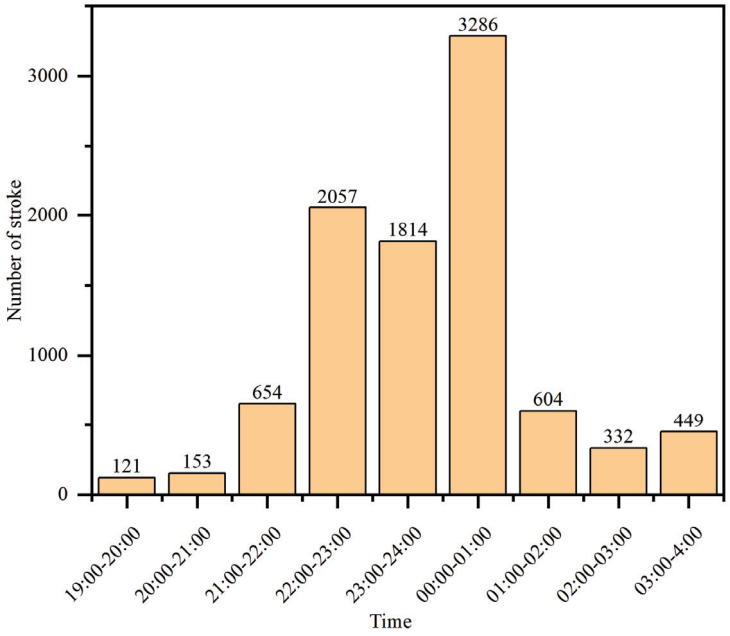

Figure 13. The number of lightning events detected by APLLN (envelope peak method) at different times.

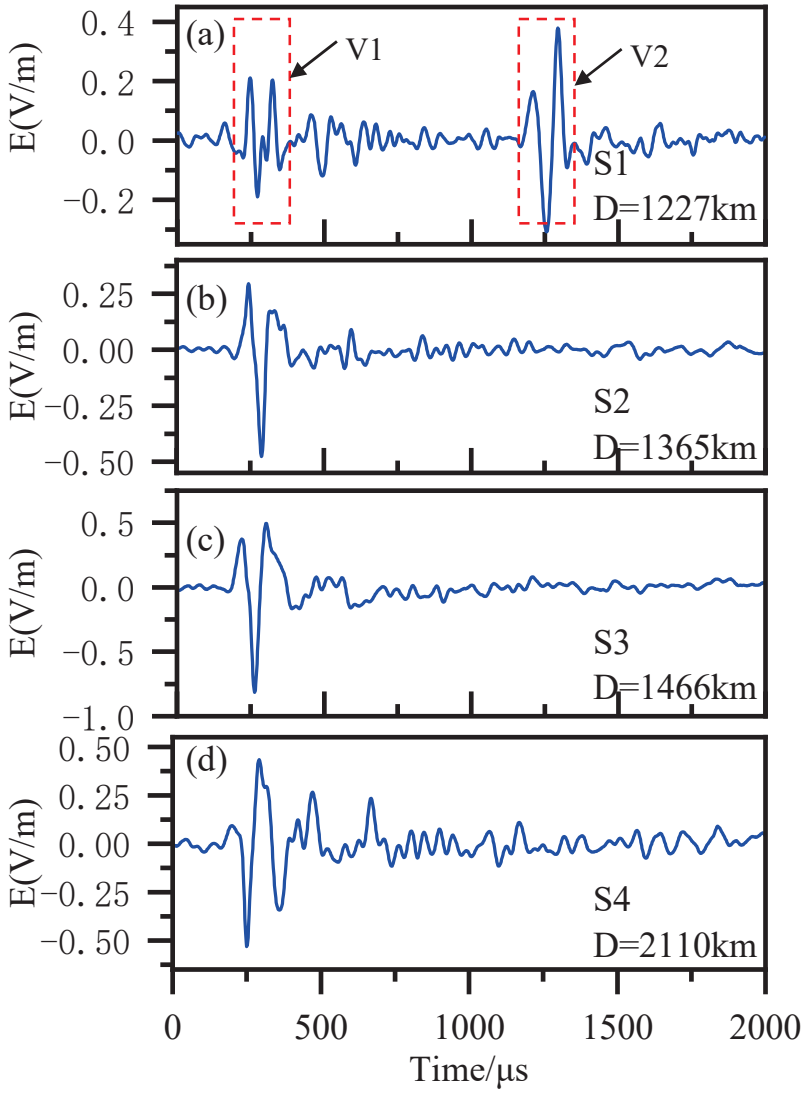

Figure 14. A set of LEMP waveform data for anomaly localization results. Subplots (**a**–**d**) represent the LEMP data received by each site. In subplot (**a**), two LEMPs are labeled with V1 and V2.

It is undeniable that using the cross-correlation method can improve the accuracy of the signal arrival time calculation and increase the success rate of localization. The statistical results from Figures 11 and 13 demonstrate this point well. But we also found that from 00:00 to 1:00, using the envelope peak method, the number of lightning localization was significantly higher than that using the signal cross-correlation method, which was significantly opposite to other times. One obvious factor is that there were 953 incorrect location results, accounting for 29% of the total. On the other hand, according to statistics, the envelope peak method may result in multiple localization results for the same lightning event due to its inability to accurately confirm the homology of events. These types of data account for approximately 3% of all data. Excluding the abnormal or erroneous data caused by these reasons, 2234 data points were located using the envelope peak method, which is less than the location results using the cross-correlation method. This also explains the abnormal situation from 00:00 to 1:00 very well.

5. Discussion

5.1. Relative Detection Efficiency

In order to compare and evaluate the data, this paper also used the three-dimensional lightning location network (advanced direction-time lightning detection system, ADTD)

data of the Institute of Electrical Engineering, Chinese Academy of Sciences [35]. The ADTD is a short-baseline lightning detection network, with an average distance between stations of about 100 km. The detection range covers most of China and some countries in Southeast Asia. It has been running stably for more than ten years; the lightning location accuracy in the network is better than 500 m, and the cloud-to-ground flash detection efficiency is better than 99%.

Within the same time, latitude, and longitude as described in Section 4.1 above, the ADTD has detected a total of 12,602 lightning strokes, including 8737 CG strokes and 3865 IC strokes. CG strokes accounted for 69.3% of all detected lightning strokes. IC strokes accounted for 30.7% of all lightning. As can be seen from Figure 15, the development trend of LEMP waveform data detected by the ADTD is consistent with that detected by the APLLN.

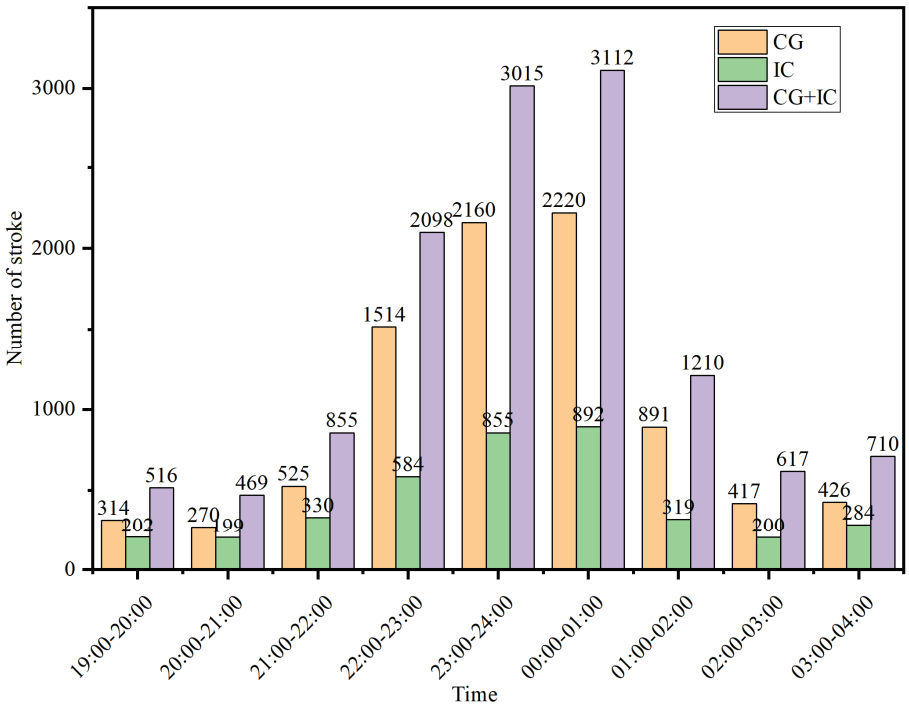

Figure 15. Distribution of LEMP waveform data detected by ADTD from 19:00 on 22 March 2023 to 4:00 on 23 March 2023. Purple means all types of lightning; orange means CG, and green means IC.

From the above discussion, it is evident that within the same latitude and longitude region at the same time, the ADTD detected a total of 12,602 lightning strokes. The APLLN (cross-correlation method) detected a total of 10,604 lightning strokes (the APLLN cross-correlation method detection rate is 84.1% of the ADTD). The APLLN (envelope peak method) detected a total of 9470 lightning strokes (the APLLN envelope peak method detection rate is 75.1% of the ADTD). In order to determine the relative detection efficiency of two detection nets, we needed to calculate the homologous events between the two detection nets. For different detection networks, there are different definitions of homologous events. Based on the characteristics of the APLLN detection network, Wang et al. [15] defined the detection distance of events less than 50 km and the time difference less than 0.5 ms as homologous events. In this paper, the same determination method was used to calculate homologous events. The method for calculating the relative detection efficiency (RDE) of APLLN is:

$$RDE = \frac{Shared\ events\ located\ by\ APLLN\ and\ ADTD}{Events\ located\ by\ ADTD} \quad (8)$$

The APLLN (cross-correlation method) detected a total of 8700 homologous lightning events with the ADTD. It accounted for 69% of the total ADTD detected. The APLLN (envelope peak method) detected a total of 5345 homologous lightning events with the ADTD. It accounted for 42.4% of the total the ADTD detected. The detection results of the APLLN (cross-correlation method) and the APLLN (envelope peak method) relative to the ADTD in different periods are shown in Figure 16.

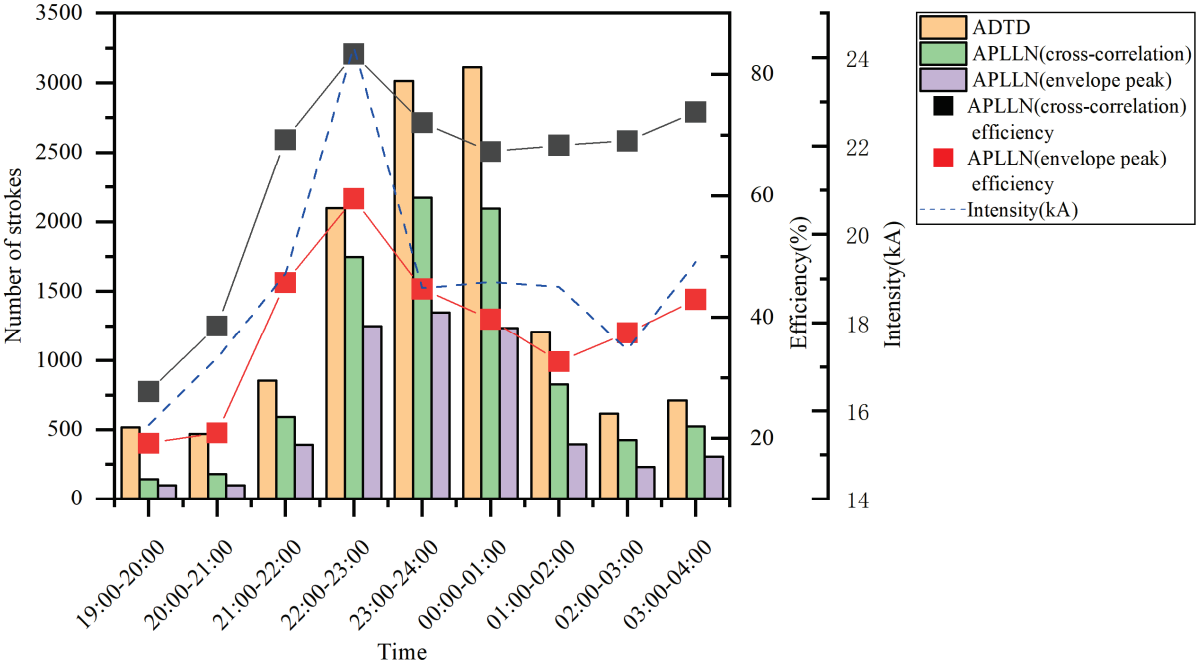

Figure 16. Distribution of lightning quantity and detection efficiency in different periods. Orange indicates the number of lightning strokes detected by ADTD. Green indicates the number of homologous data detections of APLLN (cross-correlation method) relative to ADTD. Purple represents the number of homologous data detections of APLLN (envelope peak method) relative to ADTD. The black square represents the detection efficiency of APLLN (cross-correlation method) relative to ADTD. The red square represents the detection efficiency of APLLN (envelope peak method) relative to ADTD. The blue dashed line represents the average peak current intensity of lightning detected by ADTD within each hour.

The detection efficiency is related to the peak current intensity and propagation distance of lightning. As the peak current intensity becomes stronger, the signal propagation distance becomes farther in the Earth–ionosphere waveguide and could be detected by more detection sites. From Figure 16, it can be seen that from 19:00 to 20:00, the relative detection efficiency of the APLLN is significantly lower. During this period, the average peak current intensity of lightning detected by the ADTD is 15.7 kA, which is significantly lower than other time periods. This also indicates that the improved the APLLN geolocation algorithm has a lightning detection efficiency of over 60% for lightning above 20 kA.

5.2. Relative Location Accuracy

The results of the ADTD were used as a reference in this paper. The location results of the APLLN (cross-correlation method) and the APLLN (envelope peak method) were compared with those of the ADTD. Within the same latitude and longitude region at the same time selected above, all the data located by each detection network were used for the calculation. The calculation method for relative location accuracy (RLA) can be represented by the following equation:

$$RLA = \frac{1}{n}\sum_{1}^{n}|Calculated\ value - Reference\ Value| \quad (9)$$

where the reference value and calculated value were selected from the localization results of the same lightning events in ADTD and APLLN, respectively. Considering the existence of errors, the likelihood of identical results between the two systems is relatively low. Therefore, it was necessary to determine an appropriate time tolerance. Similar to the calculation method for relative detection efficiency in Section 5.1, a time tolerance of 0.5 ms was set here. As long as the time error of the location results of the ADTD and APLLN was within 0.5 ms, it was considered as the location result of a lightning event. Finally, we calculated the mean of all errors to eliminate the influence of a small amount of data with larger errors.

To assess the location performance of the cross-correlation method and evaluate the improvement of location accuracy and detection efficiency of the cross-correlation method compared with the envelope peak method, we compared the results of the cross-correlation method and envelope peak method with those of the ADTD. The results are shown in Table 2. The APLLN (cross-correlation method) has a location accuracy of 4.5 km. This is consistent with the Monte Carlo simulation result in Figure 9. The APLLN (envelope peak method) has a location accuracy of 9.9 km. Figure 17 shows the distribution of location errors obtained using the envelope peak and the cross-correlation methods. It is obvious that the location error of the cross-correlation method is concentrated in 0~3 km, accounting for 75.6% of the total quantity. However, using the envelope method, only 27.8% of the data have a location error of less than 3 km. Table 2 summarizes the relative detection efficiency and location error of the APLLN, and it can be seen that the detection efficiency and detection accuracy of the APLLN (cross-correlation method) are greatly improved compared with the APLLN (envelope peak method).

Table 2. Performance evaluation of lightning location accuracy using different algorithms.

	Cross-Correlation Method	Envelope Peak Method
Stroke number	10,604	9470
Homologous events with ADTD	8700	5345
Detection efficiency relative to ADTD	69%	42.4%
Location accuracy relative to ADTD	4.5 km	9.9 km

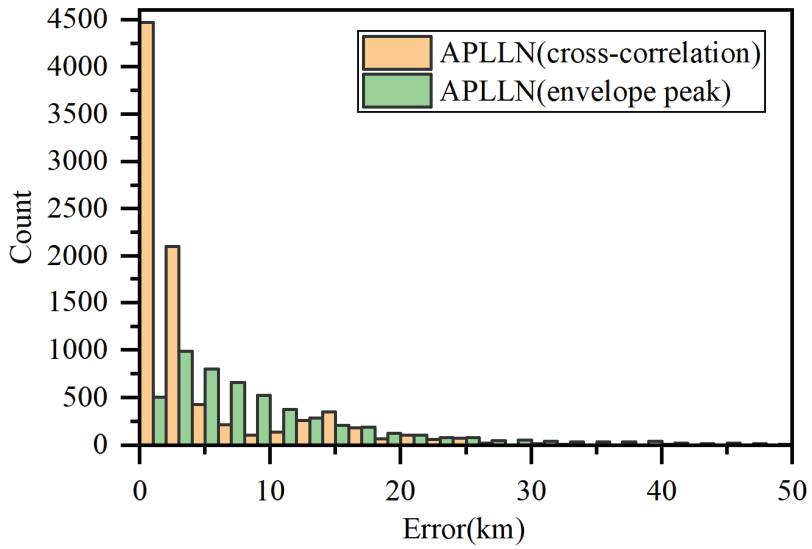

Figure 17. Distribution diagram of relative location error between envelope peak and cross-correlation method.

6. Conclusions

In this paper, we present an improved algorithm for the long-baseline lightning location network, which aims to achieve better LEMP detection efficiency and location accuracy:

(1) An LEMP waveform compression method based on PCA is proposed and applied for the first time, which realizes real-time compression and the efficient transmission of LEMP waveform data. The compression time for each data point is less than 1 ms.
(2) The cross-correlation technique of the long-baseline LEMP waveform is proposed. On the one hand, the influence of noise on location accuracy is minimized, and on the other hand, the accuracy of calculating the signal arrival time difference is improved.
(3) The relative detection efficiency and relative location accuracy of the waveform cross-correlation method and envelope peak method were evaluated with ADTD data. The detection performance of the long-baseline lightning location network can be further improved by using waveform cross-correlation technology. The lightning location accuracy can be better than 4.5 km, and the relative detection efficiency can reach 69%. It should be emphasized that the location accuracy of the proposed method is twice higher than that of the envelope peak method.

Author Contributions: Conceptualization, T.Z., J.W., Q.M. and L.F.; methodology, T.Z., J.W., Q.M. and L.F.; software, T.Z. and J.W.; validation, J.W., Q.M. and L.F.; formal analysis, Q.M. and L.F.; investigation, T.Z., J.W., Q.M. and L.F.; resources, J.W., Q.M. and L.F.; data curation, T.Z.; writing—original draft preparation, T.Z., J.W., Q.M. and L.F.; writing—review and editing, T.Z., J.W., Q.M. and L.F.; visualization, T.Z.; supervision, L.F.; project administration, J.W., Q.M. and L.F.; funding acquisition, J.W., Q.M. and L.F. All authors have read and agreed to the published version of the manuscript.

Funding: This work was funded by National Natural Science Foundation of China (NO. 42174226), National Key R&D Program of China (2023YFC3006800), the National Key Laboratory on Electromagnetic Environmental Effects and Electro-optical Engineering (No. JCKYS2022LD5), and the Fund of Institute of Electrical Engineering, Chinese Academy of Sciences (E1555401, E1555402).

Data Availability Statement: The data presented in this study are available in following resources: http://www.cnlightning.cn (accessed on 21 April 2023).

Acknowledgments: The authors thank all personnel and meteorological departments involved in the construction of the lightning location site, lightning data collection, and processing.

Conflicts of Interest: The authors declare no conflicts of interest.

References

1. Nag, A.; Murphy, M.J.; Schulz, W.; Cummins, K.L. Lightning locating systems: Insights on characteristics and validation techniques. *Earth Space Sci.* **2015**, *2*, 65–93. [CrossRef]
2. Kawasaki, Z.; Mardiana, R.; Ushio, T. Broadband and narrowband RF interferometers for lightning observations. *Geophys. Res. Lett.* **2000**, *27*, 3189–3192. [CrossRef]
3. Dong, W.; Liu, X.; Zhang, Y.; Zhang, G. Observations on the leader-return stroke of cloud-to-ground lightning with the broadband interferometer. *Sci. China Ser. D Earth Sci.* **2002**, *45*, 259–269. [CrossRef]
4. Qiu, S.; Zhou, B.-H.; Shi, L.-H.; Dong, W.-S.; Zhang, Y.-J.; Gao, T.-C. An improved method for broadband interferometric lightning location using wavelet transforms. *J. Geophys. Res. Atmos.* **2009**, *114*, D18211. [CrossRef]
5. Liu, H.; Dong, W.; Wu, T.; Zheng, D.; Zhang, Y. Observation of compact intracloud discharges using VHF broadband interferometers. *J. Geophys. Res. Atmos.* **2012**, *117*, D01203. [CrossRef]
6. Zhang, G.; Wang, Y.; Qie, X.; Zhang, T.; Zhao, Y.; Li, Y.; Cao, D. Using lightning locating system based on time-of-arrival technique to study three-dimensional lightning discharge processes. *Sci. China Earth Sci.* **2010**, *53*, 591–602. [CrossRef]
7. Budden, K.G.I. The propagation of a radio-atmospheric. *Lond. Edinb. Dublin Philos. Mag. J. Sci.* **1951**, *42*, 1–19. [CrossRef]
8. Barr, R.; Jones, D.L.; Rodger, C.J. ELF and VLF radio waves. *J. Atmos. Sol.-Terr. Phys.* **2000**, *62*, 1689–1718. [CrossRef]
9. Dowden, R.L.; Brundell, J.B.; Rodger, C.J. VLF lightning location by time of group arrival (TOGA) at multiple sites. *J. Atmos. Sol.-Terr. Phys.* **2002**, *64*, 817–830. [CrossRef]
10. Said, R.K.; Inan, U.S.; Cummins, K.L. Long-range lightning geolocation using a VLF radio atmospheric waveform bank. *J. Geophys. Res. Atmos.* **2010**, *115*, D23108. [CrossRef]

11. Pessi, A.T.; Businger, S.; Cummins, K.L.; Demetriades, N.W.S.; Murphy, M.; Pifer, B. Development of a Long-Range Lightning Detection Network for the Pacific: Construction, Calibration, and Performance. *J. Atmos. Ocean. Technol.* **2009**, *26*, 145–166. [CrossRef]
12. Rodger, C.J.; Werner, S.; Brundell, J.B.; Lay, E.H.; Thomson, N.R.; Holzworth, R.H.; Dowden, R.L. Detection efficiency of the VLF World-Wide Lightning Location Network (WWLLN): Initial case study. *Ann. Geophys.* **2006**, *24*, 3197–3214. [CrossRef]
13. Rodger, C.J.; Brundell, J.B.; Holzworth, R.H.; Lay, E.H. Growing detection efficiency of the World Wide Lightning Location Network. *Amer. IOP Conf. Proc.* **2009**, *1118*, 15–20. [CrossRef]
14. Rodger, C.J.; Brundell, J.B.; Hutchins, M.; Holzworth, R.H. The world wide lightning location network (WWLLN): Update of status and applications. In Proceedings of the 2014 XXXIth URSI General Assembly and Scientific Symposium (URSI GASS), Beijing, China, 16–23 August 2014; pp. 1–2. [CrossRef]
15. Wang, J.; Ma, Q.; Zhou, X.; Xiao, F.; Yuan, S.; Chang, S.; He, J.; Wang, H.; Huang, Q. Asia-Pacific Lightning Location Network (APLLN) and Preliminary Performance Assessment. *Remote Sens.* **2020**, *12*, 1537. [CrossRef]
16. Wang, T.; Chen, F.; Zhang, C.; Sun, Y.; Zhu, W.; Qu, X. Source Locating Algorithm for Ultra-long Baseline Lightning Detection System Based on TDOA. *High Volt. Eng.* **2020**, *46*, 1807–1813. [CrossRef]
17. Wessel, P. Compression of large data grids for Internet transmission. *Comput. Geosci.* **2003**, *29*, 665–671. [CrossRef]
18. Jolliffe, I.T.; Cadima, J. Principal component analysis: A review and recent developments. *Philos. Trans. R. Soc. A Math. Phys. Eng. Sci.* **2016**, *374*, 20150202. [CrossRef] [PubMed]
19. Ringnér, M. What is principal component analysis? *Nat. Biotechnol.* **2008**, *26*, 303–304. [CrossRef] [PubMed]
20. Cadima, J.; Cerdeira, J.O.; Minhoto, M. Computational aspects of algorithms for variable selection in the context of principal components. *Comput. Stat. Data Anal.* **2004**, *47*, 225–236. [CrossRef]
21. Pankratius, V.; Jannesari, A.; Tichy, W.F. Parallelizing Bzip2: A Case Study in Multicore Software Engineering. *IEEE Softw.* **2009**, *26*, 70–77. [CrossRef]
22. Bentley, J.L.; Sleator, D.D.; Tarjan, R.E.; Wei, V.K. A Locally adaptive data-compression scheme. *Commun. ACM* **1986**, *29*, 320–330. [CrossRef]
23. Lee, A.C.L. An experimental study of the remote location of lightning flashes using a VLF arrival time difference technique. *Q. J. R. Meteorol. Soc.* **1986**, *112*, 203–229. [CrossRef]
24. Betz, H.D.; Schmidt, K.; Laroche, P.; Blanchet, P.; Oettinger, W.P.; Defer, E.; Dziewit, Z.; Konarski, J. LINET—An international lightning detection network in Europe. *Atmos. Res.* **2009**, *91*, 564–573. [CrossRef]
25. Biagi, C.J.; Cummins, K.L.; Kehoe, K.E.; Krider, E.P. National Lightning Detection Network (NLDN) performance in southern Arizona, Texas, and Oklahoma in 2003–2004. *J. Geophys. Res. Atmos.* **2007**, *112*, D05208. [CrossRef]
26. Liu, B.; Shi, L.; Qiu, S.; Liu, H.; Dong, W.; Li, Y.; Sun, Z. Fine Three-Dimensional VHF Lightning Mapping Using Waveform Cross-Correlation TOA Method. *Earth Space Sci.* **2020**, *7*, e2019EA000832. [CrossRef]
27. Stock, M.G.; Akita, M.; Krehbiel, P.R.; Rison, W.; Edens, H.E.; Kawasaki, Z.; Stanley, M.A. Continuous broadband digital interferometry of lightning using a generalized cross-correlation algorithm. *J. Geophys. Res. Atmos.* **2014**, *119*, 3134–3165. [CrossRef]
28. Lyu, F.; Cummer, S.A.; Solanki, R.; Weinert, J.; McTague, L.; Katko, A.; Barrett, J.; Zigoneanu, L.; Xie, Y.; Wang, W. A low-frequency near-field interferometric-TOA 3-D Lightning Mapping Array. *Geophys. Res. Lett.* **2014**, *41*, 7777–7784. [CrossRef]
29. Wu, T.; Wang, D.; Takagi, N. Lightning Mapping With an Array of Fast Antennas. *Geophys. Res. Lett.* **2018**, *45*, 3698–3705. [CrossRef]
30. Bitzer, P.M.; Christian, H.J.; Stewart, M.; Burchfield, J.; Podgorny, S.; Corredor, D.; Hall, J.; Kuznetsov, E.; Franklin, V. Characterization and applications of VLF/LF source locations from lightning using the Huntsville Alabama Marx Meter Array. *J. Geophys. Res.-Atmos.* **2013**, *118*, 3120–3138. [CrossRef]
31. Koshak, W.J.; Solakiewicz, R.J.; Blakeslee, R.J.; Goodman, S.J.; Christian, H.J.; Hall, J.M.; Bailey, J.C.; Krider, E.P.; Bateman, M.G.; Boccippio, D.J.; et al. North Alabama Lightning Mapping Array (LMA): VHF source retrieval algorithm and error analyses. *J. Atmos. Ocean. Technol.* **2004**, *21*, 543–558. [CrossRef]
32. Rodger, C.J.; Brundell, J.B.; Dowden, R.L. Location accuracy of VLF World-Wide Lightning Location (WWLL) network: Post-algorithm upgrade. *Ann. Geophys.* **2005**, *23*, 277–290. [CrossRef]
33. Wang, Y.; Qie, X.S.; Wang, D.F.; Liu, M.Y.; Su, D.B.; Wang, Z.C.; Liu, D.X.; Wu, Z.J.; Sun, Z.L.; Tian, Y. Beijing Lightning Network (BLNET) and the observation on preliminary breakdown processes. *Atmos. Res.* **2016**, *171*, 121–132. [CrossRef]
34. Dowden, R.L.; Holzworth, R.H.; Rodger, C.J.; Lichtenberger, J.; Thomson, N.R.; Jacobson, A.R.; Lay, E.; Brundell, J.B.; Lyons, T.J.; O'Keefe, S.; et al. World-Wide Lightning Location Using VLF Propagation in the Earth-Ionosphere Waveguide. *IEEE Antennas Propag. Mag.* **2008**, *50*, 40–60. [CrossRef]
35. Wang, J.; Huang, Q.; Ma, Q.; Chang, S.; He, J.; Wang, H.; Zhou, X.; Xiao, F.; Gao, C. Classification of VLF/LF Lightning Signals Using Sensors and Deep Learning Methods. *Sensors* **2020**, *20*, 1030. [CrossRef] [PubMed]

Disclaimer/Publisher's Note: The statements, opinions and data contained in all publications are solely those of the individual author(s) and contributor(s) and not of MDPI and/or the editor(s). MDPI and/or the editor(s) disclaim responsibility for any injury to people or property resulting from any ideas, methods, instructions or products referred to in the content.

land

MDPI

Article

Analysis of Changes in Ecological Environment Quality and Influencing Factors in Chongqing Based on a Remote-Sensing Ecological Index Mode

Yizhuo Liu [1], Tinggang Zhou [1,2,*] and Wenping Yu [1,3,4,*]

[1] School of Geographical Sciences, Southwest University, Chongqing 400715, China; liuyizhuo@email.swu.edu.cn
[2] Three Gorges Reservoir Key Laboratory of Ecological Environment of Ministry of Education, Chongqing 400715, China
[3] Chongqing Jinfo Mountain Karst Ecosystem National Observation and Research Station, School of Geographical Sciences, Southwest University, Chongqing 400715, China
[4] Yibin Academy of Southwest University, Yibin 644000, China
* Correspondence: zhoutg@swu.edu.cn (T.Z.); ywpgis2005@swu.edu.cn (W.Y.)

Abstract: Chongqing is a large municipality in southwestern China, having the characteristics of a vast jurisdiction, complex topography, and a prominent dual urban–rural structure. It is vitally important to optimize the spatial layout of land and efficiency of natural resource allocation, achieve sustainable development, and conduct influence assessment and causation analysis in this region. Here, using the Google Earth Engine platform, we selected Landsat remote-sensing (RS) images from the period 2000–2020 and constructed a remote-sensing ecological index (RSEI) model. Considering the urban spatial pattern division in Chongqing, the Sen + Mann–Kendall analytical approach was employed to assess the fluctuating quality of the ecological environment in different sectors of Chongqing. Subsequently, single-factor and interaction detectors in the Geodetector software tool were used to conduct causation analysis on the RSEI, with the use of eight elements: elevation, slope, aspect, precipitation, temperature, population, land use, and nighttime lighting. Findings indicate that, over the course of the investigation period, the eco-quality in Chongqing displayed a pattern of degradation, succeeded by amelioration. The RSEI decreased from 0.700 in 2000 to 0.590 in 2007, and then gradually recovered to 0.716 in 2018. Overall, the eco-environment quality of Chongqing improved. Spatially, changes in the RSEI were consistent with the planning and positioning of the urban spatial pattern. The main new urban area and periphery of the central urban area showed a slight deterioration, while other regions showed marked improvement. The combined effect of any two elements enhanced the explanatory power of a single factor, with elevation, temperature, and land use being the strongest explanatory elements of eco-quality in Chongqing. The most influential factor explaining the spatial variation of the RSEI was determined to be the combined impact of elevation and land use. At the temporal scale, elements related to human activities showed the most evident trend in explanatory power.

Keywords: Google Earth Engine; Landsat; remote-sensing ecological index model; Geodetector; Chongqing

1. Introduction

With the rapid advancement in economic and social development, the influence of human activities on eco-environment change has become increasingly evident [1]. In this context, coordinating economic and social development with ecological protection and optimization of the spatial layout of land is vitally important [2]. Optimally dividing the urban spatial pattern and constructing different development strategies based on the relative

resource endowments of different regions is an important strategy for coordinating urban–rural development and resolving internal contradictions within natural ecosystems [3]. The evaluation of eco-environment quality is a crucial process in coordinating harmonious development between humans and nature. Therefore, it is essential to use appropriate methods to assess the influence of urban clusters and their surrounding natural spaces, explore key elements influencing influence change, and verify the compatibility of the chosen method with urban spatial patterns [4].

Chongqing, a large municipality in southwestern China, possesses a vast administrative jurisdiction, diverse topography, and a distinct dual urban–rural structure [5]. It is the most populous and largest directly controlled municipality in China, exhibiting marked differences in natural conditions, resource endowments, and development potential among its different regions, and between its urban and rural areas [6]. In response to this, in 2014, Chongqing proposed the "one zone, two groups" urban spatial pattern, considering the differences in natural conditions, urban distribution patterns, and development situations in various areas across the municipality. This determined the development priorities of each region and put forward new requirements for nature conservation [7]. Currently, numerous researchers have conducted assessments of eco-environment quality in the region from various perspectives. For instance, Zhang et al. (2023) focused on the upper reaches of the Yangtze River and explored the relationship between natural conditions and ecological environmental patterns in that area [8]. Kang et al. (2023) centered on the Chengdu–Chongqing urban agglomeration and conducted a preliminary evaluation of the eco-environment quality in that region [9]. Wang et al. (2023), focusing on Chongqing Municipality, conducted a preliminary exploration of the factors influencing the spatial patterns of the eco-environment in the area from 2011 to 2021 [10]. However, there is currently a lack of research on eco-environment quality from the perspective of urban spatial patterns, and the significant differences in natural conditions and development status among various regions of Chongqing Municipality have not been adequately addressed in previous studies. Thus, targeted studies in this regard are urgently needed.

Remote sensing (RS), owing to its macroscopic, multi-spectral, and multi-temporal characteristics, is extensively employed in monitoring ecological conditions [11]. However, traditional influence assessment methods often rely on a single evaluation index, making it challenging to reveal systematic changes in the eco-environment and compare the effects of various influencing elements [12]. Despite the current lack of an influence assessment system for urban spatial patterns, the remote-sensing ecological index (RSEI) has been widely applied in comprehensive regional influence assessments [13–15]. The RSEI, by coupling four evaluation elements—normalized difference vegetation index (NDVI), wetness (WET), land surface temperature (LST), and normalized difference built-up index (NDBI)—avoids the problems associated with single-index evaluations and allows for visualization. Owing to its various advantages, the RSEI has been widely applied in regions including urban [16], wetlands [17], and arid region [18], and its reliability has been validated. It thus holds the potential for application in eco-environment quality assessments tailored to urban spatial patterns.

Because the eco-environment is in constant dynamic change, conducting long-term eco-environment monitoring and exploring its influencing elements are crucial for adjusting regional development strategies, mitigating climate change, and achieving sustainable development. The Google Earth Engine (GEE) platform provides convenient access to a large amount of publicly available resources and can handle massive geospatial datasets, making it suitable for large-scale, long-term monitoring. Previous studies have demonstrated the notable advantages of the GEE platform in eco-environment assessment and natural disaster change detection [19]. Therefore, scholars have increasingly combined the GEE platform with the RSEI, conducting research in small regions [20], urban clusters [21], and river basins [22], achieving promising results. In existing studies, researchers have generally incorporated the Geodetector software tool proposed by Wang et al. (2017) [23], using common elements in natural conditions and human activities to explain the detection

results, although such analysis mainly focused on spatial patterns and the temporal resolution was relatively low. This is because the cases in which the RSEI was applied in existing research were mostly specific terrain or administrative areas, where spatial differences were not prominent, making the exploration of changes in the driving forces of different elements less meaningful [24–26]. This contributes to the limited number of application cases with high temporal resolution for the Geodetector tool.

This study is based on the complex urban spatial pattern of Chongqing, and aims to conduct a long time-series assessment of eco-environment change. It utilizes multiple elements from different perspectives to carry out Geodetector factor detection on an annual basis. This approach not only explores the eco-environment quality under different urban patterns but also, based on the advantage of high temporal resolution, introduces the Sen + Mann–Kendall and linear regression methods to fit the trends of driving elements. Therefore, this study aims to address some of the limitations of traditional RSEI applications by providing an example of a long-term sequential analysis of potential influencing factors on the eco-environment. It also seeks to explore the response of Chongqing Municipality's eco-environment to the "one zone, two groups" policy orientation, verify the effectiveness of current policies, and lay the groundwork for future ecological protection efforts in Chongqing Municipality.

2. Material and Methods

2.1. Study Area

Chongqing Municipality (28°10′–32°13′ N, 105°11′–110°11′ E) is positioned in southwestern China, on the upper reaches of the Yangtze River, within the transitional area between the Qinghai–Tibet Plateau and the middle–lower reaches plain of the Yangtze River. This region falls within the subtropical monsoon humid climate zone, characterized by a minor annual temperature fluctuation and ample rainfall. The average temperature is relatively mild throughout the year. The topography of Chongqing Municipality is predominantly hilly–mountainous, with lower elevations in the southwestern and central areas. In contrast, the eastern part of the municipality includes the Wuling and Daba Mountains, with the overall terrain height gradually decreasing from north to south along the Yangtze River valley (Figure 1). The geological structure is relatively complex and features extensive karst landscapes.

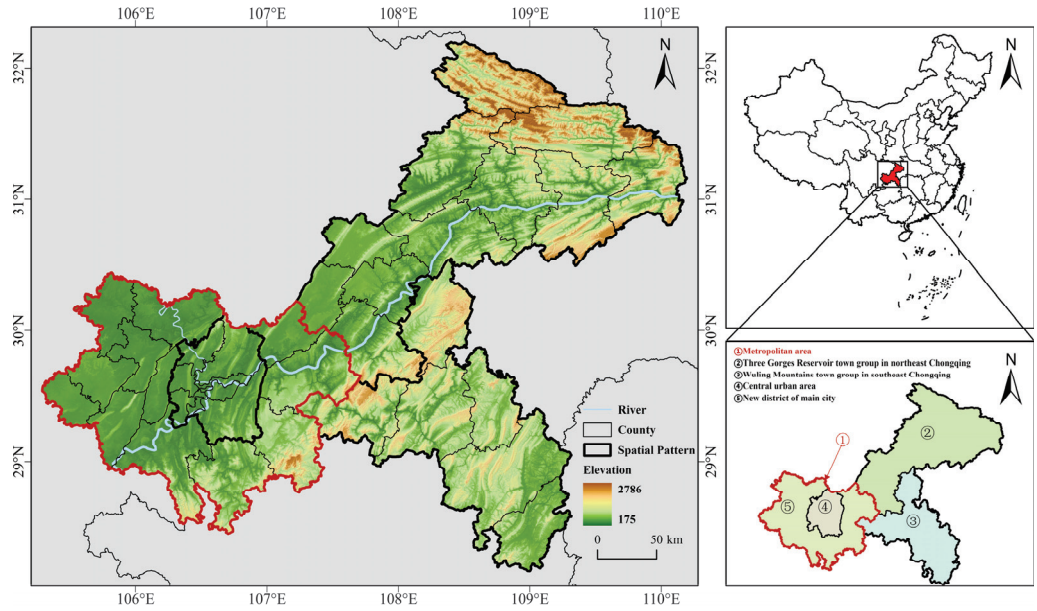

Figure 1. Geographical conditions and urban spatial pattern of Chongqing Municipality.

The primary types of vegetation include evergreen needleleaf forests, evergreen broadleaf forests, and deciduous broadleaf forests, with an overall vegetation coverage rate of 55.04%. The administrative jurisdiction of Chongqing Municipality covers a total area of 82,402.95 km^2. The urban spatial pattern is divided into the main city metropolitan area, Three Gorges Reservoir town group in northeast Chongqing, and Wuling Mountains town group in southeast Chongqing. The main city metropolitan area comprises the central urban area and new district of the main city. At the end of 2022, the permanent population was 32.13 million, with an urbanization rate of 70.96%, and a gross domestic product of CNY 2912.903 billion.

2.2. Data

The RS data utilized were sourced from Landsat images within the GEE platform database. Specifically, Landsat 5 TM images were used for the period 2000–2012, while Landsat 8 OLI images were employed for the period 2013–2020. Both datasets belong to the T1 level. These data underwent radiometric calibration, geometric correction, and atmospheric correction processes to ensure their reliability and accuracy. Considering the growth of vegetation and the weather characteristics of frequent cloud cover and fog in the study area, we focused on data from the months of June to September. To minimize the influence of atmospheric elements on the images, a thorough data quality screening process was implemented. Additionally, image mosaicking, resampling, cropping, and filling of invalid pixels were carried out to enhance the overall quality and suitability of the data for the subsequent analysis of eco-environment changes in Chongqing.

Population density data were sourced from the LandScan Global dataset (https://landscan.ornl.gov/ (accessed on 22 July 2023)) released by the Oak Ridge National Laboratory, a dataset acknowledged for its comprehensive depiction of global population distribution [27,28]. Land-use data were derived from the China Annual Land Cover Dataset, produced by researchers at Wuhan University, led by Yang et al. (2022) [29]. Nighttime light data, comprehensively reflecting elements such as transportation routes, residential areas, and urban development, is widely considered a crucial visual data source for capturing economic activities [30]. Thus, we adopted the Defense Meteorological Satellite Program/Operational Linescan System nighttime light dataset, accessible at https://dataverse.harvard.edu/ (accessed on 24 July 2023).

Digital elevation model (DEM) data for slope calculations were obtained from the National Aeronautics and Space Administration Earth Science Data Network (https://data.nasa.gov/ (accessed on 23 July 2023)). Temperature and precipitation data were sourced from the National Tibetan Plateau Data Center (https://data.tpdc.ac.cn/ (accessed on 24 July 2023)), and included datasets for monthly precipitation and average temperature spanning the period 1901–2022 [31,32]. During the monthly data processing, we aggregated the precipitation data for the months of June to September for each study year and calculated the average temperature for the same period to derive the cumulative precipitation and average temperature data for each study year from June to September. The integration of DEM, temperature, and precipitation data allows for a comprehensive analysis of eco-environment changes in Chongqing, taking into account elements such as slope, temperature, and precipitation in the assessment model.

2.3. Remote-Sensing Ecological Index Model

Xu (2013) proposed a comprehensive RSEI. This index is based on RS information and integrates various ecological elements for regional eco-environment RS evaluation [33]. The RSEI consists of four indicators: greenness (NDVI), wetness (Wet), dryness (NDBSI), and warmth (LST). The weights of these indicators are determined by their relative contributions in principal component analysis (PCA). For the calculation methods of each ecological index, please refer to Table 1.

Table 1. Calculation methods for ecological indicators.

Index	Method of Calculation
NDVI	$NDVI = (NIR - Red)/(NIR + Red)$
NDBSI	$SI = \frac{[(S_1+Red)-(Blue+NIR)]}{[(S_1+Red)+(Blue+NIR)]}$
	$IBI = \frac{\left\{\frac{2S_1}{S_1+NIR} - \left[\frac{NIR}{NIR+Red} + \frac{Green}{Green+S_1}\right]\right\}}{\left\{\frac{2S_1}{S_1+NIR} + \left[\frac{NIR}{NIR+Red} + \frac{Green}{Green+S_1}\right]\right\}}$
	$NDBSI = (SI + IBI)/2$
WET	$TM:\ WET = 0.0315Blue + 0.2021Green + 0.3102Red + 0.1594NIR - 0.6806S_1 - 0.6109S_2$
	$OIL:\ WET = 0.1511Blue + 0.1972Green + 0.3283Red + 0.3407NIR - 0.7117S_1 - 0.4559S_2$
LST	$LST = \frac{T}{\left[1+\left(\frac{\lambda T}{1.438\times10^{-2}}\right)\ln\varepsilon\right]} - 273.15$

Notes: *Red*, *Blue*, *Green*, *NIR*, S_1, and S_2 represent the reflectance values of Landsat imagery in the blue, green, red, near-infrared, shortwave infrared 1, and shortwave infrared 2 bands, respectively [34]. The calculation of *LST* employs an atmospheric correction algorithm [35]. In the *LST* formula, *T* represents the sensor's thermal value; λ denotes the center wavelength of the thermal infrared band; and ε represents the surface emissivity [36].

After obtaining the four standardized ecological indices for each year, we utilized PCA to transform these variables, yielding the first principal component (PCA1). The initial values of the RSEI can be expressed by the difference between *PCA1* and 1, namely:

$$RSEI_0 = 1 - \{PCA1[f(NDVI, LST, WET, NDBSI)]\}. \quad (1)$$

To ensure accurate analysis of the *RSEI* across different time periods, we standardized the initial *RSEI*:

$$RSEI = \frac{RSEI_0 - RSEI_{Min}}{RSEI_{Max} - RSEI_{Min}}, \quad (2)$$

where the final *RSEI* has a value ranging from 0 to 1. A greater value signifies a more positive impact. *RSEImax* signifies the highest achievable value of the influence index, whereas *RSEImin* denotes the lowest attainable value.

2.4. Geodetector

Geodetector, available at http://www.geodetector.cn/ (accessed on 23 July 2023), serves as an analytical software tool employed to identify the spatial heterogeneity of a dependent variable and unveil the contributing elements influencing it [23]. According to our research requirements, we utilized both the single-factor detector and interaction detector within Geodetector for analysis herein. The single-factor detector was employed to examine the spatial differentiation explanatory power of each influencing factor on the RSEI. This explanatory power is measured by a variable, denoted as *q*, with values ranging from 0 to 1. A greater *q* value represents a stronger explanatory power of the influencing element on the spatial differentiation characteristics of the RSEI. The expression is as follows:

$$q = 1 - \frac{\sum_{h=1}^{L} N_h \sigma_h^2}{N\sigma^2}, \quad (3)$$

where *L* represents the number of layers for the independent variable x_i, N_h represents the sample size within *N* layers and in the region, and σ^2 and σ_h^2 represent the population variances. The model is valid when $\sigma^2 \neq 0$. The interaction detector was used to assess the interaction among different elements (*xi*) to evaluate the influence on the explanatory power of variables when driven by multiple elements. Assuming $q(x_1)$ and $q(x_2)$ represent the explanatory powers of elements x_1 and x_2 on the spatial differentiation characteristics of the RSEI, $q(x_1 \cap x_2)$ represents the explanatory power after the interaction between these elements. There are five different influence patterns, as detailed in Table 2.

Table 2. Interaction types.

Criterion	Mode
$q(x_1 \cap x_2) < Min(q(x_1), q(x_2))$	Nonlinear weakening
$Min(q(x_1), q(x_2)) < q(x_1 \cap x_2) < Max(q(x_1), q(x_2))$	Single-factor nonlinear weakening
$q(x_1 \cap x_2) > Max(q(x_1), q(x_2))$	Two-factor enhancement
$q(x_1 \cap x_2) = q(x_1) + q(x_2)$	Independent
$q(x_1 \cap x_2) > q(x_1) + q(x_2)$	Nonlinear enhancement

2.5. Sen + Mann–Kendall Trend Analysis

The Theil–Sen median method is a non-parametric statistical approach for trend calculation [37–39]. Its formula is:

$$\beta = median\left(\frac{x_j - x_i}{j - i}\right), \forall j > i, \tag{4}$$

where x_j and x_i represent time-series data. A positive β value represents an ascending trend in the time series, whereas a negative value signifies a descending trend.

Similarly, the Mann–Kendall method is also a non-parametric test that does not require distribution assumptions for sample data, thereby reducing the influence of outliers on the results [40–42]. The Mann–Kendall method sets a test statistic, S, which is calculated as follows:

$$\theta = x_j - x_i, \tag{5}$$

$$S = \sum_{i=1}^{n-1} \sum_{j=i+1}^{n} sgn(\theta), \tag{6}$$

where, when $\theta > 0$, sgn(θ) = 1; when $\theta < 0$, sgn(θ) = -1; and when $\theta = 0$, sgn(θ) = 0. Based on this, we can construct the variance, Var(S), of S, which is formulated as follows:

$$Var(S) = \frac{n(n-1)(2n+5) - \sum_{i=1}^{m} t_i(t_i - 1)(2t_i + 5)}{18}, \tag{7}$$

where n represents the number of dots, m is the number of groups with the same value samples, and t_i denotes the number of ties in range i. If $n > 10$, the slope can be represented by Z, calculated as follows:

$$Z = \begin{cases} \frac{S-1}{\sqrt{VAR(S)}}, & (S > 0) \\ 0, & (S = 0) \\ \frac{S+1}{\sqrt{VAR(S)}}, & (S < 0) \end{cases}. \tag{8}$$

The Sen + Mann–Kendall trend analysis method merges the Theil–Sen median method and the Mann–Kendall method. It utilizes the parameter β from the Theil–Sen median method to determine the direction of the trend and the Z value from the Mann–Kendall method to assess the significance of the trend. For a significance level, α, of 0.05, the critical Z value is 1.96. On the basis of this value, trends are categorized as follows: if $|Z| > 1.96$ and $\beta > 0.0005$, a significant improvement is indicated; if $|Z| < 1.96$ and $\beta > 0.0005$, a slight improvement is indicated; if $|Z| > 1.96$ and $\beta < -0.0005$, a significant degradation is indicated; if $|Z| < 1.96$ and $\beta < -0.0005$, a slight degradation is indicated; and if $-0.0005 \leq \beta \leq 0.0005$, there is no significant change. These classifications were used to categorize the trends in RSEI values over multiple years.

3. Results

3.1. Eco-Environment Quality and Changes in Chongqing

The temporal variation of the RSEI in Chongqing Municipality is illustrated in Figure 2. Eco-environment changes in Chongqing between 2000 and 2020 can be divided into two phases, with 2007 as the boundary year. From 2000 to 2007, the RSEI exhibited a fluctuating descendant trend, gradually decreasing from 0.7005 in 2000 to 0.5904 in 2007. The linear fit goodness was 0.5576, indicating a distinct deteriorating trend in the eco-environment of Chongqing during this period. From 2007 to 2020, the RSEI exhibited a fluctuating upward trend, reaching 0.7163 in 2018. The linear fit goodness was 0.6091, suggesting a gradual improvement in the eco-environment during this phase. Therefore, during the study period, the eco-environment quality in Chongqing showed a V-shaped trend of deterioration followed by improvement. Overall, from 2000 to 2020, there was a slight improvement in the eco-environment quality in Chongqing.

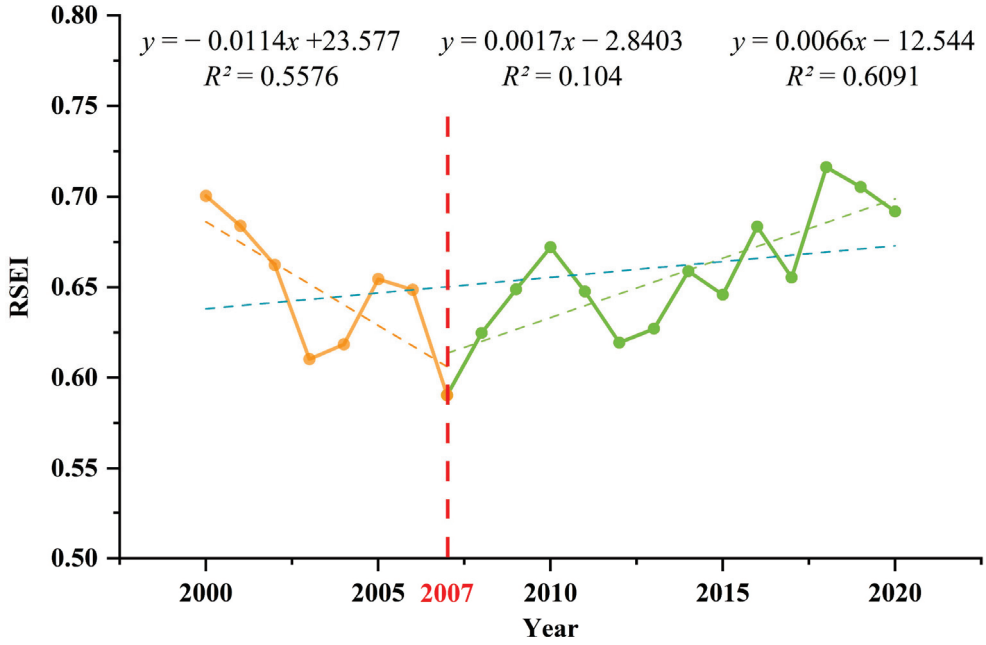

Figure 2. Trend of remote-sensing ecological index (RSEI) change in Chongqing Municipality between 2000 and 2020.

The spatial distribution pattern of the RSEI in Chongqing Municipality is illustrated in Figure 3, where it can be seen that the eco-quality exhibited substantial spatial heterogeneity. From 2000 to 2020, the spatial distribution of the RSEI in Chongqing was generally consistent. The areas with lower RSEI values are depicted in brown on the map, showing a pattern of "one block, multiple points". Specifically, the low-value areas consist of a larger block of low-value area in the southwest part of the map and scattered point-like low-value areas distributed across the entire map. The block-shaped distribution area is located within the central urban area of Chongqing, and its shape closely resembles that of the built-up area in the central urban area of Chongqing. The point-shaped low-value areas are mainly situated around the central urban area within the main urban districts of Chongqing, or scattered in the valley areas. These point-shaped low-value areas correspond to the county-level cities within Chongqing, as their built-up areas are much smaller than that of the central urban area, resulting in a point-like appearance on the map. Their RSEI values are <0.5, indicating that the RSEI values in urban built-up areas are lower than those in non-built-up areas. High-value areas can be mainly divided into two parts: the Daba Mountains in the northeast and Wuling Mountains in the southeast, corresponding to the urban spatial pattern of Chongqing. In these areas, the RSEI values are generally >0.75, indicating a better eco-environment. In the high-value RSEI areas, the distribution trend of

the RSEI reflects the parallel distribution of ridges and valleys in the Chongqing region, indicating a potential relationship between the RSEI and altitude.

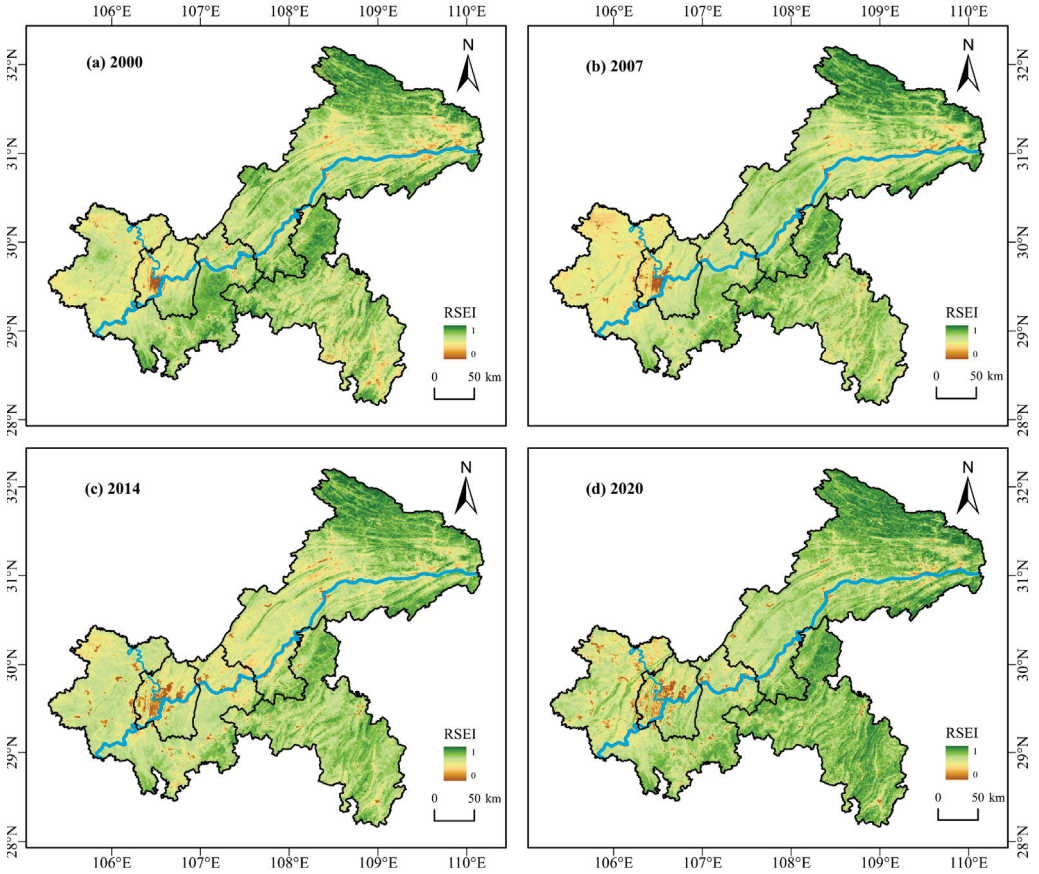

Figure 3. Spatial distribution patterns of the remote-sensing ecological index (RSEI) in Chongqing Municipality in (**a**) 2000, (**b**) 2007, (**c**) 2014, and (**d**) 2020.

To visually illustrate the spatial changes in influence in Chongqing Municipality during the study period, we employed the Sen + Mann–Kendall analysis method to examine the spatial variation of the RSEI. The results were categorized, and the proportions of each change category were calculated, as depicted in Figure 4. This revealed that >70% of the regions in Chongqing witnessed an improvement in their eco-environment during the study period. Specifically, 28.27% were classified as significantly improved and 43.59% as slightly improved. In contrast, only 18.55% of the regions exhibited slight deterioration, with no areas meeting the criteria for significant deterioration, aligning with our earlier overall assessment. Upon analyzing the spatial distribution, areas experiencing deterioration were primarily concentrated in the central urban area and the outskirts of the central city. Meanwhile, the core area of the central city, urban clusters in the Three Gorges Reservoir area of northeast Chongqing, and urban clusters in the Wuling Mountains area of southeast Chongqing exhibited a trend of improvement.

Following the accepted methodology of related studies, we classified the RSEI values into five levels: poor, fair, moderate, good, and excellent, using an equal interval approach. Considering the overall temporal variation in the RSEI, we selected four specific years, namely 2000, 2007, 2014, and 2020, as key points to reclassify and statistically analyze the RSEI results. As depicted in Figure 5, the results represent a dynamic transformation in RSEI levels across Chongqing, with approximately 67.08% of regions experiencing changes in classification during the study period. Notably, transitions between good and moderate levels stand out. The predominant transformation pattern involves a shift from a good level to moderate level at a certain point, followed by a return to a good level. This particular

transition path covers approximately 36.97% of the study area, markedly influencing the variation in influence levels across Chongqing. This pattern aligns with the observed V-shaped temporal trend in the RSEI.

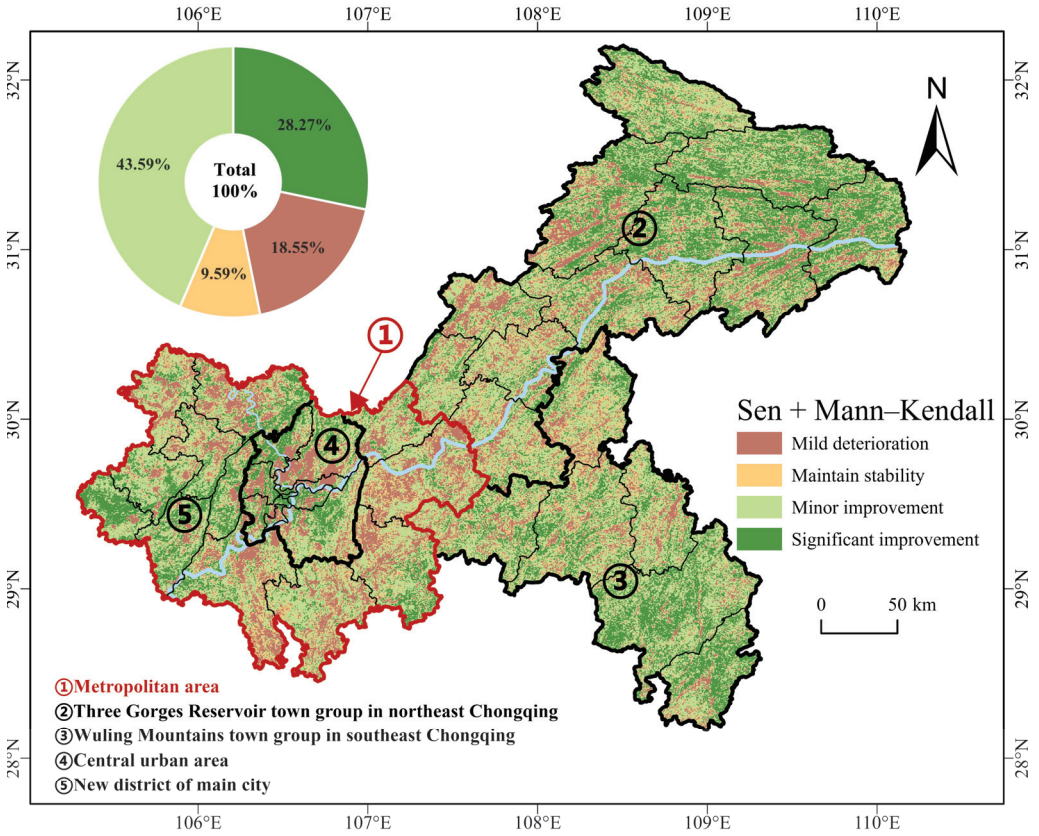

Figure 4. Spatial pattern of changes in the remote-sensing ecological index in Chongqing Municipality between 2000 and 2020.

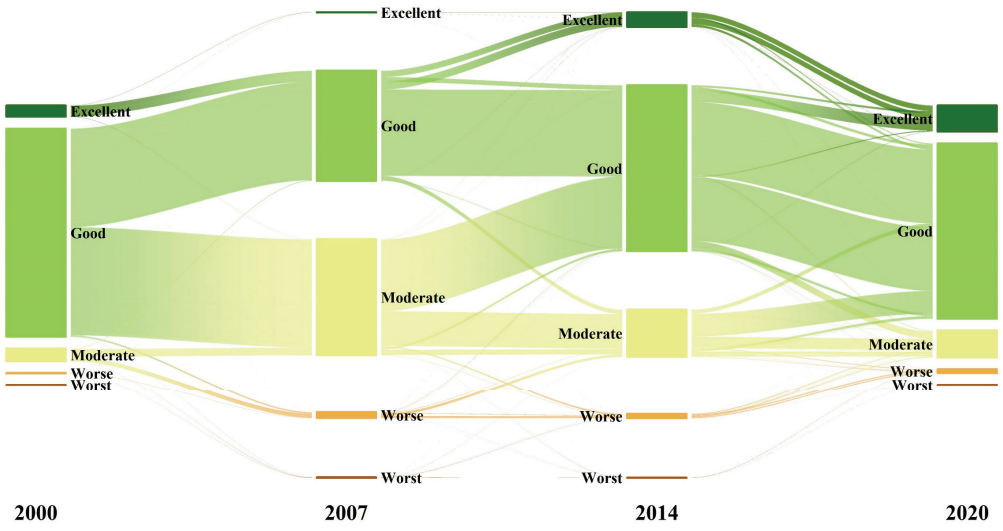

Figure 5. Changes in remote-sensing ecological index levels in Chongqing Municipality between 2000 and 2020.

3.2. Detection Results Based on Geodetectors

According to our research requirements, we selected eight elements to investigate the main elements influencing the eco-environment in Chongqing. These elements included elevation, slope, aspect, precipitation, temperature, population, land use, and nighttime

light. To align with the sampling period of RSEI, the data for precipitation and slope were collected from June to September each year. These elements exhibit significant differences and spatial heterogeneity in their distribution across Chongqing, as illustrated in Figure 6, depicting their overall spatial distribution patterns. To conduct factor detection, a 5 × 5 km grid was created, and factor attribute values corresponding to spatially relevant points were extracted. These spatially relevant points are evenly distributed across the study area, representing the geographical conditions of different regions in Chongqing. Single-factor detectors and interaction detectors were employed to study the influence of these selected elements on the RSEI-based eco-environment changes in Chongqing and their interactions.

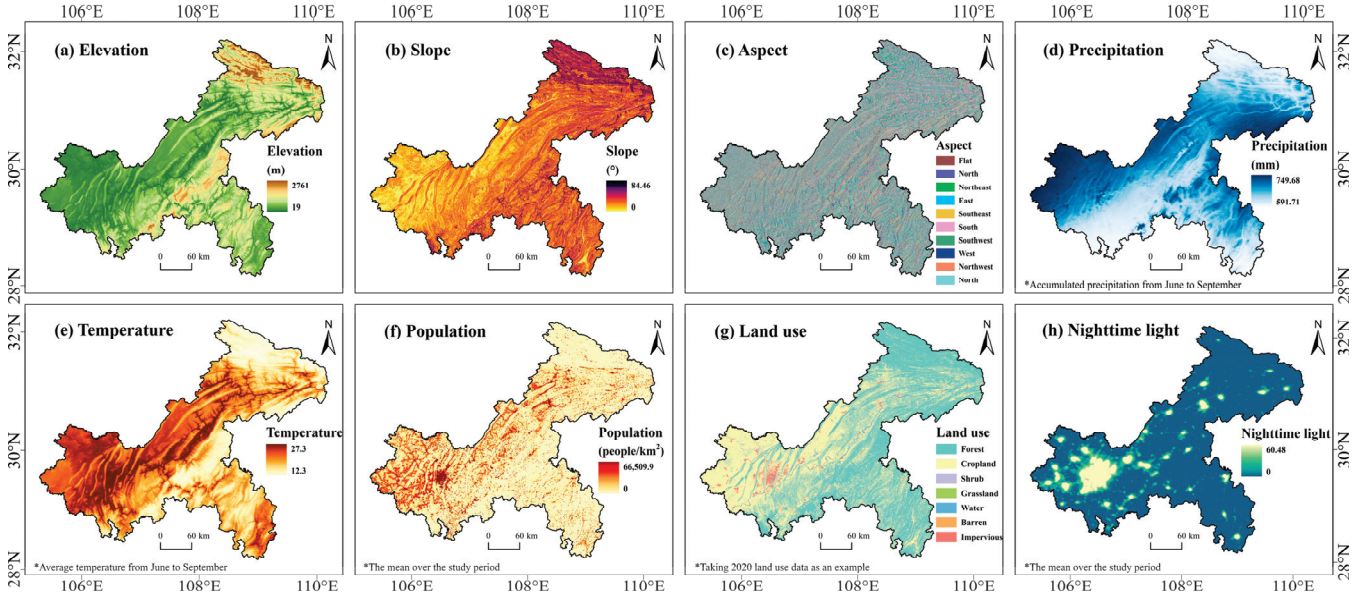

Figure 6. The spatial distribution of selected elements in Chongqing City. (**a**–**c**) represent the elevation, slope, and aspect of the study area. (**d**) represents the mean cumulative precipitation from June to September for each year from 2000 to 2020. (**e**) represents the average temperature from June to September for each year from 2000 to 2020. (**f**,**h**) represent population and nighttime light data for the study area, respectively, shown as the average values from 2000 to 2020. (**g**) represents land use data, with the example shown for the year 2020.

Using a single-factor Geodetector to detect selected years, the average interpretability and significance of each factor's separate effects on the RSEI and their variations were analyzed, as shown in Table 3. All elements passed the significance test at the 0.05 level. The ranking of interpretability for each factor was elevation > temperature > land use > nighttime light > population > slope > precipitation > aspect. The interpretability of single-factor detection for each study year was plotted over the study period to show its variation (Figure 7), wherein nighttime light, land use, and population elements exhibited a noticeable increasing trend in interpretability; when fitted with linear regression, their goodness of fit values were 0.6539, 0.6141, and 0.5470, respectively. Other elements did not show a clear trend in interpretability for the RSEI. Additionally, it is noteworthy that the interpretability of the precipitation factor showed considerable interannual variation, which may be related to the distinct differences in annual precipitation distribution across the region.

Table 3. Single-factor detection significance.

Factor	Elevation	Slope	Aspect	Precipitation	Temperature	Population	Land Use	Nighttime Light
q	0.499	0.197	0.005	0.126	0.440	0.217	0.404	0.221
p	0.000	0.000	0.048	0.000	0.000	0.000	0.000	0.000

Figure 7. Changes in the explanatory power of various elements on the remote-sensing ecological index between 2000 and 2020. (**a**) Elevation; (**b**) Slope; (**c**) Aspect; (**d**) Precipitation; (**e**) Temperature; (**f**) Population; (**g**) Land use; (**h**) Nighttime light.

Using the interaction detector to explore the interactions between different elements and the RSEI, representative years (2000, 2007, 2014, and 2020) were again chosen to construct interaction power heatmaps for pairwise coupling effects (Figure 8). The coupling effect between the elevation and land-use elements exhibited the strongest interpretability for the spatial distribution of the RSEI, reaching 0.463, 0.612, 0.617, and 0.605 for the four respective years. Additionally, the coupling effects between elevation and nighttime light, elevation and temperature, and temperature and nighttime light also showed relatively strong explanatory power. In terms of coupling mechanisms, all interaction types were enhancing effects, with the majority (74.11%) being double-factor enhancement patterns and the rest (25.89%) being nonlinear enhancement patterns.

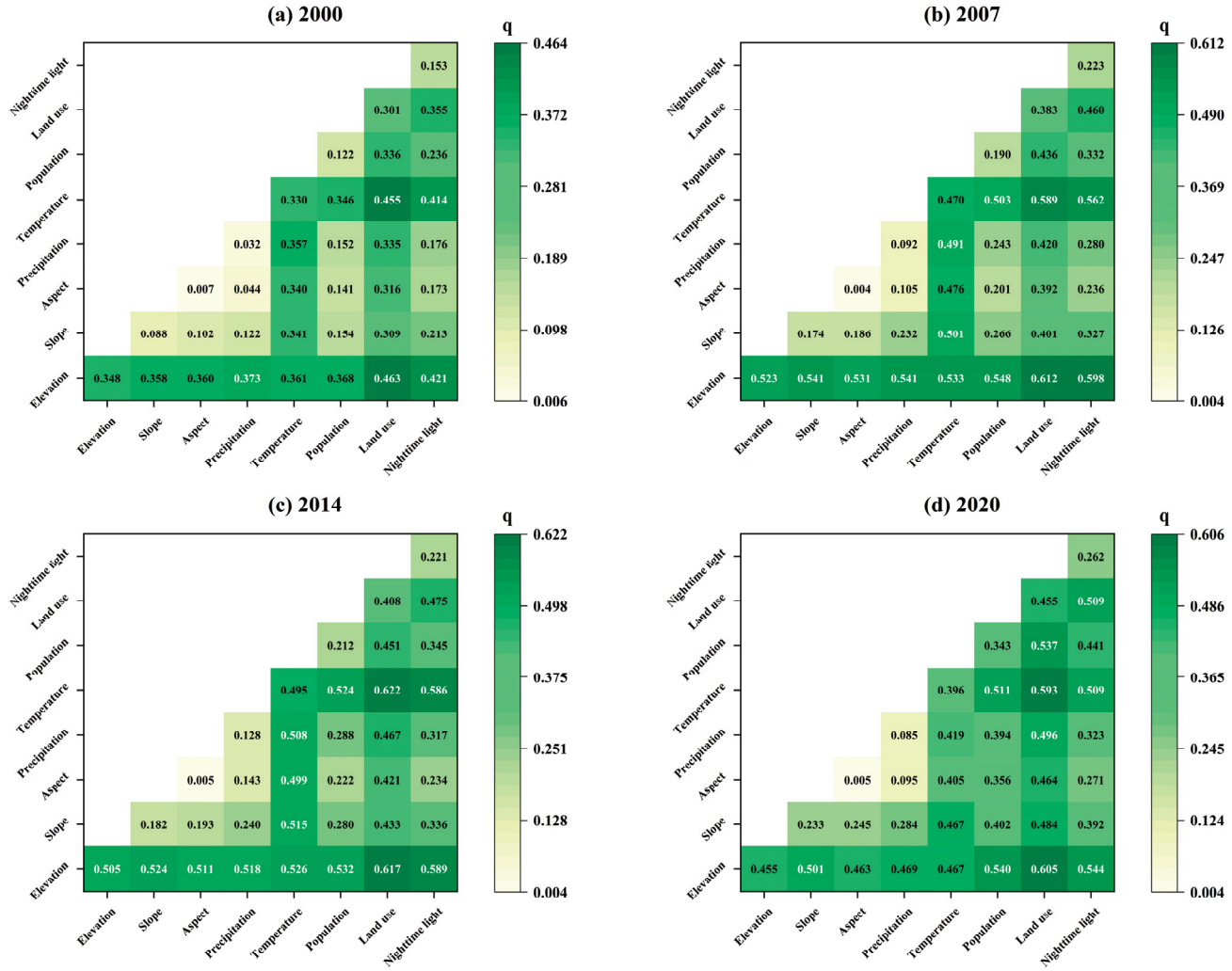

Figure 8. Interactive detector explanatory heat maps for (**a**) 2000, (**b**) 2007, (**c**) 2014, and (**d**) 2020.

4. Discussion

Our trend analysis of the RSEI revealed two phases of influence change in Chongqing Municipality over the past 20 years, with 2007 as the turning point. Before 2007, Chongqing experienced a relatively deteriorating trend in influence, associated with rapid industrial development and urbanization at that time. With the increasing frequency of human activity and irrational land-use practices, vegetation coverage in the region decreased, leading to soil erosion and negative influences on the eco-environment [43,44]. After 2007, the eco-quality in Chongqing gradually improved, possibly owing to the gradual manifestation of the ecological benefits of the Grain for Green project. China initiated the nationwide Grain for Green project in 2002; previous studies have shown that there have been significant positive effects from this project on the eco-environment in western China,

with a certain temporal lag effect [45–47]. Given the unique topography, landforms, and climatic conditions in Chongqing, afforestation is the primary form of land conversion, with such areas exceeding 25,000 hectares; this is a major type of land conversion with substantial economic benefits [48]. In studies focused on the Chengdu–Chongqing region, the dominant role of the NDVI in the improvement of urban cluster environments has been recognized [49]. Therefore, the continuous improvement of vegetation coverage may be a key factor in reversing the deteriorating trend and gradually improving the eco-environment quality in Chongqing Municipality.

Our Sen + Mann–Kendall analysis has demonstrated the spatial heterogeneity of eco-environment changes in Chongqing Municipality. It is evident that there is considerable spatial heterogeneity in the eco-environment in Chongqing. Areas exhibiting a deteriorating trend are concentrated in the southwest of Chongqing, characterized by relatively flat terrain and a comparatively dense population. In contrast, most areas in the northeast and southeast of Chongqing, which have complex terrain and small populations, exhibit an improving trend. Because the areas displaying a declining trend in southwestern Chongqing constitute a minor proportion of the entire municipality, the overall eco-environment quality in Chongqing exhibits an improving trend. Combined with the "one zone, two groups" urban spatial pattern in Chongqing, further analysis reveals that areas with deteriorating ecological conditions are concentrated on the outskirts of the main new urban area and central urban area. These areas are designated as the main focal point for the aggregation of advanced manufacturing and industrial urbanization, serving as the primary areas for expansion and construction of the central urban area and the main sites for population transfer. During the rapid development of the past 20 years, these areas have been rapidly urbanized, with the transformation of extensive forest and arable land into impervious surfaces (Figure 9); this is the main reason for the relatively deteriorating eco-environment in these regions. In this regard, Ren et al. (2021) incorporated point-of-interest data to analyze the relevant indicators of the RSEI in the main urban district of Chongqing, corroborating the results obtained herein [50]. However, the eco-quality of the old urban district of Chongqing, also part of the main urban area, has shown a marked trend of improvement. This is intricately linked to the ecological restoration activities carried out in the core area of Chongqing over the last few years. Overall, the results of our Sen + Mann–Kendall analysis are highly consistent with the policy guidance of the "one zone, two groups" urban spatial pattern in Chongqing Municipality.

The application results of the Geodetector tool indicate that, at the spatial scale, elevation, temperature, and land use are the main driving elements influencing the eco-environment in Chongqing Municipality. The explanatory power of other elements is relatively low, which aligns with conclusions reached in other studies carried out in the region [9]. Owing to the complex terrain of Chongqing and the considerable influence of elevation and temperature on vegetation growth in the region [51], complex topography affects land use, and high-altitude areas are often unsuitable for human activities owing to topographical constraints. As a result, vegetation is well preserved in these areas, contributing to better eco-environment quality. In terms of temporal changes, elements closely related to human activities, such as nighttime light, land use, and population distribution, show an increasing explanatory power for the RSEI over recent years, while the explanatory power of other natural elements does not exhibit a clear trend. Considering the development status of Chongqing Municipality during our study period, we suggest that, compared with natural elements (e.g., climate and topography). Human activities can produce more pronounced trends over a relatively short period, and further analysis suggests that human activities emerge as the predominant factor influencing the changes in RSEI over the timescale examined in this study. Compared with elements such as climate/precipitation, the intensity of human activities can undergo substantial changes over a short period. Incorporating the results of Sen + Mann–Kendall analysis, it is evident that the regions where the RSEI shows a deteriorating trend are precisely the regions with intense human activities in the "one zone, two groups" spatial pattern, while the

regions showing improvement align with areas covered by the Grain for Green project. This indicates that government policies can have a marked influence on human activities and can change the eco-quality of a region over a relatively short time frame.

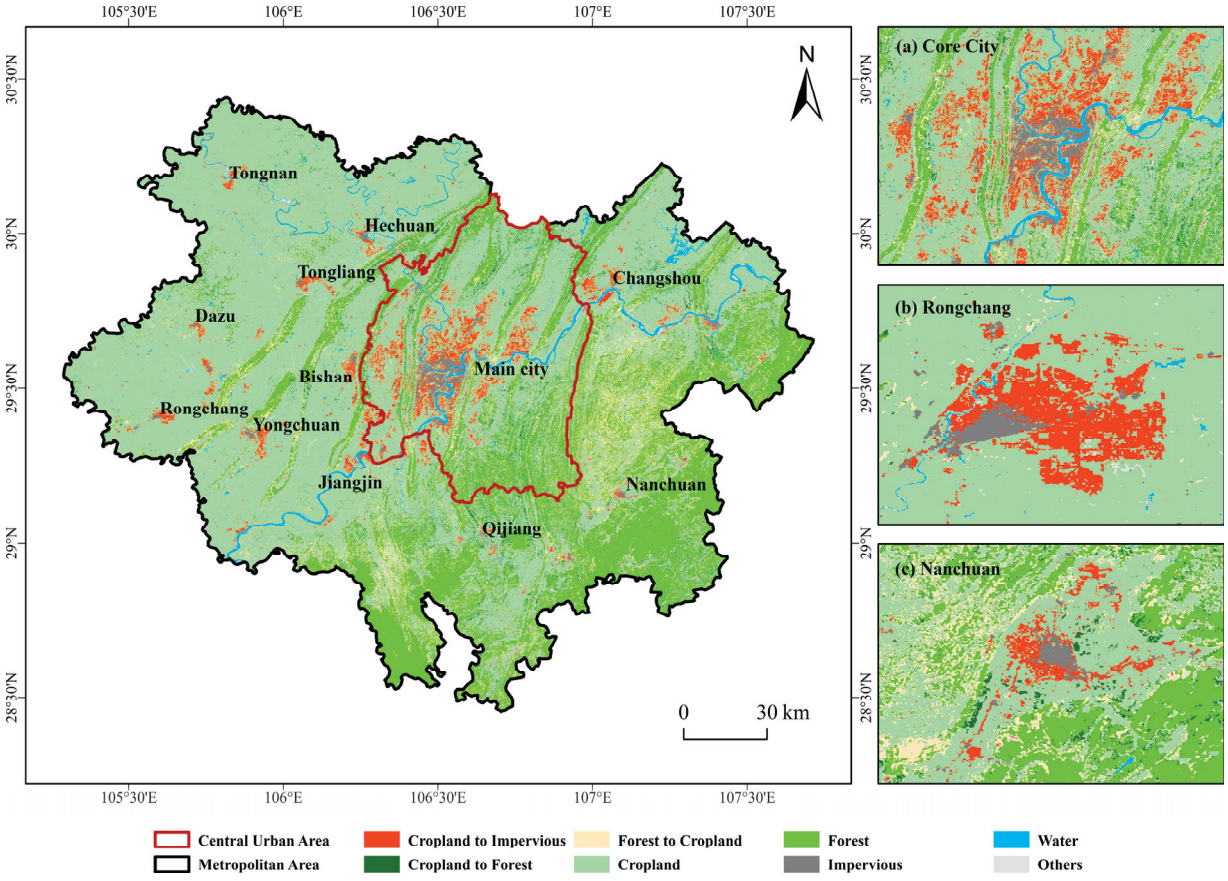

Figure 9. Land-use changes in metropolitan areas of Chongqing from 2000 to 2020.

The above results and discussion demonstrate the effectiveness of policymaking. Therefore, we suggest that policymakers continue to promote the development adjustment of ecological functional areas according to the established route. Furthermore, given the decline in the surrounding eco-environment of the central urban area and the main new urban area, we advise policymakers to carry out more comprehensive local environmental assessments prior to initiating urbanization development in order to mitigate the serious harm that intense urban development causes to the local eco-environment. Compared with the similar methodological studies conducted by Kang et al. (2023) and Wang et al. (2023) in the region, this study provides a new perspective on the urban spatial pattern for the application of RSEI [9,10]. In contrast to the element detection conducted by Zhang et al. (2023) and Wang et al. (2023), this study not only offers mean detection results but also provides element influence detection results under time series, which effectively supplements previous research [8,10]. However, this study only conducted the overall detection of driving factors in the study area using Geodetector, without fully considering the complex geographical conditions and spatial heterogeneity within the research area. Therefore, in future research, it could be beneficial to integrate the urban spatial pattern of Chongqing's "one zone, two groups" policy and conduct long-term element detection on various sub-regions, with full consideration of the differences in conditions across Chongqing to compare the differential effects of influencing elements under different conditions. This will provide more specific recommendations for tailored ecological protection measures.

5. Conclusions

In this study, we employed Landsat RS imagery to construct an RSEI model. Simultaneously, we utilized the Sen + Mann–Kendall analysis method to summarize the spatial distribution and trend changes of the RSEI in Chongqing Municipality. Additionally, we applied single-factor and interaction detectors within the Geodetector tool to analyze the impact of various detection elements on the eco-environment in Chongqing. This study yielded the following conclusions:

(1) On the basis of RS data from 2000 to 2020 in Chongqing Municipality, we revealed a changing trend in the eco-environment quality, characterized by deterioration followed by recovery. Before 2007, the eco-environment quality in Chongqing deteriorated, while, after 2007, it gradually improved. Overall, the eco-quality in Chongqing is now trending positively. In terms of spatial distribution, the changes in the eco-quality in Chongqing align with the overall development pattern of the "one zone, two groups" spatial pattern, exhibiting marked spatial heterogeneity. The eco-environment in the peripheral areas of the main new urban area and central urban area has deteriorated to some extent, while the eco-environment in the old urban district of Chongqing and other areas where ecological conservation and protection has been prioritized has significantly improved.

(2) The application of the Geodetector tool revealed that, at the spatial scale, elevation, temperature, and land use are the main explanatory elements influencing the eco-environment in Chongqing. They play a fundamental role in shaping the spatial pattern of the RSEI. Interaction detector results show that the combined effects of various influencing elements enhance the impact of a single element, with the combined influence of elevation and land use exhibiting a strong explanatory interpretability for the RSEI. On the temporal scale, compared with natural elements, elements related to human activities show a more pronounced trend in explanatory power changes. Influenced by local government policy preferences, economic development, and elements like the Grain for Green project, human activities dominate the temporal changes in the RSEI in Chongqing.

Author Contributions: Conceptualization, Y.L., T.Z. and W.Y.; methodology, Y.L.; software, Y.L.; validation, T.Z. and W.Y.; formal analysis, Y.L.; Writing—original draft, Y.L.; writing—review & editing, T.Z. and W.Y.; visualization, Y.L.; supervision, T.Z. and W.Y.; funding acquisition, Y.L and W.Y. All authors have read and agreed to the published version of the manuscript.

Funding: This work was supported by Sichuan Science and Technology Program (2023NSFSC1916), the National Natural Science Foundation of China (42371333), National Key Research and Development Program (2022YFB3903503), and Chongqing Municipal Training Program of Innovation and Entrepreneurship for Undergraduates (S202310635097).

Data Availability Statement: Data are contained within the article.

Acknowledgments: The authors are grateful for the financial support provided by Sichuan Science and Technology Program (2023NSFSC1916), the National Natural Science Foundation of China (42371333), National Key Research and Development Program (2022YFB3903503), and project S202310635097 supported by Chongqing Municipal Training Program of Innovation and Entrepreneurship for Undergraduates. Thank you for the support from the School of Geographical Sciences, Southwest University. Thank all anonymous reviewers and editors for their comments and help.

Conflicts of Interest: The authors declare no conflicts of interest.

References

1. Li, H.; Jing, H.T.; Yan, G.D.; Guo, H.C.; Luan, W.F. Long-Term Ecological Environment Quality Evaluation and Its Driving Mechanism in Luoyang City. *Sustainability* **2023**, *15*, 11866. [CrossRef]
2. Zhong, Q.; Li, Z.; He, Y. Coupling Evaluation and Spatial-Temporal Evolution of Land Ecosystem Services and Economic-Social Development in a City Group: The Case Study of the Chengdu-Chongqing City Group. *Int. J. Environ. Res. Public Health* **2023**, *20*, 5095. [CrossRef] [PubMed]

3. Fan, J. Scientific Basis of China's Main Functional Zoning. *Acta Geogr. Sin.* **2007**, *4*, 339–350. (In Chinese)
4. Chen, Y.; Cai, H.; Chen, Y. Spatial Correlation and Interaction Effect Intensity between Territorial Spatial Ecological Quality and New Urbanization Level in Nanchang Metropolitan Area, China. *Ecol. Indic.* **2023**, *156*, 111163. [CrossRef]
5. Han, S.S.; Wang, Y. City Profile—Chongqing. *Cities* **2001**, *18*, 115–125. [CrossRef]
6. Smith, N.R.Z. Urban Furnace: The Making of a Chinese City. Ph.D. Thesis, Harvard University, Cambridge, MA, USA, 2015.
7. Wang, X.; Wang, S.L.; Dong, N.Y. Study on Influencing Factors and Spatial Spillover of Regional Carbon Emission Intensity under the Background of Carbon Peak—A Case Study of Chongqing. *Soft Sci.* **2022**, *36*, 97–103. (In Chinese)
8. Zhang, C.Y.; Yang, S.K.; Dong, X.H.; Zhao, C.M.; Bo, H.J.; Liu, J. Research on the Spatiotemporal Evolution and Influencing Factors of Ecological Environment Quality in the Upper Reaches of the Yangtze River Based on RSEI Index. *Soil Water Conserv. Res.* **2023**, *30*, 356–363. (In Chinese)
9. Kang, Y.; Cui, H. Urbanization and Ecological Environmental Coordination Analysis of Five Major Urban Agglomerations. *J. Guangzhou Univ. (Nat. Sci. Ed.)* **2023**, *22*, 49–56. (In Chinese)
10. Wang, Y.X.; Xu, Y.Y.; Yang, J.J.; Chen, Y.X.; Wei, J.X.; Zhou, J.; Zhang, W.L.; Cheng, W.X. Dynamic Monitoring and Spatial-Temporal Pattern Evolution Analysis of Ecological Environment Quality in Chongqing Based on Landsat. *Acta Ecol. Sin.* **2023**, *43*, 6278–6292. (In Chinese)
11. Huang, H.P.; Li, Q.Z.; Zhang, Y. A High-Resolution Remote-Sensing-Based Method for Urban Ecological Quality Evaluation. *Front. Environ. Sci.* **2022**, *10*, 765604. [CrossRef]
12. Sun, C.J.; Li, X.M.; Zhang, W.Q.; Chen, W.; Wang, J.R. Ecological Security Assessment of Poverty-Stricken Areas in Lvliangshan Based on Remote Sensing Information. *China Environ. Sci.* **2019**, *39*, 5352–5360. (In Chinese)
13. Cui, R.H.; Han, J.Z.; Hu, Z.Q. Assessment of Spatial Temporal Changes of Ecological Environment Quality: A Case Study in Huaibei City, China. *Land* **2022**, *11*, 944. [CrossRef]
14. Gong, C.; Lyu, F.; Wang, Y. Spatiotemporal Change and Drivers of Ecosystem Quality in the Loess Plateau Based on RSEI: A Case Study of Shanxi, China. *Ecol. Indic.* **2023**, *155*, 111060. [CrossRef]
15. Yao, K.X.; Halike, A.; Chen, L.M.; Wei, Q.Q. Spatiotemporal Changes of Eco-Environmental Quality Based on Remote Sensing-Based Ecological Index in the Hotan Oasis, Xinjiang. *J. Arid Land* **2022**, *14*, 262–283. [CrossRef]
16. Yue, H.; Liu, Y.; Li, Y.; Lu, Y. Eco-Environmental Quality Assessment in China's 35 Major Cities Based on Remote Sensing Ecological Index. *IEEE Access* **2019**, *7*, 51295–51311. [CrossRef]
17. Yuan, B.; Fu, L.; Zou, Y.; Zhang, S.; Chen, X.; Li, F.; Deng, Z.; Xie, Y. Spatiotemporal Change Detection of Ecological Quality and the Associated Affecting Factors in Dongting Lake Basin, Based on RSEI. *J. Clean. Prod.* **2021**, *302*, 126995. [CrossRef]
18. Wu, S.P.; Gao, X.; Lei, J.Q.; Zhou, N.; Guo, Z.K.; Shang, B.J. Ecological Environment Quality Evaluation of the Sahel Region in Africa Based on Remote Sensing Ecological Index. *J. Arid Land* **2022**, *14*, 14–33. [CrossRef]
19. Zhang, C.K.; Zhang, H.Y.; Tian, S.J. Phenology-Assisted Supervised Paddy Rice Mapping with the Landsat Imagery on Google Earth Engine: Experiments in Heilongjiang Province of China from 1990 to 2020. *Comput. Electron. Agric.* **2023**, *212*, 108105. [CrossRef]
20. Wen, X.L.; Ming, Y.L.; Gao, Y.G.; Hu, X.Y. Dynamic Monitoring and Analysis of Ecological Quality of Pingtan Comprehensive Experimental Zone, a New Type of Sea Island City, Based on RSEI. *Sustainability* **2020**, *12*, 21. [CrossRef]
21. Zhang, Y.; She, J.; Long, X.; Zhang, M. Spatio-Temporal Evolution and Driving Factors of Eco-Environmental Quality Based on RSEI in Chang-Zhu-Tan Metropolitan Circle, Central China. *Ecol. Indic.* **2022**, *144*, 109436. [CrossRef]
22. Zhang, K.L.; Feng, R.R.; Zhang, Z.C.; Deng, C.; Zhang, H.J.; Liu, K. Exploring the Driving Factors of Remote Sensing Ecological Index Changes from the Perspective of Geospatial Differentiation: A Case Study of the Weihe River Basin, China. *Int. J. Environ. Res. Public Health* **2022**, *19*, 10930. [CrossRef]
23. Wang, J.F.; Xu, C.D. Geographic Detectors: Principles and Prospects. *Acta Geogr. Sin.* **2017**, *72*, 116–134. (In Chinese)
24. Gou, R.K.; Zhao, J. Eco-Environmental Quality Monitoring in Beijing, China, Using an RSEI-Based Approach Combined with Random Forest Algorithms. *IEEE Access* **2020**, *8*, 196657–196666. [CrossRef]
25. Zhang, X.M.; Fan, H.B.; Zhou, C.H.; Sun, L.; Xu, C.Q.; Lv, T.G.; Ranagalage, M. Spatiotemporal Change in Ecological Quality and Its Influencing Factors in the Dongjiangyuan Region, China. *Environ. Sci. Pollut. Res.* **2023**, *30*, 69533–69549. [CrossRef] [PubMed]
26. Wang, J.; Wang, J.; Xu, J.Q. Spatio-Temporal Variation and Prediction of Ecological Quality Based on Remote Sensing Ecological Index—A Case Study of Zhanjiang City, China. *Front. Ecol. Evol.* **2023**, *11*, 1153342. [CrossRef]
27. Sims, K.; Reith, A.; Bright, E.; McKee, J.; Rose, A. *LandScan Global 2021 [Data Set]*; Oak Ridge National Laboratory: Oak Ridge, TN, USA, 2021.
28. Weber, E.; Moehl, J.; Weston, S.; Rose, A.; Brelsford, C.; Hauser, T. *LandScan USA 2021 [Data Set]*; Oak Ridge National Laboratory: Oak Ridge, TN, USA, 2021.
29. Yang, J.; Huang, X. The 30 m Annual Land Cover Dataset and Its Dynamics in China from 1990 to 2019. *Earth Syst. Sci. Data* **2022**, *13*, 3907–3925. [CrossRef]
30. Cui, Y.Z.; Shi, K.F.; Jiang, L.; Qiu, L.F.; Wu, S.H. Identifying and Evaluating the Nighttime Economy in China Using Multisource Data. *Ieee Geosci. Remote Sens. Lett.* **2021**, *18*, 1906–1910. [CrossRef]
31. Peng, S. *1-km Monthly Mean Temperature Dataset for China (1901–2022)*; National Tibetan Plateau Data Center: Beijing, China, 2019.
32. Peng, S. *1-km Monthly Precipitation Dataset for China (1901–2022)*; National Tibetan Plateau/Third Pole Environment Data Center: Beijing, China, 2020.

33. Xu, H.Q. Creation and Application of Urban Remote Sensing Ecological Index. *Acta Ecol. Sin.* **2013**, *33*, 7853–7862. (In Chinese)
34. Xu, H.Q. Research on the Extraction of Water Body Information Using Improved Normalized Difference Water Index (MNDWI). *J. Remote Sens.* **2005**, *05*, 589–595. (In Chinese)
35. Benmecheta, A.; Abdellaoui, A.; Hamou, A. A Comparative Study of Land Surface Temperature Retrieval Methods from Remote Sensing Data. *Can. J. Remote Sens.* **2013**, *39*, 59–73. [CrossRef]
36. Zhu, X.M.; Song, X.N.; Leng, P.; Guo, D.; Cai, S.H. Impact of Atmospheric Correction on Spatial Heterogeneity Relations between Land Surface Temperature and Biophysical Compositions. *IEEE Trans. Geosci. Remote Sens.* **2021**, *59*, 2680–2697. [CrossRef]
37. Theil, H. A rank-invariant method of linear and polynomial regression analysis (parts 1–3). *Ned. Akad. Wetensch. Proc. Ser. A* **1950**, *53*, 1397–1412.
38. Sen, P.K. Estimates of the regression coefficient based on Kendall's tau. *J. Am. Stat. Assoc.* **1968**, *63*, 1379–1389. [CrossRef]
39. Conover, W.J. *Statistical Methods Based on Ranks: Practical Nonparametric Statistics*, 2nd ed.; John Wiley & Sons: New York, NY, USA, 1980.
40. Mann, H.B. Non-parametric tests against trend. *Econometrica* **1945**, *13*, 163–171. [CrossRef]
41. Kendall, M.G. *Rank Correlation Methods*, 4th ed.; Charles Griffin: London, UK, 1975.
42. Gilbert, R.O. *Statistical Methods for Environmental Pollution Monitoring*; Wiley: New York, NY, USA, 1987.
43. Pan, X.R.; Long, J.; Xu, Y.Y. Causes and Control Measures of Soil Erosion in the Middle and Lower Reaches of the Jialing River. *Agric. Eng. Technol.* **2018**, *38*, 28. (In Chinese)
44. Zhang, T.; Xue, D.J.; Duan, J.L.; Yang, L. Spatiotemporal Characteristics of Vegetation Cover in the Jialing River Basin from 2000 to 2019 and Its Response to Climate Change. *Resour. Environ. Yangtze Basin* **2021**, *30*, 1110–1120. (In Chinese)
45. Yang, X.D. Evaluation of the Effectiveness of Returning Farmland to Forest Project in Western China. Ph.D. Thesis, Beijing Forestry University, Beijing, China, 2004. (In Chinese).
46. He, J.Y.; Jiang, X.H.; Lei, Y.X.; Cai, W.J.; Zhang, J.J. Temporal and Spatial Variation and Driving Forces of Soil Erosion on the Loess Plateau Before and After the Implementation of the Grain-for-Green Project: A Case Study in the Yanhe River Basin, China. *Int. J. Environ. Res. Public Health* **2022**, *19*, 8446. [CrossRef] [PubMed]
47. Liu, S.H.; Zhang, H.; Ding, Z.M.; Yao, S.B. Cost-Effectiveness and Optimization of the Forest Types Investment Structure of the Grain for Green Project: A Case Study of Shaanxi Province, China. *Scand. J. For. Res.* **2022**, *37*, 241–253. [CrossRef]
48. Gao, L.; Yang, X.; Hu, H.; Lü, X.; Hou, G.; Delang, C.; Wang, X.; Chen, F. Ecological and Economic Benefits Analysis of Chongqing's Returning Farmland to Forest Project. *Soil Water Conserv. Res.* **2019**, *26*, 353–358. (In Chinese)
49. Wu, X.B.; Fan, X.Y.; Liu, X.J.; Xiao, L.; Ma, Q.M.; He, N.; Gao, S.Z.; Qiao, Y.T. Spatiotemporal Changes in Ecological Environment Quality of Chengyu Urban Agglomeration Based on Google Earth Engine Platform. *Chin. J. Ecol.* **2023**, *42*, 759–768. (In Chinese)
50. Ren, Y.N.; Zhou, T.G.; Li, H.Z.; Xie, S.L.; Yin, Z.N. Urban Ecological Environment Pattern in the Main Urban Area of Chongqing Based on Remote Sensing and POI Data. *Prog. Geophys.* **2021**, *36*, 766–778. (In Chinese)
51. Zhang, B.; Wang, D.; Wang, G.G.; Ma, Q.; Zhang, G.B.; Ji, D.M. Vegetation Cover Changes and Their Relationship with Climatic Factors in the Southwestern Region of China in the Past 14 Years. *Resour. Environ. Yangtze Basin* **2015**, *24*, 956–964. (In Chinese)

Disclaimer/Publisher's Note: The statements, opinions and data contained in all publications are solely those of the individual author(s) and contributor(s) and not of MDPI and/or the editor(s). MDPI and/or the editor(s) disclaim responsibility for any injury to people or property resulting from any ideas, methods, instructions or products referred to in the content.

remote sensing

MDPI

Article

Monitoring Soil Salinity Classes through Remote Sensing-Based Ensemble Learning Concept: Considering Scale Effects

Huifang Chen [1], Jingwei Wu [1,*] and Chi Xu [2]

[1] State Key Laboratory of Water Resources Engineering and Management, Wuhan University, Wuhan 430072, China
[2] Changjiang Institute of Survey, Planning, Design and Research, Wuhan 430010, China
* Correspondence: jingwei.wu@whu.edu.cn; Tel.: +86-138-8619-7527

Abstract: Remote sensing (RS) technology can rapidly obtain spatial distribution information on soil salinization. However, (1) the scale effects resulting from the mismatch between ground-based "point" salinity data and remote sensing pixel-based "spatial" data often limit the accuracy of remote sensing monitoring of soil salinity, and (2) the same salinity RS monitoring model usually provides inconsistent or sometimes conflicting explanations for different data. Therefore, based on Landsat 8 imagery and synchronously collected ground-sampling data of two typical study regions (denoted as N and S, respectively) of the Yichang Irrigation Area in the Hetao Irrigation District for May 2013, this study used geostatistical methods to obtain "relative truth values" of salinity corresponding to the Landsat 8 pixel scale. Additionally, based on Landsat 8 multispectral data, 14 salinity indices were constructed. Subsequently, the Correlation-based Feature Selection (CFS) method was used to select sensitive features, and a strategy similar to the concept of ensemble learning (EL) was adopted to integrate the single-feature-sensitive Bayesian classification (BC) model in order to construct an RS monitoring model for soil salinization (Nonsaline, Slightly saline, Moderately saline, Strongly saline, and Solonchak). The research results indicated that (1) soil salinity exhibits moderate to strong variability within a 30 m scale, and the spatial heterogeneity of soil salinity needs to be considered when developing remote sensing models; (2) the theoretical models of salinity variance functions in the N and S regions conform to the exponential model and the spherical model, with R^2 values of 0.817 and 0.967, respectively, indicating a good fit for the variance characteristics of salinity and suitability for Kriging interpolation; and (3) compared to a single-feature BC model, the soil salinization identification model constructed using the concept of EL demonstrated better potential for robustness and effectiveness.

Keywords: regional soil salinization; scale effects; remote sensing; geostatistical methods; ensemble learning concepts

1. Introduction

Soil salinization is a global issue of concern to resources and ecology [1,2]. It usually results from the interaction of natural or anthropogenic factors such as climate, topography, hydrogeology, and irrigated agriculture, particularly in arid or semi-arid regions [3–5]. Soil salinization can lead to changes in soil properties, resulting in a decrease in soil potential productivity and posing a serious threat to resources and the environment. It is widely recognized as one of the main factors to consider in achieving sustainable agriculture and land management [6]. Therefore, the timely and accurate assessment of the degree and distribution of soil salinization in salt-affected areas is of great significance for comprehensively formulating scientific management measures and the rational utilization of land resources.

Remote sensing (RS) technology provides a fast and reliable approach for the timely and accurate acquisition of information on salt-affected soils, enabling the dynamic monitoring of regional soil salinization [1]. In soil salinization RS monitoring, ground point

observation data are commonly used to calibrate RS information and verify inversion results [7–9]. However, due to the strong spatiotemporal heterogeneity of soil salinity [10,11], even ground point observations taken at the same time cannot fully represent the corresponding observations at the pixel scale of RS. Geostatistical methods (e.g., variograms and Kriging interpolation) are efficient for obtaining soil property information from surface data, and the obtained "RS spatial data" are more representative than information obtained from individual sampling points. However, most studies focus on the analysis of spatial heterogeneity and scale effects of ground point observation data [12,13] and rarely combine this information with RS data to better monitor soil salinization.

Over the years, the effective detection of salt-affected soils using RS has mainly relied on the spectral response characteristics of saline soils [14]. Generally, reflectance increases with an increasing quantity of salts at the terrain surface [1], providing an important scientific basis for RS monitoring of soil salinization. However, RS images are susceptible to the "same spectrum for different objects, different spectra for the same object" phenomenon due to atmospheric conditions, sensor characteristics, and other factors. This makes the correspondence between the degree of soil salinization and spectral response characteristics not always clear, making it difficult for rule-based classification methods (such as decision trees, random forests, etc.) to solve this problem effectively. Compared to rule-based classification methods, Bayesian methods are non-rule-based classification methods that achieve optimal statistical classification results based on class priors and class probability density functions. In recent years, theoretical and applied research on Bayesian statistics both nationally and in other countries has increased, and their application in research on extreme climate risk [15–17], sediment fingerprinting identification [18–20], soil properties [21,22], and many other fields has become widespread and demonstrated significant application potential.

Although Bayesian methods are ideal for soil salinity modeling, as with any other method, models may have similar performance using different input variables but offering different predictions [23,24]. Ensemble learning (EL) is a machine learning framework based on the idea of "group intelligence", which is capable of combining (averaging) the predictions of multiple participating models [25–28]. Compared to single-model predictions, EL can consistently generate more accurate and reliable predictions [29–31]. In practical applications, EL can be homogenous and heterogeneous based on whether the participating models are of the same type [32]. In recent years, EL methods have been widely applied in soil modeling and analysis, such as in determining soil classes [33], soil properties [34–36], soil micronutrients [37], soil organic carbon [38,39], soil moisture [40,41], and soil texture [42,43]. However, the application of EL in soil salinization analysis is relatively limited. Therefore, it is of great research significance to effectively apply the advanced concept and method of EL to soil salinity monitoring research based on the comparison and evaluation of existing methods and models.

Therefore, this study conducted an "RS-ground synchronization experiment" in the Hetao Irrigation District, Inner Mongolia, aiming to (1) achieve the conversion of ground point data and RS pixel-scale salinity "relative truth values" and (2) evaluate the potential of the EL concept in predicting remote sensing monitoring of soil salinization.

2. Materials and Methods

2.1. Study Area

The study was conducted in the Hetao Irrigation District of Inner Mongolia in northwestern China, which is one of the three largest irrigation districts in China and the largest in Asia. The district is located at 40°10′–41°20′N, 106°10′–109°30′E, in the Hetao Plain of the Yellow River, with a flat topography, higher in the southwest and lower in the northeast. The elevation ranges from approximately 1007 m to 1050 m (with an average elevation of 1028 m). The annual average temperature ranges from 6.5 to 7.8 °C, with low rainfall and intense evaporation. The annual average precipitation ranges from 100 to 250 mm, while the evaporation can reach as high as 2400 mm, representing a typical temperate continental

climate. The study area is an important production base for commodity grains and oil in the country and in the autonomous region, with major crops including wheat, coarse grains, maize, sugar beet, and sunflower, among others.

2.2. Data Acquisition and Processing

The research data mainly include two types of data: (1) soil salinity data and (2) satellite imagery data.

2.2.1. Salt Data Collection and Processing

In the Yichang irrigation area of the Hetao Irrigation District, a research area of 2667 ha was selected. Two experimental regions (referred to as N and S regions) with an area of 64 ha each were selected within this research area, and the same sampling scheme was adopted for these two regions. The N area primarily consists of farmland, while the S region includes both farmland and regions affected by salinization. The sampling scheme is shown in Figure 1. Field surveys and soil sample collection were conducted in May 2013. A total of 243 soil samples were collected in the N research region, and 245 soil samples were collected in the S research region, resulting in a total of 488 surface (0–5 cm) soil samples. The collected soil samples were placed in sampling bags for subsequent laboratory analysis of soil salinity. To accurately record the coordinates of the sampling points, a GPS locator was used, as shown in Figure 2.

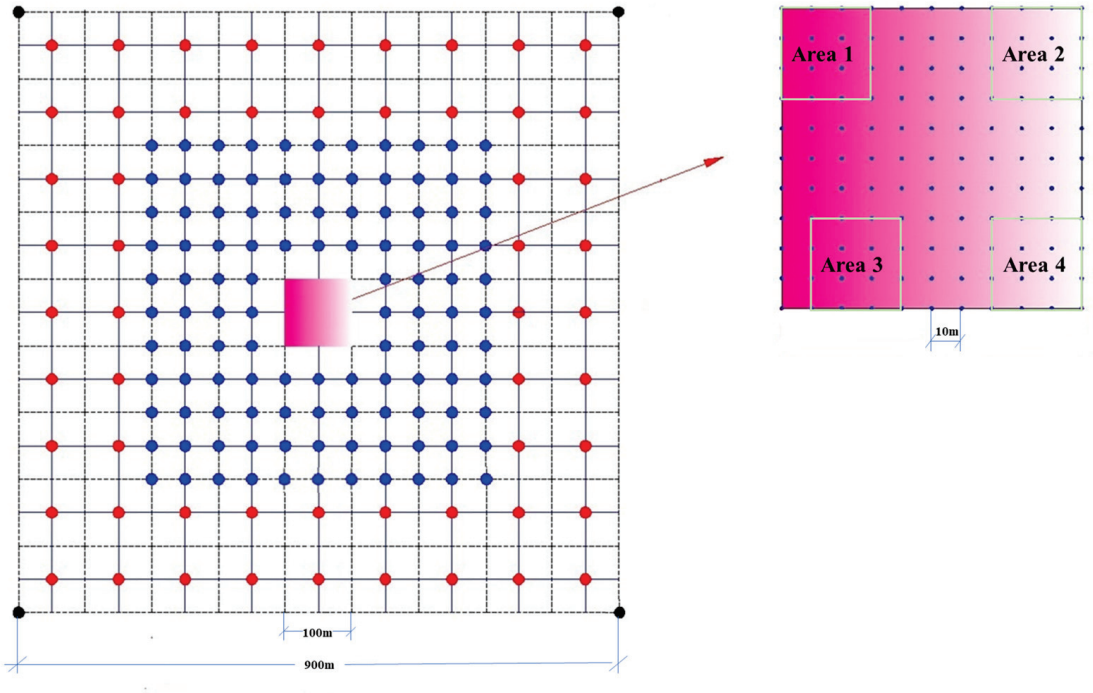

Figure 1. Soil sampling scheme.

The collected soil samples were dried, sieved, grind, and passed through a 2 mm sieve in the laboratory. The electrical conductivity of the soil extract ($EC_{1:5}$, dS/m) was determined using a conductivity meter at a soil-to-water ratio of 1:5. The soil salinity content (SSC, %) was calculated as N : $SSC = 0.0004EC_{1:5} - 0.04$, S : $SSC = 0.0003EC_{1:5}$.

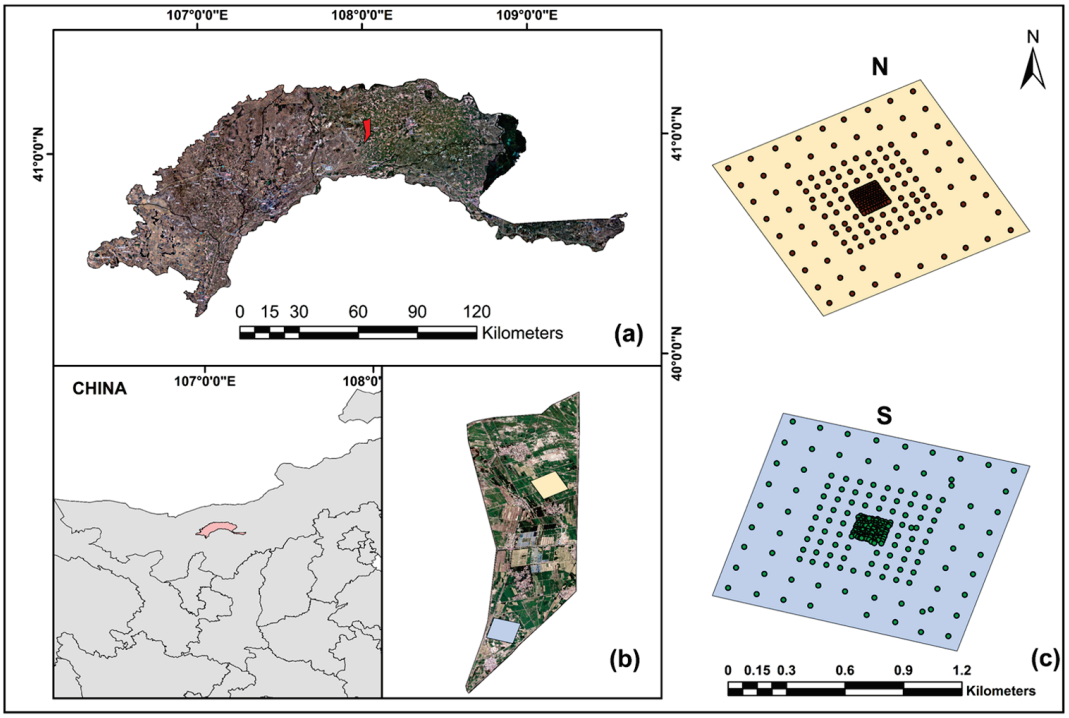

Figure 2. Study area and sampling point map. (**a**) Hetao Irrigation District; (**b**) 2667 ha experimental area; (**c**) N and S experimental regions.

2.2.2. Landsat 8 Data Acquisition and Processing

Accounting for factors such as the actual conditions of the study area, the spatial resolution of the RS images, and the ease of image acquisition, the Landsat series of satellites from the United States was selected as the target RS data source. The spatial resolution of the images was 30 m. To ensure the accuracy of the data, Landsat 8 images (20 April 2013) that were close in time to ground sampling were obtained from the United States Geological Survey (USGS) platform (https://earthexplorer.usgs.gov/).

ENVI 5.3 software was used to perform preprocessing tasks of the Landsat 8 images, such as radiometric calibration, atmospheric correction, image stitching, and cropping.

2.2.3. Remote Sensing Pixel-Scale Salt Content Acquisition

To address the scale effects resulting from the mismatch between ground-based "point" salinity data and remote sensing pixel-based "spatial" data, a geostatistical approach was adopted, using the intended remote sensing image pixel scale as the interpolation scale to convert ground "point"-scale soil salt observations to pixel-scale soil salt content. Geostatistics consist of two main components: the analysis of spatial variation and structure using variograms and their parameters and the Kriging interpolation method for spatial-localization estimation.

(1) Normality test of the data

The calculation of the variance function typically requires data to follow a normal distribution, as otherwise scale effects may occur. To assess whether the data followed a normal distribution, the Kolmogorov–Smirnov (K-S) test in SPSS 26 was used. If the data do not conform to a normal distribution, data transformation is applied to make it follow a normal distribution.

(2) Variance function

The variance function is used to describe the structural and stochastic characteristics of regionalized variables. Its empirical function expression is

$$\gamma^*(h) = \frac{1}{2N(h)} \sum_{i=1}^{N(h)} [Z(x_i) - Z(x_i + h)]^2 \quad (1)$$

where $\gamma^*(h)$ represents the average variance of all point pairs spaced h apart; $Z(x_i)$ and $Z(x_i + h)$ represent the values of the study variable (such as observed values of a certain attribute or factor) at points x_i and $x_i + h$, respectively; and $N(h)$ represents the numerical pairs with a spacing of h.

Theoretical models of the variance function are commonly used as exponential, spherical, Gaussian, and linear models. The structural characteristics of the variance function are described by four important parameters: the type of function, nugget variance (denoted as C_0), sill (denoted as $C_0 + C$, where C represents the partial sill), and range (denoted as A_0). The GS + 9.0 software is used to compute the variance function, and the optimal theoretical model of the variance function is selected based on the principles of a high R^2 approaching 1 and the minimum residual sum of squares (RSS).

The spatial variation in soil salinity is influenced by two main factors: (1) random factors C_0 (related to irrigation, fertilization, cultivation practices, land-use practices, etc., i.e., human-associated factors) and (2) structural factors denoted as C (related to topography, climate, vegetation, soil types, etc., i.e., natural factors). $C_0/(C_0 + C)$ represents spatial correlation, indicating the proportion of spatial heterogeneity caused by random factors to the total variability of the system. If $C_0/(C_0 + C) <$25%, there is a strong spatial correlation, and the spatial variation is mainly controlled by structural factors. If 25% $< C_0/(C_0 + C) <$ 75%, there is a moderate spatial correlation, where spatial variation is influenced by both structural and random factors. If $C_0/(C_0 + C) >$ 75%, there is a weak spatial correlation, and the spatial variation is mainly governed by random factors.

(3) Kriging interpolation

Kriging interpolation is an unbiased optimal estimation method based on the analysis of the distribution of the data of geographic variables and the structure of their variance functions, which is used to estimate the attribute values of unknown points [22,44]. During the interpolation process, Kriging considers the spatial relationship between the unknown points and all known sample points, fully utilizes the spatial structural characteristics of the sample point data, assigns a certain interpolation weight to each known point, and predicts the value of unknown points using a weighted average method.

In this study, the soil salinity was subjected to ordinary Kriging interpolation using the Spatial Analyst tool in ArcGIS 10.5 software. This allowed for the generation of soil salt content estimates corresponding to the Landat 8 (30 m × 30 m) pixel scale.

2.2.4. Classification Criteria for Soil Salinization

According to the soil salinization classification criteria used by Wu et al. [45], soil salinity can be divided into the following five levels: (a) Nonsaline: salt content < 0.2%; (b) Slightly saline: salt content ranging from 0.2% to 0.3%; (c) Moderately saline: salt content ranging from 0.3% to 0.6%; (d) Strongly saline: salt content ranging from 0.6% to 1.0%; and (e) Solonchak: salt content > 1.0%.

2.3. Spectral Index Construction

Spectral indices are commonly used as indirect indicators for monitoring salinized areas in bare ground or soils with very low vegetation cover. Spectral indices are obtained by combining two or more spectral bands and are widely regarded as powerful tools for identifying features of interest [8]. Based on existing research and experience, 14 commonly used salt indices were selected as candidate indicators for the monitoring model of soil salinization. The calculation formulas for these indices are shown in Table 1.

Table 1. Spectral index formula.

Salinity Index	Formula	Reference
SI	$SI = \sqrt{(B + R)}$	[46]
SI1	$SI1 = \sqrt{R * G}$	[47]
SI2	$SI2 = \sqrt{G^2 + R^2 + NIR^2}$	[47]
SI3	$SI3 = \sqrt{G^2 + R^2}$	[47]
S1	$S1 = B/R$	[48]
S2	$S2 = (B - R)/(B + R)$	[48]
S3	$S3 = G * R/B$	[48]
S4	$S4 = \sqrt{B \times R}$	[48]
S5	$S5 = B \times R/G$	[48]
S6	$S6 = R \times NIR/G$	[48]
S7	$S7 = SWIR1/SWIR2$	[11]
S8	$S8 = (SWIR1 - SWIR2)/(SWIR1 + SWIR2)$	[11]
NDSI	$NDSI = (R - NIR)/(R + NIR)$	[46]
GAEX	$GAEX = R/G$	[49]

Note: B, G, R, NIR, and SWIR represent the spectral reflectance at the blue, green, red, near-infrared, and shortwave infrared wavelengths, respectively.

2.4. Feature Selection

Feature selection is a crucial step in the development of machine learning models. It involves identifying the most important subset of input variables for prediction or decision making, which can improve the accuracy and generalization ability of the model. Among various feature selection methods, correlation-based feature selection (CFS) is a technique that considers both the correlation between feature variables and the correlation between feature variables and the dependent variable. CFS first calculates the correlation between each feature variable and the dependent variable, then calculates the correlation between each feature variable and other feature variables, and finally combines the two to select the final subset of features.

3. Modeling Methods and Evaluation Metrics

3.1. Modeling Methods

The Bayes Classifier (BC) is a classical probabilistic classification model that calculates the posterior probability of a sample based on the prior probabilities of different classes in the dataset and the conditional probability of the sample under a given class and selects the category corresponding to the category with the largest posterior probability as the final prediction type of the sample.

In this study, the soil salinization type is represented as an event w, and the salinization characteristics are represented as an event x. The soil salinization type $w_i (i = 1, 2, \ldots, c)$ and the corresponding characteristics x are two events that occur in the same spatial location. According to Bayes' theorem, the posterior probability $P(w_i|x)$ can be expressed as

$$P(w_i|x) = \frac{P(w_i)P(x|w_i)}{P(x)} \tag{2}$$

where $P(w_i)$ represents the prior probability of class w_i occurring; $P(x|w_i)$ represents the probability of observing x given that the true class is w_i, known as the likelihood; and $P(x)$ represents the probability of observing x from the entire sample, given by $P(x) = \sum_{i=1}^{k} P(w_i)P(x|w_i)$.

For a given x, $P(x)$ is determined. Let $f_i(\mathrm{x})$ represent the probability density of an unknown sample x belonging to class w_i. The likelihood can be expressed in terms

of probability density, given by $P(x|w_i) = 2bf_i(\mathrm{x})$, where b is a small interval near x. Therefore, the formula for calculating the posterior probability can be simplified as follows:

$$P(w_i|x) = \frac{P(w_i)P(x|w_i)}{P(x)} \propto P(w_i)P(x|w_i) \propto P(w_i)f_i(\mathrm{x}) \tag{3}$$

As indicated by Equation (4), the determination of the probability density function $f_i(\mathrm{x})$ becomes crucial in determining w_i. Kernel Density Estimation (KDE) is a nonparametric statistical method used for estimating the probability density function of a random variable. The formula for KDE is

$$f_i(x) = \frac{1}{nh}\sum_{i=1}^{n}\left[K\left(\frac{x - X_i}{h}\right)\right] \tag{4}$$

where n represents the total number of known samples; h denotes the bandwidth; x indicates the random sample; X_i represents the i_{th} known sample; and $K(.)$ represents the kernel function.

In this study, the bandwidth h was computed using Scott's rule method, and the Gaussian kernel was used as the kernel function: $K(u) = \frac{1}{\sqrt{2\pi}}exp\left(-\frac{u^2}{2}\right)$, $u\ \epsilon(-\infty, +\infty)$.

Many studies use EL to obtain more accurate results by combining the outputs of single models. In this study, a strategy similar to the concept of EL was adopted to integrate the single-feature BC model in order to construct an RS monitoring model for soil salinization. The settings are as follows: Assume that we construct d participating models for the sample $\hat{x} = (x_1, x_2, \ldots, x_d)$ using the BC algorithm, denoted as M_1, M_2, …, M_d. The recall rates for different classes under the m_{th} participating model are denoted as $R_m^{(k)}$, where $k = 1, 2, \ldots, c$. According to the ensemble strategy we have set, the class attribute w_i of the sample $\hat{x} = (x_1, x_2, \ldots, x_d)$ can be determined based on Equation (5):

$$w = \underset{w_i, i = 1, 2, \ldots c}{argmax} \sum_{j=1}^{d} \frac{1}{R_j^{(i)}} P\left(w_i|x_j\right) \tag{5}$$

where $Recall = \frac{TP}{TP+FN}$ and TP represents true positives (samples that are actually positive and predicted as positive) and FN represents false negatives (samples that are actually positive but predicted as negative).

3.2. Model Evaluation Metrics

Model evaluation metrics include recall, precision, F1-score, and accuracy. Recall measures the ability of the model to correctly identify positive samples. Precision measures the model's ability to not predict negative samples as positive. The F1-score is a measure of the model's robustness, and the larger its value is, the more robust the model is. Accuracy is an evaluation metric that measures the overall performance of the model. The Kappa coefficient takes into account the consistency of a model, especially in situations of imbalanced class distribution. It provides a more accurate performance evaluation, with a range of values from [−1 to 1]. A value closer to 1 indicates better model performance.

$$Precision = \frac{TP}{TP + FP} \tag{6}$$

$$F1 = \frac{2 * Recall * Precision}{Recall + Precision} \tag{7}$$

$$Accuracy = \frac{TP + TN}{TP + FP + TN + FN} \tag{8}$$

where *FP* represents false positives (samples that are actually negative but predicted as positive) and *TN* represents true negatives (samples that are actually negative and predicted as negative).

4. Results and Analysis

4.1. Descriptive Statistics of the Measured Soil Salinity

To investigate the spatial variation in soil salinity at a 30 m resolution, a descriptive statistical analysis was conducted on the selected sample areas (Table 2). From Table 2, it is evident that there are significant differences in the salinity characteristics among the sample areas. The CV for all sample areas is greater than 10%, indicating substantial spatial variability in soil surface salinity within the 30 m scale. Merely using the salinity value of any single sampling point within the 30 m range cannot represent the overall salinity conditions within that range. Therefore, when performing RS inversion, it is necessary to further obtain estimates corresponding to the pixel scale to acquire more representative salinity information.

Table 2. Statistical characteristics of soil salinity at the 30 m scale.

Study Area	Area	Minimum (%)	Maximum (%)	Mean (%)	Median (%)	SD (%)	CV (%)
N	1	0.10	0.44	0.25	0.25	0.11	44.18
	2	0.21	1.12	0.49	0.43	0.29	58.61
	3	0.21	1.50	0.41	0.32	0.31	76.13
	4	0.21	0.66	0.34	0.27	0.15	43.93
S	1	0.16	0.94	0.47	0.37	0.27	58.46
	2	0.16	2.26	0.41	0.24	0.51	125.90
	3	0.18	0.73	0.40	0.38	0.16	39.58
	4	0.13	0.50	0.28	0.26	0.13	45.12

Note: CV < 10% indicates weak variability; 10% < CV < 100% indicates moderate variability; and CV > 100% indicates strong variability.

The descriptive statistics of the soil salinity content in the N and S regions were analyzed separately, and the results are shown in Table 3. In terms of the variation, the soil salinity content in the N region varied by 3.90%, while that in the S region varied by 5.68%. In terms of the mean value, the N region belonged to the slightly saline type, while the S region belonged to the strongly saline type. In terms of the CV, both the N and S regions had variation coefficients exceeding 100%, indicating a strong variation. This phenomenon may be caused by differences in local topography, land use, irrigation systems, and cultivation practices within the regions.

Table 3. Statistical characteristics of soil salinity.

Study Region	Minimum (%)	Maximum (%)	Mean (%)	Median (%)	SD (%)	CV (%)
N	0.06	3.96	0.36	0.26	0.43	119.22
S	0.09	5.77	0.80	0.39	1.03	128.80

4.2. Transformation of "Point" to "Spatial" Scale for Soil Salinity Information Based on Geostatistical Methods

The analysis of the variance function structure of soil salinity and the results of Kriging interpolation are shown in Table 4 and Figure 3, respectively. The analysis of the variance function structure showed that the theoretical model of the soil salinity variance function in region N conformed to the exponential model, while that in region S conformed to the spherical model, but the R^2 values of both models were higher, 0.82 and 0.97, respectively, which indicated that the selected model could fit the data better and accurately reflect the

spatial variability characteristics of soil salinity at the sampling scale. The $C_0/C_0 + C$ of soil salinity in the N and S regions was 41.27% and 19.46%, respectively. This indicated that the spatial variation in soil salinity in the N region was influenced by both random factors such as irrigation and cultivation practices and structural factors such as soil type, while in the S region, the spatial variation was mainly influenced by structural factors. The A_0 in the N and S regions was 603.00 m and 762.00 m, respectively, indicating that the soil salinity in both regions had a large spatial autocorrelation distance. This was due to the sampling period being during the drought period, where continuous and intense evaporation enhances the homogeneity of surface soil salinity distribution. It was also the fallow period, and agricultural activities, such as irrigation, fertilizer application, and cultivation activities, are relatively infrequent, which decreases the spatial autocorrelation of surface soil salinity during this period.

Table 4. Soil salinity variance function model and its related parameters.

Study Region	Theoretical Model	C_0	C_0+C	C_0/C_0+C (%)	A_0 (m)	R^2	RSS
N	Exponential	0.26	0.63	41.27	603.00	0.82	0.03
S	Spherical	0.23	1.16	19.46	762.00	0.97	0.07

From the spatial distribution of soil salinity (Figures 3 and 4), the soil salt content in both the N and S regions exhibits a pattern of stripes and patches. In the N study region, the soil salinity is relatively low, and the land is mainly used for cultivating sunflowers. Therefore, microtopography, human activities, and other factors may be important factors contributing to this distribution pattern of salinity. In the S study region, soil salinity is higher and mainly concentrated in the eastern part of the study region, which is mainly due to the different land use patterns in the eastern and western parts of the S study region, with the eastern part being a saline wasteland, while the western part of the study region is mainly dominated by agricultural land. This difference in land use leads to variations in soil salinity distribution between the eastern and western regions.

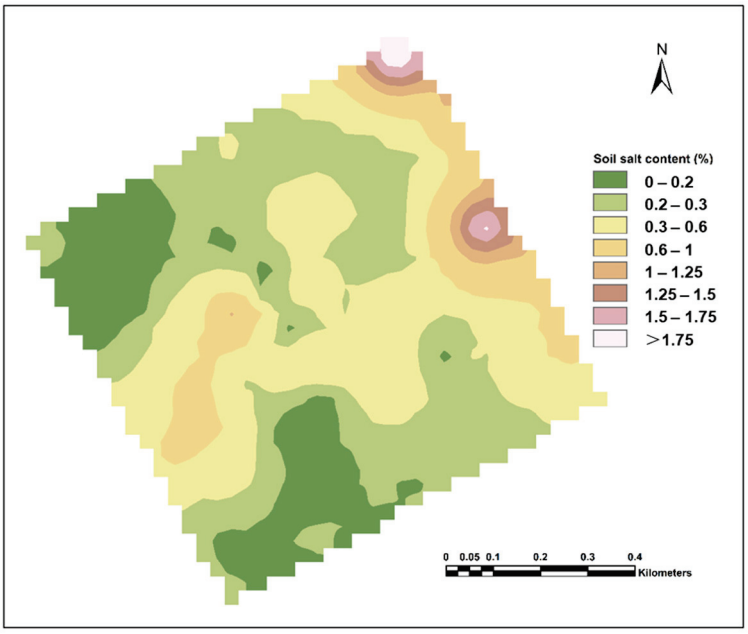

Figure 3. Spatial distribution of soil salinity in the N study region.

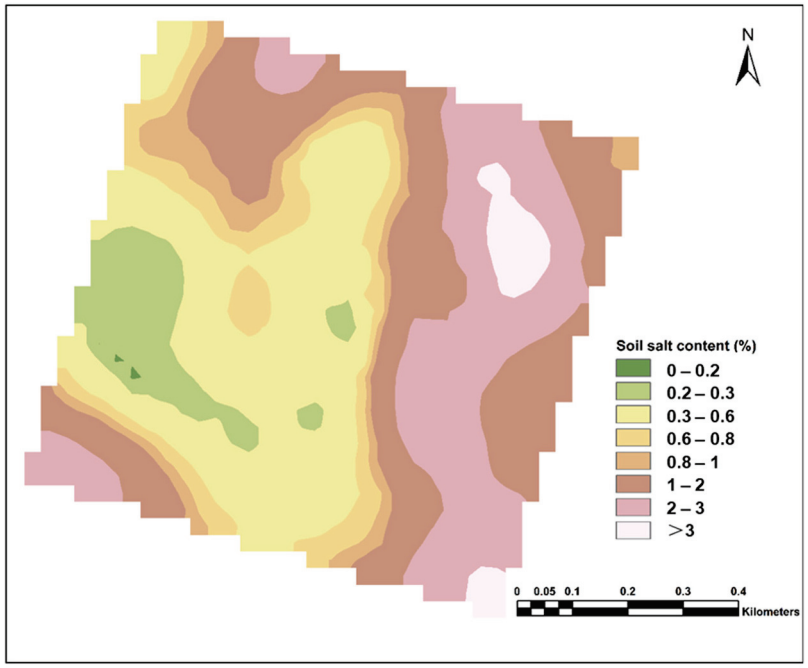

Figure 4. Spatial distribution of soil salinity in the S study region.

4.3. Model Results and Analysis

Based on the salinity Kriging interpolation results described in Section 4.2, the ground "relative truth" value corresponding to the pixel scale was generated at a scale of 30 m. Subsequently, the generated pixel-scale "relative truth" was classified according to the salt-affected classification criteria, and the classified salt-affected degrees were used as the dependent variable for sensitive spectral feature selection and subsequent model construction. During the feature selection phase, the CFS method was employed to select features, resulting in the selection of the feature subset S1, S3, S7, and GAEX. Finally, the selected subset of features was used to construct salinization remote sensing monitoring models using the BC algorithm. In constructing the model, 70% of the total samples were used as the training set, and 30% were used as the validation set. In the following analysis, the models built based on single features are referred to as KDE-BC_S1, KDE-BC_S3, KDE-BC_S7, and KDE-BC_GAEX. The combination of a single-feature BC model using the EL concept is denoted as KDE-BC_EL, and the model confusion matrix results are shown in Appendix A Figure A1.

The single-feature constructed KDE-BC model was moderately successful in predicting soil salinity based on the evaluation scores of the model (recall, precision, F1-score), and the model results was shown Table 5. However, there are still some challenges. One noteworthy issue is that different KDE-BC models had varying scores when identifying the same soil salinity type. For example, when identifying saline soil, the F1-scores of KDE-BC_S1, KDE-BC_S3, KDE-BC_S7, and KDE-BC_GAEX were 0.82, 0.89, 0.57, and 0.84, respectively. The recall and precision patterns were similar to those of the F1-score. However, when combining the single-feature constructed KDE-BC models, it was found that KDE-BC_EL significantly improved the identification of various salinity types, indicating its good applicability in classifying salinization.

Table 5. Scores of model evaluation metrics.

Model	Category	Recall	Precision	F1-Score	Accuracy	Kappa
KDE-BC_S1	Nonsaline	0.68	0.69	0.68	0.73	0.64
	Slightly saline	0.62	0.73	0.67		
	Moderately saline	0.74	0.72	0.73		
	Strongly saline	0.49	0.84	0.62		
	Solonchak	0.95	0.72	0.82		
KDE-BC_S3	Nonsaline	0.43	0.46	0.44	0.77	0.70
	Slightly saline	0.73	0.68	0.70		
	Moderately saline	0.83	0.81	0.82		
	Strongly saline	0.63	0.77	0.70		
	Solonchak	0.90	0.88	0.89		
KDE-BC_S7	Nonsaline	0.62	0.77	0.69	0.66	0.55
	Slightly saline	0.75	0.63	0.69		
	Moderately saline	0.80	0.79	0.80		
	Strongly saline	0.37	0.57	0.45		
	Solonchak	0.59	0.55	0.57		
KDE-BC_GAEX	Nonsaline	0.57	0.62	0.59	0.71	0.61
	Slightly saline	0.53	0.72	0.61		
	Moderately saline	0.81	0.64	0.72		
	Strongly saline	0.55	0.65	0.60		
	Solonchak	0.86	0.83	0.84		
KDE-BC_EL	Nonsaline	0.70	0.68	0.69	0.85	0.80
	Slightly saline	0.81	0.81	0.81		
	Moderately saline	0.89	0.90	0.90		
	Strongly saline	0.78	0.80	0.79		
	Solonchak	0.91	0.89	0.90		

Further analysis of the model accuracy revealed that among the KDE-BC models, KDE-BC_S3 performed the best, with accuracy and Kappa values of 0.77 and 0.70, respectively. On the other hand, KDE-BC_S7 performed the worst, with accuracy and Kappa values of 0.66 and 0.55, respectively. In comparison to the KDE-BC model, KDE-BC_EL provided more accurate predictions, with accuracy and Kappa reaching 0.85 and 0.80, respectively. This validated the effectiveness of the soil salinization identification model constructed based on the concept of ensemble learning. Importantly, the KDE-BC_EL model only improved the accuracy by 0.08 compared to the best KDE-BC model. However, considering the F1 score, the KDE-BC_EL model effectively enhanced the robustness of the model.

5. Discussion

Soil salinity monitoring is crucial for land management in arid and semiarid regions. With the development and application of RS technology, unconventional monitoring of soil salinity has become possible, expanding the monitoring range of soil salt content beyond traditional techniques. However, due to the significant spatial heterogeneity of soil salinity, observation data from different scales often lack comparability. Therefore, this study focuses on the spatial heterogeneity of soil salinity information at the RS pixel scale. Eight sample plots (at a pixel scale of 30 m) were selected to examine the spatial variability of soil salinity. The variation coefficient of salt content within the eight sample plots was greater than 10%, indicating that using the salt content value from any single sampling point within a 30 m scale cannot represent the salt content situation within that scale. However, most existing studies are based on the assumption of spatial homogeneity of soil salinity, using ground-level salt content observation data as the "true value" for establishing salt content RS models and validating the rationality and accuracy of RS inversion products, without considering the representativeness of the ground point salinity observation data, which is somewhat unreasonable. In addition, to obtain ground-level "relative true values" corresponding to the pixel scale, the study adopted the ordinary

Kriging method to interpolate the salinity. However, the effectiveness of different Kriging methods in salt content interpolation was not compared. Therefore, it is necessary to further explore other Kriging interpolation methods, such as cokriging and indicator Kriging.

Soil formation involves both environmental factors and human activities. Environmental factors include topography, climate, vegetation cover, and land use types, which can influence the physical, chemical, and biological properties of the soil. Human activities such as land reclamation, cultivation, fertilization, irrigation, and drainage may also alter the composition and characteristics of the soil, thereby affecting the spatial heterogeneity of soil salinity. Spatial heterogeneity is an inherent property of the spatial distribution pattern of soil salinity, encompassing heterogeneity in spatial composition, configuration, and relationships [50]. It reflects the complexity and variability of the spatial system. The spatial heterogeneity of soil salinity is shaped by the combined influence of structural and stochastic factors. Structural factors enhance spatial correlations within the same layer, while stochastic factors weaken spatial correlations, driving the system towards homogenization and uniformity [51]. This study reveals that the N and S study regions exhibit spatial heterogeneity in soil salinity. Compared to the N region influenced by both structural and stochastic factors, the S region, influenced by structural factors, exhibits stronger spatial variation induced by spatial autocorrelation.

It is generally believed that spatial variability is a natural characteristic of soil salinity itself, and regardless of the observation scale being large or small, the spatial variability of soil salinity objectively exists. The ability of remote sensing imagery to retrieve soil salinity varies with different resolutions. However, for the spatial distribution of soil salinity, a single-resolution remote sensing image is challenging to accurately represent. Moreover, there are differences in the optimal scale for the precise inversion of soil salinity spatial features and variations. In future research, it would be beneficial to better serve soil salinity remote sensing monitoring by analyzing the relationship between ground-level patchy salt content at different spatial scales and remote sensing data to select the optimal scale.

The spectral index method is the most popular method used in research when attempting to characterize the relationship between soil reflectance and soil salinity. Previous soil salinity studies have accumulated empirical evidence (spectral indices) for soil salinity identification and verified their validity and reproducibility [52]. RS modeling is a critical stage in salinity monitoring, and the choice of estimation method can greatly influence the final results. In recent years, researchers have increasingly favored the approach of EL or multi-model inference [53–55]. Therefore, this study introduces the EL concept for soil salinity identification, and the recall rate is used to quantify the advantages of each participating model. Consistent with other research findings, this study also found that the soil salinization identification model constructed using the EL concept outperforms single participating models in terms of prediction and is more robust in classifying different categories, resulting in satisfactory results. Compared to a single model, the ensemble of multiple models in this study compensated for any potential deficiencies or unreliable information in any single model and improved the robustness of the predictions. However, the homogeneous EL concept method used in this study only improved the classification accuracy by 0.08 compared to the best single participating model, which warrants further consideration. (1) The Bayesian statistical method is an unconventional classification method that has a unique advantage in mining complex data and can provide meaningful and interpretable relational models [56], which can adequately address the unclear correspondence between feature variables and target variables, as demonstrated by the classic example of the Iris flower dataset classification. Therefore, single participating models may also produce good results. (2) Previous research has mostly focused on ensembles of heterogeneous models [37,57,58]. Compared to ensembles of heterogeneous models, homogeneous model ensembles reduce training costs but may also reduce model diversity [32,59–61]. Therefore, in further research, it is necessary to explore the application of the heterogeneous EL concept in predicting soil salinity to better monitor soil salinization.

6. Conclusions

In this study, we focused on the spatial heterogeneity of soil salinity and explored the potential of an EL concept combining single-feature BC methods for soil salinity identification based on the acquisition of ground "relative truth" values at the pixel scale of RS. It was found that the scale effects resulting from the mismatch between ground-based "point" salinity data and remote sensing pixel-based "spatial" data need to be considered when performing RS inversion. The introduction of the EL concept improved the accuracy of soil salinity RS monitoring, with an overall accuracy of 0.85. Although the improvement in overall accuracy compared to the best KDE-BC model was only 0.08, there was a significant improvement in the identification of various salinization types (e.g., F1-score), effectively enhancing the robustness of the model. Therefore, it is highly recommended to explore the potential of the EL concept in soil salinization identification to develop reliable models for identifying salinized soils, as well as for further applications in quantitative RS monitoring of soil salinity.

Author Contributions: Conceptualization, H.C. and J.W.; methodology, H.C. and J.W.; software, H.C.; validation, H.C.; formal analysis, H.C.; investigation, C.X.; resources, H.C.; data curation, H.C. and H.C.; writing—original draft preparation, H.C.; writing—review and editing, H.C. and J.W.; visualization, H.C. and J.W.; supervision, J.W.; project administration, J.W.; funding acquisition, J.W. All authors have read and agreed to the published version of the manuscript.

Funding: This work was financially supported by the National Natural Science Foundation of China (Grant No. 52379047 and 52209067) and the National Key Research and Development Program of China (Grant No. 2021YFD1900804).

Data Availability Statement: Data are contained within the article.

Conflicts of Interest: The authors declare no conflicts of interest.

Appendix A

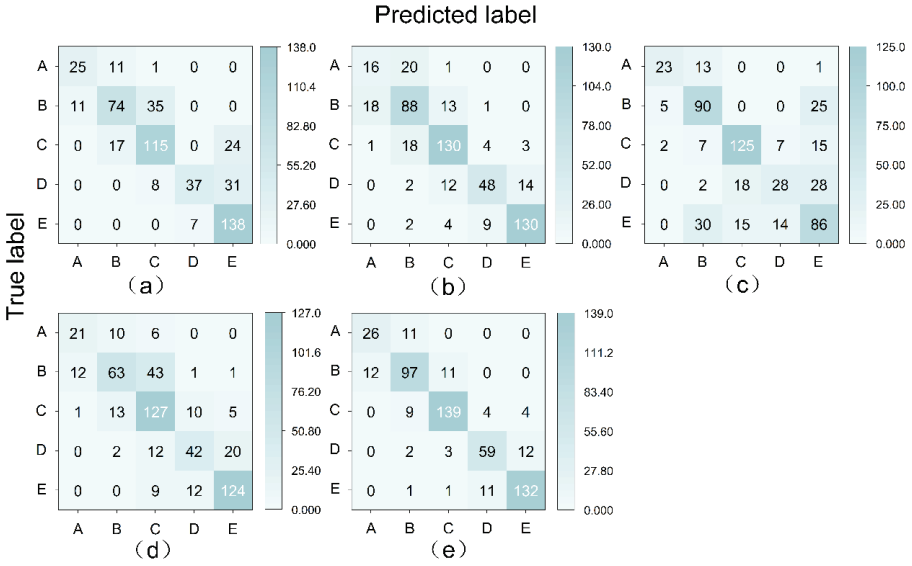

Figure A1. Confusion matrix plots. A: Nonsaline, B: Slightly saline, C: Moderately saline, D: Strongly saline, E: Solonchak; (**a**) KDE-BC_S1, (**b**) KDE-BC_S3, (**c**) KDE-BC_S7, (**d**) KDE-BC_GAEX, (**e**) KDE-BC_EL.

References

1. Metternicht, G.I.; Zinck, J.A. Remote sensing of soil salinity: Potentials and constraints. *Remote Sens. Environ.* **2003**, *85*, 1–20. [CrossRef]
2. Wang, J.; Zhen, J.; Hu, W.; Chen, S.; Lizaga, I.; Zeraatpisheh, M.; Yang, X. Remote sensing of soil degradation: Progress and perspective. *Int. Soil Water Conserv. Res.* **2023**, *11*, 429–454. [CrossRef]

3. Farifteh, J.; Farshad, A.; George, R.J. Assessing salt-affected soils using remote sensing, solute modelling, and geophysics. *Geoderma* **2006**, *130*, 191–206. [CrossRef]
4. Wang, J.; Ding, J.; Yu, D.; Teng, D.; He, B.; Chen, X.; Ge, X.; Zhang, Z.; Wang, Y.; Yang, X.; et al. Machine learning-based detection of soil salinity in an arid desert region, Northwest China: A comparison between Landsat-8 OLI and Sentinel-2 MSI. *Sci. Total Environ.* **2020**, *707*, 136092. [CrossRef] [PubMed]
5. Abuelgasim, A.; Ammad, R. Mapping soil salinity in arid and semi-arid regions using Landsat 8 OLI satellite data. *Remote Sens. Appl.* **2019**, *13*, 415–425. [CrossRef]
6. Wang, J.; Ding, J.; Ge, X.; Peng, J.; Hu, Z.W. Monitoring soil salinization based on remote sensing and proximal soil sensing: Progress and perspective. *J. Remote Sens.* **2023**, 1–23. [CrossRef]
7. Lobell, D.B.; Lesch, S.M.; Corwin, D.L.; Ulmer, M.G.; Anderson, K.A.; Potts, D.J.; Doolittle, J.A.; Motos, M.R.; Baltes, M.J. Regional-scale Assessment of Soil Salinity in the Red River Valley Using Multi-year MODIS EVI and NDVI. *J. Environ. Qual.* **2010**, *39*, 35–41. [CrossRef] [PubMed]
8. Wang, J.; Ding, J.; Ma, X.; Zhang, Z.; Ge, X.; Lizaga, I.; Li, X.; Liang, J.; Chen, X.; Yuan, L.; et al. Capability of Sentinel-2 MSI data for monitoring and mapping of soil salinity in dry and wet seasons in the Ebinur Lake region, Xinjiang, China. *Geoderma* **2019**, *353*, 172–187. [CrossRef]
9. Ge, X.; Ding, J.; Teng, D.; Wang, J.; Huo, T.; Jin, X.; Wang, J.; He, B.; Han, L. Updated soil salinity with fine spatial resolution and high accuracy. The synergy of Sentinel-2 MSI, environmental covariates and hybrid machine learning approaches. *Catena* **2022**, *212*, 106054. [CrossRef]
10. Golestani, M.; Mosleh Ghahfarokhi, Z.; Esfandiarpour-Boroujeni, I.; Shirani, H. Evaluating the spatiotemporal variations of soil salinity in Sirjan Playa, Iran using Sentinel-2A and Landsat-8 OLI imagery. *Catena* **2023**, *231*, 107375. [CrossRef]
11. Wang, L.; Hu, P.; Zheng, H.; Liu, Y.; Cao, X.; Hellwich, O.; Liu, T.; Luo, G.; Bao, A.; Chen, X. Integrative modeling of heterogeneous soil salinity using sparse ground samples and remote sensing images. *Geoderma* **2023**, *430*, 116321. [CrossRef]
12. Abidine, M.M.O.; El Aboudi, A.; Kebd, A.; Aloueimine, B.B.; Dallahi, Y.; Soulé, A.; Vadel, A. Modeling the Spatial Variability of the Electrical Conductivity of the Soil Using Differents Spatial Interpolation Methods: Case of the Dawling National Park in Mauritania. *Geogr. Tech.* **2018**, *13*, 1–11. [CrossRef]
13. Fu, T.; Gao, H.; Liu, J. Comparison of Different Interpolation Methods for Prediction of Soil Salinity in Arid Irrigation Region in Northern China. *Agronomy* **2021**, *11*, 1535. [CrossRef]
14. Howari, F.M.; Goodell, P.C.; Miyamoto, S. Spectral properties of salt crusts formed on saline soils. *J. Environ. Qual.* **2002**, *31*, 1453–1461. [CrossRef]
15. Cheng, L.; Aghakouchak, A.; Gilleland, E.; Katz, R.W. Non-stationary extreme value analysis in a changing climate. *Clim. Chang.* **2014**, *127*, 353–369. [CrossRef]
16. Nie, M.; Huang, S.; Leng, G.; Zhou, Y.; Huang, Q.; Dai, M. Bayesian-based time-varying multivariate drought risk and its dynamics in a changing environment. *Catena* **2021**, *204*, 105429. [CrossRef]
17. Yang, X.; Li, Y.P.; Huang, G.H.; Li, Y.F.; Liu, Y.R.; Zhou, X. Development of a multi-GCMs Bayesian copula method for assessing multivariate drought risk under climate change: A case study of the Aral Sea basin. *Catena* **2022**, *212*, 106048. [CrossRef]
18. Davies, J.; Olley, J.; Hawker, D.; Mcbroom, J. Application of the Bayesian approach to sediment fingerprinting and source attribution. *Hydrol. Process* **2018**, *32*, 3978–3995. [CrossRef]
19. Li, Y.; Gholami, H.; Song, Y.; Fathabadi, A.; Malakooti, H.; Collins, A.L. Source fingerprinting loess deposits in Central Asia using elemental geochemistry with Bayesian and GLUE models. *Catena* **2020**, *194*, 104808. [CrossRef]
20. Fathabadi, A.; Jansen, J.D. Quantifying uncertainty of sediment fingerprinting mixing models using frequentist and Bayesian methods: A case study from the Iranian loess Plateau. *Catena* **2022**, *217*, 106474. [CrossRef]
21. Wang, Y.; Zhao, T. Statistical interpretation of soil property profiles from sparse data using Bayesian compressive sampling. *Géotechnique* **2017**, *67*, 523–536. [CrossRef]
22. Wang, C.; Li, X.; Zhang, J.; Liu, Y.; Situ, Z.; Gao, C.; Liu, J. Using Bayesian compressed sensing and sparse dictionaries to interpolate soil properties. *Geoderma* **2022**, *428*, 116162. [CrossRef]
23. Luo, Y.; Weng, E.; Wu, X.; Gao, C.; Zhou, X.; Zhang, L. Parameter identifiability, constraint, and equifinality in data assimilation with ecosystem models. *Ecol. Appl.* **2009**, *19*, 571–574. [CrossRef]
24. Heung, B.; Ho, H.C.; Zhang, J.; Knudby, A.; Bulmer, C.E.; Schmidt, M.G. An overview and comparison of machine-learning techniques for classification purposes in digital soil mapping. *Geoderma* **2016**, *265*, 62–77. [CrossRef]
25. Tebaldi, C.; Knutti, R. The use of the multi-model ensemble in probabilistic climate projections. *Philos. Trans. R. Soc. A* **2007**, *365*, 2053–2075. [CrossRef]
26. Baker, L.; Ellison, D. The wisdom of crowds—Ensembles and modules in environmental modelling. *Geoderma* **2008**, *147*, 1–7. [CrossRef]
27. Peña, M.; van den Dool, H. Consolidation of Multimodel Forecasts by Ridge Regression: Application to Pacific Sea Surface Temperature. *J. Clim.* **2008**, *21*, 6521–6538. [CrossRef]
28. Yan, J.; Sun, R.; Liu, T.; Duan, S. Domain-adaptation-based active ensemble learning for improving chemical sensor array performance. *Sens. Actuators A-Phys.* **2023**, *357*, 114411. [CrossRef]
29. Taghizadeh-Mehrjardi, R.; Nabiollahi, K.; Minasny, B.; Triantafilis, J. Comparing data mining classifiers to predict spatial distribution of USDA-family soil groups in Baneh region, Iran. *Geoderma* **2015**, *253–254*, 67–77. [CrossRef]

30. Kim, D.; Yu, H.; Lee, H.; Beighley, E.; Durand, M.; Alsdorf, D.E.; Hwang, E. Ensemble learning regression for estimating river discharges using satellite altimetry data: The Central Congo River as a Test-bed. *Remote Sens. Environ.* **2019**, *221*, 741–755. [CrossRef]
31. Cimusa Kulimushi, L.; Bigabwa Bashagaluke, J.; Prasad, P.; Heri-Kazi, A.B.; Lal Kushwaha, N.; Masroor, M.; Mohammed, S. Soil erosion susceptibility mapping using ensemble machine learning models: A case study of upper Congo river sub-basin. *Catena* **2023**, *222*, 106858. [CrossRef]
32. Pham, K.; Kim, D.; Park, S.; Choi, H. Ensemble learning-based classification models for slope stability analysis. *Catena* **2021**, *196*, 104886. [CrossRef]
33. Taghizadeh-Mehrjardi, R.; Minasny, B.; Toomanian, N.; Zeraatpisheh, M.; Amirian-Chakan, A.; Triantafilis, J. Digital Mapping of Soil Classes Using Ensemble of Models in Isfahan Region, Iran. *Soil. Syst.* **2019**, *3*, 37. [CrossRef]
34. Malone, B.P.; Minasny, B.; Odgers, N.P.; Mcbratney, A.B. Using model averaging to combine soil property rasters from legacy soil maps and from point data. *Geoderma* **2014**, *232–234*, 34–44. [CrossRef]
35. Vaysse, K.; Lagacherie, P. Evaluating Digital Soil Mapping approaches for mapping GlobalSoilMap soil properties from legacy data in Languedoc- Roussillon (France). *Geoderma Reg.* **2015**, *4*, 20–30. [CrossRef]
36. Rasaei, Z.; Bogaert, P. Spatial filtering and Bayesian data fusion for mapping soil properties: A case study combining legacy and remotely sensed data in Iran. *Geoderma* **2019**, *344*, 50–62. [CrossRef]
37. Dasgupta, S.; Debnath, S.; Das, A.; Biswas, A.; Weindorf, D.C.; Li, B.; Shukla, A.K.; Das, S.; Saha, S.; Chakraborty, S. Developing regional soil micronutrient management strategies through ensemble learning based digital soil mapping. *Geoderma* **2023**, *433*, 116457. [CrossRef]
38. Riggers, C.; Poeplau, C.; Don, A.; Bamminger, C.; Höper, H.; Dechow, R. Multi-model ensemble improved the prediction of trends in soil organic carbon stocks in German croplands. *Geoderma* **2019**, *345*, 17–30. [CrossRef]
39. Song, X.; Wu, H.; Ju, B.; Liu, F.; Yang, F.; Li, D.; Zhao, Y.; Yang, J.; Zhang, G. Pedoclimatic zone-based three-dimensional soil organic carbon mapping in China. *Geoderma* **2020**, *363*, 114145. [CrossRef]
40. Zhu, L.; Walker, J.P.; Shen, X. Stochastic ensemble methods for multi-SAR-mission soil moisture retrieval. *Remote Sens. Environ.* **2020**, *251*, 112099. [CrossRef]
41. Nketia, K.A.; Asabere, S.B.; Ramcharan, A.; Herbold, S.; Erasmi, S.; Sauer, D. Spatio-temporal mapping of soil water storage in a semi-arid landscape of northern Ghana—A multi-tasked ensemble machine-learning approach. *Geoderma* **2022**, *410*, 115691. [CrossRef]
42. Román Dobarco, M.; Arrouays, D.; Lagacherie, P.; Ciampalini, R.; Saby, N.P.A. Prediction of topsoil texture for Region Centre (France) applying model ensemble methods. *Geoderma* **2017**, *298*, 67–77. [CrossRef]
43. Caubet, M.; Román Dobarco, M.; Arrouays, D.; Minasny, B.; Saby, N.P.A. Merging country, continental and global predictions of soil texture. Lessons from ensemble modelling in France. *Geoderma* **2019**, *337*, 99–110. [CrossRef]
44. Castrignanò, A.; Buttafuoco, G. Geostatistical Stochastic Simulation of Soil Water Content in a Forested Area of South Italy. *Biosyst. Eng.* **2004**, *87*, 257–266. [CrossRef]
45. Wu, J.; Vincent, B.; Yang, J.; Bouarfa, S.; Vidal, A. Remote Sensing Monitoring of Changes in Soil Salinity: A Case Study in Inner Mongolia, China. *Sensors* **2008**, *8*, 7035–7049. [CrossRef] [PubMed]
46. Khan, N.M.; Rastoskuev, V.V.; Sato, Y.; Shiozawa, S. Assessment of hydrosaline land degradation by using a simple approach of remote sensing indicators. *Agric. Water Manag.* **2005**, *77*, 96–109. [CrossRef]
47. Douaoui, A.E.K.; Nicolas, H.; Walter, C. Detecting salinity hazards within a semiarid context by means of combining soil and remote-sensing data. *Geoderma* **2006**, *134*, 217–230. [CrossRef]
48. Allbed, A.; Kumar, L.; Aldakheel, Y.Y. Assessing soil salinity using soil salinity and vegetation indices derived from IKONOS high-spatial resolution imageries: Applications in a date palm dominated region. *Geoderma* **2014**, *230–231*, 1–8. [CrossRef]
49. Taghizadeh-Mehrjardi, R.; Minasny, B.; Sarmadian, F.; Malone, B.P. digital mapping of soil salinity in Ardakan region, central Iran. *Geoderma* **2014**, *213*, 15–28. [CrossRef]
50. Yang, Y.; Dou, Y.; Liu, D.; An, S. Spatial pattern and heterogeneity of soil moisture along a transect in a small catchment on the Loess Plateau. *J. Hydrol.* **2017**, *550*, 466–477. [CrossRef]
51. Zhao, Y.; Feng, Q.; Yang, H. Soil salinity distribution and its relationship with soil particle size in the lower reaches of Heihe River, Northwestern China. *Environ. Earth Sci.* **2016**, *75*, 810. [CrossRef]
52. Wang, Z.; Zhang, F.; Zhang, X.; Chan, N.W.; Kung, H.; Ariken, M.; Zhou, X.; Wang, Y. Regional suitability prediction of soil salinization based on remote-sensing derivatives and optimal spectral index. *Sci. Total Environ.* **2021**, *775*, 145807. [CrossRef] [PubMed]
53. Liao, K.; Lai, X.; Zhou, Z.; Zhu, Q. Combining the ensemble mean and bias correction approaches to reduce the uncertainty in hillslope-scale soil moisture simulation. *Agric. Water Manag.* **2017**, *191*, 29–36. [CrossRef]
54. Yao, Y.; Liang, S.; Li, X.; Chen, J.; Liu, S.; Jia, K.; Zhang, X.; Xiao, Z.; Fisher, J.; Mu, Q.; et al. Improving global terrestrial evapotranspiration estimation using support vector machine by integrating three process-based algorithms. *Agric. For. Meteorol.* **2017**, *242*, 55–74. [CrossRef]
55. Zhang, R.; Xu, X.; Guo, J.; Sheng, Z. Multi-model ensemble approaches for simulation of evapotranspiration of karst agroforestry ecosystems. *Agric. Water Manag.* **2022**, *273*, 107869. [CrossRef]

56. Zhao, K.; Wulder, M.; Hu, T.; Bright, R.M.; Brown, M.E. Detecting change-point, trend, and seasonality in satellite time series data to track abrupt changes and nonlinear dynamics: A Bayesian ensemble algorithm. *Remote Sens. Environ.* **2019**, *232*, 111181. [CrossRef]
57. Chen, W.; Pourghasemi, H.R.; Kornejady, A.; Zhang, N. Landslide spatial modeling: Introducing new ensembles of ANN, MaxEnt, and SVM machine learning techniques. *Geoderma* **2017**, *305*, 314–327. [CrossRef]
58. Zhang, Y.; Shen, F.; Sun, X.; Tan, K. Marine big data-driven ensemble learning for estimating global phytoplankton group composition over two decades (1997–2020). *Remote Sens. Environ.* **2023**, *294*, 113596. [CrossRef]
59. Kuncheva, L.I.; Whitaker, C.J. Measures of Diversity in Classifier Ensembles and Their Relationship with the Ensemble Accuracy. *Mach. Learn.* **2003**, *51*, 181–207. [CrossRef]
60. Akay, H. Spatial modeling of snow avalanche susceptibility using hybrid and ensemble machine learning techniques. *Catena* **2021**, *206*, 105524. [CrossRef]
61. Sylvain, J.; Anctil, F.; Thiffault, E. Using bias correction and ensemble modelling for predictive mapping and related uncertainty: A case study in digital soil mapping. *Geoderma* **2021**, *403*, 115153. [CrossRef]

Disclaimer/Publisher's Note: The statements, opinions and data contained in all publications are solely those of the individual author(s) and contributor(s) and not of MDPI and/or the editor(s). MDPI and/or the editor(s) disclaim responsibility for any injury to people or property resulting from any ideas, methods, instructions or products referred to in the content.

remote sensing

MDPI

Article

Machine-Learning-Assisted Characterization of Regional Heat Islands with a Spatial Extent Larger than the Urban Size

Yin Du [1], Zhiqing Xie [2,3,*], Lingling Zhang [2], Ning Wang [2], Min Wang [1] and Jingwen Hu [1]

[1] Key Laboratory of Meteorological Disaster of Ministry of Education (KLME)/Collaborative Innovation Center on Forecast and Evaluation of Meteorological Disasters (CIC-FEMD)/Joint International Research Laboratory of Climate and Environment Change (ILCEC), Nanjing University of Information Science & Technology, Nanjing 210044, China; ydu@nuist.edu.cn (Y.D.); 202212010018@nuist.edu.cn (M.W.); 202212010132@nuist.edu.cn (J.H.)
[2] Jiangsu Climate Center, Nanjing 210019, China; bellbellzhang@163.com (L.Z.); ningwang0309@hotmail.com (N.W.)
[3] Jiangsu Institute of Meteorological Science, Nanjing 210019, China
* Correspondence: xiezhiqing9896@163.com

Abstract: Surface urban heat islands (SUHIs) can extend beyond the urban boundaries and greatly affect the thermal environment of continuous regions over an agglomeration. Traditional urban-rural dichotomy depending on the built-up and non-urban lands is challenged in characterizing regional SUHIs, such as how to accurately quantify the intensity, spatial pattern, and scales of SUHIs, which are vulnerable to SUHIs, and what the optimal scale for conducting measures to mitigate the SUHIs. We propose a machine-learning-assisted solution to address these problems based on the thermal similarity in the Yangtze River Delta of China. We first identified the regional-level SUHI zone of approximately 42,328 km^2 and 38,884 km^2 and the areas that have no SUHI effects from the annual cycle of land surface temperatures (LSTs) retrieved from Terra and Aqua satellites. Defining SUHI as an anomaly on background condition, random forest (RF) models were further adopted to fit the LSTs in the areas without the SUHI effects and estimate the LST background and SUHI intensity at each grid point in the SUHI zone. The RF models performed well in fitting rural LSTs with a simulation error of approximately 0.31 °C/0.44 °C for Terra/Aqua satellite data and showed a good generalization ability in estimating the urban LST background. The RF-estimated daytime Aqua/SUHI intensity peaked at approximately 6.20 °C in August, and the Terra/SUHI intensity had two peaks of approximately 3.18 and 3.81 °C in May and August, with summertime RF-estimated SUHIs being more reliable than other SUHI types owing to the smaller simulation error of less than 1.0 °C in July–September. This machine-learning-assisted solution identified an optimal SUHI scale of 30,636 km^2 and a zone of approximately 23,631 km^2 that is vulnerable to SUHIs, and it provided the SUHI intensity and statistical reliability for each grid point identified as being part of the SUHI. Urban planners and decision-makers can focus on the statistically reliable RF-estimated summertime intensities in SUHI zones that have an LST annual cycle similar to that of large cities in developing effective strategies for mitigating adverse SUHI effects. In addition, the selection of large cities might strongly affect the accuracy of identifying the SUHI zone, which is defined as the areas that have an LST annual cycle similar to large cities. Water bodies might reduce the RF performance in estimating the LST background over urban agglomerations.

Keywords: surface urban heat islands; urban agglomerations; random forest; land surface temperature; MODIS

1. Introduction

Urban areas are usually warmer than their surrounding rural regions [1]. This phenomenon, known as the urban heat island (UHI), has been expanding to a regional level in many urban agglomerations experiencing rapid urbanization, new industrialization,

and fast transportation in recent years [2–4]. Regional UHIs greatly affect the thermal environment of continuous regions and threaten regional-level environmental sustainability, biodiversity, and resource and energy consumption, and they are thus increasingly drawing attention from residents, urban climate researchers, and policymakers [5,6]. Accurate UHI information on urban agglomerations, including the intensity, spatial pattern, and scale of UHIs and their spatiotemporal variations, is of practical importance to urban planning and environmental management in terms of shaping rational urban clusters, mitigating heat-related health risks and improving human comfort [4,7].

UHIs are defined differently depending on the layers in which the highest temperatures are recorded, namely surface UHIs (SUHIs), canopy-layer UHIs (CUHIs), and boundary-layer UHIs (BLUHIs) [1]. The three types of UHIs have strong differences in intensity, extent, spatial pattern, and diurnal and seasonal variations within a single city. It is difficult for policymakers in urban design to select a UHI type as a reference in developing effective strategies to mitigate the adverse effects of UHIs [7]. CUHIs and BLUHIs, with the intensity notably lower than that of SUHIs and peaking in winter [8–11], can be markedly enhanced by upstream urbanization and have a nonlocal distribution due to atmospheric thermal advection and local wind circulation [12,13]. Being the main heating source of CUHIs and BLUHIs, SUHIs explain 70–87% of the land surface temperature (LST) variation in urban areas, with a spatial pattern similar to built-up land and a high sensitivity to land cover and human activities [4,14,15]. The SUHI intensity peaks in the summer daytime owing to the seasonal and diurnal variations of solar radiation and notably exacerbates summer heatwave stress on human health in urban areas [16]. Hence, it is more important that urban planners and decision-makers have accurate information on summertime SUHIs than on other UHI types in establishing effective strategies for coping with urban heat waves and heat-related health risks.

Against a background of rapid urbanization and global warming, key decision-makers and urban planners are becoming increasingly concerned with mitigating regional-level SUHIs over urban agglomerations from the perspective of climatology in actively incorporating UHI-related considerations [7]. However, it is a great challenge to accurately characterize the intensity, spatial pattern, and scale of SUHIs in urban agglomerations, mainly because the daytime SUHIs extend beyond the urban boundaries, with the extent being approximately 2.3–3.9, 1–3, 1.3–2.5, and 1.5–2.0 times the urban size over many large cities and metropolitan areas in the world [4,17–19]. The SUHI extent also has notable diurnal, seasonal, and inter-city differences [9,10], which further increase the difficulty of characterizing the SUHIs in urban agglomerations [20–22]. An ambiguous classification of the urban areas and surrounding rural areas could be responsible for disagreements on the spatial extent and intensity of SUHIs [21]. Fine-resolution mesoscale models and regional climate models have been developed to investigate the effects of urbanization on the thermal and physical properties of the land surface at various spatiotemporal scales [19,23–26], but complex data collection, data pre-and post-processing, and model validation make it difficult to simulate complex urbanization processes and human activities over urban agglomerations at a high spatial resolution [27,28]. Recent advances in machine-learning approaches have made it possible to extract valuable SUHI information from a variety of widely available high-spatial-resolution satellite data [21]; e.g., the two-dimensional Gaussian, decision regression tree, random forest (RF), and support vector machine models are becoming useful tools that support heat-related active policy measures in urban planning [29–34]. Integrating machine-learning and remote-sensing methods has improved the insights into the relationship between urbanization, climatic, geographical, and biophysical conditions, as well as the SUHIs [35,36]. A myriad of factors affecting micro-scale SUHIs, including the albedo, roughness, geographical location, topography, urban geometry, land cover, thermal capacity and conductivity, and anthropogenic heat have been investigated using machine-learning methods and high-resolution satellite products for the Yangtze River Delta, Pearl River Delta, and Jing-Jin-Ji urban agglomerations of China and European and American cities [37–42]. A convolutional neural network model was used to predict

the impact of urban structure patterns on the thermal environment and achieved a high accuracy rate of 81.97% in identifying low and medium thermal risks [43]. RF regression shows high accuracy in predicting the LSTs and identifying the main drivers of SUHI [44]. The nonlinear relationships between two-dimensional and three-dimensional factors and the LST were investigated by applying the RF method over the Olympic Area of Beijing and identified four dominant factors affecting the land thermal environments [45], among which the vegetation and buildings were the domain factors influencing daytime and nighttime LST on a block scale, and the urban greenery coverage is the most important for urban heat mitigation [46,47].

Urbanization-induced impacts on global SUHI trends have shown strong divergent features since the 1980s [48]. Under the 1.5 °C global warming limit, addressing UHI-related challenges is urgent not only for environmental, ecosystem, social, and health consequences but also for economic impacts relevant to labor, capital, and goods or services due to the UHIs being a common issue for many metropolitans in the world [49]. Accurate UHI information on urban agglomerations is of practical importance to future urban planning and environmental management. However, the extent of SUHIs being larger than the urban size and varying with the background climate state and land cover means that urban and built-up land cannot accurately represent the spatial scale and distribution of SUHIs. As a phenomenon of any area being warmer than its surroundings, heat islands also can develop in a non-urban area, such as a wetland, water body at nighttime, or seasonally bare soil lands. These non-urban heat islands do not represent a risk to humans or the environment but strongly increase the difficulty of identifying the SUHI spatial pattern, scale, and intensity in an urban agglomeration. How do you quantify the intensity, spatial pattern, and scale of SUHIs, where are they vulnerable to the SUHIs, and what is the optimal scale for conducting measures to mitigate the SUHIs over an urban agglomeration? Using the Yangtze River Delta urban agglomeration (YRDUA) of China as an example, we propose a machine-learning-assisted solution to address these problems by separately characterizing the SUHI spatial features from the thermal similarity of land cover types and the SUHI intensity according to the definition of urban heat islands as an anomaly on background condition. The new solution can reasonably estimate the SUHI extent being larger than the urban size and the SUHI intensity at each grid point with statistical reliability and has great potential for rapidly developing urban agglomerations in the field of urban planning and design.

2. Materials and Methods

2.1. Data Sources and Preprocessing

A daily 1 km all-weather LST dataset for 2000–2021 retrieved from the Moderate Resolution Imaging Spectroradiometer (MODIS) sensors on Terra and Aqua satellites was used to quantify the SUHIs in the YRDUA region [50]. A 500 m-resolution land cover dataset for 2020 from Terra and Aqua satellites (MCD12Q1) was used to extract the land cover types of croplands, forests, and large cities [51]. A global 8-day composite fractional vegetation coverage (FVC) dataset generated from a suite of the global land surface satellite products (GLASS) in 2000–2020 [52], a 30 m-resolution satellite-retrieved human settlement dataset for 1978–2017 [53], a 30 m-resolution Landsat impervious surface dataset at a 5-year interval in 1985–2020 [54], and a suite of global 1 km topographic variables for environmental and biodiversity modeling [55] were used to input features into RF models to estimate the SUHI intensity based on the 8-day composite MODIS/LST in the YRDUA region. All these data are spatially and temporally continuous with no gaps and missing values, and they are of great use in regional-level SUHIs over urban agglomerations from the perspective of climatology. The global 1 km topographic products provide fully standardized topographic variables to quantify the impacts of complex terrain on the regional-level SUHIs in the YRDUA region.

Determined by the data source of MODIS/LSTs, GLASS products, and 1 km topographic variables, we investigated the regional-level SUHIs in the YRDUA region at a

spatial resolution of 1 km × 1 km with an 8-day composite. The data were preprocessed with spatiotemporal matching as the following procedure. First, a simple 8-day averaging method was conducted for the daily 1 km all-weather MODIS/LST dataset to fit the 8-day composite GLASS products in 2000–2020. Second, the 30 m-resolution Landsat impervious surface and satellite-retrieved human settlement data were merged by their union at each grid point in the period from 2015–2020 and upscaled to 1 km to generate more continuous imperviousness density data in space by summarizing the merged impervious surface area to the 1 km grid. Finally, all these data without gaps and missing values were reprojected to the latitude–longitude grid at 30 arc seconds (about 1 km × 1 km spatial resolution) to generate all variables for training the RF models.

2.2. Definition of the SUHI Intensity on Each Grid Point in Urban Agglomerations

Here, local LST anomaly is calculated as the difference between the actual and background LSTs at each grid point:

$$\Delta T_i = T_i - TB_i, \quad (1)$$

When defining SUHI as the additional anomaly on background condition [16], ΔT_i, T_i, and TB_i are the SUHI intensity and actual and background LSTs at grid point i in the areas that have an SUHI phenomenon. Actual LSTs in the areas that have no SUHIs are well-associated with climate, geographical, topographical, and biophysical conditions, all of which have been well-retrieved from high-quality satellite datasets without gaps and missing values [50,56]. When the LSTs in the areas that have no SUHIs are selected as the background condition and fitted by machine-learning algorithms with geographical and biophysical parameters, ΔT_i is the background simulation error at grid point i. Hence, it is critical for quantifying the SUHI intensity on each grid point in urban areas to identify the non-SUHI areas, which are mainly attributed to the LSTs in non-SUHI areas being used to train the machine-learning models that are used to estimate the LST background in areas that have an SUHI effect.

2.3. Identifying the SUHI and Non-SUHI Zones in Urban Agglomerations

Land cover types mainly consist of cropland, forests, water bodies, and urban and built-up land in the YRDUA region at [117.5–123°E, 28.5–33.7°N] (Figure 1a), with the total area of urban and built-up land of approximately 31,663 km^2 in 2020. Spatially continuous large cities with a built-up area exceeding 100 km^2 along the Yangtze River and Hangzhou Bay have been identified as representative areas that have notable SUHI effects [4]. These cities are located along the Yangtze River and in Hangzhou Bay and are surrounded by cropland and many medium-size (<100 km^2) cities (Figure 1a). Applying the urban population criteria of being more than 1 million, 1 million to 500,000, and below 500,000 from the China Urban Construction Statistical Yearbook [57,58], 15 large, nine medium, and 36 small cities are obtained in the YRD region, with an average built-up area of approximately 414.2, 113.6, and 49.4 km^2. Small towns have an average built-up area of approximately 4.6 km^2 according to the China Urban–Rural Construction Statistical Yearbook [57,58]. Therefore, large, medium, and small cities and villages are identified from the MCD12Q1 urban and built-up lands by using continuously built-up areas that are ≥100 km^2, 50–100 km^2, 5–50 km^2, and <5 km^2.

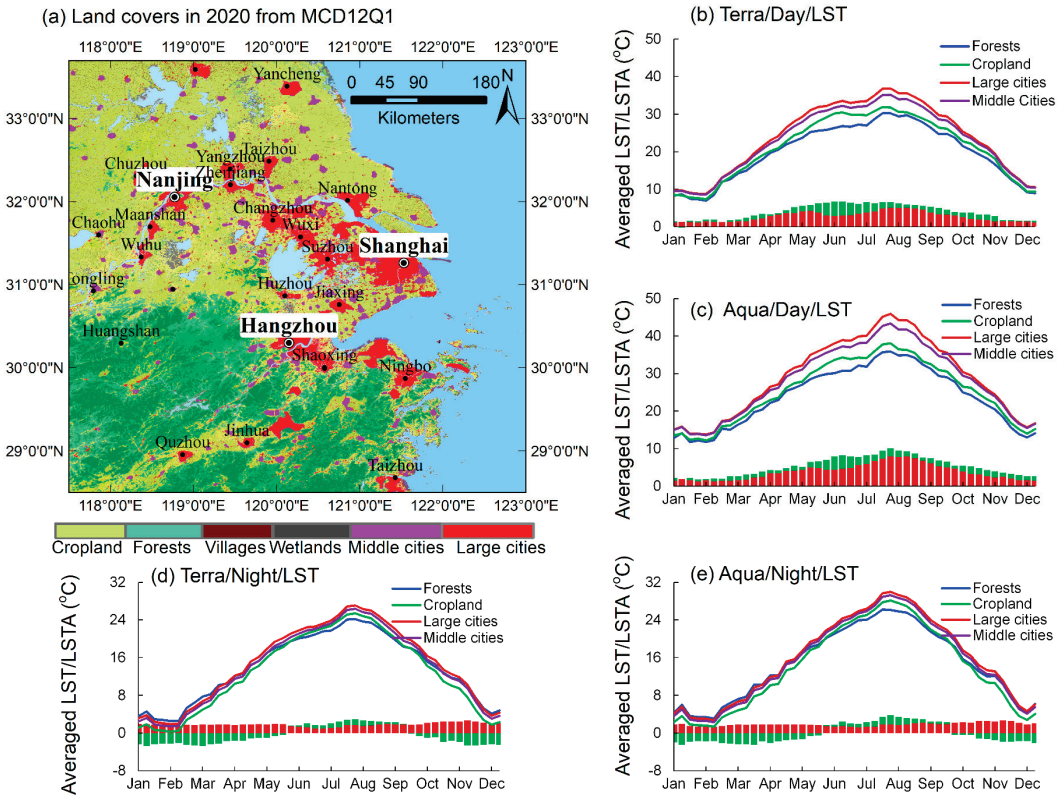

Figure 1. The MCD12Q1 land cover types in 2020 (**a**) and long-term mean land surface temperature (LST) annual cycles (lines) during the day and at night for croplands, forests, and medium and large cities, and LST differences between large cities and cropland (red bars), and between cropland and forests (green bars) for Terra (**b**,**d**) and Aqua data (**c**,**e**) between 2015–2020.

Here, the SUHI zones were defined as areas that have an LST annual cycle similar to that of large cities. Since the Chinese government implemented a development plan to restrict urban expansion in the YRDUA region in 2016, large- and medium-sized cities have maintained a stable urban and built-up area of approximately 7787.6–7818.4 km^2 according to the China Urban Construction Statistical Yearbook for 2015–2020 [57,58]. We thus investigated the land thermal features based on differences in the LST annual cycle between medium-sized cities (50–100 km^2), large cities, cropland, and forests for the period 2015–2020. Statistically significant differences in the daytime LST annual cycle were found among large cities, medium cities, cropland, and forests in an *F*-test variance analysis at a 0.01 significance level (lines in Figure 1b,c). There were large LST differences of approximately 4–8 °C between April–September and small differences of less than 2 °C between October–March (red bars in Figure 1b,c). Medium and large cities, cropland, and forests had similar nighttime LST annual cycles, with LST differences of approximately −3 to 3 °C. The daytime LST annual cycle was thus suitable for classifying the land surface thermal zones owing to its statistically significant differences among large cities, medium cities, cropland, and forests.

A spatial similarity regression model (S_i) proposed by Xie et al. in 2022 [4] was used to identify areas that have LST annual cycles similar to those of large cities, cropland, and forests. The spatial similarity of the LST annual cycle (S_i) to the LST annual cycle of the large cities, cropland, or forests at a grid point was quantified using the explained variance (R^2) and the root mean square error ($RMSE_i$), defined as

$$S_i = \begin{cases} \left(1 - R_i^2 \sin(R\pi/2)\right) RMSE_i \ (R_i < 0) \\ \left(1 - 0.5 R_{mode} R_i^2 \sin(R_i\pi/2)\right) RMSE_i \ (R_i \geq 0) \end{cases}, \quad (2)$$

$$RMSE_i = \sqrt{\sum_{j=1}^{N}\left((T_{ij} - \overline{T_i}) - \left(T_{ij} - \overline{T_r}\right)\right)^2 / N}, \quad (3)$$

$$R_i = \frac{\sum_{j=1}^{N}(T_{ij} - \overline{T_i})(T_{rj} - \overline{T_r})}{\sqrt{\sum_{j=1}^{N}(T_{ij} - \overline{T_i})^2 \sum_{j}^{N}(T_{rj} - \overline{T_r})^2}}, \quad (4)$$

where R_i is the correlation coefficient, R_{mode} is the mode of R_i frequencies, T_{rj} is the regionally averaged LST in large cities, cropland, or forests, $RMSE_i$ is the root mean square error, $\overline{T_r}$ is the average value of T_{rj}, T_{ij} and $\overline{T_i}$ denote the LST series at grid point i and the average value, N is the series length, and $\left(1 - R_i^2 \sin(R\pi/2)\right)$ and $\left(1 - 0.5R_{mode}R_i^2 \sin(R_i\pi/2)\right)$ are adjustment factors adopted to avoid the excessive reduction of $RMSE_i$. S_i is the spatial similarity of the LST annual cycle to the LST annual cycle of large cities, cropland, or forests at the grid point i, with a statistical confidence level from the chi-square variable $\chi_i^2 = \sum_{j=1}^{N}(T_{ij} - \overline{T_r} + \overline{T_i})^2 / \frac{1}{N}\sum_{j=1}^{N}(T_{rj} - \overline{T_r})^2$. Applying a natural-break algorithm, all S_i values were classified into five types that were two zones with strong positive/negative values R~±1.0, two transition zones with positive/negative correlation, and an uncorrelated zone (R~0) by using a natural-break algorithm.

2.4. Estimation of the SUHI Intensity on Each Grid Point in Urban Agglomerations

RF regression is a nonlinear machine-learning technique based on decision trees with good generalization ability, and increasing the critical hyper-parameter ntree can improve the RF model performance and stability [59]. Non-urban LSTs in the background, cropland, and forest zones well-related to the geographical factors, the topographic variables, and biophysical and urbanization parameters, were used to train the RF models adopting the input features listed in Table 1.

Table 1. Influencing factors of the LST used in random forest models.

Categories of Variables	Variables	Meaning of Variables
Climate factors	LON	Longitude in grid
	LAT	Latitude in grid
Geographical factor	ELE	Mean value of elevation in grid
Topographic variables	RUG	Mean value of roughness in grid
	SLP	Mean value of slope in grid
	TRI	Mean value of terrain ruggedness index in grid
	VRM	Mean value of vector ruggedness measure in grid
Biophysical parameter	FVC	Fractional vegetation cover in grid
Urbanization parameter	ISA	Percentage of impervious surface area in grid

Theoretically, there is no need for any additional accuracy estimation procedures like cross-validation or a separate test set to get an estimate of the training error for RF regression owing to the out-of-bag error being estimated internally during the training. Hence, three critical hyper-parameters used in the RF models, the tree depth max_depth, the minimum samples required at a leaf node min_sample_count, and the maximum tree number ntree, were determined by the out-of-bag error at the respective ranges of 5–25, 0.5%–3%, and 5–300 with the increments of 1, 0.1%, and 5 during the training. As a result, all RF models showed a small out-of-bag error of less than 1.0 °C and 1.4 °C at the critical hyper-parameters min_sample_count = 1%, max_depth = 10 and ntree = 200 for the 8-day composite long-term Terra and Aqua LSTs in the period between 2015–2020. The min_sample_count = 1%, max_depth = 10, and ntree = 200 thus were selected as the optimal values. Considering the urban LST background value at each grid point in the SUHI zone as a missing value, these RF models trained by the non-urban LSTs were further

used to estimate the urban LST background owing to the advantage of RF regression in estimating a large proportion of missing data with a good accuracy.

The SUHI intensity at each grid point was estimated by adopting the following procedure. (1) Applying the spatial similarity regression model proposed by Xie et al. (2022) [4], the SUHI zone and its spatial pattern and scale were first identified from the MODIS/LST annual cycle for the YRDUA region between 2015–2020. (2) Strong SUHI zones, vulnerable SUHI zones, background zones, cropland zones, and forest zones were then identified from long-term LST annual cycles similar to those of large cities, cropland, and forests. The LST samples in the background, cropland, and forest zones were used to train RF models. (3) A series of RF models with the hyper-parameters min_sample_count = 1%, max_depth = 10, and ntree = 200 were obtained from each long-term 8-day composite *FVC* field and non-urban LST field between 2015–2020, and the LST-simulating error was calculated at each grid point. These RF models were further used to estimate the vegetation background FVC_{bkg} with ISA = 0 and the temperature background LST_{bkg} with ISA = 0 and FVC = FVC_{bkg} at each grid point over strong SUHI zones and the vulnerable SUHI zones. (4) The SUHI intensity was finally obtained from the difference between actual and background LSTs at each grid point over urban agglomerations. The framework is shown in Figure 2.

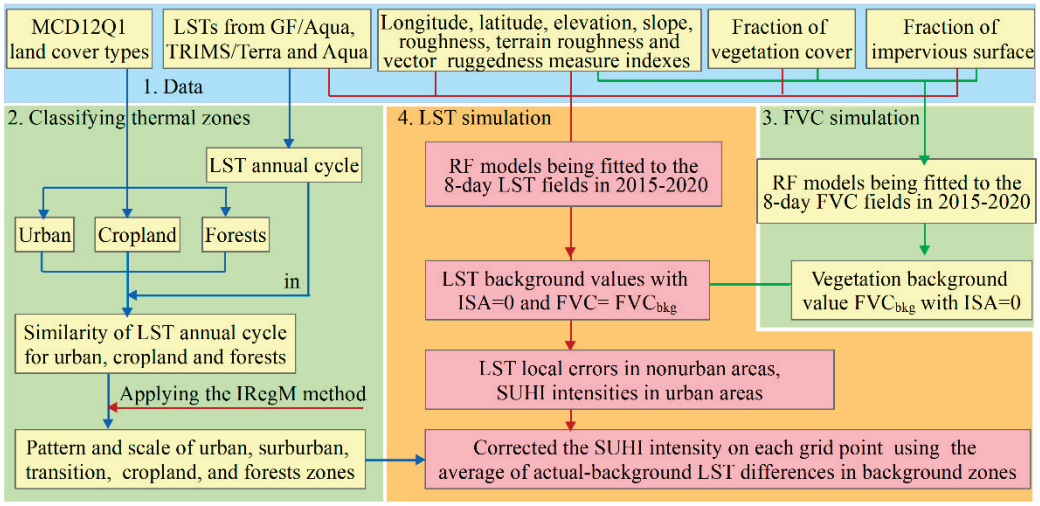

Figure 2. Framework for characterizing the SUHI spatial pattern and scale and intensity in urban agglomerations.

3. Results

Applying the proposed solution described in Section 2, the strong SUHI zone and the zones being vulnerable to SUHIs were identified out on the similarity of long-term LST annual cycles and successfully excluded the heat islands unrelated to urbanization in the YRDUA region. We also obtained the SUHI intensity, spatial pattern, and scale for each case of the long-term 8-day composite MODIS/LST data between 2015–2020, which were further used to investigate the seasonal variations of the regional SUHIs related to vegetation changes and urbanization. All these are conducive to urban planning and environmental management in terms of shaping rational urban clusters and improving human comfort.

3.1. The SUHI Spatial Pattern and Scale and the Land Surface Thermal Types

Terra/SUHI and Aqua/SUHI zones were obtained from the spatial similarity of LST annual cycles similar to those in large cities with a chi-square test at 0.05 confidence level, (Figure 3a,b), with the spatial extents of approximately 42,328 km^2 and 38,884 km^2. Their intersections represented a stable daytime SUHI phenomenon over the middle and large cities (Figure 3c) and were identified as the optimal SUHI zone, with statistical reliability

belonging to the SUHIs at each grid point and a spatial scale of approximately 30,636 km^2. The thermal zones that have a long-term LST annual cycle similar to that of cropland (forests) were identified from Terra and Aqua satellites, and their union was identified as the cropland (forests) zones (Figure 3d,e). The SUHI zone had notable overlapping areas with cropland and forest zones (Figure 3c–e), which were the mixed areas of built-up land and natural and agricultural vegetation land according to the MCD12Q1 data in 2020. These overlapping areas had an LST annual cycle simultaneously similar to that of large cities, cropland, and forests and were identified as the SUHI vulnerable zone related to urbanization, with a spatial extent of approximately 23,631 km^2. A strong SUHI zone was then defined as the difference between the SUHI zone and the SUHI vulnerable zone and had a spatial extent of approximately 7005 km^2 compatible with the urban and built-up area of large- and medium-sized cities. Intersections between the cropland and forest zones and the areas uncorrelated with large cities were further defined as background zones without notable UHI effects. Ultimately, the YRDUA region was divided into a strong SUHI zone, vulnerable SUHI zone, background zone, cropland zone, and forest zone (Figure 3f). In summary, the SUHI effects steadily occurred in the strong SUHI zone, they could deteriorate with the urbanization in the vulnerable zone, and they did not occur in the background, cropland, and forest zones. According to the SUHI zone and the urban and built-up land in 2020 MCD12Q1 data, approximately 24,784 km^2 of urban and built-up land and 14,098 km^2 of non-urban land around large cities showed notable SUHI phenomenon and approximately 6879 km^2 of urban and built-up land in small cities and villages that have no SUHI phenomenon. Hence, urban and built-up lands cannot accurately represent the spatial scale and pattern of SUHIs.

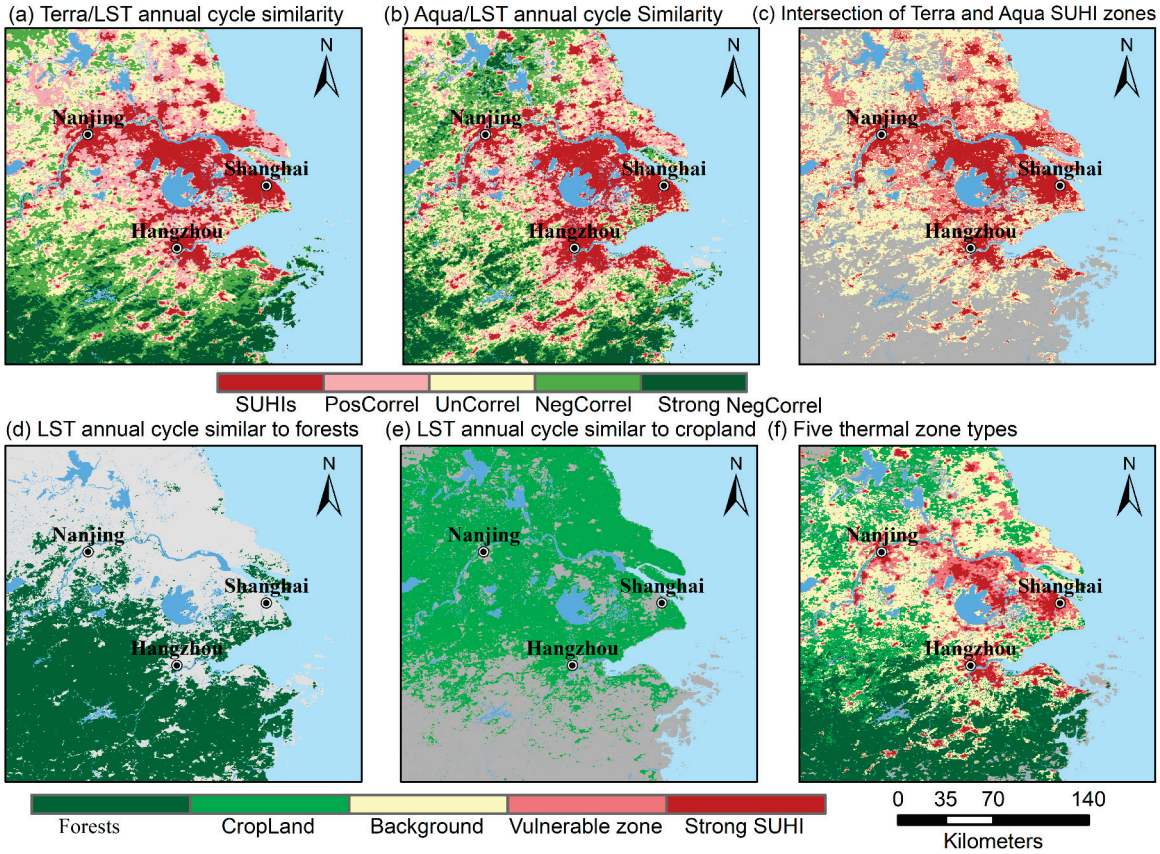

Figure 3. Strongly positively correlated (also referred to as SUHI), positively correlated, uncorrelated, negatively correlated, and strongly negatively correlated zones that have the Terra/LST (**a**) and Aqua/LST (**b**) annual cycles similar to those of large cities and the intersections of Terra/SUHI and Aqua/SUHI zones (**c**); areas having the LST annual cycle similar to that of forests (**d**) and the cropland (**e**); and five thermal zone types (**f**).

3.2. Estimation of the FVC and LST Backgrounds and the SUHI Intensity

The nonurban LST is well-associated with climate, geographical, topographical, and biophysical conditions, all of which have been well-retrieved from high-quality satellite datasets without gaps or missing values [50,56]. RF regression models were with geographical, biophysical, and urbanization parameters to fit the nonurban LST in the background, cropland, and forest zones and estimate the urban LST background and SUHI intensity at each grid point in the SUHI zone.

Figure 4 shows an example of estimating the urban FVC and LST backgrounds and quantifying the SUHI intensity on Day 225 of the long-term LST annual cycle between 2015–2020. An RF model was first trained by the FVC samples in the background, cropland, and forest zones with the input features listed in Table 1 at the optimal hyper-parameter ntree = 200 and was used to estimate the vegetation background FVC_{bkg} without the urban effect (ISA = 0) at each grid point in the SUHI zone. In the same way, the LST samples in the background, cropland, and forest zones were used to train another RF model with the input features listed in Table 1 at the optimal hyper-parameter ntree = 200. This RF model was further used to estimate the temperature background LST_{bkg} with ISA = 0 and FVC = FVC_{bkg} at each grid point in the SUHI zone. As shown in the left and middle panels of Figure 4, the actual FVC and LST values and their estimated backgrounds from the geographical factors, topographic variables, and vegetation background had similar spatial patterns and comparable values in the background, cropland, and forest zones. Almost no urban effects on the FVC and LST backgrounds were observed in the urban areas. Large actual background differences in the FVC and LST (right panel in Figure 4) thus represented urban effects and showed a spatial pattern similar to the urban and built-up land (Figure 1a). The SUHIs reached a maximum intensity of approximately 5 °C during the day and approximately 2 °C at night in the urban areas and valleys of the YRDUA region. Small actual background LST differences below 1 °C were due to RF simulation errors in the cropland and forest zones. Therefore, the RF models simulated the FVC and LST values in the non-SUHI zone well and reasonably estimated the FVC and LST backgrounds in the SUHI zone on Day 225 of the long-term LST annual cycle between 2015–2020.

Adopting RF models to fit the nonurban LSTs and estimate the LST background in the SUHI zone for all long-term mean 8-day composite MODIS/LST data between 2015–2020, the results revealed that all RF models performed well in fitting the LSTs in the non-SUHI zone (Figure 5), with the annual MAE value being approximately 0.31 °C for Terra data and 0.44 °C for Aqua data. There were strong seasonal variations of the MAE in the background zones for the daytime LST, with peaks of approximately 0.65 and 0.80 °C for Terra/LST and Aqua/LST data between May–June (Figure 5a,b). The RF models performed well in simulating the LST over background, cropland, and forest zones, with the average MAE being approximately 0.14–0.65, 0.18–0.43, and 0.22–0.38 °C for daytime Terra/LST data and 0.28–0.80, 0.30–0.57, and 0.15–0.50 °C for daytime Aqua/LST data. The cropland and forest zones had a stable MAE of approximately 0.29 and 0.40 °C for the daytime LST of Terra and Aqua data. All RF models simulated the nighttime LST well, with a stable MAE of approximately 0.20–0.30 °C (Figure 5c,d).

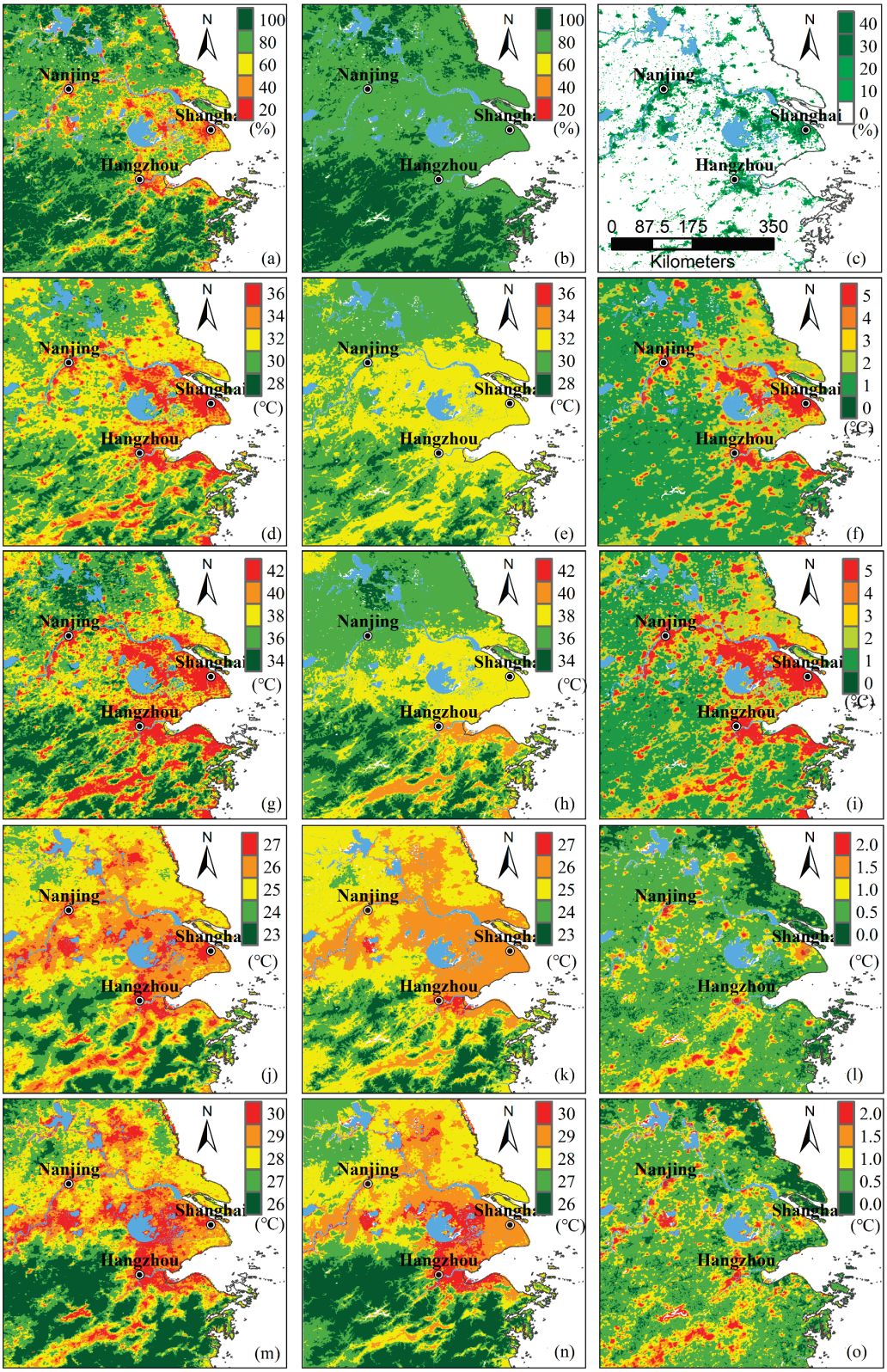

Figure 4. Example of estimating the background (middle panel) and the urban effect (right panel) of the fractional vegetation coverage (**a**–**c**) and land surface temperature (LST, **d**–**o**) on Day 225 of the long-term annual cycle between 2015–2020 using the Random Forest method. Actual value, the RF-estimated background and SUHI intensity for the daytime Terra/LST in (**d**–**f**) and Aqua/LST (**g**–**i**), and the nighttime Terra/LST (**j**–**l**) and Aqua/LST (**m**–**o**).

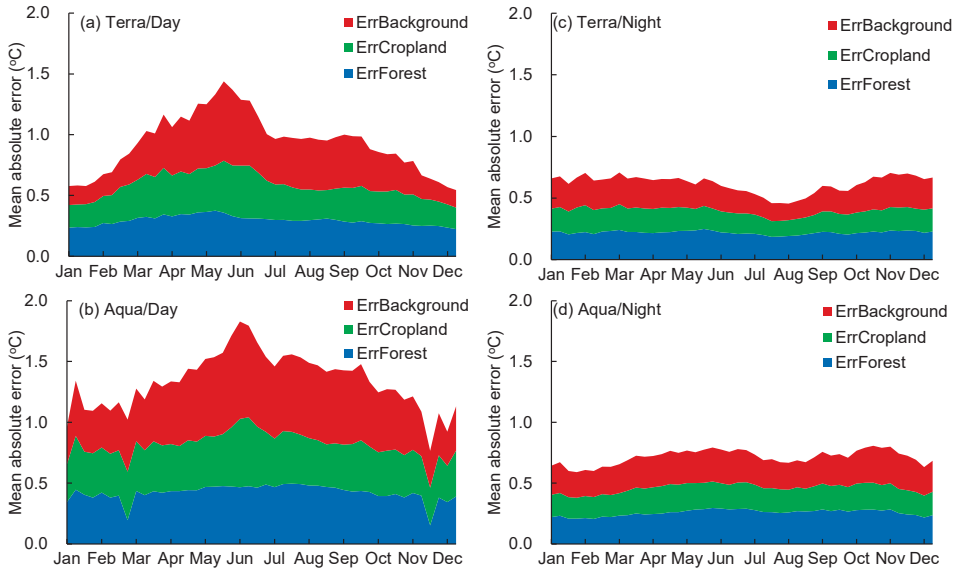

Figure 5. Seasonal variation of mean absolute errors of the random-forest-estimated land surface temperature (LST) in background, cropland, and forest zones for daytime (**a**,**b**) and nighttime (**c**,**d**) LSTs from the Terra (**a**,**c**) and Aqua (**b**,**d**) satellites.

3.3. Seasonal Variations of the SUHI Intensity in the YRDUA Region

As shown in Figure 6, the daytime SUHI intensity in the strong SUHI zone had a strong seasonal variation in the range between 0.93–6.20 °C for Aqua data and 0.29–3.81 °C for Terra data, with an Aqua/SUHI peak in August and two Terra/SUHI peaks of approximately 3.18 and 3.81 °C in May and August (Figure 6a,b). The zone vulnerable to SUHIs had daytime Terra/SUHI and Aqua/SUHI intensities of approximately 0.12–1.85 °C and 0.43–2.74 °C, being half of the intensity in the strong SUHI zone. The strongest daytime SUHI intensity between July–September corresponded to a small RF simulation error of less than 1.0 °C (Figure 5), meaning that the RF models can provide reliable summertime SUHI information for urban planners and decision-makers to design strategies for coping with urban heat waves in the YRDUA region. The cropland zone had a weak cold effect of approximately −1.0 to 0.0 °C for Terra and Aqua data. Nighttime SUHIs had a weak intensity of less than 1.0 °C for Terra and Aqua data (Figure 6c,d).

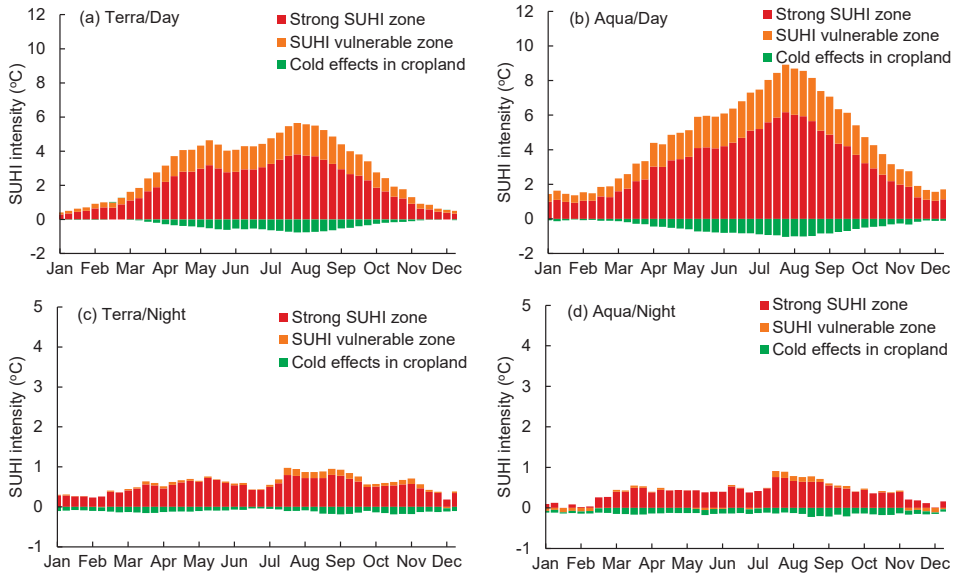

Figure 6. Seasonal variations of the regionally averaged intensity in the strong SUHI, vulnerable SUHI, and cropland zones from the Terra (**a**,**c**) and Aqua (**b**,**d**) data.

3.4. Spatial Distribution and Scale of the RF-Estimated SUHI Intensities

Applying the Jenks–Fisher natural-break algorithm, all daytime SUHIs were divided into weak, medium, strong, and extreme types according to the regionally averaged intensity in the SUHI zones, with the SUHI possessing intensities of 0.18–0.45, 0.46–1.68, and 1.69–2.00 and 2.01–2.59 °C for Terra and 0.60–0.88, 0.89–2.00, 2.01–2.90, and 2.91–4.03 °C for Aqua. The spatial distribution of SUHI intensities of four types is shown in Figure 7a–h. Strong and extreme SUHIs with an intensity of at least 1 °C had spatial extents of approximately 39,528–45,121 km^2 for the Terra satellite and 50,078–56,665 km^2 for the Aqua satellite, which were larger than the spatial extents of 42,328 km^2 and 38,884 km^2 obtained from the Terra and Aqua LST annual cycles (Table 2). After the spring sowing of maize, and early harvesting of rice from late July to August over the southern valleys and along the northern coast, some cropland is transformed to bare soil and contributes to the nonurban heat island phenomenon that enhanced the SUHI spatial extent in the strong and extreme types. With the threshold of SUHI intensity increasing from 1.0 °C to 2.0 °C, strong and extreme SUHIs rapidly shrank to the middle and large cities and had the Terra/SUHI and Aqua/SUHI spatial extents of approximately 27,694 km^2 and 26,841 km^2, which were notably less than those obtained from the Terra and Aqua LST annual cycles. Weak and medium SUHIs had an underestimated extent in the large cities and an overestimated extent in southern YRDUA, with spatial extents of approximately 6612–39,109 km^2 and a spatial pattern different from the strong and extreme types. The SUHIs in winter, spring, autumn, and summer showed spatial patterns and variations similar to weak, medium, strong, and extreme types (Figure 7i–p). Therefore, a small amplitude variation in the intensity ranging from 0.5–3.0 °C corresponded to a highly varying spatial extent of the SUHIs among four seasons and the four types of SUHI. The RF models generated more reliable Terra/SUHI and Aqua/SUHI intensities in the extreme type and summer than in other types and seasons owing to the clear urban–rural cliff, low MAE, and statistical reliability at the 0.05 confidence level (purple shading in Figure 7).

Table 2 lists the spatial extent of SUHIs for the Terra and Aqua satellites at different intensity thresholds. Compared with the SUHI extents of 42,328 km^2 and 38,884 km^2 obtained from the Terra and Aqua LST annual cycles, strong and extreme SUHIs had larger spatial extents of approximately 39,528–45,121 km^2 for the Terra satellite and 50,078–56,665 km^2 for Aqua satellite (Table 2). When the threshold of SUHI intensity varies in the range of 1.0–2.0 °C, strong and extreme SUHIs had smaller spatial extents of approximately 27,694–32,983 km^2 for the Terra satellite and 38,798–45,759 km^2 for the Aqua satellite. Weak and medium SUHIs had a spatial pattern of approximately 6612–39,109 km^2. The SUHIs in winter, spring, autumn, and summer also showed a varying spatial extent at different intensities. In short, it was difficult to identify the reasonable intensity threshold for quantifying the optimal scale and pattern of SUHIs in the YRDUA region. Fortunately, two compatible spatial extents of the SUHI were obtained from the spatial similarity of LST annual cycles similar to those in large cities (Figure 3a,b). Their intersections represented a stable daytime SUHI phenomenon over the middle and large cities and were identified as the optimal SUHI zone of approximately 30,636 km^2 for urban design and urban planning.

3.5. Relative Importance of the RF-Model Input Features

The relative importance values of nine input features were obtained using the RF model regression to fit all actual LSTs in the YRDUA region between 2015–2020. A large importance value means that the feature notably affected the RF model performance in the simulation of the LST spatial distribution and the accuracy of the RF-estimated SUHI intensity. The ISA, FVC, LAT, ELE, and LON features explained approximately 80% of the LST spatial heterogeneity in the YRDUA region (Figure 8a,b). The LAT feature had the largest importance value, exceeding 50%, in the cold season between October–March, and the ISA and FVC features had a large combined importance of approximately 40%–60% and anchored the spatial heterogeneity of the daytime LST in the warm season between April–September. The terrain features of ELE, RUG, SLP, TRI, and VRM, as well as the

LON feature, had a stable combined importance of approximately 40% in the daytime LST. In contrast, the ISA and FVC features had small importance values of approximately 15% for the nighttime LST (Figure 8c,d). The topographic variables of RUG, SLP, TRM, and VRM had a combined importance value of less than 20%. The LAT, LON, and ELE features contributed approximately 68% and 63% of the spatial variation of the nighttime Terra/LST and Aqua/LST. The LAT feature contributed more than 50% of the nighttime LST spatial variation between October–May and approximately 20–50% for the Lon feature between June–September. The ISA feature had the lowest importance value of approximately 1–3% in the nighttime LST spatial variation.

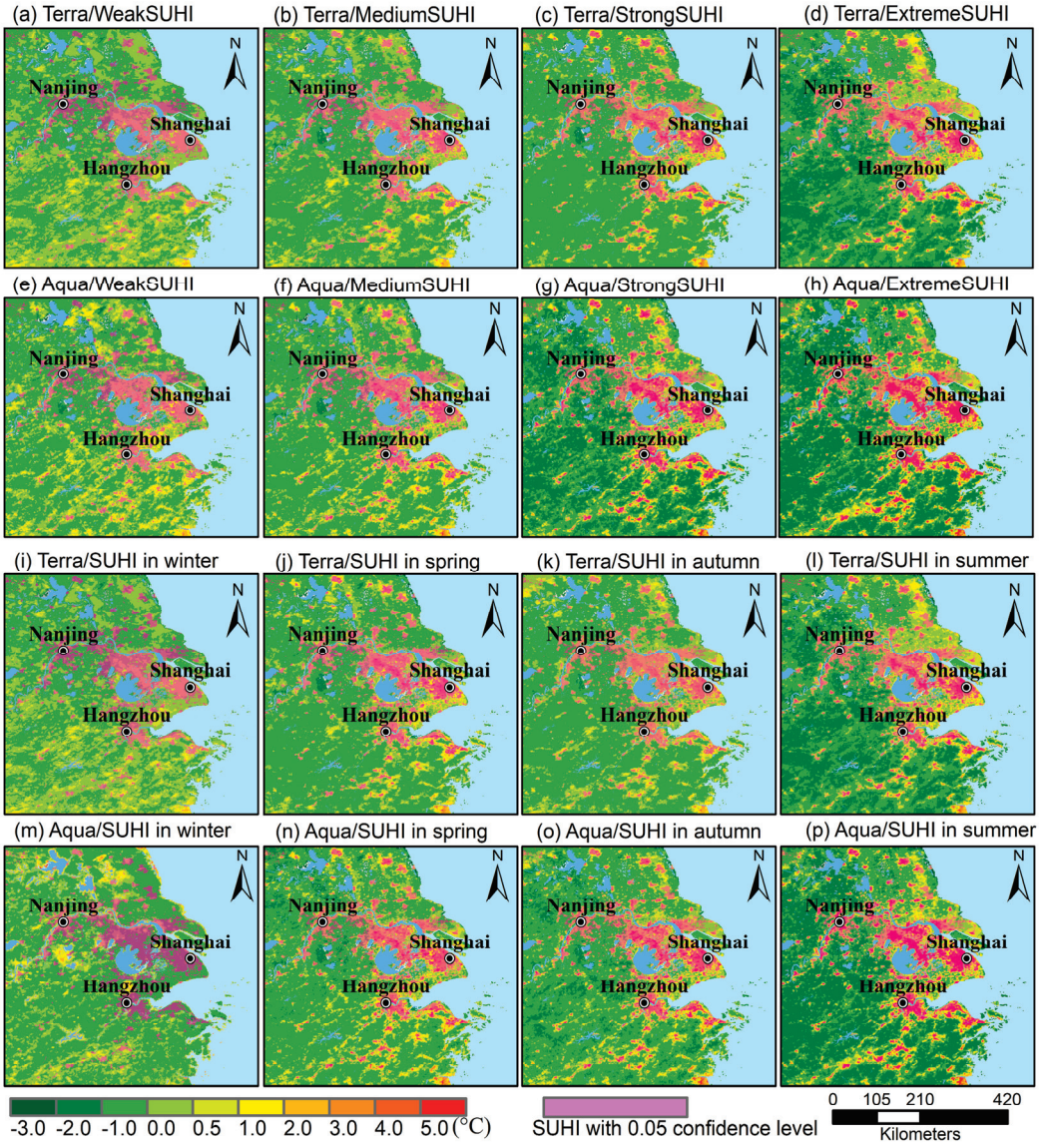

Figure 7. Spatial pattern and intensity at each grid point for the weak, medium, strong, and extreme SUHI types (**a**–**h**) and four seasons (**i**–**p**) in the YRDUA region. Green dots represent the grid point identified as the SUHI with a 0.05 confidence level.

Table 2. The spatial extent of SUHIs at different intensity thresholds.

Satellite	SUHI Extent (km^2)	SUHI Types	Sample Size	The SUHI Intensity (°C)		The Spatial Extent of SUHIsat Different Intensities (km^2)				
				Strong Zones	VulnerableZones	≥1 °C	≥1.5 °C	≥2 °C	≥3 °C	≥4 °C
Terra	42,328	Weak	15	0.6	0.26	6612	1305	242	0	0
		Medium	8	1.63	0.75	25,237	12,990	6489	725	25
		Strong	11	2.73	1.28	39,528	27,694	18,863	7663	1590
		Extreme	12	3.39	1.61	45,121	32,983	24,405	12,435	4322
Aqua	38,884	Weak	11	1.09	0.51	23,830	9000	3347	474	40
		Medium	14	2.38	1.09	39,109	24,992	15,252	4237	895
		Strong	11	4.08	1.83	50,078	38,798	30,591	18,467	9433
		Extreme	10	5.55	2.45	56,665	45,759	38,007	26,841	18,555
Terra	42,328	Spring	11	2.31	1.05	35,671	22,562	14,038	4178	451
		Summer	12	3.31	1.56	44,940	32,601	24,028	12,016	4142
		Autumn	11	1.94	0.93	30,334	17,087	9203	1151	52
		Winter	12	0.51	0.21	2235	1043	176	0	0
Aqua	38,884	Spring	11	2.96	1.32	44,686	31,680	22,079	9067	2372
		Summer	12	5.24	2.32	55,139	44,127	36,407	25,231	16,869
		Autumn	11	3.36	1.54	45,942	34,036	25,431	12,702	4243
		Winter	12	1.11	0.54	24,286	9266	3490	484	39

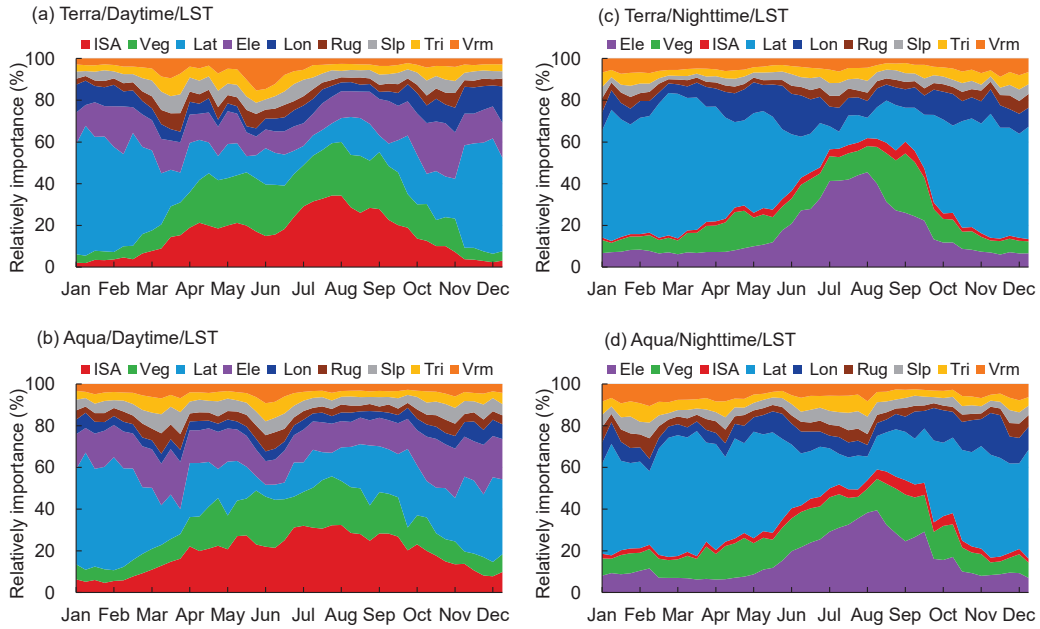

Figure 8. Seasonal variations in the relative importance of nine inputting features for fitting all actual LST values retrieved from the Terra (**a**,**c**) and Aqua (**b**,**d**) satellites at day (**a**,**b**) and night (**c**,**d**) in the YRDUA region.

4. Discussion

4.1. Potential Applications of the Quantitative Regional SUHIs in Urban Planning and Decision-Making

As a phenomenon of any area being warmer than its surroundings, heat islands also can develop in a non-urban area, such as a wetland and water body at nighttime or seasonally bare soil land. These heat islands do not represent a risk to humans or the environment but increase the difficulty of identifying the SUHI spatial pattern and scale and intensity in an urban agglomeration. Anthropogenic heat from vehicles, air-conditioning units, buildings, thermal plants, and other industrial facilities further increase this difficulty [60]. Fortunately, from the perspective of climatology, large cities usually have a daytime LST annual cycle that is statistically significantly different from that of other land cover types at a 0.05 statistical confidence level (Figure 1). Quantifying regional SUHI spatial scales from the spatial similarity of LST annual cycles excluded the heat islands unrelated to the urbanization and captured the SUHI phenomenon extending beyond

the urban boundaries over large cities (Figure 2f). Relative to the varying SUHI spatial extents obtained at different intensity thresholds, the statistically reliable spatial pattern and extent identified from the LST annual cycle are more conducive to urban design and planning. The vulnerable SUHI zones that have an LST annual cycle similar to that of large cities, cropland, and forests can provide important references for urban planners and decision-makers in urban design to restrain the rapid expansion of the SUHI spatial extent over urban agglomerations. The strong SUHI zones that have the strongest SUHI intensity and highly urbanized levels should be paid more attention to developing effective mitigation strategies.

Defining the SUHI intensity as the difference between the actual and background LSTs, the non-urban thermal types without SUHI effects: background, cropland, and forest zones that are identified out from the spatial similarity of LST annual cycles at a 0.05 statistical confidence level. The three non-urban thermal types can be used in selecting suitable non-urban LSTs to train the RF models, in which the non-urban LST samples that have notable SUHI effects have been removed to improve the accuracy of estimating the LST background. RF regression can quantify the contribution of various landscape compositions, and biophysical and climate conditions on the LST. Thus, the non-urban LST with the averaged simulation error of approximately 0.31 °C and 0.44 °C is well-fitting for Terra and Aqua satellites, and it reasonably estimated the urban LST background in the YRDUA region. The reliable RF-estimated SUHI intensity in the areas that have an LST annual cycle similar to that of large cities is conducive for urban planners and decision-makers to develop effective mitigation strategies.

4.2. Advantages and Limitations of the Proposed Solution in Quantifying Regional SUHIs

The SUHI spatial heterogeneity in cities cannot be adequately addressed using the traditional urban–rural dichotomy [61]. Defining the SUHI intensity as the difference between the actual and background LSTs, RF regression has clearly shown advantages in estimating the LST background and SUHI intensity at each grid point. It describes the SUHI phenomena based on empirical knowledge and the statistical relationships between LSTs and the geographical, topographic, biophysical, urbanization parameters, and other factors. Although fine-resolution mesoscale simulating models can estimate the LST background and SUHI intensity at each grid point over urban agglomerations, complex data collection, data pre- and post-processing, and model validation make it difficult to simulate complex urbanization processes and human activities over urban agglomerations at a high spatial resolution [27,28]. The two-dimensional Gaussian surface model has been widely used to estimate the SUHI intensity and footprint owing to its good performance in quantifying SUHIs [9,17,30]. Applying a two-dimensional Gaussian surface model to quantify the SUHIs in a single city includes two key steps: First, identifying the rural LST pixels in a single city according to the land cover data. Second, the two-dimensional Gaussian surface models are used to fit the rural LSTs and estimate the urban LST background and SUHI intensity on each grid point in urban areas. Its performance strongly depends on the accuracy of the land cover data and is influenced by the complex terrain and urban geometry. The proposed machine-learning-assisted solution identifies the SUHI zone and rural LST samples from the statistically significant differences in the LST annual cycle between the large cities and other land cover types and reduces the dependence on the land cover data accuracy. More importantly, this solution provides clear urban–rural cliffs and more reliable RF-estimated intensity on each grid point over an agglomeration with a 0.05 statistical confidence level and avoids some heat islands unrelated to urbanization being wrongly marked as SUHIs. Hence, it has great potential in urban planning and design and in mitigating heat-related health risks in rapidly developing urban agglomerations.

Compared with other machine-learning methods [4,7,32], the RF regression avoids the additional accuracy estimation procedures like cross-validation or a separate test set to obtain an estimate of the training error and can quantify the contribution of each inputting feature on the spatial heterogeneity of SUHIs and LSTs over urban agglomerations. The

ISA, FVC, LAT, ELE, and LON features explained approximately 80% of the LST spatial heterogeneity in the YRDUA region (Figure 8). The LAT feature had the largest importance value, exceeding 50%, between October–March, and the ISA and FVC features had a large, combined importance of approximately 40–60% and anchored the spatial heterogeneity of the daytime LST between April–September. In contrast, the ISA and FVC features had small importance values of approximately 15% for the nighttime LST, and the LAT, LON, and ELE features contributed approximately 68% and 63% of the spatial variation of the nighttime Terra/LST and Aqua/LST. The main SUHI-related factors are solar radiation, evapotranspiration, land cover type, climate, and geographical factors, topographical and biophysical conditions, and rapid urbanization and other human activities. Most of these factors are well-quantified by high-quality and high-accurate datasets without gaps or missing values [56], and a suite of global 1 km topographic variables has been developed to represent the environmental geographical and topographical conditions [55]. We need to select suitable seasonally varying factors to estimate the urban LST background when quantifying the regional SUHI intensities in urban agglomerations according to the data availability of biophysical parameters for day and night. Among the seasonally varying factors, including the FVC index, normalized difference vegetation index, enhanced vegetation index, leaf area index, surface albedo, downward shortwave radiation, soil moisture, and evapotranspiration, the FVC feature was ultimately identified as the optimal biophysical parameter by adopting RF models owing to its data availability and the ease of estimating the FVC urban background from environmental, geographical, and topographical conditions. The ISA and FVC features represented the effects of urbanization and vegetation relating to solar radiation and biophysical conditions in the YRDUA region.

The proposed solution also has some limitations. A selection of the large cities might strongly affect the accuracy of identifying the SUHI zone and rural LST samples in urban agglomerations, mainly because the SUHI zones are defined as the areas having an LST annual cycle similar to that of the large cities. Spatially continuous large cities with a built-up area of $\geq$100 km^2 have been identified as representative areas that have notable SUHI effects in the YRDUA region. The criterion of built-up areas exceeding 100 km^2 for large cities might need further validation before applying it to identify the regional-level SUHIs over other urban agglomerations. Statistically significant differences in the LST annual cycle between large cities and other land cover types are prerequisites for identifying the SUHI zone, but these differences also might not exist in some large cities over arid and desert areas. In addition, the inputting features of RUG, SLP, TRI, VRM, FVC, and ISA for training the RF models usually have a zero value over large lakes, rivers, and large reservoirs, which can lead to the failure of simulating the LSTs over water bodies. In this study, LST samples in large water bodies have been removed from the rural LST samples to generate more accurate RF models in estimating the urban LST background and SUHI intensity (Figures 4 and 7).

5. Conclusions

Since SUHIs have expanded to a regional level and have changed the climate over many urban agglomerations worldwide, mitigating regional SUHIs from the perspective of climatology has become a growing concern for decision-makers and urban planners in terms of actively incorporating UHI-related considerations. Complex urban geometry and human activities, weather and terrain conditions, and some nonurban land being warmer than its surroundings greatly increase the difficulty of characterizing the SUHI intensity, spatial pattern, and scale. Instead of quantifying the complex effects of the urban geometry and human activities on the urban LST, reasonably estimating the urban LST background is a feasible solution for quantifying regional SUHIs in urban agglomerations when defining the SUHI intensity as the difference between the actual and background LSTs. We thus proposed a machine-learning-assisted solution to quantify the SUHI spatial features and intensity at each grid point based on the LST annual cycle in large cities being statistically significantly different from that for other land cover types. This solution

provides clear urban–rural cliffs and more reliable RF-estimated intensities of regional SUHIs based on a chi-square testing statistical variable at a 0.05 statistical confidence level and avoids some heat islands unrelated to urbanization being wrongly marked as SUHIs in urban agglomerations. More importantly, we can focus on quantifying the intensity on each grid point without the consideration of the nonurban heat islands when applying machine-learning methods to characterize the SUHIs and the SUHI spatial features that can be reasonably identified from the LST annual cycle over urban agglomerations.

Using the YRDUA as an example and applying the proposed solution, two compatible SUHI spatial scales of approximately 42,328 and 38,884 km^2 were obtained from long-term Terra and Aqua LST annual cycles between 2015–2020. The SUHI spatial pattern and scales were identified from the spatial similarity of LST annual cycles at a 0.05 confidence level and excluded the heat island effects of non-urban land such as wetlands, water bodies, and seasonally bare soils. We further adopted an RF method to estimate the urban LST background and SUHI intensity at each 1 km $\times$ 1 km grid point using the MODIS-retrieved LST as the response variable and nine satellite-retrieved input variables. By avoiding the quantification of complex effects of the urban morphological factors and human activities on the urban LST, RF models performed well in fitting the nonurban LST values with a low MAE of approximately 0.31 °C for Terra/LST data and 0.44 °C for Aqua/LST data. In addition, the RF models estimated the urban LST background and SUHI intensity in the YRDUA region well. The daytime SUHI intensity in urban zones had a maximum value of approximately 6.20 °C for Aqua/LST data in August and had two peaks of approximately 3.18 and 3.81 °C for Terra/LST data in May and August; these values were approximately 2.2 times the SUHI intensity in suburban zones. The RF models provide more reliable summertime SUHI information in the YRDUA region owing to the low MAE errors of less than 1.0 °C between July–September. This information includes the SUHI spatial pattern and the intensity at each grid point. This feasible solution identifies the strong SUHI and the vulnerable zones and the reliable summertime SUHI intensity on each grid point, all of which are conducive to developing suitable mitigation strategies in different SUHI zones for urban planners and decision-makers. The vulnerable zone, with the SUHI intensity being half of that in the strong SUHI zone, should be paid more attention in urban design to restrain the rapid expansion of the SUHI spatial extent over urban agglomerations.

The reasonable selection of input features in machine-learning methods is critical to quantifying the SUHI intensities in urban agglomerations. SUHI-related factors mainly comprise solar radiation, evapotranspiration, land cover type, climate and geographical factors, topographical and biophysical conditions, and urbanization and human activities. A lack of high-precision and high-resolution climate and weather conditions and human activities could increase the uncertainty in quantifying SUHIs in the YRDUA region. Fortunately, the ISA, VEG, LAT, and ELE explained approximately 80% of the spatial variation of the long-term mean 8-day composite MODIS/LST data between 2015–2020 and anchored the seasonal variation of the daytime SUHIs in the YRDUA region, meaning that it is important to ensure sufficient vegetation to alleviate the SUHIs during rapid urbanization. Our simple solution allows the non-expert to quantify regional SUHIs over urban agglomerations. It is a powerful tool that clarifies urban–rural LST boundaries and provides the reliable land thermal types, the SUHI spatial patterns, and the SUHI intensity on each grid point, and it also indicates the zones that are vulnerable to SUHIs with statistical reliability in urban agglomerations. All these features are conducive to urban planning and environmental management in terms of shaping rational urban clusters, mitigating heat-related health risks, and improving human comfort.

Regional SUHIs gradually extend beyond the urban boundaries in some urban agglomerations and greatly affect the thermal environment of continuous regions and threaten regional-level environmental sustainability, biodiversity, and resource and energy consumption. Machine-learning methods have shown great potential in characterizing the intensity, spatial pattern, and scale of regional SUHIs and their spatiotemporal variations over urban agglomerations. Fine-scale simulation experiments should be conducted

simultaneously as a complementary method to machine-learning methods to improve interpretability in future studies, particularly in urban agglomerations that have complex terrain and weather conditions, which could provide more valuable insights for urban design and decision-making.

Author Contributions: Conceptualization, Y.D. and Z.X.; methodology, Z.X.; software, M.W.; validation, N.W. and J.H.; formal analysis, Y.D.; investigation, Y.D. and N.W.; resources, L.Z.; data curation, Y.D.; writing—original draft preparation, Y.D. and Z.X.; writing—review and editing, Z.X.; visualization, N.W. and M.W.; supervision, Z.X.; project administration, Z.X.; funding acquisition, Z.X. All authors have read and agreed to the published version of the manuscript.

Funding: This research was funded by the National Natural Science Foundation of China (Grant 42075118 and Grant 42075027) and the National Key Research and Development Program (Grant 2020YFA0608901).

Data Availability Statement: The daily LST data used in identifying SUHI effects are freely available at the National Tibetan Plateau Data Center (https://doi.org/10.11888/Meteoro.tpdc.271252). The 500 m-resolution yearly land cover type dataset from 2001 to 2020 (MODIS/MCD12Q1) is freely available at https://lpdaac.usgs.gov/products/mcd12q1v061/, accessed on 1 May 2023. The global 30-m-resolution impervious surface dataset with a 5-year interval (1985–2020) is freely available at https://zenodo.org/record/5220816, accessed on 1 May 2023. Data pre- and post-processing and the RF models training are supported by the C/C++ libraries of GDAL at https://gdal.org, accessed on 1 March 2023, Dlib at https://github.com/davisking/dlib, accessed on 1 March 2023, and OpenCV at https://opencv.org/, accessed on 1 March 2023.

Conflicts of Interest: The authors declare no conflicts of interest.

References

1. Oke, T.R.; Mills, G.; Christen, A.; Voogt, J.A. *Urban Climates*; Cambridge University Press: Cambridge, UK, 2017. [CrossRef]
2. Du, Y.; Xie, Z.Q.; Zeng, Y.; Shi, Y.F.; Wu, J.G. Impact of urban expansion on regional temperature change in the Yangtze River Delta. *J. Geogr. Sci.* **2007**, *17*, 387–398. [CrossRef]
3. Fang, C.; Yu, D. Urban agglomeration: An evolving concept of an emerging phenomenon. *Landsc. Urban Plan.* **2017**, *162*, 126–136. [CrossRef]
4. Xie, Z.Q.; Du, Y.; Miao, Q.; Zhang, L.L.; Wang, N. An approach to characterizing the spatial pattern and scale of regional heat islands over urban agglomerations. *Geophys. Res. Lett.* **2022**, *49*, e2022GL099117. [CrossRef]
5. Manoli, G.; Fatichi, S.; Schläpfer, M.; Yu, K.; Crowther, T. Magnitude of urban heat islands largely explained by climate and population. *Nature.* **2019**, *573*, 55–60. [CrossRef]
6. Masoudi, M.; Tan, P.Y. Multi–year comparison of the effects of spatial pattern of urban green spaces on urban land surface temperature. *Landsc. Urban Plan.* **2019**, *184*, 44–58. [CrossRef]
7. Kim, S.W.; Brown, R.D. Urban heat island (UHI) intensity and magnitude estimations, a systematic literature review. *Sci. Total Environ.* **2021**, *779*, 146389. [CrossRef] [PubMed]
8. Chakraborty, T.; Sarangi, C.; Tripathi, S.N. Understanding diurnality and interseasonality of a sub-tropical urban heat island. *Bound.-Layer Meteor.* **2017**, *163*, 287–309. [CrossRef]
9. Hu, J.; Yang, Y.B.; Zhou, Y.Y.; Zhang, T.; Ma, Z.F.; Meng, X.J. Spatial patterns and temporal variations of footprint and intensity of surface urban heat island in 141 China cities. *Sustain. Cities Soc.* **2022**, *77*, 103585. [CrossRef]
10. Yang, C.B.; Yan, F.Q.; Zhang, S.W. Comparison of land surface and air temperatures for quantifying summer and winter urban heat island in a snow climate city. *J. Environ. Manag.* **2020**, *265*, 110563. [CrossRef]
11. Venter, Z.S.; Chakraborty, T.; Lee, X.H. Crowdsourced air temperatures contrast satellite measures of the urban heat island and its mechanisms. *Sci. Adv.* **2021**, *7*, eabb9569. [CrossRef]
12. Zhang, D.L.; Shou, Y.X.; Dickerson, R.R. Upstream urbanization exacerbates urban heat island effects. *Geophys. Res. Lett.* **2009**, *36*, L24401. [CrossRef]
13. Zhang, N.; Chen, Y. A case study of the upwind urbanization influence on the urban heat island effects along the Suzhou-Wuxi Corridor. *J. Appl. Meteorol. Climatol.* **2014**, *53*, 333–345. [CrossRef]
14. Imhoff, M.L.; Zhang, P.; Wolfe, R.E.; Bounoua, L. Remote sensing of the urban heat island effect across biomes in the continental USA. *Remote Sens. Environ.* **2010**, *114*, 504–513. [CrossRef]
15. Li, X.M.; Asrar, G.R.; Imhoff, M.; Li, X.C. The surface urban heat island response to urban expansion: A panel analysis for the conterminous United States. *Sci. Total Environ.* **2017**, *605*, 426–435. [CrossRef]
16. Zhao, L.; Lee, X.H.; Smith, R.B.; Oleson, K. Strong contributions of local background climate to urban heat islands. *Nature* **2014**, *511*, 216–219. [CrossRef] [PubMed]

17. Zhou, D.C.; Zhao, S.Q.; Zhang, L.X.; Sun, G.; Liu, Y.Q. The footprint of urban heat island effect in China. *Sci. Rep.* **2015**, *5*, 11160. [CrossRef] [PubMed]
18. Sun, Y.W.; Gao, C.; Li, J.L.; Wang, R.; Liu, J. Evaluating urban heat island intensity and its associated determinants of towns and cities continuum in the Yangtze River Delta urban agglomerations. *Sustain. Cities Soc.* **2019**, *50*, 101659. [CrossRef]
19. Wang, Z.A.; Meng, Q.Y.; Allam, M.; Hu, D.; Zhang, L.L.; Menenti, M. Environmental and anthropogenic drivers of surface urban heat island intensity: A case study in the Yangtze River Delta, China. *Ecol. Indic.* **2021**, *128*, 107845. [CrossRef]
20. Zhou, D.C.; Xiao, J.F.; Bonafoni, S.; Berger, C.; Deilami, K.; Zhou, Y.Y.; Frolking, S.; Yao, R.; Qiao, Z.; Sobrino, J.A. Satellite remote sensing of surface urban heat islands: Progress, challenges, and perspectives. *Remote Sens.* **2019**, *11*, 48. [CrossRef]
21. Acosta, M.P.; Vahdatikhaki, F.; Santos, J.; Hammad, A.; Dor′ee, A.G. How to bring UHI to the urban planning table? A data-driven modeling approach. *Sustain. Cities Soc.* **2021**, *71*, 102948. [CrossRef]
22. Chen, S.Z.; Yu, Z.W.; Liu, M.; Da, L.J.; Faiz, M. Trends of the contributions of biophysical (climate) and socioeconomic elements to regional heat islands. *Sci. Rep.* **2021**, *11*, 12696. [CrossRef] [PubMed]
23. Wang, Y.; Li, Y.G.; Xue, Y.; Martilli, A.; Shen, J.; Chan, P.W. City-scale morphological influence on diurnal urban air temperature. *Build. Environ.* **2020**, *169*, 106527. [CrossRef]
24. Back, Y.; Bach, P.M.; Jasper-Tönnies, A.; Rauch, W.; Kleidorfer, M. A rapid fine-scale approach to modeling urban bioclimatic conditions. *Sci. Total Environ.* **2021**, *756*, 143732. [CrossRef] [PubMed]
25. Du, R.; Song, J.; Huang, X.; Wang, Q.; Zhang, C.; Brousse, O.; Chan, P.W. High-resolution regional modeling of urban moisture island: Mechanisms and implications on thermal comfort. *Build. Environ.* **2022**, *207*, 108542. [CrossRef]
26. Zhu, D.; Ooka, R. WRF-based scenario experiment research on urban heat island: A review. *Urban Clim.* **2023**, *49*, 101512. [CrossRef]
27. Feng, Y.; Li, H.; Tong, X.; Chen, L.; Liu, Y. Projection of land surface temperature considering the effects of future land change in the Taihu Lake Basin of China. *Glob. Planet Chang.* **2018**, *167*, 24–34. [CrossRef]
28. Shen, C.H.; Hou, H.; Zheng, Y.Y.; Murayama, Y.J.; Wang, R.C.; Hu, T.G. Prediction of the future urban heat island intensity and distribution based on landscape composition and configuration: A case study in Hangzhou. *Sustain. Cities Soc.* **2022**, *83*, 103992. [CrossRef]
29. Hsu, A.; Sheriff, G.; Chakraborty, T.; Manya, D. Disproportionate exposure to urban heat island intensity across major US cities. *Nat. Commun.* **2021**, *12*, 2721. [CrossRef]
30. Yang, Q.Q.; Huang, X.; Tang, Q.H. The footprint of urban heat island effect in 302 Chinese cities: Temporal trends and associated factors. *Sci. Total Environ.* **2019**, *655*, 652–662. [CrossRef]
31. Yao, L.; Sun, S.; Song, C.X.; Li, J.; Xu, W.T.; Xu, Y. Understanding the spatiotemporal pattern of the urban heat island footprint in the context of urbanization, a case study in Beijing, China. *Appl. Geogr.* **2021**, *133*, 102496. [CrossRef]
32. Adilkhanova, I.; Ngarambe, J.; Yun, G.Y. Recent advances in black box and white-box models for urban heat island prediction: Implications of fusing the two methods. Renew. *Sust. Energ. Rev.* **2022**, *165*, 112520. [CrossRef]
33. Oukawa, G.Y.; Krecl, P.; Targino, A.C. Fine-scale modeling of the urban heat island: A comparison of multiple linear regression and random forest approaches. *Sci. Total Environ.* **2022**, *815*, 152836. [CrossRef]
34. Wang, Q.; Wang, X.N.; Meng, Y.; Zhou, Y.; Wang, H.T. Exploring the impact of urban features on the spatial variation of land surface temperature within the diurnal cycle. *Sustain. Cities Soc.* **2023**, *91*, 104432. [CrossRef]
35. Li, F.; Yigitcanlar, T.; Nepal, M.; Nguyen, K.; Dur, F. Machine learning and remote sensing integration for leveraging urban sustainability: A review and framework. *Sustain. Cities Soc.* **2023**, *96*, 104653. [CrossRef]
36. Lin, J.Y.; Qiu, S.X.; Tan, X.J.; Zhuang, Y.Y. Measuring the relationship between morphological spatial pattern of green space and urban heat island using machine learning methods. *Build. Environ.* **2023**, *228*, 109910. [CrossRef]
37. Du, H.; Wang, D.; Wang, Y.; Zhao, X.; Qin, F.; Jiang, H.; Dai, Y. Influences of land cover types, meteorological conditions, anthropogenic heat and urban area on surface urban heat island in the Yangtze River Delta Urban Agglomeration. *Sci. Total Environ.* **2016**, *571*, 461–470. [CrossRef]
38. Deilami, K.; Kamruzzaman, M.; Liu, Y. Urban heat island effect: A systematic review of spatio-temporal factors, data, methods, and mitigation measures. *Int. J. Appl. Earth Obs. Geoinf.* **2018**, *67*, 30–42. [CrossRef]
39. Peng, J.; Jia, J.; Liu, Y.; Li, H.; Wu, J. Seasonal contrast of the dominant factors for the spatial distribution of land surface temperature in urban areas. *Remote Sens. Environ.* **2018**, *215*, 255–267. [CrossRef]
40. Yu, Z.; Yao, Y.; Yang, G.; Wang, X.; Vejre, H. Spatiotemporal patterns and characteristics of remotely sensed region heat islands during the rapid urbanization (1995–2015) of southern China. *Sci. Total Environ.* **2019**, *674*, 242–254. [CrossRef] [PubMed]
41. Li, Y.F.; Schubert, S.; Kropp, J.P.; Rybski, D. On the influence of density and morphology on the Urban Heat Island intensity. *Nat. Commun.* **2020**, *11*, 2647. [CrossRef]
42. Xiang, Y.; Huang, C.B.; Huang, X.; Zhou, Z.X.; Wang, X.S. Seasonal variations of the dominant factors for spatial heterogeneity and time inconsistency of land surface temperature in an urban agglomeration of central China. *Sustain. Cities Soc.* **2021**, *75*, 103285. [CrossRef]
43. Lau, T.K.; Chen, Y.C.; Lin, T.P. Application of local climate zones combined with machine learning to predict the impact of urban structure patterns on thermal environment. *Urban Clim.* **2023**, *52*, 101731. [CrossRef]
44. Jato-Espino, D.; Manchado, C.; Roldán-Valcarce, A.; Moscardó, V. ArcUHI: A GIS add-in for automated modelling of the Urban Heat Island effect through machine learning. *Urban Clim.* **2022**, *44*, 101203. [CrossRef]

45. Hu, Y.F.; Dai, Z.X.; Guldmann, J.M. Modeling the impact of 2D/3D urban indicators on the urban heat island over different seasons: A boosted regression tree approach. *J. Environ. Manag.* **2020**, *266*, 110424. [CrossRef]
46. Han, D.R.; An, H.M.; Cai, H.Y.; Wang, F.; Xu, X.L.; Qiao, Z.; Jia, K.; Sun, Z.Y.; An, Y. How do 2D/3D urban landscapes impact diurnal land surface temperature: Insights from block scale and machine learning algorithms. *Sustain. Cities Soc.* **2023**, *99*, 104933. [CrossRef]
47. Hou, H.R.; Longyang, Q.Q.; Su, H.B.; Zeng, R.J.; Xu, T.F.; Wang, Z.H. Prioritizing environmental determinants of urban heat islands: A machine learning study for major cities in China. *Int. J. Appl. Earth Obs.* **2023**, *122*, 103411. [CrossRef]
48. Li, L.; Zhan, W.F.; Hu, L.Q.; Chakraborty, T.C.; Wang, Z.H.; Fu, P.; Wang, D.Z.; Liao, W.L.; Huang, F.; Fu, H.Y.; et al. Divergent urbanization-induced impacts on global surface urban heat island trends since 1980s. *Remote Sens. Environ.* **2023**, *295*, 113650. [CrossRef]
49. He, B.J.; Wang, J.S.; Zhu, J.; Qi, J.D. Beating the urban heat: Situation, background, impacts and the way forward in China. *Renew. Sust. Energ. Rev.* **2022**, *161*, 112350. [CrossRef]
50. Tang, W.B.; Zhou, J.; Ma, J.; Wang, Z.W.; Ding, L.R.; Zhang, X.D.; Zhang, X. TRIMS LST: A daily 1 km all-weather land surface temperature dataset for China's landmass and surrounding areas (2000–2022). *Earth Syst. Sci. Data* **2024**, *16*, 387–419. [CrossRef]
51. Abercrombie, S.P.; Friedl, M.A. Improving the consistency of multitemporal land cover maps using a hidden Markov model. *IEEE Trans. Geosci. Remote Sens.* **2016**, *54*, 703–713. [CrossRef]
52. Yang, L.Q.; Jia, K.; Liang, S.L.; Liu, J.C.; Wang, X.X. Comparison of four machine learning methods for generating the GLASS fractional vegetation cover product from MODIS data. *Remote Sens.* **2016**, *8*, 682. [CrossRef]
53. Gong, P.; Li, X.C.; Zhang, W. 40-Year (1978–2017) human settlement changes in China reflected by impervious surfaces from satellite remote sensing. *Sci. Bull.* **2019**, *64*, 756–763. [CrossRef]
54. Zhang, X.; Liu, L.L.; Zhao, T.T.; Gao, Y.; Chen, X.D.; Mi, J. GISD30: Global 30m impervious-surface dynamic dataset from 1985 to 2020 using time-series Landsat imagery on the Google Earth Engine platform. *Earth Syst. Sci. Data* **2022**, *14*, 651–664. [CrossRef]
55. Amatulli, G.; Domisch, S.; Tuanmu, M.N.; Parmentier, B.; Ranipeta, A.; Malczyk, J.; Jetz, W. A suite of global, cross-scale topographic variables for environmental and biodiversity modeling. *Sci. Data* **2018**, *5*, 180040. [CrossRef]
56. Liang, S.L.; Cheng, J.; Jia, K.; Jiang, B.; Liu, Q.; Xiao, Z.Q.; Yao, Y.J.; Yuan, W.P.; Zhang, X.T.; Zhao, X.; et al. The Global Land Surface Satellite (GLASS) products suite. *Bull. Am. Meteorol. Soc.* **2021**, *102*, E323. [CrossRef]
57. Zhao, H.Z.; Ge, Q.H.; Ni, K. *China Urban Construction Statistical Yearbook–2015: National Urban Population and Construction Land by City*; China Statistics Press: Beijing, China, 2015; pp. 52–85.
58. Hu, Z.J.; Wu, W.J.; Xin, Y.N. *China Urban Construction Statistical Yearbook–2020: National Urban Population and Construction Land by City*; China Statistics Press: Beijing, China, 2021; pp. 48–83. [CrossRef]
59. Breiman, L. Random forests. *Mach. Learn.* **2001**, *45*, 5–32. [CrossRef]
60. U.S. Environmental Protection Agency. Reducing Urban Heat Islands: Compendium of Strategies. 2008. Available online: https://www.epa.gov/heat-islands/heat-island-compendium (accessed on 20 October 2023).
61. Wang, Z.H. Reconceptualizing urban heat island: Beyond the urban-rural dichotomy. *Sustain. Cities Soc.* **2022**, *77*, 103581. [CrossRef]

Disclaimer/Publisher's Note: The statements, opinions and data contained in all publications are solely those of the individual author(s) and contributor(s) and not of MDPI and/or the editor(s). MDPI and/or the editor(s) disclaim responsibility for any injury to people or property resulting from any ideas, methods, instructions or products referred to in the content.

land

MDPI

Article

Analysis and Prediction of Spatial and Temporal Evolution of Ecosystem Service Value on the Northern Slopes of the Kunlun Mountains Based on Land Use

Zhichao Zhang, Yang Wang *, Haisheng Tang and Zhen Zhu

College of Grassland Science, Xinjiang Agricultural University, Urumqi 830052, China;
320212453@xjau.edu.cn (Z.Z.); 320222396@xjau.edu.cn (H.T.); 320222416@xjau.edu.cn (Z.Z.)
* Correspondence: wangyang@xjau.edu.cn; Tel.: +86-13999252425

Abstract: The ecological environment in the mountainous areas of southern Xinjiang is very sensitive and fragile, and identifying the ecological asset retention within the mountainous areas is a top priority at the current stage in the context of comprehensive environmental management in arid zones. This study examines the conversion and ecosystem service values between different land types within the mountainous areas based on a time series of land-use data from 1990 to 2020, and the results show that: (1) The value of ecosystem services on the northern slopes of the Kunlun Mountains shows an overall increasing trend. It increased from CNY 308.645 billion in 1990 to CNY 326.550 billion in 2020. Among them, the value of ecosystem services increased significantly between 2000 and 2010, with an increase of CNY 39.857 billion. Regulatory services accounted for more than 66% of the value of each ecosystem service. (2) Land use on the northern slopes of the Kunlun Mountains has changed significantly since 1990. The areas of cropland, forest land, grassland, watershed, and construction land have all shown an upward trend, with the greatest increase in construction land. The area of unutilized land, on the other hand, has slightly decreased. (3) The value of ecosystem services within the northern slopes of the Kunlun Mountains was spatially high in the south, low in the north, and higher in the west than in the east. The study also found a significant positive spatial correlation between ecosystem service values. In the spatial distribution, the increasing areas were mainly distributed in the southeast, and the decreasing areas were in the north. Changes in land types are expected to include an increase in the area of grassland and woodland, a decrease in unutilized land and cropland, and an overall improvement in the ecological environment of the northern slopes of the Kunlun Mountains in the next decade. This study also provides lessons and references for sustainable development and ecological protection in ecologically fragile regions.

Keywords: land use; ecosystem service values; Spatio-temporal evolution characteristics

1. Introduction

Ecosystem services are service functions that humans derive directly or indirectly from the structure, function, and construction of ecosystems that benefit human development and productive life [1]. They include service functions that can be commercialized, i.e., direct values such as provisioning services (food, water, production of raw materials, etc.) and cultural services (recreation, cultural benefits, etc.), and service functions that are difficult to commercialize, i.e., indirect values such as regulating services (flooding, climate regulation, etc.) and supporting services (carbon dioxide fixation, etc.). Commercialized service functions are usually derived from services that are difficult to commercialize [2].

Ecosystem services are also the most important bridge for humans to connect with nature. Following the development of a global ecosystem service value (ESV) paradigm by Daily and Costanza et al. [1,3] in the 1990s, ecosystem service research has made enormous progress. In 1999, Chinese scholar Ouyang et al. [4] clarified the basic concept of ecosystem

services in China, proposing that the value of terrestrial ecosystem services can be applied to the process of valuation developed by Chinese scholars Xie et al. [5]. Based on the Costanza assessment model, this approach adjusts ESV coefficients according to the actual situation of Chinese ecosystems. It also establishes a set of ESV coefficients that can be widely used to assess the value of ecosystems in Chinese provinces and cities [6], lakes [7], and plateaus [8], providing Chinese scholars with verified calculation methods when conducting regional ecosystem research. This approach is now widely used in China.

Currently, there are two types of methods for valuing the value of ecosystem services. One is the functional value method, which is based on the functional price per unit of service, and the other is the equivalent factor method, which is based on the equivalent factor of value per unit of area [9–11]. The functional value method requires more input parameters and a cumbersome calculation process and has no way to standardize the evaluation methods and parameters of different service values, which estimates different types of service values prone to error [12]. On the contrary, the equivalent factor approach not only requires less data, but is also more intuitive and convenient and is more suitable for valuing the value of ecosystem services on a regional or global scale. Compared with the functional value approach, the equivalent factor approach has the advantages of fewer data requirements, more objective results, and comprehensive assessment types, so it is commonly used in the study of valuing the value of ecosystem services in China [13].

Land is a prerequisite for human agricultural production activities and regional socio-economic progress [14]. Land-use datasets are the most fundamental manifestation of the interaction between humans and the terrestrial natural environment. Land-use datasets are also a major driver of environmental change in the biosphere [15]. The transformation of land-use types leads to changes in ecosystem service functions and structures, and these changes affect ESV [16,17]. Currently, in the context of intensified modernization and excessive human intervention in ecosystems, the harmful use of land has accelerated the degree of convergence between land-use types, leading to serious damage to ecosystems, intensified changes in the value of ecosystem services, and deterioration of the ecological environment [18].

The Kunlun Mountains are located at the northern edge of the Qinghai-Tibet Plateau [19], which is an extremely fragile ecological area in the arid zone of northwest China. As such, it is highly sensitive to climate change. The northern slopes of these mountains provide the source for many of the rivers and streams flowing into the Tarim River. However, in the context of global warming and the acceleration of the water cycle [20,21], the excessive expansion of human activities and the unreasonable deployment of environmental resources in recent years have caused the ecology of the Kunlun Mountains to be seriously affected. This has resulted in several major ecological problems, such as the degradation of natural grasslands, the decrease in glacier area, the unsustainable use of water resources, and the intensification of desertification [22–26], causing the already fragile ecological environment of the Kunlun Mountains to become even more fragile [27,28]. At present, other scholars' studies on the value of ecosystem services in southern Xinjiang have focused on the Tarim River Basin [29], the Aksu River [30], the Kaidu River [31], etc., and there are fewer long-term time-series studies on the value of ecosystem services on the northern slopes of the Kunlun Mountains, and this study fills in the blank period of ecological monitoring of the northern slopes of the Kunlun Mountains, and provides scientific basis for the construction of the northern slopes of the Kunlun Mountains ecological environment.

In view of the above, the present paper assesses the value of ecosystem services on the northern slopes of the Kunlun Mountains based on long-term remote sensing data. It also uses an exploratory spatial analysis method to quantitatively analyze the spatial and temporal trends of ESV in the study area and to explore the root causes of the region's ecosystem problems. This work will provide a scientific basis for the sustainable utilization of resources and ecological and environmental management in the mountainous areas of the Kunlun Mountains.

2. Data and Materials

2.1. Study Area

The northern slopes of the Kunlun Mountains are in the arid center of Asia and Europe at 74°80′–93°02′ E and 34°83′–40°55′ N (Figure 1), covering an area of up to 4.34×10^5 km^2. To the north, it includes the Tarim Basin. The southern portion of the study area is connected to the Qinghai-Tibet Plateau, creating an overall gradual rise in elevation from east to west. The northern slopes of the Kunlun Mountains constitute five main parts, namely the Kumkuri Basin, the Qarqan River Basin, the Keriya Valley, the Hotan River Basin, and the Yarkant River Basin. All these areas are important sources of external water recharge for the oases on the southern edge of the Tarim River Basin.

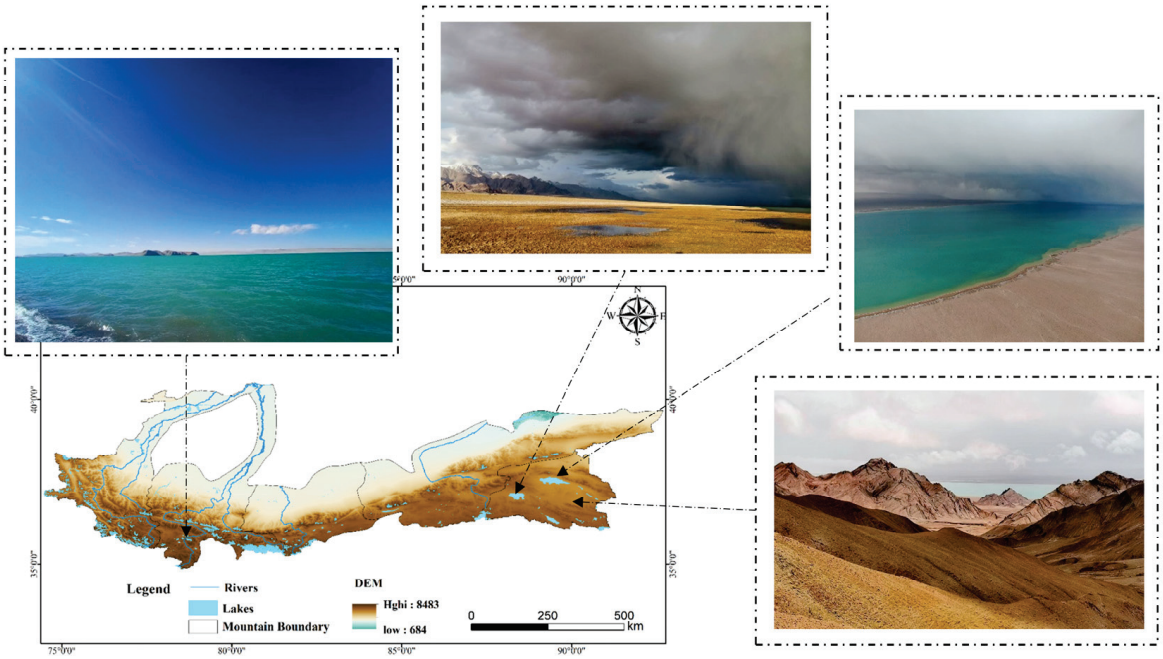

Figure 1. Overview map of the study area.

The study area is part of the Mongolian-Siberian dry anticyclone control range and features a continental climate characterized by strong aridity and little precipitation. The arid climate combines with the high altitude and low temperatures to result in an ecological environment dominated by grasslands and little species variety, along with oases that are mainly distributed at 1360–1500 m above sea level. Elevation (DEM) is an important factor affecting the distribution of plants and animals in the study area, and the Gobi, where plants and animals are scarce, is mainly distributed in the range of 1500–1950 m above sea level. As DEM increases, vegetation types such as mountain desert grassland, mountain typical grassland, and alpine grassland appear. Similar to other parts of the study area, precipitation in the oases and Gobi is scarce, with an average annual precipitation of only 34.8 mm.

2.2. Data Sources

The current land-use data were obtained from the annual China Land Cover Dataset published by Wuhan University [32]. These data cover the northern slopes of the Kunlun Mountains from 1990 to 2020, with a spatial resolution of 30 m and an overall classification accuracy of more than 80%. The classification of land types was selected from the unified land-use classification of the Chinese Academy of Sciences, and the dataset was reclassified into six land-use types: cropland, woodland, grassland, water, construction land, and barren land (Table 1). Around 80~110 sample points were randomly selected for each land

type. The accuracy of interpretation was verified with the help of Google Earth images (Kappa > 0.78), and the results met the requirements of the study.

Table 1. Classification of Land Use.

Serial Number	Land-Use Type	Land Type
1	Cropland	Paddy fields, drylands, mountains, hills, plains, sloping land, etc.
2	Woodland	Woodlands, open woodlands, shrublands, and other woodlands, etc.
3	Grassland	High-coverage grassland, medium-coverage grassland, low-coverage grassland, etc.
4	Water	Rivers and canals, lakes, reservoirs, wetlands, ponds, etc.
5	Construction land	Urban land, rural settlements, etc.
6	Barren land	Sandy land, Gobi, saline land, etc.

Temperature and precipitation data were obtained from the National Heating Data Center, which is part of the National Oceanic and Atmospheric Administration, with a spatial resolution of 1km. Differences in the stations included in the study area were processed using the spatial interpolation module of ArcGIS 10.2 software in accordance with the needs of the study. Topographic and slope data were taken from the SRTM DEM data in the Geospatial Data Cloud (http://www.gscloud.cn (accessed on 8 March 2023)) with a spatial resolution of 30 m.

Socio-economic data mainly include population density data and GDP (Gross Domestic Product) data, which were obtained from the Center for Resource and Environmental Science and Data (http://www.resdc.cn(accessed on 16 March 2023)) with a spatial resolution of 1 km. Some other data come from the Xinjiang Statistical Yearbook, Xinjiang Production and Construction Corps Statistical Yearbook, and the website of the Xinjiang Uygur Autonomous Region Bureau of Statistics (http://www.xjtj.gov.cn/ (accessed on 16 March 2023)) for the period 1990–2020.

2.3. Single Land-Use Dynamic Attitude

Based on the dynamic attitude, it is possible to understand and analyze the transformation rates between various land types on the northern slopes of the Kunlun Mountains for different time periods. Additionally, it is possible to estimate and predict change trends in land type [33] using land-use data in the study area for 1990, 2000, 2010, and 2020, as follows:

$$K = \frac{M_a - M_b}{M_b} \times \frac{1}{T} \times 100\% \quad (1)$$

where M_a and M_b are the areas of one type of land use in the designated area at the beginning and end of the study, T is the length of the study time, and K is the annual rate of change in one land-use type during the study period.

2.4. Calculation of the Value of Ecosystem Services

In this study, the improved Costanza evaluation model, which was modified by Xie et al. [34], was used to derive the Chinese ESV equivalents (Table 2). The model was modified again to fit the actual situation of the northern slopes of the Kunlun Mountains [35]. Please note that construction land only has the ESV of cultural recreation [36]. With the help of the ArcGIS 10.2 software fishnet tool, the study area was divided into 11,309 grids measuring 8 km × 8 km [37]. The area of each category within the grids was calculated separately using the natural breakpoint method to spatialize ESV and its gains and losses, which are calculated as follows:

$$\begin{aligned} ESV &= \sum A_a \times VC_a \\ ESV_b &= \sum A_a \times VC_{ba} \end{aligned} \quad (2)$$

where ESV is ecosystem service value, ESV_b is the value of ecosystem services in item b, A_a is the area of land-use type a in the study area, and VC_a is the coefficient of ecological

service value of land-use type *a*. VC_{ba} represents the value of the *b* ecosystem services of land-use type *a*.

Table 2. ESV Coefficient for the Northern Slopes of the Kunlun Mountains/CNY·hm^{-2}.

Ecosystem Service Function	Land-Use Type					
	Cropland	Woodland	Grassland	Water	Construction Land	Barren Land
Gas regulation	940.91	6586.37	1505.46	0	0	0
Climate regulation	1674.82	5080.92	1693.64	865.64	0	0
Water conservation	1129.09	6021.83	1505.46	38,351.50	0	56.45
Soil formation and protection	2747.46	7339.10	3669.55	18.82	0	37.64
Waste disposal	3086.19	2465.18	2465.18	34,211.50	0	18.82
Biodiversity conservation	1336.09	6134.74	2051.18	4685.73	0	639.82
Food production	1881.82	188.18	564.55	188.18	0	18.82
Raw material production	188.18	4892.73	94.09	18.82	0	0
Entertainment culture	18.82	2408.73	75.27	8167.10	82.60	18.82
Total	13,003.38	41,117.78	13,624.38	86,507.29	82.60	790.36

2.5. Ecosystem Service Change Index

Changes in the value of ecosystem services are determined by the value of the ecosystem services Change Index (ESCI) [38], with the "±" in ESCI indicating the relative gain or loss of each ecosystem service. It is calculated by the formula

$$ESCI_x = \frac{ES_{CUR_x} - ES_{HIS_s}}{ES_{HIS_s}} \quad (3)$$

where $ESCI_x$ denotes the single ecosystem service change index, and ES_{HISs} and ES_{CURx} correspond to the value of ecosystem services in the initial and final states during the study period, respectively. $ESCI > 0$ indicates a gain, $ESCI < 0$ indicates a loss, and $ESCI = 0$ indicates no change.

2.6. Spatial Autocorrelation Analysis

In this study, the Global Moran's I and Univariate Local Moran's I of the GeoDa model were used to explore clustering and anomalies in the ESV spatial distribution pattern [39]. The LISA (Local Indicators of Spatial Association) model is a statistical model used to analyze geospatial data. It is mainly used to study the degree of spatial aggregation and spatial correlation of geographic phenomena [40]. The core idea of the LISA model is based on the concept of spatial autocorrelation. In this paper, we use Moran's I Index to analyze and determine the spatial distribution pattern of geographic phenomena and finally obtain the LISA clustering map. The output of the LISA model is usually a LISA clustering map, which is used to visualize the spatial distribution pattern of geographic phenomena. The LISA clustering map divides the geographic units into four quadrants: High–High (H–H), Low–Low (L–L), High–Low (H–L), and Low–High (L–H). The H–H quadrant indicates that high-value geographic units are surrounded by clusters of high-value geographic units, the L–L quadrant indicates that low-value geographic units are surrounded by clusters of low-value geographic units, the H–L quadrant indicates that high-value geographic units are surrounded by discrete areas of low-value geographic units, and the L–H quadrant indicates that low-value geographic units are surrounded by discrete areas of high-value geographic units. LISA can show the spatial heterogeneity of ecosystem service values on the northern slopes of the Kunlun Mountains and provide a reference for trade-offs and synergies among ecosystem service values on the northern slopes of the Kunlun Mountains. Furthermore, G_i^* was used to explore special values of spatial variations of ESV clustering

distribution characteristics, i.e., high-value clustering (hot spots) and low-value clustering (cold spots). The equations are, respectively:

$$I_i = \frac{x_i - \overline{X}}{S_i^2} \sum_{j=1, j \neq i}^{n} w_{ij}\left(x_j - \overline{X}\right) \tag{4}$$

$$S_i^2 = \frac{\sum_{j=1, j \neq i}^{n} \left(x_j - \overline{X}\right)^2}{n-1} \tag{5}$$

where x_i is the value of factor i, $\overline{x}$ is the average of the factor values, w_{ij} is the spatial weight matrix between factors i and j, n is the total number of factors, and s is the standard deviation of all factors from 1 to n.

$$G_i^* = \frac{\sum_{j=1}^{n} w_{ij} x_j - X \sum_{i=1}^{n} w_{ij}}{\sqrt{s}\left[n \sum_{j=1}^{n} w_{ij}{}^2 - \left(\sum_{j=1}^{n} w_{ij}\right)^2\right]/(n-1)} \tag{6}$$

$$X = \frac{1}{n} \sum_{i=1}^{n} x_i, S = \sqrt{\frac{1}{n} \sum_{i=1}^{n} x_i^2 - (X)^{-2}} \tag{7}$$

where x_j is the original attribute value of factor j, w_{ij} is the weight representation between factor i and factor j (adjacent weight value is 1; non-adjacent weight value is 0), and n is the total number of all sampled points. X is the mean of all factors from 1 to n, and S is the standard deviation of all factors from 1 to n.

2.7. CA–Markov Model

In this study, the CA–Markov model was used to simulate future land use on the northern slopes of the Kunlun Mountains. Markov modeling is a prediction method based on Markov chains that predicts the changing conditions of events at various moments in the future based on their current conditions [41]. The Markov prediction method is one of the important prediction methods in geographic prediction research. Land use is consistent with the Markov prediction process [42]. The formula is:

$$S_{(t+1)} = P_{ij} \times S_t \tag{8}$$

$$P_{ij} = \begin{bmatrix} P_{11} & \cdots & P_{1n} \\ \vdots & \ddots & \vdots \\ P_{n1} & \cdots & P_{nn} \end{bmatrix} \tag{9}$$

$$[0 \leq P_{ij} < 1 \; and \sum_{j=1}^{n} P_{ij} = 1 (i.j = 1, 2 \cdots n)] \tag{10}$$

where $S_{(t+1)}$ is the system state at period $t + 1$ and P_{ij} is the state transfer probability matrix.

In this study, in order to test the accuracy and feasibility of the CA–Markov model for future land-use analysis, we first simulated the land-use data in 2010 with the CA–Markov model in Idrisi 17.0 prediction software and then compared the simulated land-use data in 2010 with the real values, which verified the model's reliability is more, and it meets the research requirements. The real land-use value in 2010 was used as the starting year to simulate the land-use changes in the study area in 2030, and all the images processed in Idrisi software were raster data. The land raster size used in this paper is 30 m × 30 m, and the spatial data processing is carried out in ArcGIS 10.2 software.

3. Results and Analysis

3.1. Spatial and Temporal Variation Characteristics of Land-Use Types

The current land-use status (Figure 2) and land-use structure (Figure 3a) of the northern slopes of the Kunlun Mountains from 1990 to 2020 show that the largest and most widely distributed land type in the study area is barren land. This land type dominates the ecosystem, accounting for 72.92% of the total area as of 2020, followed by grassland, which accounts for 19.15% of the total area. In contrast, water and cropland account for only 4.93% and 2.93% of the total area, respectively. Woodland and construction land are the smallest, accounting for only 0.04% of the total area.

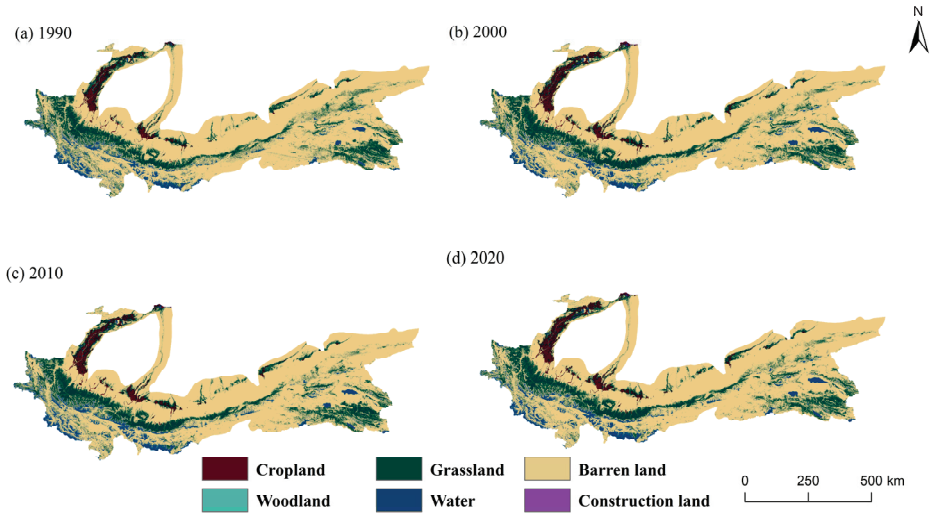

Figure 2. Status of land use on the northern slopes of the Kunlun Mountains.

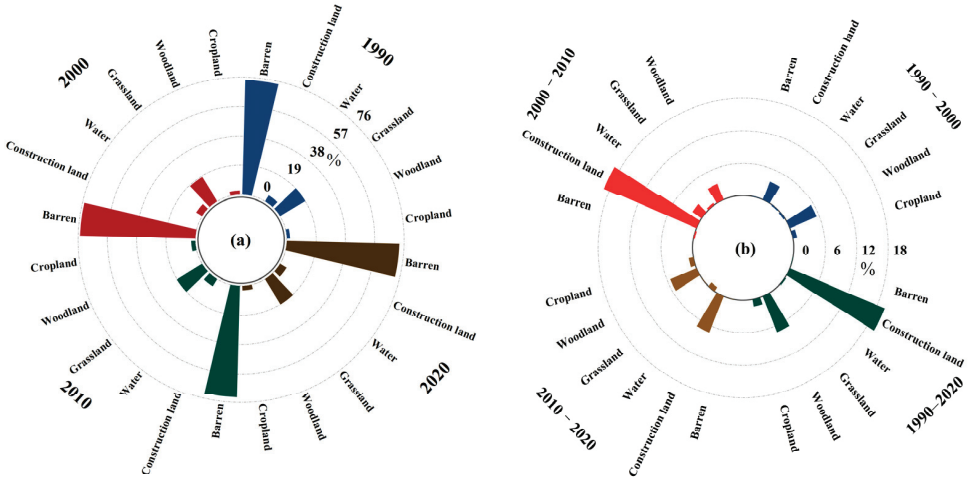

Figure 3. (**a**) Structure of land-use types (%); (**b**) dynamic attitude of land-use types (%).

Although each land type changed during the study period, the change characteristics differed according to land type and time period. The area of grassland, construction land, woodland, cropland, and water increased, while the area of barren land decreased. Cropland experienced the largest growth in the area, showing a total growth of 364.69 $\times$ 10^3 hm^2. The fastest growth rate for this land type occurred from 2000 to 2010, with a kinetic attitude of 1.97% (Figure 3b). Most of the cropland was converted from grassland (385.81 $\times$ 10^3 hm^2) and barren land (100.8 $\times$ 10^3 hm^2), with human large-scale land reclamation being an important factor in this phenomenon.

During the study period, the increase in population resulted in construction land having the largest proportional growth among all land-use types. The most significant change occurred from 2000 to 2010, with construction land expanding from 3.3 × 10^3 hm^2 in 1990 to 9.61 × 10^3 hm^2 in 2020 (Figure 4), at a growth rate of 291.04% and a moving attitude of up to 19.1%. The growth trend of forested land is also dramatic, with the fastest growth rate of forested land in 1990–2000, with a forested land movement rate of 5.49%, and the growth of forested land from 5.17 × 10^3 hm^2 in 1990 to 8 × 10^3 hm^2 in 2000, which was mainly converted from grassland (12.7 × 10^3 hm^2).

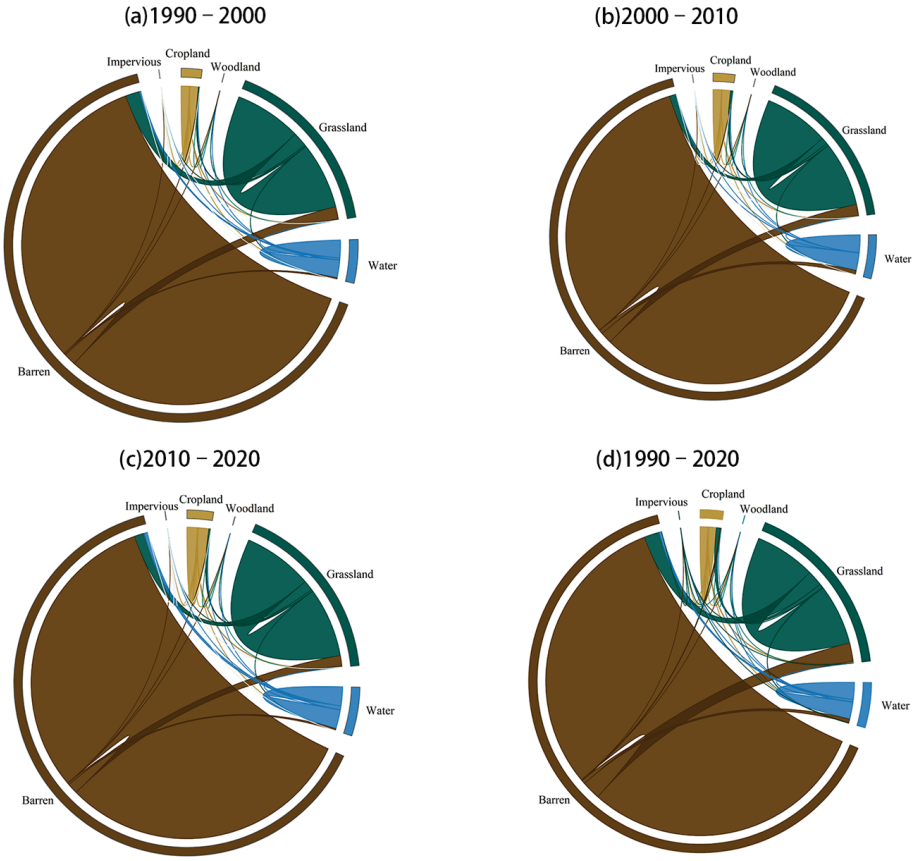

Figure 4. Status of land-use flow on the northern slopes of the Kunlun Mountains from 1990 to 2020.

The area of unutilized land was 30,885.24 × 10^3 hm^2 in 1990 and 30,341.86 × 10^3 hm^2 in 2020, with an area reduction of 1.08%, and the fastest rate of reduction was in the time period of 2000–2010, with a momentum of −0.29%, which was mainly transformed into a land area consisting of grassland (1594.49 × 10^3 hm^2), water (241.77 × 10^3 hm^2), and cropland (100.8 × 10^3 hm^2), which is mainly due to the increase in temperature, the increase in mountain runoff, and the increase in precipitation in the recent years, which makes the study area gradually move towards ecological restoration.

Meanwhile, The growth trend of grassland in the past 30 years is a small increase of 155.26 × 10^3 hm^2 (Table 3), and the grassland is mainly transformed by unutilized land (1929.37 × 10^3 hm^2) and arable land (119.95 × 10^3 hm^2), and the large-scale reclaiming of the grassland (184.59 × 10^3 hm^2) into arable land and overgrazing from 1990 to 2000 led to the large-scale reduction of grassland (345.27 × 10^3 hm^2), and after 2000, in response to the national policy, people began to pay attention to ecological conservation, and the area of grassland was recovered. From 1990 to 2000, human beings massively reclaimed grassland (184.59 × 10^3 hm^2) as arable land and overgrazed it, resulting in the large-scale reduction of grassland (345.27 × 10^3 hm^2).

Table 3. Land-Use Transfer Matrix for the Northern Slopes of the Kunlun Mountains, 1990–2020 ($\times 10^3$ hm^2).

Land-Use Type	Cropland	Woodland	Grassland	Water	Construction Land	Barren Land	Total	Transfer
Cropland	769.44	0	119.95	1.36	2.64	2.11	895.50	126.06
Woodland	0	4.33	0.75	0.02	0.38	0	5.48	1.15
Grassland	385.81	12.70	6251.13	60.32	1594.49	10.15	8314.59	2063.46
Water	4.04	0.07	25.07	1748.17	241.77	0.36	2019.48	271.31
Construction land	100.80	0.36	1929.37	364.82	29,672.65	2.64	32,070.65	2398.00
Barren land	0.10	0	0.54	0.05	0.14	1.65	2.48	0.83
Total	1260.19	17.46	8326.82	2174.74	31,512.07	16.91		
Transfer in	490.75	13.13	2075.69	426.56	1839.42	15.26		

Furthermore, over the past 30 years, the area of the watershed has increased by 155.26 $\times$ 10^3 hm^2, and the fastest rate of increase was during the period of 2000–2010, with a motivation of 2.09%, which was mainly made up of unused land (364.82 $\times$ 10^3 hm^2), grassland (60.32 $\times$ 10^3 hm^2), and arable land (1.36 $\times$ 10^3 hm^2). During 2000–2010, the transformation of unutilized land and grassland to water was the most drastic, respectively (550.42 $\times$ 10^3 hm^2 and 19.27 $\times$ 10^3 hm^2). In general, the increase of water and the decrease of unutilized land area have certain spatial synergies with the decrease of glacier area in the Kunlun Mountains and the intensification of the water cycle in arid zones, which also indicates that the ecological environment in the study area is developing in a good direction. It also indicates that the ecological environment in the study area is developing in a favorable direction.

3.2. Spatial and Temporal Variation Characteristics of ESV

3.2.1. Characteristics of Changes in the Temporal Dimension of ESV

In this study, the ecosystem service values of the northern slopes of the Kunlun Mountains were estimated for 1990, 2000, 2010, and 2020 based on the primary land-use classification (Table 4). Overall, ESV showed a rising trend, with a total increase of CNY 17.906 billion (or about 5.8%), while for the four above-stated years, the ESV was 3086.45, 3032.90, 343.147, and 326.550 billion, respectively. It can be concluded from these figures that the ESV trend first slowly decreased, then significantly increased, and finally flatly decreased while generally showing an upward trend. Specifically, from 1990 to 2000, the ESV slowly decreased by CNY 5.535 billion. From 2000 to 2010, it increased dramatically by CNY 39.857 billion, and from 2010 to 2020, it showed a significant downward trend, dropping CNY 16.579 billion.

Table 4. Changes in ESV by Land-Use Type on the Northern Slopes of the Kunlun Mountains, 1990–2020/10^8 CNY.

Land-Use Type		Cropland	Woodland	Grassland	Water	Construction Land	Barren Land	Total
1990	ESV	112.43	2.12	1083.72	1644.06	0	244.11	3086.45
	Proportion	3.64%	0.07%	35.11%	53.27%	0%	7.91%	100%
2000	ESV	121.53	3.29	1047.68	1614.50	0	245.89	3032.90
	Proportion	4.01%	0.11%	34.54%	53.23%	0%	8.11%	100%
2010	ESV	145.45	4.36	1090.76	1952.11	0.01	238.78	3431.47
	Proportion	4.24%	0.13%	31.79%	56.89%	0%	6.96%	100%
2020	ESV	158.47	6.72	1085.42	1775.06	0.01	239.81	3265.50
	Proportion	4.85%	0.21%	33.24%	54.36%	0%	7.34%	100%
ESV changes from 1990 to 2020		46.04	4.59	1.70	131.00	0.01	−4.29	179.06
ESV change rate from 1990 to 2020		40.95%	216.28%	0.16%	7.97%	587.41%	−1.76%	5.80%

Furthermore, in looking at the changes in ESV for each category for the whole study period (Table 5), we can see that woodland and cropland ESV changed the most, increasing by CNY 459.00 and 4.604 billion, respectively, which was 216.28% and 40.95%, respectively. The ESV of barren land, on the other hand, showed a decreasing trend, reducing by CNY 429 million. This is some indication that the ecology of the study area is, in general, in a state of improvement. There is an improvement in the ecosystem health of the protected areas, and the globally warming environment has led to an increase in the ESV of woodland and water areas. At the same time, the intensification of human activities and the speed of socio-economic development have led to a continuous increase in the ESV of cropland.

Table 5. Changes in Various ESVs in the Northern Slopes of the Kunlun Mountains, 1990–2020 (10^8 CNY).

Type 1	Type 2	1990		2000		2010		2020	
Regulation services	Gas regulation	128.22	4.15%	125.09	4.12%	121.23	3.53%	132.48	4.06%
	Climate regulation	165.91	5.38%	162.45	5.36%	174.40	5.08%	173.93	5.33%
	Water conservation	876.12	28.39%	860.13	28.36%	1016.28	29.62%	938.75	28.75%
	Waste disposal	878.90	28.48%	862.96	28.45%	1009.84	29.43%	942.11	28.85%
	Subtotal	2049.15	66.39%	2010.62	66.29%	2321.75	67.66%	2187.28	66.98%
Support services	Soil formation and protection	328.00	10.63%	320.51	10.57%	337.09	9.82%	338.83	10.38%
	Biodiversity conservation	461.69	14.96%	457.21	15.07%	478.85	13.95%	470.98	14.42%
	Subtotal	789.69	25.59%	777.72	25.64%	815.93	23.78%	809.81	24.80%
Provision of services	Food production	70.58	2.29%	70.38	2.32%	76.20	2.22%	77.51	2.37%
	Raw material production	9.72	0.31%	9.74	0.32%	10.58	0.31%	10.97	0.34%
	Subtotal	80.30	2.60%	80.12	2.64%	86.78	2.53%	88.49	20.50%
Cultural services	Entertainment culture	167.30	5.42%	164.44	5.42%	196.48	5.73%	179.93	5.51%
	Total	3086.45		3032.90		3420.95		3265.50	

The dominant service value in the study area is the regulating function, which consists of four main aspects: gas regulation, climate regulation, water connotation, and waste treatment. The overall service functions of these regulations during the study period show an upward trend of CNY 42.56, 80.21, 626.3, and 63.217 billion, respectively, with a slight decrease from 1990 to 2000. There is also a significant upward trend in water connotation and waste treatment from 2000 to 2010, followed by a slight decrease from 2010 to 2020. The increase in water area also plays a key role in regulating services. For the service functions of water source containment and waste treatment, the decrease followed by an increase is consistent with grassland and water area changes.

The two service functions of soil formation/conservation and biodiversity conservation are called support services. Between 1990 and 2020, these two services showed a decrease followed by an increase. They are mainly influenced by cropland, woodland, and grassland, so their value increased due to the expansion of woodland and cropland areas and the fluctuating increase in grassland.

Supply services include the two service functions of food production and raw material production, whereas cultural services include only recreational and cultural functions and thus account for a relatively small proportion of the value of ecosystem services in the study area. Furthermore, the supply function is mainly influenced by cropland, woodland, and grassland, so when cropland and grassland areas expand, there is a subsequent increase in the production of crops and livestock products. The result is a gentle upward trend in the food production function, which in the study area occurred from 1990 to 2000, followed by a more dramatic increase from 2000 to 2020. The function of raw material production service experienced a slight upward trend from 1990 to 2020, similar to the changing trend of cropland and grassland areas. The changes in supply services are mainly due to the combined effect of cropland, woodland, and grassland, charting an overall upward trend.

In contrast, the cultural service function shows an upward trend from 1990 to 2010 and a downward trend from 2010 to 2020, with an especially dramatic upward trend from 2000 to 2010. This service function is mainly influenced by woodland, grassland, and water areas, and its change trend is consistent with changes in woodland and water areas.

Overall, the value of ecosystem services on the northern slopes of the Kunlun Mountains from 1990 to 2020 maintained an upward trend, consistent with changes in regulating services. The data show a slight decline followed by a sharp upward trend from 2000 to 2010 and then another slight decline from 2010 to 2020.

3.2.2. Characteristics of Changes in ESV Spatial Dimension

The spatial distribution pattern shows that the highest values are mainly concentrated in grassland and watersheds in the western and southeastern portions of the study area (Figure 5). This is highly consistent with the unique landscape type distribution characteristics of the region, which includes vast desert areas and barren land in the northeast (low ESV), the Yarkand River Basin in the northwest (high ESV), mountainous areas in the southwest (high ESV), and the Kumkuri Basin in the southeast within the Alpine Reserve (high ESV). Comparing the spatial distribution changes of ESV from 1990 to 2022, the high-value areas showed an expanding trend, while the low-value zone showed a decrease in size. Overall, the ESV in the study area showed a significant increasing trend.

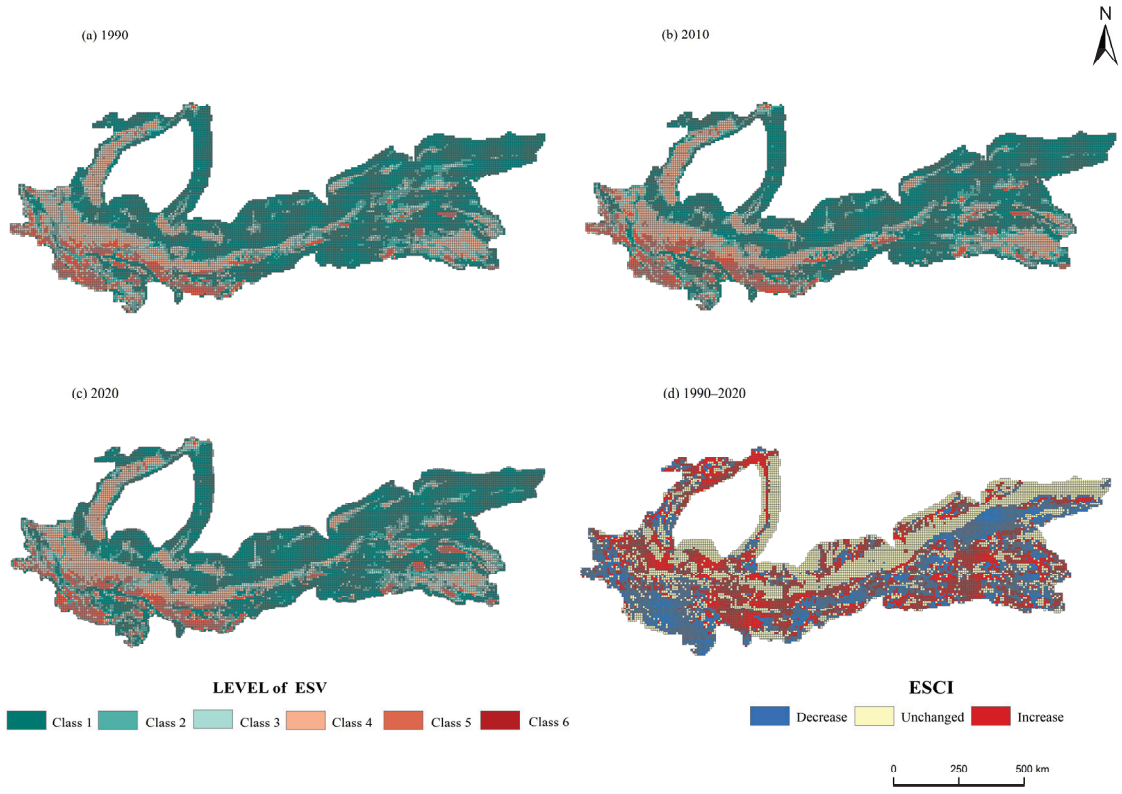

Figure 5. Spatial variation distribution characteristics of ESV on the northern slopes of the Kunlun Mountains.

Similarly, the loss and gain value of ecosystem services for the northern slopes of the Kunlun Mountains from 1990 to 2020 shows an increasing trend, mainly due to the acceleration of the global water cycle. The result was the conversion of land types with lower ESV (barren land) to land types with higher ESV (grassland, water). In the northeastern and northern parts of the study area, there are slab-like portions of gain, primarily resulting from the expansion of water and grassland areas. There are also some point-like gain sections in the northeast, mainly due to the local increase in grassland and water areas

post-ecological restoration. Meanwhile, the ESV gain areas in the west are thanks to the increase in grassland cover in some areas due to the development of water resources.

3.3. Spatial Correlation Analysis of ESV

3.3.1. Spatial Autocorrelation Analysis

The present study conducted global autocorrelation analysis using the GeoDa model to find the spatial pattern characteristics of the ecosystem service values for the northern slopes of the Kunlun Mountains from 1990 to 2020. According to the calculated results, there is a very significant spatial correlation in the ESV distribution, i.e., the spatial distribution is clustered in places with high ESV values and vice versa. The global Moran's I Index for the four periods of 1990, 2000, 2010, and 2020 (Figure 6) shows a maximum value of 0.692 in 1990. This trend is consistent with the spatial correlation of ESV in the study area, which reveals a yearly increase in area and higher ESV for grassland and water. Analysis of the correlation of the dynamic change in ESV indicated a changing trend of initial gradual increase. With the help of the Local Moran's I Index, a LISA clustering map was created (Figure 7).

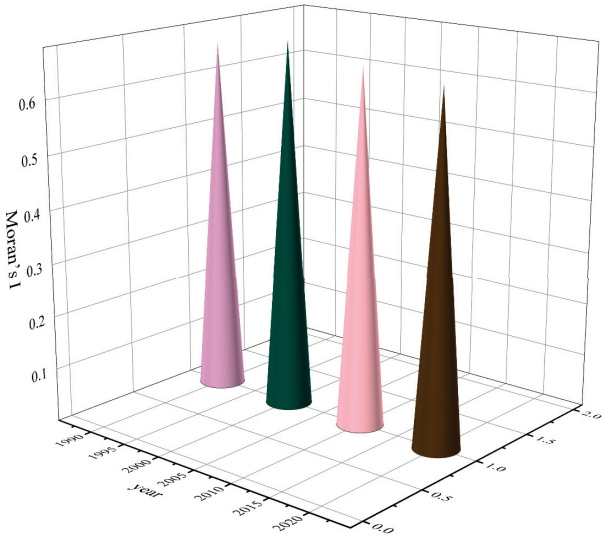

Figure 6. Moran Index for the northern slopes of the Kunlun Mountains, 1990–2020.

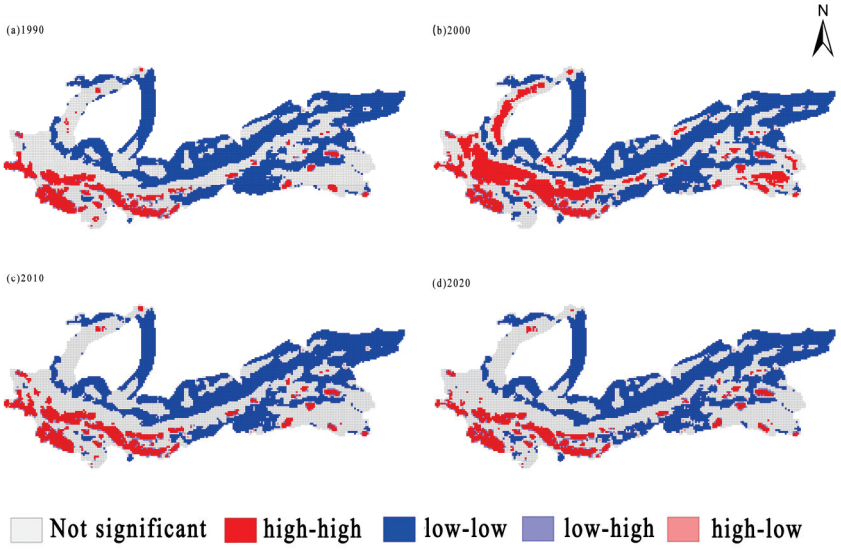

Figure 7. LISA clustering map of ESV on the northern slopes of the Kunlun Mountains, 1990–2020.

The main spatial clustering types of ESV in the study area are High–High, Low–High, and Low–Low. The High–High ESV value areas from 1990 to 2020 were mainly distributed throughout the north, west, and south, with a small amount distributed in the southeast, all of which are rich in grassland and water resources. The northern region is also characterized by intensive human activities, which then leads to more cropland and a higher level of socio-economic development. The low–high ESV areas were mainly distributed in the west and southeast from 1990 to 2020, covering barren land and grassland. The Low–Low type areas are mainly distributed in the central and northeastern regions of the study area, where the land is barren, has low ESV value, is ecologically fragile, and is difficult to develop and use.

3.3.2. Cold Hot Spot Analysis

With the help of the ArcGIS 10.2 software cold and hotspot analysis tool, the ESV dynamics of the study area were spatially expressed by selecting the statistically significant spots with a confidence level of 90% or more from the obtained results (Figure 8).

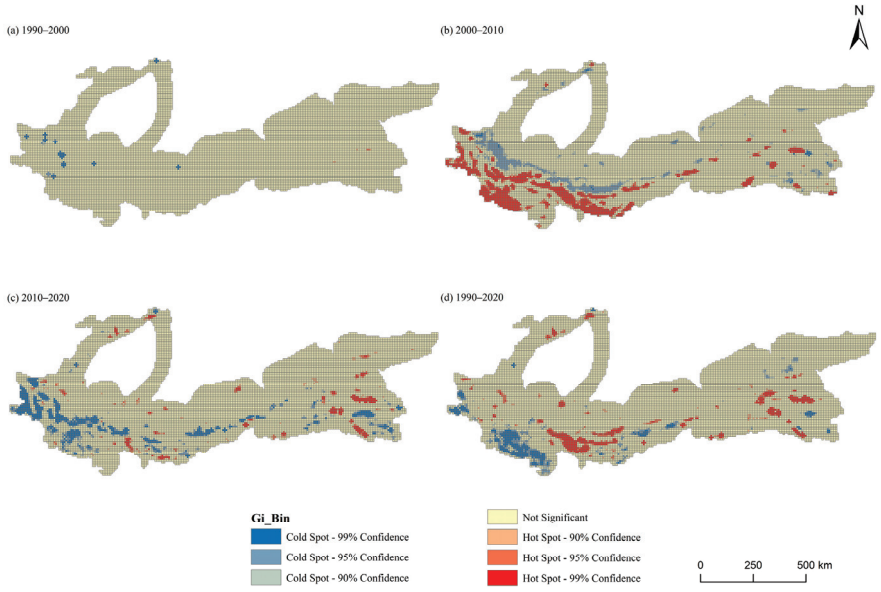

Figure 8. Cold hotspot analysis of ESV on the northern slopes of the Kunlun Mountains.

The results indicate that the ESV value-added hotspots in the study area from 1990 to 2000 were dispersed throughout the oasis-desert intersection and some areas in the south. The dispersion pattern is mostly due to the conversion of barren land to cropland and the growth of water area, which led to the growth of ESV in some places. The cold spots were mainly distributed in the southwest and were primarily caused by the shrinkage of water and grassland area, resulting in the loss of ESV. In 2010–2020, ESV gain hotspots were concentrated in the southwest, with some patchy hotspots in the southeast and center. The intensification of the global water cycle and rising temperatures resulted in the conversion of significant amounts of barren land into grassland and water, resulting in an increase in ESV in 2010. The loss of ESV mainly occurred at the border between the Taklamakan Desert and the western portion of the study area, where the degree of desertification was greater and ESV, therefore, lower.

The ESV gain hotspots in 2010–2020 were primarily located in the southeast, which is mostly due to the increase in water resources in that area caused by rising temperatures and accelerating snow melt. However, this change, to some extent, improved the grassland ecosystem in the region, increasing grassland and water area and a subsequent uptick in ESV. The cold spots designating ESV loss were mainly located in the northern and western parts of the study area and were mostly the result of increased human activities, which included some behaviors such as large-scale reclamation and grazing activities. The

outcome of these activities was the conversion of land types with high ESV value, such as grassland, into land types with low ESV value, such as barren land.

Overall, the changes in cold hot spots from 1990 to 2020 are similar to those in ESV gains and losses in terms of spatial distribution characteristics. The ESV value-added hotspots were concentrated in the southeastern and southern regions and were due mainly to the increase in grassland and water area. The cold spots were mainly located in the north and southwest and were the direct result of human activities leading to the conversion of grassland and water into cropland and barren land. The distribution area of ESV loss hotspots shows an overall increase in ESV in the study area for the 30-year study period.

3.4. CA–Markov Model Simulation and Prediction

In this study, the equivalent factor method was used to calculate the ecosystem service value, and the change in land-use type is closely related to the ecosystem service value. We analyzed the change in ecosystem service value on the northern slopes of the Kunlun Mountains from 1990 to 2020. Based on the land-use data of 2020, the CA–Markov model is used to simulate and predict the period from 2020 to 2030. Based on the impact of land-use type conversion on the value of ecosystem services, we discussed the reasons for the increase in the value of ecosystem services and provided a scientific basis for ecological protection in the study area in the future.

Through simulation and prediction, it can be concluded that the conversion between various land types in different periods on the northern slopes of the Kunlun Mountains is quite frequent, and its main feature is the mutual conversion between grassland, forest land, unused land, and other land types (Figure 9). The area of grassland, forest land, construction land and water area is increasing, and the area of grassland is increasing the most. The increase was 4534.89 $\times$ 10^3 hm^2 (Table 6). In the study area, the water area increased by 644.97 $\times$ 10^3 hm^2, and the unused land and cultivated land both showed a decreasing trend. The unused land decreased by 4830.42 $\times$ 10^3 hm^2 with the largest amplitude. The unused land was transformed into grassland and water area by 6417.17 $\times$ 10^3 hm^2 and 515.09 $\times$ 10^3 hm^2, respectively. Grassland increased mainly in the Yerqiang River basin in the southwest and the upper Chelson River basin in the east. Unused land in the Hotan River Basin and Keriya River Basin is also partially converted to grassland and water.

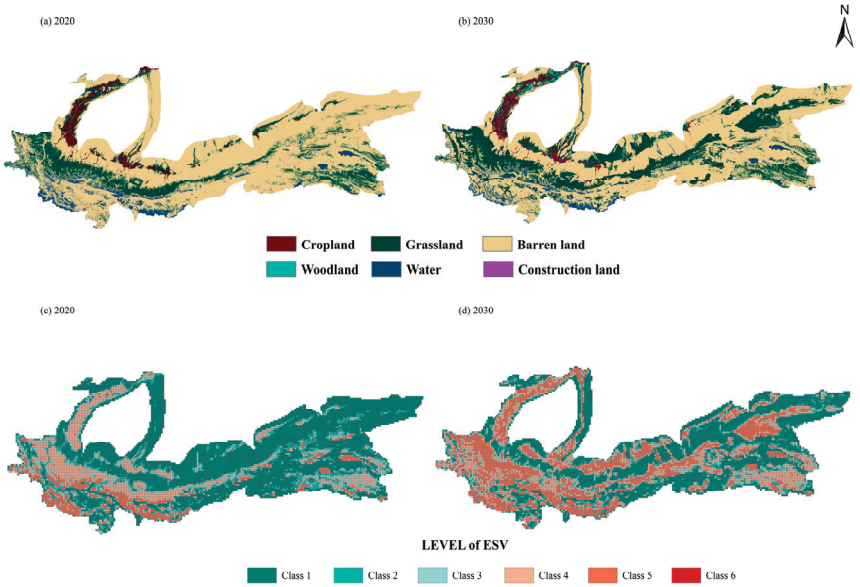

Figure 9. Future land change and future ecosystem service values on the northern slopes of the Kunlun Mountains: (**a**) 2020; (**b**) actual and simulated land-use change results from the CA–Markov model in 2030; (**c**) ecosystem service values in 2020; and (**d**) projected ecosystem service values in 2030.

Table 6. Simulated projected land-use transfer matrix for the northern slopes of the Kunlun Mountains, 2020–2030 ($\times 10^3$ hm^2).

Land-Use Type	Cropland	Woodland	Grassland	Water	Construction Land	Barren Land	Total	Transfer
Cropland	896.58	52.77	182.78	18.26	37.82	71.91	1260.12	363.54
Woodland	0	2.44	13.20	0.06	0	1.55	17.25	14.81
Grassland	256.98	195.72	6177.14	110.21	21.11	1566.64	8327.82	2150.67
Water	0.71	0.23	65.52	1548.90	0.01	560.27	2175.68	626.74
Construction land	2.27	2.98	6.89	1.36	3.10	0.19	16.79	13.68
Barren land	31.99	65.21	6417.17	515.09	1.53	24,481.08	31,512.13	7030.99
Total	1188.53	319.34	12,862.71	2193.88	60.66	26,684.56		
Transfer in	291.95	316.90	6685.57	644.97	60.47	2200.57		

The ecosystem service value of the northern slopes of the Kunlun Mountains predicted by the simulation will increase from 2020 to 2030. According to the simulation prediction, the ecosystem service value of the northern slopes of the Kunlun Mountains in 2030 is CNY 455.495 billion (Table 7), which increases by CNY 128.945 billion compared with 2020. Among them, the adjustment services, support services, supply services, and cultural services have, respectively, increased relative to 2020: 765.1, 422.76, 62.33, and CNY 3.924 billion. We found that the main increase in the value of ecosystem services predicted by the simulation in 2030 comes from the regulation services. Through the study, we concluded that grassland, water area, and forest land are the main factors that increase the regulation services. The decrease in unused land and cultivated land and the increase in grassland, forest, and water areas on the northern slopes of the Kunlun Mountains indicate that the ecology in the study area is gradually recovering. Therefore, strengthening the ecological protection in the study area is of great significance to the ecological restoration of the northern slopes of the Kunlun Mountains.

Table 7. Prediction of various ESVs on the northern slopes of the Kunlun Mountains in the future 2030 (10^8 CNY).

Type 1	Type 2	Land-Use Type						
		Cropland	Woodland	Grassland	Water	Construction Land	Barren Land	Total
Regulation services	Gas regulation	12.65	24.05	214.74	0	0	0	251.44
	Climate regulation	22.52	18.56	241.58	20.54	0	0	303.19
	Water conservation	15.18	21.99	214.74	909.81	0	16.74	1178.46
	Waste disposal	41.49	9.00	351.63	811.60	0	5.58	1219.30
	Subtotal	91.84	73.61	1022.68	1741.94	0	22.32	2952.38
Support services	Soil formation and protection	36.94	26.80	523.42	0.45	0	11.16	598.77
	Biodiversity conservation	17.96	22.40	292.58	111.16	0	189.70	633.81
	Subtotal	54.90	49.21	815.99	111.61	0	200.86	1232.57
Provision of services	Food production	25.30	0.69	80.53	4.46	0	5.58	116.56
	Raw material production	2.53	17.87	13.42	0.45	0	0	34.27
	Subtotal	27.83	18.56	93.95	4.91	0	5.58	150.82
Cultural services	Entertainment culture	0.25	8.80	10.74	193.75	0.06	5.58	219.17
	Total	174.83	150.17	1943.35	2052.21	0.06	234.34	4554.95

4. Discussion

4.1. Methods for Valuing Ecosystem Services

Ecosystem service value assessment translates the current state of the ecosystem into many ecological assets [43]. Its intuitive form is more suitable for interpretation by policymakers and the public and helps to identify problems. Research on the assessment of ecosystem service values and their driving mechanisms provides an in-depth analysis of the development trends and change mechanisms of the ecological environment [44]. Furthermore, the assessment of ESV gives a scientific basis for promoting regional ecological civilization construction and optimizing management decisions.

However, despite the obvious advantages of evaluating ESV, such evaluations can be controversial in terms of the methods applied. One study found that the evaluation of ecological status and remote sensing data combination areas is currently the most important research tool, but the degree of accuracy and timeliness of ESV evaluation may be questionable [45]. At this stage, the valuation of ecosystem services can be broadly divided into two types: methods based on the functional price per unit of service and methods based on the value equivalent factor per unit area [46]. Of these two options, the value equivalent method is more intuitive, has a uniform evaluation method and parameter criteria, and is suitable for regional ecosystem service valuation [47]. The equivalence factor approach has been applied to global regions and has been very fruitful. For example, Belay et al. estimated the value of ecosystem services in the African highlands of the Guna Mountains in northwestern Ethiopia for the period 1995–2020 and found a decreasing trend [48]. Hoque et al., estimating the value of ecosystem services in the coastal zone of Bangladesh, found that increased mangrove area and human activities led to a decrease in the value of ecosystem services in the overall coastal zone [49]. Deloyde et al. estimated the value of ecosystem services in southern Ontario, Canada, between 2002 and 2015 and found that the value of regulating services declined while the value of cultural services increased [50]. Therefore, this paper adopted a modified equivalence factor method for unit area values, which combines the ecosystem characteristics of the study area to provide a more accurate assessment of ESV. The value of ecosystem services has significant spatial variation, which is the result of the interaction between natural and socio-economic factors. Therefore, attention should be paid to spatial differentiation when exploring the influence mechanisms of value of ecosystem services.

4.2. Impacts of Land Use on the Value of Ecosystem Services

Our study area is an important part of China's ecologically fragile northwest. It is also the core of the Silk Road Economic Belt, so ecological monitoring of this area is crucial. Since 1990, the transformation between land-use types has been dramatic, due mostly to the combined effects of global warming and socio-economic development. A large amount of grassland has been transformed into cropland and barren land, while the water area has maintained an upward trend after initially increasing and then decreasing. The fastest increase occurred from 2000 to 2010. The conversion of barren land to water is mostly the result of the accelerated water cycle and global warming [51].

In general, the conversion of ESV low-value land types to high-value land types is one of the main reasons for the increase in ESV. This suggests that the northern slopes of the Kunlun Mountains are in a zone that is sensitive to global changes and responds more directly to temperature increases and intensified water cycles within the arid zone. Accordingly, when further developing the economy in the north, attention should be paid to the impact of the significant reduction in grassland areas on the fragile ecological environment. Furthermore, ecological problems such as the waste of water resources and the shortage of ecological water supply downstream due to the increase in cropland areas and water conservancy facilities should also be considered [52]. Alongside vigorously promoting living standards, we still need to focus on improving the quality of the living environment. The increase and protection of ecological land will, to a certain extent, alleviate the human/land conflict and improve the region's overall ESV.

Although the ESV benefits in the study area have increased, enormous ecological problems remain in the region. The impact of multiple factors should be considered when exploring the balance point of loss and gain of regional ESV, and ecological restoration projects should be implemented according to the regional environmental characteristics to achieve the purpose of maintaining regional ecological assets and promoting green and high-quality development. María [53] argued that increased land-use intensity alters key components critical to ecosystem functioning and changes the synergies between biodiversity and ecosystem functions and services and that different land-use types respond differently to the valuation of ecological services. In the spatial deployment of the value of ecosystem services, policymakers should thus focus on the trade-offs between land market returns, ecosystem restoration, and biodiversity conservation [54].

In addition, there is as yet no universally accepted method to explore the impact of land-use change on ESV based on a spatial scale. In this paper, we applied the spatial autocorrelation analysis method based on grid cells, as we hoped this approach would better express the response of ESV to land-use change from a spatial perspective. We also used the LISA clustering map and ESV hotspot map to show the characteristics of ESV distribution change. This combined approach can provide a feasible way for future exploration of the impact of land-use evolution on the value of ecosystem services.

Moreover, in our research, we found that High–High-type areas are mostly located in the mountains and at the intersection of mountains and plains, indicating that the vegetation area is significantly increasing. This finding further supports that the increase in surface water resources leads to the expansion of vegetation area under climate change, thus affecting ESV changes. The increase in Low–High type areas points to an increase in cropland area, which is highly aggregated in space. However, ESV remains of low value because the ecosystem service capacity of agricultural land is weak.

In the spatial correlation analysis from 2010 to 2020, a decreasing trend was found in the High–High-type area, mainly due to a reduction in the watershed. The change in the area of water resources was affected by numerous factors, including increases in temperature and the conversion of ecological land such as grassland, wetland, and watershed into agricultural land and wasteland by excessive reclamation.

4.3. Ecological Conservation and Development in the Study Area

To explore the value of ecosystem services on the northern slopes of the Kunlun Mountains, land-use data from 1990 to 2020 were selected and combined with the CA–Markov model, and the status and future changes in ecosystem services on the northern slopes of the Kunlun Mountains were analyzed. By comparing the changing characteristics of ESV between the study area and other regions in Xinjiang, China, it was found that the changing trends are not the same. For example, the ESV of the Aksu River Basin in Xinjiang showed a fluctuating upward trend from 1990 to 2020 [55], while the ESV of the northern edge of the Tarim River Basin showed a continuous downward trend from 1994 to 2016 [56]. From a regional perspective, from 2000 to 2015, the overall ESV of Xinjiang showed a downward trend [57]. The differences in ESV between regions are mainly caused by differences in land-use structure, terrain, time scale, and research area scale. Zuripia et al. estimated that the ecosystem service value of the Kashgar River Basin showed an upward trend from 2000 to 2020 [58]. The CA–Markov model is also one of the more accurate prediction methods currently available. Gasirabo et al. Predictive assessment of land use in Chittagong Hill Tracts, Bangladesh, using CA–Markov modeling [59]. Amir Siddique et al., in their study of Beijing's urban heat, also used the CA–Markov model to predict Beijing's land use for the period 2004–2050 [60]. Therefore, we concluded that the ecosystem service value of the northern slopes of the Kunlun Mountains showed an upward trend between 1990 and 2030.

In addition, the ecological problems of the northern slopes of the Kunlun Mountains, which are at the core of the Silk Road Economic Belt, are one of the biggest obstacles to the ecological restoration process of China's "green water and green mountains". In recent years, against a background of global changes and the intensification of human

activities [61], the ecological environment of the study region has become increasingly fragile, and the conflict between humans and land has intensified, seriously hindering the progress of ecological civilization construction in the basin. This paper takes the spatial and temporal changes in ESV as an entry point to map the ecological assets of the watershed at both temporal and spatial scales to measure the current ecological status of the watershed and visual changes in ecological assets and to provide more general theoretical support for decision-makers in formulating ecological restoration policies. In addition, the study of dynamic changes in ESV at spatial scales provides basic support for delineating regions to formulate ecological restoration policies to ensure their implementation in accordance with local conditions.

5. Conclusions

Based on long-term land-use data and spatial autocorrelation analysis, this paper explores the impacts of land-use pattern evolution on ecosystem service values on the northern slopes of the Kunlun Mountains from 1990 to 2020 and the analysis of future simulation prediction. The study uses grid cells to cover the study area and the modified unit area equivalent factor method. The main findings are as follows:

(1) Unexploited land, grassland, and watershed are the land-use types that account for more than 85% of the study area. During the study period, the water area showed a continuous growth trend, while grassland, cropland, woodland, and construction land showed a fluctuating growth trend and barren land charted a continuous decline. Among these land types, construction land had the highest increase (291.04%), followed by woodland, whereas grassland had the lowest increase. Only barren land showed a decrease.

(2) The ESV of the study area trended slightly downward from 1990 to 2000 and sharply upward from 2000 to 2010, and then reverted to a slight downward trend from 2010 to 2020. The overall ESV showed an upward trend from 1990 to 2020, with a total increase of CNY 17.906 billion. The upward trend of watershed areas intensified the most from 2000 to 2010, with ESV increasing by CNY 39.857 billion due mainly to low-value land-use types shifting to high-value land-use types.

(3) In terms of space, the value-added areas of ESV in the study area from 1990 to 2020 are mainly concentrated in the northwest and southern regions of the study area. the loss area of ESV is mainly distributed in the northern part of the study area. Based on the cold and hot spot map of ESV changes in the study area, it can be seen that the ecosystem service value of the northern slopes of the Kunlun Mountains is increasing. According to the CA–Markov model analysis, the grassland, forest land, and water area in the study area will increase from 2020 to 2030. The growth trend of the ecosystem service value of the northern slopes of the Kunlun Mountains is obvious in 2030, and the ecological environment will steadily improve. This is due to the conversion of unused land into grassland and forest land. We also found that the conversion of unused land into grassland has a positive impact on the ecology of the region. In the future, we will continue to research the northern slopes of the Kunlun Mountains, explore the driving factors of ecosystem service value, and conduct in-depth research on the impact of climate change on the ecosystem service value of the northern slopes of the Kunlun Mountains.

Author Contributions: Y.W. contributed to the formulation of the research questions; Z.Z. (Zhichao Zhang) performed the data analysis and paper writing; H.T. and Z.Z. (Zhen Zhu) were responsible for data processing and interpretation of the results. Y.W. managed the project and funded this paper. All authors have read and agreed to the published version of the manuscript.

Funding: This research was funded by the Third Xinjiang Scientific Expedition Program (Grant No: 2021xjkk010202).

Data Availability Statement: The data presented in this study are available on request from the corresponding author.

Conflicts of Interest: The authors declare no conflict of interest.

References

1. Costanza, R.; D'Arge, R.; Groot, R.D.; Farber, S.; Grasso, M.; Hannon, B.; Limburg, K.; Naeem, S.; Neill, R.V.; Paruelo, J.; et al. The value of the world's ecosystem services and natural capital. *Nature* **1997**, *387*, 253–260. [CrossRef]
2. Darvill, R.; Lindo, Z. The inclusion of stakeholders and cultural ecosystem services in land management trade-off decisions using an ecosystem services approach. *Landsc. Ecol.* **2016**, *31*, 533–545. [CrossRef]
3. Daily, G.C. *Nature's Services: Societal Dependence on Natural Ecosystems*; Island Press: Washington, DC, USA, 1997; p. 3.
4. OuYang, Z.Y.; Wang, X.K.; Miao, H. A preliminary study on the service functions of terrestrial ecosystems and their ecological and economic values in China. *J. J. Ecol.* **1999**, *5*, 19–25.
5. Xie, G.D.; Zhang, C.X.; Zhang, C.S.; Xiao, Y.; Lu, C.X. The value of ecosystem services in China. *Resour. Sci.* **2005**, *37*, 1740–1746.
6. Parron, L.M.; Villanueva, A.J.; Glenk, K. Estimating the value of ecosystem services in agricultural landscapes amid intensification pressures: The Brazilian case. *Ecosyst. Serv.* **2022**, *57*, 101476. [CrossRef]
7. Shi, F.; Zhou, B.; Zhou, H.; Zhang, H.; Li, H.; Li, R.; Guo, Z.; Gao, X. Spatial Autocorrelation Analysis of Land Use and Ecosystem Service Value in the Huangshui River Basin at the Grid Scale. *Plants* **2022**, *11*, 2294. [CrossRef]
8. Braun, D.; de Jong, R.; Schaepman, M.E.; Furrer, R.; Hein, L.; Kienast, F.; Damm, A. Ecosystem service change caused by climatological and non-climatological drivers: A Swiss case study. *Ecol. Appl. A Publ. Ecol. Soc. Am.* **2019**, *29*, e01901. [CrossRef]
9. Pan, N.; Guan, Q.; Wang, Q.; Sun, Y.; Li, H.; Ma, Y. Spatial differentiation and driving mechanisms in ecosystem service value of arid region:a case study in the middle and lower reaches of shule river basin, nw china. *J. Clean. Prod.* **2021**, *319*, 128718. [CrossRef]
10. Nelson, E.; Mendoza, G.; Regetz, J.; Polasky, S.; Tallis, H.; Cameron, D.R.; Chan, K.M.A.; Daily, G.C.; Goldstein, J.; Kareiva, P.M. Modeling multiple ecosystem services, biodiversity conservation, commodity production, and tradeoffs at landscape scales. *Front. Ecol. Environ.* **2009**, *7*, 4–11. [CrossRef]
11. Felipe-lucia, M.R.; Comín, F.A.; Bennett, E.M. Interactions among ecosystem services across land uses in a floodplain agroecosystem. *Ecol. Soc.* **2014**, *19*, 360–375. [CrossRef]
12. Gren, I.M.; Groth, K.H.; Sylvén, M. Economic values of danube floodplains. *J. Environ. Manag.* **1995**, *45*, 333–345. [CrossRef]
13. Benez, S.; Fabio, J.D.; Puneet, F.; Susana, H.C.; Jeffrey, W. Trade-offs Between the Value of Ecosystem Services and Connectivity Among Protected Areas in the Upper Chattahoochee Watershed. *J. Environ. Manag.* **2022**, *69*, 937–951.
14. Wu, C.Y.; Chen, B.; Huang, X.J.; Wei, Y.H.D. Effect of land-use change and optimization on the ecosystem service values of Jiangsu province, China. *J. Ecol. Indic.* **2020**, *117*, 106507. [CrossRef]
15. Gagarin, L.; Wu, Q.; Cao, W. Icings of the Kunlun Mountains on the Northern Margin of the Qinghai-Tibet Plateau, Western China: Origins, Hydrology and Distribution. *J. Water* **2022**, *14*, 2396. [CrossRef]
16. Kang, L.; Jia, Y.; Zhang, S.L. Spatiotemporal distribution and driving forces of ecological service value in the Chinese section of the "Silk Road Economic Belt". *J. Ecol. Indic.* **2022**, *141*, 109074. [CrossRef]
17. Ma, X.; Zhang, H. Land-Use/Land-Cover Change and Ecosystem Service Provision in Qinghai Province, China: From the Perspective of Five Ecological Function Zones. *J. Land.* **2023**, *12*, 656. [CrossRef]
18. Chen, Y.; Xu, E. The Spatiotemporal Change in Land Cover and Discrepancies within Different Countries on the Qinghai–Tibet Plateau over a Recent 30-Year Period. *Land* **2023**, *12*, 1797. [CrossRef]
19. Hughes-Allen, L.; Bouchard, F.; Séjourné, A.; Fougeron, G.; Léger, E. Automated Identification of Thermokarst Lakes Using Machine Learning in the Ice-Rich Permafrost Landscape of Central Yakutia (Eastern Siberia). *Remote Sens.* **2023**, *15*, 1226. [CrossRef]
20. Mantas, V.; Caro, C. User-Relevant Land Cover Products for Informed Decision-Making in the Complex Terrain of the Peruvian Andes. *Remote Sens.* **2023**, *15*, 3303. [CrossRef]
21. Druckenmiller, H. Accounting for ecosystem service values in climate policy. *J. Nat. Clim. Chang.* **2022**, *12*, 596–598. [CrossRef]
22. Maimaiti, B.; Chen, S.; Kasimu, A. Coupling and Coordination Relationships between Urban Expansion and Ecosystem Service Value in Kashgar City. *Remote Sens. J.* **2022**, *14*, 2557. [CrossRef]
23. Niu, S.; Sun, M.; Wang, G.; Wang, W.; Yao, X.; Zhang, C. Glacier Change and Its Influencing Factors in the Northern Part of the Kunlun Mountains. *Remote Sens.* **2023**, *15*, 3986. [CrossRef]
24. Zhang, Z.; Xia, F.; Yang, D.; Huo, J.; Chen, H. Spatiotemporal characteristics in ecosystem service value and its interaction with human activities in Xinjiang, China. *J. Ecol. Indic.* **2020**, *110*, 105826. [CrossRef]
25. Beaudon, E.; Sheets, J.M.; Martin, E.; Sierra-Hernández, M.R.; Mosley-Thompson, E.; Thompson, L.G. Aeolian Dust Preserved in the Guliya Ice Cap (Northwestern Tibet): A Promising Paleo-Environmental Messenger. *Geosciences* **2022**, *12*, 366. [CrossRef]
26. Zhu, S.; Zhao, Y.; Huang, J.; Wang, S. Analysis of Spatial-Temporal Differentiation and Influencing Factors of Ecosystem Services in Resource-Based Cities in Semiarid Regions. *J. Remote Sens.* **2023**, *15*, 871. [CrossRef]
27. Ma, X.; Yan, W.; Zhao, C.; Kundzewicz, Z.W. Snow-Cover Area and Runoff Variation under Climate Change in the West Kunlun Mountains. *Water* **2019**, *11*, 2246. [CrossRef]

28. Li, C.G.; Wang, M.; Liu, W.; Lee, S.Y.; Hou, J. Quantitative estimates of Holocene glacier meltwater variations on the Western Tibetan Plateau. *J. Earth Planet. Sci. Lett.* **2021**, *559*, 116766. [CrossRef]
29. Lu, Q.; Hua, D.; Li, Y.; Wang, D. Estimation of Water Resource Ecosystem Service Value inTarim River Basin—From a Full Value Chain Perspective. *Water* **2022**, *14*, 2355. [CrossRef]
30. Xu, H.; Yang, J.; Xia, G.; Lin, T. Spatio-temporal Differentiation of Coupling Coordination between Ecological Footprint and Ecosystem Service Functions in the Aksu Region, Xinjiang, China. *Sustainability* **2022**, *14*, 3483. [CrossRef]
31. Adila, A.; Abudukeyimu, A.; Abdugheni, A.; Abdulla, A.; Jiao, J.; Bin, O. Land Use and Land Cover Change Effects on the Value of Ecosystem Services in the Konqi River Basin, China, under Ecological Water Conveyance Conditions. *Forests* **2023**, *14*, 1028.
32. Yang, J.; Huang, X. The 30 m annual land cover dataset and its dynamics in China from1990 to 2019. *J. Earth Syst. Sci. Data* **2021**, *13*, 3907–3925. [CrossRef]
33. Liu, C.; Xu, R.; Xu, K.; Lin, Y.; Cao, Y. Carbon Emission Effects of Land Use in Chaobai River Region of Beijing–Tianjin–Hebei, China. *Land* **2023**, *12*, 1168. [CrossRef]
34. Xie, G.D.; Zhang, C.X.; Zhen, L.M.; Chen, W.H.; Li, S.M. Dynamic changes in the value of China's ecosystem services—ScienceDirect. *J. Ecosyst. Serv.* **2017**, *26*, 146–154. [CrossRef]
35. Zhang, S.; Wang, Y.; Wang, Y.; Li, Z.; Hou, Y. Spatiotemporal Evolution and Influencing Mechanisms of Ecosystem Service Value in the Tarim River Basin, Northwest China. *Remote Sens.* **2023**, *15*, 591. [CrossRef]
36. Ling, H.B.; Yan, J.J.; Xu, H.L.; Guo, B.; Zhang, Q.Q. Estimates of shifts in ecosystem service values due to changes in key factors in the Manas River basin, northwest China. *J. Sci. Total Environ.* **2019**, *659*, 177–187. [CrossRef]
37. Orna, R.; Shiri, Z.; Ido Izhaki, A.L. The effect of wildfire and land-cover changes on the economic value of ecosystem services in Mount Carmel Biosphere Reserve, Israel. *J. Ecosyst. Serv.* **2021**, *49*, 101291.
38. Wan, L.H.; Wang, S.W.; Chen, X.H. Spatial correlation of GDP in Hadazhi industrial corridor based on GeoDA. *Geogr. Res.* **2011**, *30*, 8.
39. Wu, X.; Zhang, L.; Gao, L.; Li, Y.; Liu, X. Change and Tradeoff/Synergy Analysis of Watershed Ecosystem Services: A Case Study of Qinghai Lake Basin. *Sustainability* **2023**, *15*, 11711. [CrossRef]
40. Guo, C.Y.; Gao, S.; Zhou, B.Y.; Gao, J.H. Effects of land use change on ecosystem service value in Funiu Mountain based upon a grid square. *J. Acta Ecol. Sin.* **2019**, *39*, 3482–3493.
41. Di-Gregaria, A.; Jonsen, L.J. *Land Cover Classification System, Concepts and User Manual*; FAO: Rome, Italy, 2005.
42. Bcp, A.; Dgb, B.; Bas, C.; Gam, D. Using neural networks and GIS to forecast land use changes: A Land Transformation Model. Computers. Environ. *Urban Syst.* **2002**, *26*, 553–575.
43. Ouyang, Z.; Zheng, H.; Xiao, Y.; Polasky, S.; Liu, J.; Xu, W.; Wang, Q.; Zhang, L.; Xiao, Y.; Rao, E.; et al. Improvements in ecosystem services from investments in natural capital. *J. Sci.* **2016**, *352*, 1455–1459. [CrossRef]
44. Long, X.R.; Lin, H.; An, X.X.; Chen, S.D.; Qi, S.Y.; Zhang, M. Evaluation and analysis of ecosystem service value based on land use/cover change in Dongting Lake wetland. *J. Ecol. Indic.* **2022**, *136*, 108619. [CrossRef]
45. Li, C.; Zheng, H.; Li, S.Z.; Chen, X.S.; Li, J.; Zeng, W.H.; Liang, Y.C.; Polasky, S.; Feldman, M.W.; Ruckelshaus, M.; et al. Impacts of conservation and human development policy across stakeholders and scales. *Proc. Natl. Acad. Sci. USA* **2015**, *112*, 7396–7401. [CrossRef]
46. Cheng, Q.; Zhou, L.; Wang, T. Assessment of ecosystem services value in Linghekou wetland based on landscape change. *Environ. Sustain. Indic.* **2022**, *15*, 100195. [CrossRef]
47. Xiao, Y.; Huang, M.D.; Xie, G.D.; Zhen, L. Evaluating the impacts of land use change on ecosystem service values under multiple scenarios in the Hunshandake region of China. *J. Sci. Total Environ.* **2022**, *850*, 158067. [CrossRef]
48. Belay, T.; Melese, T.; Senamaw, A. Impacts of land use and land cover change on ecosystem service values in the Afroalpine area of Guna Mountain, Northwest Ethiopia. *Heliyon* **2022**, *8*, e12246. [CrossRef]
49. Hoque, M.Z.; Islam, I.; Ahmed, M.; Hasan, S.S.; Prodhan, F.A. Spatio-temporal changes of land use land cover and ecosystem service values in coastal Bangladesh. *Egypt. J. Remote Sens. Space Sci.* **2022**, *25*, 173–180.
50. DeLoyde, C.N.M.; Mabee, W.E. Ecosystem service values as an ecological indicator for land management decisions: A case study in southern Ontario, Canada. *Ecol. Indic.* **2023**, *151*, 110344. [CrossRef]
51. Hang, X.; Chen, D.C.; Fan, J.D.; Yu, C.; Zhou, Y.; Tang, J.J. Study on the change of ecosystem service value and its correlation with human activities: Taking Changzhou City as an example. *J. Environ. Eng. Technol.* **2022**, *12*, 2124–2131.
52. Liu, W.; Liu, Z.; An, Z. Late Miocene episodic lakes in the arid Tarim Basin, western China. *Proc. Natl. Acad. Sci. USA* **2014**, *111*, 16292–16296. [CrossRef] [PubMed]
53. María, R.F.L.; Soliveres, S.; Penone, C. Land-use intensity alters networks between biodiversity, ecosystem functions, and services. *Proc. Natl. Acad. Sci. USA* **2020**, *117*, 28140–28149.
54. Gui, D.; Lei, J.; Mu, G.; Zeng, F. Effects of different management intensities on soil quality of farmland during oasis development in southern Tarim Basin, Xinjiang, China. *J. Int. J. Sustain. Dev. World Ecol.* **2009**, *16*, 295–301. [CrossRef]
55. Xie, L.; Wang, H.W.; Liu, S.H. The ecosystem service values simulation and driving force analysis based on land use/land cover: A case study in inland rivers in arid areas of the Aksu River Basin, China. *J. Ecol. Indic.* **2022**, *138*, 108828. [CrossRef]
56. Ling, H.B.; Guo, B.; Zhang, G.P.; Xu, H.L.; Deng, X.Y. Evaluation of the ecological protective effect of the "large basin" comprehensive management system in the Tarim River basin, China. *Sci. Total Environ.* **2019**, *650*, 1696–1706. [CrossRef]

57. Wang, Y.; Shataer, R.; Zhang, Z.C.; Zhen, H.; Xia, T. Evaluation and Analysis of Influencing Factors of Ecosystem Service Value Change in Xinjiang under Different Land Use Types. *J. Water* **2022**, *14*, 1424. [CrossRef]
58. Kulaixi, Z.; Chen, Y.; Li, Y.; Wang, C. Dynamic Evolution and Scenario Simulation of Ecosystem Services under the Impact of Land-Use Change in an Arid Inland River Basin in Xinjiang, China. *J. Remote Sens.* **2023**, *15*, 2476. [CrossRef]
59. Yu, X.; Xiao, J.; Huang, K.; Li, Y.; Lin, Y.; Qi, G.; Liu, T.; Ren, P. Simulation of Land Use Based on Multiple Models in the Western Sichuan Plateau. *Remote Sens.* **2023**, *15*, 3629. [CrossRef]
60. Amir Siddique, M.; Wang, Y.; Xu, N.; Ullah, N.; Zeng, P. The Spatiotemporal Implications of Urbanization for Urban Heat Islands in Beijing: A Predictive Approach Based on CA–Markov Modeling (2004–2050). *Remote Sens.* **2021**, *13*, 4697. [CrossRef]
61. Huang, X.; Ma, J.L. Changes in the ecosystem service values of typical river basins in arid regions of Northwest China. *J. Ecohydrol.* **2013**, *6*, 1048–1056. [CrossRef]

Disclaimer/Publisher's Note: The statements, opinions and data contained in all publications are solely those of the individual author(s) and contributor(s) and not of MDPI and/or the editor(s). MDPI and/or the editor(s) disclaim responsibility for any injury to people or property resulting from any ideas, methods, instructions or products referred to in the content.

land

MDPI

Article

Assessing the Effects of Subjective and Objective Measures on Housing Prices with Street View Imagery: A Case Study of Suzhou

Jin Zhu [1,2,*], Yao Gong [1], Changchang Liu [1], Jinglong Du [1], Ci Song [2,3], Jie Chen [2,3] and Tao Pei [2,3,4,*]

[1] School of Geography Science and Geomatics Engineering, Suzhou University of Science and Technology, Suzhou 215009, China; 2113021105@post.usts.edu.cn (Y.G.); liuchangchang1025@163.com (C.L.); jldu@mail.usts.edu.cn (J.D.)
[2] State Key Laboratory of Resources and Environmental Information System, Institute of Geographical Sciences and Natural Resources Research, Chinese Academy of Sciences, Beijing 100101, China; songc@lreis.ac.cn (C.S.); chenj@lreis.ac.cn (J.C.)
[3] University of Chinese Academy of Sciences, Beijing 100101, China
[4] Jiangsu Center for Collaborative Innovation in Geographical Information Resource Development and Application, Nanjing 210023, China
* Correspondence: zhujin@usts.edu.cn (J.Z.); peit@lreis.ac.cn (T.P.)

Abstract: The price of a house is affected by both the subjective and objective factors of the street environment in a neighborhood. However, the relationships between these factors and housing prices are not fully understood. Street view imagery (SVI) has recently emerged as a new data source for housing price studies. The SVI contains both objective and subjective information and can be used to extract objective measurements describing the physical environment and subjective measurements depicting human perceptions. Compared to conventional methods, there is consistency between subjective and objective information extracted from SVIs, and the two types of information are acquired from the perspective of the human visual perceptual system. Therefore, using both objective and subjective information extracted from street view images to study their relationship with housing prices has several advantages. In this study, focusing on the city of Suzhou, China, we extracted subjective perception and objective view indices from SVIs and systematically assessed their effects on housing prices. The global ordinary least squares (OLS) regression model and the local geographically weighted regression (GWR) model were used to model the correlations between these measures and housing prices. The OLS reveals that overall objective measures have stronger explanatory power, and built environment factors have a greater impact on housing prices. GWR shows that subjective factors can explain more variance in housing prices on the local scale and that home buyers care more about the subjective perceptions of the neighborhood's surroundings. The map of the GWR local coefficients demonstrates that the perception indicators have both positive and negative effects on housing prices in different places. In addition, a Monte Carlo test was performed to verify the spatially varying relationships between these measures. Our findings provide important references for urban designers and guide various applications, such as safe neighborhood design and sustainable city planning.

Keywords: street view imagery; housing prices; human perception; Simpson's paradox; geographically weighted regression

1. Introduction

Housing price studies have received growing attention in recent years because of the availability of housing data and the important role of housing in human life [1–3]. Housing prices are determined by several groups of characteristics, such as structural, locational and neighborhood attributes [4]. Streets near houses can provide residents with opportunities for strolling and socializing [5]. The streetscape is the "outdoor room" one encounters

when turning the corner or stepping out the door into the street [6]. The quality of a streetscape is associated with user well-being [7]. People tend to live in houses surrounded by high-quality streetscapes with many trees or that are perceived as beautiful and safe [8,9]. Understanding the relationship between streetscapes and housing prices can provide new insights into the composition of housing prices and is beneficial for applications, such as urban planning and real estate.

Conventional approaches to streetscape evaluation include field surveys and interviews. These methods may lead to potential biases and are costly and time consuming [10]. Street view imagery (SVI) has recently become widely used as an emerging source of big data [11,12]. The SVI is publicly available and provides an alternative to traditional methods [11]. Owing to machine learning and deep learning, the SVI has become highly effective for assessing streetscapes in urban environments. There are two types of indicators for measuring streetscape qualities from the SVI [13]. The first is an objective measure that describes the physical appearance of streets, such as the green view index (GVI) [14], pedestrian volume [15], and sidewalk length [16]. Prior studies have mainly used objective measures to study the relationship between streetscape quality and housing prices [8,17]. For example, visible street greenery has been found to have a significant positive effect on housing prices [8]. However, we can only learn about one side of a street from objective measurements. Specifically, they do not capture a street's human perceptions, which may have subtle or complex relationships with physical elements [18]. The second category includes subjective measures depicting human perceptions, such as beautiful, safe and enclosure [19]. They described the raters' overall perceptions of street view images. Analyzing the effects of the street environment's human perceptions on housing prices may provide a comprehensive understanding of housing prices [13]. For example, the enclosure measurement was found to have a negative relationship with housing prices [13]. Although objective and subjective measures have distinct effects on housing prices, the strength of the association between these measures and housing prices is not fully understood.

Previous research has focused on the perceptions favored by urban planners [13,20,21]. These perceptions included enclosure, human scale, complexity, imageability, safety, greenness, and walkability. These are the professional opinions of urban planners, which are difficult for ordinary house buyers to comprehend. Personal perceptions, which are more subjective than professional perceptions [18], such as safety, wealthy, lively, beautiful, boring, depressing [9], class, and uniqueness [22], are closely related to residents' daily lives. Therefore, for housing buyers and renters, these personal perceptions offer additional references and values. However, prior studies usually employed the Place Pulse dataset (Place Pulse 1.0 and 2.0) [9] created by MIT Senseable City Lab researchers to measure the visual perceptions of Google Street View images, which may not be appropriate for Chinese cities. The Place Pulse 2.0 dataset contains 110,988 SVIs spanning 56 cities in 28 countries [23] and does not include SVIs from mainland China. Although the Place Pulse 2.0 dataset can be applied to other cities, each city has its own socio-economic status or physical environments, such as building styles [24–26], which may pose problems and lead to perceptual biases in people. To estimate premiums on housing prices, it would be ideal to use a perception dataset with locally obtained SVIs and local evaluations.

This study aimed to understand the impact of subjective emotional and objective view measures on housing prices using locally obtained SVIs in China through a comprehensive assessment. In this study, we extracted subjective perception and objective view indices from SVIs and systematically compared their effects on housing prices. We considered Suzhou City, China, as an example. The subjective perceptions were safety, wealthy, lively, beautiful, boring, and depressing, and they were more relevant to people's daily lives. Locally collected SVIs were used to train a deep learning model to predict human perceptions of the street environment. The effects of subjective and objective measures on housing prices were assessed with ordinary least squares (OLS) regression. To account for spatial heterogeneity, GWR was also performed.

This study makes three main contributions to the literature. First, we comprehensively assessed the relationship between objective/subjective measures and housing prices. Second, we discussed how certain perceptions may affect housing prices. Third, we explored the effects of these measures on housing prices, both globally and locally. We do not intend to make any causal statements. Our study aims to use this correlation to demonstrate the need to incorporate human perceptions into housing price studies. Our study provides a significant reference for urban planners to enhance urban environments from the viewpoint of human perception.

2. Literature Review

2.1. Housing Price Modeling and Spatial Heterogeneity

Extensive research has been conducted to analyze the different factors that affect housing prices [1,27,28]. The willingness to pay for these attributes can be inferred using the hedonic price modeling (HPM) method [4] in environmental economics. Due to its simplicity and interpretability, OLS regression is the most popular HPM technique.

OLS provides a set of coefficients for all observations and is, therefore, a global model. OLS ignores spatial heterogeneity, implying that different locations within a given area exhibit distinct features or patterns. This may lead to the Simpson's paradox, which refers to the reversal of results when datasets are analyzed separately and then combined. This indicates that it is risky to analyze aggregated data. It is essential to mitigate this problem by modeling spatially varying relationships [29].

Geographically weighted regression (GWR) [30] has been used as an effective model to detect spatially varying relationships. GWR estimates different coefficients for observations at different locations and is, therefore, a local model that can reduce the problem of Simpson's paradox. While OLS establishes the baseline, GWR is recommended for improving the estimation of housing prices.

2.2. Streetscape Measures from SVI

Both the objective and the subjective groups of information can be derived from SVIs. Examples of common objective measurements include the GVI [31,32], the sky view index (SVI) [33], blue spaces (e.g., rivers, lakes) [34], and frontage [35]. As objective measures are simpler to extract than subjective measures, some studies first extract view indices from SVIs and then use view indices to compute subjective human perceptions through specific mathematical models. For example, the view indices of psychological greenery, visual crowdedness, outdoor enclosure, and visual pavement were combined to constitute an integrated visual walkability index [36]. Ito employed both objective and subjective SVI indicators and other non-SVI indicators to construct a comprehensive bikeability index [37]. Ma [38] used objective view indices to form perceptions of openness, greenness, enclosure, walkability, and imageability. Subjective measures are believed to depict the environment more completely than objective measures [16]. Subjective measures have complex and subtle relationships with objective measures. Ewing presented operational definitions of five perceptions (imageability, enclosure, human scale, transparency, and complexity) and provided novel insights into the relationships between physical features and perceptions [18]. Street-level perceptions can be measured subjectively through surveys or objectively by recombining view indices extracted from SVI [38].

2.3. Effects of Streetscape Measures on Housing Prices

An important aspect of assessing the effectiveness of environmental policies in improving streetscapes is the quantitative measurement of the economic value of the benefits. Houses surrounded by better streetscapes will have this benefit capitalized into their value, and this should be reflected in a higher sales price. Regarding objective measures, Ye found that visible street greenery had a significant positive effect on housing prices [8]. Fu showed that greenery and sky view indices could significantly increase housing prices [17]. Chen found that the impacts of the green view index and sky view index on housing prices were

nonlinear; the green view index had a positive effect, whereas the sky view index had a negative effect [39] on housing prices. Objective measures can only describe the physical settings of the street environment and cannot fully capture people's overall perceptions of the streetscape [18].

For subjective measures, Buonanno confirmed that security perception was positive for a property's average value in Barcelona [40]. Kang incorporated six human perceptions (safe, beautiful, depressed, lively, wealthy, and boring) into the HPM and found that positive perceptions (beautiful, lively, safe, and wealthy) had a positive correlation with housing prices, and negative perceptions (depressing and boring) had a negative correlation [9]. The US cities of Boston and Los Angeles were selected as case studies for Kang's study. Based on the assumption that subjective indicators provide a more complete picture of the street environment, Qiu compared the strength of objective measures and subjective urban design-related measures (enclosure, human scale, complexity, imageability, and safety) and revealed that the subjective measures individually had stronger strength than the objective measures [13]. Despite employing the GWR to map the effects of various measures on housing prices, Qiu neglected to thoroughly examine the positive and negative effects of objective and subjective measures. Qiu subjectively and objectively measured six perceptions (greenness, safety, walkability, imageability, enclosure, and complexity) and found that the collective strengths of perception indicators were nearly equal for both subjective scores and objective counterparts; however, the subjective and objective indicators all had opposite individual signs in explaining price variance [20]. Xu took a similar approach and discovered that subjective scores explained more variance than objective scores and that perceptions could not be fully represented by objective indicators [21]. For professional perceptions (e.g., imageability), subjective indicators can explain more variance, but for self-evident perceptions (e.g., greenness), objective indicators perform better. Qiu and Xu used only the global model and did not consider local models, such as GWR [20,21]. Table 1 summarizes the models and measures used in studies on the effects of streetscape perceptions on housing prices.

Table 1. Models and measures of studies related to the effects of streetscape perceptions on housing prices.

Research	Model	Measures	Case Study
Buonanno [40]	OLS	security perception	Barcelona, Spain
Kang [9]	OLS, GWR, PCA	beautiful, lively, safe, wealthy, depressing and boring	Boston and Los Angeles, USA
Qiu [13]	OLS, GWR, Spatial Regression	enclosure, human scale, complexity, imageability, and safety	Shanghai, China
Qiu [20]	OLS	greenness, safety, walkability, imageability, enclosure, and complexity, with subjective survey and objective equations	Shanghai, China
Xu [21]	OLS	greenness, safety, walkability, imageability, enclosure, and complexity	Shanghai, China
this study	OLS, GWR	beautiful, lively, safe, wealthy, depressing and boring	Suzhou, China

2.4. Summary

The following three knowledge gaps regarding the effects of streetscape measures on housing prices are summarized:

First, personal perceptions have received little attention in the research on housing prices. The perceptions (safe, beautiful, depressing, lively, wealthy, and boring) are more relevant to local residents than Qiu and Xu's chosen perceptions (enclosure, human scale, complexity, imageability, and safety), which are based on urban planning theory [18]. Subjective measures of urban design are more readily available to designers and planners than to the general public. Therefore, they have fewer actionable implications for homebuyers

and residents [13]. The effects of these perceptions on housing prices are not very clear, and they have not been assessed or compared with objective measures.

Second, little research has been conducted on personal perceptions of housing prices in China. Kang's study focused on American cities, and the human perception dataset was the Place Pulse dataset, which primarily comprised Western cities. However, each city has unique characteristics. Urban perceptions obtained from the global Place Pulse dataset may not apply to Chinese cities. Using a perception dataset with locally obtained SVIs and local evaluations may be more appropriate for predicting perceptions.

Third, the global and local models have rarely been considered simultaneously. Most studies have employed global models, such as OLS. However, inferring a policy from the average results of a global model may be misleading. Local models, such as GWR, should be used to reveal the spatially varying effects of streetscape measures.

Based on the aforementioned analysis, we assessed and compared the effects of personal perceptions of housing prices with those of objective measures. Locally collected SVIs were used to train a deep learning model to predict human perceptions. The effects of these measures were assessed using OSL. To avoid misleading interpretations, GWR was employed to account for the spatial heterogeneity of these measures.

3. Data and Methods

3.1. Research Framework

The major steps of the research framework are listed below and presented in Figure 1. First, street view images were collected from the Baidu online map and fed into the deep learning models PSPNet and convolutional neural network (CNN) separately to obtain objective view indices (sky view index, tree view index) and subjective perception scores. Community housing price data and other related variables were gathered from the Anjuke online platform, and community price was set as the dependent variable. The road network and the point-of-interest (POI) datasets were used to calculate hedonic variables. Finally, the subjective perception scores and objective view indices were regarded as two groups of interpretable variables and added with control variables. Using these two groups of variables, we compared and analyzed the results of stepwise regression and GWR.

3.2. Study Area

Our analysis was conducted in Suzhou, a city located in the Jiangsu province of China ranging from 119° 55′ E to 121° 20′ E longitude and from 30° 47′ N to 32°02′ N latitude. The total area of Suzhou was 8657.32 km^2 and its population was 12.75 million as of 2020 [41]. Suzhou lies with Shanghai to the east and is the most populous city in Jiangsu Province. It is one of the first national historical and cultural cities, known as "the heaven on the earth". The central city consists of the Gusu District, Industrial Park District, Wuzhong District, Xin District, and Xiangcheng District. In 2020, the GDP of Suzhou exceeded 2 trillion Chinese Yuan(CNY) for the first time, making it the sixth 2 trillion CNY city in China, and the city's housing prices have been growing rapidly in recent years. Suzhou is characterized by a network of canals, rivers, and numerous small lakes. These waterways have earned Suzhou the nickname "Venice of the East". The city is known for its traditional architecture, with well-preserved historic areas featuring narrow streets, stone bridges, and traditional Chinese buildings. The central region of Suzhou was selected as the study area in the present study.

3.3. Data

3.3.1. Housing Prices

Housing prices for 1389 communities as of December 2022 were collected through web crawling technology from the Anjuke website [42]. Anjuke is a large website that offers real-estate information services and serves numerous cities in China. Community attributes, such as address, building year, property fee, floor area ratio, and greenspace proportion, were also gathered. Duplex flats and villas were not included in the scope of

this study, thus avoiding potential biases and increasing the reliability of the findings. Price is the average price of the properties currently on sale for the current month. The latitude and longitude coordinates of residential communities were gathered using Baidu Map's geocoding service, and community attributes were combined with housing price data, as shown in Figure 2.

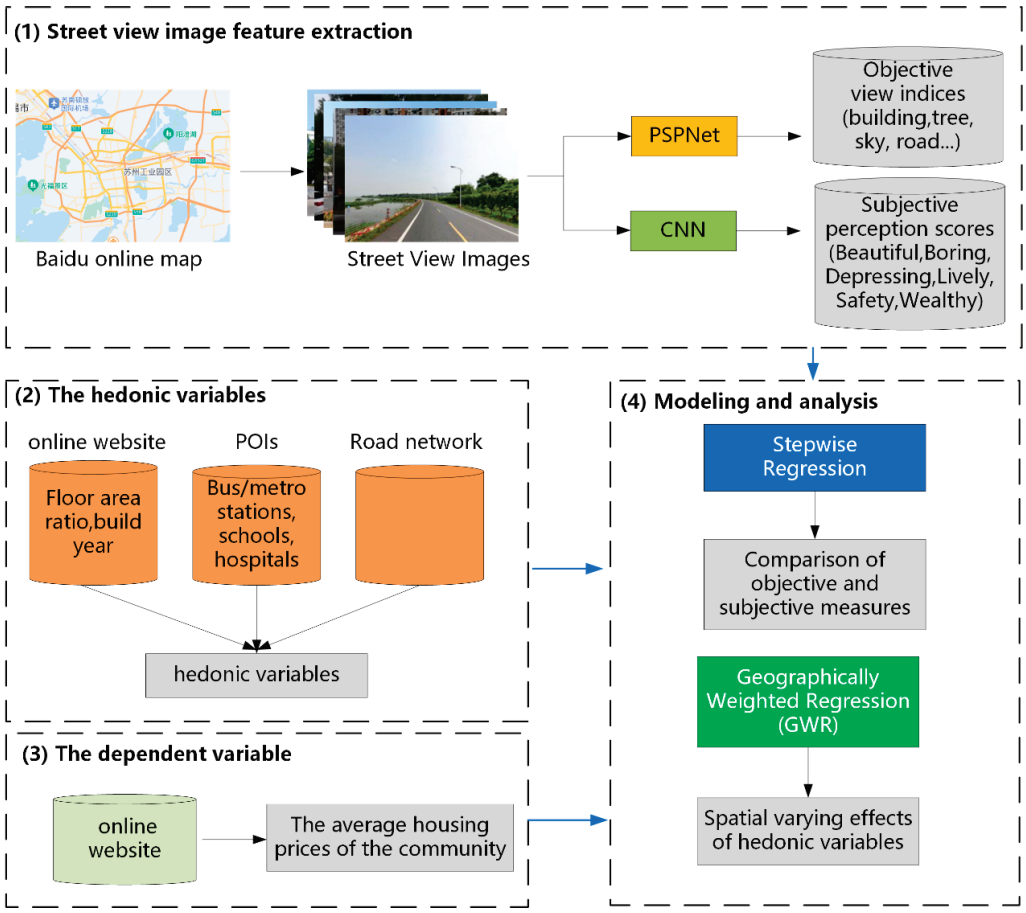

Figure 1. Research framework.

3.3.2. POI and Road Network

Additionally, POI data for Suzhou were gathered from the Baidu map platform using web crawling technology. The categories in the POI data were utilized to extract bus stations, metro stations, primary/middle schools, and hospitals, which were then used to compute the locational and neighborhood attributes in the HPM. The road network of Suzhou was extracted from the Open Street Map (OSM, https://www.openstreetmap.org (accessed on 21 May 2023)) and used to calculate the network distances between communities and amenities.

3.3.3. Street View Images

Subjective human perceptions and objective view indices of the street environment were obtained using SVIs. The SVIs of Suzhou were collected from the Baidu Map in December 2022. Baidu Maps, a Chinese map service provider, is comparable to Google Maps in that it provides street viewing services to numerous Chinese cities. We used the road network data of Suzhou City to construct sampling points for street view images at 100 m intervals along the streets. Based on the location of the sampling points, images in the horizontal direction closest to the sampling points were obtained through web requests. Four acquisition directions (90°, 180°, 270°, and 360°) were specified at each sampling

point to capture its full view. Each image had a resolution of 960 × 720 pixels. There were 43,382 sampling points in the study area, and 173,528 images were collected.

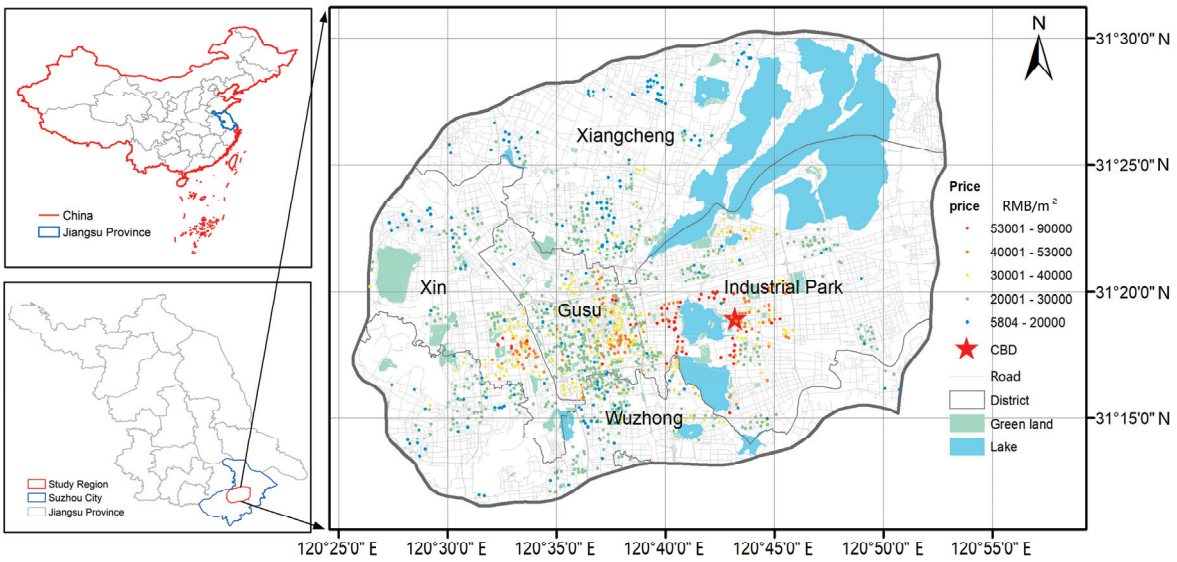

Figure 2. Spatial distribution of community housing prices in Suzhou.

3.4. Data Preprocessing

3.4.1. Calculation of Subjective Perception Scores

Deep learning is the primary method used to extract human perceptions from SVIs. Deep learning can be used to obtain human perception in two ways. One fits the human perception scores directly and automatically learns the deep features of an image. For instance, Dubey et al. trained an end-to-end Siamese-like convolutional neural model on the Place Pulse 2.0 dataset to predict the human perception score of a street view image [23]. Wang et al. [43] designed a CNN model based on VGGNet and trained it on a Chinese urban perception dataset [44]. Another method extracts image features using deep learning semantic segmentation techniques and uses additional machine learning models, such as the random forest model, to fit the human perception scores. For example, Yao et al. employed a fully convolutional network to semantically segment the features of SVIs and estimate the areal ratio of each semantic object [24]. The areal ratios were then fed into a random forest model to fit human perceptions. Zhang et al. developed a CNN model based on a residual network to learn the deep features of SVIs and trained an SVM classifier to predict the human perception score [19].

The accuracies of the CNN approach and Yao's method were compared by Wang et al. [24], and it was discovered that the former was superior to the latter because it considered the topological properties of semantic objects [44]. The former method is faster and simpler. Furthermore, the CNN model introduced by Wang et al. was open-source (https://doi.org/10.6084/m9.figshare.12552233 (accessed on 23 May 2023)), trained on a Chinese (Wuhan city) urban perception dataset, and was more suitable for the present study than other models trained on the global Place Pulse 2.0 dataset. Therefore, we employed Wang's CNN model to quantify the human perception scores of the SVIs.

The architecture of Wang's model is illustrated in Figure 3. Traditional CNN models are typically used for image classification tasks. Wang modified the traditional CNN model and replaced the softmax layer used for classification with a fully connected layer to gather deep-image features and predict human perceptions.

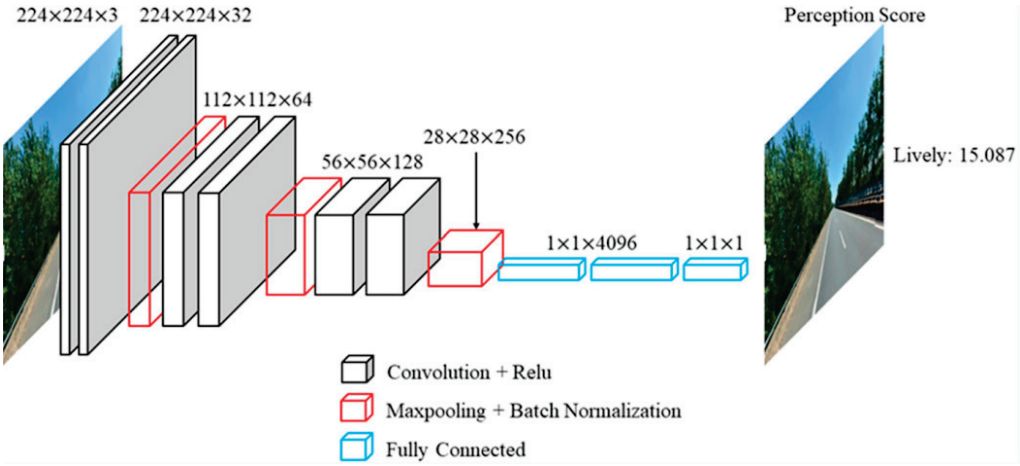

Figure 3. Subjective perception score calculations via the CNN model [44].

After predicting the six perception scores for each SVI, the average SVI scores for the SVIs of all four directions at each sampling point were calculated. Then, the scores of the SVIs with a 1 km buffer (15 min walking distance) of a community were averaged to represent the street perception of the community [13,36]. Descriptive statistics for the six perceptions are presented at the bottom of Table 2.

3.4.2. Extracting Objective View Indices

The objective view index of a street view image is the areal ratio of a semantic object to the total number of pixels in the image. This can be calculated using Equation (1).

$$VI_{obj} = \frac{\sum_{i=1}^{m} Area_{obj_i}}{\sum_{i=1}^{m} Area_{total_i}} \times 100\% \quad (1)$$

where $Area_{obj_i}$ is the number of pixels of a particular object obj (e.g., building, sky, or tree) obtained by the deep learning semantic segmentation algorithm in direction i. $Area_{total_i}$ is the total number of pixels of one SVI. The number m represents the number of SVI orientations that a camera will capture at one sample point, which was four in this study.

To extract semantic features from the SVIs, the Pyramid Scene Parsing Network (PSP-Net) model [45] was employed. PSPNet is a deep-learning-based semantic segmentation network that extracts scene information from global to local scales to better recognize and distinguish between various objects. Figure 4 shows the PSPNet architecture. PSPNet has a wide range of applications in image segmentation and scene understanding tasks, with advantages such as high accuracy, high speed, and low computational cost. This is appropriate for various high-level computer vision tasks.

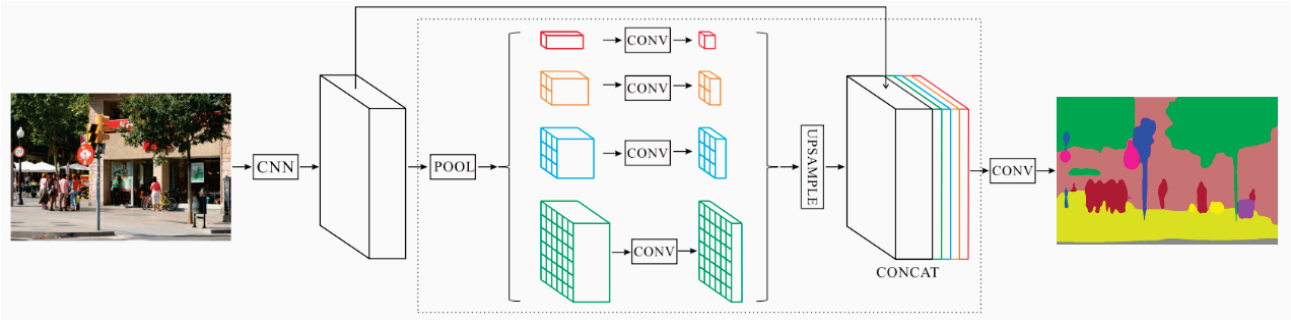

Figure 4. PSPNet model to semantically segment an SVI [45].

Table 2. Descriptive statistics of all variables.

Variable	Definition	Mean	Std
Ln_Price	RMB (Chinese currency)/m^2, dependent variable, the natural logarithm of the original price	10.197	0.354
Structural attributes	**Description**	**Mean**	**Std**
FAR	Floor area ratio	1.68	0.835
Age	Age of the building	18.862	7.322
Locational attributes	**Description**	**Mean**	**Std**
D_CBD	Network distance (km) to the CBD (the Suzhou Industrial Park)	13.739	6.213
D_Bus	Network distance to the nearest bus station (km)	0.306	0.210
D_Metro	Network distance to the nearest metro station (km)	1.042	1.249
D_School	Network distance to the nearest primary/middle school (km)	0.424	0.369
D_Hospital	Network distance to the nearest hospital (km)	0.552	0.542
Neighborhood attributes	**Description**	**Mean**	**Std**
N_Bus	Number of bus stations in 1000 m walking distance	7.534	4.837
N_Metro	Number of metro stations in 1000 m walking distance	1.433	1.368
N_School	Number of schools in 1000 m walking distance	6.34	4.536
N_Hospital	Number of hospitals in 1000 m walking distance	2.788	1.309
Subjective perceptions	**Description**	**Mean**	**Std**
S_Beautiful	Beautiful perception	37.818	4.416
S_Lively	Lively perception	36.256	2.817
S_Safe	Safe perception	37.143	1.725
S_Wealthy	Wealthy perception	42.717	2.482
S_Boring	Boring perception	60.134	1.516
S_Depressing	Depressing perception	53.568	2.391
Objective view index	**Description**	**Mean**	**Std**
O_Sky	Sky view index	30.069	7.13
O_Building	Building view index	20.976	9.237
O_Tree	Tree view index	17.369	6.917
O_Road	Road view index	13.796	3.053
O_Wall	Wall view index	2.856	2.148
O_Car	Car view index	2.548	1.372
O_Sidewalk	Sidewalk view index	2.67	0.963
O_Plant	Plant view index	2.335	1.26
O_Grass	Grass view index	1.534	1.256
O_Earth	Earth view index	0.867	1.136
O_Fence	Fence view index	0.831	0.592
O_Ceiling	Ceiling view index	0.52	1.417

Using MIT ADE20K [46], the largest open-source dataset for semantic segmentation and scene parsing, PSPNet achieved a high accuracy of 80.13%. ADE20K is a collection of 20,000 photographs with pixel-level annotations covering 150 object types in various scenes, including street scenes. It is useful for comprehending the semantics of urban environments. This study used the PyTorch implementation of a pretrained PSPNet based on the ADE20K dataset (https://pypi.org/project/mit-semseg/ (accessed on 19 May 2023)).

After semantic segmentation, 150 view indices were obtained. However, many view indices were zero because the ADE20K object categories contained a large number of indoor objects, which were uncommon in street scenes.

To eliminate objects whose view indices were extremely small for these 150 classes of objects, the average view indices of each class of objects in all street view images were calculated, and only objects with an average view index greater than 0.5% were retained. Twelve classes of objects—sky, building, tree, road, wall, car, sidewalk, plant, grass, earth, fence, and ceiling—were retained after preprocessing.

The average view indices for the SVIs in all four directions at each sampling point were calculated for the 12 classes of view indices. Then, the average view indices of the SVIs with a 1 km buffer (15 min walking distance) of a community were averaged to represent the view indices for the community. The descriptive statistics of the 12 view indices are shown at the bottom of Table 2.

3.4.3. Correlation Analysis

Zhang found that the Pearson's correlation coefficients of subjective perceptions were highly correlated, like beautiful–safe, beautiful–wealthy and depressing–safe [19]. The view indices were also correlated and could lead to multicollinearity issues in multiple linear regression (MLR). To inspect the linear relationship between the 12 view indices and the six subjective perceptions, pairwise Pearson's correlation coefficients were generated.

3.4.4. Analyzing the Importance of View Indices

View indices [13] or POI [24] can be used to predict and explain subjective perceptions to a certain degree. The lightGBM model [47] was fitted to examine the relative importance of each view index for each perception using the 12 view indices as explanatory variables and the 6 perception scores as response variables. LightGBM is a gradient boosting framework that uses a tree-based learning algorithm and is designed to be faster and more memory-efficient. To analyze the importance of a feature, LightGBM measures the extent to which each feature contributes to a model's accuracy by calculating the average gain of the splits where the feature is used.

3.4.5. Other Explanatory Variables

Other explanatory variables were selected based on data availability and a literature review [1–3,8,9] and can be divided into structural, locational, and neighborhood attributes. Building type, floor area ratio (*FAR*), and age of the building (*Age*) are common structural attributes. Owing to data availability, the latter two indicators were selected. Locational attributes are road network distances to various amenities, such as education, health care, and commercial facilities. Educational institutions, including primary and middle schools, can contribute to increases in housing prices. Healthcare facilities provide medical services to various types of hospitals. The central business district (CBD) plays a crucial role in the economic and commercial life of a city, and the CBD of Suzhou (the central region of the industrial park district) was considered a commercial facility in this study. The locational attributes comprised the distance to the CBD (*D_CBD*), nearest bus station (*D_Bus*), metro station (*D_Metro*), primary or middle school (*D_School*), and hospital (*D_Hospital*). The neighborhood attributes were the number of different facilities around the community, including the number of bus stations (*N_Bus*), metro stations (*N_Metro*), primary and middle schools (*N_School*), and hospitals (*N_Hospital*) in community neighborhoods within a radius of 1000 m. The locational and neighborhood attributes were computed using ArcGIS with POI and road network data. Table 2 provides the descriptive statistics for these variables.

3.5. Modeling Methodology

3.5.1. HPM

The HPM has been widely used to estimate the willingness to pay for a house based on its characteristics, quality, and features [9,48]. The HPM assumes that the price of a house is influenced by its characteristics, as well as the characteristics of market demand and supply [4]. The HPM estimates the contribution of each feature to the house price and helps identify the relative importance of each feature in determining the final price.

This study aimed to compare the contributions of subjective perception scores and objective view indices to community housing prices. The subjective perception scores and objective view indices belong to neighborhood attributes, and we distinguished these two groups of neighborhood attributes from traditional neighborhood attributes. All of

these attributes are independent variables of the HPM, and Table 2 shows their descriptive statistics.

The dependent variable of the HPM is community housing prices. We used the natural logarithm of community housing prices as the dependent variable, which is called the semi-logarithmic form of the HPM. It has several advantages over other functional forms, including interpretability, flexibility, improved accuracy, and reduced heteroscedasticity.

3.5.2. Stepwise Regression

The conventional HPM uses the MLR model to model the relationship between two or more attributes and community housing prices [13,28,49]. OLS is the most common method for estimating the coefficients of variables in the MLR model.

We employed a specific type of MLR called stepwise regression, which is a variable selection technique that iteratively adds or removes variables from the model and tests for statistical significance after each iteration until the best set of variables is obtained [50]. By selecting the most influential variables, stepwise regression can produce a more parsimonious model that is easier to interpret. Therefore, stepwise regression rather than MLR was chosen for this study.

Seven attributes were chosen using stepwise regression out of 11 structural, locational, and neighborhood attributes, with a backward stepwise regression model that iteratively removed variables. These seven attributes were *FAR*, *Age*, *D_CBD*, *D_Hospital*, *N_Bus*, *N_Metro*, and *N_School*.

Using the seven attributes as control variables and subjective perception scores and objective view indices as interpretable variables, two groups of backward stepwise regression models were constructed. There were seven control variables plus six subjective perception scores and seven control variables plus twelve objective view indices. The threshold for significance was set at $p < 0.05$. Variables with p-values > 0.05 were removed, and significant variables were retained. Finally, S_Boring and S_Safe from the subjective perception score group and *O_Sky*, *O_Tree*, *O_Building*, *O_Plant*, *O_Car*, *O_Fence*, and *O_Ceiling* from the objective view index group were retained and regarded as explanatory variables. The MLR model is expressed by Equations (2) and (3) for subjective perception scores and objective view indices, respectively.

$$\begin{aligned} Ln_Price = {} & \beta_0 + \beta_1 * FAR + \beta_2 * Age + \beta_3 * D_CBD + \beta_4 * D_Hospital \\ & + \beta_5 * N_Bus + \beta_6 * N_Metro + \beta_7 * N_School + \beta_8 \\ & * S_Boring + \beta_9 * S_Safe \end{aligned} \tag{2}$$

$$\begin{aligned} Ln_Price = {} & \beta_0 + \beta_1 * FAR + \beta_2 * Age + \beta_3 * D_CBD + \beta_4 * D_Hospital + \beta_5 \\ & * N_Bus + \beta_6 * N_Metro + \beta_7 * N_School + \beta_8 * O_Sky + \beta_9 \\ & * O_Tree + \beta_{10} * O_Building + \beta_{11} * O_Plant + \beta_{12} * O_Car + \beta_{13} \\ & * O_Fence + \beta_{14} * O_Ceiling \end{aligned} \tag{3}$$

where β_0 is the intercept, and $\beta_i (i = 1, \ldots, 9)$ in Equation (2) and $\beta_i (i = 1, \ldots, 14)$ in Equation (3) represent the coefficients of the independent variables.

The MLR model can also be expressed in matrix form:

$$\boldsymbol{Y} = \beta_0 1_n + \boldsymbol{X}\boldsymbol{\beta} + \varepsilon \tag{4}$$

where $\boldsymbol{Y}$ is an $n \times 1$ column vector of dependent variables for each community $\boldsymbol{i}$ in the sample ($\boldsymbol{i} = 1, \ldots, \boldsymbol{n}$), 1_n is an $n \times 1$ column vector of ones associated with intercept β_0, $\boldsymbol{X}$ is an $n \times p$ matrix of the explanatory variables, $\boldsymbol{\beta}$ is a $p \times 1$ column vector of coefficients, ε is an $n \times 1$ column vector of random errors, n is the number of communities, and p is the number of explanatory variables.

3.5.3. GWR

MLR is a global stationary regression model. This implies that the coefficients of the MLR are constant in space. However, owing to the complex spatial heterogeneity caused by urban spatial structures, the modeling relationships vary across space.

To capture the spatially varying effects in modeling the relationships between the dependent and independent variables, GWR establishes local functions corresponding to each observation. The GWR model is expressed in Equation (5).

$$y_i = \beta_{i0} + \sum_{k=1}^{p} \beta_{ik} x_{ik} + \varepsilon_i, \quad i = 1, \ldots, n, \tag{5}$$

For each location i, y_i is the dependent variable, β_{i0} is the location-specific intercept term, β_{ik} is the local regression coefficient of the kth explanatory variable, x_{ik} is the kth explanatory variable, and ε_i is the random error following a normal distribution. In this study, a bisquare kernel function was selected to calculate the spatial weight matrix.

4. Results

4.1. Extracting Perceptual Scores and View Indices

Figure 5 displays four sample SVIs, semantic segmentation results, six predicted perceptual scores, and eight dominant view indices. Different SVIs have different perceptual scores and viewing indices. The perceptual scores and results of the semantic segmentation appeared to be reasonable.

Owing to the Image A's large tree and sky view indices, Image A had the highest beautiful perceptual score. Despite being in a shopping district, Image B's wealthy perceptual score was low, likely because the image lacked trees. Image C appeared to be the wealthiest, safest, lively, and boring image because of its extensive collection of urban scene objects. Image D was believed to be the most depressing. This may be because the majority of the images consisted of artificial buildings and were dark in hue.

4.2. Correlation Analysis

Six different types of perceptions are correlated, as Zhang (2018) showed [19]. The Pearson correlation coefficients for the six indicators are displayed in Figure 6. Some correlation pairs had a strong positive correlation, including "lively–safety" (0.56), "lively–wealthy" (0.64), and "safety–wealthy" (0.52). In contrast, "beautiful–depressing" had a strong negative correlation (-0.55).

This outcome deviates somewhat from that of Zhang's study. According to Zhang's examination of the six perceptual indicators for Beijing and Shanghai in China, "beautiful–safety" (0.819 and 0.667 for Beijing and Shanghai, respectively) and "beautiful–wealthy" (0. 834 and 0. 639 for Beijing and Shanghai, respectively) were strongly positively correlated. However, "beautiful–safety" (-0.06) and "beautiful–wealthy" (-0.07) were almost uncorrelated in our analysis. This can be noted in Image A in Figure 5, which had the highest beautiful score; however, its safety and wealthy scores were relatively low. This was probably caused by the distinct urban environments in these cities and the different datasets (Place Pulse 2.0 and the local dataset) used to train the perception prediction models.

In addition to the perceptual scores, the Pearson correlation coefficients of the top 12 view indices were calculated and are shown in Figure 7. Except for the "sky–tree" (-0.54) and "sky–building" (-0.48) pairs, which were relatively highly correlated, most correlations of view index pairs were weakly or moderately correlated, and this is consistent with Qiu's work [13].

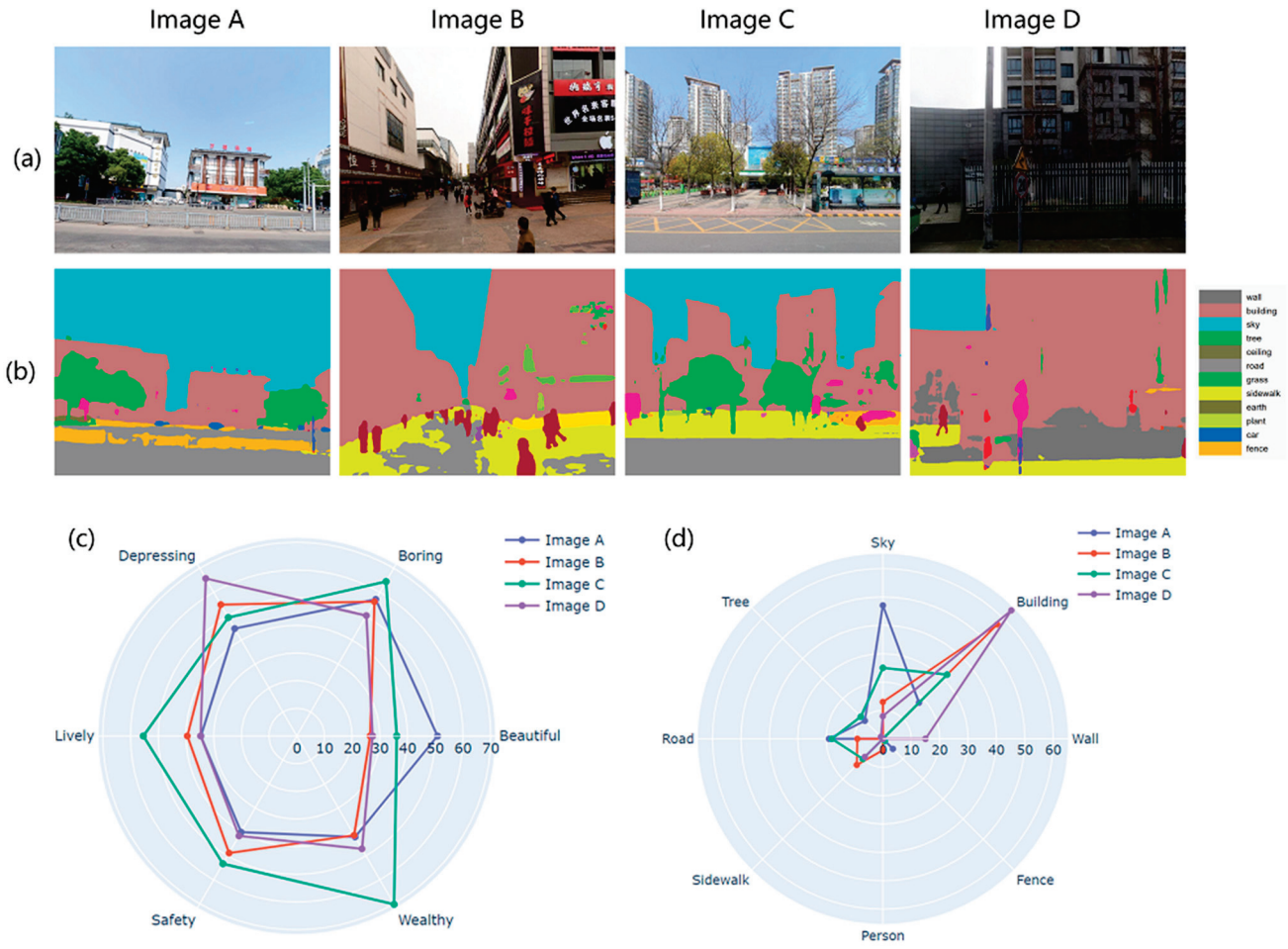

Figure 5. Sample SVIs. (**a**) Four SVIs. (**b**) Semantic segmentation result of SVIs. (**c**) Six perceptual scores for the SVIs. (**d**) Eight dominant view indices calculated with the semantic segmentation result.

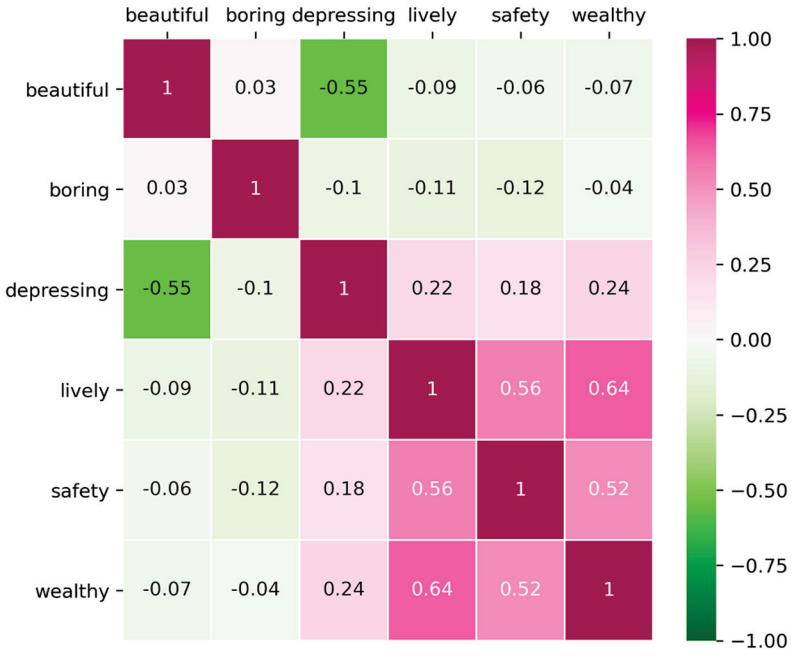

Figure 6. Pearson correlation coefficients of six perceptual scores.

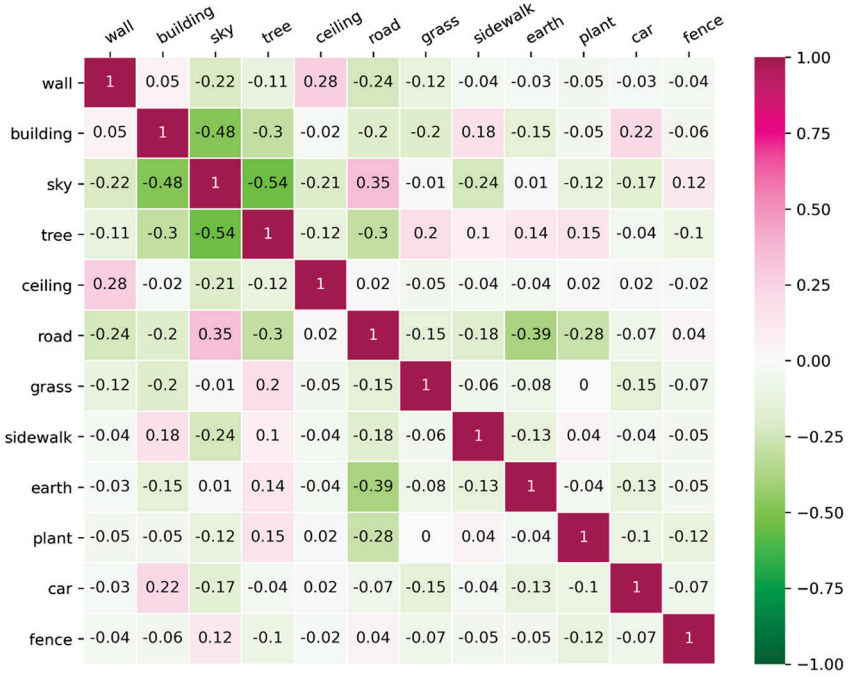

Figure 7. Pearson correlation coefficients of top 12 view indices.

4.3. Feature Importance

The LightGBM was employed using the 12 most important view indices to predict the six perceptual scores. The R^2 metrics for measuring the fit performance of the six perceptions are presented in Table 3. The R^2 values for the six perceptions showed non-negligible variance. Depression had the highest R^2, which shows that the view indices could explain 54% of the variance in depression scores. Boring had the lowest R^2, and these view indices could only account for 17% of the variance in boring scores.

Table 3. The R^2 of LightGBM for the six perceptions.

Perceptions	Beautiful	Boring	Depressing	Lively	Safety	Wealthy
R^2	36%	17%	54%	33%	24%	39%

The feature importance of the view indices based on the total gain across all splits in LightGBM is displayed in Figure 8. In each view index group (sky, road, etc.), the six bars represent the importance of a specific view index in predicting the six perceptions. In general, the view indices with larger ratios are more important than those with lower ratios. For instance, the sky, roads, trees, and buildings are more important than walls, grass, fences, and earth. The contributions of the one-view index to the various perception scores varied significantly. Compared to the importance of the lively (132) and wealthy (151), the road view index for boring (50) was substantially less significant. The importance of the plant view index for the beautiful (65) was significantly higher than that for the lively (5) and wealthy (6). According to common sense, the earth view index can influence boring and depressing more than other perception scores. Trees, cars, and sidewalks contribute significantly to lively, safety, and wealthy, which is consistent with Zhang's research [19].

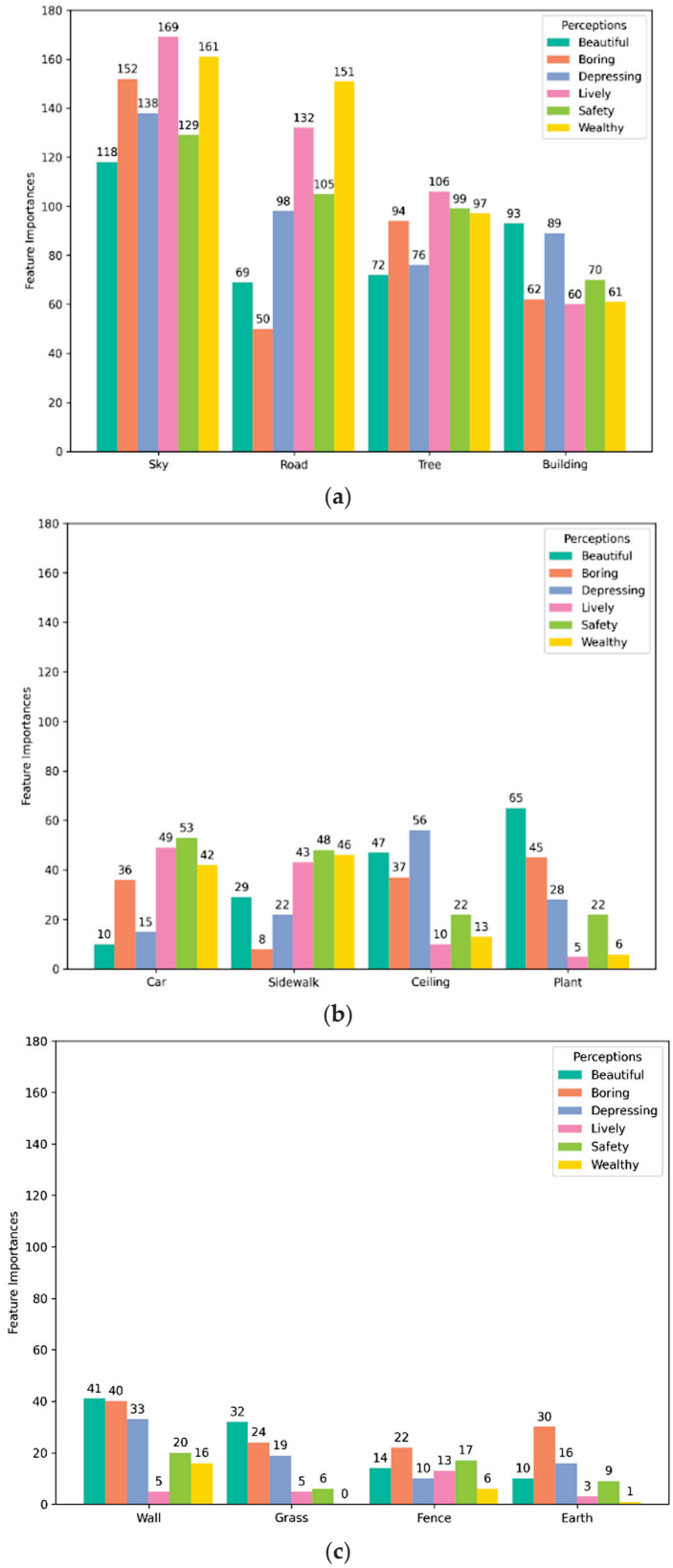

Figure 8. Feature importance for predicting the six perceptual scores. In each view index group (sky, road, and so on), there were six bars representing the importance of the specific view index in predicting the six perceptions. (**a**) The feature importance of sky, road, tree and building. (**b**) The feature importance of car, sidewalk, ceiling and plant. (**c**) The feature importance of wall, grass, fence, and earth.

4.4. Stepwise Regression

Stepwise regression was applied to select the significant variables. The baseline model, Model 0, was fitted with the attributes FAR, Age, D_CBD, D_Hospital, N_Bus, N_Metro, and N_School, accounting for 33.98% of the variance in housing prices. Then, stepwise regression was performed again to construct Models 1 and 2 using Equations (2) and (3), as follows:

Table 4 summarizes the regression diagnostic data for each model, including the adjusted R^2, AICc, AIC, and residual sum of squares (RSS). In terms of adjusted R^2, Model 1 (adjusted R^2 = 34.46%) and Model 2 (adjusted R^2 = 39.26%) improved by 0.48% and 5.28%, respectively, compared with Model 0 (adjusted R^2 = 33.98%). The values of the AICc, AIC, and RSS metrics of Model 0 were higher than those of Models 1 and 2. This indicates the effectiveness of the perception scores and view indices. Furthermore, the view indices were slightly stronger than the perception scores. This is consistent with Qiu's study [13], although our subjective and objective indicators were not exactly the same.

Table 4. Regression diagnostic information of OLS and GWR estimations.

	Model 0	**Model 1**	**Model 2**	**Model 3**	**Model 4**
Model	OLS(Stepwise)			GWR	
Variables	Baseline	Perception scores	View Indices	Perception scores	View Indices
Adjusted R^2	33.98%	34.46%	39.26%	72.3%	70.1%
AICc	493.244	485.178	384.592	−453.945	−230.686
AIC	491.113	482.987	382.196	−276.803	−370.407

Table 5 lists the regression coefficients for each model. Notably, the absolute values of these coefficients were small because the dependent variable was the natural logarithm of the original house price. For Model 0, the signs of these coefficients were consistent with prior studies. The expected sign of the coefficient of D_Hospital was positive in some studies while negative in others, and it was positive in this study, indicating if a community is closer to a hospital, its price is lower. The signs of structural, locational, and neighborhood variables of Model 1 were the same as the ones of Model 0, and the magnitude of these variables changed little. The signs of S_Safe and S_Boring were both negative. All of the coefficients were significant at the 1% level, except that the coefficient of S_Safe was significant at the 5% level. The view index variables had positive and negative signs, and their coefficients were all significant at the 1% level.

4.5. GWR

In this study, the adaptive bisquare kernel function of the GWR model was employed. The adaptive kernel bandwidths (i.e., a fixed number of local observations) were estimated as 95 and 168 for Models 3 and 4, respectively. The effects of perception scores on housing prices were more localized than those of view indices.

The GWR models offer better fitting performance than the OLS models. The adjusted R^2 values for Models 3 and 4 were 72.3% and 70.1%, respectively, which were much higher than those of the OLS. Interestingly, the adjusted R^2 of Model 3 (perceptions) was higher than that of Model 4 (view indices) for GWR, which is the opposite of the results of OLS, whose adjusted R^2 for perceptions was lower than that of the view indices. The high adjusted R^2 and low AICc values in Table 3 suggest that the GWR model had the strongest fitting performance.

Table 5. Regression coefficients of models.

Model	Model 0	Model 1	Model 2
cons	10.5238 ***	12.000 ***	12.437 ***
Structural attributes			
FAR	−0.0415 ***	−0.03956 ***	−0.0102 ***
Age	−0.0131 ***	−0.01281 ***	−0.0447 ***
Locational attributes			
D_CBD	−0.000024 ***	−0.000023 ***	−0.000022 ***
D_Hospital	0.000063 ***	0.000060 ***	0.000039 **
Neighborhood attributes			
N_Bus	0.01123 ***	0.01094 ***	0.00979 ***
N_Metro	0.01164 ***	0.01264 ***	0.01283 ***
N_School	0.00529 ***	0.00543 ***	0.00648 ***
Subjective perception			
S_Safe	/	−0.01226 ** (0.015)	/
S_Boring	/	−0.01722 ***	/
Objective view index			
O_Sky	/	/	−0.03284 ***
O_Tree	/	/	−0.02427 ***
O_Building	/	/	−0.02704 ***
O_Plant	/	/	0.02419 ***
O_Car	/	/	−0.02317 ***
O_Fence	/	/	0.04223 ***
O_Ceiling	/	/	−0.05011 ***

Note: Significant *p*-values are marked in parentheses: ** $p < 0.05$, *** $p < 0.01$.

The values of local R^2 for Models 3 and 4 are shown in Figure 9. In general, for both models, the industrial park and Xin district had greater local R^2 values than the central region of the Gusu district. The spatial pattern of the local R^2 matched that of the housing price map shown in Figure 1. In other words, areas with higher housing prices exhibited a better fitting performance.

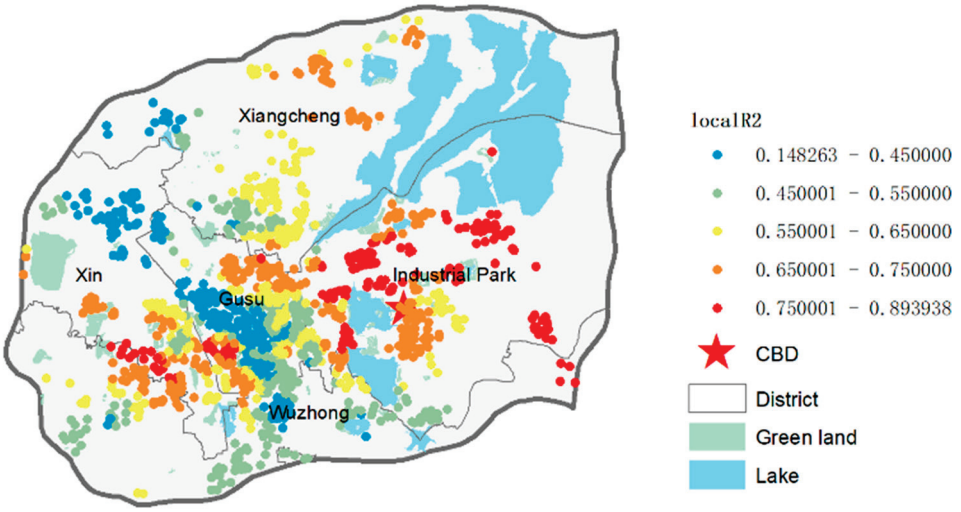

(**a**)

Figure 9. *Cont*.

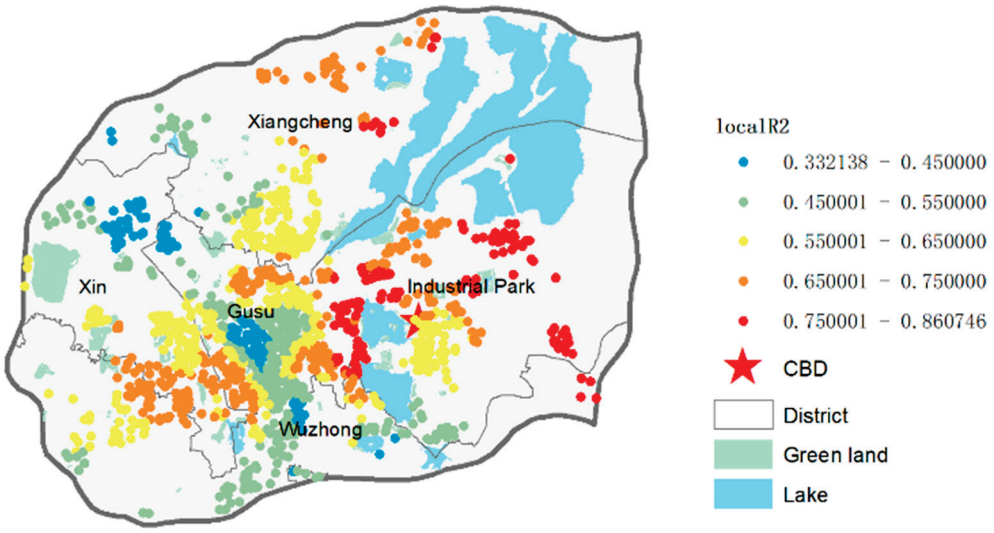

(**b**)

Figure 9. Local R^2 of Model 3 and Model 4. (**a**) Local R^2 of Model 3 (perception scores). (**b**) Local R^2 of Model 4 (view indices).

The Monte Carlo test was used to evaluate the significance of the GWR-estimated coefficients and determine whether they were spatially stationary. The Monte Carlo test was performed 999 times with random permutations of the observations in space. The results of the descriptive statistics and the *p*-values of the Monte Carlo significance test for Models 3 and 4 are presented in Tables 6 and 7, respectively. The *p*-values of all coefficients in both models were zero, suggesting that the impact of the variables on housing prices varies spatially. Therefore, it was necessary to use GWR to model the spatial heterogeneity of these variables.

Table 6. Summary statistics and Monte Carlo significance test results for Model 3 (perception scores) parameter estimates.

Variable	Mean	STD	Min	Median	Max	*p*-Value
FAR	−0.074	0.096	−0.432	−0.072	0.178	0 ***
Age	−0.014	0.011	−0.046	−0.012	0.017	0 ***
D_CBD	0	0	0	0	0	0 ***
D_Hospital	0	0	−0.001	0	0.001	0 ***
N_Bus	0.006	0.013	−0.023	0.004	0.051	0 ***
N_Metro	0.007	0.024	−0.057	0.006	0.093	0 ***
N_School	−0.002	0.023	−0.093	0.002	0.055	0 ***
S_Boring	−0.005	0.038	−0.111	−0.001	0.116	0 ***
S_Safe	−0.012	0.04	−0.144	−0.008	0.098	0 ***

Note: Significance value, *** $p < 0.01$.

The estimated coefficients of the GWR varied from place to place. The spatial distributions of the coefficients for Models 3 and 4 are shown in Figures 10 and 11, respectively. The natural break (Jenks) classification method divides coefficients into five classes. To distinguish between the positive and negative effects of these factors on housing prices, a zero value was purposefully set in one of the classes to distinguish between the positive and negative coefficient groups.

Table 7. Summary statistics and Monte Carlo significance test results for Model 4 (view indices) parameter estimates.

Variable	Mean	STD	Min	Median	Max	*p*-Value
FAR	−0.064	0.075	−0.302	−0.062	0.118	0 ***
Age	−0.013	0.009	−0.034	−0.011	0.007	0 ***
D_CBD	0	0	0	0	0	0 ***
D_Hospital	0	0	0	0	0	0 ***
N_Bus	0.006	0.009	−0.017	0.005	0.032	0 ***
N_Metro	0.007	0.015	−0.032	0.008	0.059	0 ***
N_School	0.002	0.014	−0.048	0.004	0.033	0 ***
O_Sky	−0.021	0.027	−0.115	−0.019	0.035	0 ***
O_Building	−0.02	0.025	−0.114	−0.017	0.03	0 ***
O_Tree	−0.015	0.026	−0.105	−0.016	0.047	0 ***
O_Ceiling	−0.047	0.071	−0.286	−0.035	0.287	0 ***
O_Plant	0.018	0.033	−0.057	0.019	0.107	0 ***
O_Fence	0.018	0.077	−0.247	0.012	0.311	0 ***
O_Car	−0.017	0.036	−0.115	−0.022	0.067	0 ***

Note: Significance value, *** $p < 0.01$.

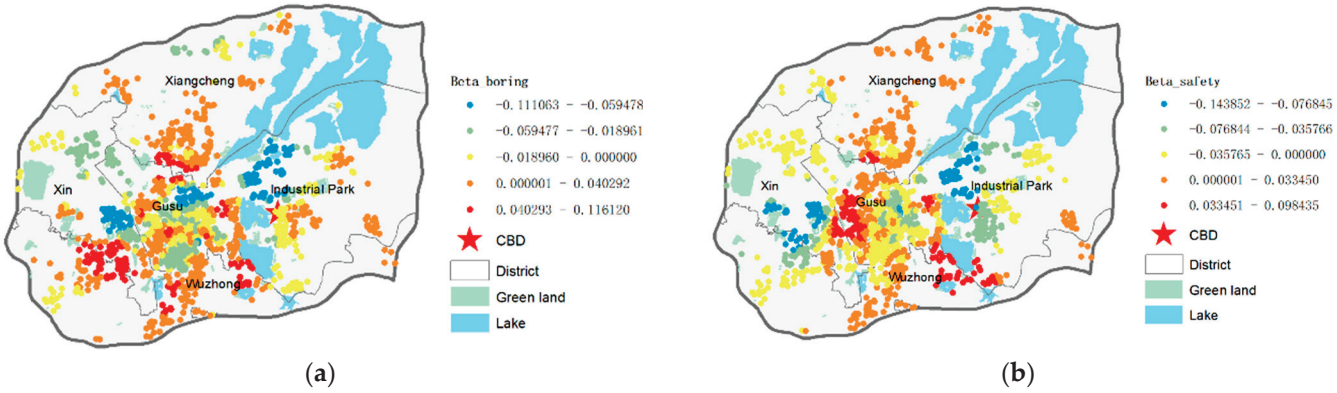

(**a**) (**b**)

Figure 10. Coefficient estimates for Model 3 (perception scores). (**a**) Coefficients of the boring score. (**b**) Coefficients of the safety score.

Boring is a negative and unlively perception [9], and a substantial portion of the boring coefficients were negative in Figure 10a, indicating that the boring perception in these communities was inversely proportional to housing prices. However, many communities had positive boring coefficients, such as several communities in the Wuzhong and Xiangcheng districts. This implies that an increase in boring scores may increase the housing price. Safety is a positive perception, and several communities in the Gusu, Xiangcheng, and Wuzhong districts had positive safety coefficients, indicating that safety perception is proportional to housing prices. Meanwhile, the safety coefficients were negative in certain outlying suburbs, indicating that an increasing safety score may decrease housing prices. This may be due to the fact that these areas are in suburbs and life is not convenient.

Figure 11a–c show similar spatial patterns for the sky, building, and tree-view index coefficients, respectively. Some communities in the city center had positive coefficients, whereas others in the surrounding regions had negative coefficients. The number of communities with negative coefficients was greater than those with positive coefficients. This indicates that increasing the sky, building, and tree indices may decrease housing prices in most communities. The spatial distributions of the other view index coefficients differed significantly from one another.

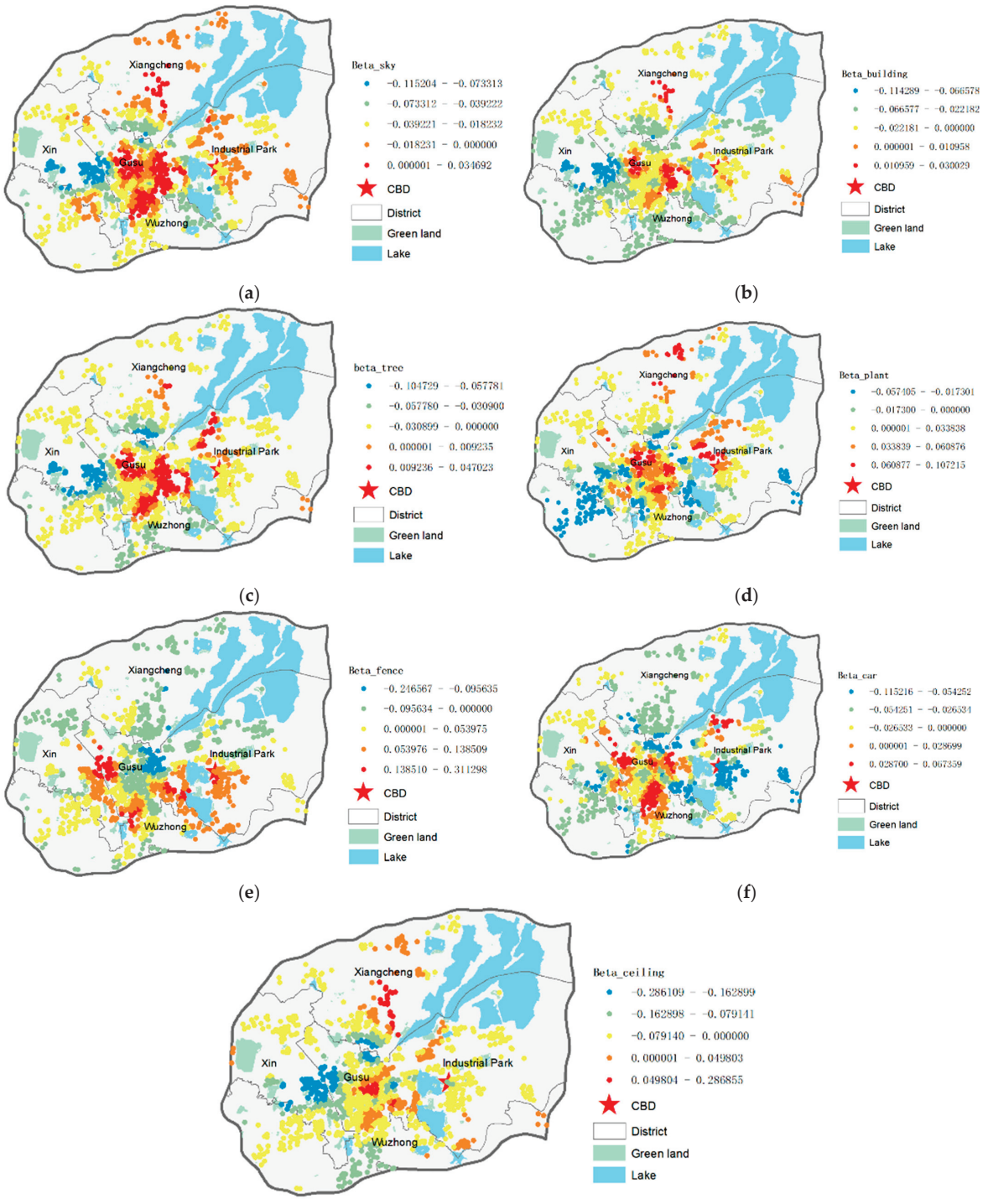

Figure 11. Coefficient estimates for Model 4 (view indices). (**a**) Sky view index coefficients. (**b**) Building view index coefficients. (**c**) Coefficients of the tree view index. (**d**) Coefficients of the plant view index. (**e**) Coefficients of fence view index (**f**) Coefficients of car view index. (**g**) Coefficients of the ceiling view index.

5. Discussion

5.1. Effects of Subjective and Objective Measures on Housing Prices

The objective measures may generally explain more variance than the subjective measures, according to the adjusted R^2 of the OLS in Table 3. The adjusted R^2 of Model 2 (39.26%) for OLS was 4.8 percentage points higher than that of Model 1 (34.46%). Overall,

the objective measures had stronger explanatory power, and built environment factors had a greater impact on housing prices. This is in line with a study by Qiu [13]. In addition to the sky, tree, and building view indices having the largest proportions, the plant, car, fence, and ceiling view indices also have a considerable impact on housing prices.

The global OLS model determines a single corresponding parameter for each variable in each observation. By contrast, GWR is a local model that estimates the model parameters for every observation within a local neighborhood. In Table 3, the adjusted R^2 of Model 3 (72.3%) was greater than that of Model 4 (70.1%), which is an interesting contrast to the OLS relationship. This contradicts Qiu [13] and demonstrates that for GWR, perceptual measures can explain more variance in housing prices than view indices on the local scale. This indicates that home buyers care more about their subjective perceptions of their neighborhoods' surroundings.

The GWR produces a different result than OLS, suggesting that the result of the local model is opposite to that of the global model. This phenomenon is, in fact, the Simpson's paradox. It is essential to mitigate this problem by modeling spatially varying relationships [29]. The results of the Monte Carlo test also demonstrate that the impacts of the explanatory variables vary spatially.

Specifically, the coefficients of the boring and safety scores were both negative for OLS. For GWR, some communities had positive coefficients for boring and safety scores, whereas others had negative coefficients. Boring is a negative perception that usually has a negative impact on housing prices, indicating that a boring community environment is associated with low housing prices. Safety is a positive perception and usually has a positive impact on housing prices. This indicates that people are prepared to pay premiums for safe communities.

However, some communities had positive coefficients for boring perceptions. This appears counterintuitive. One reason is that older residential communities usually have stores on the first floor and are cheaper, whereas newer residential communities do not have stores on the first floor and are usually more expensive than older communities. Owing to stores and shoppers, older and cheaper residential communities have lower boring scores. By contrast, newer residential communities had higher boring scores. Therefore, the boring coefficients were positive for some communities.

A potential explanation for the negative safety coefficients was provided. According to Figure 8b, the car and sidewalk view indices (53 and 48) had the highest feature importance in predicting the safety perception. More cars can bring not only safety but also more air pollution and noise. This has a negative effect on housing prices. This justification is comparable to the effect of metro stations on housing prices [51]. The closer a community is to a metro station, the more convenient it is to travel. Thus, property prices property will increase. However, if they are too close, housing prices may be lowered due to noise and other considerations.

In addition, the effect of the tree view index on housing prices was negative for the OLS. This is counterintuitive and inconsistent with Ye's work [8]. Figure 11c shows that the tree view index had both positive and negative effects. The positive effects were mainly concentrated in the city center. The negative effects were in the suburbs, and a possible reason was that trees around new residential communities in the suburbs were not tall or large because of their relatively young age, resulting in a low tree view index. Thus, new communities have high housing prices and a low tree view index.

It is critical to pay attention to both the model and the selected variables when analyzing housing prices because the result of OLS is the opposite of that of GWR. In particular, the Simpson's paradox may result from utilizing global models, such as OLS. Thus, OLS should be used with caution when attempting to explain the influence of various variables on housing prices. It is indispensable to use a local model, such as GWR, to analyze the spatially varying effects of variables.

The outcomes we obtained differed from those of Kang's study [9]. Kang first employed the principal component analysis technique and then used OLS to analyze the

effects of various factors on housing prices. The principal components were linear combinations of individual perceptions. Kang analyzed only the principal components' impacts on housing prices rather than individual perceptions. In addition, although Kang applied GWR, Kang did not demonstrate or analyze the spatially varying coefficients.

5.2. Pros and Cons of Subjective and Objective Measures

The GWR discloses that subjective perceptual scores can explain more variance in housing prices than objective view indices. This highlights the importance of "sense of place" and humanistic insights in evaluating the effects of various features on housing prices [9]. Perceptual scores measure how people perceive a place psychologically and are related to the socioeconomic environment, such as land use [52], poverty status [53], and crime rates [54]. Human perceptions of places depict a complete picture. Table 3 shows that the 12 most important view indices could only explain a small proportion of the perceptual variance (17–54%). The boring and safety perceptions had the two lowest R^2 values (17% and 24%, respectively), and the two perceptions were selected using the stepwise regression model to fit housing prices. This reflects the fact that the two perceptions contain more sensory information than view indices. The multicollinearity issue with subjective measurements makes it challenging to incorporate all of them into OLS, which is one of their drawbacks.

Objective view indices can supplement subjective perceptual scores even if they cannot fully characterize a place, such as subjective measures. The view indices are distinct, unambiguous, easy to measure, and have a low correlation.

5.3. Implications for Urban Planning

This research integrates and compares the effects of subjective perceptions and objective view indices on housing prices and has broad and practical applications in urban planning. First, housing prices were significantly affected by subjective perceptions. Governments and policymakers should pay attention not only to the built environment, but also to perceptions of the micro-scale street environment around residential districts. Sidewalks and fences, which may affect residents' perceptions of safety, should receive more attention. Currently, only the green ratio and road construction have received attention in other cities. Perception indicators should be carefully selected because of the multicollinearity problem. Second, a street environmental fee can be imposed to compensate for public funds invested in improving streetscapes [8]. This is because real estate developers profit financially from the surrounding street environment, whereas cities create, invest in, and maintain streetscapes. Tax amounts can be determined using both subjective and objective indices. Third, boring and safety perceptions were selected to represent negative and positive perceptions, respectively. This study can serve as a reference for future research. These subjective perceptions can be used to model economics and other urban plans outside of settlement assessments. For example, they can provide new measures for street design guidelines [38]. Urban designers and practitioners can examine the social, psychological, and emotional meanings of the street environment and better guide various applications, such as lively and safe neighborhood design, sustainable city planning, and urban micro-renovation.

5.4. Limitations and Potential Improvements

This study has several limitations that should be addressed in future studies. First, human perception may have been biased. The deep learning model used to appraise the SVIs of Suzhou was trained using SVIs collected in Wuhan City. Although both cities are located in China, each city has a unique street environment [55]. These two datasets have distinct data distributions. To assess the performance of the model in future studies, Suzhou's sample SVIs may need to be collected and annotated by humans.

Second, human perceptions were predicted with a deep learning model. Experiencing a place does not involve the observation of specific objects. In addition to the visual

elements in SVIs, other elements are related to human perceptions. Quercia pointed out that the history, culture, interactions, and experiences of a place cannot be easily captured by images [56]. Future research could expand the incorporation of additional datasets, such as social media datasets.

Third, previous studies have shown that the spatial scale impacts the hedonic price model's results. The scale of the research object has a modifiable areal unit problem [57]. A fine-scale community was selected as the study object. More coarse-level regions (such as zip code regions) can be applied in other research to conduct experiments [2].

6. Conclusions

Using SVIs, this study analyzed the effects of subjective perceptions and objective view indices on housing prices. Subjective perceptions and objective view indices were extracted from the SVIs using deep-learning models. The effects of the subjective and objective measures were analyzed and compared using OLS and GWR. The global model OLS explored the overall impact of these measures on housing prices. GWR was employed to reveal the spatial variation in these factors from a local perspective, as opposed to the global approach that OLS uses. The main findings are summarized as follows:

First, for OLS, the overall objective measures explained more variance than the subjective measures. This result is consistent with that reported by Qiu et al. [13]. This suggests that the built environment factors have a greater impact on housing prices.

Second, compared to the view indices, the perceptual scores for the GWR exhibited stronger explanatory power. This indicates that home buyers care more about their subjective perceptions of their neighborhoods' surroundings. The results of the local GWR model were opposite to those of the global OLS model. The GWR result highlighted the importance of "sense of place" and humanistic insights in evaluating the effects of various indicators on housing prices. Furthermore, human perceptions of a place can provide a more complete picture.

Third, the results of the Monte Carlo test showed that the effects of the explanatory variables varied spatially and were statistically significant. However, this demonstrates the value of using GWR.

These results have important implications for governments and urban planners. They should focus on the perceptions of the microscale street environment around residential areas, as well as the built environment. Urban designers and practitioners can examine the social, psychological, and emotional meanings of street environments and guide various applications.

Author Contributions: Conceptualization, J.Z.; Formal analysis, J.D.; Resources, T.P.; Software, Y.G. and C.L.; Writing—original draft, J.Z.; Writing—review and editing, Y.G., C.S., J.C. and T.P. All authors have read and agreed to the published version of the manuscript.

Funding: This work was funded by Jiangsu Province Industry-University-Research Cooperation Program (No. BY20221316), National Natural Science Foundation of China (No. 42071436, 42071435 and 71874110), and Grant of State Key Laboratory of Resources and Environmental Information System (No. 201816).

Data Availability Statement: OSM data: https://www.openstreetmap.org (accessed on 21 May 2023), Housing price data: https://suzhou.anjuke.com/ (accessed on 21 December 2022), Stree view data: https://map.baidu.com/ (accessed on 19 May 2023).

Acknowledgments: We would like to thank the reviewers for their valuable comments and suggestions, which played a positive role in improving the content of our paper.

Conflicts of Interest: The authors declare that they have no known competing financial interests or personal relationships that could have appeared to influence the work reported in this paper.

References

1. Hu, L.; He, S.; Han, Z.; Xiao, H.; Su, S.; Weng, M.; Cai, Z. Monitoring Housing Rental Prices Based on Social Media:An Integrated Approach of Machine-Learning Algorithms and Hedonic Modeling to Inform Equitable Housing Policies. *Land Use Policy* **2019**, *82*, 657–673. [CrossRef]
2. Kang, Y.; Zhang, F.; Peng, W.; Gao, S.; Rao, J.; Duarte, F.; Ratti, C. Understanding House Price Appreciation Using Multi-Source Big Geo-Data and Machine Learning. *Land Use Policy* **2021**, *111*, 104919. [CrossRef]
3. Li, S.; Jiang, Y.; Ke, S.; Nie, K.; Wu, C. Understanding the Effects of Influential Factors on Housing Prices by Combining Extreme Gradient Boosting and a Hedonic Price Model (XGBoost-HPM). *Land* **2021**, *10*, 533. [CrossRef]
4. Rosen, S. Hedonic Prices and Implicit Markets: Product Differentiation in Pure Competition. *J. Political Econ.* **1974**, *82*, 34–55. [CrossRef]
5. Li, X.; Ratti, C.; Seiferling, I. Mapping urban landscapes along streets using Google Street View. In *Advances in Cartography and GIScience*; Peterson, M.P., Ed.; Lecture Notes in Geoinformation and Cartography; Springer International Publishing: Cham, Switzerland, 2017; pp. 341–356. ISBN 978-3-319-57335-9.
6. Cullen, G. *Concise Townscape*; Routledge: London, UK, 1961.
7. Park, K.; Ewing, R.; Sabouri, S.; Larsen, J. Street Life and the Built Environment in an Auto-Oriented US Region. *Cities* **2019**, *88*, 243–251. [CrossRef]
8. Ye, Y.; Xie, H.; Fang, J.; Jiang, H.; Wang, D. Daily Accessed Street Greenery and Housing Price: Measuring Economic Performance of Human-Scale Streetscapes via New Urban Data. *Sustainability* **2019**, *11*, 1741. [CrossRef]
9. Kang, Y.; Zhang, F.; Gao, S.; Peng, W.; Ratti, C. Human Settlement Value Assessment from a Place Perspective: Considering Human Dynamics and Perceptions in House Price Modeling. *Cities* **2021**, *118*, 103333. [CrossRef]
10. Gupta, K.; Kumar, P.; Pathan, S.K.; Sharma, K.P. Urban Neighborhood Green Index—A Measure of Green Spaces in Urban Areas. *Landsc. Urban Plan.* **2012**, *105*, 325–335. [CrossRef]
11. Biljecki, F.; Ito, K. Street View Imagery in Urban Analytics and GIS: A Review. *Landsc. Urban Plan.* **2021**, *215*, 104217. [CrossRef]
12. Kang, Y.; Zhang, F.; Gao, S.; Lin, H.; Liu, Y. A Review of Urban Physical Environment Sensing Using Street View Imagery in Public Health Studies. *Ann. GIS* **2020**, *26*, 261–275. [CrossRef]
13. Qiu, W.; Zhang, Z.; Liu, X.; Li, W.; Li, X.; Xu, X.; Huang, X. Subjective or Objective Measures of Street Environment, Which Are More Effective in Explaining Housing Prices? *Landsc. Urban Plan.* **2022**, *221*, 104358. [CrossRef]
14. Li, X.; Zhang, C.; Li, W.; Ricard, R.; Meng, Q.; Zhang, W. Assessing Street-Level Urban Greenery Using Google Street View and a Modified Green View Index. *Urban For. Urban Green.* **2015**, *14*, 675–685. [CrossRef]
15. Chen, L. Estimating Pedestrian Volume Using Street View Images: A Large-Scale Validation Test. *Comput. Environ. Urban Syst.* **2020**, *11*, 101481. [CrossRef]
16. Lin, L.; Moudon, A.V. Objective versus Subjective Measures of the Built Environment, Which Are Most Effective in Capturing Associations with Walking? *Health Place* **2010**, *16*, 339–348. [CrossRef] [PubMed]
17. Fu, X.; Jia, T.; Zhang, X.; Li, S.; Zhang, Y. Do Street-Level Scene Perceptions Affect Housing Prices in Chinese Megacities? An Analysis Using Open Access Datasets and Deep Learning. *PLoS ONE* **2019**, *14*, e0217505. [CrossRef]
18. Ewing, R.; Handy, S. Measuring the Unmeasurable: Urban Design Qualities Related to Walkability. *J. Urban Des.* **2009**, *14*, 65–84. [CrossRef]
19. Zhang, F.; Zhou, B.; Liu, L.; Liu, Y.; Fung, H.H.; Lin, H.; Ratti, C. Measuring Human Perceptions of a Large-Scale Urban Region Using Machine Learning. *Landsc. Urban Plan.* **2018**, *180*, 148–160. [CrossRef]
20. Qiu, W.; Li, W.; Liu, X.; Zhang, Z.; Li, X.; Huang, X. Subjective and Objective Measures of Streetscape Perceptions: Relationships with Property Value in Shanghai. *Cities* **2023**, *132*, 104037. [CrossRef]
21. Xu, X.; Qiu, W.; Li, W.; Liu, X.; Zhang, Z.; Li, X.; Luo, D. Associations between Street-View Perceptions and Housing Prices: Subjective vs. Objective Measures Using Computer Vision and Machine Learning Techniques. *Remote Sens.* **2022**, *14*, 891. [CrossRef]
22. Salesses, P.; Schechtner, K.; Hidalgo, C.A. The Collaborative Image of The City: Mapping the Inequality of Urban Perception. *PLoS ONE* **2013**, *8*, e68400. [CrossRef]
23. Dubey, A.; Naik, N.; Parikh, D.; Raskar, R.; Hidalgo, C.A. Deep Learning the City: Quantifying Urban Perception at a Global Scale. In Proceedings of the Computer Vision–ECCV 2016: 14th European Conference, Amsterdam, The Netherlands, 11–14 October 2016; Proceedings, Part I 14; Springer: Berlin/Heidelberg, Germany, 2016; pp. 196–212.
24. Yao, Y.; Liang, Z.; Yuan, Z.; Liu, P.; Bie, Y.; Zhang, J.; Wang, R.; Wang, J.; Guan, Q. A Human-Machine Adversarial Scoring Framework for Urban Perception Assessment Using Street-View Images. *Int. J. Geogr. Inf. Sci.* **2019**, *33*, 2363–2384. [CrossRef]
25. Zhang, L.; Pei, T.; Wang, X.; Wu, M.; Song, C.; Guo, S.; Chen, Y. Quantifying the Urban Visual Perception of Chinese Traditional-Style Building with Street View Images. *Appl. Sci.* **2020**, *10*, 5963. [CrossRef]
26. Sun, M. Understanding Architecture Age and Style through Deep Learning. *Cities* **2022**, *128*, 103787. [CrossRef]
27. Su, S.; Zhang, J.; He, S.; Zhang, H.; Hu, L.; Kang, M. Unraveling the Impact of TOD on Housing Rental Prices and Implications on Spatial Planning: A Comparative Analysis of Five Chinese Megacities. *Habitat Int.* **2021**, *107*, 102309. [CrossRef]
28. Wu, C. Spatial Effects of Accessibility to Parks on Housing Prices in Shenzhen, China. *Habitat Int.* **2017**, *10*, 45–54. [CrossRef]
29. Fotheringham, A.S.; Sachdeva, M. Scale and Local Modeling: New Perspectives on the Modifiable Areal Unit Problem and Simpson's Paradox. *J. Geogr. Syst.* **2022**, *24*, 475–499. [CrossRef]

30. Fotheringham, A.S.; Brunsdon, C.; Charlton, M. *Geographically Weighted Regression: The Analysis of Spatially Varying Relationships*; John Wiley & Sons: Hoboken, NJ, USA, 2003.
31. Dong, R.; Zhang, Y.; Zhao, J. How Green Are the Streets Within the Sixth Ring Road of Beijing? An Analysis Based on Tencent Street View Pictures and the Green View Index. *Int. J. Environ. Res. Public Health* **2018**, *22*, 1367. [CrossRef]
32. Long, Y.; Liu, L. How Green Are the Streets? An Analysis for Central Areas of Chinese Cities Using Tencent Street View. *PLoS ONE* **2017**, *12*, e0171110. [CrossRef]
33. Yin, L.; Wang, Z. Measuring Visual Enclosure for Street Walkability: Using Machine Learning Algorithms and Google Street View Imagery. *Appl. Geogr.* **2016**, *76*, 147–153. [CrossRef]
34. Helbich, M. Using Deep Learning to Examine Street View Green and Blue Spaces and Their Associations with Geriatric Depression in Beijing, China. *Environ. Int.* **2019**, *11*, 107–117. [CrossRef]
35. Law, S.; Seresinhe, C.I.; Shen, Y.; Gutierrez-Roig, M. Street-Frontage-Net: Urban Image Classification Using Deep Convolutional Neural Networks. *Int. J. Geogr. Inf. Sci.* **2020**, *34*, 681–707. [CrossRef]
36. Zhou, H.; He, S.; Cai, Y.; Wang, M.; Su, S. Social Inequalities in Neighborhood Visual Walkability: Using Street View Imagery and Deep Learning Technologies to Facilitate Healthy City Planning. *Sustain. Cities Soc.* **2019**, *50*, 101605. [CrossRef]
37. Ito, K.; Biljecki, F. Assessing Bikeability with Street View Imagery and Computer Vision. *Transp. Res. Part C Emerg. Technol.* **2021**, *132*, 103371. [CrossRef]
38. Ma, X.; Ma, C.; Wu, C.; Xi, Y.; Yang, R.; Peng, N.; Zhang, C.; Ren, F. Measuring Human Perceptions of Streetscapes to Better Inform Urban Renewal: A Perspective of Scene Semantic Parsing. *Cities* **2021**, *110*, 103086. [CrossRef]
39. Chen, L.; Yao, X.; Liu, Y.; Zhu, Y.; Chen, W.; Zhao, X.; Chi, T. Measuring Impacts of Urban Environmental Elements on Housing Prices Based on Multisource Data—A Case Study of Shanghai, China. *ISPRS Int. J. Geo-Inf.* **2020**, *9*, 106. [CrossRef]
40. Buonanno, P.; Montolio, D.; Raya-Vílchez, J.M. Housing Prices and Crime Perception. *Empir. Econ.* **2013**, *45*, 305–321. [CrossRef]
41. Suzhou Statistics and Information Bureau Suzhou Statistical Yearbook. 2021. Available online: http://tjj.suzhou.gov.cn/sztjj/tjnj/2021/zk/indexce.htm (accessed on 7 August 2023).
42. Anjuke. Available online: https://suzhou.anjuke.com/ (accessed on 21 December 2022).
43. Simonyan, K.; Zisserman, A. Very Deep Convolutional Networks for Large-Scale Image Recognition. *arXiv* **2015**, arXiv:1409.1556.
44. Wang, R.; Ren, S.; Zhang, J.; Yao, Y.; Wang, Y.; Guan, Q. A Comparison of Two Deep-Learning-Based Urban Perception Models: Which One Is Better? *Comput. Urban Sci.* **2021**, *1*, 3. [CrossRef]
45. Zhao, H.; Shi, J.; Qi, X.; Wang, X.; Jia, J. Pyramid Scene Parsing Network. In Proceedings of the 2017 IEEE Conference on Computer Vision and Pattern Recognition (CVPR), Honolulu, HI, USA, 21–26 July 2017; pp. 6230–6239.
46. Zhou, B.; Zhao, H.; Puig, X.; Fidler, S.; Barriuso, A.; Torralba, A. Scene Parsing through ADE20K Dataset. In Proceedings of the 2017 IEEE Conference on Computer Vision and Pattern Recognition (CVPR), Honolulu, HI, USA, 21–26 July 2017; pp. 5122–5130.
47. Ke, G.; Meng, Q.; Finley, T.; Wang, T.; Chen, W.; Ma, W.; Ye, Q.; Liu, T.-Y. LightGBM: A highly efficient gradient-boosting decision tree. *Adv. Neural Inf. Process. Syst.* **2017**, *30*, 2–9.
48. Huang, Z.; Chen, R.; Xu, D.; Zhou, W. Spatial and Hedonic Analysis of Housing Prices in Shanghai. *Habitat Int.* **2017**, *67*, 69–78. [CrossRef]
49. Lu, J. The Value of a South-Facing Orientation: A Hedonic Pricing Analysis of the Shanghai Housing Market. *Habitat Int.* **2018**, *81*, 24–32. [CrossRef]
50. James, G.; Witten, D.; Hastie, T.; Tibshirani, R. *An Introduction to Statistical Learning: With Applications in R*; Springer: Berlin/Heidelberg, Germany, 2013.
51. Tan, R.; He, Q.; Zhou, K.; Xie, P. The Effect of New Metro Stations on Local Land Use and Housing Prices: The Case of Wuhan, China. *J. Transp. Geogr.* **2019**, *79*, 102488. [CrossRef]
52. Pei, T.; Sobolevsky, S.; Ratti, C.; Shaw, S.-L.; Li, T.; Zhou, C. A New Insight into Land Use Classification Based on Aggregated Mobile Phone Data. *Int. J. Geogr. Inf. Sci.* **2014**, *28*, 1988–2007. [CrossRef]
53. Fan, Z.; Zhang, F.; Loo, B.P.Y.; Ratti, C. Urban Visual Intelligence: Uncovering Hidden City Profiles with Street View Images. *Proc. Natl. Acad. Sci. USA* **2023**, *120*, e2220417120. [CrossRef] [PubMed]
54. Kang, Y.; Abraham, J.; Ceccato, V.; Duarte, F.; Gao, S.; Ljungqvist, L.; Zhang, F.; Näsman, P.; Ratti, C. Assessing Differences in Safety Perceptions Using GeoAI and Survey across Neighbourhoods in Stockholm, Sweden. *Landsc. Urban Plan.* **2023**, *236*, 104768. [CrossRef]
55. Lynch, K. *The Image of the City*; MIT Press: Cambridge, MA, USA, 1960.
56. Quercia, D.; O'Hare, N.K.; Cramer, H. Aesthetic Capital: What Makes London Look Beautiful, Quiet, and Happy? In Proceedings of the Proceedings of the 17th ACM conference on Computer Supported Cooperative Work & Social Computing, Baltimore, MD, USA, 15 February 2014; pp. 945–955.
57. Fotheringham, A.S.; Wong, D.W.S. The Modifiable Areal Unit Problem in Multivariate Statistical Analysis. *Environ. Plan. A* **1991**, *23*, 1025–1044. [CrossRef]

Disclaimer/Publisher's Note: The statements, opinions and data contained in all publications are solely those of the individual author(s) and contributor(s) and not of MDPI and/or the editor(s). MDPI and/or the editor(s) disclaim responsibility for any injury to people or property resulting from any ideas, methods, instructions or products referred to in the content.

remote sensing

MDPI

Technical Note

Dynamics of Spring Snow Cover Variability over Northeast China

Taotao Zhang [1,2,*] and Xiaoyi Wang [3]

[1] Key Laboratory of Meteorological Disaster, Ministry of Education (KLME)/International Joint Research Laboratory of Climate and Environment Change (ILCEC)/Collaborative Innovation Center on Forecast and Evaluation of Meteorological Disasters (CIC-FEMD), Nanjing University of Information Science & Technology (NUIST), Nanjing 210044, China
[2] School of Atmospheric Sciences, Nanjing University of Information Science & Technology (NUIST), Nanjing 210044, China
[3] State Key Laboratory of Tibetan Plateau Earth System and Resources Environment (TPESRE), Institute of Tibetan Plateau Research, Chinese Academy of Sciences, Beijing 100101, China; xiaoyiwang@itpcas.ac.cn
* Correspondence: ttzhang@nuist.edu.cn

Abstract: Spring snow cover variability over Northeast China (NEC) has a profound influence on the local grain yield and even the food security of the country, but its drivers remain unclear. In the present study, we investigated the spatiotemporal features and the underlying mechanisms of spring snow cover variability over NEC during 1983–2018 based on the satellite-derived snow cover data and atmospheric reanalysis products. The empirical orthogonal function (EOF) analysis showed that the first EOF mode (EOF1) explains about 50% of the total variances and characterizes a coherent snow cover variability pattern over NEC. Further analyses suggested that the formation of the EOF1 mode is jointly affected by the atmospheric internal variability and the sea surface temperature (SST) anomaly at the interannual timescale. Specifically, following a negative phase of the atmospheric teleconnection of the Polar–Eurasian pattern, a prominent cyclonic circulation appears over NEC, which increases the snowfall over the east of NEC by enhancing the water vapor transport and decreases the air temperature through reducing the solar radiation and intensifying the cold advection. As a result, the snow cover has increased over NEC. Additionally, the tripole structure of the North Atlantic spring SST anomaly could excite a wave-train-type anomalous circulation propagating to NEC that further regulates the snow cover variability by altering the atmospheric dynamic and thermodynamic conditions and the resultant air temperature and snowfall. Our results have important implications on the understanding of the spring snow cover anomaly over NEC and the formulation of the local agricultural production plan.

Keywords: Northeast China; spring snow cover; interannual variability; Polar–Eurasian pattern; North Atlantic SST

1. Introduction

Northeast China (NEC) is one of the most important commercial grain bases, where the crop yield accounts for more than 20% of the total production of the country, thus playing a crucial role in the local socioeconomic development and even the country's food security [1–3]. Owing to the long cold season over NEC, abundant snow cover accumulates in winter and is preserved into spring, which has notable impacts on local agricultural production. For example, the melting of snow cover during spring provides precious water resources for crop sowing by regulating runoff and soil moisture [4,5]. In addition, by the snow albedo and hydrological effect, spring snow cover can influence the air temperature and precipitation during spring and summer [6–11], which are the key factors affecting seedling emergence, crop growth, and final yield. Therefore, it is critical to advance the

understanding of the spring snow cover variability over NEC for the formulation of the local agricultural production plan and the promotion of socioeconomic development.

The snow cover variability over NEC has been a widely considered topic in the recent global warming scenario [12–15]. Numerous studies explored the changes in various snow cover parameters, such as the snow volume, phenology, and duration [16–19]. Some studies found that the snow cover days have significantly increased in recent decades and attributed this to the influence of the mean air temperature [16,17,19], while others suggested that the snow depth has decreased over NEC [18]. These studies have improved our understanding on the responses of snow cover over NEC to the warming climate, but the spatiotemporal features of the snow cover variability on the interannual timescale have not been well documented as yet.

Previous researches suggested that both the atmospheric internal variability and the external forcings play important roles in the snow cover variability over Eurasia and its sub-regions [20–26]. For example, the dominant modes of Eurasian snow cover variations in spring and autumn were found to be influenced by multiple teleconnection patterns, such as the Arctic Oscillation (AO), East Atlantic (EA), Polar–Eurasian pattern (POL), EA-Western Russia (EAWR), West Pacific (WP), and Scandinavia (SCAND) pattern [24–26]. Moreover, North Atlantic Oscillation (NAO) could affect the snow cover variability over Europe during winter through regulating the thermal advection [20–23]. Sun et al. [27] also found that NAO is an important factor shaping the winter snowfall variability over North China. Lu et al. [18] indicated that the snow depth over NEC during spring and autumn is negatively correlated with the intensity of the East Asian Trough and the polar vortex, while the winter snow depth has a close linkage with the Subtropical High intensity.

As for the lower boundary forcings, the sea surface temperature (SST) anomaly over the North Atlantic has been recognized as a crucial driver that can affect the Eurasian snow cover by exciting the eastward propagated wave-train-type anomalous circulations [25,26,28]. The transition of the North Atlantic SST anomaly from a cold phase to a warm phase around the 1990s contributed to the decadal increase in heavy snowfall over NEC [29]. Recently, studies indicated that the Arctic sea ice variabilities also act as a considerable factor responsible for the anomalies of temperature and precipitation over Eurasia, which then could lead to the variations in snow cover [26,30–32]. However, it remains unclear whether there is any influence of the above factors on the spring snow cover variability over NEC.

Therefore, in this study, we aim to, firstly, clarify the characteristics of the interannual variability in the spring snow cover over NEC, and, secondly, unravel the physical mechanism responsible for the snow cover anomalies.

2. Study Area

In the present study, NEC denotes the region of China over 40°–55°N, 115°–135°E, including the Heilongjiang, Jilin, and Liaoning Provinces and the east part of Inner Mongolia (Figure 1). The Inner Mongolia Plateau lies in western NEC, which is mainly covered by grassland and sparse vegetation. Forests are mainly distributed in the Greater and Lesser Khingan Mountains and Changbai Mountain, which stretch from the north to the east and south of NEC. There are wide range of croplands located in the central and east tip of NEC, with flat terrain and low elevation.

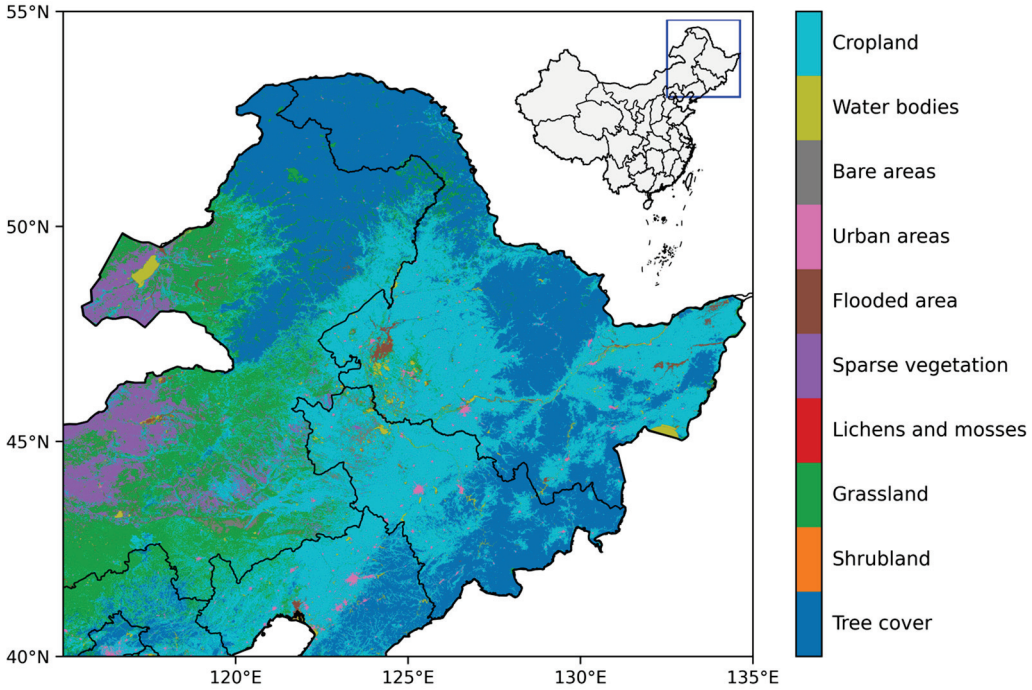

Figure 1. The location and land cover types [33] of Northeast China.

3. Materials and Methods

In the present study, the snow cover fraction (SCF) data were derived from the Northern Hemisphere EASE-Grid 2.0 Weekly Snow Cover and Sea Ice Extent, Version 4, which was provided by the National Snow and Ice Data Center (NSIDC). The NSIDC snow data are available from 1966 to the present with a spatial resolution of 0.25° × 0.25° [34]. We also employed the SCF data from the Japan Aerospace Exploration Agency Satellite Monitoring for Environmental Studies (JASMES) to confirm the reliability of the results from the NSIDC data. The JASMES data are available from 1978 to 2019 with a resolution of 5 km × 5 km [35]. For ease of analysis, we transformed both the NSIDC and JASMES snow cover data to a monthly 1° × 1° grid based on the linear interpolation.

The monthly surface air temperature (SAT) and precipitation were from the Climate Research Unit, University of East Anglia (CRU TS v4.03). This dataset is available from 1901 to 2020 and has a spatial resolution of 0.5° × 0.5° [36]. The SST data were obtained from the National Oceanic and Atmospheric Administration Extended Reconstructed Sea Surface Temperature (ERSST) v5 dataset. These monthly SST data are on a regular 2° × 2° grid and are available after 1854 [37]. The monthly sea ice concentration data, with a resolution of 1° × 1° and covering 1870 to 2020, are provided by the Hadley Centre Sea Ice and Sea Surface Temperature data set (HadISST1) [38]. The monthly atmospheric variables, including air temperature, horizontal wind, geopotential height, and energy fluxes, were extracted from the National Centers for Environmental Prediction-National Center for Atmospheric Research (NCEP-NCAR) Reanalysis 1 product [39]. The indices of atmospheric teleconnections were downloaded from the National Oceanic and Atmospheric Administration Climate Prediction Center. These datasets have been widely used in previous studies and confirmed to be suitable for climate investigations [34–39].

In order to analyze the variability in SAT, we diagnosed the horizontal thermal advection (T_{adv}), which is calculated according to the following formula [40]:

$$T_{adv} = -u\frac{\partial T}{r\cos\varphi\partial\lambda} - v\frac{\partial T}{r\partial\varphi} \quad (1)$$

where φ and λ represent the latitude and longitude, respectively. u, v, r, and T are the zonal and meridional winds, radius of Earth, and air temperature, respectively.

To detect the propagation of the Rossby wave train, we computed the wave activity flux (WAF) following Takaya and Nakamura [41,42]. The horizontal components of WAF can be written as follows:

$$\mathrm{WAF} = \frac{p\cos\varphi}{2|\mathbf{U}|}\left\{\begin{array}{c}\frac{U}{\alpha^2\cos^2\varphi}\left[\left(\frac{\partial\psi'}{\partial\lambda}\right)^2 - \psi'\frac{\partial^2\psi'}{\partial\lambda^2}\right] + \frac{V}{\alpha^2\cos\varphi}\left[\frac{\partial\psi'}{\partial\lambda}\frac{\partial\psi'}{\partial\varphi} - \psi'\frac{\partial^2\psi'}{\partial\lambda\partial\varphi}\right] \\ \frac{U}{\alpha^2\cos\varphi}\left[\frac{\partial\psi'}{\partial\lambda}\frac{\partial\psi'}{\partial\varphi} - \psi'\frac{\partial^2\psi'}{\partial\lambda\partial\varphi}\right] + \frac{V}{\alpha^2}\left[\left(\frac{\partial\psi'}{\partial\varphi}\right)^2 - \psi'\frac{\partial^2\psi'}{\partial\varphi^2}\right]\end{array}\right\} \quad (2)$$

where $|\mathbf{U}|$ represents the climatological wind speed; p is the pressure scaled by 1000 hPa; α means the radius of the Earth; φ and λ represent the latitude and longitude; V and U indicate the climatological meridional and zonal wind, respectively; and ψ' denotes the perturbed geostrophic streamfunction.

The Eady growth rate (*EGR*) is employed to quantify the atmospheric baroclinicity [43,44]. The *EGR* can be calculated based on the following equation:

$$EGR = 0.31\frac{|fU_z|}{N} \quad (3)$$

where the f is the Coriolis parameter, U_z denotes the vertical wind shear, and the N is the Brunt–Väisälä frequency. Moreover, the variance in the 2–8-day bandpass-filtered daily geopotential height at 300 hPa is used to indicate the storm track activity.

In light of the lack of part of snow cover data from JASMES and NSIDC in 1981 and 1982, the research period of this paper was set as 1983–2018. The spring snow cover means the average snow cover in March, April, and May. This study aimed to investigate the variations on the interannual timescale; all of the variables needed to be filtered by a 9-year high-pass filter to avoid the potential contamination of the signals of decadal changes and long-term trends. We employed the empirical orthogonal function (EOF) analysis to extract the spatiotemporal features of the spring snow cover variability over NEC. The snow cover anomalies in EOF analysis were weighted by the cosine of the latitudes to account for the reduction in the area toward the higher latitudes [45]. In addition, we calculated the linear correlations of the timeseries of the leading mode of snow cover variability with teleconnections, SST, and sea ice to detect the potential relationships between them. Moreover, the responses of the atmospheric dynamic and thermodynamic conditions to the teleconnections and SST anomalies were examined through linear regression analyses to explore the physical processes responsible for the snow cover variability. The statistical significance was estimated on the basis of the two-tailed Student's *t*-test.

4. Results

4.1. The Leading Mode of Spring Snow Cover Anomaly over NEC

Figure 2 presents the first EOF mode (EOF1) of the interannual variability in NEC spring snow cover during 1983–2018. The EOF1 mode derived from the NSIDC SCF data (Figure 2a) can explain about 50% of the total variances and can be separated from other modes based on the method proposed by North et al. [46]. The spatial pattern of EOF1 characterizes a coherent variation in the spring snow cover over most areas of NEC, with large loading located in the east and north parts of NEC (Figure 2a). The principal component of EOF1 (PC1) shows prominent interannual fluctuation, and the magnitude has experienced an obvious increasing trend since the late 1990s (Figure 2b). This denotes that the interannual variability in the spring snow cover over NEC has strengthened in recent years.

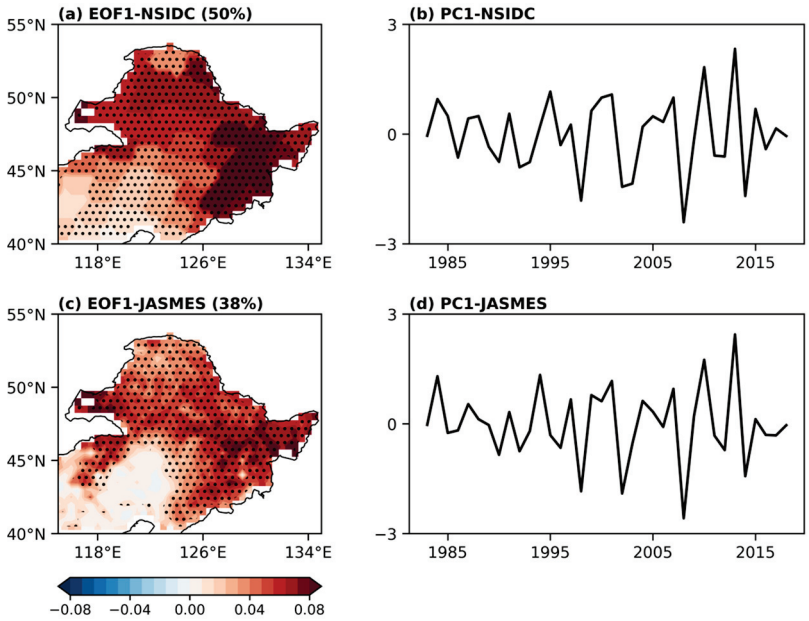

Figure 2. The EOF1 mode of NEC spring snow cover anomaly during 1983–2018. (**a**,**c**) illustrate the spatial patterns of EOF1 mode derived from NSIDC and JASMES snow cover data, respectively. (**b**,**d**) show the corresponding principal component (PC1) of two datasets. The spatial patterns of the EOF1 mode are expressed as the regression of SCF against the respective PC1. The dots represent areas significant at 95% confidence level.

In order to further corroborate the results from the NSIDC data, we also conducted an EOF analysis on the JASMES SCF data. The spatial pattern of the EOF1 mode of the snow cover variability from the JASMES bears a close resemblance to that from the NSIDC, but with a relatively lower variance explanation rate of 38% (Figure 2c). In addition, the correlation coefficient between the PC1 from the JASMES and that from the NSIDC reaches 0.89, exceeding the 99% confidence level (Figure 2d). The consistencies of the EOF results regarding both the spatial pattern and its temporal evolution between two SCF datasets verify the robustness of the features of the EOF1 mode of NEC spring snow cover variability. Although the spatiotemporal features of the snow cover variability from the two datasets are consistent with each other, the EOF1 mode from the NSIDC can explain a larger proportion of the total variances than that from JASMES. Therefore, in the following sections, we mainly use the NSIDC data to investigate the mechanisms of the NEC spring snow cover variability. The main results do not change when the JASMES snow cover data are employed (See Supplementary Material).

4.2. Mechanisms of the Spring Snow Cover Variability over NEC

Variation in snow cover is mainly controlled by the anomalies of snowfall and air temperature, which determine the processes of snow melt and accumulation. In theory, a lower temperature and excessive snowfall in the cold season are conducive to the accumulation of snow cover on the ground, and vice versa [25,26]. Furthermore, the variabilities in snowfall and air temperature are the products of atmospheric circulation anomalies [27,47]. Therefore, the first step is to analyze the EOF1-related simultaneous anomalous atmospheric circulations to identify the potential influencing factors.

Figure 3 exhibits the anomalies of horizontal winds and geopotential height at 200 hPa, 500 hPa, and 850 hPa, which are obtained through regression with the PC1. It is apparent that the anomalous atmospheric circulation patterns at different levels of the troposphere are generally consistent with each other (Figure 3), indicating a quasi-barotropic structure. Specifically, corresponding to the positive phase of PC1, NEC is dominated by a prominent anomalous cyclonic circulation that may contribute to the excessive snow cover over NEC by modulating the precipitation and temperature. From a wider view, there is a clear

meridional dipole pattern of geopotential height anomalies over the north polar region and northeast Asia (Figure 3). This circulation pattern closely resembles that related to the atmospheric teleconnection patterns of AO and POL [48–50], implying that they could act as the potential drivers of the NEC snow cover variability. In addition, a zonal wave-train-type circulation can be seen over the mid–high latitudes that stems from the North Atlantic to NEC (Figure 3), indicating the possible impact of the North Atlantic SST anomaly on the NEC snow cover variation. Therefore, in the following section, we explore the physical mechanisms of the NEC spring snow cover anomaly by mainly considering the contributions of the atmospheric teleconnections and the North Atlantic SST.

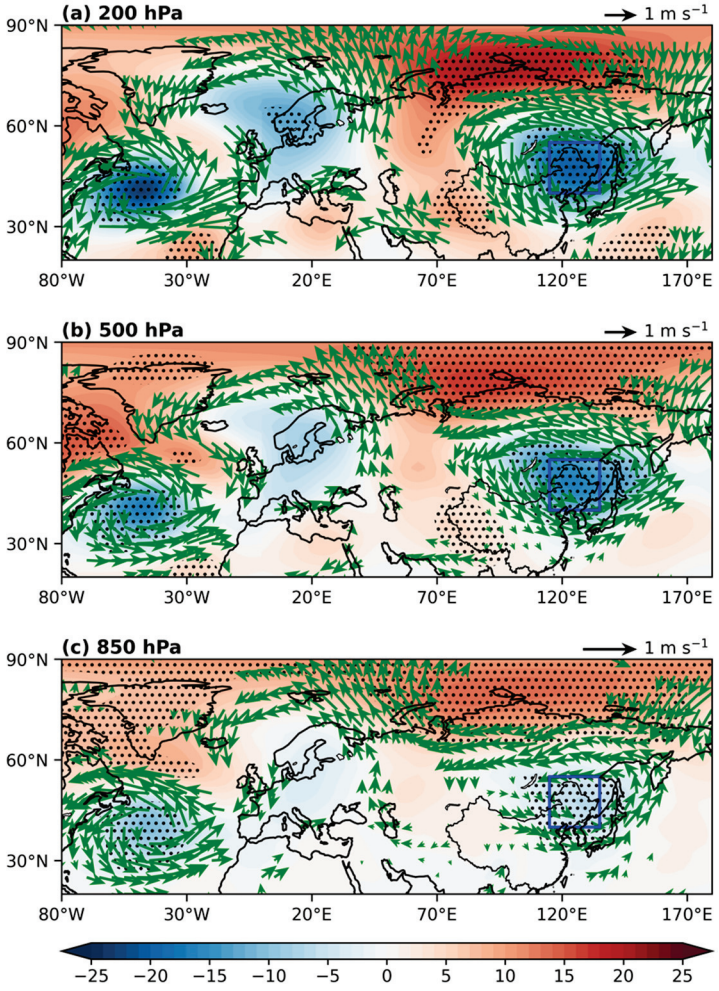

Figure 3. Anomalies of geopotential height (shading; gpm) and wind (vectors; m s^{-1}) at 200 hPa (**a**), 500 hPa (**b**), and 850 hPa (**c**) obtained by regression onto PC1 during 1983–2018. Green vectors and black dots indicate the anomalies of wind and geopotential height reaching the 95% confidence level, respectively. The blue boxes represent the domain of NEC.

4.2.1. Effect of the Polar–Eurasia Pattern

Correlation analyses confirm that the AO and POL have a close connection with the PC1 of the leading mode of NEC snow cover variability, with correlation coefficients of −0.35 ($p < 0.05$) and −0.45 ($p < 0.01$), respectively (Table 1). We also calculated the correlations of PC1 with other major teleconnections that prevailed over Eurasia [48,49], but none of them have a significant correlation with PC1 (Table 1). These results are also robust when the JASMES snow data are used (Table S1). In addition, we note that there is a close connection between AO and POL, with a correlation coefficient of 0.43 ($p < 0.01$). This implies that the linkages of AO and POL with PC1 may not be independent of each other. To check this speculation, we calculated the partial correlations between PC1 and AO (POL)

after removing the effect of POL (AO), respectively. The results show that the correlation between PC1 and POL is still significant after excluding the signal of AO (Figure 4b), suggesting that the influence of POL on the EOF1 mode of NEC snow cover variability is independent of AO. In contrast, the relationship between PC1 and AO substantially weakens when the signal of POL is excluded (Figure 4a). This denotes that the linkage between PC1 and AO may be an artifact of the effect of POL. Therefore, we suggest that the POL is the major factor responsible for the formation of the leading mode of NEC snow cover variation.

Table 1. Correlation coefficients (R) between the PC1 of NEC snow cover variability with the contemporary atmospheric teleconnections. One asterisk and double asterisks indicate the R exceeding the 95% and 99% confidence levels, respectively.

Teleconnection Indices	R
AO	−0.35 *
NAO	−0.11
EA	−0.21
EAWR	−0.04
POL	−0.45 **
SCAND	−0.17
WP	−0.02

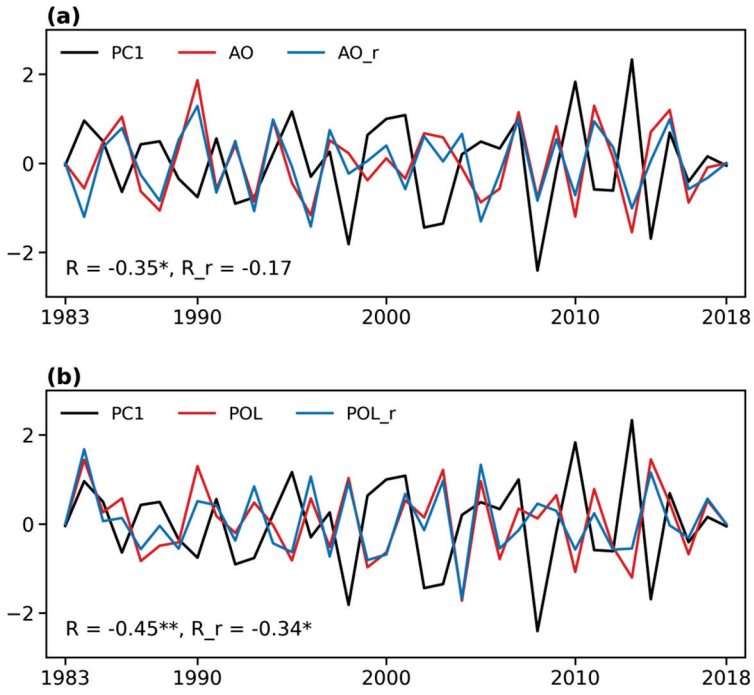

Figure 4. (**a**) The correlations of PC1 with the AO (R) and AO_r (R_r). The AO_r represents the residuals of AO where the signal of POL has been linearly removed. (**b**) is the same as (**a**) except for with POL and POL_r. POL_r is the residual of POL where the signal of AO has been linearly removed. The correlation coefficients exceeding the 95% and 99% confidence levels are labeled by one asterisk and double asterisks, respectively.

What are the physical processes involved in the effect of the POL on NEC snow cover anomalies? To answer this question, we explored the POL-related anomalies of geopotential height and horizontal winds. As shown in Figure 5a, in response to the negative phase of POL, the anomalous circulations exhibit a tripole structure at 500 hPa, with two positive anomalies centers of geopotential height over the north high latitudes and northwest Pacific, and one negative anomaly centering around northeast Asia. Accordingly, two anomalous anticyclones and one anomalous cyclone are observed over the corresponding regions

(Figure 5a). The anomalous circulation pattern at the lower troposphere (Figure 5b) closely resembles that at 500 hPa, implying a quasi-barotropic vertical structure of the circulation anomalies related to the POL.

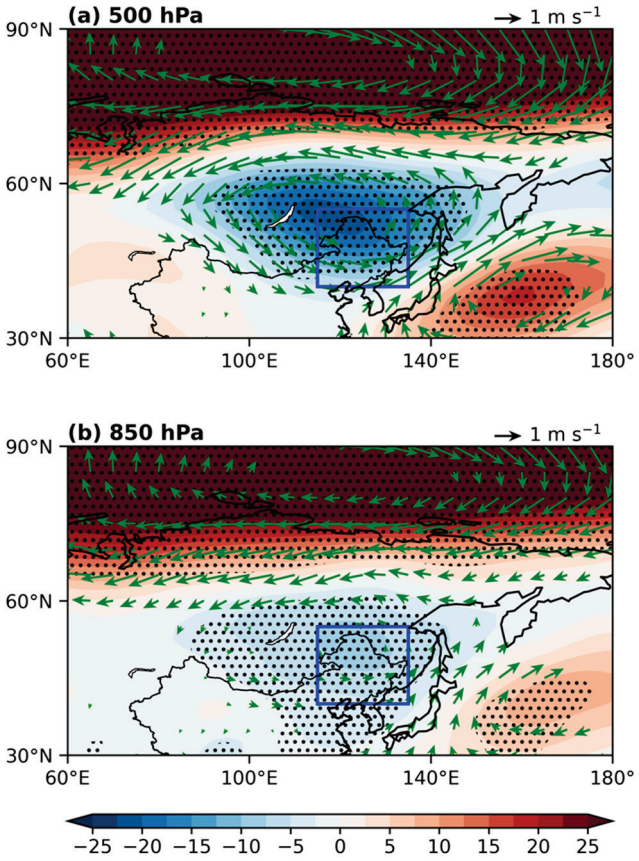

Figure 5. The anomalies of horizontal wind (vectors; m s^{-1}) and geopotential height (shading; gpm) at 500 hPa (**a**) and 850 hPa (**b**) obtained by regression onto the sign-reversed POL index during 1983–2018. The anomalies of wind and geopotential height exceeding the 95% confidence level are labeled by green vectors and black dots, respectively. The blue boxes represent the domain of NEC.

Focusing on northeast Asia, the anomalous southeast flow on the east side of the anomalous cyclone transports the warm and moist air flow northward from the Japan Sea and then converges over the east and north sides of the NEC (Figure 6a), leading to excessive snowfall over the region (Figure 6g). Moreover, the increased cloud cover (Figure 6b) induced by the moisture convergence contributes to the decreased downward shortwave radiation to the north and east boundaries of NEC (Figure 6c), which in turn causes the negative anomalies of SAT there (Figure 6f). As a result, the reduced SAT and the increased snowfall jointly lead to the above normal snow cover over the north and east boundaries of NEC (Figure 6h). In addition, the anomalous northwesterly air flow on the west side of the cyclonic circulation could lead to the invasion of cold and dry air from the higher latitudes to the central part of NEC (Figure 5), which directly results in the negative anomalies of SAT (Figure 6f) through cold advection (Figure 6e). On the other hand, the intrusion of the northwest flow could further indirectly decrease the SAT by reducing the downward longwave radiation (Figure 6d) owing to the lower emissivity of longwave radiation of the dry cold air. Therefore, the positive anomalies of snow cover over central NEC (Figure 6h) may mainly result from the decreased SAT because the snowfall has not changed significantly over the region (Figure 6g). In general, the POL-induced snow cover anomaly pattern is consistent with that related to the EOF1 mode, verifying the crucial role of POL in shaping the spring snow cover variability over NEC.

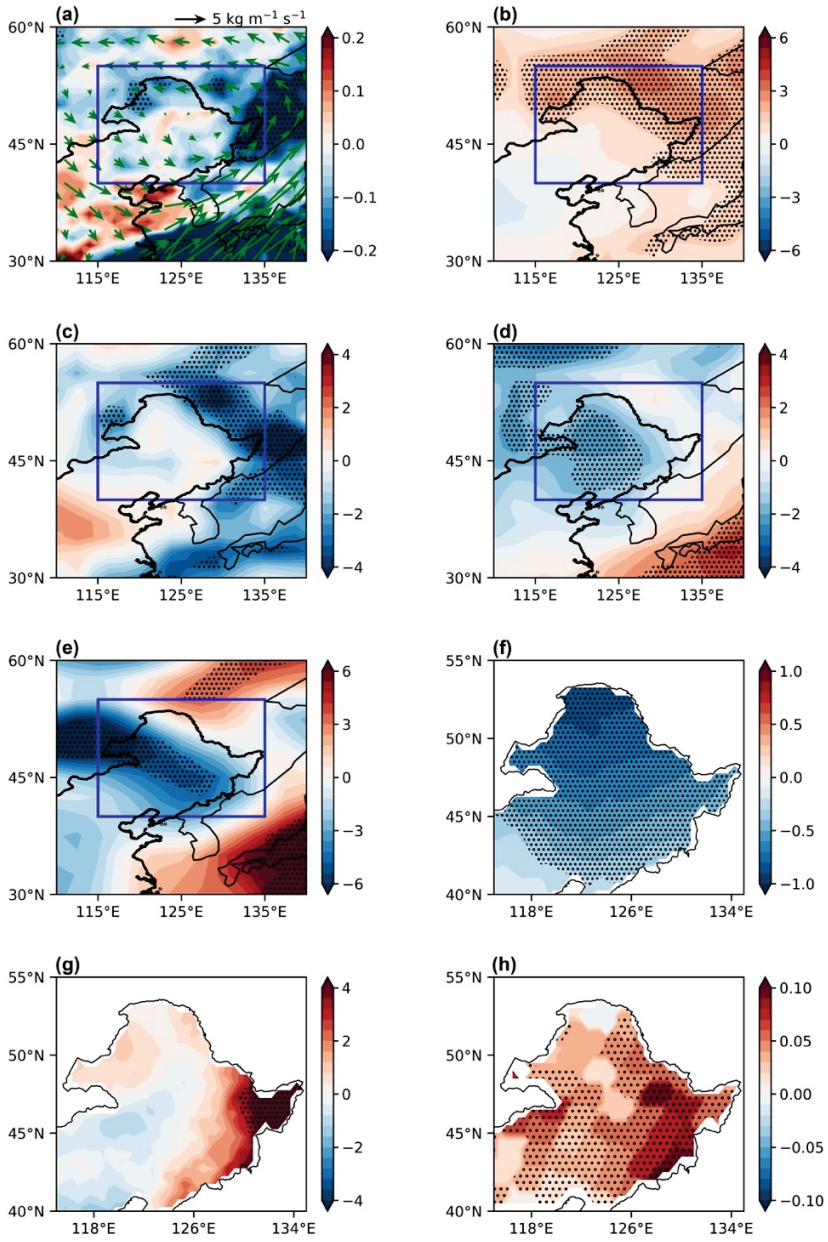

Figure 6. The anomalies of various variables obtained by regression against the sign-reversed POL index. (**a**) Vertical integrated moisture flux (vectors; kg m^{-1} s^{-1}) and its divergence (10^{-5} kg m^{-2} s^{-1}), (**b**) total cloud cover (%), downward shortwave (**c**) and longwave (**d**) radiation flux (W m^{-2}), (**e**) temperature advection (°C month^{-1}), (**f**) SAT (°C), (**g**) snowfall (mm), (**h**) SCF. Black dots imply where the anomalies reach the 95% confidence level. The blue boxes represent the domain of NEC.

4.2.2. Impact of the North Atlantic SST Anomaly

In order to explore the relationship of the North Atlantic SST with the dominant mode of the NEC snow cover anomaly, a regression between the anomalies of the spring SST and PC1 were examined. As illustrated in Figure 7a, the North Atlantic SST anomalies exhibit an apparent tripole pattern, with one negative anomaly centering over the east of North America, and two positive anomalies centering over the subtropics and the south of Greenland, respectively. We further constructed an SST index (SSTI) to quantitatively depict the variability in the tripole SST anomalies. The SSTI is defined as the standardized difference in the area-average SST over the two positive centers and the negative center. There is an intimate connection between PC1 and SSTI, with the correlation coefficient reaching 0.56, exceeding the 99% confidence level (Figure 7b), confirming the potential role

of the North Atlantic tripole SST anomalies in the variability in NEC spring snow cover. Note that these results are supported by the analyses based on the JASMES snow data (Figure S1).

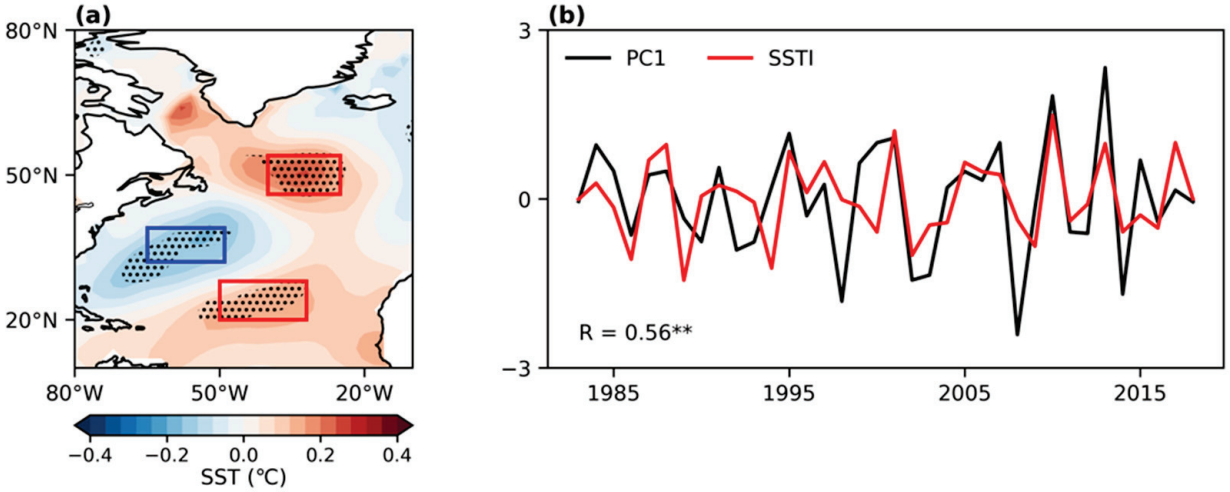

Figure 7. (**a**) SST anomalies over North Atlantic obtained by regression against PC1. (**b**) Timeseries of the SSTI and PC1. Black dots in (**a**) denote the SST anomalies exceeding 95% confidence level. Double asterisks in (**b**) indicate the R exceeding the 99% confidence levels. The regions enclosed by blue and red rectangles are used to compute the SSTI. The domains of three key regions are 46°–54°N, 25°–40°W; 32°–39°N, 49°–65°W; and 20°–28°N, 32°–50°W for the north, central, and south regions, respectively.

Previous studies indicated that the North Atlantic SST anomalies' tripole pattern can regulate climate variations over Eurasia by exciting a wave-train-like anomalous circulation [25,51,52]. Here, we find that following the positive phase of the SSTI, the geopotential height anomalies at 300 hPa exhibit a clear wave train structure (Figure 8a). According to the WAF, we can see that the wave-train-type circulation propagates from the North Atlantic to east Asia, thus acting like a bridge spreading the influence of the North Atlantic SST anomalies on the NEC climate (Figure 8a). How does the tripole SST anomaly excite such a Rossby wave train? Previous studies suggested that the response of the transient eddy activities to the low-level atmospheric baroclinicity is the crucial process responsible for the forcing of the SST anomaly on the atmosphere [53–56]. To unravel this mechanism, we investigated the SSTI-related meridional temperature gradient and the atmospheric baroclinicity at 850 hPa, and anomalies of the storm track at 300 hPa (Figure 8b–d). Following the positive polarity of the SSTI, the temperature gradient has increased over the region between the areas with the negative SST anomalies over the central North Atlantic and the positive SST anomalies over the subtropics (Figure 8b). On the contrary, the decreased temperature gradient is seen over the area between the positive SST anomalies centers over the south of Greenland and the central North Atlantic (Figure 8b). Correspondingly, the strengthened (weakened) atmospheric baroclinicity presents over the regions with an increased (decreased) temperature gradient (Figure 8c). In response to the changes in the atmospheric baroclinicity, reduced and intensified storm tracks are observed over the south of Greenland and the central North Atlantic, respectively (Figure 8d). The enhanced (weakened) transient eddy activity tends to be accompanied by cyclonic (anticyclonic) eddy forcing to its north [57,58]. As a result, the tripole SST anomalies could lead to the positive and negative geopotential height anomalies over southern Greenland and central North Atlantic, respectively, which further excite the wave train propagating to east Asia (Figure 8a).

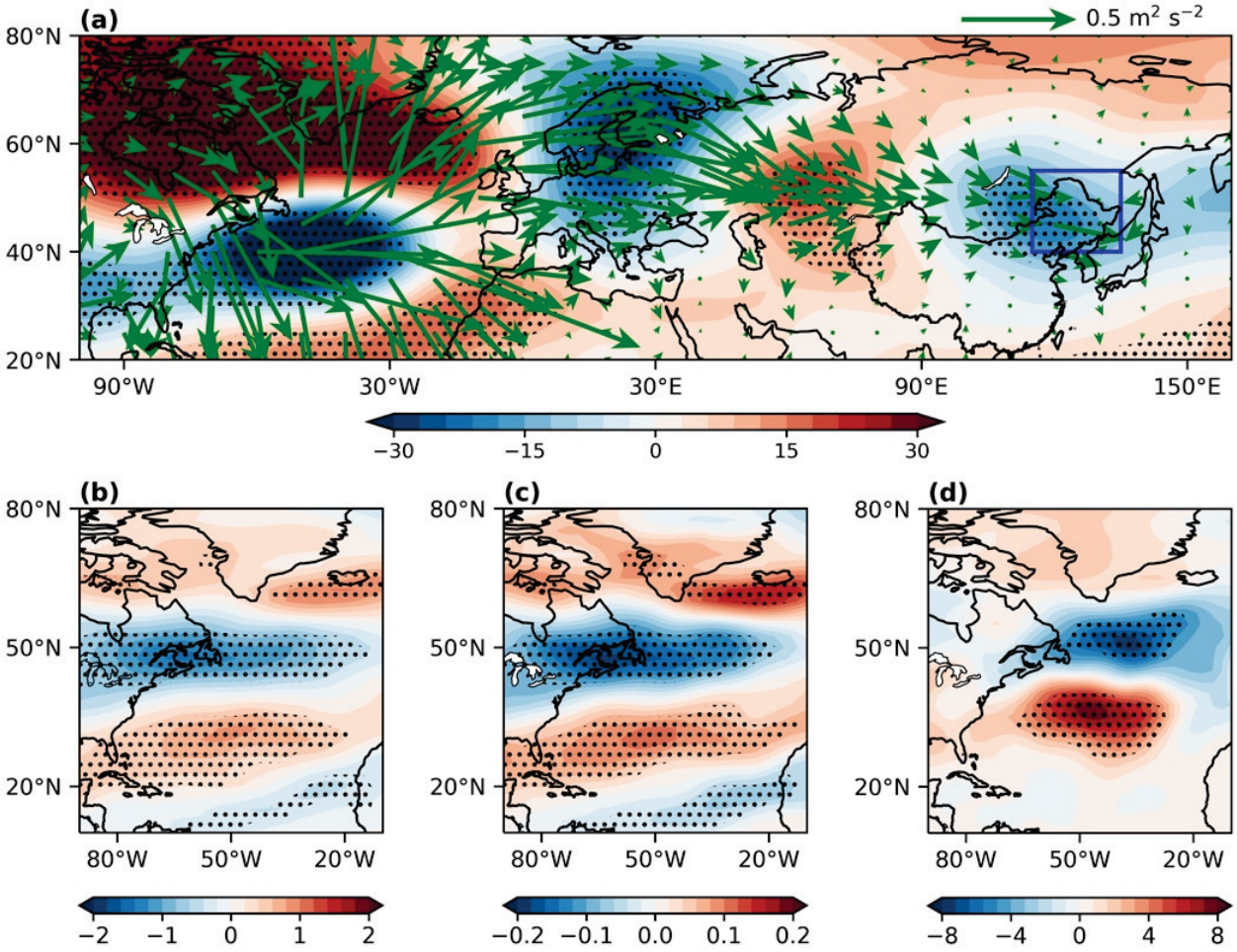

Figure 8. Anomalies of (**a**) geopotential height (shading; gpm) and the related WAF (vectors) at 300 hPa, (**b**) meridional air temperature gradient (10^{-6} K m^{-1}) and (**c**) Eady growth rate (day^{-1}) at 850 hPa, (**d**) storm track at 300 hPa (gpm) obtained by regression onto SSTI. Stippling indicates the 95% confidence level. The blue box represents the domain of NEC.

The wave train type circulation has significantly negative height anomalies centering around the NEC (Figures 8a and 9a). Controlled by this cyclonic circulation, the south and southeast winds on the east side of the cyclonic circulation bring abundant water vapor northward (Figure 9b) and lead to above-normal snowfall over the south NEC (Figure 9g). In addition, the convergence of the water vapor results in the positive anomalies of cloud cover over the north NEC (Figure 9c), which would further reduce the incoming solar radiation and hence the decreased SAT over there (Figure 9d,f). On the west side of the cyclone, the northwesterly air flow causes the decreased SAT over the south NEC through cold advection (Figure 9e,f). The SSTI-related snow cover variability over NEC shows a coherent positive anomalies pattern, with two prominent anomalies centering over the south and north parts of NEC, respectively (Figure 9h). According to our above analyses, the snowfall has no significant change over north NEC (Figure 9g), which would exert limited influence on the snow cover anomaly over the region. Therefore, the increased snow cover in the north center mainly results from the decreased SAT, while that in the south center could be attributed to the combined effect of the reduced SAT and increased snowfall (Figure 9f–h).

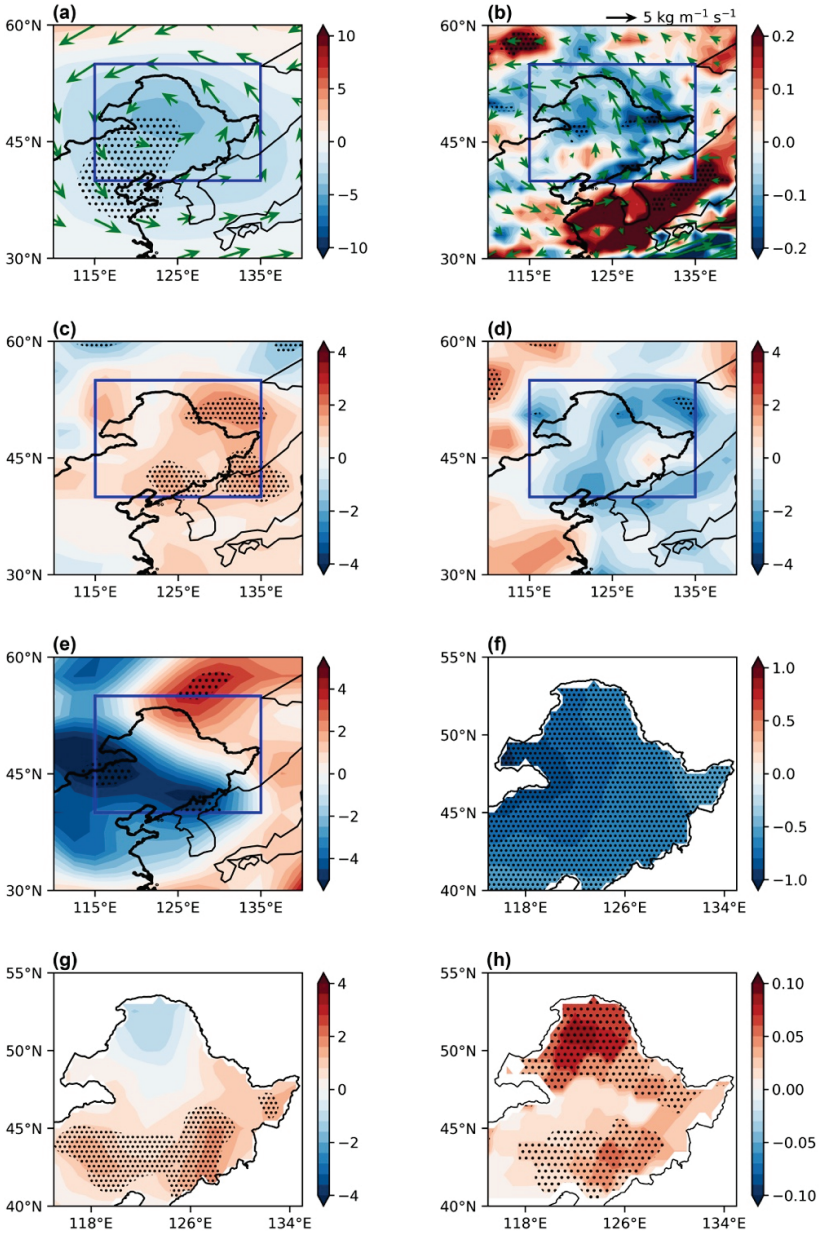

Figure 9. The anomalies of various variables obtained by regression against the SSTI. (**a**) Geopotential height and wind at 850 hPa, (**b**) vertical integrated moisture flux (vectors; kg m^{-1} s^{-1}) and its divergence (10^{-5} kg m^{-2} s^{-1}), (**c**) total cloud cover (%), (**d**) downward shortwave radiation flux (W m^{-2}), (**e**) temperature advection (°C month^{-1}), (**f**) SAT (°C), (**g**) snowfall (mm), and (**h**) SCF. Dotted areas indicate where the anomalies are significant at the 95% confidence level. The blue boxes represent the domain of NEC.

5. Conclusions and Discussion

This study successfully achieved both of its objectives by (1) clarifying the characteristics of the interannual variability in NEC spring snow cover (1983–2018) and (2) identifying the physical mechanisms responsible for the main drivers creating the variability in NEC spring snow cover. This was accomplished by analyzing satellite-derived snow cover data along with the analysis of the effects of atmospheric patterns and SST. The EOF analysis was used to obtain the leading mode of the NEC snow cover anomaly. The EOF1 mode can explain about half of the total variances and features a coherent snow cover variability over NEC. Further analyses found that the atmospheric teleconnection pattern of POL and the tripole SST anomalies over the North Atlantic play a major role in the formation of the

EOF1 mode. Specifically, the POL-related anomalous circulations transport moisture to the east and north sides of NEC, resulting in excessive snowfall over the region. In addition, the circulation-induced cold advection and reduced solar radiation lead to the negative anomalies of SAT dominating the whole NEC. The decreased air temperature and increased snowfall contribute to the excessive snow cover over NEC. The North Atlantic tripole SST anomalies can shape the NEC spring snow cover variability by exciting a wave-train-type anomalous circulation that propagates from the North Atlantic to NEC. Controlled by the SST-induced anomalous cyclone, the snowfall has increased over the south part of NEC, while the SAT over the whole NEC has significantly decreased. These anomalies of SAT and snowfall are conducive to the accumulation of snow cover. Our results can substantially improve the understanding of the variability in spring snow cover over NEC and provide scientific support for making local agricultural policies.

We note that although the POL and the tripole SST anomalies have profound impacts on the dominant mode of the spring snow cover variability over NEC, they can jointly account for about 50% of the variances. This implies that there should be other influencing factors responsible for the NEC snow cover variability. Previous studies suggested that the Arctic sea ice variation can exert important influence on the NEC climate variability [27,59]. Here, we additionally examined the possible relationship between Arctic sea ice and NEC snow cover. As exhibited in Figure 10 (also in Figure S2), the correlations between PC1 and the spring sea ice are generally weak, suggesting the limited contribution of the Arctic sea ice variation on the NEC spring snow cover variations. Therefore, in future studies, we should investigate other potential drivers to further improve the understanding of the mechanisms of the snow cover variability over NEC. Previous studies found that the connections between some influencing factors and regional climate anomalies have weakened [60–62] or strengthened [10,63,64] in recent years. It remains unknown if the influences of the POL and the tripole SST anomalies on the NEC snow cover variability would change in a future warming climate. In addition, this study only concentrates on the interannual variability; the characters and the underlying physical mechanisms of the decadal change and the long-term trend of the NEC snow cover have not been well documented as yet. These issues should be explored in the following studies using longer observational data and model simulation. Moreover, the extraction of snow cover data from satellite images can be influenced by vegetation [65]. It is necessary to strengthen snow monitoring over vegetation-covered areas, which is beneficial to improve the accuracy of snow cover data.

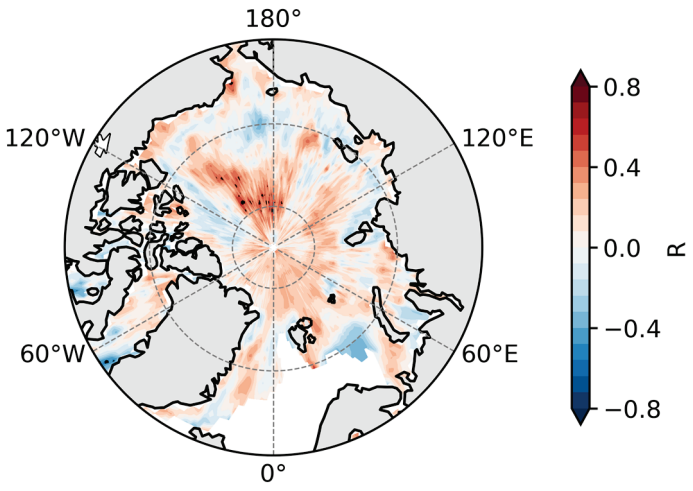

Figure 10. Correlations between PC1 of NEC spring snow cover variability and simultaneous sea ice variations. Dots denote the correlations exceeding the 95% confidence level.

Supplementary Materials: The following supporting information can be downloaded at: https://www.mdpi.com/article/10.3390/rs15225330/s1, Figure S1: (a) SST anomalies over North Atlantic obtained by regression against PC1 of JASMES data. (b) Timeseries of the SSTI and PC1. Black dots in (a) denote the SST anomalies exceeding 95% confidence level. The regions enclosed by rectangles are used to compute the SSTI. The domains of three key regions are 46°–54°N, 25°–40°W; 34°–41°N, 46°–62°W; and 20°–28°N, 32°–50°W for the north, central, and south regions, respectively; Figure S2: Correlations between PC1 of NEC spring snow cover variability from the JASMES data and simultaneous sea ice variations. Dots denote the correlations exceeding the 95% confidence level; Table S1: Correlation coefficients (R) between the PC1 of NEC snow cover variability from the JASMES data with the contemporary atmospheric teleconnections. One asterisk and double asterisks indicate the R exceeding the 95% and 99% confidence levels, respectively.

Author Contributions: Conceptualization, T.Z. and X.W.; methodology, T.Z.; validation, X.W.; formal analysis, T.Z.; investigation, T.Z.; data curation, X.W.; writing—original draft preparation, T.Z.; writing—review and editing, X.W.; visualization, T.Z.; supervision, X.W. All authors have read and agreed to the published version of the manuscript.

Funding: This research was jointly supported by the National Natural Science Foundation of China (42305023, 42371118), Natural Science Foundation of Jiangsu Province (BK20230432), Natural Science Foundation of the Jiangsu Higher Education Institutions of China (23KJB170011), and the Startup Foundation for Introducing Talent of NUIST (2022r002).

Data Availability Statement: All data that support the findings of this study are included within the article.

Acknowledgments: We gratefully acknowledge the National Snow and Ice Data Center for providing the snow cover data.

Conflicts of Interest: The authors declare no conflict of interest.

References

1. Yang, J.; Chen, Y.; Wang, Q. Cultivated Land Resources and Grain Production Potential in the Three Northeast Provinces. *Chin. J. Soil Sci.* **2017**, *48*, 1055–1060. (In Chinese)
2. Han, D.; Zhao, J.; Hu, Q. Study on the change characteristics of food crop yield in Northeast China and its response to meteorological drought. *J. China Agricul. Uni.* **2021**, *26*, 188–200. (In Chinese)
3. Zhen, Z.; Chen, S.; Yin, T.; Gastellu-Etchegorry, J.-P. Improving Crop Mapping by Using Bidirectional Reflectance Distribution Function (BRDF) Signatures with Google Earth Engine. *Remote Sens.* **2023**, *15*, 2761. [CrossRef]
4. Qi, W.; Feng, L.; Liu, J.; Yang, H. Snow as an important natural reservoir for runoff and soil moisture in Northeast China. *J. Geophys. Res. Atmos.* **2020**, *125*, e2020JD033086. [CrossRef]
5. Li, Y.; Liu, D.; Li, T.; Fu, Q.; Liu, D.; Hou, R.; Meng, F.; Li, M.; Li, Q. Responses of spring soil moisture of different land use type to snow cover in Northeast China under climate change background. *J. Hydrol.* **2022**, *608*, 127610. [CrossRef]
6. Barnett, T.P.; Dumenil, L.; Schlese, U.; Roeckner, E.; Latif, M. The effect of Eurasian snow cover on regional and global climate variations. *J. Atmos. Sci.* **1989**, *46*, 661–685. [CrossRef]
7. Cohen, J.; Rind, D. The Effect of Snow Cover on the Climate. *J. Clim.* **1991**, *4*, 689–706. [CrossRef]
8. Wu, R.; Zhao, P.; Liu, G. Change in the contribution of spring snow cover and remote oceans to summer air temperature anomaly over Northeast China around 1990. *J. Geophys. Res. Atmos.* **2014**, *119*, 663–676. [CrossRef]
9. Halder, S.; Dirmeyer, P.A. Relation of Eurasian snow cover and Indian summer monsoon rainfall: Importance of the delayed hydrological effect. *J. Clim.* **2017**, *30*, 1273–1289. [CrossRef]
10. Zhang, T.; Wang, T.; Feng, Y.; Li, X.; Krinner, G. An emerging impact of Eurasian spring snow cover on summer rainfall in Eastern China. *Env. Res. Lett.* **2021**, *16*, 054012. [CrossRef]
11. Sun, Y.; Chen, H.; Zhu, S.; Zhang, J.; Wei, J. Influence of the Eurasian spring snowmelt on summer land surface warming over Northeast Asia and its associated mechanism. *J. Clim.* **2021**, *34*, 4851–4869. [CrossRef]
12. Chen, S.; Yang, Q.; Xie, H.; Zhang, H.; Lu, P.; Zhou, C. Spatiotemporal variations of snow cover in northeast China based on flexible multiday combinations of moderate resolution imaging spectroradiometer snow cover products. *J. Appl. Remote Sens.* **2014**, *8*, 084685. [CrossRef]
13. Ma, N.; Yu, K.; Zhang, Y.; Zhai, J.; Zhang, Y.; Zhang, H. Ground observed climatology and trend in snow cover phenology across China with consideration of snow-free breaks. *Clim. Dyn.* **2020**, *55*, 2867–2887. [CrossRef]
14. Wang, Y.; Zheng, Z. Spatial Representativeness Analysis for Snow Depth Measurements of Meteorological Stations in Northeast China. *J. Hydrometeorol.* **2020**, *21*, 791–805. [CrossRef]
15. Zou, Y.; Sun, P.; Ma, Z.; Lv, Y.; Zhang, Q. Snow Cover in the Three Stable Snow Cover Areas of China and Spatio-Temporal Patterns of the Future. *Remote Sens.* **2022**, *14*, 3098. [CrossRef]

16. Zhang, X.; Zang, S.; Sun, L. Spatial-temporal variation characteristics of snow cover days in Northeast China in the past 40 years and their relationship with climatic factors. *Adv. Earth Sci.* **2018**, *33*, 958–968. (In Chinese)
17. Zhou, X.; Zhao, C.; Li, N. Spatiotemporal Variation of Snow and its Response to Climate Change in Northeast China. *Plateau Meteor.* **2021**, *40*, 875–886. (In Chinese)
18. Lu, Q.; Li, B.; Wang, Z. The relationship between spatial and temporal change of snow cover depth and atmospheric circulation in Northeast China from 1979 to 2014. *J. Glaciol. Geocryol.* **2018**, *40*, 907–915. (In Chinese)
19. Guo, H.; Wang, X.; Guo, Z.; Chen, S. Assessing Snow Phenology and Its Environmental Driving Factors in Northeast China. *Remote Sens.* **2022**, *14*, 262. [CrossRef]
20. Henderson, G.R.; Leathers, D.J. European snow cover extent variability and associations with atmospheric forcings. *Int. J. Climatol.* **2010**, *30*, 1440–1451. [CrossRef]
21. Seager, R.; Kushnir, Y.; Nakamura, J.; Ting, M.; Naik, N. Northern Hemisphere winter snow anomalies: ENSO, NAO and the winter of 2009/10. *Geophys. Res. Lett.* **2010**, *37*, L14703. [CrossRef]
22. Kim, Y.; Kim, K.-Y.; Kim, B.-M. Physical mechanisms of European winter snow cover variability and its relationship to the NAO. *Clim. Dyn.* **2013**, *40*, 1657–1669. [CrossRef]
23. Wegmann, M.; Rohrer, M.; Santolaria-Otín, M.; Lohmann, G. Eurasian autumn snow link to winter North Atlantic Oscillation is strongest for Arctic warming periods. *Earth Syst. Dynam.* **2020**, *11*, 509–524. [CrossRef]
24. Gastineau, G.; García-Serrano, J.; Frankignoul, C. The influence of autumnal Eurasian snow cover on climate and its link with Arctic sea ice cover. *J. Clim.* **2017**, *30*, 7599–7619. [CrossRef]
25. Zhang, T.; Wang, T.; Zhao, Y.; Xu, C.; Feng, Y.; Liu, D. Drivers of Eurasian Spring Snow-Cover Variability. *J. Clim.* **2021**, *34*, 2037–2052. [CrossRef]
26. Zhang, T.; Feng, Y.; Chen, H. Revealing the formation of the dipole mode of Eurasian snow cover variability during late autumn. *J. Geophys. Res. Atmos.* **2023**, *128*, e2022JD038233. [CrossRef]
27. Sun, B.; Wang, H.J.; Wu, B.W.; Xu, M.; Zhou, B.T.; Li, H.X.; Wang, T. Dynamic Control of the Dominant Modes of Interannual Variability of Snowfall Frequency in China. *J. Clim.* **2021**, *34*, 2777–2790. [CrossRef]
28. Sun, C.; Zhang, R.; Li, W.; Zhu, J.; Yang, S. Possible impact of North Atlantic warming on the decadal change in the dominant modes of winter Eurasian snow water equivalent during 1979–2015. *Clim. Dyn.* **2019**, *53*, 5203–5213. [CrossRef]
29. Zhou, B.T.; Wang, Z.Y.; Sun, B.; Hao, X. Decadal Change of Heavy Snowfall over Northern China in the Mid-1990s and Associated Background Circulations. *J. Clim.* **2021**, *34*, 825–837. [CrossRef]
30. Bailey, H.; Hubbard, A.; Klein, E.S.; Mustonen, K.R.; Akers, P.D.; Marttila, H.; Welker, J.M. Arctic sea-ice loss fuels extreme European snowfall. *Nat. Geosci.* **2021**, *14*, 283–288. [CrossRef]
31. Xu, B.; Chen, H.; Gao, C.; Zhou, B.; Sun, S.; Zhu, S. Regional response of winter snow cover over the Northern Eurasia to late autumn Arctic sea ice and associated mechanism. *Atmos. Res.* **2019**, *222*, 100–113. [CrossRef]
32. Santolaria-Otín, M.; García-Serrano, J.; Ménégoz, M.; Bech, J. On the observed connection between Arctic sea ice and Eurasian snow in relation to the winter North Atlantic Oscillation. *Env. Res. Lett.* **2020**, *15*, 124010. [CrossRef]
33. ESA. Land Cover CCI Product User Guide Version 2. Tech. Rep. 2017. Available online: https://maps.elie.ucl.ac.be/CCI/viewer/download/ESACCI-LC-Ph2-PUGv2_2.0.pdf (accessed on 30 October 2023).
34. Brodzik, M.J.; Armstrong, R. *Northern Hemisphere EASE-Grid 2.0 weekly snow cover and sea ice extent, version 4*; NASA National Snow and Ice Data Center Distributed Active Archive Center. 2013. Available online: https://doi.org/10.5067/P7O0HGJLYUQU (accessed on 10 November 2022).
35. Hori, M.; Sugiura, K.; Kobayashi, K.; Aoki, T.; Tanikawa, T.; Kuchiki, K.; Niwano, M.; Enomoto, H. A 38-year (1978–2015) Northern Hemisphere daily snow cover extent product derived using consistent objective criteria from satellite-borne optical sensors. *Remote Sens. Env.* **2017**, *191*, 402–418. [CrossRef]
36. Harris, I.; Osborn, T.J.; Jones, P.; Lister, D. Version 4 of the CRU TS monthly high-resolution gridded multivariate climate dataset. *Sci. Data* **2020**, *7*, 109. [CrossRef]
37. Huang, B.; Thome, P.W.; Banzon, V.F.; Boyer, T.; Cherupin, G.; Lawrimore, J.H.; Menne, M.J.; Smith, T.M.; Vose, R.S.; Zhang, H.-M. Extended Reconstructed Sea Surface Temperature, version 5 (ERSSTv5): Upgrades, validation and intercomparisons. *J. Clim.* **2017**, *30*, 8179–8205. [CrossRef]
38. Rayner, N.A.; Parker, D.E.; Horton, E.B.; Folland, C.K.; Alexander, L.V.; Rowell, D.P.; Kent, E.C.; Kaplan, A. Global analyses of sea surface temperature, sea ice, and night marine air temperature since the late nineteenth century. *J. Geophys. Res. Atmos.* **2003**, *108*, 4407. [CrossRef]
39. Kalnay, E.; Kanamitsu, M.; Kistler, R.; Collins, W.; Deaven, D.; Gandin, L.; Iredell, M.; Saha, S.; White, G.; Woollen, J.; et al. The NCEP/NCAR 40-Year Reanalysis Project. *Bull. Amer. Meteorol. Soc.* **1996**, *77*, 437–472. [CrossRef]
40. Holton, J.R. *An introduction to Dynamic Meteorology*; Academic Press: London, UK, 1992.
41. Takaya, K.; Nakamura, H. A formulation of a wave-activity flux for stationary Rossby waves on a zonally varying basic flow. *Geophys. Res. Lett.* **1997**, *24*, 2985–2988. [CrossRef]
42. Takaya, K.; Nakamura, H. A formulation of a phase-independent wave-activity flux for stationary and migratory quasigeostrophic eddies on a zonally varying basic flow. *J. Atmos. Sci.* **2001**, *58*, 608–627. [CrossRef]
43. Eady, E.T. Long waves and cyclone waves. *Tellus* **1949**, *1*, 33–52. [CrossRef]

44. Lindzen, R.S.; Farrell, B. A simple approximate result for the maximum growth rate of baroclinic instabilities. *J. Atmos. Sci.* **1980**, *37*, 1648–1654. [CrossRef]
45. North, G.R.; Moeng, F.J.; Bell, T.L.; Cahalan, R.F. The latitude dependence of the variance of zonally averaged quantities. *Mon. Wea. Rev.* **1982**, *110*, 319–326. [CrossRef]
46. North, G.R.; Bell, T.L.; Cahalan, R.F.; Moeng, F.J. Sampling Errors in the Estimation of Empirical Orthogonal Functions. *Mon. Weather Rev.* **1982**, *110*, 699–706. [CrossRef]
47. Chen, S.F.; Wu, R.; Liu, Y. Dominant modes of interannual variability in Eurasian surface air temperature during boreal spring. *J. Clim.* **2016**, *29*, 1109–1125. [CrossRef]
48. Wallace, J.M.; Gutzler, D.S. Teleconnections in the geopotential height field during the Northern Hemisphere winter. *Mon. Weather Rev.* **1981**, *109*, 784–812. [CrossRef]
49. Barnston, A.G.; Livezey, R.E. Classification, seasonality and persistence of low-frequency atmospheric circulation patterns. *Mon. Wea. Rev.* **1987**, *115*, 1083–1126. [CrossRef]
50. Thompson, D.W.J.; Wallace, J.M. The Arctic oscillation signature in the wintertime geopotential height and temperature fields. *Geophys. Res. Lett.* **1998**, *25*, 1297–1300. [CrossRef]
51. Han, Z.; Luo, F.; Wan, J. The observational influence of the North Atlantic SST tripole on the early spring atmospheric circulation. *Geophys. Res. Lett.* **2016**, *43*, 2998–3003. [CrossRef]
52. Song, Y.; Chen, H. Influence of the Late-Winter North Atlantic Tripole Sea Surface Temperature Anomalies on Spring Land Surface Temperature in Mid-to-High Latitudes of Western Eurasia. *J. Clim.* **2023**, *36*, 4933–4950. [CrossRef]
53. Peng, S.; Mysak, L.A.; Ritchie, H.; Derome, J.; Dugas, B. The differences between early and midwinter atmospheric responses to sea surface temperature anomalies in the Northwest Atlantic. *J. Clim.* **1995**, *8*, 137–157. [CrossRef]
54. Kushnir, Y.; Robinson, W.A.; Bladé, I.; Hall, N.M.J.; Peng, S.; Sutton, R. Atmospheric GCM response to extratropical SST anomalies: Synthesis and evaluation. *J. Clim.* **2002**, *15*, 2233–2256. [CrossRef]
55. Nie, Y.; Zhang, Y.; Chen, G.; Yang, X. Delineating the barotropic and baroclinic mechanisms in the midlatitude eddy-driven jet response to lower-tropospheric thermal forcing. *J. Atmos. Sci.* **2016**, *73*, 429–448. [CrossRef]
56. Chen, S.F.; Wu, R.; Chen, W.; Hu, K.M.; Yu, B. Structure and dynamics of a springtime atmospheric wave train over the North Atlantic and Eurasia. *Clim. Dyn.* **2020**, *54*, 5111–5126. [CrossRef]
57. Lau, N.C. Variability of the Observed Midlatitude Storm Tracks in Relation to Low-Frequency Changes in the Circulation Pattern. *J. Atmos. Sci.* **1988**, *45*, 2718–2743. [CrossRef]
58. Cai, M.; Yang, S.; Dool, H.; Kousky, V. Dynamical implications of the orientation of atmospheric eddies: A local energetics perspective. *Tellus Dyn. Meteorol. Oceanogr.* **2007**, *59*, 127–140. [CrossRef]
59. Gao, K.; Tang, Y.; Chen, D. Influence of Arctic Sea ice and Interdecadal Pacific Oscillation on the recent increase of winter extreme snowfall in Northeast China. *Atmos. Res.* **2023**, *295*, 107030. [CrossRef]
60. Wu, R.; Liu, G.; Ping, Z. Contrasting Eurasian spring and summer climate anomalies associated with western and eastern Eurasian spring snow cover changes. *J. Geophys. Res. Atmos.* **2014**, *119*, 7410–7424. [CrossRef]
61. Wang, Z.; Wu, R.; Duan, A.-M.; Qu, X. Influence of eastern Tibetan Plateau spring snow cover on North American air temperature and its interdecadal change. *J. Clim.* **2020**, *33*, 5123–5139. [CrossRef]
62. Zhang, T.; Wang, T.; Krinner, G.; Wang, X.; Gasser, T.; Peng, S.; Piao, S.; Yao, T. The Weakening Relationship between Eurasian Spring Snow Cover and Indian Summer Monsoon Rainfall. *Sci. Adv.* **2019**, *5*, eaau8932. [CrossRef]
63. Han, T.; Tang, G.; Zhou, B.; Hao, X.; Li, S. Strengthened relationship between sea ice in East Siberian Sea and midsummer rainfall in Northeast China. *Clim. Dyn.* **2023**, *60*, 3749–3763. [CrossRef]
64. Chen, S.; Wu, R. Interdecadal changes in the relationship between interannual variations of spring North Atlantic SST and Eurasian surface air temperature. *J. Clim.* **2017**, *30*, 3771–3787. [CrossRef]
65. Zhen, Z.; Chen, S.; Yin, T.; Gastellu-Etchegorry, J.-P. Globally quantitative analysis of the impact of atmosphere and spectral response function on 2-band enhanced vegetation index (EVI2) over Sentinel-2 and Landsat-8. *ISPRS J. Photogramm. Remote Sens.* **2023**, *205*, 206–226. [CrossRef]

Disclaimer/Publisher's Note: The statements, opinions and data contained in all publications are solely those of the individual author(s) and contributor(s) and not of MDPI and/or the editor(s). MDPI and/or the editor(s) disclaim responsibility for any injury to people or property resulting from any ideas, methods, instructions or products referred to in the content.

remote sensing

MDPI

Article

Influence of Climate, Topography, and Hydrology on Vegetation Distribution Patterns—Oasis in the Taklamakan Desert Hinterland

Lei Peng, Yanbo Wan, Haobo Shi, Abudureyimu Anwaier and Qingdong Shi *

College of Ecology and Environment, Xinjiang University, Urumqi 830046, China;
penglei1028@stu.xju.edu.cn (L.P.); wanyb1995@stu.xju.edu.cn (Y.W.); shi_haobo@stu.xju.edu.cn (H.S.);
anwar_jan@stu.xju.edu.cn (A.A.)
* Correspondence: shiqd@xju.edu.cn

Abstract: Vegetation in natural desert hinterland oases is an important component of terrestrial ecosystems. Determining how desert vegetation responds to natural variability is critical for a better understanding of desertification processes and their future development. The aim of this study is to characterize the spatial distribution of vegetation in the natural desert hinterland and to reveal how different environmental factors affect vegetation changes. Taking a Taklamakan Desert hinterland oasis as our research object, we analyzed the effects of different environmental factors on desert vegetation using a time-series normalized difference vegetation index (NDVI) combined with meteorological, topographic, and hydrological data, including surface water and groundwater data. Vegetation was distributed in areas with high surface water frequency, shallow groundwater levels, relatively flat terrain, and dune basins. NDVI datasets show greening trends in oasis areas over the past 20 years. The frequency of surface water distribution influences water accessibility and effectiveness and shapes topography, thus affecting the spatial distribution pattern of vegetation. In this study, areas of high surface water frequency corresponded with vegetation distribution. The spatial distribution of groundwater depth supports the growth and development of vegetation, impacting the pattern of vegetation growth conditions. Vegetation is most widely distributed in areas where the groundwater burial depth is 3.5–4.5 m. This study provides data for restoring riparian vegetation, ecological water transfer, and sustainable development.

Keywords: Taklamakan Desert hinterland; climate change; topography; hydrological processes; vegetation pattern

1. Introduction

Vegetation is an important component of terrestrial ecosystems with a critical role in maintaining the sustainable development of global and regional ecosystems [1]. Desert vegetation supports the survival and development of oases. While vegetation in desert areas is typically sparse, it is instrumental in anchoring sand dunes and countering desertification [2]. Understanding how desert vegetation adapts to shifts in natural and human-induced stressors is crucial for a deeper comprehension of desertification dynamics and its prospective progression.

According to the fifth report from the Intergovernmental Panel on Climate Change (IPCC), global climate change has significantly intensified in recent years. In fact, the last 30 years have seen the highest average temperatures since 1400; meanwhile, rainfall has increased in humid zones and decreased in arid zones, with the frequency of extreme rainfall increasing [3]. These notable changes in climate impact the vegetation growth environment, which in turn affects the phenology, distribution, and growth of vegetation, thus affecting the ecosystem material–energy conversion and carbon cycle [4,5]. Climate influences the long-term evolution of vegetation and causes changes in vegetation growing

seasons by altering the duration and rate of photosynthesis and respiration of plants, which affects the global vegetation–atmosphere pattern of carbon, water, and energy cycles [6,7]. Among the abiotic factors affecting plant growth, the most immediate and significant influences are temperature and precipitation [8,9]. Climate change can alter temperature and soil moisture levels. Such shifts in hydrothermal conditions can profoundly influence the health and growth of vegetation.

In arid and semi-arid areas, where soil moisture primarily constrains plant growth, a temperature rise elevates evapotranspiration rates, reducing soil water content when temperature and precipitation are negatively and positively correlated with vegetation health, respectively [10]. Considering that spatiotemporal changes in vegetation are closely related to climate change, detecting the spatiotemporal correlation between climate change and vegetation characteristics is important for understanding the impact of climate change on vegetation ecosystems.

Topography, as the most prominent and complex geographical factor in the region, is an important source of environmental spatial and temporal heterogeneity. It influences changes in temperature, precipitation, wind speed, insolation, and evapotranspiration, which are spatially redistributed and can cause local environmental changes, forming microclimate zones and affecting vegetation growth [11]. Topographic factors regulate soil conditions, microclimate, and water availability across regions at small scales [12–14]. As such, they shape the locational conditions for plant growth and drive abiotic and biotic interactions [15], determining plant community diversity, structure, and function [13]. Topography is also important in providing spatial species diversity and expanding ecological niches at different scales, increasing species diversity and resistance to harsh environments [14,16].

More specifically, in the top and slope areas of dunes, nutritious soil and water are often not stored, making the vegetation more competitive for light and nutrients than at the bottom of the dune [13,17]. Currently, the use of variability in topographic features to reveal the spatial distribution patterns of vegetation and the influence of natural factors on vegetation distribution has been widely deployed in the analysis of vegetation patterns at landscape and community scales.

As typical desert vegetation ecosystems, natural oasis regions in the desert hinterlands of China are strongly dependent on water resources. Thus, analyzing the spatial distribution and dynamic changes in vegetation in response to water resources is necessary for the sustainable management and maintenance of healthy ecosystems [18,19]. Relatively abundant and stable water sources in oases provide the necessary water and nutrients for vegetation growth and are prerequisites for the development of natural oases in arid zones [20]. Surface water and its distribution are key factors shaping the spatial vegetation distribution patterns of oases [21].

Groundwater controls vegetation ecosystems [22,23] as a water supply source that supports vegetation growth and transpiration [24,25]. Physiological and ecological indicators of vegetation, water-use strategies, patch distribution characteristics, community abundance, age structure, and succession are closely related to groundwater [26]. Surface water and groundwater jointly influence the survival and development of oasis vegetation. Surface hydrological processes, including the frequency and duration of flooding, determine the distribution pattern of vegetation in riparian zones at the watershed scale, whereas subsurface hydrological processes influence the mechanism between the spatial and temporal ecological succession of natural vegetation, affecting the critical depth of burial of vegetation, ecological water demand of vegetation, and optimum suitable water level for vegetation.

Dramatic climate changes can impact vegetation cover; however, scientific opinions on the drivers of vegetation growth in the Northern Hemisphere are divided. Some researchers posit that global warming is the main cause of increased vegetation cover in the Northern Hemisphere [27]. In contrast, others postulate that global warming increases evaporation and rapidly depletes soil moisture in the arid zones of the Northern Hemisphere, inhibiting

the increase in vegetation cover [28]. Meanwhile, in extremely arid conditions, such as the hinterland of the Taklamakan Desert, although climate change may have an impact, the hydrological processes and topography have an extremely important influence on vegetation cover, significantly affecting the survival and development of vegetation. Within this region, most studies have focused on large-scale assessments, such as the response of vegetation on the Tibetan Plateau to climate change [29] or the impact of climate change on vegetation productivity in the dry zone of Central Asia [30]. Meanwhile, fewer studies have reported small- or medium-scale assessments with regard to changes in vegetation cover.

Located in the desert hinterland, the Daliyabui oasis covers an area of approximately 342 km^2; it represents an area for small- to medium-scale assessments. The use of long-term remotely sensed data is an effective method for studying vegetation changes and atmospheric processes at different spatial and temporal scales [31]. Remotely sensed NDVI calculated from red and near-infrared reflectance has been recognized as an indicator of vegetation cover [32]. Of all the NDVI products, Moderate Resolution (MODIS) NDVI and Landsat NDVI are the most widely used because of their simultaneous high spatial and temporal resolution [33].

Therefore, we selected a natural oasis in the hinterland of the Taklamakan Desert as our research object, with the desert riparian vegetation ecosystem as the core, and explored the effects of climate change, topography, and water resource changes on the spatiotemporal distribution patterns of oasis vegetation. Additionally, we identified the general patterns in desert vegetation characteristics, provided basic datasets for restoring riparian vegetation and curbing oasis desertification, and provided scientific support for oasis health management and sustainable development.

2. Materials and Methods

2.1. Study Area

Nestled within the heart of the Taklamakan Desert—China's grandest desert—lies the Daliyabui oasis, with the borders of 81°90′15″–82°23′41″E and 37°20′39″–39°10′35″N. The core area of the oasis covers an area of 324 km^2, with a relatively flat topography (1061–1177 m) and an average elevation of 1108 m above sea level. The Kriya River traverses this area, flowing from south to north, vanishing into the desert's deep interiors. The oasis predominantly sits on the alluvial plain formed by the tail end of the Kriya River, from which it emerged, presenting a relatively untouched natural sanctuary (Figure 1). The area has a temperate continental arid desert climate characterized by high evaporation, low rainfall, a large diurnal temperature difference, and a long frost-free period. The average annual precipitation is <10 mm, and the average annual temperature is 11 °C. The oasis vegetation composition is dominated by poplars, tamarisks, and reeds, which are representative of the desert ecosystem. Oasis vegetation is mostly distributed in lowlands with shallow groundwater. Poplars primarily grow on both sides of the fine river network, washed out by rivers, shrubs, and annual herbs sparsely growing on sand dunes. In some large inter-mound basins in the interior of the desert, shrubs dominate the plant community, forming relatively large vegetation patches with low coverage.

2.2. Methods

2.2.1. Meteorological and Topographic Data

The impact of climate change on vegetation trends was analyzed using precipitation and temperature data from 2000 to 2020. Ground-based observations were not used in this study as no meteorological stations provided long-term observations in the study area. Therefore, a high-precision 1 km resolution precipitation and temperature dataset was selected and generated for the study area using delta spatial downscaling (http://data.tpdc.ac.cn, accessed on 23 April 2023). Data from 496 independent meteorological observation points were used for validation (Figure 2). Correlation analysis between multi-year meteorological data and NDVI data was performed using Matlab (2021b) software to derive the effect of meteorological factors on vegetation.

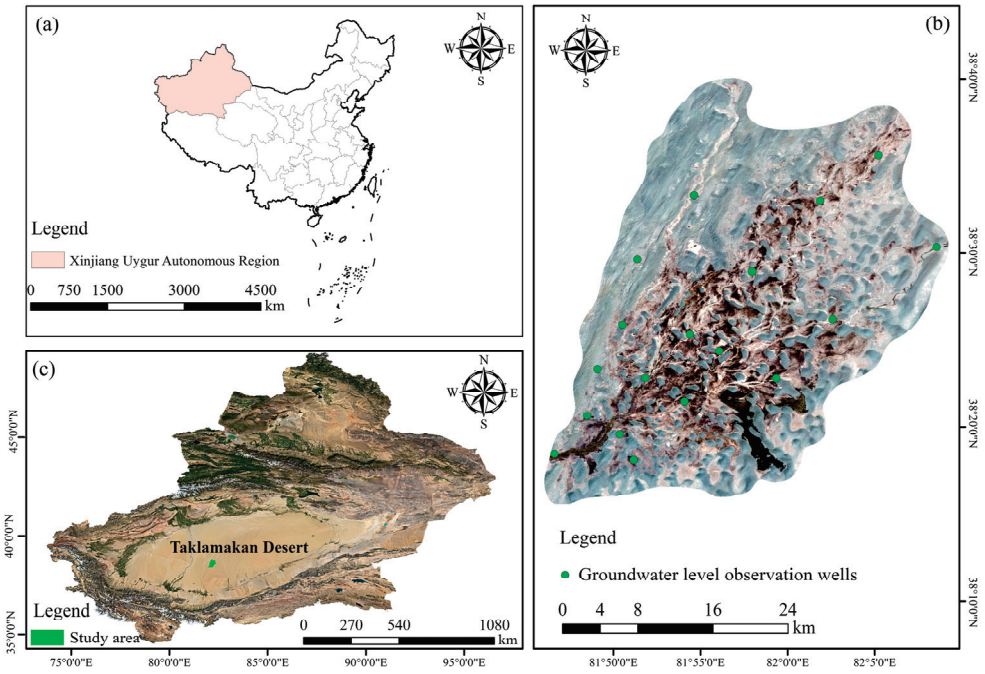

Figure 1. (**a**) Location of study area in China. (**b**) Desert hinterland oasis and ecological water level observation wells. (**c**) Location of the Taklamakan Desert within Xinjiang.

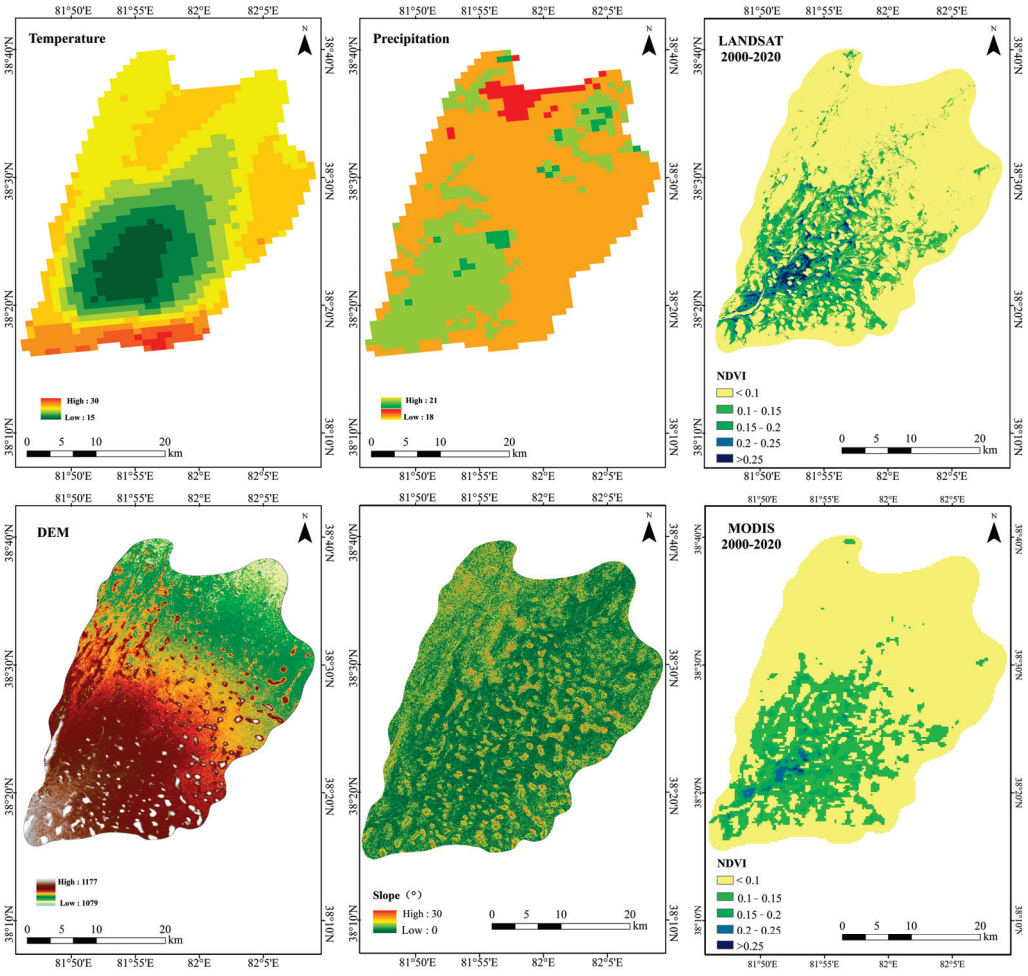

Figure 2. Temperature, rainfall, elevation, slope, and vegetation data for the study area.

To understand the response of vegetation distribution patterns to topography, the 90 m resolution digital elevation model data were used to generate topographic data, calculate and correlate the slope of the study area with vegetation indices, and derive the factors influencing the growth of vegetation (Figure 2). The topographic data were obtained from the U.S. Geological Survey (USGS, https://earthexplorer.usgs.gov/, accessed on 23 April 2023).

2.2.2. Hydrological Data

Surface Water Data

The United States Geological Survey (USGS) provided 130 cloud-free Landsat images from 2000 through 2020 for this investigation. The data were preprocessed using ENVI 5.3 to obtain better-quality images. Then, 13 water body indices were selected to extract water bodies in the study area. This selection considered the degree of numerical differentiation between the surface water image elements and background image elements, that is, the numerical size difference, and the larger the difference, the more conducive it is to the application of automatic thresholding to determine the method of extracting the distribution range of the water bodies and obtaining a better accuracy. Based on a previous analysis [21], the $AEWI_{no\ shadow}$ water body index is the most effective. Mapping the spatial distribution of the surface water was achieved using the maximum entropy threshold segmentation method (Figure 3). Finally, the relative distribution frequency of surface water was obtained by using the TOTAL function to sum the images at the image element scale and dividing by the number of images, N, to normalize the image element values between 0 and 1; 0 indicated that no surface water reached the image element during the study period, and 1 indicated that surface water was always present during the study period. It should be noted that due to image availability and the influence of clouds and cloud shadows, the resulting surface water frequency does not absolutely indicate the presence or absence of surface water, which is in flux, and is only used to characterize the differences in the spatial and temporal distributions of surface water as continuous data for surface water are not available.

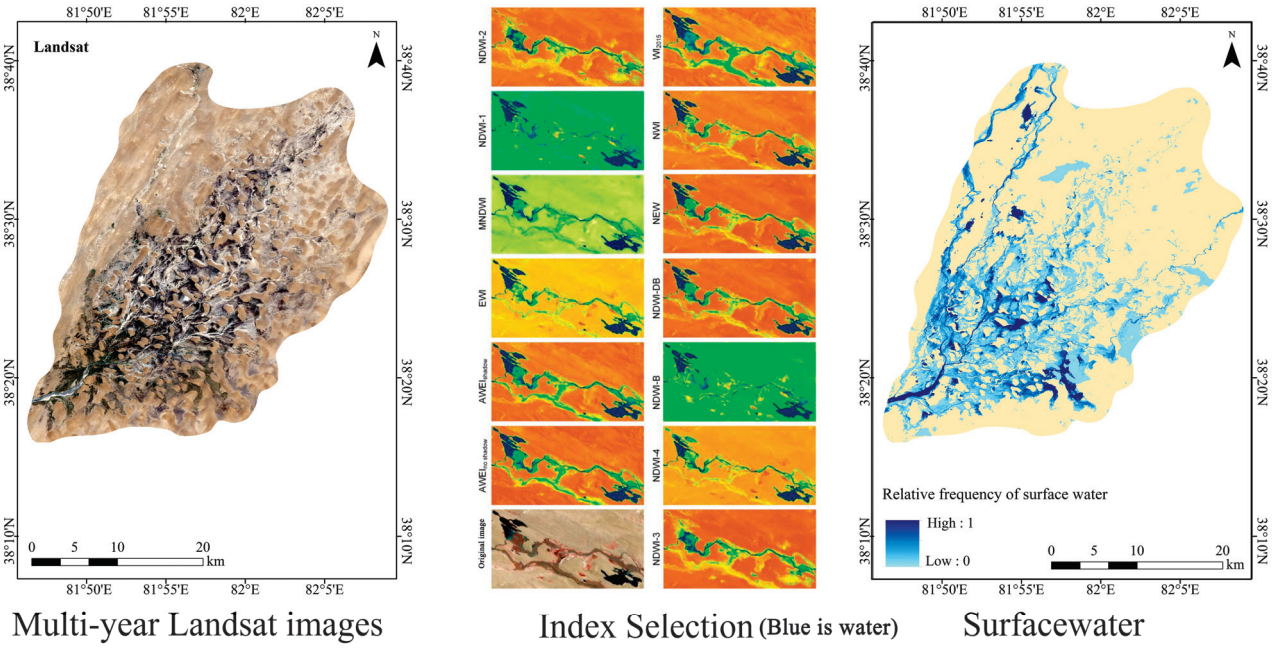

Figure 3. Extraction of surface water processes from remote sensing imagery.

Groundwater Data

To invert the groundwater burial depth, data from 19 groundwater level observation wells (HOBO water level observation meters) in the study area were used to build a model by combining 16 environmental covariates (Figure 4) with high correlation with

groundwater (topographic, meteorological, and vegetation data), and the spatial resolution of the environmental covariates was uniformly re-sampled to 90 m using ArcGIS 10.8. Finally, a groundwater level model was created with Matlab (2021b) software based on the random forest (RF) model, and a remote sensing inversion of the groundwater level in the research region was carried out and mapped.

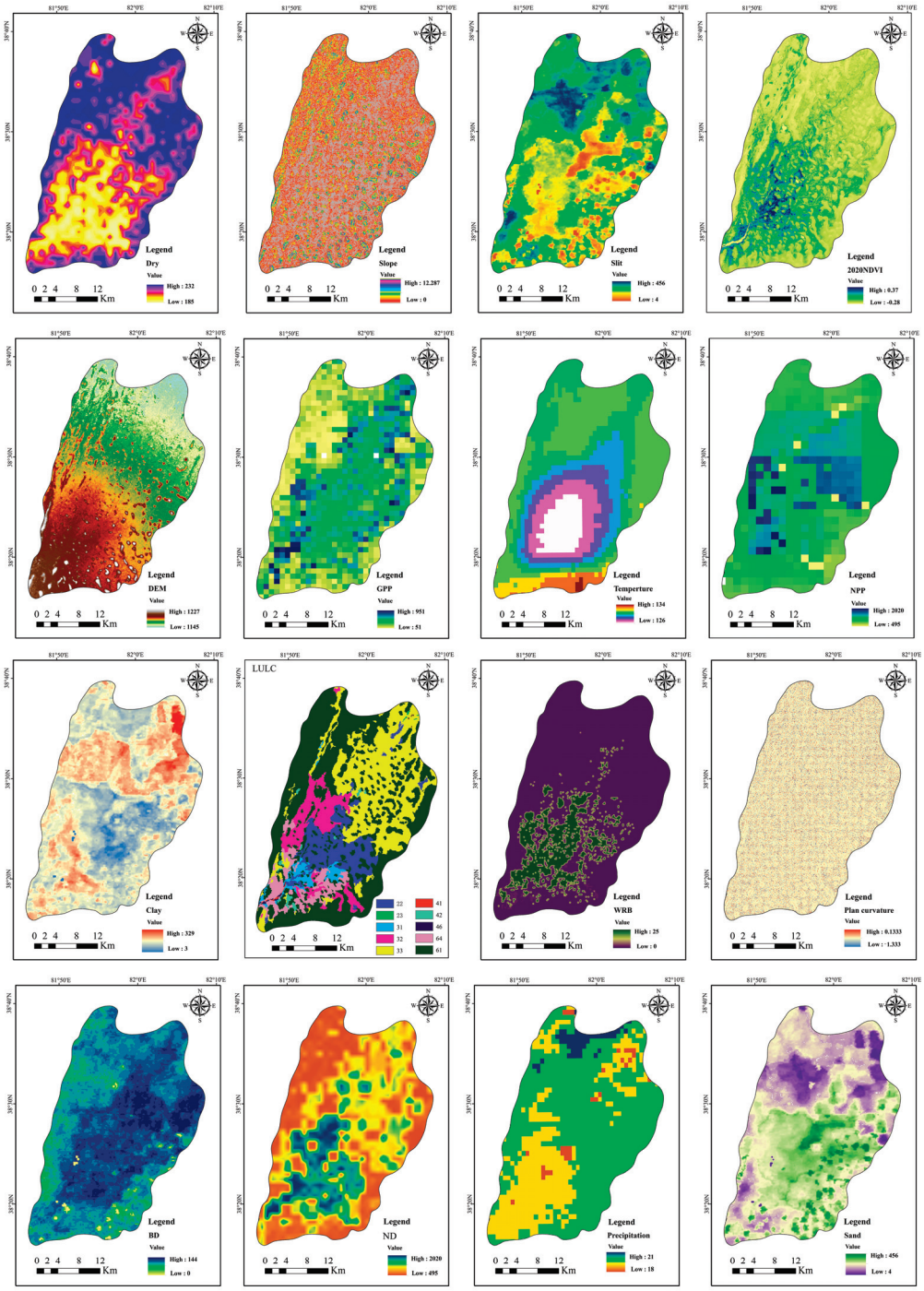

Figure 4. Environmental covariates used for modeling the spatial patterns of groundwater parameters in the Daliyabui oasis (In LULC, 22, 23, 31, 32, 33, 41, 42, 46, 64, 61 represent shrubwood, sparse shrub, high cover grassland, medium cover grassland, low cover grassland, graff, lake, bottomland, marsh, bare land respectively).

To validate the model's ability to predict groundwater burial depth data, we split the entire sample into two. One copy contained samples 9/10 for modeling and 1/10 for validation, yielding ten groups for cross-validation. The model's validity was assessed using root-mean-square error (RMSE) and the coefficient of determination (R^2). The temporal and geographical predictive capacity of the RF model for groundwater parameters may be completely assessed by combining the validation technique for time-varying prediction of the RF model with 10-fold cross-validation (Figure 5).

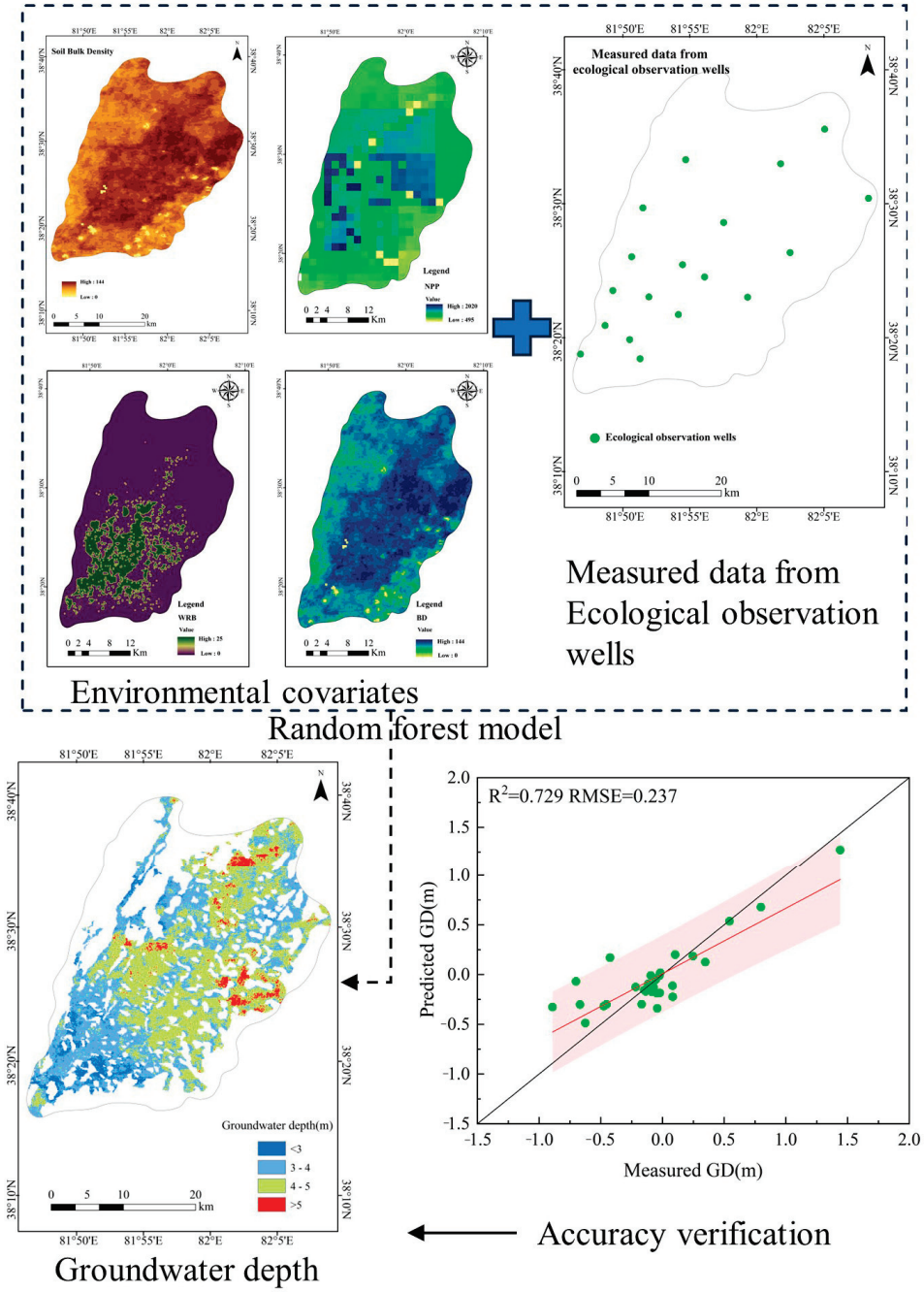

Figure 5. Remote sensing extraction process for groundwater (The green dots represent the coordinates of the measured and predicted points; The red area represents the 95% prediction interval).

2.2.3. Vegetation Data

NDVI is a critical measure for tracking changes in plant distribution patterns in a research region. The Google Earth Engine (GEE) platform was used to calculate NDVI for

the Landsat and MODIS (MODIS/006/MOD13A2) datasets (Table 1) with resolutions of 30 m and 250 m, respectively. The NDVI raster images were obtained by masking the vector range of the study area, cropping the monthly NDVI raster images for 2000–2020, and obtaining the annual average NDVI raster images using the mean method. The comparison of the two time series revealed differences in the Landsat and MODIS satellite sensors that led to uncertainties.

Table 1. Landsat and MODIS satellite sensor information.

Satellites Sensors	Year	Resolution (m)	Period (Days)
Landsat-5 MSS, TM	2000–2013	90	16
Landsat-8 OLI	2013–2020	90	16
MODIS	2000–2020	250	16

Statistical analyses of the Landsat and MODIS NDVI image elements were used to obtain the NDVI distribution characteristics for the entire desert, including the frequency distribution of the NDVI and the mean value. Finally, the nonparametric Mann–Kendall test was performed to determine the statistical significance of the trends for each NDVI dataset for each picture element over the observation period. The calculated statistical indicator Z was used to classify the trends as significant increase ($Z > 1.96$, significant at 5%), significant decrease ($Z < -1.96$, significant at 5%), and no significant change.

2.2.4. NDVI Calculation

NDVI is an important monitoring indicator for quantifying changes in plant cover due to climate change, and it is especially sensitive in arid areas with scant vegetation [34]. The formula is presented in Equation (1):

$$NDVI = \frac{\rho_{nir} - \rho_{red}}{\rho_{nir} + \rho_{red}} \quad (1)$$

where ρ_{nir} is for the near-infrared band and ρ_{red} is for the infrared band.

2.2.5. Water Index Calculation

The $AWEI_{no\ shadow}$ can effectively threshold segment water bodies with high accuracy and improved detection at the surface water distribution's boundaries. It is ideal for monitoring complex water environments in desert areas [35] and is calculated using Equation (2):

$$AWEI_{no\ shadow} = 4(\rho_{green} - \rho_{swir1}) - (0.25\rho_{nir} + 0.75\rho_{swir2}) \quad (2)$$

where ρ_{green}, ρ_{swir1}, ρ_{nir}, and ρ_{swir2} are the reflectance values of the green, *swir*1, near-infrared, and *swir*2 bands, respectively.

2.2.6. Mann–Kendall Test and Sen's Slope Estimator—Trend Detection [36]

Sen's *slope* is widely used in ecohydrological climates and is calculated as per Equation (3):

$$slope = \text{Median}\left[(x_j - x_i)/(j - i)\right], \forall j > i \quad (3)$$

where Median [] represents the median value; if the slope is >0, a positive trend is assigned to the vegetation cover; if the slope is <0, a decreasing trend is assigned.

The Mann–Kendall test is a nonparametric statistical test used to detect the significance of changes in trends and is calculated using Equations (4) and (5):

$$S = \sum_{i=l}^{n-1} \sum_{j=i+1}^{n} sgn(x_j - x_i) \quad (4)$$

$$sgn(x_j - x_i) = \begin{cases} 1(x_j - x_i) > 0 \\ 0(x_i - x_i) = 0 \\ -1(x_j + x_i) < 0 \end{cases} \quad (5)$$

The Z test statistic was used to perform the trend test in Equation (6):

$$\boldsymbol{Z} = \begin{cases} \frac{S}{\sqrt{\mathbf{Var}(S)}} & (\boldsymbol{S} > 0) \\ 0 & (\boldsymbol{S} = 0)^{+}_{-} \\ \frac{S+1}{\mathrm{Var}(S)} & (\boldsymbol{S} < 0) \end{cases} \quad (6)$$

where n is the length of the sample and x_i and x_j are the data values in time series i and j, respectively. The formula for Var is presented as Equation (7):

$$\mathrm{Var}(\boldsymbol{s}) = \frac{\mathbf{n(n-1)(2n+5)}}{\mathbf{18}} \quad (7)$$

2.2.7. Calculation of Correlation Analysis

Correlation analysis of vegetation with precipitation and temperature was performed using Pearson's correlation coefficient as presented in Equation (8):

$$\boldsymbol{R} = \frac{\boldsymbol{Cov(x,y)}}{\sigma_x \sigma_y} = \frac{\boldsymbol{n\sum xy - \sum x \sum y}}{\sqrt{\left[\boldsymbol{n\sum x^2 - (\sum x)^2}\right] \cdot \left[\boldsymbol{n\sum y^2 - (\sum y)^2}\right]}} \quad (8)$$

where R is the correlation coefficient, Cov is the covariance, and σ is the standard deviation.

2.2.8. Random Forest (RF) Model

RF models [37] utilize integrated learning methods and are nonlinear tree-based models. These models use multiple decision trees, making them less prone to oversaturation. Their accuracy is also improved due to the voting of multiple decision trees. Moreover, when dealing with high-dimensional data, there is no need to select features to obtain the value of each. The parallel computing implemented by the RF algorithm is fast and easy to implement, and the introduction of stochasticity reduces the variance of the model run, making it insensitive to multivariate covariances and improving the computation of data with missing values.

Modeling between groundwater level and environmental covariates was performed using RF models in Matlab2018b. Indeed, RFs have better performance in multivariate inversion and can effectively invert groundwater levels, making the results more reliable.

3. Results

3.1. Vegetation Distribution Pattern

The pixel levels of the multiyear average NDVI of the Daliyabui oasis were calculated based on the Landsat and MODIS (Figure 2) NDVI datasets. Although these datasets differ in spatial resolution, they both display comparable distribution patterns. In general, the NDVI at the oasis inlet in the central region was higher than at the tail of the oasis. Higher-resolution Landsat data showed that several sizable vegetation patches with higher NDVI were also distributed in the inner desert region. According to a field survey, these patches of vegetation in the middle of the desert were mostly distributed on both sides of wider river channels, as well as in large open interdune basins surrounded by large sand dunes.

Based on the MODIS and Landsat NDVI datasets, the frequency distribution of NDVI for each image element in the oasis showed a clear single-peaked distribution with a main peak close to 0.06 (Figure 6). This indicated the predominance of sparsely vegetated active dunes in the oasis. The NDVI showed a positively skewed distribution, with the right side > 0.15 representing vegetation patches. This indicates that the oasis is dominated

by low-coverage vegetation with a very small and scattered area of high-density vegetation. This reflects the effects of hydrological and climatic drought conditions on normal vegetation growth.

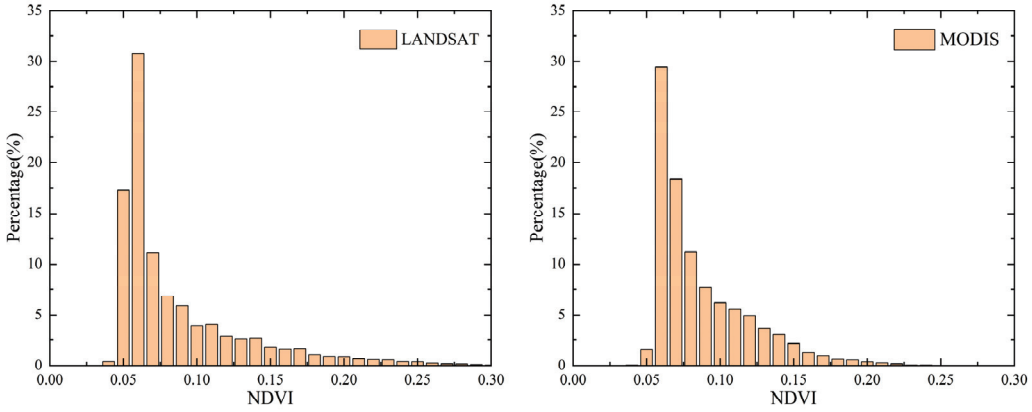

Figure 6. Frequency distribution characteristics of Landsat and MODIS NDVI.

3.2. Greening Trends in the Daliyabui Oasis

The mean values of the Landsat and MODIS NDVI time series were fairly low; both showed a clear rising tendency (Figure 7). The interannual variation in mean NDVI values of both time series was similar, based on Landsat and MODIS NDVI growth rates of 0.001 and 0.0075 per decade during 2000–2020, respectively. Temporally, the oasis vegetation showed an overall greening trend, and degradation existed in local areas. Spatially, the vegetation greening area was primarily distributed in the oasis's western and center areas; the declining area was mainly distributed north of the oasis end and in the eastern region. The stable region was primarily concentrated in the southeastern part of the oasis (Figure 8).

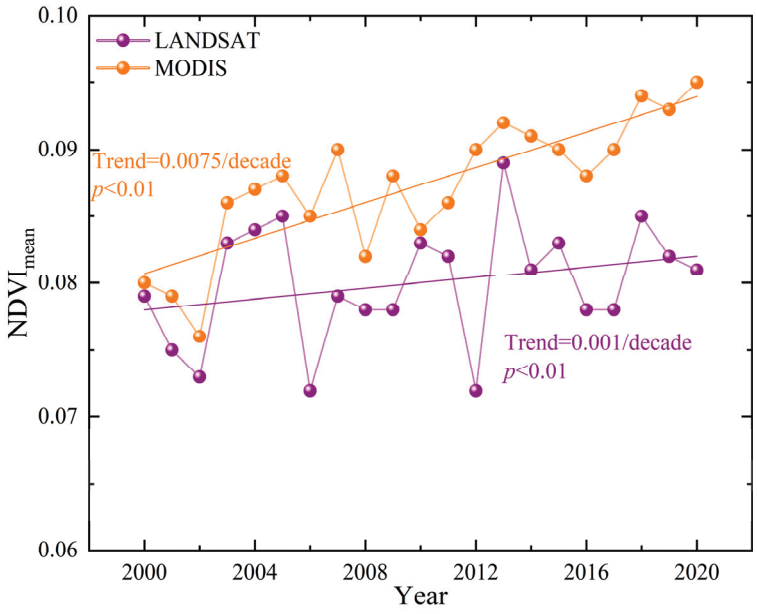

Figure 7. Time series of annual NDVI averages for the entire oasis based on Landsat (purple line) and MODIS (orange line).

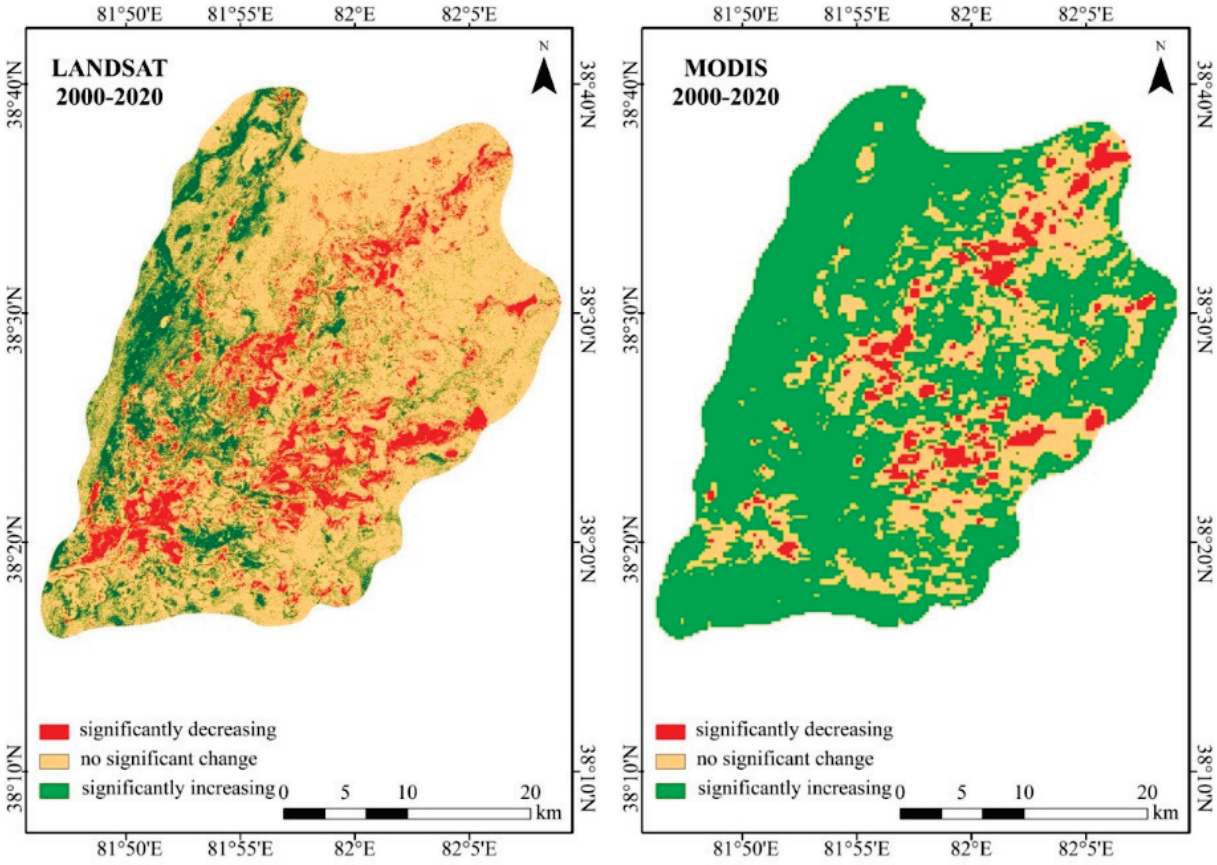

Figure 8. Spatial distribution of annual trends in oasis NDVI.

3.3. Climate Effects of Climate on Oasis Vegetation

Among the various climatic variables that drive vegetation change, the most basic and important are solar radiation, temperature, and precipitation, which provide the light, heat, and water conditions necessary for vegetation growth, respectively [38]. Radiation is the source of energy for plant photosynthesis, which can only proceed under suitable light conditions. Temperature affects the rates of photosynthesis and respiration, as well as the efficiency of nutrient utilization by plants, and precipitation is the main source of plant water [39–41]. Precipitation is thus a key factor for plant growth [42].

Since the 1980s, Northwest China's dry and semi-arid areas have become increasingly warm and humid. The analysis of climatic data showed that the mean and maximum temperatures in the desert hinterland oases increased during the study period (Figure 9a,c). Rainfall showed insignificant interannual variability, while in 2010, there were significant extreme precipitation events (Figure 9b), which had a profound effect on plant growth. At the image metric scale, the relationship between climatic elements such as temperature, precipitation, and NDVI was investigated (Figure 10). The findings revealed that NDVI was positively associated with temperature and precipitation in most of the research locations but was only significant in certain regions ($p < 0.05$). This may be because of the complex response of the NDVI to climate environment changes, which is nonlinear and influenced by topography and hydrological processes [43].

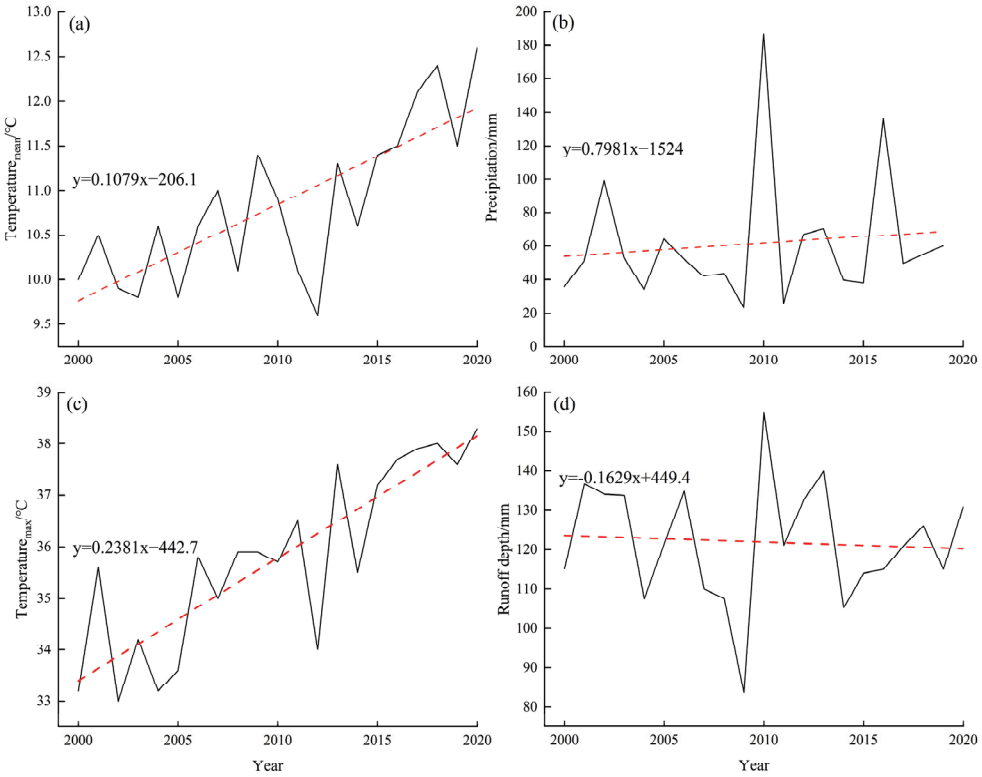

Figure 9. Climatic conditions in the oasis during 2000–2020: (**a**) mean temperature; (**b**) precipitation; (**c**) maximum temperature; (**d**) runoff.

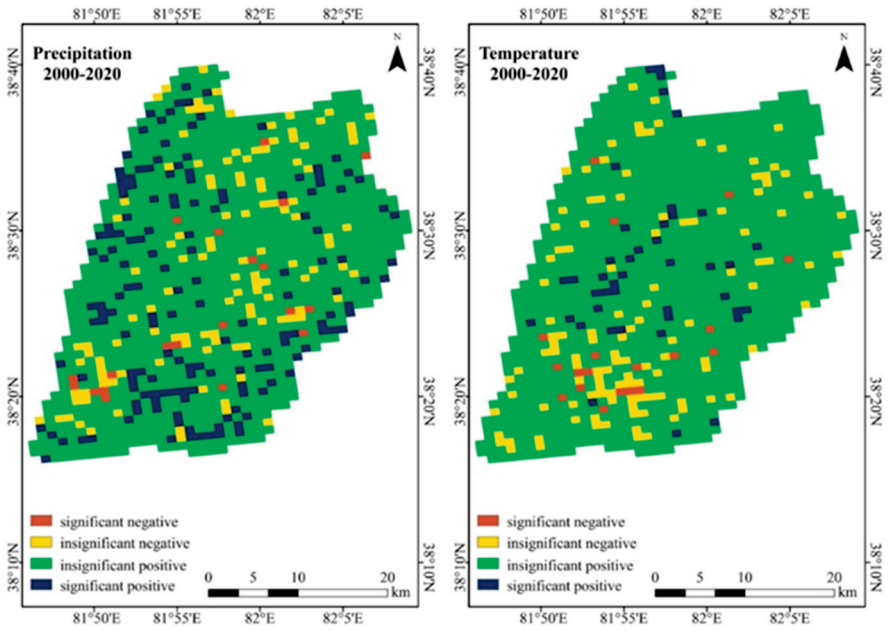

Figure 10. Pearson correlation coefficients between NDVI and precipitation and NDVI and temperature for 2000–2020.

3.4. Effect of Topography on Oasis Vegetation

As shown in Figure 11, regional topography affected the geographic heterogeneity of the observed NDVI distribution. Huge pockets of flora in the hinterland of the desert oasis, which include banded vegetation patches in the middle of the oasis, were typically found in lowlands or vast inter-mound basins with level landscapes, corresponding to the visual interpretation of unmanned aerial vehicle (UAV) images, high-resolution data,

and field surveys (Figure 6). The slopes of the desert hinterland oasis varied greatly in space. (Figure 11). The NDVI pixel values for slopes <8° were larger than those for slopes >8°, where the NDVI was typically below 0.1. Previous research has revealed that local environmental factors regulated by topography impact the development of plants [44].

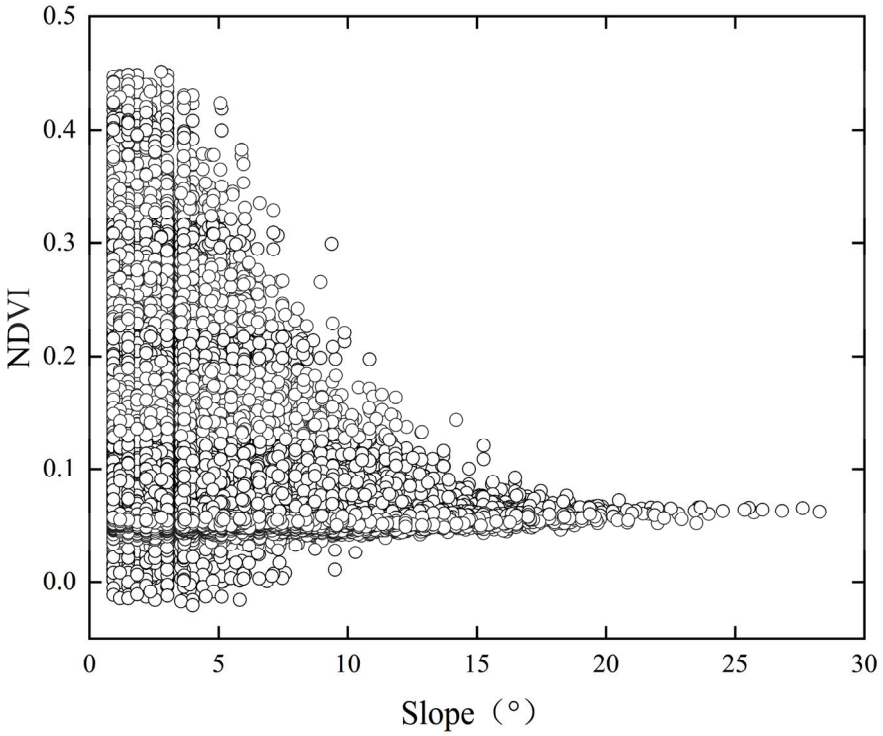

Figure 11. Slope of the study area and NDVI versus slope scatter plot.

Vegetation cover was negatively correlated with slope; that is, the greater the slope, the lower the vegetation cover. The significant variation in vegetation cover with slope is due to the fact that slopes influence surface runoff and water redistribution, creating substantial habitat heterogeneity [45]. Similarly, the size and movement of sand dunes have a significant impact on the geographical distribution pattern of vegetation in desert hinterlands. The geographic spatial distribution pattern of sand dunes affects the distribution and effectiveness of, and accessibility to, surface water, which indirectly affects the spatial distribution of vegetation. Surface water movement has a remodeling effect on sand dunes, driving the transformation of nearby riparian deserts into riverbanks; with the considerable mobility of sand, plants living on dunes are endangered by sand burial.

Meanwhile, in the bottom area of the tall dunes, more water and nutrients can be gathered, providing a good substrate for vegetation growth and development. However, the slope at the top and profile of the dunes prevents water and nutrients from being stored, which is not conducive to the growth of vegetation [46]. Furthermore, the basins formed between individual dunes can provide a more favorable environment for plants to survive in the harsh desert environment by shielding them from wind, sand, and direct sunlight, reducing sand burial and evaporation [47].

3.5. Effects of Spatial Distribution Frequency of Surface Water on Vegetation

Surface water was extracted using the $AEWI_{no\ shadow}$ water body index with the maximum entropy threshold segmentation method from 2000 to 2020. Surface water's relative distribution frequency was obtained by summing all images at the image element scale and dividing by the number (N); this was used to characterize the differences in the spatiotemporal distribution of surface water. The relative distribution frequency of surface water was 1.29. Regarding spatial distribution, the western, central, and southeastern

regions of the oasis were the main distribution areas of surface water; the range was consistent with the vegetation distribution range of the oasis (Figures 7 and 12).

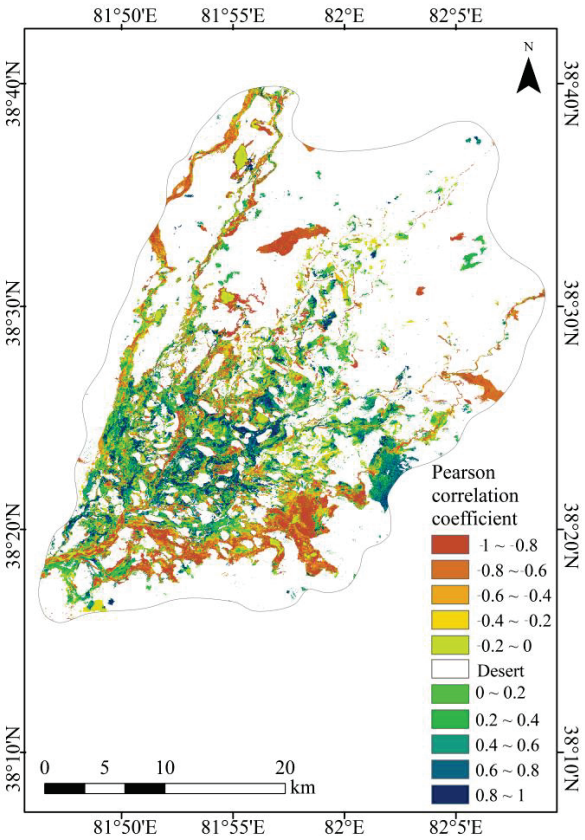

Figure 12. Relative frequency of surface water distribution and correlation with NDVI.

Directionally, 45.54% of the regional surface water frequency in the oasis was positively correlated with NDVI, and 54.46% was negatively correlated with NDVI, owing to the presence of rivers, lakes, waterlogged depressions, and high salinity in high-frequency waterlogged areas (Table 2). Oasis vegetation, water bodies, and sand dunes interact and influence each other, constituting the natural factors controlling changes in the oasis landscape. With the recent change in upstream runoff (Figure 9d), surface water enters the oasis and scours the sand dunes to form the internal river network of the oasis; the accessibility and effectiveness of its water profoundly affect the vegetation on both sides of the river network water system. The surface water end is reduced by the decreased water velocity and flow and the tall sand dunes. This is consistent with the results showing that the topographic slope of the oasis affects vegetation distribution and growth.

Table 2. Frequency correlation of NDVI and surface water distribution from 2000 to 2020.

Classification		Relevance	Percentage	Total
Positive correlation	0.8–1	Very strong positive correlation	8.27%	45.54%
	0.6–0.8	Strong positive correlation	9.41%	
	0.4–0.6	Moderate positive correlation	9.84%	
	0.2–0.4	Weak positive correlation	9.32%	
	0–0.2	Very weak positive correlation	8.70%	
Negative correlation	−0.2–0	Very weak negative correlation	10.20%	54.46%
	−0.4–0.2	Weak negative correlation	8.08%	
	−0.6–0.4	Moderate negative correlation	7.60%	
	−0.8–0.6	Strong negative correlation	11.02%	
	−1–0.8	Very strong negative correlation	17.56%	

3.6. Effect of Groundwater Level on Oasis Vegetation

Groundwater is the main factor influencing plant growth and development [48]. Some studies have concluded that riparian zones are groundwater-sustained ecosystems and that many riparian-zone plants are groundwater-dependent [49]. Groundwater properties (depth of water table burial and groundwater mineralization) determine the distribution of plant composition and diversity in the arid zone [50]. Groundwater can be taken up directly by deep-rooted plants or supplied for the growth of plants with shallow roots as a result of the regulation of the moisture content of the envelope [51]. Changes in groundwater levels can affect water use efficiency and the physiological and ecological responses of plants [52]. To maintain plant growth in riparian zones, the burial depth of the water table must be maintained at a suitable interval. In this study, the burial depth of groundwater in the oasis was mapped based on the environmental covariates selected for correlation with the groundwater level and measured groundwater data. The average depth of groundwater in the vegetated area of the oasis was 3.75 m.

Figure 13 shows that the groundwater burial depth in the vegetated region of the Daliyabui oasis decreased from southwest to northeast, with shallow water table areas at the river inlets on both sides of the oasis, a high groundwater table in the central area owing to topography, and greater groundwater depth in the coccyx area owing to low water accessibility. The groundwater burial depth in the vegetated areas of the oasis ranged from 2 to 7 m, with the minimum and maximum values occurring in small areas in the southern and northern parts of the oasis, respectively. Most of the vegetation was distributed in areas with a groundwater burial depth of 3–5 m, and the distribution range was largest when the groundwater burial depth was 3.5–4.5 m.

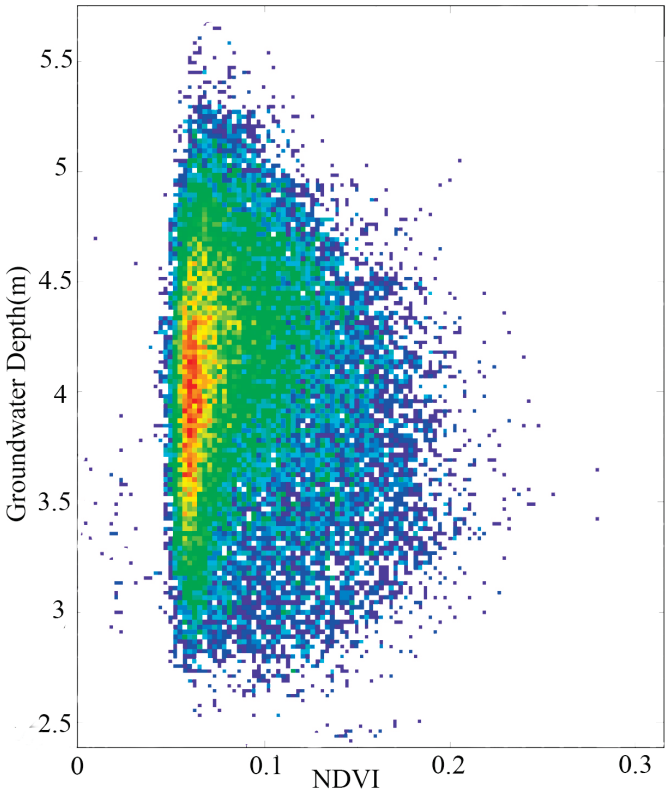

Figure 13. NDVI and groundwater depth scatter plot.

4. Discussion

Arid and semi-arid zones are ecologically fragile, highly sensitive to climate change, and contain vegetation as the main terrestrial ecosystem with vegetation activities producing a dynamic, nonlinear response law that reflects the interaction between hydrothermal

elements and vegetation activities [53]. Although previous studies have provided a preliminary understanding of the increase in vegetation cover change, the results varied widely due to the use of different collection methods, multiple sources of NDVI data, and short NDVI time series [54]. In comparison with Landsat NDVI, LTDR NDVI is more accurate than GIMMS NDVI at the regional scale, in terms of static values and dynamics; however, GIMMS LTDR NDVI data are slightly more accurate than LTDR NDVI data in terms of most vegetation dynamics. This may be due to the GIMMS NDVI values being spatially biased and temporally less biased [55]. Therefore, the use of NDVI data from the same sensor platform and long time series can reduce the data errors caused by different sensor platforms, enabling a better understanding of the changes in vegetation cover in desert hinterland oases and providing a more accurate theoretical basis for predicting changes in vegetation cover and modeling the relationship between vegetation and climate at the global and regional scales. In this study, Landsat, MODIS, and meteorological data did not respond well to the vegetation changes in response to environmental factors due to the limited spatial resolution. However, Sentinel and GF data with higher resolution could be utilized for analysis in subsequent studies. Moreover, this paper only considered the effect of a single environmental factor on vegetation and did not consider the effect of coupling between environmental factors on vegetation. In addition, only climatic, topographic, and hydrological environmental factors were considered, whereas others, such as soil organic matter, nutrient elements, and microclimate, also affect vegetation.

In the present study, 130 Landsat images from 2000 to 2020 were utilized to extract surface water data by adopting the water body index and threshold segmentation method. Although this method achieved better results in water body extraction, the quality and quantity of images and the limitation of spatial and temporal resolution made it difficult for the extracted water bodies to characterize the surface water distribution in the study area accurately. Moreover, only the depth of groundwater burial was modeled using the RF algorithm, with an overall accuracy of 0.729 (Figure 5), indicating that the direct modeling strategy has a limited ability to predict groundwater levels. Zhu et al. improved the prediction accuracy of SPAD using the RF algorithm and a GMM clustering model [56]. Meanwhile, Yang et al. used K-mean and RF machine learning methods, reporting a significant improvement in the accuracy of estimating SPAD [57]. Hence, machine learning methods that are more predictive of groundwater should be introduced in subsequent studies. Moreover, only 16 environmental covariates were included when estimating the depth of groundwater, whereas Zhang et al. selected 24 environmental covariates and used principal component analysis to determine the main variables for predicting soil organic matter in the whole country, which improved the prediction accuracy. Hence, additional environmental covariates should be selected for groundwater level prediction in subsequent studies [37].

5. Conclusions

This study reveals the influence of the distribution pattern of natural oasis vegetation in the hinterland of the Taklamakan Desert by studying the patterns of change in climate, topography, and hydrological processes, and it explores the response of natural oasis vegetation to a series of environmental factors. In general, the oasis vegetation showed a greening trend over time. Spatially, the vegetation showed backward shrinkage in the central region and significant greening in the northwest region. As a result of the effects of climate change, NDVI was positively linked with both temperature and precipitation in the majority of the research locations, but the association was only significant in some parts of the positive correlation region. In natural desert hinterland oases, the most essential element influencing plant growth is water availability, and the combined effects of surface water and groundwater profoundly affect the survival and development of oasis vegetation. A higher frequency of surface water distribution means that the area has better accessibility and water use efficiency, which is also a key factor in shaping the topography of the oasis and determines the distribution pattern of vegetation in the riparian zone at the watershed

scale. The major spatial extent of surface water distribution coincides with vegetation distribution. Meanwhile, a shallow groundwater level affects the mechanism between spatial and temporal ecological succession, critical depth, ecological water demand, and optimal water level of vegetation. Vegetation is most widely distributed in areas with a groundwater burial depth of 3.5–4.5 m. Therefore, this study is informative in exploring how climate change affects oasis vegetation and the impact of water resources on vegetation to guide future water delivery policies for oases.

Author Contributions: Conceptualization and formal analysis, L.P.; funding acquisition, Q.S.; investigation, L.P., Y.W. and H.S.; methodology, L.P.; project administration, Q.S.; software, and A.A.; supervision, Q.S.; validation, L.P., H.S. and A.A.; visualization, L.P.; writing—original draft, L.P.; writing—review and editing, Q.S. All authors have read and agreed to the published version of the manuscript.

Funding: This study was funded by the National Natural Science Foundation of China (Grant No. U1703237).

Data Availability Statement: Data are contained within the article.

Acknowledgments: We are very grateful to our laboratory colleagues for their help in essay writing. We sincerely thank the Editor-in-Chief (Markus Egli) and the two anonymous reviewers for their helpful comments on improving this paper.

Conflicts of Interest: The authors declare no conflict of interest.

References

1. Liang, Y.; Zhang, Z.; Lu, L.; Cui, X.; Qian, J.; Zou, S.; Ma, X. Trend in Satellite-Observed Vegetation Cover and Its Drivers in the Gannan Plateau, Upper Reaches of the Yellow River, from 2000 to 2020. *Remote Sens.* **2022**, *14*, 3849. [CrossRef]
2. Zhang, X.; Jin, X.; Liang, X.; Ren, J.; Han, B.; Liu, J.; Fan, Y.; Zhou, Y. Implications of land sparing and sharing for maintaining regional ecosystem services: An empirical study from a suitable area for agricultural production in China. *Sci. Total Environ.* **2022**, *820*, 153330. [CrossRef] [PubMed]
3. Marques, A.C.; Veras, C.E.; Rodriguez, D.A. Assessment of water policies contributions for sustainable water resources management under climate change scenarios. *J. Hydrol.* **2022**, *608*, 127690. [CrossRef]
4. Alexander, L.V. Global observed long-term changes in temperature and precipitation extremes: A review of progress and limitations in IPCC assessments and beyond. *Weather Clim. Extrem.* **2016**, *11*, 4–16. [CrossRef]
5. Gu, Q.; Wei, J.; Luo, S.; Ma, M.; Tang, X. Potential and environmental control of carbon sequestration in major ecosystems across arid and semi-arid regions in China. *Sci. Total Environ.* **2018**, *645*, 796–805. [CrossRef] [PubMed]
6. Cleland, E.E.; Chiariello, N.R.; Loarie, S.R.; Mooney, H.A.; Field, C.B. Diverse responses of phenology to global changes in a grassland ecosystem. *Proc. Natl. Acad. Sci. USA* **2006**, *103*, 13740–13744. [CrossRef]
7. Piao, S.; Ciais, P.; Friedlingstein, P.; Peylin, P.; Reichstein, M.; Luyssaert, S.; Margolis, H.; Fang, J.; Barr, A.; Chen, A. Net carbon dioxide losses of northern ecosystems in response to autumn warming. *Nature* **2008**, *451*, 49–52. [CrossRef]
8. Nemani, R.R.; Keeling, C.D.; Hashimoto, H.; Jolly, W.M.; Piper, S.C.; Tucker, C.J.; Myneni, R.B.; Running, S.W. Climate-driven increases in global terrestrial net primary production from 1982 to 1999. *Science* **2003**, *300*, 1560–1563. [CrossRef]
9. Wang, H.; Liu, D.; Lin, H.; Montenegro, A.; Zhu, X. NDVI and vegetation phenology dynamics under the influence of sunshine duration on the Tibetan plateau. *Int. J. Climatol.* **2015**, *35*, 687–698. [CrossRef]
10. Yang, L.; Wei, W.; Chen, L.; Chen, W.; Wang, J. Response of temporal variation of soil moisture to vegetation restoration in semi-arid Loess Plateau, China. *Catena* **2014**, *115*, 123–133. [CrossRef]
11. Auslander, M.; Nevo, E.; Inbar, M. The effects of slope orientation on plant growth, developmental instability and susceptibility to herbivores. *J. Arid. Environ.* **2003**, *55*, 405–416. [CrossRef]
12. Ali, A.; Lin, S.-L.; He, J.-K.; Kong, F.-M.; Yu, J.-H.; Jiang, H.-S. Climatic water availability is the main limiting factor of biotic attributes across large-scale elevational gradients in tropical forests. *Sci. Total Environ.* **2019**, *647*, 1211–1221. [CrossRef]
13. Jucker, T.; Bongalov, B.; Burslem, D.F.; Nilus, R.; Dalponte, M.; Lewis, S.L.; Phillips, O.L.; Qie, L.; Coomes, D.A. Topography shapes the structure, composition and function of tropical forest landscapes. *Ecol. Lett.* **2018**, *21*, 989–1000. [CrossRef]
14. Moeslund, J.E.; Arge, L.; Bøcher, P.K.; Dalgaard, T.; Svenning, J.C. Topography as a driver of local terrestrial vascular plant diversity patterns. *Nord. J. Bot.* **2013**, *31*, 129–144. [CrossRef]
15. Stein, A.; Gerstner, K.; Kreft, H. Environmental heterogeneity as a universal driver of species richness across taxa, biomes and spatial scales. *Ecol. Lett.* **2014**, *17*, 866–880. [CrossRef]
16. Lundholm, J.T. Plant species diversity and environmental heterogeneity: Spatial scale and competing hypotheses. *J. Veg. Sci.* **2009**, *20*, 377–391. [CrossRef]
17. Srinivasan, M.P.; Bhatia, S.; Shenoy, K. Vegetation-environment relationships in a South Asian tropical montane grassland ecosystem: Restoration implications. *Trop. Ecol.* **2015**, *56*, 201–217.

18. Gow, L.; Barrett, D.J.; Renzullo, L.J.; Phinn, S.R.; O'Grady, A. A detection problem: Sensitivity and uncertainty analysis of a land surface temperature approach to detecting dynamics of water use by groundwater-dependent vegetation. *Environ. Model. Softw.* **2016**, *85*, 342–355. [CrossRef]
19. Shanafield, M.; Cook, P.G.; Gutiérrez-Jurado, H.; Faux, R.; Eamus, D. Field comparison of methods for estimating groundwater discharge by evaporation and evapotranspiration in an arid-zone playa. *J. Hydrol.* **2015**, *527*, 1073–1083. [CrossRef]
20. Saber, M.; Mokhtar, M.; Bakheit, A.; Elfeky, A.M.; Gameh, M.; Mostafa, A.; Sefelnasr, A.; Kantoush, S.A.; Sumi, T.; Hori, T. An integrated assessment approach for fossil groundwater quality and crop water requirements in the El-Kharga Oasis, Western Desert, Egypt. *J. Hydrol. Reg. Stud.* **2022**, *40*, 101016. [CrossRef]
21. Li, H.; Shi, Q.; Wan, Y.; Shi, H.; Imin, B.; Li, M.S. Influence of Surface Water on Desert Vegetation Expansion at the Landscape Scale: A Case Study of the Daliyabuyi Oasis, Taklamakan Desert. *Sustainability* **2021**, *13*, 9522. [CrossRef]
22. Fan, Y.; Li, H.; Miguez-Macho, G. Global patterns of groundwater table depth. *Science* **2013**, *339*, 940–943. [CrossRef] [PubMed]
23. Shen, C.; Niu, J.; Phanikumar, M.S. Evaluating controls on coupled hydrologic and vegetation dynamics in a humid continental climate watershed using a subsurface-land surface processes model. *Water Resour. Res.* **2013**, *49*, 2552–2572. [CrossRef]
24. Imin, B.; Dai, Y.; Shi, Q.; Guo, Y.; Li, H.; Nijat, M. Responses of two dominant desert plant species to the changes in groundwater depth in hinterland natural oasis, Tarim Basin. *Ecol. Evol.* **2021**, *11*, 9460–9471. [CrossRef] [PubMed]
25. Mcdonald, A.K.; Wilcox, B.P.; Moore, G.W.; Hart, C.R.; Sheng, Z.; Owens, M.K. Tamarix transpiration along a semiarid river has negligible impact on water resources. *Water Resour. Res.* **2015**, *51*, 5117–5127. [CrossRef]
26. Shi, H.; Shi, Q.; Zhou, X.; Imin, B.; Li, H.; Zhang, W.; Kahaer, Y. Effect of the competition mechanism of between co-dominant species on the ecological characteristics of Populus euphratica under a water gradient in a desert oasis. *Glob. Ecol. Conserv.* **2021**, *27*, e01611. [CrossRef]
27. Slayback, D.A.; Pinzon, J.E.; Los, S.O.; Tucker, C.J. Northern hemisphere photosynthetic trends 1982–1999. *Glob. Chang. Biol.* **2003**, *9*, 1–15. [CrossRef]
28. Braswell, B.; Schimel, D.S.; Linder, E.; Moore Iii, B. The response of global terrestrial ecosystems to interannual temperature variability. *Science* **1997**, *278*, 870–873. [CrossRef]
29. Ma, S.; Wang, L.-J.; Jiang, J.; Chu, L.; Zhang, J.-C. Threshold effect of ecosystem services in response to climate change and vegetation coverage change in the Qinghai-Tibet Plateau ecological shelter. *J. Clean. Prod.* **2021**, *318*, 128592. [CrossRef]
30. Wu, L.; Ma, X.; Dou, X.; Zhu, J.; Zhao, C. Impacts of climate change on vegetation phenology and net primary productivity in arid Central Asia. *Sci. Total Environ.* **2021**, *796*, 149055. [CrossRef]
31. Yang, J.; Gong, P.; Fu, R.; Zhang, M.; Chen, J.; Liang, S.; Xu, B.; Shi, J.; Dickinson, R. The role of satellite remote sensing in climate change studies. *Nat. Clim. Chang.* **2013**, *3*, 875–883. [CrossRef]
32. Baniya, B.; Tang, Q.; Huang, Z.; Sun, S.; Techato, K.-a. Spatial and temporal variation of NDVI in response to climate change and the implication for carbon dynamics in Nepal. *Forests* **2018**, *9*, 329. [CrossRef]
33. Beck, P.S.; Atzberger, C.; Høgda, K.A.; Johansen, B.; Skidmore, A.K. Improved monitoring of vegetation dynamics at very high latitudes: A new method using MODIS NDVI. *Remote Sens. Environ.* **2006**, *100*, 321–334. [CrossRef]
34. Jiang, Z.; Huete, A.R.; Chen, J.; Chen, Y.; Li, J.; Yan, G.; Zhang, X. Analysis of NDVI and scaled difference vegetation index retrievals of vegetation fraction. *Remote Sens. Environ.* **2006**, *101*, 366–378. [CrossRef]
35. Fisher, A.; Flood, N.; Danaher, T. Comparing Landsat water index methods for automated water classification in eastern Australia. *Remote Sens. Environ.* **2016**, *175*, 167–182. [CrossRef]
36. Mann, H.B. Nonparametric tests against trend. *Econom. J. Econom. Soc.* **1945**, *13*, 245–259. [CrossRef]
37. Zhang, Z.; Ding, J.; Zhu, C.; Chen, X.; Wang, J.; Han, L.; Ma, X.; Xu, D. Bivariate empirical mode decomposition of the spatial variation in the soil organic matter content: A case study from NW China. *Catena* **2021**, *206*, 105572. [CrossRef]
38. King, D.A.; Bachelet, D.M.; Symstad, A.J.; Ferschweiler, K.; Hobbins, M. Estimation of potential evapotranspiration from extraterrestrial radiation, air temperature and humidity to assess future climate change effects on the vegetation of the Northern Great Plains, USA. *Ecol. Model.* **2015**, *297*, 86–97. [CrossRef]
39. Lenihan, J.M. Climate Cahnge Effects on Vegetation Distribution, Carbon Stocks, and Fire Regimes in California. *AGU Fall Meet. Abstr.* **2002**, *2002*, B21A-0719.
40. Tan, S.Y. The influence of temperature and precipitation climate regimes on vegetation dynamics in the US Great Plains: A satellite bioclimatology case study. *Int. J. Remote Sens.* **2007**, *28*, 4947–4966. [CrossRef]
41. Wang, J.; Price, K.; Rich, P. Spatial patterns of NDVI in response to precipitation and temperature in the central Great Plains. *Int. J. Remote Sens.* **2001**, *22*, 3827–3844. [CrossRef]
42. Chen, H.; Huo, Z.; Dai, X.; Ma, S.; Xu, X.; Huang, G. Impact of agricultural water-saving practices on regional evapotranspiration: The role of groundwater in sustainable agriculture in arid and semi-arid areas. *Agric. For. Meteorol.* **2018**, *263*, 156–168. [CrossRef]
43. Wang, L.; Qiu, Y.; Han, Z.; Xu, C.; Wu, S.-Y.; Wang, Y.; Holmgren, M.; Xu, Z. Climate, topography and anthropogenic effects on desert greening: A 40-year satellite monitoring in the Tengger desert, northern China. *Catena* **2022**, *209*, 105851. [CrossRef]
44. Scherrer, D.; Körner, C. Topographically controlled thermal-habitat differentiation buffers alpine plant diversity against climate warming. *J. Biogeogr.* **2011**, *38*, 406–416. [CrossRef]
45. Bärlocher, F.; Corkum, M. Nutrient enrichment overwhelms diversity effects in leaf decomposition by stream fungi. *Oikos* **2010**, *101*, 247–252. [CrossRef]

46. Chambers, J.C.; Bradley, B.A.; Brown, C.S.; D'Antonio, C.; Germino, M.J.; Grace, J.B.; Hardegree, S.P.; Miller, R.F.; Pyke, D.A. Resilience to stress and disturbance, and resistance to *Bromus tectorum* L. invasion in cold desert shrublands of western North America. *Ecosystems* **2014**, *17*, 360–375. [CrossRef]
47. Akkouche, S.; Guerrache, N.; Bouderbala, R.; Kadik, L. Choice of fixing species dunes and their effect on vegetation. *Int. J.* **2014**, *2*, 21–30.
48. Liu, X.; Lai, Q.; Yin, S.; Bao, Y.; Qing, S.; Mei, L.; Bu, L. Exploring sandy vegetation sensitivities to water storage in China's arid and semi-arid regions. *Ecol. Indic.* **2022**, *136*, 108711. [CrossRef]
49. Balestrini, R.; Delconte, C.; Sacchi, E.; Buffagni, A. Groundwater-dependent ecosystems as transfer vectors of nitrogen from the aquifer to surface waters in agricultural basins: The fontanili of the Po Plain (Italy). *Sci. Total Environ.* **2021**, *753*, 141995. [CrossRef]
50. Xia, J.; Zhang, S.; Zhao, X.; Liu, J.; Chen, Y. Effects of different groundwater depths on the distribution characteristics of soil-Tamarix water contents and salinity under saline mineralization conditions. *Catena* **2016**, *142*, 166–176. [CrossRef]
51. Eamus, D.; Hatton, T.; Cook, P.; Colvin, C. *Ecohydrology: Vegetation Function, Water and Resource Management*; Csiro Publishing: Clayton, Australia, 2006.
52. Antunes, C.; Diaz Barradas, M.C.; Zunzunegui, M.; Vieira, S.; Pereira, Â.; Anjos, A.; Correia, O.; Pereira, M.J.; Máguas, C. Contrasting plant water-use responses to groundwater depth in coastal dune ecosystems. *Funct. Ecol.* **2018**, *32*, 1931–1943. [CrossRef]
53. Zeng, B.; Zhang, F.; Wei, L.; Zhang, X.; Yang, T. An improved IBIS model for simulating NPP dynamics in alpine mountain ecosystems: A case study in the eastern Qilian Mountains, northeastern Tibetan Plateau. *Catena* **2021**, *206*, 105479. [CrossRef]
54. Zhou, J.; Jia, L.; Menenti, M. Reconstruction of global MODIS NDVI time series: Performance of Harmonic Analysis of Time Series (HANTS). *Remote Sens. Environ.* **2015**, *163*, 217–228. [CrossRef]
55. Beck, H.E.; McVicar, T.R.; van Dijk, A.I.; Schellekens, J.; de Jeu, R.A.; Bruijnzeel, L.A. Global evaluation of four AVHRR–NDVI data sets: Intercomparison and assessment against Landsat imagery. *Remote Sens. Environ.* **2011**, *115*, 2547–2563. [CrossRef]
56. Zhu, C.; Ding, J.; Zhang, Z.; Wang, J.; Wang, Z.; Chen, X.; Wang, J. SPAD monitoring of saline vegetation based on Gaussian mixture model and UAV hyperspectral image feature classification. *Comput. Electron. Agric.* **2022**, *200*, 107236. [CrossRef]
57. Yang, X.; Yang, R.; Ye, Y.; Yuan, Z.; Wang, D.; Hua, K. Winter wheat SPAD estimation from UAV hyperspectral data using cluster-regression methods. *Int. J. Appl. Earth Obs. Geoinf.* **2021**, *105*, 102618. [CrossRef]

Disclaimer/Publisher's Note: The statements, opinions and data contained in all publications are solely those of the individual author(s) and contributor(s) and not of MDPI and/or the editor(s). MDPI and/or the editor(s) disclaim responsibility for any injury to people or property resulting from any ideas, methods, instructions or products referred to in the content.

land

MDPI

Article

Production–Living–Ecological Spatial Function Identification and Pattern Analysis Based on Multi-Source Geographic Data and Machine Learning

Ziqiang Bu [1,2], Jingying Fu [1,2,*], Dong Jiang [1,2,3] and Gang Lin [1,2,*]

[1] Institute of Geographic Sciences and Natural Resources Research, Chinese Academy of Sciences, Beijing 100101, China; buziqiang3314@igsnrr.ac.cn (Z.B.); jiangd@igsnrr.ac.cn (D.J.)
[2] College of Resources and Environment, University of Chinese Academy of Sciences, Beijing 100049, China
[3] Key Laboratory of Carrying Capacity Assessment for Resource and Environment, Ministry of Natural Resources, Beijing 100101, China
* Correspondence: fujy@igsnrr.ac.cn (J.F.); ling@lreis.ac.cn (G.L.); Tel.: +86-010-6488-9221 (J.F.); +86-188-1175-9109 (G.L.)

Abstract: Land use cannot be simply understood as land cover. The same land may carry different functions, such as production, living, and ecological applications; the dominant function of land will affect and restrict other uses. Disorderly urbanization and industrialization have led to an intensification of conflicts among the production, living, and ecological functions of land, which is a major constraint on regional sustainable development. This paper took the perspective of land-use function and used multi-source data such as Sentinel remote-sensing imagery, VIIRS night-time light data, and POIs to classify land-use functions on a large scale in the Beijing–Tianjin–Hebei (BTH) urban agglomeration. The specific research process was as follows. Firstly, the BTH region was multi-scale-segmented based on Sentinel remote-sensing data. Then, the spectral, texture, shape, and socio-economic features of each small area after segmentation were extracted. Moreover, a PLES land-use classification system oriented towards land-use function was established, and a series of representative samples were selected. Subsequently, a random forest model was trained using these samples; then, the trained model was used for the large-scale analysis of land use in the entire BTH region. Finally, the spatial distribution patterns and temporal–spatial evolution characteristics of PLES in the BTH region from 2016 to 2021 were analyzed from the macro level to the micro level.

Keywords: multi-source data; multi-scale segmented; PLES; random forest

1. Introduction

The problems caused by urbanization and industrialization, such as resource constraints, unbalanced urban–rural development, and increased risks to food security, are constantly deteriorating. Land-use conflicts between various stakeholders are intensifying, and interactions between production, living, and ecological spaces are gradually becoming unbalanced [1,2]. For example, the development of farmland and the construction of factories continue to encroach on living and ecological spaces, in the same time, The disorderly expansion of urban residential buildings and the large number of new buildings in the countryside have encroached on cultivated land and ecological land to some extent. On the contrary, the occupied and destroyed ecological space may have negative feedback on the production space and living space by natural disasters such as landslide and sand storm and the reduction in ecological service value. It can be seen that the rational layout of production, living, and ecological spaces and the balanced play of their functions are important contents in realizing sustainable land use. From a realistic perspective, with the development and growth of urban scale, cities are connected into urban agglomerations, and the flow of production, living, and ecological factors within urban agglomerations

is very close. The functional changes in land use in different cities may have similar laws or mutual influences [3]. Therefore, identifying the land-use patterns of cities and urban agglomerations from the perspective of function can elucidate the dynamic changes in and impacts between the production, living, and ecological functions of land during urbanization and industrialization, so as to evaluate and diagnose the sustainability of land use.

Traditional land-use classification mainly identifies land cover through the spectral, textural, and other advanced features of remote-sensing images. These can mainly be divided into the following three categories: pixel-based classification methods, object-oriented classification methods, and scene-based classification methods [4]. Various classification methods are applicable to different remote-sensing image features. Pixel-based classification methods mainly analyze differences in the spectral information of pixels for classification. Some simpler machine-learning methods are being trialed that do not require many input features [5–7]; they are suitable for low- and medium-resolution remote-sensing images. For example, Fei Yuan et al. used the maximum likelihood method to classify most of the Minnesota urban area pixel by pixel in tandem with multi-temporal Landsat series data, and quantified the land-cover change patterns of the city with an overall classification accuracy between 80% and 90% [8]. However, pixel-based classification methods neglect the shape and texture features of land cover, and are constrained by the "spectral confusion" issue, which may lead to misclassification and omission errors of land cover [9,10]. Object-based image analysis (OBIA) uses geographic objects as the basic unit for land-cover classification [11,12], which reduces intra-class variation and eliminates the salt-and-pepper effect caused by misclassification. The advantage of OBIA is that it incorporates various information sources, enabling the use of the texture, shape, and location of feature objects as the basis for classification [13–15], which can reveal more image information. For example, Mengmeng Li et al. applied OBIA classification methods, bifurcated segmentation trees, and energy minimization algorithms to the image segmentation of very-high-resolution (VHR) satellite images, which can effectively distinguish buildings from other man-made objects [16]. Scene-based land-use classification, mainly utilizing convolutional neural network methods, is suitable for extracting deep image features from ultra-high-resolution images [17]. For example, Nimrabanu Memon et al. applied CNNs for the automatic land-cover classification of multi-resolution dual-polarized data and found that CNN models trained on low-spatial-resolution images were more adept at performing migration learning to predict higher-resolution images [18]. Recently, the demand for the fine-grained planning of functional areas within major urban areas and the increasing availability of socioeconomic big data (SBD) have given rise to a boom in fusing high-resolution remote-sensing imagery and SBD for urban functional area identification [19–23]. For example, Feng et al. proposed a scene–object–economy recognition framework that fuses building vectors, POIs, and high-resolution remote-sensing image features to compensate for the inability of remote-sensing images to mine 3D features [24]. However, the difficulty of data acquisition and the incoherence of data have created bottlenecks in this field of research, because higher-resolution remote-sensing satellites tend to have long re-entry cycles and are costly and expensive to acquire. In addition, convolutional neural networks can be expensive in terms of hardware costs and time costs for training and prediction [25]. Therefore, it is difficult to apply scenario-based land-use classification and urban functional area identification to large-scale land-use mapping. Taken together, the OBIA approach has a higher accuracy than image-based detection methods [26], and it is more feasible than approaches using scenario-based and multi-source data in the field of long time series large-scale land-use mapping; In addition, the OBIA approach can be used in conjunction with complex machine-learning algorithms, and the influence of input variables on the results can be analyzed after the results are produced which makes it more suitable for large-scale, multi-feature input land-use classification. Taken together, all three classification methods apply machine-learning algorithms for classification to a greater or lesser extent, due to the fact that machine-learning models, which can be based on features extracted from

classification objectives and manually given labels, have become an indispensable process for automated land-use classification.

The function of production–living–ecological space (PLES) refers to the characteristics or functions displayed by different types of national spatial areas in terms of residents' production and living activities under the joint influence of internal composition elements and external influencing factors, forming a complex community in terms of economic, social, and geographic elements. The rational layout and balanced functioning of PLES is important for coordinated regional development and sustainable land use. However, few existing classification studies have used PLES as a classification system. Existing relevant research mainly uses the merged classification method [27–29] and the index system measurement method [30–32] to identify PLES based on existing publicly available land-use products. For example, Li et al. constructed a classification system for urban PLES functions using the index system measurement method from a comprehensive perspective of land function, ecosystem services, and landscape functions, and integrated spatial function value accounting functions based on ecosystem service value evaluation. They determined the dominant type of spatial function through vertical and horizontal comparisons [33]. While Nan et al. used the merged classification method to produce the spatial and temporal distribution data of PLES in Xinjiang from 2000 to 2020, the center of gravity transfer model and Moran's I method were used to analyze and summarize its distribution pattern and spatio-temporal evolution [34].

However, both of these methods used in most of the PLES classification studies are overly dependent on traditional land-use classification products and have certain limitations: Firstly, traditional land-use classification products do not take into account the functionality of the land use; for example, they cannot differentiate between factories, subdivisions, and rural home sites. And publicly available land-use products are limited in their accuracy and have a resolution that is difficult to satisfy. Therefore, a small number of studies has begun to focus on directly dividing land functions based on the PLES classification system from socioeconomic or remote-sensing data. For example, using POIs as the data source, Fu et al. effectively identified PLES in the central urban area of Wuhan, China, revealing influencing factors through the application of the analytic hierarchy process (AHP), spatial analysis, and quadrat proportion method [35]. However, due to data limitations, these studies are predominantly limited to the main urban areas of a single city and cannot consider the impact of rural living space, agricultural production space, and ecological land outside the city on the distribution and combination patterns of functional urban PLES. In addition, previous studies have been unable to characterize the interactions of PLES functions among different cities within an urban agglomeration. Therefore, it is necessary to classify land based on PLES functions at a larger scale, which encompasses complex geographic areas with diverse geographic environments and socio-economic activities such as the urban agglomeration scale. This study took the Beijing–Tianjin–Hebei city cluster (BTH) as the study area, adopted a PLES classification system based on a functional perspective, used POI data with long time series and night-time lighting data to assist, and employed a classification algorithm with object-oriented integrated machine-learning (random forest) for the large-scale land-use mapping of Sentinel images in order to provide more reliable basic data (10 m resolution) for researchers to conduct subsequent research on land issues.

2. Materials and Methods

2.1. Study Area

The Beijing–Tianjin–Hebei city cluster(Figure 1) located at latitude 37°27′~42°40′ N and longitude 113°27′~119°50′ E, is situated in the area north of the lower reaches of the Yellow River in northern China, east of the Bohai Sea, including the 2 municipalities directly under the central government of Beijing and Tianjin, and 11 prefecture-level cities such as Shijiazhuang and Tangshan in Hebei province, with a land area of approximately 180,000 km^2, accounting for 3.8% of the total urban land area of the country. BTH is

situated within the temperate continental monsoon climate zone, with high topography in the northwest and low topography in the southeast; the arable land is generally devoted to dryland farming. The BTH region, which has a high population density, a long history of agriculture, and rapid industrial development, is the largest urban agglomeration in the Bohai Sea region of Northeast Asia, and it is the largest and most dynamic economic zone in northern China. Separately, Beijing is the economic, political, and cultural center of China, with an important development status, and is a city of significant status in China. Tianjin is located in the center of the Bohai Sea region, and has a port known as "the largest port in northern China". Tianjin is also the economic hinterland of the Beijing–Tianjin–Hebei region, with a vast land area, abundant natural resources, and developed high-tech industries, which has enormous potential for development. Hebei province, located in the heart of the Bohai Sea region, contains 11 prefecture-level cities. It has tremendous development advantages in terms of natural resources, distribution, production, markets, talents, and location, making it one of the fastest-growing economic regions in China. In recent years, Beijing and Tianjin, as the central growth points of the region, have stimulated the integrated development of sub-cities in the region, enabling the BTH to achieve a regional GDP of RMB 9.6 trillion in 2021 [36,37]. However, the siphoning effect of large cities has led to unbalanced development within the BTH, exhibiting polarization; rapid urbanization and industrialization have led to ecological degradation, reductions in arable land area, traffic congestion, and deterioration of the population's living environment, which affects sustainable economic and social development [38]. The rapid development of non-agriculturalization in rural areas of the BTH region has been attributed to the advancement of urbanization and industrialization. This has also resulted in a strong transition of rural production spaces and living spaces towards urban production and living spaces, causing certain encroachment and damage to ecological spaces in the process. However, research on the distribution and evolution of land-use functions in the BTH from a PLES perspective is relatively scattered. Therefore, this study selected the BTH region as the study area to investigate the functional utilization of land use at different scales, which has typical significance.

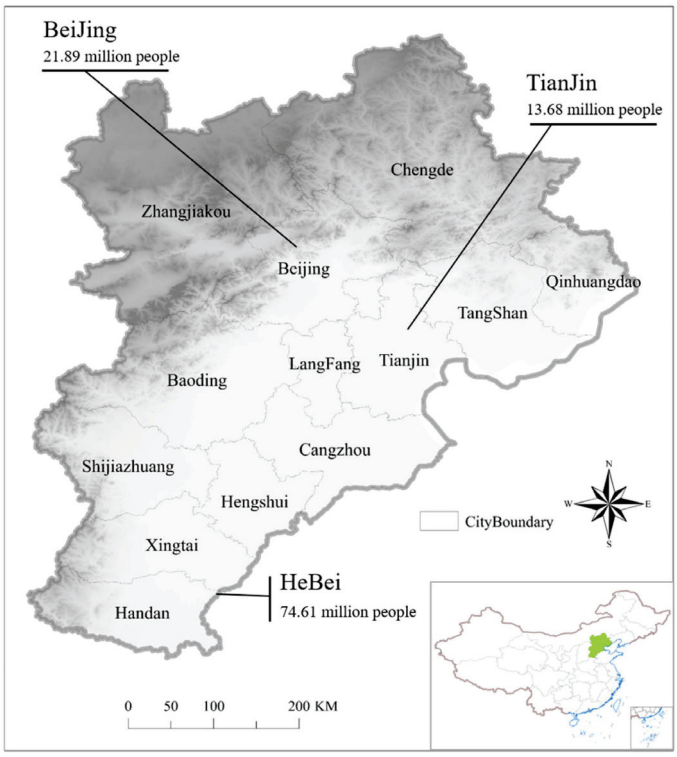

Figure 1. Study area location.

2.2. Research Data

2.2.1. Sentinel-2A Remote-Sensing Data

Sentinel-2A has 13 bands with a width of 290 km and a revisit period of 10 d. The remote-sensing images for this study were downloaded from the Google Earth Engine platform (https://earthengine.google.com/ (accessed on 20 February 2023)), and the images were collected during the crop-growing periods of 2016 and 2021 (1 April to 31 October). Additionally, pre-processing steps such as image de-clouding, cropping, mosaic, mean fusion, etc., were completed online by means of code on the platform, and four bands of red, green, blue, and near-infrared were screened.

For the spectral features required for the study, the red, green, blue, and near-infrared bands of Sentinel-2A were fused by interrogating the built-in module of the Google Earth Engine (GEE) platform; then, the texture features were extracted according to the principal component bands to obtain 18 texture features of the principal component bands within the BTH. The corner second-order, correlation, and entropy texture features were finally determined by feature analysis moment, correlation, and entropy as the classification features.

2.2.2. Night-Time Lighting Data and POI Data

Night-light remote sensing is recognized as a good data source for the large-scale simultaneous monitoring of socioeconomic activities and has been widely used in the fields of population estimation, economic estimation, urbanization monitoring, and energy consumption studies [39]. The spatial resolution of NPP/VIIRS is 15″ at the monthly scale; this sensor has a sensitive perception of faint lights at night across a long time series. In this study, the annual synthesis, cropping, and mosaic visualization of these data were accomplished using the Google Earth Engine platform. POI data refer to points of interest, which record the name, category, latitude, and longitude of various activities on the ground and other basic information. It has been shown that POI data can effectively describe the function of a plot [40]. In this study, Python was used to crawl POI data of 13 cities in the BTH for 2016 and 2021 from the Baidu map platform, and then convert POIs from vector point data to raster density data and resample them to a 10 m resolution through kernel density analysis in the ArcGIS platform to perform the fusion analysis of multi-source data.

The final acquired features and data sources are shown in Table 1, where the shape features are the area, perimeter, and structure ratio of the object after object-oriented multiscale segmentation. Spectral features and texture features are used to distinguish different subsurface types, which are often used in traditional studies; whereas shape features and socioeconomic features are added to our algorithm, which help to distinguish different building categories for the PLES functional identification, which is the innovation of this paper.

Table 1. Classification features and data source.

Feature Type	Bands	Data Source
Spectral features	B8	Sentinel-2A
	B4	Sentinel-2A
	B3	Sentinel-2A
	B2	Sentinel-2A
	NDVI	Sentinel-2A
Shape features	Area	Object segmentation
	Perimeter	Object segmentation
Texture features	Structure ratio	Object segmentation
	Second-order moment	GEE
	Relevance	GEE
	Entropy	GEE
Socioeconomic features	Night light value	NPP/VIIRS
	POIs density	Nucleation density of POIs

2.3. Research Methods

This paper proposes a large-scale land-use identification method using a production–living–ecological network as the classification system, which can represent the functionality of land use. In concrete terms, object-oriented segmentation on remote-sensing images was performed first. After completing the segmentation, the segmented objects were converted into vector polygons, and the subsequent extraction of features and selection of samples and labels are based on the vector polygons after object-oriented segmentation. Then, we extracted the spectral, shape, texture, and socioeconomic features of each pixel within the object from Sentinel optical images, NPP/VIIRS night-time lighting images, and POI data and constructed a PLES spatial classification system. Subsequently, some representative samples for labeling were selected. These samples were used to extract features from multi-source data, and the optimal random forest model was trained by adjusting each parameter. Finally, the trained models were used to perform large-scale classification on the whole area of the study area. The specific research process is shown in Figure 2.

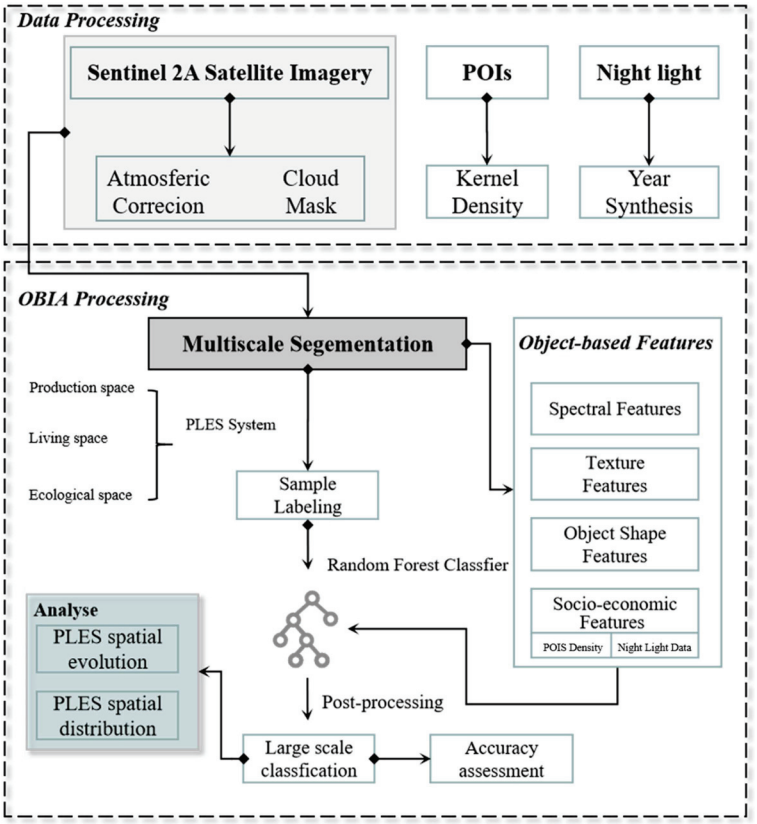

Figure 2. Technical framework.

2.3.1. PLES Spatial Classification System

Traditional land-use classification is mostly based on land-cover discrimination, using remote-sensing image features to discriminate ground attachments for land-use classification; however, land is an integrated functional whole, and its production, living, and ecological functions are interlinked. In this study, a PLES classification system (Table 2) was constructed that considers the surface cover and land-use functionality, and divides the regional land into three primary classifications and nine secondary classifications. This is important for analyzing functional PLES conflicts and the coupling characteristics of city clusters, and studying the sustainable development of urban clusters. This classification system is important for analyzing the conflict and coupling characteristics of the PLES functions of city clusters and studying the sustainable development of urban agglomerations.

Table 2. PLES classification system.

Level 1 Classification	Level 2 Classification	Code
Production area	Agricultural space	11
	Industrial space	12
	Transportation space	13
Living area	Rural living space	21
	Urban living space	22
Ecological area	Waters	31
	Urban ecological space	32
	Non-urban ecological space	33
	Unused space	34

2.3.2. Object-Oriented Multi-Scale Segmentation Algorithm

The object-oriented multi-scale segmentation algorithm views an image as a neighborhood graph consisting of topological relationships between sub-regions and within an image region [41]. Starting from a single image element card, segmentation is performed according to a specified scale, and adjacent image regions are merged and grown two by two. To ensure that the merged regions have a high degree of homogeneity, it is necessary to set a threshold to control the process of patch growth so as to segment feature objects at the optimal scale. The basic idea of the algorithm is that starting from a single image element, the difference metrics are calculated separately with the neighboring image elements, and merging is carried out within the allowed range of the heterogeneity threshold; after the completion of one round of merging, objects generated in the previous round are used as the basic unit, and calculations are continued separately with the neighboring objects; the above steps are iterated until no more objects can be merged under the specified heterogeneity threshold.

The heterogeneity between objects consists of spectral heterogeneity and shape heterogeneity. Initially, each pixel is treated as a region, and the disparity metric (f) is calculated.

$$f = w_1 x + (1 - w_1) y \tag{1}$$

where w_1 is the weight value, $0 \leq w_1 \leq 1$, x is the spectral heterogeneity, and y is the shape heterogeneity. The spectral heterogeneity and shape heterogeneity methods are expressed as follows:

$$x = \sum_{i=1}^{n} p_i \sigma_i \tag{2}$$

$$y = w_2 u + (1 - w_2) v \tag{3}$$

where p_i is the weight of the ith image layer, σ_i is the standard deviation of the spectral value of the ith image layer, u is the overall tightness of the image area, v is the smoothness of the image area boundary, and w_2 is the weight, $0 \leq w_2 \leq 1$. The formula for the calculation is:

$$u = E/\sqrt{N} \tag{4}$$

$$v = E/L \tag{5}$$

where E is the actual boundary length of the image area, N is the total number of image elements in the image area, and L is the total length of the rectangular boundary containing the extent of the images.

2.3.3. Random Forest Classification Algorithm

Random forest is a machine-learning algorithm proposed by Breiman et al. [42]; it is an integrated learning algorithm in which multiple decision trees are integrated together for decision making. A random forest consists of numerous decision trees, each of which grows independently and forks at nodes with randomly selected parameters of the characteristic variables, and the final prediction results are selected by each decision tree. Decision tree

models are usually tuned by the number of iterations of decision trees and the number of feature parameters contained in each tree. After sampling the data in random forests, the features are also randomly sampled to ensure independence of the predictor; thus, random forest systems can handle a large amount of high-dimensional data and can determine the interactions between various features. In this study, multi-source data from 2016 and 2021 were collected, and then the same sample points were used to extract objects, shapes, and socioeconomic features from these two periods of data, respectively. And through field research and manual visual interpretation, labels were set according to the actual functional land-use changes, and the resulting datasets were used to train two different random forest models. During the training process, iterating the three hyperparameters of the depth of the decision tree in a random forest, the maximum number of features, and the minimum number of samples contained in the leaf nodes was specially focused on.

3. Results

3.1. Object-Oriented Segmentation and Accuracy Evaluation of the Random Forest Algorithm

In this study, the GEE platform was first used to perform the atmospheric correction, cloud removal, clipping, and mosaicking of Sentinel images at different times in the study area, and calculate texture features. Then, downloaded images of the BTH region were subjected to multi-scale segmentation using ArcGIS Pro 2.8 software and Python programs. After segmentation, 1956 sample points were selected in the BTH region through visual interpretation, considering the surface coverage and land-use function, covering three primary classifications and nine secondary classifications, and fully considering the characteristics of developed and undeveloped areas within the urban agglomeration. The spectral, shape, textural, and socio-economic features of these samples were then extracted as input data and fed into the random forest algorithm for training. By calculating the confusion matrix of the classification results for different schemes, the classification accuracy of each category and the overall classification accuracy could be obtained.

Specifically, in order to test and validate that the combination of spectral, shape, textural, and socio-economic features is more conducive to functionally oriented PLES classification, three different training plans were implemented, including Plan A, using only Sentinel spectral and textural features; Plan B, using remote-sensing features and object-based segmented shape features; and Plan C, using a combination of spectral features. As shown in Table 3. The overall accuracy rates of Plan A, Plan B, and Plan C were 85.06%, 87.64%, and 93.97%, respectively. The Kappa coefficients were 82.66, 85.74, and 92.98, respectively. It can be seen that as the number of features involved in the classification gradually increased, the classification accuracy was gradually improved to a certain extent.

In Plan A, the results obtained using only remote-sensing image features for classification were poor, especially due to the confusion between urban living space and rural living space, as well as urban green space and non-urban green space, because these two groups of land-cover types were only distinguished through the land-use function and had similar visual effects in land cover, which may have caused "same spectrum different object" and "same object different spectrum" phenomena in the spectral domain. After adding shape features (Plan B), this problem was somewhat improved, with an overall accuracy improvement of 2.58%. Shape features help to identify subtle differences between certain land-cover types from other dimensions. For example, agricultural production spaces and rural living spaces on the North China Plain generally exhibit regular shapes, while living spaces in urban areas have larger patch areas, and road land appears elongated. In Plan B, the prediction accuracy of industrial production spaces increased by 4%, and the prediction accuracy of road land increased by 8%. However, the misclassification phenomenon between the main urban area and the non-main urban area remained significant.

Table 3. Classification accuracy of different plans.

	Plan A				Plan B				Plan C			
	PA/%	UA/%	OA/%	Kappa	PA/%	UA/%	OA/%	Kappa	PA/%	UA/%	OA/%	Kappa
Agricultural space	0.87	0.89			0.82	0.98			0.98	0.96		
Industrial space	0.89	0.96			0.93	0.96			0.93	1.00		
Transportation space	0.76	0.76			0.94	0.61			0.89	0.89		
Rural living space	0.89	0.91			0.90	0.93			0.97	0.97		
Urban living space	0.90	0.86	85.06	82.66	0.89	0.96	87.64%	85.74%	1.00	0.96	93.97	92.98
Waters	0.95	0.93			1.00	0.91			0.84	0.84		
Urban ecological Space	0.68	0.73			0.75	0.77			0.94	1.00		
Non-urban ecological space	0.53	0.47			0.77	0.67			0.79	0.81		
Unused space	0.86	0.60			0.83	0.62			1.00	0.57		

In Plan C, both night-time light features and POI density were added, which could effectively distinguish urban central areas from non-urban areas (urban central areas generally exhibit a high economic activity density, numerous POIs, and high night-time light brightness, while suburbs are the opposite). This led to an overall accuracy increase of 6.33% and a Kappa coefficient increase of 7.24, greatly improving the model's ability to distinguish between urban and agricultural living spaces, urban green spaces, and non-urban ecological green spaces. The confusion matrix of the validation set for Plan C is shown in Figure 3, which indicates that the overall performance of the algorithm and dataset is good, but errors still occur in distinguishing between roads and agricultural living land and between agricultural production space and non-urban green space. To some extent, the shape features obtained from object-oriented segmentation and the socio-economic features provided by night-time light and POI density data help to solve the problems of "same object, different spectrum" and "same spectrum, different object" (which is more typical in function-type classification) and can significantly improve the accuracy of the spatial classification of PLES based on functionality.

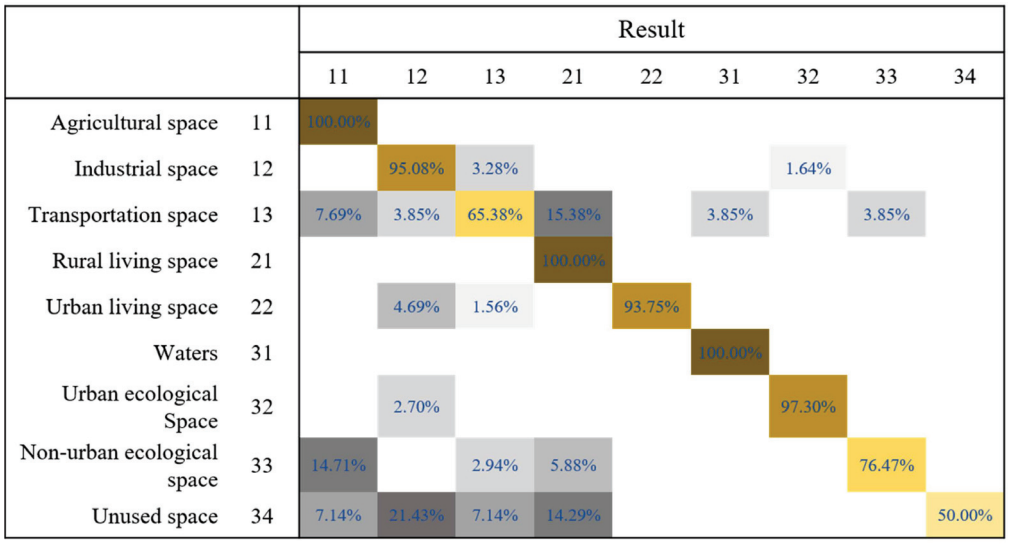

Figure 3. Confusion matrix on the validation set of the dataset in 2021 (Warm colors indicate correct classification, while gray indicates incorrect classification).

In addition, the representativeness of the selected samples is important for PLES classification at such a large scale (the BTH region). Therefore, Google imagery, Sentinel imagery, and other base maps were utilized to validate the accuracy of the large-scale land-use classification data obtained from the Plan-C-based trained model. We randomly selected a portion of the validation points and obtained an accuracy of only 84.17%, which can meets the needs of large-scale land-use analysis, although the actual accuracy has decreased to a certain extent compared with the accuracy on the model validation set.

The above results indicate that the feature set composed of spectral, texture, shape, and socioeconomic features can effectively train a model for fine-grained PLES classification. To evaluate the numerous features extracted from multi-source data, the contribution rates of each feature to the classification results were calculated (as shown in Figure 4a). Among the 23 features, there is a significant difference in the contribution rates of each feature to the classification results (spectral features contributed a total of 57.8%, while texture features, shape features, and socio-economic features cumulatively contributed 19.0%, 5.6%, and 17.6%, respectively). Specifically, the average value of the red band from Sentinel in the spectral features demonstrated the highest contribution rate: approximately 13.53%. Additional features with high contribution rates included the average NDVI value of land objects and the average night-time light brightness of land objects. Although some textural and shape features have relatively low contribution rates, they still play a positive role in improving the accuracy of the final classification.

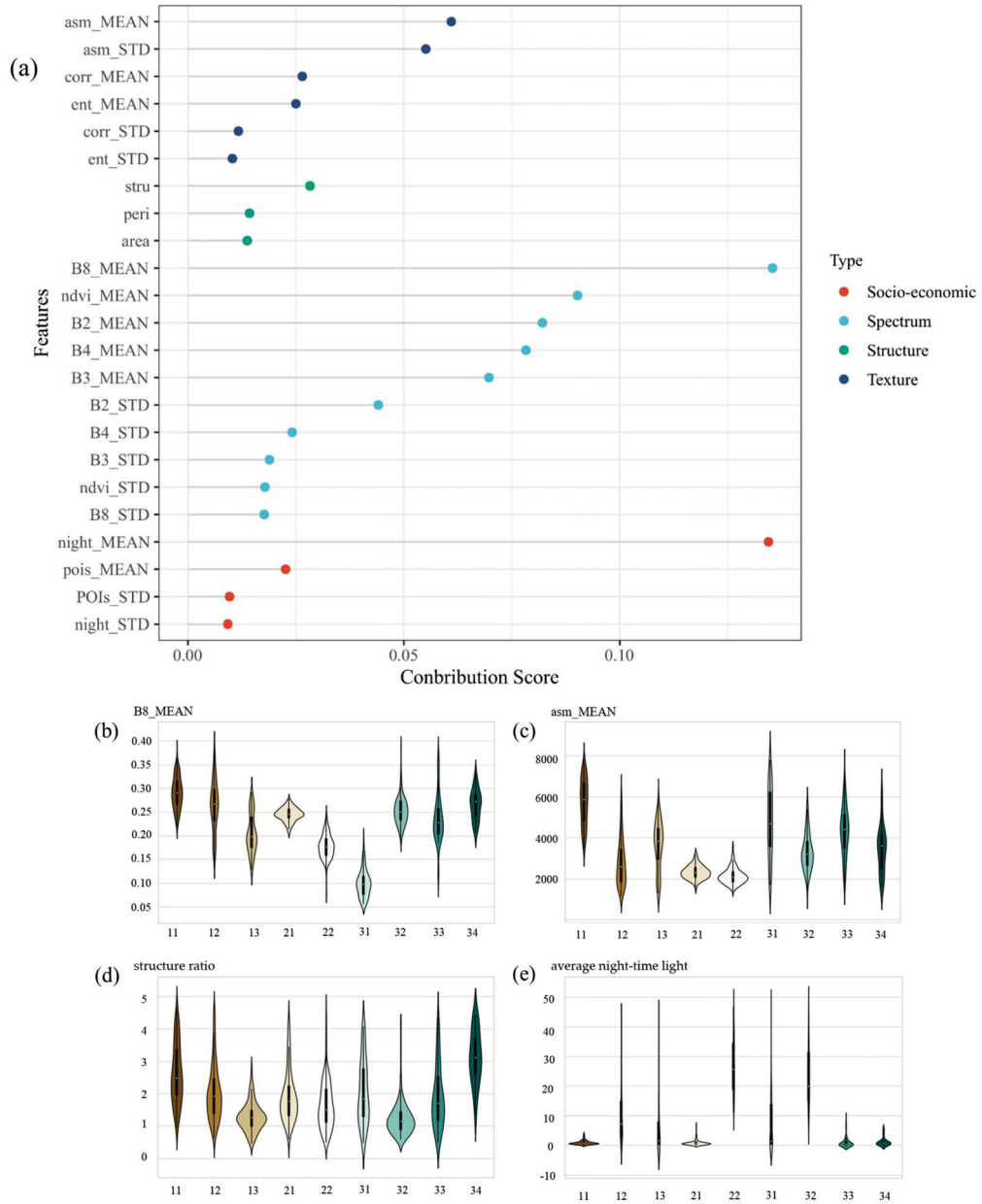

Figure 4. (**a**) Contribution of each feature to the final classification model; (**b**–**e**) Distribution of the values of the four typical features at the sample points.

To specifically explore the discriminative effect of different features on PLES categories, the feature values of typical four categories were computed (as shown in Figure 4b–d): the average red band value of each object (B8_MEAN refers to the mean of the red band values of all image elements of an object, which is a typical representative of spectral features); the average value of the angle second-order moment band (asm_MEAN is the mean of angular second-order moments of all image elements of an object, which is a typical representative of texture features); the structure ratio (the more prominent shape feature); and the average night-time light brightness (the more prominent socio-economic feature) of each object. These four categories represent spectral, textural, shape, and socioeconomic features, respectively. Different land covers have different observable reflectance values in the red band, with vegetation exhibiting the highest values, followed by buildings and water bodies. The red band also aids in distinguishing different types of built-up areas; the red band reflectance in agricultural residential spaces is generally higher than in urban residential spaces. The structural complexity of land objects helps to differentiate land classes from a different perspective. For instance, urban green spaces and non-urban green spaces have similar surface-cover characteristics, making it difficult to distinguish them based on spectral and texture features alone. However, due to human development activities, such as roads and buildings, urban green spaces exhibit a higher fragmentation and tend to have more irregular shapes. In contrast, non-urban green spaces are less affected by human activities, resulting in more regular shapes. Therefore, the structural complexity of non-urban green spaces far exceeds that of other land classes. The night-time light brightness of land patches greatly contributes to distinguishing rural residential areas from urban residential areas. As depicted in Figure 4, roads, factories, and water bodies are widely distributed, exhibiting significant variations in night-time light brightness. Conversely, urban areas have a high population density and more nocturnal production and living activities, leading to a higher night-time light brightness. In contrast, cropland and rural residential areas have lower night-time light brightness values, making it easier to differentiate between urban and rural areas.

However, certain features or combinations of features have limited discriminatory power for functional PLES types. Therefore, it is necessary to integrate multiple sources of data and consider various features using ensemble learning methods for the identification of functional PLES types.

3.2. Analysis of the Spatial Evolution Pattern of PLES in the BTH Region

The PLES spatial structure refers to the proportions of various land-use types in different areas in the study region. Changes in land-use structure can indicate future trends and help to better understand the impact of natural, economic, and population factors on land-use structure changes. This can also clarify the spatial distribution rules of PLES and promote the coordinated development of PLES land use. The PLES spatial distribution map of 2021 of the BTH region displayed in Figure 5 shows clear zonality, influenced by the Taihang Mountains running through the west of the city cluster and the Yan Mountains and the Bashang Plateau located to the north. Large areas of the western and northern regions of the study area are covered by natural ecological land such as forests and grasslands. Only some valleys and flat areas have been cultivated into farmland, with scattered villages. Covering the central and southeast areas of the BTH is the vast and flat North China Plain, most of which is used as agricultural and living space. Rural living spaces are responsible for maintaining agricultural production and are interspersed with agricultural production spaces in a sporadic manner.

The spatial distribution patterns and proportions of human-induced PLES land use (refers to the land that mainly performs the function of serving for human activities, including agricultural space, industrial space, transportation space, rural living space, urban living space, urban ecological space) in Beijing, Tianjin, and other cities in Hebei province are significantly different. Figure 6 depicts the proportion of land-cover types under artificial utilization in various cities within the Beijing–Tianjin–Hebei region. Urban

areas in Beijing and Tianjin, as megacities each with a population of over 10 million, occupy 43.67% of the urban living space within the entire urban agglomeration. The urban living space in Beijing and Tianjin is huge and concentrated, and there are extensive urban green spaces distributed throughout the city, including the central area, accounting for 17.76% and 7.95% of the urban land use, respectively. Industrial production spaces are distributed in the peripheral areas further away from the city center, indicating a high level of coordination in the PLES. In contrast, cities in the rest of Hebei are much less developed than Beijing and Tianjin, and land development and utilization are dominated by agricultural production spaces, covering approximately 6.72 million hectares of arable land in 2021, accounting for 90.17% of the arable land area of the entire BTH region and 27.17% of the total land area. In Hebei province, construction land is mainly devoted to enhancing rural living spaces, and the urban living space is relatively small in patches. The proportion of urban ecological land area is only 0.73%, and a large amount of industrial land is distributed on the edge of urban living space or even in the core area, resulting in more obvious conflicts in PLES. In general, the land in the study area is covered by natural vegetation, with non-urban ecological land and unused land accounting for 54.77% of the total area. Artificially utilized land is used for production spaces, especially for agricultural production space, accounting for 59.43% of the total area of artificially transformed land. Industrial production space and rural living space are scattered, while urban living space is mainly concentrated around several large cities. At the micro level, rural living space in plain areas is generally surrounded by agricultural production space, and a proportion of rural living areas has industrial production space distributed internally or on the periphery. Industrial production land is generally located on the outskirts of cities, but in some less developed cities in Hebei, such as Baoding, industrial production space surrounds the main urban area; there are also scattered industrial production spaces within the rural living space. Urban living space in the main urban area and some suburban centers outside the main urban area is continually expanding, gradually replacing the original "agricultural production space–rural living space" system with an "industrial production space–urban living space" system.

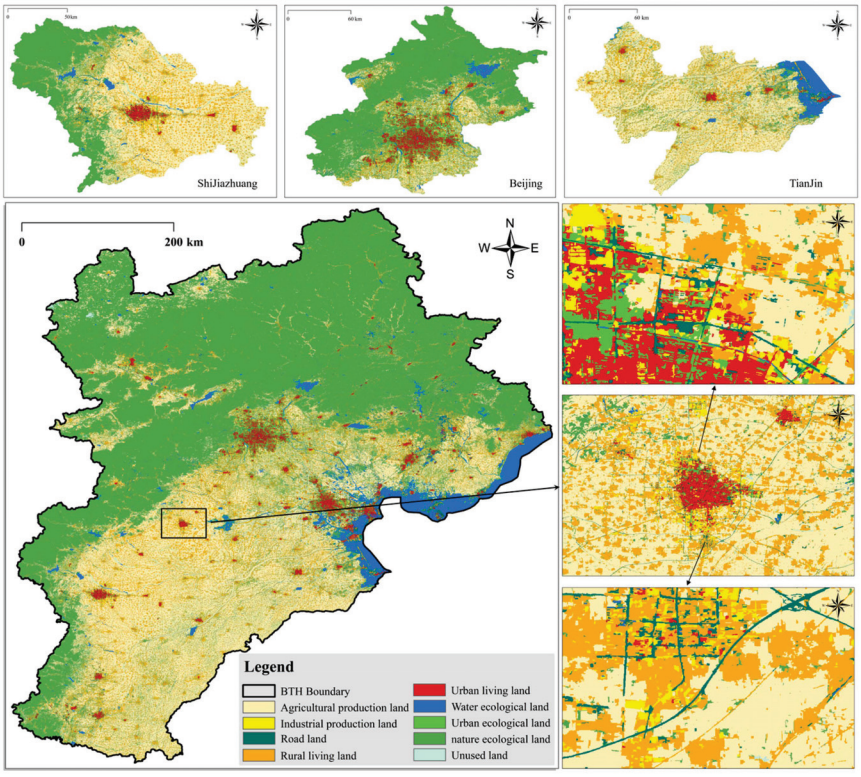

Figure 5. PLES classification results of 2021 of the BTH at different scales.

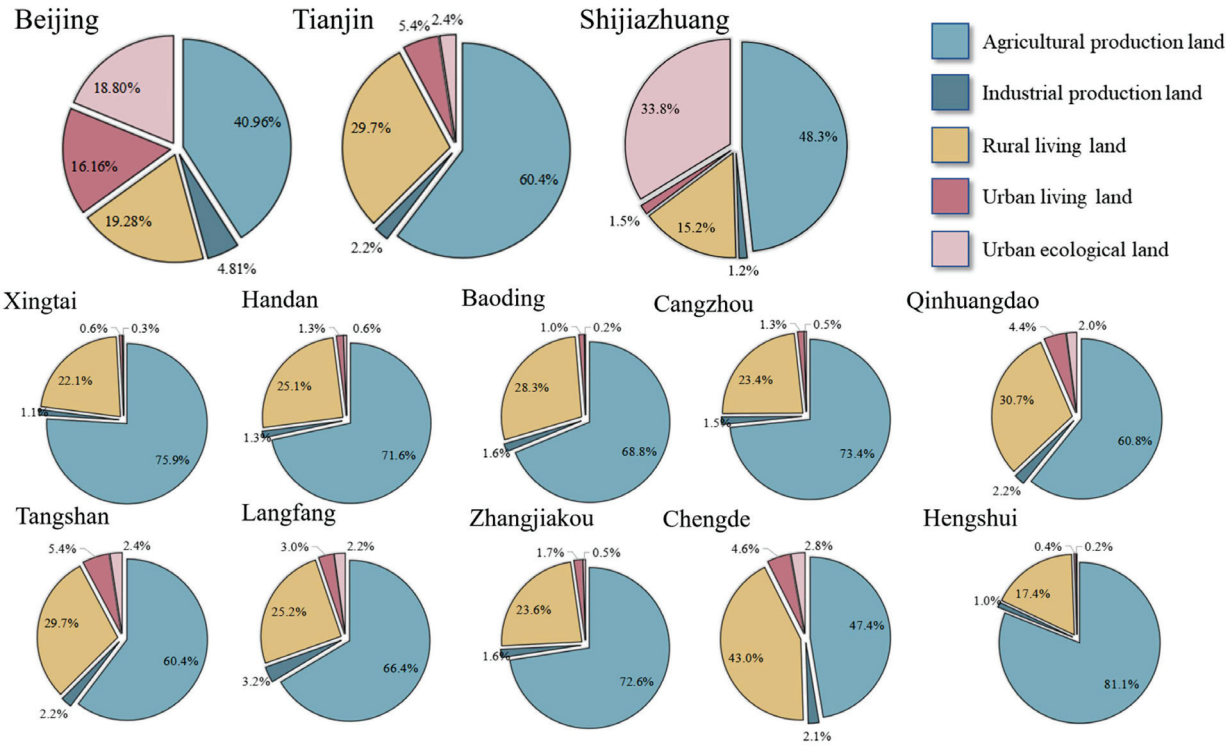

Figure 6. Distribution patterns of artificial PLES areas in different cities.

PLES in the BTH region for the years 2016 and 2021 was classified using the method and model described in the previous section. According to the classification result statistics shown in Table 4, during the 5-year period from 2016 to 2021, in the process of urbanization and industrialization in the BTH region, a small proportion of cultivated land was converted into rural living space and urban living space, resulting in a slight decrease in the overall area of cultivated land. The area of industrial production space increased slightly, but only by 0.01%, and the base area of industrial production space is relatively small; therefore, the overall area of production space slightly decreased. The changes in living space are reflected in the decrease in rural living space and the increase in urban living space, which is caused by the transformation of urban villages and village settlements on the outskirts of cities into land devoted into high-rise buildings, for example. The urban living space in Beijing and Tianjin has expanded, with a tendency towards connecting into a continuous area, while the main urban areas of other cities in Hebei, such as Shijiazhuang, are gradually becoming connected to surrounding counties to the north. Rural living space is shrinking due to the encroachment of agricultural production space and swallowing up by urban living space; however, the magnitude of this change is not significant. At the same time, due to the expansion of urban areas and the construction of urban green spaces, the area of urban ecological land has increased.

Table 4. PLES area statistics results.

PLES Type	Area in 2016 (km^2)	Area in 2021 (km^2)
Agricultural space	807.86	786.45
Industrial space	26.05	27.14
Transport space	61.42	44.46
Rural living space	280.15	267.63
Urban living space	35.13	40.02
Waters	100.99	107.37
Urban ecological space	22.17	28.89
Non-urban ecological space	1500.08	1527.95
Unused space	6.74	10.68

4. Discussion

Many scientific research teams [43–46] have been engaged in large-scale land-use classification, striving to improve the precision and accuracy of classification through finer granularity, and they have achieved meaningful results. A set of high-precision, high-availability land-use products have been produced and shared on open platforms for use by other scholars. Researchers in planning, environmental, and other fields have relied on these public data for a series of secondary classifications, exploring and summarizing the regional development laws. However, traditional large-scale land-use classification data divide the land surface into categories such as forests, cultivated land, and buildings based on the natural attributes of land cover. They do not specifically distinguish categories within buildings, which is completely inadequate for assessing the population's living environment and the sustainable development of cities, or typical regions undergoing rapid industrialization and urbanization. Therefore, this study has proposed a production–living–ecological classification system which includes nine secondary classifications, such as agricultural production space and industrial production space. Based on the functionality of land use, the classification results can facilitate fine-grained land-use analysis, providing reliable data support for the analysis of PLES in city clusters and typical regions and the sustainable development of city clusters. Figure 7 illustrates a comparison between the land-use product of the European Space Agency (ESA LUCC) [43], the land-use product of the Resource and Environmental Science Data Center of the Chinese Academy of Sciences (CNLUCC) [44], and our PLES classification product (functional PLES LUCC). As shown in Figure 7, the ESA LUCC focuses on the natural attributes of ground attachments and does not consider the fine-scale classification of different buildings. Therefore, it is not suitable for the secondary analysis of functional land use, such as production–living–ecological functions. Although the CNLUCC can distinguish between urban construction land and rural construction land, the product resolution is 30 m, which results in relatively fuzzy boundaries between different functional land parcels and prominent misclassification phenomena. In contrast, the functional PLES LUCC developed in this study has a spatial resolution of 10 m and, with the assistance of multi-source data, can differentiate between different functional types such as rural living space and urban living space. Therefore, the PLES classification dataset developed in this study has a high practicality in studies of regional development pattern evolution. And the multi-scale classification algorithm of the PLES space function in this article is applicable to both rural and urban land-use classification, taking into account both natural and artificial land-use functional characteristics. It has a wide application scope and high practical value. It needs to be emphasized in particular that, as mentioned in the introduction, the same piece of land may carry production, living, and ecological functions, and our classification system and resulting dataset focuses on identifying their dominant functions.

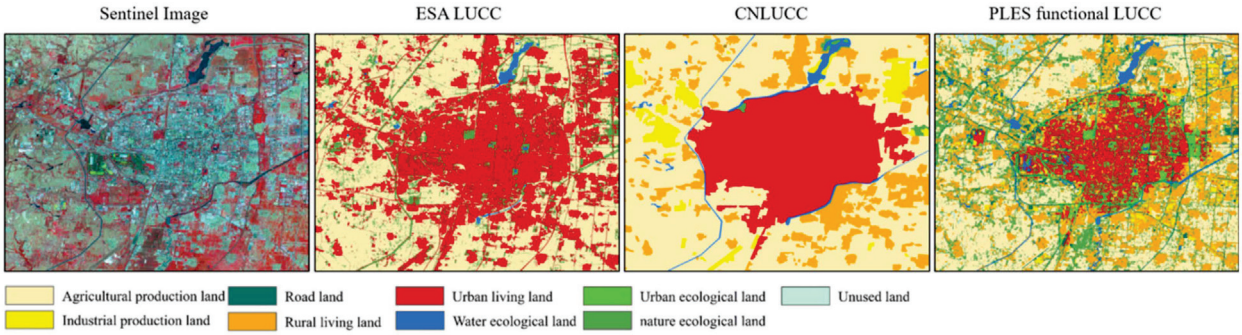

Figure 7. Comparison of our PLES classification results with other products.

However, due to the lack of strong representativeness in sample selection or insufficient sample size, the overall accuracy of the classification is limited. Moreover, this study adopted an object-oriented and multi-source data fusion spatial PLES classification

method, which required downloading remote-sensing data from the Google Earth Engine for multi-scale segmentation and multi-source data fusion. This local operation is time-consuming and laborious, rendering this method temporarily unsuitable for larger-scale land-use classification, such as at the national or global level.

In future research, facing the demand for the classification of complex urban and urban functional types, it is necessary to perform the classification of land-use functional types utilizing novel geographic big data. We will strive to select more representative samples and data sources to improve classification accuracy, improve the method system of PLES spatial classification to improve classification efficiency, and reduce data processing and classification costs to adapt our method for larger-scale classification and application.

5. Conclusions

With the rapid development of remote-sensing satellite technology, pixel-based, object-oriented, and scene-based land-use methods have gradually been formed and improved, each with their own applicable classification tasks, advantages, and disadvantages. For monitoring land-use conflicts caused by the spatial competition of PLES in the process of urbanization and industrialization, pixel-based land-use classification cannot represent the shape features and combined texture features of land cover, making it difficult to identify the functional land use; scene-based functional zone recognition has high data and computing performance requirements and is costly, which is not suitable for large-scale land-use classification. Simultaneously, the classification method based on multi-scale object-oriented segmentation can easily extract and synthesize features from complex data sources. And the object-oriented segmentation model requires a low computational performance and data resolution. Therefore, this study identified PLES in the BTH region using multi-source geographic data and an object-oriented method combined with machine-learning algorithms. The main results and conclusions are as follows.

1. Firstly, multiple-scale segmentation of the study area was performed based on remote-sensing images (Sentinel); then, the spectral, textural, shape, and socio-economic characteristics of the objects were extracted from the remote-sensing image data, night-time light data, and POI data using the segmented objects. Representative samples were selected and labeled based on the nine secondary classifications under PLES categories. These samples were used to train a random forest algorithm, which was then used to classify all the objects in the entire study area. The results showed that features extracted based on object-oriented and multi-source data can better reflect the characteristics of objects from multiple dimensions, which is effective for identifying the functional types of PLES.
2. In this study, the segmentation parameters were iteratively optimized using a multi-scale segmentation algorithm, resulting in a good segmentation effect, with the size of the segmented objects depending on the image features, and clear boundaries between different land covers. Nearly 2000 samples covering 9 second-level classifications were selected, and 11 features were extracted from multiple sources of data and used to train the random forest algorithm. The results showed that the random forest model had a strong anti-overfitting ability, could monitor the mutual influence between features, and identified small differences between different land covers. Finally, the model achieved an accuracy of 84.17% on the validation set and can thus meet the demands for large-scale land-use classification.
3. The trained model was used to identify the spatial functional PLES types of land in the BTH region in 2016 and 2021, generating a 10 m resolution spatial distribution dataset. Based on this dataset, the spatial distribution patterns and development evolution of the PLES in the BTH region were statistically analyzed. It was found that the PLES in the study area exhibited a zonal distribution. The distribution between Beijing and Tianjin and across Hebei is extremely uneven, with Beijing and Tianjin occupying a substantial proportion of the urban living space, while other cities in Hebei, such as Shijiazhuang, have more clear land-use conflicts in terms of PLES. Furthermore, this

imbalance has widened in the past 5 years. Overall, the production space in the BTH has decreased, while the living space and ecological space have increased. As the urban living space expands, urban green space also increases, and the overall layout of the PLES tends to be more reasonable.

Author Contributions: Methodology, D.J.; supervision, G.L.; writing—original draft, Z.B.; writing—review and editing, J.F. All authors have read and agreed to the published version of the manuscript.

Funding: This work was supported by a grant from the National Natural Science Foundation of China (Grant No. 41971250), State Key Laboratory of Resources and Environmental Information System, and Institute of Geographical Sciences and Natural Resources Research, Chinese Academy of Sciences (Grant No. E0V00112YZ).

Data Availability Statement: The data that support the findings of this study are available from the corresponding author upon reasonable request.

Conflicts of Interest: The authors declare no conflict of interest.

References

1. Gutman, G.; Janetos, A.C.; Justice, C.O.; Moran, E.F.; Mustard, J.F.; Rindfuss, R.R.; Skole, D.; Turner, B.L., II; Cochrane, M.A. *Land Change Science: Observing, Monitoring, and Understanding Trajectories of Change on the Earth's Surface*; Springer: Berlin/Heidelberg, Germany, 2004.
2. Chen, X.; Yu, L.; Du, Z.; Liu, Z.; Qi, Y.; Liu, T.; Gong, P. Toward sustainable land use in China: A perspective on China's national land surveys. *Land Use Policy* **2022**, *123*, 106428. [CrossRef]
3. Yang, X.; Chen, X.; Qiao, F.; Che, L.; Pu, L. Layout optimization and multi-scenarios for land use: An empirical study of production-living-ecological space in the Lanzhou-Xining City Cluster, China. *Ecol. Indic.* **2022**, *145*, 109577. [CrossRef]
4. Navin, M.S.; Agilandeeswari, L. Comprehensive review on land use/land cover change classification in remote sensing. *J. Spectr. Imaging* **2020**, *9*, a8. [CrossRef]
5. Pierdicca, N. Bayesian Techniques in Remote Sensing. *Adv. Glob. Chang. Res.* **2003**, *13*, 49–64.
6. Toth, D.; Aach, T. Improved minimum distance classification with gaussian outlier detection for industrial inspection. In Proceedings of the International Conference on Image Analysis & Processing, Palermo, Italy, 26–28 September 2001; IEEE Computer Society: Washington, DC, USA, 2001; pp. 584–588.
7. Kandrika, S.; Roy, P.S. Land use land cover classification of Orissa using multi-temporal IRS-P6 awifs data: A decision tree approach. *Int. J. Appl. Earth Obs. Geoinf.* **2008**, *10*, 186–193. [CrossRef]
8. Yuan, F.; Sawaya, K.E.; Loeffelholz, B.C.; Bauer, M.E. Land cover classification and change analysis of the Twin Cities (Minnesota) Metropolitan Area by multitemporal Landsat remote sensing. *Remote Sens. Environ.* **2005**, *98*, 317–328. [CrossRef]
9. Atkinson, P.M.; Lewis, P. Geostatistical classification for remote sensing: An introduction. *Comput. Geosci.* **2000**, *26*, 361–371. [CrossRef]
10. Khatami, R.; Mountrakis, G.; Stehman, S.V. A meta-analysis of remote sensing research on supervised pixel-based land-cover image classification processes: General guidelines for practitioners and future research. *Remote Sens. Environ.* **2016**, *177*, 89–100. [CrossRef]
11. Dorren, L.K.A.; Maier, B.; Seijmonsbergen, A.C. Improved Landsat-based forest mapping in steep mountainous terrain using object-based classification. *For. Ecol. Manag.* **2003**, *183*, 31–46. [CrossRef]
12. Peña, J.M.; Gutiérrez, P.A.; Hervás-Martínez, C.; Six, J.; Plant, R.E.; López-Granados, F. Object-based image classification of summer crops with machine learning methods. *Remote Sens.* **2014**, *6*, 5019–5041. [CrossRef]
13. Li, M.; Zang, S.Y.; Zhang, B.; Li, S.S.; Wu, C.S. A review of remote sensing image classification techniques: The role of spatio-contextual information. *Eur. J. Remote Sens.* **2014**, *47*, 389–411. [CrossRef]
14. Hussain, M.; Chen, D.; Cheng, A.; Wei, H.; Stanley, D. Change detection from remotely sensed images: From pixel-based to object-based approaches. *ISPRS J. Photogramm. Remote Sens.* **2013**, *80*, 91–106. [CrossRef]
15. Moskal, L.M.; Styers, D.M.; Halabisky, M. Monitoring urban tree cover using object-based image analysisand public domain remotely sensed data. *Remote Sens.* **2011**, *3*, 2243–2262. [CrossRef]
16. Li, M.; Bijker, W.; Stein, A. Use of binary partition tree and energy minimization for object-based classification of urban land cover. *ISPRS J. Photogramm. Remote Sens.* **2015**, *102*, 48–61. [CrossRef]
17. Yin, J.; Dong, J.; Hamm, N.A.; Li, Z.; Wang, J.; Xing, H.; Fu, P. Integrating remote sensing and geospatial big data for urban land use mapping: A review. *Int. J. Appl. Earth Obs. Geoinf.* **2021**, *103*, 102514. [CrossRef]
18. Memon, N.; Parikh, H.; Patel, S.B.; Patel, D.; Patel, V.D. Automatic land cover classification of multi-resolution dualpol data using convolutional neural network (CNN). *Remote Sens. Appl. Soc. Environ.* **2021**, *22*, 100491. [CrossRef]
19. Bao, H.; Ming, D.; Guo, Y.; Zhang, K.; Zhou, K.; Du, S. DFCNN-based semantic recognition of urban functional zones by integrating remote sensing data and POI data. *Remote Sens.* **2020**, *12*, 1088. [CrossRef]

20. Chang, S.; Wang, Z.; Mao, D.; Guan, K.; Jia, M.; Chen, C. Mapping the essential urban land use in changchun by applying random forest and multi-source geospatial data. *Remote Sens.* **2020**, *12*, 2488. [CrossRef]
21. Hu, T.; Yang, J.; Li, X.; Gong, P. Mapping urban land use by using landsat images and open social data. *Remote Sens.* **2016**, *8*, 151. [CrossRef]
22. Zhang, S.; Li, C.; Sun, J.; Wang, J. Identification of Urban Functional Zones Using High-Resolution Remote Sensing Images and Socioeconomic Big Data. *ISPRS Int. J. Geo-Inf.* **2021**, *10*, 242.
23. Zhang, X.; Du, S.; Wang, Q. Hierarchical semantic cognition for urban functional zones with VHR satellite images and POI data. *ISPRS J. Photogramm. Remote Sens.* **2017**, *132*, 170–184. [CrossRef]
24. Feng, Y.; Huang, Z.; Wang, Y.; Wan, L.; Liu, Y.; Zhang, Y.; Shan, X. An SOE-Based Learning Framework Using Multisource Big Data for Identifying Urban Functional Zones. *IEEE J. Sel. Top. Appl. Earth Obs. Remote Sens.* **2021**, *14*, 7336–7348. [CrossRef]
25. Kamusoko, C.; Kamusoko, O.W.; Chikati, E.; Gamba, J. Mapping urban and peri-urban land cover in Zimbabwe: Challenges and opportunities. *Geomatics* **2021**, *1*, 114–147. [CrossRef]
26. Bruzzone, L.; Demir, B. A review of modern approaches to classification of remote sensing data. *Land Use Land Cover. Mapp. Eur. Pract. Trends* **2014**, *18*, 127–143.
27. Zhang, H.B.; Li, M.H.; Zhang, Q.L. Construction of land classification system and land type identification for territorial spatial planning based on multi-source data. *Trans. Chin. Soc. Agric. Eng.* **2020**, *36*, 261–269.
28. Jin, X.; Lu, Y.; Lin, J.; Qi, X.; Hu, G.; Li, X. Research on the evolution of spatiotemporal patterns of production-living-ecological space in an urban agglomeration in the Fujian Delta region, China. *Acta Ecol. Sin.* **2018**, *38*, 4286–4295.
29. Liu, J.L.; Liu, Y.S.; Li, Y.R.; Liu, J.L.; Liu, Y.S.; Li, Y.R. Classification evaluation and spatial-temporal analysis of "production-living-ecological" spaces in China. *Acta Geogr. Sin.* **2017**, *72*, 1290–1304.
30. Lin, J.; Wu, Y.X.; Wu, J.Y. Construction of the spatial planning system: With discussions on the relationship between spatial planning, territorial spatial regulation, and natural resources supervision. *City Plan. Rev.* **2018**, *42*, 9–17.
31. Ji, Z.X.; Liu, C.; Xu, Y.Q.; Huang, A.; Lu, L.H.; Duan, Y.M. Identification and optimal regulation of the production-living-ecological space based on quantitative land use functions. *Trans. Chin. Soc. Agric. Eng.* **2020**, *36*, 222–231.
32. Fu, J.; Bu, Z.; Jiang, D.; Lin, G.; Li, X. Sustainable land use diagnosis based on the perspective of production–living–ecological spaces in China. *Land Use Policy* **2022**, *122*, 106386. [CrossRef]
33. Li, G.D.; Fang, C.L. Quantitative function identification and analysis of urban ecological-production-living spaces. *Acta Geogr. Sin.* **2016**, *71*, 49–65.
34. Xia, N.; Hai, W.; Tang, M.; Song, J.; Quan, W.; Zhang, B.; Ma, Y. Spatiotemporal evolution law and driving mechanism of production–living–ecological space from 2000 to 2020 in Xinjiang, China. *Ecol. Indic.* **2023**, *154*, 110807. [CrossRef]
35. Fu, C.; Tu, X.; Huang, A. Identification and characterization of Production–living–ecological space in a central urban area based on POI data: A case study for Wuhan, China. *Sustainability* **2021**, *13*, 7691. [CrossRef]
36. Hao, L.; Yu, J.; Du, C.; Wang, P. A policy support framework for the balanced development of economy-society-water in the Beijing-Tianjin-Hebei urban agglomeration. *J. Clean. Prod.* **2022**, *374*, 134009. [CrossRef]
37. Wang, Y.; Xie, Y.; Qi, L.; He, Y.; Bo, H. Synergies evaluation and influencing factors analysis of the water–energy–food nexus from symbiosis perspective: A case study in the Beijing–Tianjin–Hebei region. *Sci. Total Environ.* **2022**, *818*, 151731. [CrossRef] [PubMed]
38. Cui, Y. The coordinated relationship among industrialization, environmental carrying capacity and green infrastructure: A comparative research of Beijing-Tianjin-Hebei region, China. *Environ. Dev.* **2022**, *44*, 100775. [CrossRef]
39. Zheng, Y.; Tang, L.; Wang, H. An improved approach for monitoring urban built-up areas by combining NPP-VIIRS nighttime light, NDVI, NDWI, and NDBI. *J. Clean. Prod.* **2021**, *328*, 129488. [CrossRef]
40. Jiang, S.; Alves, A.; Rodrigues, F.; Ferreira, J., Jr.; Pereira, F.C. Mining point-of-interest data from social networks for urban land use classification and disaggregation. *Comput. Environ. Urban Syst.* **2015**, *53*, 36–46. [CrossRef]
41. Fathizad, H.; Ardakani, M.A.H.; Mehrjardi, R.T.; Sodaiezadeh, H. Evaluating desertification using remote sensing technique and object-oriented classification algorithm in the Iranian central desert. *J. Afr. Earth Sci.* **2018**, *145*, 115–130. [CrossRef]
42. Carbonell, J.G.; Michalski, R.S.; Mitchell, T.M. Machine learning: A historical and methodological analysis. *AI Mag.* **1983**, *4*, 69.
43. Zanaga, D.; Van De Kerchove, R.; Daems, D.; De Keersmaecker, W.; Brockmann, C.; Kirches, G.; Wevers, J.; Cartus, O.; Santoro, M.; Fritz, S.; et al. ESA WorldCover 10 m 2021 v200. 2022. Available online: https://zenodo.org/records/7254221 (accessed on 20 February 2023).
44. Xu, X.; Liu, J.; Zhang, S.; Li, R.; Yan, C.; Wu, S. *China's Multi-Period Land Use Land Cover Remote Sensing Monitoring Data Set (CNLUCC)*; Resource and Environment Data Cloud Platform: Beijing, China, 2018.
45. Rosier, J.F.; Taubenböck, H.; Verburg, P.H.; van Vliet, J. Fusing Earth observation and socioeconomic data to increase the transferability of large-scale urban land use classification. *Remote Sens. Environ.* **2022**, *278*, 113076. [CrossRef]
46. Zhang, X.; Liu, L.; Wang, Y.; Hu, Y.; Zhang, B. A SPECLib-based operational classification approach: A preliminary test on China land cover mapping at 30 m. *Int. J. Appl. Earth Obs. Geoinf.* **2018**, *71*, 83–94. [CrossRef]

Disclaimer/Publisher's Note: The statements, opinions and data contained in all publications are solely those of the individual author(s) and contributor(s) and not of MDPI and/or the editor(s). MDPI and/or the editor(s) disclaim responsibility for any injury to people or property resulting from any ideas, methods, instructions or products referred to in the content.

climate

MDPI

Article

Homogenous Climatic Regions for Targeting Green Water Management Technologies in the Abbay Basin, Ethiopia

Degefie Tibebe [1,2], Mekonnen Adnew Degefu [1,3,*], Woldeamlak Bewket [1,4], Ermias Teferi [1,5], Greg O'Donnell [6] and Claire Walsh [6]

[1] Water and Land Resource Center (WLRC), Addis Ababa University, Addis Ababa P.O. Box 3880, Ethiopia; d.tibebe@cgiar.org (D.T.); woldamlak.b@wlrc-eth.org (W.B.); ermias.t@wlrc-eth.org (E.T.)
[2] Alliance Bioversity International and International Center for Tropical Agriculture (CIAT), Addis Ababa P.O. Box 5689, Ethiopia
[3] Department of Geography and Environmental Studies, Debre Markos University, Debre Markos P.O. Box 269, Ethiopia
[4] Department of Geography & Environmental Studies, Addis Ababa University, Addis Ababa P.O. Box 1176, Ethiopia
[5] Center for Environment and Development, Addis Ababa University, Addis Ababa P.O. Box 3880, Ethiopia
[6] School of Engineering, Newcastle University, Newcastle upon Tyne NE1 7RU, UK; g.m.o'donnell@newcastle.ac.uk (G.O.); claire.walsh@ncl.ac.uk (C.W.)
* Correspondence: author: mekonnen.a@wlrc-eth.org

Abstract: Spatiotemporal climate variability is a leading environmental constraint to the rain-fed agricultural productivity and food security of communities in the Abbay basin and elsewhere in Ethiopia. The previous one-size-fits-all approach to soil and water management technology targeting did not effectively address climate-induced risks to rain-fed agriculture. This study, therefore, delineates homogenous climatic regions and identifies climate-induced risks to rain-fed agriculture that are important to guide decisions and the selection of site-specific technologies for green water management in the Abbay basin. The k-means spatial clustering method was employed to identify homogenous climatic regions in the study area, while the Elbow method was used to determine an optimal number of climate clusters. The k-means clustering used the Enhancing National Climate Services (ENACTS) daily rainfall, minimum and maximum temperatures, and other derived climate variables that include daily rainfall amount, length of growing period (LGP), rainfall onset and cessation dates, rainfall intensity, temperature, potential evapotranspiration (PET), soil moisture, and AsterDEM to define climate regions. Accordingly, 12 climate clusters or regions were identified and mapped for the basin. Clustering a given geographic region into homogenous climate classes is useful to accurately identify and target locally relevant green water management technologies to effectively address local-scale climate-induced risks. This study also provided a methodological framework that can be used in the other river basins of Ethiopia and, indeed, elsewhere.

Keywords: climate homogenization; k-means clustering; green water; technology targeting; abbay basin

1. Introduction

Spatiotemporal climate variability is a leading environmental factor that determines the rain-fed agricultural productivity and food security of communities in a given geographical region by affecting the amount and spatiotemporal distribution of green water resources; the water held in the soil and available to crops and plants [1,2]. The effect of temperature and rainfall variability causes inter-annual variability in cereal crop productivity by about 30–50% in rain-fed agriculture [3]. The impact of climate variability is extremely high in countries like Ethiopia, where there is very high spatiotemporal rainfall and temperature variability caused by the complex topography and north–south oscillation

of overhead solar radiation [4]. An annual-based north–south oscillation of overhead solar radiation over Ethiopia determines the location of the Inter Tropical Convergence Zone (ITCZ), then by the direction and magnitude of rain-producing wind flow [4]. The impact of climate on rain-fed agriculture is not only caused by inter-annual rainfall variability but also by fluctuations in annual rainfall cycles, length of growing period (LGP), rainfall intensity, rainfall onset and cessation dates, and outbreaks of climate-related crop diseases and pests [5–7]. Temperature also determines the spatial and temporal distribution of green water and crop productivity in the rain-fed agriculture system by influencing the rate of water loss from the soil through evapotranspiration [7,8].

Evidence from empirical studies such as [4] indicates that the occurrence and impact of climate-induced risks on rain-fed agriculture differ from region to region significantly. Furthermore, except for temperature, which showed a steadily increasing trend over large areas, trends in rainfall amount and extremes are complex and varied from place to place in the Abbay basin in particular and across Ethiopia in general [4,9]. Similarly, scenario-based studies indicate that the impacts of future climate change on rain-fed agriculture and crop productivity vary from place to place in Ethiopia [10,11]. In addition to the climatic factors, there are other environmental factors such as topography, soil condition, land use, and cover, as well as anthropogenic factors such as agricultural practices and management decisions that can affect the availability of green water in a given area and at a particular time [12]. Recent evidence also confirms that climate change, population growth, and land cover conversation are significantly affecting the availability and distribution of green water resources [13–15].

Poor water utilization and management practices are another set of drivers for the low productivity of primary smallholder rain-fed agriculture in the county [16]. Although many soil and water conservation programs and projects have been implemented since the 1980s, the outcomes have not been adequate nor sustainable as both design and implementations followed top-down and one-size-fits-all approaches without considering spatial climatic variations [16,17]. Moreover, the traditional agroecological zone (AEZ)-based recommendations for green water and agronomic management practices [18] poorly capture local-scale climate-driven green water-related risks. Hence, there is a need to improve green water management practices and the targeting of green water management interventions in the country by considering local scale patterns and risks of climate variability and climate change. Clustering areas into homogenous climatic units can facilitate the identification and characterization of major agricultural water security risks, as well as foster the selection and implementation of site-specific green water management technologies [16].

BCEOM [19] is the only available study that has classified the Abbay basin into four climate clusters by considering the spatial variation of rainfall amount and its seasonal distribution. The four climate clusters include (1) the southeastern part of the basin, which receives more than 1400 mm mean annual rainfall and has a relatively longer monomodal rainfall pattern; (2) the central part of the basin which is characterized by short-length monomodal rainfall pattern; (3) the eastern part of the basin that has small and bimodal rainfall pattern; and (4) the northwestern part of the basin that has monomodal rainfall pattern and receives less than 1200 mm mean annual rainfall amount. Another national-scale study conducted by [20] classified the Abbay basin into five rainfall clusters based on seasonal rainfall cycles and interannual rainfall variability. These rainfall-based clustering studies have identified the broader regional classes but have not captured local scale rainfall variability and water availability and, hence, are not suitable for local scale planning and operational activities. There is a need for a higher resolution classification that uses multiple climate and non-climate (e.g., topography) variables to support effective green water management.

The objective of this study is to produce and characterize climate clusters for the Abbay basin. The clustering was made for the *kiremt* (June–September) primary rainy season, which supports 70–80% of the rain-fed agricultural production of the country. Different from previous studies such as [19,21–24] that considered only the spatial variation of the

annual rainfall cycle, we used other rainfall variables (rainfall amount, onset and cessation dates, length of growing period, and rainfall intensity), temperature, evapotranspiration, and soil moisture in our climate classification. These climate variables are important determinants of the productivity of the rain-fed agricultural system of the country [25–29]. The results generated from this study are useful to optimize the selection and application of site-specific green water management technologies in the study area.

2. Data and Methods

2.1. Study Area

The Abbay basin, also called the Upper Blue Nile Basin (UBNB), is located in the northwestern part of Ethiopia between 7°40′ N and 12°51′ N and 34°25′ E and 39°49′ E and covers a total area of 199,812 km^2 (Figure 1). Rugged topography in the central and eastern parts and flat lowlands in the western parts is the major terrain feature of the basin. About 60% of the basin's area is highland, with elevations of ≥1500 m asl. It is an important basin in the country as it contributes approximately 45% of the total surface water resources, accommodates 25% of the population, accounts for 20% of the area, and contributes about 40% of the agricultural production in the country [30]. The mean annual runoff generated from the Abbay basin is estimated at 49 BCM. The rugged topography, together with the north–south oscillation of the Inter Tropical Convergence Zone (ITCZ), controls the geographical and temporal distribution of the climate system in the Abbay basin [31]. The climate in the Abbay basin varies between hot and semi-arid conditions in the lowlands along the Ethio-Sudanese border and cool and humid conditions in the highlands located in the eastern part of the basin [32].

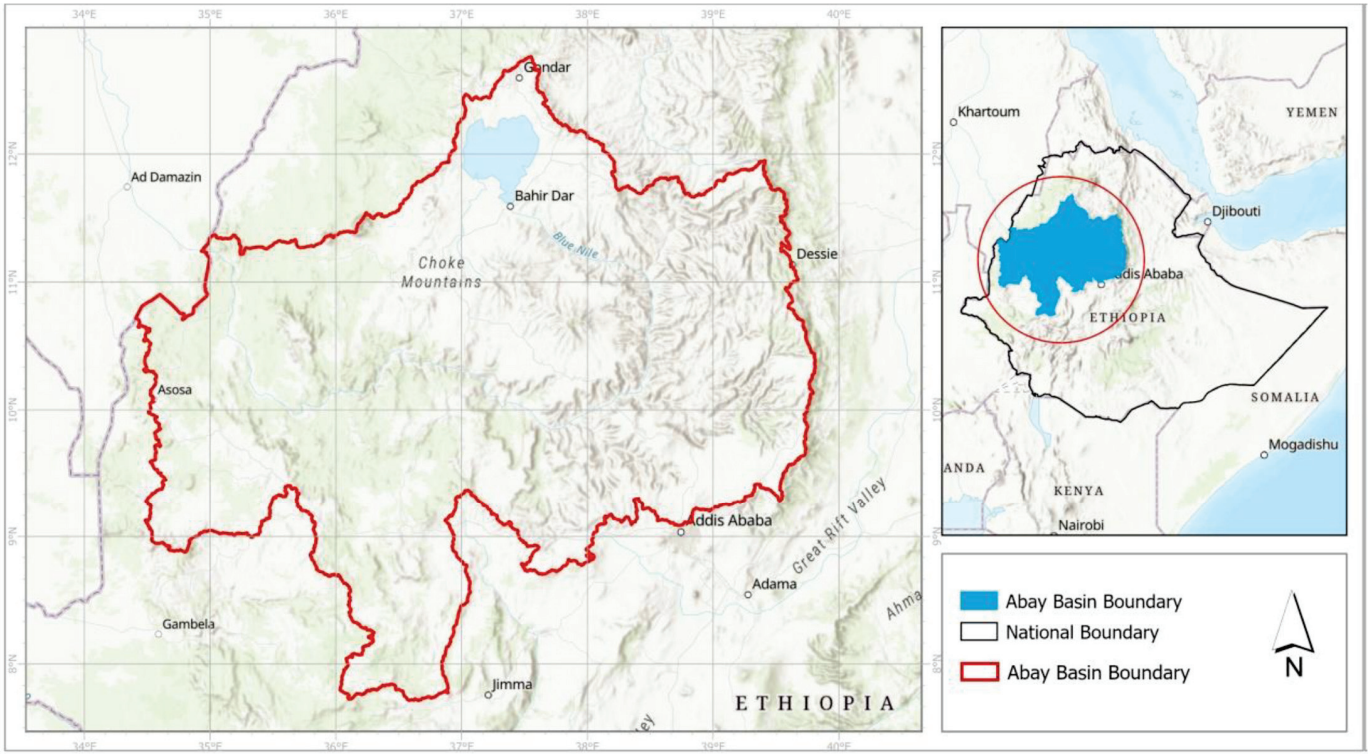

Figure 1. Map of Abbay River basin.

2.2. Data and the Sources

For this study, different climatic data were used for processing and development of homogeneous climate clusters (Table 1). The Enhancing National Climate Services (ENACTS) daily time scale 4 km resolution rainfall and minimum and maximum temperature datasets [33] were used. These datasets were also used to derive the onset date, cessation

date, and length of growing period (LGP), which were used as inputs in the analysis. Climate variability controls the practice and productivity in the rain-fed agricultural system by determining the start and end of the farming calendar, LGP, soil moisture balance, and types of crops that can be grown in an area [5,6].

Table 1. Data used for climatic regionalization in the Abbay basin.

No	Data Type	Source	Spatial Resolution	Temporal Resolution
1	Precipitation	ENACTS	~4 km	1981–2018 (daily)
2	Maximum temperature (Tmax)	ENACTS	~4 km	1981–2018 (daily)
3	Minimum temperature (Tmin)	ENACTS	~4 km	1981–2018 (daily)
4	Onset date	Own analysis	~4 km	1981–2018 (Annual)
5	Cessation	Own analysis	~4 km	1981–2018 (Annual)
6	Length of growing period (LGP)	Own analysis	~4 km	1981–2018 (Annual)
7	Potential evapotranspiration (PET)	Own analysis	~4 km	1981–2018 (daily)
8	Precipitation Concentration Index (PCI)	Own analysis	~4 km	1981–2018 (Annual)
9	Soil moisture	Own analysis	~4 km	1981–2018 (daily)
10	Elevation	AsterDEM v2		

The rainfall onset and cessation dates were defined using a modified version of the Food and Agricultural Organization (FAO, 1986) method. It was defined as the day n after 1 June (i) or 1 March (i), depending on the season, when the daily precipitation exceeds half of the potential evapotranspiration.

$$\sum_{i=1}^{n} R > \sum_{i=1}^{n} PET/2$$

Rainfall cessation was defined as the period when this relationship no longer holds. It is important to mention here that the indicated cessation dates do not mean that there is no rainfall after those dates; rather, the cessation dates refer to the dates when the amount of rainfall becomes less than half of the PET. The length of the growing season (LGP) is simply defined as the number of days between the onset and cessation. The rainfall onset, cessation, and LGP computations were performed for two rainy seasons, which occurred during June–July–August–September (JJAS) and March–April–May (MAM). Most parts of the study area received rainfall during JJAS; however, some areas received short rain during MAM, apart from the JJAS. Potential evapotranspiration was computed using the Hargreaves method, considering the daily minimum and maximum temperature from the ENACT dataset. Soil moisture was estimated using a simple bucket 1D water balance model at the daily timescale and was used as the input. In this method, soil moisture was generated at the daily timescale by assuming the soil to be a reservoir that periodically fills by rainfall events in the form of randomly distributed patterns [34]. This water balance mode was used to estimate soil moisture dynamics in a single top soil layer and conceptualized as a bucket receiving and filled by infiltration driven by gravity and lost by evapotranspiration and/or drainage [35]. The precipitation concentration index was generated from the precipitation data and used to capture the temporal distribution of rainfall and its spatial pattern. It is used to quantify the relative distribution of rainfall patterns. According to Oliver [36], a PCI value < 10.0 represents a mostly uniform precipitation distribution. A PCI between 11 and 15 represents moderate precipitation concentration. A PCI between 16 and 20 represents an irregular distribution. A PCI value above 20 represents strong irregularity.

Topography is another dimension that was considered in the study since it is an important local climate modifier as well as determines surface moisture conditions. Overall, 10 variable input layers were prepared for the clustering analysis (Table 1).

2.3. Data Processing

A stepwise data processing technique was employed for the study (Figure 2). The first step was making all data layers have the same boundary and spatial resolution; the

data layers were clipped to the Abbay basin boundary and resampled to a 4 km grid resolution. The second step involved the calculation of exceedance probabilities to capture the temporal variability of the climate variables. The exceedance probability indicates the likelihood that up to a certain value occurs based on historical data. Typically, an 80% exceedance probability is used in long-term climate analysis, and this reference was used here. Subsequent to the exceedance probabilities computation, variable selection was carried out to reduce the variable space and allow parsimonious model-based clustering. For this, principal component analysis (PCA) was used to reduce the data dimension and maintain only important variables by excluding those that carry redundant information. PCA axes with eigenvalues greater than 1 were retained to ensure that only PCA axes with a significant contribution were used for further analysis [37]. However, we retained a climate variable (cessation date) due to its importance in determining the timing and availability of green water resources in the rain-fed agricultural system. The final data processing step was clustering, and in this study, the k-means spatial clustering [38–41] was employed to find homogenous climatic regions of the study area. k-means clustering is generally simple to implement, and it can be used with large datasets having medium to coarse spatial resolution.

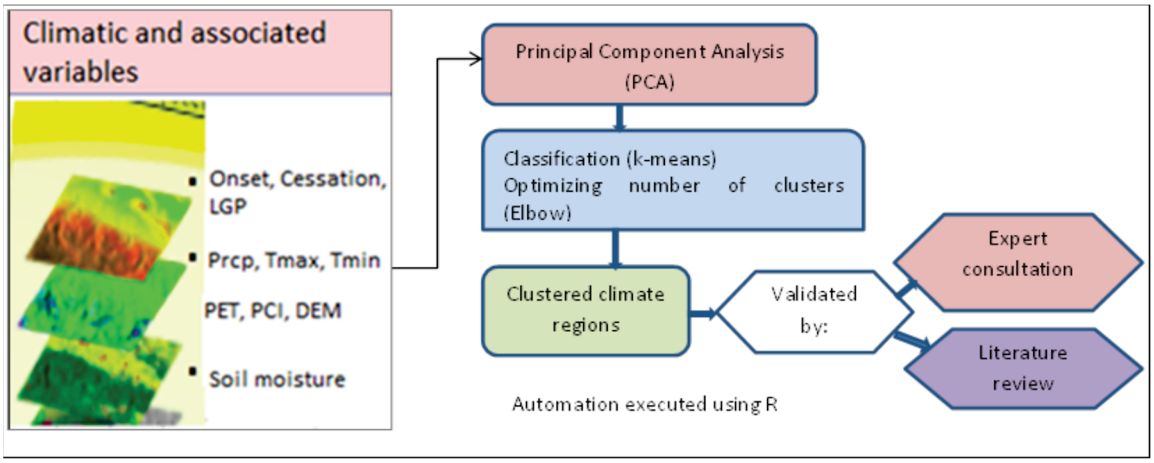

Figure 2. General framework of clustering.

k-means clustering is defined as the sum of squared distances of Euclidean distances between items and the corresponding centroid, which is shown as follows:

$$W(C_k) = \sum_{x_i \in C_k} (Xi - \mu k)^2$$

Here, xi is the ith data point of cluster k (C_k), and μk is the mean value of points in cluster k. The total within-cluster variation is defined as follows:

Total within-cluster variation =

$$\sum_{k=1}^{k} W(C_k) = \sum_{k=1}^{k} \sum_{x_i \in C_k} (Xi - \mu k)^2$$

The total within-cluster sum of squares measures the goodness of the clustering, which increases as the sum of squares measures decreases.

The k-means algorithm requires the user to specify the number of clusters. To reduce subjectivity, the elbow method was used to select the optimal number of clusters. The Elbow method helps to find the optimal number of clusters. This method uses the concept

of Within Cluster Sum of Squares (WCSS), which defines the total variations within a cluster. WCSS is calculated with the following formula:

$$WCSS = \sum P_{i\ in\ cluster\ 1}\ distance\ (P_i\ C_1\ )^2\ + P_{i\ in\ cluster\ 2}\ distance\ (P_i\ C_2\ )^2 + P_{i\ in\ cluster\ 3}\ distance\ (P_i\ C_3\ )^2$$

In the formula of WCSS, $\sum P_{i\ in\ cluster\ 1}\ distance\ (P_i\ C_1\ )^2$ is the sum of the square of the distances between each data point and its centroid within cluster 1. To measure the distance between data points and the centroid, Euclidean distance or Manhattan distance can be used. The elbow method uses a graphical representation to select the optimal K.

The 1st moment and 2nd moment descriptive statistics were applied to characterize each homogeneous climate cluster and interpret it with respect to water availability and agricultural water management. In this regard, mean, median, range, standard deviation, and variance statistics were used. The climate classification was performed for the *Kiremt* growing season. The length of the growing period (LGP) was defined as the number of days taken for the cumulative precipitation to exceed half the cumulative potential evapotranspiration. The rainfall onset and cessation dates were also determined by considering this water balance approach.

3. Results

3.1. Variables Used for Clustering

The variables used for the clustering were selected by applying PCA. The variance, cumulative variance, and Eigenvalues generated from the PCA are shown in Figure 3. The result reveals that the two components with an Eigenvalue greater than one explain more than 77% of the variance. Of this, 52.3% of the variance was explained by the first component, and the remaining 25.2% of the variance was explained by the second component. The Eigenvalues after the second dimension are less than one, indicating that these PCs explain less than the original variables (Figure 3). Accordingly, only the first and second principal components were retained and selected for further analysis.

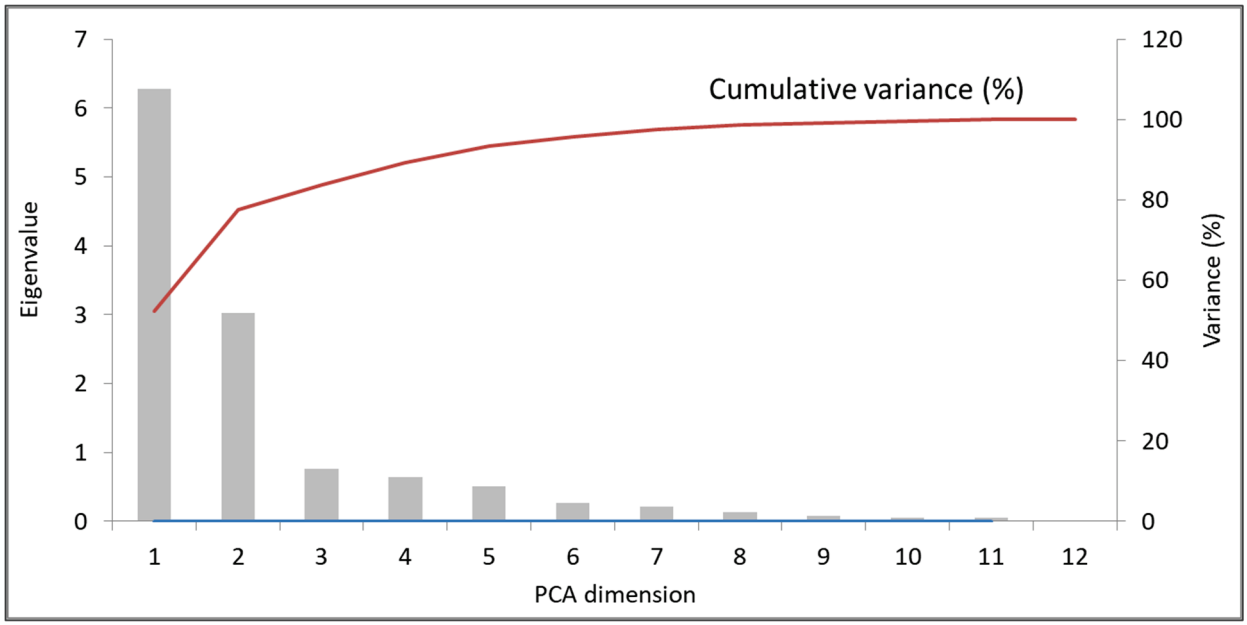

Figure 3. PCA dimensions, Eigenvalue, and cumulative variance.

The quality of variable representation was analyzed and demonstrated on a Cos2 factor map (Figure 4). The results are presented in the Cos2 factor map, on which the variables that are better represented by the two PCs appear close to the circumference of

the correlation circle. The variables are well represented by the principal components, with the exception of the rainfall cessation date, which has a lower representation. This latter variable was kept in the analysis due to its importance for agriculture.

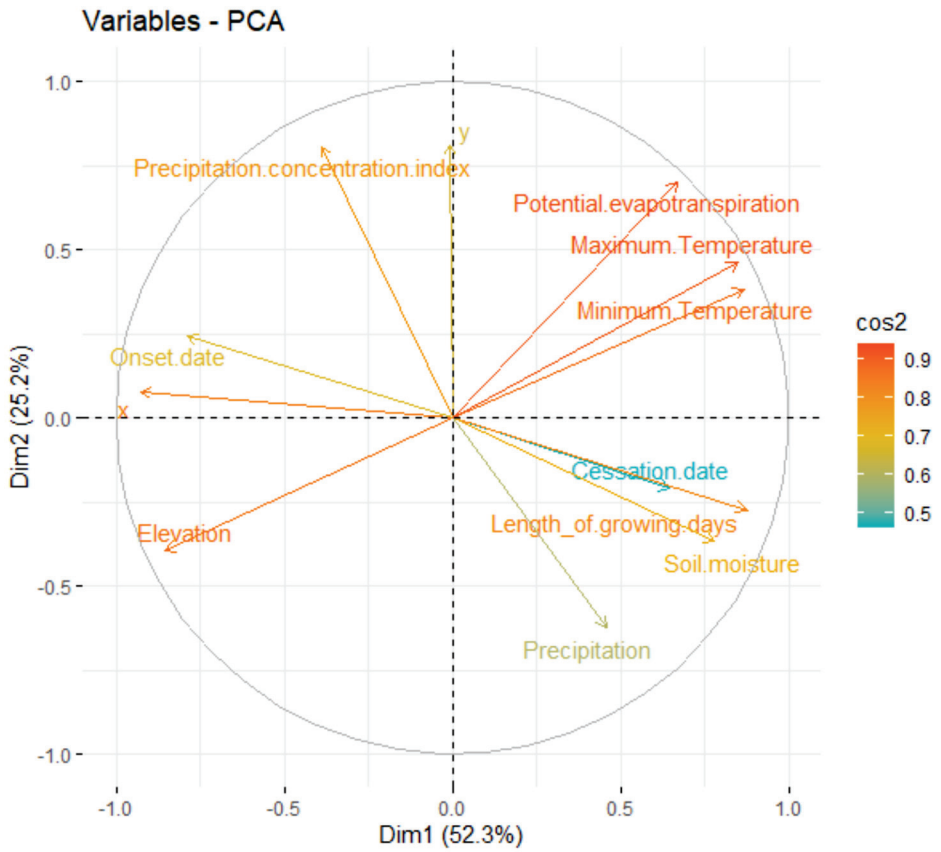

Figure 4. Cos2 factor map representing the quality of variables.

The result shows that the elevation, length of growing season, rainfall onset date, maximum and minimum temperatures, soil moisture, and potential evapotranspiration contribute the most to dimension one, while the precipitation concentration index, PET, and precipitation contribute to dimension two. Furthermore, Figure 4 displays that the distances of the variables from the origin in all covariates are relatively high, demonstrating that most of these variables are very useful for cluster analysis. The result further shows that the PET, elevation, and maximum and minimum temperatures have relatively high Cos2 values.

3.2. Climate Clusters of the Abbay River Basin

The unsupervised k-means clustering considered classifications using up to 150 clusters (Figure 5), from which the optimal number of clusters was selected using the elbow method. The Elbow method is a graphical quasi-objective method in which the optimal number of clusters is selected at the point where the graph of the number of clusters versus WCSS starts to bend and flatten out.

Based on the Elbow graph (Figure 5), 12 climate clusters were identified and mapped (Figure 6). The climate clusters are simply labeled by numbers from 1 to 12.

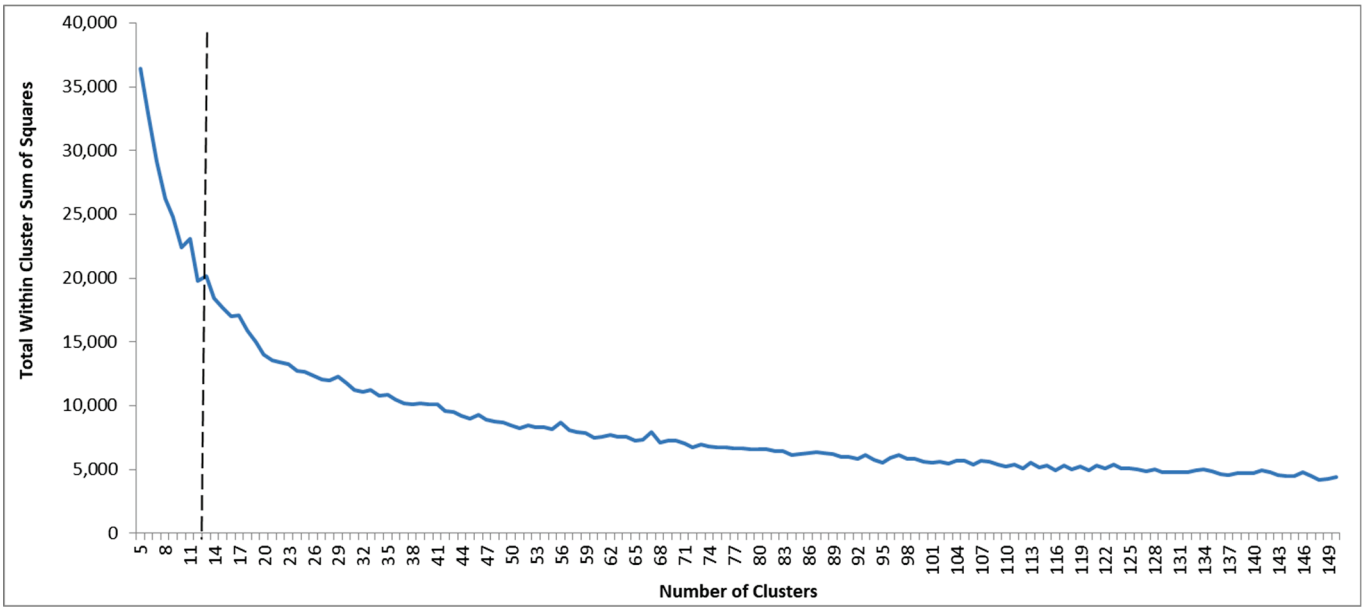

Figure 5. Total number of climate clusters generated by the k-means clustering and optimal number of clusters determined by the Elbow method. The broken line indicate the number of clusters determined by the Elbow method.

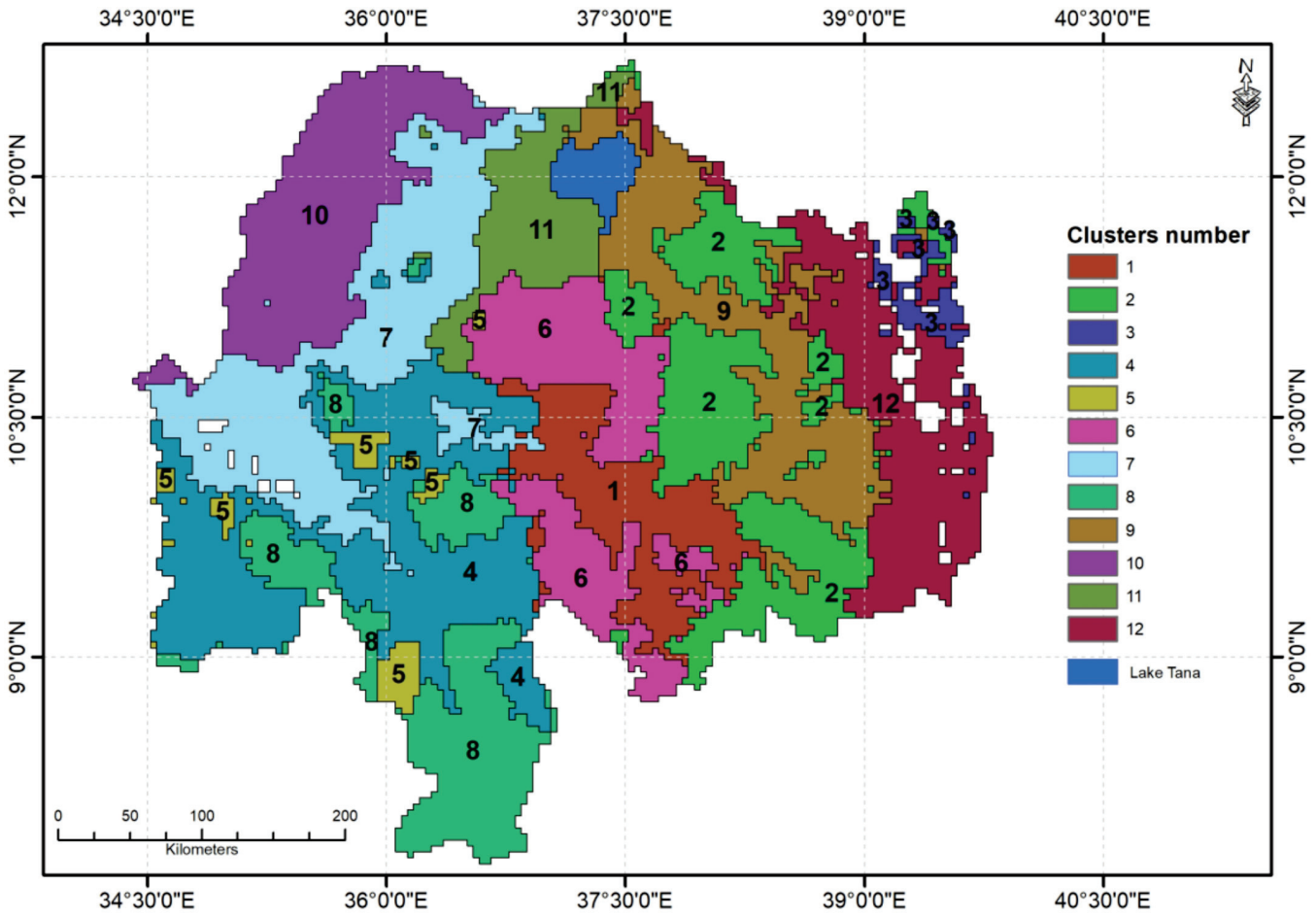

Figure 6. Climate clusters in the Abbay Basin generated by the k-means clustering method.

3.3. Climate Variation between Clusters

Table 2 presents the areal mean annual value of the climate variables for the 12 climate clusters of the Abbay River basin. The climate variables that were used for the study are important determinant factors of spatiotemporal variability and availability of green water for rain-fed agriculture.

Table 2. Characteristics of the climate variables in the 12 climate clusters.

Climate Clusters	Rainfall Onset Date (Pentad)	Rainfall Cessation Date (Pentad)	LGP (Pentad)	PCI	Annual Rainfall (mm)	PET (mm)	Soil Moisture (mm)	Min Tem. (°C)	Max Tem. (°C)	Mean Elevation (m asl)	Rainfall Cycle (number)
1	32.3	53.4	21.1	16.6	1386.4	1432.7	24.7	13.8	26.7	1561.9	1
2	33.8	53.6	19.8	18.1	1190.2	1261.2	13.4	9.2	23.1	2538.5	2
3	19.2	49.5	30.4	20.3	1006.3	1303.0	13.8	8.9	22.4	2620.3	2
4	26.1	54.3	28.2	16.2	1514.2	1425.6	62.5	14.5	28.7	1401.2	1
5	26.1	60.0	33.9	15.9	1603.8	1409.8	75.5	14.6	28.0	1458.7	1
6	31.8	53.7	21.9	16.2	1645.8	1289.1	33.5	10.8	24.3	2267.5	1
7	27.2	54.0	26.8	18.2	1423.5	1655.8	60.1	16.4	31.2	974.8	1
8	25.5	53.9	28.5	14.6	1769.5	1320.7	79.9	12.9	26.2	1846.8	1
9	33.6	53.7	20.0	19.9	1157.8	1467.0	10.6	12.4	27.0	1798.6	2
10	27.2	54.2	27.0	19.5	1198.9	1846.8	51.6	19.1	34.8	698.0	1
11	30.4	54.1	23.6	19.0	1427.5	1449.4	58.3	12.9	27.6	1755.9	1
12	34.4	49.2	14.8	21.1	1006.6	1301.3	11.5	9.0	22.0	2511.5	2

Note: Pentad is a period of five days.

The results demonstrate that four of the climate clusters (2, 3, 9, and 12) experience a bimodal (*Belg* and *Kiremt*) rainfall pattern and are located in the eastern part of the basin (Figure 6). The remaining eight clusters experience monomodal rainfall patterns or the *Kiremt* season only. The mean length of growing period (LGP) for the *Kiremt* season varies between 2.5 months in climate region 12 and 5.6 months in climate region 5. The climate regions located in the western part of the basin have relatively long growing periods (4.5–5.6 months). In contrast, the LGP was relatively short (3.3–3.9 months) for those climate regions located in the central and eastern parts of the basin, except for region three, where the LGP is 5.1 months. The relatively longer LGP for region three, which is located in the eastern part of the basin, is attributable to the early onset of rainfall. Rainfall in this region exceeds half of the PET in early March, while this occurs in early May in the other regions of the eastern and central parts of the basin.

The rainfall onset and cessation dates were earliest for region 3; in this region, rainfall exceeds half of the PET in early April and drops to half of PET in early September. Region 12 has a similar rainfall cessation date (early September). The rainfall onset time in five regions (4, 5, 7, 8, and 10) is in the first two weeks of May. The rainfall onset for the other six regions is between early May (regions 6 and 11) and the third week of May (regions 2, 9, and 12). The rainfall cessation date for four climate regions (1, 2, 6, and 9) is in the last week of September, while it is in early October in five regions (4, 7, 8, 10, and 11). The fall of rainfall amount to less than half of the PET can be caused by the decrease in rainfall amount or increase in the PET amount as the temperature starts to rise with the decreasing cloud cover over the region. The rainfall cessation time for region 5 is in October.

In general, the mean annual rainfall decreases from the southwestern towards the northern and northeastern parts of the basin. The mean annual rainfall is relatively small (less than 1200 mm) for climate regions 2, 3, 9, and 12, which are all located in the eastern and central parts of the basin. The mean annual rainfall is relatively high (1514.2–1769.5 mm) in four climate regions (4, 5, 6, and 8) which are located in the southwestern part of the basin. The mean annual rainfall in regions 7, 10, and 11, which are located in the northwestern part of the basin, is 1423.5 mm, 1198.9 mm, and 1427.5 mm, respectively. Furthermore, the mean annual rainfall for region 1 is 1386.4 mm.

The intensity of rainfall, as represented by PCI, is lowest (14.6 mm) in region 8 and highest (21.1 mm) in region 12. The PCI is relatively low (14.6–16.6) for regions 1, 4, 5, 6, and

8, and all of these regions are located in the southwestern part of the basin. These climate clusters are also known for their extended rainfall season. The PCI is high (19.9–21.1) in regions 3, 9, and 12; all of these regions are located in the extreme eastern part of the basin. The mean annual PET amount is lowest (1261.2 mm) in region 2 and highest (1846.8 mm) in region 10. In general, the mean annual PET is high in climate regions 7 (1655.8 mm) and 10 (1846.8 mm); both of these regions are located in the western lowland part of the basin. It is relatively low (1261.2–1301.3 mm) in regions 2, 3, 6, 8, and 12. The mean annual PET in the five regions (1, 4, 5, 9, and 11) varies between 1409.8 mm and 1467.0 mm. The spatial variation of annual PET is due to the variation of temperature between the climate clusters. The mean annual minimum and maximum temperatures vary between 8.9 °C and 19.1 °C and 22.0 °C and 34.8 °C, respectively. The mean minimum and maximum temperatures are high in the two climate regions (7 and 10) that are located in the western part of the basin. The mean minimum and maximum temperatures are 16.4 °C and 31.2 °C in region 7 and 19.1 °C and 34.8 °C in region 10, respectively. Low mean minimum (8.9–9.2 °C) and maximum (22.0–23.1 °C) temperatures characterize the three climate regions, which are located in the eastern part of the basin.

Soil moisture content also reveals significant variation between the climate clusters. The lowest (10.6 mm) mean annual soil moisture content is found for climate region 9, and the highest (79.9 mm) mean annual soil moisture content is found for climate region 8. In general, the mean annual soil moisture content is relatively high (60.1–79.9 mm) in four climate regions (4, 5, 7, and 8). In contrast, four climate regions that include regions 2, 3, 9, and 12 have relatively low (10.6–13.8 mm) mean soil moisture content; all of these regions are located in the eastern part of the Abbay basin. The mean annual soil moisture content for the other climate regions varies between 24.7 mm in region 1 and 58.3 mm in region 11.

The mean altitude of climate regions varied between 698 m asl for climate region 10 and 2620.3 m asl for climate region 3 (Table 2). As shown in Table 2, the mean altitudes for climate regions 7 and 10 are relatively low at 974.8 m asl and 698 m asl, respectively. Both of these climate regions are located in the northwestern part of the basin. In contrast, climate regions 2, 3, 6, and 12, which are located in the eastern part of the basin, have relatively high ranges from 2267.2 m asl and 2620.3 m asl. The results further showed the absence of a systematic relationship between rainfall variables and altitude in the Abbay basin. In contrast, the distribution of PET, temperature, and soil moisture displayed a systematic relationship with altitude. In this regard, temperature and PET are relatively higher in lowland climate regions (7 and 10) and low in highland climate regions (e.g., 2, 3, 9, and 12). On the other hand, the mean annual soil moisture amount is relatively high in the lowland climate regions (7 and 10) and relatively low in highland climate regions (e.g., 2, 3, 9, and 12).

In general, regions 2, 3, 9, and 12 have two rain cycles; most of the climate characteristics are relatively similar, except climate region 3 has early rainfall onset and longer LGP, and climate region 9 has higher temperature values. Of the others, climate region 5 is distinct as it has a relatively longer LGP, which is attributed to the late cessation date. On the other hand, climate region 10, followed by climate region 7, has a high PET. Furthermore, climate regions 1 and 6 are very similar in all rainfall characteristics, except climate region 6 is slightly wetter. Similarly, all the rainfall indicators and PET amounts are relatively similar for climate regions 2 and 9.

4. Implications for Targeting Green Water Management Technologies

This study produced data-driven homogenous climate clusters that are useful for identifying local scale climate-induced risks for rain-fed agriculture systems and for facilitating the selection of site-specific green water management technologies in the Abbay River basin. The assumption is that spatiotemporal climate variability is the leading environmental determinant factor to the productivity of rain-fed agriculture in the basin. Climate variability controls the practice and productivity in the rain-fed agricultural system by determining the start and end of the farming calendar, LGP, soil moisture balance,

and types of crops that can be grown in an area. It also relates to many risks to rain-fed agriculture, such as shortage of water associated with seasonality of the rainfall or due to excessive evapotranspiration or both, the occurrence of flood and soil erosion due to a high amount or intensity of rainfall or both, water logging and soil acidity caused by the seasonal high-intensity rainfall, and soil salinity caused by high rates of evapotranspiration. These risks can significantly constrain rain-fed agricultural practices and crop productivity [2,5,7,9,41,42]. It is important to note that the prevalence, severity, and effects of these climate variability-induced agricultural challenges vary spatially across the Abbay basin [16]. Previous soil and water conservation practices, as well as other agronomic interventions, did not achieve the intended outcomes as they followed a one-size-fits-all top-down approach without considering regional and local-scale climate variability [17,32].

The results generated from this study have contributed to identifying appropriate green water management technologies to address climate-induced risks to the rain-fed agricultural system. For example, all climate regions located in the eastern part of the basin, except climate region three, have relatively short LGP (2.5–3.9 months), which means longer dry periods. This suggests that agricultural productivity in these regions is constrained by the short LGP. Some of the climate regions (2, 9, and 12) experience a bimodal (*Kiremt* and *Belg*) rainfall pattern; the rainfall amount during the later season is too erratic, unreliable, and exceeded by PET. In these regions, rainwater harvesting and supplementary irrigation can be used to complement the short LGP and improve agricultural productivity.

Climate regions 2, 9, 11, and 12 have relatively high PCI (18.1–21.1), which means there is high rainfall seasonality that can generate excessive surface runoff during the *Kiremt* season. Rainwater harvesting, such as small-scale water reservoirs and well-designed private ponds, is a useful strategy to extend the period of water availability in these regions. Using water-efficient technologies and agronomic practices are also appropriate interventions in these regions. It is important to note that most of these areas have dense populations, which means a large number of the workforce remains idle for an extended period (6.5–7.5 months) of the year. Rainwater harvesting and dry season production activities are therefore important from the perspective of improved use of labor resources.

Many empirical studies confirm the significant contribution of small-scale irrigation to poverty reduction [43–46] and improved food security [47–49] in the rural areas of Ethiopia. Furthermore, the construction of rainwater harvesting schemes in regions that experience short LGP and high PCI can reduce the frequency and intensity of flood events during the peak rainfall season and increase groundwater storage and low flows. The presence of a water harvesting scheme at an upper part of the river basin can significantly regulate soil erosion and reduce sediment yields [50].

Soil management practices emerge as priority interventions in climate regions 2, 3, 9, 11, and 12, where the PCI is high. This is because high rainfall concentration results in low infiltration and high surface runoff, causing severe soil erosion [16]. Soil acidity management should be a top priority green water management strategy in climate regions 4, 5, 6, and 8, where annual rainfall amount is in excess of 1500 mm.

For climate regions 2, 3, 9, and 12 (all located in the eastern part of the basin), where soil moisture contents are low (10.6–13.8 mm), soil water conservation technologies are important interventions. Although these climate regions have bimodal rainfall cycles *(Kiremt* and *Belg*), the *Kiremt* rainfall has a short duration (2.5–3.3 months), except for region 3, where the LGP is 5.1 months, and the *Belg* season's rainfall is decreasing and highly unreliable for agricultural production. A recent study by Tibebe [16] indicated that agricultural productivity in the Abbay basin is negatively affected not only by the high level of climate variability but also by the low and poor utilization and management of the available water. Hence, it is important to enhance or introduce water utilization technologies to efficiently use the available moisture that occurs during the two rainy seasons. There are very large areas in region 12, particularly in Semien Shewa and Debub Wollo, where farmers cannot cultivate crops during the *Kiremt* season due to water logging [51]. This problem is observed in the highland areas, where barley is the dominant type of crop. The

water logging problem is not only caused by the occurrence of excessive rainfall but also by the nature of the soil. Therefore, water logging management should be a top priority green water management issue in these areas.

Opportunities extend the crop season using available moisture in those climate regions that have relatively long LGP (3, 4, 5, 7, 8, and 10). The LGP in these climate regions varies between 4.5 and 5.6 months, and all except region 3 are located in the western part of the basin. It is important to target short-maturing crop varieties and other agronomic and agro-climate services to enable crop production for more than a single season.

The climate regions 2 and 9 experience short LGP, heavy rainfall during the *kiremt* season, soil erosion, and shortage of soil moisture in the dryland areas. Hence, the impact of such multiple risks on the rain-fed agriculture should be addressed by carefully understanding their co-occurrences and synergies and through targeted package-based interventions. For example, structural measures used to protect soil erosion in moisture-stressed highland areas can be designed in a way to enhance on-farm soil moisture and groundwater recharge by reducing the velocity of surface runoff.

5. Conclusions

Clustering a given geographic region into homogenous climate units is important to identify site-specific climate-related water security risks and facilitate the selection and implementation of appropriate green water management technologies for improved productivity of rain-fed agricultural systems. This study undertook a climate classification scheme for the Abbay basin, where rain-fed agriculture is highly constrained by spatiotemporal climate variability. The k-means unsupervised clustering approach was employed to define homogeneous climate clusters by using climate variables (daily rainfall amount, rainfall intensity, rainfall onset and cessation dates, LGP, PCI, PET, and soil moisture) that have determinant impacts on rain-fed agriculture.

The climate classification scheme generated 12 homogenous climate clusters for the basin. The results are discussed with reference to climatic characteristics, potential climate-related risks to rain-fed agriculture, and green water management options across the identified climate clusters. The climate classification approach and results presented in this study have multiple implications for transformative green water management by facilitating the selection and targeted implementation of technologies tailored to local circumstances. The overall outcome is the efficient utilization of the scarce water and land resources and improved agricultural production and food security in the area. Furthermore, the study provides a methodological framework that can be used in the other river basins of Ethiopia and, indeed, elsewhere.

Author Contributions: Conceptualization, D.T. and W.B.; methodology and data analysis, D.T.; formal analysis, M.A.D.; writing—original draft preparation, M.A.D.; supervision, W.B.; writing—review and editing, W.B., E.T., G.O. and C.W. All authors have read and agreed to the published version of the manuscript.

Funding: This research work was financially supported by the Water and Land Resource Center (WLRC), Addis Ababa University (AAU), funded by the UKRI GCRF (Grant Number: ES/S008179/1) Water Security and Sustainable Development Hub Project.

Data Availability Statement: Data can be shared up on request, except the ENACT climate date, which is restricted to share to third party by NMA policy.

Acknowledgments: We thank the Ethiopian Meteorological Institute (EMI) for providing climate data for the study.

Conflicts of Interest: The authors declare no conflict of interest.

References

1. Brown, C.; Hansen, J.W. *Agricultural Water Management and Climate Risk. Report to the Bill and Melinda Gates Foundation*; IRI Tech. Rep. No. 08-01; International Research Institute for Climate and Society: Palisades, NY, USA, 2008; p. 19.
2. Kotir, J.S. Climate change and variability in Sub-Saharan Africa: A review of current and future trends and impacts on agriculture and food security. *Environ. Dev. Sustain.* **2010**, *13*, 587–605. [CrossRef]
3. Holleman, C.; Rembold, F.; Crespo, O.; Conti, V. The impact of climate variability and extremes on agriculture and food security—An analysis of the evidence and case studies. In *Background Paper for The State of Food Security and Nutrition in the World*; FAO Agricultural Development Economics Technical Study No. 4; FAO: Rome, Italy, 2018. [CrossRef]
4. Conway, D.; Schipper, E.L.F. Adaptation to climate change in Africa: Challenges and opportunities identified from Ethiopia. *Glob. Environ. Chang.* **2011**, *21*, 227–237. [CrossRef]
5. Ademe, F.; Kibret, K.; Beyene, S.; Getinet, M.; Mitike, G. Rainfall analysis for rain-fed farming in the Great Rift Valley Basins of Ethiopia. *J. Water Clim. Chang.* **2020**, *11*, 812–828. [CrossRef]
6. Ademe, D.; Zaitchik, B.F.; Tesfaye, K.; Simane, B.; Alemayehu, G.; Adgo, E. Analysis of agriculturally relevant rainfall characteristics in a tropical highland region: An agroecosystem perspective. *Agric. For. Meteorol.* **2021**, *311*, 108697. [CrossRef]
7. Mubenga-Tshitaka, J.; Dikgang, J.; Mwamba, J.W.M.; Gelo, D. Climate variability impacts on agricultural output in East Africa. *Cogent Econ. Financ.* **2023**, *11*, 2181281. [CrossRef]
8. Ochieng, J.; Kirimi, L.; Mathenge, M. Effects of climate variability and change on agricultural production: The case of small scale farmers in Kenya. *NJAS Wagening. J. Life Sci.* **2016**, *77*, 71–78. [CrossRef]
9. Bewket, W. Climate change perceptions and adaptive responses of smallholder farmers in central highlands of Ethiopia. *Int. J. Environ. Stud.* **2012**, *69*, 507–523. [CrossRef]
10. Evangelista, P.; Young, N.; Burnett, J. How will climate change spatially affect agriculture production in Ethiopia? Case studies of important cereal crops. *Clim. Chang.* **2013**, *119*, 855–873. [CrossRef]
11. Ginbo, T. Heterogeneous impacts of climate change on crop yields across altitudes in Ethiopia. *Clim. Chang.* **2022**, *170*, 12. [CrossRef]
12. Tamene, L.; Abera, W.; Bendito, E.; Erkossa, T.; Tariku, M.; Sewnet, H.; Tibebe, D.; Sied, J.; Feyisa, G.; Wondie, M.; et al. Data-driven similar response units for agricultural technology targeting: An example from Ethiopia. *Exp. Agric.* **2022**, *58*, e27. [CrossRef]
13. Zang, C.; Liu, J.; van der Velde, M.; Kraxner, F. Assessment of spatial and temporal patterns of green and blue water flows under natural conditions in inland river basins in Northwest China. *Hydrol. Earth Syst. Sci.* **2012**, *16*, 2859–2870. [CrossRef]
14. Zhang, Y.; Tang, C.; Ye, A.; Zheng, T.; Nie, X.; Tu, A.; Zhu, H.; Zhang, S. Impacts of climate and land-use change on blue and green water: A case study of the upper Ganjiang River Basin, China. *Water* **2020**, *12*, 2661. [CrossRef]
15. Lyu, L.; Wang, X.; Sun, C.; Ren, T.; Zheng, D.-F. Quantifying the Effect of Land Use Change and Climate Variability on Green Water Resources in the Xihe River Basin, Northeast China. *Sustainability* **2019**, *11*, 338. [CrossRef]
16. Tibebe, D.; Teferi, E.; Bewket, W.; Zeleke, G. Climate induced water security risks on agriculture in the Abbay river basin: A review. *Front. Water* **2022**, *4*, 961948. [CrossRef]
17. Zimale, F.A.; Tilahun, S.A.; Tebebu, T.Y.; Guzman, C.D.; Hoang, L.; Schneiderman, E.M.; Langendoen, E.J.; Steenhuis, T.S. Improving watershed management practices in humid regions. *Hydrol. Process.* **2017**, *31*, 3294–3301. [CrossRef]
18. FAO. *Agro-Ecological Zoning Guidelines*; FAO Soils Bulletin 73, Soil Resources, Management and Conservation Service, FAO Land and Water Development Division; Food and Agriculture Organization of the United Nations: Rome, Italy, 1996; p. 78, ISBN 92-5-103890-2.
19. BCEOM. *Abbay River Basin Integrated Development Master Plan-Phase 2—Data Collection—Site Investigation Survey and Analysis—Volume I—Natural Resources—Geology; Ministry of Water Resource*; BCEOM: Addis Ababa, Ethiopia, 1998; p. 144.
20. Cheung, W.H.; Senay, G.B.; Singh, A. Trends and spatial distribution of annual and seasonal rainfall in Ethiopia. *Int. J. Climatol.* **2008**, *28*, 1723–1734. [CrossRef]
21. Mengistu, D.; Bewket, W.; Lal, R. Recent spatiotemporal temperature and rainfall variability and trends over the Upper Blue Nile River Basin, Ethiopia. *Int. J. Climatol.* **2014**, *34*, 2278–2292. [CrossRef]
22. Degefu, M.A.; Rowell, D.; Bewket, W. Teleconnections between Ethiopian rainfall variability and global SSTs: Observations and methods for model evaluation. *Meteorol. Atmos. Phys.* **2017**, *129*, 173–186. [CrossRef]
23. Degefu, M.A.; Tadesse, Y.; Bewket, W. Observed changes in rainfall amount and extreme events in southeastern Ethiopia, 1955–2015. *Theor. Appl. Climatol.* **2021**, *144*, 967–983. [CrossRef]
24. Degefu, M.A.; Bewket, W.; Amha, Y. Evaluating performance of 20 global and quasi-global precipitation products in representing drought events in Ethiopia: Visual analysis. *Weather Clim. Extrem.* **2022**, *35*, 100416. [CrossRef]
25. Abdisa, T.B.; Diga, G.M.; Tolessa, A.R. Impact of climate variability on rain-fed maize and sorghum yield among smallholder farmers. *Cogent Food Agric.* **2022**, *8*, 2057656. [CrossRef]
26. Desta, G.; Kassawmar, T.; Tadesse, M.; Zeleke, G. Extent and distribution of surface soil acidity in the rainfed areas of Ethiopia. *Land Degrad. Dev.* **2021**, *32*, 5348–5359. [CrossRef]
27. Abate, E.; Hussein, S.; Laing, M.; Mengistu, F. Soil acidity under multiple land-uses: Assessment of perceived causes and indicators, and nutrient dynamics in small-holders' mixed-farming system of northwest Ethiopia. *Acta Agric. Scand. B Soil Plant Sci.* **2017**, *67*, 134–147. [CrossRef]

28. Bedane, H.R.; Beketie, K.T.; Fantahun, E.E.; Feyisa, G.L.; Anose, F.A. The impact of rainfall variability and crop production on vertisols in the central highlands of Ethiopia. *Environ. Syst. Res.* **2022**, *11*, 26. [CrossRef]
29. Hasanuzzaman, M.; Nahar, K.; Alam, M.M.; Roychowdhury, R.; Fujita, M. Physiological, biochemical, and molecular mechanisms of heat stress tolerance in plants. *Int. J. Mol. Sci.* **2013**, *14*, 9643–9684. [CrossRef] [PubMed]
30. Erkossa, T.; Awulachew, S.B.; Haileslassie, A.; Yilma, A.D. Impacts of improving water management of smallholder agriculture in the upper Blue Nile Basin. In *CP 19 Project Workshop Proceedings*; IWMI: Addis Ababa, Ethiopia, 2009; Available online: https://publications.iwmi.org/pdf/H042504.pdf (accessed on 12 September 2022).
31. Fazzini, M.; Bisci, C.; Billi, P. The Climate of Ethiopia. In *Landscapes and Landforms of Ethiopia, World Geomorphological Landscapes*; Billi, P., Ed.; Springer Science + Business Media: Dordrecht, The Netherlands, 2015. [CrossRef]
32. Tebebu, T.Y.; Bayabil, H.K.; Stoof, C.R.; Giri, S.K.; Gessess, A.A.; Tilahun, S.A.; Steenhuis, T.S. Characterization of degraded soils in the humid Ethiopian Highlands. *Land Degrad. Develop.* **2017**, *28*, 1891–1901. [CrossRef]
33. Dinku, T.; Hailemariam, K.; Maidment, R.; Tarnavsky, E.; Connor, S. Combined use of satellite estimates and rain gauge observations to generate high-quality historical rainfall time series over Ethiopia. *Int. J. Climatol.* **2014**, *34*, 2489–2504. [CrossRef]
34. Romano, N.; Palladino, M.; Chirico, G.B. Parameterization of a bucket model for soil-vegetation-atmosphere modeling under seasonal climatic regimes. *Hydrol. Earth Syst. Sci.* **2011**, *15*, 3877–3893. [CrossRef]
35. Mao, W.; Yang, J.; Zhu, Y.; Ye, M.; Liu, Z.; Wu, J. An efficient soil water balance model based on hybrid numerical and statistical methods. *J. Hydrol.* **2018**, *559*, 721–735. [CrossRef]
36. Oliver, J.E. Monthly precipitation distribution: A comparative index. *Prof. Geogr.* **1980**, *32*, 300–309. [CrossRef]
37. Kaiser, H.F.; Rice, J. Little jiffy, mark IV. Educ. *Psychol. Meas.* **1974**, *34*, 111–117. [CrossRef]
38. Jain, A.K.; Duin, R.P.W.; Mao, J. Statistical pattern recognition: A review. *IEEE Trans. Pattern Anal. Mach.* **2000**, *22*, 4–37. [CrossRef]
39. Rahmani, M.K.I.; Pal, N.; Arora, K. Clustering of image data using K-means and fuzzy K-means. *Int. J. Adv. Comput. Sci. Appl.* **2014**, *5*, 160–163.
40. Hot, E.; Popović-Bugarin, V. Soil data clustering by using K-means and fuzzy K-means algorithm. In Proceedings of the 2015 23rd Telecommunications Forum Telfor (TELFOR), Belgrade, Serbia, 24–26 November 2015; pp. 890–893.
41. Shukla, R.K.; Agrawal, J.; Sharma, S.; Chaudhari, N.S.; Shukla, K.K. (Eds.) *Social Networking and Computational Intelligence: Proceedings of SCI-2018*; Springer Nature Singapore Pte Ltd.: Singapore, 2020; Volume 100.
42. Zeweld, W.; Huylenbroeck, G.V.; Hidgot, A.; Chandrakanth, M.; Speelman, S. Adoption of small-scale irrigation and its livelihood impacts in Northern Ethiopia. *Irrigat. Drain.* **2015**, *64*, 655–668. [CrossRef]
43. Mengistie, D.; Kidane, D. Assessment of the impact of small-scale irrigation on household livelihood improvement at Gubalafto District, North Wollo, Ethiopia. *Agriculture* **2016**, *6*, 27. [CrossRef]
44. Abebe, A. The determinants of small-scale irrigation practice and its contribution on household farm income: The case of Arba Minch Zuria Woreda, Southern Ethiopia. *Afr. J. Agric. Res.* **2017**, *12*, 1136–1143.
45. Kassie, K.E.; Alemu, B.A. Does irrigation improve household's food security? The case of Koga irrigation development project in northern Ethiopia. *Food Secur.* **2021**, *13*, 291–307. [CrossRef]
46. Assefa, E.; Ayalew, Z.; Mohammed, H. Impact of small-scale irrigation schemes on farmers livelihood, the case of Mekdela Woreda, North-East Ethiopia. *Cogent Econ. Finan.* **2022**, *10*, 2041259. [CrossRef]
47. Wondimagegnhu, B.A.; Bogale, B.A. Small-scale irrigation and its effect on food security of rural households in North-West Ethiopia: A comparative analysis. *Ethiop. J. Sci. Technol.* **2020**, *13*, 31–51. [CrossRef]
48. Jambo, Y.; Alemu, A.; Tasew, W. Impact of small-scale irrigation on household food security: Evidence from Ethiopia. *Agricu. Food Secur.* **2021**, *10*, 21. [CrossRef]
49. Maru, H.; Haileslassie, A.; Zeleke, T. Impacts of small-scale irrigation on farmers' livelihood: Evidence from the drought prone areas of upper Awash sub-basin, Ethiopia. *Heliyon* **2023**, *16*, e16354. [CrossRef] [PubMed]
50. Dile, Y.T.; Karlberg, L.; Daggupati, P.; Srinivasan, R.; Wiberg, D.; Rockström, J. Assessing the implications of water harvesting intensification on upstream-downstream ecosystem services: A case study in the Lake Tana basin. *Sci. Total Environ.* **2016**, *542*, 22–35. [CrossRef] [PubMed]
51. Gebrehiwot, K.A. A review on waterlogging, salinization and drainage in Ethiopian irrigated agriculture. *Sustain. Water Resour. Manag.* **2018**, *4*, 55–62. [CrossRef]

Disclaimer/Publisher's Note: The statements, opinions and data contained in all publications are solely those of the individual author(s) and contributor(s) and not of MDPI and/or the editor(s). MDPI and/or the editor(s) disclaim responsibility for any injury to people or property resulting from any ideas, methods, instructions or products referred to in the content.

remote sensing

MDPI

Article

Identifying Major Diurnal Patterns and Drivers of Surface Urban Heat Island Intensities across Local Climate Zones

Yongjuan Guan [1,2], Jinling Quan [1,2,*], Ting Ma [1,2], Shisong Cao [3], Chengdong Xu [1,2] and Jiali Guo [1,2]

[1] State Key Laboratory of Resources and Environmental Information System, Institute of Geographic Sciences and Natural Resources Research, Chinese Academy of Sciences, Beijing 100101, China; guanyongjuan5548@igsnrr.ac.cn (Y.G.); mting@lreis.ac.cn (T.M.); xucd@lreis.ac.cn (C.X.); gjl1521660chd@gmail.com (J.G.)
[2] College of Resources and Environment, University of Chinese Academy of Sciences, Beijing 100190, China
[3] School of Geomatics and Urban Spatial Informatics, Beijing University of Civil Engineering and Architecture, Beijing 100044, China; caoshisong@bucea.edu.cn
* Correspondence: quanjl@lreis.ac.cn

Abstract: Deepening the understanding of diurnal characteristics and driving mechanisms of surface urban heat islands (SUHIs) across different local climate zones (LCZs) and time scales is of great significance for guiding urban surface heat mitigation. However, a comprehensive investigation of SUHIs from the diurnal, local, multi-seasonal, and interactive perspectives remains a large gap. Here, we generalized major diurnal patterns of LCZ-based SUHI intensities (SUHIIs) throughout 2020 over the urban area of Beijing, China, based on diurnal temperature cycle modeling, block-level LCZ mapping, and hierarchical clustering. A geographical detector was then employed to explore the individual and interactive impacts of 10 morphological, socioeconomic, and meteorological factors on the multi-temporal spatial differentiations of SUHIIs. Results indicate six prevalent diurnal SUHII patterns with distinct features among built LCZ types. LCZs 4 and 5 (open high- and mid-rise buildings) predominantly display patterns one, two, and five, characterized by an afternoon increase and persistently higher values during the night. Conversely, LCZs 6, 8, and 9 (open, large, and sparsely built low-rise buildings) mainly exhibit patterns three, four, and six, with a decrease in SUHII during the afternoon and lower intensities at night. The maximum/minimum SUHIIs occur in the afternoon–evening/morning for patterns 1–3 but in the morning/afternoon for patterns 5–6. In all four seasons, the enhanced vegetation index (EVI) and gross domestic product (GDP) have the top two individual effects for daytime spatial differentiations of SUHIIs, while the air temperature (TEM) has the largest explanatory power for nighttime differentiations of SUHIIs. All factor interactions are categorized as two-factor or nonlinear enhancements, where nighttime interactions exhibit notably greater explanatory powers than daytime ones. The strongest interactions are EVI ∩ GDP (q = 0.80) during the day and TEM ∩ EVI (q = 0.86) at night. The findings of this study contribute to an improved interpretation of the diurnal continuous dynamics of local SUHIIs in response to various environmental conditions.

Keywords: surface urban heat island; land surface temperature; local climate zone; geographical detection; diurnal dynamics

1. Introduction

Urban heat island (UHI) is a worldwide phenomenon characterized by significantly higher temperatures in cities compared to the surrounding rural areas [1–3]. It has significant impacts on regional climate, energy consumption, air quality, vegetation ecology, and population health [4,5]. Gaining a deeper understanding of the spatiotemporal variations and driving mechanisms of UHIs is crucial for guiding urban thermal management.

Previous studies have mainly relied on a fuzzy urban–rural dichotomy to assess temperature differences [6,7]. However, there is a lack of a consistent standard for urban–

rural division, which has hampered comparisons and led to contradictions among UHI studies [8,9]. Moreover, it is difficult to portray complex intra-urban variability in local thermal environments [10,11]. To describe internal urban structures and properties in a more objective, standardized, and quantitative way [12], Stewart et al. [10] introduced the concept of local climate zones (LCZs), consisting of 17 building types and land cover types with uniform surface covers, structures, materials, and human activities.

LCZ-based UHI studies have been rising in recent years and are divided into two main categories: canopy UHIs (CUHIs) [13–15] and surface UHIs (SUHIs) [8,16,17]. The former mainly reveals the near-surface temperature differences among different LCZ types through station observations [13,18], mobile measurements [14], and numerical simulations [10,15]. However, the spatial representativeness of station observations is usually insufficient, the financial investment in mobile measurements is substantial, and the model uncertainty for realistic scenario simulations can be considerable. Alternatively, others utilized remotely sensed land surface temperature (LST) observations with the advantages of wide coverage and low cost to characterize SUHIs via inter-LCZ comparative analysis [16,19–22]. SUHIs are closely related to, yet distinct from, CUHIs, particularly at the diurnal scale, where they can exhibit contrasting patterns of variation [23,24]. However, due to the limited temporal frequency of fine-resolution LST observations, previous LCZ-based SUHI studies have primarily focused on the annual patterns and several discrete moments [8,17,25], posing challenges in capturing the diurnal continuous dynamics of SUHIs. For instance, Bechtel et al. [8] used LCZs to conduct a comprehensive comparison of SUHIs among 50 global cities at four MODIS overpass times, and Chang et al. [25] examined thermal patterns of each LCZ in Xi'an, China at several moments of ECOSTRESS observations.

Regarding these limitations, researchers have begun to utilize spatiotemporally enhanced LSTs for diurnal investigation. For example, Quan [20] generated hourly 100 m LSTs based on an integrated fusion of Landsat, MODIS, and FengYun-2F LSTs and then analyzed the multi-temporal thermal differences among LCZ types in Beijing, China. However, their analysis focused on LSTs rather than SUHIs. Dong et al. [16], on the other hand, investigated the characteristic parameters of diurnal SUHI intensities (SUHIIs) for built LCZ types in Nanjing, China, via monthly composite diurnal LSTs of 100 m from the combination of spatial downscaling and diurnal temperature modeling. Nevertheless, temporal averaging by month/season/year is somewhat subjective and insufficient to characterize major patterns from complex diurnal dynamics of SUHIIs across varied LCZs and times.

In terms of interpretation of the diurnal SUHII variability, previous studies have often investigated single or multiple drivers through spatial comparative analysis [26] and linear regression/correlation [27,28]. The former compares the SUHI differences among surface categories, which is often used in LCZ-based SUHI studies. However, this method presents challenges in quantifying the contribution of each factor. The latter assumes linear dependencies between SUHI and drivers, whereas there is no strict standard linear correspondence between them, and complex interactions exist during SUHI formation and evolution [29]. Alternatively, the geographical detector (geodetector) measures geographic attributions and driver interactions based on spatial heterogeneity without linear assumptions [30]. The use of geodetector to explore the diurnal SUHII variations would help improve our understanding of the individual and interactive effects of different factors, especially at a diurnal scale; however, such exploration is in great lack [31].

Overall, despite the remarkable progress that has been made, there are still gaps in the generalization of the diurnal continuous variation patterns of SUHIIs across diverse LCZs and the quantification of interactive driving effects behind the spatial differentiations of SUHIIs. Consequently, the current understanding of the variety and taxonomy of the prevalent diurnal SUHII patterns across LCZs remains a large deficiency. To address these issues, here we identify the major diurnal patterns of SUHIIs across different built LCZ types and months in Beijing, China, based on diurnal temperature cycle (DTC) modeling, block-level LCZ mapping, and hierarchical clustering. We then adopt the geodetector to

quantify the individual and interactive impacts of multiple morphological, socioeconomic, and meteorological factors on the spatial stratified heterogeneity of SUHIIs during the day–night and across seasons. The findings of this study contribute to an improved interpretation of SUHI variability in response to the local environment at a diurnal scale and provide valuable insights for enhancing urban thermal regulation.

2. Study Area and Data

2.1. Study Area

Beijing (39°28′N–41°05′N, 115°25′E–117°30′E) covers a total area of 16,410 km^2 with an average altitude of 1000–1500 m in the western and northern mountainous areas and 20–60 m in the southeastern plains. It has a warm, temperate, semi-humid, and semi-arid monsoon climate, experiencing hot and rainy summers and cold and dry winters. The annual average temperature and precipitation in the plain areas are 11–13 °C and 500–600 mm, respectively. Beijing has a dense population of approximately 21.9 million and a high urbanization rate of around 87.5% (Beijing Statistical Yearbook, 2020), and has been exhibiting significant UHI effects for years in the city core area, i.e., around and within the Fifth Ring Road, which was therefore chosen as our main study area (Figure 1).

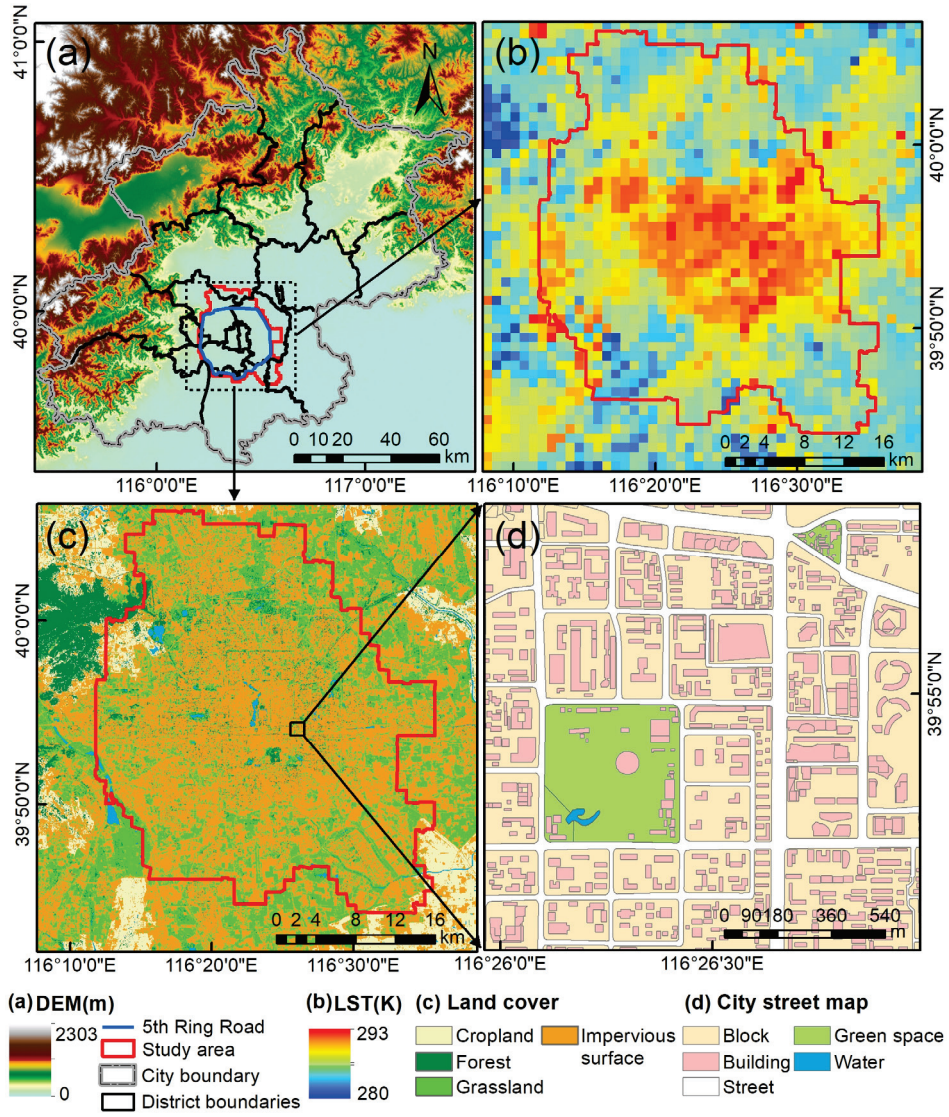

Figure 1. Study area. (**a**) Location and elevations of the study area; (**b**) annual average MODIS land surface temperatures in 2020; (**c**) land cover map (LCM); and (**d**) city street map (CSM).

2.2. Data for DTC Modeling

We downloaded MODIS daily 1 km LST products throughout 2020 (Collection 6.1, https://appeears.eartHD_Batacloud.nasa.gov/, accessed on 16 April 2022), including MOD11A1, acquired at ~10:30 and ~22:30, and MYD11A1, acquired at ~13:30 and ~01:30 local time. These products were retrieved by a generalized split-window algorithm [32] with an overall accuracy within 2 K [33]. Pixels affected by clouds and aerosols were excluded based on the associated QA file. For the DTC modeling over the study area, we selected four consecutive MODIS images with the clearest LST observations per month, i.e., on 30 January, 22 February, 4 March, 30 April, 18 May, 12 June, 23 July, 2 August, 18 September, 18 October, 9 November, and 20 December 2020.

2.3. Data for LCZ Mapping

We obtained a vector-based city street map (CSM, Figure 1d, http://www.navinfo.com/en/aboutus/index.aspx, accessed on 10 March 2022) that contains key attribute information to characterize the urban morphology, including blocks, buildings (height), roads, green spaces, and water. It was converted to 30 m × 30 m grids to match the other two auxiliary data: Landsat 8 and land cover map (LCM). The Landsat 8 data, downloaded from the USGS (http://earthexplorer.usgs.gov/, accessed on 10 March 2022), contain red and near-infrared (VNIR) bands for calculating vegetation fractions. The LCM (Figure 1c) was collected from the Peng Cheng Laboratory (http://data.starcloud.pcl.ac.cn/zh, accessed on 11 March 2022). It was retrieved from the Landsat series through supervised classification, consisting of forest, cropland, grassland, shrubland, water, wetland, impervious land, and bare land. The LCM was mainly used here as a reference for distinguishing vegetation types.

2.4. Driving Factors

A total of 10 morphological [34–36], socioeconomic [27,37], and meteorological [37] factors were selected for the geodetector-based attribution analysis. For the sake of brevity, their details are listed in Table 1, and spatial distributions are shown in Figure 2. The collection of these drivers followed four main criteria: (1) they have demonstrated influences on SUHIs in previous studies; (2) they are easily quantifiable in space and time; (3) they encompass various dimensions and perspectives; and (4) they avoid information redundancy as much as possible. The hourly atmospheric pressure (PRS), relative humidity (RHU), and air temperature (TEM) data were measured at 800 ground stations, interpolated to 1 km grid cell using the spline strategy, and then composed into eight (2 × 4) datasets to facilitate daytime (08:00–16:00) and nighttime (20:00–04:00) analysis across four seasons. The monthly enhanced vegetation index (EVI) data were also aggregated to a seasonal scale but served as a common independent variable for both day and night. The yearly data, including modified normalized difference water index (MNDWI), building surface fraction (BSF), mean building height (BH), gross domestic product (GDP), population density (PD), and road density (RD), were used as constants throughout days and seasons.

Table 1. Details on the driving factors.

Indicator	Description	Temporal Resolution	Spatial Resolution	Source	Calculation
Morphological Factors					
EVI	Enhanced vegetation index	Monthly	500→1000 m	MOD13A3 [1]	
MNDWI [2]	Modified normalized difference water index	Yearly	10→1000 m	Sentinel 2	(Green–MIR)/(Green+MIR)
BSF	Building surface fraction	Yearly	10→1000 m	CSM	Total building area/grid area [3]
BH	Mean building height	Yearly	10→1000 m	CSM	Total building height/total building numbers

Table 1. *Cont.*

Indicator	Description	Temporal Resolution	Spatial Resolution	Source	Calculation
Socioeconomic Factors					
GDP	Gross domestic product	Yearly	1000 m	RESDC [4]	
PD	Population density	Yearly	1000 m	RESDC	
RD	Road density	Yearly	1000 m	CSM	Total road area/grid area
Meteorological Factors					
PRS	Atmospheric pressure	Hourly	Site→1000 m	CMDC [5]	Spline interpolation
RHU	Relative humidity	Hourly	Site→1000 m	CMDC	Spline interpolation
TEM	Air temperature	Hourly	Site→1000 m	CMDC	Spline interpolation

[1] downloaded from https://appeears.earthdatacloud.nasa.gov/, accessed on 4 June 2022. [2] calculated from all clear-sky Sentinel 2 data in 2020 and averaged to a yearly dataset. [3] grid area = 1 km × 1 km. [4] Resource and Environment Science and Data Center (http://www.resdc.cn, accessed on 19 September 2022). [5] China Meteorological Data Service Center (https://data.cma.cn/en, accessed on 10 October 2022).

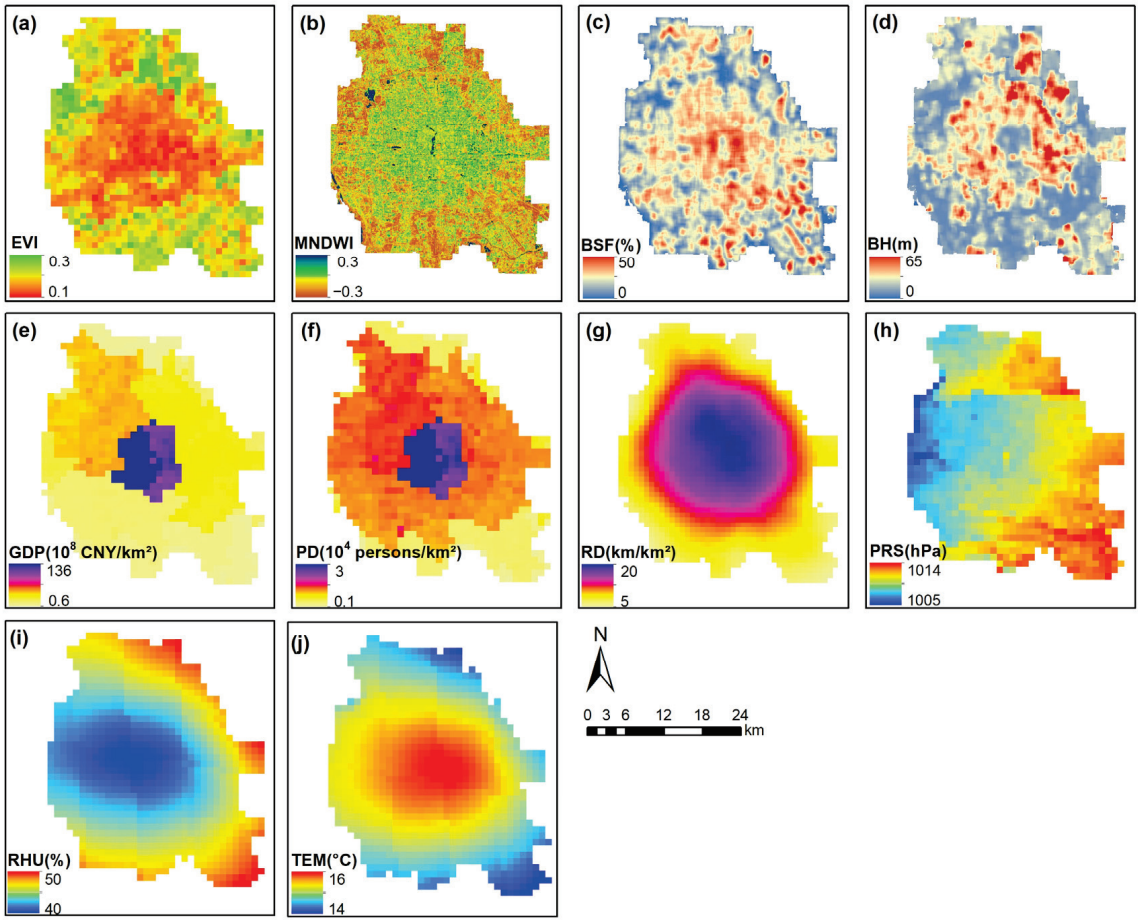

Figure 2. Spatial distributions of the driving factors at a yearly scale. (**a**) Enhanced vegetation index (EVI); (**b**) Modified normalized difference water index (MNDWI); (**c**) Building surface fraction (BSF); (**d**) Mean building height (BH); (**e**) Gross domestic product (GDP); (**f**) Population density (PD); (**g**) Road density (RD); (**h**) Atmospheric pressure (PRS); (**i**) Relative humidity (RHU); and (**j**) Air temperature (TEM).

3. Methodology

The research framework of this study consists of four main steps (Figure 3): (1) reconstruction of diurnal LSTs based on the selected MODIS LSTs and a modified four-parameter DTC model; (2) classification of LCZs by a GIS-based block-level mapping

approach [38] for built-up and land-cover types; (3) identification of major diurnal patterns of SUHIIs across different LCZs and months; and (4) geographical detection of SUHII differentiations with 10 driving factors at multiple time scales.

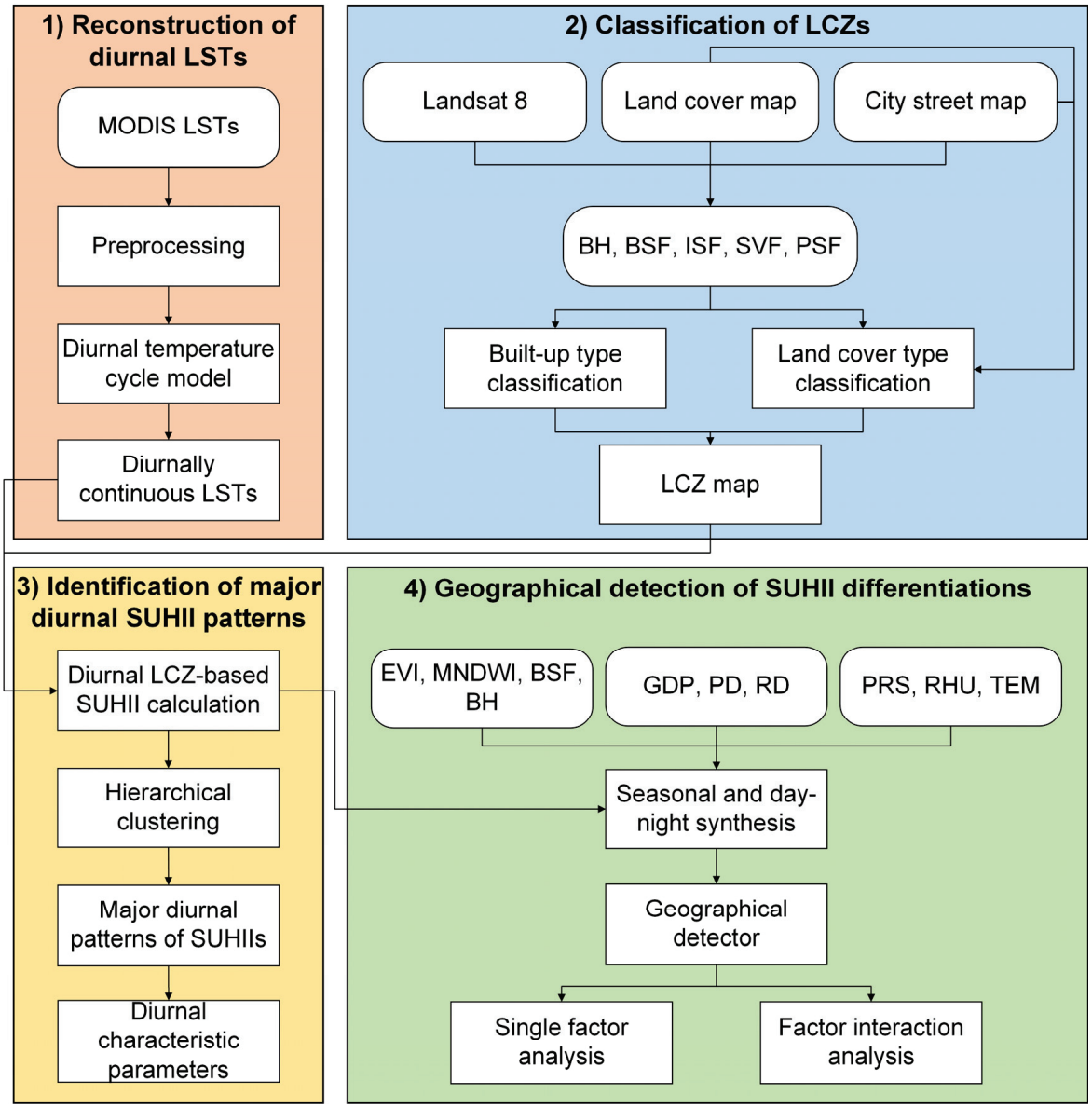

Figure 3. Flowchart of this study.

3.1. Reconstruction of Diurnal LSTs

Many DTC models have been proposed to reconstruct diurnal continuous LSTs from sporadic thermal observations with four or more parameters [39–44]. There is usually a trade-off between applicability and accuracy [45,46]. Given the maximum of four MODIS observations per day and the focus of this study on major patterns across seasons, the model proposed by Inamdar et al. [43] was adopted with a zero assumption on the temperature difference between adjacent sunrise times [39]. Specifically, the diurnal temperature variation with time ($T(t)$) is described as a combination of harmonic and hyperbolic functions based on thermal diffusion and Newton's cooling law:

$$T(t) = \begin{cases} T_{\text{day}}(t) = T_0 + T_a \cos\left[\left(\frac{\pi}{\omega}\right)(t - t_m)\right], t < t_s \\ T_{night}(t) = T_0 + \left[T_a \cos\left(\frac{\pi}{\omega}(t_s - t_m)\right)\right] \frac{k}{(k+t-t_s)}, t \geq t_s \end{cases} \quad (1)$$

with

$$\begin{cases} \mathrm{k} = \frac{\omega}{\pi}\tan^{-1}\left(\frac{\pi}{\omega}(t_s - t_m)\right) \\ \omega = \frac{2}{15}\arccos(-\tan\phi\tan\delta) \\ \delta = 23.45\sin\left(\frac{360}{365}(284 + DOY)\right) \end{cases}$$

where T_0 is the lowest early morning temperature; T_a is the diurnal temperature amplitude; t_m is the time when the temperature reaches its maximum; t_s is the time when the temperature begins to decay freely; ω represents the half period of the cosine term; k is the attenuation constant; ϕ is the latitude; δ is the solar declination; and DOY is the day of year.

T_0, T_a, t_m and t_s are the four unknown parameters, which were solved pixel-by-pixel with the nonlinear least square fitting method in MATLAB using the four MODIS LST images selected per month (Section 2.2). Subsequently, diurnally continuous LSTs were reconstructed for the specified day each month by substituting the solved parameters into Equation (1).

3.2. Classification of LCZs

The study area was classified into 15 LCZ types using a simple GIS-based block-level mapping method we proposed previously [38]. The basic idea of this approach is to calculate five key morphological and coverage indicators for each block, based on which blocks are hierarchically assigned with the most appropriate LCZ types regarding their typical ranges defined in the LCZ scheme. The five indicators include BSF, BH, pervious surface fraction (PSF), impervious surface fraction (ISF), and sky view factor (SVF). They were calculated from the CSM attributes, Landsat VNIR bands, and LCM and averaged for each block. The hierarchical classification principle is illustrated in Figure 4: LCZs 1, 2, 4, 5, and 9 were first distinguished based on BSF and BH; LCZs 3, 6, 7, and 8 were then classified by combining BSF, BH, and one of the remaining indicators; and finally blocks with BH < 10 m and BSF < 10% were classified as LCZs A–G according to the natural land surface types provided in CSM and LCM. More details on the approach can be found in Quan [38].

3.3. Identification of Major Diurnal Patterns of SUHIIs

As one of the most representative indicators for SUHI, the SUHII was calculated hour-by-hour for different LCZs based on the diurnal LST data and LCZ map generated earlier. Specifically, the LCZ-based SUHII is defined as the average LST difference between a specific built LCZ type and a land cover type (typically LCZ D) [16,19]:

$$SUHII(t)_{LCZX} = \frac{\sum_{i=1}^{m} T(i,t)_{LCZX}}{m} - \frac{\sum_{j=1}^{n} T(j,t)_{LCZD}}{n} \quad (2)$$

where $SUHII(t)_{LCZX}$ represents the SUHII of LCZ X at time t; $T(i,t)_{LCZX}$ and $T(j,t)_{LCZD}$ denote the LSTs of pixel i in LCZ X and pixel j in LCZ D at t, respectively; m and n are the total numbers of i and j, respectively. Herein, X = 4, 5, 6, 8, and 9, while other built LCZ types were excluded from this calculation owing to their insufficient samples in the study area in comparison to those of LCZ D.

To identify the major diurnal patterns of SUHIIs across different LCZs and months, a hierarchical clustering analysis was performed on the 60 groups (12 months × 5 main built LCZ types) of diurnal SUHII curves. Specifically, each of the samples was initially assigned to a separate class, and those with the smallest distance were merged iteratively to form a comprehensive class. There are several methods to measure the distance between classes. In this study, the longest distance was adopted according to the practical clustering performance, and the sum of distances and a similarity of 40 were employed as the criteria for clustering centroids and divisions. Five characteristic parameters were then calculated for each clustered diurnal pattern, including the maximum SUHII ($I_{\max}$), minimum SUHII ($I_{\min}$), nocturnal (20:00–04:00) average SUHII (I_{night}), time of $I_{\max}$ ($t_{\max}$), and time of $I_{\min}$ ($t_{\min}$).

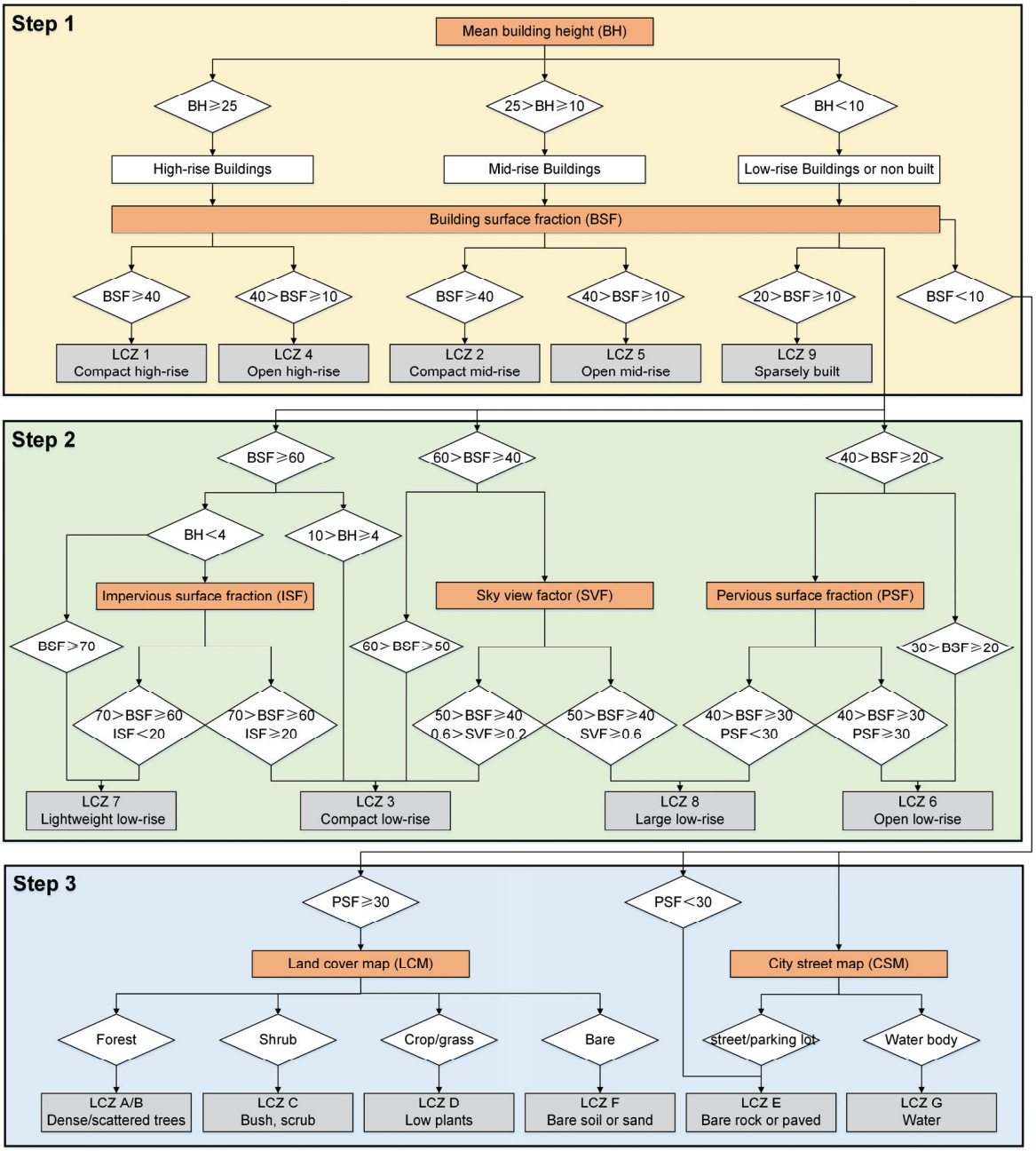

Figure 4. Hierarchical classification of LCZs according to the five indicators, CSM and LCM.

3.4. Geographical Detection of SUHII Differentiations

The geodetector q statistic was applied to analyze the spatial stratified heterogeneity of SUHIIs and their driving mechanisms across different seasons and day–night periods [47]. The basic concept is that if independent variables significantly affect the dependent variable, they would have consistent spatial distribution characteristics and stratified heterogeneity [48]. The q statistic can be expressed as follows:

$$q(X) = 1 - \frac{\sum_{h=1}^{L} N_h \sigma_h^2}{N\sigma^2} \tag{3}$$

where h is the layer Y based on X stratification; L is the total number of layers; N and N_h are the numbers of pixels in the entire region and layer h, respectively; σ^2 and σ_h^2 are the variances of Y in the entire region and layer h, respectively. The calculation software and

tutorial can be found on the Geodetector Learning website at http://www.geodetector.cn/, accessed on 30 September 2023.

Herein, the Y variable represents the seasonal daytime (08:00–16:00) and nighttime (20:00–04:00) average SUHIIs at the pixel level, with respect to the average LST in LCZ D. The X variable is one of the 10 driving factors (Table 1). Each X was stratified into 9 layers using a quantile classification method. The resultant q ranges from 0 to 1, indicating the individual explanatory power of a given factor X on the spatial stratified heterogeneity of SUHIIs, expressed as $q \times 100\%$. By further calculating and comparing $q(X_1)$, $q(X_2)$, and $q(X_1 \cap X_2)$, the interaction effect of any two factors can be determined, as shown in Table 2.

Table 2. Types of interactions between two variables.

Creterion	Interaction Type
$q(X_1 \cap X_2) < \text{Min}(q(X_1), q(X_2))$	Nonlinear weakening
$\text{Min}(q(X_1), q(X_2)) < q(X_1 \cap X_2) < \text{Max}(q(X_1), q(X_2))$	Single-factor nonlinear weakening
$q(X_1 \cap X_2) > \text{Max}(q(X_1), q(X_2))$	Two-factor enhancement
$q(X_1 \cap X_2) = q(X_1) + q(X_2)$	Independent
$q(X_1 \cap X_2) > q(X_1) + q(X_2)$	Nonlinear enhancement

4. Results

4.1. A general View of the LCZs and Corresponding LSTs

The four DTC parameters (T_0, T_a, t_m and t_s) derived for the 12 months are illustrated in Figure 5. T_0 reaches its peak in summer (close to 300 K) and slump in winter (<275 K). The overall trend accords with the annual temperature cycle driven by solar radiation in Beijing. T_a mostly ranges from 15 K to 20 K, while dropping by 1–3 K in August, December, and January, i.e., the hottest and coldest months. t_m (11:00–14:00) and t_s (15:00–18:00) have similar monthly variations, indicating that an earlier temperature peak is usually accompanied by an earlier temperature decay and vice versa. The absolute fitting error in comparison to the MODIS input is 0.76 K. The resulting hourly LSTs were further compared to the hourly seamless LST product (0.02°) generated by Cheng et al. [49], yielding a mean absolute difference of 2.52 K.

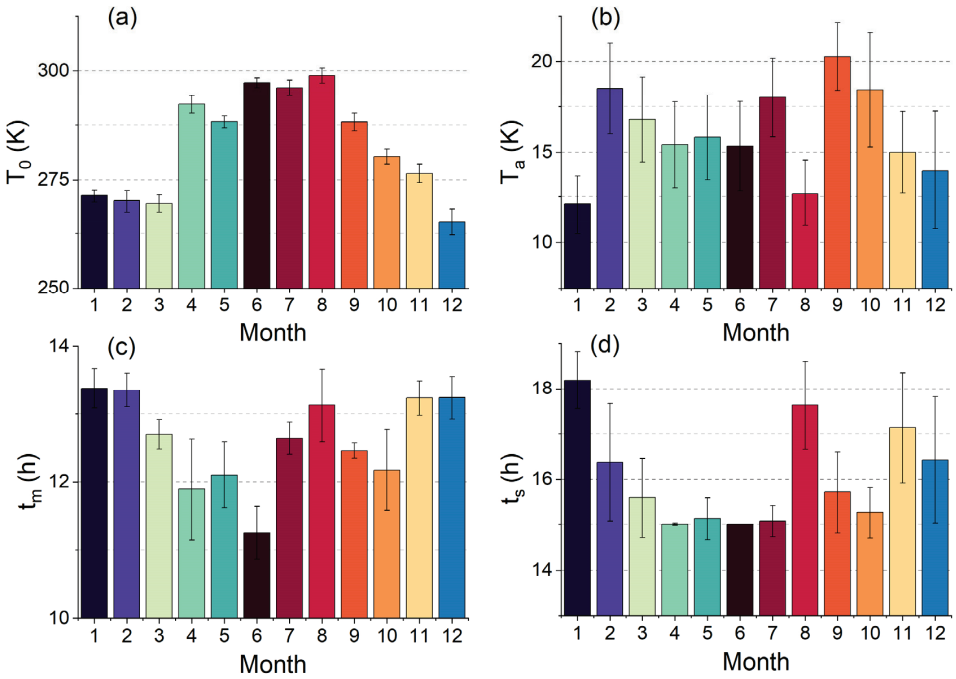

Figure 5. Monthly Distribution of T_0, T_a, t_m, and t_s. (**a**) T_0 is the lowest early morning temperature; (**b**) T_a is the diurnal temperature amplitude; (**c**) t_m is the local time when the temperature reaches its maximum; and (**d**) t_s is the local time when the temperature begins to decay freely.

Figure 6 shows the LCZ map generated over the study area. Previous validation against field samples reveals an agreement of ~90% [38]. The dominant built LCZ types are open high-rise (LCZ 4), open mid-rise (LCZ 5), open low-rise (LCZ 6), large low-rise (LCZ 8), and sparsely built (LCZ 9), each accounting for more than 5% of the total. Among them, LCZ 5 is the most widely distributed (28.8%), followed by LCZ 6 (12.9%). These five built LCZ types were selected for subsequent LCZ-based SUHII calculations considering the sufficient samples that are comparable to those of LCZ D (low plants, 4.7%). In terms of spatial distributions, Figure 6 shows a general progression from low-rise to mid-rise and then to low-rise again, moving from the center to the outskirts. Specifically, the central area consists mainly of open low-rise buildings (LCZ 6), encompassing landmarks like the Forbidden City and Hutongs. Extending towards the Third and Fourth Ring Roads, open mid-rise buildings (LCZ 5) become more prevalent, interspersed with open high-rise buildings (LCZ 4). Continuing towards the Fifth Ring Road, a mixed distribution of open low-rise buildings (LCZ 6) and sparse buildings (LCZ 9) is observed. Vegetation types (LCZs A–D) mainly comprise parks and farmlands scattered in the surroundings.

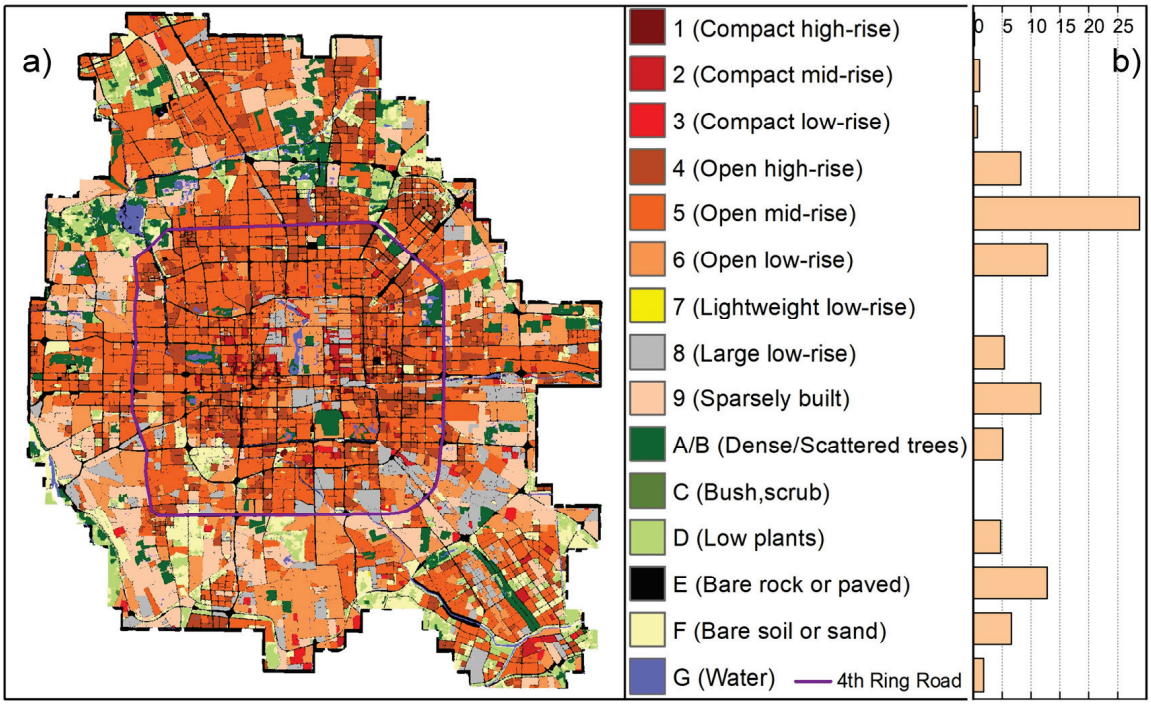

Figure 6. Local climate zones (LCZs) of the study area. (**a**) shows the LCZ map and (**b**) lists the proportion (%) of each LCZ type.

Combining the LCZ map and diurnal LSTs, Figure 7 exhibits distinct thermal characteristics of various LCZs during the day and night. The LST differences among LCZs are relatively small and generally stable during the daytime (except for spring), while the nighttime shows significant variability. At night, the LSTs of both compact (LCZs 1–3) and open buildings (LCZs 4–6) decline with decreasing building height, with compact buildings being more affected in summer and winter. During the daytime, the thermal impact of building height on compact buildings is generally negative in spring and summer and less significant in autumn and winter. This is consistent with previous findings that growing building height decreases daytime LSTs and increases nighttime LSTs [25,34]. Furthermore, for high-rise buildings, compact ones tend to have higher LSTs than open ones. From an average perspective, vegetation types (LCZs A/B and D) generally have lower LSTs than built LCZ types for all seasons and day–night periods (except for spring), suggesting that a SUHI phenomenon constantly controls the study area.

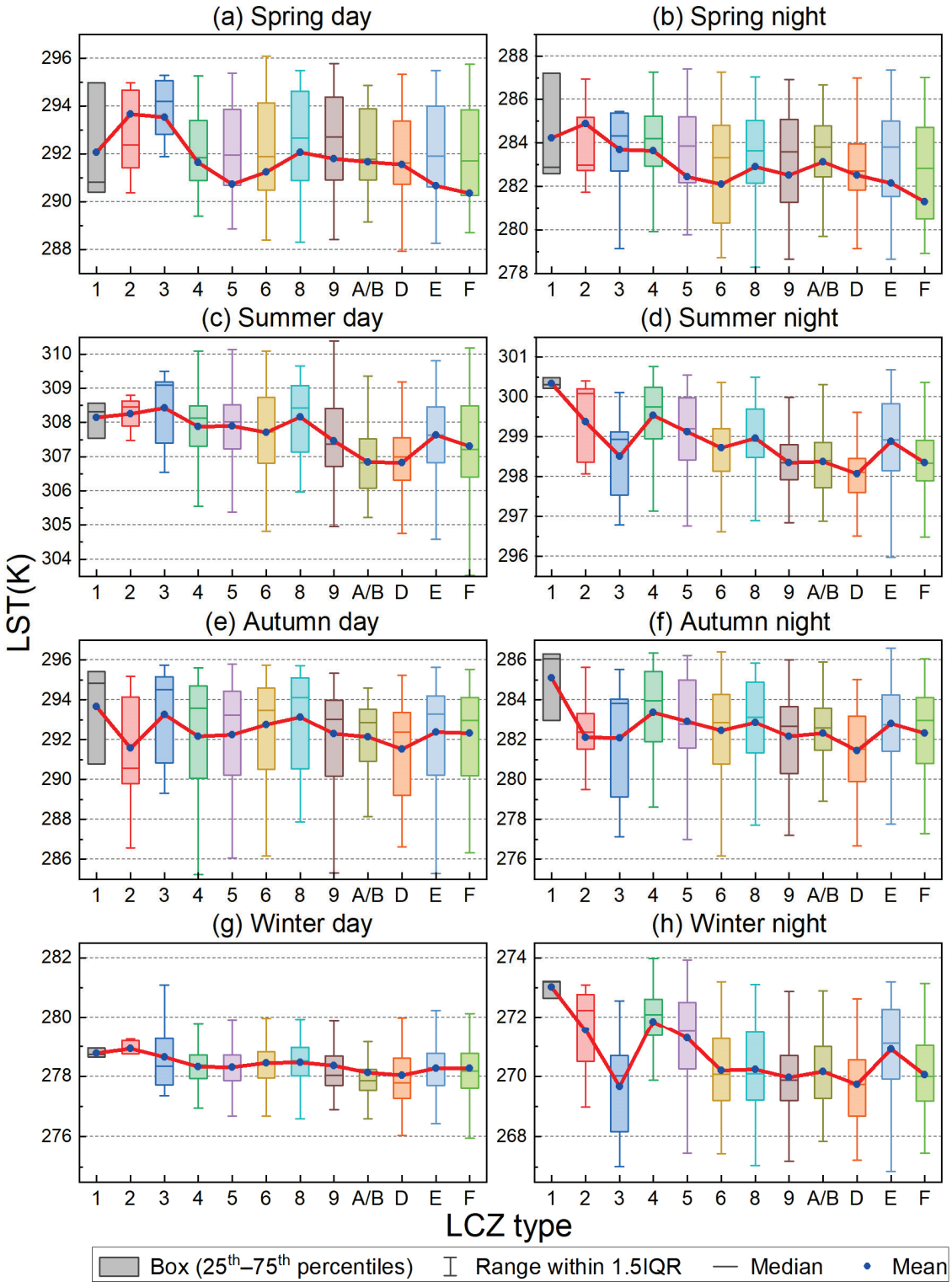

Figure 7. Thermal characteristics of different LCZs during the daytime (08:00–16:00) and nighttime (20:00–04:00) in four seasons.

4.2. Diurnal Patterns of SUHIIs across Different LCZs and Months

Figure 8 shows the diurnal variations of SUHIIs of five main built LCZ types (LCZs 4, 5, 6, 8, and 9) in 12 months and four seasons. It illustrates a similar diurnal pattern between LCZs 4 (open high-rise) and 5 (open mid-rise), which is characterized by a rapid decrease in the morning, followed by a sharp increase in the afternoon, peaking around 18:00, and

then exhibiting slow changes during the night. However, there are differences between the seasons. Specifically, for LCZs 4 and 5, the diurnal SUHII amplitudes in autumn and winter are larger than those in spring and summer, and an overall increasing/decreasing trend in SUHII after ~18:00 is presented in summer/autumn. As for SUHIIs of LCZs 6 (open low-rise), 8 (large low-rise), and 9 (sparsely built), the variations after ~15:00 are consistent throughout the seasons, i.e., SUHIIs decrease from ~15:00 to ~19:00 and remain low at night; however, the patterns from ~9:00 to ~15:00 are rather different, with a predominant decrease in spring and summer but an increase in autumn and winter. Meanwhile, the diurnal variations of LCZ-based SUHIIs significantly differ within seasons [16]. Specifically, in March and April, the SUHII variation in each LCZ accords closely with its average in spring; however, in May, the patterns are opposite to its seasonal average. For the months of June–August, the diurnal SUHII patterns are similar to the summer average, but LCZs 6, 8, and 9 exhibit peak values around 15:00 in August, while the peak values occur between 8:00 and 12:00 in June and July. In autumn, there are substantial differences in SUHIIs among various built LCZ types across months, but both LCZs 4 and 5 show sharp peaks around 18:00 throughout the season. The winter months experience the most stable and consistent diurnal SUHII patterns for a given LCZ type. Notably, LCZ 4 exhibits a cold island phenomenon between 10:00 and 14:00 in December and January, which may be partially attributed to shading effects from high-rise buildings [50,51].

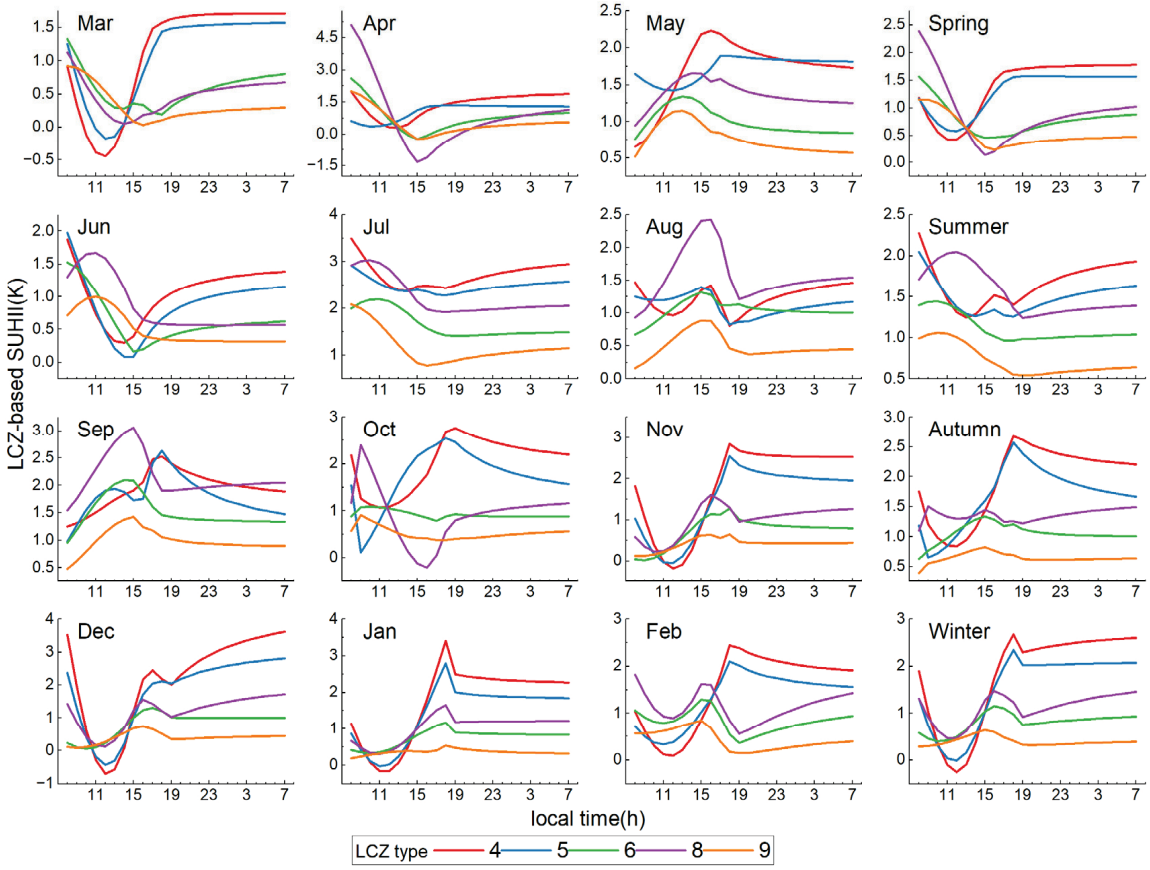

Figure 8. Diurnal SUHIIs of five main built LCZ types (LCZs 4, 5, 6, 8, and 9) in 12 months and four seasons.

It can be seen that the seasonally averaged diurnal curve, a common approach in previous studies, still has some insufficiency and complexity in expressing major diurnal patterns of SUHIIs across different LCZs and months. In order to promote a more general understanding of these variation characteristics, a hierarchical clustering analysis was conducted (Section 3.3), and six primary diurnal patterns with distinct features were identified (Figures 9–11). In general, LCZs 4 and 5 predominantly display patterns one,

two, and five, characterized by an afternoon increase in SUHII, which then sustains at higher values at night (I_{night} > 1.2 K). Conversely, LCZs 6, 8, and 9 mainly exhibit patterns three, four, and six, showing a decrease in SUHII during the afternoon hours and lower intensities at night ($I_{night} \leq$ 1.2 K), except that during November–January, pattern two dominates instead probably due to increased LSTs in these low-rise buildings caused by extensive winter heating. Moreover, opposite trends in the timing of extreme SUHIIs are observed between patterns 1–3 and patterns 5–6: t_{max} and t_{min} for patterns 1–3 occur in the afternoon/evening and morning, respectively, whereas for patterns 5–6, they appear in the morning and afternoon, respectively.

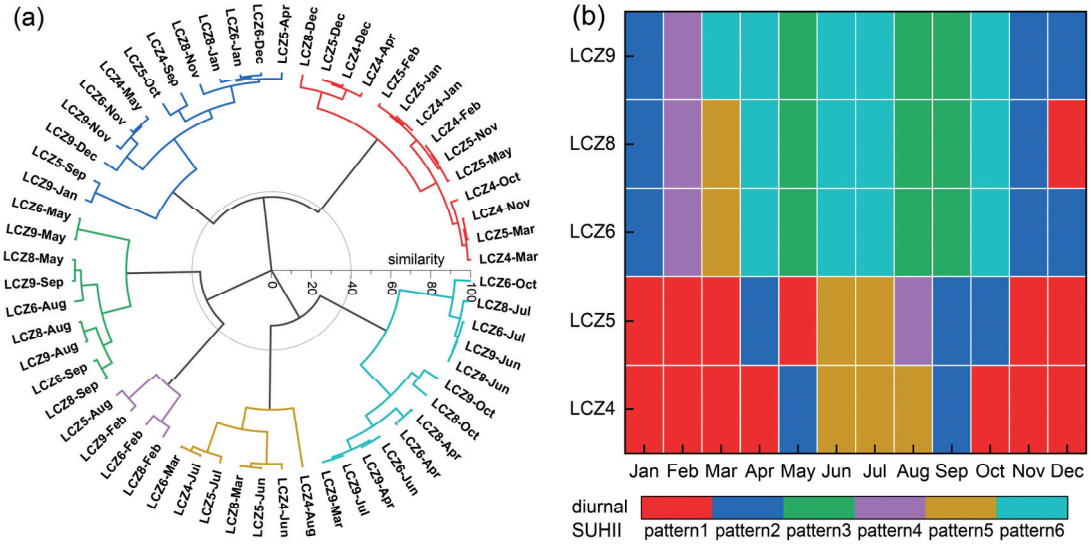

Figure 9. Hierarchical clustering of diurnal SUHII variations across different LCZs and months. (**a**) The spectral plot of clustering patterns, where the 'LCZX-Month' indicates the diurnal variation in LCZ X in that month. (**b**) The division of LCZX-Month into the six major diurnal patterns of SUHIIs.

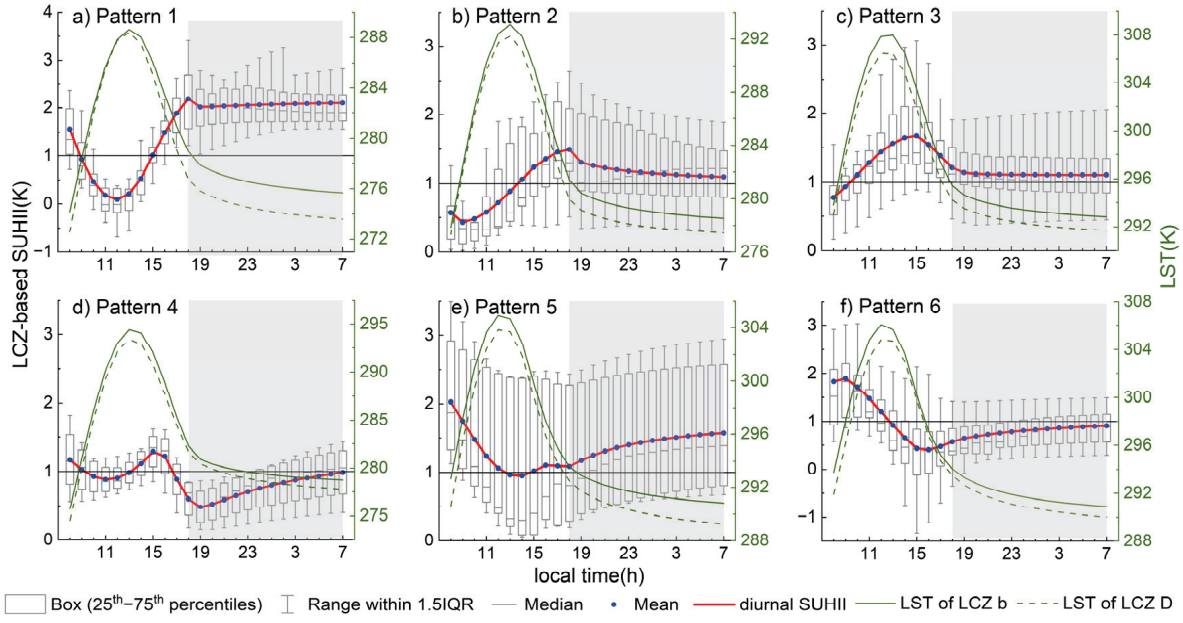

Figure 10. Six major diurnal SUHII patterns of various LCZs and their associated LST cycles in-built LCZ types (LCZ b) and LCZ D. For each pattern, the boxplot includes the contemporaneous SUHIIs in all LCZs and months classified into that pattern in Figure 9, and the mean value is adopted to form the major pattern. Similarly, the associated LSTs are averages among these LCZs and months.

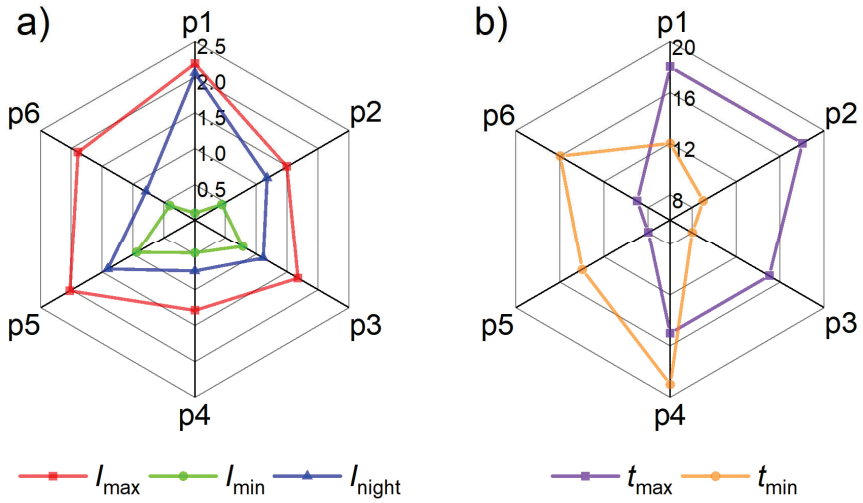

Figure 11. Characteristic parameters of the major diurnal SUHII patterns in Figure 10 (p is an abbreviation for "pattern"). (**a**) shows the maximum SUHII (I_{max}), minimum SUHII (I_{min}) and nocturnal (20:00–04:00) average SUHII (I_{night}), and (**b**) shows the time of I_{max} (t_{max}) and time of I_{min} (t_{min}).

The specific features of the six major diurnal patterns are described as follows.

Pattern one (Figure 10a): SUHII decreases rapidly after sunrise, reaching its lowest value around noon, followed by a sharp increase, exhibiting the highest rate of change during the day among these patterns. After 18:00, SUHII remains consistent at ~2 K, stronger than that during the day. It has the largest I_{max} and I_{night}, and the lowest I_{min} (close to zero), indicating the strongest diurnal variations in SUHII. The LST curves also demonstrate a close resemblance between the built LCZ types and LCZ D around noon, with the most significant differences during the night. This pattern is common in open high- and mid-rise buildings (LCZs 4 and 5), covering most months in winter, spring, and autumn.

Pattern two (Figure 10b): SUHII shows a minor decrease followed by an increase during the day, with a peak around 18:00, and then slightly decreases to around 1.2 K during the night. Its primary difference from pattern one lies in the morning evolution of SUHII and the weaker magnitude of change throughout the day. The short-term decrease in SUHII after sunrise may be attributed to a shadow effect at the low solar altitude that alleviates the heating rate of building types [52]. Nevertheless, the shadow effect will soon be overpowered by the contrasting thermal inertia difference between buildings and low plants as the solar altitude increases with time, leading to a subsequent rise in SUHII. This rationalizes why this pattern occurs mostly in low-rise buildings (LCZs 6, 8, and 9) in winter and high-/mid-rise buildings (LCZs 4 and 5) in April–May and September–October.

Pattern three (Figure 10c): SUHII continues to increase until a prominent peak appears around 15:00, followed by a decrease until ~19:00 and constancy at ~1 K throughout the night. This pattern is present in low-rise buildings (LCZs 6, 8, and 9) in May, August, and September. It differs from all the other patterns in the continuous rise of SUHII from morning to early afternoon, which is probably related to the dominant cooling effect of abundant vegetation coverage in LCZ D in growing seasons.

Pattern four (Figure 10d): SUHII exhibits a peak around 15:00 and two valleys around 11:00 and 19:00, with a gradual increase during the night. The overall SUHII and diurnal variations are weak, mostly ranging from 0.5 K to 1 K. This pattern occurs less frequently than others, appearing only in LCZs 6, 8, and 9 in February and LCZ 5 in August.

Pattern five (Figure 10e): SUHII decreases until ~14:00 and then rises slowly to around 1.5 K for the rest of the day. This pattern maintains a relatively high level of SUHII (>1 K) throughout the day in comparison to others. It primarily occurs in LCZs 4 and 5 during June–August.

Pattern six (Figure 10f): SUHII rises just before 9:00, drops from about 2 K to 0.5 K by ~16:00, and then slowly rises to around 1 K. This pattern is often observed in LCZs 6, 8, and 9 and from April to October.

4.3. Individual and Interactive Effects of Driving Factors

Table 3 shows that the explanatory power of each driving factor exhibits significant seasonal and day–night differences, where all q-values pass the significance test ($p < 0.01$), except for those of MNDWI, BH, and PRS during the spring daytime. In general, the explanatory power is lower in spring than in other seasons, which may be attributed to the significant reduction in human activities during the COVID-19 lockdown in Beijing and the associated substantial weakening of SUHII and spatial variations [53]. For daytime spatial differentiations of SUHIIs, EVI, and GDP have the top two impact degrees in all four seasons, while BSF, PD, RD, and RHU rank third from spring to winter, respectively. TEM has the largest explanatory power for nighttime spatial differentiations of SUHIIs across seasons, which is followed by PD and RD in spring and by EVI and RHU in summer–winter. In terms of mean q-value, the top three factors are EVI > TEM > GDP = RHU, while MNDWI exhibits the least explanatory power.

Table 3. The geodetector q statistic of each driving factor on the spatial stratified heterogeneity of SUHIIs across four seasons and day–night periods.

Factors	Spring		Summer		Autumn		Winter		Average
	Day	Night	Day	Night	Day	Night	Day	Night	
Morphological Factors									
EVI	**0.21**	0.32	**0.60**	**0.66**	**0.58**	**0.63**	**0.23**	**0.54**	**0.47**
MNDWI	0.04 *	0.14	0.19	0.22	0.14	0.23	0.06	0.19	0.15
BSF	**0.19**	0.15	0.26	0.21	0.30	0.18	0.19	0.17	0.21
BH	0.02 *	0.22	0.12	0.37	0.08	0.20	0.03	0.34	0.17
Socioeconomic Factors									
GDP	**0.21**	0.45	**0.37**	0.41	**0.43**	0.46	**0.32**	0.45	**0.39**
PD	0.08	**0.52**	**0.28**	0.46	0.34	0.44	0.22	0.46	0.35
RD	0.08	**0.47**	0.19	0.41	**0.42**	0.52	0.20	0.45	0.34
Meteorological Factors									
PRS	0.02 *	0.27	0.27	0.36	0.16	0.28	0.13	0.26	0.22
RHU	0.15	0.44	**0.28**	**0.57**	0.26	**0.53**	**0.26**	**0.64**	**0.39**
TEM	0.11	**0.61**	0.16	**0.73**	0.15	**0.73**	0.10	**0.71**	**0.41**
Ranking of the 10 factors for each column									10 th → 1 st

* $p > 0.01$.

Among the morphological factors, EVI exhibits the strongest average explanatory power. Particularly during the summer daytime, a q-value of up to 0.60 is obtained. This is mainly due to the well-known cooling effect via vegetation evapotranspiration and canopy shading [54]. Accordingly, the q-value of EVI gradually changes with vegetation phenology and solar insolation, reaching the lowest value during the daytime of cold (leaf-off) seasons [34]. EVI also presents significant controls ($q \geq 0.54$) on the spatial differentiations of summer, autumn, and winter nighttime SUHIIs, which is most likely related to the albedo-induced radiative warming effect of plant canopies [55]. This is consistent with the pronounced nocturnal variation characteristics of LSTs/SUHIIs among LCZs (Figures 7–11). Meanwhile, as many studies have noted, BSF is a key factor influencing the local-scale thermal differentiation [56], especially during the daytime when building canyons and materials demonstrate strong heat storage capacities and eventually substantial contributions to increased SUHIIs [57]. In contrast to BSF, BH exhibits a higher explanatory power for the nighttime SUHIIs ($0.20 \leq q \leq 0.37$) than for the daytime SUHIIs ($0.02 \leq q \leq 0.12$). This supports to some extent the general dichotomy between high-/mid-rise buildings (LCZs 4 and 5) and low-rise buildings (LCZs 6, 8, and 9) in terms of major diurnal SUHII patterns

with significant I_{night} differences in each month (Figures 9 and 11). The overall explanatory power of BH is slightly lower than that of BSF.

Among the socioeconomic factors, GDP has the strongest power to explain the daytime SUHII variations ($0.21 \leq q \leq 0.43$), which could be attributed to its comprehensiveness with respect to PD and RD regarding human activity, surface morphology, and zonal function. For nighttime SUHII variations, GDP, PD, and RD show close contribution magnitudes (0.41–0.52), mainly revealing the impact of anthropogenic heat emissions [58]. Among them, PD and RD are the second- and third-ranked explanatory variables during the spring nighttime. One possible reason for this is the strict COVID-19 lockdown in Beijing in the spring of 2020, which has led to reduced human mobility and increased transportation of goods, thus maybe increasing the explanatory powers of the annual PD and RD datasets at night.

Among the meteorological factors, TEM plays a dominant role in determining the spatial variation in nighttime SUHIIs, with an explanatory power ranging from 61% to 73%. This is consistent with previous studies, indicating a strong correlation between nighttime atmospheric and surface temperatures [59]. Research has also suggested that nighttime humidity can control surface cooling [60], which may explain the higher explanatory power of RHU (44% to 64%) at night. On the other hand, the daytime q-values of TEM and RHU are notably lower. This could be attributed to the fact that the daytime SUHII mechanism is more complex [61] and influenced more by surface morphology and human activities. Compared to RHU and TEM, the influence of PRS on the spatial variation in SUHIIs is limited.

Furthermore, interactive effects among 10 driving factors are shown in Figure 12. The interaction types are either two-factor enhancement or nonlinear enhancement, indicating that the driving effects on SUHII are not independent but rather interdependent, and the interaction between any two factors can enhance the impact on SUHIIs. The nonlinear enhancement interaction primarily occurs during the daytime, while nighttime interactions are mostly categorized as two-factor enhancement, implying that the daytime driving mechanism may be more complex than the nighttime counterpart.

During the spring daytime, all the interactions are nonlinear enhancement. The largest individual effect is 0.21 (q(EVI) and q(GDP)), while the interactive effect can reach 0.53 (q(TEM $\cap$ GDP)) and 0.51 (q(RHU $\cap$ GDP)). This may suggest that the urban thermal environment in the spring of 2020 is more dependent on the response of local socioeconomics to variable meteorological conditions. The winter daytime has the second largest number of factor pairs with nonlinear enhancement. Particularly, MNDWI, BH, PRS, and TEM have extremely low individual effects; nonetheless, their explanatory powers are highly strengthened by nonlinear interactions with any other factor. In summer and autumn, the strongest interaction factors for daytime SUHIIs are EVI $\cap$ GDP, EVI $\cap$ PD, EVI $\cap$ RHU, and EVI $\cap$ TEM ($q \geq 0.69$). They are also the factors with the highest individual effects (Table 3). During the nighttime, the top three interactive effects always involve TEM, regardless of the season. This further confirms the substantial part played by TEM in characterizing the nighttime thermal patterns, whether as a single factor or interacting with other factors.

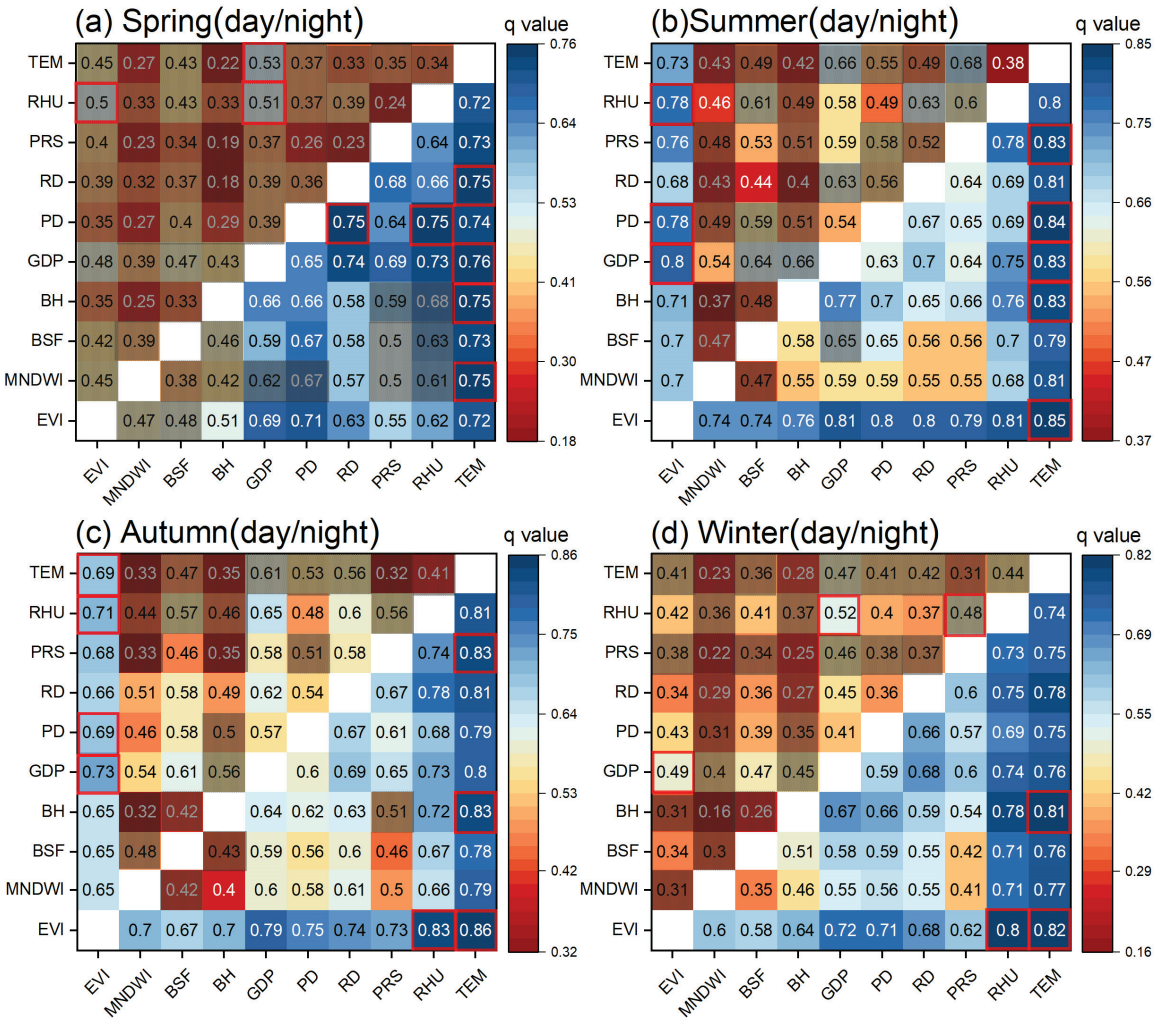

Figure 12. Interactive effects (q(X1 ∩ X2)) among 10 driving factors on the seasonal and day–night spatial differentiations of SUHIIs. The upper and lower triangles show the daytime and nighttime results, respectively. The red frames indicate the top three *q*-values for each scenario. The shadowed squares represent the nonlinear enhancement effect, while the others represent two-factor enhancement.

5. Discussion

This study focused on the combined use of a series of methods (i.e., DTC modeling, LCZ mapping, hierarchical clustering, and geodetector analysis) to identify the major diurnal patterns of SUHIIs of built LCZ types and the driving factors for spatial differentiations of SUHIIs that have not been fully understood before. It mainly innovated in three aspects. First, SUHIIs based on an LCZ scheme were comprehensively examined at a continuous diurnal scale and over 12 months. Second, six major diurnal patterns of SUHIIs were generalized and elucidated in detail across different built LCZ types and months based on hierarchical clustering analysis. Third, the spatial stratified heterogeneity of SUHIIs during four seasons and day–night periods was explored from both individual and interactive perspectives using the geodetector.

The results contribute to expanding our understanding of the diurnal variations in the local thermal environment associated with different types of urban buildings and the complex driving effects of urban morphological, socioeconomic, and meteorological conditions. For example, the major pattern one and pattern two identified in this study accord well with the "weak-spoon" pattern and "quasi-spoon" pattern defined by Lai et al. [52], respectively; nevertheless, the major patterns 3–6 are not recognized as the

typical diurnal patterns of SUHIIs in their study. This is mainly because they focused on nationwide cities with higher levels of urbanization based on the urban–rural dichotomy and thus may have difficulties capturing the diurnal variations primarily associated with low-rise buildings (LCZs 6, 8, and 9). Pattern one was found common in open high- and mid-rise buildings (LCZs 4 and 5) in winter, spring, and autumn. This rationalizes the diurnal SUHII change during this period in Beijing characterized by an urban–rural delineation in the study of Zhou et al. [62], as LCZs 4 and 5 have larger numbers and greater variations than other built LCZ types and exert a higher impact on the urban-averaged SUHII. This pattern also supports Dong et al. [16] on the transition of SUHII around sunset for high-rise built LCZ types in winter. Moreover, unlike many previous studies [63,64], this study obtained a high q-value ($\geq$0.54) of EVI for explaining the spatial SUHII differentiations during the summer, autumn, and winter nighttime. This difference may be due to the fact that the geodetector here measures the zonal heterogeneity affected by drivers, while previous studies primarily evaluate the pixel-by-pixel linear relationship, further indicating that the vegetation albedo-based radiative effect on the nighttime SUHII is likely to be nonlinear and/or hierarchical [52]. Meanwhile, EVI presents the strongest interaction effects with GDP, PD, RHU and TEM during the summer and autumn daytime, implying that it is important to reasonably configure the spatial distribution of vegetation with locally specific socioeconomic and climatological conditions for further surface heat mitigation in warm/hot seasons.

Despite these progresses, this study has certain limitations and future aspects as follows.

(1) In terms of the LST reconstruction and LCZ classification

The DTC model describes clear-sky LST evolutions and requires at least four observations per day; therefore, the diurnal LSTs were reconstructed under the assumption of 24 h of cloudlessness with a resolution of 1 km on a monthly basis. This could lead to slightly reduced magnitudes of spatiotemporal variations in LCZ-based SUHIIs [11], difficulties in characterizing practical diurnal thermal patterns under all-weather/overcast/rainy conditions [65], and the lack of appropriateness in tropical and high-latitude regions [66]. The use of microwave and/or reanalysis data associated with sophisticated spatiotemporal reconstruction models to generate all-weather diurnal high-resolution LSTs [67] would improve the stability and comprehensiveness of the research results. However, such products are not currently accessible, and advanced data modeling is not the focus of the current study. Considering that this study mainly concentrated on the major building LCZ types that have certain aggregation features with sufficient sizes, it is inferred that the overall patterns of diurnal variations are less affected during the clustering analysis and most likely still hold at a higher spatial resolution. Another caveat of the DTC model is that it does not incorporate the directionality of thermal radiation with urban 3D structures and multi-angle satellite observations. This may disturb the diurnal curves of SUHIIs in vertical buildings, reduce their comparability over space and time, and lower the explanatory powers of 3D morphological factors [68]. Additionally, the GIS-based LCZ mapping approach heavily depends on high-resolution 3D building and plant information, which are often unavailable, particularly in under-developed countries and cities. Therefore, it is desirable to adopt/develop a more widely applicable yet highly accurate LCZ classification framework to further explore the diurnal SUHII patterns of different LCZ types across multiple cities or even globally.

(2) In terms of the geographical detection

The geodetector is susceptible to a partitioning effect, meaning that different methods of discretizing and classifying independent variables would affect the attribution results to some extent [69]. Therefore, following previous research [37,69], we classified all independent variables into the same number of classes using the quantile classification method and made analyses based on the relative importance or ranks among driving factors. Further improvements in the reclassification of drivers may consider the regional characteristics

of each independent variable. Also, incorporating a sufficient number of driving factors helps avoid fortuitous outcomes of geographical detection. Here, we combined 10 factors covering distinct perspectives of urban morphology, socioeconomics, and meteorology. However, due to the limited access to frequent records of socioeconomic conditions, yearly data were used for seasonal and day–night attribution analysis. This may introduce biases in assessing the multi-temporal impacts of socioeconomic activities [70], which could be mitigated by utilizing real-time data on crowd statistics and behaviors (e.g., mobile phone and microblogging) as well as anthropogenic heat emissions. In addition, while the geodetector enables analysis of both single-factor and interaction-factor effects, it is still limited in capturing the collective interactions among multiple driving factors, which are crucial for gaining a comprehensive understanding of complex geographic phenomena.

6. Conclusions

In this study, we first reconstructed diurnal LSTs of Beijing in 2020 using MODIS LST data and a DTC model. Combined with the LCZ classification, we then analyzed the multi-temporal thermal characteristics of different LCZs. On this basis, diurnal SUHII patterns were clustered across different built LCZ types and months, and their characteristic parameters were identified. The geodetector q statistic was further employed to investigate the driving mechanisms behind multi-temporal spatial differentiations in SUHIIs in association with the urban morphological, socioeconomic, and meteorological factors. The main conclusions are as follows:

(1) There exist six primary diurnal SUHII patterns among five main built types and 12 months. LCZs 4 and 5 (open high- and mid-rise) predominantly exhibit patterns one, two, and five, with an increase in SUHII in the afternoon, which is maintained at higher values (I_{night} > 1.2 K) at night. LCZs 6, 8, and 9 (open, large, and sparsely-built low-rise) mainly display patterns three, four, and six, with a decrease in SUHII during the afternoon and lower intensities at night ($I_{night} \leq$ 1.2 K). $t_{\max}$ and $t_{\min}$ for patterns 1–3 are in the afternoon–evening, and morning, respectively, whereas those for patterns 5–6 are in the morning and afternoon, respectively.

(2) EVI and GDP have the top two explanatory powers for daytime spatial differentiations of SUHIIs in all four seasons, while BSF, PD, RD, and RHU rank third from spring to winter. TEM has the strongest individual effect for nighttime spatial differentiations of SUHIIs, followed by PD and RD in spring and EVI and RHU in summer–winter.

(3) Factor interaction types are two-factor and nonlinear enhancement across four seasons. The former/latter mainly exists during the nighttime/daytime, where the nighttime explanatory powers are greater than the daytime ones. The strongest interactions are EVI ∩ GDP (q = 0.80) during the day and TEM ∩ EVI (q = 0.86) at night.

Future works may incorporate sophisticated models for diurnal all-weather LST reconstruction with a high spatial resolution covering 3D facets, examine diurnal LCZ-based SUHIIs for varied cities and climates by combining widely applicable yet highly accurate LCZ classification frameworks, and explore collective interactions among dynamic driving factors for a further comprehensive understanding of the complex SUHI phenomena.

Author Contributions: Conceptualization, J.Q. and T.M.; Methodology, Y.G. and J.Q.; Investigation and Data Curation, Y.G.; Writing—Original Draft, Y.G. and J.Q.; Writing—Review and Editing, J.Q., T.M., S.C., C.X. and J.G. All authors have read and agreed to the published version of the manuscript.

Funding: The Youth Project of Innovation LREIS (YPI008); the Youth Innovation Promotion Association, CAS (2021051).

Conflicts of Interest: The authors declare no conflict of interest.

References

1. Oke, T.R. The energetic basis of the urban heat island. *Q. J. R. Meteorol. Soc.* **1982**, *108*, 1–24. [CrossRef]
2. Rizwan, A.M.; Dennis, L.Y.C.; Liu, C. A review on the generation, determination and mitigation of Urban Heat Island. *J. Environ. Sci.* **2008**, *20*, 120–128. [CrossRef] [PubMed]
3. Voogt, J.A.; Oke, T.R. Thermal remote sensing of urban climates. *Remote Sens. Environ.* **2003**, *86*, 370–384. [CrossRef]
4. Zhou, D.; Zhao, S.; Liu, S.; Zhang, L.; Zhu, C. Surface urban heat island in China's 32 major cities: Spatial patterns and drivers. *Remote Sens. Environ.* **2014**, *152*, 51–61. [CrossRef]
5. Kong, J.; Zhao, Y.; Carmeliet, J.; Lei, C. Urban heat island and its interaction with heatwaves: A review of studies on mesoscale. *Sustainability* **2021**, *13*, 10923. [CrossRef]
6. Mishra, V.; Ganguly, A.R.; Nijssen, B.; Lettenmaier, D.P. Changes in observed climate extremes in global urban areas. *Environ. Res. Lett.* **2015**, *10*, 024005. [CrossRef]
7. Chu, P.; Jiang, Z.; Li, Q.; Dong, L. Analysis of the effect of uncertainty in urban and rural classification on urbanization impact assessment. *Trans. Atmos. Sci.* **2016**, *39*, 661–671. [CrossRef]
8. Bechtel, B.; Demuzere, M.; Mills, G.; Zhan, W.; Sismanidis, P.; Small, C.; Voogt, J. SUHI analysis using local climate zones—A comparison of 50 cities. *Urban Clim.* **2019**, *28*, 100451. [CrossRef]
9. Verdonck, M.-L.; Okujeni, A.; van der Linden, S.; Demuzere, M.; De Wulf, R.; Van Coillie, F. Influence of neighbourhood information on 'Local Climate Zone' mapping in heterogeneous cities. *Int. J. Appl. Earth Obs. Geoinf.* **2017**, *62*, 102–113. [CrossRef]
10. Oke, T.R.; Stewart, I.D. Local climate zones for urban temperature studies. *Bull. Am. Meteorol. Soc.* **2012**, *93*, 1879–1900. [CrossRef]
11. Jiang, S.; Zhan, W.; Yang, J. Urban heat island studies based on local climate zones: A systematic overview. *Acta Geogr. Sin.* **2020**, *75*, 1860–1878. [CrossRef]
12. Kaloustian, N.; Bechtel, B. Local climatic zoning and urban heat island in Beirut. *Procedia Eng.* **2016**, *169*, 216–223. [CrossRef]
13. Beck, C.; Straub, A.; Breitner, S.; Cyrys, J.; Philipp, A.; Rathmann, J.; Schneider, A.; Wolf, K.; Jacobeit, J. Air temperature characteristics of local climate zones in the Augsburg urban area (Bavaria, southern Germany) under varying synoptic conditions. *Urban Clim.* **2018**, *25*, 152–166. [CrossRef]
14. Leconte, F.; Bouyer, J.; Claverie, R.; Pétrissans, M. Using local climate zone scheme for UHI assessment: Evaluation of the method using mobile measurements. *Build. Environ.* **2015**, *83*, 39–49. [CrossRef]
15. Stewart, I.D.; Oke, T.R.; Krayenhoff, E.S. Evaluation of the 'Local Climate Zone' scheme using temperature observations and model simulations. *Int. J. Climatol.* **2014**, *34*, 1062–1080. [CrossRef]
16. Dong, P.; Jiang, S.; Zhan, W.; Wang, C.; Miao, S.; Du, H.; Li, J.; Wang, S.; Jiang, L. Diurnally continuous dynamics of surface urban heat island intensities of local climate zones with spatiotemporally enhanced satellite-derived land surface temperatures. *Build. Environ.* **2022**, *218*, 109105. [CrossRef]
17. Xia, H.; Chen, Y.; Song, C.; Li, J.; Quan, J.; Zhou, G. Analysis of surface urban heat islands based on local climate zones via spatiotemporally enhanced land surface temperature. *Remote Sens. Environ.* **2022**, *273*, 112972. [CrossRef]
18. Yang, X.; Yao, L.; Jin, T.; Peng, L.L.H.; Jiang, Z.; Hu, Z.; Ye, Y. Assessing the thermal behavior of different local climate zones in the Nanjing metropolis, China. *Build. Environ.* **2018**, *137*, 171–184. [CrossRef]
19. Geletič, J.; Lehnert, M.; Savić, S.; Milošević, D. Inter-/intra-zonal seasonal variability of the surface urban heat island based on local climate zones in three central European cities. *Build. Environ.* **2019**, *156*, 21–32. [CrossRef]
20. Quan, J. Multi-temporal effects of urban forms and functions on urban heat islands based on local climate zone classification. *Int. J. Env. Res. Public Health* **2019**, *16*, 2140. [CrossRef]
21. Stewart, I.D.; Krayenhoff, E.S.; Voogt, J.A.; Lachapelle, J.A.; Allen, M.A.; Broadbent, A.M. Time evolution of the surface urban heat island. *Earth's Future* **2021**, *9*, 2178. [CrossRef]
22. Hu, J.; Yang, Y.; Pan, X.; Zhu, Q.; Zhan, W.; Wang, Y.; Ma, W.; Su, W. Analysis of the spatial and temporal variations of land surface temperature based on local climate zones: A case study in Nanjing, China. *IEEE J. Sel. Top. Appl. Earth Obs. Remote Sens.* **2019**, *12*, 4213–4223. [CrossRef]
23. Anniballe, R.; Bonafoni, S.; Pichierri, M. Spatial and temporal trends of the surface and air heat island over Milan using MODIS data. *Remote Sens. Environ.* **2014**, *150*, 163–171. [CrossRef]
24. Roth, M.; Oke, T.R.; Emery, W.J. Satellite-derived urban heat islands from three coastal cities and the utilization of such data in urban climatology. *Int. J. Remote Sens.* **2007**, *10*, 1699–1720. [CrossRef]
25. Chang, Y.; Xiao, J.; Li, X.; Middel, A.; Zhang, Y.; Gu, Z.; Wu, Y.; He, S. Exploring diurnal thermal variations in urban local climate zones with ECOSTRESS land surface temperature data. *Remote Sens. Environ.* **2021**, *263*, 112544. [CrossRef]
26. Jiang, Y.; Fu, P.; Weng, Q. Assessing the impacts of urbanization-associated land use/cover change on land surface temperature and surface moisture: A case study in the midwestern United States. *Remote Sens.* **2015**, *7*, 4880–4898. [CrossRef]
27. Peng, J.; Jia, J.; Liu, Y.; Li, H.; Wu, J. Seasonal contrast of the dominant factors for spatial distribution of land surface temperature in urban areas. *Remote Sens. Environ.* **2018**, *215*, 255–267. [CrossRef]
28. Ramamurthy, P.; Bou-Zeid, E. Heatwaves and urban heat islands: A comparative analysis of multiple cities. *J. Geophys. Res. Atmos.* **2017**, *122*, 168–178. [CrossRef]
29. Arnfield, A.J. Two decades of urban climate research: A review of turbulence, exchanges of energy and water, and the urban heat island. *Int. J. Climatol.* **2003**, *23*, 1–26. [CrossRef]
30. Wang, J.-F.; Hu, Y. Environmental health risk detection with GeogDetector. *Environ. Model. Softw.* **2012**, *33*, 114–115. [CrossRef]

31. You, M.; Lai, R.; Lin, J.; Zhu, Z. Quantitative analysis of a spatial distribution and driving factors of the urban heat island effect: A case study of Fuzhou central area, China. *Int. J. Env. Res. Public Health* **2021**, *18*, 13088. [CrossRef] [PubMed]
32. Zhengming, W.; Dozier, J. A generalized split-window algorithm for retrieving land-surface temperature from space. *IEEE Trans. Geosci. Remote Sens.* **1996**, *34*, 892–905. [CrossRef]
33. Wan, Z. New refinements and validation of the collection-6 MODIS land-surface temperature/emissivity product. *Remote Sens. Environ.* **2014**, *140*, 36–45. [CrossRef]
34. Hu, D.; Meng, Q.; Schlink, U.; Hertel, D.; Liu, W.; Zhao, M.; Guo, F. How do urban morphological blocks shape spatial patterns of land surface temperature over different seasons? A multifactorial driving analysis of Beijing, China. *Int. J. Appl. Earth Obs. Geoinf.* **2022**, *106*, 102648. [CrossRef]
35. Lai, J.; Zhan, W.; Quan, J.; Liu, Z.; Li, L.; Huang, F.; Hong, F.; Liao, W. Reconciling debates on the controls on surface urban heat island intensity: Effects of scale and sampling. *Geophys. Res. Lett.* **2021**, *48*, e2021GL094485. [CrossRef]
36. Hu, Y.; Dai, Z.; Guldmann, J.M. Modeling the impact of 2D/3D urban indicators on the urban heat island over different seasons: A boosted regression tree approach. *J. Env. Manag.* **2020**, *266*, 110424. [CrossRef]
37. Chen, L.; Wang, X.; Cai, X.; Yang, C.; Lu, X. Seasonal variations of daytime land surface temperature and their underlying drivers over Wuhan, China. *Remote Sens.* **2021**, *13*, 323. [CrossRef]
38. Quan, J. Enhanced geographic information system-based mapping of local climate zones in Beijing, China. *Sci. China Technol. Sci.* **2019**, *62*, 2243–2260. [CrossRef]
39. Göttsche, F.-M.; Olesen, F.S. Modelling of diurnal cycles of brightness temperature extracted from METEOSAT data. *Remote Sens. Environ.* **2001**, *76*, 337–348. [CrossRef]
40. Göttsche, F.-M.; Olesen, F.-S. Modelling the effect of optical thickness on diurnal cycles of land surface temperature. *Remote Sens. Environ.* **2009**, *113*, 2306–2316. [CrossRef]
41. Jiang, G.-M.; Li, Z.-L.; Nerry, F. Land surface emissivity retrieval from combined mid-infrared and thermal infrared data of MSG-SEVIRI. *Remote Sens. Environ.* **2006**, *105*, 326–340. [CrossRef]
42. Bergh, F.v.d.; Wyk, M.A.v.; Wyk, B.J.v.; Udahemuka, G. A comparison of data-driven and model-driven approaches to brightness temperature diurnal cycle interpolation. *SAIEE Afr. Res. J.* **2007**, *98*, 81–86. [CrossRef]
43. Inamdar, A.K.; French, A.; Hook, S.; Vaughan, G.; Luckett, W. Land surface temperature retrieval at high spatial and temporal resolutions over the southwestern United States. *J. Geophys. Res. Atmos.* **2008**, *113*, D07107. [CrossRef]
44. Schädlich, S.; Göttsche, F.M.; Olesen, F.S. Influence of land surface parameters and atmosphere on METEOSAT brightness temperatures and generation of land surface temperature maps by temporally and spatially interpolating atmospheric correction. *Remote Sens. Environ.* **2001**, *75*, 39–46. [CrossRef]
45. Duan, S.-B.; Li, Z.-L.; Wang, N.; Wu, H.; Tang, B.-H. Evaluation of six land-surface diurnal temperature cycle models using clear-sky in situ and satellite data. *Remote Sens. Environ.* **2012**, *124*, 15–25. [CrossRef]
46. Meng, X.; Liu, H.; Cheng, J. Evaluation and characteristic research in diurnal surface temperature cycle in China using FY-2F data. *J. Remote Sens.* **2019**, *23*, 570–581. [CrossRef]
47. Wang, J.; Xu, C. Geodetector: Principle and prospective. *Acta Geogr. Sin.* **2017**, *72*, 116–134. [CrossRef]
48. Wang, J.F.; Li, X.H.; Christakos, G.; Liao, Y.L.; Zhang, T.; Gu, X.; Zheng, X.Y. Geographical detectors-based health risk assessment and its application in the neural tube defects study of the Heshun region, China. *Int. J. Geogr. Inf. Sci.* **2010**, *24*, 107–127. [CrossRef]
49. Cheng, J.; Dong, S.; Shi, J. 0.02° Seamless Hourly Land Surface Temperature Dataset over East Asia (2016–2021). 2022. Available online: https://data.tpdc.ac.cn/en/data/06414391-abd4-4d28-a844-bd036a0b8c55/ (accessed on 30 September 2023).
50. Chun, B.; Guhathakurta, S. The impacts of three-dimensional surface characteristics on urban heat islands over the diurnal cycle. *Prof. Geogr.* **2017**, *69*, 191–202. [CrossRef]
51. Erell, E. The application of urban climate research in the design of cities. *Adv. Build. Energy Res.* **2008**, *2*, 95–121. [CrossRef]
52. Lai, J.; Zhan, W.; Huang, F.; Voogt, J.; Bechtel, B.; Allen, M.; Peng, S.; Hong, F.; Liu, Y.; Du, P. Identification of typical diurnal patterns for clear-sky climatology of surface urban heat islands. *Remote Sens. Environ.* **2018**, *217*, 203–220. [CrossRef]
53. Liu, Z.; Lai, J.; Zhan, W.; Bechtel, B.; Voogt, J.; Quan, J.; Hu, L.; Fu, P.; Huang, F.; Li, L.; et al. Urban heat islands significantly reduced by COVID-19 lockdown. *Geophys. Res. Lett.* **2022**, *49*, e2021GL096842. [CrossRef]
54. Berry, R.; Livesley, S.J.; Aye, L. Tree canopy shade impacts on solar irradiance received by building walls and their surface temperature. *Build. Environ.* **2013**, *69*, 91–100. [CrossRef]
55. Alkama, R.; Forzieri, G.; Duveiller, G.; Grassi, G.; Liang, S.; Cescatti, A. Vegetation-based climate mitigation in a warmer and greener World. *Nat. Commun.* **2022**, *13*, 606. [CrossRef] [PubMed]
56. Guo, G.; Zhou, X.; Wu, Z.; Xiao, R.; Chen, Y. Characterizing the impact of urban morphology heterogeneity on land surface temperature in Guangzhou, China. *Environ. Model. Softw.* **2016**, *84*, 427–439. [CrossRef]
57. Liu, W.Y.; Gong, A.D.; Zhou, J.; Zhan, W.F. Investigation on relationships between urban building materials and land surface temperature through a mult-resource remote sensing approach. *Remote Sens. Inf.* **2011**, *31*, 46–53+110. [CrossRef]
58. Wu, X.; Wang, G.; Yao, R.; Wang, L.; Yu, D.; Gui, X. Investigating surface urban heat islands in south America based on MODIS data from 2003–2016. *Remote Sens.* **2019**, *11*, 1212. [CrossRef]
59. Yang, P.; Chen, J.; Hou, X.; Gao, Q.; Zhao, Q. Study of urban heat island based on multi-source data—By the example of the Shijiazhuang area. *Meteorol. Mon.* **2013**, *39*, 1304–1313. [CrossRef]
60. Rongbo, X. A review of the eco-environmental consequences of urban heat islands. *Acta Ecol. Sin.* **2005**, *25*, 2055–2060.

61. Hu, N.; Ren, Z.; Dong, Y.; Fu, Y.; Guo, Y.; Mao, Z.; Chang, X. Spatio-temporal evolution of heat island effect and its driving factors in urban agglomerations of China. *Sci. Geogr. Sin.* **2022**, *42*, 1534–1545. [CrossRef]
62. Zhou, J.; Chen, Y.; Zhang, X.; Zhan, W. Modelling the diurnal variations of urban heat islands with multi-source satellite data. *Int. J. Remote Sens.* **2013**, *34*, 7568–7588. [CrossRef]
63. Lu, Y.; Wu, P.; Ma, X.; Yang, H.; Wu, Y. Monitoring seasonal and diurnal surface urban heat islands variations using Landsat-scale data in Hefei, China, 2000–2017. *IEEE J. Sel. Top. Appl. Earth Obs. Remote Sens.* **2020**, *13*, 6410–6423. [CrossRef]
64. Long, L.; Yong, Z.; Jiahua, Z. Spatial and dynamic perspectives on surface urban heat island and their relationships with vegetation activity in Beijing, China, based on Moderate Resolution Imaging Spectroradiometer data. *Int. J. Remote Sens.* **2020**, *41*, 882–896. [CrossRef]
65. Wang, X.; Zhang, C.; Dong, N.; Yao, W. Urban heat island effect under different meteorological conditions in Jining of Shandong province. *J. Nanjing Univ. Inf. Sci. Technol.* **2016**, *8*, 160–165. [CrossRef]
66. Hong, F.; Zhan, W.; Göttsche, F.M.; Liu, Z.; Dong, P.; Fu, H.; Fan, H.; Zhang, X. A global dataset of spatiotemporally seamless daily mean land surface temperatures: Generation, validation, and analysis. *Earth Syst. Sci. Data* **2022**, *14*, 3091–3113. [CrossRef]
67. Ma, J.; Shen, H.; Wu, P.; Wu, J.; Gao, M.; Meng, C. Generating gapless land surface temperature with a high spatio-temporal resolution by fusing multi-source satellite-observed and model-simulated data. *Remote Sens. Environ.* **2022**, *278*, 113083. [CrossRef]
68. Berger, C.; Rosentreter, J.; Voltersen, M.; Baumgart, C.; Schmullius, C.; Hese, S. Spatio-temporal analysis of the relationship between 2D/3D urban site characteristics and land surface temperature. *Remote Sens. Environ.* **2017**, *193*, 225–243. [CrossRef]
69. Wang, R.; Wang, M.; Zhang, Z.; Hu, T.; Xing, J.; He, Z.; Liu, X. Geographical detection of urban thermal environment based on the local climate zones: A case study in Wuhan, China. *Remote Sens.* **2022**, *14*, 1067. [CrossRef]
70. Sun, Z.J.; Xie, S.Y. Spatiotemporal variation in net primary productivity and factor detection in Yunnan Province based on geodetector. *Chin. J. Ecol.* **2021**, *40*, 3836–3848. [CrossRef]

Disclaimer/Publisher's Note: The statements, opinions and data contained in all publications are solely those of the individual author(s) and contributor(s) and not of MDPI and/or the editor(s). MDPI and/or the editor(s) disclaim responsibility for any injury to people or property resulting from any ideas, methods, instructions or products referred to in the content.

remote sensing

MDPI

Article

Unexpected Expansion of Rare-Earth Element Mining Activities in the Myanmar–China Border Region

Emmanuel Chinkaka [1,2,*], Julie Michelle Klinger [1], Kyle Frankel Davis [1,3] and Federica Bianco [4,5,6]

[1] Department of Geography and Spatial Sciences, University of Delaware, Newark, DE 19716, USA; klinger@udel.edu (J.M.K.); kfdavis@udel.edu (K.F.D.)
[2] Department of Earth Sciences, Malawi University of Science and Technology, Limbe P.O. Box 5196, Malawi
[3] Department of Plant and Soil Sciences, University of Delaware, Newark, DE 19716, USA
[4] Department of Physics and Astronomy, University of Delaware, Newark, DE 19716, USA; fbianco@udel.edu
[5] Joseph R. Biden, Jr. School of Public Policy and Administration, University of Delaware, Newark, DE 19716, USA
[6] Data Science Institute, University of Delaware, Newark, DE 19716, USA
* Correspondence: echinka@udel.edu; Tel.: +1-(302)-442-1907

Abstract: Mining for rare earth elements is rapidly increasing, driven by current and projected demands for information and energy technologies. Following China's Central Government's 2012 strategy to shift away from mining in favor of value-added processing, primary extraction has increased outside of China. Accordingly, changes in mineral exploitation in China and Myanmar have garnered considerable attention in the past decade. The prevailing assumption is that mining in China has decreased while mining in Myanmar has increased, but the dynamic in border regions is more complex. Our empirical study used Google Earth Engine (GEE) to characterize changes in mining surface footprints between 2005 and 2020 in two rare earth mines located on either side of the Myanmar–China border, within Kachin State in northern Myanmar and Nujiang Prefecture in Yunnan Province in China. Our results show that the extent of the mining activities increased by 130% on China's side and 327% on Myanmar's side during the study period. We extracted surface reflectance images from 2005 and 2010 from Landsat 5 TM and 2015 and 2020 images from Landsat 8 OLI. The Normalized Vegetation Index (NDVI) was applied to dense time-series imagery to enhance landcover categories. Random Forest was used to categorize landcover into mine and non-mine classes with an overall accuracy of 98% and a Kappa Coefficient of 0.98, revealing an increase in mining extent of 2.56 km^2, covering the spatial mining footprint from 1.22 km^2 to 3.78 km^2 in 2005 and 2020, respectively, within the study area. We found a continuous decrease in non-mine cover, including vegetation. Both mines are located in areas important to ethnic minority groups, agrarian livelihoods, biodiversity conservation, and regional watersheds. The finding that mining surface areas increased on both sides of the border is significant because it shows that national-level generalizations do not align with local realities, particularly in socially and environmentally sensitive border regions. The quantification of such changes over time can help researchers and policymakers to better understand the shifting geographies and geopolitics of rare earth mining, the environmental dynamics in mining areas, and the particularities of mineral extraction in border regions.

Keywords: mining extent; rare earth elements; Google Earth Engine; Landsat; change detection; NDVI; geopolitics; remote sensing; Kachin State; Nujiang; Nujiang Prefecture; Yunnan Province

1. Introduction

Rare earth elements (REEs) refer to the fifteen elements that comprise the lanthanide series, ranging in atomic number from 57 (lanthanum) to 71 (lutetium), as well as scandium (Sc) and yttrium (Y) [1]. REEs have garnered heightened attention since 2010 because of China's historic dominance in the sector, the international impacts of China's industrial policy changes, and, more recently, the increased global demand for REEs in the renewable

energy transition [2]. Although rare earth elements are essential inputs to many types of technologies, their usage in renewable energy technologies such as batteries, catalysts, electric vehicles (EVs), and wind turbines [3] has stimulated increased REE exploration programs by various countries [4]. Since the 1990s, China has dominated global REE mining and production, followed by a few other countries, including the United States and Myanmar [5]. Sanctions against Myanmar's military regime [6] and grassroots accounts of mining-driven violence and expropriation in northern Myanmar [7] have intensified concerns around REE supply chain ethics, security, and traceability. In particular, Western firms are under pressure to ensure the REEs used in their technologies are not sourced from Myanmar [7]. This has proven challenging because of the general assumption that REE mining in China has decreased or stopped while production in Myanmar has increased, driven by demand from China. Proving or disproving this is challenging because of the global importance of value-added processing that takes place within China [8]. Mineral processing facilities combine material from many parts of the world, meaning that while it is possible to trace REEs from the mine to the processor and to trace refined materials from the processor to downstream users, the processors, refiners, and smelters are often a kind of 'black box' in mineral commodity flows because they combine raw materials from diverse sources into a single refined product. Therefore, examining the changing footprint of mining activities over time can provide important insights into the actual origins of raw materials, particularly in cross-border regions.

The observations that the decrease in REE mine production in China is related to the expansion of REE mining in Myanmar are broadly accurate, with notable landscape recovery in former rare earth mining areas in Jiangxi Province, China, for example [9]. But this generalization cannot be extrapolated into a causal relationship based on remote sensing analysis alone. Such analyses must be enriched with qualitative research in situ to avoid obscuring important local realities, particularly in sensitive border regions. This study offers empirically substantiated evidence that mining activities are increasing in the region, but increases or decreases in activity are not neatly determined by the location of a deposit relative to national borders. This finding is significant for three major reasons.

First, we have chosen REE mines on either side of the Myanmar–China border, in Kachin State in northern Myanmar and Nujiang Prefecture in Yunnan Province in China, in order to investigate whether policy changes have translated into changing mining footprints on the ground. If the broader narratives are correct and China's strategies to shift from being a net importer of rare earth elements to being a net exporter have had their intended impacts, then we should expect to see increased rare earth mining in Myanmar and a decrease in rare earth mining activity in China in the context of this border region. Our findings show a more complex situation. This raises important questions about the relationship between policy change, geopolitical shifts, and landcover change in extractive border regions and should enrich ongoing debates about the shifting geographies of rare-earth element supply chains.

Second, the emphasis on the importance of rare earth elements for renewable energy infrastructure has intensified concerns around the social and environmental conditions at mining sites. Reports of land theft, threats of violence, and little to no pollution controls in Myanmar illustrate the practical sustainability concerns surrounding the material needs for the renewable energy transition. However, it is important to note that rare earth elements are used in every major form of energy generation, so these concerns should not be treated as unique to renewable energy technology or solely driven by projected demand increases for electric vehicles. Over the past decade, the demand for consumer electronics and military equipment, both major sectors of REE applications, has also increased [10].

Third, mining operations can produce severe environmental degradation, including air pollution, water contamination, and deforestation, as the mine extent expands over time [11–13]. This impairs ecosystem function and landcover dynamics [14,15]. Therefore, it is critical to monitor the development of mining activities on the landscape as a measure of effective environmental protection and mine management. By using open-source data

and demonstrating a novel application of established methods to this particular issue, our study shows one reproducible and adaptable method to investigate this dynamic in other contexts where extractive activities are taking place on both sides of a national border dividing two very different regulatory contexts, such as south Texas, US, and Tamaulipas, Mexico [16], or between Copper Belt, Zambia, and Katanga Province, Democratic Republic of the Congo [17], to name just two examples.

The development of remote sensing technology and sensors has advanced the manner in which mining land surfaces in most areas of the earth's surface can be monitored in a multi-temporal, multi-resolution, and multi-scale manner [12]. Accordingly, many studies have been conducted using satellite remote sensing data to monitor the surface landscape of mining areas in general [18–20] and rare earth mines and impacts in particular [9,21]. Mining and restoration assessment indicators (MRAIs) and land surface temperature (LST) of multi-temporal Landsat TM, ETM+, and OLI images were used by Xie et al. [9] to monitor the impacts of REE mining and restoration on the environment. Vorovencii [22] used a Support Vector Machine (SVM) classifier to detect changes and land restoration in the mining areas using multi-temporal Landsat data in Jiu Valley, Romania. The Normalized Difference Vegetation Index (NDVI), Soil Adjusted Vegetation Index (SAVI), and Modified Soil Adjusted Vegetation Index-2 (MSAVI-2) were used to identify and quantify active mines and reclaimed areas within the study area [22]. The Sentinel-2 satellite imagery dataset was used by Juanda et al. [23] to pinpoint surface areas of land degradation on mining sites using a comparative analysis of vegetation indices. Laari et al. [24] applied a maximum likelihood classifier to determine landcover changes in the mining areas of Wa East District, Ghana, using Landsat ETM imagery. Change detection was utilized by Li et al. [25] to monitor the ground-surface environment in the Lingbei rare earth mining area. The landcover change dynamics in mining areas are an essential indicator for determining the impacts of mining operations [26,27]. Landcover mapping algorithms include Artificial Neural Network (ANN) [28], Support Vector Machine (SVM) [29], Random Forest (RF) [30], and Deep Learning (DL) [31,32]. However, among these classifiers, RF has gained great popularity in landcover mapping due to its higher accuracy and relatively low computational cost [30,33,34]. Currently, the Google Earth Engine (GEE) platform provides access to remotely sensed datasets such as Landsat mission data, Sentinel-2, and MODIS for earth observation analysis [35,36]. It allows fast and powerful tools for landuse and landcover mapping in the cloud, which is efficient in processing big geo-data, including dense time-series images, as applied in this study [37,38]. Therefore, based on the GEE platform, this study analyzes the development of REEs' mining extents from the 2005–2020 period using Landsat missions' satellite data through landcover change detection. Remote sensing imagery for 2005 and 2010 from Landsat 5 TM and 2015 and 2020 images from Landsat 8 Operational Land Imager (OLI) were processed to determine changes in mining and non-mining areas, and a change detection analysis was performed to quantify the landcover change dynamics of mine and non-mine areas. This is part of a larger global study that aims to map, measure, and characterize the shifting geographies of licit and illicit supply networks of several energy-critical materials, including rare earth elements.

2. Materials and Methods

2.1. Study Area

The study area is located in the mining region in the Myanmar–China border in the Myitkyina area in the eastern Kachin State in northern Myanmar and the Nujiang Prefecture area in the western Yunnan Province in southwest China (Figure 1). The study area consists of multiple open-pit mining operations within a long rectangular area located near 98.53°E and 25.89°N, with a total area coverage of about 57.76 km^2. The area is characterized by rough mountainous terrain, extensive plateaus, and very heavy and dense vegetation, with no major urban settlements. It is home to several diverse ethnolinguistic groups and has historically hosted largely autonomous agrarian and agropastoral livelihoods [39,40]. The climate of the study area is subtropical, humid, and highland oceanic [41,42]. Rainfall

occurs mainly in the monsoon season (between June and October) and is between 1900 and 2540 mm on average [43]. This climate context is important to bear in mind when considering the potential impacts of mining activities, particularly on water quality, soil erosion, and landslides that may result from excavation activities in mountainous regions with heavy rainfall.

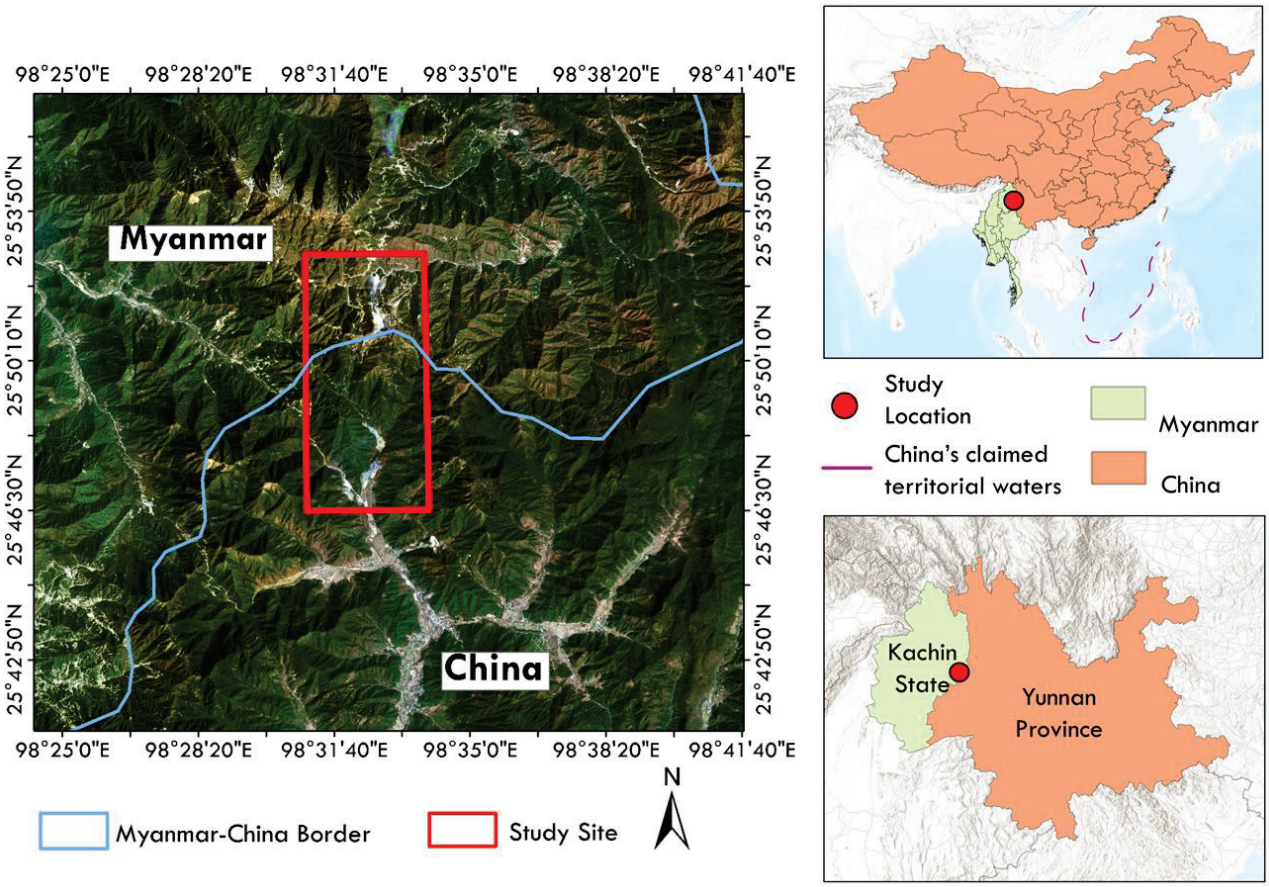

Figure 1. Study area (Myanmar–China border)—Myitkyina (Kachin State) and Nujiang Prefecture (Yunnan Province) and Planet satellite data imagery (RGB = 642, Natural Color Composite).

2.2. Geological and Tectonic Setting

Tectonically, the study area forms part of the Alpine–Himalayan Orogenic Belt and the Indonesian Island Arc System [44]. In the northern part of the area, in Myanmar, the orogenic belt is bent around the Eastern Himalayan Syntaxis into a north–south direction and passes southwards through the resource-rich Indo-Myanmar Ranges, while in the south and eastern parts, in China, the area forms a great part of the Shan Plateau known as the Sibumasu block of rocks [45,46]. The local geology comprises a complex succession of metamorphic rocks (the Mogok–Mandalay–Mergui Belt, Figure 2) that forms the boundary of the Burma Terrane [47]. The area is endowed with mineral resources such as rare earth elements and precious metals, including jadeite and "Burmese Amber" (burmite) [48]. These precious stones were formed due to the metasomatic alteration of peridotites in a subduction zone [49,50].

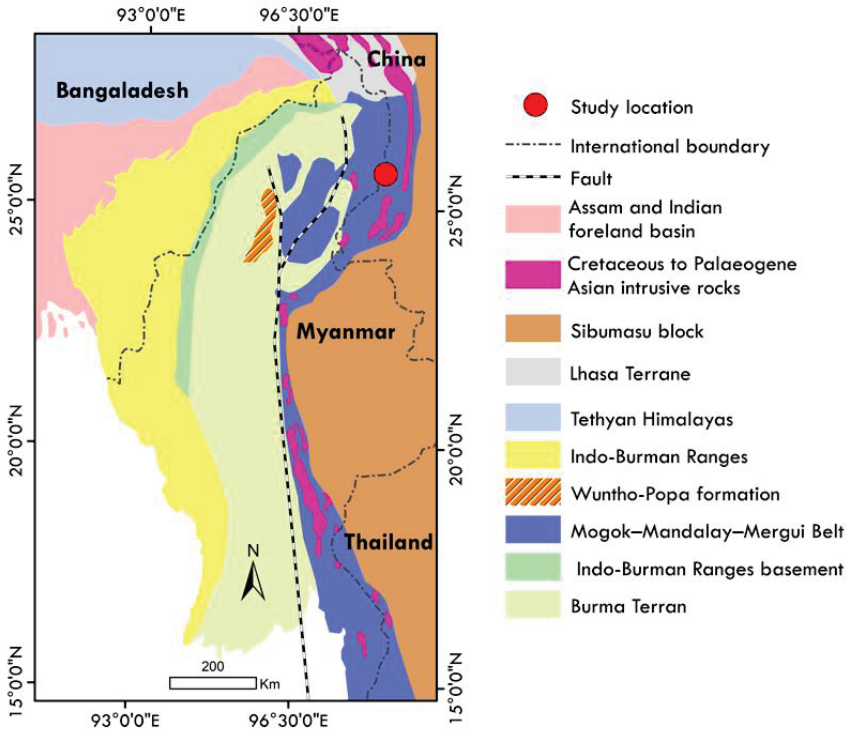

Figure 2. Generalized geologic map of the study area: China–Myanmar border and neighboring countries. Modified from [44].

Detailed geological and mineralogical survey data are not freely available in China and Myanmar; therefore, it is necessary to verify the type of mining activity in the study area to confirm that the mining is indeed for rare earth elements. We utilized satellite remote sensing and the United States Geological Survey (USGS) Spectroscopy Laboratory Library for the hyperspectral signature of rare earth elements and host minerals of monazite to verify the presence of rare earth elements in these mines as described by Karimzadeh and Tangestani [51]. Monazite (Nd, Ce, La, Y, Th) PO_4 is a phosphate of the group of rare earth metals usually found as a comparatively rare accessory mineral in granitic rocks and pegmatites. It is a reddish-brown phosphate mineral that contains rare earth elements, primarily neodymium (Nd) [52]. Neodymium expresses spectral diagnostic absorption features around 0.53 µm, 0.74 µm, 0.80 µm, and 0.87 µm [51]. As such, any spectral absorption features around these frequencies are related to rare earth elements' occurrences. Obtaining a monazite spectrum from a sample or image confirms the presence of rare earth metals. Among the available elements in monazite, neodymium has a unique absorption feature around 0.74 µm. This feature is indicative of monazite presence with multiple rare earth combinations (Nd, Ce, La, Y, Th) [53]. The USGS monazite reflectance sample was obtained from Miguel County, New Mexico, USA, as a pure monazite sample and was analyzed spectroscopically in the USGS Spectroscopy Laboratory to obtain its unique spectral reflectance [54]. We used Sentinel-2 MSI spectral reflectance collected from Sentinel-2 MSI images on an open-pit mine in the study site (Figure 3c, red box) to detect a neodymium diagnostic absorption feature at 0.74 µm. We compared the monazite HS255.3B spectrum (Figure 3a) exhibiting a neodymium absorption feature at 0.74 µm wavelength with various rare earth-bearing minerals, including fluorapatite WS416, goethite WS222, and hematite GDS27 [54]. Following Karimzadeh and Tangestani [51], we compared the USGS spectrum of Monazite HS55.3B [54] resampled to Sentinel-2 MSI bandpasses (Figure 3b) with the Sentinel-2 MSI image spectrum at an open pit with ENVI 5.3 coordinates (X:5455 Y:4081). The retained absorption feature of neodymium at 0.74 µm in Band 6 of Sentinel-2 MSI from the image (Figure 3d) provided a high level of certainty that indeed the mines in the study area are for rare earth elements.

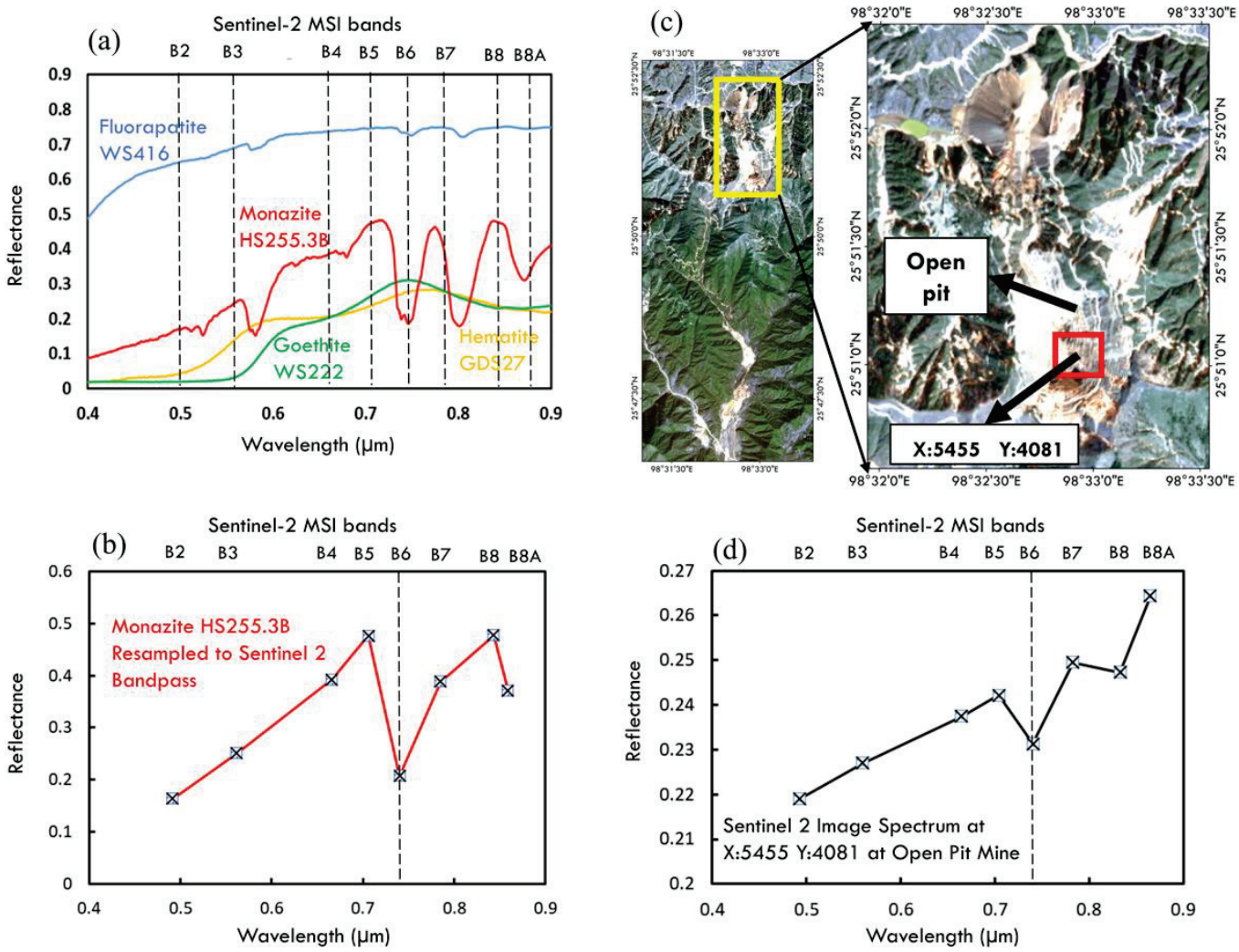

Figure 3. (**a**) Reflectance spectra of fluorapatite, monazite, goethite, and hematite selected from the USGS spectral library [54]; (**b**) Monazite HS255.3B from the USGS Library resampled to Sentinel-2 MSI bandpass for comparison (a vertical line indicates the REE neodymium absorption feature); (**c**) Sentinel-2 MSI imagery with a Natural Color Composite (RGB = 4/3/2) showing study area site in yellow box and the open pit for REE minerals mining in a red box where the image spectrum was extracted at the middle of the open pit (X:5455 Y:4081); (**d**) Sentinel-2 image spectrum from the study site's open-pit mine (X:5455 Y:4081), showing a vertical line indicating the REE neodymium absorption feature, confirming the presence of REEs. In this study, Sentinel-2 MSI has only been used for rare earth mineral confirmation because it has a band configuration that enables the detection of neodymium absorption features, but Sentinel-2's launch dates do not align well with the study period to allow multi-temporal analysis.

2.3. Satellite Data and Image Preprocessing

Landsat 5 Thematic Mapper™ and Landsat 8 OLI time-series imagery from the USGS database (which provides level 1 and level 2 Landsat data (https://espa.cr.usgs.gov/, accessed on 15 October 2022) were extracted in GEE, obtaining geometrically and atmospherically corrected cloud-free time-series reflectance images for the years 2005 to 2020 (Table 1). Landsat missions' datasets are freely available on the GEE platform. This study uses open-source platforms for data access and analysis to increase accessibility, adaptability, and reproducibility. Figure 4 shows the location of the study area.

Table 1. Data description summary.

Sensor	Band Number	Description	Bandwidth (μm)	Resolution (m)
Landsat 5 TM	1	Visible Blue	0.45–0.52	30
	2	Visible Green	0.52–0.60	30
	3	Visible Red	0.63–0.69	30
	4	Near-Infrared 1	0.76–0.90	30
	5	Near-Infrared 2	1.55–1.75	30
	6	Thermal-Infrared	10.40–12.50	120
	7	Mid-Infrared	2.08–2.35	30
Landsat 8 OLI	1	Coastal/Aerosol	0.43–0.45	30
	2	Visible Blue	0.45–0.51	30
	3	Visible Green	0.53–0.59	30
	4	Visible Red	0.64–0.67	30
	5	Near-Infrared	0.85–0.88	30
	6	Shortwave-Infrared 1	1.57–1.65	30
	7	Shortwave-Infrared 2	0.43–0.45	30
	8	Panchromatic	0.50–0.68	15
	9	Cirrus	1.36–1.38	30
	10	Longwave-Infrared 1	10.6–11.19	100
	11	Longwave-Infrared 2	11.5–12.51	100

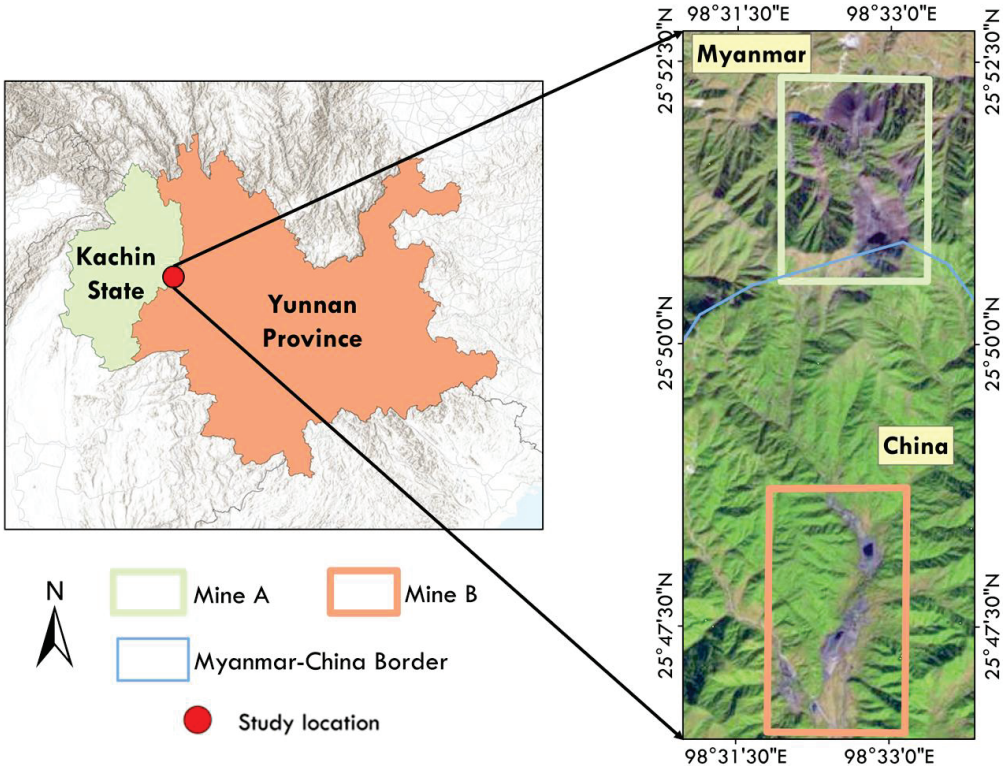

Figure 4. Landsat 8 OLI image for the study area in Natural Color Composite (Red = 4, Green = 3, Blue = 2).

Multi-spectral vegetation indices such as the NDVI measure the ratio of reflectance at different wavelengths as measured in remotely sensed data as a proxy for vegetation health. In particular, the NDVI measures relative reflected energy in the near-infrared wavelengths, which are reflected by healthy chlorophyll, and at red wavelengths [55–57]. We measured the NDVI as an indicator of changes in vegetation in mining areas that may be associated with mining operations [22]. The NDVI, proposed by Rouse et al. [58], is defined as follows (Equation (1)):

$$\mathrm{NDVI} = \frac{\mathrm{NIR} - \mathrm{Red}}{\mathrm{NIR} + \mathrm{Red}} \quad (1)$$

The possible values of the NDVI range between 1 and −1, where 1 indicates a likely high density of green vegetation and 0 or negative values indicate no vegetation [59,60]. Table 2 reports the data specifications of four spectral images that were utilized for landcover mapping and change detection analysis. A detailed methodological flow is illustrated in Figure 5.

Table 2. Specifications of satellite data that were used in the Random Forest image classification.

Sensor	Acquisition Date	Path/Row	Resolution
L5 TM	13 January 2005	167/71	30
L5 TM	13 December 2010	161/71	30
L8 OLI	9 November 2015	161/71	30
L8 OLI	6 December 2020	161/71	30

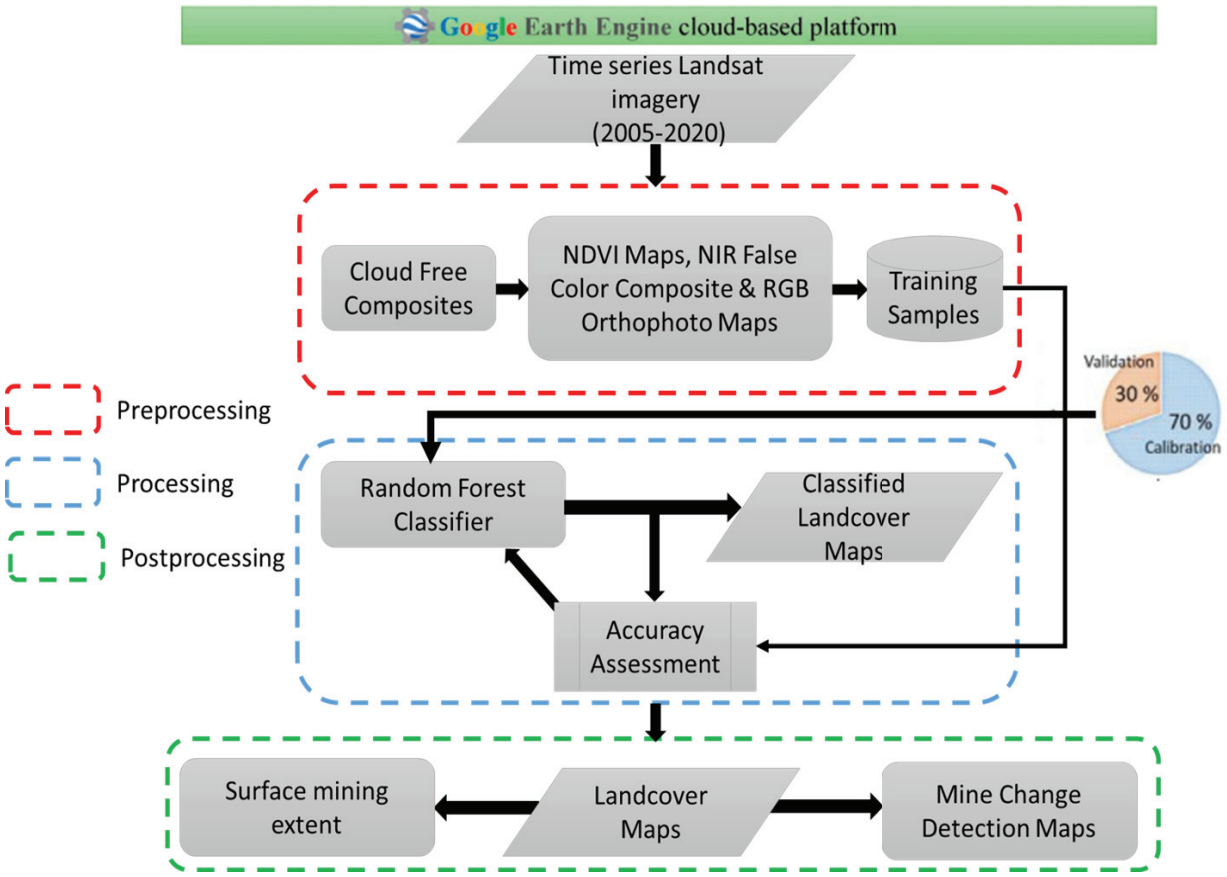

Figure 5. Research Methodology Workflow.

Classification Scheme and Sampling for Ground Truthing

Fieldwork in the study area on this topic is not possible for non-local researchers due to the political sensitivity of claims to mineral resources, including armed violence in northern Myanmar [61]. Therefore, reference data for model training and validation were collected remotely. Territorial conflicts surrounding mining activities in international border regions are not unique to the China–Myanmar context, so in theory, the method presented here can be applied to other contexts where field-based ground truthing is not possible. We applied a remote sensing-based integrated approach to identify pixel areas of interest in the images. This includes simultaneous visual inspection and interpretation of maps generated from Landsat 5TM/8OLI images: NDVI maps, Near Infrared False Color Composite (with band combinations of 4, 3, 2 for Landsat 5 TM and 5, 4, 3 for Landsat 8 OLI), RGB Orthophoto Composite Maps (Natural Color Composite with band combinations of 3, 2, 1 for Landsat 5 TM and 4, 3, 2 for Landsat 8 OLI), and high-resolution Google Earth imagery (Figure 5). This approach allows flexibility in the inclusion of different satellite data types depending on data availability and the research question of interest. While we acknowledge the importance of fieldwork-based ground truthing, we are confident that we were able to obtain a reliable set of reference labels that were used as ground-truth datasets for model training and accuracy assessment. We applied a random design when collecting these reference pixels. Training and validation data were randomly selected across each of the images over the areas of interest (AOIs). Random sampling is extensively used for landuse/landcover mapping, as reported in the literature [12,62–67]. We obtained 282 labels for randomized pixels in the AOIs. Out of these samples, 100 labels were for mine class and 182 labels were for non-mine class (Tables 3 and 4).

Table 3. Landcover classification categories and their corresponding descriptions.

Category	Description
Mine area	Areas with surface mine operations, mine excavated areas, open-pit mine areas, mine wet and dry tailings, mine stockpiles, and mine operation buildings, including mine processing facilities.
Non-mine area	Areas with dense vegetation cover, sparse vegetation cover, mixed vegetation cover, and bare land.

Table 4. Confusion matrix for the accuracy assessment of classified maps (2005, 2010, 2015, and 2020).

Landcover Class	Mine Area	Non-Mine Area	Total	User's Accuracy (%)
		2005		
Mine area	98	1	99	98.99
Non-mine area	2	181	183	98.90
Total	100	182	282	
Producer's Accuracy (%)	98	99.45		
Overall Accuracy (%)		98.94		
Kappa Coefficient		0.9877		
		2010		
Mine area	98	0	98	100
Non-mine area	2	182	184	98.91
Total	100	182	282	
Producer's Accuracy (%)	98	100		
Overall Accuracy (%)		99.29		
Kappa Coefficient		0.9918		

Table 4. *Cont.*

Landcover Class	Mine Area	Non-Mine Area	Total	User's Accuracy (%)
		2015		
Mine area	100	1	101	99
Non-mine area	0	181	181	100
Total	100	182	282	
Producer's Accuracy (%)	100	99.45		
Overall Accuracy (%)		99.64		
Kappa Coefficient		0.9962		
		2020		
Mine area	99	0	99	100
Non-mine area	1	182	183	99.45
Total	100	182	282	
Producer's Accuracy (%)	99	100		
Overall Accuracy (%)		99.64		
Kappa Coefficient		0.9958		

2.4. Random Forest Classification

Random Forest (RF) classification was performed in the GEE platform, categorizing the study site landscape into mine and non-mine areas by labeling pixels within the images [68–71]. RF is a non-parametric machine learning classifier that deploys an ensemble of decision trees, each of which divides input pixels into mutually exclusive groups [30]. An RF classifier is essentially a set of flow charts, or "tree models", where observations (here pixels) are associated into groups based on consecutive binary cuts on subsets of the input features and observations. The cuts are made in the so-called "nodes". The final groups of observations are referred to as "leaves". Each node can be subdivided until it is representative of one of the final classes, but the number of allowed splits can also be limited [72]. RF was chosen in this research due to its higher accuracy and relatively low computational cost [30,65,73]. Tamiminia et al. [74] reviewed 349 GEE peer-reviewed papers in a span of 10 years and showed that RF is the most frequently used classification model for landcover in the remote sensing community. RF models, in particular, are less susceptible to overfitting than single decision trees [30]. The large number of trees, each using a randomized subset of the input features, reduces the correlation between trees. This and the strength of the individual trees control the generalization error of forests. The GEE implementation of the RF classifier algorithm allows control of six model hyperparameters: (1) the number of decision trees to create, (2) the number of variables that are used by each node, (3) the bagged fraction of the input variables for each decision tree, (4) the minimum leaf population, (5) the maximum number of node splits, and (6) a random seed to enable reproducibility [65,75]. Panuju et al. [76] suggest that controlling the number of decision trees to create and the number of variables that are used by each node is a sufficient precaution to limit the risk of overfitting (and we see that our performance on the validation test is extremely high, with minimal to no degradation compared to the training set performance). Our model takes the input of the reflectance at each of the eight wavelengths of bands 1 to 8 for each pixel in each image from each year. In this study, we leave the number of variables that are used by each node set to the default GEE value of the square root of the number of variables ($variablesPerSplit = int\sqrt{8}$). This is consistent with the recommendation of keeping $variablesPerSplit << N_variables$ to prevent overfitting [30,77], while we optimize the number of decision trees, ultimately setting it to 50 based on validation accuracy and visual inspection of the classification results. We separated the reference data into a training and a testing set using a 70:30 ratio, where 70%

of the points were used for model training and the rest for testing. To assert the validity of the classification results [78], we used the Overall Accuracy (OA) and Cohen's Kappa Coefficient (k) in a confusion matrix analysis [79,80], as follows:

$$k = \frac{N \sum_{i=1}^{2} m_{i,i} - \sum_{i=1}^{2} C_i G_i}{N^2 - \sum_{i=1}^{2} C_i G_i} \quad (2)$$

where i stands for the class number, N denotes the total number of classified pixels, $m_{i,i}$ represents the number of pixels of class i that have been assigned to class i, Ci is the total number of classified pixels in class i, and G_i denotes the total number of field data pixels in class i.

2.5. Change Detection

A change matrix depicting changes in mine areas and non-mine areas from the initial analysis year (2005) to the final year of analysis (2020) was computed from the classified maps. To quantify spatiotemporal changes [64,81,82], we generated maps of gains and losses of mine and non-mine cover. Further, change detection statistics were used to compile a detailed tabulation of changes between images acquired during the study period. The open-pit mine area extents and their corresponding quantities from the two identified mines (Mine A in Myanmar and Mine B in China) were extracted from the classified maps. Classified and change analysis area estimate calculations were based on pixel-level calculations of the landcover class, that is, the number of pixels in a particular class. The area changes of the classes, which are mine and non-mine areas in our study case, are a result of the post-classification, which corresponds to the area unit covered by the class pixels [83]. We show the post-classification area change analysis that generates pixel classes of the "from–to" information of binary change maps through change vector analysis [84].

3. Results

3.1. Analysis of Landcover Distribution and Dynamics

The analysis of landcover distribution and expansion over the study area was based on the classified images of the 2005, 2010, 2015, and 2020 RF model classification outputs.

We revealed continued increases in mine areas over the years from 2005 to 2020. The mine area increased from 1.22 km^2 in 2005 to 3.78 km^2 in 2020. The RF model classifier in GEE detected the development of REEs excavations in the open pits and excavated areas shown in red in Figure 6. For instance, the mine area depicted in red patches on the peripherals of the two mine boundaries, mine A and mine B, could be related to possible small-scale mining excavations. The mine areas in the study area show no trace of environmental reclamation or remediation activities. Figure 7 shows that the non-mine area, which is predominantly composed of bare land and dense, thick vegetation, decreased from 56.54 km^2 to 53.98 km^2 over the study period.

Accuracy assessments for the 2005, 2010, 2015, and 2020 images indicated an average overall accuracy of 98% and a Kappa Coefficient of 0.98. This is a good accuracy result based on [85], since the overall accuracies for all classifications were above 85%. The pixel-based landcover classification is appropriate in mining landscapes where the morphology of many mine-related structures is complex and varied, which is a challenge for object detection models. In mining sites, the texture and emissivity of the surfaces are sufficiently distinct, and with a simple classification scheme, as in our case (binary or few-class), there are more risks to the accuracy of object-based analysis than pixel-level analysis.

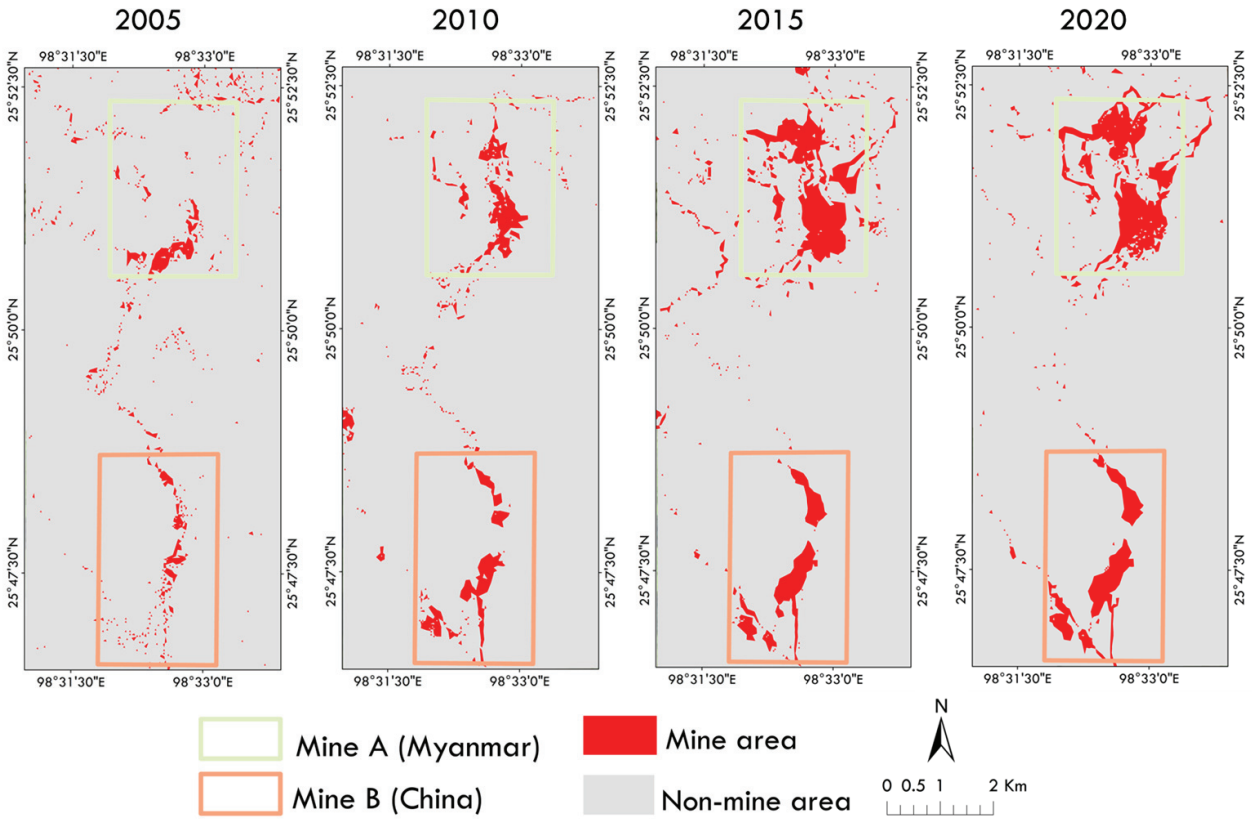

Figure 6. Landcover maps of Landsat-5 and Lansat-8 images using RF classifiers for the years 2005, 2010, 2015, and 2020.

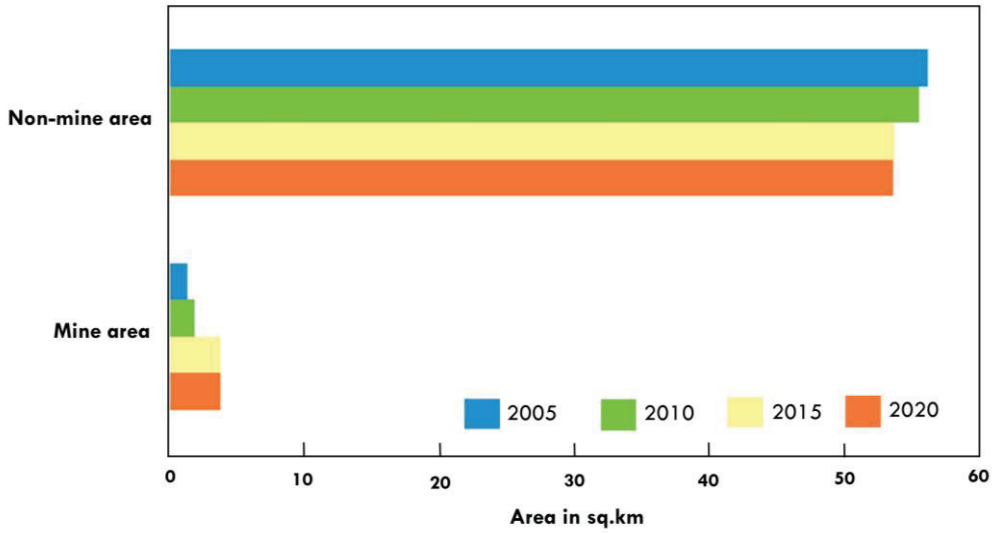

Figure 7. Landcover changes using RF classifier of Landsat-5 and Landsat-8 for the years 2005, 2010, 2015, and 2020.

3.2. Change Detection Trajectories

The post-classification and categorization comparison change detection analysis results show that both the mine areas and non-mine areas have rapidly changed over the study area. The change analysis between 2005 and 2010 shows that the non-mine area has changed to mine area by 1.4 km^2, and, from 2010 to 2015, a non-mine area cover of about 2.2 km^2 was converted to mine area. Further, a total of 1.0 km^2 of non-mine area cover was converted to mine area between 2015 and 2020. This is indicative of active mining operations taking

place in the area (Figure 8). However, the changes from mine area to non-mine area are minimal in comparison to the changes from non-mine area to mine area as depicted in Figure 9. Throughout the period between 2005 and 2020 (Table 5), only 0.64 km^2 of mine area was converted to non-mine area. This could be attributed to abandoned small-scale excavations and is not related to mine area reclamation. Meanwhile, a non-mine area amounting to 3.2 km^2 was converted to mine area within the same period.

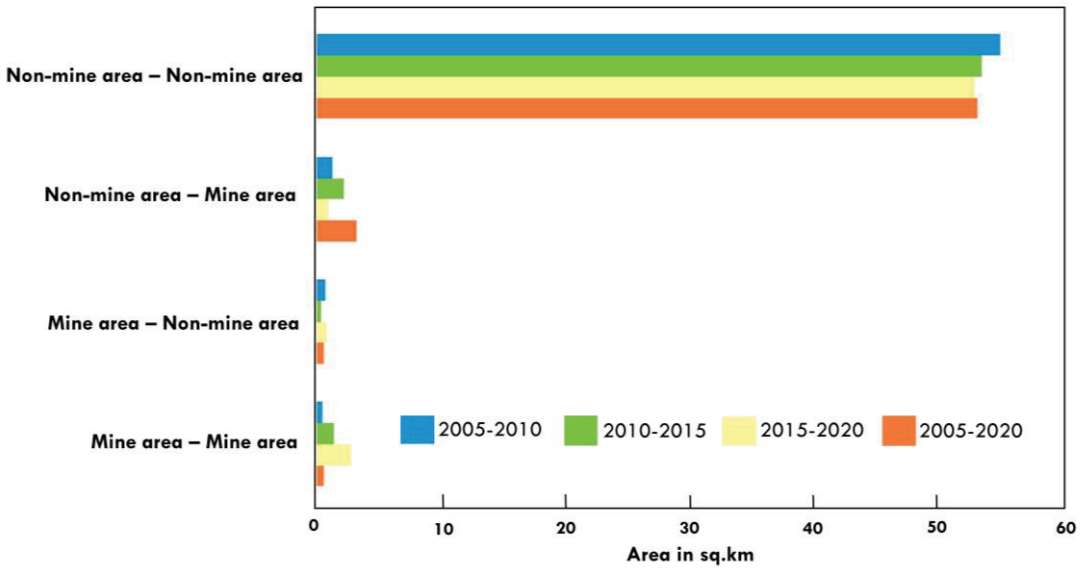

Figure 8. Area change detection quantifications in square kilometers over time: 2005–2020.

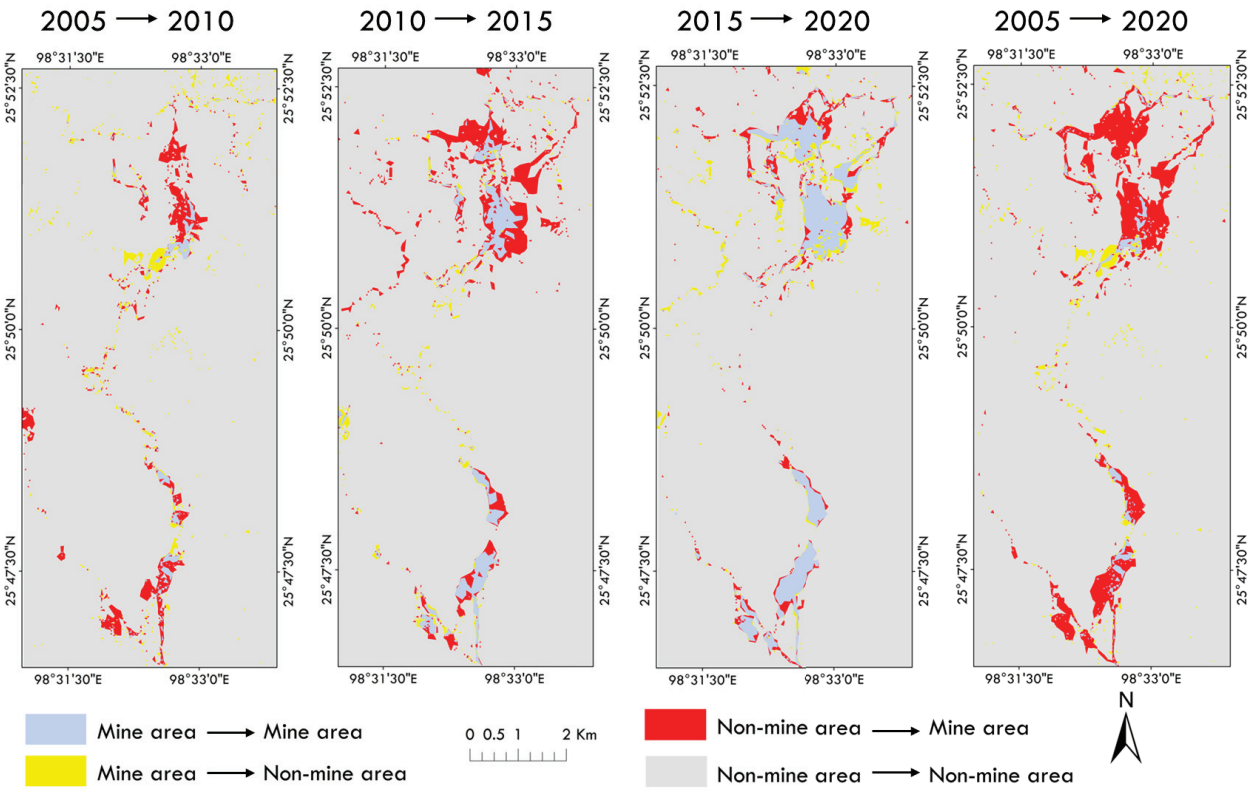

Figure 9. Change detection maps with "from–to" information: Mine area–Mine area, Mine area–Non-mine area, Non-mine area–Mine area, and Non-mine area–Non-mine area.

Table 5. Overall change detection statistics (2005–2020).

Landcover Change	Area Change (km^2)
Mine area–Mine area	0.57
Mine area–Non-mine area	0.64
Non-mine area–Mine area	3.20
Non-mine area–Non-mine area	53.33

3.3. Surface Mining Extent Changes

Rapid growth in the use of energy-critical minerals, including rare earth elements, is raising concerns about supply chain security, the quality of life of the impacted communities, and the need to prevent irreversible damage to the environment [86,87]. Increased mining extents, which usually infer an increase in mining operations, are an indication of the presence of potential environmental and social impacts at the mining sites. Surface mining extent is considered to cover all areas of the mining site operations, including the stock piles, mining dam tailings, mining paths, open-pit rocks, and mining operation buildings [88]. In this study, the concept of mine area has been defined in this holistic manner. Figure 10 shows the expansion of the REEs mining footprint from 2005 to 2020.

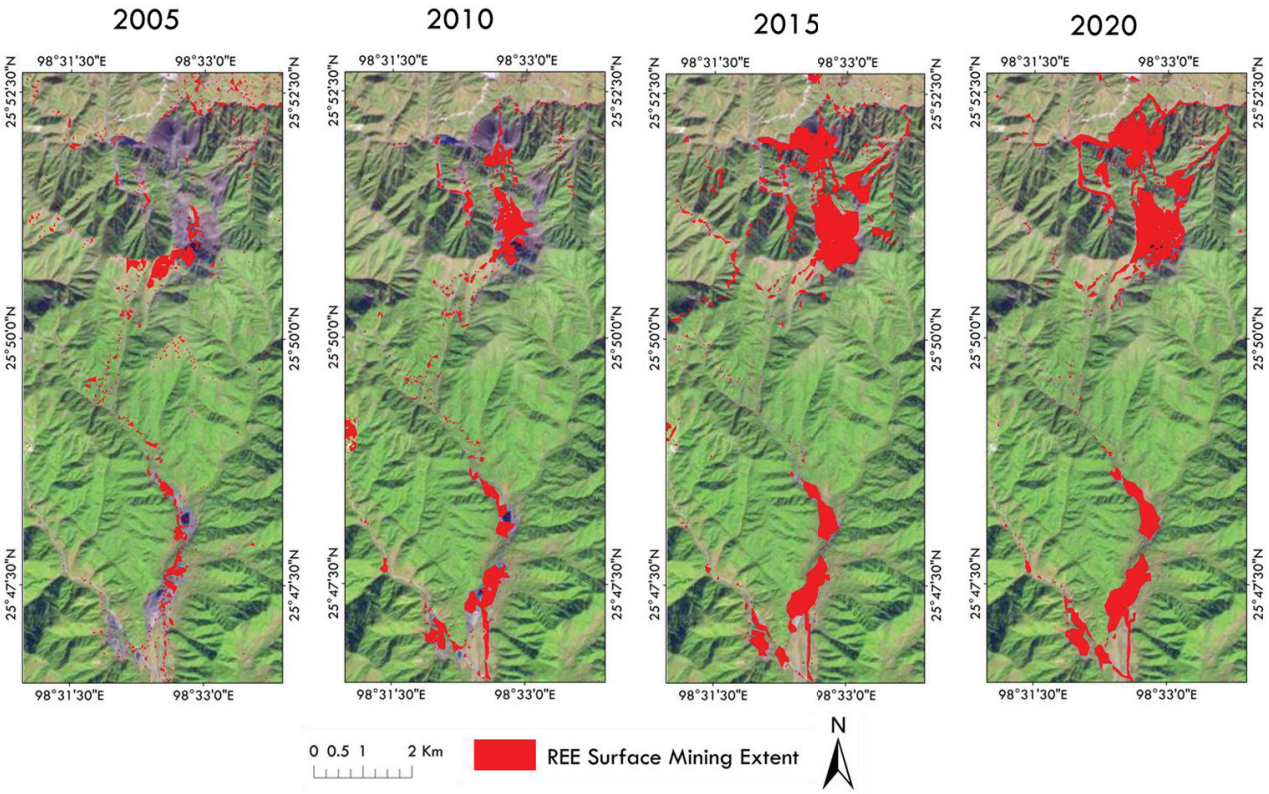

Figure 10. Surface mining extents for 2005, 2010, 2015, and 2020 draped on 2020 Landsat 8 OLI natural color imagery.

Comparison of the Results from Mining Sites with High-Resolution Google Earth Images

In order to validate the automated mapping extent of this study in mining areas, we compared the mining extent changes using high-resolution Google Earth images for the specific years (2005 and 2020) with the results from this study. Mine site A was compared in terms of the development of its mining extent from 2005 (Figure 11a, Google Earth image), which is consistent with the yellow patches in Figure 11c (which indicate the mining extent mapped from this study). The same was performed for 2020 on Google Earth images

(Figure 11b), and it also matched with the results mapped from this study (red patches on Figure 11c). This analysis shows a multi-temporal increase in mining extents.

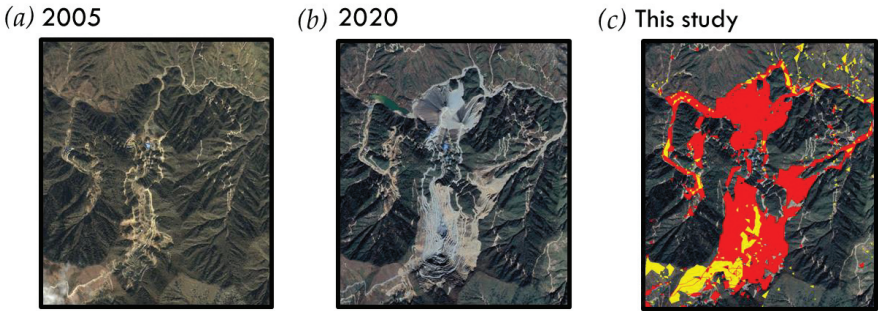

Figure 11. (**a**) Google Earth image for Mine site A in 2005; (**b**) Google Earth image for Mine site A in 2020 illustrating mine area expansion; (**c**) surface mine area expansion analysis result for Mine site A from this study, depicting surface mining extent in 2005 (visualized in yellow) and surface mining extent in 2020 (visualized in red).

Mine site B expansion extents have been illustrated in Figures 12 and 13. These images show the expansion of the mining site from Google Earth images for 2005 (Figures 12a and 13a) and 2020 (Figures 12b and 13b). The results from this study showing the spatial expansion of the mining extent are depicted in Figures 12c and 13c.

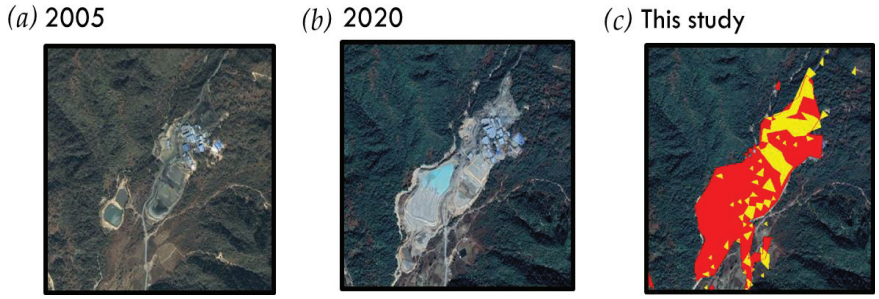

Figure 12. (**a**) Google Earth image for northern part of Mine site B in 2005; (**b**) Google Earth image for northern part of Mine site B in 2020 illustrating mine area expansion; (**c**) surface mine area expansion analysis result for northern part of Mine site B from this study, depicting surface mining extent in 2005 (visualized in yellow) and surface mining extent in 2020 (visualized in red).

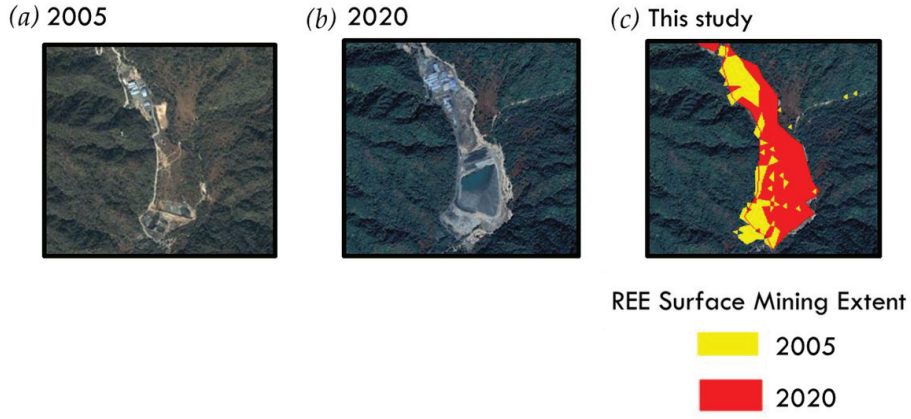

Figure 13. (**a**) Google Earth image for southern part of Mine site B in 2005; (**b**) Google Earth image for part southern of Mine site B in 2020 illustrating mine area expansion; (**c**) surface mine area expansion analysis result for southern part of Mine site B from this study, depicting surface mining extent in 2005 (visualized in yellow) and surface mining extent in 2020 (visualized in red).

4. Discussion

Characterization of Rare Earth Mining Extents and Related Social and Environmental Impacts

Mining covers less than 1% of the Earth's surface [89]. Though this may seem small, open-pit mine operations can cause significant environmental and human health impacts through physical disturbance of the landscape, sedimentation of water bodies, and contamination [90]. The World Bank [91] has listed several sources related to environmental impacts and pollution pathways due to mining activities, including for rare earth elements (Table 6).

Table 6. World Bank list of mining activity related to environmental impacts and pollution pathways [91].

Sources, Environmental Impacts, and Pollution Pathways
• Drainage from mining sites, including processing water discharge and the breaching of mining tailings impoundments;
• Direct dumping of mine/domestic waste;
• Sediment runoff from mining activities;
• Anthropogenic heavy metal pollution of terrestrial and aquatic ecosystems;
• Leaching of pollutants from tailings residues, disposal areas, and contaminated soils;
• Air emissions from mineral-processing diesel equipment;
• Dust emissions.

Decades of REE mining in China have caused considerable environmental degradation [92]. More recent social and environmental harms associated with the expansion of rare earth mining have been reported for Kachin State in northern Myanmar [93,94]. Monitoring the development of surface mining expansion over time and in relation to broader political and economic changes can help better understand and potentially manage these effects. This study shows that surface mine extents throughout the REE mining areas in both China and Myanmar (the area of this study) have increased by 211% from 2005 to 2020. This increase is revealed at a time when there is high global demand for REEs for energy and other technologies, including electric vehicle production [88,89]. A reduction in dense forest inferred from the non-mine cover and the high-resolution Google Earth images of the study site indicate increased land degradation, with no evidence of land or forest reclamation in the area. Our analysis also suggests small-scale mining in the area; through time-series analysis and visual inspection of Google Earth satellite images, we identify several patches that we hypothesize to be small-scale REE excavation areas. Their inconsistency on multiple time-series images indicates that these excavated areas were abandoned at a later stage, allowing the regeneration of trees and suggesting the presence of small-scale excavations around the study area. This can compound social and environmental impacts but requires verification. Figure 14 shows potential negative impacts on surface water from the creek where it is no longer usable for drinking or crop irrigation due to rare earth mining activities in Myanmar's Kachin State [61].

Our findings are contrary to the prevailing narrative that rare earth mining has decreased in China and increased in Myanmar. While overall domestic mining has decreased in China, our study shows that mining has continued to increase in border regions. On the Chinese side of the study area, the REE surface mining extent has increased from 0.63 km^2 to 1.45 km^2, representing a 130% increase in extractive mining area, and on Myanmar's side of the border, the surface mining area extraction has increased by 327% within the same study period, during which the mine area increased from 0.58 km^2 in 2005 to 2.49 km^2 in 2020 (Figure 15). This increase in REE surface mining extents in Myanmar is influenced by its proximity to China, as reported in the literature by Nakano [95], Sophia [96], and Klinger [97].

Figure 14. Environmental impacts from rare earth mines in Myanmar's Kachin State. Local villagers have indicated that water from the creek is no longer usable for drinking or growing crops and that their skin itches after being exposed to water near rare earth mining sites [61].

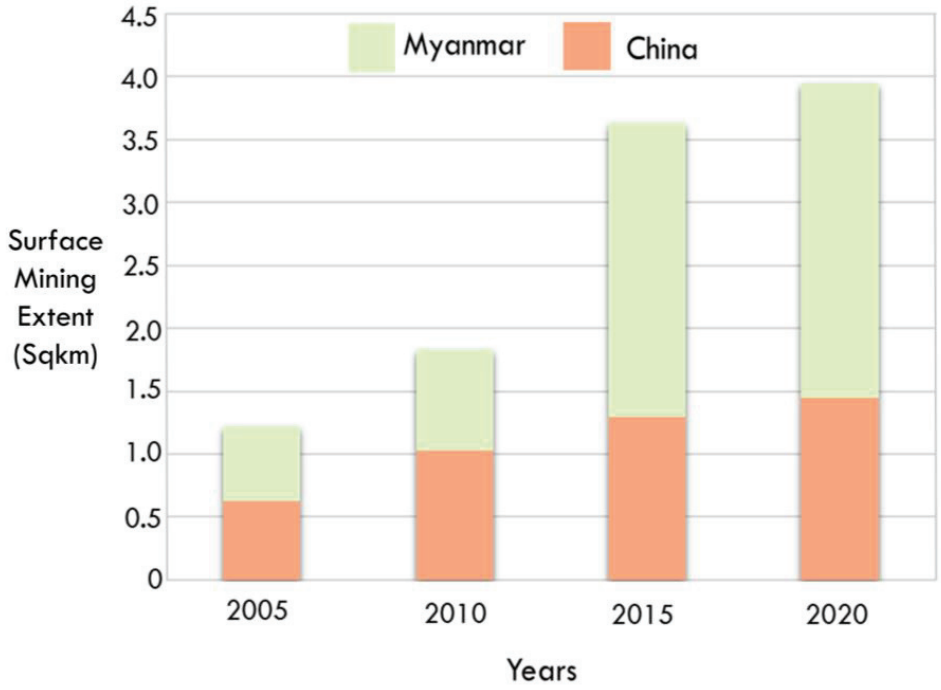

Figure 15. Change in Rare Earth Mining Surface Extents in Myanmar and China (over the study area) between 2005 and 2020.

With projected demand increases, including those driven by the necessary transition to renewable energy to reach net zero by 2050 [98], there is increasing pressure on areas with rare earth elements and other critical raw material reserves. Mining in sensitive border regions (especially when it is occurring against stated government goals) requires improved transparency, as there are many opportunities for those extracted minerals to enter supply chains undetected. Understanding these dynamics more broadly can offer insights into the ways in which REEs are sourced and how their extraction may be better tracked and monitored.

5. Conclusions

In this present study, Landsat 5 TM and Landsat OLI time-series data from 2005 to 2020, in combination with landcover reference data from high-resolution Google Earth images, were used in a machine learning-powered, multi-temporal change detection analysis to map and monitor the development of mining extent activities in the rare earth mining fields of the Myanmar–China geopolitical border within Kachin State in northern Myanmar and the Nujiang Prefecture area in China using the GEE cloud computing platform. We performed a machine learning-supervised Random Forest classification [30] to determine the landcover dynamics in the study area with two main classes: mine area and non-mine area. From the analysis, we noted that the non-mine landcover decreased from 56.54 km^2 to 53.98 km^2, representing a decrease of 4.7%, and the mining area extent increased from 1.22 km^2 to 3.78 km^2. The mine area and non-mine area maps generated in this study showed changes in the landscape over the study period. Such information is crucial to understanding the transformation processes and human–environment interactions within mine sites as mining footprints expand over time. Leveraging the properties of the terrain in the area of interest, with heavy forest cover, this study focused on two main landcover classes: mine and non-mine. The typical size of mine-related landmarks is supported by the low spatial resolution of the Landsat data, which provided temporal coverage over our entire study period of 2005–2020. Access to new innovative commercial satellite data providers with low-cost and high-spatial-resolution datasets could be used to track seasonal or annual changes in mining patterns, including landuse/landcover changes, and the wider landscape related to future REE mining operations on a case-by-case scenario. For instance, the 30 m resolution of Landsat data supports our study because of the typical size of mining areas; using a resolution higher than 30 m is unlikely to make any significant difference in a binary classification, as was the case in this study. It is also critical to consider that spatial resolutions higher than 30 m would increase computational burdens without making significant improvements to the actual results. Our approach has successfully been used in mapping and monitoring the development of surface mine footprint expansion while mapping landcover changes using open-source tools. For similar operations and future research work, we recommend the integrated use of multiple methods as applied in this study for landcover categorization, visual inspection, and interpretation as a standard operating protocol to remotely collect ground-truthing data where fieldwork is not possible. This includes a selection of satellite imagery based on image resolution, the purpose of the landcover analysis, and the temporal scale of the study. Further, simultaneous use of visual inspection and interpretation of maps generated from satellite imagery (NDVI maps, Near Infrared False Color Composite (with band combinations of 4, 3, 2 for Landsat 5 TM and 5, 4, 3 for Landsat 8 OLI), RGB Orthophoto Composite Maps (Natural Color Composite with band combinations of 3, 2, 1 for Landsat 5 TM and 4, 3, 2 for Landsat 8 OLI), and high-resolution Google Earth images) are vital. Our approach allows flexibility in the inclusion of different satellite data types, depending on data availability and the research question of interest. This will contribute to the progress of remote sensing technologies in monitoring surface mining footprints, enhance the development of sustainable resource management initiatives, and potentially contribute to more sustainable mining development between the two neighboring countries.

Author Contributions: Conceptualization, E.C. and J.M.K.; methodology, E.C. and F.B.; formal analysis, E.C.; data curation, E.C. and J.M.K.; writing—original draft preparation, E.C. and J.M.K.; writing—review and editing, F.B., K.F.D., E.C. and J.M.K.; visualization, E.C., F.B. and K.F.D.; supervision, J.M.K.; project administration, J.M.K.; funding acquisition, J.M.K. All authors have read and agreed to the published version of the manuscript.

Funding: This material is based upon work supported by the National Science Foundation under Award No. 2039857. Any opinions, findings and conclusions or recommendations expressed in this material are those of the author(s) and do not necessarily reflect the views of the National Science Foundation.

Data Availability Statement: Administrative boundaries of China and Myanmar were accessed through the DIVA-GIS website (https://www.diva-gis.org/gdata, accessed on 1 November 2020); Planet satellite data was accessed on Planet website (https://www.planet.com/products/planet-imagery/, accessed on 1 February 2023); Landsat 5 TM and Landsat 8 OLI were accessed from the USGS through the Google Earth Engine platform (https://code.earthengine.google.com/, accessed on 15 October 2022); Google Earth images and training (referenced) data were accessed through Google Earth Pro (https://www.google.com/earth/versions/#earth-pro, accessed on 25 October 2022); Sentinel-2 data was downloaded from https://scihub.copernicus.eu/dhus/#/home, accessed on 20 October 2022 and pre-proposed in QGIS (https://www.qgis.org/en/site/forusers/download.html, accessed on 21 October 2022); and the USGS Spectroscopy Laboratory Library for rare earth elements was accessed from https://crustal.usgs.gov/speclab/QueryAll07a.php, accessed on 24 November 2022. The GEE codes were modified from https://www.eefabook.org/, accessed on 18 October 2022 and can be accessed on the Github repository through https://github.com/EmmanuelChinkaka/Monitoring-Mining-Extents, accessed on 3 July 2023. Any further information on the data presented in this work can be obtained from the authors.

Acknowledgments: Special thanks to members of the Klinger Lab, Department of Geography and Spatial Sciences, University of Delaware, and Romain Richaud for working on, and helping with the graphical abstract.

Conflicts of Interest: The authors declare no conflict of interest.

References

1. Wu, B.; Fang, C.; Yu, L.; Huang, X.; Zhang, Q. A Fully Automatic Method to Extract Rare Earth Mining Areas from Landsat Images. *Photogramm. Eng. Remote Sens.* **2016**, *82*, 729–737. [CrossRef]
2. Muavhi, N.; Mavhungu, M.E.; Ndivhudzannyi, R. Mapping of potential rare earth deposits in the Schiel alkaline complex using sentinel-2B multispectral sensor. *Egypt. J. Remote Sens. Space Sci.* **2021**, *24*, 609–617. [CrossRef]
3. Haque, N.; Hughes, A.; Lim, S.; Vernon, C. Rare Earth Elements: Overview of Mining, Mineralogy, Uses, Sustainability and Environmental Impact. *Resources* **2014**, *3*, 614–635. [CrossRef]
4. Nguyen, R.T.; Imholte, D.D. China's Rare Earth Supply Chain: Illegal Production, and Response to new Cerium Demand. *JOM* **2016**, *68*, 1948–1956. [CrossRef]
5. Schlinkert, D.; Boogaart, K.G.v.D. The development of the market for rare earth elements: Insights from economic theory. *Resour. Policy* **2015**, *46*, 272–280. [CrossRef]
6. The White House, United States of America. 31 CFR Part 525—Burma Sanctions Regulations. Available online: https://www.ecfr.gov/current/title-31/subtitle-B/chapter-V/part-525 (accessed on 28 March 2023).
7. Chen, S. 'The Sacrifice Zone': Myanmar Bears Cost of Green Energy | AP News. Available online: https://apnews.com/article/technology-forests-myanmar-75df22e8d7431a6757ea4a426fbde94c (accessed on 28 March 2023).
8. Institute for Energy Research. China and the Rare Earth Supply Chain. IER. 23 February 2021. Available online: https://www.instituteforenergyresearch.org/renewable/china-and-the-rare-earth-supply-chain-policy-brief/ (accessed on 28 March 2023).
9. Xie, L.; Wu, W.; Huang, X.; Ou, P.; Lin, Z.; Zhiling, W.; Song, Y.; Lang, T.; Huangfu, W.; Zhang, Y.; et al. Mining and Restoration Monitoring of Rare Earth Element (REE) Exploitation by New Remote Sensing Indicators in Southern Jiangxi, China. *Remote Sens.* **2020**, *12*, 3558. [CrossRef]
10. Haq, I.U.; Ferreira, P.; Maneengam, A.; Wisetsri, W. Rare Earth Market, Electric Vehicles and Future Mobility Index: A Time-Frequency Analysis with Portfolio Implications. *Risks* **2022**, *10*, 137. [CrossRef]
11. Silva, M.P.d.S.; Câmara, G.; Escada, M.I.S.; de Souza, R.C.M. Remote-sensing image mining: Detecting agents of land-use change in tropical forest areas. *Int. J. Remote Sens.* **2008**, *29*, 4803–4822. [CrossRef]
12. Zhang, M.; He, T.; Li, G.; Xiao, W.; Song, H.; Lu, D.; Wu, C. Continuous Detection of Surface-Mining Footprint in Copper Mine Using Google Earth Engine. *Remote Sens.* **2021**, *13*, 4273. [CrossRef]
13. Soni, A.K. Estimation of Mine Water Quantity: Development of Guidelines for Indian Mines. *Mine Water Environ.* **2020**, *39*, 397–406. [CrossRef]
14. Nascimento, F.S.; Gastauer, M.; Souza-Filho, P.W.M.; Nascimento, W.R.; Santos, D.C.; Costa, M.F. Land Cover Changes in Open-Cast Mining Complexes Based on High-Resolution Remote Sensing Data. *Remote Sens.* **2020**, *12*, 611. [CrossRef]
15. Luo, P.; Han, X.; Chen, N. Study on Complexity Planning Model of Pumped Storage in Abandoned Open-Pit Mine: A Case Study of Fushun Open-Pit Mine. *Front. Earth Sci.* **2022**, *10*, 808371. [CrossRef]

16. Page, W.R.; VanSistine, D.P.; Turner, K.J. *Preliminary Geologic Map of Southernmost Texas, United States, and Parts of Tamaulipas and Nuevo Leon, Mexico: Environmental Health Investigations in the United States-Mexico Border Region*; U.S. Geological Survey: Denver, CO, USA, 2005. Available online: https://pubs.usgs.gov/of/2005/1409/ (accessed on 21 August 2023).
17. Rubbers, B. *Inside Mining Capitalism: The Micropolitics of Work on the Congolese and Zambian Copperbelts*; Boydell & Brewer: Suffolk, UK, 2021. [CrossRef]
18. Chaussard, E.; Kerosky, S. Characterization of Black Sand Mining Activities and Their Environmental Impacts in the Philippines Using Remote Sensing. *Remote Sens.* **2016**, *8*, 100. [CrossRef]
19. Mimouni, M.E.; Aarab, A.; Lakhloufi, A.; Hamzaoui, A.; Benammi, E.M.; Benyas, K. New Targets of Potential Mining Interest Using Gravimetric and Satellite Data: Case Study of Hercynian Rehamna Massif, Morocco. *Iraqi Geol. J.* **2022**, *55*, 14–26. [CrossRef]
20. Brown, C.; Boyd, D.S.; Kara, S. Landscape Analysis of Cobalt Mining Activities from 2009 to 2021 Using Very High Resolution Satellite Data (Democratic Republic of the Congo). *Sustainability* **2022**, *14*, 9545. [CrossRef]
21. Zhiqiang, L.; Peihong, L.; Yimin, Y. Research on Multi-scale Segmentation of Remote Sensing Images of Typical Feature in Rare Earth Mining Area. *IOP Conf. Ser. Earth Environ. Sci.* **2021**, *671*, 012025. [CrossRef]
22. Vorovencii, I. Changes detected in the extent of surface mining and reclamation using multitemporal Landsat imagery: A case study of Jiu Valley, Romania. *Environ. Monit. Assess.* **2021**, *193*, 30. [CrossRef]
23. Juanda, E.T.; Martono, D.N.; Saria, L. Analysis vegetation change on coal mine reclamation using Normalized Difference Vegetation Index (NDVI). *IOP Conf. Ser. Earth Environ. Sci.* **2021**, *716*, 012035. [CrossRef]
24. Basommi, P.L.; Guan, Q.; Cheng, D. Exploring Land use and Land cover change in themining areas of Wa East District, Ghana usingSatellite Imagery. *Open Geosci.* **2015**, *7*, 20150058. [CrossRef]
25. Li, H.; Wu, L.; Liu, X. Change detection of ground-surface environment in rare earth mining area based on multi-temporal remote sensing: A case in Lingbei rare earth mining area. *Zhongguo Kuangye Daxue Xuebao J. China Univ. Min. Technol.* **2014**, *43*, 1087–1094.
26. Rawat, J.; Kumar, M. Monitoring land use/cover change using remote sensing and GIS techniques: A case study of Hawalbagh block, district Almora, Uttarakhand, India. *Egypt. J. Remote Sens. Space Sci.* **2015**, *18*, 77–84. [CrossRef]
27. Arıkan, C.; Tümer, İ.N.; Aksoy, S.; Sertel, E. Determination of burned areas using Sentinel-2A imagery and machine learning classification algorithms. *Intercont. Geoinf. Days* **2022**, *4*, 43–46.
28. Korytkowski, M.; Rutkowski, L.; Scherer, R. Fast image classification by boosting fuzzy classifiers. *Inf. Sci.* **2016**, *327*, 175–182. [CrossRef]
29. Sanghvi, K.; Aralkar, A.; Sanghvi, S.; Saha, I. A Survey on Image Classification Techniques. *SSRN Electron. J.* **2021**. [CrossRef]
30. Breiman, L. Random forests. *Mach. Learn.* **2001**, *45*, 5–32. [CrossRef]
31. Naushad, R.; Kaur, T.; Ghaderpour, E. Deep Transfer Learning for Land Use and Land Cover Classification: A Comparative Study. *Sensors* **2021**, *21*, 8083. [CrossRef]
32. Alzubaidi, L.; Zhang, J.; Humaidi, A.J.; Al-Dujaili, A.; Duan, Y.; Al-Shamma, O.; Santamaría, J.; Fadhel, M.A.; Al-Amidie, M.; Farhan, L. Review of deep learning: Concepts, CNN architectures, challenges, applications, future directions. *J. Big Data* **2021**, *8*, 53. [CrossRef]
33. Thanh Noi, P.; Kappas, M. Comparison of Random Forest, k-Nearest Neighbor, and Support Vector Machine Classifiers for Land Cover Classification Using Sentinel-2 Imagery. *Sensors* **2018**, *18*, 18. [CrossRef]
34. Khelifi, L.; Mignotte, M. Deep Learning for Change Detection in Remote Sensing Images: Comprehensive Review and Meta-Analysis. *IEEE Access* **2020**, *8*, 126385–126400. [CrossRef]
35. Gorelick, N.; Hancher, M.; Dixon, M.; Ilyushchenko, S.; Thau, D.; Moore, R. Google Earth Engine: Planetary-scale geospatial analysis for everyone. *Remote Sens. Environ.* **2017**, *202*, 18–27. [CrossRef]
36. Bahşi, K.; Ustaoglu, B.; Aksoy, S.; Sertel, E. Estimation of emissions from crop residue burning in Türkiye using remotely sensed data and the Google Earth Engine platform. *Geocarto Int.* **2022**, *38*, 2157052. [CrossRef]
37. Huang, H.; Chen, Y.; Clinton, N.; Wang, J.; Wang, X.; Liu, C.; Gong, P.; Yang, J.; Bai, Y.; Zheng, Y.; et al. Mapping major land cover dynamics in Beijing using all Landsat images in Google Earth Engine. *Remote Sens. Environ.* **2017**, *202*, 166–176. [CrossRef]
38. Bayrakdar, H.Y.; Kavlak, M.; Yilmazel, B.; Çabuk, A. Assessing the performance of machine learning algorithms in Google Earth Engine for land use and land cover analysis: A case study of Muğla province, Türkiye. *J. Des. Resil. Arch. Plan.* **2022**, *3*, 224–236. [CrossRef]
39. Woods, K. Expansion of Agribusiness in Myanmar: Driver of deforestation, conversion timber and land conflicts in Myanmar. 2015. Available online: https://www.forest-trends.org/publications/commercial-agriculture-expansion-in-myanmar-links-to-deforestation-conversion-timber-and-land-conflicts/ (accessed on 29 March 2023).
40. Ting, Z. A Study of the Impacts of Shifting Cultivation on the Environment and Local People in Kachin State, Myanmar. 2014. Available online: https://www.academia.edu/49165530/A_Study_of_the_Impacts_of_Shifting_Cultivation_on_the_Environment_and_Local_People_in_Kachin_State_Myanmar (accessed on 29 March 2023).
41. Sun, H.; Wang, J.; Xiong, J.; Bian, J.; Jin, H.; Cheng, W.; Li, A. Vegetation Change and Its Response to Climate Change in Yunnan Province, China. *Adv. Meteorol.* **2021**, *2021*, 8857589. [CrossRef]
42. Ranjitkar, S.; Sujakhu, N.M.; Lu, Y.; Wang, Q.; Wang, M.; He, J.; Mortimer, P.E.; Xu, J.; Kindt, R.; Zomer, R.J. Climate modelling for agroforestry species selection in Yunnan Province, China. *Environ. Model. Softw.* **2016**, *75*, 263–272. [CrossRef]
43. Zomer, R.J.; Xu, J.; Wang, M.; Trabucco, A.; Li, Z. Projected impact of climate change on the effectiveness of the existing protected area network for biodiversity conservation within Yunnan Province, China. *Biol. Conserv.* **2015**, *184*, 335–345. [CrossRef]

44. Licht, A.; Dupont-Nivet, G.; Win, Z.; Swe, H.H.; Kaythi, M.; Roperch, P.; Ugrai, T.; Littell, V.; Park, D.; Westerweel, J.; et al. Paleogene evolution of the Burmese forearc basin and implications for the history of India-Asia convergence. *GSA Bull.* **2018**, *131*, 730–748. [CrossRef]
45. The Geology of Burma (Myanmar): An Annotated Bibliography of Burma's Geology, Geography and Earth Science. Available online: https://www.researchgate.net/publication/235104805_The_Geology_of_Burma_Myanmar_An_Annotated_Bibliography_of_Burma\T1\textquoterights_Geology_Geography_and_Earth_Science (accessed on 12 January 2023).
46. Barber, T. Book Review. *Am. Miner.* **2020**, *105*, 287–288. [CrossRef]
47. Westerweel, J.; Roperch, P.; Licht, A.; Dupont-Nivet, G.; Win, Z.; Poblete, F.; Ruffet, G.; Swe, H.H.; Thi, M.K.; Aung, D.W. Burma Terrane part of the Trans-Tethyan arc during collision with India according to palaeomagnetic data. *Nat. Geosci.* **2019**, *12*, 863–868. [CrossRef]
48. Searle, M.P.; Morley, C.K.; Waters, D.J.; Gardiner, N.J.; Htun, U.K.; Nu, T.T.; Robb, L.J. Chapter 12 Tectonic and metamorphic evolution of the Mogok Metamorphic and Jade Mines belts and ophiolitic terranes of Burma (Myanmar). *Geol. Soc. Lond. Mem.* **2017**, *48*, 261–293. [CrossRef]
49. Parlak, O.; Delaloye, M.; Bíngöl, E. Mineral chemistry of ultramafic and mafic cumulates as an indicator of the arc-related origin of the Mersin ophiolite (southern Turkey). *Int. J. Earth Sci.* **1996**, *85*, 647–661. [CrossRef]
50. Liu, T.; Liu, C.; Chen, Y.; Guo, S.; Sein, K.; Dong, X. Petrology and geochemistry of ultramafic rocks in the Mogok belt, Myanmar: Cumulates from high-pressure crystallization of hydrous arc melts. *Geol. J.* **2021**, *57*, 886–905. [CrossRef]
51. Karimzadeh, S.; Tangestani, M.H. Potential of Sentinel-2 MSI data in targeting rare earth element (Nd3+) bearing minerals in Esfordi phosphate deposit, Iran. *Egypt. J. Remote Sens. Space Sci.* **2022**, *25*, 697–710. [CrossRef]
52. Lavenir, N.M.J.; Cyrille, S.; Paul, N.J.; Suh, C.E. Mineral chemistry (EMPA) of monazites in metamorphic rocks from Edea region: Implications of the monazite chemistry on the metamorphic evolution of the Nyong Complex. *Arab. J. Geosci.* **2022**, *15*, 1665. [CrossRef]
53. Purwadi, I.; van der Werff, H.; Lievens, C. Targeting rare earth element bearing mine tailings on Bangka Island, Indonesia, with Sentinel-2 MSI. *Int. J. Appl. Earth Obs. Geoinf.* **2020**, *88*, 102055. [CrossRef]
54. Kokaly, R.F.; Clark, R.N.; Swayze, G.A.; Livo, K.E.; Hoefen, T.M.; Pearson, N.C.; Wise, R.A.; Benzel, W.M.; Lowers, H.A.; Driscoll, R.L.; et al. *USGS Spectral Library Version 7*; U.S. Geological Survey: Reston, VA, USA, 2017; 61p. [CrossRef]
55. Ditian; Devy, M.; Eko, W.; Sanjaya, H.; Hartono, R. Mangrove Extent and Change Mapping of Muaragembong from 1990 to 2020 using Google Earth Engine (GEE). In Proceedings of the IEEE Ocean Engineering Technology and Innovation Conference: Ocean Observation, Technology and Innovation in Support of Ocean Decade of Science (OETIC), Jakarta, Indonesia, 8–9 November 2021; Sanjaya, H., Ed.; pp. 35–38. [CrossRef]
56. Liu, Y.; Xie, M.; Liu, J.; Wang, H.; Chen, B. Vegetation Disturbance and Recovery Dynamics of Different Surface Mining Sites via the LandTrendr Algorithm: Case Study in Inner Mongolia, China. *Land* **2022**, *11*, 856. [CrossRef]
57. Ma, C.; Guo, Z.-Z.; Zhang, X.-K.; Han, R.-M. Annual integral changes of time serial NDVI in mining subsidence area. *Trans. Nonferrous Met. Soc. China* **2011**, *21*, s583–s588. [CrossRef]
58. Rouse, J.W.; Haas, R.H.; Schell, J.A.; Deering, D.W. Monitoring vegetation systems in the Great Plains with ERTS. In *Third Earth Resources Technology Satellite-1 Symposium*; NASA Sp-351 I: Greenbelt, MA, USA, 1973; Volume 351, pp. 309–317.
59. Fan, X.; Guan, Y.; Bai, Z.; Zhou, W.; Zhu, C. Optimization of Reclamation Measures in a Mining Area by Analysis of Variations in Soil Nutrient Grades under Different Types of Land Usage—A Case Study of Pingshuo Coal Mine, China. *Land* **2022**, *11*, 321. [CrossRef]
60. Liu, X.; Cao, Y.; Bai, Z.; Wang, J.; Zhou, W. Evaluating relationships between soil chemical properties and vegetation cover at different slope aspects in a reclaimed dump. *Environ. Earth Sci.* **2017**, *76*, 805. [CrossRef]
61. China-led Rare Earth Mining in Myanmar Fuels Rights Abuses, Pollution: Report. Radio Free Asia. Available online: https://www.rfa.org/english/news/myanmar/rareearths-08092022183340.html (accessed on 4 April 2023).
62. Hansen, M.C.; Roy, D.P.; Lindquist, E.; Adusei, B.; Justice, C.O.; Altstatt, A. A method for integrating MODIS and Landsat data for systematic monitoring of forest cover and change in the Congo Basin. *Remote Sens. Environ.* **2008**, *112*, 2495–2513. [CrossRef]
63. Rabiei-Dastjerdi, H.; Amini, S.; McArdle, G.; Homayouni, S. City-region or city? That is the question: Modelling sprawl in Isfahan using geospatial data and technology. *GeoJournal* **2022**. [CrossRef]
64. Zhu, Z.; Zhang, Z.; Zuo, L.; Pan, T.; Zhao, X.; Wang, X.; Sun, F.; Xu, J.; Liu, Z. Study on the Classification and Change Detection Methods of Drylands in Arid and Semi-Arid Regions. *Remote Sens.* **2022**, *14*, 1256. [CrossRef]
65. Amini, S.; Saber, M.; Rabiei-Dastjerdi, H.; Homayouni, S. Urban Land Use and Land Cover Change Analysis Using Random Forest Classification of Landsat Time Series. *Remote Sens.* **2022**, *14*, 2654. [CrossRef]
66. Zhai, H.; Lv, C.; Liu, W.; Yang, C.; Fan, D.; Wang, Z.; Guan, Q. Understanding Spatio-Temporal Patterns of Land Use/Land Cover Change under Urbanization in Wuhan, China, 2000–2019. *Remote Sens.* **2021**, *13*, 3331. [CrossRef]
67. Tu, Y.; Chen, B.; Zhang, T.; Xu, B. Regional Mapping of Essential Urban Land Use Categories in China: A Segmentation-Based Approach. *Remote Sens.* **2020**, *12*, 1058. [CrossRef]
68. Pal, M. Random forest classifier for remote sensing classification. *Int. J. Remote Sens.* **2005**, *26*, 217–222. [CrossRef]
69. Somayajula, V.K.; Ghai, D.; Kumar, S. Land Use/Land Cover Change Analysis Using NDVI, PCA. In Proceedings of the 5th International Conference on Computing Methodologies and Communication (ICCMC), Erode, India, 8–10 April 2021; pp. 849–855. [CrossRef]

70. Madanian, M.; Soffianian, A.R.; Koupai, S.S.; Pourmanafi, S.; Momeni, M. Analyzing the effects of urban expansion on land surface temperature patterns by landscape metrics: A case study of Isfahan city, Iran. *Environ. Monit. Assess.* **2018**, *190*, 189. [CrossRef]
71. Mantero, P.; Moser, G.; Serpico, S. Partially Supervised classification of remote sensing images through SVM-based probability density estimation. *IEEE Trans. Geosci. Remote Sens.* **2005**, *43*, 559–570. [CrossRef]
72. Wulder, M.A.; Li, Z.; Campbell, E.M.; White, J.C.; Hobart, G.; Hermosilla, T.; Coops, N.C. A National Assessment of Wetland Status and Trends for Canada's Forested Ecosystems Using 33 Years of Earth Observation Satellite Data. *Remote Sens.* **2018**, *10*, 1623. [CrossRef]
73. Lechner, M.; Dostálová, A.; Hollaus, M.; Atzberger, C.; Immitzer, M. Combination of Sentinel-1 and Sentinel-2 Data for Tree Species Classification in a Central European Biosphere Reserve. *Remote Sens.* **2022**, *14*, 2687. [CrossRef]
74. Tamiminia, H.; Salehi, B.; Mahdianpari, M.; Quackenbush, L.; Adeli, S.; Brisco, B. Google Earth Engine for geo-big data applications: A meta-analysis and systematic review. *ISPRS J. Photogramm. Remote Sens.* **2020**, *164*, 152–170. [CrossRef]
75. Rudiastuti, A.W.; Lumban-Gaol, Y.; Silalahi, F.E.S.; Prihanto, Y.; Pranowo, W.S. Implementing Random Forest Algorithm in GEE: Separation and Transferability on Built-Up Area in Central Java, Indonesia. *JOIV Int. J. Inform. Vis.* **2022**, *6*, 74–82. [CrossRef]
76. Maxwell, A.E.; Warner, T.A.; Fang, F. Implementation of machine-learning classification in remote sensing: An applied review. *Int. J. Remote Sens.* **2018**, *39*, 2784–2817. [CrossRef]
77. Phan, T.N.; Kuch, V.; Lehnert, L.W. Land Cover Classification using Google Earth Engine and Random Forest Classifier—The Role of Image Composition. *Remote Sens.* **2020**, *12*, 2411. [CrossRef]
78. He, H.; Garcia, E.A. Learning from Imbalanced Data. *IEEE Trans. Knowl. Data Eng.* **2009**, *21*, 1263–1284. [CrossRef]
79. Więckowska, B.; Kubiak, K.B.; Jóźwiak, P.; Moryson, W.; Stawińska-Witoszyńska, B. Cohen's Kappa Coefficient as a Measure to Assess Classification Improvement following the Addition of a New Marker to a Regression Model. *Int. J. Environ. Res. Public Health* **2022**, *19*, 10213. [CrossRef]
80. de Raadt, A.; Warrens, M.J.; Bosker, R.J.; Kiers, H.A.L. A Comparison of Reliability Coefficients for Ordinal Rating Scales. *J. Classif.* **2021**, *38*, 519–543. [CrossRef]
81. Meier, J.; Mauser, W. Irrigation Mapping at Different Spatial Scales: Areal Change with Resolution Explained by Landscape Metrics. *Remote Sens.* **2023**, *15*, 315. [CrossRef]
82. Zhang, C.; Dong, J.; Zuo, L.; Ge, Q. Tracking spatiotemporal dynamics of irrigated croplands in China from 2000 to 2019 through the synergy of remote sensing, statistics, and historical irrigation datasets. *Agric. Water Manag.* **2022**, *263*, 107458. [CrossRef]
83. Panuju, D.R.; Paull, D.J.; Griffin, A.L. Change Detection Techniques Based on Multispectral Images for Investigating Land Cover Dynamics. *Remote Sens.* **2020**, *12*, 1781. [CrossRef]
84. Reis, M.S.; Dutra, L.V.; Sant'anna, S.J.S.; Escada, M.I.S. Examining Multi-Legend Change Detection in Amazon with Pixel and Region Based Methods. *Remote Sens.* **2017**, *9*, 77. [CrossRef]
85. Baig, M.F.; Mustafa, M.R.U.; Baig, I.; Takaijudin, H.B.; Zeshan, M.T. Assessment of Land Use Land Cover Changes and Future Predictions Using CA-ANN Simulation for Selangor, Malaysia. *Water* **2022**, *14*, 402. [CrossRef]
86. Rakhmangulov, A.; Burmistrov, K.; Osintsev, N. Selection of Open-Pit Mining and Technical System's Sustainable Development Strategies Based on MCDM. *Sustainability* **2022**, *14*, 8003. [CrossRef]
87. Zhou, Y.; Zhou, W.; Lu, X.; Jiskani, I.M.; Cai, Q.; Liu, P.; Li, L. Evaluation Index System of Green Surface Mining in China. *Mining, Metall. Explor.* **2020**, *37*, 1093–1103. [CrossRef]
88. Dutta, T.; Kim, K.-H.; Uchimiya, M.; Kwon, E.E.; Jeon, B.-H.; Deep, A.; Yun, S.-T. Global demand for rare earth resources and strategies for green mining. *Environ. Res.* **2016**, *150*, 182–190. [CrossRef]
89. LaJeunesse Connette, K.J.; Connette, G.; Bernd, A.; Phyo, P.; Aung, K.H.; Tun, Y.L.; Thein, Z.M.; Horning, N.; Leimgruber, P.; Songer, M. Assessment of Mining Extent and Expansion in Myanmar Based on Freely-Available Satellite Imagery. *Remote Sens.* **2016**, *8*, 912. [CrossRef]
90. Dlamini, L.Z.D.; Xulu, S. Monitoring Mining Disturbance and Restoration over RBM Site in South Africa Using LandTrendr Algorithm and Landsat Data. *Sustainability* **2019**, *11*, 6916. [CrossRef]
91. D'Souza, K. *Artisanal Mining in the DRC: Key Issues, Challenges and Opportunities*; Communities and Small-Scale Mining; World Bank: Washington, DC, USA, 2007; Available online: https://delvedatabase.org/uploads/resources/2007_CASM_DSouza_DRC-Artisianal-Mining-Key-Issues-Challenges-Opportunities.pdf (accessed on 4 April 2023).
92. Klinger, J.M. Social and Environmental Impacts of Rare Earth Mining, Processing, and Proliferation: Scoping and Preliminary Assessment. In *Critical Minerals, the Climate Crisis and the Tech Imperium*; Kalantzakos, S., Ed.; Springer Nature Switzerland: Cham, Switzerland, 2023; pp. 149–165. [CrossRef]
93. Rare Earths in Myanmar: Unobtanium? Available online: https://thediplomat.com/2021/06/rare-earths-in-myanmar-unobtanium/ (accessed on 4 April 2023).
94. Zapp, P.; Schreiber, A.; Marx, J.; Kuckshinrichs, W. Environmental impacts of rare earth production. *MRS Bull.* **2022**, *47*, 267–275. [CrossRef]
95. Nakano, J. The Geopolitics of Critical Minerals Supply Chains. 2021. Available online: https://www.csis.org/analysis/geopolitics-critical-minerals-supply-chains (accessed on 1 May 2023).
96. Sophia, K. The Geopolitics of Critical Minerals. *Professional Paper*. 2017. Available online: https://www.academia.edu/41546280/The_Geopolitics_of_Critical_Minerals (accessed on 8 May 2023).

97. Klinger, J.M. *Rare Earth Frontiers: From Terrestrial Subsoils to Lunar Landscapes*; Illustrated Edition; Cornell University Press: Ithaca, NY, USA, 2018.
98. Balaram, V. Potential Future Alternative Resources for Rare Earth Elements: Opportunities and Challenges. *Minerals* **2023**, *13*, 425. [CrossRef]

Disclaimer/Publisher's Note: The statements, opinions and data contained in all publications are solely those of the individual author(s) and contributor(s) and not of MDPI and/or the editor(s). MDPI and/or the editor(s) disclaim responsibility for any injury to people or property resulting from any ideas, methods, instructions or products referred to in the content.

remote sensing

MDPI

Article

A Comparison of Six Forest Mapping Products in Southeast Asia, Aided by Field Validation Data

Bin Liu [1,2,†], Xiaomei Yang [1,2,†], Zhihua Wang [1,2,*], Yaxin Ding [1,2], Junyao Zhang [1,2] and Dan Meng [1,2]

[1] State Key Laboratory of Resources and Environmental Information System, Institute of Geographic Sciences and Natural Resources Research, Chinese Academy of Sciences, Beijing 100101, China; liub@lreis.ac.cn (B.L.); yangxm@lreis.ac.cn (X.Y.); ddyx0111@gmail.com (Y.D.); zhangjy@lreis.ac.cn (J.Z.); mengdan0428@igsnrr.ac.cn (D.M.)
[2] University of Chinese Academy of Sciences, Beijing 100049, China
* Correspondence: zhwang@lreis.ac.cn
† These authors contributed equally to this work.

Abstract: Currently, many globally accessible forest mapping products can be utilized to monitor and assess the status of and changes in forests. However, substantial disparities exist among these products due to variations in forest definitions, classification methods, and remote sensing data sources. This becomes particularly conspicuous in regions characterized by significant deforestation, like Southeast Asia, where forest mapping uncertainty is more pronounced, presenting users with challenges in selecting appropriate datasets across diverse regions. Moreover, this situation impedes the further enhancement of accuracy for forest mapping products. The aim of this research is to assess the consistency and accuracy of six recently produced forest mapping products in Southeast Asia. These products include three 10 m land cover products (Finer Resolution Observation and Monitoring Global LC (FROM-GLC10), ESA WorldCover 10 m 2020 (ESA2020), and ESRI 2020 Land Cover (ESRI2020)) and three forest thematic mapping products (Global PALSAR-2 Forest/Non-Forest map (JAXA FNF2020), global 30 m spatial distribution of forest cover in 2020 (GFC30_2020), and Generated_Hansen2020, which was synthesized based on Hansen TreeCover2010 (Hansen2010) and Hansen Global Forest Change (Hansen GFC) for the year 2020). Firstly, the research compared the area and spatial consistency. Next, accuracy was assessed using field validation points and manual densification points. Finally, the research analyzed the geographical environmental and biophysical factors influencing consistency. The results show that ESRI2020 had the highest overall accuracy for forest, followed by ESA2020, FROM-GLC10, and Generated_Hansen2020. Regions with elevations ranging from 200 to 3000 m and slopes below 15° or above 25° showed high spatial consistency, whereas other regions showed low consistency. Inconsistent regions showed complex landscapes heavily influenced by human activities; these regions are prone to being confused with shrubs and cropland and are also impacted by rubber and oil palm plantations, significantly affecting the accuracy of forest mapping. Based on the research findings, ESRI2020 is recommended for mountainous areas and abundant forest regions. However, in areas significantly affected by human activities, such as forest and non-forest edges and mixed areas of plantations and natural forests, caution should be taken with product selection. The research has identified areas of forest inconsistency that require attention in future forest mapping. To enhance our understanding of forest mapping and generate high-precision forest cover maps, it is recommended to incorporate multi-source data, subdivide forest types, and increase the number of sample points.

Keywords: forest mapping products; FROM-GLC10; ESA WorldCover 10 m 2020; ESRI 2020 Land Cover; Hansen TreeCover2010; GFC30_2020; FNF; spatial consistency; field validation; accuracy assessment

1. Introduction

Forests are of great importance in global ecology, specifically in terms of biodiversity conservation and carbon balance [1–5]. In particular, tropical forests play a significant role

in mitigating climate change [6,7]. Southeast Asia is home to approximately 15% of the world's tropical forests [7], encompassing at least four biodiversity hotspots [8]. Moreover, these forests are essential for the region's development [9,10]. However, human activities have led to rapid changes in the forests of this region [9,11], which in turn have significant implications for the natural environment [10]. Therefore, gaining a comprehensive understanding of the distribution and changes in Southeast Asia forests is of great importance. Remote sensing technology has greatly aided the mapping of large-scale tropical forests, leading to the production of numerous land cover products that include forest in recent years [12–14], for example, 10 m resolution Finer Resolution Observation and Monitoring Global LC (FROM-GLC10) [12], ESA WorldCover 10 m 2020 (ESA2020) [13], and ESRI 2020 Land Cover (ESRI2020) [14]. Forest thematic mapping products, such as global 30 m spatial distribution of forest cover in 2020 (GFC30_2020) [15], have also been developed, alongside continuously updated forest products like Hansen Global Forest Change (Hansen GFC) [16] and the Global PALSAR-2 Forest/Non-Forest map (JAXA FNF) [17]. Nevertheless, variations in definitions, classification algorithms, and data sources lead to limited comparability among products, particularly regarding the spatial consistency of forests across different regions [18–20]. This complicates the precise measurement of forests and spatial distribution. Thus, the identification of the spatial distribution of forests necessitates cross-validation among various products.

Numerous studies have been conducted to analyze the consistency of multiple forest mapping products, focusing on two aspects: (1) consistency analysis within land cover products, including forests as one of the land cover classes [21–24]; (2) consistency analysis specifically targeting forests, using land cover data to extract forests for analysis [25–27]. However, these studies still have certain limitations. On one hand, Southeast Asia boasts vast tropical rainforests, but these rainforests have been impacted by global forestry demand [10], such as the extensive cultivation of oil palm in Malaysia and Indonesia, which account for over 90% of global palm oil production [28,29]. As the balance between forestry supply and demand changes, the types and spatial distribution of forest resources in each country experience corresponding changes. Analyzing the Southeast Asian region aids in comprehending forest distribution, identifying hotspots with inconsistent forest distribution, and determining the primary factors of spatial inconsistency. This approach prevents overly biased and inaccurate analysis of the influencing factors of inconsistency in individual countries or smaller regions. On the other hand, the lack of field validation points has left the accuracy of numerous remote sensing products unassessed [30]. Even if assessment is feasible, ensuring the reliability of accuracy evaluation is challenging due to the difficulty of guaranteeing the accuracy of the obtained validation points. The availability of field validation points allows them to be used as references during other point collection processes, thereby making the manual densification points more reflective of real land cover features and significantly improving the reliability of accuracy evaluation results. Therefore, it is of great significance to conduct accuracy evaluations on medium-high resolution forest products, compare the accuracy and strengths and weaknesses of multiple forest mapping products, and analyze potential factors of the observed differences.

The aim of this research was to utilize field validation data collected by the research team [21,23] to analyze and assess the consistency and accuracy of multiple forest mapping products. Furthermore, we sought to analyze the factors that influence consistency by considering the geographical environmental (elevation, slope) and biophysical (land cover, LC) factors [26,31,32]. This analysis provides users with guidance for selecting and using forest products in tropical rainforest regions and identifying areas for improvement and optimization in future forest extraction and updates. Moreover, it serves as a reference for improving the accuracy of forest mapping. Specifically, we used six forest mapping products with resolutions ranging from 10 m to 30 m, including three land cover products (FROM-GLC10, ESA2020, and ESRI2020) and three forest thematic products (JAXA FNF2020, GFC30_2020, and Generated_Hansen2020, which was synthesized based on Hansen TreeCover2010 (Hansen2010) and Hansen GFC). The year for FROM-GLC10 was

2017, while the other products were for 2020. We compared the area and spatial consistency among the different products and evaluated their accuracy using field validation points and manual densification points. Additionally, in regions exhibiting spatial inconsistency, we investigated the impact of elevation, slope, and various land cover classes (including rubber and oil palm) on the variations in forest distribution.

2. Study Area and Data Preprocessing

2.1. Southeast Asia

Southeast Asia (SEA) is located in the southeastern part of Asia, covering an area of approximately 430 million hectares. SEA is abundant in forest resources, holding nearly 15% of the world's tropical forests. These forests are predominantly distributed in the northeastern part of the Indochina Peninsula, as well as the Malay Archipelago and the island of New Guinea. Forests play a vital role in the region's development, offering employment opportunities across various sectors for the local population. However, population growth and economic transformation have led to an escalating demand for forests, resulting in rapid changes in forested areas. Consequently, Southeast Asia is recognized as one of the significant hotspots for tropical forest logging and forest degradation [31]. During the period from 1990 to 2010, forest cover in Southeast Asia experienced a decline from 268 million hectares to 236 million hectares [9,10], with ongoing large-scale deforestation.

Southeast Asia boasts expansive plantations and serves as a significant producer of tropical cash crops, including rubber, oil palm, coconut, and banana fiber. It stands as the world's largest production region, encompassing 85% of the world's rubber plantations and 90% of rubber production [33]. Additionally, Southeast Asia is home to over 80% of oil palm plantations and contributes to more than 90% of global palm oil production [28]. The dynamic changes in forest resources within this region exert substantial impacts on society, politics, economy, and climate. So we chose Southeast Asia as the study area (Figure 1), including eight countries: Cambodia, Indonesia, Laos, Malaysia, Myanmar, Philippines, Thailand, and Vietnam. East Timor, Singapore, and Brunei are excluded from the research due to their smaller land area, limited forest resources, and negligible influence on the analysis of large-scale forest patterns. By comparing and validating six forest mapping products, our aim is to offer insights into the utilization of such products for studying changes in forest ecosystems, human–environment interactions, and environmental conservation.

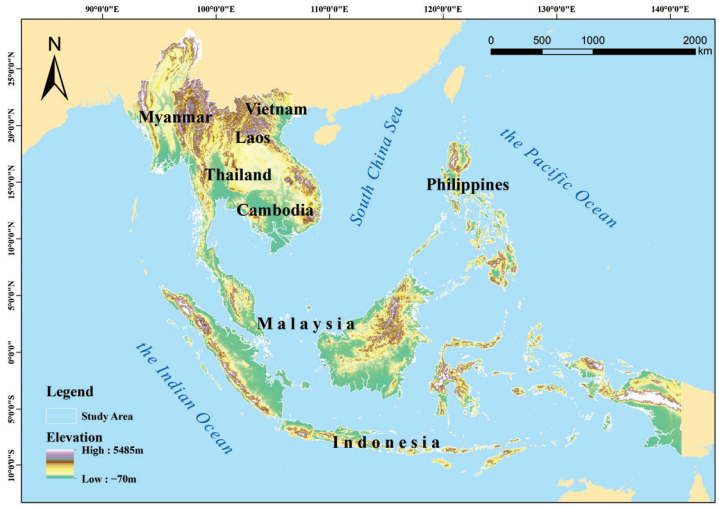

Figure 1. Location and topography of Southeast Asia.

2.2. Data and Preprocessing

The forest products selected for this research consist of three land cover products: FROM-GLC10, ESA2020, and ESRI2020. Additionally, three forest thematic products were chosen: JAXA FNF2020, GFC30_2020 and Hansen2010, which was used to synthesize

the Generated_Hansen2020 for the year 2020. The land cover products currently offer the highest resolution available for free, with a 10 m resolution. Conversely, the forest thematic products are either recent releases or continuously updated products with a medium resolution of 25–30 m. These products possess high timeliness and resolution, enabling a more precise comprehension of the present forest conditions and facilitating the analysis of the strengths, weaknesses, and distribution of the data products.

(1) FROM-GLC10

The FROM-GLC10 [12] is a global land cover product created by Gong Peng et al., from Tsinghua University, in 2017 (http://data.starcloud.pcl.ac.cn/zh/resource/1, accessed on 31 August 2023). It is based on 10 m resolution Sentinel-2 imagery and was produced using a random forest classifier. The forest class is coded as 20 and is defined as areas with trees higher than 3 m and tree cover of more than 15%. The product was generated using a multi-seasonal sample library, collecting over 300,000 training samples of various sizes from around 93,000 sample points worldwide. The validation set consists of approximately 140,000 samples from different seasons, covering 38,000 sample points. The overall accuracy of the product is 72.76%, with a user's accuracy for the forest class of about 83.47%.

(2) ESA2020

The ESA2020 [13] is a global land cover product for the year 2020 (https://developers.google.com/earth-engine/datasets/catalog/ESA_WorldCover_v100, accessed on 31 August 2023). It is a collaborative effort between the European Space Agency (ESA) and multiple research institutions worldwide, utilizing imagery from Sentinel-1 and Sentinel-2. The forest class is coded as 10 and is defined as areas where tree cover is more than 10%. This land cover includes classes below the canopy, like shrubs, built-up areas, and plantations, like oil palm and olive trees. It also includes tree-covered areas with seasonally or permanently flooded with freshwater, except for mangroves. The product assesses accuracy through statistical verification, map visual comparison, and spatial accuracy verification. More than 200,000 reference points were used in the map visual comparison to evaluate its accuracy and assess its spatial uncertainty. Its overall accuracy was determined to be 74.4%.

(3) ESRI2020

The ESRI2020 [14] is a global land cover product for the year 2020 (https://www.arcgis.com/home/item.html?id=8214141a576848f69f440c793144f6ce, accessed on 31 August 2023). It was developed using Sentinel-2 imagery with a 10 m resolution and deep learning methods. In this product, the forest class is coded as 2 and defined as dense vegetation clustering of trees taller than 15 m, typically with a closed or dense canopy. This class includes various types of vegetation, such as wooded vegetation and clusters of dense tall vegetation within savannas, plantations, swamps, and mangroves. The model utilized over 5 billion Sentinel-2 pixels, manually annotated from more than 20,000 sampling points distributed worldwide. By processing images captured on multiple dates throughout the year, the model generated a representative map. The overall accuracy is reported to be 85%.

(4) Hansen2010

The Hansen 2010 [16] is a global forest thematic mapping product for the year 2010 (https://glad.umd.edu/dataset/global-2010-tree-cover-30-m, accessed on 31 August 2023). It is a collaborative effort between the Global Land Analysis and Discovery (GLAD) lab at the University of Maryland, Google, the United States Geological Survey (USGS), and the National Aeronautics and Space Administration (NASA). Tree cover is defined as all vegetation taller than 5 m, including both natural forests and planted forests that meet the criteria. The spatial resolution is 30 m, and the tree cover is represented as a percentage from 1% to 100%. The data are derived from Landsat 7 reflectance measurements obtained during the growing season. Over 600,000 Landsat 7 images were analyzed using the Google Earth Engine (GEE) to accurately classify and supervise tree cover at the pixel level.

(5) JAXA FNF2020

The JAXA FNF2020 [17] is a forest product for the year 2020 (https://developers.google.com/earth-engine/datasets/catalog/JAXA_ALOS_PALSAR_YEARLY_FNF4, accessed on 31 August 2023). It was developed by the Japan Aerospace Exploration Agency (JAXA) using L-band synthetic aperture radar sensors on the Advanced Land Observing Satellite-2 (ALOS-2 PALSAR-2) and Advanced Land Observing Satellite (ALOS PALSAR). It was generated through random forest, utilizing variances in the backscattering coefficients among different land cover classes in diverse ecological regions. The product has a spatial resolution of 25 m. Forests are defined as land spanning more than 0.5 hectares with trees higher than 5 m and a canopy cover of more than 10%. This includes forested areas that have not yet reached but are expected to reach the criteria, as well as forest roads, firebreaks, and other small open areas. It includes rubberwood, cork oak, and Christmas tree plantations, but excludes plantations in agricultural production systems, such as oil palm plantations, fruit tree plantations, and olive grove orchards. The accuracy was evaluated using ground photographs and high-resolution optical satellite images. The overall accuracy for three classes—forests, non-forests, and water—was higher than 86%.

(6) GFC30_2020

The GFC30_2020 [15] is a global forest cover product for the year 2020 (https://data.casearth.cn/sdo/detail/625e1760819aec2a46dcd2d8, accessed on 31 August 2023), and it was developed through a collaboration between the Aerospace Information Research Institute of the Chinese Academy of Sciences and other institutions. It was created using a random forest algorithm based on Landsat satellite images and images from GF-1 and GF-6 satellites. The product employs global ecological geographical zoning and crowd-sourced sample data. Its resolution is 30 m. Forests are defined as land spanning more than 0.5 hectares with trees higher than 5 m and a canopy cover of more than 10%, or areas that have not yet reached but are expected to reach the criteria. It excludes forests primarily used for agricultural and urban purposes. The primary data source consists of multi-temporal Landsat images captured during the global forest vegetation growing season. The random forest algorithm was applied for large-scale learning and model training, resulting in the creation of a global forest zoning classifier and the production of the global forest cover product. The product's accuracy was evaluated through a combination of direct validation and cross-validation. For direct validation, a stratified random sampling approach was adopted, with 1500 points randomly selected for each class. These points were manually inspected and verified using high-resolution images from Google Earth/GF, referencing relevant data products from the United States, Japan, and other sources, and incorporating some field survey data to ensure the reliability of the validation points. In total, 39,900 validation points were obtained globally, and the overall accuracy of the product exceeded 85%.

Table 1 shows the varying resolutions and forest definitions of these forest mapping products. Data preprocessing mainly involves three steps. First, considering the resolution ranges from 10 m to 30 m, we used the nearest neighbor method to resample the spatial resolution to 10 m. Second, we adopted Hansen2010, combined with Hansen GFC loss and gain, to synthesize the forest cover for 2020 based on net changes, and named it Generated_Hansen2020. These products exhibit significant differences in their forest definitions, with the minimum forest cover ranging from 10% to 15% and the minimum tree height ranging from 3 m to 15 m. These variations greatly impacted our assessment of forest distribution and are among the reasons for inconsistency [34]. Therefore, for effective comparison, we appropriately adjusted the products to ensure consistency when comparing different products. In detail, for FROM-GLC10, ESA2020, ESRI2020, JAXA FNF2020, and GFC30_2020, where forests are mapped as a separate class, we directly extracted the forest from the products. For Generated_Hansen2020, to maintain consistency with the other five products, we converted the percentage into a forest category. Therefore, referring to the Global Forest Review (GFR) (https://research.wri.org/gfr/key-terms-definitions#glossary, accessed on 31 August 2023), we extracted areas with tree cover exceeding 30% and considered them forests.

Table 1. Comparison of different forest products.

Products	Forest Definition	Special Provisions in the Definition	Spatial Resolution	Data Source	Algorithm	Product Accuracy	Sample Size and Sample Acquisition Method
FROM-GLC10	Areas with trees higher than 3 m and tree cover of more than 15%	——	10 m	Sentinel-2 satellite data	Supervised classification	Overall accuracy is 72.76%	Validation set consists of approximately 140,000 samples from different seasons, covering 38,000 sample points
ESRI2020	Dense vegetation clustering of trees taller than 15 m, typically with a closed or dense canopy	Including wooded vegetation, clusters of dense tall vegetations within savannas, plantations, swamp, or mangroves	10 m	Sentinel-2 satellite data	Deep learning	Overall accuracy is 85%	Over 5 billion manually annotated Sentinel-2 pixels in over 20,000 sampling points worldwide
ESA2020	Tree cover is more than 10%	① Including land cover classes below the canopy, like shrubs and built-up areas; ② including plantations like oil palm and olive trees and tree covered areas with seasonally or permanently flooded with freshwater except for mangroves	10 m	Sentinel-1 and Sentinel-2 satellite data	Supervised classification	Overall accuracy is 74.4%	Over 200,000 reference points
Hansen2010	All vegetation taller than 5 m in height	Including both natural forests and planted forests that meet the criteria	30 m	Landsat7 reflectance characteristic indicators during the growing season	Supervised classification		Stratified random sampling based on random forest

Table 1. *Cont.*

Products	Forest Definition	Special Provisions in the Definition	Spatial Resolution	Data Source	Algorithm	Product Accuracy	Sample Size and Sample Acquisition Method
JAXA FNF2020	Land spanning more than 0.5 hectares with trees higher than 5 m and a canopy cover of more than 10%	① Including forested areas that have not yet reached but are expected to reach the criteria; ② including forest roads, firebreaks, and other small open areas; ③ including rubberwood, cork oak, and Christmas tree plantations; ④ excluding plantations in agricultural production systems, such as oil palm plantations, fruit tree plantations, and olive grove orchards	25 m	PALSAR mosaic dataset	Supervised classification	By forest, non-forest, and water classes, the overall accuracy is higher than 86%	Used ground photographs and high-resolution optical satellite images
GFC30_2020	Land spanning more than 0.5 hectares with trees higher than 5 m and a canopy cover of more than 10%	① Including areas that have not yet reached but are expected to reach the criteria; ② excluding forest primarily used for agricultural and urban purposes	30 m	Landsat series satellite images of the global forest vegetation growth season in 2020, China's GF-1, GF-6 and other satellite imagery	Machine learning algorithms	Overall accuracy is higher than 90.94%	Using high-resolution images such as Google Earth/GF for manual inspection and verification, referencing relevant data products from the United States and Japan, and combining some field survey data, a total of 39,900 verification points were obtained

3. Methods

This research utilized field validation points and manual densification points to assess the accuracy, consistency, and disparities among six extensively utilized forest mapping products in Southeast Asia. The processing flowchart is shown in Figure 2. Firstly, we compared the consistency of their area and spatial distribution. Subsequently, accuracy assessment was performed using samples from both forest and non-forest areas. Lastly, we analyzed factors influencing spatial consistency, considering geographical environmental factors, such as elevation and slope, and biophysical factors, such as confusion with other land cover types in spatially inconsistent areas.

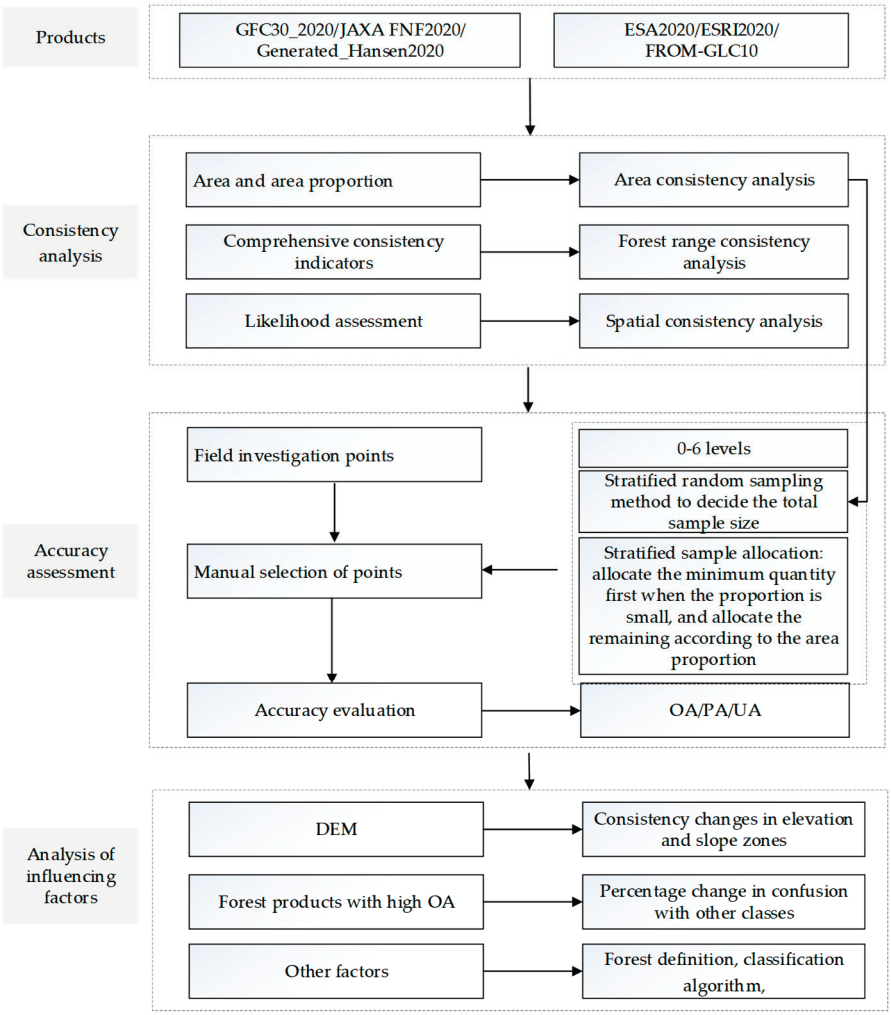

Figure 2. Flowchart of forest consistency, accuracy assessment, and influencing factor analysis.

3.1. Area and Spatial Consistency Analysis

For area consistency, we used GEE to calculate the differences in the areas among the six products. Furthermore, we analyzed the areas within each country to emphasize the regional disparities throughout Southeast Asia.

For spatial consistency, we used the likelihood assessment method to analyze and compare discrepancies among the different products in terms of spatial differences [35]. By measuring the determinacy and uncertainty of each product, this method evaluates the consistency of individual pixels across different products. It is commonly applied in situations where determining the credibility of multiple products poses challenges [36]. Conceptually, this method can be likened to a voting mechanism for the products and is implemented through spatial overlay techniques. If all products identify a pixel as

forest, it results in a high voting score for that pixel, indicating a high level of consistency across the products.

In this research, the forest products were recorded, with a value of 1 for the forest class and 0 for other classes. Spatial overlay was conducted using GEE to obtain the spatial consistency results of forests. The pixel values range from 0 to 6, where each value corresponds to the number of votes for the forest. For instance, a value of 6 signifies that the pixel is classified as forest in all six forest products, whereas a value of 0 indicates that the pixel is not classified as forest in any of the products. Higher pixel values indicate a greater probability of being classified as forest, indicating higher consistency among the products. The spatial consistency was categorized into six levels based on the pixel value range: Level 1 represents areas of complete inconsistency, Levels 2–5 represent partially consistent areas, and Level 6 represents areas of complete consistency. Moreover, a value of 0 signifies non-forest areas. It is crucial to address a specific matter accurately: a value of 0 indicates that the six products do not classify the area as forest; however, this does not necessarily mean there is no forest there. Rather, it suggests an extremely low likelihood of forest presence in that area.

Additionally, we computed a comprehensive index to assess the overall level of spatial consistency. The formula is defined as follows:

$$A = \frac{A_{HF}}{\sum A_{\mathrm{i}(F)}/6} \tag{1}$$

In this formula, A_{HF} represents the forest area in completely consistent regions, while $A_{\mathrm{i}(F)}$ represents the forest area in the ESRI2020, ESA2020, FROM-GLC10, GFC30_2020, Generated_Hansen2020, and JAXA FNF2020 products, respectively.

3.2. Verification Point Design and Accuracy Assessment

We evaluated the accuracy of the forest products using field validation points and manual densification points. The design of the validation points involved determining the sampling method, the number of sample points, and the attributes of the sample types.

We utilized a stratified random sampling method. Adequate samples were necessary to validate product accuracy and capture the confusion between different classes. Stratified random sampling is a practical and commonly used sampling design scheme [37,38] for accuracy assessment purposes. Cochran [39] provided the following sample size formula (assuming equal sampling costs across strata):

$$n = \frac{(\sum w_i s_i)^2}{[S(\hat{O})] + (1/N)\sum w_i {s_i}^2} \approx \left(\frac{\sum w_i s_i}{S(\hat{O})}\right)^2 \tag{2}$$

where N represents the number of pixels in the study area, $S(\hat{O})$ represents the standard error of the desired estimation accuracy, w_i indicates the area percentage of the class i, and s_i represents the standard deviation of the stratum i. $s_i = \sqrt{U_i(1-U_i)}$ [39]. When N is sufficiently large, the equation can be approximated, where U_i denotes the user accuracy. For instance, in the sampling stratum ranked 1, indicating complete inconsistency, the forest accuracy within this stratum is significantly low. The area percentage w_i can be acquired through area statistics. Assuming that the confusing class in this stratum is shrub, with user accuracies of 60%, 70%, and 50% for shrub in three land cover products, the average value of s_i was determined as 60%. $S(\hat{O})$ is specified as a standard error of 0.01.

The different levels of the spatial consistency analysis results are regarded as distinct sampling strata, and the allocation of sample quantities is based on the area percentage of each stratum determined by the area statistics [38,39]. Moreover, given the intricate nature of land cover types in regions with low spatial consistency, it is essential to appropriately augment the number of sample points while ensuring that the sample size for each class in every level remains at a minimum of 100.

To facilitate the accuracy assessment, we obtained and processed the sample points from reference [23]. These sample points encompass a wide range of types, considering the quantity, richness, and spatial distribution of the samples, including field validation points and manual densification points from Google high-resolution images. However, since our research focuses on forest areas, these sample points are needed to undergo processing and coordination. We enhanced and refined the attribute types by augmenting the original sample data attribute table with two additional attributes: a primary class and a secondary class. The primary class classifies the samples as either forest or non-forest. Moreover, the secondary class expands the forest samples to rubber, oil palm, and other forest types, thereby facilitating the analysis of confused land cover classes. During the expansion of the secondary classes, we meticulously examined all sample data and rectified certain attribute errors. As rubber and oil palm areas are relatively small, we adjusted some rubber and oil palm points located at the edges to the nearest spatial positions with similar types in the clustered distribution of the current samples during the expansion process. Additionally, we randomly added around 100 rubber and oil palm samples. While this presented challenges to meet the minimum requirement of 100 samples for each level, we made sure that each sample class had a total count of at least 100.

We conducted an accuracy assessment using the overall accuracy (OA), user's accuracy (UA), and producer's accuracy (PA) [40]. This formed the confusion matrix for each product, enabling the analysis of the accuracy of the forest products. The OA can directly reflect the proportion of correct categorization. It is equal to the sum of correctly categorized pixels divided by the total number of pixels. UA refers to the ratio of the total number of pixels correctly classified into class A to the total number of pixels of the entire image classified into class A by the classifier. PA refers to the ratio of the number of pixels of the whole image correctly classified by the classifier into class A to the total number of true references of class A. We also calculated the commission error and omission error to assess the accuracy of the products. The commission error refers to how many of the classification results are incorrect. The omission error refers to how many true results were missed in the classification results.

3.3. Analysis of Geographical Environmental and Biophysical Influencing Factors

To investigate the factors of inconsistent spatial patterns, we carefully selected the most representative geographical environmental factors, such as the elevation and slope, along with biophysical factors related to land cover, specifically focusing on the distribution of rubber and oil palm [41–45]. Subsequently, we conducted an analysis of the factors behind these spatial inconsistencies. Following the references [41,42], elevation was categorized into six intervals: 0–200 m, 200–500 m, 500–1000 m, 1000–2000 m, 2000–3000 m, and above 3000 m. Moreover, using the digital elevation model (DEM), we derived slope and divided them into the following intervals: 0–5°, 5–15°, 15–25°, 25–35°, 35–45°, and above 45°. We then computed the consistency between different elevation and slope zones. The formulas used to calculate the percentage of each elevation and slope zone are as follows:

$$\mathrm{p}_{ij(DEMF)} = \frac{A_{ij(DEMF)}}{A_{i(DEMF)}} \tag{3}$$

$$\mathrm{p}_{ij(slopeF)} = \frac{A_{ij(slopeF)}}{A_{i(slopeF)}} \tag{4}$$

In these formulas, $\mathrm{p}_{ij(DEMF)}$ and $\mathrm{p}_{ij(slopeF)}$ represent the respective percentages of forest area in the *j*th level of both the elevation zone *i*th and the corresponding slope zone.$A_{ij(DEMF)}$ and $A_{ij(slopeF)}$ denote the forest area of the *j*th level in the same elevation zone and slope zone, while $A_{i(DEMF)}$ and $A_{i(slopeF)}$ indicate the total forest area within the elevation zone *i*th and the corresponding slope zone. The variable *j* ranges from 1 to 6.

We utilized land cover products of higher accuracy to calculate the area and percentage of diverse land cover types within the inconsistent regions. This analysis aimed to analyze

the impact of land cover on forest distribution, as described by Formulas (5) and (6). We further analyzed the land cover area and percentage of forest inconsistency across various countries, with a focus on highlighting the variations in Southeast Asia. By superimposing detailed samples within the inconsistent regions, the percentages of accurately classified samples for rubber, oil palm, and other forests were calculated. Furthermore, the elevation and slope values were extracted for these sample points, followed by an analysis of the elevation and slope distributions for these types.

$$\mathrm{p}_{j(LC)} = \frac{A_{j(LC)}}{A_{(LC)}} \tag{5}$$

$$\mathrm{p}_{ij(LC)} = \frac{A_{ij(LC)}}{A_{i(LC)}} \tag{6}$$

These formulas use $\mathrm{p}_{j(LC)}$ to represent the percentage of land cover area for the *j*th class within the inconsistent region, while $\mathrm{p}_{ij(LC)}$ represents the percentage of land cover area for the *j*th class in the *i*th level. $A_{j(LC)}$ represents the forest area for the *j*th class, and $A_{(LC)}$ represents the total land cover area. Similarly, $A_{ij(LC)}$ represents the forest area for the *j*th class in the *i*th level, and $A_{i(LC)}$ represents the forest area in the *i*th level. Here, the value of *i* ranges from 1 to 5.

4. Results

4.1. Area Consistency Comparison

Regarding the comparison of area consistency, we calculated the forest area and area percentage for six products (Figure 3). Substantial differences exist in the areas among the products. The forest area of GFC30_2020 is the smallest, covering 2.49 million square kilometers, which represents 56.32% of the total area. The largest forest area belongs to ESA2020, covering 3.31 million square kilometers, which accounts for 74.86% of the total area. There is an area difference of 820,000 square kilometers between the two. ESRI2020 and FROM-GLC10 have forest areas of 2.98 million square kilometers and 2.85 million square kilometers, respectively, with a relatively minor discrepancy of around 120,000 square kilometers. Except for Generated_Hansen2020, the land cover products generally exhibit higher forest area values compared to the forest thematic products. Discrepancies arise due to variations in resolution and forest definition among the products. Among the products, GFC30_2020, which has the lowest resolution, exhibits the most pronounced differences. Furthermore, the consistency of the products can be influenced by different data sources. For instance, the utilization of optical imagery in GFC30_2020 might result in a lower classification performance in regions of Southeast Asia characterized by cloudiness and rainfall. In conclusion, notable differences in area exist among the various products, particularly for GFC30_2020. Hence, it is vital to analyze the consistency of the products.

By analyzing regional statistics, we obtained the forest area coverage percentages for different countries across six products, as shown in Figure 4. First and foremost, notable disparities exist in the forest area percentages among different countries in Southeast Asia and across different forest products. Malaysia, Thailand, and the Philippines demonstrate the most significant variations in forest area percentages. The difference between the highest and lowest forest area percentages in Malaysia is 30.76%, while other countries exhibit percentage ranges surpassing 20%. In contrast, Laos and Myanmar exhibit relatively smaller discrepancies compared to other countries; nevertheless, their percentage differences still reach approximately 15%.

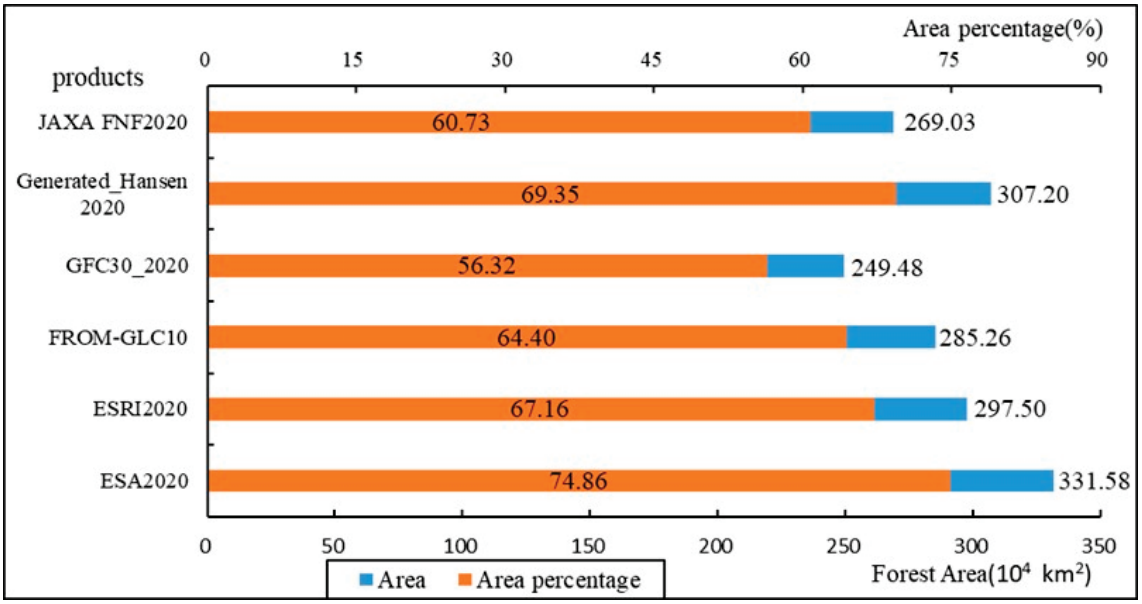

Figure 3. Comparison of forest area and area percentage distribution in 6 products.

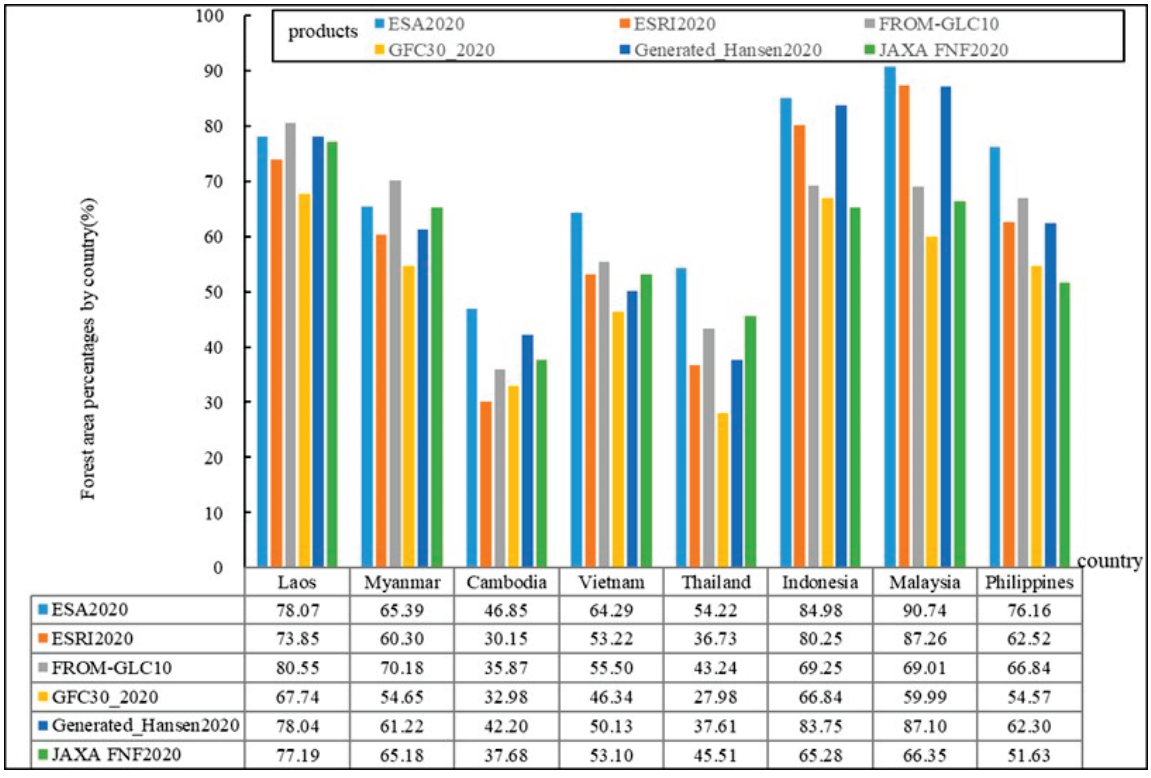

	Laos	Myanmar	Cambodia	Vietnam	Thailand	Indonesia	Malaysia	Philippines
ESA2020	78.07	65.39	46.85	64.29	54.22	84.98	90.74	76.16
ESRI2020	73.85	60.30	30.15	53.22	36.73	80.25	87.26	62.52
FROM-GLC10	80.55	70.18	35.87	55.50	43.24	69.25	69.01	66.84
GFC30_2020	67.74	54.65	32.98	46.34	27.98	66.84	59.99	54.57
Generated_Hansen2020	78.04	61.22	42.20	50.13	37.61	83.75	87.10	62.30
JAXA FNF2020	77.19	65.18	37.68	53.10	45.51	65.28	66.35	51.63

Figure 4. Forest area percentage comparison of different countries in 6 products.

4.2. Spatial Consistency Comparison

Figures 5 and 6 show the results of the spatial consistency of six forest products. The forest area percentages for consistency levels 6, 5, 4, 3, 2, and 1 are 48.59%, 16.19%, 10.74%, 9.02%, 7.53%, and 7.94%, respectively (see Table 2). The spatial distribution exhibits good consistency due to the substantial percentage of forest areas classified as levels 6 and 5. This is also evidenced by the spatial comprehensive consistency index, which measures 62.62%. Moreover, Figures 5 and 6 reveal concentrated regions of high consistency in forest areas, including northern Myanmar, the western coast of Sumatra in Indonesia, the western and

northern portions of Kalimantan, Sulawesi, and West Papua, as well as western Malaysia. These regions are characterized by higher elevations or minimal human activity impact. Conversely, regions exhibiting low consistency in forest areas are more scattered, primarily located in the southeastern coastal areas of Sumatra in Indonesia, Jakarta, the southeastern coastal areas of Kalimantan, and the southern coastal areas of Vietnam. Thus, regions with concentrated forest distribution can be readily identified in remote sensing images and show greater consistency.

Figure 5. The spatial consistency distribution maps of the six products. Values range from 6 to 1, where 6 represents completely consistent areas, 1 represents completely inconsistent areas, and 2–5 represent partially consistent areas. Areas with 0 indicate non-forest. The areas in the red box are the enlarged display regions.

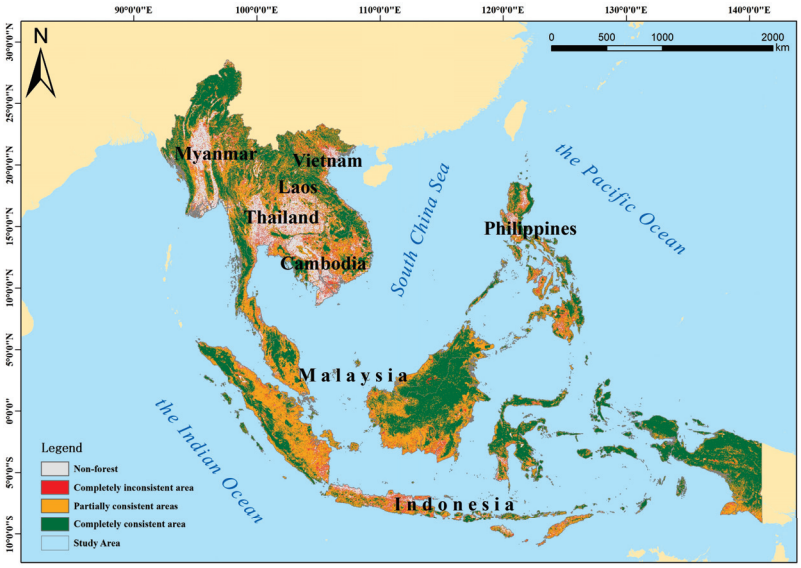

Figure 6. The spatial consistency distribution of 6 products is divided into three levels: completely consistent areas (corresponding to value 6), partially consistent areas (corresponding to values 2–5), and completely inconsistent areas (corresponding to value 1).

Table 2. Area and percentage of different spatial consistency levels.

Spatial Consistency Level	1	2	3	4	5	6
Forest area (10^4 km^2)	29.54	28.04	33.57	39.97	60.27	180.87
Forest area percentage (%)	7.94	7.53	9.02	10.74	16.19	48.59

4.3. Accuracy Assessment

The accuracy evaluation involved utilizing field survey verification points and manual densification points to acquire sample points. The minimum sample size of 941 was calculated based on the designed sampling scheme. However, with the collection of 1133 field samples, the sample points were expanded, resulting in a total of 6985 forest samples and 7809 non-forest samples, as illustrated in Figure 7.

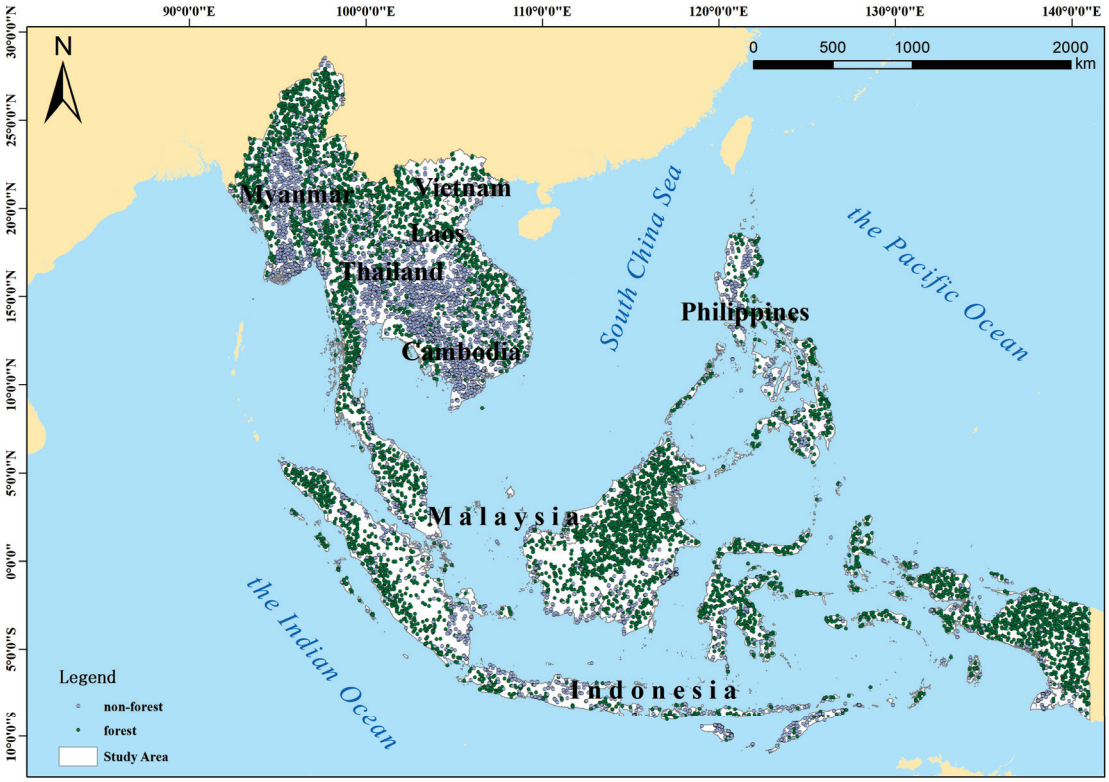

Figure 7. Forest and non-forest sample points in Southeast Asia.

Table 3 shows the validation results of 6 products generated by the overall accuracy (OA), user's accuracy (UA), producer's accuracy (PA), commission error, and omission error. Generally, the forest areas in the six products exhibited high overall accuracy, surpassing 85%. ESRI2020 had the highest overall accuracy at 91.64%, while both ESA2020 and FROM-GLC10 both had overall accuracies, above 89%, and GFC30_2020 had the lowest accuracy at 87.47%. Except for GFC30_2020, the user's accuracy for the remaining five forest products surpassed 90%. All products, except ESA2020 and Generated_Hansen2020, achieved producer's accuracies, exceeding 85%. Particularly, the user's accuracy for forest areas in GFC30_2020 was only 84.5%, resulting in a 15.5% commission error of forest areas as non-forest. Furthermore, the producer's accuracy for non-forest was 86.97%, accompanied by a 13.03% omission error where non-forest areas were inaccurately extracted. Regarding the ESA2020 and Generated_Hansen2020, the producer's accuracy for forest areas reached 83.49% and 83.9%, respectively, suggesting an approximate 16% of unidentified forest areas. Additionally, a notable commission error existed for non-forest areas, with roughly 16% of non-forest areas not accurately identified.

Table 3. Validation results of 6 products.

Accuracy (%)		ESA2020	ESRI2020	FROM-GLC10	GFC30_2020	Generated_Hansen2020	JAXA FNF2020
UA	Forest	95.50	93.00	93.01	84.50	92.91	89.04
	Non-forest	83.57	90.46	87.06	90.06	84.49	88.31
PA	Forest	83.49	89.45	86.21	88.09	83.90	86.89
	Non-forest	95.52	93.69	93.47	86.97	93.20	90.26
Commission error	Forest	4.50	7.00	6.99	15.50	7.09	10.96
	Non-forest	16.43	9.54	12.94	9.94	15.51	11.69
Omission error	Forest	16.51	10.55	13.79	11.91	16.10	13.11
	Non-forest	4.48	6.31	6.53	13.03	6.80	9.74
OA		89.12	91.64	89.83	87.47	88.41	88.65

Additionally, we conducted a comparison of accuracy across different countries and forest products (Figure 8). The results indicate minimal variation in the overall accuracy across different products and countries. However, notable discrepancies exist in the user's accuracy and producer's accuracy among some countries. Thailand and the Philippines demonstrated more significant disparities in the user's accuracy. FROM-GLC10 showed the highest user's accuracy in Thailand, reaching 89.96%, whereas GFC30_2020 exhibited the lowest at 72.65%, resulting in an accuracy difference of approximately 17%. Similarly, in the Philippines, ESRI2020 demonstrated the highest user's accuracy at 90.69%, while FROM-GLC10 had the lowest at 80.18%, resulting in a 10% difference. Notably, there were substantial variations in the producer's accuracy between Thailand and Cambodia. ESRI2020 attained the highest producer's accuracy in Thailand, at 84%, whereas ESA2020 exhibited the lowest at 65%, resulting in an accuracy difference of approximately 19%. In Cambodia, ESRI2020 showed the highest producer's accuracy at 67%, while ESA2020 demonstrated the lowest at 48%, resulting in a 19% difference.

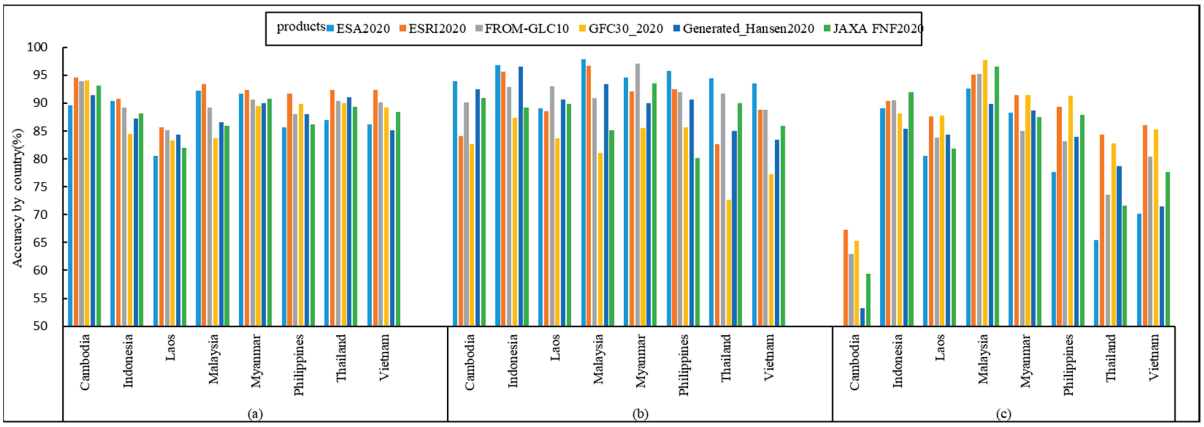

Figure 8. OA, UA, and PA of different products in different countries. (**a**) Overall accuracy (OA), (**b**) user's accuracy (UA), (**c**) producer's accuracy (PA).

4.4. Factors Influencing Spatial Consistency

To analyze the geographical environmental factors influencing the inconsistency in forest spatial distribution, we utilized DEM data to extract the elevation and slope, and then calculated the percentages of different elevation zones and slope zones with consistency levels (Figures 9 and 10). The forest consistency was divided into six levels, where Level 6 represents complete consistency, Levels 5 to 2 represent partial consistency, and Level 1 represents complete inconsistency. Figure 9 illustrates the percentage of spatial consistency

distributions in different elevation intervals. Figure 9a shows six levels, while in Figure 9b, we consolidated the six levels into three levels, where Level 6 in Figure 9a corresponds to Level 3 in Figure 9b. Levels 5 to 2 in Figure 9a were merged into Level 2, and Level 1 remains the same as Level 1 in Figure 9a. The percentage of complete consistency is lower for elevations below 200 m and reaches its lowest for elevations above 3000 m. However, within the elevation range of 200–3000 m, the percentage of complete consistency for forest areas is remarkably high, exceeding 60%. In the plain areas below 200 m, the consistency between products is lower. The spatial pattern of consistency distribution exhibits variation with elevation. Consistency is high within the elevation range of 200–3000 m, whereas the percentage of consistency distribution is low below 200 m and above 3000 m.

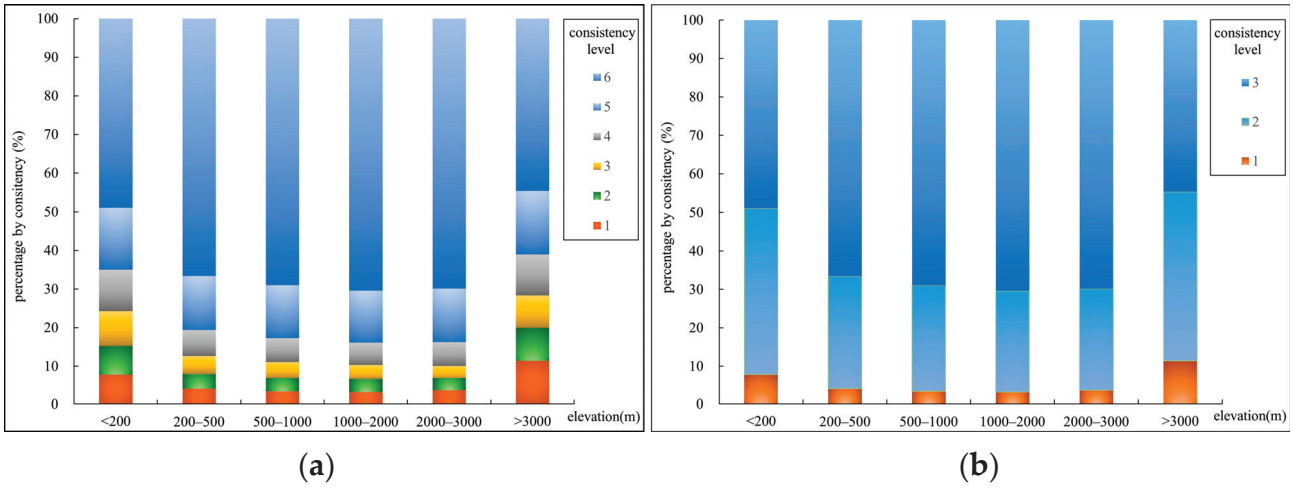

Figure 9. The spatial consistency distribution percentage of different elevation intervals. (**a**) Six-level consistency percentages, (**b**) three-level consistency percentages, from high to low.

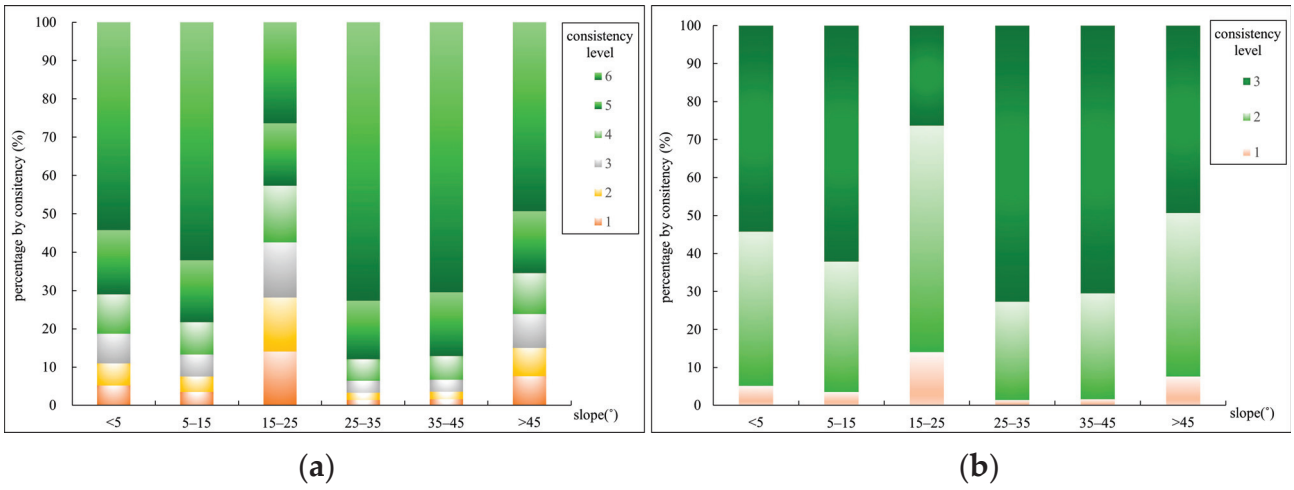

Figure 10. The spatial consistency distribution percentage of different slope intervals. (**a**) Six-level consistency percentages; (**b**) three-level consistency percentages, from high to low.

Figure 10 reflects the percentage of spatially consistent distributions among different slope intervals, where Figure 10a shows six levels, while Figure 10b shows three levels, following the same merging method as in Figure 9. In Figure 10a, the percentage of complete consistency is highest between slopes 25° and 45°, reaching 70%. It remains substantial, exceeding 50%, when the slope is below 15°. However, it is at its lowest when the slope falls within the range of 15° to 25°. Dividing the slope range into 15°–25° and below 15°, we found that as the slope increases within the 0–15° range, the percentage

of consistent areas increases, while the percentages of partially consistent and completely inconsistent areas decrease. Conversely, when the slope exceeds 25°, consistent areas decrease while partially consistent and completely inconsistent areas increase. In the slope range of 15°–25°, consistent areas are at their lowest at 26%, while partially consistent and completely inconsistent areas peak at 14%. Figure 10b consolidates the six levels, reflecting a spatial consistency pattern for these levels with respect to slope variation. Complete consistency is high below 15° and above 25°, while it is lower within the 15°–25° range, with a higher percentage of partially consistent areas.

Utilizing the ESRI 2020 land cover product, we selected alternative land cover types as biophysical factors to calculate the area and percentage of forest that is confused with other types (Figure 11). From the standpoint of land cover, forests are regarded as distinctive ecosystems or vegetation types characterized by unique compositions of flora and fauna [46]. In such instances, accurately distinguishing between forest and shrub poses a challenge. The findings presented in Figure 11a reveal that the classes prone to the greatest confusion with forest, in descending order, are shrub, crops, and built area, whereas the level of confusion with other classes is minimal. Within all regions exhibiting inconsistencies in forest, shrub accounts for 46%, crops for 28%, and built area for 14%. The outcomes shown in Figure 11b demonstrate the variability of land cover types that impact the distribution of forest across different levels of inconsistency. In areas characterized by complete inconsistency, crops exhibit the highest level of confusion with forest, reaching 38%, followed by shrub at 31%. Additionally, the built area demonstrates notable confusion at a percentage of 20%. In partially consistent areas, particularly within the range of Levels 2–5, shrub shows the highest percentage of confusion, surpassing 40%. Moreover, we conducted calculations to determine the percentages of various land cover types that lead to confusion with forest in inconsistent areas across different countries, aiming to illustrate intercountry discrepancies, as depicted in Figure 11c. In Indonesia, Thailand, Vietnam, and the Philippines, the disparities in the percentages between crops and shrub being confused with forest are relatively minor, suggesting that forest is prone to being confused with crops and shrub in these countries. In Laos, Cambodia, and Myanmar, there is a significant likelihood of confusion between forest and shrub, leading to inconsistency. Malaysia exhibits substantial percentages of confusion between forest and crops, shrub, built area, and grassland. Except for Laos, Cambodia, and Myanmar, all countries demonstrate some level of confusion between areas of forest inconsistency and built area.

Considering the extensive rubber and oil palm plantations in Southeast Asia, which have a notable impact on the spatial distribution of forests, we computed the percentages of planted forests and other forests within the areas exhibiting inconsistency, as depicted in Figure 12a. Planted forests and other forests exhibit broad distributions and are present in all areas characterized by inconsistency. Notably, in Level 1, the percentage of planted forest samples is substantially higher than that of other forests, reaching 34.62%. Conversely, in Level 5, the percentage of other forests is significantly higher than that of planted forests. In Level 2, the number of planted forest samples slightly surpasses that of other forests, with percentages of 47.58% and 52.42%, respectively. In Levels 3–5, the percentage of other forests experiences a substantial increase from 52% to 99%, whereas the percentage of planted forests declines from 47% to 8%. While the sample points cannot fully represent the distribution of planted forests and other forests across the entire region, they still enable us to analyze the land cover types responsible for the inconsistencies in these areas. Furthermore, the results presented in Figure 12a indicate that planted forests play a significant role in the inconsistency of forest products.

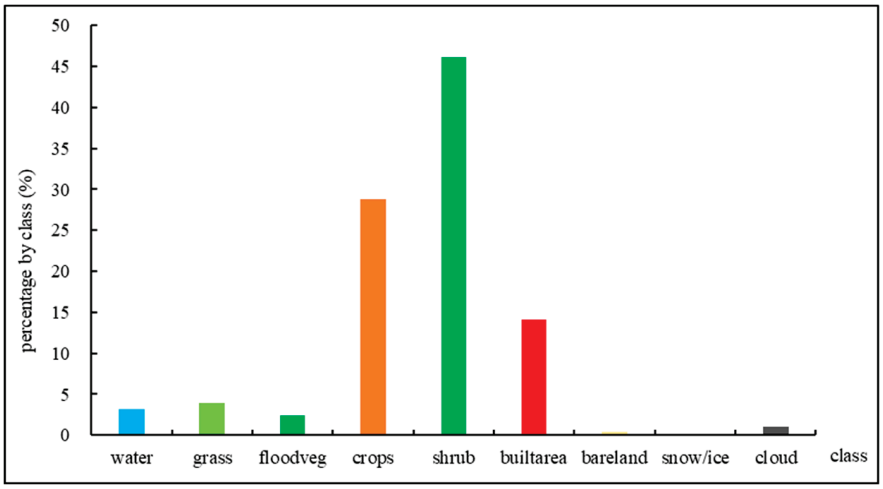

(**a**)

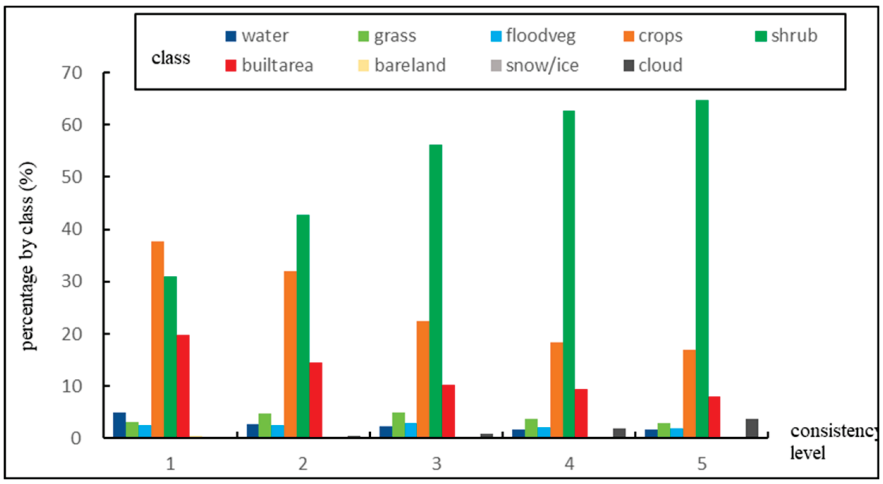

(**b**)

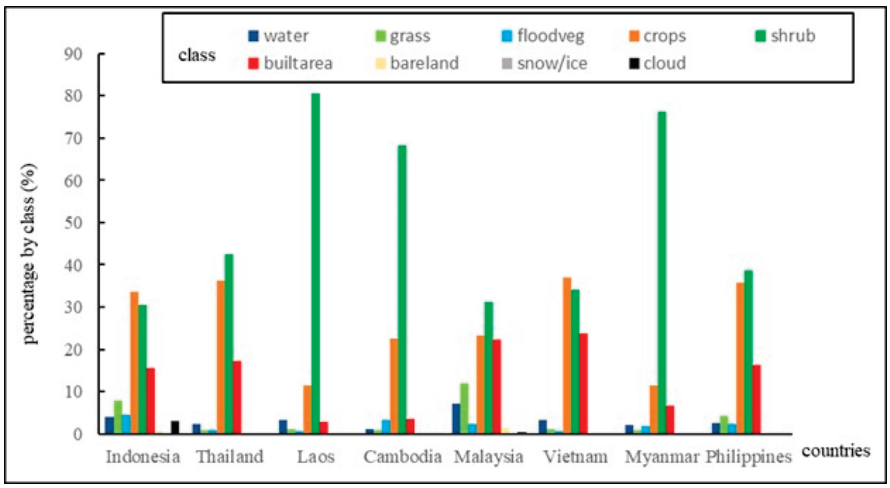

(**c**)

Figure 11. Percentage of forest areas with inconsistency and their confusion with other land cover types in ESRI2020. (**a**) Forest areas with inconsistency and confused land cover classes. (**b**) Forest areas with different consistency levels and confused land cover, (**c**) Forest areas with easily confused land cover in different countries.

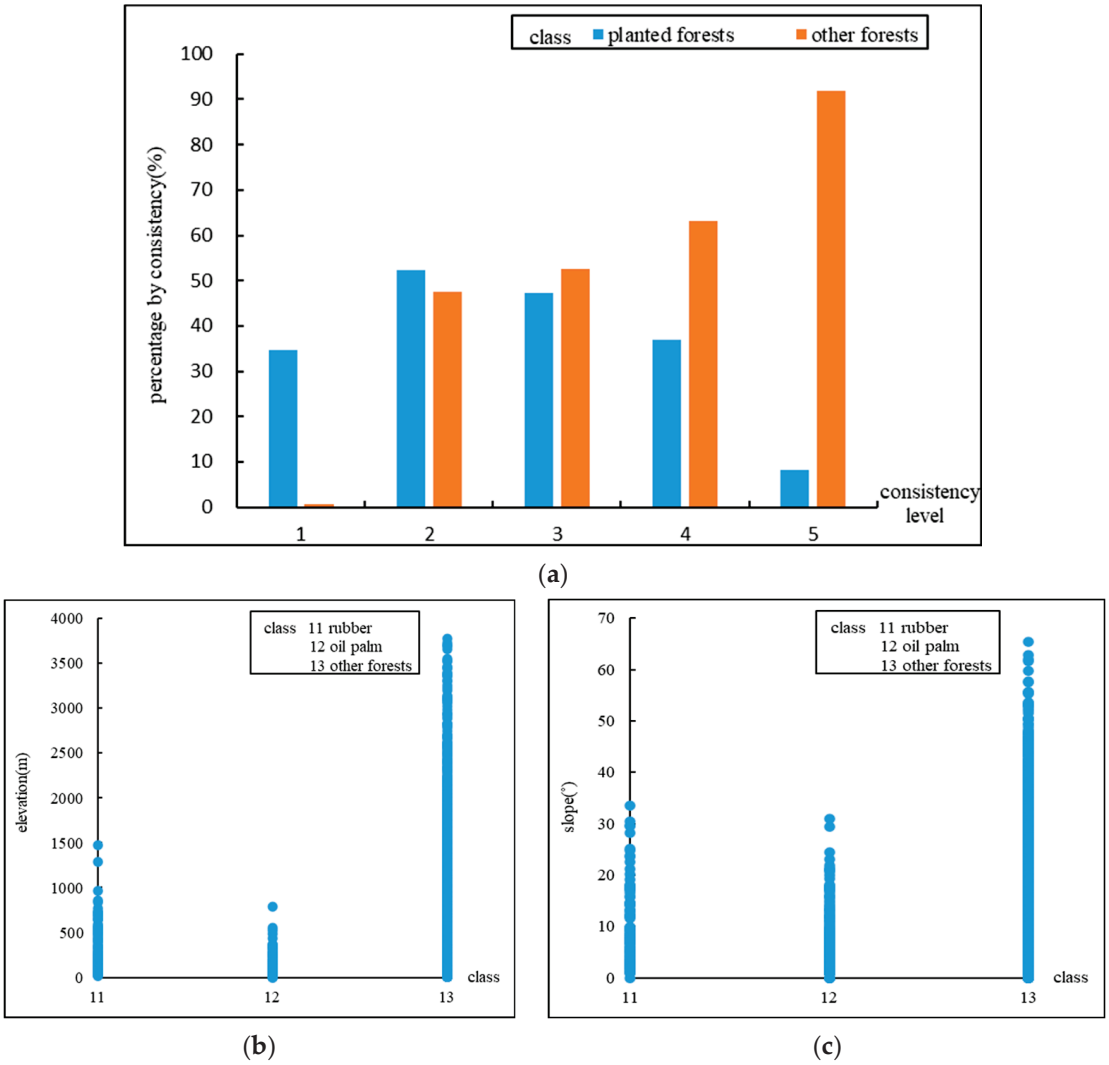

Figure 12. The impact of rubber, oil palm, and other forests on inconsistent areas. (**a**) Percentage of sample distribution of planted forests and other forests in inconsistent areas. (**b**) Elevation distribution of sample points in rubber, oil palm, and other forests. (**c**) Slope distribution of sample points in rubber, oil palm, and other forests.

Additionally, we utilized the sample points to determine the distribution of planted forests in relation to elevation and slope, as depicted in Figure 12b,c. The results reveal that the distribution of planted forests corresponds to the distribution of elevation and slope in the areas of inconsistent forest. In Figure 12b, numbers 11, 12, and 13 represent the distribution of sample points for rubber, oil palm, and other forests across various elevation zones. It is evident that rubber is primarily distributed at elevations below 1000 m, whereas oil palm exhibits a concentration below 600 m, and other forests show a relatively extensive distribution below 3500 m in elevation. Figure 12c illustrates the distribution of rubber, oil palm, and other forests across various slope zones. The findings indicate that rubber is distributed on slopes below 30°, oil palm shows concentration below 25°, and other forests are prevalent across all slope angles.

5. Discussion

5.1. Comparison of Precision with Existing Local Area Studies Results

We assessed the accuracy of six forest mapping products using field verification points and manual densification points. ESRI2020 achieved the highest overall accuracy of 91.64%. However, in the reference [26], it was found that FROM-GLC10 achieved higher accuracy in

the consistency of forest mapping products in Myanmar, with an overall accuracy of 84.48%. It is apparent that our research attained higher accuracy, primarily due to the utilization of field verification products and the improved referencing of field verification points during the manual densification of Google's high-resolution image verification points. To establish the reliability of the findings, we conducted a review of specific verification points. Additionally, we obtained World Imagery high-resolution historical images for 10 June 2020 from World Imagery Wayback (https://www.arcgis.com/home/item.html?id=ca2adf1589524e29a1c754405cde15af, accessed on 31 August 2023) and performed visual comparisons among ESRI2020, ESA2020, and FROM-GLC10, thereby affirming the accuracy of our results. Figure 13 undeniably supports the assertion of ESRI2020's superior accuracy, thereby enhancing the reliability of our findings. Nonetheless, it is important to note that our selection of a limited number of illustrative points may not fully encapsulate the entire scope of the research, thereby acknowledging potential limitations. To further bolster the reliability and accuracy of the results, it is recommended to augment the number of sample points in the areas exhibiting inconsistency, thereby enhancing accuracy.

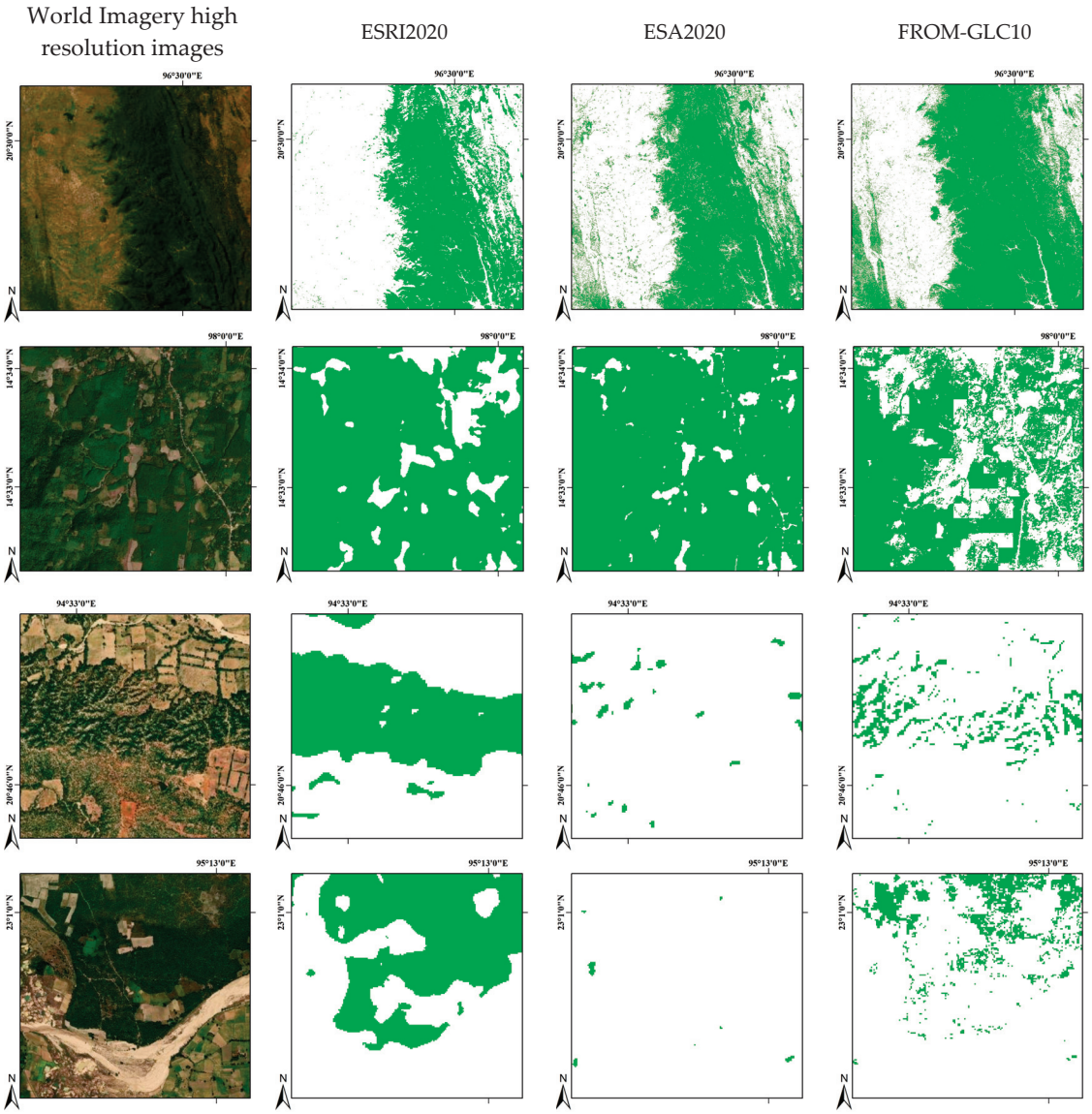

Figure 13. Comparison of forest in partial areas of ESRI2020, ESA2020, and FROM-GLC10. The second to fourth columns display the forest cover areas for three products (ESRI2020, ESA2020, and FROM-GLC10) corresponding to the high-resolution imagery in the first column.

5.2. Analysis of Inconsistent Forest Mapping Products in Southeast Asia

Despite the high forest coverage in Southeast Asia, there are still significant discrepancies in the six products. First, forest inconsistencies may stem from varying forest definitions [34]. During the creation of forest mapping products using remote sensing images, producers establish forest definitions based on a range of factors, including research objectives, study regions, and data sources. In the cases of ESA2020 and Generated_Hansen2020, ESA2020 utilizes Sentinel-1 and Sentinel-2 imagery, whereas Generated_Hansen2020 relies on the Landsat series imagery. Differences in data sources can impact forest definitions, consequently impacting forest areas and causing uncertainty. Furthermore, Generated_Hansen2020 is a synthetic dataset based on Hansen2010 and Hansen GFC, introducing uncertainties itself. Thus, when performing consistency analyses with different forest products, standardizing forest criteria becomes imperative to maintain the fundamental consistency of product comparisons. Various data sources and classification algorithms are equally crucial factors influencing consistency. In this study, ESRI2020 employed Sentinel-2 imagery generated through deep learning, whereas JAXA_FNF2020 utilized PALSAR mosaic imagery generated via random forests. The forest extent varies by approximately 280,000 square kilometers between these two datasets. These factors, including forest definitions, data sources, and classification methods, among others, contribute to spatial inconsistencies.

Forest inconsistencies are primarily concentrated on the border regions between forest and non-forest areas, where small and fragmented patches can emerge due to factors like forest logging and planted afforestation [32,47]. Within this research, the areas of inconsistency predominantly occurred in high mountainous regions above 3000 m, low-lying plains areas below 200 m, and areas with slopes ranging from 15 to 25 degrees. The complex and diverse terrain leads to variations in elevation and slope across forest. In regions of high altitude, differences in people's perception of forest may arise. From an economic standpoint, gentle slopes accommodate the cultivation of various land cover types, resulting in a less organized assortment of planting types and diminished consistency.

Forest is susceptible to confusion with land cover types like crops, shrub, and grass [12,14,16,46]. When extracting forest from remote sensing images, situations inevitably arise where "same spectrum, different objects" and "same object, different spectra" occur. Diverse interpretations of forest will introduce confusion between forest and other land cover types, thereby causing inconsistencies in forest mapping products.

The encroachment of plantations has extended into certain regions of natural forests, causing spatial disparities between plantations and other forest types, thus introducing inconsistencies in forest mapping products. Rubber and oil palm represent the primary plantation types in Southeast Asia. Our results indicate that rubber is distributed below 1000 m in elevation, with a minor extension between 1000 and 1500 m, and on slopes with gradients less than 35°. Oil palm is distributed below 800 m in elevation and on slopes with gradients less than 30°. Recent studies have demonstrated that rubber plantations are gradually expanding into less favorable zones characterized by higher elevations and steeper slopes, which were previously considered less conducive for rubber cultivation [44,48,49]. Additionally, oil palm, which was commonly found at elevations below 500 m and slopes less steep than 25°, is also expanding into higher elevation areas [50], and the area of oil palm cultivation within the range of slopes from 0.5° to 2.5° has significantly increased. This is due to the expansion of rubber and oil palm into areas less favorable for their growth, encroaching upon the growing space of other forests, that spatial inconsistency in forest products has been affected.

5.3. Suggestions for Usage of Forest Mapping Products in Southeast Asia

30]The overall accuracy of the ESA2020, FROM-GLC10, Generated_Hansen2020, GFC30_2020, and JAXA FNF2020 for forest areas in Southeast Asia exceeded 85%. However, ESRI2020 achieved the highest overall accuracy, reaching 91.64%. Nevertheless, variations persist in specific local areas. Therefore, we have the following recommenda-

tions: (1) For forest areas located in hilly or mountainous terrain, or characterized by gentle or steep slopes, we recommend utilizing the ESRI2020 forest dataset. In such areas, the forest exhibits relatively homogeneous internal patterns and can be effectively differentiated from other land cover classes. (2) In cases where the study area borders between forest and non-forest regions or includes a substantial presence of artificial forests, refining the forest type classification from these six datasets is necessary to mitigate errors resulting from inconsistent forest areas. (3) Regarding protected areas (PA), the ESRI2020 dataset attains the highest accuracy, indicating superior precision. This outcome can be attributed to the utilization of deep learning, scalable cloud-based computing, and a large-scale labeled sample dataset [14]. These findings align with those presented in the study [23]. Consequently, we recommend considering the inclusion of sample points during dataset production to enhance classification accuracy. (4) In terms of urban areas (UA), the accuracy of forest classification exceeds 90%. ESA2020, FROM-GLC10, ESRI2020, Generated_Hansen2020, ESA2020, and FROM-GLC10 offer higher levels of detail compared to ESRI2020. Considering points (1) and (2), we recommend users integrate and employ these four forest products, with particular attention given to spatially inconsistent areas.

5.4. Recommendations for Future Large-Scale Forest Mapping

When undertaking research on large-scale forest mapping, it is imperative to take regional characteristics into account and establish a precise forest definition [46]. In countries such as Malaysia, Indonesia, Thailand, and others, where significant areas are dominated by oil palm plantations, the influence of these plantations on forest extraction must be considered.

Through the analysis of six forest mapping products, we determined that the process of large-scale forest mapping is affected by the combined impact of image resolution and classification methods. Presently, forest mapping commonly employs optical imagery data and radar data with resolutions ranging from 10 to 30 m, and classification tasks are frequently carried out through machine learning techniques. Notwithstanding the similarities in data and methods, certain limitations persist. Studies have revealed that forest thematic products with a resolution of 30 m exhibit slightly lower overall accuracy compared to those with a resolution of 10 m. Elevating the spatial resolution of imagery can enhance pixel purity, diminish the percentage of mixed pixels [51], and thereby improve the accuracy to a certain extent. Despite using the same Sentinel-2 data with enhanced resolution, discrepancies in accuracy persist. The ESRI2020 product exhibited the highest overall accuracy, followed by ESA2020 and FROM-GLC10, which possessed slightly lower accuracies. This disparity can be attributed to variances in the classification methods. ESRI2020 employs deep learning techniques and incorporates a substantial number of manually labeled samples during the dataset creation process [14], leading to enhanced accuracy. Therefore, we suggest that producers enhance the spatial image resolution and expand the sample size to generate highly accurate forest cover maps encompassing extensive regions in the future.

In the production of remote sensing mapping products, the synergistic use of multi-source data can enhance the accuracy of remote sensing classification and feature recognition [52,53]. The process of producing forest mapping products benefits from the integration of multi-source data, enabling the capture of additional features and facilitating large-scale forest mapping. For example, the integration of optical and radar data enables the utilization of spectral and textural characteristics, facilitating the extraction of forest structure information and enhancing forest mapping [54,55]. Moreover, the inclusion of time-series data, such as NDVI and EVI, enables the capturing of vegetation phenological traits, thereby further improving forest identification accuracy [56]. In a study [57], researchers introduced the notion of a geoscientific knowledge graph to tackle the challenges associated with comprehensive analysis of remote sensing big data. This concept strives to advance the accuracy of geoscientific knowledge within the remote sensing big data era, enhance

the interpretability and practicality of remote sensing data, and deepen the comprehension of geoscientific principles, and it holds significant potential.

6. Conclusions

We conducted a comparative analysis and comprehensive evaluation of six extensively utilized forest mapping products in Southeast Asia. Field validation points and manual densification points were used to analyze the consistency and assess the accuracy of each product. We compared the variations in area and spatial distribution among these products and analyzed the error factors that affect the spatial consistency of forest, such as terrain and land cover classes that are prone to confusion. The primary conclusions are as follows:

(1) The ESRI2020 forest product achieved the highest overall accuracy in Southeast Asia, followed by ESA2020, FROM-GLC10, Generated_Hansen2020, and finally, JAXA FNF2020 and GFC30_2020.

(2) Among the six forest mapping products, there is a notable spatial consistency for elevations ranging from 200 to 3000 m, with high consistency observed for slopes below 15° or above 25°. Forest is predominantly characterized by natural attributes and demonstrates a relatively even distribution across elevations ranging from 200 to 3000 m. Below 200 m, forest experiences rapid changes and lower consistency due to human activities, such as forest exploitation and logging. Above 3000 m, discrepancies in people's perception of forest may lead to inconsistency. Forest demonstrates high consistency for slopes below 15° or above 25°, but lower consistency within the range of 15–25°.

(3) Among the six products, forest is susceptible to confusion with shrub, cropland, and built areas. This is primarily due to the significant spectral similarity between forest and shrub, resulting in confusion. The land cover types that contribute to forest inconsistency differ among different countries. The research also utilized samples to analyze the percentage of planted forest samples, including rubber and oil palm, among other forest samples within areas of inconsistent forest, highlighting the significant impact of planted forests on the distribution of forest consistency.

Therefore, comparing multiple products can assist users in selecting suitable products for different regions during forest mapping in Southeast Asia, which is of great value. When mapping different regions, it is necessary to consider the characteristics of forest in that particular area. Additionally, the utilization of high spatial resolution imagery, radar imagery, and appropriate classification methods for forest monitoring should be considered.

Author Contributions: Conceptualization, X.Y. and Z.W.; data curation, B.L. and Y.D.; formal analysis, B.L.; funding acquisition, X.Y.; investigation, X.Y., Z.W., B.L., Y.D., J.Z. and D.M.; methodology, X.Y., Z.W. and B.L.; supervision, B.L.; validation, Y.D. and B.L.; visualization, B.L.; writing—original draft, B.L.; writing—review and editing, B.L., X.Y. and Z.W. All authors have read and agreed to the published version of the manuscript.

Funding: This research was funded by the National Key R&D Program of China (Grant No. 2021YFB3900501).

Acknowledgments: We thank the anonymous reviewers for improving the quality of the paper. We would also like to thank the other project team members who provided help: Yueming Liu, Xiaoliang Liu, Ku Gao, Guo Yu, QingyangZhang, Junmei Kang, and Jun Wang.

Conflicts of Interest: The authors declare that they have no conflict of interest. The authors also declare that this paper has not been published previously, that it is not under consideration for publication elsewhere, and that its publication has been approved by all of the authors and has been tacitly or explicitly approved by the responsible authorities in the area where the work was carried out.

References

1. Estoque, R.C.; Dasgupta, R.; Winkler, K.; Avitabile, V.; Johnson, B.A.; Myint, S.W.; Gao, Y.; Ooba, M.; Murayama, Y.; Lasco, R.D. Spatiotemporal pattern of global forest change over the past 60 years and the forest transition theory. *Environ. Res. Lett.* **2022**, *17*, 084022. [CrossRef]
2. Oldekop, J.A.; Rasmussen, L.V.; Agrawal, A.; Bebbington, A.J.; Meyfroidt, P.; Bengston, D.N.; Blackman, A.; Brooks, S.; Davidson-Hunt, I.; Davies, P.; et al. Forest-linked livelihoods in a globalized world. *Nat. Plants* **2020**, *6*, 1400–1407. [CrossRef] [PubMed]
3. Sudmeier-Rieux, K.; Arce-Mojica, T.; Boehmer, H.J.; Doswald, N.; Emerton, L.; Friess, D.A.; Galvin, S.; Hagenlocher, M.; James, H.; Laban, P.; et al. Scientific evidence for ecosystem-based disaster risk reduction. *Nat. Sustain.* **2021**, *4*, 803–810. [CrossRef]
4. Hansen, A.J.; Noble, B.P.; Veneros, J.; East, A.; Goetz, S.J.; Supples, C.; Watson, J.E.M.; Jantz, P.A.; Pillay, R.; Jetz, W.; et al. Toward monitoring forest ecosystem integrity within the post-2020 Global Biodiversity Framework. *Conserv. Lett.* **2021**, *14*, e12822. [CrossRef]
5. Grassi, G.; House, J.; Dentener, F.; Federici, S.; den Elzen, M.; Penman, J. The key role of forests in meeting climate targets requires science for credible mitigation. *Nat. Clim. Chang.* **2017**, *7*, 220–226. [CrossRef]
6. Estoque, R.C.; Ooba, M.; Avitabile, V.; Hijioka, Y.; DasGupta, R.; Togawa, T.; Murayama, Y. The future of Southeast Asia's forests. *Nat. Commun.* **2019**, *10*, 1829. [CrossRef] [PubMed]
7. Sodhi, N.S.; Posa, M.R.C.; Lee, T.M.; Bickford, D.; Koh, L.P.; Brook, B.W. The state and conservation of Southeast Asian biodiversity. *Biodivers. Conserv.* **2010**, *19*, 317–328. [CrossRef]
8. Stibig, H.J.; Achard, F.; Carboni, S.; Raši, R.; Miettinen, J. Change in tropical forest cover of Southeast Asia from 1990 to 2010. *Biogeosciences* **2014**, *11*, 247–258. [CrossRef]
9. FAO. *Global Forest Resources Assessment 2020*; Main Report; Food and Agriculture Organization of the United Nations: Rome, Italy, 2020.
10. FAO. *Southeast Asian Forests and Forestry to 2020: Subregional Report of the Second Asia-Pacific Forestry Sector Outlook Study*; Asia-Pacific Forestry Commission; Food and Agriculture Organization of the United Nations: Bangkok, Thailand, 2011.
11. Keenan, R.J.; Reams, G.A.; Achard, F.; de Freitas, J.V.; Grainger, A.; Lindquist, E. Dynamics of global forest area: Results from the FAO Global Forest Resources Assessment 2015. *For. Ecol. Manag.* **2015**, *352*, 9–20. [CrossRef]
12. Gong, P.; Liu, H.; Zhang, M.; Li, C.; Wang, J.; Huang, H.; Clinton, N.; Ji, L.; Li, W.; Bai, Y.; et al. Stable classification with limited sample: Transferring a 30-m resolution sample set collected in 2015 to mapping 10-m resolution global land cover in 2017. *Sci. Bull.* **2019**, *64*, 370–373. [CrossRef] [PubMed]
13. Zanaga, D.; Van De Kerchove, R.; De Keersmaecker, W.; Souverijns, N.; Brockmann, C.; Quast, R.; Wevers, J.; Grosu, A.; Paccini, A.; Vergnaud, S.; et al. ESA2020 WorldCover 10 m 2020 v100. 2021. Available online: https://zenodo.org/record/5571936 (accessed on 14 September 2023).
14. Karra, K.; Kontgis, C.; Statman-Weil, Z.; Mazzariello, J.C.; Mathis, M.; Brumby, S.P. Global land use/land cover with Sentinel 2 and deep learning. In Proceedings of the 2021 IEEE International Geoscience and Remote Sensing Symposium IGARSS, Brussels, Belgium, 11–16 July 2021; pp. 4704–4707.
15. Zhang, X.; He, G.; Long, T. *Global 30-m Spatial Distribution of Forest Cover in 2020 (GFC30_2020)*; International Research Center of Big Data for Sustainable Development Goals (CBAS): Beijing, China, 2022.
16. Hansen, M.C.; Potapov, P.; Moore, R.; Hancher, M.; Turubanova, S.; Tyukavina, A.; Thau, D.; Stehman, S.; Goetz, S.; Loveland, T.; et al. High-Resolution Global Maps of 21st-Century Forest Cover Change. *Science* **2013**, *342*, 850–853. [CrossRef] [PubMed]
17. Shimada, M.; Itoh, T.; Motooka, T.; Watanabe, M.; Shiraishi, T.; Thapa, R.; Lucas, R. New global forest/non-forest maps from ALOS PALSAR data (2007–2010). *Remote Sens. Environ.* **2014**, *155*, 13–31. [CrossRef]
18. Liang, J.; Gamarra, J.G.P. The importance of sharing global forest data in a world of crises. *Sci. Data* **2020**, *7*, 424. [CrossRef] [PubMed]
19. Nesha, K.; Herold, M.; De Sy, V.; Duchelle, A.E.; Martius, C.; Branthomme, A.; Garzuglia, M.; Jonsson, O.; Pekkarinen, A. An assessment of data sources, data quality and changes in national forest monitoring capacities in the Global Forest Resources Assessment 2005–2020. *Environ. Res. Lett.* **2021**, *16*, 054029. [CrossRef]
20. Estoque, R.C.; Johnson, B.A.; Dasgupta, R.; Gao, Y.; Matsuura, T.; Toma, T.; Hirata, Y.; Lasco, R.D. Rethinking Forest monitoring for more meaningful global forest landscape change assessments. *J. Environ. Manag.* **2022**, *317*, 115478. [CrossRef]
21. Kang, J.; Wang, Z.; Sui, L.; Yang, X.; Ma, Y.; Wang, J. Consistency Analysis of Remote Sensing Land Cover Products in the Tropical Rainforest Climate Region: A Case Study of Indonesia. *Remote Sens.* **2020**, *12*, 1410. [CrossRef]
22. Kang, J.; Sui, L.; Yang, X.; Wang, Z.; Huang, C.; Wang, J. Spatial Pattern Consistency among Different Remote-Sensing Land Cover Datasets: A Case Study in Northern Laos. *ISPRS Int. J. Geo-Inf.* **2019**, *8*, 201. [CrossRef]
23. Ding, Y.; Yang, X.; Wang, Z.; Fu, D.; Li, H.; Meng, D.; Zeng, X.; Zhang, J. A Field-Data-Aided Comparison of Three 10 m Land Cover Products in Southeast Asia. *Remote Sens.* **2022**, *14*, 5053. [CrossRef]
24. Gao, Y.; Liu, L.; Zhang, X.; Chen, X.; Mi, J.; Xie, S. Consistency Analysis and Accuracy Assessment of Three Global 30-m Land-Cover Products over the European Union using the LUCAS Dataset. *Remote Sens.* **2020**, *12*, 3479. [CrossRef]
25. Arjasakusuma, S.; Pribadi, U.; Aria Seta, G. Accuracy and Spatial Pattern Assessment of Forest Cover Change Datasets in Central Kalimantan. *Indones. J. Geogr.* **2018**, *50*, 222. [CrossRef]
26. Xing, H.; Niu, J.; Liu, C.; Chen, B.; Yang, S.; Hou, D.; Zhu, L.; Hao, W.; Li, C. Consistency Analysis and Accuracy Assessment of Eight Global Forest Datasets over Myanmar. *Appl. Sci.* **2021**, *11*, 11348. [CrossRef]

27. Li, Y. *Analysis of Multi-Source Forest Cover Products and Research on Forest Information Extraction*; Wuhan University: Wuhan, China, 2019.
28. Meijaard, E.; Brooks, T.M.; Carlson, K.M.; Slade, E.M.; Garcia-Ulloa, J.; Gaveau, D.L.A.; Lee, J.S.H.; Santika, T.; Juffe-Bignoli, D.; Struebig, M.J.; et al. The environmental impacts of palm oil in context. *Nat. Plants* **2020**, *6*, 1418–1426. [CrossRef] [PubMed]
29. Kenney-Lazar, M.; Ishikawa, N. Mega-Plantations in Southeast Asia: Landscapes of Displacement. *Environ. Soc.* **2019**, *10*, 63–82. [CrossRef]
30. Bos, A.B.; De Sy, V.; Duchelle, A.E.; Herold, M.; Martius, C.; Tsendbazar, N.-E. Global data and tools for local forest cover loss and REDD+ performance assessment: Accuracy, uncertainty, complementarity and impact. *Int. J. Appl. Earth Obs. Geoinf.* **2019**, *80*, 295–311. [CrossRef]
31. Fagan, M.E.; Kim, D.-H.; Settle, W.; Ferry, L.; Drew, J.; Carlson, H.; Slaughter, J.; Schaferbien, J.; Tyukavina, A.; Harris, N.L.; et al. The expansion of tree plantations across tropical biomes. *Nat. Sustain.* **2022**, *5*, 681–688. [CrossRef]
32. Ma, J.; Li, J.; Wu, W.; Liu, J. Global Forest fragmentation change from 2000 to 2020. *Nat. Commun.* **2023**, *14*, 3752. [CrossRef] [PubMed]
33. Li, Y.; Liu, C.; Zhang, J.; Zhang, P.; Xue, Y. Monitoring Spatial and Temporal Patterns of Rubber Plantation Dynamics Using Time-Series Landsat Images and Google Earth Engine. *IEEE J. Sel. Top. Appl. Earth Obs. Remote Sens.* **2021**, *14*, 9450–9461. [CrossRef]
34. Qin, Y.; Dong, J.; Xiao, X. Analysis of Differences and Uncertainties in Forest Cover Products in China. *Biodiversity* **2015**, *23*, 5.
35. Wang, H.; Cai, L.; Wen, X.; Fan, D.; Wang, Y. Land cover change and multiple remotely sensed datasets consistency in China. *Ecosyst. Health Sustain.* **2022**, *8*, 2040385. [CrossRef]
36. Fang, X.; Zhao, W.; Zhang, C.; Zhang, D.; Wei, X.; Qiu, W.; Ye, Y. Methodology for credibility assessment of historical global LUCC datasets. *Sci. China Earth Sci.* **2020**, *63*, 1013–1025. [CrossRef]
37. Huang, C.; Goward, S.N.; Masek, J.G.; Thomas, N.; Zhu, Z.; Vogelmann, J.E. An automated approach for reconstructing recent forest disturbance history using dense Landsat time series stacks. *Remote Sens. Environ.* **2010**, *114*, 183–198. [CrossRef]
38. Olofsson, P.; Foody, G.M.; Herold, M.; Stehman, S.V.; Woodcock, C.E.; Wulder, M.A. Good practices for estimating area and assessing accuracy of land change. *Remote Sens. Environ.* **2014**, *148*, 42–57. [CrossRef]
39. Stehman, S.V.J.R.S.L. Impact of sample size allocation when using stratified random sampling to estimate accuracy and area of land-cover change. *Remote Sens. Lett.* **2012**, *3*, 111–120. [CrossRef]
40. Stehman, S.V. Estimating area from an accuracy assessment error matrix. *Remote Sens. Environ.* **2013**, *132*, 202–211. [CrossRef]
41. Yang, Z.; Dong, J.; Liu, J.; Zhai, J.; Kuang, W.; Zhao, G.; Shen, W.; Zhou, Y.; Qin, Y.; Xiao, X. Accuracy Assessment and Inter-Comparison of Eight Medium Resolution Forest Products on the Loess Plateau, China. *ISPRS Int. J. Geo-Inf.* **2017**, *6*, 152. [CrossRef]
42. Blasco, F.; Whitmore, T.C.; Gers, C. A framework for the worldwide comparison of tropical woody vegetation types. *Biol. Conserv.* **2000**, *95*, 175–189. [CrossRef]
43. Li, W.; Fu, D.; Su, F.; Xiao, Y. Spatial–Temporal Evolution and Analysis of the Driving Force of Oil Palm Patterns in Malaysia from 2000 to 2018. *ISPRS Int. J. Geo-Inf.* **2020**, *9*, 280. [CrossRef]
44. Liu, X.; Feng, Z.; Jiang, L.; Li, P.; Liao, C.; Yang, Y.; You, Z. Rubber plantation and its relationship with topographical factors in the border region of China, Laos and Myanmar. *J. Geogr. Sci.* **2013**, *23*, 1019–1040. [CrossRef]
45. Selvalakshmi, S.; Kalarikkal, R.K.; Yang, X. Predicting the habitat distribution of rubber plantations with topography, soil, land use, and climatic factors. *Environ. Monit. Assess.* **2020**, *192*, 598. [CrossRef] [PubMed]
46. Chazdon, R.L.; Brancalion, P.H.S.; Laestadius, L.; Bennett-Curry, A.; Buckingham, K.; Kumar, C.; Moll-Rocek, J.; Vieira, I.C.G.; Wilson, S.J. When is a forest a forest? Forest concepts and definitions in the era of forest and landscape restoration. *Ambio* **2016**, *45*, 538–550. [CrossRef]
47. Chen, H.; Yi, Z.-F.; Schmidt-Vogt, D.; Ahrends, A.; Beckschäfer, P.; Kleinn, C.; Ranjitkar, S.; Xu, J.; Schmidt-Vogt, Y.; Ahrends, D. Pushing the Limits: The Pattern and Dynamics of Rubber Monoculture Expansion in Xishuangbanna, SW China. *PLoS ONE* **2016**, *11*, e0150062. [CrossRef] [PubMed]
48. Liu, X. *Research on Land Use: Land Cover Change in the Border Area between China, Laos and Myanmar*; University of Chinese Academy of Sciences: Beijing, China, 2013.
49. Liao, C.; Feng, Z.; Li, P. Land use change information mining and country comparison in the border area between China, Laos, Myanmar, and Thailand. *J. Nat. Resour.* **2015**, *30*, 1785–1797.
50. Cheng, Y. *Analysis of Dynamic Changes in Oil Palm Planting in Malaysia*; Henan University: Kaifeng, China, 2017.
51. Cui, L.; Du, H.; Zhou, G.; Li, X.; Mao, F.; Xu, X.; Fan, W.; Li, Y.; Zhu, D.; Liu, T.; et al. Combination of decision tree and mixed pixel decomposition for extracting bamboo forest information in China. *Yaogan Xuebao/J. Remote Sens.* **2019**, *23*, 166–176. [CrossRef]
52. Wang, Z.; Zhang, J.; Yang, X.; Huang, C.; Su, F.; Liu, X.; Liu, Y.; Zhang, Y. Global mapping of the landside clustering of aquaculture ponds from dense time-series 10 m Sentinel-2 images on Google Earth Engine. *Int. J. Appl. Earth Obs. Geoinf.* **2022**, *115*, 103100. [CrossRef]
53. Kang, J.; Yang, X.; Wang, Z.; Huang, C.; Wang, J. Collaborative Extraction of Paddy Planting Areas with Multi-Source Information Based on Google Earth Engine: A Case Study of Cambodia. *Remote Sens.* **2022**, *14*, 1823. [CrossRef]

54. Reiche, J.; Hamunyela, E.; Verbesselt, J.; Hoekman, D.; Herold, M. Improving near-real time deforestation monitoring in tropical dry forests by combining dense Sentinel-1 time series with Landsat and ALOS-2 PALSAR-2. *Remote Sens. Environ.* **2018**, *204*, 147–161. [CrossRef]
55. Reddy, C.S.; Pasha, S.V.; Satish, K.V.; Unnikrishnan, A.; Chavan, S.B.; Jha, C.S.; Diwakar, P.G.; Dadhwal, V.K. Quantifying and predicting multi-decadal forest cover changes in Myanmar: A biodiversity hotspot under threat. *Biodivers. Conserv.* **2019**, *28*, 1129–1149. [CrossRef]
56. Lossou, E.; Owusu-Prempeh, N.; Agyemang, G. Monitoring Land Cover changes in the tropical high forests using multi-temporal remote sensing and spatial analysis techniques. *Remote Sens. Appl. Soc. Environ.* **2019**, *16*, 100264. [CrossRef]
57. Wang, Z.; Yang, X.; Zhou, C. The concept of geoscience knowledge graph for remote sensing big data. *J. Earth Inf. Sci.* **2021**, *23*, 13.

Disclaimer/Publisher's Note: The statements, opinions and data contained in all publications are solely those of the individual author(s) and contributor(s) and not of MDPI and/or the editor(s). MDPI and/or the editor(s) disclaim responsibility for any injury to people or property resulting from any ideas, methods, instructions or products referred to in the content.

drones

MDPI

Article

An Evaluation of Sun-Glint Correction Methods for UAV-Derived Secchi Depth Estimations in Inland Water Bodies

Edvinas Tiškus *, Martynas Bučas, Diana Vaičiūtė, Jonas Gintauskas and Irma Babrauskienė

Marine Research Institute, Klaipeda University, 92294 Klaipeda, Lithuania; martynas.bucas@ku.lt (M.B.); diana.vaiciute@ku.lt (D.V.); jonas.gintauskas@ku.lt (J.G.); irma.babr@gmail.com (I.B.)
* Correspondence: edvinas.tiskus@ku.lt

Abstract: This study investigates the application of unoccupied aerial vehicles (UAVs) equipped with a Micasense RedEdge-MX multispectral camera for the estimation of Secchi depth (SD) in inland water bodies. The research analyzed and compared five sun-glint correction methodologies—Hedley, Goodman, Lyzenga, Joyce, and threshold-removed glint—to model the SD values derived from UAV multispectral imagery, highlighting the role of reflectance accuracy and algorithmic precision in SD modeling. While Goodman's method showed a higher correlation (0.92) with in situ SD measurements, Hedley's method exhibited the smallest average deviation (0.65 m), suggesting its potential in water resource management, environmental monitoring, and ecological modeling. The study also underscored the quasi-analytical algorithm (QAA) potential in estimating SD due to its flexibility to process data from various sensors without requiring in situ measurements, offering scalability for large-scale water quality surveys. The accuracy of SD measures calculated using QAA was related to variability in water constituents of colored dissolved organic matter and the solar zenith angle. A practical workflow for SD acquisition using UAVs and multispectral data is proposed for monitoring inland water bodies.

Keywords: UAVs; Secchi depth; multispectral imagery; sun glint; quasi-analytical algorithm; remote sensing

1. Introduction

Secchi depth (SD), an essential measure of water transparency in aquatic ecosystems, provides a critical indication of water quality and ecological health [1–3]. In Europe, SD is important for following the water quality rules set by the European Water Framework Directive (WFD), which mandates member states to uphold ecological standards [4]. SD thus helps identify impairments affecting water quality and aids in devising and executing management plans to protect water bodies [5].

The Secchi disk is the main tool used for obtaining SD measurements, particularly in vast and complex aquatic ecosystems [6–8]. However, traditional methods—visual observations using a white Secchi disk—can be labor-intensive, time-consuming, and potentially influenced by observer bias [9,10]. They also typically offer point-level measurements, which may not reflect water transparency over larger areas [11,12].

The limitations of traditional methods have spurred interest in remote sensing techniques for estimating SD in complex aquatic ecosystems. Techniques ranging from satellite data to unoccupied aerial vehicles (UAVs) equipped with light detection and ranging (LiDAR) systems and hyperspectral imagery have been explored for accuracy [13]. These techniques promise cost-effective and efficient high-resolution spatial data on water transparency over large areas, with multispectral imagery from UAVs emerging as a promising alternative [14].

UAVs can provide higher-resolution images than satellites, allowing for more precise measurements of water bodies, including small and shallow ponds [15,16], which are

often not well captured by satellite imagery [16,17]. Furthermore, UAVs can be flown at a specific time and location, which is particularly important for SD measurements, as the measurement of water transparency can be influenced by various environmental factors, such as partial cloud cover, water turbidity, and the angle of the sun [18,19]. Although weather conditions influence the ability of UAV flight (with Inspire 2 UAV if winds exceed around 10 m/s), UAVs can collect data during fully cloudy conditions, where optical satellite data are heavily affected by clouds. Additionally, they can be equipped with diverse sensors for capturing multispectral or hyperspectral images, thus providing valuable data on water quality and ecology [14,20]. Furthermore, UAVs can serve as ground truth to validate satellite data [21,22], thereby enhancing accuracy for the monitored area, e.g., one tile coverage of Sentinel-2 can reach from 100,000 ha, while UAVs cannot cover relatively large areas. Moreover, UAV technology presents a strategic advantage in regions where conventional methodologies struggle due to logistical complications.

SD is primarily influenced by three optical components: Chl-a, colored dissolved organic matter (CDOM), and total suspended matter (TSM) [23,24]. Different wavelengths of light penetrate water bodies to different extents. For instance, blue light can penetrate deeper into clear waters than green or red light. Conversely, in more turbid waters, red and near-infrared (NIR) light is absorbed more rapidly and scatters quickly, leading to a diminished signal at the surface. Hence, the spectral signatures captured by remote sensors are significantly influenced by the composition and clarity of the water body.

Various algorithms exist to calculate water parameters from multispectral data, including mechanistic models [25], artificial neural networks [26], and regression algorithms [27]. Each offers unique advantages and applicability, depending on the specific characteristics of the data and the aquatic ecosystem under study. For instance, a study by Chusnah and Chu [28] demonstrated the application of machine learning in estimating Chl-a concentrations, which are commonly used as indicators for assessing the trophic level of lakes and the state of water quality. The study utilized machine learning to implement a band ratio algorithm and generate Chl-a maps from Sentinel-2 and Sentinel-3 satellite images. However, mechanistic models, relying on physical laws and principles to simulate light attenuation and scattering processes in water, often provide the most reliable and accurate predictions, particularly when dealing with smaller datasets, which would not be sufficient for machine learning models [29].

Lee et al. [30] provided a foundational understanding of the optical properties influencing SD, which significantly contributed to the development of the quasi-analytical algorithm (QAA) for more accurate and reliable water clarity estimations. The QAA, a commonly used mechanistic model for SD, has been utilized in various water bodies [29,31,32]. It has been applied to MODIS and MERIS satellite data, where it reduced the root-mean-square error (RMSE) of SD estimation from 1.5 m to 1.0 m. Furthermore, the QAA has been used to account for the residual error in reflectance data from MODIS satellite data, demonstrating its potential for remote sensing in monitoring and managing water resources [33]. The algorithm showed excellent results (R^2 = 0.96, MAPD = 0.18) when validated with independent measurements covering oceanic, coastal, and lake waters [34]. However, previous studies have not delved into the potential benefits of utilizing multispectral cameras onboard UAVs in combination with the QAA algorithm. The integration of these cameras with UAVs offers potential improvements in spatial resolution and data availability, bridging the gap between in situ and satellite remote sensing measurements [18].

It is important to accurately account for reflected light from the water surface—more specifically, the sun-glint effect—as it can lead to inaccuracies in further processing of water quality algorithms [18,35,36]. The simplest way of avoiding sun glint is careful UAV flight time and direction planning; however, since the water surface is often uneven, it is hard to reduce sun glint completely [37]. There are several methods of reducing the sun-glint effect in multispectral UAV images during postprocessing, for example, M Muslim et al. [36] tested four methods proposed by Lyzenga et al. [38], Joyce [39], Hedley et al. [40], and Goodman et al. [41] and applied them to either the whole image or just the glinted area.

Other studies used the methods of Hochberg et al. [42], removing glinted pixels as NIR threshold or using HydroLight simulations [18]. The application of these methods should align with the specific requirements of the study. For instance, if the primary objective entails bottom mapping, the method proposed by Lyzenga offers superior results, as demonstrated in M Muslim's et al. [36] study. On the other hand, if the analysis is focused on assessing surface water quality parameters, the Hedley method emerged as the preferred choice by Windle and Silsbe [18]. Thus, the selection of sun-glint correction techniques requires careful consideration of the objectives, ensuring the most effective and accurate outcomes in different scenarios.

By yielding accurate, timely, and spatially inclusive data on water transparency, UAVs equip decision-makers with invaluable resources, necessitating immediate intervention or remediation measures. This is particularly evident when we consider the capabilities of UAVs for mapping vast areas. A single UAV flight, which takes approximately 25 min, can effectively map an area as large as 25 ha.

This research aimed to evaluate the effectiveness of QAA for the determination of SD using multispectral cameras onboard UAVs. It was performed by testing QAA on image datasets preprocessed using five different methods of sun-glint correction. Additionally, the study examined how water constituents and solar zenith angle affected the discrepancy between actual and modeled SD values. We hypothesize that the radiometric accuracy of a calibrated UAS sensor should meet the required accuracy of 5%, expected with ocean color remote sensing, when compared to in situ measures of Hooker et al. [43] and application of sun-glint correction methods will improve usability in SD modeling, by deviation of RMSD of the same 5% from in situ measures, which would still provide practical results for water quality assessment.

2. Materials and Methods

The study was performed in 43 water bodies in Lithuania (Figure 1), represented by high variability and proportion of optically active in-water components—turbidity, Chl-a and CDOM (Supplementary Table S1)—thus bolstering the robustness and generalizability of the findings. The research was conducted from May 2021 to May 2023.

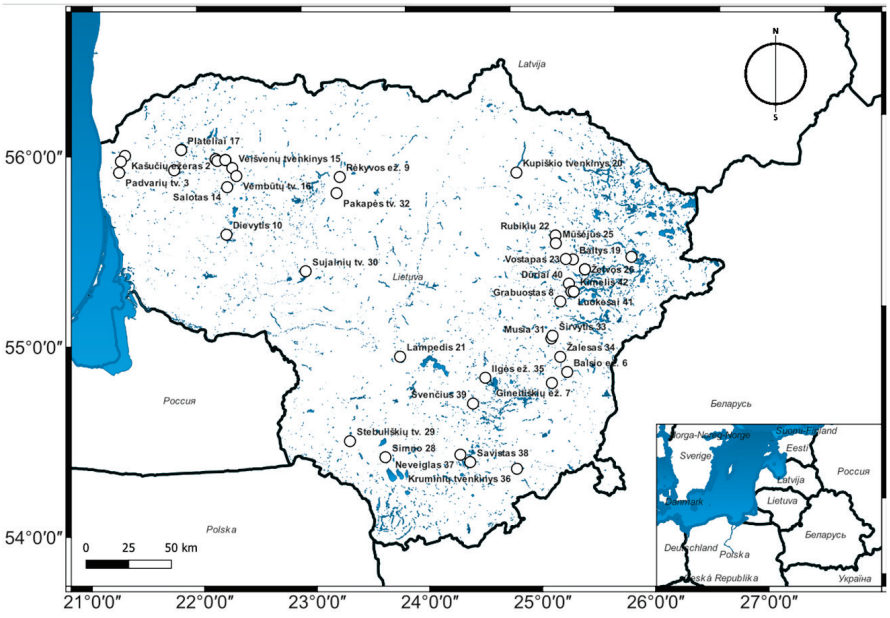

(**a**)

Figure 1. *Cont.*

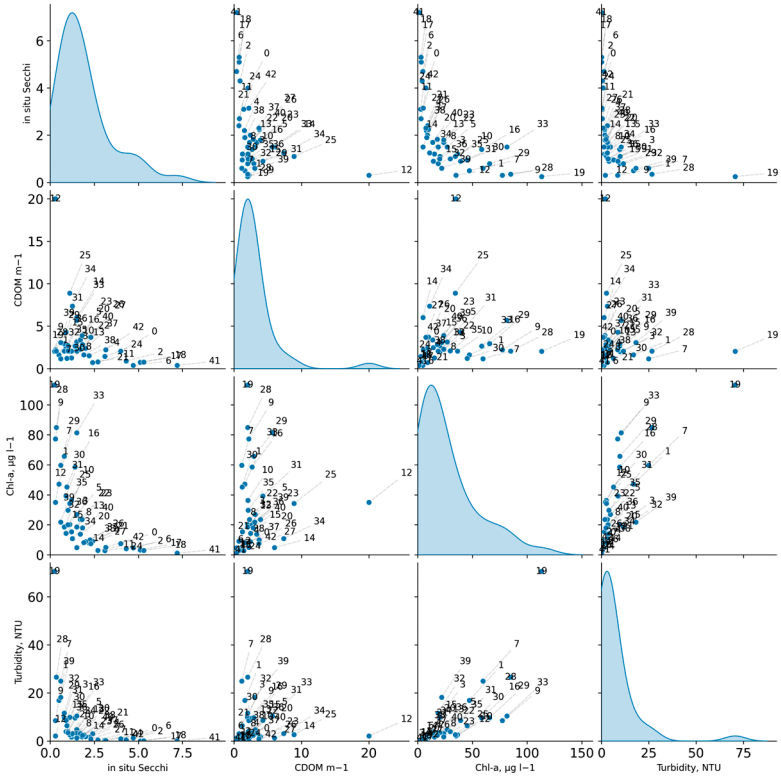

Figure 1. (**a**) Study area with indicated study sites. (**b**) Pair plot between in situ parameters, measured in the areas of interest. The diagonal plots show kernel density estimations for each parameter, offering a smoothed representation of the distribution of data values. ID numbers in pair plots represent the lake number after the name in the map with $n = 43$.

2.1. UAV Data Collection and Calibration

An Inspire 2 UAV equipped with a RedEdge-MX camera was used to facilitate the acquisition of data [44]. The camera features five bands: blue (475 nm ± 16 nm), green (560 nm ± 13 nm), red (668 nm ± 8 nm), red edge (717 nm ± 6 nm), and NIR (842 nm ± 28 nm). To ensure optimal image capture, the UAV was flown at a height of 60 m to optimize the balance between spatial resolution and the area covered in each image, allowing for both relatively high-resolution imagery (from 3 to 4 cm/pixel) and a reasonable area coverage per flight (around 40–50 m^2), with the camera programmed to capture images every three seconds. This frequency was necessitated by the inability to view the live feed and capture images in desired areas from the Micasense RedEdge-MX camera at a distance. The maximum distance between the SD measurement site, where GPS coordinates were recorded, and the image GPS coordinates were approximately 40 m, while the minimum distance was 0 when the measurement was above the boat. For the majority of water bodies, a single measurement site was selected in alignment with the methods of the Environmental Protection Agency of Lithuania. However, for a few larger water bodies, two sampling points were obtained for a more comprehensive understanding. The operation of the UAV was coordinated by two individuals: one controlling the UAV from the shore and the other onboard a boat, both communicating via phone during the Secchi disk measurements. The onboard operator also concurrently measured other water quality parameters outlined in Section 2.2.

For image calibration, the original Micasense RedEdge calibration panel was used. In accordance with Micasense's guidelines, a calibration panel image was captured at the shore before and after each flight, ensuring no shadows were cast on the reference panel or drone [44]. Three images were taken each time for assurance. Furthermore, the

Downwelling Light Sensor (DLS2) provides real-time, continuous measurements of the ambient light conditions during the flight, ensuring that the images captured are properly calibrated regardless of changes in the lighting environment.

2.2. In Situ Data

Concurrently with the UAV image capturing, in situ SD measurements were performed using a 30 cm white Secchi disk, a widely accepted method for assessing water transparency in lakes, rivers, and oceans [45].

The parameters of CDOM—the light-absorbing component of dissolved organic matter, Chl-a (an indicator of phytoplankton biomass), and turbidity (a measure of the cloudiness or haziness of water)—were measured alongside SD to assess their potential influence on water transparency. Parameters were only measured in areas where SD was lower than the depth of the specific point being assessed.

Water samples for Chl-a measurements were filtered through glass fiber GF/F filters with a nominal pore size of 0.7 μm and extracted into 90% acetone. Photosynthetic pigments were measured spectrophotometrically and estimated according to the trichromatic method [46,47]. CDOM was measured spectrophotometrically after filtration through 0.22 μm membrane filters. The CDOM absorption coefficient at 440 nm was derived according to Kirk [48]. A Shimadzu UV-2600 spectrophotometer was used for the analysis of Chl-a and CDOM. Turbidity was measured with a portable turbidity meter (Eutech InstrumentsTN-100, Landsmeer, The Netherlands) in the Nephelometric Turbidity Unit (NTU). The instrument has a light-emitting diode in the near-infrared range (Hach Lange at 860 nm and Eutech Instruments at 850 nm), and the detector measures the scatter at a 90° angle. This method is based on International Organization for Standardization (ISO) 7027.

In situ remote sensing reflectance R_{rs} was acquired to validate wavelengths from UAV observations of water surface reflectance. R_{rs} was measured in the spectral range of 400–800 nm by simultaneous measurements of downwelling irradiance, upwelling radiance, and downwelling radiance, performed with a WISP-3 spectroradiometer [49]. R_{rs} was calculated according to Equation (1):

$$R_{rs} = \frac{L_u - \rho L_d}{E_d}. \quad (1)$$

where L_u is the upwelling radiance, L_d the downwelling radiance, E_d the downwelling irradiance, and ρ a water surface reflectance factor equal to 0.028.

Central wavelengths of the Rededge MX camera were used (475 nm, 560 nm, 668 nm, 717 nm, 842 nm). NIR data were excluded from comparison with in situ reflectance, which was not measured at 842 nm; however, NIR was still used for the sun-glint correction step Section 2.4.

2.3. Preprocessing the UAV Data

The collected UAV images underwent preprocessing of correcting atmospheric effects and standardizing the format suitable for analysis (Figure 2). The conversion of raw images to radiance involves several corrective steps to eliminate biases and errors, accounting for dark-pixel offset, vignette effect, as well as aligning images due to distances between sensors, which could potentially affect the accuracy and reliability of the data. These steps were achieved using the Micasense Python (version 3.7, Python Software Foundation, 2018) workflow, mainly the function raw_image_to_radiance, as described in the Micasense Github repository for users [44].

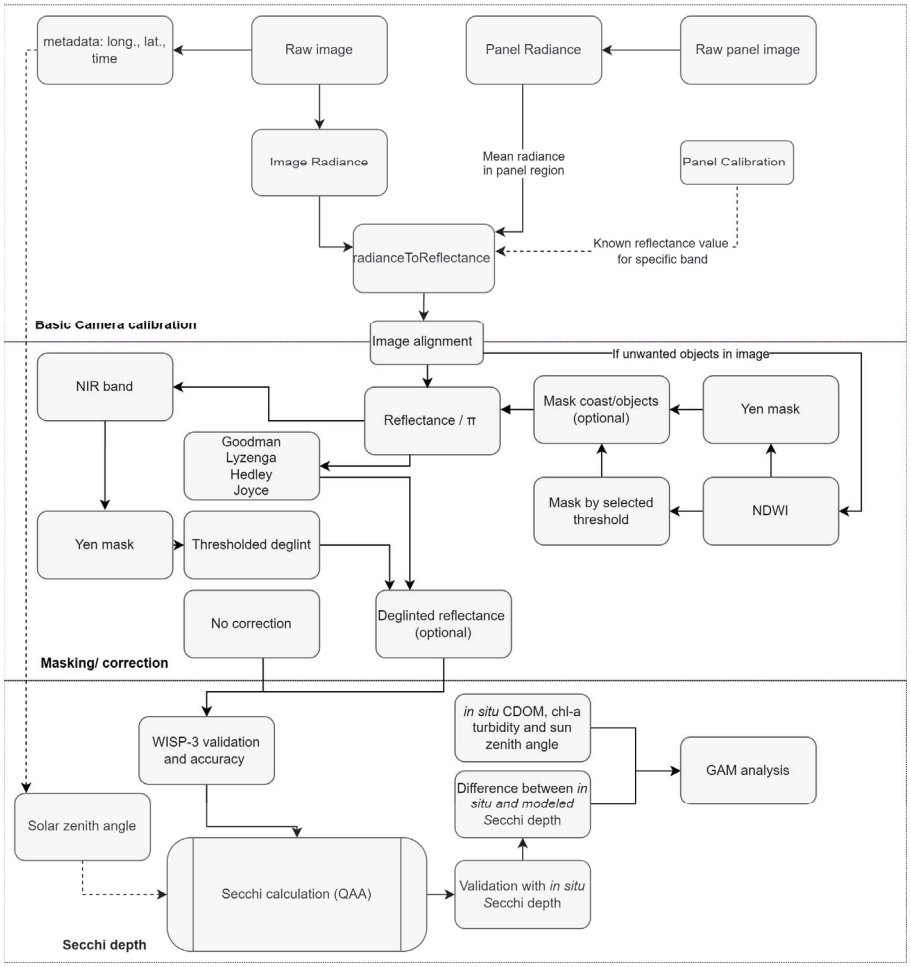

Figure 2. Processing workflow for selected UAV images. Arrows represent image processing and the dashed line arrows represent metadata. NDWI, normalized difference water index.

Since reflectance is relatively independent of illumination conditions [11,50], it is preferred for calculating SD using remote sensing images. The conversion of radiance to reflectance was performed using a reference panel of known reflectance to determine a scale factor between radiance and reflectance. This scale factor was applied to the entire image to obtain a reflectance image. The accuracy of the reflectance image was verified by extracting and checking the same reflectance panel region used to calculate the scale factor for any trends or inconsistencies [44].

Reflectance was further normalized by dividing it by π, assuming water as a Lambertian body, following the mathematical model (2).

$$\text{Reflected radiance} = \rho \times (\cos \theta_i)/\pi \quad (2)$$

Here, cos θ_i represents the cosine of the angle between the incident light and the surface normal and ρ–a surface reflectance factor [50]. This normalization ensures that the reflectance values fall within a standardized range (0 to 1), facilitating consistent comparisons and calculations across different surfaces, lighting conditions, and measurement devices [51,52].

2.4. Image Masking and Sun-Glint Correction

From the initial set of water bodies, four were eliminated (Tūbausių Reservoir, Grabuostas Lake, Ilgis Lake, and Mušėjus Lake) from further analysis. One was excluded due to excessive cloud glint, while the other three measurements were performed too close to the shore or contained emerged macrophytes, leaving no sufficient area where the reflectance

would not be affected (Figure 3a). One water body (Kruminių Reservoir) was surveyed at late in the day, when the zenith angle was approximately 80 degrees, resulting in shadows covering half the area; however, the unshaded area was able to be used for the analyses (Figure 3b), removing the shadowed area using binary thresholding. In total, 39 water bodies were left for statistical analysis after discarding unsuitable ones.

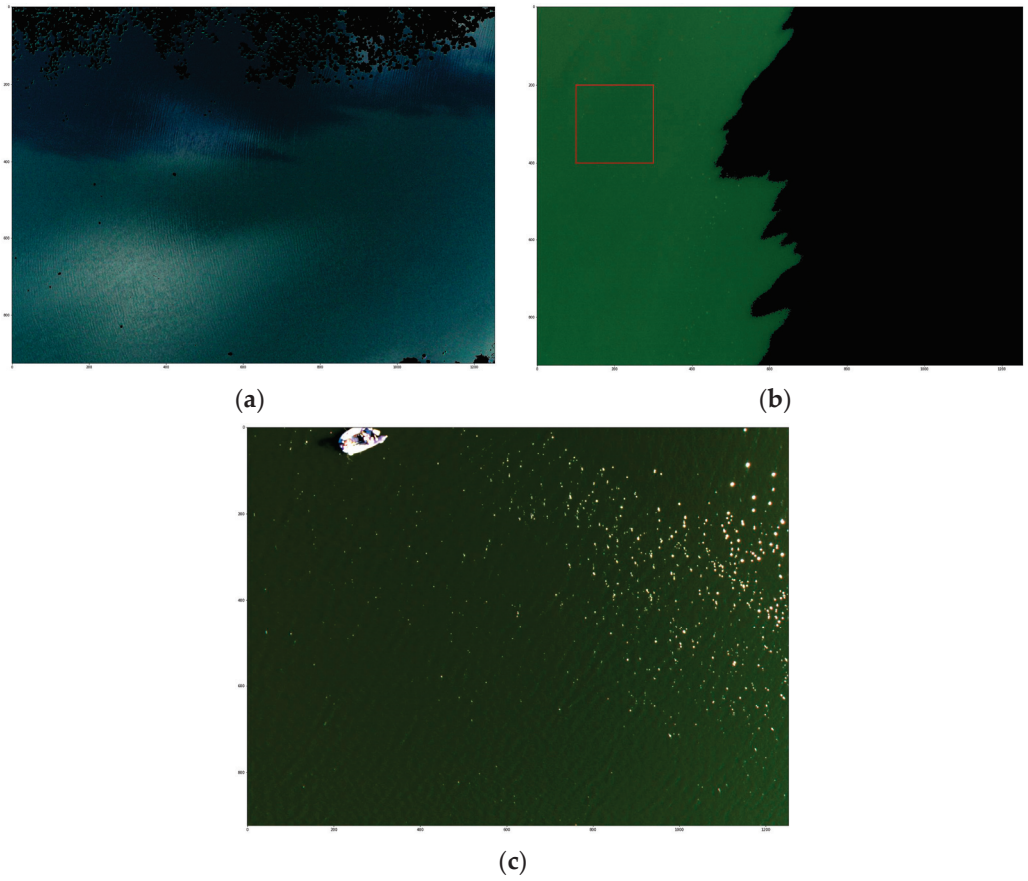

(**a**) (**b**)

(**c**)

Figure 3. (**a**) RGB of an image affected by shadows, bottom reflectance and floating macrophytes after thresholding (Grabuostas Lake), (**b**) RGB of contaminated image (Kruminių Reservoir) with shadow and shore, but where values can still be used by selecting an area (red square) that was good, (**c**) RGB example of a relatively good image (Musia Lake) before removing sun glint and boat.

To ensure accurate SD measurements, objects (boats, coast, macrophytes) and shadows potentially affecting the measurements' accuracy were removed. Firstly, the normalized difference water index (NDWI) was calculated to distinguish between water and non-water pixels (3). This index was then classified into binary parts using Yen thresholding [53,54], where non-water pixels were masked as NaN values. Yen method was used also on just the NIR band to classify areas where pixels were affected by sun glint and masked as NaN in one of the sun-glint removal tests. This sun-glint removal method was later called the threshold-removed glint method.

$$NDWI = \frac{RrsGreen - RrsNir}{RrsGreen + RrsNir} \quad (3)$$

In 11 images, water waves caused a substantial amount of sun glint (Figure 4a), despite images being captured early in the morning around 10 a.m. GMT+3, when the sun reflection from calm water should not have reached the lens. Therefore, the sun-glint correction was performed using the algorithms developed by Hedley et al. [40], Goodman et al. [41], Lyzenga et al. [38], and Joyce [39], which assume that the water surface reflectance is a

linear combination of water reflectance and sun-glint reflectance. The models were fitted using a set of training data consisting of image pixels where sun glint was absent, calculated from an area with 10% lowest value NIR pixels [18]. The model was then used to predict water reflectance for sun-glint-affected pixels, reducing reflectance values according to Equations (4)–(7).

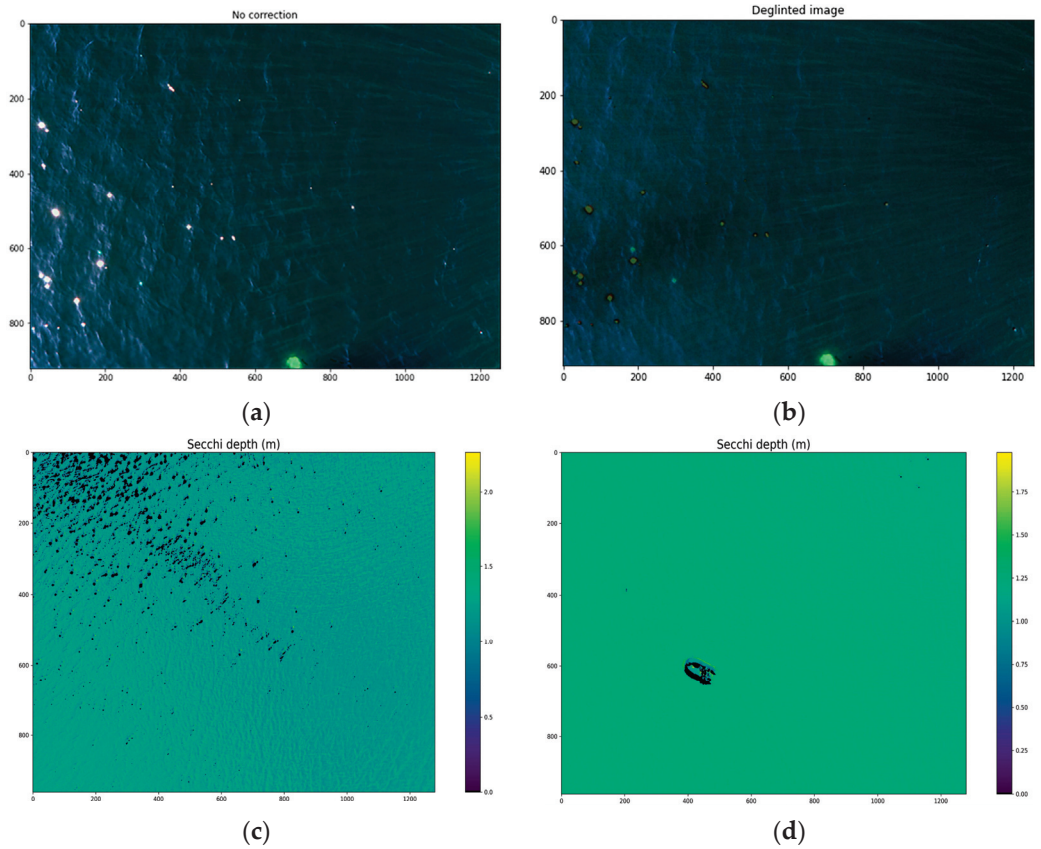

Figure 4. (**a**) RGB image before the sun-glint correction. (**b**) Deglinted RGB image using Hedley's method. (**c**) Threshold-removed sun-glint area from NDWI image, recalculated to SD; black areas represent removed values. (**d**) The boat removed from NDWI using Yen's threshold and recalculated to SD; black areas represent removed values.

The Hedley method (4) calculates the remote sensing reflectance (R_{rs}) for each pixel in each band. The method first finds the minimum NIR value and then calculates the slope for each band using linear regression. The Lyzenga and Joyce methods ((5) and (6)) are similar to the Hedley method, but use the mean and mode, respectively, of the lowest 10% of NIR values instead of the minimum NIR value. The Goodman method (7) calculates the Rrs for each pixel in each band using a constant A (0.000019) and a factor B (0.1) that is multiplied by the difference between the red and NIR bands:

$$\text{Hedley } R_{rs\lambda} = \lambda + bi_{\lambda} \times (NIR - NIR_{min}) \quad (4)$$

$$\text{Lyzenga } R_{rs\lambda} = \lambda + bij_{\lambda} \times (NIR - NIR_{mean}) \quad (5)$$

$$\text{Joyce } R_{rs\lambda} = \lambda + bi_{\lambda} \times (NIR - NIR_{mode}) \quad (6)$$

$$\text{Goodman } R_{rs\lambda} = \lambda - NIR + \delta, \text{ where } \delta = A + B \times (Red\lambda - NIR\lambda) \quad (7)$$

where λ is the band of interest (blue, green, red, red edge, NIR), bi_{λ} is the slope of the band, bij_{λ} is equal to covariance between λ and NIR divided by variance in NIR, and NIR_{min}, NIR_{mode}, and NIR_{mean} are the minimum, mode, and mean NIR values, respectively. For

Goodman's method, δ is a constant offset across all wavelengths where A and B are constants (A = 0.000019 and B = 0.1). Additionally, removing only sun-glint-affected areas (determined by the binary thresholding Yen algorithm) was compared as an alternative approach to sun-glint correction methods (Figure 4c).

The images of four water bodies (Vembutų, Stebuliškių, Pakapės, and Krūminių reservoirs) were also affected by either shore or cloud-glint artefacts. However, most of these artefacts were successfully removed using binary thresholding, except for one image (Figure 3b) where the area had to be manually chosen because the thresholding method was unable to accurately separate the unwanted areas.

2.5. Secchi Depth Model

The quasi-analytical algorithm (QAA) proposed by Lee et al. [30] provides a robust framework for monitoring SD (8), particularly in scenarios where in situ measurements may be unavailable. Compared to the empirical approach, this semianalytical method offers a significant advantage: it does not necessitate the recalibration of the retrieval algorithm with in situ data [31]. This enhances its utility in diverse settings. As such, it was considered more suitable for monitoring SD in various water bodies.

Lee et al. [30] introduced a mechanistic model that accounts for the effects of light attenuation, scattering, and reflection in the water column, as well as the properties of the Secchi disk itself, in determining the SD. The parameters that determine SD in this algorithm are the total absorption coefficient '*a* and the total backscattering coefficient '*bb*. From these parameters, the diffuse attenuation coefficient K_d was calculated, which is the main variable in the SD formula, besides the R_{rs} band:

$$K_T_K_d = \frac{1.04 * (1 + 5.4u)^{0.5}}{1/\left(1 - \frac{sin(\theta)^2}{RI^2}\right)^{0.5}}. \quad (8)$$

$$SD = \frac{1}{kt_kd \ * \ minKd} \ ln\left(\frac{0.14 - minRrs}{0.013}\right) \quad (9)$$

where minKd is the minimum value of K_d chosen from K_d calculated with blue, green and red bands and minRrs is the above-surface remote sensing reflectance of the band that had the lowest K_d value. $K_t_K_d$ is the upwelling radiance diffuse attenuation coefficient and was used instead of a constant value of 1.5 as suggested by Jiang et al. [31], where θ is the solar zenith angle, *RI* is the refractive index value of water equal to 1.33 and u denotes the ratio of backscattering coefficient to the sum of absorption and backscattering coefficient.

The sun zenith angle was computed from in situ measurements using the time and location of the observation. This information was then used to calculate the solar position using the Python library pytz [55]. This approach provided a reliable means of determining the solar zenith angle, which is an important parameter in applications related to SD acquisition from R_{rs}.

Selecting the appropriate reference wavelength is of major importance for the final SD value [34]. The green band (560 nm) was used as a reference if the red band R_{rs} (668 nm) was <0.0015 sr^{-1}. Otherwise, the red band (668 nm) was used, with accordingly modified calculations of other parameters, as suggested by Lee et al [30].

SD was calculated using the QAA method for images of 6 types: corrected after Hedley, Lyzenga, Joyce and Goodman sun-glint algorithms, threshold-removed images and images with no correction.

2.6. Validation and Interpretation of Results

All of the final modeled SD values and reflectance images were averaged to ensure that images could be compared with in situ data. Pearson correlation coefficients were calculated to assess multicollinearity between the reflectance values of different wavelengths. The final reflectances obtained after applying various correction methods and no correction

(Sections 2.3 and 2.4) were validated with in situ reflectances (WISP-3). The accuracy of these methods was evaluated by bias (9), while the root-mean-square deviation (RMSD) was used as an indicator of the QAA model's precision (10), and the Pearson's correlation coefficient (r) described the relationship strength between the model's output and the real data values.

$$\text{Bias} = \frac{1}{N}\sum_{i=1}^{N}(X_{estimated,i} - X_{measured,i}) \quad (10)$$

$$\text{RMSD} = \sqrt{\frac{\sum_{i=1}^{N}(X_{estimated,i} - X_{measured,i})^2}{N}} \quad (11)$$

The same accuracy and precision measures were applied to modeled SD values. Generalized additive models (GAMs) were employed [56] to investigate the relationships between the difference in modeled and in situ SD (the response variable) and a set of independent variables: CDOM, Chl-a, turbidity, and solar zenith. The GAMs were chosen due to their flexibility in modeling nonlinear relationships and their ability to handle interactions between predictors. The GAMs were utilized using R programing language with the mgcv [57] library for statistical parameters and ggplot2 [58] library for visualization. Before analysis, the cross-correlation (based on the Pearson correlation coefficient) between the independent variables was determined. The correlation was relatively high (r = 0.76) between Chl-a and turbidity; therefore, turbidity was not included in the GAMs. Before the interpretation of the GAM results, the residuals were visually inspected with diagnostic plots for normality and equal variance against the fitted values. F and p values were obtained to assess the relative importance and significance of the independent variables ($p < 0.05$ was considered a statistically significant relationship). The fit of the model was evaluated using the explained deviance. A response plot was graphically represented to visualize the relationship between an explanatory variable and the response. As there were multiple predictors, each one was plotted separately with a smooth curve and the confidence interval of the effect.

To visualize the SD results, a subset of images with calculated SD values were exported as TIFF and mosaiced according to image metadata GPS coordinates in QGIS version 3.16 [59]. The result was then visualized on top of the RGB mosaic that was mosaiced using OpenDroneMap [60] photogrammetry software.

3. Results

3.1. Band Validation after Sun-Glint Correction

Across all correction methods and the in situ data, the green band (560 nm) consistently showed the peak mean value, while the blue band (475 nm) indicated the valley or lowest mean value. The general shape of the data appears to peak at the green band, with decreasing values on either side at the blue and red bands (668 nm), and a slight increase at the red edge band (717 nm). This pattern was consistent across all the correction methods and the in situ data, indicating the robustness of this spectral feature in the multispectral UAV image data. In terms of multicollinearity, the green and red exhibited the strongest correlation of 0.97, closely followed by correlations between the green and red edge at 0.96 and the red and red edge at 0.95. The blue band also exhibited strong multicollinearity with the other bands: 0.97 with green, 0.94 with red and 0.91 with red edge.

The highest mean values across all bands were observed with the Lyzenga correction method, while the lowest was observed with the Goodman correction method (Figure 5). The in situ values were generally lower than the corrected values, except for the Goodman correction method.

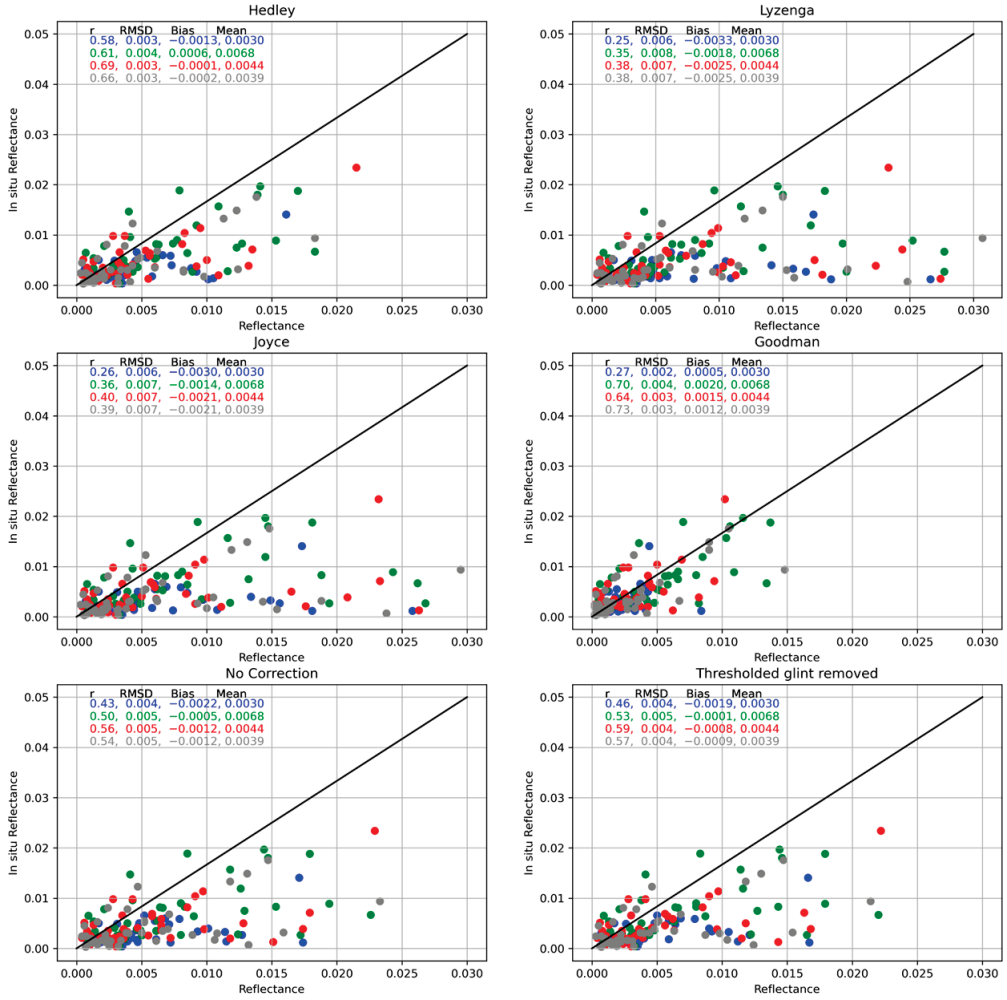

Figure 5. Spectral scatterplots demonstrating the agreement between in situ measured and sun-glint-corrected (or not corrected) reflectances in the UAV images. Statistics (r, RMSD, bias) and points are color-coded accordingly, except for the red edge, which is gray. A diagonal black line marks perfect agreement (1:1).

Removing the two outlier points, one from green and one from the red edge band, decreases r values and the r mean becomes similar to the red bands. However, it also decreases RMSD and bias for these bands, thus not decreasing the accuracy of the data.

The validation results provided robust evidence regarding the performance of the correction methods and the reliability of the final reflectance values. The correlation for all methods (Figure 6) had the same trend, where it was the lowest for the blue band ($r = 0.38 \pm 0.12$) as well as for the red band ($r = 0.56 \pm 0.14$), but higher for the green band ($r = 0.75 \pm 0.11$) and red edge band ($r = 0.80 \pm 0.10$). However, RMSD was relatively low for the blue band ($RMSD = 0.0043 \pm 0.0016$) and red ($RMSD = 0.0048 \pm 0.0018$) bands and slightly higher for the green ($RMSD = 0.0060 \pm 0.0013$) and red edge ($RMSD = 0.0053 \pm 0.0014$) bands. Bias for most methods followed a similar trend of larger underestimation for the blue band and green bands, then slight overestimation for the red band with Goodman, Hedley and threshold-removed glint methods, but still undervaluation for other methods, and slightly lower undervaluation for the red edge band. Goodman's method was exceptional to these trends, as green, red and red edge bands were overestimated.

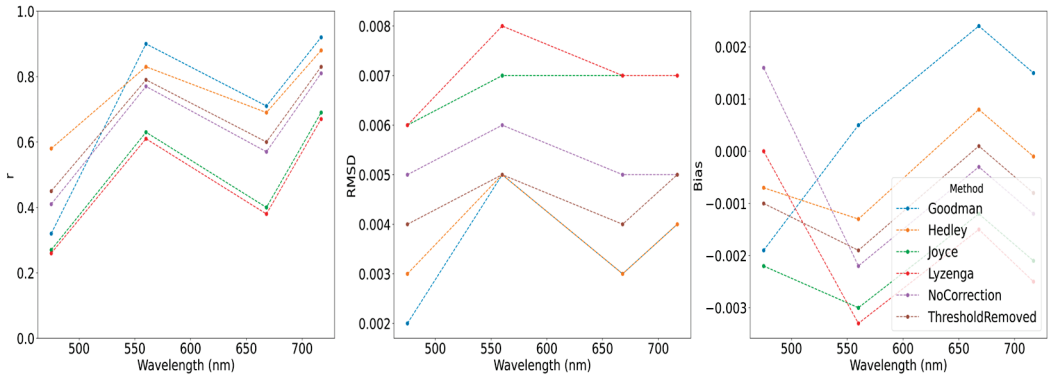

Figure 6. Mean r, RMSD and bias between corrected reflectances with each method and in situ measured reflectances across all available wavelengths. RMSD and bias are presented in reflectance values.

Overall, Goodman's algorithm showed the highest correlation for the green and red edge bands, with r values of 0.90 and 0.92, respectively. However, it had low r values for the blue and red bands, with 0.32 and 0.71, respectively. The RMSD values for Goodman were relatively low across all bands, ranging from 0.002 to 0.005. Similarly, the Hedley algorithm consistently performed well across all bands, with r values ranging from 0.58 to 0.88. The RMSD values were similar to those of Goodman, ranging from 0.003 to 0.005.

The Joyce and Lyzenga algorithms showed matching performances, with lower r values and higher RMSD and bias values compared to Goodman and Hedley. The r values ranged from 0.27 to 0.69 for Joyce and from 0.26 to 0.67 for Lyzenga. The RMSD values ranged from 0.006 to 0.007 for both algorithms.

The control group with no correction applied showed moderate r values, ranging from 0.41 to 0.81. The RMSD values were similar to those of Goodman and Hedley, ranging from 0.005 to 0.006.

3.2. Validation of QAA SD Model

The performance of the QAA model's (Figure 7) ability to predict SD when compared with in situ measurements showed a relatively high correlation across all methods, with r ranging from 0.74 (threshold-removed glint) to 0.92 (Hedley glint correction). RMSD (from 0.65 to 1.05 m) and bias (from −0.78 to 0.58 m) showed acceptable results for all methods as well.

Comparing methods between themselves, the accuracy of all parameters had similar trends as accuracy for band comparison with in situ measurements (Section 2.1), where the SD values were overestimated for the smaller SD values and underestimated for the larger ones, except for Goodman's method, where most of the SD values were overestimated.

Hedley's sun-glint-corrected images achieved the best results according to the RMSD measures (0.65 m), while r was just slightly smaller (0.91) than with Goodman's method (0.92), which achieved the best results based on the r value of 0.92. However, the RMSD value for Goodman's method was relatively high (1.00 m) compared to the values of other methods. This method overestimated most of the values for both small and large SD values.

The Joyce and Lyzenga methods showed similar results between themselves with r values of 0.87 and 0.85, respectively. The RMSD values for Joyce and Lyzenga were 0.79 and 0.86 m, respectively, and biases showed underestimation.

The worst-performing method was when only sun-glint-affected pixels were removed and all other pixels were left unchanged (r = 0.75, RMDS = 1.05 m, bias = 0.13 m). The control group with no correction showed slightly better results: r value of 0.89, RMSD value of 0.74 m and underestimation according to bias.

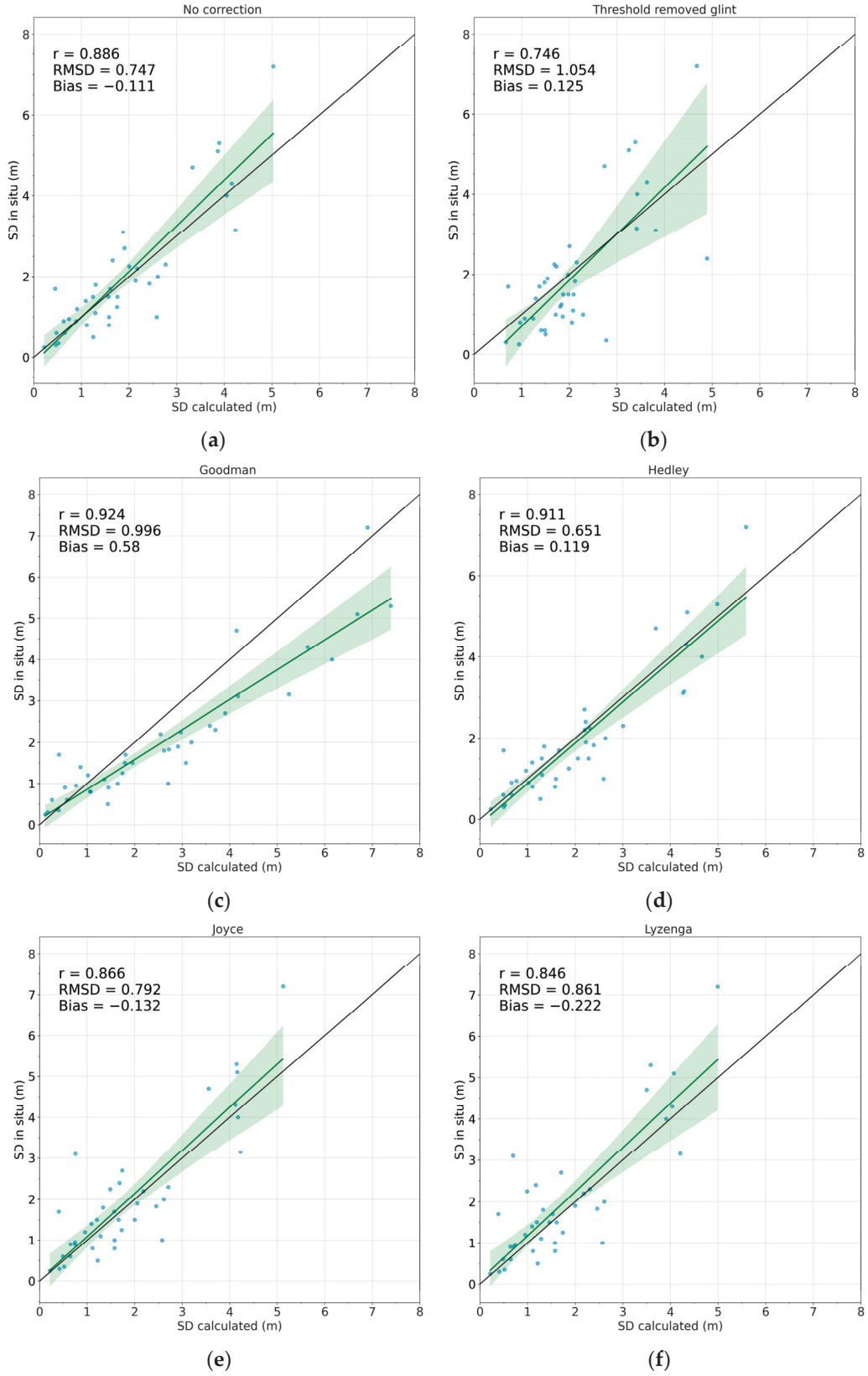

Figure 7. Scatterplots with linear regression line and 95% degrees of freedom (green) of modeled and in situ SD. Best-fit line (1:1) (black) for each image dataset, using different preprocessing methods: (**a**) no correction, (**b**) threshold-removed glint, (**c**) Goodman, (**d**) Hedley, (**e**) Joyce, (**f**) Lyzenga (n = 39).

3.3. Relation with Water Constituents

The average in situ SD of the lakes was 1.91 ± 1.53 m (±standard deviation), ranging from a minimum of 0.25 to a maximum of 7.2 m. The mean CDOM was 2.95 ± 3.2 m^{-1} (min–max: 0.37–20.01 m^{-1}), the mean Chl-a concentration 26.59 ± 26.48 (1.13–113.23) and the mean turbidity 6.76 ± 11.8 NTU (0.00–70.62 NTU).

The environmental factors in GAMs significantly explained (38.3%) the variance in the difference in SD measurements. The interaction term of the sun zenith angle and CDOM was significant (F = 6.808, p-value < 0.05), suggesting that these factors together affect the accuracy of SD retrieval (Figure 8). The most important and statistically significant factor was CDOM (F = 10.47, $p < 0.05$), followed by the solar zenith (F = 4.84, $p = 0.02$). Chl-a values did not have a significant effect on the GAM model (F = 0.295, $p = 0.59$).

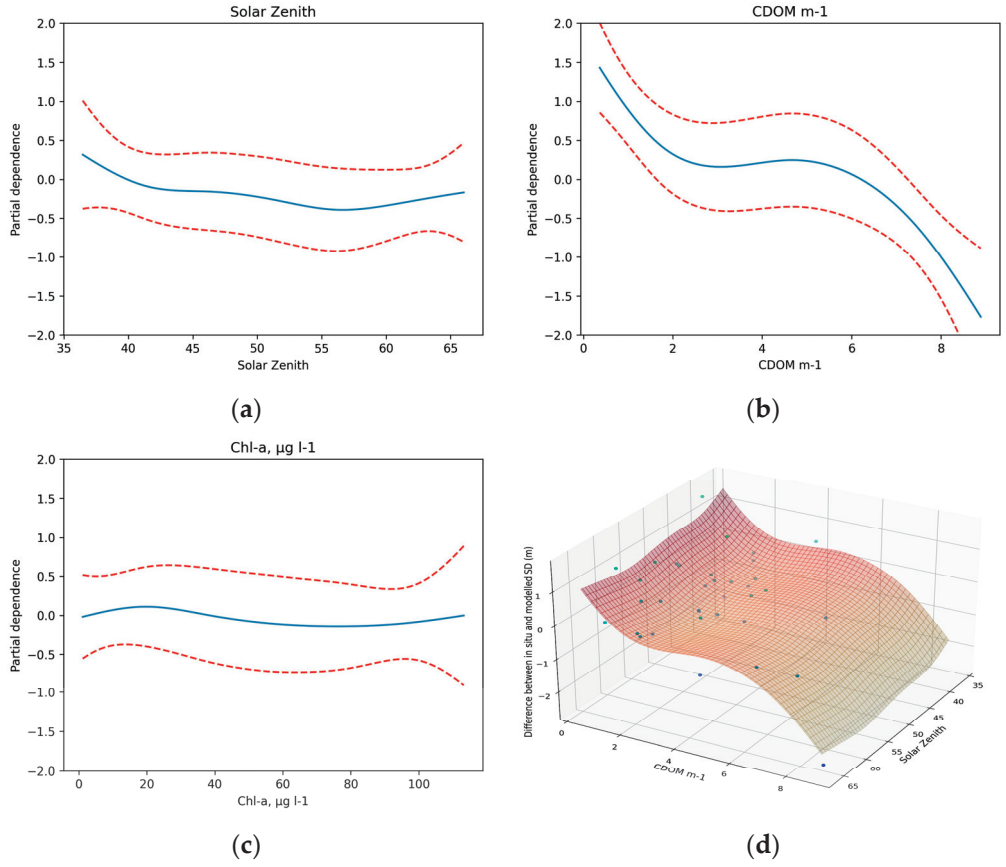

Figure 8. GAMs fitted smooth lines (blue lines) between the difference in SD (modeled vs. in situ) and graphs for each independent environmental factor: (**a**) solar zenith (**b**) CDOM (**c**) Chl-a and (**d**) interaction plot of solar zenith angle. CDOM and predicted difference plane between in situ and modeled SD (m). The red dashed lines show a 95% confidence interval for fitted lines.

In the residual plots of the model a random scatter of points was observed (Figure 9), with no discernible pattern or trend. This scatter indicates that the residuals have a constant variance, which suggests homoscedasticity. The absence of any systematic structure or pattern in the residuals reinforces the notion that nonlinear relationships assumed by our model are an adequate representation of this dataset. Additionally, we did not identify any significant outliers that could unduly influence our model's predictions.

The modeled SD values were overestimated (to over 1.3 m) when CDOM values were <7.5 m^{-1}, while underestimated (over 1 m) when CDOM was >7.5 (although underestimation did not significantly change when CDOM > 12). For the solar zenith, the SD values were overestimated (over 0.7 m) at the lower solar zenith angles (<45 degrees), and then a relatively low effect (within ±0.5 m) was between 45 and 75 degrees of the solar zenith

angle and the underestimation sharply increased to over 1.5 m when the solar zenith angle was >75 degrees.

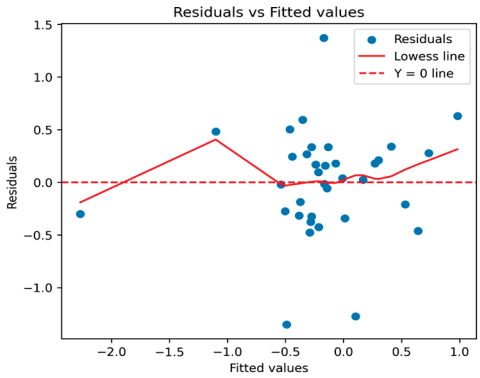

Figure 9. A scatterplot of residuals and fitted values with the red line presenting the best fit and dashed red line representing the Y = 0 line.

4. Discussion

4.1. Advancements in SD Measurements

This research focused on evaluating the effectiveness of the QAA for determining SD using a multispectral camera onboard UAVs. This novel approach expands the current understanding of measuring SD by introducing the potential use of UAVs, balancing the broad coverage provided by remote sensing methods with the high accuracy characteristic of in situ measurements, thereby serving as a more comprehensive alternative to traditional methods.

The experimental results did not uniformly support our hypothesis that the application of sun-glint correction methods would enhance the utility of multispectral images in SD modeling by reducing the RMSD by about 5% and reducing the bias by a similar amount. The precision observed across all bands appears to correspond with the spectral band reflectance intensity, where bands demonstrating relatively lower reflectance intensity (e.g., blue band) typically displayed a lower compliance between the reflectance measured from the UAV and the in situ reflectance measurements and the reverse held true for bands with relatively higher reflectance intensity. Environmental factors such as weak water surface signal and roughness of the water surface can introduce systematic and random errors, respectively, into water surface detection [13]. The correlation with the blue was identified as the least robust (Figure 7), which can be ascribed to increased vulnerability to scattering, a trait inherent to these bands in the water environment [61].

Among the tested glint correction methods, the Hedley and Goodman methods emerged as the most effective across all bands, with Hedley demonstrating the lowest RMSD across all bands. For instance, a study conducted by M Muslim et al. [36] employed a similar methodology to our study, testing multiple sun-glint correction methods. Their findings indicated that the Lyzenga method yielded the most accurate results. However, it is important to note that the primary objective of their research was to map coral reefs, and in most of the study area, the bottom was visible, which may have influenced their results. In contrast, Windle and Silsbe [18] found that the Hedley method provided the highest correlation coefficient (r) and the lowest RMSD, corresponding closely with the results of our study.

The key distinction between the three glint correction methods (excluding the Goodman method) lies in the slope or covariance index of NIR band values. In the case of the Hedley method, the slope was the largest, as it takes the minimum value of the band as the starting point, as opposed to the mode (Joyce method) or the mean (Lyzenga method) [38–40]. This suggests that the images used in our study required a larger numeric correction due to the lowest initial reflectance values.

The results showed that the Goodman's method reflectance intensity values tend to be significantly different from other methods for the blue, red and red edge bands. This method, which was ranked as the second-best-performing in our study, adopted a different approach, using constant values to correct for the sun-glint effect [41]. This approach led to overall better r values between in situ and the green, red, and red edge bands onboard the UAV. However, the performance of the blue band was significantly lower than when using the Hedley method. Despite this, the Goodman method demonstrated the lowest RMSD values and small overestimation bias, underscoring its effectiveness in applications where low reflectance intensity deviation from in situ radiometer is required.

The results also indicated that applying glint correction to the entire image rather than just the binary thresholded area can yield better results in terms of the overall accuracy of the reflectance values. This observation implies that the method of applying glint correction solely to the binary thresholded area might not be the most effective strategy, as it may overlook potential glint effects present beyond this area. Additional sun-glint correction research should be considered in the future for better generalization of reflectance correction [62].

The overall agreement between the in situ SD measurements and the modeled SD values might be connected to their handling of in-water constituents such as colored dissolved organic matter (CDOM) and solar zenith angles, which significantly influenced the accuracy of the models. CDOM was found to predominantly influence the discrepancies between in situ measurements and modeled SD. Given that CDOM primarily absorbs light in the ultraviolet (UV) and blue regions of the spectrum, resulting in a relatively low acquired signal by sensor [63], this agrees with our observation that the blue band demonstrated one of the weakest correlations between in situ and UAV-derived reflectance measurements [64]. It is plausible that Goodman's and Hedley's methods more effectively managed this factor, where Hedley's had the highest r and Goodman's had the lowest RMSD for blue band reflectance, resulting in a closer match with in situ values. Another potential interference is bottom reflection, particularly in clear waters, where the difference between the SD and the actual water depth is minimal. While the SD was consistently less than the water body depth in our study, situations where this difference is minimal could lead to bottom influences on the measurements.

Similarly, high solar zenith angles above 70° impacted the accuracy of modeled SD, leading to underestimations by up to 1.5 m. This is likely due to increased scattering and absorption of light at higher zenith angles, resulting in less light reaching the water's surface and thus larger differences between modeled and in situ SD values [65]. This reinforces the need for sophisticated algorithms that can accurately model these complex environmental factors in SD predictions.

4.2. Practical Applications

Accurate SD determination in large areas is particularly important given the increasing demand for high-resolution data on water transparency for applications including water resource management, environmental monitoring, and ecological modeling [66]. Measures of SD can reduce the need for boat measurements in lakes, also allowing for data collection at a higher frequency, surpassing traditional monthly monitoring intervals that may be inadequate for dynamic water bodies with recurring algal blooms, which in some cases can be inaccessible due to terrain or vegetation around the lake [67]. UAVs could also be used in shallow coastal waters (<1.5 m), where a research vessel usually cannot access them, e.g., in the Curonian Lagoon [68].

The optimal fit model using Hedley sun-glint correction on the whole image was used to construct a mosaic from 45 individual images (Figure 10) of Kašučių Lake on 20 September 2021. All of the pixels were left unmasked to show how shadows affect the final results, and therefore this aspect should be taken into consideration while planning the acquisitions.

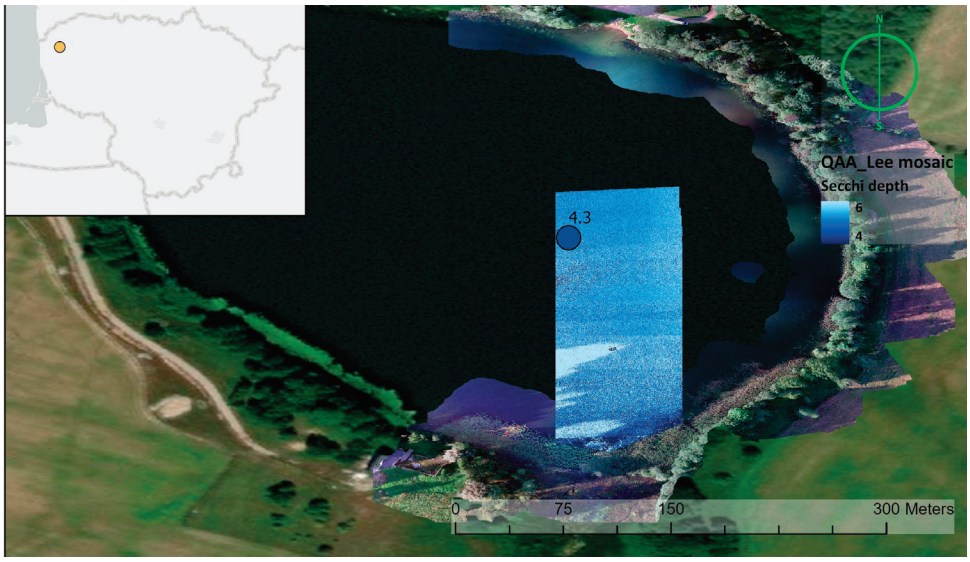

Figure 10. An SD transect of 45 mosaiced images in Kašučių Lake 20 September 2021. The dot with color represents in situ SD of 4.3 m.

This example shows the efficacy of the QAA best-fit model in transforming discrete data into a coherent, large-scale representation of SD. The SD varied from 4 to 6 m, where the highest values were determined in the areas covered by tree shadows. Elsewhere, SD values were more homogeneous (4.0 to 4.8 m), but some noise was still apparent in the orthomosaic (snow-like effect), as SD values are calculated for each pixel. For this reason, the mean value of the whole image was compared to in situ measurements in the area, instead of selecting a small square or point in the images, which would have resulted in lower accuracies.

This method has potential applications in shaping policies and regulations related to water bodies. With the methods provided in this paper, processing workflow for one 5 ha lake should not take longer than 20 min. Moreover, this process can be fully automated, requiring only the supervision of the final results. To put this into context, Lithuania has around 6000 lakes, and about 340 of them are larger than 5 ha [69], which would be suitable for monitoring using a Sentinel-2 satellite, assuming that the shape is not elongated. The rest of the smaller lakes could be monitored by applying methodology from this study and potentially could improve the accuracy and coverage of current national monitoring conducted by the Environmental Protection Agency, which currently covers around 80 lakes every 6 years in Lithuania.

4.3. Future Research and Potential Limitations

The QAA model possesses the flexibility to process remote sensing data sourced from an array of sensors, including but not limited to MODIS, MERIS, OLCI, MSI and GOCI. By integrating a more diverse set of global in situ measurements corresponding to various water types, it is conceivable to further refine the precision and effectiveness of the QAA model.

While the research results demonstrate potential, it is essential to emphasize that the investigation was conducted across a broad range of unique aquatic environments and included measurements captured under variable sun zenith angles. Consequently, for future work, there is potential to modify the existing QAA used for SD estimations to better account for CDOM and sun zenith angle, which in this study have been shown to be critical parameters. This modification could improve our understanding and predictions in the context of diverse and changeable aquatic conditions. Several limitations need to be addressed in future research. One of the main limitations is the assumption of linearity in the Hedley method. This method requires at least one dark pixel unaffected by glint [40] to

be visible in the image, and if the whole image is affected by glint, this deglinting method will provide incorrect data. Understanding these limitations aids in contextualizing the results and fosters the development of more refined glint correction methodologies in the future. This is also relevant for a partial cloud glint when clouds are reflected from the water surface in some, but not all areas of the image, for the analysis of multispectral drone imagery [40,70]. Most methodological studies on water surface mapping using UAVs suggest careful planning of flight time, preferably during conditions of clear skies and low sun glint [37]; however, this restricts one of the main advantages of UAVs—obtaining data on demand—especially if there is a need to visit several inland water bodies on the same day.

Many studies underscore the importance of choosing the appropriate quasi-analytical algorithm (QAA) for different optical water types [13,29,34]. The optical properties of coastal and inland waters, which are primarily influenced by the concentrations of suspended particulate matter, phytoplankton, and dissolved organic material, exhibit spatial and temporal variability, leading to diverse optical water types [71,72]. Applying a universal algorithm in these optically complex waters often results in significant uncertainties [71,72]. This insight highlights the importance of optical water classification to enhance retrieval accuracy, as indicated by numerous studies that developed class-specific algorithms for bio-optical parameters and achieved improvements by applying optical classification in the retrieval of these parameters [72–75]. In our study, relatively high concentrations of CDOM significantly affected the optical properties of the water, thereby introducing uncertainties in the results. One possible approach to improve the accuracy of the QAA is to calibrate the algorithm for the CDOM-dominated water bodies.

In addition to the aforementioned limitations, another significant challenge to consider is the interference of high-vegetation pixels in the analysis of multispectral drone imagery [76]. Vegetation and their shadows, especially when in close proximity to water bodies, can skew the reflectance measurements and thus influence the accuracy of Secchi depth estimates. Consequently, implementing strategies to exclude these pixels during image analysis can enhance the reliability of the measurements.

The applicability of water parameters extends beyond SD, allowing for the calculation of additional parameters. Prior research has demonstrated the feasibility of employing multispectral UAVs for turbidity [77–79], Chl-a [77,79–81], CDOM [79], TSS [80,82], cyanobacteria [80] and macrophytes [16,53,83]. Given the inherent scalability of the UAV-based methodology, it stands as a promising tool for extensive SD assessments and water quality surveys, thereby facilitating large-scale studies focused on water transparency. This advancement brings us a step closer to exploiting the full potential of UAV-based remote sensing for assessing and monitoring aquatic environments.

5. Conclusions

This study revealed that the accuracy of SD measurements is profoundly influenced by sun-glint correction methods employed in UAV flights. There was a consistent agreement across all methods and the in situ radiometric data, particularly for the green band, emphasizing the robustness of multispectral UAV image data. Among the tested methods, Hedley's method demonstrated superior accuracy (RMSD = 0.65 m) and precision, thereby significantly contributing to the accuracy of the UAV-derived SD data.

Moreover, findings underscored the significant role of environmental factors, particularly the CDOM and solar zenith angle, causing inaccuracies in SD measurements: a solar zenith angle > 70° resulted in an underestimation of up to 1.5 m in modeled SD, while CDOM > 12 m^{-1} caused similar underestimations. Our research, therefore, supports the use of UAVs equipped with multispectral cameras as a viable method for SD determination in inland water bodies with SD of up to 7 m and lower than 12 m^{-1} CDOM. The results point towards an approach capable of reaching a correlation as high as 0.91 and reducing the RMSD by up to 12.85% (Hedley's method), thereby enhancing the versatility and reliability of SD measurements.

Supplementary Materials: The following supporting information can be downloaded at https://www.mdpi.com/article/10.3390/drones7090546/s1. Table S1. Summary of investigated lakes and reservoirs in Lithuania. Descriptive statistics of in situ-measured SD, chlorophyll-a, CDOM and turbidity.

Author Contributions: E.T.: conceptualization, methodology, software, validation, formal analysis, investigation, resources, data curation, writing—original draft, writing—review and editing, visualization, supervision; M.B.: conceptualization, methodology, validation, investigation, resources, data curation, writing—review and editing, supervision; D.V.: conceptualization, validation, investigation, resources, data curation, writing—review and editing, supervision; J.G.: conceptualization, validation, investigation, resources, writing—review and editing; I.B.: resources, data curation, funding acquisition. All authors have read and agreed to the published version of the manuscript.

Funding: This research was supported by a doctorate scholarship program in Ecology and Environmental Sciences at Klaipeda University, Lithuania. The field campaigns were cofunded by the Environmental Protection Agency contract "Assessment of the water condition and its more efficient management of the remote monitoring data collection, processing, use and storage system, to ensure accurate results (NUOTOLIS)" (grant 28T-2021-64/SUT-21P-20).

Data Availability Statement: The data presented in this study are available on request from the corresponding author.

Conflicts of Interest: The authors declare no conflict of interest.

References

1. Cloern, J.E.; Abreu, P.C.; Carstensen, J.; Chauvaud, L.; Elmgren, R.; Grall, J.; Greening, H.; Johansson, J.O.R.; Kahru, M.; Sherwood, E.T.; et al. Human Activities and Climate Variability Drive Fast-Paced Change across the World's Estuarine–Coastal Ecosystems. *Glob. Chang. Biol.* **2016**, *22*, 513–529. [CrossRef] [PubMed]
2. MacKay, M.D.; Neale, P.J.; Arp, C.D.; De Senerpont Domis, L.N.; Fang, X.; Gal, G.; Jöhnk, K.D.; Kirillin, G.; Lenters, J.D.; Litchman, E.; et al. Modeling Lakes and Reservoirs in the Climate System. *Limnol. Oceanogr.* **2009**, *54*, 2315–2329. [CrossRef]
3. Paerl, H.W. Nuisance Phytoplankton Blooms in Coastal, Estuarine, and Inland Waters1. *Limnol. Oceanogr.* **1988**, *33*, 823–843. [CrossRef]
4. European Parliament, Council of the European Union. *Directive 2000/60/EC of the European Parliament and of the Council of 23 October 2000 Establishing a Framework for Community Action in the Field of Water Policy*; European Environment Agency: Luxembourg, 2000.
5. Aas, E.; Høkedal, J.; Sørensen, K. Secchi Depth in the Oslofjord–Skagerrak Area: Theory, Experiments and Relationships to Other Quantities. *Ocean Sci.* **2014**, *10*, 177–199. [CrossRef]
6. Ibelings, B.W.; Portielje, R.; Lammens, E.H.R.R.; Noordhuis, R.; Van Den Berg, M.S.; Joosse, W.; Meijer, M.L. Resilience of Alternative Stable States during the Recovery of Shallow Lakes from Eutrophication: Lake Veluwe as a Case Study. *Ecosystems* **2007**, *10*, 4–16. [CrossRef]
7. Schultze-Lam, S.; Schultze-Lam, S.; Beveridge, T.J.; Des Marais, D.J. Whiting Events: Biogenic Origin Due to the Photosynthetic Activity of Cyanobacterial Picoplankton. *Limnol. Oceanogr.* **1997**, *42*, 133–141. [CrossRef]
8. Spyrakos, E.; O'Donnell, R.; Hunter, P.D.; Miller, C.; Scott, M.; Simis, S.G.H.; Neil, C.; Barbosa, C.C.F.; Binding, C.E.; Bradt, S.; et al. Optical Types of Inland and Coastal Waters. *Limnol. Oceanogr.* **2018**, *63*, 846–870. [CrossRef]
9. Jiang, H. Research on Transparency Derived from Remote Sensing and Its Spatial-Temporal Changes in Poyang Lake. *China Rural. Water Hydropower* **2012**, *1*, 30–33.
10. Yu, D.F.; Xing, Q.G.; Lou, M.J.; Shi, P. Retrieval of Secchi Disk Depth in the Yellow Sea and East China Sea Using 8-Day MODIS Data. *IOP Conf. Ser. Earth Environ. Sci.* **2014**, *17*, 012112. [CrossRef]
11. Pham, T.N.; Ho, A.P.H.; Nguyen, T.V.; Nguyen, H.M.; Truong, N.H.; Huynh, N.D.; Nguyen, T.H.; Dung, L.T. Development of a Solar-Powered IoT-Based Instrument for Automatic Measurement of Water Clarity. *Sensors* **2020**, *20*, 2051. [CrossRef]
12. Stock, A. Satellite Mapping of Baltic Sea Secchi Depth with Multiple Regression Models. *Int. J. Appl. Earth Obs. Geoinf.* **2015**, *40*, 55–64. [CrossRef]
13. Wang, D.; Xing, S.; He, Y.; Yu, J.; Xu, Q.; Li, P. Evaluation of a New Lightweight UAV-Borne Topo-Bathymetric LiDAR for Shallow Water Bathymetry and Object Detection. *Sensors* **2022**, *22*, 1379. [CrossRef] [PubMed]
14. Manfreda, S.; McCabe, M.F.; Miller, P.E.; Lucas, R.; Pajuelo Madrigal, V.; Mallinis, G.; Ben Dor, E.; Helman, D.; Estes, L.; Ciraolo, G.; et al. On the Use of Unmanned Aerial Systems for Environmental Monitoring. *Remote Sens.* **2018**, *10*, 641. [CrossRef]
15. Flynn, K.; Chapra, S. Remote Sensing of Submerged Aquatic Vegetation in a Shallow Non-Turbid River Using an Unmanned Aerial Vehicle. *Remote Sens.* **2014**, *6*, 12815–12836. [CrossRef]
16. Müllerová, J.; Gago, X.; Bučas, M.; Company, J.; Estrany, J.; Fortesa, J.; Manfreda, S.; Michez, A.; Mokroš, M.; Paulus, G.; et al. Characterizing Vegetation Complexity with Unmanned Aerial Systems (UAS)—A Framework and Synthesis. *Ecol. Indic.* **2021**, *131*, 108156. [CrossRef]

17. Yang, S.; Wang, J.; Wang, P.; Gong, T.; Liu, H. Low Altitude Unmanned Aerial Vehicles (UAVs) and Satellite Remote Sensing Are Used to Calculated River Discharge Attenuation Coefficients of Ungauged Catchments in Arid Desert. *Water* **2019**, *11*, 2633. [CrossRef]
18. Windle, A.E.; Silsbe, G.M. Evaluation of Unoccupied Aircraft System (UAS) Remote Sensing Reflectance Retrievals for Water Quality Monitoring in Coastal Waters. *Front. Environ. Sci.* **2021**, *9*, 674247. [CrossRef]
19. Yunlin, Z. Distribution, Seasonal Variation and Correlation Analysis of the Transparency in Taihu Lake. *Trans. Oceanol. Limnol.* **2003**, *96*, 36–39.
20. Rahman, A.; Maulud, K.N.A.; Mohd, F.; Jaafar, O.; Tahar, K.N. Volumetric Calculation Using Low Cost Unmanned Aerial Vehicle (UAV) Approach. *IOP Conf. Ser. Mater. Sci. Eng.* **2017**, *270*, 012032. [CrossRef]
21. Otsu, K.; Pla, M.; Vayreda, J.; Brotóns, L. Calibrating the Severity of Forest Defoliation by Pine Processionary Moth with Landsat and UAV Imagery. *Sensors* **2018**, *18*, 3278. [CrossRef]
22. Zhang, H.; Sun, Y.; Chang, L.-D.; Qin, Y.; Chen, J.; Qin, Y.; Du, J.; Yi, S.; Wang, Y. Estimation of Grassland Canopy Height and Aboveground Biomass at the Quadrat Scale Using Unmanned Aerial Vehicle. *Remote. Sens.* **2018**, *10*, 851. [CrossRef]
23. Castagna, A.; Amadei Martínez, L.; Bogorad, M.; Daveloose, I.; Dassevile, R.; Dierssen, H.M.; Beck, M.; Mortelmans, J.; Lavigne, H.; Dogliotti, A.; et al. Optical and Biogeochemical Properties of Belgian Inland and Coastal Waters. *Earth Syst. Sci. Data* **2022**, *14*, 2697–2719. [CrossRef]
24. Garaba, S.P.; Friedrichs, A.; Voß, D.; Zielinski, O. Classifying Natural Waters with the Forel-Ule Colour Index System: Results, Applications, Correlations and Crowdsourcing. *Int. J. Environ. Res. Public Health* **2015**, *12*, 16096–16109. [CrossRef] [PubMed]
25. Giardino, C.; Bresciani, M.; Stroppiana, D.; Oggioni, A.; Morabito, G. Optical Remote Sensing of Lakes: An Overview on Lake Maggiore. *J. Limnol.* **2013**, *73*, 201–214. [CrossRef]
26. Anuar, N.N.M.; Fauzi, N.F.; Halim, H.; Khairudin, N.I.; Bakhtiar, N.S.A.; Shafii, N.H.B. Implementation of Long-Short Term Memory Neural Network (LSTM) for Predicting the Water Quality Parameters in Sungai Selangor. *J. Comput. Res. Innov.* **2021**, *6*, 40–49. [CrossRef]
27. Coskun, H.G.; Tanik, A.; Alganci, U.; Cigizoglu, H.K. Determination of Environmental Quality of a Drinking Water Reservoir by Remote Sensing, GIS and Regression Analysis. *Water Air Soil Pollut.* **2008**, *194*, 275–285. [CrossRef]
28. Chusnah, W.N.; Chu, H.-J. Estimating Chlorophyll-a Concentrations in Tropical Reservoirs from Band-Ratio Machine Learning Models. *Remote Sens. Appl. Soc. Environ.* **2022**, *25*, 100678. [CrossRef]
29. Zhang, Y.; Zhang, Y.; Shi, K.; Zhou, Y.; Li, N. Remote Sensing Estimation of Water Clarity for Various Lakes in China. *Water Res.* **2021**, *192*, 116844. [CrossRef]
30. Lee, Z.; Shang, S.; Hu, C.; Du, K.; Weidemann, A.; Hou, W.; Lin, J.; Lin, G. Secchi Disk Depth: A New Theory and Mechanistic Model for Underwater Visibility. *Remote Sens. Environ.* **2015**, *169*, 139–149. [CrossRef]
31. Jiang, D.; Matsushita, B.; Setiawan, F.; Vundo, A. An Improved Algorithm for Estimating the Secchi Disk Depth from Remote Sensing Data Based on the New Underwater Visibility Theory. *ISPRS J. Photogramm. Remote Sens.* **2019**, *152*, 13–23. [CrossRef]
32. Wei, L.; Wang, Z.; Huang, C.; Zhang, Y.; Wang, Z.; Xia, H.; Cao, L. Transparency Estimation of Narrow Rivers by UAV-Borne Hyperspectral Remote Sensing Imagery. *IEEE Access* **2020**, *8*, 168137–168153. [CrossRef]
33. Chen, J.; Han, Q.; Chen, Y.; Li, Y. A Secchi Depth Algorithm Considering the Residual Error in Satellite Remote Sensing Reflectance Data. *Remote Sens.* **2019**, *11*, 1948. [CrossRef]
34. Qing, S.; Cui, T.; Lai, Q.; Bao, Y.; Diao, R.; Yue, Y.; Hao, Y. Improving Remote Sensing Retrieval of Water Clarity in Complex Coastal and Inland Waters with Modified Absorption Estimation and Optical Water Classification Using Sentinel-2 MSI. *Int. J. Appl. Earth Obs. Geoinf.* **2021**, *102*, 102377. [CrossRef]
35. De Keukelaere, L.; Moelans, R.; Knaeps, E.; Sterckx, S.; Reusen, I.; De Munck, D.; Simis, S.G.H.; Constantinescu, A.M.; Scrieciu, A.; Katsouras, G.; et al. Airborne Drones for Water Quality Mapping in Inland, Transitional and Coastal Waters—MapEO Water Data Processing and Validation. *Remote Sens.* **2023**, *15*, 1345. [CrossRef]
36. Muslim, A.M.; Wei Sheng, C.; Che Din, M.S.; Khalil, I.; Hossain, M. Coral Reef Mapping of UAV: A Comparison of Sun Glint Correction Methods. *Remote Sens.* **2019**, *11*, 2422. [CrossRef]
37. Joyce, K.E.; Duce, S.; Leahy, S.M.; Leon, J.; Maier, S.W. Principles and Practice of Acquiring Drone-Based Image Data in Marine Environments. *Mar. Freshw. Res.* **2019**, *70*, 952. [CrossRef]
38. Lyzenga, D.R.; Malinas, N.P.; Tanis, F.J. Multispectral Bathymetry Using a Simple Physically Based Algorithm. *IEEE Trans. Geosci. Remote Sens.* **2006**, *44*, 2251–2259. [CrossRef]
39. Joyce, K.E. A Method for Mapping Live Coral Cover Using Remote Sensing. Ph.D. Thesis, The University of Queensland, Brisbane, QLD, Australia, 2005.
40. Hedley, J.D.; Harborne, A.R.; Mumby, P.J. Technical Note: Simple and Robust Removal of Sun Glint for Mapping Shallow-water Benthos. *Int. J. Remote Sens.* **2005**, *26*, 2107–2112. [CrossRef]
41. Goodman, J.A.; Lee, Z.; Ustin, S.L. Influence of Atmospheric and Sea-Surface Corrections on Retrieval of Bottom Depth and Reflectance Using a Semi-Analytical Model: A Case Study in Kaneohe Bay, Hawaii. *Appl. Opt.* **2008**, *47*, F1. [CrossRef]
42. Hochberg, E.J.; Andréfouët, S.; Tyler, M.R. Sea Surface Correction of High Spatial Resolution Ikonos Images to Improve Bottom Mapping in Near-Shore Environments. *IEEE Trans. Geosci. Remote Sens.* **2003**, *41*, 1724–1729. [CrossRef]
43. Hooker, S.B.; Firestone, E.R.; Mcclain, C.R.; Esaias, W.E.; Barnes, W.; Guenther, B.; Endres, D.; Mitchell, B.G.; Barnes, R. *SeaWiFS Calibration and Validation Plan, Volume 3*; NASA: Washington, DC, USA, 1992.

44. User Guide for MicaSense Sensors. Available online: https://support.micasense.com/hc/en-us/articles/360039671254-User-Guide-for-MicaSense-Sensors (accessed on 13 March 2023).
45. Preisendorfer, R.W. Secchi Disk Science: Visual Optics of Natural Waters1. *Limnol. Oceanogr.* **1986**, *31*, 909–926. [CrossRef]
46. Jeffrey, S.W.; Humphrey, G.F. New Spectrophotometric Equations for Determining Chlorophylls a, b, C1 and C2 in Higher Plants, Algae and Natural Phytoplankton. *Biochem. Physiol. Pflanz.* **1975**, *167*, 191–194. [CrossRef]
47. Parsons, T.R.; Maita, Y.; Lalli, C.M. A Manual of Chemical and Biological Methods for Sea Water Analysis. *Deep Sea Res. Part A Oceanogr. Res. Pap.* **1984**, *31*, 1523. [CrossRef]
48. Kirk, J. Light and Photosynthesis in Aquatic Systems. In *Light and Photosynthesis in Aquatic Ecosystems*, 3rd ed.; Cambridge University Press: Cambridge, UK, 2010; Volume VI, pp. 1–651. [CrossRef]
49. Hommersom, A.; Kratzer, S.; Laanen, M.; Ansko, I.; Ligi, M.; Bresciani, M.; Giardino, C.; Beltran-Abaunza, J.M.; Moore, G.; Wernand, M.R.; et al. Intercomparison in the Field between the New WISP-3 and Other Radiometers (TriOS Ramses, ASD FieldSpec, and TACCS). *JARS* **2012**, *6*, 063615. [CrossRef]
50. Mobley, C. Estimation of the Remote-Sensing Reflectance from Above-Surface Measurements. *Appl. Opt.* **2000**, *38*, 7442–7455. [CrossRef] [PubMed]
51. Qiu, R.; Wang, S.; Shi, J.; Shen, W.; Zhang, W.; Zhang, F.; Li, J. Sentinel-2 MSI Observations of Water Clarity in Inland Waters across Hainan Island and Implications for SDG 6.3.2 Evaluation. *Remote Sens.* **2023**, *15*, 1600. [CrossRef]
52. Wang, D.; Ma, R.; Xue, K.; Loiselle, S.A. The Assessment of Landsat-8 OLI Atmospheric Correction Algorithms for Inland Waters. *Remote Sens.* **2019**, *11*, 169. [CrossRef]
53. Tiškus, E.; Vaičiūtė, D.; Bučas, M.; Gintauskas, J. Evaluation of Common Reed (Phragmites Australis) Bed Changes in the Context of Management Using Earth Observation and Automatic Threshold. *Eur. J. Remote Sens.* **2023**, *56*, 2161070. [CrossRef]
54. Yen, J.-C.; Chang, F.-J.; Chang, S. A New Criterion for Automatic Multilevel Thresholding. *IEEE Trans. Image Process.* **1995**, *4*, 370–378. [CrossRef]
55. Bishop Pytz Python Historical Timezone Library and Database. Available online: https://github.com/stub42/pytz (accessed on 3 April 2023).
56. Wood, S.N. Fast Stable Restricted Maximum Likelihood and Marginal Likelihood Estimation of Semiparametric Generalized Linear Models. *J. R. Stat. Soc. Ser. B Stat. Methodol.* **2011**, *73*, 3–36. [CrossRef]
57. Wood, S.N. *Generalized Additive Models: An Introduction with R*; CRC Press: Boca Raton, FL, USA, 2017. [CrossRef]
58. Wickham, H. *Ggplot2: Elegant Graphics for Data Analysis*; Springer: New York, NY, USA, 2009; ISBN 978-0-387-98140-6.
59. QGIS Version 3.16. Available online: https://qgis.org/en/site/ (accessed on 20 July 2023).
60. Drone Mapping Software. Available online: https://www.opendronemap.org/ (accessed on 20 July 2023).
61. Zaneveld, J.R.V.; Barnard, A.H.; Boss, E. Theoretical Derivation of the Depth Average of Remotely Sensed Optical Parameters. *Opt. Express* **2005**, *13*, 9052. [CrossRef] [PubMed]
62. Overstreet, B.; Legleiter, C. Removing Sun Glint from Optical Remote Sensing Images of Shallow Rivers: Removing Sun Glint from River Imagery. *Earth Surf. Process. Landf.* **2016**, *42*, 318–333. [CrossRef]
63. Warren, M.; Simis, S.; Martinez-Vicente, V.; Poser, K.; Bresciani, M.; Alikas, K.; Spyrakos, E.; Giardino, C.; Ansper, A. Assessment of Atmospheric Correction Algorithms for the Sentinel-2A MultiSpectral Imager over Coastal and Inland Waters. *Remote Sens. Environ.* **2019**, *225*, 267–289. [CrossRef]
64. Mamaghani, B.; Salvaggio, C. Multispectral Sensor Calibration and Characterization for SUAS Remote Sensing. *Sensors* **2019**, *19*, 4453. [CrossRef] [PubMed]
65. Hashimoto, N.; Saito, Y.; Maki, M.; Homma, K. Simulation of Reflectance and Vegetation Indices for Unmanned Aerial Vehicle (UAV) Monitoring of Paddy Fields. *Remote. Sens.* **2019**, *11*, 2119. [CrossRef]
66. Soulignac, F.; Vinçon-Leite, B.; Lemaire, B.J.; Scarati Martins, J.R.; Bonhomme, C.; Dubois, P.; Mezemate, Y.; Tchiguirinskaia, I.; Schertzer, D.; Tassin, B. Performance Assessment of a 3D Hydrodynamic Model Using High Temporal Resolution Measurements in a Shallow Urban Lake. *Environ. Model. Assess.* **2017**, *22*, 309–322. [CrossRef]
67. Alikas, K.; Kratzer, S. Improved Retrieval of Secchi Depth for Optically-Complex Waters Using Remote Sensing Data. *Ecol. Indic.* **2017**, *77*, 218–227. [CrossRef]
68. Tyrimų laivas „Vėjūnas“. Aplinkos Apsaugos Agentūra. Available online: https://www.gamta.lt/apie-agentura/tyrimu-laivas-vejunas/45 (accessed on 20 July 2023).
69. Vaitekūnas, S.; Valančienė, E. *Lietuvos Geografija (Geography of Lithuania)*; Alma Litera: Vilnius, Lithuania, 2004.
70. Partama, I.G.Y.; Kanno, A.; Ueda, M.; Akamatsu, Y.; Inui, R.; Sekine, M.; Yamamoto, K.; Imai, T.; Higuchi, T. Removal of Water-Surface Reflection Effects with a Temporal Minimum Filter for UAV-Based Shallow-Water Photogrammetry. *Earth Surf. Process. Landf.* **2018**, *43*, 2673–2682. [CrossRef]
71. Le, C.; Li, Y.; Zha, Y.; Sun, D.; Huang, C.; Zhang, H. Remote Estimation of Chlorophyll a in Optically Complex Waters Based on Optical Classification. *Remote Sens. Environ.* **2011**, *115*, 725–737. [CrossRef]
72. Cui, T.W.; Zhang, J.; Wang, K.; Wei, J.W.; Mu, B.; Ma, Y.; Zhu, J.H.; Liu, R.J.; Chen, X.Y. Remote Sensing of Chlorophyll a Concentration in Turbid Coastal Waters Based on a Global Optical Water Classification System. *ISPRS J. Photogramm. Remote Sens.* **2020**, *163*, 187–201. [CrossRef]
73. Jackson, T.; Sathyendranath, S.; Mélin, F. An Improved Optical Classification Scheme for the Ocean Colour Essential Climate Variable and Its Applications. *Remote Sens. Environ.* **2017**, *203*, 152–161. [CrossRef]

74. Yu, X.; Lee, Z.; Shen, F.; Wang, M.; Wei, J.; Jiang, L.; Shang, Z. An Empirical Algorithm to Seamlessly Retrieve the Concentration of Suspended Particulate Matter from Water Color across Ocean to Turbid River Mouths. *Remote Sens. Environ.* **2019**, *235*, 111491. [CrossRef]
75. Zhang, F.; Li, J.; Shen, Q.; Zhang, B.; Tian, L.; Ye, H.; Wang, S.; Lu, Z. A Soft-Classification-Based Chlorophyll-a Estimation Method Using MERIS Data in the Highly Turbid and Eutrophic Taihu Lake. *Int. J. Appl. Earth Obs. Geoinf.* **2019**, *74*, 138–149. [CrossRef]
76. Doña, C.; Morant, D.; Picazo, A.; Rochera, C.; Sánchez, J.M.; Camacho, A. Estimation of Water Coverage in Permanent and Temporary Shallow Lakes and Wetlands by Combining Remote Sensing Techniques and Genetic Programming: Application to the Mediterranean Basin of the Iberian Peninsula. *Remote Sens.* **2021**, *13*, 652. [CrossRef]
77. McEliece, R.; Hinz, S.; Guarini, J.-M.; Coston-Guarini, J. Evaluation of Nearshore and Offshore Water Quality Assessment Using UAV Multispectral Imagery. *Remote Sens.* **2020**, *12*, 2258. [CrossRef]
78. Su, T.-C. A Study of a Matching Pixel by Pixel (MPP) Algorithm to Establish an Empirical Model of Water Quality Mapping, as Based on Unmanned Aerial Vehicle (UAV) Images. *Int. J. Appl. Earth Obs. Geoinf.* **2017**, *58*, 213–224. [CrossRef]
79. Zeng, C.; Richardson, M.; King, D.J. The Impacts of Environmental Variables on Water Reflectance Measured Using a Lightweight Unmanned Aerial Vehicle (UAV)-Based Spectrometer System. *ISPRS J. Photogramm. Remote Sens.* **2017**, *130*, 217–230. [CrossRef]
80. Becker, R.H.; Sayers, M.; Dehm, D.; Shuchman, R.; Quintero, K.; Bosse, K.; Sawtell, R. Unmanned Aerial System Based Spectroradiometer for Monitoring Harmful Algal Blooms: A New Paradigm in Water Quality Monitoring. *J. Great Lakes Res.* **2019**, *45*, 444–453. [CrossRef]
81. Choo, Y.; Kang, G.; Kim, D.; Lee, S. A Study on the Evaluation of Water-Bloom Using Image Processing. *Environ. Sci. Pollut. Res.* **2018**, *25*, 36775–36780. [CrossRef]
82. Olivetti, D.; Roig, H.; Martinez, J.-M.; Borges, H.; Ferreira, A.; Casari, R.; Salles, L.; Malta, E. Low-Cost Unmanned Aerial Multispectral Imagery for Siltation Monitoring in Reservoirs. *Remote Sens.* **2020**, *12*, 1855. [CrossRef]
83. Doughty, C.L.; Ambrose, R.; Okin, G.; Cavanaugh, K. Characterizing Spatial Variability in Coastal Wetland Biomass across Multiple Scales Using UAV and Satellite Imagery. *Remote Sens. Ecol. Conserv.* **2021**, *7*, 411–429. [CrossRef]

Disclaimer/Publisher's Note: The statements, opinions and data contained in all publications are solely those of the individual author(s) and contributor(s) and not of MDPI and/or the editor(s). MDPI and/or the editor(s) disclaim responsibility for any injury to people or property resulting from any ideas, methods, instructions or products referred to in the content.

MDPI AG
Grosspeteranlage 5
4052 Basel
Switzerland
Tel.: +41 61 683 77 34

MDPI Books Editorial Office
E-mail: books@mdpi.com
www.mdpi.com/books

Disclaimer/Publisher's Note: The title and front matter of this reprint are at the discretion of the Topic Editors. The publisher is not responsible for their content or any associated concerns. The statements, opinions and data contained in all individual articles are solely those of the individual Editors and contributors and not of MDPI. MDPI disclaims responsibility for any injury to people or property resulting from any ideas, methods, instructions or products referred to in the content.

Academic Open
Access Publishing

mdpi.com

ISBN 978-3-7258-4712-9